

**A Celebration of a Great Partnership:**  
**CODAR and RU COOL**  
**1998-2025**  
**Volume 1**

# The SeaSonde Papers

A Celebration of a Great Partnership: CODAR & RUCOOL 1998-2025

For four decades, the Rutgers University Center for Ocean Observing Leadership (RUCOOL) and CODAR Ocean Sensors have partnered in pioneering efforts of ocean observation, applying CODAR's SeaSonde high-frequency (HF) radar technology to address critical scientific and societal challenges. This book is a curated compilation of the scientific publications authored by our team, all of which share a common foundation: the use of SeaSonde systems to observe the coastal ocean.

Our partnership with CODAR Ocean Sensors began in 1998, driven by the need for continuous, synoptic surface current data along the New Jersey coast. At the time, there were few observational tools that could deliver this kind of coverage in real time. The SeaSonde filled that gap—and quickly became central to our research and education missions. Over the years, we have deployed these systems across from the heavily populated Mid-Atlantic coast to the tropical Caribbean and Gulf of Mexico, to the remote polar Arctic and Antarctic regions.

This body of work would not have been possible without our long-standing collaboration with Dr. Don Barrick, founder of CODAR Ocean Sensors and a pioneer in HF radar technology. Don's willingness to share his ideas and engage with ours, support field deployments, and co-develop new techniques—ranging from bistatic radar configurations to vessel detection algorithms—transformed our science and advanced the state of the art.

Each paper in this compilation represents not only a contribution to oceanography and coastal science, but also a chapter in the evolving story of radar-based ocean observing. From operational ocean forecasting and model validation to environmental response, fisheries management, and maritime security, SeaSonde technology has enabled us to turn observations into action and data into impact.

A cornerstone of this partnership has been our shared commitment to education and workforce development. At Rutgers, SeaSonde technology has not only fueled research but also served as a powerful teaching tool. Through hands-on training in the classroom, field deployments, and thesis work, our students have gained critical experience in ocean observing technologies. Together with CODAR, we have expanded the HF Radar community by hosting workshops, developing open-source tools, and fostering regional and global networks. What began as two radar stations in southern New Jersey has matured into a globally connected observing system—one in which the next generation of scientists and engineers will play a central role.

This book is intended as both a scientific record and a resource for the growing community of HF Radar users. It reflects the dedication of our students, staff, and collaborators, the vision of our funding partners, and the enduring innovation at CODAR. We hope it serves to inform, inspire, and guide those who continue to explore our dynamic coastal ocean.

– The Rutgers University HF Radar Team







*The SeaSonde proved its utility in directing ship and AUV sampling operations, and improving circulation model forecasts, during the summer of 1998 off New Jersey. A high standard of SeaSonde surface-current measurement accuracy was established by ADCP comparisons.*

By Josh Kohut, Student and Scott Glenn, Professor at the Rutgers University and Don Barrick, President of CODAR Ocean Sensors, Ltd.

# SeaSonde Is Integral to Coastal Flow Model Development

The Rutgers University Long-term Eco-system Observatory (LEO-15) is an instrumented natural laboratory located on the inner continental shelf off Tuckerton, New Jersey in approximately 15 m of water. LEO-15 was developed to study coupled physical, optical, biological, chemical and sediment transport processes by maintaining a continuous observational presence in a 30 km x 30 km coastal region. The numerous remote sensing, shipboard, and underwater ob-

serving systems at LEO-15 transmit their measurements in real time to a central shore station in Tuckerton where they are made available via the World Wide Web (<http://marine.rutgers.edu/mrs>) for research, education and recreational purposes.

The first in a four-year series of Coastal Predictive Skill Experiments was conducted last summer at LEO-15. The July 1998 experiment was sponsored by the National Ocean Partnership Program (NOPP), the Of-

fice of Naval Research, and the Mid-Atlantic Bight National Undersea Research Center. The purpose of these experiments is to evaluate a new coastal-ocean forecast model and the influence of sub-surface adaptive sampling in a data- and process-rich environment. The processes studied focus on the development of recurrent coastal upwelling centres along the New Jersey coast and how they influence phytoplankton concentrations and dissolved oxygen levels. Assimilation datasets for the forecast model include spatially-extensive surface current as mapped by the SeaSonde HF radar, temperature distributions from NOAA satellites, and limited subsurface currents and temperature profiles from ships, moorings and Autonomous Underwater Vehicles (AUVs). A major goal is to optimise the usefulness of the expensive subsurface observations by adapting shipboard and AUV sampling strategies to the present oceanographic conditions based on the real-time data and previous model forecasts. The desired end result is a validated coastal forecast model which can be relocated to other regions with knowledge of what surface and subsurface datasets are required to maintain a specific level of forecast accuracy. Using large phased array antennas on San Clemente Island, CA, Barrick and his colleagues established the utility of HF radars for coastal surface-current mapping over 25 years ago<sup>1</sup>. HF radar signals propagate beyond the horizon and backscatter from short waves (e.g., 6 m whose periods are 2 s). The current speed toward or away from a single radar is measured

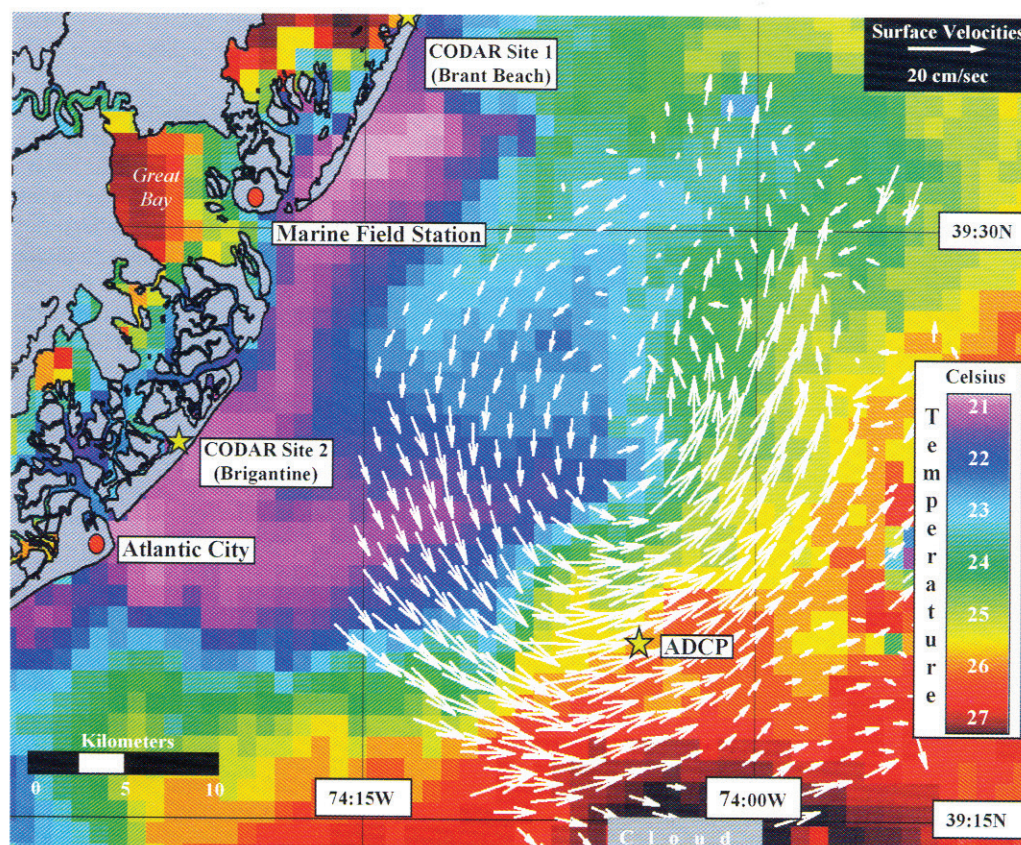


Figure 1: Real-time 'nowcast' obtained from overlaid AVHRR and SeaSonde data for July 23, 1998



as the Doppler shift of the echo signal. Because a single radar detects only the radial speed toward or away from its site, normally two or more radars are deployed to synthesise a total horizontal current vector at each point on their common map area. Ranges out to 70 km and spatial resolutions as good as 300 m are achieved by choice of operating frequency and waveform. The information from a pair of HF radars is equivalent to that of thousands of closely spaced drifters which would need to be released every day.

The major impediment to widespread HF radar use has been their large phased-array antenna sizes, demanding at least 100 m of coast per site, not including their transmit antennas. Besides high costs, this was a major inconvenience factor that often limited access to points with desirable views. This obstacle was overcome by inventions at U.S. NOAA's research laboratories headed by Barrick in the 1970s. Compact direction-finding antennas replaced the large beam-forming phased arrays. The Sea-

Sonde is its commercial culmination. Its compact antenna can be kept out of reach, either on posts or building rooftops. Along with a unique, highly efficient waveform, this low-power compact system allows unmanned real-time operation which at some sites has continued for six years uninterrupted. But it is also suited for quick-response deployments because of its small size and ease of set-up.

### Summer '98 Findings

A SeaSonde radar pair was deployed on the New Jersey coast in the vicinity of LEO-15 to measure surface currents associated with coastal upwelling. Historically, LEO-15 has been an area of strong upwelling characterised by uniform offshore flow. After the initial winds relax, the cold upwelled water concentrates into distinct upwelling centres characterised by a cold eddy surrounded by a northward flowing jet. Hourly SeaSonde surface-current maps complemented many other instruments, including moored, towed and AUV-mounted ADCPs, in an intense sampling of upwelling during the month of July 1998.

The SeaSonde data were initially detided using a least squares fit of regional tidal constituents. The detided data were then filtered using a low pass filter with a cut off frequency of thirty hours. The filtered data showed expected upwelling features, including strong offshore flow and eddy development. This data set was used to plan daily cruise transects and to improve numerical model forecasts through assimilation.

Real-time SeaSonde-derived vector fields were used to plan daily transects near LEO-15 as an alternative to past operations which used an arbitrary cross-shore line. During July of 1998, SeaSonde maps coupled with AVHRR imagery allowed researchers to develop a 'nowcast' of the upwelling area and identify specific areas of interest. The 'nowcast' obtained each morning enabled the in situ sampling to concentrate on these critical areas. For example, the data illustrated in Figure 1 prompted sampling along transects drawn through the centre of the eddy. This efficient sampling regime coupled the surface-current maps with subsurface profiles providing a more complete representation of upwelling dynamics.

The HF radar data were also assimilated into a numerical model to improve weekly forecasts. To test this assimilation, the model was initiated both with and without the surface-current information. The assimilated model depicted the development of an upwelling eddy while the non-assimilative model did not (Figure 2). The assimilations based on the SeaSonde data led to predictions of common flow features associated with upwelling, thus providing a more accurate forecast.

### Use and Validation of SeaSonde

Besides differing from deeper currents in their direct response to the surface winds, the highly important surface flows also have greater spatial variability over small scales.

Nonetheless, the assimilation of HF radar data with that from other instruments into models requires one to establish how they relate to one another, i.e., comparisons. Since each radar directly feels the radial component of the surface current, it makes most sense to relate this radial speed to the velocity component from the other instrument directed toward the radar. This way, a comparative assessment for each radar is established separately, before the two data sets have been combined into a total vector.

An example of a raw time series at hourly increments over one week is shown in Figure 3. Here the South SeaSonde radial component at the ADCP location (shown in Figure 1 located ~29 km directly out from this radar site) is compared to its own radar-directed component from the bin 4.5 m below the mean surface. This is the closest measurable bin to the surface. Also shown is a scatter plot between these two raw measurements, but over a 30 day time period during July 1998 (a total of ~720 data points). The rms difference between the two (i.e.,  $\text{Avg}[\sqrt{(v_a - v_r)^2}]$ ) is 6.7 cm/s.

This difference has four causes: (i) residual random variability due to a finite ensemble average of the sensor signals; (ii) the different nature of the two measurements; (iii) error in the ADCP used for the comparison; (iv) error in the HF radar measurement. Careful studies examining the partitioning of these errors have been done elsewhere for phased-array HF

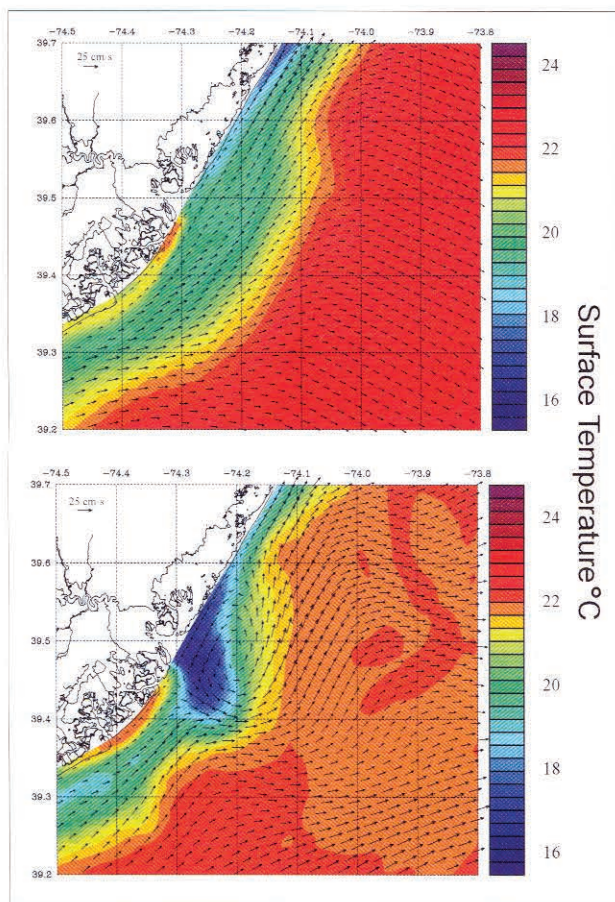


Figure 2: Ocean model outputs for July 17, 1998 both with (lower) and without (upper) SeaSonde data assimilation. Model fails to predict observed eddy without SeaSonde input



radar systems, e.g., Chapman and Graber<sup>1</sup>. Finding upper bounds in total rms velocity of 10-15 cm/s, those studies concluded that the portion due to the HF radar might be 6-7 cm/s. Since our total rms difference is 6.7, our radar error at the radial level must be less by several cm/s than this number.

The tidal part of the currents measured by different instruments at the same location is expected to agree more closely, with the short-term wind and wave effects near the surface removed. Only those components at the known tidal frequencies are extracted, using a least-squares filter over a long time period (30 days). Remaining differences include any real depth and spatial variations, as well as long-term errors due to inherent instrument biases. Examples of the tidal time series over one week are shown in Figure 4 for both sites. Again, the SeaSonde radial tidal speeds at the ADCP are compared to the component which points toward each of the two radar sites. The degree of overlay suggests little bias. The rms differences between these radial tidal components over the entire 30-day period are 2.5 cm/s and 2.4 cm/s for the North and South sites, respectively.

### Conclusions

Adaptive sampling programmes at LEO-15 before 1998 relied solely on satellite-derived sea-surface temperature fields for mission planning. Overhead passes from the operational NOAA AVHRR satellites are only available four times per day, and un-

fortunately the satellite's view of the ocean surface can be obscured by clouds or fog. During the July 1998 experiment, 9 out of 27 days were completely obscured from view by dense cloud cover. Since fog often develops over the cold upwelling centres and does not burn off until late in the day, the upwelling centres often were not visible even on relatively clear days until after the adaptive sampling ships and AUVs had left the dock.

In contrast, continuous SeaSonde surface current fields were available every hour in real-time regardless of the weather conditions. The continuous nature of the SeaSonde observations allowed us to decompose the observed current fields into tidal and low frequency components, the latter clearly revealing the wind-driven upwelling centres. Real-time maps that showed regions of surface convergence and divergence expedited our biological adaptive sampling operations. We also found convincing evidence that assimilation of SeaSonde currents into the numerical model will improve weekly forecasts; without these surface inputs, the model often failed to predict the observed eddies produced by cold upwelling features. Finally, ADCP comparisons support the conclusion that radar error in radial current measurement near the centre of the coverage area is better than 6 cm/s. Future plans for the SeaSonde under NOPP will see expanded versatility and coverage.

Over the next two years, a 'bistatic' capability is to be added to the SeaSonde.

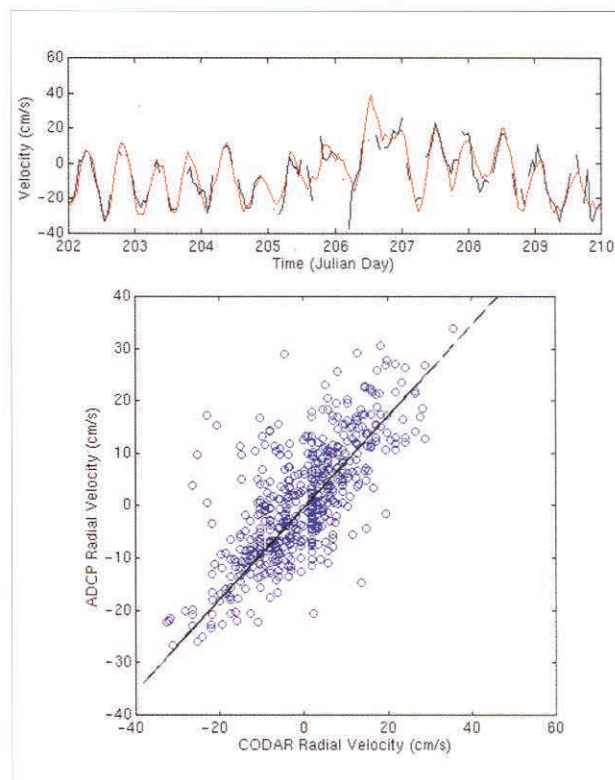


Figure 3: Raw data comparisons between South-site SeaSonde and ADCP bin at 4.5 m depth. Lower is scatter plot for month of July (6.7 cm/s rms difference); upper is one-week time series

### Footnote

<sup>1</sup> A recommended collection of readable articles summarising the evolution and progress of HF current-mapping radars is found in a special issue of the journal *Oceanography*, vol. 10, no. 2, 1997

National Oceanographic Partnership Program (NOPP) is a collaboration of twelve federal agencies to promote co-operative activities among government, academia, and industry, for the advancement of ocean science, technology, and education.

### Biographies

Don Barrick is President of CODAR Ocean Sensors, Ltd., the group which invented and developed HF radar surface-current mapping over the past 25 years.

Josh T Kohut is a second year graduate student at the Rutgers University Institute of Marine and Coastal Sciences studying the coastal dynamics of upwelling.

Scott M Glenn, a Professor at the Rutgers University Institute of Marine and Coastal Sciences, is Principal Investigator for NOPP-sponsored research at LEO-15. ■

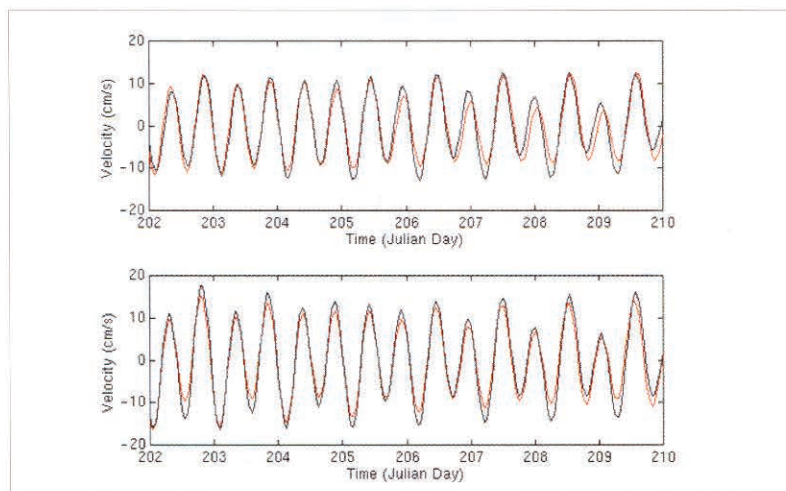
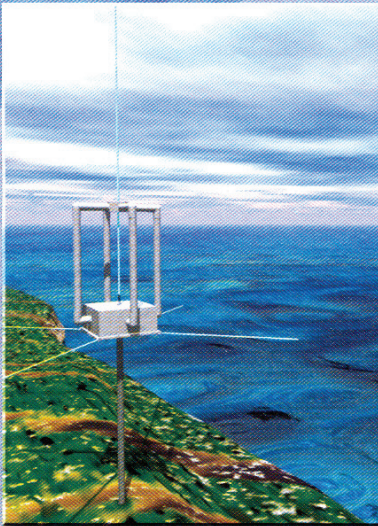


Figure 4: Tidal time series comparison over one week for North-site (upper) and South-site (lower) SeaSonde radial currents and ADCP radar-directed velocities

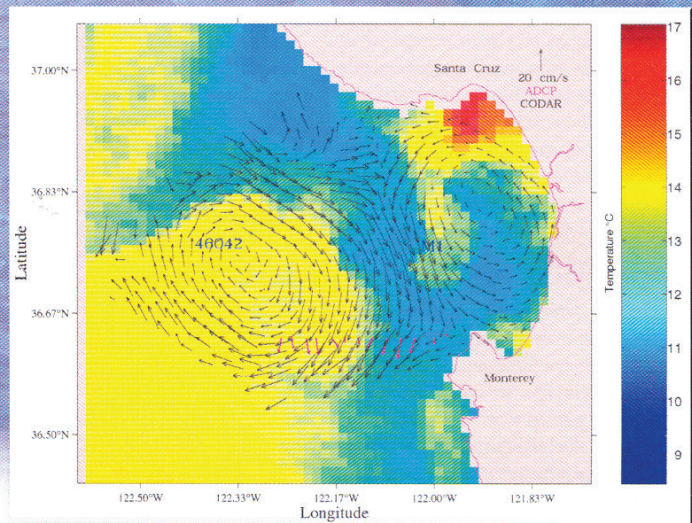


# The No-Hassle Way to Map Surface Currents from Shore



Receive Antenna — Actual size less than 1m<sup>3</sup>

Actual data set from Monterey Bay showing SeaSonde® current velocity vectors, and AVHRR temperatures in colored background.  
The Journal of Geophysical Research, 1996, vol. 101, by J. D. Paduan & L. K. Rosenfeld



## The SeaSonde® Radar System

- Compact Size
- Rapid Deployment
- Wide Coverage Area (100 x 60km)
- Real-Time Data Acquisition
- Remote System Monitoring
- The Most Advanced System Available





## Improving HF Radar Surface Current Measurements with Measured Antenna Beam Patterns

JOSH T. KOHUT AND SCOTT M. GLENN

*Institute of Marine and Coastal Sciences, Rutgers University, New Brunswick, New Jersey*

(Manuscript received 20 December 2001, in final form 5 December 2002)

### ABSTRACT

A high-frequency (HF) radar system is deployed on the New Jersey continental shelf as part of a coastal ocean observatory. The system includes two remote transmit-receive sites in Brant Beach and Brigantine, New Jersey, and a central processing site in Tuckerton, New Jersey. The system uses radio waves scattered off the ocean to measure the radial velocity, range, and bearing of the scattering surface. Calculation of the bearing for HF radar systems depends on the actual beam pattern of the receive antennas. A series of antenna beam pattern measurements conducted on the New Jersey system shows that these patterns are often distorted when an antenna is deployed in the field. Tests indicate that the local environment, not system hardware, causes the most significant distortion of the pattern from the theoretical shape. Correlation with an in situ acoustic Doppler current profiler (ADCP) indicates that the beam pattern distortion can bias the bearing estimate. It is shown that this bias can be removed if the measured beam patterns are used to estimate the bearing.

### 1. Introduction

High-frequency (HF) radar systems have matured to the point where they are now integral components of coastal ocean observation networks and prediction systems (Glenn et al. 2000b; Paduan et al. 1999). An HF radar uses scattered radio waves to measure surface currents, wave parameters, and surface wind fields (Paduan and Graber 1997; Wyatt 1997; Graber and Heron 1997; Fernandez et al. 1997). Surface currents, the most common product of HF radar systems, are used for real-time applications (Kohut et al. 1999), data assimilation, model validation (Breivik and Sætra 2001; Oke et al. 2002; Shulman et al. 2000), and dynamical studies (Shay et al. 1995; Kosro et al. 1997; Paduan and Cook 1997). This expanding HF radar user community necessitates a better understanding of system operation and accuracy.

There is a 30-year history of validation studies using in situ observations to ground truth HF radar data. Early studies compared total vector current data measured with HF radar and in situ current meters, including acoustic Doppler current profilers (ADCPs) and drifters, reporting rms differences ranging from 9 to 27 cm s<sup>-1</sup> [for a review see Chapman and Graber (1997)]. All agree that physical differences between the types of measurements must be considered when validating HF

radar data with in situ instruments. These differences can be separated into three categories: velocity gradients (vertical and horizontal), time averaging, and geometric error associated with total vector combination.

An HF radar system operating at a typical frequency of 25 MHz uses the scattered signal off of a 6-m-long surface gravity wave to infer near-surface current velocities. These current measurements are vertically averaged over the depth felt by the wave. Assuming a linear velocity profile, Stewart and Joy (1974) estimate that for a 6-m-long ocean wave, this depth is about 1 m. At this frequency, any velocity shear between the upper 1 m of the water column and the depth of the in situ measurement will affect the rms difference. Graber et al. (1997) demonstrate that the contribution of specific upper-ocean processes including Ekman fluxes can lead to differences between remote HF radar and in situ current measurements. Additional horizontal differences occur since HF radars are calculating currents based on a return signal that, for a typical 25-MHz system, is averaged over a patch of the ocean surface that can be as large as 3 km<sup>2</sup>, while typical in situ current meters measure at a single point. Any surface inhomogeneity like fronts or small eddies will contribute to the observed rms difference.

The second contribution to the difference is the time sampling of the two instruments. A typical 25-MHz system averages the continuous backscattered data into hourly bins. Often in situ measurements are burst sampled because of battery power and data storage requirements. High-frequency oscillations such as internal

*Corresponding author address:* Dr. Josh T. Kohut, Institute of Marine and Coastal Sciences, Rutgers University, 71 Dudley Rd., New Brunswick, NJ 08901-8521.  
E-mail: jtkohut@rci.rutgers.edu

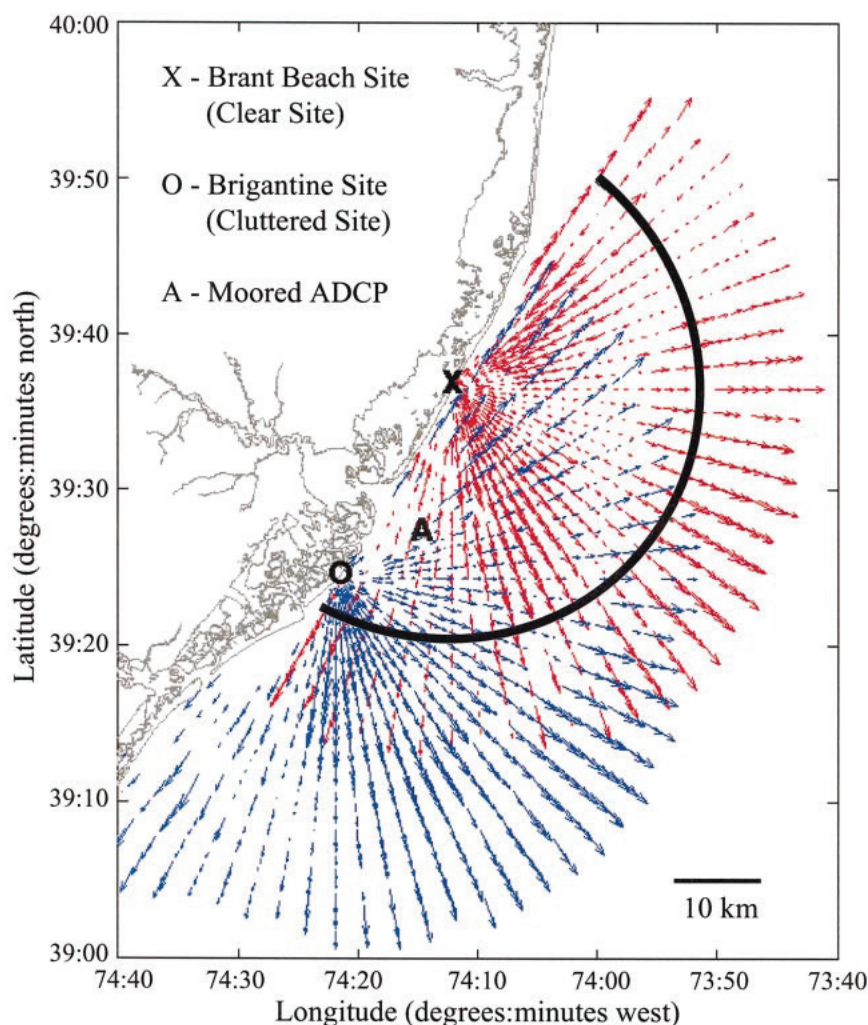


FIG. 1. Study area off the southern coast of New Jersey including hourly radial maps from the Brant Beach (red) and Brigantine (blue) sites. The solid semicircle highlights a range cell for the Brant Beach site.

waves could contaminate a short burst in the in situ measurement and could be averaged over in the HF radar data.

The third possible contribution to the rms difference between HF radar and in situ measurements is related to the geometric combination of radial velocity vectors. Since HF radar systems use Doppler theory to extract surface current information, standard backscatter systems can only resolve the radial current component directed toward or away from the antenna site. At least two spatially separated sites are necessary to calculate the total vector currents for the ocean surface. An example of a radial component velocity map is shown for two coastal sites in Fig. 1. When estimating the total current vector from radial components, the further the two radials are from orthogonality, the larger the potential error in the total vector. This is described by Chapman et al. (1997) as the geometric dilution of pre-

cision (GDOP). By using the independent radial velocity measurements from the two remote sites, this study eliminates this error seen exclusively in the total vector calculations.

More recently, the role of receive antenna patterns on system accuracy has been the focus of HF radar validation. Barrick and Lipa (1986) used an antenna mounted on an offshore oil rig to illustrate that near-field interference can cause significant distortion from ideal patterns. Their study defines this near field as a circle around the antenna with a radius equal to one wavelength of the broadcast signal. Through simulations, they show that typical pattern distortion can introduce an angular bias as large as  $35^\circ$  if they are not taken into account. Comparisons of radial velocity vectors calculated directly between two HF radar sites located on opposite shores of Monterey Bay, California, have also shown an angular bias between the baseline and the best

correlation (Fernandez and Paduan 1996). It is suggested that this bias could be caused by distorted antenna patterns. More recently, Paduan et al. (2001) show that the HF radar correlation with observed currents from an ADCP improves if pattern distortion is taken into account. Kohut et al. (2001) also show the importance of pattern distortion and go on to identify possible sources of this distortion including hardware and the local environment. The HF radar validation results presented here will investigate several sources of antenna pattern distortion as measured in the field and will quantify how this distortion impacts system accuracy. Section 2 briefly describes those features of the operation of HF radar systems relevant to the ensuing discussion. Section 3 outlines the specific instrumentation and methods used in this study. Section 4 discusses the source of antenna pattern distortion and the impact of this distortion on system accuracy, and section 5 presents some concluding remarks.

## 2. Background

High-frequency radar systems use the return signal scattered off the ocean surface to measure the range, bearing, and radial velocity of the scattering surface toward or away from the antenna. The radial velocity is determined using Bragg peaks in the spectra of the backscattered signal (Barrick 1972; Barrick et al. 1977; Lipa and Barrick 1986). Crombie (1955) first recognized that these peaks were the result of an amplification of a transmitted signal by surface gravity waves with a wavelength equal to half that of the transmitted signal. The range of the scattering surface is measured using either a time delay or a frequency modulation technique. The methods used to measure the range and radial velocity of the scattering surface are similar for all HF radar systems (Paduan and Graber 1997). Bearing determination, however, differentiates HF radar systems into two major types: beam forming (BF) and direction finding (DF). Both types illuminate the ocean surface over all angles with a transmitted signal. The difference arises in the reception and interpretation of the backscattered signal. A BF system uses a linear array of vertical elements to steer the receive antenna look angle to different bearings. The bearing of the measured return signal is the look angle of the receive antenna. Some systems mechanically rotate the transmit and receive antenna array (Furukawa and Heron 1996) and others use the relative phases of the antenna elements and their antenna beam patterns to move the receive antenna look angle across the ocean surface. The angular width of the look angle depends on the length of the linear array. A typical 25-MHz system requires an 80-m length to resolve  $5^\circ$  bins. In contrast, a DF system measures the return signal continuously over all angles. The beam patterns of independent antenna elements are used to determine the direction of the incoming signals. The angular resolution, set in the processing, is typically  $5^\circ$ .

For a description of the mechanics and operation of these two HF radar systems, the reader is referred to Teague et al. (1997) and Barrick and Lipa (1996).

Coastal Ocean Dynamics Applications Radar (CODAR), a DF system, uses a three-element receive antenna mounted on a single post. These elements include two directionally dependent cross-loops and a single omnidirectional monopole (Lipa and Barrick 1983; Barrick and Lipa 1996). Since the monopole is omnidirectional, the antenna pattern is a circle of constant radius around the antenna post. Since the absolute patterns of each element cannot be measured, all of the patterns discussed in this paper are those of the loops normalized by the monopole (Fig. 2). This normalized pattern can be measured in the field and used in the current processing algorithms. The theoretical (ideal) pattern has a peak in loop 1 that coincides with the null of loop 2 and vice versa. Using a frequency modulation technique (Teague et al. 1997), the continuous data measured by each antenna is separated into distinct range cells. One range cell of a typical radial field is highlighted in Fig. 1. The Bragg peaks are used to calculate all of the radial velocities measured in the range cell. The bearing of each radial velocity is then determined using the frequency spectra from each receive antenna element. Since its inception, the CODAR system has used several different algorithms to determine the bearing of a given radial velocity, including a closed form solution and a least squares fit to the incoming data (Lipa and Barrick 1983; Barrick and Lipa 1986). More recently, a much more robust multiple signal classification (MUSIC) algorithm enables the CODAR configuration to resolve more complicated flow fields, including conditions when the same radial velocity comes from two different directions. MUSIC was first developed by Schmidt (1986) to locate radio signal sources from aircraft. Barrick and Lipa (1999) have modified MUSIC for the specific task of extracting the bearing of a given signal measured by  $N$  isolated antenna elements. The algorithm has been evaluated and fine-tuned using simulations to recreate known radial velocity fields (Barrick and Lipa 1997; Laws et al. 2000). In its present form, MUSIC can use the shape of either the ideal or measured normalized beam pattern to determine the bearing of a signal scattered off the ocean surface.

The measured antenna pattern differs from the ideal due to distortion caused by coupling with any object other than air within the near field (about one broadcast wavelength). The most significant coupling will occur with objects larger than one-quarter wavelength, especially vertical conductors since the HF radar signals are vertically polarized to enable propagation over the ocean surface. The vertical antenna elements in any HF radar system are more susceptible to beam pattern distortion. For the CODAR-type system the cross-loops are less sensitive since any additional current induced on one side of the loop is approximately balanced by an opposing current induced on the opposite side. Rather than



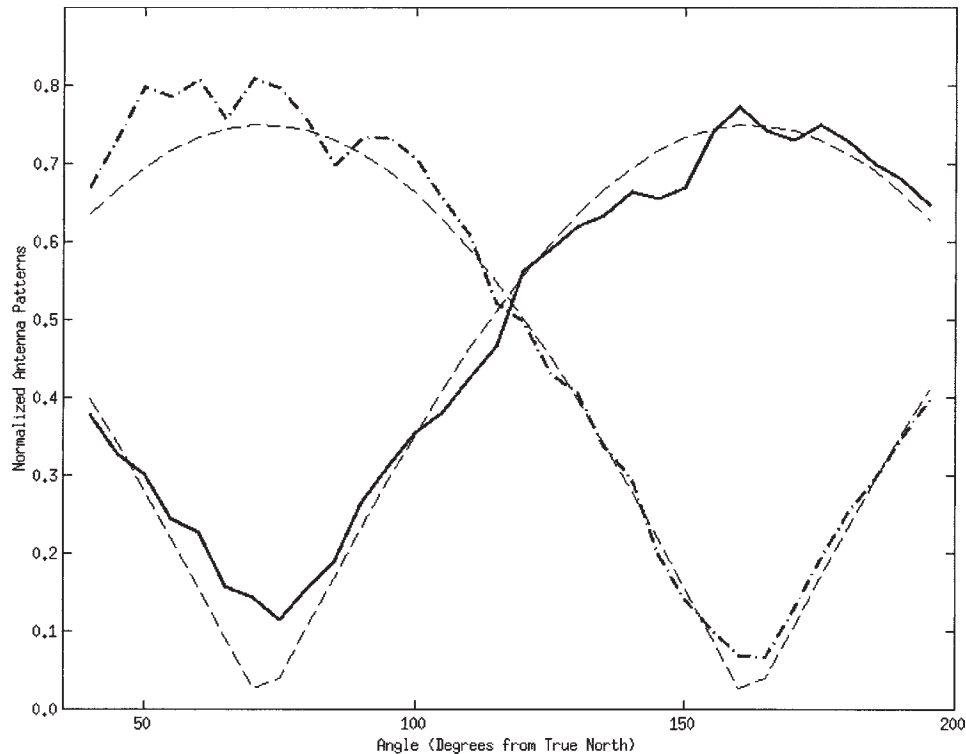


FIG. 2. Ideal (thin dashed) and measured antenna patterns for loop 1 (thick solid) and loop 2 (thick dash-dot) normalized by the monopole. The measured pattern data were collected during run 2.

normalizing one cross-loop by the other, measured beam patterns for each loop will be normalized by the monopole (as in Fig. 2) to maximize our ability to identify distortion. Under ideal conditions, the geometry of a CODAR-type system with a single monopole and two cross-loop elements is such that all current carrying paths of the elements are orthogonal to each other. This orthogonality inhibits any one element from interacting with the other two. When the antenna is mounted in the field, either the local environment or system hardware could induce coupling and change this ideal condition. If the geometry breaks down, the antenna elements interact, causing the normalized ideal pattern to distort. This study will examine the effect of system hardware and the local environment on antenna patterns and compare ocean currents estimated with both the ideal and measured patterns with in situ surface current measurements.

### 3. Methods

#### a. HF radar setup

The 25-MHz CODAR system used here includes two remote antenna sites separated by 26 km in Brant Beach and Brigantine, New Jersey (Fig. 1). The first deployment of this system ran from May 1998 to August 1998. The success of this first summer test prompted a second continuous deployment that began nine months later in

May of 1999 and is continuing to sample in real time, surviving tropical storm Floyd (Kohut 2002) and many nor'easters. Since the remote sites can only resolve the component of the velocity moving toward or away from the antennas, radial current maps are generated at each site. Each field has a range resolution of 1.5 km and an angular resolution of  $5^\circ$ . The radial velocities are based on hourly averaged backscatter data. The fields are center averaged at the top of the hour. This study uses radial velocities collected between 16 October 1999 and 24 January 2000. By using the radial velocity components from each site, the contribution of GDOP is eliminated from the investigation.

The normalized antenna patterns were measured using a transponder that modifies and reradiates the transmitted signal (Barrick and Lipa 1986, 1996). The small battery-operated transponder is mounted on the deck of a boat that tracks along a semicircle around the receive antenna, maintaining a constant speed and radius. For this particular study, the boat maintained a range of 1 km and a speed of 5 kt. At the remote site, raw time series data were measured by each receive element. The time series were combined with the boat's GPS data to determine how the transponder signal varied with angle for each antenna element.

Table 1 summarizes the pattern runs completed at the two CODAR sites. Each pattern run is the average of two boat transects, one circling north to south and the

TABLE 1. Antenna pattern measurement runs.

Run number	Ground plane (m)	Environment	Antenna	Receiver	Date
1	2.4	Cluttered	B	B	Oct 1999
2	1.2	Cluttered	B	B	Oct 1999
3	2.4	Clear	A	A	Oct 1999
4	1.2	Clear	A	A	Oct 1999
5	1.2	Clear	A	A	Sep 2000
6	1.2	Clear	B	A	Sep 2000
7	1.2	Clear	B	B	Sep 2000
8	1.2	Clear	A	A	Sep 2000
9	1.2	Cluttered	B	B	Nov 2000
10	1.2	Cluttered	A	B	Nov 2000
11	1.2	Cluttered	B	B	Nov 2000
12*	1.2	Cluttered	B	B	Nov 2000
13	1.2	Cluttered (new)	B	B	Oct 2001

\* Same as run 11 except different cable location.

other circling south to north. The distortion for each run is calculated by subtracting the measured pattern from the ideal pattern. Since the pattern amplitudes are continually adjusted with sea echo (Lipa and Barrick 1983), the ideal pattern is taken as the best-fit cosine through the measured pattern (Fig. 2). The sites in Table 1 are labeled according to the characteristics of the near field. Both sites, operating at 25.41 and 24.70 MHz, have a near field with a radius of about 12 m. The antenna setup in Brant Beach is mounted on a sand dune close to the surf zone where there are no buildings or any other known interference within several wavelengths of the antenna. This site has a clear near field and will be referred to as the clear site. In Brigantine, the antenna is mounted on a sand dune within one wavelength of a four-story condominium. The presence of this large building clutters the antenna's near field, so the Brigantine site will be referred to as the cluttered site. The ground plane length referred to in Table 1 is the length of the four horizontal fiberglass whips that make up the ground plane of the monopole element. During normal operation, antenna A and receiver A are the receive antenna and receiver setup at the clear site, and antenna B and receiver B are setup in the cluttered site.

The bearing of each radial velocity in a given range cell was calculated once with the ideal pattern and twice with the measured pattern, both with and without outlier elimination, angular interpolation, and smoothing. Outliers were identified using the median of the vectors that fall within  $20^\circ$  of the data point. If the data value is more than  $25 \text{ cm s}^{-1}$  from the median value, it is eliminated from the radial field. The interpolation algorithm then uses a Gaussian window with a half-power width of  $20^\circ$  degrees to smooth and interpolate the data. Radial velocities that are more than  $10^\circ$  from the interpolated value are weighted significantly less than data within  $10^\circ$  of the interpolated radial velocity (Barrick and Lipa 1996). This algorithm is used exclusively on the measured pattern current estimates.

#### b. ADCP setup

A single bottom-mounted ADCP was deployed at the Longterm Ecosystem Observatory (LEO-15) from 21 September 1999 to 29 February 2000 (Grassle et al. 1998; Glenn et al. 2000a; Schofield et al. 2002). Real-time data were sent from the seafloor node through a fiber-optic cable to a computer on shore. The location of this ADCP is shown in Fig. 1. The ADCP operated at 1200 kHz with a bin resolution of 1 m. The ADCP continuously sampled in mode 1 at a sample rate of 400 pings per 1-min ensemble. Since the ADCP was continuously sampled, the potential difference due to burst sampling was eliminated from the dataset. These data were hourly averaged centered at the top of the hour to exactly match the sampling of the CODAR systems. The shallowest bin without sidelobe interference was used in the comparisons. This bin was determined for each data point using the ADCP pressure record by maintaining a depth of about 2.5 m below the surface. The resulting ADCP comparison is then as close to the surface as possible throughout the entire record. The north-south and east-west components of the velocity measured in the surface bin were rotated into a radial/cross-radial coordinate system for each site. The radial component of the ADCP data was compared directly to the radial CODAR data, eliminating the error due to GDOP.

## 4. Results and discussion

### a. Antenna pattern distortions

#### 1) GROUND PLANE

The ground plane of the monopole is made up of four horizontal fiberglass whips at the base of the antenna box. These four orthogonal whips are oriented in the alongshore and cross-shore directions. For the remainder of the discussion, all patterns refer to the patterns of loops 1 and 2 normalized by the monopole. Pattern measurement runs tested two whip lengths, 1.2 and 2.4

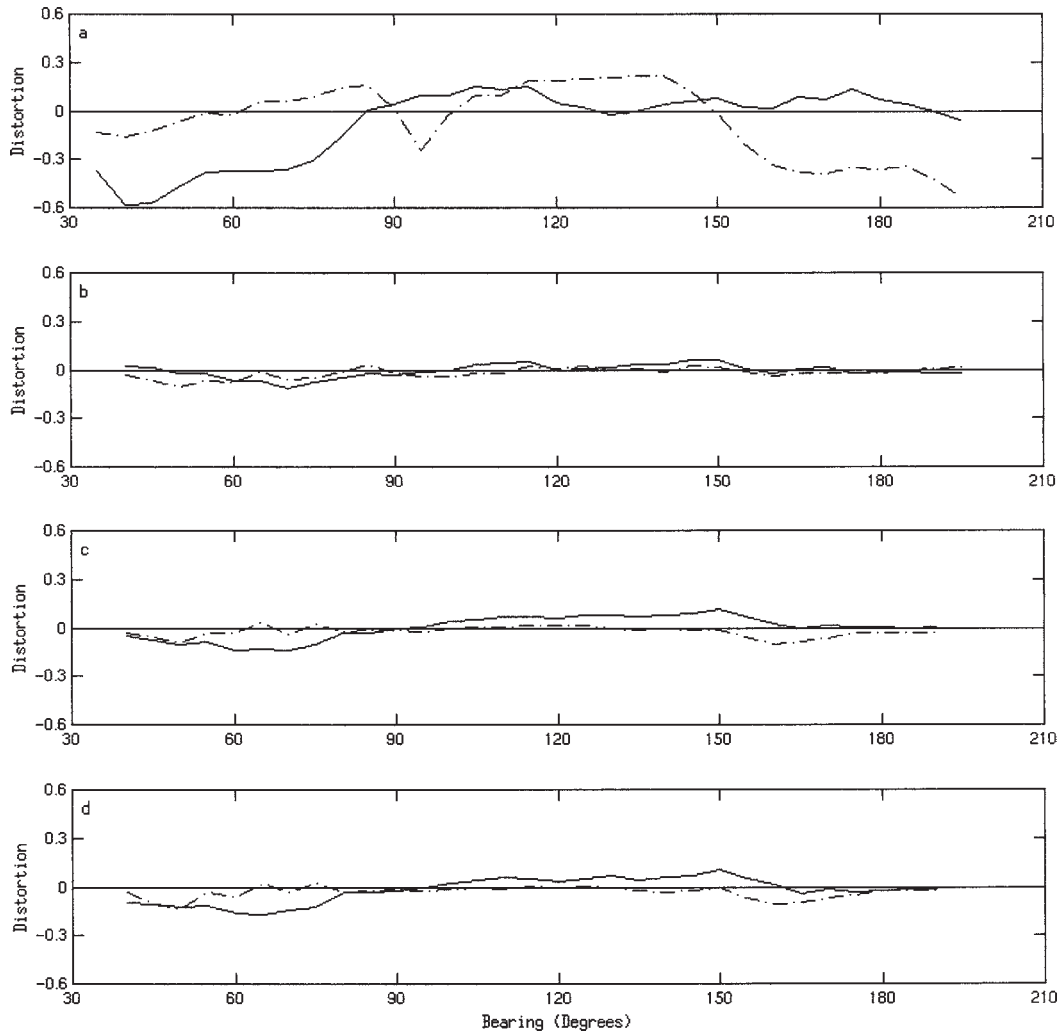


FIG. 3. Normalized antenna pattern distortion for loop 1 (solid) and loop 2 (dash-dot) measured at the clear Brant Beach site for runs (a) 3, (b) 4, (c) 6, and (d) 7.

m, in each environment. Runs 3 and 4, completed approximately 30 min apart, measured the pattern of antenna A with the two different ground planes in the clear environment. The patterns show that the 2.4-m ground plane causes a much larger distortion than the shorter ground plane (Figs. 3a,b). The patterns indicate a stronger coupling between the ground plane and the two loops with the longer ground plane. At an operating frequency of 25 MHz, 2.4 m is a quarter-wavelength. This quarter-wave ground plane is resonant and therefore very efficient. The stronger currents within the ground plane induce strong signals on the two loops resulting in significant pattern distortion. When the whips are reduced to 1.2 m, the efficiency of the ground plane is reduced and the magnitude of the coupling diminishes. The influence of element interaction on antenna pattern distortion has been studied theoretically using an exact industry standard numerical electromagnetics code (NEC) ideally suited for HF (Burke

1981a,b,c). These studies have shown that the resonant ground plane will amplify the coupling between antenna elements. The observations measured in the clear environment support the theoretical results of the NEC.

The distortion of the pattern measured with the resonant (2.4 m) ground plane is relatively larger near the endpoints (Fig. 3a). Since these patterns are measured using a transponder mounted on a boat, the pattern endpoints correspond to the coast on either side of the antenna. As the transponder gets close to the coast, the signal must travel over more of the beach to get to the antenna. When a signal travels over a less conductive surface, like sand, the signal strength quickly drops off. The increased distortion seen near the edges of the pattern is correlated with this weaker transponder signal. Theory suggests that pattern distortions caused by coupling between the individual elements will be relatively larger for angles with relatively weaker signals (Burke 1981a,b,c). The larger distortion at the endpoints of the

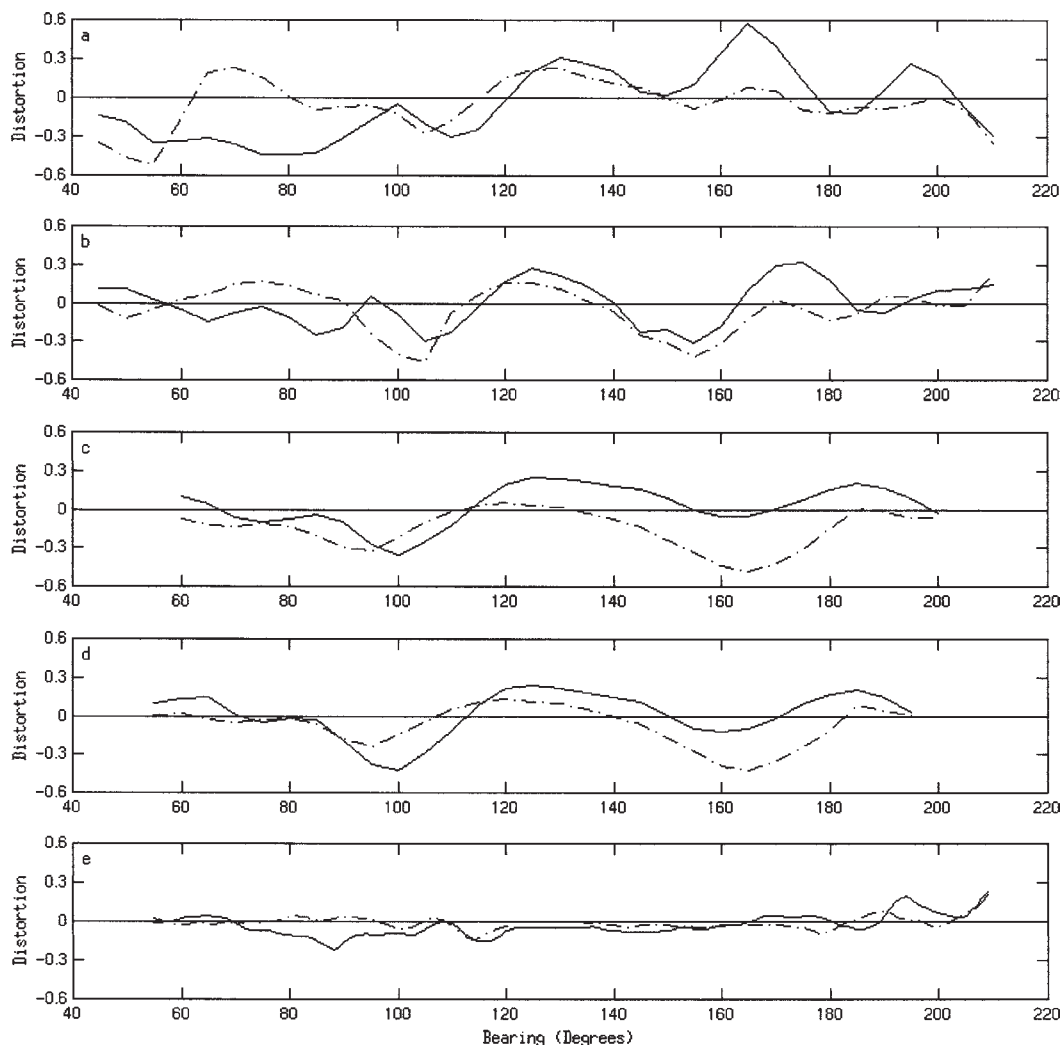


FIG. 4. Normalized antenna pattern distortion for loop 1 (solid) and loop 2 (dash-dot) measured at the cluttered Brigantine site for runs (a) 1, (b) 2, (c) 12, (d) 10, and (e) 13.

pattern further supports the antenna element interaction seen with the resonant ground plane.

The sensitivity of the antenna pattern to the length of the ground plane was also tested in the cluttered environment. Runs 1 and 2 measured the pattern of antenna B with the resonant (2.4 m) and nonresonant (1.2 m) ground planes. The pattern measured with the resonant ground plane has significant distortion over all angles (Fig. 4a). The pattern with the nonresonant ground plane has less distortion, especially near the edges (Fig. 4b). While changing the ground plane improves the pattern near the edges, the nonresonant pattern remains more distorted than the pattern measured in the clear site with the same setup. The remainder of this section will test and discuss the contribution of several possible sources responsible for this difference, including system hardware and the local environment.

## 2) RECEIVER

The receiver is the interface between the computer, the receive antenna, and the transmitter. It houses the hardware components responsible for generating the transmitted signal and receiving the backscattered signal. The three coaxial cables from the antenna elements are attached to the back of the chassis. During these tests, beam patterns using receivers A and B were measured in the clear environment. The patterns measured with the different receivers in the same environment show no significant difference (Figs. 3b,d). Both patterns show relatively small distortion over all angles. The similarity between these two patterns indicates that the receiver does not account for the difference seen in the patterns measured at the clear and cluttered environments with the nonresonant ground plane.

### 3) CABLES

The receive cables run from the receiver to the antenna elements. Electrical currents can build up along the cables and disrupt the ideal geometry discussed previously. If these currents exist, then the location of the cables with respect to the antenna could change the measured pattern. During normal operation these currents are inhibited by a tight loop in the cables near the base of the antenna. To test the effectiveness of this loop, the same system setup was measured with two different cable locations. During run 2, the cables were run as they would be during normal continuous operation. For run 12, the cables were moved closer to the ocean, maintaining the tight loop near the base of the antenna. A comparison between these runs shows that there is no significant difference between the patterns (Figs. 4b,c). Based on these results, we conclude that the cable loop is an effective way to reduce electrical currents along the receive cables that can lead to pattern distortion.

### 4) RECEIVE ANTENNA

The receive antenna consists of three independent antenna elements. Antennas A and B were switched so that the normalized patterns of both antennas could be measured in each environment. Runs 4 and 6 illustrate the difference between the patterns of antennas A and B in the clear environment. The patterns of the two antennas in the clear environment are not significantly different (Figs. 3b,c). There are some small differences; however, they are much smaller than those seen in the patterns of the two antennas in different environments. Patterns for the two antennas were also measured in the cluttered environment (Figs. 4b,d). Again they are very similar and both show significant distortion across much of the pattern. These results indicate that the antenna hardware does not account for the difference in the patterns measured at each site with the nonresonant ground plane.

### 5) LOCAL ENVIRONMENT

Patterns measured with the same hardware in the clear and cluttered environments were used to determine the impact of the local environment on antenna pattern distortion. Antenna B was measured in the clear and cluttered environments. The pattern in the cluttered environment is significantly distorted from the theoretical ideal pattern (Fig. 4b). When this antenna is moved to the clear site these distortions are significantly reduced (Fig. 3c). The results for antenna A show a similar trend in that the patterns measured at the cluttered site are significantly more distorted than those measured at the clear site (Figs. 3b, 4d). Recently the cluttered site was moved 500 m to the southwest to a more stable beach location. The new location offers a more open near field

on a dune similar in composition to the setup at the clear site. After antenna B was moved the patterns were re-measured. The pattern measured at the new location is much closer to ideal than at the previous location (Fig. 4e). These observations clearly indicate that interference within the antenna's near field significantly influences pattern distortion. If either antenna A or B is set up in a clear environment, the patterns are much closer to ideal than if the same antenna is measured in a cluttered environment.

### 6) TIME DEPENDENCE

The time dependence of the measured patterns is very important to document since the patterns can be used to improve HF radar measurements. The timescale of the pattern changes will dictate the frequency of the measurement necessary to maintain accurate systems. The time dependencies of these patterns were determined by comparing like runs measured at different times. Both runs 4 and 5 measured the same system hardware in the clear environment 11 months apart. The measurements indicate that while the amplitude of the pattern changed over time, the angular dependence of the pattern did not (Figs. 2 and 5a). These patterns are normalized by the omnidirectional monopole. If the strength of the monopole decreases, the amplitude of the normalized pattern will increase. Since the change in the pattern is felt equally over all angles, the difference in the normalized pattern can only be attributed to a weaker monopole. During the hardware changes for runs 6 and 7, the cable connecting the receiver to the monopole was disconnected and reconnected. The same hardware was then measured again in run 8. After the cable was reconnected, the pattern amplitude returned to the same order seen 11 months before (Figs. 2 and 5b). Again the directional dependence of the pattern did not change. The tighter cable connection strengthened the monopole and decreased the amplitude of the normalized pattern. This indicates that the only change seen in the antenna pattern over the 11-month period is the strength of the monopole.

Similar tests were completed in the cluttered environment. These runs measured the same system setup 13 months apart. Again the amplitude, not the directionality, of the pattern was affected. The amplitude measured in October 1999 is on the order of 0.80. The amplitude of the same system setup measured 13 months later increased to about 1.50. After several hardware changes, the monopole connection was strengthened and the pattern amplitude returned to 0.65, the same order as that measured 13 months before. Through all of these runs the directional dependence of the patterns remained the same. Since the pattern amplitudes are adjusted with measured sea echo (Lipa and Barrick 1983), it is only required that the directional dependence of the pattern be maintained. The results from both sites indicate that the directionality of the normalized pattern measured in

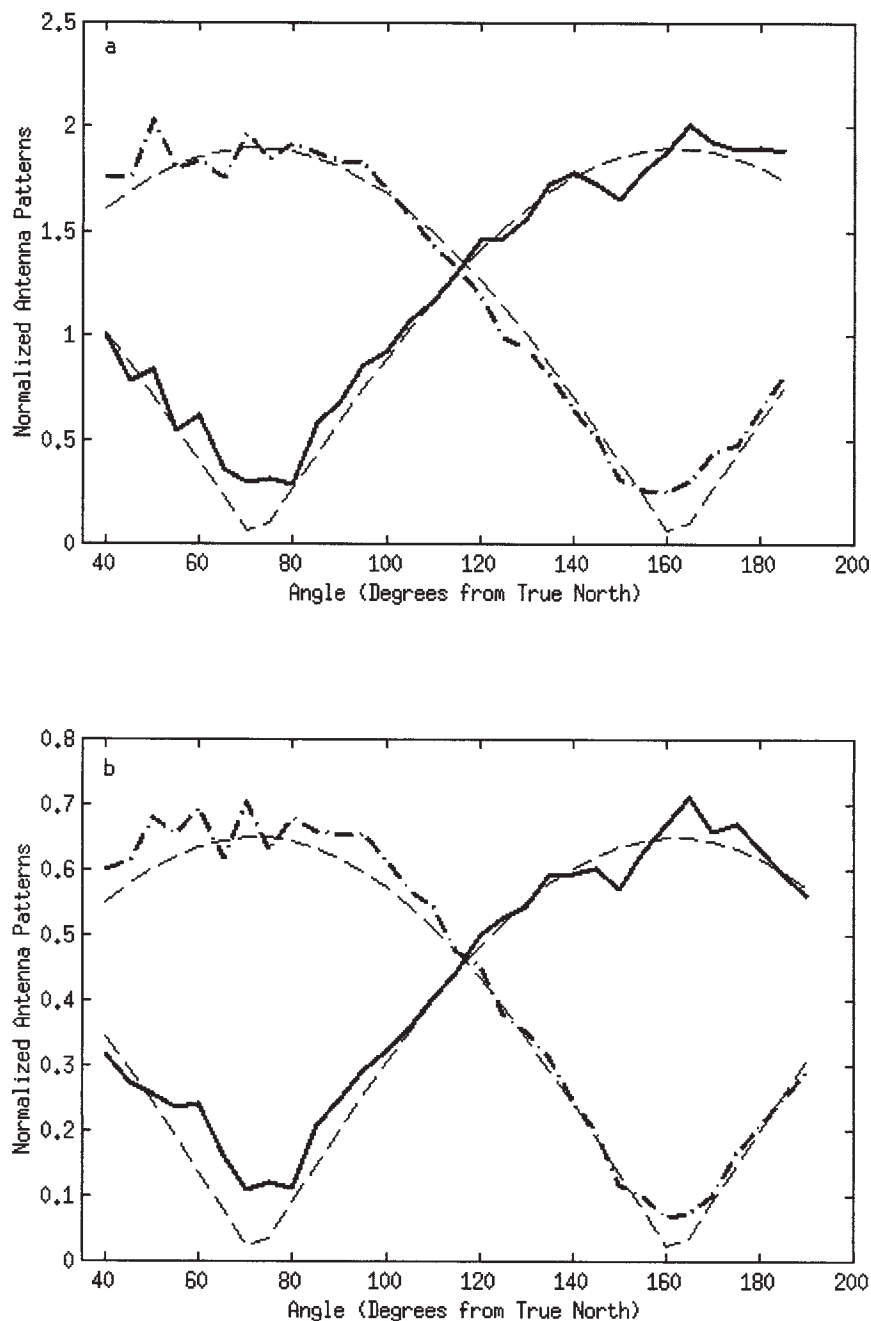


FIG. 5. Antenna patterns of loop 1 (thick solid) and loop 2 (thick dash-dot) normalized by the monopole at the clear site during runs (a) 5 and (b) 8.

either environment did not significantly change over annual timescales. Based on these conclusions, annual antenna pattern runs appear to be sufficient to maintain the accuracy of a CODAR site.

The pattern measurements shown here indicate that the length of the monopole ground plane and the local environment play an important role in antenna pattern distortion. If the ground plane is resonant or there is interference within the antennas near field, the ideal

geometry of the antenna breaks down and the elements interact. This breakdown has also been shown theoretically to cause interelement interaction that distorts the antenna pattern (Burke 1981a,b,c).

#### *b. ADCP comparisons*

The MUSIC algorithm can use either the measured or ideal pattern to determine the bearing of a given radial

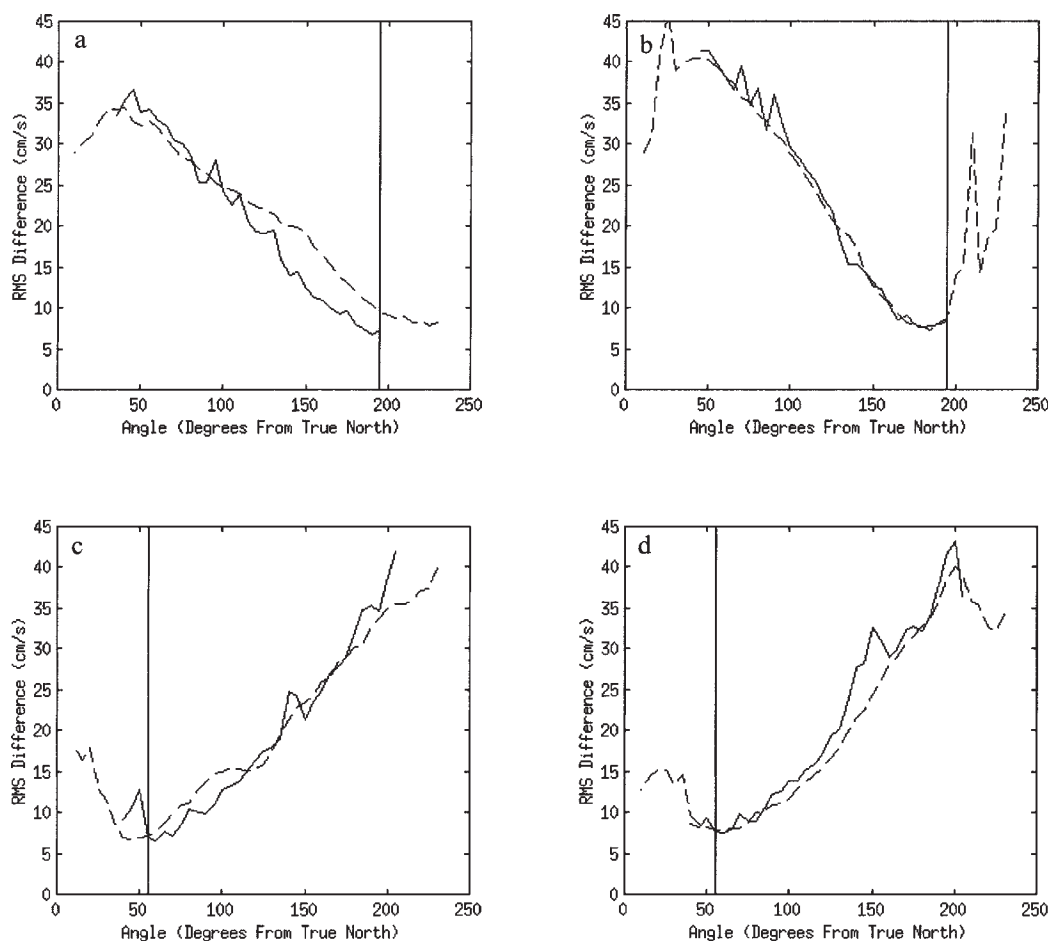


FIG. 6. The rms difference between the radial velocities of the ADCP and each CODAR angular bin within the range cell passing through the ADCP using the measured (solid) and ideal (dashed) antenna patterns. Comparisons were made at the clear site with the (a) resonant and (b) nonresonant ground planes, and repeated at the cluttered site with both the (c) resonant and (d) nonresonant ground planes. The angular bin containing the ADCP is shown as a vertical black line.

velocity. For the purpose of this study, results obtained with the ideal pattern will be called ideal pattern results and those obtained with the measured pattern will be labeled the measured pattern results. The processing can also utilize an angular interpolation scheme to fill in radial data gaps. Since the measured pattern results usually have more data gaps than the ideal pattern results (Paduan et al. 2001), the interpolation was used exclu-

sively on these data. The ideal, measured, and measured-interpolated CODAR results were each independently validated against a moored ADCP. As previously mentioned, the CODAR measurement is the average over the surface meter of the water column and the ADCP is a 1-m average at a depth of 2.5 m. Between 16 October 1999 and 24 January 2000, the CODAR

TABLE 2. ADCP comparison statistics for the clear environment.

Ground plane (m)	Antenna pattern	Rms difference (cm s <sup>-1</sup> )	R <sup>2</sup>	Number of points
2.4	Ideal	9.53	71%	682
2.4	Measured	7.37	90%	314
2.4	Measured-interpolated	7.75	86%	594
1.2	Ideal	8.30	81%	99
1.2	Measured	8.40	83%	224
1.2	Measured-interpolated	7.80	88%	549

TABLE 3. ADCP comparison statistics for the cluttered environment.

Ground plane (m)	Antenna pattern	Rms difference (cm s <sup>-1</sup> )	R <sup>2</sup>	Number of points
2.4	Ideal	7.19	84%	699
2.4	Measured	6.83	94%	190
2.4	Measured-interpolated	7.65	82%	722
1.2	Ideal	7.76	90%	694
1.2	Measured	7.68	93%	632
1.2	Measured-interpolated	6.70	90%	920



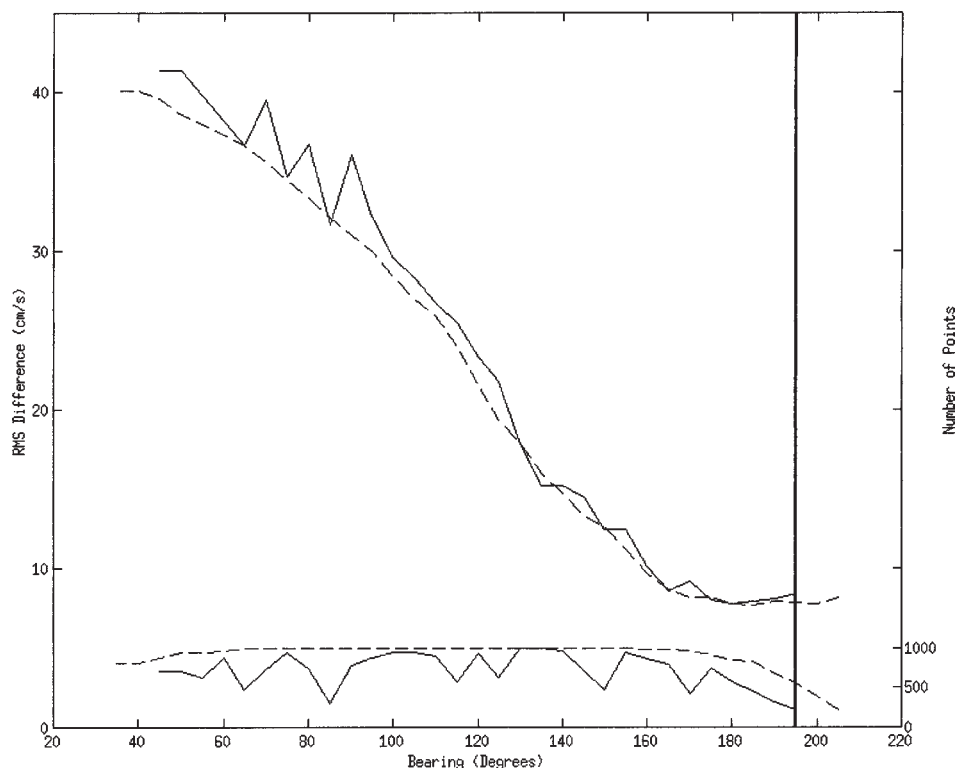


FIG. 7. The rms difference (upper lines) at the clear site between the radial velocities of the ADCP and each CODAR angular bin within the range cell passing through the ADCP using the measured antenna pattern with (dashed) and without (solid) the interpolation-smoothing algorithm. The number of data points (lower lines) for each angular bin with (dashed) and without (solid) the interpolation-smoothing algorithm.

sampling was separated into two regimes. From 16 October 1999 to 4 December 1999, the antennas were set up with the resonant 2.4-m ground plane. From 6 December 1999 to 24 January 2000, the ground plane was shortened to the nonresonant 1.2 m. These tests take advantage of the amplified distortion observed with the resonant ground plane so that the effect of this distortion on system accuracy is more easily observed. Additionally, the ADCP was moored near the edge of the antenna pattern for each remote site, so these comparisons also focus on the portion of the pattern most affected by antenna element interaction. Results from the clear site indicate the influence of the pattern distortion on the ADCP comparisons (Table 2). When the larger ground plane was tested, the ideal pattern results had an rms difference of  $9.53 \text{ cm s}^{-1}$  and a correlation of 71%. When the large distortion was accounted for in MUSIC by using the measured pattern, the rms difference improved to  $7.37 \text{ cm s}^{-1}$  with a correlation of 90%. With the nonresonant ground plane, the distortion is significantly reduced and there is only a small difference between the ideal and measured pattern results. The ADCP comparisons show that either pattern has rms differences on the order of  $8 \text{ cm s}^{-1}$  with an average correlation of 82%. With the near-ideal pattern, the accuracy of the CODAR measurement is independent of the pattern used in the processing. However, if these patterns are

distorted, surface current measurements are in better agreement when MUSIC uses the measured pattern.

Table 2 also shows the number of concurrent data points from each instrument used in the comparison. One consequence of using the measured pattern in the MUSIC processing is that certain radial directions are favored over others. The number of points used in each comparison indicates this asymmetry in the radial fields. The angular interpolation within a given range cell was used in the processing to fill in these gaps. The interpolated data was compared to the ADCP to assess the validity of the algorithm. With an rms difference of  $7.75 \text{ cm s}^{-1}$  and a correlation of 86%, the measured-interpolated data correlation is on the same order as the measured pattern data without interpolation. These results hold true for both the resonant and nonresonant cases. With both ground planes, the measured-interpolated data had similar statistical comparisons as the corrected data and prove to be an effective algorithm for filling in radial data gaps.

The same study was repeated in the cluttered environment. This site differs from the clear site in that the patterns are distorted with both the resonant and nonresonant ground planes. The only similarity is that the distortion near the endpoints was reduced with the shorter ground plane. With the resonant ground plane, the results using the measured pattern improved the ADCP



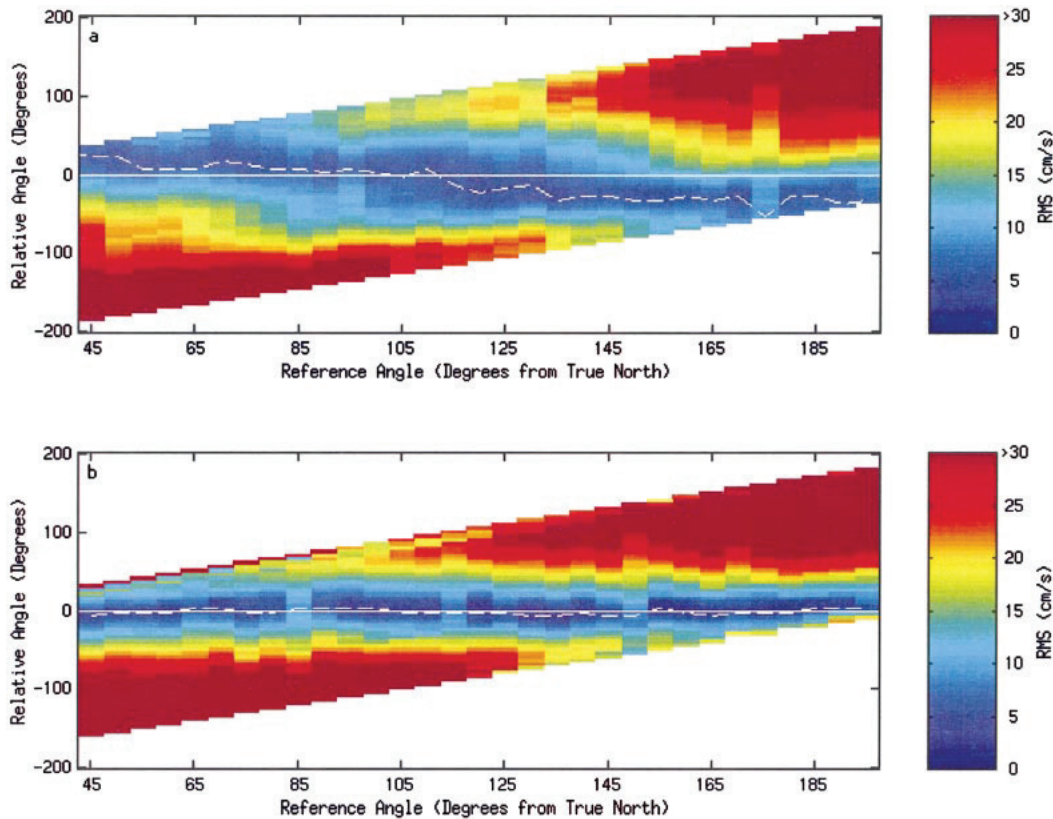


FIG. 8. The rms difference between the measured and ideal pattern current estimates at the clear site with the (a) resonant and (b) nonresonant ground planes. The lowest rms difference for each bin is shown as a dashed line.

correlation from 84% to 94% (Table 3). These results are consistent with those found at the clear site. With the nonresonant ground plane, the results did not differ significantly between the measured and ideal pattern data. Even with the distortion near the center of the pattern, the reduced distortion near the endpoints is sufficient to equalize the two results. These observations suggest that the distortion near the center of the pattern may not influence the radial data distribution near the edge of the pattern.

Since MUSIC uses the antenna pattern to determine the bearing of each radial velocity observed in a given range cell, comparisons between the ADCP and radial currents from all other angles in the CODAR range cell may indicate why pattern measurements improve system accuracy. The rms difference between the ADCP and all CODAR grid points was determined for the ideal, measured, and measured-interpolated CODAR data. Since bearing solutions estimated with the ideal pattern are found over  $360^\circ$  and solutions with the measured pattern only occur over the range covered by the boat measurement, solutions over land sometimes are included in the ideal data. Paduan et al. (2001) suggest that the ideal solutions outside the measured pattern domain result from pattern distortion. The angular dependence of the rms difference between the ADCP and

the CODAR data estimated with the ideal pattern has a very broad minimum shifted to the right of the ADCP (Fig. 6a). When the data are processed with the measured pattern, the rms value at the ADCP is lower and the narrower minimum is shifted toward the ADCP. With the nonresonant ground plane, the angular dependence of the rms comparison does not differ significantly for the two patterns (Fig. 6b). This is to be expected since the two patterns are almost identical and the CODAR estimates should be similar. If the patterns are distorted, the correlation statistics are improved by more consistently placing radial velocities in the appropriate angular bin.

The angular validation at the cluttered site supports the results found in the clear site. If the pattern is distorted, the lowest rms difference is closer to the ADCP when the measured pattern is used (Fig. 6c). Even with the pattern distortion seen with the nonresonant ground plane, the ADCP correlation statistics did not change (Table 3). Similarly, the angular dependence of the rms difference does not change between the ideal and measured pattern estimates (Fig. 6d). With the ADCP location near the edge of the pattern, these results indicate that pattern distortion may only affect local bearing estimates.

The measured and interpolated data for the entire

clear site range cell was also compared to the ADCP. If the interpolation is used, the data gaps or spokes seen in the estimates processed with the measured pattern are filled in (Fig. 7). The rms curves for the measured pattern and measured–interpolated pattern data are nearly identical, indicating that the two datasets compare similarly to the ADCP. Since the algorithm is using a  $20^\circ$  window for interpolation and smoothing, the rms minimum in the interpolated data is broader than the measured result without interpolation (Fig. 7). The algorithm used here is an effective method for filling in radial data gaps in the measured pattern data.

The comparisons with the ADCP show that the CODAR data processed with the measured antenna pattern have a higher correlation. These results are especially evident if the patterns are significantly distorted, as is the case with the resonant ground plane. If the measured and ideal patterns do not significantly differ, the correlation remains high regardless of the pattern used in the processing. This study takes advantage of the ADCP's proximity to the endpoint of the pattern, the area most affected by antenna element interaction. The next section will expand these results over all angles by looking at comparisons between CODAR data processed with the measured and ideal antenna pattern.

### c. Measured versus ideal

The results of the previous section showed that for the angles looking toward the ADCP, system accuracy improved with the measured pattern if significant distortion exists. To spatially extend the ADCP results, this section discusses comparisons between CODAR currents generated with the ideal and the measured antenna patterns over all angles. In the following analysis, data from the clear site CODAR range cell passing through the ADCP were used. Measured pattern currents from a specific angular bin were compared to the ideal pattern currents from all angular bins. The rms difference calculations were then repeated for each angular bin in the range cell. Figure 8 shows contour plots of the rms difference between the measured and ideal pattern results. The  $x$  axis is the reference angle from true north for each angular bin of the measured pattern. The  $y$  axis is the relative angle between the measured angular bin and the ideal angular bin. Zero relative angle means the measured and ideal angular bins are collocated, and positive relative angles imply that the ideal angular bin is north of the measured angular bin. The dashed line indicates the ideal bin with the lowest rms difference. Since the reference angle in each plot does not match the relative angle near the edges, the measured pattern focuses the possible angle solutions to a narrower range and the ideal pattern spreads the possible solutions over more angles. When the patterns are distorted, the measured and ideal pattern data measured at the same angular bin do not have the lowest rms difference (Fig. 8a). The dashed line shows that the lowest rms differ-

ence could be with a grid point as far as  $50^\circ$  away. This angular offset is shown to be dependent on the reference angle, with a larger offset near the edges. This appears to be related to the increased distortion observed near the coast. If the resonant ground plane is replaced with a shorter nonresonant ground plane, the distortion near the edge of the pattern is reduced. The ideal bin with the best correlation to the measured pattern result is much closer to the measured pattern data point (Fig. 8b). This is to be expected since the measurement pattern is almost ideal.

## 5. Conclusions

As the role of HF radar becomes increasingly more important in coastal observatories and regional modeling efforts, it is imperative to properly maintain accurate systems to ensure high data quality. System accuracy is shown to be dependent on the distortion of the measured pattern. For the CODAR-type DF system, this distortion is related to the interaction between the individual elements, whether caused by a resonant ground plane or the local environment. In many cases distortion is unavoidable due to site location constraints. For these instances it is necessary to process the data with the measured pattern. Unless the measured pattern is nearly ideal, ADCP comparisons indicate that the CODAR bearing estimates are more accurate if MUSIC uses the measured pattern. A direct CODAR-to-CODAR comparison shows that the offset between the measured and ideal angular bins with the lowest rms difference extends over all angles when the pattern is distorted over all angular bins. To maximize an HF radar's usefulness for scientific and operational applications, the antenna patterns for each site must be measured and, if distorted, these patterns should be used in the processing to improve the surface current measurements.

*Acknowledgments.* This work was funded by the Office of Naval Research (N00014-97-1-0797, N00014-99-1-0196, N00014-00-1-0724), the National Ocean Partnership Program (N00014-97-1-1019, N00014-98-1-0815), and the great state of New Jersey. ADCP data provided by the Mid-Atlantic Bight National Undersea Research Center with additional support from the National Science Foundation.

## REFERENCES

- Barrick, D. E., 1972: First-order theory and analysis of mf/hf/vhf scatter from the sea. *IEEE Trans. Antennas Propag.*, **AP-20**, 2–10.
- , and B. J. Lipa, 1986: Correcting for distorted antenna patterns in CODAR ocean surface measurements. *IEEE J. Oceanic Eng.*, **OE-11**, 304–309.
- , and —, 1996: Comparison of direction-finding and beam-forming in hf radar ocean surface current mapping. Phase 1 SBIR Final Report, Contract 50-DKNA-5-00092. National Oceanic and Atmospheric Administration, Rockville, MD, 81 pp.

- , and —, 1997: Evolution of bearing determination in hf current mapping radars. *Oceanography*, **10**, 72–75.
- , and —, 1999: Radar angle determination with MUSIC direction finding. U.S. Patent 5 990 834.
- , M. W. Evens, and B. L. Weber, 1977: Ocean surface currents mapped by radar. *Science*, **198**, 138–144.
- Breivik, O., and O. Sætra, 2001: Real time assimilation of hf radar currents into a coastal ocean model. *J. Mar. Syst.*, **28**, 161–182.
- Burke, G. J., and A. J. Poggio, 1981a: Numerical Electromagnetics Code (NEC)—Method of moments. Part I: Program description—Theory. NOSC Tech. Doc. 116, Vol. 1, Lawrence Livermore National Laboratory, 84 pp.
- , and —, 1981b: Numerical Electromagnetics Code (NEC)—Method of moments. Part II: Program description—Code. NOSC Tech. Doc. 116, Vol. 1, Lawrence Livermore National Laboratory, 433 pp.
- , and —, 1981c: Numerical Electromagnetics Code (NEC)—Methods of moments. Part III: User's guide. NOSC Tech. Doc. 116, Vol. 2, Lawrence Livermore National Laboratory, 179 pp.
- Chapman, R. D., and H. C. Graber, 1997: Validation of hf radar measurements. *Oceanography*, **10**, 76–79.
- , L. K. Shay, H. C. Graber, J. B. Edson, A. Karachintsev, C. L. Trump, and D. B. Ross, 1997: On the accuracy of hf radar surface current measurements: Intercomparisons with ship-based sensors. *J. Geophys. Res.*, **102**, 18 737–18 748.
- Crombie, D. D., 1955: Doppler spectrum of sea echo at 13.56 Mc/s. *Nature*, **175**, 681–682.
- Fernandez, D. M., and J. D. Paduan, 1996: Simultaneous CODAR and OSCAR measurements of ocean surface currents in Monterey Bay. *Proc. IEEE IGARSS '96*, Vol. 3, Lincoln, NE, IEEE, 1746–1750.
- , H. C. Graber, J. D. Paduan, and D. E. Barrick, 1997: Mapping wind direction with hf radar. *Oceanography*, **10**, 93–95.
- Furukawa, K., and M. L. Heron, 1996: Vortex modeling and observation of a tidally induced jet. *Coastal Eng.*, **43**, 371–375.
- Glenn, S. M., W. Boicourt, B. Parker, and T. D. Dickey, 2000a: Operational observation networks for ports, a large estuary and an open shelf. *Oceanography*, **13**, 12–23.
- , T. D. Dickey, B. Parker, and W. Boicourt, 2000b: Long-term real-time coastal ocean observation networks. *Oceanography*, **13**, 24–34.
- Graber, H. C., and M. L. Heron, 1997: Wave height measurements from hf radar. *Oceanography*, **10**, 90–92.
- , B. K. Haus, L. K. Shay, and R. D. Chapman, 1997: Hf radar comparisons with moored estimates of current speed and direction: Expected differences and implications. *J. Geophys. Res.*, **102**, 18 749–18 766.
- Grassle, J. F., S. M. Glenn, and C. von Alt, 1998: Ocean observing systems for marine habitats. *Proc. OCC '98*, Baltimore, MD, Marine Technology Society, 567–570.
- Kohut, J. T., 2002: Spatial current structure observed with a calibrated HF radar system: The influence of local forcing, stratification, and topography on the inner shelf. Ph.D. thesis, Rutgers University, 141 pp.
- , S. M. Glenn, and D. E. Barrick, 1999: SeaSonde is integral to coastal flow model development. *Hydro International*, Vol. 3, GITC, 32–35.
- , —, and —, 2001: Multiple hf-radar system development for a regional long term ecosystem observatory in the New York bight. Preprints, *Fifth Symp. on Integrated Observing Systems*, Albuquerque, NM, Amer. Meteor. Soc., 4–7.
- Kosro, P. M., J. A. Barth, and P. T. Strub, 1997: The coastal jet: Observations of surface currents over the Oregon continental shelf from hf radar. *Oceanography*, **10**, 53–56.
- Laws, K., D. M. Fernandez, and J. D. Paduan, 2000: Simulation-based evaluations of hf radar ocean current algorithms. *IEEE J. Oceanic Eng.*, **25**, 481–491.
- Lipa, B. J., and D. E. Barrick, 1983: Least-squares methods for the extraction of surface currents from CODAR cross-loop data: Application at ARSLOE. *IEEE J. Oceanic Eng.*, **OE-8**, 226–253.
- , and —, 1986: Extraction of sea state from hf-radar sea echo: Mathematical theory and modeling. *Radio Sci.*, **21**, 81–100.
- Oke, P. R., J. S. Allen, R. N. Miller, G. D. Egbert, and P. M. Kosro, 2002: Assimilation of surface velocity data into a primitive equation coastal ocean model. *J. Geophys. Res.*, **107**, 3122, doi: 10.1029/2000JC000511.
- Paduan, J. D., and M. S. Cook, 1997: Mapping surface currents in Monterey Bay with CODAR-type hf radar. *Oceanography*, **10**, 49–52.
- , and H. C. Graber, 1997: Introduction to high-frequency radar: Reality and myth. *Oceanography*, **10**, 36–39.
- , L. K. Rosenfeld, S. R. Ramp, F. Chavez, C. S. Chiu, and C. A. Collins, 1999: Development and maintenance of the ICON observing system in Monterey Bay. Preprints, *Third Conf. on Coastal Atmospheric and Oceanic Prediction and Processes*, New Orleans, LA, Amer. Meteor. Soc., 226–231.
- , D. E. Barrick, D. M. Fernandez, Z. Hallock, and C. C. Teague, 2001: Improving the accuracy of coastal hf radar current mapping. *Hydro International*, Vol. 5, GITC, 26–29.
- Schmidt, R. O., 1986: Multiple emitter location and signal parameter estimation. *IEEE Trans. Antennas Propag.*, **AP-34**, 276–280.
- Schofield, O., T. Bergmann, W. P. Bissett, F. Grassle, D. Haidvogel, J. Kohut, M. Moline, and S. Glenn, 2002: The long term ecosystem observatory: An integrated coastal observatory. *IEEE J. Oceanic Eng.*, **27**, 146–154.
- Shay, L. K., H. C. Graber, D. B. Ross, and R. D. Chapman, 1995: Mesoscale ocean surface current structure detected by hf radar. *J. Atmos. Oceanic Technol.*, **12**, 881–900.
- Shulman, I., and Coauthors, 2000: Development of the high resolution, data assimilation numerical model of the Monterey Bay. *Estuarine and Coastal Modeling*, M. L. Spaulding and H. L. Butler, Eds., 980–994.
- Stewart, R. H., and J. W. Joy, 1974: Hf radio measurement of surface currents. *Deep-Sea Res.*, **21**, 1039–1049.
- Teague, C. C., J. F. Vesecky, and D. M. Fernandez, 1997: Hf radar instruments, past to present. *Oceanography*, **10**, 40–44.
- Wyatt, L. R., 1997: The ocean wave directional spectrum. *Oceanography*, **10**, 85–89.

# Flow reversals during upwelling conditions on the New Jersey inner shelf

Robert J. Chant, Scott Glenn, and Josh Kohut

Institute of Marine and Coastal Science, Rutgers University, New Brunswick, New Jersey, USA

Received 30 April 2003; revised 15 June 2004; accepted 22 July 2004; published 13 November 2004.

[1] The temporal evolution of a flow reversal during upwelling conditions along New Jersey's inner shelf is characterized with shipboard, moored, and remote observations. The flow reversal occurs nearshore in the form of a subsurface jet with maximum velocities exceeding 30 cm/s. The jet is most intense in the thermocline, commences during maximum alongshore wind stress, and has a spin-up time approximately equal to the local inertial period. The jet also has a surface signature apparent in ocean current radar data that shows the jet veering offshore and feeding an upwelling center that drifts southward at 5 cm/s. Moored instrumentation within the upwelling center indicates that cross-shelf transport in the warm surface layer is consistent with the predicted Ekman transport prior to the spin-up of the jet, but exceeds Ekman transport thereafter. However, onshore transport in the lower layer never compensates for offshore flow in the surface layer, suggestive that the mass balance requires a three-dimensional closure. Finally, we suggest that the flow reversal provides a significant fraction of cool water to the evolving upwelling center, and that the offshore veering is due to enhanced friction over a shoaling and rougher topography.

**INDEX TERMS:** 4279 Oceanography: General: Upwelling and convergences; 4524 Oceanography: Physical: Fine structure and microstructure; 4520 Oceanography: Physical: Eddies and mesoscale processes; **KEYWORDS:** upwelling, flow reversal, Ekman Transport Index

**Citation:** Chant, R. J., S. Glenn, and J. Kohut (2004), Flow reversals during upwelling conditions on the New Jersey inner shelf, *J. Geophys. Res.*, 109, C12S03, doi:10.1029/2003JC001941.

## 1. Introduction

[2] The most simplistic model of coastal upwelling, based on Ekman dynamics, consists of an offshore transport of warm surface water that is compensated by an onshore transport of cold fluid in the bottom layer. The transport of fluid in the surface layer is the Ekman transport,  $\tau/\rho f$ , where  $\tau$ ,  $\rho$ , and  $f$  are the alongshore wind stress, density, and the Coriolis frequency, respectively. Numerous theoretical and experimental studies have been motivated by this simple two-dimensional model, and the results have produced a more sophisticated view of coastal circulation processes. Huyer [1983] described an alongshore downwind baroclinic surface jet that is in thermal wind balance with the tilted isopycnals of an upwelling front. Lentz and Trowbridge [1991], Trowbridge and Lentz [1991], and MacCready and Rhines [1993] have invoked the combined effects of baroclinicity and Ekman dynamics over a sloping bottom to characterize the arrested Ekman layer and the resulting asymmetries in coastal circulation in response to upwelling and downwelling wind forcing. Recently, Austin and Barth [2002] have characterized the time-dependent nature of upwelling based on a series of high-resolution cross-shelf temperature sections.

[3] Although many aspects of coastal upwelling are captured by these two-dimensional models [Winant *et al.*, 1987; Wang, 1997; Chen and Wang, 1990], many observa-

tions clearly indicate that upwelling processes are often three-dimensional. Perhaps the most cited example is a summary by Smith [1981], who notes that while observations of wind-driven offshore transport in the upper layer off the American west and African coasts are consistent with Ekman's theory, the onshore transport at depth is not, and that this implies a divergence/convergence in the alongshore currents. Three-dimensional structure is also suggested in satellite-derived sea surface temperature imagery that emphasizes a rich alongshore structure characterized by offshore squirts and upwelling centers [Bernstein *et al.*, 1977; Traganza *et al.*, 1981; Glenn *et al.*, 1996]. Alongshore variability may be triggered by coastal promontories [Kosro, 1987] and the underlying bathymetry [Glenn *et al.*, 1996; Song *et al.*, 2001] as well as internal dynamics alone that can drive instabilities and produce coherent alongshore structure [Barth, 1994].

[4] While the classic textbook upwelling model highlights the cross-shelf flows, currents are predominately in the alongshore direction. This is particularly true in the nearshore where currents are highly polarized and aligned in the alongshore direction [Kosro, 1987]. This polarization makes estimates of the cross-shelf flows sensitive to the definition of the along-shelf direction. Nevertheless, while synoptic current maps show a complex flow field that rarely resembles the conceptual model, many of the idealized features do appear in the averaged fields [Kosro, 1987; Winant *et al.*, 1987; Munchow and Chant, 2000].



[5] *Munchow and Chant* [2000] provide a statistical description of wind-driven flows on New Jersey's inner shelf during the summer months when mean winds are upwelling favorable (to the north). During this period the mean currents have an appreciable offshore component in the surface with a weaker and noncompensating onshore transport at depth. Alongshore mean flows contain a downwind surface jet, similar to the thermal wind jet described by *Huyer* [1983] and *Kosro* [1987], and a subsurface flow in the opposite direction that is strongest near the coast. Flow reversals at depth have also been reported to occur along the U.S. west coast [*Winant et al.*, 1987; *Kosro*, 1987; *Huyer*, 1983]. *Kosro* [1987] indicates that this return flow can surface near the coast. Model hindcasts of the CODE observations indicate that the return flow is driven by an alongshore pressure gradient [*Chen and Wang*, 1990]. Flow reversals also occur as upwelling winds relax [*Wang*, 1997] or during times of appreciable wind stress curl [*Wang*, 1997]. These nearshore flow reversals occurred frequently during CODE and contributed significantly to the heat budget and emphasize that upwelling can be a fully three-dimensional process [*Send et al.*, 1987]. Of particular relevance to observations presented in this paper are results from numerical simulations by *Gan and Allen* [2002a, 2002b], who elucidate the dynamics of topographically driven flow reversal when upwelling winds relax. Specifically, they demonstrate that the flow reversals are driven by an adverse pressure gradient that develops downstream of coastal promontories.

[6] Many of these processes are evident in data collected during upwelling conditions along New Jersey's inner shelf. In particular, the development of a flow reversal during upwelling conditions appear to impact the development of a recurrent upwelling center in the vicinity of Rutgers University's Long-term Ecosystem Observatory (LEO) located on New Jersey's inner shelf (Figure 1). Note that the flow reversal discussed in this paper occurs during upwelling conditions in contrast to the aforementioned west-coast studies where flow reversals are often reported to occur during relaxation. The evolution of the flow reversal described in this paper is based on data collected from shipboard, moored, and remote platforms in July of 1998. This event typifies numerous upwelling events that have been observed along the New Jersey shelf over the last decade [*Glenn et al.*, 1996; *Munchow and Chant*, 2000; *Song et al.*, 2001]. For example, the temporal and spatial evolution of the event is similar to EOF analysis presented by *Munchow and Chant* [2000] where the phasing between mode 1 and mode 2 time series reveals a cyclonic rotating eddy with inshore flow reversals as upwelling winds relax. This structure is also apparent in the theoretical study by *Song et al.* [2001], a study motivated by the interaction between upwelling circulation and topographic variability on the New Jersey shelf. They revealed that topography enhances onshore transport of cold bottom fluid in the bottom Ekman layer downwind of topographic highs while reducing lower layer transport upwind of a high. This along-shelf structure was characterized in terms of a topographic perturbation velocity in the bottom Ekman layer that, like in our observations, contains a flow reversal at the coast.

[7] The New Jersey shelf becomes strongly thermally stratified during the summer months when surface to bottom temperature differences can exceed 15°C in 20 m of water. The stratification is characterized by a two-layer system separated by a sharp thermocline, generally less than 5 m in thickness. Upwelling occurs during the summer months in response to the prevailing summertime southwesterly winds driven by the Bermuda High. The cool upwelled water is supplied by the shoreward side of New York Bight's cold pool within which minimum summertime bottom temperatures off the New Jersey coast occur on the mid-shelf in the late summer due to advective processes [*Houghton et al.*, 1982]. In contrast, surface water temperature reaches a maximum during July. The combination of the supply of cold water to the cold pool and surface heating maintains strong stratification throughout the summer months.

[8] The data on which this paper is based were collected as part of an interdisciplinary study to investigate interactions between wind-driven circulation and primary production. The field program was conducted in July 1998 in the vicinity of LEO. LEO is located in one of three recurring upwelling centers that develop along the New Jersey coast in response to summertime southerly winds [*Glenn et al.*, 1996]. These upwelling centers occur to the north of topographic highs that are remnant river deltas. Topographic contours in Figure 1 contain one of these highs along the C-line and show that the high is associated with increased roughness. The rougher topography is due to larger ridge and swale features that are evident in the southern half of the figure.

## 2. Field Experiment

[9] The 1998 field experiment characterized the evolving three-dimensional structure of a coastal upwelling event. It was comprised of two ADCP moorings (Figure 1), a thermistor string, multiple shipboard ADCP/CTD sections that focused on two cross-shore sections, sea surface temperature from AVHRR imagery, and surface currents fields from a land-based CODAR system [*Kohut and Glenn*, 2003]. The offshore mooring was in 23 m of water. Velocity measurement spanned from 1.6 m above bottom to 20.6 mab (2.4 m below the surface) at a vertical resolution of 1 m. The inshore mooring was in 12 m of water with vertical resolution of 1 m from 1.6 mab to 10.6 mab (1.4 m below surface). The thermistor string at the offshore moorings contained a thermistor every 50 cm from 1.5 m below the surface to 19 m below the surface.

[10] Shipboard instrumentation included a 1200-kHz broadband RDI-ADCP towed abeam of the ship. The ADCP was operated in mode 1 and collected single ping data in 1-m bins. Astern of the ship we towed a Guildline minibat equipped with a CTD and fluorometer. Data from the minibat were screened to include only downcasts providing a horizontal resolution of 200–400 m. ADCP data were screened for excessive acceleration and averaged into 2-min ensembles, which, at our typical ship speed of 3 m/s, represents a 200-m footprint. Meteorological data were taken from the NOAA buoy off Delaware Bay, approximately 100 km from the site.

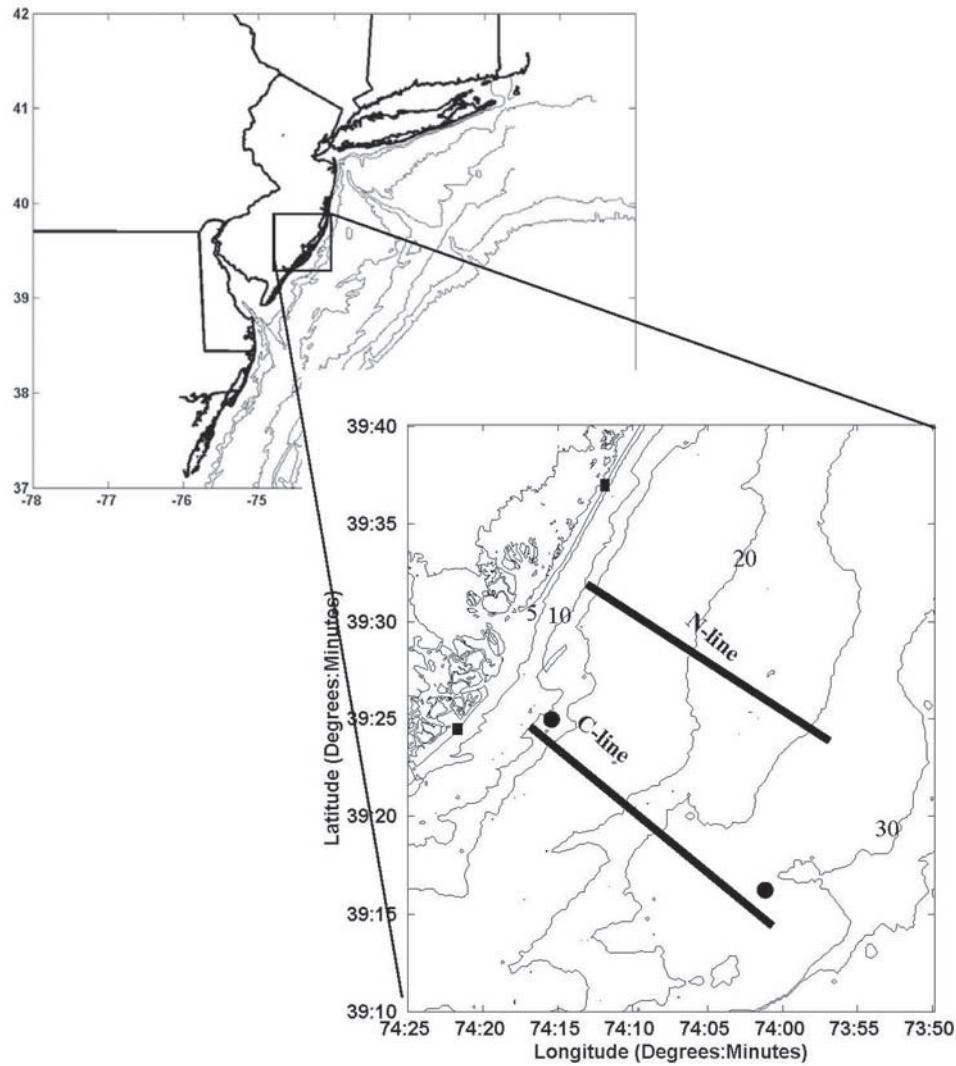


**Figure 1.** Study area. Shipboard transects are depicted by thick lines on lower map. Current meter locations are depicted as solid circles. LEO-15 is the inshore circle. Solid black squares depict the CODAR sites. Isobaths in the large-scale map are 15, 20, 40, 60, 80, 100, and 200 m. Isobaths in small-scale figure are in increments of 5 m.

[11] Time series of currents from the moorings and CODAR unit have been low-pass filtered with a cutoff period of 32 hours to remove tidal and inertial period motion. Tidal motion was removed from the towed ADCP data by a tidal model described below. Note that the detided shipboard ADCP data still contain tidal period motion not included in the tidal model, such as intermittent internal tides, and near-inertial motion. Inertial motion has been shown to at times dominate currents during upwelling periods at this location [Chant, 2001], but because our shipboard survey repeated sections 2–3 times inside of a tidal cycle, we can assess to what extent the results are aliased by tidal period motion not included in the tidal model.

[12] The coordinate system used in this paper defines  $x$  and  $y$  as the offshore and up-shelf directions, while  $u$  and  $v$  represent offshore and up-shelf flow. Up-shelf is defined

to the north, opposite to the direction of Kelvin wave propagation.

### 3. Tidal Model

[13] The depth-averaged shipboard ADCP data collected in July 1998 and July 1999 were fit to the  $M_2$  tidal constituent with a *Candela et al.* [1992] type method using a second-order polynomial for the cross-shore structure of the alongshore and cross-shore  $M_2$  tidal motion along lines C and N (Figure 2). To include the spring/neap modulation of amplitude and phase of the semidiurnal motion, we used a method similar to that described by *Signell and Geyer* [1991] whereby the horizontal structure of the tidal motion is determined by the shipboard data, and this horizontal structure is temporally modulated by spring/neap variability from a nearby fixed point time series. In our

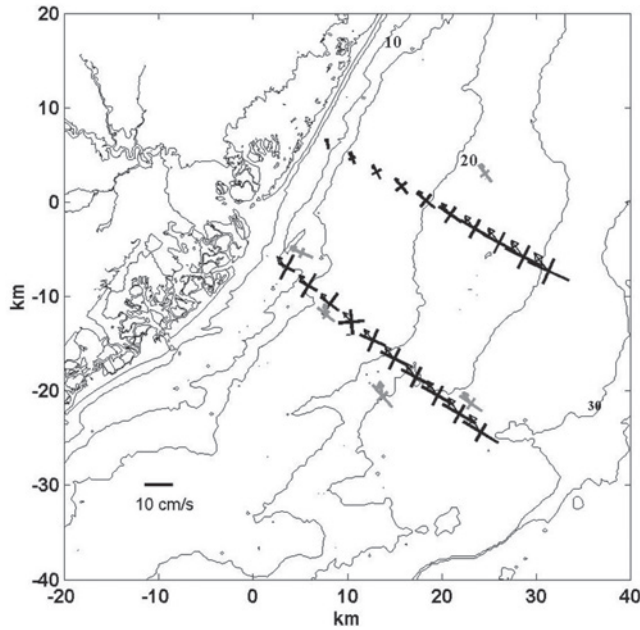


**Figure 2.** Depth-averaged semidiurnal tidal ellipses. Black ellipses are obtained from shipboard surveys. Shaded ellipses were obtained from moored instruments. Moorings from 1998 are the two just north of the C-line. Other moorings are from 1996. Arrows indicate the phase of the tide. Depth contours are in increments of 5 m.

case we used the depth-averaged current from the offshore mooring to modulate the amplitude and phase of the  $M_2$  tidal constituent obtained from the shipboard data. Specifically, the amplitude of the tidal motion was modulated by  $A(t)/A_{M2}$  where  $A(t)$  is the amplitude of the time series demodulated at the  $M_2$  frequency and  $A_{M2}$  is the least squares estimate of the depth-averaged  $M_2$  tidal motion at the mooring. Similarly, the phase of the  $M_2$  tide is modulated by the difference between the phase of the demodulated time series and the phase of the  $M_2$  tidal constituent at the mooring ( $\Delta\theta = \theta_{\text{dmd}} - \theta_{M2}$ ). Thus for the depth-averaged cross-shore motion the tidal motion is

$$U = \frac{A_{\text{dmd}}}{A_{M2}} \times A_i(x) \times \cos(\omega t + \theta_i(x) - \Delta\theta(t)), \quad (1)$$

where  $A_i(x)$  and  $\theta_i(x)$  are obtained from the second-order polynomial fit of the shipboard data, and the index  $i$  represents the fit along the C-line ( $i = 1$ ) and N-line ( $i = 2$ ). The alongshore semidiurnal motion is calculated in an identical fashion.

[14] The vertical structure of the tidal motion was determined with the offshore mooring as follows. The depth was transformed to a sigma coordinate system, and the depth-dependent tidal motion was characterized by the ratio of the depth-dependent  $M_2$  tidal amplitude to the depth-averaged  $M_2$  tidal amplitude (Figure 3, left panel) and the difference in phase between the depth-dependent and depth-averaged motion (Figure 3, right panel). The final step in the tidal model is to multiply the depth-averaged tidal model (1) by the depth-dependent structure to get the depth-dependent amplitude of the tidal motion. Similarly, the phase of the

depth-averaged motion is shifted by the vertical phase structure as is shown in Figure 3 (right panel).

[15] The leakage of the along-shelf flows into estimates of diurnal tidal motion made with the shipboard data was severe and likely due the fact that shipboard surveys were only 12 hours and do not cover the entire diurnal period. However, moored data from 1998 and 1996 indicate that there is little cross-shelf structure to the diurnal motion (Figure 4), and subsequently, diurnal motion in the tidal model is estimated by a least squares fit to the moored data. The modeled diurnal tide is based on data collected between days 190 and 210 from the offshore mooring. Thus the diurnal tidal model has a vertical structure, but no horizontal variability.

## 4. Results

### 4.1. Forcing

[16] We focus on a single upwelling event that occurred between July 20 and July 25 (days 201–206) in response to a 4- to 5-day period of upwelling-favorable winds (Figure 5). On the basis of winds from the NOAA buoy off Delaware Bay, we estimate the alongshore wind stress,  $\tau_{sy}$ , with a quadratic formulation  $\tau_{sy} = \rho_a C_d W_a |W|$ , where  $W_a$  is the alongshore wind speed,  $|W|$  is the wind's magnitude,  $\rho_a$  is the density of air ( $1.2 \text{ kg/m}^3$ ), and  $C_d = 1.2 \times 10^{-3}$  [Large and Pond, 1981]. The alongshore direction is defined by the orientation of the coastline (taken to be  $34^\circ$  east of north). The maximum alongshore wind stress of  $0.7 \text{ dynes/cm}^2$  occurred during day 200. Weak wind reversals occur on days 205–206 followed by weak upwelling-favorable winds up to day 210.

### 4.2. Surface Signature

[17] The response of this shallow, stratified shelf to the wind is rapid. On 21 July (day 202), 1 day after the

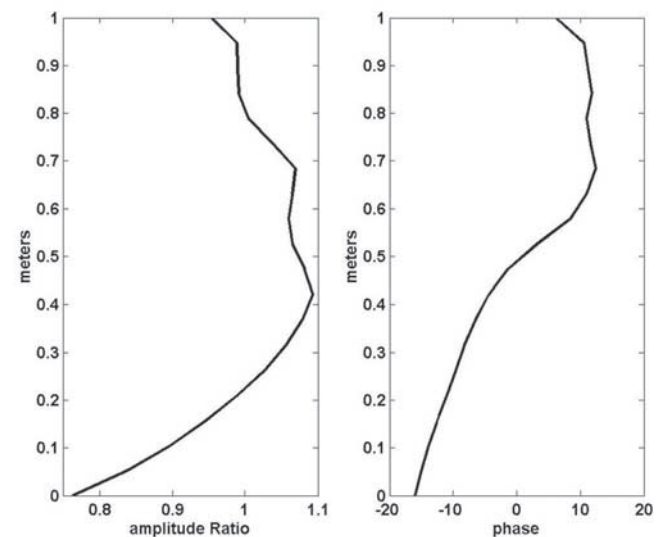


**Figure 3.** (top) Vertical structure of the ratio of the major axis of the depth dependent  $M_2$  tidal constituent to the major axis of the depth averaged  $M_2$  tidal motion from the offshore mooring. (bottom) Vertical phase structure of the  $M_2$  tide used in the tidal model defined as the difference between the depth-dependent and depth-averaged phase.



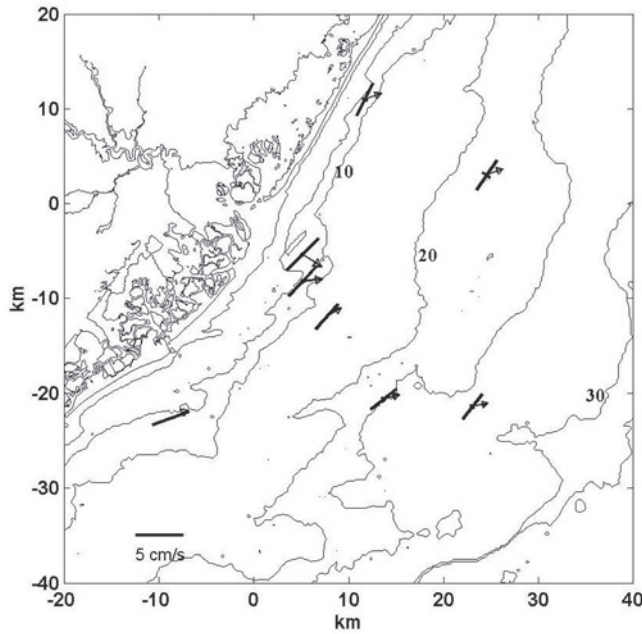


**Figure 4.** Depth-averaged diurnal tidal ellipses from moored data. Arrows indicate the phase of the tide. Depth contours are in increments of 5 m.

commencement of upwelling-favorable winds, AVHRR imagery indicates that cool water has surfaced at the coast and extends offshore just to the north of LEO (Figure 6). By 23 July the offshore extension of upwelled water has moved to the south, despite continued upwelling-favorable winds. On both days, low-passed CODAR data reveal cyclonically rotating surface current fields. On 21 July the center of recirculation is at  $39^{\circ}30'N$ ,  $74^{\circ}05'W$ . On 23 July (day 203) the feature has migrated to the south into the full view of the CODAR footprint with the center of recirculation located at  $39^{\circ}25'N$ ,  $74^{\circ}05'$ . Between these two images the center of recirculation has moved approximately 9 km in 45 hours, corresponding to an average speed of 5 cm/s. Both images reveal a strong nearshore upwind southerly flow of cool water that turns offshore over the rougher topography at the inshore side of the C-line. Unfortunately the CODAR unit was down due to a power outage during the onset of upwelling (18–19 July), so we are unable to depict the flow structure prior to the development of the nearshore jet.

[18] During the commencement of this upwelling event and subsequent spin-up of the nearshore-upwind jet, we

conducted numerous cross-shelf surveys along the N and C lines. On the basis of these sections, we describe in detail the spin-up of the nearshore upwind jet.

#### 4.3. Upwind Jet

[19] Cross-shelf sections of detided along-shelf currents and temperature obtained on 23 and 24 July are presented in Figure 7. Both figures show a nearshore subsurface jet that flows down-shelf with maximum flow speeds exceeding 30 cm/s. The highest velocities in the jet occur at approximately the  $18^{\circ}C$  isotherm. Isotherms in the jet are spread, suggestive of enhanced mixing in the jet or of a convergence of fluid in the thermocline. Offshore, the flow is to the north where up-shelf currents exceed 25 cm/s. The offshore jet is situated just seaward of upward sloping isotherms, and the sign and magnitude of the vertical shear is consistent with a thermal wind balance. Estimates of the terms  $f\frac{\partial v}{\partial z}$  and  $\frac{g\partial\rho}{\rho\partial x}$  from the 23 July section indicates that both are both approximately  $5 \times 10^{-6} s^{-2}$ , suggesting that the vertical shear is in near-thermal balance. A sharp thermocline 3–5 m thick separates these warm surface waters from a cold bottom mixed layer where temperatures are below  $12^{\circ}C$ . The flow reversal is not associated with a buoyant coastal current associated with fresh water flows from the Hudson River, as described by Yankovsky *et al.* [2000]. The salinity field (not shown) is characterized by a low saline lower layer (31.5 psu) and a fresh upper layer (30.5 psu) that is associated with shelf-wide two-layer structure rather than a coastal buoyant current.

[20] From the cross-shelf shipboard sections the volume of down-shelf transport is estimated (Figure 8) as  $\int_{Z_t}^{Z_b} \int_{X_1}^{X_2} \min(v_{dt}, 0) dx dz$ , where  $Z_t$  and  $Z_b$  are the top and bottom ADCP bin,  $X_1$  and  $X_2$  are distances from shore of the inshore and offshore sides of the section, and  $v_{dt}$  is the detided along-shelf flow and is defined as negative for down-shelf flow. Prior to day 201, sampling occurred only on the C-line, during which time down-shelf flows are weak. Up-shelf flows of approximately  $20,000 m^3/s$  are observed on both 16 and 17 July (not shown). On 20 July (day 201) we sampled the C-line once and the N-line twice. On all three transects the down-shelf transport is again weak. Up-shelf transport along the N-line is slightly less than  $20,000 m^3/s$ , while it exceeds  $30,000 m^3/s$  along the C-line (not shown). The spin-up of the jet occurs between days 201 and 202. On 21 July (day 202) the N-line was completed three times, from which three consistent estimates of down-shelf transport of  $\sim 30,000 m^3/s$  were made. The onset of down-shelf

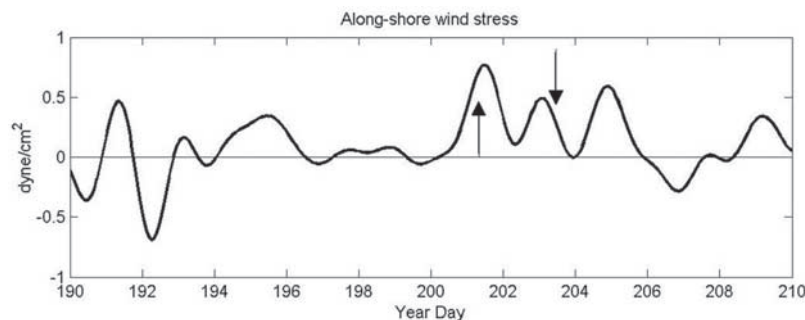


**Figure 5.** Alongshore wind stress. Arrows indicate times of current maps shown in Figure 6.



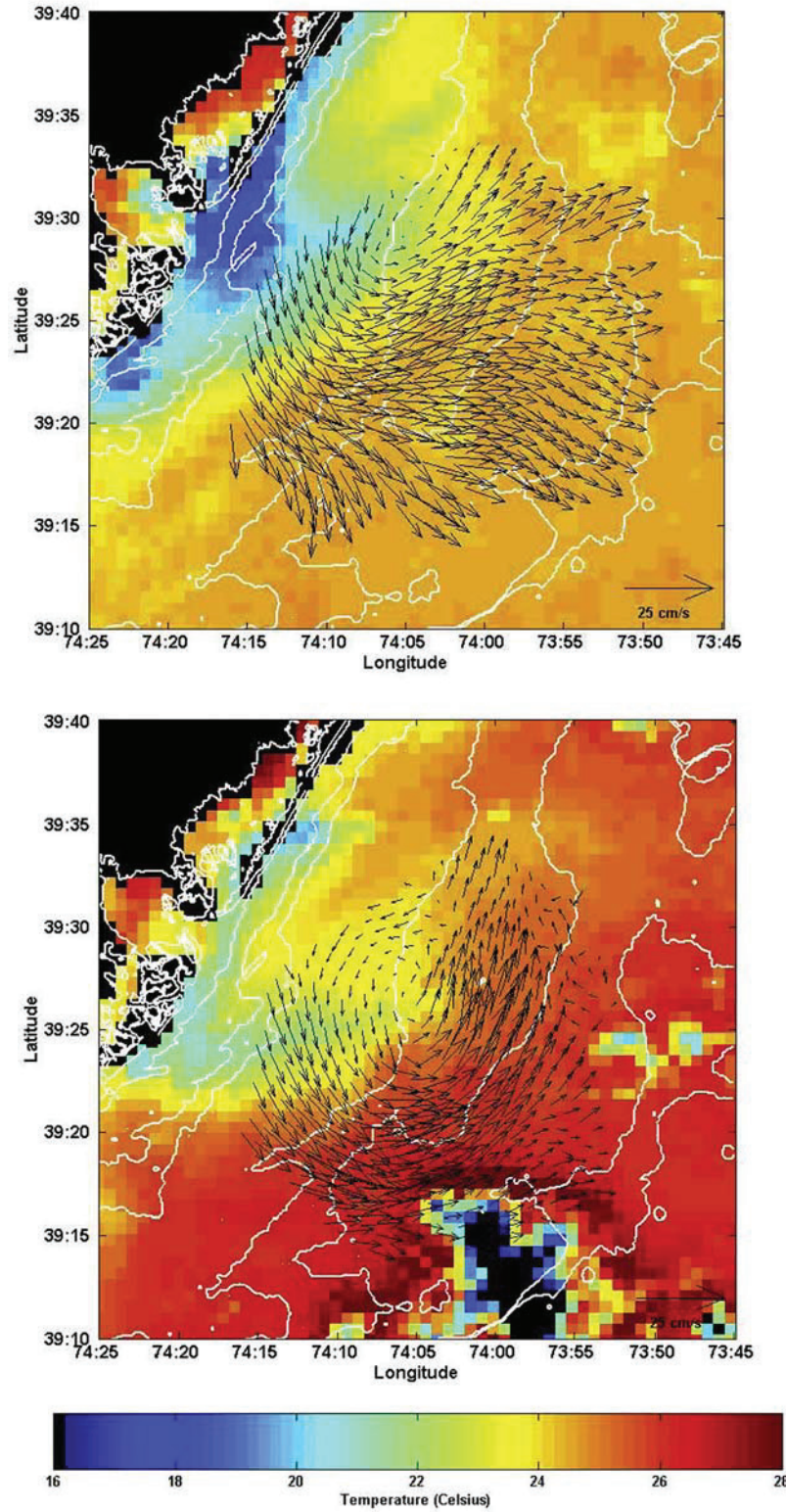


**Figure 6.** Overlay of sea-surface temperature from AVHRR and low-passed surface currents from CODAR for (top) 21 July 0820 GMT and (bottom) 23 July 1135 GMT.

transport coincides with the maximum along-shelf wind stress, and the spin-up time of the jet is on the order of an inertial period. This temporal evolution is depicted by the curve  $Q = 35,000 \times (e^{-t/T} - 1)$  in Figure 8 (bottom panel),

where  $T$  is the local inertial period (18.8 hours), and emphasizes that the spin-up of the jet occurs at the local inertial period. On subsequent days the upwind transport remains high, averaging nearly  $35,000 \text{ m}^3/\text{s}$ . The fact that

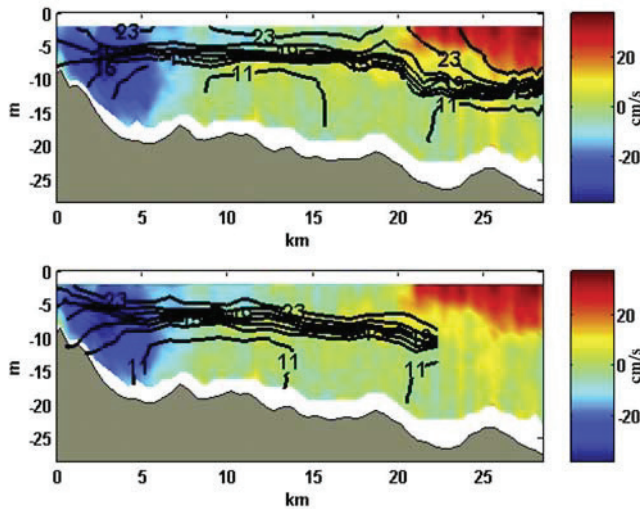


**Figure 7.** Detided along-shelf current speed and temperature from transects run along the N-line on (top) 23 July 1998 and (bottom) 24 July 1998.

transport estimates between repeat sections are fairly consistent indicates that these results are not significantly impacted by tidal period motion that remains in our estimates of the “detided” along-shelf flow.

#### 4.4. Moored Data

[21] The thermal structure at the offshore mooring during the entire upwelling event can be characterized as a two-layer system (Figure 9), where a surface mixed layer with temperatures exceeding  $22^{\circ}\text{C}$  is separated from the cold lower layer with temperatures below  $11^{\circ}\text{C}$ , by a thermocline 3–4 m thick. Low-passed cross-shore flows (colors in Figure 9) depict the strong offshore flow in the surface

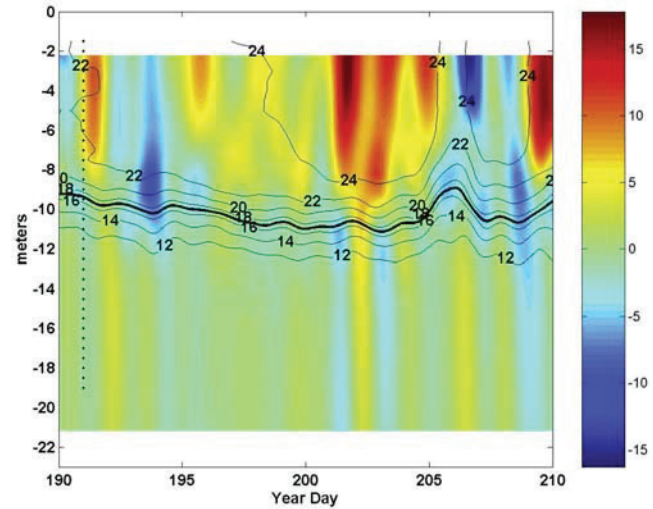


**Figure 9.** Low-passed temperature from a thermistor chain from the offshore mooring (contours) and low-passed cross-shelf current speed (colors). Positive current is directed offshore. Thick contour line depicts the  $17^{\circ}$  isotherm that is used to define the interface between the upper and lower layers. Black dots indicate position of thermistors.

layer following the onset of upwelling-favorable winds toward the end of day 200. Cross-shore flows are significantly weaker in the lower layer and oscillate with the wind variability. Selecting the  $17^{\circ}\text{C}$  isotherm as the interface (thick contour line in Figure 9) we calculated the low-passed along-shelf and cross-shelf transport per unit width ( $\text{m}^2/\text{s}$ ) in each layer and plot the result along with the alongshore wind stress in Figure 10 (the alongshore direc-

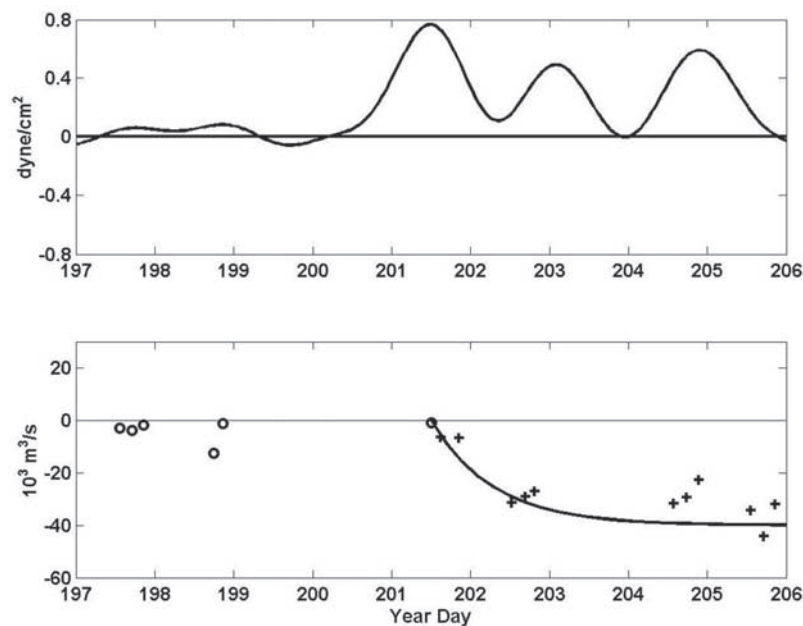


**Figure 8.** (top) Along-shelf wind stress (reproduction of Figure 4). (bottom) Down-shelf transport from detided shipboard ADCP sections. Circles are estimates made along the C-line; crosses are estimates made along the N-line.

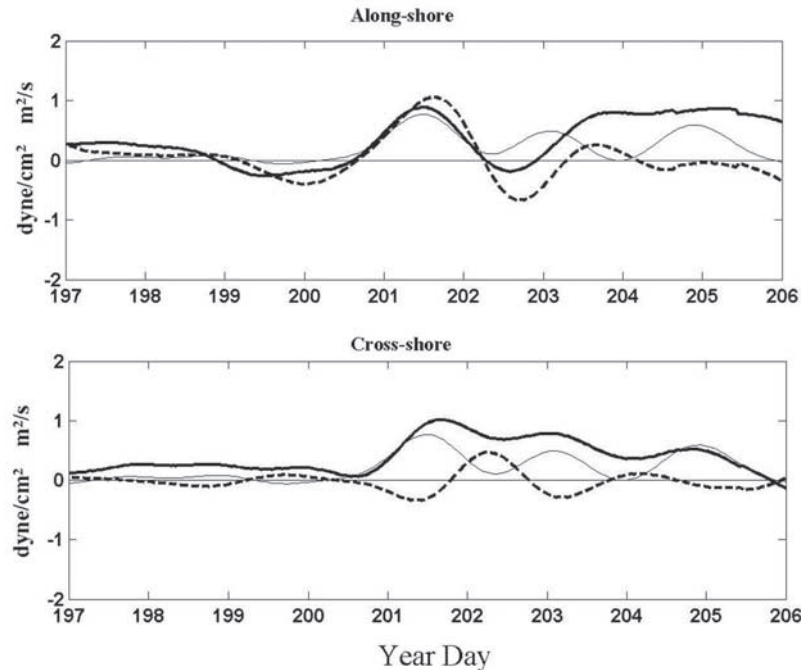


**Figure 10.** Upper and lower layer flow from the offshore mooring. (top) Along-shelf volume transport per unit width (thick solid line), lower layer (dashed line), and alongshore wind stress (thin solid line). (bottom) Cross-shelf volume transport per unit width in upper layer (thick solid line), lower layer (dashed line), and along-shelf wind stress (thin solid line).

tion for the current, as with the wind, is defined as  $34^\circ$  east of north). Note that these estimates are probably low by 20% due to the near-bottom and near-surface blanking regions. The initial pulse of along-shelf flow in the upper layer on day 201 occurs in phase with the along-shelf wind stress. In the lower layer, along-shelf current response lags the wind forcing. Following this pulse of wind, however, along-shelf currents do not follow the wind forcing, yet upper and lower layers tend to oscillate in a similar fashion, with the lower layer lagging the upper layer. In the cross-shelf direction (bottom panel in Figure 10) the surface layer begins to flow offshore as up-shelf wind accelerates on day 200. Offshore transport in the surface layer peaks shortly after a maximum in along-shelf wind stress. The offshore transport also modulates weakly in phase with the time-varying alongshore wind stress. Weak on-shelf transport is evident in the lower layer, but does not compensate the offshore transport in the surface. Furthermore, the cross-shelf oscillations in the lower layer are more pronounced than those in the upper layer. Cross-shore flow oscillations in the lower layer occur  $180^\circ$  out of phase with those in the surface layer. This is in contrast to oscillations in the alongshore flow where upper and lower layers fluctuations occur with only a small phase difference.

[22] The bottom panel in Figure 11 presents the time integral of the cross-shore transport in the upper and lower layer along with the time integral of  $\tau_{sy}/\rho f$ , which represents the cross-shore volume of fluid that Ekman dynamics would predict. To include the transport omitted in the near-surface and near-bottom blanking intervals, the layer transports shown in Figure 10 were increased by 20%. During the first day of upwelling-favorable winds, offshore transport in

the upper layer is consistent with that predicted by Ekman's theory: The thick and thin solid lines overlap. However, after day 201, offshore flow in the surface layer exceeds that predicted by Ekman's theory, and this timing coincides with initiation of the jet. We suggest that the increased transport in the surface layer is associated with the convergence of upwelled water driven by the flow reversal as it impinges on the shoaling and rougher topography to the south.

[23] At the inshore mooring the alongshore flow in the surface layer is initially to the north but begins to accelerate to the south after day 201 (Figure 12), coinciding with the jet's spin-up. The time lag between the appearance of the jet across N-line and fully developed southward flow at the inshore mooring is consistent with advective speeds of 5–10 cm/s. This speed is more consistent with the speed at which the eddy drifts southward, based on the CODAR imagery, than the observed currents in the jet, which exceed 30 cm/s.

[24] The cross-shore transport in the surface layer at the LEO ADCP is considerably weaker than at the offshore mooring (Figure 12). Furthermore, cross-shore flows here are directed offshore throughout the water column. This is in contrast to the offshore mooring where surface and bottom mean cross-shore flows are in opposite directions. The spatial structure of the mean cross-shore flow during the upwelling event is depicted in Figure 13 along with the cross-shelf transport predicted by Ekman theory (arrow above sea surface). At the offshore mooring the cross-shelf transport at the surface exceeds that predicted by Ekman's theory. At neither the inshore or offshore mooring, however, does the flow in the bottom layer compensate for the offshore flow in the upper layer, and consequently, at both



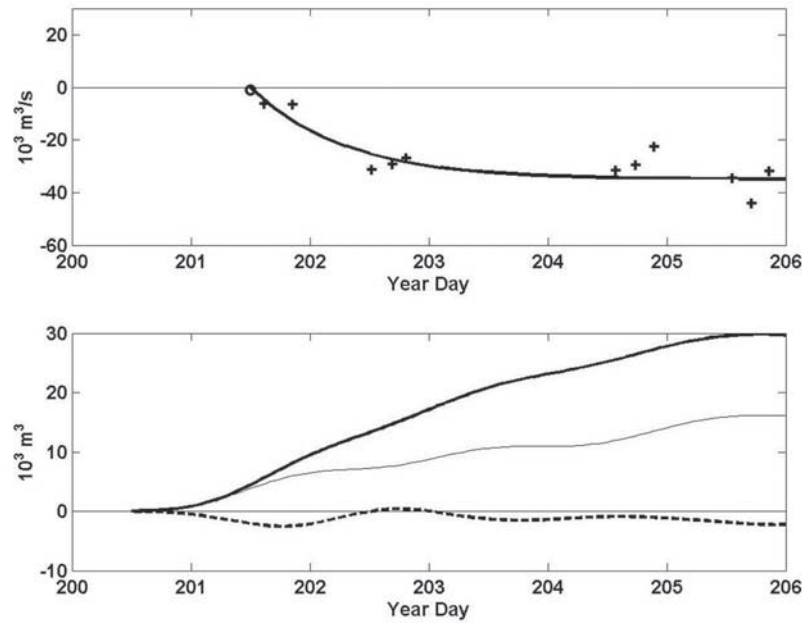


**Figure 11.** (top) Reproduction of Figure 9 but only plotting days 200–206. (bottom) Time integral of the cross-shelf transport in the upper layer (thick solid line) and lower layer (dashed line), and that predicted by Ekman's theory (thin solid line).

moorings, there is a significant time-mean depth-averaged offshore flow. The basic result does not change for defining the along-shelf direction based on the 10- to 20-km-scale topographic variability. This offshore flow must be maintained by a divergence in the alongshore flow. This divergence is a result of the trajectory of the jet that flows down-shelf along the N-line and veers offshore in the

vicinity of LEO. The mean cross-shelf flow from the two moorings indicate that the divergence in the upper layer is equal to the convergence in the lower layer, yet it corresponds to an upwelling velocity of approximately 1 m per day, significantly slower than what is required to drive the rapid upwelling response apparent in the AVHRR imagery. Rather, we suggest that much of the cool water in the

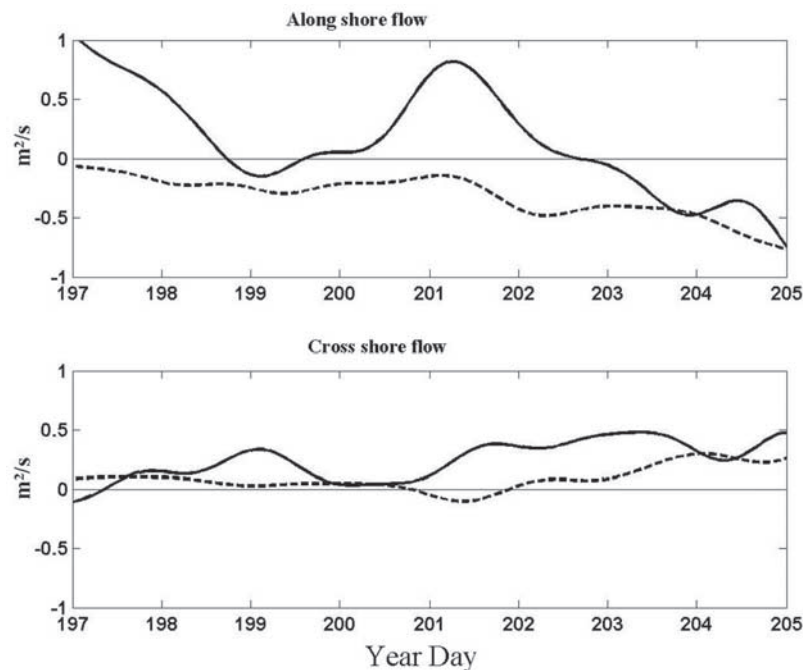


**Figure 12.** Upper and lower layer flow at LEO-15. (top) Along-shelf flow in upper layer (thick solid line) and lower layer (dashed line). (bottom) Cross-shelf flow in upper layer (thick solid line) and lower layer (dashed line).

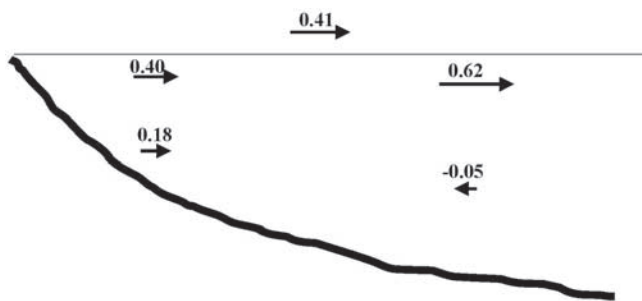


**Figure 13.** Schematic showing the mean cross-shelf transport per unit width ( $\text{m}^2/\text{s}$ ) in upper and lower layer during the upwelling event. The mean cross-shelf transport predicted by Ekman's theory is shown above surface.

upwelling center is fed by the nearshore jet of cool water that veers offshore in the vicinity of LEO.

## 5. Discussion

[25] We have characterized the temporal evolution of a flow reversal during upwelling conditions and the subsequent development of an upwelling center in the vicinity of LEO-15. In particular, moored observations reveal that offshore transport in the surface mixed layer is initially consistent with an Ekman response to an alongshore wind stress. However, flow in the lower layer, while directed onshore, does not compensate for the offshore transport in the surface layer. This imbalance is evident at the daily timescale as well as at the event timescale (3–5 days) and is consistent with the findings of *Munchow and Chant* [2000], indicating that even on the seasonal timescales the mass balance is three-dimensional on this inner shelf.

[26] The mass balance at the event timescale is impacted by a nearshore flow reversal that veers offshore as it impinges on a shoaling and rougher topography. The evolution of the flow reversal was captured by towed ADCP data showing that it commenced during maximum alongshore wind stress and spins up in an inertial period. The flow reversal's structure is characterized by a jet where maximum velocities exceed 30 cm/s in the interior of the water column. The jet is 5 km wide and transports  $\sim 20 \text{ km}^3/\text{s}$  of thermocline fluid to the south. An additional  $10\text{--}25 \text{ km}^3/\text{s}$  of down-shelf transport occurs offshore in the thermocline. As the jet spins up, the cross-shelf transport in the surface layer at the offshore mooring also increases. Prior to the flow reversal, off-shelf transport in the surface layer is consistent with Ekman transport, while following the flow reversal, offshore transport in the surface exceeds that predicted by Ekman's theory. Surface currents from CODAR indicate that the jet turns left and offshore as it impinges on the rougher topography at LEO-15. A similar veering of a coastal buoyant current has been observed at this location [*Yankovsky et al.*, 2000], and in the mean upwelling circulation pattern from CODAR [*Kohut et al.*, 2004].

[27] During this upwelling event, approximately  $10 \text{ km}^3$  of fluid has been transported southward across the N-line and toward the upwelling center. This fluid tends to be a combination of thermocline water on the inshore side and

colder lower layer water on the offshore side of the transect. This volume is approximately the volume of fluid contained in the southward drifting upwelling center observed with the AVHRR imagery on 23 July, assuming a mean water column depth of 15 m. Although upwelling is obviously associated with the onshore and upward movement of the western edge of the cold pool, we suggest that the down-shelf transport and offshore extension of the upwelling center is in part due to a convergence of the upwind nearshore jet as it veers offshore over the increasing rougher topography in the vicinity of LEO-15.

[28] Aspects of this structure are consistent with modeling results of *Song et al.* [2001]. Specifically, their results indicate that upwelled water is preferentially transported onshore downwind of a topographic high and forms a coastal current, opposed to the upwelling winds. This flow then turns offshore on the upwind side of the high where it competes with onshore flow in the bottom Ekman layer. On one hand, this is consistent with our observation of onshore flow in the bottom boundary layer that does not compensate the offshore flow in the surface layer. On the other hand, our observations indicate that the jet veers offshore upwind of the topographic high (Figure 6, top panel), and this differs from the *Song et al.* [2001] result that shows the nearshore return flow veering offshore south of the topographic high.

[29] The CTD sections indicate that the flow reversal is not associated with a buoyant current, and so the dynamics driving this differs from that described by *Yankovsky et al.* [2000] where fresh water from the Hudson's outflow impinged on the region. Rather we suggest that this flow reversal is driven by an adverse pressure gradient, similar to the modeling study by *Gan and Allen* [2002b], associated with flow curvature. Steerage of surface currents in this region by bottom topography is reported by *Kohut et al.* [2004] and apparent in surface current radar fields presented by *Chant* [2001]. Figure 14 presents idealized bottom topography used by *Song et al.* [2001] to depict topographic variability along the New Jersey shelf with a radius of curvature of 25 km. During the early phases of upwelling conditions, the up-shelf wind-driven flow meanders around these topographic features with a characteristic velocity of 0.15 cm/s [*Song et al.*, 2001; *Chant*, 2001; *Munchow and Chant*, 2000]. Assuming that the flow curvature ( $V^2/R$ ) is balanced by a cross-shelf barotropic pressure gradient ( $g_{\partial\eta/\partial x}$ ) ( $R = 25 \text{ km}$ ) results in a coastal setdown due to cyclostrophic forcing of approximately 0.4 cm at the topographic high and a coastal setup of the same magnitude where the flow curvature changes sign in the trough, 25 km to the north. Consequently, this would result in an alongshore sea surface slope of  $0.8 \text{ cm}/25 \text{ km} = 3 \times 10^{-7}$ . Note that while upwelling winds will drive a coastal setdown, it is the alongshore flow variability (i.e., flow curvature) that gives rise to the alongshore pressure gradients.

[30] An alongshore pressure gradient of a similar magnitude was revealed in EOF analysis of bottom pressure data collected here in 1996 [*Munchow and Chant*, 2000]. The first EOF mode, which contained nearly 95% of the variance, shows an alongshore barotropic pressure gradient that is enhanced on the shoreward side of the mooring array. During upwelling conditions the along-shelf pressure gra-

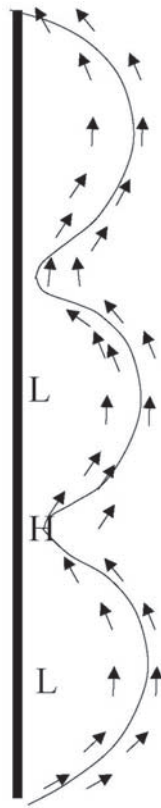


**Figure 14.** Schematic of flow bathymetry and flow curvature after Song *et al.* [2001].

dient is characterized by a sea level that slopes down-shelf 1.5 cm across the 40-km mooring array corresponding to a slope of approximately  $4 \times 10^{-7}$  and similar to the one inferred from the conceptual model (Figure 14).

[31] This estimate of the sea surface slope is of the right order to accelerate the flow reversal. Assuming an initial momentum balance between acceleration and the adverse pressure gradient, we can estimate that the down-shelf surface slope must be at least  $\frac{\partial v}{\partial x} g^{-1}$ , where  $v$  is the characteristic flow in the jet. The shipboard sections show that the flow reversal accelerates from rest to 20 cm/s in an inertial period (18.8 hours), and this requires a surface slope to the south of  $3 \times 10^{-7}$ , consistent with our other estimates of the adverse pressure gradient. Finally, after the jet has reached steady state, a balance between the pressure gradient and friction would yield a slope of  $\frac{\tau_{by}}{gH} = \frac{C_d v^2}{gH}$ , where  $H = 15$  m,  $v$  is 0.20 m/s, and the bottom drag coefficient  $C_d = 2 \times 10^{-3}$  yields a slope of  $5.4 \times 10^{-7}$ , again consistent in magnitude to the other estimates of the alongshore slope.

[32] What causes the jet to veer offshore and detach from the topography? Laboratory experiments by Klinger [1994] indicate that flow will separate from topography when the radius of curvature is less than  $v/f$ . However, during the event described in this paper,  $v/f$  is approximately 2000 m while the radius of curvature of the major bathymetric features are at least an order of magnitude larger. Yet other topographic scales are present. Specifically, a 5-km-scale ridge/swale topography with undulations spanning over 25% of the water column is superimposed on the topo-

graphic high (Figures 15a and 15b). One impact of the shoaling and rougher topography would be increased bottom friction due to wave-current interaction, because bottom wave orbital velocities will be larger over the rough topographic high south of LEO than orbital velocities north of LEO. In addition, large ripples form in response to the wave motion in these sandy sediments [Traykovski *et al.*, 1999].

[33] During this upwelling and relaxation event the period of surface gravity waves was typically 6 s, significant wave heights were 0.5–1 m, and bottom orbital velocities at LEO (12 m of water) were 20 cm/s (Figure 16). We estimate near-bottom wave orbital velocities on a transect north of LEO and transect south of LEO based on the dispersion relationship  $\omega^2 = gk \tanh(kH)$ , [Leblond and Mysak, 1978], where  $\omega$  and  $k$  are the wave's frequency and wave number and  $g$  and  $H$  are gravity and water column depth. For 6-s waves the bottom orbital velocities ( $\omega A / \sinh(kH)$  where  $A$  is the waves amplitude) are 50% higher and wave kinetic energy is twice as large on the southern line as on the northern line (Figures 15c and 15d). Furthermore, these increased near-bottom velocities would also be augmented by increased tidal currents near the coast in the vicinity of the inlet in contrast to the weaker tidal currents near the coast to the north (Figure 2).

[34] Traykovski *et al.* [1999] suggests that over 75% of the time, wave orbital velocities are large enough to initiate sediment motion and form wave orbital ripples at LEO. For 6- to 8-s-period waves [Traykovski *et al.*, 1999, Figure 18], initiation of sediment motion occurs with significant wave heights of 0.5–1 m. During the upwelling event described in this paper, wave conditions are near this transitional region and thus we expect ripples to form, particularly in the shoaling depths along the southern reaches of our study where wave orbital bottom velocities are larger. Furthermore, Styles and Glenn [2002] show that the largest ripples, often exceeding 10 cm, occur at this transitional point. From the law-of-the-wall scaling the coefficient of quadratic bottom drag  $C_d = (\kappa / \ln(z/z_0))^2$  can be estimated. In the absence of sand ripples and wave-current interaction, typical  $z_0$  are less than 1 mm, while in the shallower depths the combination of ripple formation and a wave bottom boundary layer can produce an apparent  $z_0$  exceeding 20 cm [Styles and Glenn, 2002] corresponding to a factor of 10 increase in the bottom drag coefficient. In an environment where bottom drag is a dominant term in the momentum balance [Lentz *et al.*, 1999] an order of magnitude increase in the bottom drag coefficient must impact the flow structure. We suggest that increased drag will cause the flow to decelerate and drive the alongshore convergence characterized by the increased cross-shelf motion that we observe in the moored data.

[35] Form drag over the larger-amplitude ridge and swale topography would also augment bottom drag there. MacCready and Pawlak [2001] indicate that form drag over a single ridge can dominate the drag and drive an offshore transport. Since bottom friction is a first-order term in the along-shelf momentum balance on the inner shelf [Lentz *et al.*, 1999], a dramatic increase in drag over the rougher topography could reduce alongshore velocities and drive an offshore flow due to this convergence. This frictional increase in drag would be further aug-

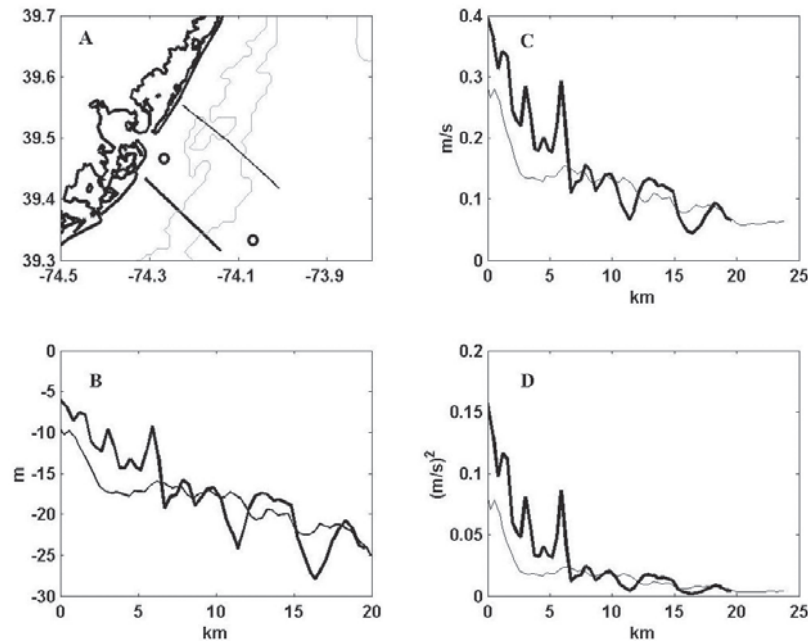


**Figure 15.** (a) Map showing cross-shelf sections used in ensuing three panels. In all figures, the thick line depicts the southern transect and the thin line depicts the northern transect. (b) Depth along transects shown in Figure 13 (top panel). (c) Wave orbital velocities at the bottom assuming a 6-s 1-m wave and a wave dispersion from *LeBlond and Mysak* [1978]. (d) Kinetic energy of wave orbital velocity.

mented by increased bottom friction associated with increased wave/current interaction and ripple formation over the ridges.

## 6. Conclusions

[36] With moored, shipboard, and remotely sensed data we have characterized the temporal evolution of a flow

reversal during upwelling conditions and the subsequent development of an upwelling center on New Jersey's inner shelf. The flow reversal was initiated after a peak in upwelling-favorable winds and spins up in an inertial period. The flow reversal veers offshore as it impinges upon shoaling and rougher topography to the south and feeds a growing upwelling center. Moored data indicate that while offshore transport in the surface layer was initially

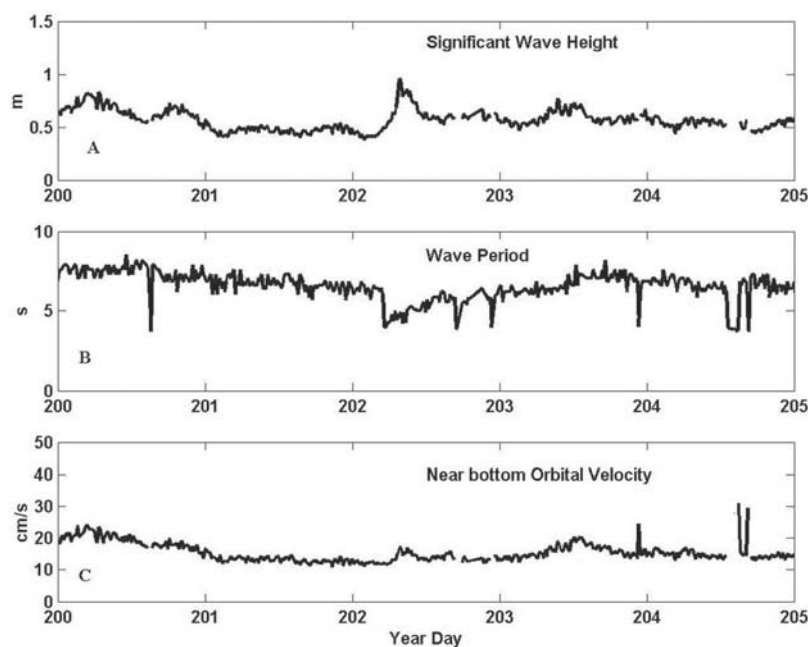


**Figure 16.** Wave parameters measured at LEO-15. (a) Significant wave height. (b) Peak wave period. (c) Bottom orbital wave velocity.



consistent with Ekman's theory, as the flow reversal spins up, the offshore transport in the surface layer exceeds the Ekman transport. The three dimensionality of the upwelling circulation is further emphasized by the fact that onshore flow in the bottom Ekman layer at the mooring site never compensates for the offshore transport in surface layer. The transport of fluid associated with the flow reversal is of the same order of magnitude as the volume of fluid in the evolving upwelling center, suggesting that the growth of the upwelling center is due to convergences in the alongshore flow rather than in the cross-shore flow. Estimates of alongshore pressure gradients required to maintain the flow curvature around the topography along the New Jersey shelf, as characterized by Song *et al.* [2001], are similar to those calculated in EOF analysis of bottom pressure records presented by Munchow and Chant [2000]. Furthermore, these estimates of the alongshore pressure gradient are consistent with both the pressure gradient required to spin up the flow reversal and maintain a steady flow when the pressure gradient is eventually balanced by friction. We further speculate that increased friction, due to both enhanced wave/current interactions and form drag, over shoaling and rougher topography causes the alongshore flow in the jet to converge and drive the flow offshore where it feeds a growing upwelling center. Insofar as the ridge and swale topography impacts the larger-scale dynamics, more detailed bathymetric data may be required to faithfully model this system.

[37] **Acknowledgments.** The authors acknowledge funding from the Office of Naval Research, the National Ocean Partnership Program (NOPP), and the Mid-Atlantic Bight National Undersea Research Center. Six of the current meter moorings used to generate the tidal model were deployed in 1996 as part of a National Science Foundation grant OCE-95-2839 of which Andreas Munchow, Rich Garvine, and Scott Glenn were the principal investigators. We thank Jennifer Bosch and Mike Crowley for the processing and plotting of AVHRR and CODAR data. We also thank two anonymous reviewers whose insights and comments have greatly improved this paper.

## References

- Austin, J. A., and J. A. Barth (2002), Variation in the position of the upwelling front on the Oregon shelf, *J. Geophys. Res.*, **107**(C11), 3180, doi:10.1029/2001JC000858.
- Barth, J. A. (1994), Short wavelength instabilities on coastal jets and fronts, *J. Geophys. Res.*, **99**, 16,095–16,105.
- Bernstein, R. L., L. Breaker, and R. Whitner (1977), California Current eddy formation, *Science*, **195**, 353–359.
- Candela, J., R. C. Beardsley, and R. Limeburner (1992), Separation of tidal and subtidal currents in ship-mounted acoustic Doppler current profiler observations, *J. Geophys. Res.*, **97**, 769–788.
- Chant, R. J. (2001), Evolution of near-inertial waves during an upwelling event on the New Jersey inner shelf, *J. Phys. Oceanogr.*, **31**, 746–764.
- Chen, D., and D. P. Wang (1990), Simulating the time-variable coastal upwelling during CODE 2, *J. Mar. Res.*, **48**, 335–358.
- Gan, J. P., and J. S. Allen (2002a), A modeling study of shelf circulation off northern California in the region of the Coastal Ocean Dynamics Experiment: 2: Simulations and comparisons with observations, *J. Geophys. Res.*, **107**(C11), 3184, doi:10.1029/2001JC001190.
- Gan, J. P., and J. S. Allen (2002b), A modeling study of shelf circulation off northern California in the region of the Coastal Ocean Dynamics Experiment: Response to relaxation of upwelling favorable winds, *J. Geophys. Res.*, **107**(C9), 3123, doi:10.1029/2000JC000768.
- Glenn, S. M., M. F. Crowley, D. B. Haidvogel, and T. S. Song (1996), Underwater observatory captures coastal upwelling events off New Jersey, *Eos Trans. AGU*, **77**, 233, 236.
- Houghton, R. W., R. Schlitz, R. C. Beardsley, B. Butman, and J. L. Chamberlin (1982), The Middle Atlantic Bight cold pool: Evolution of the temperature structure during summer 1979, *J. Phys. Oceanogr.*, **12**, 1019–1029.
- Huyer, A. (1983), Coastal upwelling in the California current system, *Prog. Oceanogr.*, **12**, 259–284.
- Klinger, B. A. (1994), Inviscid current separation from rounded cape, *J. Phys. Oceanogr.*, **24**, 1805–1811.
- Kohut, J. T., and S. M. Glenn (2003), Improving HF radar surface current measurements with measured antenna beam patterns, *J. Atmos. Oceanic Technol.*, **20**, 1303–1316.
- Kohut, J. T., S. M. Glenn, and R. J. Chang (2004), Seasonal current variability on the New Jersey inner shelf, *J. Geophys. Res.*, **109**, C07S07, doi:10.1029/2003JC001963.
- Kosro, P. M. (1987), Structure of the coastal current field off northern California during the Coastal Ocean Dynamics Experiment, *J. Geophys. Res.*, **92**, 1637–1654.
- Large, W. G., and S. Pond (1981), Open ocean momentum flux measurements in moderate to strong winds, *J. Phys. Oceanogr.*, **11**, 324–336.
- LeBlond, P. H., and L. A. Mysak (1978), *Waves in the Ocean*, 602 pp., Elsevier Sci., New York.
- Lentz, S. J., and J. H. Trowbridge (1991), The bottom boundary layer over the northern California shelf, *J. Phys. Oceanogr.*, **21**, 1186–1201.
- Lentz, S., R. T. Guza, S. Elgar, F. Feddersen, and T. H. C. Herbers (1999), Momentum balances on the North Carolina inner shelf, *J. Geophys. Res.*, **104**, 18,205–18,226.
- MacCready, P., and G. Pawlak (2001), Stratified flow along a corrugated slope: Separation drag and wave drag, *J. Phys. Oceanogr.*, **31**, 2824–2839.
- MacCready, P., and P. B. Rhines (1993), Slippery bottom boundary layers on a slope, *J. Phys. Oceanogr.*, **23**, 5–22.
- Munchow, A., and R. J. Chant (2000), Kinematics of inner shelf motion during the summer stratified season off New Jersey, *J. Phys. Oceanogr.*, **30**, 247–268.
- Send, U., R. C. Beardsley, and C. D. E. Winant (1987), Relaxation from upwelling in the coastal ocean dynamics experiment, *J. Geophys. Res.*, **92**, 1683–1698.
- Signell, R. P., and W. R. Geyer (1991), Transient eddy formation around headlands, *J. Geophys. Res.*, **96**, 2561–2575.
- Smith, R. L. (1981), A comparison of the structure and variability of the flow field in three coastal upwelling regions: Oregon, northwest Africa, and Peru, in *Coastal Upwelling, Coastal Estuarine Stud.*, vol. 1, edited by F. A. Richards, pp. 108–118, AGU, Washington, D. C.
- Song, Y. T., D. B. Haidvogel, and S. M. Glenn (2001), Effects of topographic variability on the formation of upwelling centers off New Jersey: A theoretical model, *J. Geophys. Res.*, **106**, 9223–9240.
- Styles, R., and S. M. Glenn (2002), Modeling bottom roughness in the presence of wave-generated ripples, *J. Geophys. Res.*, **107**(C8), 3110, doi:10.1029/2001JC000864.
- Traganza, E. C., J. C. Conrad, and L. C. Breaker (1981), Satellite observations of a cyclonic upwelling system and giant plume in the California Current, in *Coastal Upwelling, Coastal Estuarine Stud.*, vol. 1, edited by F. A. Richards, pp. 228–241, AGU, Washington, D. C.
- Traykovski, P., A. E. Hay, J. D. Irish, and J. F. Lynch (1999), Geometry, migration and evolution of wave orbital ripples at LEO-15, *J. Geophys. Res.*, **104**, 1505–1524.
- Trowbridge, J. H., and S. J. Lentz (1991), Asymmetric behavior of an oceanic boundary layer over a sloping bottom, *J. Phys. Oceanogr.*, **21**, 1171–1185.
- Wang, D. P. (1997), Effects of small-scale wind on coastal upwelling with application to Point Conception, *J. Geophys. Res.*, **102**, 15,555–15,570.
- Winant, C. D., R. C. Beardsley, and R. E. Davis (1987), Moored wind, temperature and current observations made during Coastal Ocean Dynamics Experiments 1 and 2 over the northern California continental shelf and upper slope, *J. Geophys. Res.*, **92**, 1569–1604.
- Yankovsky, A. E., R. W. Garvine, and A. Munchow (2000), Mesoscale currents on the inner New Jersey shelf driven by the interaction of buoyancy and wind forcing, *J. Phys. Oceanogr.*, **30**, 2214–2230.

R. J. Chant, S. Glenn, and J. Kohut, Institute of Marine and Coastal Science, Rutgers University, 74 Dudley Road, New Brunswick, NJ 08901, USA. (chant@imcs.rutgers.edu)





## Seasonal current variability on the New Jersey inner shelf

Josh T. Kohut, Scott M. Glenn, and Robert J. Chant

Institute of Marine and Coastal Sciences, Rutgers University, New Brunswick, New Jersey, USA

Received 16 May 2003; revised 7 November 2003; accepted 12 March 2004; published 31 July 2004.

[1] The well-sampled ocean off the coast of New Jersey provides a data-rich environment in which to study ocean current variability over the inner shelf. Using a year-long HF radar data set, complemented with in situ and meteorological observations, the annual- and seasonal-scale variabilities are examined. The hydrographic variability of the inner shelf off New Jersey is largely bimodal between summer stratification and winter mixing. An annual oceanographic and atmospheric data set was separated into these two regimes. The influence of stratification is evident through a relatively steady current response strongly correlated with the wind during the stratified season and a more variable response less correlated with the wind during the mixed season. When the water column is mixed, the influence of the local topography on the surface current variability is dependent on the slope, with a tendency for the variability to be more aligned with steeper topography. **INDEX TERMS:** 6959 Radio Science: Radio oceanography; 4512 Oceanography: Physical: Currents; 4520 Oceanography: Physical: Eddies and mesoscale processes; 4536 Oceanography: Physical: Hydrography; 4572 Oceanography: Physical: Upper ocean processes; **KEYWORDS:** coastal dynamics, HF radar

**Citation:** Kohut, J. T., S. M. Glenn, and R. J. Chant (2004), Seasonal current variability on the New Jersey inner shelf, *J. Geophys. Res.*, 109, C07S07, doi:10.1029/2003JC001963.

### 1. Introduction

[2] The Middle Atlantic Bight (MAB) has been a regional focus of coastal research since the early 1900s. *Beardsley and Boicourt* [1981] present a literature review of the estuarine and coastal circulation studied from Cape Cod, Massachusetts south to Cape Hatteras, North Carolina. Early observations described by *Bigelow* [1933] and *Bigelow and Sears* [1935] show the hydrography of the MAB has a strong seasonal cycle. Typically strong stratification, brought on by warmer temperatures and increased freshwater runoff, exists beginning in the early spring and continuing through the summer. This stratification is broken down in the fall and early winter by strong storms and cooler temperatures. The first dynamical model for the MAB showed a southwest drift of shelf and slope waters from Cape Cod toward Cape Hatteras [*Svedrup et al.*, 1942]. *Beardsley and Winant* [1979] show numerically that the southwest flow of this cold glacial water is primarily driven as a boundary current connected to the larger-scale circulation of the western North Atlantic Ocean. *Chapman and Beardsley* [1989] also suggest that the origin of the shelf water is from glacial melt along the southern Greenland coast that flows south to the MAB as a buoyant coastal current. Early on, *Miller* [1952] found that there was strong variability about this mean drift in the form of eddies and current filaments. Improved technology enabled more long-term measurements of currents, water temperature and salinity, and meteorological forcing in the 1960s. *Beardsley and Boicourt* [1981] describe much of the work from these

longer time series, confirming that transient currents modulate the mean southwest drift.

[3] The focus of dynamical research in the 1970s shifted from the mean southwest flow to the current variability. *Beardsley et al.* [1976] suggest that the current variability of the MAB is mostly wind-driven. *Saunders* [1977] shows that the wind forcing driving this variability is predominately from the west/northwest except in the summer months when the wind is typically from the southwest. The typical timescale of the wind forcing is on the order of 2–10 days [*Moore et al.*, 1976]. On the basis of observations, *Ou et al.* [1981] suggest that the variability is composed of a wind forced component and a larger-scale free wave component that is not correlated with the wind and propagates downshelf. Modeling studies also suggest that these current fluctuations do have a local and nonlocal response. The local response is related to local geometry, topography and forcing and the nonlocal response is due to forcing “distant in time and space” [*Beardsley and Haidvogel*, 1981].

[4] More recent work in the MAB focused on the locally forced variability, particularly in the summer months when the water column is strongly stratified. The strongest signal typically observed along the New Jersey coast during the summer stratification season is coastal upwelling/downwelling. Traditionally, upwelling studies have focused on eastern boundaries such as the Peruvian coast [*Brink et al.*, 1980], coastal waters off California [*Narimousa and Maxworthy*, 1987] and Oregon [*Halpern*, 1976] as well as western Africa [*Halpern*, 1977]. A series of observational and numerical studies of the coastal ocean focused on the region off the Northern California coast [*Beardsley and Lentz*, 1987]. The Coastal Ocean Dynamics Experiment

(CODE) looked at both the local and regional response of the coastal ocean to atmospheric and freshwater forcing. *Davis and Bogden* [1989] describe the difference seen in the current response over a deep (greater than 60 m) and shallow (less than 60 m) shelf. They suggest that the geostrophic response seen over the deep shelf breaks down over the shallow shelf where frictional surface layers extend all the way to the bottom. More recently, upwelling regions on the eastern continental coasts have been identified. These include the coast of Nova Scotia [*Barth*, 1994] and the North Carolina coast [*Austin*, 1999].

[5] The shelf waters off the New Jersey coast offer a slightly different context to study upwelling. Most of the upwelling research outlined above has focused on regions with narrow continental shelves adjacent to very deep slope waters. The shelf waters off the coast of New Jersey, on the other hand, are characterized by a relatively wide continental shelf with slope waters about 200 km offshore. The strong summer stratification over the shallow shelf complemented with generally alongshore winds make this region subject to frequent upwelling/downwelling events. Using 50 years of temperature data from Cape Cod to the Florida Keys, *Walford and Wicklund* [1968] describe a cold pool of water on the MAB continental shelf. The cell, which is composed of water less than 8°C, is trapped below the thermocline by the highly stratified ocean during the spring and summer [*Houghton et al.*, 1982; *Hicks and Miller*, 1980]. *Hicks and Miller* [1980] also observed that meteorological forcing, if persistent, has the potential to move the western boundary of the cell nearshore and surface along the New Jersey coast. After the annual cycle, the largest fluctuation in sea surface temperature along the New Jersey coast is due to coastal upwelling/downwelling (S. M. Glenn et al., Biogeochemical impact of summertime coastal upwelling in the Mid-Atlantic Bight, submitted to *Journal of Geophysical Research*, 2003, hereinafter referred to as S. M. Glenn et al., submitted manuscript, 2003). While the upwelling observed along the New Jersey coast may initially appear uniformly distributed, after a period of days the cold water develops into distinct upwelling centers. Along the southern New Jersey coast, three upwelling centers develop about 50 km apart and are collocated with three areas of recurrent bottom hypoxia [*Glenn et al.*, 1996]. Using numerical models [*Glenn et al.*, 1996] and analytical simulations [*Song et al.*, 2001], both with ideal topography, the recurrent upwelling centers are shown to be the direct result of the interaction of surface wind forcing and local bathymetry. The centers are found both in models and observations to form on the downwind side of topographic highs and are composed of a nearshore cyclonic circulation cell bounded by the coast onshore and a downwind alongshore jet offshore [*Glenn et al.*, 1996; *Song et al.*, 2001]. One recurring center forms in this study site offshore of Tuckerton, New Jersey.

[6] Additional research in this region has looked at both the sea level and current response to short wind events during the highly stratified summer season. For example, *Yankovski and Garvine* [1998] document a strong interaction between the wind-forced response and a coastal buoyant jet driven by fresh Hudson River outflow during a very wet year. They describe an intensification of the wind-driven currents in the buoyant water as it extends offshore.

Additionally, *Münchow and Chant* [2000] show that the vertical and horizontal variability of the subinertial response to an alongshore wind stress are characterized by a coupling between wind forced and buoyancy regimes that rotates counterclockwise with depth. *Chant* [2001] focuses on the near-inertial band of the wind driven response. The energy within this band is initially uniform across the surface and propagates into the thermocline within two inertial periods.

[7] This paper examines the local response of the surface current fields to the local wind forcing over longer seasonal scales. As the summer months pass and the cold winter sets in, the stratification sharply decreases and the forcing changes from light summer breezes to strong winter storms. This study uses spatial time series observations from an HF radar and a bottom-mounted ADCP to describe the structure of the three-dimensional response to local forcing. Since stratification varies significantly on seasonal scales, analysis is performed separately on stratified and unstratified conditions. The role of the local forcing and topography also influence the local dynamics on seasonal timescales.

## 2. Instrumentation

[8] The 25 MHz CODAR-type HF radar network deployed around Tuckerton consists of two remote sites located in Brant Beach and Brigantine, New Jersey (Figure 1). Using Doppler theory, each site measures the radial components of the ocean surface velocity directed toward or away from the site [*Crombie*, 1955; *Barrick*, 1972; *Barrick et al.*, 1977]. Since the systems are using surface gravity waves to estimate these velocity components, the measured currents at this frequency are the weighted average of the currents within the upper one meter of the water column [*Stewart and Joy*, 1974]. The sites were first deployed along the southern New Jersey coast in May 1998 as part of a coastal predictive skill experiment. Since this 3-month test deployment, the two sites were redeployed in May 1999 and continue to operate in real-time. Radial component velocities measured at the two sites are combined into hourly total surface current maps. The dynamical study discussed here focuses on surface fields measured between May 1999 and May 2000. This time span was selected because it includes periods with both strongly stratified and mixed water columns and the stratified period is subject to several upwelling/downwelling events. In addition, the spring and summer of 1999 were anomalously dry, minimizing the freshwater contribution to the local circulation.

[9] All data were processed using measured antenna beam patterns as described by *Kohut and Glenn* [2003]. This technique was demonstrated to produce the best comparison with concurrent in situ current meter data. The radial data were combined into hourly averaged total vector maps on a fixed grid using the CODAR Ocean Sensors software package. The entire record at each grid point was detided using a least squares fit of the five strongest constituents ( $M_2$ ,  $S_2$ ,  $N_2$ ,  $K_1$ , and  $O_1$ ) to the raw time series data. The subtidal data were then low-pass filtered with a cutoff period of 30 hours. The surface data used in this study only included grid points that had at least 70% return over the annual record (Figure 2). The Geometric Dilution of Precision (GDOP) describes the spatial error

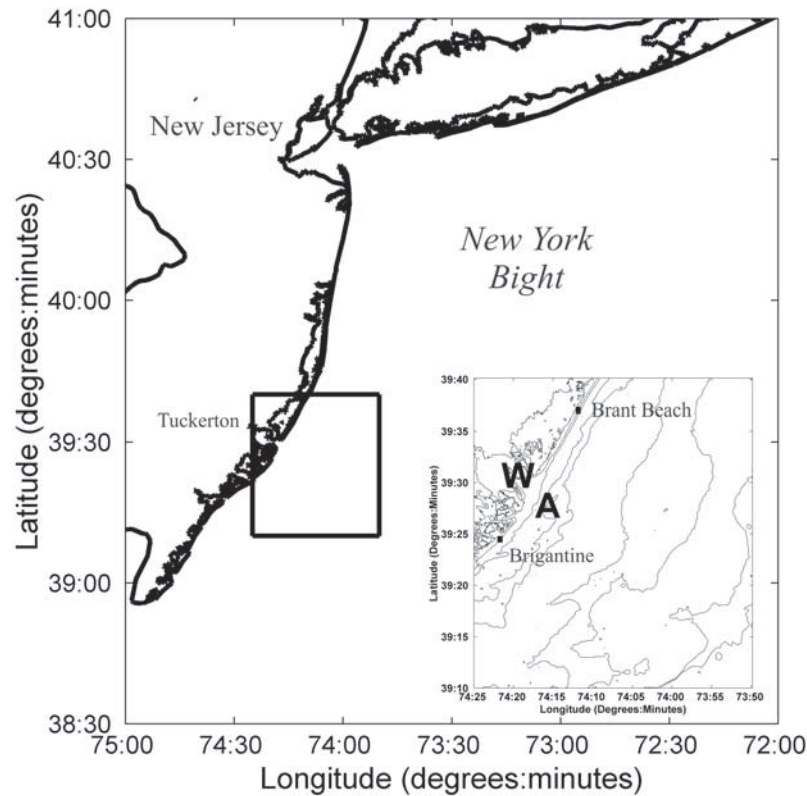


**Figure 1.** Map of the research area. The locations of the HF radar sites (solid squares), ADCP (A) and meteorological station (W) are shown in the inset. The 5 m depth contours range from 5 m nearshore to 35 m offshore.

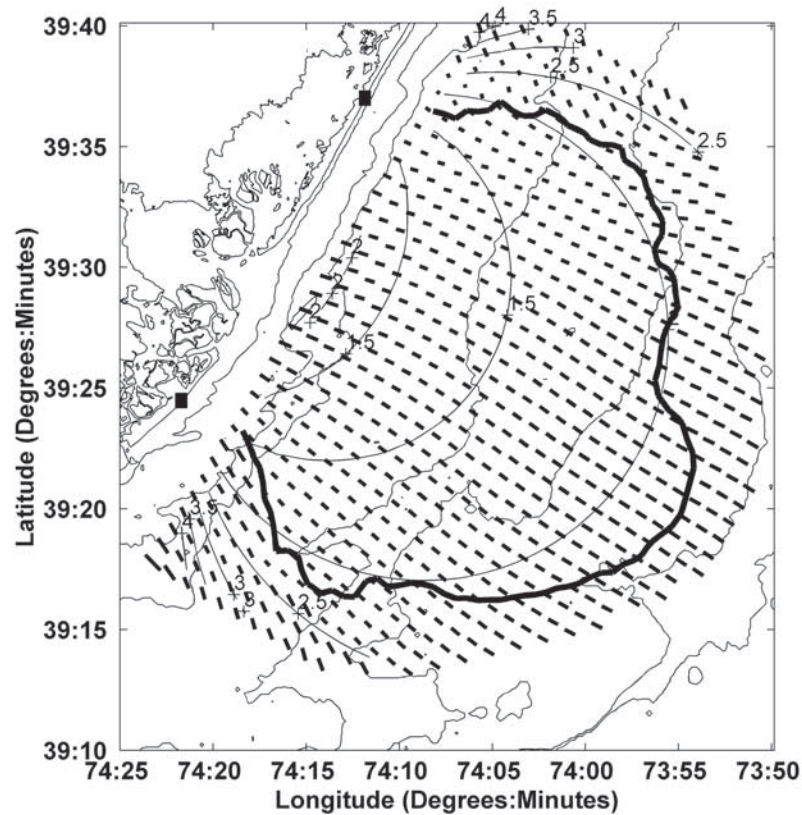


**Figure 2.** The GDOP contours (thin) of the HF radar system, tidal ellipses for the M2 constituent, and the 70% coverage contour (thick) of the annual data set.



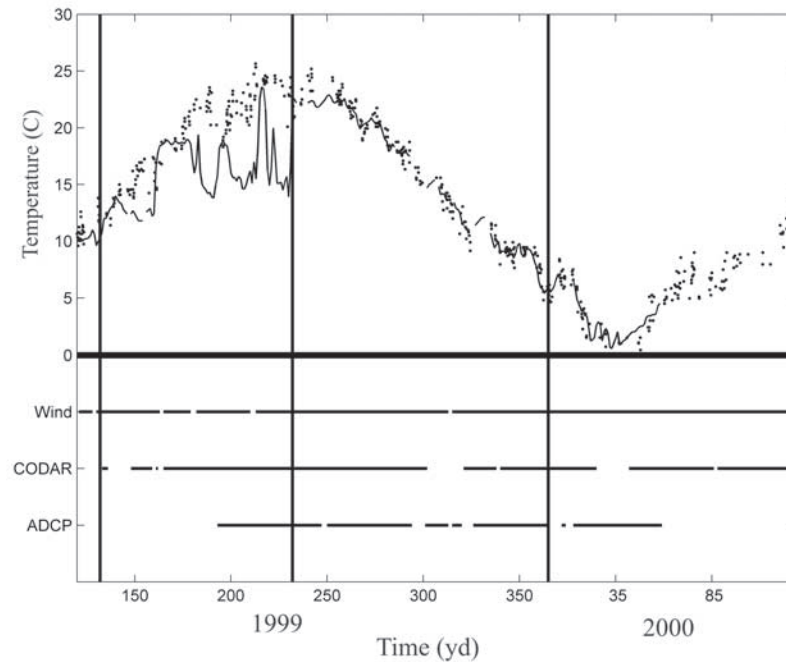


**Figure 3.** Time series of sea surface temperature (dots), bottom temperature (solid line), and the availability of wind velocity, HF radar, and ADCP data. The stratified and mixed regimes are delineated by vertical lines.

associated with the geometric combination of the radial velocity measurements [Chapman *et al.*, 1997]. The specific GDOP for this HF radar setup indicates that the geometric error increases rapidly toward the northwest and southwest nearshore corners of the coverage (Figure 2). The selected 70% coverage area is within GDOP values of 2.5 or less. The tidal estimates from the detiding step were used to further verify the data quality of the selected grid since the orientation of the major axis of the tidal ellipse should not vary significantly over the grid [Battisti and Clarke, 1982]. The  $M_2$  tidal ellipses (Figure 2) confirm that areas in which the major axes vary are collocated with larger GDOP, indicating that these regions contain less reliable total vectors. Since the data within the 70% contour has low GDOP and consistent tides, these data were used in the following analysis.

[10] Complimentary in situ data were obtained from the Long-term Ecosystem Observatory (LEO) [Grassle *et al.*, 1998; Glenn *et al.*, 2000; Schofield *et al.*, 2001], located midway between the two CODAR sites (Figure 1). Remotely operated profilers that sample subsurface properties (including temperature, salinity, and pressure) and a bottom mounted Acoustic Doppler Current Profiler (ADCP) are located about 5 km offshore in 12 meters of water (Figure 1). Using a least squares fit, the ADCP data was detided using the  $M_2$ ,  $S_2$ ,  $N_2$ ,  $K_1$ , and  $O_1$  constituents to match the CODAR data processing. A meteorological tower at the Rutgers University Marine Field Station compliments the ocean observations with a suite of atmospheric data. Satellite imagery obtained from the Rutgers University Coastal Ocean Observation Lab provides continuous spatial coverage of sea surface temperature over the region. This particular study utilizes surface map time series of currents and temperature from the HF radar and satellites, bottom

temperature and subsurface ADCP velocity profiles from LEO, and local wind measurements from the meteorological tower (Figure 3). The detided ADCP and wind data were centered averaged on the hour and filtered to match the HF radar sampling.

### 3. Results

#### 3.1. Annual Mean

[11] The annual mean between May 1999 and May 2000 is a relatively weak flow generally alongshore toward the southwest (Figure 4). While consistent with historical results, the surface flow is clearly influenced by the underlying topography. On the northern side of the domain, the topography is relatively deep and flat rising sharply at the beach. On the southern side, however, steep rises are encountered offshore between 20 m and 25 m and again between 15 m and 10 m. The resulting topographic bump is also the site of numerous kilometer-scale shore oblique sand ridges. Southward heading flows thus encounter isobaths that veer offshore in the center of the domain. The flow generally follows these isobaths, veering offshore and accelerating. Downstream of the topographic bump the flow returns to an alongshore direction. The HF radar field indicates that on annual timescales, the surface currents are significantly influenced by local topography on the order of the baroclinic Rossby radius  $O(10 \text{ km})$ . In the absence of stratification, surface and bottom boundary layers will often overlap in coastal ocean water depths less than 30 m [Brink, 1997]. Topographic steering of the annual mean flow indicates that this timescale may be influenced by a longer unstratified season during which the entire water column is dominated by coupled surface and bottom boundary layers. Here we discuss the role of stratification



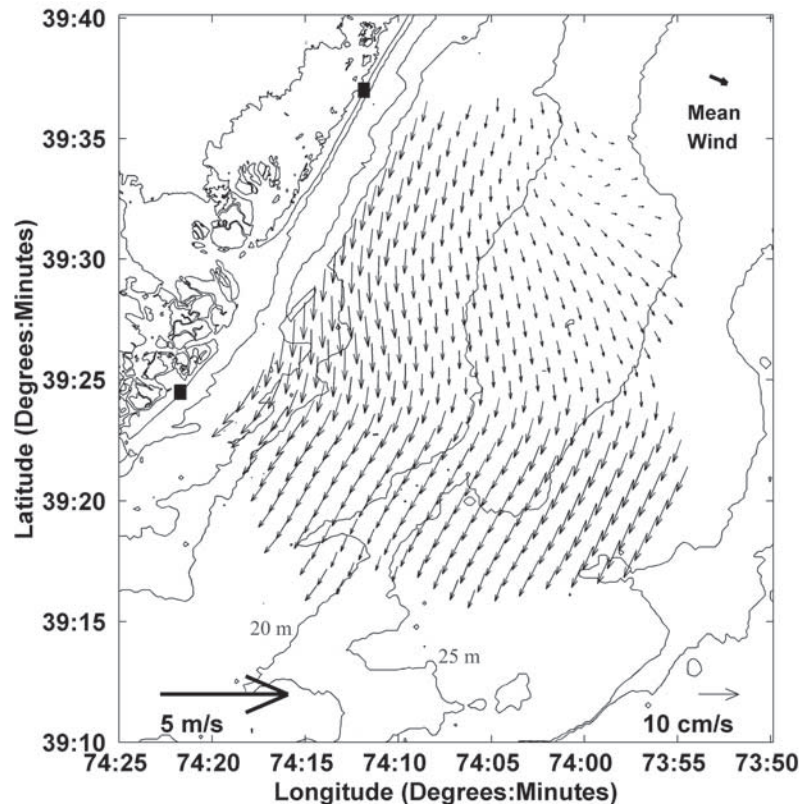


**Figure 4.** Annual mean currents measured between May 1999 and May 2000 with the HF radar system. The mean wind measured at the marine field station (upper right), the current scale (lower right), and wind scale (lower left) are also shown.

on the interaction and how this interaction influences the current response on seasonal timescales.

### 3.2. Mixed Versus Stratified

[12] To see the effect of stratification on the surface current field, the annual record was divided into two regimes, stratified and mixed. The stratification was quantified using the surface temperature from a satellite advanced very high resolution radiometer (AVHRR) and the bottom temperature from the LEO SeaBird conductivity-temperature-depth (CTD) sensor. The AVHRR data used here are a subset of a nine year time series (S. M. Glenn et al., submitted manuscript, 2003). The data in this subset were collected locally from the NOAA 12, NOAA 14, and NOAA 15 satellites at the Rutgers University remote sensing lab. Sea surface temperatures were derived from the AVHRR data using the MultiChannel Sea Surface Temperature (MCSST) algorithm [Bernstein, 1982]. Any grid point more than 4 degrees different than the surrounding points was eliminated to remove the effect of clouds. All images were manually navigated to approximately one pixel in error. For this analysis the pixel directly over the LEO node was used for the SST time series.

[13] Within the annual data there are two clear regimes, one with significantly different surface and bottom temperatures, labeled stratified, and one with very similar surface and bottom temperatures, labeled mixed (Figure 3). The transition from stratified to mixed is usually associated with a September mixing storm. For this particular year, the

stratified regime runs from year-day (yd) 133 to yd 231 and the mixed regime runs from yd 232 to yd 365. Both the current and wind data were divided into these two seasonal regimes so that the influence of stratification on the surface current fields could be studied.

### 3.3. Stratified Regime

#### 3.3.1. Forcing

[14] The forcing during the summer-stratified season is typically driven by winds and buoyancy. Using the techniques described by Yankovski and Garvine [1998], the influence of buoyancy in the research area was determined by the magnitude of freshwater outflow leaving the Hudson River. Yankovski and Garvine [1998] describe an approximate 40-day lag between freshwater outflow at Watertown, New York and arrival off the southern New Jersey coast. On the basis of this 40-day lag, the brackets of Figure 5 indicate the freshwater outflow at Watertown, NY that would influence the dynamics of the stratified regime in southern New Jersey. Unlike the spring of 1996 with many record or near record high outflows, the spring of 1999 is characterized by many record or near record low outflows of fresh Hudson River water (Figure 5). The average outflow affecting the circulation during the stratified regime was  $187 \text{ m}^3/\text{s}$  in 1999 and  $467 \text{ m}^3/\text{s}$  in 1996. The summer stratification season of 1999 is likely to have a much smaller buoyant forced response than that observed in previous years.

[15] The wind forcing during the stratified regime was strong and predominantly alongshore. A histogram of the

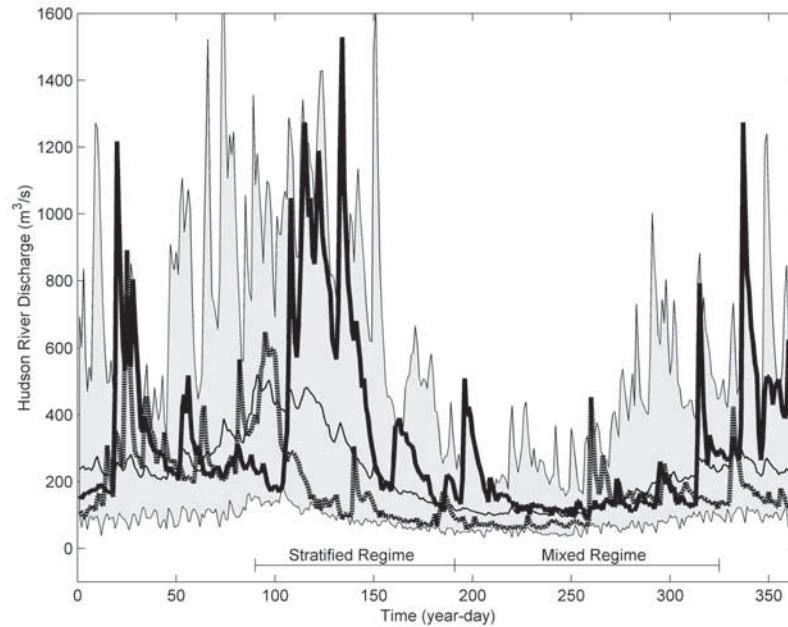


**Figure 5.** The daily averaged Hudson River outflow for 1996 (thick) 1999 (dashed), and the 25 year mean (thin) measured at a USGS station near Watertown, New York. The 25 year data envelope is shaded.

low-passed filtered winds shows that the wind was mostly from the northeast (downwelling favorable) and the southwest (upwelling favorable) with the southwest winds dominating (Figure 6). The mean and standard deviation of the wind velocities from each direction indicates that the strongest velocities with the most variability were from the upwelling favorable direction. The forcing of the 1999 summer stratification season was dominated by an oscillation between upwelling and downwelling favorable winds.

### 3.3.2. Response

[16] The current response during the stratified regime was separated into a mean and transient using a Reynolds decomposition approach,  $U = \bar{U} + U'$ , so that  $\bar{U}$  is the mean and  $U'$  is the transient. The mean response is relatively weak across the field with an average magnitude of 3.6 cm/s (Figure 7a). The current direction varies significantly across the field and indicates a weak relationship with the mean southwesterly alongshore wind. The

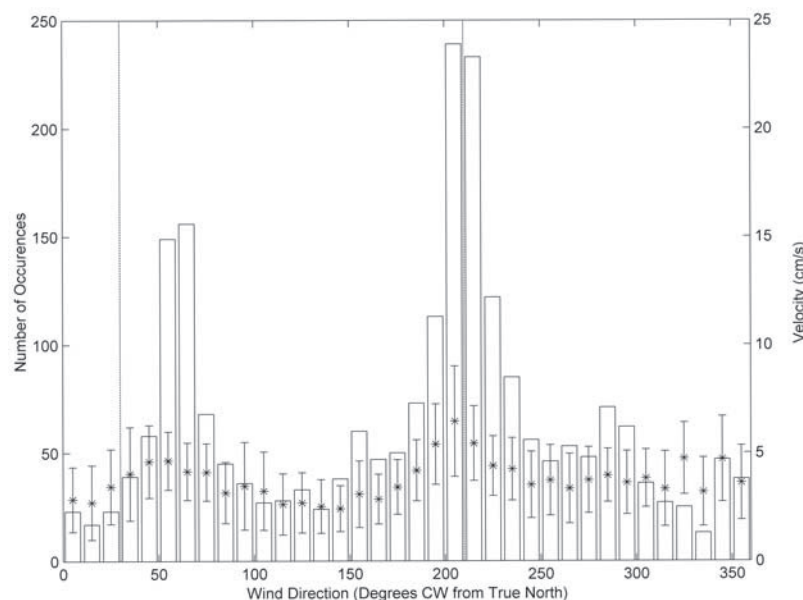


**Figure 6.** Histogram of wind forcing over the stratified regime. The mean (stars) and standard deviation (bars) of the wind velocity in each angular bin are also shown. The dashed lines indicate the bearing of the coast to the north and south.

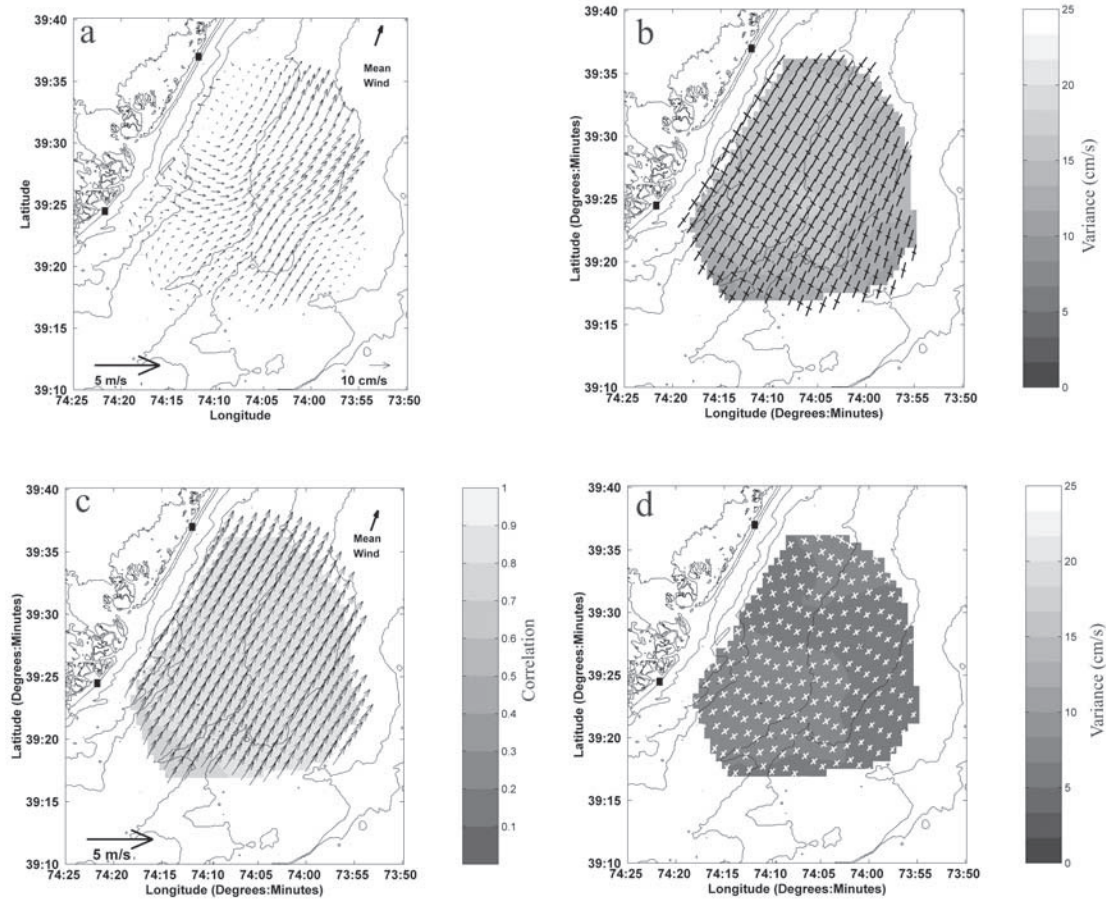


**Figure 7.** (a) The mean stratified regime current response. The mean stratified wind measured at the field station (upper right), the current scale (lower right), and wind scale (lower left) are also shown. (b) Principle components of the stratified regime transient response. (c) The magnitude of the complex correlation of the stratified regime transient current response with the local winds is shaded. The angle between the mean wind (upper right) and each grid point (black vectors) indicates the offset between the highest correlated current and wind. (d) Variance of the uncorrelated current component of the stratified regime transient response.

cyclonic rotation north of the bump hints at the interaction between surface currents and topography described by *Glenn et al.* [1996] and *Song et al.* [2001]. The transient, on the other hand, is fairly uniform and much more energetic (Figure 7b). The principle components are strongly rectilinear indicating a tendency for the variability to be aligned with the coast. This combined with a weak mean indicates that over the entire stratified regime the response is highly variable in magnitude but tends to be oriented along the coast.

[17] The complex correlation between the local wind time series and the transient current response at each HF radar grid point shows a very strong correlation, with a mean of 0.82, a mean range of  $\pm 0.065$  for the 95% confidence interval, and a standard deviation of 0.05 across the entire field (Figure 7c). In addition to the magnitude, the vectors indicate that the current direction with the highest correlation is shifted to the right of the wind. This offset fluctuates slightly across the field with a maximum of 23 degrees at the center of the field, a minimum of 4 degrees near the northern edge, and a mean of 14.2 degrees. The vertical variability of this correlation was determined from the

ADCP. As expected, the surface currents are more correlated with the wind than the bottom currents (Figure 8). The phase indicates that the highest correlated currents are shifted to the right of the wind at the surface and rotate to the left with depth. The spiral is a fairly typical picture of an upwelling/downwelling regime in which the surface layer moves to the right of the forcing and the bottom layer moves to the left.

[18] A linear correlation was used to identify that component of the observed flow most correlated with the wind. The complex correlation between the wind and each HF radar grid point indicates the magnitude and direction between the best correlated wind and current response. For each grid point, the wind was rotated according to the complex correlation and a best fit-linear regression was used to describe the relationship between the wind and current so that:

$$u_{cor}(x, y, t) = slope_x(x, y) * u_{wind}(t) \quad (1)$$

$$v_{cor}(x, y, t) = slope_y(x, y) * v_{wind}(t) \quad (2)$$



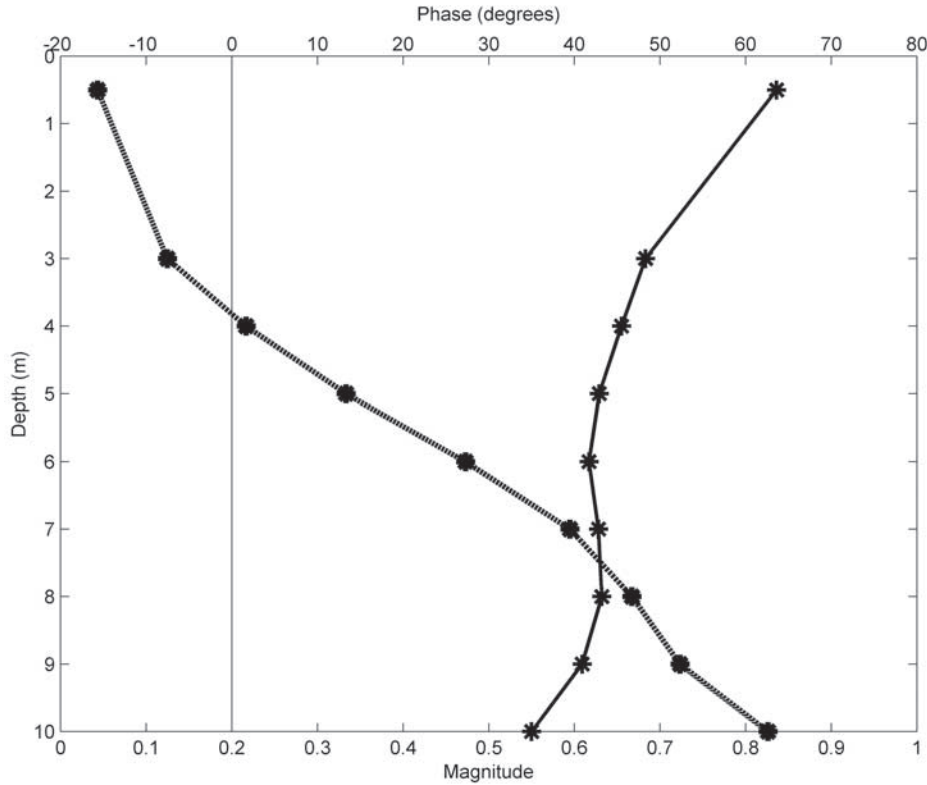


**Figure 8.** Magnitude (thick) and phase (dashed) of the complex correlation between the vertical current profile and the local wind forcing during the stratified regime. The markers indicate the centers of the measurement bins for the ADCP and CODAR (surface). Negative phase indicates that the highest correlated current is to the right of the wind. The thin line indicates zero phase.

where  $slope_x$ , and  $slope_y$  are the slopes of the linear fit for the east and north current components, respectively. The predicted flow,  $u_{cor}$  and  $v_{cor}$ , are the east and north components of the wind-correlated current. If this correlated response is subtracted from the total response, the residual is labeled the component of the flow uncorrelated with the wind.

$$u_{total} = u_{cor}(x, y, t) + u_{uncor}(x, y, t) \quad (3)$$

$$v_{total} = v_{cor}(x, y, t) + v_{uncor}(x, y, t) \quad (4)$$

[19] The magnitude of this uncorrelated current for each directional component,  $u_{uncor}$  and  $v_{uncor}$ , is a function of the scatter about the linear fit (Figure 9). The variance of the current uncorrelated with the wind is significantly less than the total variance (Figure 7d). Therefore the wind forcing accounts for the majority of the variability seen in the stratified transient response. This indicates a tightly linked system between the wind forcing and the current response. Since the orientation of the forcing and response are both along the coast, a better representation of the current structure related to the local forcing can be achieved by separating the stratified regime into upwelling and downwelling regimes.

### 3.3.3. Upwelling Regime

[20] The mean surface response during upwelling favorable winds is, as expected, up-shelf and shifted to the right

of the wind. (Figure 10a). Nevertheless, an interesting spatial variability exists in this mean upwelling response that is more evident after subtracting the spatial mean from each vector (Figure 10b). The spatial variability in the mean flow during upwelling favorable conditions is characterized by an eddy like feature that rotates cyclonically immediately north of the topographic high.

[21] This flow variability is similar in structure to the circulation observed when upwelling winds relax as described by R. J. Chant et al. (Flow reversals during upwelling conditions on the New Jersey inner shelf, submitted to *Journal of Geophysical Research*, 109, 2003) and Chant [2001]. The recirculation north of the bump would advect with it the cool upwelled water along the coast, move it offshore in the vicinity of LEO, and feed a growing upwelling center. The eddy location also coincides with numerical results in which the upwelling center north of the bump is characterized by a cyclonic eddy [Glenn et al., 1996] within an upwelling center.

### 3.3.4. Downwelling Regime

[22] The mean surface response to downwelling favorable winds is again relatively strong (Figure 11a). The horizontal shear of the downwelling regime is more uniform than the upwelling regime and appears to be related to the stratification (Figure 11b). During a typical downwelling event, the thermocline intersects the bottom. Offshore of this intersection the water column remains stratified, while onshore of the intersection the water column becomes mixed. The spatial structure of the mean can also be



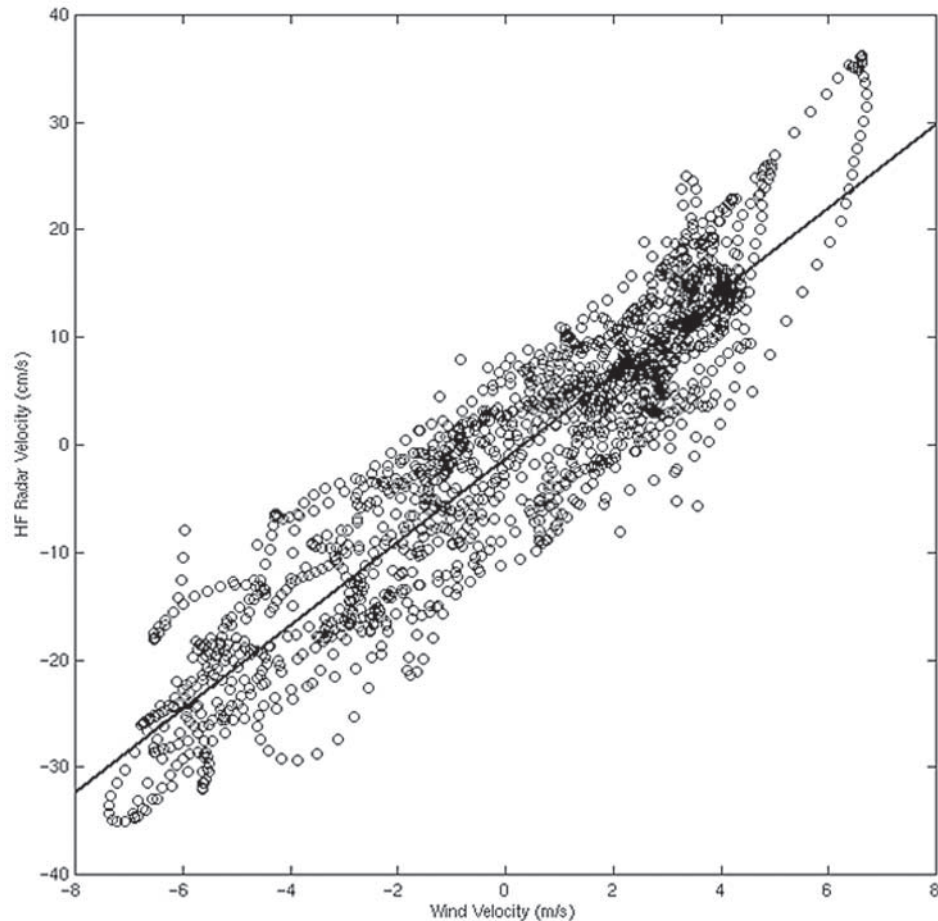


**Figure 9.** Scatterplot of wind and surface velocity for a single HF radar grid point. The line indicates the slope used to predict the wind-correlated component of the flow.

separated into two regions. The nearshore response of the mixed region is alongshore toward the south and oriented to the left of the wind (Figure 11b). The convergence zone in the southwest sector of the coverage is indicative of an acceleration of the flow over the bump and deceleration downwind of the bump. The offshore response of the stratified region, no longer oriented with the coast, is more closely aligned with the wind.

[23] When the current response is divided into upwelling and downwelling regimes, relatively strong means and weak variability result. In both responses the nearshore region is more influenced by topography where stratification is reduced.

### 3.4. Mixed Regime

#### 3.4.1. Forcing

[24] The buoyancy forcing during the mixed regime was again below the 25 year mean through much of the time period (Figure 5). The peak seen around yd 260 in the Watertown outflow is from a large rain event associated with the passing of tropical storm Floyd. While Floyd was a significant freshwater event, over the seasonal scale studied here the influence of the buoyancy is relatively low. Similar to the stratified regime, the contribution of buoyancy to the local circulation is assumed small relative to that of the local wind forcing.

[25] The wind forcing throughout the mixed regime was much more evenly distributed than observed during the stratified regime with a peak in the northwest direction (Figure 12). This is consistent with the climatology described by *Saunders* [1977] in which the winds measured over much of the year tend to be from the northwest. The mean and standard deviation of the wind measured in each directional bin show that the forcing is stronger and more variable than observed in the stratified regime (Figures 12 and 6).

#### 3.4.2. Response

[26] The mean response closely resembles that seen in the annual mean (Figures 4 and 13a). Again the currents follow the local topography north of the bump and turn more alongshore south of the bump. The magnitude of the flow is on the order of 4.5 cm/s. The spatial structure of the variance also reflects the underlying topography with an energy maximum centered over the bump (Figure 13b). The mean and transient indicate that the response is relatively steady surrounding the bump and much more variable over the bump.

[27] Correlation between the wind forcing and this response indicate the current is now less correlated with the wind than during the stratified regime, with a mean of 0.69, a mean range of  $\pm 0.09$  for the 95% confidence interval, and a standard deviation of 0.03 across the field. The vectors

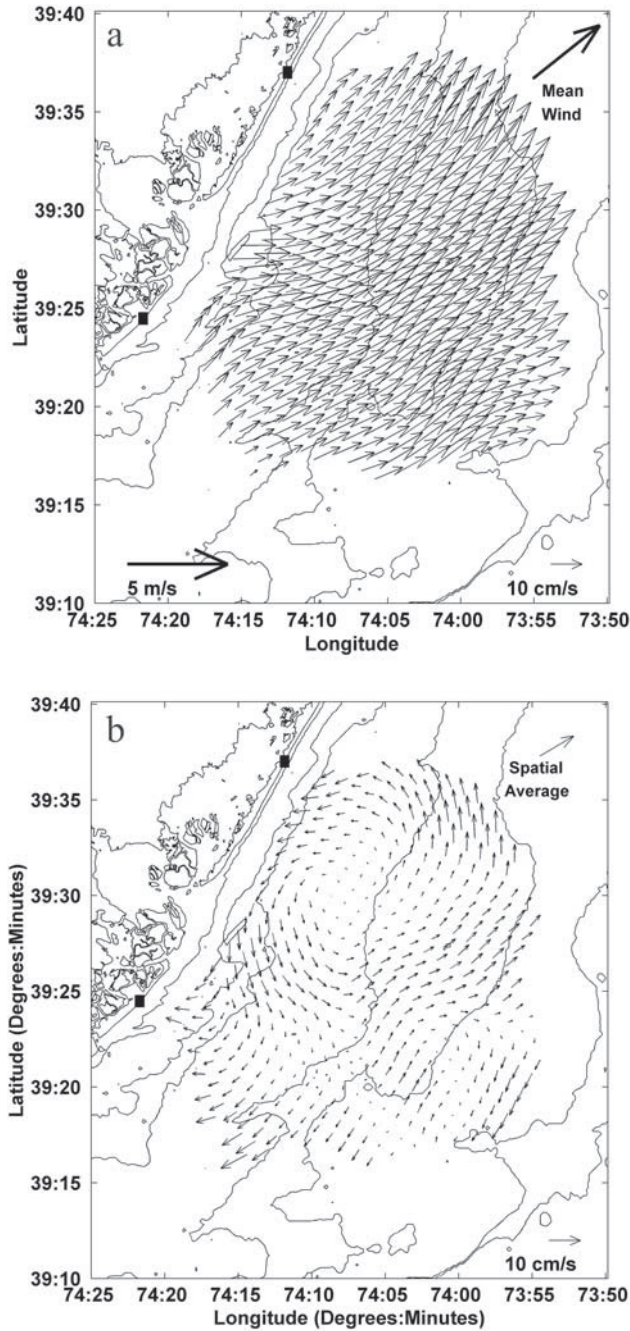


**Figure 10.** (a) Mean upwelling regime response. The mean upwelling wind measured at the marine field station (upper right), the current scale (lower right), and wind scale (lower left) are also shown. (b) Spatial structure of the mean upwelling response. The vector field is the difference between the temporal mean at each grid point and the spatial mean (upper right).

indicate that the angular offset between the wind and the currents with the highest correlation is now shifted to the left of the wind, with a mean of 14.9 degrees and a maximum of 31 degrees nearshore (Figure 13c). The vertical structure of the correlation at the ADCP is highest at the surface and decreases with depth (Figure 14). The angular shear from surface to bottom is relatively small

suggesting that the system is acting as a single layer. The single layer rotation to the left could be an indication of a bottom Ekman layer extending to the surface. Assuming a standard linear eddy viscosity,  $K = \kappa u^* z$  [Smith and Long, 1976; Forristall et al., 1977], the scale height of the bottom boundary layer for geophysical flows is:

$$l = \frac{\kappa u^*}{f} \quad (5)$$

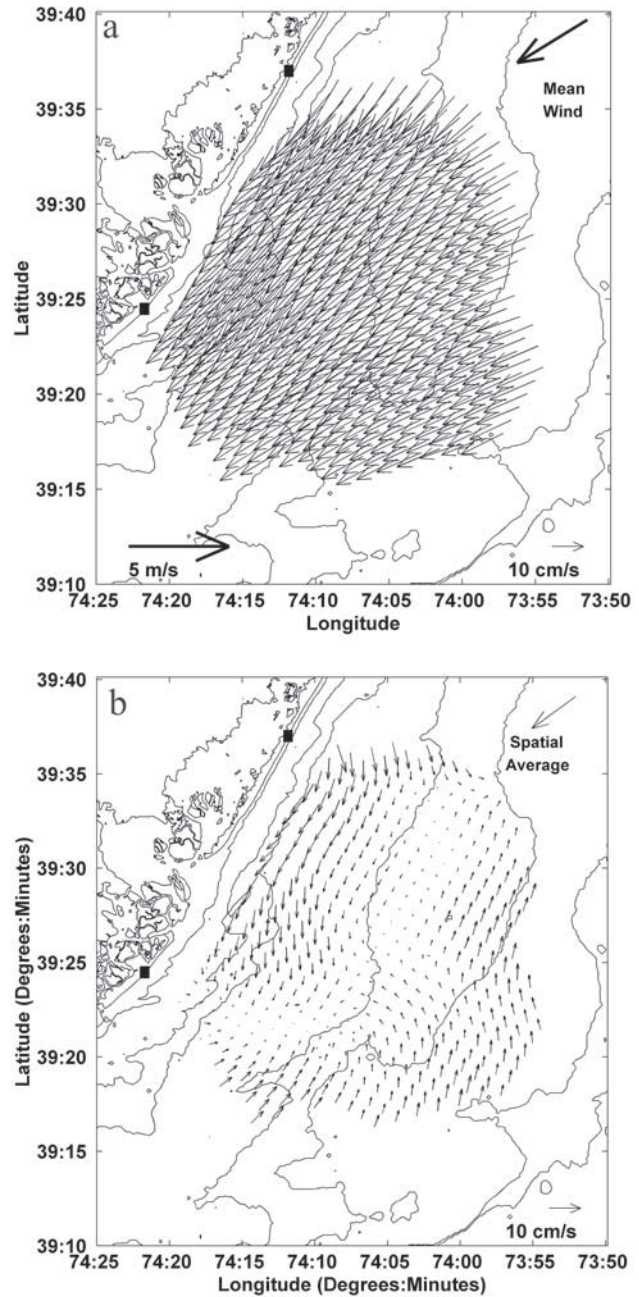


**Figure 11.** (a) Mean downwelling regime response. The mean downwelling wind measured at the field station (upper right), the current scale (lower right), and wind scale (lower left) are also shown. (b) Spatial structure of the mean downwelling response. The vector field is the difference between the temporal mean at each grid point and the spatial mean (upper right).

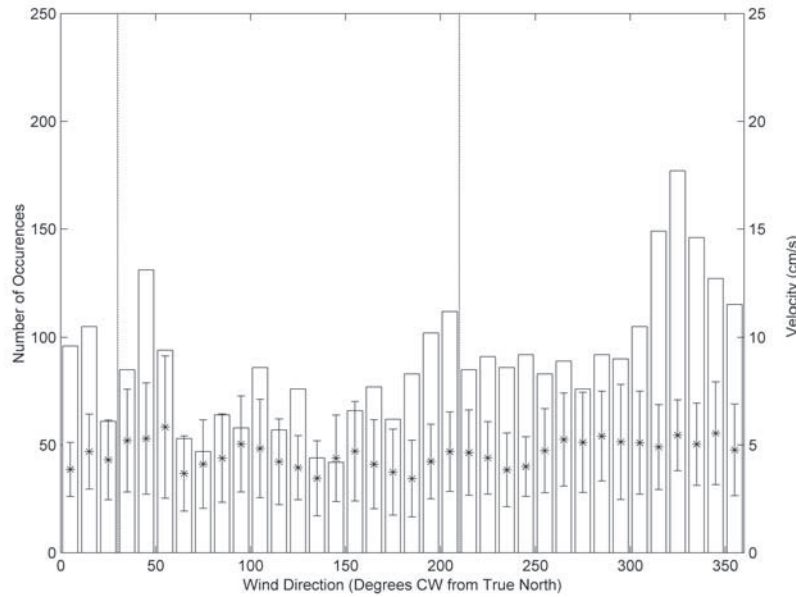


**Figure 12.** Histogram of wind forcing over the mixed regime. The mean (stars) and standard deviation (bars) of the wind velocity in each angular bin are also shown. The dashed lines indicate the direction of coast to the north and south.

where  $\kappa$  is von Karman's constant,  $u^*$  is the frictional velocity, and  $f$  is the Coriolis parameter [Long, 1981; Glenn, 1983]. Since  $\kappa$  and  $f$  are constants, the frictional velocity,  $u^*$ , is the only unknown. Assuming a near-bed constant stress layer:

$$u(z) = \frac{u^*}{\kappa} \ln\left(\frac{z}{z_o}\right) \quad (6)$$

where  $z_o$  is the height above the bed at which the current goes to zero. The velocities at two different heights ( $u_1$  at  $z_1$  and  $u_2$  at  $z_2$ ) can be used to solve for  $u^*$ :

$$u^* = \frac{(u_2 - u_1)\kappa}{\ln\left(\frac{z_2}{z_1}\right)} \quad (7)$$

The two bottom bins of the ADCP, 1.25 m and 2.25 m above the bed, are used to estimate  $u^*$ , which is then substituted into equation (5) to estimate the scale height,  $l$ . A time series of  $l$  indicates that the bottom boundary layer scale height frequently exceeds the water depth (Figure 15). With a mean value of 65 m and a standard deviation of 50 m, the shallow water column (<30 m) within the HF radar grid is dominated by overlapping boundary layers.

[28] Using the linear model described in equations (1) and (2),  $u_{cor}$  and  $v_{cor}$  was subtracted from the total transient leaving the uncorrelated variance. The principle components have less energy than the total response, however the structure observed in the total variance of the mixed regime is still evident in the uncorrelated field (Figure 13d). The wind forcing appears to amplify the mixed response but does not drive it. Even without the wind forcing, the spatial structure of the variance remains.

### 3.4.3. Bottom Topography

[29] Since the entire water column is moving as a frictional layer, the influence of the underlying topography

should be evident in the surface currents. There is already an indication of this interaction in the mixed, stratified, and annual fields. To quantify the role of the topography, the along isobath direction was calculated at each HF radar grid point using the depth gradient vector,  $\vec{H}$ .

$$\vec{H} = \frac{\partial h}{\partial L_x} \hat{i} + \frac{\partial h}{\partial L_y} \hat{j} \quad (8)$$

Where  $\hat{i}$  and  $\hat{j}$  are unit vectors,  $h$  is depth, and  $L_x(L_y)$  is the east (north) component of the horizontal scale. By definition the along-isobath direction is orthogonal to  $\vec{H}$ . Since the small-scale ridge and swale topography common along the United States east coast is on the order of 5 km [McBride and Moslow, 1991], this length scale was chosen for this analysis. Equation (8) was solved using finite differences such that  $L_x = L_y = 5$  km. The magnitude of the depth gradient at this 5 km scale is characterized by four regions of relatively steep topography over our domain (Figure 16a). Two regions fall along the 20 m isobath, one further offshore along the 25 m isobath, and a final area nearshore associated with the topographic bump. The effect of these regions of steeper topography on the surface current variability of the mixed regime is seen when the major axis of the variability is differenced from the along-isobath direction (Figure 16b). Regions in the coverage with small angular offsets indicate that the current variability tends to be more aligned with the topography compared to regions with larger angular offsets. Over our domain the four regions with relatively steeper topography correspond with regions of smaller angular offsets, indicating that the current variability tends to be more aligned with the steeper topography than the flatter topography (Figure 16b). There is a clear trend in which the angular offset is more variable over topography with small slopes (Figure 16c). As the topography steepens, the variability in the angular offset



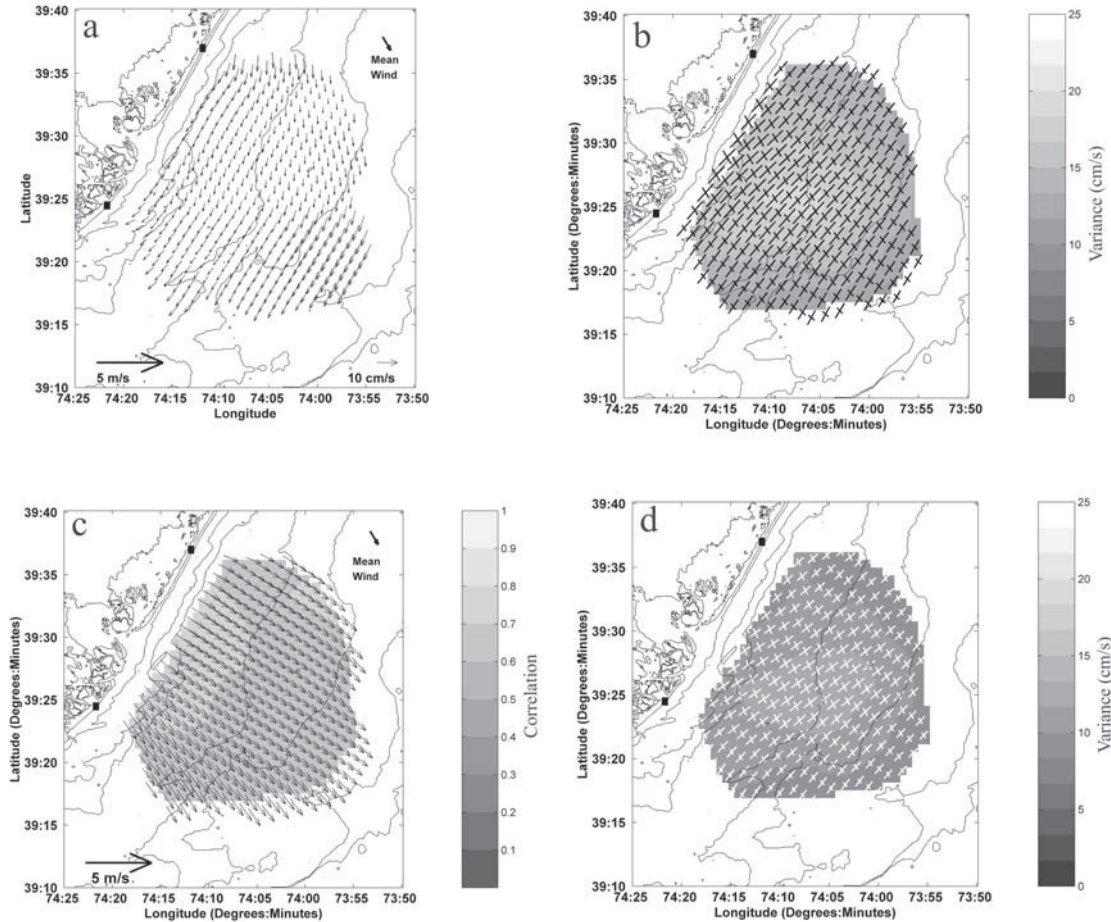


**Figure 13.** (a) The mean mixed regime response. The mean mixed wind measured at the field station (upper right), the current scale (lower right), and wind scale (lower left) are also shown. (b) Principle components of the mixed regime transient response. (c) The magnitude of the complex correlation of the mixed regime transient response with the local winds is shaded. The angle between the mean wind (upper right) each grid point (black vectors) indicates the offset between the highest correlated current and wind. (d) Variance of the uncorrelated current component of the mixed regime transient response.

decreases and favors smaller angles. The current response of the mixed regime is closely linked to this 5 km scale topography. At this scale the angular offset between the current variability and the topography tends to be more random over areas of relatively flat topography and more aligned over areas with relatively steep topography.

#### 4. Discussion and Conclusions

[30] Throughout the year the influence of topography was observed in the surface current response. Over annual timescales the southward current is steered around a topographic bump seen along the nearshore edge of the data coverage. Using finite difference on the mean surface current fields, vorticity fields were calculated for the mixed, stratified, upwelling and downwelling regimes. In both the mixed and stratified mean flows, there is a ridge of positive vorticity to the north of the bump and a ridge of negative vorticity to the south (Figure 17). This pattern is also seen in the upwelling (Figure 17c) and downwelling (Figure 17d) subsets of the stratified regime. While this pattern persists throughout the year, there is evidence of a seasonal depen-

dence. During the stratified regime, in both the upwelling and downwelling regimes, the magnitude of the vorticity is higher and concentrated closer to the coast than during the mixed regime. Stratification appears to shorten the horizontal length scale in which the influence of the bump is felt, but the response is more intense. When the water column is mixed, the vorticity associated with the bump extends further offshore and is much weaker.

[31] During the summer stratified season the surface layer is very highly correlated with the local wind forcing, with the highest correlated currents at the surface to the right of the wind. The vertical structure of the correlation shows a two-layer system in which the surface layer flows to the right of the wind and the bottom layer flows to the left. Both the forcing and the response show that the stratified regime is dominated by upwelling/downwelling events. During these events the surface current response to the wind is dependent on both local topography and stratification. In contrast, the mixed regime forcing and response is much more variable. The response tends to be aligned with the coast even though the stronger wind fields no longer favor the alongshore direction. The mean flow during



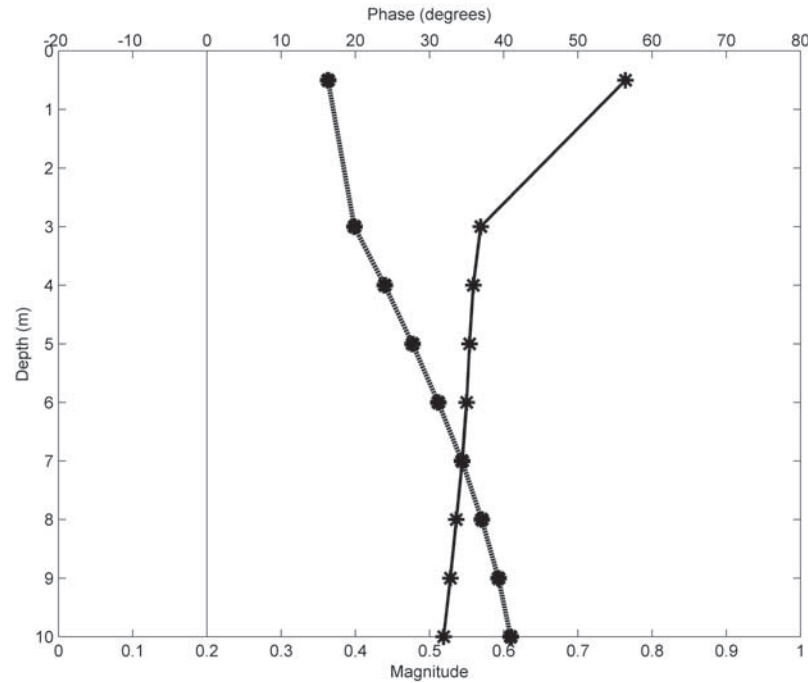


**Figure 14.** Magnitude (thick) and phase (dashed) of the complex correlation between the vertical current profile and the local wind forcing during the mixed regime. The markers indicate the centers of the measurement bins for the ADCP and CODAR (surface). Negative phase indicates that the highest correlated current is to the right of the wind. The thin line indicates zero phase.

mixed conditions resembles the annual mean having a general flow toward the southwest with perturbations around the local topography. The vertical structure of the correlation shows a single layer in which the most wind-correlated current is to the left of the wind throughout the water column. The left offset of the most correlated current

increases with depth. The frictional length scale calculated throughout this period indicates that the entire water column is composed of a single frictional layer. As a single layer, the surface response is strongly influenced by the local topography, especially over those regions in which the slope exceeds 1.3 m/km.

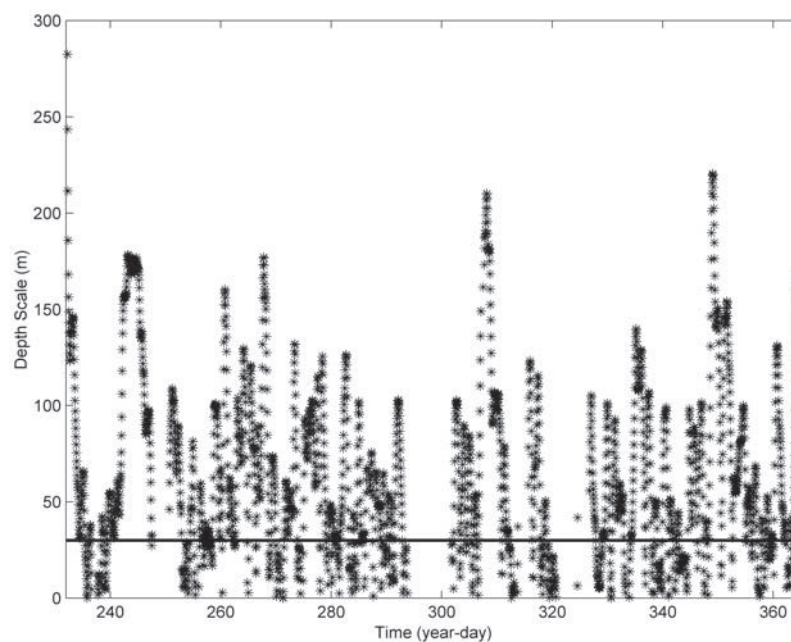


**Figure 15.** Time series of frictional layer thickness,  $l$ , defined by equation (3.5). For reference, the solid black line indicates the 30 m isobath.

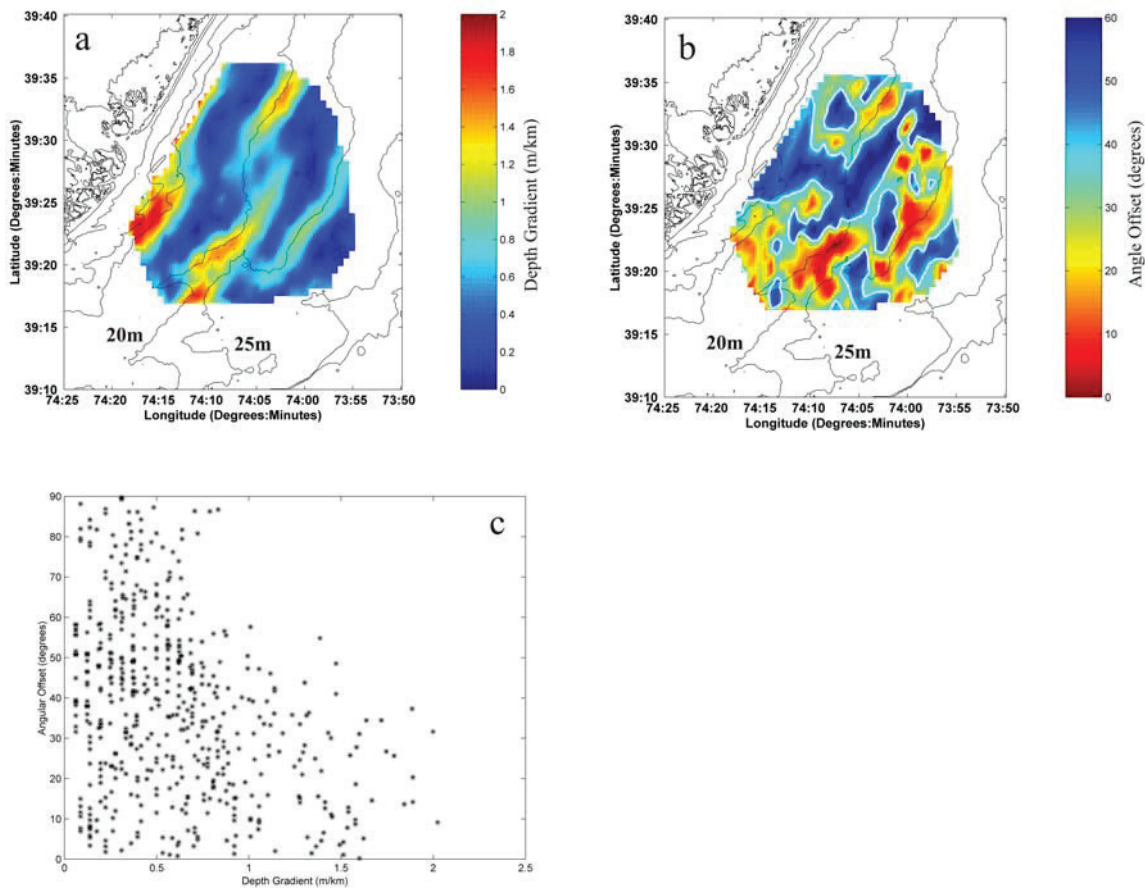


**Figure 16.** (a) The magnitude of the 5 km scale depth gradient. The 20 m and 25 m isobaths are also labeled. (b) The difference between the 5 km scale along-isobath direction and the major axis of the mixed residual response (Figure 13d). (c) Scatterplot of the depth gradient (Figure 16a) and angular offset between the along-isobath direction and the major axis of the mixed residual response (Figure 16b).

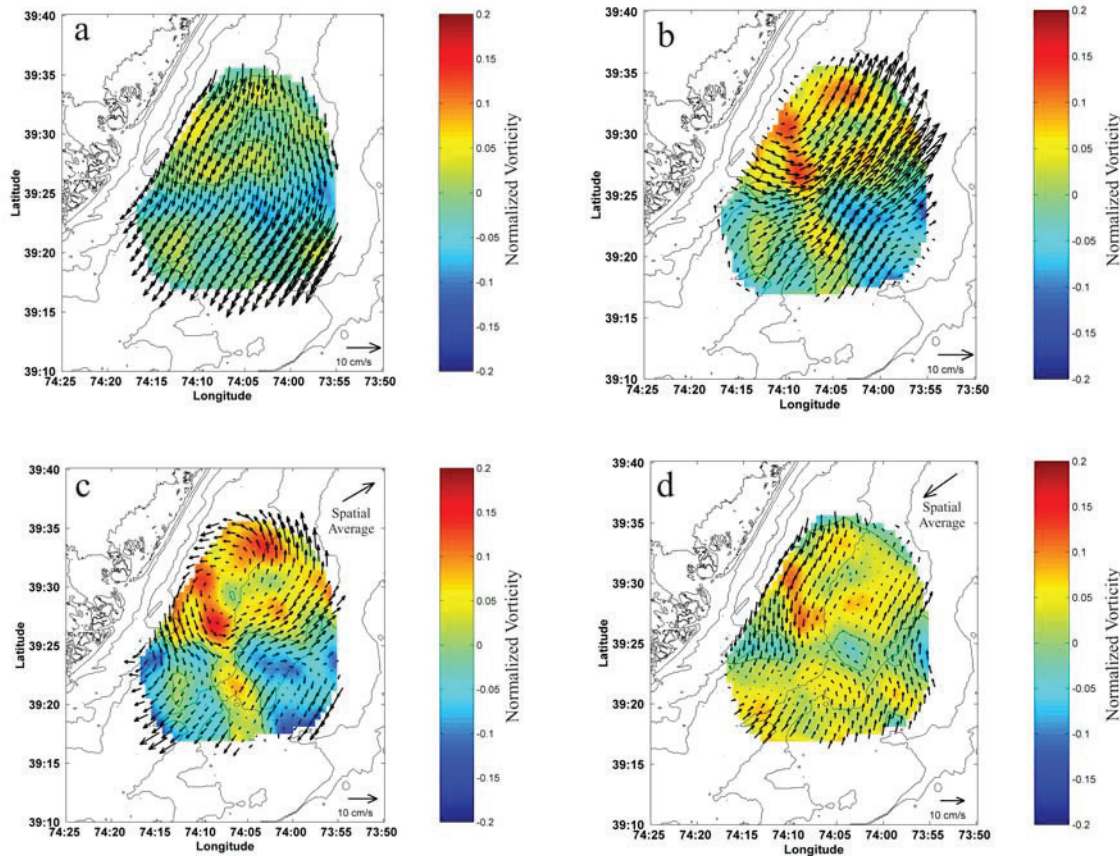


**Figure 17.** Relative vorticity normalized by the local Coriolis parameter for the mean (a) mixed, (b) stratified, (c) upwelling stratified, and (d) downwelling stratified regimes. The vector fields in Figures 17a and 17b are the temporal mean. The vector fields in Figures 17c and 17d are the difference between the temporal mean at each grid point and the spatial mean (upper right).

[32] Stratification clearly influences the response of the surface currents to local forcing. The results suggest that the complex correlation of the wind with the current could be a proxy of the strength of the stratification. If the water column is stratified, the highly correlated surface layer motion is shifted to right of the wind and, in some locations, also influenced by the underlying topography. If the water column is mixed, the less correlated response is shifted to the left of the wind and is significantly influenced by the underlying topography, especially where the depth gradients are at maximum.

[33] **Acknowledgments.** We would like to thank Dale Haidvogel, Jeff Paduan, Matt Oliver, and two anonymous reviewers for their comments and review. This work was funded by the Office of Naval Research (N00014-97-1-0797, N00014-99-1-0196, N00014-00-1-0724, N00014-02-1-0917), the National Ocean Partnership Program (N00014-97-1-1019, N00014-98-1-0815), and the great state of New Jersey. ADCP data provided by the Mid-Atlantic Bight National Undersea Research Center with additional support from the National Science Foundation.

## References

- Austin, J. A. (1999), The role of the alongshore wind in the heat balance of the North Carolina inner shelf, *J. Geophys. Res.*, *104*, 18,187–18,203.
- Barrick, D. E. (1972), First-order theory and analysis of mf/hf/vhf scatter from the sea, *IEEE Trans. Antennas Propag.*, *AP-20*, 2–10.
- Barrick, D. E., M. W. Evens, and B. L. Weber (1977), Ocean surface currents mapped by radar, *Science*, *198*, 138–144.
- Barth, J. A. (1994), Stability of a coastal upwelling front: 2. Model results and comparisons with observations, *J. Geophys. Res.*, *99*, 10,857–10,883.
- Battisti, D. S., and A. J. Clarke (1982), A simple method for estimating barotropic tidal currents on the continental margins with specific application to the M2 tide off the Atlantic and Pacific coasts of the United States, *J. Phys. Oceanogr.*, *12*, 8–16.
- Beardsley, R. C., and W. C. Boicourt (1981), On estuarine and continental-shelf circulation in the Middle Atlantic Bight, in *Evolution in Physical Oceanography*, edited by B. A. Warren and C. Wunsch, pp. 198–233, MIT Press, Cambridge, Mass.
- Beardsley, R. C., and D. B. Haidvogel (1981), Model studies of wind-driven transient circulation in the Middle Atlantic Bight, part 1: Adiabatic boundary conditions, *J. Phys. Oceanogr.*, *11*, 355–375.
- Beardsley, R. C., and S. J. Lentz (1987), The Coastal Ocean Dynamics Experiment collection: An introduction, *J. Geophys. Res.*, *92*, 1455–1463.
- Beardsley, R. C., and C. D. Winant (1979), On the mean circulation in the Mid-Atlantic Bight, *J. Phys. Oceanogr.*, *9*, 612–619.
- Beardsley, R. C., W. C. Boicourt, and D. V. Hansen (1976), Physical oceanography of the Middle Atlantic Bight, *Limnol. Oceanogr. Spec. Symp.*, *2*, 20–34.
- Bernstein, R. L. (1982), Sea surface temperature estimation using the NOAA-6 advanced very high resolution radiometer, *J. Geophys. Res.*, *87*, 9455–9465.
- Bigelow, H. B. (1933), Studies of the waters on the continental shelf, Cape Cod to Chesapeake Bay. I. The cycle of temperature, *Pap. Phys. Oceanogr. Meteorol.*, *2*, 135 pp.
- Bigelow, H. B., and M. Sears (1935), Studies of the waters on the continental shelf, Cape Cod to Chesapeake Bay. II. Salinity, *Pap. Phys. Oceanogr. Meteorol.*, *4*, 94 pp.
- Brink, K. H. (1997), Observational coastal oceanography, paper presented at National Science Foundation OCE Workshops, Natl. Sci. Found., Monterey, Calif.



- Brink, K. H., D. Halpern, and R. L. Smith (1980), Circulation in the Peruvian upwelling system near 15°S, *J. Geophys. Res.*, **85**, 4036–4048.
- Chant, R. J. (2001), Evolution of near-inertial waves during an upwelling event on the New Jersey inner shelf, *J. Phys. Oceanogr.*, **31**, 746–763.
- Chapman, D. C., and R. C. Beardsley (1989), On the origin of shelf water in the Middle Atlantic Bight, *J. Phys. Oceanogr.*, **19**, 384–391.
- Chapman, R. D., L. K. Shay, H. C. Graber, J. B. Edson, A. Karachintsev, C. L. Trump, and D. B. Ross (1997), On the accuracy of HF radar surface current measurements: Intercomparisons with ship-based sensors, *J. Geophys. Res.*, **102**, 18,737–18,748.
- Crombie, D. D. (1955), Doppler spectrum of sea echo at 13.56 Mc/s, *Nature*, **175**, 681–682.
- Davis, R. E., and P. S. Bogden (1989), Variability on the California shelf forced by local and remote winds during the Coastal Ocean Dynamics Experiment, *J. Geophys. Res.*, **94**, 4763–4783.
- Forristall, G. Z., R. C. Hamilton, and V. J. Cardone (1977), Continental shelf currents in tropical storm Delia: Observations and theory, *J. Phys. Oceanogr.*, **7**, 532–546.
- Glenn, S. M. (1983), A continental shelf bottom boundary layer model: The effect of waves, currents, and a moveable bed, Ph.D. diss., 237 pp., Woods Hole Oceanogr. Inst./Mass. Inst. of Technol. Joint Program, Woods Hole.
- Glenn, S. M., M. F. Crowley, D. B. Haidvogel, and Y. T. Song (1996), Underwater observatory captures coastal upwelling events off New Jersey, *Eos Trans. AGU*, **77**, 233–236.
- Glenn, S. M., W. Boicourt, B. Parker, and T. D. Dickey (2000), Operational observation networks for ports, a large estuary and an open shelf, *Oceanography*, **13**, 12–23.
- Grassle, J. F., S. M. Glenn, and C. von Alt (1998), Ocean observing systems for marine habitats, *OCC '98 Proceedings*, Mar. Technol. Soc., Baltimore, Md.
- Halpern, D. (1976), Structure of a coastal upwelling event observed off Oregon during July 1973, *Deep Sea Res.*, **23**, 495–508.
- Halpern, D. (1977), Description of wind and of upper ocean currents and temperature variation on the continental shelf off northwest Africa during March and April 1977, *J. Phys. Oceanogr.*, **7**, 422–430.
- Hicks, D. C., and J. R. Miller (1980), Meteorological forcing and bottom water movement off the northern New Jersey coast, *Estuarine Coastal Sci.*, **11**, 563–571.
- Houghton, R. W., R. Schlitz, R. C. Beardsley, B. Butman, and J. L. Chamberlin (1982), The Middle Atlantic Bight cold pool: Evolution of the temperature structure during summer 1979, *J. Phys. Oceanogr.*, **12**, 1019–1029.
- Kohut, J. T., and S. M. Glenn (2003), Improving HF radar surface current measurements with measured antenna beam patterns, *J. Atmos. Oceanic Technol.*, **20**, 1303–1316.
- Long, C. E. (1981), A simple model for time-dependent stably stratified turbulent boundary layers, *Spec. Rep. 95*, 170 pp., Dep. of Oceanogr., Univ. of Washington, Seattle, Wa.
- McBride, R. A., and T. F. Moslow (1991), Origin, evolution, and distribution of shoreface sand ridges, Atlantic inner shelf, U.S.A., *Mar. Geol.*, **97**, 57–85.
- Miller, A. R. (1952), A pattern of surface coastal circulation inferred from surface salinity-temperature data and drift bottle recoveries, *WHOI Tech. Rep. 52–28*, 14 pp., Woods Hole Oceanogr. Inst., Woods Hole, Mass.
- Moores, C. N. K., J. Fernandez-Partagas, and J. F. Price (1976), Meteorological forcing fields of the New York Bight (first year's progress report), *Tech. Rep. TR76–8*, Rosenstiel School of Mar. and Atmos. Sci., Univ. of Miami, Miami, Fla.
- Münchow, A., and R. J. Chant (2000), Kinematics of inner shelf motions during the summer stratified season off New Jersey, *J. Phys. Oceanogr.*, **30**, 247–267.
- Narimousa, S., and T. Maxworthy (1987), Coastal upwelling on a sloping bottom: The formation of plumes, jets and pinched-off cyclones, *J. Fluid Mech.*, **176**, 169–190.
- Ou, H. W., R. C. Beardsley, D. Mayer, W. C. Boicourt, and B. Butman (1981), An analysis of subtidal fluctuations in the Middle Atlantic Bight, *J. Phys. Oceanogr.*, **11**, 1383–1392.
- Saunders, P. M. (1977), Wind stress on the ocean over the eastern continental shelf of North America, *J. Phys. Oceanogr.*, **7**, 555–566.
- Schofield, O., T. Bergmann, W. P. Bissett, F. Grassle, D. Haidvogel, J. Kohut, M. Moline, and S. Glenn (2001), The long term ecosystem observatory: An integrated coastal observatory, *IEEE J. Oceanic Eng.*, **27**, 146–154.
- Smith, J. D., and C. E. Long (1976), The effect of turning in the bottom boundary layer on continental shelf sediment transport, *Mem. Soc. R. Sci. Liège Coll. 6°*, **X**, 369–396.
- Song, Y. T., D. B. Haidvogel, and S. M. Glenn (2001), Effects of topographic variability on the formation of upwelling centers off New Jersey: A theoretical model, *J. Geophys. Res.*, **106**, 9223–9240.
- Stewart, R. H., and J. W. Joy (1974), HF radio measurement of surface currents, *Deep Sea Res.*, **21**, 1039–1049.
- Svedrup, H. U., M. W. Johnson, and R. H. Fleming (1942), *The Oceans: Their Physics, Chemistry, and General Biology*, 1087 pp., Prentice-Hall, Old Tappan, N. J.
- Walford, L. A., and R. I. Wicklund (1968), Monthly sea temperature structure from the Florida Keys to Cape Cod, *Serial Atlas of the Marine Environment*, folio 15, Am. Geogr. Soc. of New York, New York.
- Yankovski, A. E., and R. W. Garvine (1998), Subinertial dynamics on the inner New Jersey shelf during the upwelling season, *J. Phys. Oceanogr.*, **28**, 2444–2458.

J. T. Kohut, S. M. Glenn, and R. J. Chant, Institute of Marine and Coastal Sciences, Rutgers University, New Brunswick, NJ, USA. (kohut@imcs.rutgers.edu)

## Inner shelf response to Tropical Storm Floyd

Josh T. Kohut,<sup>1</sup> Scott M. Glenn,<sup>1</sup> and Jeffrey D. Paduan<sup>2</sup>

Received 20 October 2003; revised 23 May 2005; accepted 30 January 2006; published 27 September 2006.

[1] A continuously operated coastal observatory off the southern coast of New Jersey provides an opportunity to study both long-term trends and episodic events. On the evening of 16 September 1999, Tropical Storm Floyd moved up the New Jersey coast directly over the observatory. The response of the inner shelf is characterized using a depth-averaged (DA) and surface layer (SL) model in conjunction with direct observations. During the storm, the DA model was more representative of the observed response. While there was a peak in the near-inertial band of the depth average current, the response was not the typical clockwise ringing response seen in deepwater stratified regions. Instead the shallow, well-mixed inner shelf responded with an alongshore current oscillation balanced by the alongshore pressure gradient and bottom stress. The increased influence of bottom friction damps the typical inertial tail seen in deeper ocean responses and shortens the relaxation phase from several days to hours. Immediately following the storm, the surface layer model better represents the observed currents. It appears that the excessive rainfall associated with the storm and the resulting freshening of the inner shelf isolate the surface layer from the effect of bottom friction. The large waves and currents associated with the storm increase the potential for a sediment resuspension and transport event. Unlike the typical nor'easter in which the transport in this location is alongshore toward the south and onshore, the currents coinciding with the largest waves are alongshore toward the south but with an offshore component.

**Citation:** Kohut, J. T., S. M. Glenn, and J. D. Paduan (2006), Inner shelf response to Tropical Storm Floyd, *J. Geophys. Res.*, **111**, C09S91, doi:10.1029/2003JC002173.

### 1. Introduction

[2] Tropical storms and hurricanes force strong current responses over relatively short timescales. Since the generation and propagation of these storms is difficult to predict, most studies have utilized analytical and numerical models in conjunction with sparse observations to describe the structure of the current response. It has been shown that random wind forcing [Kundu, 1984] and fronts [Kundu, 1986; Paduan *et al.*, 1989] can generate a clockwise (CW) rotating near-inertial current. Most studies of wind forced responses associated with passing storms have focused on this frequency band. The typical deep ocean stratified response consists of a forced phase followed by an inertial tail that persists for several days [Price *et al.*, 1994]. This response has been described for several storms including Hurricane Allen in the gulf of Mexico [Brooks, 1983] and Hurricane Frederic off the coast of Alabama [Shay and Elsberry, 1987]. As is the case in the above examples, hurricanes are predominantly experienced in summer stratified waters. In the Mid-Atlantic Bight (MAB), Hurricane Belle forced two different responses on the outer and middle shelf [Mayer *et al.*, 1981]. The near-inertial middle shelf

response lasted only 2 days compared to the longer response observed in the deeper water over the outer shelf. Mayer *et al.* [1981] identify friction as a possible contributor to this difference.

[3] Using the measured wind forcing as a boundary condition, a linear, inviscid model was used to predict the current response [Shay *et al.*, 1990; Shay and Chang, 1997]. During the storm, the stratified water column responded with a weak barotropic and strong baroclinic component. The baroclinic modes were independent of the free surface boundary condition and propagated energy out of the local surface layer within 4 inertial periods. A less energetic barotropic oscillation was added when the surface rigid lid condition was eased. Keen and Glenn [1999] found that the energy of the barotropic response propagated away from the storm as a Kelvin wave set up by the storm surge near the coast. Keen and Glenn [1995] modeled an inshore barotropic response where bottom friction increases shear in the full water column. Offshore the response remains a baroclinic two-layer response where bottom friction results in turning within the bottom Ekman layer [Keen and Glenn, 1995]. So over a shallow inner shelf, the relative importance of friction during storm forcing is increased.

[4] Both observations and models show that storm energy dissipates from the surface of a stratified ocean within several days and that the timescale of the dissipation can be shortened by friction. We test this mechanism for the shallow inner shelf during the passage of Tropical Storm Floyd. The local forcing and current response was captured

<sup>1</sup>Institute of Marine and Coastal Sciences, Rutgers–State University of New Jersey, New Brunswick, New Jersey, USA.

<sup>2</sup>Naval Postgraduate School, Monterey, California, USA.

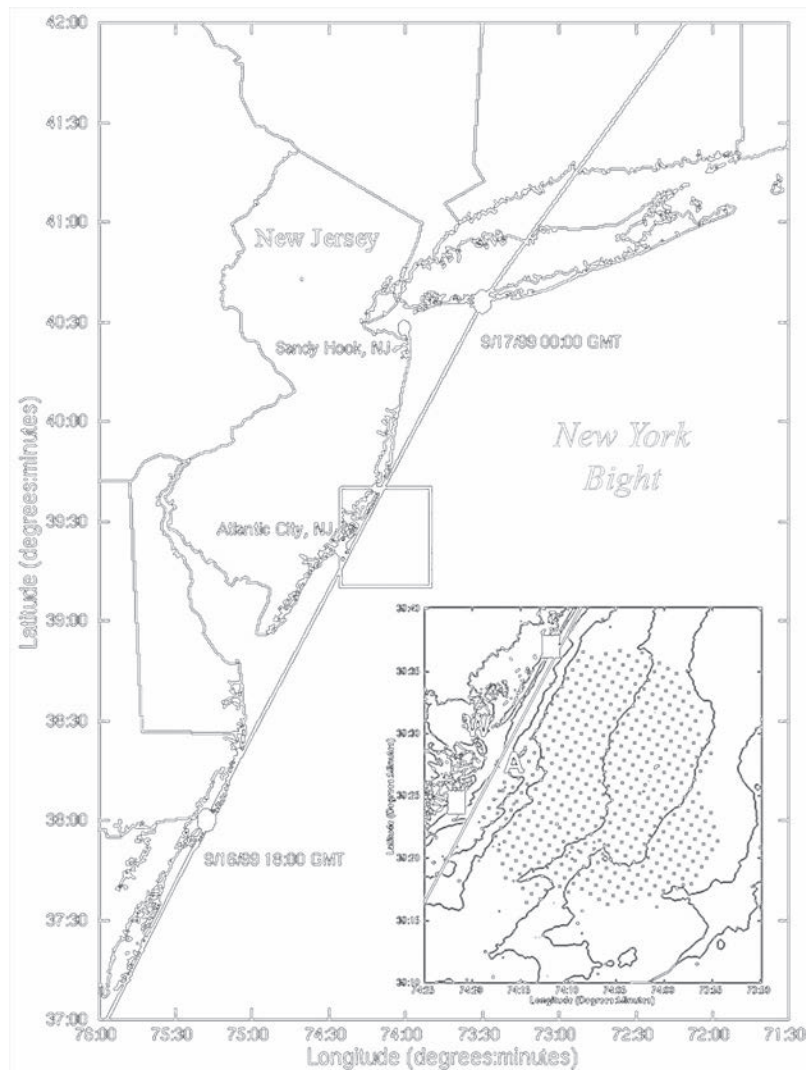


**Figure 1.** Storm track for Hurricane Floyd and the locations of the NOAA coastal sites in Atlantic City and Sandy Hook. The locations of the HF radar sites (squares), HF radar grid (asterisks), ADCP/CTD (A), and met station (W) are shown in the inset.

by a coastal ocean observatory located in Tuckerton New Jersey. Unlike the stratified and/or deep water seen in the responses outlined above, the shallow water column O(30 m) along the New Jersey inner shelf during Floyd was initially well mixed. The shallow water combined with the weak stratification increases the influence of bottom friction. While near-inertial currents have been observed within the study site, this response is typically seen during the summer months when the water column is stratified [Chant, 2001]. The observations are complimented with analytical models to characterize the current structure during and after the passing of Tropical Storm Floyd. Comparisons are drawn between this unstratified shallow water response and the deeper stratified, rotating response discussed above. Section 2 describes the instrumentation used in the study. An overview of the forcing associated with Tropical Storm Floyd is presented in section 3. Section 4 describes the current response to this forcing with observations and

analytical models. Finally, section 5 presents implications to sediment transport and some concluding remarks.

## 2. Methods

### 2.1. Instrumentation

[5] The forcing and response to Tropical Storm Floyd was captured by several different components of an ocean observatory off the New Jersey coast (Figure 1). Remote systems including satellites and high-frequency (HF) radar provided coverage of ocean surface parameters such as sea surface temperature and surface velocity fields. The HF radar system uses two sites in Brant Beach and Brigantine, New Jersey (Figure 1) to generate hourly surface current maps [Barrick *et al.*, 1977; Barrick and Lipa, 1986]. All radial HF radar data were processed by the optimal techniques described by Kohut and Glenn [2003]. These techniques were demonstrated to produce the best comparison with concurrent in situ current meter data. The total vector



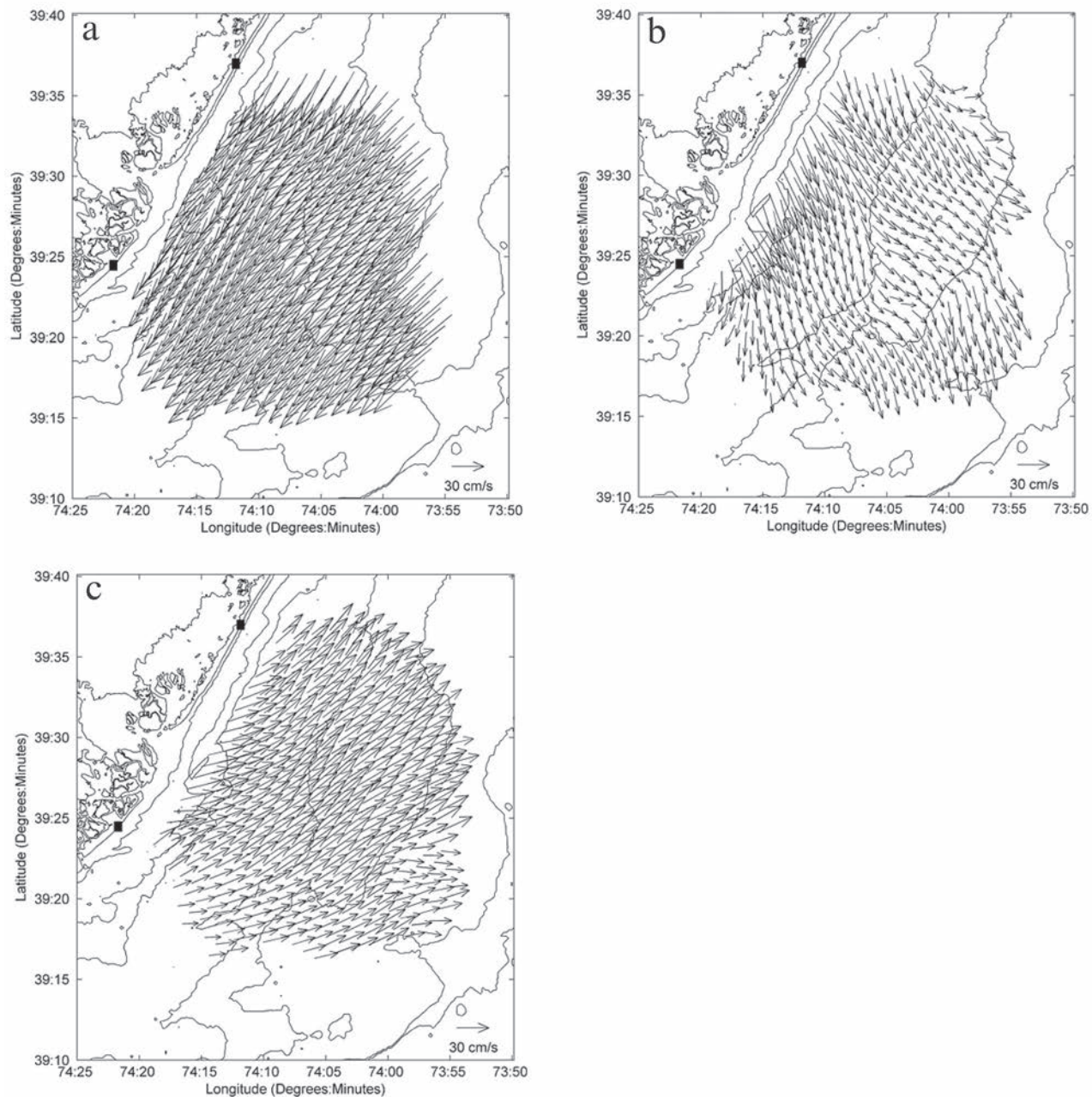


**Figure 2.** Detided surface current fields (a) before (YD 259.125), (b) at the peak significant wave height (YD 260.2083) of, (c) and following (YD 260.75) Tropical Storm Floyd.

HF radar grid stretches 40 km in the alongshore direction and about 30 km in the cross-shore direction (Figure 1). The Floyd data set is a subset of the annual record discussed by Kohut *et al.* [2004]. As discussed there, the time series data at each grid point were detided with a least squares fit of the dominant regional tidal constituents to a yearlong time series.

[6] Subsurface velocity was measured with a bottom-mounted ADCP located at the Long-term Ecosystem Observatory (LEO) [Grassle *et al.*, 1998; Glenn *et al.*, 2000a; Schofield *et al.*, 2001]. The ADCP is located about 5 km offshore in 12 m of water (Figure 1). The subsurface data were center averaged on the top of the hour and detided to match the sampling of the HF radar system. The depth-averaged flow discussed in this paper is an average of the

ADCP data from 3 to 10 m and a surface measurement from an HF radar grid point closest to the ADCP. In addition to subsurface velocity, the LEO CTD provided time series data of bottom temperature, pressure and salinity. Using the time series of the measured temperature and salinity to calculate density and assuming a hydrostatic balance in the vertical, the sea level height was estimated at the LEO site. The sea level anomaly (SLA) is based on a 45 day mean. The measured SLA was corrected for atmospheric pressure and detided using the harmonic fit described above. SLA based on mean sea level (MSL) was also measured at two NOAA coastal sites in Sandy Hook (station 8531680) and Atlantic City (station 8534720), New Jersey ([http://tidesandcurrents.noaa.gov/data\\_res.html](http://tidesandcurrents.noaa.gov/data_res.html)) (Figure 1). These data were also

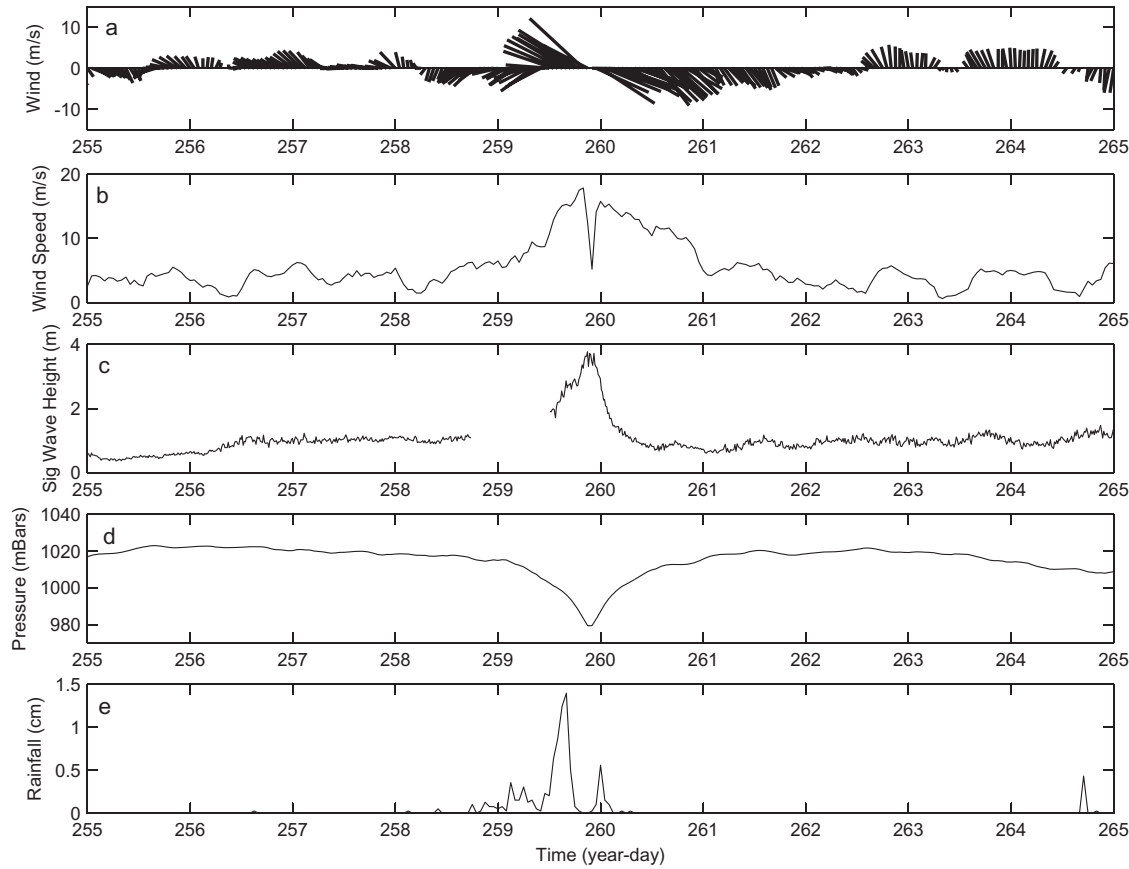


**Figure 3.** Time series of (a) wind velocity, (b) wind magnitude, (c) significant wave height, (d) barometric pressure, and (e) hourly Atlantic City precipitation surrounding Tropical Storm Floyd.

corrected for atmospheric pressure and detided. The meteorological data, measured at the Rutgers University Marine Field Station (Figure 1), includes time series data of atmospheric pressure, winds, temperature, and relative humidity.

## 2.2. Depth-Averaged Model

[7] *Fandry and Steedman* [1994] use the depth averaged shallow water equations to predict the nearshore response to a tropical storm propagating perpendicular and parallel to the coast. In both simulations, the pressure gradient is an important term in the balance [Fandry and Steedman, 1994]. The governing equations of the analytical model are

$$\frac{\partial u}{\partial t} = -g \frac{\partial \eta}{\partial x} + f v + \frac{\tau_{wx}}{\rho H} - \frac{\tau_{bx}}{\rho H} \quad (1)$$

$$\frac{\partial v}{\partial t} = -g \frac{\partial \eta}{\partial y} - f u + \frac{\tau_{wy}}{\rho H} - \frac{\tau_{by}}{\rho H} \quad (2)$$

where  $u$  and  $v$  are the depth-averaged cross-shore and alongshore velocity components,  $f$  is the local Coriolis parameter,  $\eta$  is the sea surface height,  $\rho$  is the water density,  $H$  is the water depth,  $\tau_{wx}$  ( $\tau_{bx}$ ) is the wind stress (bottom stress) in the cross-shore direction, and  $\tau_{wy}$  ( $\tau_{by}$ ) is the wind stress (bottom stress) in the alongshore direction. The nonlinear terms are not expected to be large for this forcing and response, and therefore are left out of equations (1) and (2) [Shay and Elsberry, 1987]. This is confirmed for this case by the observed surface current fields (Figure 2) in

which the time varying flow is nearly parallel and uniform in space. The alongshore flow is about 40 cm/s toward the southwest before the storm, offshore at about 25 cm/s during the peak wave heights associated with the storm, and alongshore at about 30 cm/s toward the northeast after the storm (Figure 2). In the following analysis the acceleration (first term) and Coriolis force (third term) of equations (1) and (2) are calculated with the observed depth-averaged current.

### 2.2.1. Wind Stress

[8] The TOGA-COARE2.6 algorithm, modified for high wind, uses the wind velocity, air and sea temperatures, atmospheric pressure, and the relative humidity to predict the magnitude of the wind stress,  $\tau_w$  [Fairall et al., 1996]. All the atmospheric inputs are available from the meteorological tower. The direction of the wind stress is taken to be the observed wind direction.

### 2.2.2. Bottom Stress

[9] The magnitude of the bottom stress ( $\tau_b$ ) can be represented as

$$\tau_b = \rho u_*^2 \quad (3)$$

where  $u_*$  is the frictional velocity. Assuming a standard linear eddy viscosity,  $K = \kappa u_* z$  and a constant stress layer, we get the following expression for  $u_*$ :

$$u_* = \frac{(u_2 - u_1) \kappa}{\ln\left(\frac{z_2}{z_1}\right)} \quad (4)$$

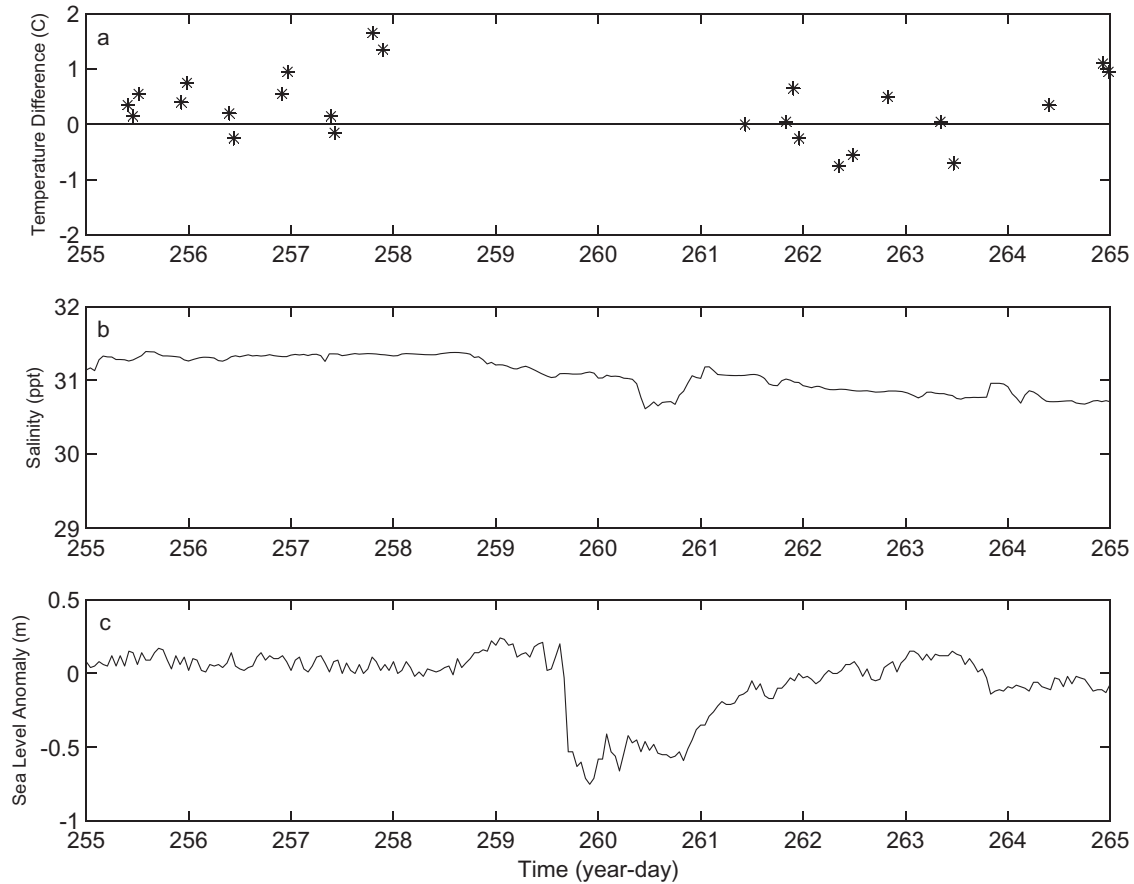


**Figure 4.** (a) Temperature gradient, (b) bottom salinity, and (c) sea level anomaly during the passage of Tropical Storm Floyd.

where  $u_1[z_1]$  and  $u_2[z_2]$  are the raw velocity (height above the seafloor) of the bottom two ADCP bins. *Forristall et al.* [1977] used this expression to calculate bottom stress during Tropical Storm Delia in the Gulf of Mexico. The frictional velocity,  $u_*$ , was then substituted into equation 3 to get the magnitude of the bottom stress,  $\tau_b$ . The direction of the bottom stress is taken to be opposite the bottom current,  $u_1$ .

### 2.2.3. Pressure Gradient

[10] The sea surface slope,  $\left(\frac{\partial \eta}{\partial x}, \frac{\partial \eta}{\partial y}\right)$ , could not be measured directly at the offshore site. Instead it was inferred by requiring the measured terms and the unknown slopes in the model equations to balance. This inferred pressure gradient was compared to the sea level observations from the LEO and the NOAA coastal sites.

### 2.3. Surface Layer Model

[11] Immediately after the storm, there is evidence of a large freshwater input to the system (Figures 3 and 4). The freshwater potentially stratifies the water column changing the vertical structure of the current response. Both the magnitude and direction of the ADCP profiles show evidence of a two-layer system in which the surface layer is much less sheared than the bottom layer. Since the flow is stratified, the surface layer is separated from the bottom and no longer feels the effect of the bottom stress. For this reason, a second version of the model, more representative

of a surface layer, was used. The model equations for the surface layer of this model are

$$\frac{\partial u_s}{\partial t} = -g \frac{\partial \eta}{\partial x} + f v_s + \frac{\tau_{wx}}{\rho H_s} \quad (5)$$

$$\frac{\partial v_s}{\partial t} = -g \frac{\partial \eta}{\partial y} - f u_s + \frac{\tau_{wy}}{\rho H_s} \quad (6)$$

where  $u_s$  and  $v_s$  are the surface layer averaged cross-shore and alongshore velocity components,  $f$  is the local Coriolis parameter,  $\eta$  is the sea surface height,  $\rho$  is the water density,  $H_s$  is the depth of the surface layer, and  $\tau_{wx}$  ( $\tau_{wy}$ ) is the wind stress in the cross-shore (alongshore) direction. We assume the stress at the interface is small compared to the other terms due to stratification. For comparison, both the DA and surface layer (SL) models were run through the entire record. Using these models, the subtidal ocean response to the forcing both during, and immediately after the passing of Tropical Storm Floyd are discussed.

## 3. Forcing

[12] During the morning hours of 8 September 1999, Tropical Storm Floyd first formed about 1400 km east of the Leeward Islands. After two days, the storm strengthened



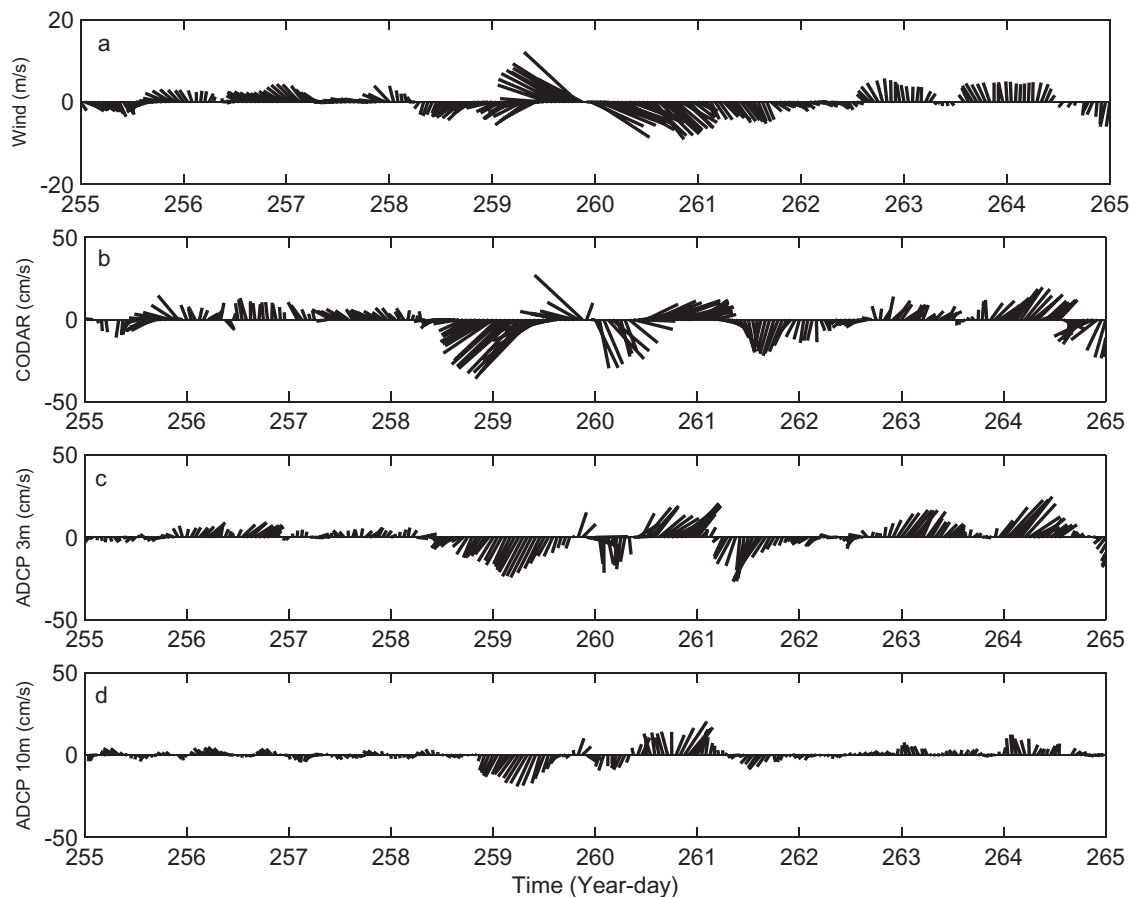


**Figure 5.** Time series of (a) wind velocity, (b) surface current, (c) current at 3 m depth, and (d) current at 10 m depth surrounding Tropical Storm Floyd.

to hurricane status and continued on a west/northwest track toward the eastern United States. Floyd's intensification fluctuated between category one and four on the Saffir/Simpson Hurricane Scale with sustained winds from 150 to 250 km/hr. The hurricane made landfall along the southern North Carolina coast at 0630 GMT on 16 September. At this time Floyd was a category 2 hurricane with sustained winds near 167 km/hr and a forward speed of about 28 km/hr. After landfall, the heavy rains caused extreme flooding as the storm weakened and accelerated toward the north/northeast. The effect of Floyd's rains and winds was seen at the mouth of the Chesapeake Bay with large freshwater outflow strong enough to reverse the flood tide [Valle-Levinson *et al.*, 2002]. Floyd was downgraded to a Tropical Storm just south of the study site at 1800 GMT on 16 September with sustained winds of 111 km/hr. The strong tropical storm continued moving toward the northeast along the New Jersey coast with a forward speed of about 54 km/hr (Figure 1). Wind data from the Rutgers meteorological station clearly shows the center of the storm arriving late on year day (YD) 259 (16 September) (Figure 3). The eye of the storm seen in the local winds and barometric pressure, passes through the study site at 2200 GMT on 16 September (YD 259.9167). Prior to the eye, the strong southeast winds peaked at 18 m/s (65 km/hr). Within the eye, the winds diminished to 5 m/s before 15 m/s northwest winds accom-

panied the second half of the storm. Throughout the period, the winds were predominately in the cross-shore direction. There was also locally heavy rainfall associated with the storm measured at Atlantic City, New Jersey (station 280311) (<http://www.ncdc.noaa.gov>) that peaked at 1.4 cm/hr prior to the storm eye (Figure 3e). This rainfall potentially increases the freshwater flux to the inner shelf after the storm.

[13] The inner shelf observatory focuses on the coastal ocean within the 30 m isobath. Within this shallow system, temperature gradients, calculated with surface satellite data and bottom CTD data, never exceed 2°C during and proceeding the storm (Figure 4a). Compared to the bottom water temperature, there is also a tendency for warmer water near the surface before the storm and cooler water near the surface after the storm, suggesting a freshening of the ocean surface after the storm. The bottom salinity minimum just after the storm also supports a freshwater pulse into the coastal ocean coincident with the storm rains (Figure 4b). Perhaps the strongest ocean signal associated with Floyd was seen in the sea surface height. A surge of 20 cm at the offshore site was followed by an 80 cm drop coincident with the eye of the storm (Figure 4c). This 80 cm drop is about 6% of the total water column. While the water column is initially well mixed prior to the storm, following the sea

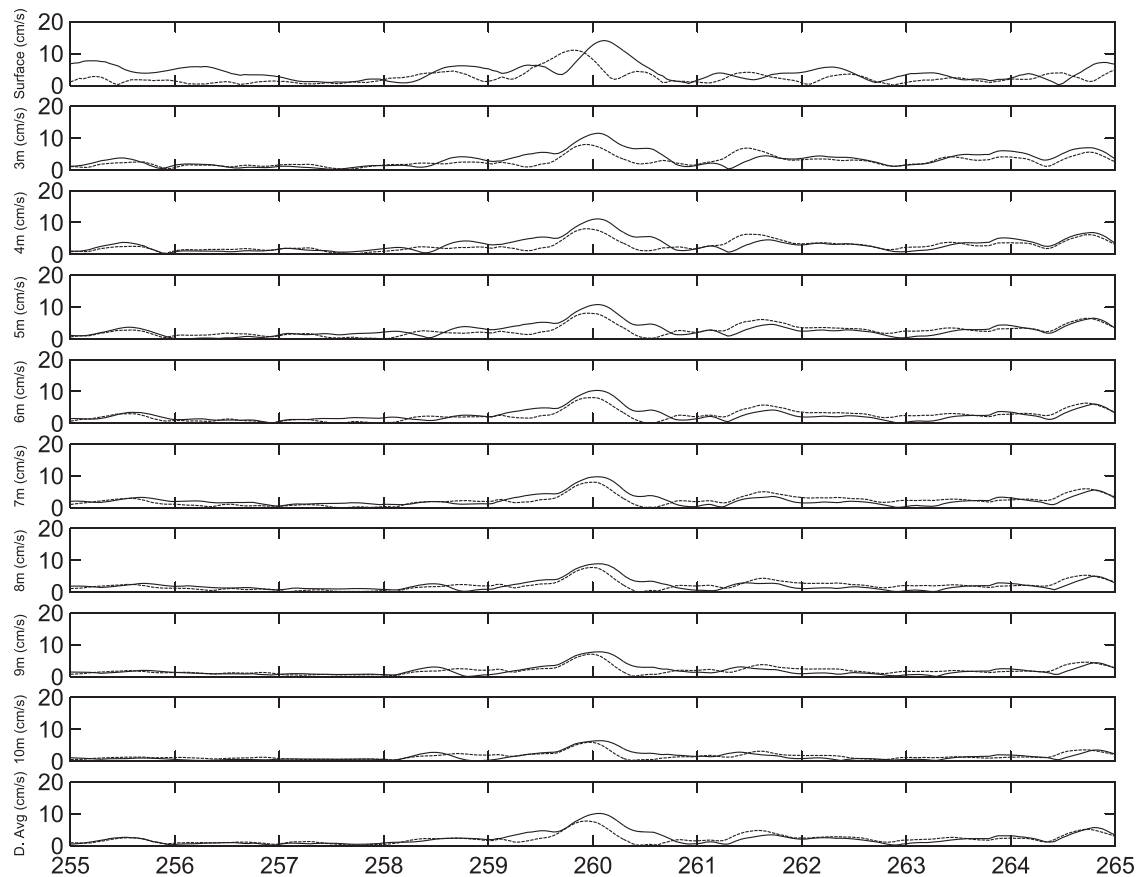


**Figure 6.** Vertical structure of the CW rotating (solid lines) and CCW rotating (dashed lines) components of the near-inertial response.

surface perturbation there is a freshwater pulse onto the inner shelf that potentially stratifies the system.

## 4. Response

### 4.1. Observed Response

[14] The vertical current structure several days before the storm was highly sheared (Figure 5). The stronger currents near the surface tend to follow the winds more closely than the weaker currents near the bottom. There is also a slight rotation to the left with depth. This rotation is representative of the typical vertical structure seen throughout the fall of 1999 [Kohut *et al.*, 2004]. As the storm approaches, this climatology breaks down and the currents increase and become more uniform with depth (Figure 5). Even though the wind forcing is primarily in the cross-shore direction (NW or SE), the depth-independent current response is predominately alongshore (NE or SW). Within 48 hours of the storm onset, the episodic response is replaced by the seasonal structure observed before the storm.

[15] Like the storm response papers outlined in the introduction, we looked at the spatial and temporal structure of the near-inertial current response. The near inertial component of the flow was obtained using a least squares fit to the detided time series. The local inertial period of 18.87 hours was fit to the data using a 1.5 day moving window. This technique has been used in previous dynam-

ical studies and is the mathematical equivalent to complex demodulation [Chant, 2001].

[16] The near-inertial band has a peak during the storm, between YD 259 and YD 261 (Figure 6). There is very little vertical structure in the band except for slightly weaker amplitudes near the bottom. The equal amplitude of the clockwise and counterclockwise rotating components indicates that, like the forcing and unlike the deepwater response discussed in the introduction, the ocean response is rectilinear. Throughout the duration of the storm, the kinetic energy within the near-inertial band is 68% of the kinetic energy of the subtidal, depth-averaged currents.

[17] Spatial maps of the near-inertial motion show that this rectilinear response is oriented in the alongshore direction (Figure 7). At one half inertial period before the storm, the strongest response is seen in the shallower water near the coast. There is a slight  $5^\circ$  advance in phase between the center and northern edges of the field with the center leading the northern edge. The phase propagation speed can be approximated using the local inertial period of 18.87 hours, the  $5^\circ$  phase shift, and the alongshore distance of approximately 20 km. The resulting phase propagation speed of 75 km/hr is consistent with the 54 km/hr translation speed estimate for the storm. When the eye is directly over the study site, the response is in phase and reaches its peak amplitude over the entire field. Within half an inertial period after the storm, the response, still in phase, has significantly decreased across the field. Throughout the

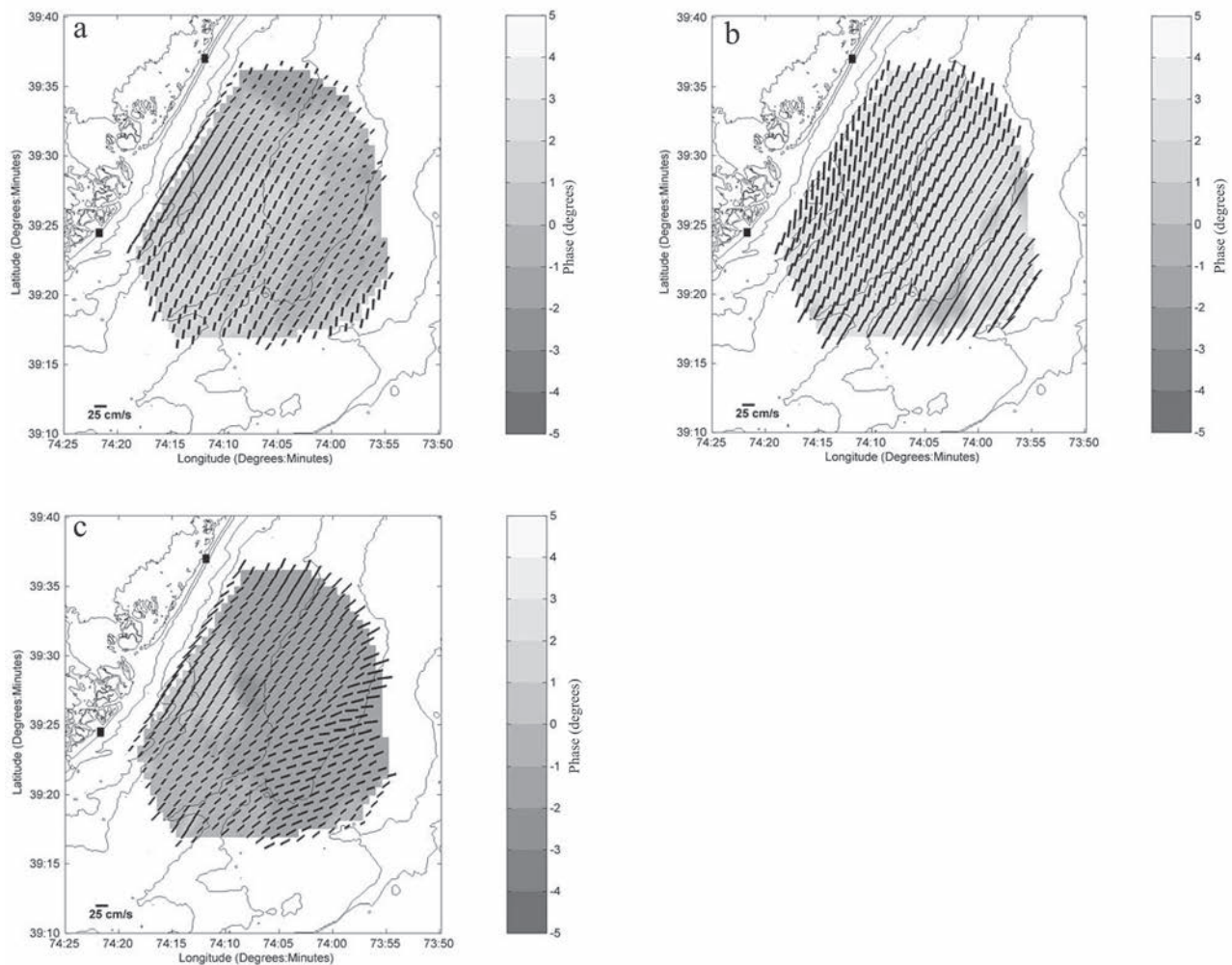


**Figure 7.** Amplitude, orientation, and phase of the near-inertial ellipses (a) one half inertial period before, (b) during, and (c) one half inertial period after the passing of Tropical Storm Floyd.

entire event, the near-inertial response is nearly uniform across the HF radar field and peaks with the storm.

[18] The near-inertial band of the subsurface response is also rectilinear with a mean eccentricity on the order of  $10^{-3}$ , equivalent to an aspect ratio 1000 to 1 between the major and minor axis. Half an inertial period before the eye, the amplitudes are relatively weak with an 8 cm/s maximum near the surface (Figure 8). There is a slight rotation to the left with depth, however, the ellipses are generally oriented along the coast. Similar to the surface response the amplitudes peak near the center of the eye with amplitudes reaching 18 cm/s near the surface and 12 cm/s near the bottom. Once again, the ellipses are oriented with the coast and in phase throughout the water column.

[19] The near-inertial response observed here is not a typical CW rotating response. Unlike the deeper more stratified responses, the currents here slosh back and forth in the alongshore direction. The energy observed in the near-inertial band is not the CW “ringing” response observed in a deeper, more stratified water column, but rather a consequence of the timescale of the storm forcing. During the deeper more stratified response, the near-inertial energy occurs after the storm and last several days. In this shallow

well-mixed response the near-inertial energy peaks during the direct forcing and quickly dissipates following the storm.

[20] The remainder of the paper will focus on the short-lived, rectilinear response using the DA and SL models. Since the larger-scale response is relatively uniform in space, the nearshore response during the direct storm forcing and immediate response, will utilize the ADCP and CODAR derived depth-averaged and surface layer flows. The analysis is described for two periods, the first during the storm and the second immediately after. These time periods were chosen based on the storm characteristics. Assuming a propagation speed of 54 km/hr and an approximate storm radius on the order of 400 km, the study site was directly impacted by the storm for approximately 15 hours. So the first time period was chosen to be 15 hours long, centered at the passing of the eye over the offshore site. The period following the storm was chosen to begin immediately after the storm forcing and continue for 15 hours. On the basis the representative vertical current structure following the storm (Figure 9), the depth of the surface layer,  $H_s$ , in the SL model is taken to be 8 m. Since this response is not a typical rotating, ringing response and



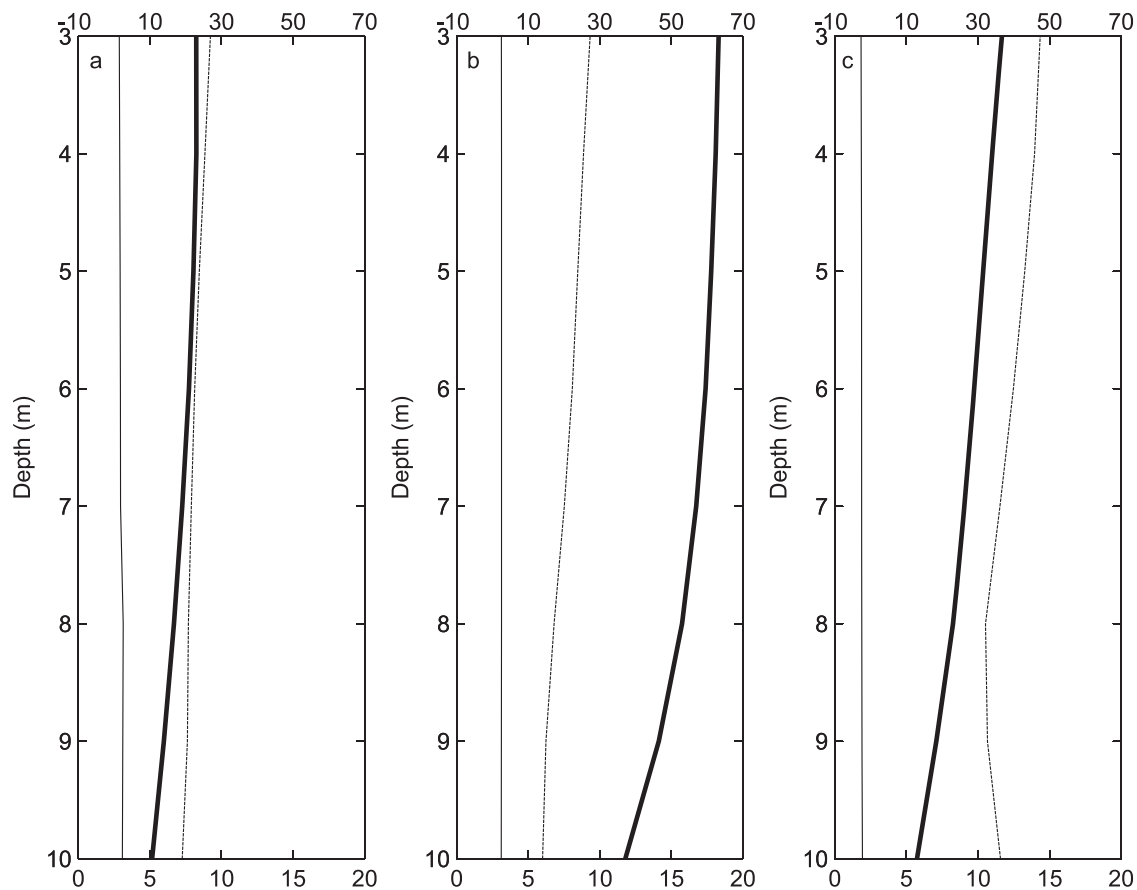


**Figure 8.** Magnitude (thick lines), inclination (dashed lines), and phase (thin lines) of the near-inertial rectilinear response (a) one half inertial period before, (b) during, and (c) one half inertial period after the passing of Tropical Storm Floyd.

the energy in the near-inertial band is 68% of the total kinetic energy, the following analysis describes the entire subtidal ocean response of the storm. The model data will be presented within these time periods, during and after the direct storm forcing.

#### 4.2. Modeled Response During the Storm

[21] As Floyd approaches the study site, the current response accelerates up and down the coast with a weak cross-shore component. The cross-shore balance of the DA model is between the onshore wind stress and the inferred pressure gradient (Figure 10b). In the eye, the onshore winds decrease and the cross-shore current accelerates offshore with the pressure gradient. Bottom friction then increases to balance the large inferred pressure gradient associated with the storm surge. The direction of the spike indicates that the surge is larger near the coast than offshore at the ADCP/CTD. Immediately after the eye, the sea surface flattens in the cross-shore direction and the weak offshore currents are again balanced primarily by the inferred pressure gradient and the wind stress. With the SL model, the cross-shore velocity of the surface layer is very similar to that seen in the DA model (Figure 10). There is initially a weak onshore flow followed by an offshore flow coincident with the eye of the storm. Since the surface layer doesn't feel the effect of bottom stress, the inferred pressure gradient is balanced by the wind stress. This results

in a sloping sea surface that changes sign with the changing winds on either side of the storm eye.

[22] Since the pressure gradient term in both models is inferred to balance the measured terms, each inferred pressure gradient was compared to a measured sea surface slope to determine which model better represents the true force balance. Available coastal sites (Figure 1) were chosen for the alongshore and cross-shore components. The storm propagates very quickly through the study area, about 50 km/hr, covering the 15 km alongshore distance between the Atlantic City site and the LEO-15 site in 18 min. Therefore the sea level difference measured between these two sites is assumed to be representative of the cross-shore pressure gradient particular to the storm. Both the inferred DA model and measured slopes tilt up toward the coast for the duration of the storm, indicating a larger storm surge near the coast (Figure 11a). The SL model slope, on the other hand, changes sign as the storm moves through the region. Even though the measured surge is an order of magnitude larger than that seen in the DA model, the slope is always negative. The discrepancy between the magnitude of the measured and the DA model slopes indicates that nearshore processes may amplify the surge near the coast. This is consistent with long wave theory over irregular-shaped basins that suggests that the cross-shore slope of the storm surge is steeper over shallower water [Dean and Dalrymple, 1991]. Dean and Dalrymple [1991] go on to

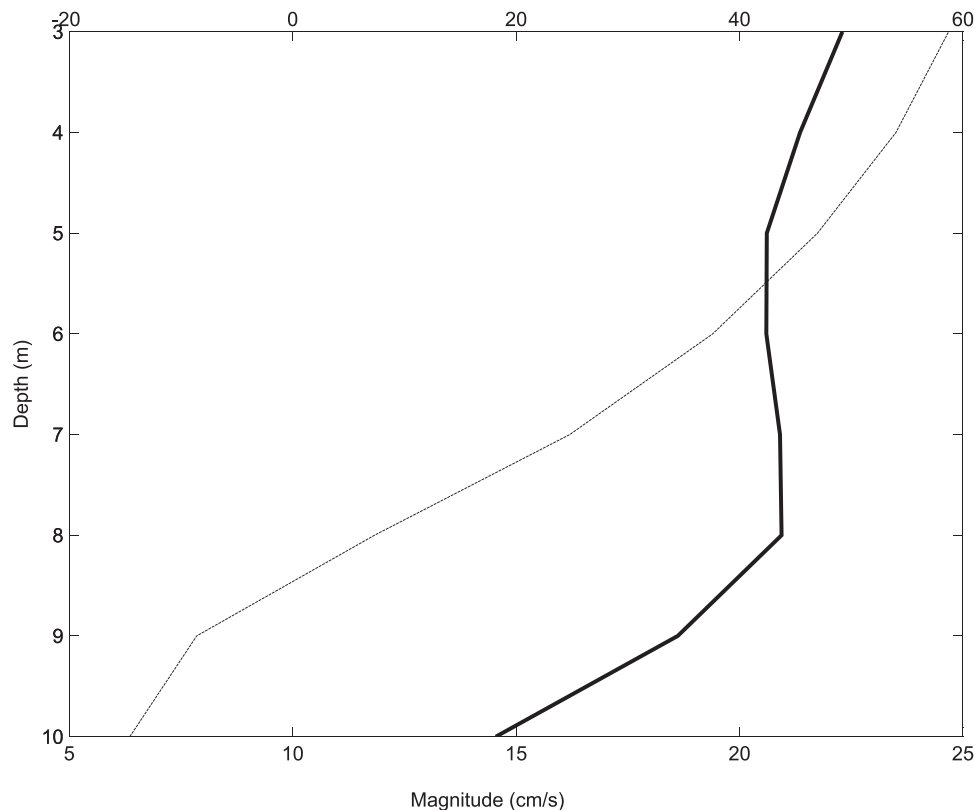


**Figure 9.** Vertical structure of the magnitude (solid line) and direction (dashed line) of the two-layer flow observed after Floyd.

show that for a given bottom stress, the steeper the bottom slope, the steeper the storm surge near the coast. Therefore most of the measured 2.5 m rise observed between the Atlantic City site and the offshore site could occur very close to shore. The 25 cm rise seen in the DA model is likely more representative of the slope acting on the depth-averaged current in the deeper 12 m water column. A time series of the SLA measured at both Atlantic City and the offshore site clearly illustrates the larger surge near the coast (Figure 12). Since the slope of the SL model changes sign during the storm and does not maintain the slope seen in the DA model, it appears that the DA model is more on track with the observations during this segment.

[23] In the alongshore direction, there are three current events associated with the storm. The important terms in the DA model are a combination of the bottom stress, pressure gradient and acceleration (Figure 13). As the storm approaches, the surge south of the study site tilts the sea surface down toward the north. This is seen in the term balance as an acceleration to the north followed by a balance between the pressure gradient and bottom stress. Immediately after the storm, the surge moves through the site and the pressure gradient changes sign. This event starts as acceleration toward the south followed again by a balance between the pressure gradient and bottom stress. After the storm has left the area there is another acceleration toward the south that once again is followed by a balance between the pressure gradient and bottom stress. This small event is correlated with the large rainfall associated with the storm (Figure 3e) and the salinity minimum observed

offshore near the bottom (Figure 4b). The three current events are also seen in the mean surface layer flow of the SL model, however the force balance of this model shows an acceleration driven by the pressure gradient term. Since there is no bottom stress in this model, the influence of the wind stress on the overall balance is increased (Figure 13d).

[24] Once again the inferred pressure gradient of each model was compared to a measured sea surface slope. For the alongshore component, the slope was calculated between the Sandy Hook and the Atlantic City sites. In the measured, DA model, and SL model there is evidence of all three events (Figure 11). The largest is seen during the second event associated with a surge north of the site. While there is evidence of all three events in both the DA and SL inferred pressure gradients, the second event is much smaller in the SL model (Figure 11b). Both the measured and DA model slopes are on the order of 10 cm over 10 km. There is a 1 hour time offset in which the measured slope leads the DA modeled slope. This offset between the 2 peaks could be due to differences that occur when comparing a sea level difference measured across 115 km (distance between the Atlantic City and Sandy Hook sites) to a predicted gradient based on observations collected at a single point 5 km offshore. The magnitude of the three event structure is similar in both the observations and the DA model. The SL model, however, underestimates the slope, especially that associated with the second event. Once again it appears that the DA model is more on track for the period during the storm. Both the cross-shore and alongshore components of the DA model indicate the

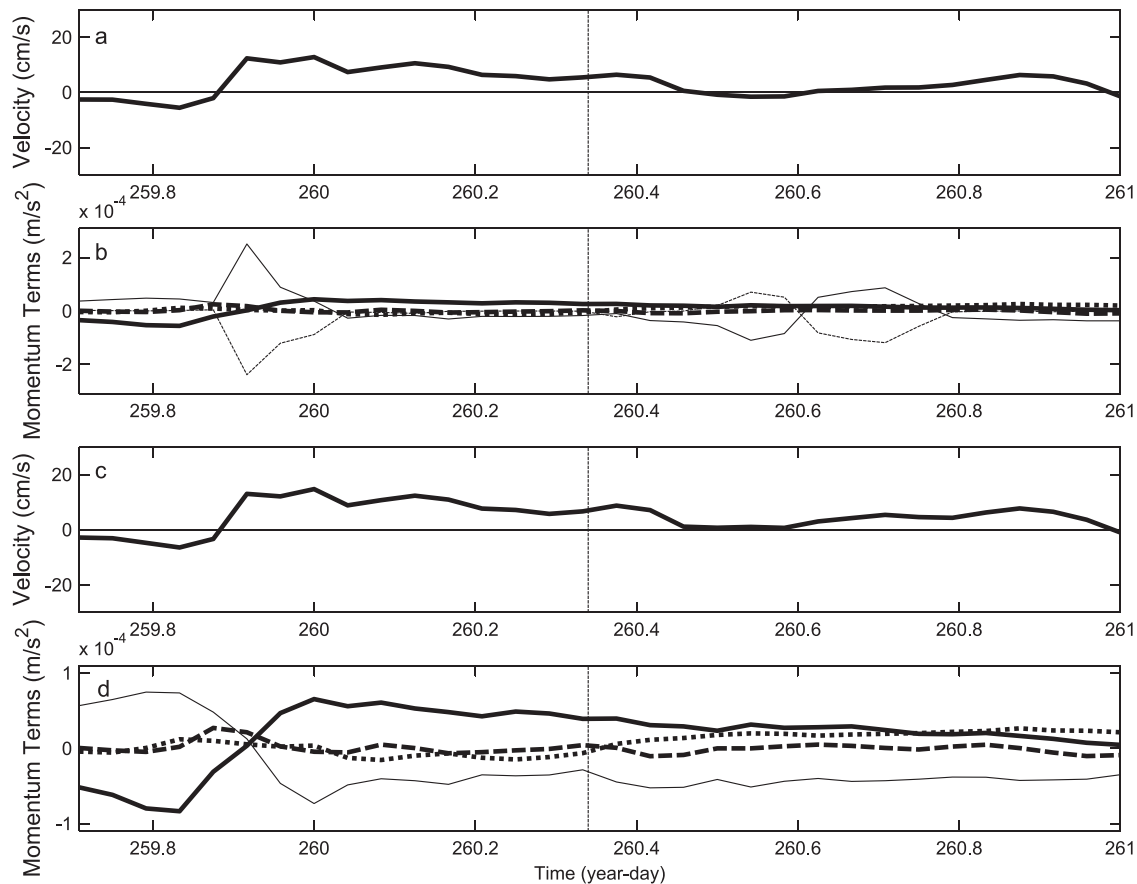


**Figure 10.** Cross-shore (a) depth-averaged velocity, (b) depth-averaged momentum balance, including the acceleration (thick dashed line), Coriolis (dotted line), wind stress (thick solid line), bottom stress (thin dashed line), and pressure gradient (thin solid line) terms, (c) surface layer velocity, (d) surface layer momentum balance, including the acceleration (thick dashed line), Coriolis (dotted line), wind stress (thick solid line), and pressure gradient (thin solid line) terms. The vertical dashed line separates the data into the during and after storm regimes.

currents associated with the storm slosh back and forth with the pressure gradient.

### 4.3. Modeled Response After the Storm

[25] After the storm, freshwater from the strong rains associated with Floyd potentially stratifies the water column. The cross-shore component of the SL model has a steady cross-shore surface layer flow in which the pressure gradient balances both the wind stress and Coriolis (Figure 10). The DA model is a multiterm balance between the wind stress, pressure gradient, Coriolis, and bottom stress. The exception to this multiterm balance is between YD 260.4 and 260.8 when the balance is dominated by two terms, the pressure gradient and bottom stress (Figure 10). During this time, the sea surface slope changes sign several times to balance the bottom stress. This oscillation is not seen in either the measured or SL model slopes (Figure 11). This fluctuation, seen only in the DA model, is due to an apparent overprediction of the influence of bottom stress on the surface currents. The large bottom stress requires that the sea surface slope compensate to keep the model in balance.

[26] Similarly in the alongshore direction, the DA model is predominately a two-term balance between the pressure gradient and the bottom stress terms (Figure 13). In the SL model there is a multiterm balance between acceleration, pressure gradient, Coriolis, and wind stress. The resulting pressure gradient is much smaller than that seen in the DA model (Figure 13). The measured alongshore pressure gradient between the two coastal sites in Sandy Hook and Atlantic City agrees much closer with the SL model slope than that seen in the DA model (Figure 11b).

[27] In both the alongshore and cross-shore direction, the bottom stress term in the DA model leads to an overprediction of the sea-surface slope. On the basis of comparisons to the observed sea surface slopes, it appears that the SL model, where bottom stress does not affect the surface layer, better represents the upper ocean force balance immediately following the storm. Even though the water column is largely isothermal (Figure 4a), the large input of freshwater by the storm into the system likely stratifies the fluid. Since the vertical temperature gradient after the storm is negative (Figure 4a), the water column must be composed of a cold, fresher layer over a warm, more saline layer. The



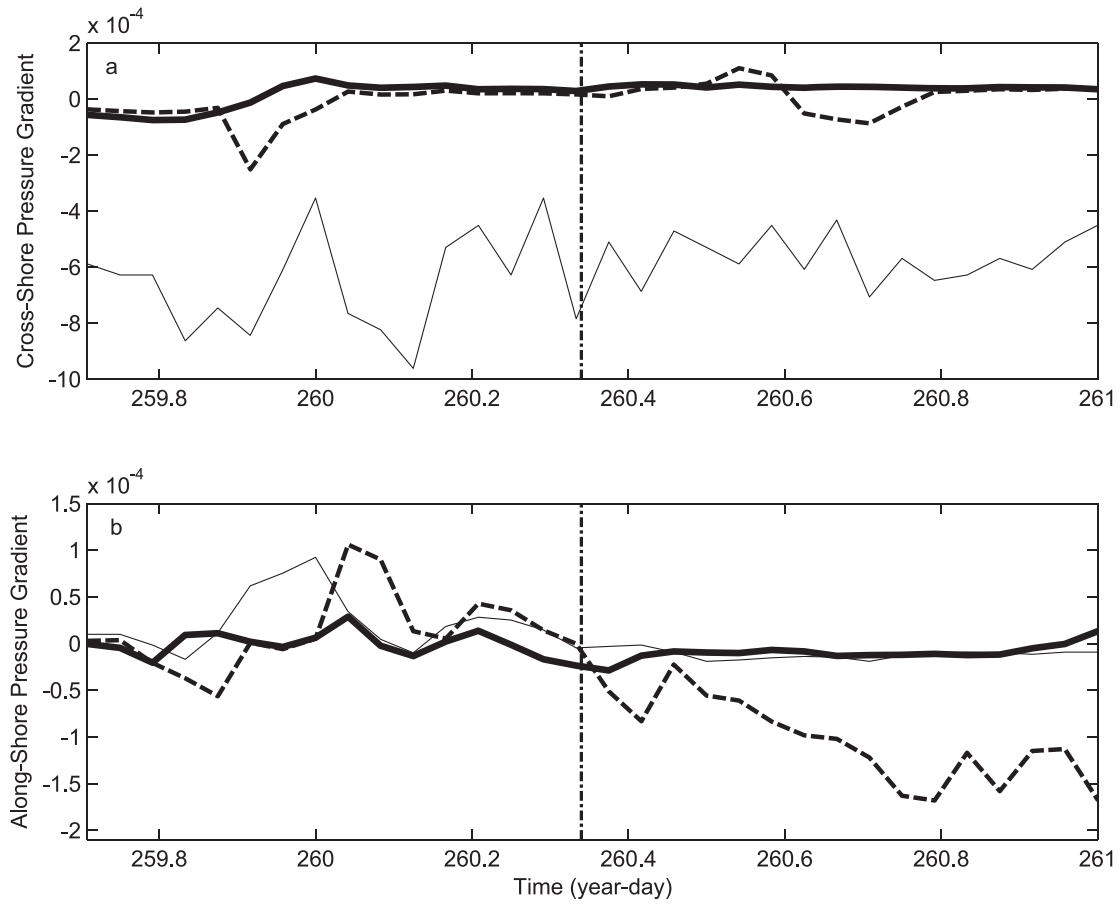


**Figure 11.** (a) Cross-shore and (b) Alongshore components of the measured (thin lines), inferred depth averaged (dashed lines), and inferred surface layer (thick lines) pressure gradient. The vertical dashed line separates the data into the during and after storm regimes.

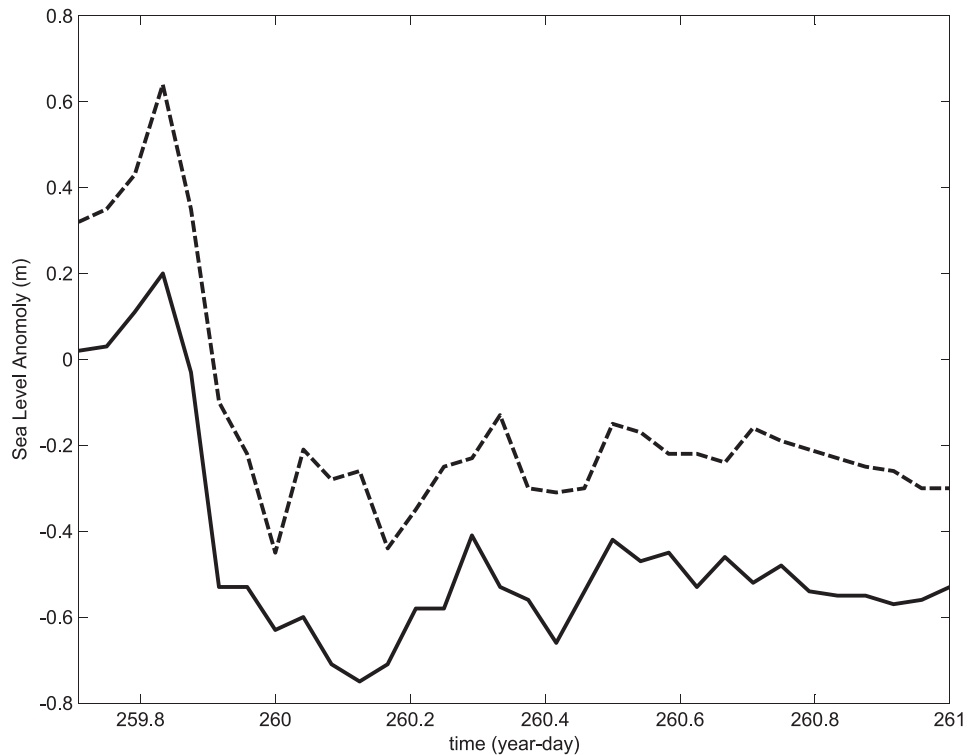


**Figure 12.** SLA measured at Atlantic City (dashed line) and the offshore node (solid line).

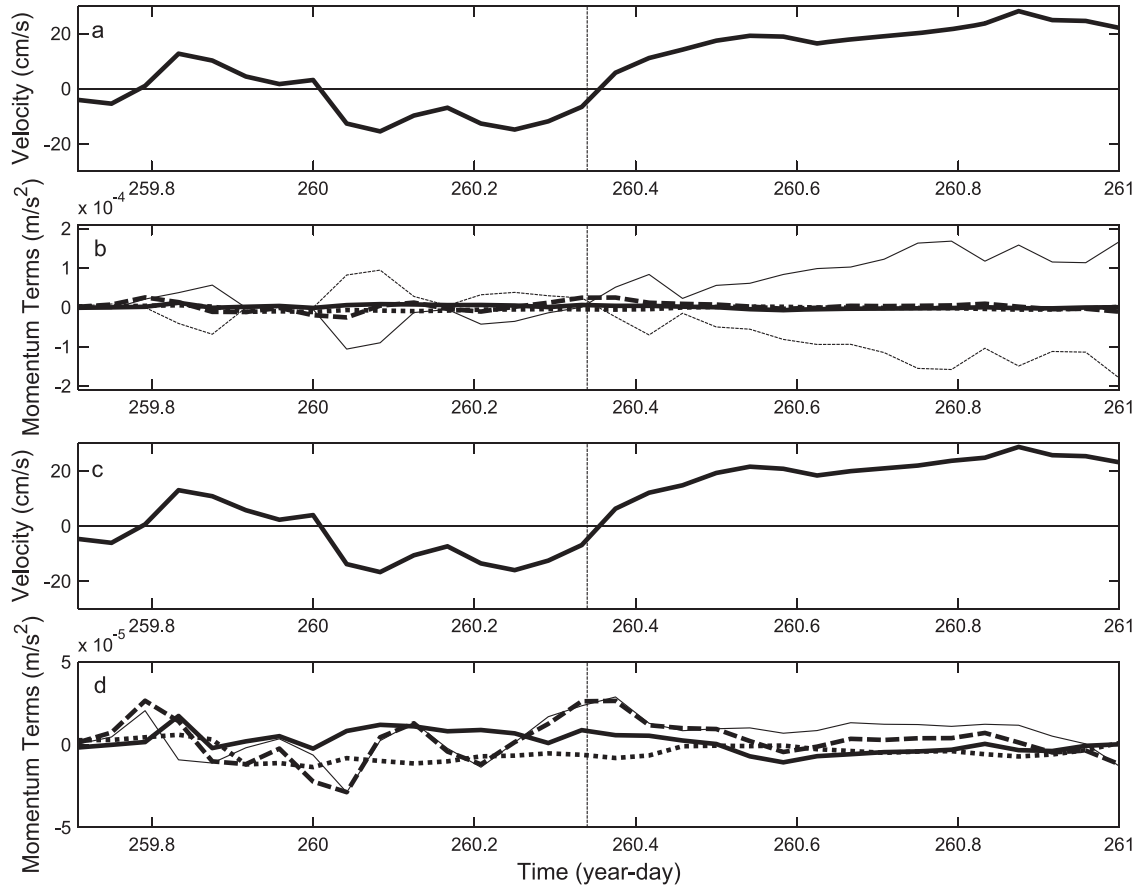


**Figure 13.** Alongshore (a) depth-averaged velocity, (b) depth-averaged momentum balance, including the acceleration (thick dashed line), Coriolis (dotted line), wind stress (thick solid line), bottom stress (thin dashed line), and pressure gradient (thin solid line) terms, (c) surface layer velocity, (d) surface layer momentum balance, including the acceleration (thick dashed line), Coriolis (dotted line), wind stress (thick solid line), and pressure gradient (thin solid line) terms. The vertical dashed line separates the data into the during and after storm regimes.

SL model and measured alongshore pressure gradients indicate a rise of about 1 cm over 10 km. The stratification induced by the large rain event appears to isolate the surface layer from the effect of bottom friction in the observed response. The structure of the current response after the storm is more representative of a two-layer flow in which the acceleration of the surface layer is balanced by the alongshore pressure gradient.

#### 4.4. Energy Flux of the Response

[28] The energy associated with the storm response differentiates the shallow water response from the deep water responses outlined in the introduction. In deep water, the energy put into the system by the passing storm was predominately in the near-inertial band and dissipates very slowly over several days. This is referred to as the “relaxation stage” of the response by Price *et al.* [1994]. This relaxation stage typically lasts for 5 to 10 days. For the specific case of Floyd and the shallow inner shelf, the entire event is much shorter. The energy put into the system dissipates much faster.

[29] The energy pathways associated with Tropical Storm Floyd were identified with a work equation based on the DA model during the initial time period in which it appears

to be more representative. The work done by each term was calculated by multiplying equations 1 and 2 by velocity so that

$$\frac{\partial KE_x}{\partial t} = -g \frac{\partial \eta}{\partial x} \bullet u + f v \bullet u + \frac{\tau_{wx}}{\rho H} \bullet u - \frac{\tau_{bx}}{\rho H} \bullet u \quad (7)$$

$$\frac{\partial KE_y}{\partial t} = -g \frac{\partial \eta}{\partial y} \bullet v - f u \bullet v + \frac{\tau_{wy}}{\rho H} \bullet v - \frac{\tau_{by}}{\rho H} \bullet v \quad (8)$$

Each term on the right side of the equations is the work done by the respective term in equations 1 and 2. The work done by the wind and bottom friction was then compared to the change in kinetic energy (KE) of the entire system with time. The following discussion focuses on the energy input and dissipation particular to the storm.

[30] The kinetic energy associated with the storm increases sharply around YD 259.8 as the storm approaches (Figure 14a). Throughout the storm there are three distinct peaks in the kinetic energy. Preceding each of these peaks is an increase in the total work (term 1 in equations (7) and (8)) (Figures 14b and 14c). Since the peaks in the work done by the wind do not appear to coincide with these energy

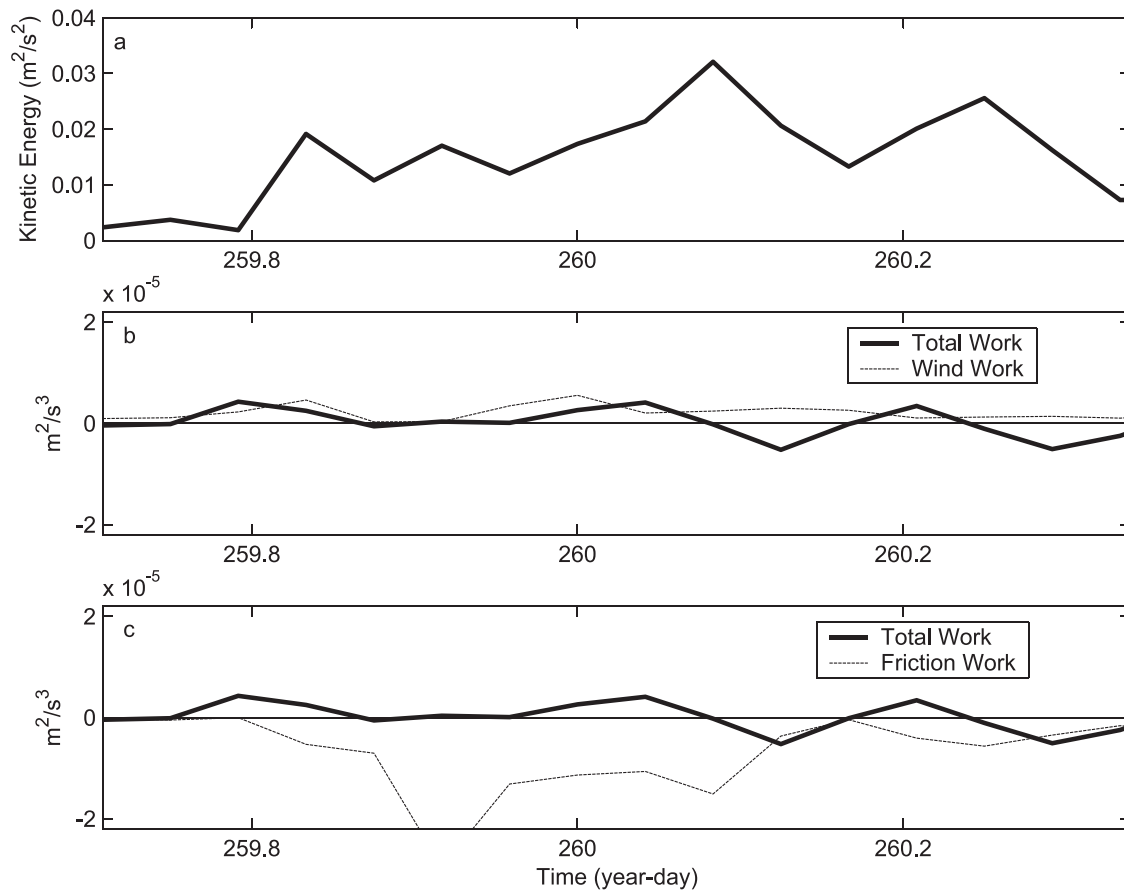


**Figure 14.** Total (a) kinetic energy, (b) work done by the wind, and (c) work done by bottom friction. The total work is quantified as the change in kinetic energy.

peaks, the wind does not appear to contribute significantly to the net increase in the total work. These three peaks are instead associated with the oscillating sea surface slope. With each increase in the kinetic energy there is an increase in the magnitude of the work done by the bottom friction term. So any energy added to the system by the oscillating pressure gradient is quickly dissipated by bottom friction. A closer look at the individual components of the energy equations shows a clear interaction between the cross-shore and alongshore components of the total work.

#### 4.4.1. Cross-Shore Energy

[31] The kinetic energy of the cross-shore current component is very weak throughout most of the study period except for the peak coincident with the eye of the storm (Figure 15a). As the storm approaches, the cross-shore wind adds energy to the system without changing the kinetic energy (Figure 15b). Instead the wind work builds up the potential energy of the system in the form of a pressure gradient. It is not until the wind dies in the storm eye that this potential energy is turned into kinetic. Following the peak in kinetic energy, the bottom friction work peaks, quickly dissipating the energy added by the wind (Figure 15c).

#### 4.4.2. Alongshore Energy

[32] The alongshore currents are more energetic than that seen in the cross-shore balance (Figure 16a). Since the wind forcing during the storm is predominately in the cross-shore

direction, the work done by the alongshore wind stress is very small throughout the study period (Figure 16b). During the storm, kinetic energy is added and taken away from the system with each sea level oscillation observed and discussed in the previous section. Like the cross-shore direction, a peak in bottom friction work follows each input of kinetic energy so that the energy put into the system by the oscillating pressure gradient is quickly taken out by bottom friction (Figure 16c).

[33] By separating the energy budget into the cross-shore and alongshore directions, the contribution of the cross-shore winds to the oscillating sea level is more evident. The storm winds set up an alongshore pressure gradient that moves up the coast with the storm. The energy associated with the moving pressure gradient is quickly diminished by bottom friction. In this shallow well-mixed ocean there is no time for the energy to propagate away before the bottom stress dissipates all the energy. For this reason, the response to this storm is shorter relative to the modeled and observed responses of a deeper more strongly stratified ocean.

## 5. Conclusions

[34] The two analytical models chosen for this study provide insight on the apparent force balances responsible for the observed response to Tropical Storm Floyd. While



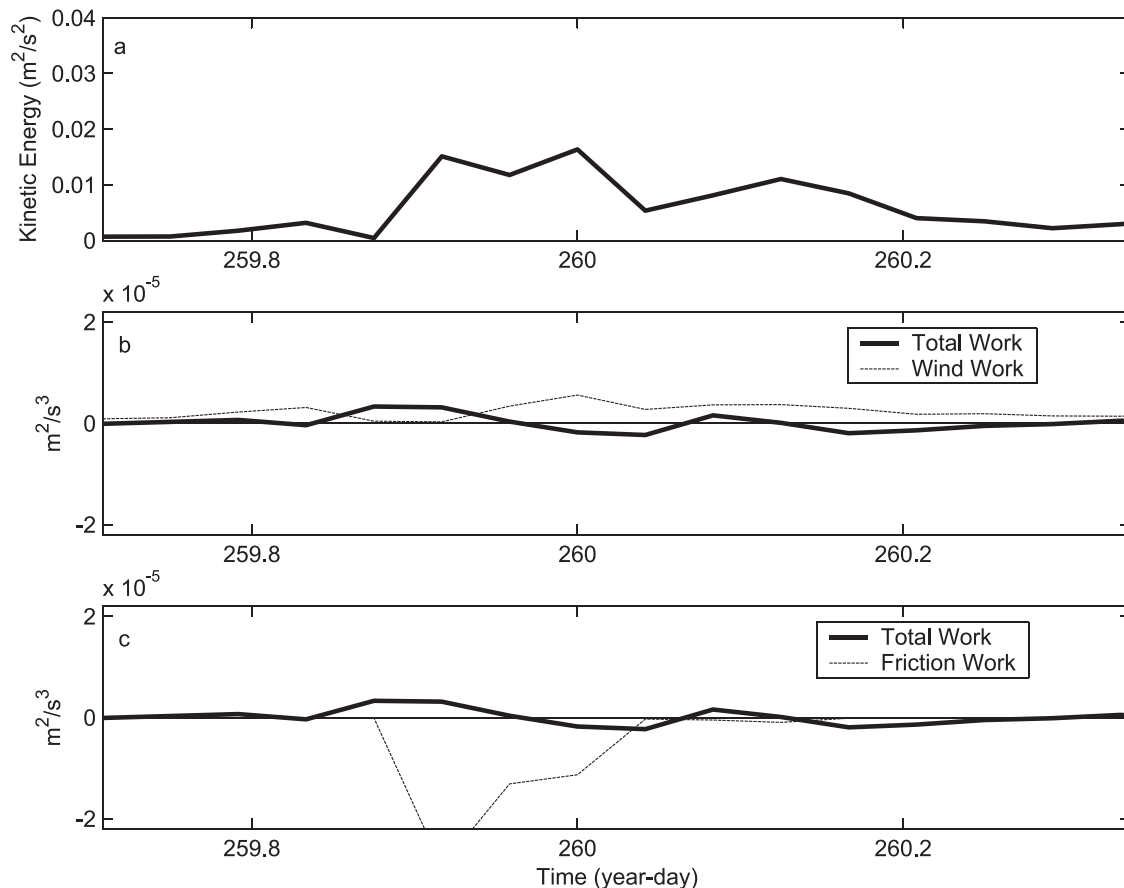


**Figure 15.** Cross-shore (a) kinetic energy, (b) work done by the wind, and (c) work done by bottom friction. The total work is quantified as the change in kinetic energy (equation (7)).

there were no direct measurements of the local pressure gradient term, the DA model pressure gradient was more consistent with the sign of the available observations during the storm and the SL model was more consistent after the storm. During the storm forcing, the dominant balance was between the pressure gradient and the bottom stress, driving an alongshore current that switched from northward to southward (Figure 2). After the storm, freshwater stratifies the system and the dominant balance of the surface layer is between the acceleration and local wind stress. In the future, better estimates of sea surface slopes from arrays of bottom pressure sensors could help to describe the response in more detail.

[35] Floyd also generated large waves as it propagated up the coast so there is potential for a large sediment resuspension and transport event. The largest waves observed at the offshore LEO site coincide with the southward current event immediately following the passage of the storm eye (Figure 17). With equivalent bottom wave orbital velocities [Styles and Glenn, 2002] on the order of 80–100 cm/s and depth averaged currents on the order of 20 cm/s toward the south, the integrated sediment transport during the storm will be to the south and offshore. This is consistent with the regional response modeled by Keen and Glenn [1995]. Typical nor'easter storm transport events observed at the LEO site have an alongshore component to the south and a cross-shore component toward the coast [Styles, 1998;

Styles and Glenn, 2005]. Styles [1998] suggests that the onshore component is steered by the local topography. Since the event seen during Floyd has an offshore component, it appears that the direction and possibly the duration of the tropical storm forcing is sufficient to overcome the local steering effects of topography. Unlike nor'easters in which the winds are from the northeast, the winds immediately following Floyd had a strong offshore component (Figure 3) that steers the alongshore flow slightly offshore (Figure 10), leading to net transport away from the coast.

[36] The shallow well-mixed response to the passing of Tropical Storm Floyd is a short episodic event. The effect of the storm perturbs the current structure for about 48 hours before the seasonal climatology returns. While there is energy in the near-inertial band, it is not the typical clockwise rotation seen with baroclinic responses in a deeper stratified ocean. Instead the oscillating sea surface slope associated with the fast moving storm and the increased influence of the bottom stress drives an alongshore current that accelerates to the north and south with the changing sea surface. Following the storm, freshwater stratifies the water column, shifting the response from a single layer to a two-layer system. Through the entire event the energy put into the system by the storm is quickly dissipated by bottom friction. The results presented here show that the response of the inner shelf to a passing tropical storm is much shorter than that seen in deeper more

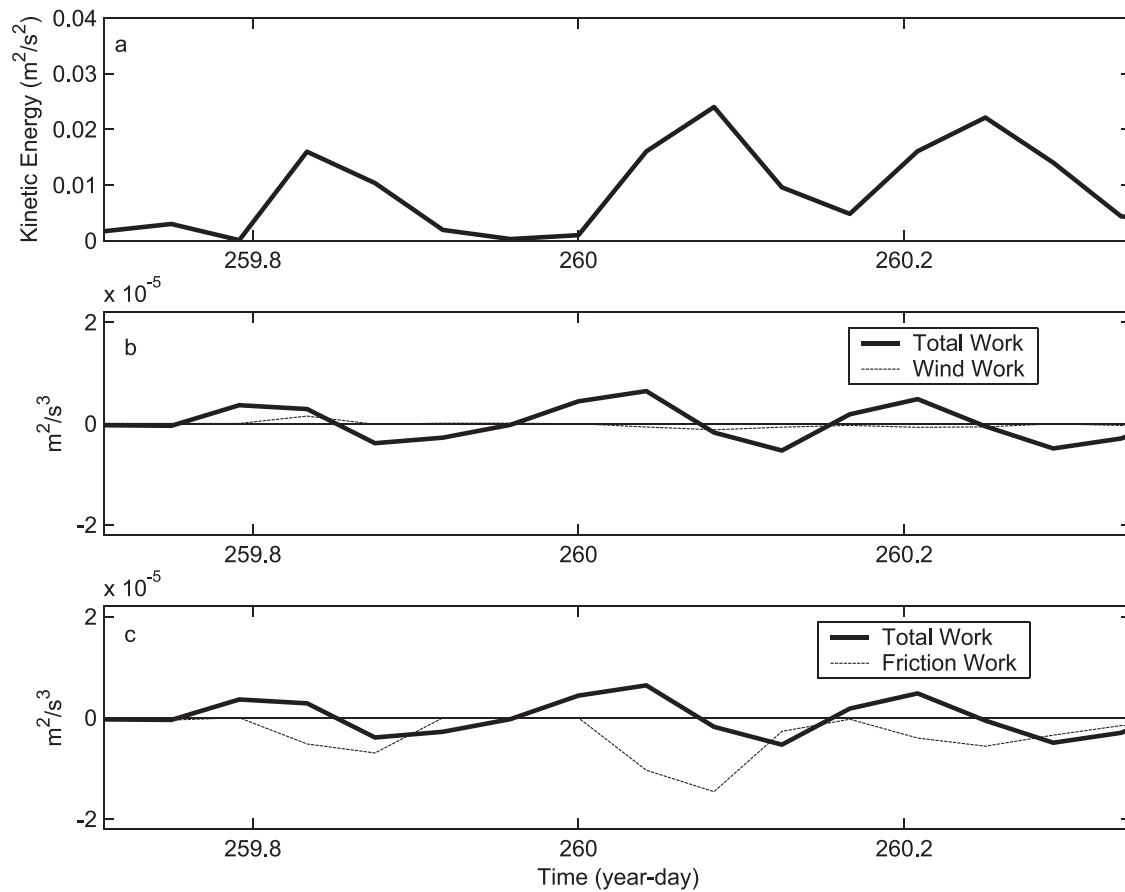


**Figure 16.** Alongshore (a) kinetic energy, (b) work done by the wind, and (c) work done by bottom friction. The total work is quantified as the change in kinetic energy (equation (8)).

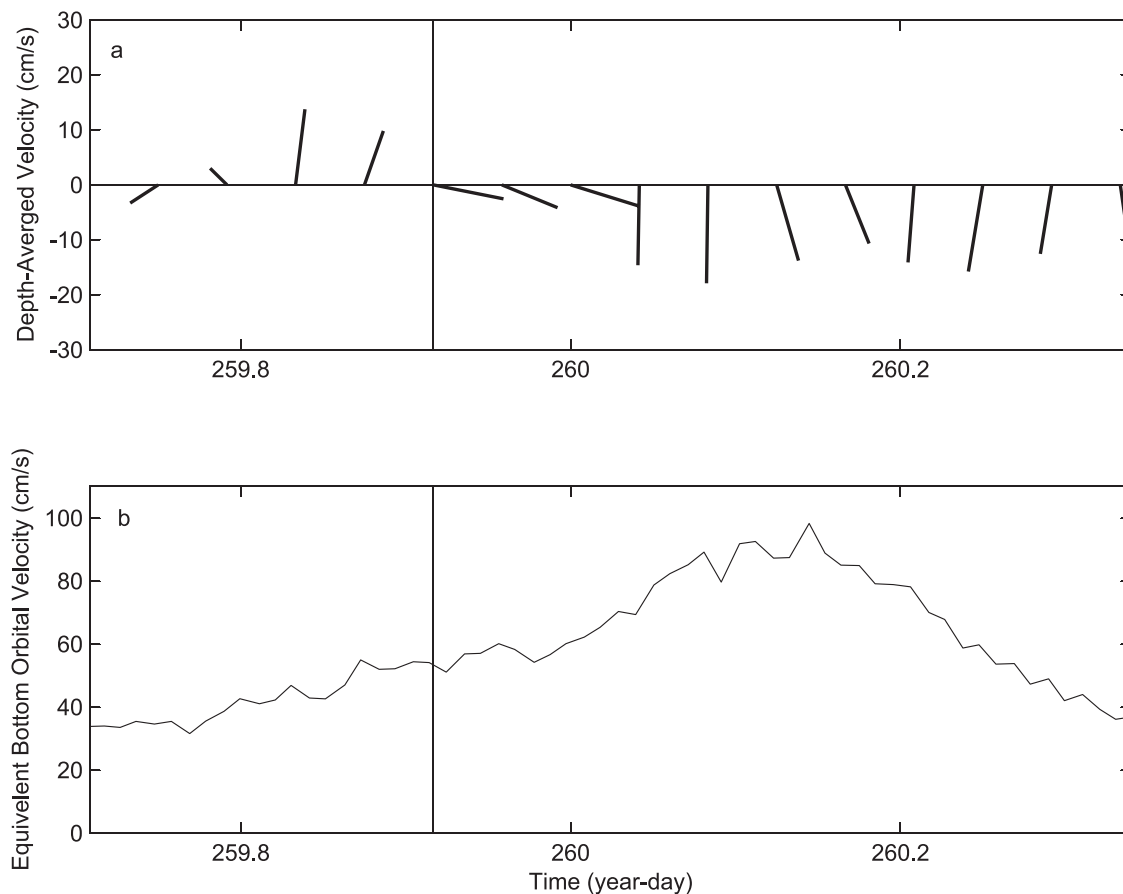


**Figure 17.** (a) Depth-averaged currents and (b) equivalent bottom wave orbital velocities associated with Tropical Storm Floyd. The vertical line indicates the passage of the storm eye.

stratified domains. This response is a largely barotropic, setup by the storm surge and local winds. The oscillating alongshore flow is an immediate response to the direct storm forcing that quickly dissipates. The larger-scale northward flow, setup by the cross-shore winds is then maintained for a day after the storm by the continued offshore winds.

[37] Timing of the storm surge occurs during the unstratified initial response when bottom friction is important to the force balance. Thus storm surge models should contain accurate representations of the bottom friction that include the influence of the waves.

## References

- Barrick, D. E., and B. J. Lipa (1986), Correcting for distorted antenna patterns in CODAR ocean surface measurements, *IEEE J. Oceanic Eng.*, *11*, 304–309.
- Barrick, D. E., M. W. Evens, and B. L. Weber (1977), Ocean surface currents mapped by radar, *Science*, *198*, 138–144.
- Brooks, D. A. (1983), The wake of Hurricane Allen in the western Gulf of Mexico, *J. Phys. Oceanogr.*, *13*, 117–129.
- Chant, R. J. (2001), Evolution of near-inertial waves during an upwelling event on the New Jersey inner shelf, *J. Phys. Oceanogr.*, *31*, 746–763.
- Dean, R. G., and R. A. Dalrymple (1991), Storm surge, in *Water Wave Mechanics for Engineers and Scientists*, edited by P. L. Liu, pp. 157–163, World Sci., Hackensack, N. J.
- Fairall, C. W., E. F. Bradley, D. P. Rogers, J. B. Edson, and G. S. Young (1996), Bulk parameterization of air-sea fluxes for TOGA COARE, *J. Geophys. Res.*, *101*, 3747–3764.
- Fandry, C. B., and R. K. Steedman (1994), Modelling the dynamics of the transient, barotropic response of continental shelf waters to tropical cyclones, *Cont. Shelf Res.*, *14*, 1723–1750.
- Forristall, G. Z., R. C. Hamilton, and V. J. Cardone (1977), Continental shelf currents in Tropical Storm Delia: Observations and theory, *J. Phys. Oceanogr.*, *7*, 532–546.
- Glenn, S. M., W. Boicourt, B. Parker, and T. D. Dickey (2000), Operational observation networks for ports, a large estuary and an open shelf, *Oceanography*, *13*, 12–23.
- Grassle, J. F., S. M. Glenn, and C. von Alt (1998), Ocean observing systems for marine habitats, paper presented at OCC '98, Mar. Technol. Soc., Baltimore, Md.
- Keen, T. R., and S. M. Glenn (1995), A coupled hydrodynamic-bottom boundary layer model of storm and tidal flow in the Middle Atlantic Bight of North America, *J. Phys. Oceanogr.*, *25*, 391–406.
- Keen, T. R., and S. M. Glenn (1999), Shallow water currents during Hurricane Andrew, *J. Geophys. Res.*, *104*, 23,443–23,458.
- Kohut, J. T., and S. M. Glenn (2003), Improving HF radar surface current measurements with measured antenna beam patterns, *J. Atmos. Oceanic Technol.*, *20*, 1303–1316.
- Kohut, J. T., S. M. Glenn, and R. J. Chant (2004), Seasonal current variability on the New Jersey inner shelf, *J. Geophys. Res.*, *109*, C07S07, doi:10.1029/2003JC001963.
- Kundu, P. K. (1984), Generation of coastal inertial oscillations by time-varying wind, *J. Phys. Oceanogr.*, *14*, 1901–1913.
- Kundu, P. K. (1986), A two-dimensional model of inertial oscillations generated by a propagating wind field, *J. Phys. Oceanogr.*, *16*, 1399–1411.
- Mayer, D. A., H. O. Mofjeld, and K. D. Leaman (1981), Near-inertial waves observed on the outer shelf in the Middle Atlantic Bight in the wake of Hurricane Belle, *J. Phys. Oceanogr.*, *11*, 87–106.
- Paduan, J. D., R. A. De Szoeke, and R. A. Weller (1989), Inertial oscillations in the upper ocean during the Mixed Layer Dynamics Experiment (MILDEX), *J. Geophys. Res.*, *94*, 4835–4842.
- Price, J. F., T. B. Sanford, and G. Z. Forristall (1994), Forced stage response to a moving hurricane, *J. Phys. Oceanogr.*, *24*, 233–260.



- Schofield, O., T. Bergmann, W. P. Bissett, F. Grassle, D. Haidvogel, J. Kohut, M. Moline, and S. Glenn (2001), The long term ecosystem observatory: An integrated coastal observatory, *IEEE J. Oceanic Eng.*, 27, 146–154.
- Shay, L. K., and S. W. Chang (1997), Free surface effects on the near-inertial ocean current response to a hurricane: A revisit, *J. Phys. Oceanogr.*, 27, 23–39.
- Shay, L. K., and R. L. Elsberry (1987), Near-inertial ocean current response to Hurricane Frederic, *J. Phys. Oceanogr.*, 17, 1249–1269.
- Shay, L. K., S. W. Chang, and R. L. Elsberry (1990), Free surface effects on the near-inertial ocean current response to a hurricane, *J. Phys. Oceanogr.*, 20, 1405–1424.
- Styles, R. (1998), A continental shelf bottom boundary layer model: Development, calibration, and applications to sediment transport in the Middle Atlantic Bight, Ph.D. dissertation, 261 pp., Rutgers–State Univ. of N. J., New Brunswick.
- Styles, R., and S. M. Glenn (2002), Modeling bottom roughness in the presence of wave-generated ripples, *J. Geophys. Res.*, 107(C8), 3110, doi:10.1029/2001JC000864.
- Styles, R., and S. M. Glenn (2005), Long-term sediment mobilization at a sandy inner shelf site, LEO-15, *J. Geophys. Res.*, 110, C04S90, doi:10.1029/2003JC002175.
- Valle-Levinson, A., K. Wong, and K. T. Bosley (2002), Response of the lower Chesapeake Bay to forcing from Hurricane Floyd, *Cont. Shelf Res.*, 22, 1715–1729.

---

S. M. Glenn and J. T. Kohut, Institute of Marine and Coastal Sciences, Rutgers–State University of New Jersey, 71 Dudley Road, New Brunswick, NJ 08901, USA. (kohut@imcs.rutgers.edu)

J. D. Paduan, Code OC/Pd, Naval Postgraduate School, Monterey, CA 93943, USA.

# Trajectory prediction using HF radar surface currents: Monte Carlo simulations of prediction uncertainties

David S. Ullman,<sup>1</sup> James O'Donnell,<sup>2</sup> Josh Kohut,<sup>3</sup> Todd Fake,<sup>2</sup> and Arthur Allen<sup>4</sup>

Received 18 May 2006; accepted 15 August 2006; published 8 December 2006.

[1] An important aspect of particle trajectory modeling in the ocean is the assessment of the uncertainty in the final particle position. Monte Carlo particle trajectory simulations using surface currents derived from standard-range and long-range CODAR HF radar systems were performed using random-walk and random-flight models of the unresolved velocities. Velocity statistics for these models were derived from the covariance functions of differences between CODAR and drifter estimates of surface currents. Comparison of predicted trajectories and drifter tracks demonstrate that these predictions are superior to assuming the drifters stay at their initial position. Vertical shear between the effective depth of long-range CODAR measurements ( $\sim 2.4$  m) and that of drifters (0.65 m) causes the drifters to move more rapidly downwind than predicted. This bias is absent when standard-range CODAR currents (effective depth  $\sim 0.5$  m) are used, implying that drifter leeway is not the cause of the bias. Particle trajectories were computed using CODAR data and the random-flight model for 24-hour intervals using a Monte Carlo approach to determine the 95% confidence interval of position predictions. Between 80% and 90% of real drifters were located within the predicted confidence interval, in reasonable agreement with the expected 95% success rate. In contrast, predictions using the random-walk approach proved inconsistent with observations unless the diffusion coefficient was increased to approximately the random-flight value. The consistency of the random-flight uncertainty estimates and drifter data supports the use of our methodology for estimating model parameters from drifter-CODAR velocity differences.

**Citation:** Ullman, D. S., J. O'Donnell, J. Kohut, T. Fake, and A. Allen (2006), Trajectory prediction using HF radar surface currents: Monte Carlo simulations of prediction uncertainties, *J. Geophys. Res.*, *111*, C12005, doi:10.1029/2006JC003715.

## 1. Introduction

[2] Accurate prediction of Lagrangian trajectories in the coastal ocean is valuable to search and rescue (SAR) operations as well as for improving our understanding of how physical processes influence coastal ecosystems. The SAR challenge is to make a prediction of the path of a drifting search target given estimates of an initial location and the evolution of the velocity field. In addition, it is essential that the statistics of the prediction uncertainties be provided so that search planners can use available assets most effectively.

[3] Understanding the role of circulation variability in the coastal ocean on the recruitment of benthic species with pelagic larval stages poses a related ecological question [see, e.g., *James et al.*, 2002]. Given a source area and an

Eulerian description of the circulation, what are the trajectories of larvae and how do the uncertainties in measurements and unresolved motions determine the statistics of the dispersion? Coastal radars and numerical models can provide estimates of the evolution of the velocity field, however, the dispersion or spread of particles, the uncertainty region in the SAR example, is more difficult to specify.

[4] The recent proliferation of coastal high frequency (HF) surface wave radar installations for mapping surface ocean currents provides a rapidly expanding capability for near real-time observation of surface currents. These data have the potential to dramatically improve the efficiency and success rate of SAR operations in coastal waters. For this reason, the U.S. Coast Guard (USCG) Research and Development Center has initiated a program to assess the effectiveness of trajectory predictions using currents derived from HF radar, and if warranted to implement the use of this technology on an operational basis. Preliminary work toward this end was reported by *Ullman et al.* [2003] and *O'Donnell et al.* [2005].

[5] Trajectory modeling applied for SAR operations must provide a measure of the uncertainty in the surface current portion of drift of the SAR object in order for an optimal search area to be delineated. The search area is a compromise between the need to define a large enough area to ensure that it encloses the target and the fact that search

<sup>1</sup>Graduate School of Oceanography, University of Rhode Island, Narragansett, Rhode Island, USA.

<sup>2</sup>Department of Marine Sciences, University of Connecticut, Groton, Connecticut, USA.

<sup>3</sup>Institute of Marine and Coastal Studies, Rutgers University, New Brunswick, New Jersey, USA.

<sup>4</sup>U.S. Coast Guard Office of Search and Rescue, Groton, Connecticut, USA.

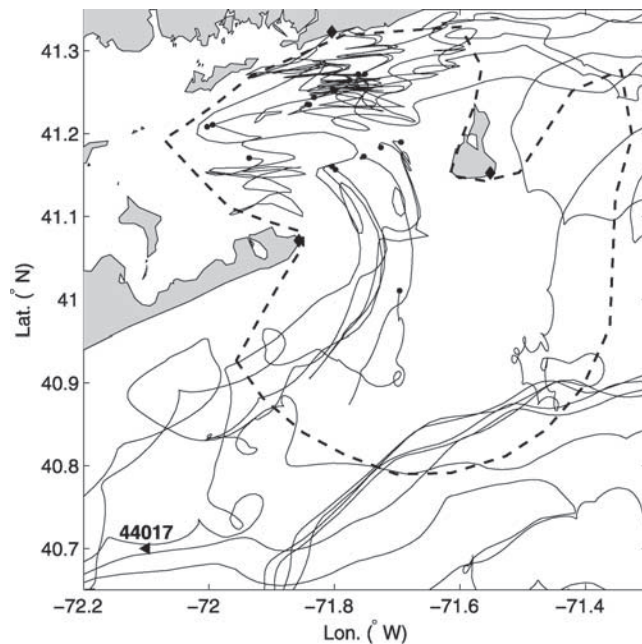


**Figure 1.** Trajectories of surface drifters deployed during December 2002 and March 2003 in the BI CODAR region. The black dots show the release points of each drifter (note that some were retrieved and redeployed). The black diamonds show the locations of the CODAR sites and the dashed line shows the approximate 10% coverage region. The location of NDBC buoy 44017 is denoted by the triangle.

resources are finite. The size of an operational search area is related to the magnitude of various uncertainties including those introduced by poorly known initial target position and time, velocity errors, and target leeway.

[6] The main objective of this paper is to evaluate a methodology for estimating uncertainty regions for simulated particle trajectories. The focus is on the uncertainty region, or search area in SAR terminology, due only to uncertainties in the drifter advective velocity provided by HF radar systems. The velocity uncertainties are modeled as a stochastic component representing a combination of unresolved or subgrid-scale motion and errors in the HF radar velocity retrieval. The parameters describing the stochastic variability are determined using a comparison of radar velocities and velocities of all available drifters passing through the radar domain. A secondary focus is the evaluation of the accuracy of trajectory predictions simulated using HF radar currents. Although the motivation of the project was the improvement of SAR trajectory predictions, we believe that the methodology described here is also applicable to the general Lagrangian prediction problem.

[7] Uncertainty regions are estimated using a Monte-Carlo approach whereby the trajectories of an ensemble of 1000 particles are simulated for 24-hour intervals. The Eulerian velocity is decomposed into a deterministic, large-scale component measured by the radar plus a stochastic component representing a combination of subgrid-scale motion and errors in the radar velocity. To simulate the

Lagrangian motion, we make use of the hierarchy of particle trajectory models outlined by *Griffa* [1996], in particular the random-walk and random-flight models.

## 2. Data Sources

### 2.1. Drifter Trajectories

[8] A number of drifter releases in the mid-Atlantic Bight were performed by the U.S. Coast Guard Research and Development Center over the period 2002–2004 with the objective of providing a data set with which to assess trajectory predictions. Drifters were released in Block Island Sound within the coverage region of the standard-range CODAR system operated by the Universities of Rhode Island and Connecticut (Figure 1). Some of these drifters eventually passed through the coverage region of Rutgers University's long-range CODAR system and a number of additional drifters were released within that zone as well (Figure 2).

[9] Drifters were deployed in December 2002 in the Block Island (BI) region and again in March 2003. A subset of the latter group subsequently moved southwest on the shelf and passed through the New Jersey (NJ) shelf CODAR coverage region. A deployment of drifters was also made in March 2003 within the NJ shelf domain. A final set of deployments was made during July 2004 in both regions, however the drifters released in the BI region rapidly exited that domain and did not provide useful trajectory segments. Table 1 summarizes the drifter deployments. Separate analyses are presented for each of three drifter data sets: (1) drifters within the BI region during winter-spring 2002–2003, (2) drifters within the NJ shelf region during early spring 2003, and (3) those within the latter region during summer of 2004.

[10] The drifters employed were self-locating datum marker buoys (SLDMB) which are a USCG operational version of the Coastal Ocean Dynamics Experiment (CODE) drifter [Davis, 1985]. The physical dimensions of the SLDMB are identical to those of a CODE drifter except that the height of the drag vanes is reduced from 1.0 m to 0.7 m [Allen, 1996]. The center of the drag vanes is located at a depth of 0.65 m, which is assumed to be the effective depth of a velocity estimate from the drifter. The drifters recorded Global Positioning System (GPS) fixes at  $\frac{1}{2}$  hour intervals and the fixes were transmitted to shore via the Argos communications network. With  $\frac{1}{2}$  hour sampling and a nominal GPS position uncertainty of 10 m, the uncertainty in the velocity of the drifter due to position uncertainty is  $O(1 \text{ cm/s})$ . Davis [1985] concluded, from comparisons of drifter velocities with near-surface vector measuring current meters, that the drifter velocity is accurate to approximately 3 cm/s. More recent measurements, using small current meters mounted within either end of the body tube of a CODE drifter, indicate that drifter slippage relative to the water is in the range of 2–5 cm/s (P. Poulain, personal communication, 2005).

### 2.2. HF Radar Surface Currents

[11] HF radar surface currents were obtained with CODAR SeaSonde systems located in the mid-Atlantic Bight in the region around Block Island and on the shelf east of New Jersey. A 3-site standard-range ( $\sim 25 \text{ MHz}$ )



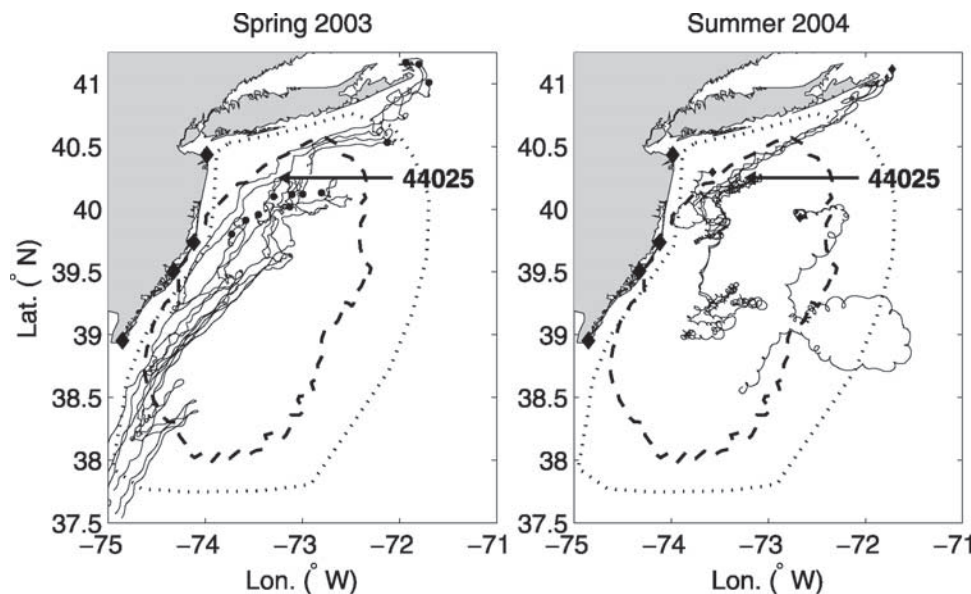


**Figure 2.** Trajectories of surface drifters deployed during March 2003 (left) and July 2004 (right) which passed through the NJ shelf CODAR domain. The black dots show the release points of each drifter. The black diamonds show the locations of the CODAR sites. The dotted line shows the nominal coverage zone, and the dashed line shows the approximate 10% coverage region. The location of NDBC buoy 44025 is indicated by the arrow.

system in the BI region provided hourly surface currents at 1.5 km resolution over the region shown in Figure 1. Radial velocities observed at each of the 3 sites were obtained with the Multiple Signal Classification (MUSIC) algorithm [Schmidt, 1986] using measured antenna patterns. The radial components were combined to produce vector velocities using the manufacturer's (CODAR Ocean Sensors) software. The NJ shelf surface currents were provided by a 4-site long-range ( $\sim 5$  MHz) system with spatial resolution of 6 km in the area shown in Figure 2. Radial velocities averaged over 3-hour periods, estimated using measured antenna patterns, were output on an hourly basis and were combined using the Naval Postgraduate School's HF Radar Toolbox. A screening methodology, utilizing a threshold on the estimated geometric dilution of precision (GDOP) [Gurgel, 1994], was used to remove current vectors derived from combinations of radials with poor geometry. The GDOP, a nondimensional scalar was calculated for every grid point in the field at each time step. Larger GDOP values indicate poor geometry in which the available radial component vectors do not adequately resolve both components of the current. For the analysis in this paper, an empirically determined threshold of 1.25 was used, whereby vectors for which the GDOP was greater than the threshold were eliminated from consideration.

[12] HF radar estimation of surface currents relies on Bragg scattering from surface gravity waves having a wavelength exactly  $\frac{1}{2}$  the radar wavelength and traveling either towards or away from the radar site [Stewart and Joy, 1974]. The backscattered signal is Doppler shifted by an amount proportional to the sum of the wave phase velocity, which is known via the deep-water dispersion relation, and the radial component of the surface current upon which the Bragg waves are carried. The surface current is then the difference between the velocity of the Bragg waves esti-

mated from the measured Doppler shift and the computed phase velocity. The effective depth of the surface current measurement depends on the wavelength of the Bragg waves, and thus on the radar frequency. Stewart and Joy [1974] showed that, for a linear surface current vertical profile, the effective measurement depth is given by:

$$d_{\text{eff}} = \frac{\lambda_{\text{bragg}}}{4\pi} = \frac{\lambda_{\text{radar}}}{8\pi} \quad (1)$$

Using this equation, the effective depths of the current measurements are estimated to be  $\sim 0.5$  m for the 25 MHz standard range system in the BI region, and  $\sim 2.4$  m for the 5 MHz long range system along the NJ coast.

[13] Estimates of the uncertainties associated with surface currents derived from CODAR systems have been provided using in situ velocity observations from acoustic Doppler current profilers (ADCPs). Chapman and Graber [1997] cite differences of  $O(15 \text{ cm/s})$  between HF radar current estimates and in situ current measurements. However, as Kohut et al. [2006] point out, these error estimates include a large component that is due to the different spatial scales and depths sampled by HF radar and ADCPs. They estimate the intrinsic CODAR radial uncertainty to be of  $O(5 \text{ cm/s})$

**Table 1.** U.S. Coast Guard Research and Development Center Mid-Atlantic Bight Drifter Releases During 2002–2004

Date	Region	Number	Notes
16–18 Dec 2002	BI	9	Retrieved and redeployed several.
27 Mar 2003	BI	4	Passed through NJ Shelf region.
27 Mar 2003	NJ Shelf	8	
27 Jul 2004	BI	3	Rapidly left domain.
27 Jul 2004	NJ Shelf	4	Passed through NJ Shelf region.

for the NJ shelf long-range systems used in the present study. Vector uncertainties for the BI region were estimated to be 3–15 cm/s with the larger values observed along the outer boundaries of the coverage regions where the combining geometry is nonoptimal and where signal to noise ratios increase [Ullman and Codiga, 2004].

[14] Interpolation of velocities from the CODAR grid to the location of a drifter was performed using a weighted, nearest neighbor scheme in which velocities from the 4 nearest neighbor grid points were weighted inversely with distance. This method is more robust than bi-linear interpolation because it tolerates some data gaps and allows for extrapolation beyond the instantaneous zone of CODAR coverage if desired. In our analysis, we restrict the trajectory prediction evaluation to those drifter tracks that start within the nominal coverage zones shown in Figures 1 and 2. There is, however, variability in the extent of the area within which long range CODAR data is available and Figure 2 also shows where current estimates are available at least 10% of the time during the drifter deployment periods. Note that in the BI region the 10% coverage region and the nominal coverage region were the same. The 10% coverage regions were used to perform more stringent screening of the trajectories, confining them to regions of more reliable CODAR currents.

### 2.3. Comparison of Surface Currents From Radar and Drifters

[15] Drifter velocities at times (hourly) corresponding to CODAR observations were computed from time series of drifter positions at half-hour intervals using a central difference scheme. CODAR velocities were then spatially interpolated to the drifter location using the weighted nearest neighbor method described above. Velocities at locations outside of the 10% coverage zones (see Figures 1 and 2) were eliminated from the analysis.

[16] Velocity differences (drifter minus CODAR) were rotated into a right-handed coordinate system with  $x$  oriented in the direction of the instantaneous wind and  $y$  oriented in the cross-wind direction. Hourly wind measurements from National Data Buoy Center buoys 44017 and 44025 were used for the BI and NJ shelf regions respectively (see Figures 1 and 2 for the location of these buoys). Winds were assumed to be spatially uniform over each of the CODAR domains. In the NJ shelf region, downwind drifter-CODAR differences are weakly correlated ( $r = 0.28$ ) with wind speed indicating a tendency for the drifters to move faster downwind than the CODAR measurements (Figure 3a). The correlation is significantly different from zero assuming N/24 degrees of freedom, where  $N = 5895$  is the number of hourly data points in Figure 3a and the factor 24 is the estimated integral timescale in hours of the wind speed (not shown). In the BI region, downwind drifter-CODAR differences are uncorrelated with the wind speed, and crosswind differences are uncorrelated in both regions (Figure 3).

[17] The effective depth of the 25 MHz BI region CODAR ( $\sim 0.5$  m) is very close to the effective depth of the drifters ( $\sim 0.65$  m). The lack of correlation between downwind drifter-CODAR difference and wind speed in this case suggests that drifter leeway is indeed small. The positive correlation exhibited in the NJ shelf region with long-range CODAR measurements at  $\sim 5$  MHz is consistent

with the presence of vertical shear between the drifter depth and the effective depth of the CODAR measurement (2.4 m). To demonstrate this, we estimated the vertical shear between the drifter and CODAR effective depths as a superposition of a steady-state Ekman spiral and the Stokes drift. Ekman currents were computed using a constant eddy viscosity of  $10^{-2}$  m<sup>2</sup>/s at 40° N and the Large and Pond drag coefficient formulation [Large and Pond, 1981]. The Stokes drift was estimated using the Pierson and Moskowitz [1964]  $n = 4$  spectrum for a fully developed wave field following Kenyon [1969]. To simplify the calculation, angular spreading of the energy spectrum was neglected. The estimated velocity difference between  $z = 0.65$  m and  $z = 2.4$  m from the combined Ekman and Stokes currents is plotted in Figure 3a as a function of wind speed (green line). Although the scatter is large, the estimated difference appears to explain the general trend, suggesting that the correlation between drifter-CODAR differences and wind speed arises due to vertical shear between the depths of the drifter and the CODAR measurements.

## 3. Trajectory Modeling

### 3.1. Monte-Carlo Trajectory Prediction

[18] The motion of a particle in a two-dimensional velocity field can be described by the equation:

$$\frac{d\mathbf{r}}{dt} = \mathbf{u}(t, \mathbf{r}), \quad (2)$$

where  $\mathbf{r} = (x, y)$  denotes the position of the particle and  $\mathbf{u} = (u, v)$  is the Eulerian velocity at position  $\mathbf{r}$  and time  $t$ . The velocity can be decomposed into a large-scale, slowly varying component  $\mathbf{U}$ , and a component  $\mathbf{u}_t$  representing subgrid-scale deviations which will be referred to as turbulence:

$$\mathbf{u} = \mathbf{U} + \mathbf{u}_t. \quad (3)$$

Surface current mapping radars such as CODAR can provide estimates of  $\mathbf{U}$  at spatial scales of approximately 1.5 km (6 km) and temporal scales of 1 hour (3 hours) for standard-range (long-range) systems, thus the turbulent component represents velocity fluctuations on scales smaller than these. The radar-derived velocity is subject to significant uncertainties and so the large-scale component can be expressed as:

$$\mathbf{U} = \mathbf{U}_{\text{radar}} + \delta\mathbf{u}, \quad (4)$$

where  $\mathbf{U}_{\text{radar}}$  is the radar measurement and  $\delta\mathbf{u}$  is the measurement error. Combining (3) and (4), the total Eulerian velocity can be written:

$$\mathbf{u} = \mathbf{U}_{\text{radar}} + \mathbf{u}_t + \delta\mathbf{u} = \mathbf{U}_{\text{radar}} + \mathbf{u}', \quad (5)$$

where  $\mathbf{u}'$  includes both the turbulent velocity and the measurement error.

[19] Prediction of particle trajectories in a region of HF radar coverage was achieved by integrating (2) using a predictor-corrector scheme with the velocity given by (5).

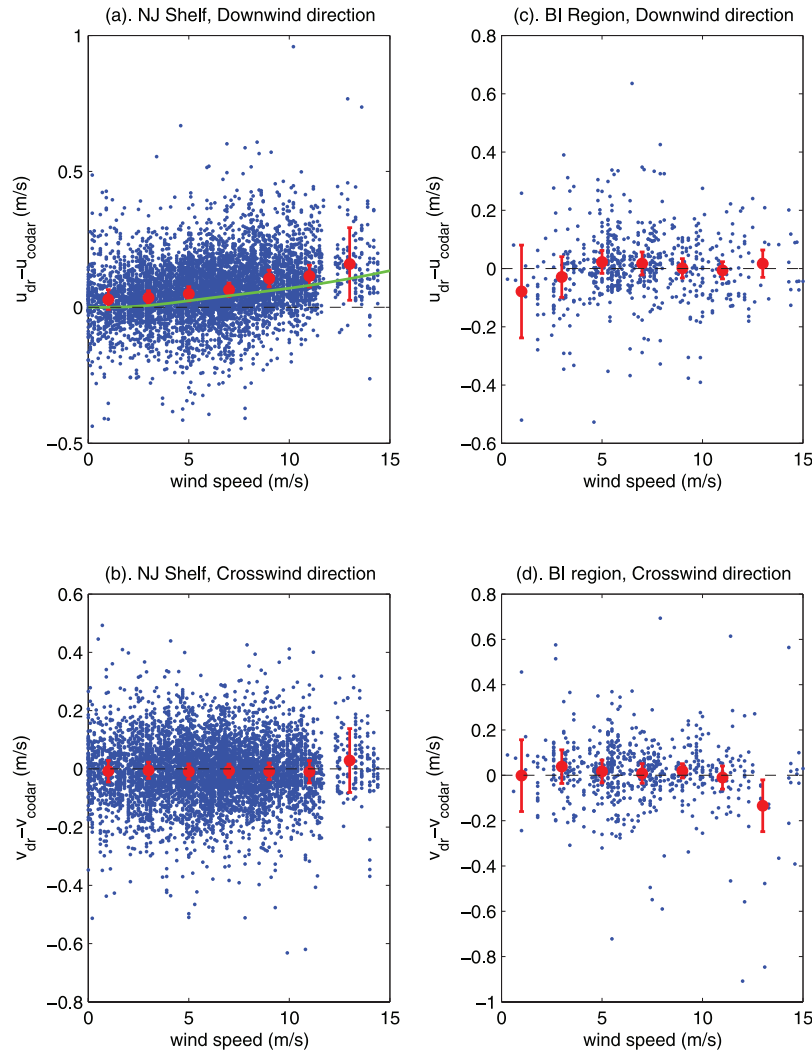


**Figure 3.** Differences between drifter and CODAR velocity resolved into the downwind and crosswind directions versus wind speed for drifters in (a, b) the NJ shelf region and (c, d) the BI region. Wind data are from NDBC buoy 44025 for the NJ shelf comparisons and buoy 44017 for the BI comparisons. The red circles are mean differences within 2 m/s wind speed bins. The error bars on the means are at the 95% level, computed using a  $t$ -test with  $N/24$  degrees of freedom, where  $N$  is the number of hourly values in the bin and 24 hours is the approximate integral timescale of the wind speed. The green line in Figure 3a is an estimate of the shear between the effective depths of the drifter (0.65 m) and the long-range CODAR (2.4 m) due to the sum of the Ekman component and the Stokes drift.

A time-step of 1 hour was used and radar velocities were interpolated to the particle location using the weighted nearest neighbor approach. The methodology for specifying  $\mathbf{u}'$  is described in the following section.

### 3.2. Subgrid-Scale Velocity Model

[20] Although  $\mathbf{u}'$  is a combination of radar measurement errors, unresolved motion, and true geophysical turbulent fluctuations, we assume that its properties can be described by models that have been used to describe turbulence alone. We are somewhat compelled to combine the components of  $\mathbf{u}'$  as there is no simple way to separate them. However, since drifters are now routinely launched during U.S. Coast Guard SAR operations and coastal current radar systems are proliferating, there is potentially substantial value in a methodology that allows the estimation of the statistics of

$\mathbf{u}'$  from comparison of drifter and radar velocities. The assumption that the properties of  $\mathbf{u}'$  can be described by models of turbulence will be shown in the following to yield predictions that are consistent with observations.

[21] Two models of turbulence (by which we mean  $\mathbf{u}'$ ) were examined. Both are members of the hierarchy of stochastic particle models reviewed by *Griffa* [1996] and assume that the two horizontal components are independent. The so-called random-walk and random-flight models both assume that the particle position is Markovian. The latter also assumes that the particle velocity is a Markovian variable. Physically, the random-flight model recognizes that the turbulent velocity fluctuations have a finite temporal correlation scale whereas the random-walk model assumes that the correlation scale is infinitesimal. When the same turbulent velocity variance is used in the two models, one



expects greater particle dispersion with the random-flight version.

[22] The random-walk formulation for the components of  $\mathbf{u}'$  ( $u'$  and  $v'$ ) can be expressed as:

$$u' = \sigma_u \frac{T_u^{1/2}}{dt} \cdot dw, \quad (6)$$

where  $\sigma_u$  is the velocity standard deviation and  $dw$  is a normally distributed random increment with zero mean and second moment  $\langle dw \cdot dw \rangle = 2 \cdot dt$  where  $dt$  the time step for the integration of (2). Note that the turbulent timescale  $T_u$  in the discrete problem is not actually infinitesimal but is constrained to equal  $dt/2$  to obtain consistency between (6) and the definition of velocity variance [Griffa, 1996].

[23] The evolution of the turbulent velocity in the random-flight turbulence model is described by:

$$du' = -\frac{u'}{T_u} dt + \frac{\sigma_u}{T_u^{1/2}} dw. \quad (7)$$

The first term on the right of (7) introduces “memory” with a timescale  $T_u$  to the model of the turbulent fluctuations and the second term is, as in the random-walk model, a random impulse. As is easily demonstrated, the autocorrelation function of the  $u'$  in (7) decays exponentially with an  $e$ -folding time, or integral timescale, equal to  $T_u$  [Griffa, 1996].

[24] It is important to note that the diffusion coefficient for particles in homogeneous turbulence at times large compared with  $T_u$  is defined as:

$$K_x = \sigma_u^2 \cdot T_u \quad (8)$$

[Csanady, 1973]. Since for the random-walk case,  $T_u = dt/2$ , the dispersion for a specified  $\sigma^2$  is dependent on the time step employed in the numerical implementation of this model.

### 3.3. Estimating Turbulent Velocity Statistics

[25] Practical implementation of the aforementioned turbulence models to determine the random velocity components in (5) requires specification of the velocity variance  $\sigma^2$ , and, for the random-flight case, the turbulent timescale  $T$ . If the tracks of clusters of drifters, released simultaneously at a variety of locations were available, one could estimate the dispersion coefficient  $K$  and compute  $\sigma^2$  and  $T$  if necessary. However, few such deployments have been undertaken. Much more frequently, a few drifters are deployed as part of a SAR operation. We propose an approach to exploit the drifter data obtained from this type of deployment, in conjunction with HF radar derived surface currents to estimate the fluctuating velocity statistics directly. From (5), the fluctuating velocity is:

$$\mathbf{u}' = \mathbf{u} - \mathbf{U}_{\text{radar}}.$$

Although clearly, the true velocity  $\mathbf{u}$  is not known, we argue that the drifter velocity is our best estimate of it and is the natural choice especially for SAR applications. Previous work suggests that the leeway associated with CODE-type

drifters is small, and further support for this result is provided by Figure 3c, which shows no discernable relation between downwind drifter-CODAR velocity difference and wind speed for the case where the effective depth of drifter and CODAR are equal. The positive relationship found for drifter-CODAR differences in the NJ shelf long-range CODAR domain are associated with the difference in effective depth of the two velocity measurements. Even in this region, other sources of errors clearly dominate the observed differences. Moreover, if the objective is to predict the motion of a drifting object at the surface, it seems eminently sensible to take the drifter velocity as the true velocity.

[26] Time series of  $\mathbf{u}'$  for each drifter, the difference of the drifter and the interpolated CODAR velocities, were used to compute autocovariance functions for the  $u'$  and  $v'$  components. These were subsequently averaged over all drifter tracks to produce the curves shown in Figure 4. The autocovariance functions for both the BI and NJ shelf regions exhibit rapid decay at lags of several hours. Low amplitude periodicities at the semi-diurnal period are evident in the BI region and in a broad band around the inertial period in the NJ shelf region during 2004 (Figure 4). The cross-covariances (not shown) are generally low, consistent with the assumption that the horizontal velocity components fluctuate independently. We estimate the turbulent variances as the zero-lag values of the autocovariance functions for each deployment. Turbulent integral timescales for the two velocity components were estimated by fitting exponential autocovariance functions to the observed autocovariances at lags of 1 and 2 hours. Although computationally much simpler than the method of moments technique used by Griffa *et al.* [1995], this method is similar to theirs in that only autocovariances at short lags, which are statistically most reliable, are used to estimate the turbulent timescale. The best fit exponential autocovariance functions are shown as dashed curves in Figure 4 and the parameter estimates are given in Table 2. Integral timescales are approximately 1.5 hours in the BI region and 3–5 hours in the NJ shelf region, with higher values during the spring 2003 deployment in the latter region.

### 3.4. Sensitivity to Number of Particles and Time Step

[27] It is well known that the results of stochastic particle modeling can be sensitive to the particular details of the methodology used [e.g., Brickman and Smith, 2002]. One of the most important methodological parameters in the simulation of particle dispersion is the number of trials (particles) simulated. If too few particles are used, the estimate of dispersion will have a large uncertainty, while a simulation with too many particles can be computationally costly. To investigate the sensitivity of dispersion estimates on the number of simulated particles, we performed a 24-hour, 10,000-particle simulation using the random-flight model with zero large-scale flow. From the 10,000 particle trajectories, we randomly subsampled 100 ensembles of  $N$  particles, with  $N$  ranging from 100 to 5000 particles. The variance of final particle position was computed for each ensemble and was compared with the analytical solution given by Griffa [1996]. Figure 5 shows that as the number of particles increases, the potential error in the estimated dispersion decreases. With 100 particles, the error in dispersion can be

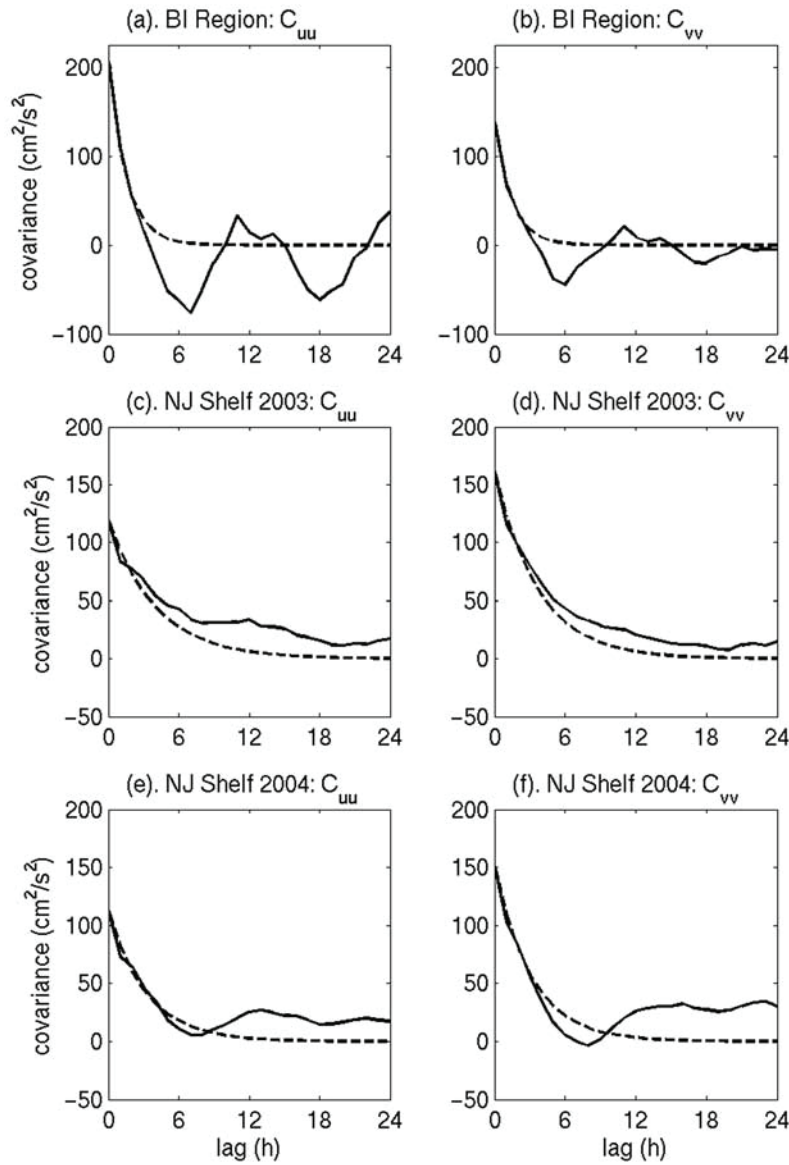


**Figure 4.** Lagged autocovariance functions of time series of differences between drifter velocity and CODAR velocity averaged over all drifters within the BI region for (a) the eastward component and (b) the northward component. The solid curves are the computed autocovariance functions, and the dashed lines are the best fit exponential covariance functions. Covariance functions for the NJ shelf region (c, d) during 2003 and (e, f) for 2004.

up to  $5\text{--}6\text{ km}^2$ , whereas the use of 5000 particles reduces the expected error to less than  $\sim 1\text{ km}^2$ . In order to reduce the computational load, we used 1000 particles for the results presented in section 4, in which case the error in dispersion is at most  $\sim 2\text{ km}^2$ .

[28] Although the CODAR currents are produced on an hourly basis, we nonetheless investigated the sensitivity of the dispersion estimates to the time step of the particle advection scheme. The CODAR velocities within the BI region were interpolated in time to  $\frac{1}{2}$  hour intervals and the random-walk and random-flight simulations performed using a  $\frac{1}{2}$  hour time step in the integration. The turbulent velocity statistics were as given in Table 2. Although not shown here, we found that the dispersion, and thus the search areas, for the random-flight case were essentially

unchanged from the results using a 1-hour time step. The random-walk results, as noted above in section 3.2, are expected to depend on the time step, and indeed we found reduced dispersion occurring for the case of  $dt = 0.5\text{ h}$ . However, the conclusions we reach, in section 4.2, regarding the relative merits of the random-walk and random-flight methods using a 1-hour time step would not have changed had we performed the simulations using a reduced time step.

#### 4. Results

[29] To evaluate our approach to modeling dispersion and to the estimation of parameters, we compared observed drifter trajectories to those predicted retrospectively using

**Table 2.** Estimates of Random-Flight Turbulence Parameters From Least Squares Fits to the Autocovariance Functions of Drifter-CODAR Velocity Differences for the Three Drifter Deployments

Region	$\sigma_u$ , m/s	$T_u$ , h	$K_x$ , m <sup>2</sup> /s	$\sigma_v$ , m/s	$T_v$ , h	$K_y$ , m <sup>2</sup> /s
BI (2003)	0.14	1.5	106	0.12	1.4	73
NJ Shelf (2003)	0.11	4.1	179	0.13	3.7	225
NJ Shelf (2004)	0.11	3.3	144	0.12	3.1	161

CODAR velocities. Each drifter trajectory was divided into 24-hour segments with each segment overlapping the previous one by 12 hours for drifters within the BI region. Example simulations are shown in Figure 6 together with the 95th percentile confidence regions for the final pseudo-drifter location (the gray polygons). To define the confidence interval, we first computed the two-dimensional frequency histogram of the terminal pseudo-drifter locations and then rank ordered the spatial bins by frequency. Proceeding from the most to the least frequent, bins were included in the confidence interval and shaded gray until 95% of the total number of simulations (1000) was included.

[30] In the analysis that follows, we present the statistics of the trajectory differences for all trajectories that begin within the area of CODAR coverage as well as for a subset with the end position also located within the coverage region. The number of trajectory comparisons versus the time since the start of the prediction is shown in Figure 7. The decrease with time in the BI region results from the retrieval and redeployment of drifters that left the CODAR domain; thus a number of “short” trajectories (<24 hours) is present in the trajectory ensemble.

#### 4.1. Accuracy of Predictions

[31] The accuracy of a drifter trajectory prediction is measured by the distance between the real drifter and the pseudo-drifter. This was computed for each hour of each 24-hour trajectory segment. The ensemble mean separation and the 95th percentile separation are presented in Figures 8–10 for the three deployments. Mean separation generally increases with time in a linear fashion with some indication that separations at short times increase at a slightly faster rate. At 24 h, mean separation is approximately 7 km (6 km) for the BI unscreened (screened) ensembles (Figure 8). In the NJ shelf region, using the screened (unscreened) ensembles, 24-hour separations are 11 km (9 km) during the spring 2003 deployment (Figure 9) and 8 km (7 km) during the summer 2004 deployment (Figure 10). The 95th percentile separation values are also somewhat higher in the NJ shelf domain, especially during 2003, with 24-hour values for the unscreened subset reaching 25 km during 2003 and 20 km during 2004 compared to about 18 km for the BI drifters. When drifters leaving the CODAR region are screened from the analyses, the 95th percentile separations (24 hours) are about 17 km and 15 km for the 2003 and 2004 deployments in the NJ shelf region and 12 km in the BI region. The general decrease in error with screening is not surprising, and is consistent with the occurrence of relatively large trajectory prediction errors along the outer boundary of the CODAR domain where radar-derived velocity errors increase.

[32] To assess the value of the CODAR-based drifter predictions, we compare the performance to the simplest

alternative prediction strategy, which is to assume that the drifter stays where it was initially released. The error in the so-called persistence, or last known position, forecast is simply the distance traveled by the drifter, and the mean and 95th percentile values are also shown in Figures 8–10. Drifters released in the BI region and during the 2003 shelf deployment tend to travel farther than those released on the shelf during summer 2004. Using the unscreened trajectories, the mean (95th percentile) distance traveled after 24 hours in the BI region is 15 km (38 km) compared with about 20 km (44 km) during 2003 and 11 km (23 km) during 2004 in the NJ shelf region. The net result is that drifter locations predicted using CODAR currents in the BI

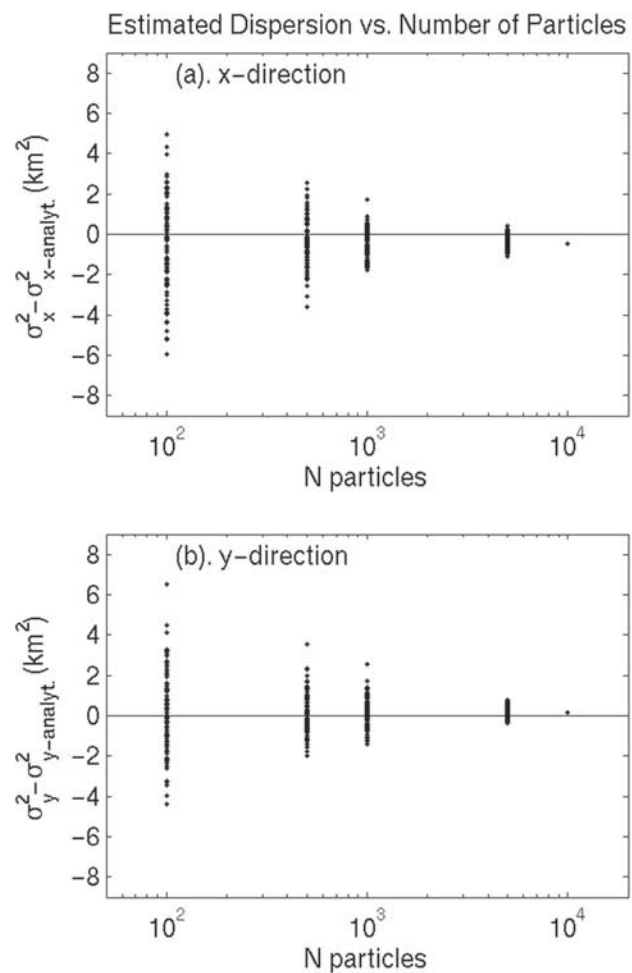


**Figure 5.** Variance in particle position in the (a)  $x$ -direction and (b)  $y$ -direction compared to the analytical solution for variance, as a function of the number of particles sampled. The simulation was performed using the random-flight turbulence model with  $\sigma_u = \sigma_v = 10$  cm/s and  $T_u = T_v = 3$  h.



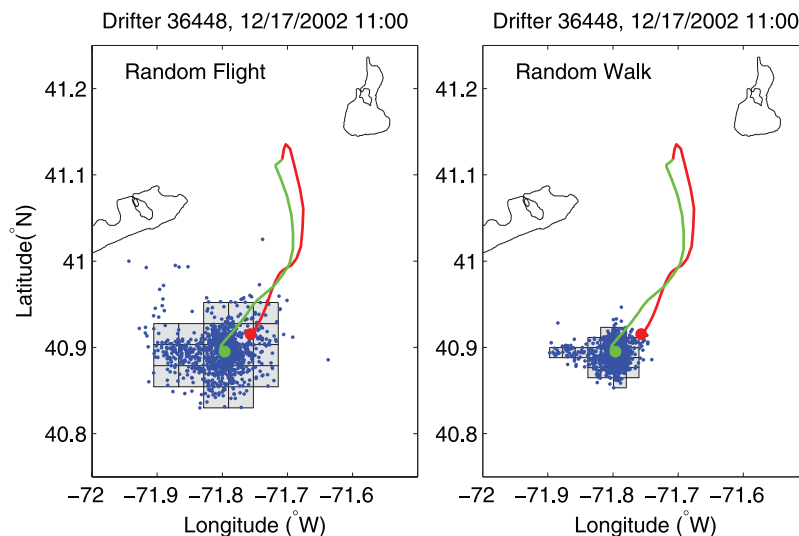


**Figure 6.** Example drifter trajectory within the BI CODAR region showing the real drifter path over 24 hours in red and the CODAR predicted position in green, with final positions denoted by the circles. The ensemble of trajectory prediction endpoints using the random-flight (left) and random-walk (right) models are shown as blue dots. The gray polygons denote the region within which 95% of the drifter final positions lie.

region are on average approximately 50% closer to the real drifter position than are the last known positions. This is also true for the NJ shelf deployment during 2003, but this effect is less pronounced on the shelf where the mean distance from the predicted position to the real drifter is about 70% of the distance traveled. Similar conclusions are reached using the screened drifter subsets, although the screening can be seen to sharply reduce the 95th percentile separation value in the BI region.

[33] The observed correlation between drifter-CODAR velocity differences and wind speed for the NJ shelf long-range CODAR (Figure 3a) suggests that the accuracy of predicted drifter positions should also be correlated with wind speed. For each trajectory, the mean eastward and northward wind components were computed over the entire 24-hour prediction time. The separation vector between the real and simulated positions at 24 hours was then rotated into a coordinate system oriented in the mean downwind and crosswind directions. For the NJ shelf drifters, Figure 11 shows that the downwind component is in fact correlated ( $r = 0.49$ , significant at the 95% level) with the magnitude of the vector-averaged wind. No such correlation is found for the drifters in the BI region (not shown), which is consistent with the lack of a relationship between wind and drifter-CODAR velocity differences in that region (Figure 3c).

#### 4.2. Uncertainty Bounds for Predictions

[34] The Monte Carlo simulation of trajectories provides an ensemble of final drifter locations that are extremely valuable in the important practical problem of defining a search area. If we take the interval containing 95% of the pseudo-drifter positions computed using the random-walk and random-flight turbulence models as the search area, then it is important to know whether the real drifters (search targets) are found within this area at the expected frequency. At each hour of each drifter trajectory, the search area was

computed as described at the beginning of this section and the position of the real drifter checked to see whether it was inside or outside the search area. The number of real drifters within the search area was summed for each hour and this quantity was then divided by the number of trajectories to compute the fraction inside the predicted search area (the percent success).

[35] Figures 12 and 13 compare the time evolution of the percentage of real drifters found inside the simulated search areas using the two turbulence models and shows clearly that the random-flight method is superior for all three drifter deployments whether the drifter tracks that exit the CODAR coverage area are screened or not. Without screening 70–90% of all random-flight derived search areas enclosed the real drifter position and there was little variation with time. Screening the drifter data increased the fraction by 5–10% yielding percent success in the range 80–90% for the BI and 2003 NJ shelf deployment, and 85–95% for the 2004 shelf deployment. In the BI region, there appears to be semi-diurnal variability in the percent success (Figure 12) which may be related to the presence of a significant semidiurnal signal in the autocovariance functions in this area (Figures 4a and 4b).

[36] In contrast, search areas estimated using the random-walk model of turbulence appear to be too small, with percent success, for the unscreened drifter subset, dropping from about 70–85% at a prediction time of 1 hour to 20–60% after 24 hours. As for the random-flight results, the comparison using the screened subset improves by about 5% at all prediction times. The discrepancy between the search areas produced using the two turbulence models is most apparent for the simulations on the NJ shelf (Figure 13).

#### 5. Discussion

[37] Drifter positions predicted over 24 hours using CODAR surface currents are clearly superior to the persis-

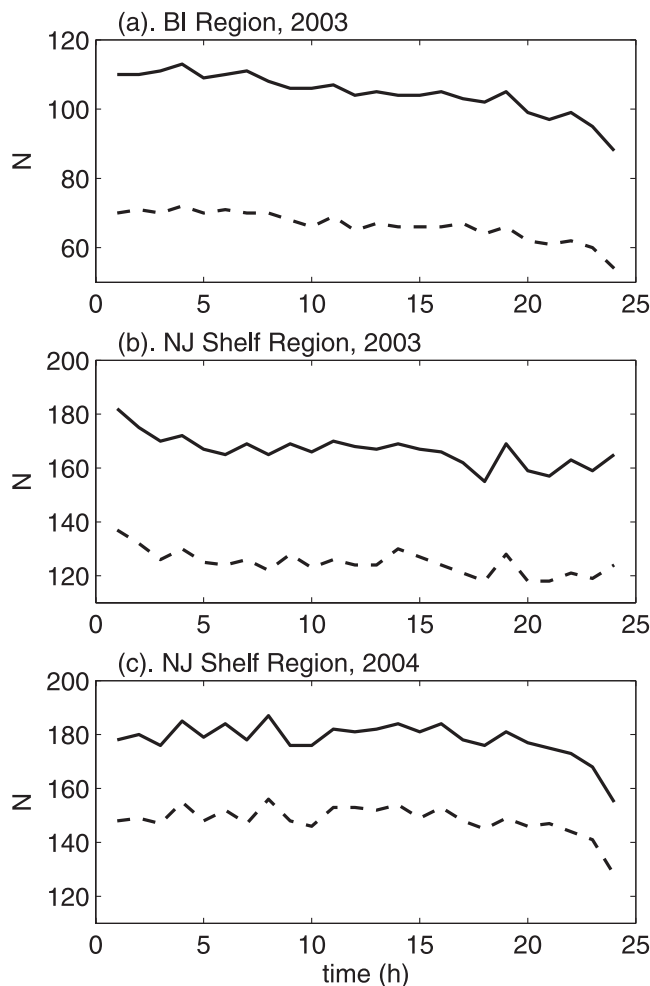


**Figure 7.** The number of comparisons between predicted and true drifter position versus time with no screening (solid lines) and with screening using the 10% coverage zone (dashed lines) for the (a) BI region, (b) NJ Shelf region during 2003, and (c) NJ Shelf region during 2004.

tence forecast in estimating the final drifter location. The mean separation between predicted and observed drifter location is 50–70% of the separation using the persistence forecast. Using currents from a numerical circulation model, *Thompson et al.* [2003] simulated the trajectories of a number of surface drifters on the Scotian Shelf. They estimated the 50th percentile separation value after 24 hours to be 6 km, which is very similar to the mean separation of 6–7 km found in the present study. This suggests that trajectory predictions using CODAR surface currents have comparable skill in predicting target trajectories as predictions using numerical model currents.

[38] Using long-range CODAR currents, trajectory predictions can be significantly in error under high-wind conditions. This appears to arise because of velocity shear between the effective measuring depths of the drifter ( $\sim 0.65$  m) and the CODAR ( $\sim 2.4$  m at 5 MHz). In this case, the real drifter experiences a greater wind-driven current in the direction of the wind. Such inaccuracies in trajectory predictions are not found when standard-range (25 MHz) CODAR currents (effective depth of  $\sim 0.65$  m)

are used for predictions. This suggests that, for SAR operations, it is important to utilize near-surface current data from a depth that is comparable to the effective depth of the drifting object. The correspondence, seen in Figure 3a,

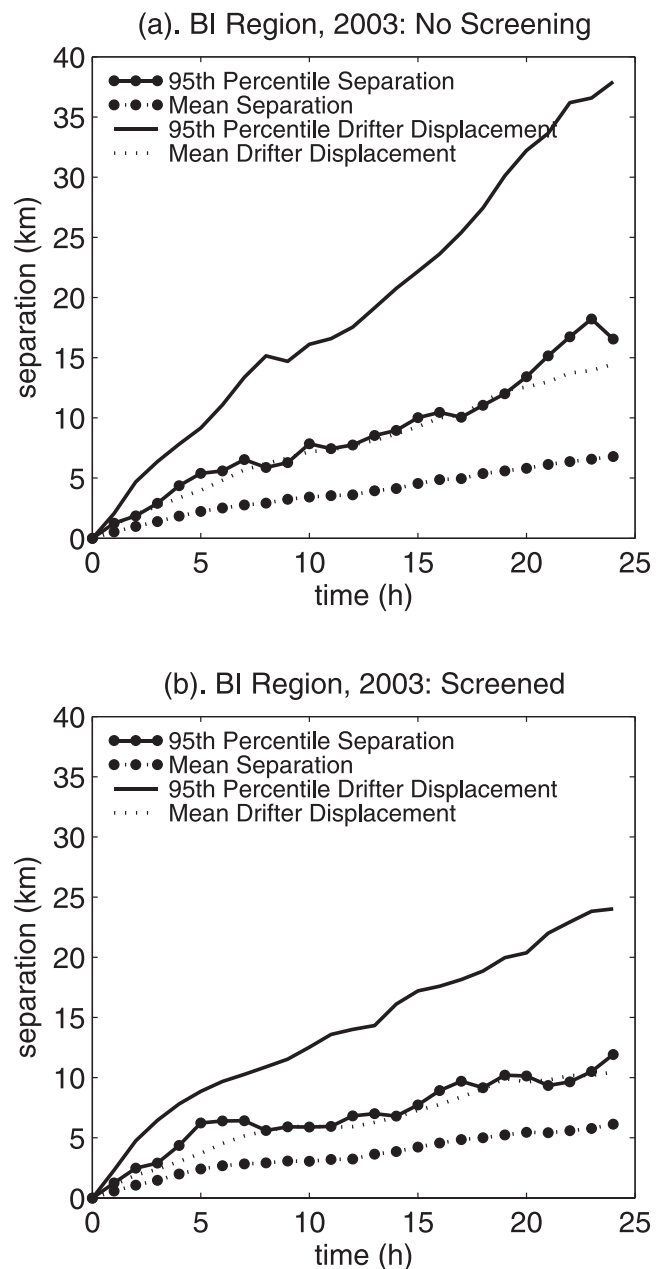


**Figure 8.** (a) Separation between actual and predicted drifter position as a function of time since start of prediction, averaged over all trajectory segments that start within the nominal coverage zone for the BI region. The curves with symbols show the mean separation (dashed line and circles) and the 95th percentile separation (solid line and circles) between the real drifter and the predicted position. The dashed and solid lines show respectively the mean distance and the 95th percentile distance that the real drifter moved over the prediction time. (b) The same statistical measures averaged over all segments that both start and end within the 10% coverage zone.

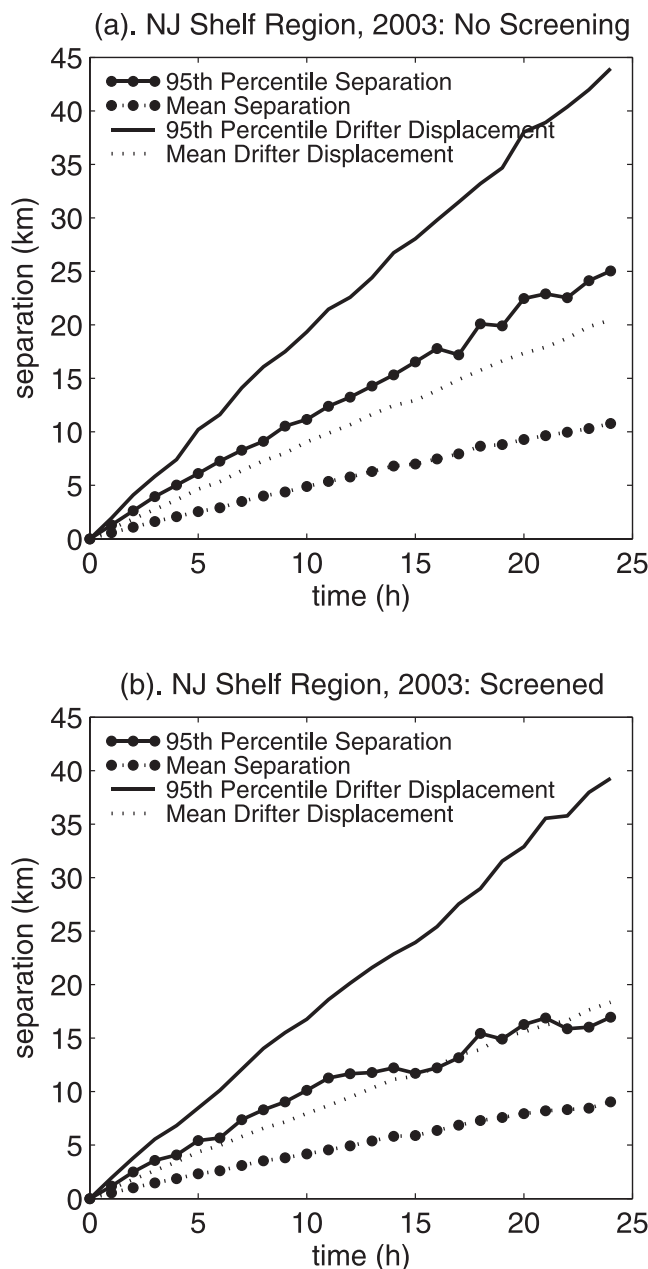


**Figure 9.** Same as Figure 8, but for the NJ shelf region during 2003.

between the predicted difference in velocity from 0.65 to 2.4 m and the observed drifter-CODAR differences indicates the possibility of correcting observed CODAR velocities to drifter depths if simultaneous wind data are available.

[39] The search area evaluations can be used to assess the consistency of the turbulence models and their associated parameters. A consistent turbulence model would be expected to provide, for instance, a 95% confidence region that is successful (with the real drifter location within it) 95% of the time. The random-flight method provides search areas that enclose the real drifter approximately 90% of the time, whereas the random-walk formulation does significantly worse. This suggests that, with the parameter(s) estimated

from the drifters, the random-flight model is nearly self-consistent while the random-walk model is definitely not. The difference between the random-flight success rate and the expected 95% suggests a slight underestimate of either the turbulent variance or the timescale. The latter seems the more likely candidate here, as we have estimated the turbulent timescale from a least squares fit to the observed autocovariance at short lags. Figure 4 shows that the empirical exponential functions generally underestimate the covariance at large time lags, suggesting an underestimate of the timescale. Note that evaluation of the integral timescale by integration of the autocovariance to infinite lags is problematic in the presence of the quasi-periodic motions evident in the covariance functions of Figure 4.

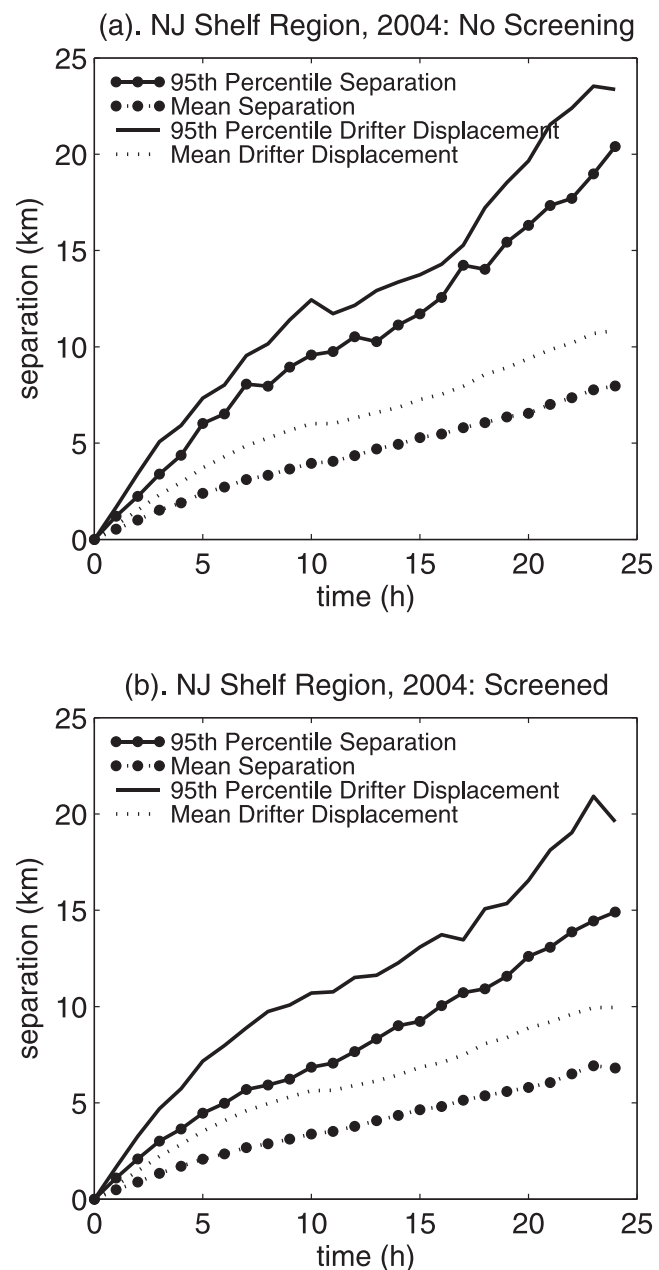


**Figure 10.** Same as Figure 8, but for the NJ shelf region during 2004.



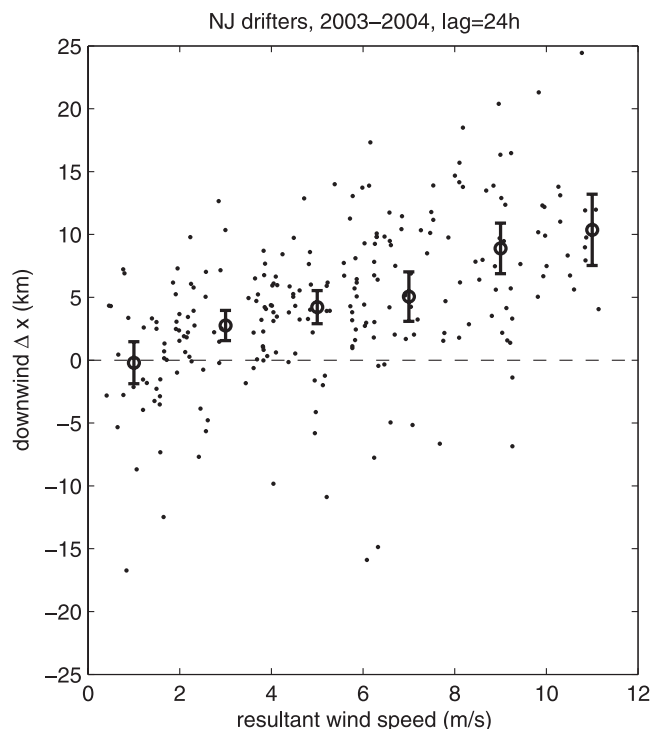


**Figure 11.** Downwind component of the difference in position between the real drifter position and the predicted position at 24 hours after the start of the prediction as a function of the vector mean wind speed over the 24-hour period for all drifters within the NJ shelf region. The dots denote individual trajectory segments, and the open circles represent the mean difference within 2 m/s bins. The error bars on the mean values are 95% confidence limits on the mean values estimated using a *t*-test.

[40] The wind speed bias observed in the NJ shelf region using long-range CODAR currents has a noticeable effect on search areas only near the end of the 24-hour prediction interval. A velocity bias  $\Delta v$  in the presence of diffusion will be negligible until such time,  $t$ , as the consequent error in displacement,  $L_E = t\Delta v$ , becomes of the order of the size of the diffusive particle cloud  $L_D = \sqrt{Kt}$ . For diffusivities of  $\sim 200 \text{ m}^2/\text{s}$  (Table 2) and velocity bias of  $\sim 0.07 \text{ m/s}$  (predicted velocity bias for 10 m/s wind),  $t$  is of order 11 hours. Examination of Figure 13a shows a gradual decrease in search area effectiveness at times greater than 15 hours for the 2003 NJ shelf drifters. Restricting the evaluation of the predicted search areas to cases of weak wind ( $<7 \text{ m/s}$ ) showed that search area effectiveness remained approximately uniform from 15 to 24 hours after the prediction start (not shown). This suggests that the gradual decrease in search area effectiveness observed in Figure 13a at large times is likely due to the inclusion of high-wind cases where the effect of the wind speed bias becomes noticeable.

[41] It is important to note that in the comparison of the effectiveness of random-walk and random-flight derived drifter dispersion the same turbulent velocity fluctuation variance ( $\sigma^2$ ) has been used. If a larger value were chosen for the random-walk simulations then the search areas would be larger and the percent success consequently higher. If an estimate of the effective diffusivity ( $K$ ) were

available and the fluctuation variances in both turbulence models and turbulent timescale in the random-flight model were chosen to be consistent with this value, the simulations of *Zambianchi and Griffa* [1994] show that the random-walk model overestimates the particle dispersion for  $t < T_u$ . At times large compared to the turbulent timescale, the two models predict that the particle cloud size increases at the same rate, though the offset introduced by the initial overestimate persists. For turbulent timescales of 1–4 hours as determined in the present study, the difference is 10–20% at 12–24 hours after the start of the prediction.

[42] The result of increasing the random-walk diffusion coefficient to the random-flight value ( $\sigma^2 T$ ) for the 2004 NJ shelf deployment is demonstrated in Figure 14. In this case, search areas using the random-walk model are more effective in enclosing the real drifter position than those from random-flight simulations at prediction times less than about 10 hours and essentially equivalent at longer times consistent with theory [*Zambianchi and Griffa*, 1994]. However, it is important to note that the improved effectiveness is simply due to a positive bias in the search area, which, in the SAR problem, dilutes the search effort.

[43] Horizontal dispersion coefficients estimated from fitting the random-flight turbulence model to autocovariance functions of CODAR-drifter differences are in the range of 70–225  $\text{m}^2/\text{s}$  (Table 2). Higher values are estimated in the NJ shelf region ( $>140 \text{ m}^2/\text{s}$ ) than in the BI region ( $<110 \text{ m}^2/\text{s}$ ). We note here that although horizontal dispersion coefficients can be estimated directly using

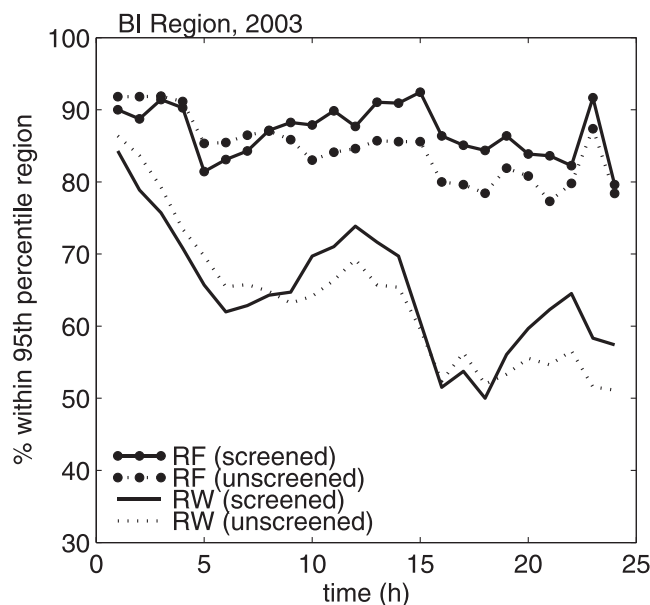


**Figure 12.** Comparison of the uncertainty bounds for predicted drifter position using the random-flight (lines and circles) and random-walk (lines) turbulence models for the BI region. The solid curves are computed using only those trajectories that both start and end within the 10% coverage zone, while the dotted curves are computed based on all trajectories that start within the nominal coverage zone. For each prediction time we plot the percent of cases where the actual drifter location at that time fell within the estimated 95% confidence region.

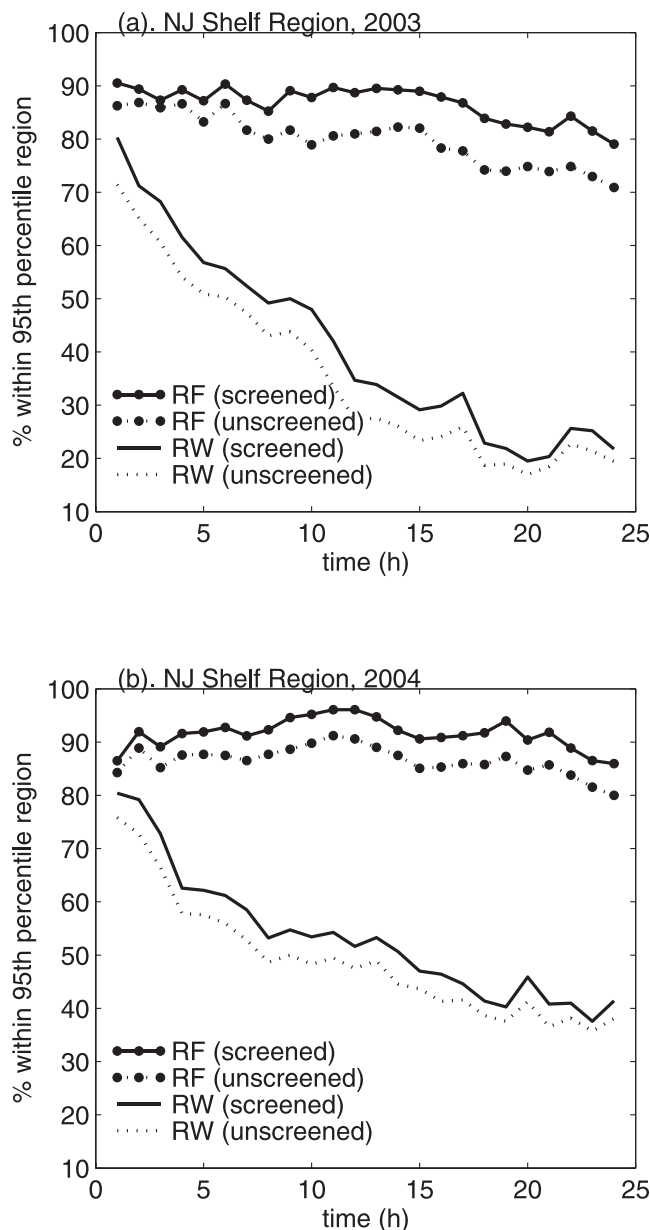


**Figure 13.** Same as Figure 12 for the NJ shelf region during (a) 2003 and (b) 2004.

drifter tracks from a cluster of drifters, this was not possible here because we did not have enough simultaneous drifter releases to form statistically meaningful clusters. Using Okubo's [1971] empirical formula for the apparent horizontal diffusion as a function of horizontal length scale of diffusion, we compute a diffusion coefficient of  $\sim 25 \text{ m}^2/\text{s}$  using a length scale of 25 km (a typical value of the 95th percentile separation in Figures 8–10). The significantly larger values obtained in this study may result from the fact that the turbulent statistics in Table 2 were computed from time series of velocity difference between drifters and CODAR. The drifter-CODAR differences arise from turbulent motions at scales unresolved by CODAR measurements as well as from errors in the CODAR measurements themselves, including those that arise from differing effective depths between the drifters and CODAR. Thus, the esti-

mated dispersion coefficients may have a large component due to CODAR uncertainties that is unrelated to geophysical turbulence. Consequently, if currents from a numerical model of the circulation were employed instead of the CODAR currents, then the statistics of the differences would be different. However, the approach we have demonstrated would still be applicable.

[44] The turbulent velocity statistics estimated in this study were computed as averages over the region and time period sampled by the drifter ensembles. Comparison of the statistics from the two deployments in the NJ shelf region (Table 2) indicate substantial differences in dispersion between the spring and summer. It is likely that horizontal dispersion is also spatially variable, although the available drifter data are not sufficient to quantify this. Note that comparison of the statistics from the BI region and the NJ shelf region is complicated by the fact that the two regions are observed with CODAR systems using different frequencies with corresponding differences in effective depths.

## 6. Summary and Conclusions

[45] Comparison of real drifter trajectories and trajectories predicted using CODAR-derived surface currents illustrates the value of these data for search and rescue operations. For prediction times of 1–24 h, the mean (and 95th percentile) distance between the CODAR-predicted position and the real position is smaller than the distance traveled by the drifter. This indicates that predictions using CODAR velocities are more accurate than the so-called “persistence” forecast (zero drifter velocity). Although, not shown here, CODAR trajectory predictions are also superior

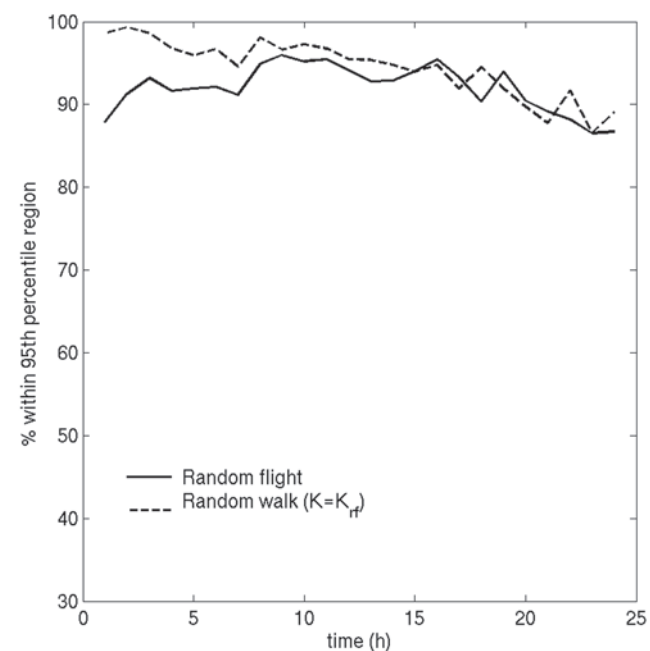


**Figure 14.** Comparison of the uncertainty bounds for predicted drifter position using the random-flight model (solid) and random-walk model with increased diffusivity (dashed) for the 2004 NJ shelf deployment. The random-walk diffusivity in this case was increased to equal the corresponding random-flight value.

to those produced using present U.S. Coast Guard practice, in which the advective velocity is obtained from NOAA tidal current predictions in nearshore waters and a surface current climatology offshore [O'Donnell *et al.*, 2005].

[46] The statistics of the combination of subgrid-scale velocity and CODAR velocity error that contribute to the dispersion of a cloud of pseudo-drifters have been estimated using the ensemble-averaged covariance functions of CODAR-drifter velocity differences. Approximate consistency of the estimates of turbulent velocity variance and timescale was demonstrated for the random-flight turbulence model by evaluation of the resulting search areas, defined as the region in which 95% of the pseudo-drifters are located. The random-flight search areas include the real drifter location in 80–95% of cases. Using the turbulent velocity variances estimated from the zero-lag autocovariance function, as for the random-flight model, the random-walk search areas were significantly less effective. This is a consequence of the fact that the effective turbulent timescale in the random-walk formulation is one half of the time step used in the integration of the Eulerian velocity, 0.5 hours in this study. One can achieve satisfactory search area predictions using the random-walk model only by specifying a diffusion coefficient that is estimated using a model of turbulence that allows for finite turbulent integral timescales, such as the random-flight model, and inflating the turbulent velocity variance to achieve more rapid dispersion at short times.

[47] This study has demonstrated the value of surface current data derived from HF radar in combination with drifter observations for the practical prediction of particle trajectories in the coastal ocean. The methodology used here for estimating uncertainty regions for predictions does not require the deployment of drifter clusters, from which explicit horizontal diffusivity can be estimated. Instead, velocity observations from an ensemble of drifters passing through the radar domain are used to estimate effective fluctuation statistics that are employed in a stochastic particle model. The method is therefore well suited to the use of “drifters of opportunity” that may be deployed for other purposes but that eventually pass through an HF radar coverage region. The question of how many such drifters are needed to accurately characterize the velocity fluctuation statistics is a question that will require further study.

[48] **Acknowledgments.** Funding for this study was provided by the U.S. Coast Guard Research and Development Center through contract DTCG39-00-D-R00008 to Anteon Corporation. We thank Adam Houk and Hugh Roarty for their efforts in maintaining continuous operation of the CODAR systems and acknowledge the U.S. Coast Guard for their invaluable assistance in the deployment of the drifters. This work would not have been conducted without the effective advocacy of Lew Lewandowski and Sean Lester. We thank Malcolm Spaulding, Eoin Howlett, Paul Hall, Tatsu Isaji, Liz Anderson, Tom McClay, and Grant McCardell for insightful comments on our work and drafts of this report. We also acknowledge the two anonymous reviewers whose comments led to significant improvements of this paper.

## References

- Allen, A. A. (1996), Performance of GPS/Argos Self-Locating Datum Marker Buoys (SLDMBs), in *Proceedings of Coastal Ocean-Prospects for the 21st Century (Oceans '96)*, pp. 857–861, Mar. Technol. Soc., Columbia, Md.
- Brickman, D., and P. C. Smith (2002), Lagrangian stochastic modeling in coastal oceanography, *J. Atmos. Oceanic Technol.*, **19**, 83–99.
- Chapman, R. D., and H. C. Graber (1997), Validation of HF radar measurements, *Oceanography*, **10**, 76–79.
- Csanady, G. T. (1973), *Turbulent Diffusion in the Environment*, 248 pp., Springer, New York.
- Davis, R. E. (1985), Drifter observations of coastal surface currents during CODE: The method and descriptive view, *J. Geophys. Res.*, **90**, 4741–4755.
- Griffa, A. (1996), Applications of stochastic particle models to oceanographic problems, in *Stochastic Modelling in Physical Oceanography*, edited by R. J. Adler, P. Müller, and B. L. Rozovskii, Springer, New York.
- Griffa, A., K. Owens, L. Piterbarg, and B. Rozovskii (1995), Estimates of turbulence parameters from Lagrangian data using a stochastic particle model, *J. Mar. Res.*, **53**, 371–401.
- Gurgel, K. W. (1994), Shipborne measurement of surface current fields by HF radar, *L'Onde Electr.*, **74**, 54–59.
- James, M. K., P. R. Armsworth, L. B. Mason, and L. Bode (2002), The structure of reef fish metapopulations: modelling larval dispersal and retention patterns, *Proc. R. Soc. London, Ser. B*, **269**, 2079–2086.
- Kenyon, K. E. (1969), Stokes drift for random gravity waves, *J. Geophys. Res.*, **74**, 6991–6994.
- Kohut, J. T., H. J. Roarty, and S. M. Glenn (2006), Characterizing observed environmental variability with HF Doppler radar surface current mappers and acoustic Doppler current profilers, *IEEE J. Oceanic Eng.*, in press.
- Large, W. G., and S. Pond (1981), Open ocean momentum flux measurements in moderate to strong winds, *J. Phys. Oceanogr.*, **11**, 324–336.
- O'Donnell, J., *et al.* (2005), Integration of Coastal Ocean Dynamics Application Radar (CODAR) and Short-Term Prediction System (STPS) surface current estimates into the Search and Rescue Optimal Planning System (SAROPS), *U.S. Coast Guard Tech. Rep.*, DTCG39-00-D-R00008/HSCG32-04-J-100052.
- Okubo, A. (1971), Oceanic diffusion diagrams, *Deep Sea Res.*, **18**, 789–802.
- Pierson, W. J., and L. Moskowitz (1964), A proposed spectral form for fully developed wind seas based on the similarity theory of S. A. Kitaigorodskii, *J. Geophys. Res.*, **69**, 5181–5190.
- Schmidt, R. O. (1986), Multiple emitter location and signal parameter estimation, *IEEE Trans. Antennas Propag.*, **AP-34**, 276–280.
- Stewart, R. H., and J. W. Joy (1974), HF radio measurements of surface currents, *Deep Sea Res.*, **21**, 1039–1049.
- Thompson, K. R., J. Sheng, P. C. Smith, and L. Cong (2003), Prediction of surface currents and drifter trajectories on the inner Scotian Shelf, *J. Geophys. Res.*, **108**(C9), 3287, doi:10.1029/2001JC001119.
- Ullman, D. S., and D. L. Codiga (2004), Seasonal variation of a coastal jet in the Long Island Sound outflow region based on HF radar and Doppler current observations, *J. Geophys. Res.*, **109**, C07S06, doi:10.1029/2002JC001660.
- Ullman, D., J. O'Donnell, C. Edwards, T. Fake, D. Morschauser, M. Sprague, A. Allen, and B. Krenzien (2003), Use of Coastal Ocean Dynamics Application Radar (CODAR) technology in U. S. Coast Guard search and rescue planning, *U. S. Coast Guard Rep.*, CG-D-09-03.
- Zambianchi, E., and A. Griffa (1994), Effects of finite scales of turbulence on dispersion estimates, *J. Mar. Res.*, **52**, 129–148.
- A. Allen, U.S. Coast Guard Office of Search and Rescue, Groton, CT 06340, USA.
- T. Fake and J. O'Donnell, Department of Marine Sciences, University of Connecticut, Groton, CT 06340, USA.
- J. Kohut, Institute of Marine and Coastal Studies, Rutgers University, New Brunswick, NJ 08901, USA.
- D. S. Ullman, Graduate School of Oceanography, University of Rhode Island, Narragansett, RI 02882, USA. (d.ullman@gso.uri.edu)



# Characterizing Observed Environmental Variability With HF Doppler Radar Surface Current Mappers and Acoustic Doppler Current Profilers: Environmental Variability in the Coastal Ocean

Josh T. Kohut, Hugh J. Roarty, and Scott M. Glenn

**Abstract**—A network of high-frequency (HF) radars is deployed along the New Jersey coast providing synoptic current maps across the entire shelf. These data serve a variety of user groups from scientific research to Coast Guard search and rescue. In addition, model forecasts have been shown to improve with surface current assimilation. In all applications, there is a need for better definitions and assessment of the measurement uncertainty. During a summer coastal predictive skill experiment in 2001, an array of *in situ* current profilers was deployed near two HF radar sites, one long-range and one standard-range system. Comparison statistics were calculated between different vertical bins on the same current profiler, between different current profilers, and between the current profilers and the different HF radars. The velocity difference in the vertical and horizontal directions were then characterized using the observed root-mean-square (rms) differences. We further focused on two cases, one with relatively high vertical variability, and the second with relatively low vertical variability. Observed differences between the top bin of the current profiler and the HF radar were influenced by both system accuracy and the environment. Using the *in situ* current profilers, the environmental variability over scales based on the HF radar sampling was quantified. HF radar comparisons with the current profilers were on the same order as the observed environmental difference over the same scales, indicating that the environment has a significant influence on the observed differences. Velocity variability in the vertical and horizontal directions both contribute to these differences. When the potential effects of the vertical variability could be minimized, the remaining difference between the current profiler and the HF radar was similar to the measured horizontal velocity difference ( $\sim 2.5$  cm/s) and below the resolution of the raw radial data at the time of the deployment.

**Index Terms**—Coastal oceanography, Doppler radar, marine technology, remote sensing.

## I. INTRODUCTION

COASTAL ocean current mapping using high-frequency (HF) radar has matured to the point where it is now considered an essential component of regional ocean observing systems. HF radar networks are being constructed with high-resolution standard-range systems nested within lower resolution

long-range systems. HF radar also provides a relatively new but important spatial data set for assimilation into coastal forecast models, enabling us to advect and evolve features into the future. Several data assimilation studies [1]–[3] have recently tested new methods to assimilate CODAR HF radar data. Wilkin *et al.* [3] have shown that coastal ocean dynamics applications radar (CODAR) HF radar surface current maps combined with subsurface conductivity–temperature–density (CTD) data assimilated via intermittent melding produce the greatest improvements in model forecasts when compared to withheld validation data. These data assimilation studies require the specification of uncertainties. HF radar uncertainties are set at two levels, first at the level of the radial currents from individual radars, second at the level of the total vector currents constructed from multiple radars.

HF radar surface currents have been validated at both levels with many different types of *in situ* current measurements, including surface drifters and subsurface current meters. To date, much of the validation has focused on the higher resolution HF radar systems. These analyses cite differences between HF radar measurements and various *in situ* measurements on the order of 9 to 27 cm/s (for a review, see [4]). In all of these studies, the instruments used for “ground truth” measure the currents over different spatial and/or temporal scales than those of the HF radar site being validated.

Since HF radar uses the scattered signal off surface gravity waves to measure the ocean current, the observations are limited to the near surface. Even with modern subsurface acoustic current profilers, the depth of the measurement bin closest to the surface differs from the surface radar measurement by a few meters. Any vertical variability in the upper water column will contribute to differences between the two measurements. A drifter, while at the surface, is a Lagrangian measurement and spends only a finite amount of time within each HF radar cell. Spatially, an HF radar measurement cell can be as large as 3 km<sup>2</sup> for a standard-range system compared to a point measurement of a subsurface current meter. For a long-range system, this area can be as large as 20 km<sup>2</sup>. Any horizontal variability over scales of the radar cell will contribute to observed differences. In the past, validation studies acknowledged that these discrepancies exist but do not go on to quantify the real environmental variability during the validation analysis [5]. The vertical and horizontal variability of the raw, tidal, and subtidal surface currents

Manuscript received October 1, 2004; revised February 3, 2006; accepted March 10, 2006. Associate Editor: L. R. Wyatt.

The authors are with the Coastal Ocean Observation Laboratory, Institute of Marine and Coastal Sciences, Rutgers, The State University of New Jersey, New Brunswick, NJ 08901 USA (e-mail: kohut@marine.rutgers.edu).

Color versions of one or more of the figures in this paper are available online at <http://ieeexplore.ieee.org>.

Digital Object Identifier 10.1109/JOE.2006.886095

in the coastal ocean can be significant [6], [7], compared to the cited rms differences. Without knowing the magnitude of the horizontal and vertical gradients over the relevant scales during the study period, there is no way to conclude what part of the observed difference is due to system uncertainties and what part is due to real environmental variability.

In this analysis, an array of acoustic Doppler current profilers (ADCPs) is used to quantify the radial velocity difference in the vertical and horizontal directions over the same scales as the HF radar cells. Comparisons are then drawn between various ADCP bins and the closest long-range HF radar measurement cell. The observed differences between the HF radar and *in situ* current measurements are then put into the context of the observed variability. The combined CODAR/ADCP data were then used to characterize the velocity differences in the upper water column during two events, one with relatively high vertical variability and one with low vertical variability.

## II. BACKGROUND

Rutgers, The State University of New Jersey, operates a nested array of CODAR-type HF radar systems. CODAR is a direction finding system that uses a compact receive antenna design with three elements, two directionally dependent loops and a single omnidirectional monopole [8]–[10]. The systems provide continuous radial component vector maps. The effective depth is the assumed depth at which the radar measurement applies. Stewart and Joy [11] estimate the effective depth as

$$D = \lambda/4\pi \quad (1)$$

where  $D$  is the effective depth and  $\lambda$  is the wavelength of the scattering ocean wave. This estimate assumes that the shear is linear between the surface and the effective depth ( $D$ ).

With an operating frequency around 5 MHz, the effective depth of the long-range CODAR system observations is 2.4 m below the surface, assuming linear shear [11]. Typical spatial resolutions are on the order of 6 km in range and  $5^\circ$  in azimuth with maximum ranges exceeding 200 km. Four long-range sites along the coast of New Jersey from Wildwood to Sandy Hook provide surface current maps over the entire New Jersey shelf (Fig. 1). These four sites form one cluster of systems within the Mid-Atlantic Bight (MAB).

Nested within the long-range system are two standard-range sites originally deployed along the southern New Jersey coast [12], [7] and recently moved to the New York Bight Apex to support river plume research (Fig. 1). Assuming linear shear, the effective depth of the 25-MHz CODAR systems is on the order of 48 cm [11]. Typical spatial resolutions are on the order of 1 km in range and  $5^\circ$  in azimuth with maximum ranges out to 40 km.

## III. METHODS

### A. HF Radar Setup

The comparisons presented here will focus on a single standard-range system deployed in Brigantine, NJ and a single long-range system deployed in Tuckerton, NJ (Fig. 1). These particular sites were chosen because they provide overlapping cov-

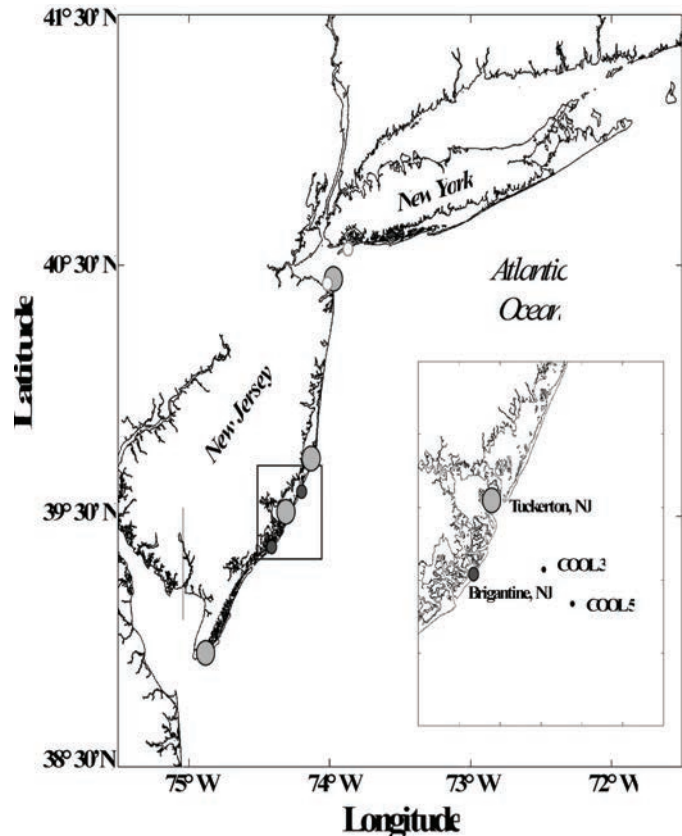


Fig. 1. Study site off the coast of New Jersey. The location of the long-range (light gray), original standard-range (dark gray), and present standard-range (white) are shown. The inset shows the locations of the ADCPs offshore and the two CODAR sites discussed here.

erage of the region occupied by the ADCPs (Fig. 2) and sample over different space and time scales (Table I). In addition, this analysis will concentrate on the first level of uncertainty, the radial level. Since the total vector error bars are based on the radial uncertainties with the geometric errors introduced in the vector combination [13], understanding the accuracy of the radial vectors is crucial when quantifying HF radar uncertainty.

The long-range site operates at 4.55 MHz with a sweep width of 25 KHz, giving an average range of 180 km and a range resolution of 5.85 km. Raw cross spectra were created every 17 min using a 1024-point fast Fourier transform (FFT). These spectra were then hourly averaged, centered on each half hour (Table I). Using the multiple signal classification (MUSIC) direction finding algorithm [14], [15] with the measured beam patterns [12], [16], these overlapping hourly averaged spectra were used to generate radial current maps. These radial current vector maps were then averaged into 4-h files generated every 3 h. Any given gridpoint in the field could have up to seven vectors going into the final average. For example, a file at 12:00:00Z was generated with hourly averaged radial files centered at 10:30:00Z, 11:00:00Z, 11:30:00Z, 12:00:00Z, 12:30:00Z, 13:00:00Z, and 13:30:00Z.

The standard site operated at 24.7 MHz with a sweep width of 100 KHz giving an average range of 40 km and a range resolution of 1.51 km (Table I). The raw cross spectra were written every 4.27 min using a 512-point FFT and used to create 15-min

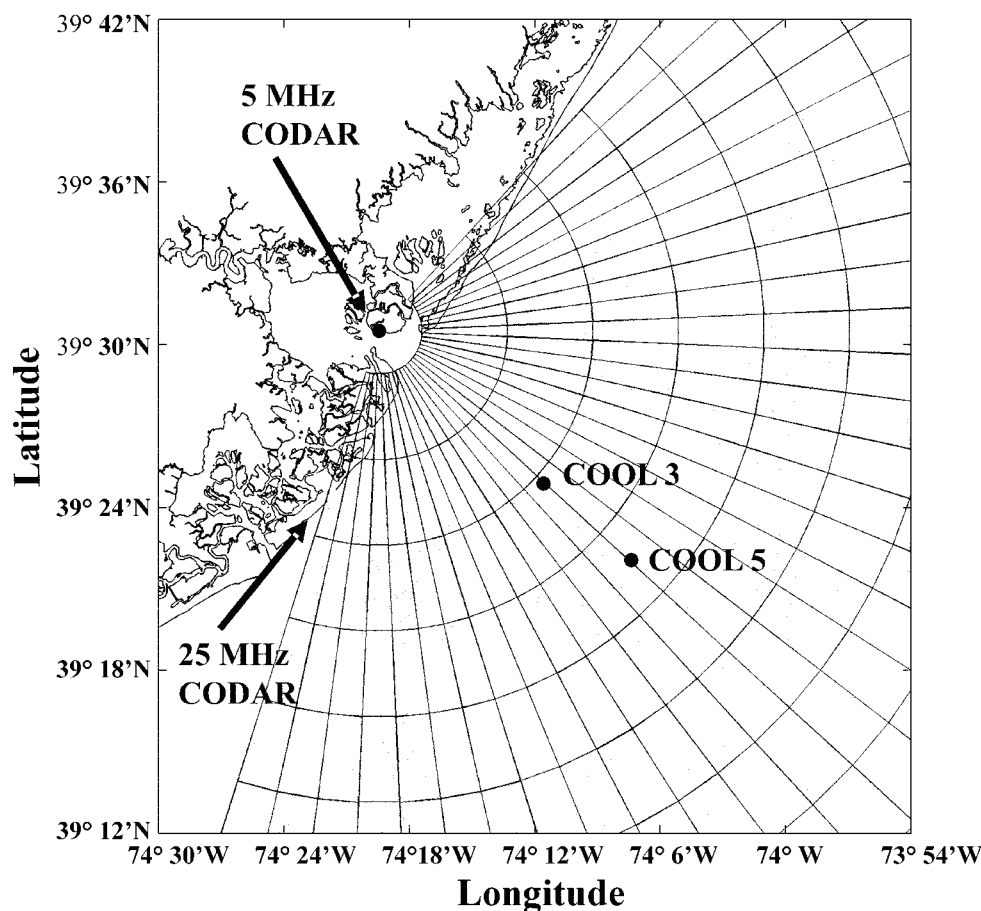


Fig. 2. Radial data grids for the 5-MHz system (dark gray) and the 25-MHz system (light gray). The locations of the ADCPs are also shown.

TABLE I  
OPERATING SETTINGS FOR ADCP, LONG RANGE, AND STANDARD RANGE

	Frequency (MHz)	Sweep Rate (Hz)	FFT Length (min)	Spectra Average (min)	Currents Averaging time (h)	Output Frequency (h)	Depth of Measurement (m)	Spatial Coverage of Measurement (km <sup>2</sup> )
ADCP	0.60	0.5	NA	NA	Match CODAR	Match CODAR	3.5 (top bin)	0.00012
Long-range CODAR	4.55	1.0	17.07	60	4	3	2.4	12
Standard-range CODAR	24.70	2.0	4.27	15	1.25	1	0.5	3

radial files, outputted every 10 min. These 10-min files were then averaged into hourly files.

The two different sampling schemes of the long- and standard-range systems are due to the differences in the transmitted signal. Since CODAR is a Doppler radar, the radial currents are manifest as frequency offsets. The frequency resolution and, through calculation, the radial current resolution of the Doppler spectra is dependent on the operating frequency, sweep rate, and FFT length used in the processing. The long-range system, with a 1-Hz sweep rate and an operating frequency of 4.55 MHz, needs a 1024-point FFT length to resolve currents to 3.22 cm/s. The standard system, with a sweep rate of 2 Hz and an operating

frequency of 24.7 MHz, needs a 512-point FFT to resolve currents to 2.31 cm/s.

### B. ADCP Setup

Two bottom mounted RD Instruments, San Diego, CA, ADCPs were deployed off the coast of New Jersey near the Longterm Ecosystem Observatory (LEO) as part of the Coastal Predictive Skill Experiments (CPSE) [17], [18] (Fig. 2). They were deployed for 37 d between July 10, 2001 and August 16, 2001. The inshore ADCP at Coastal Oceanographic Observation Lab (COOL3) was moored in 18 m of water. The second ADCP at COOL5, 8 km further offshore, was moored



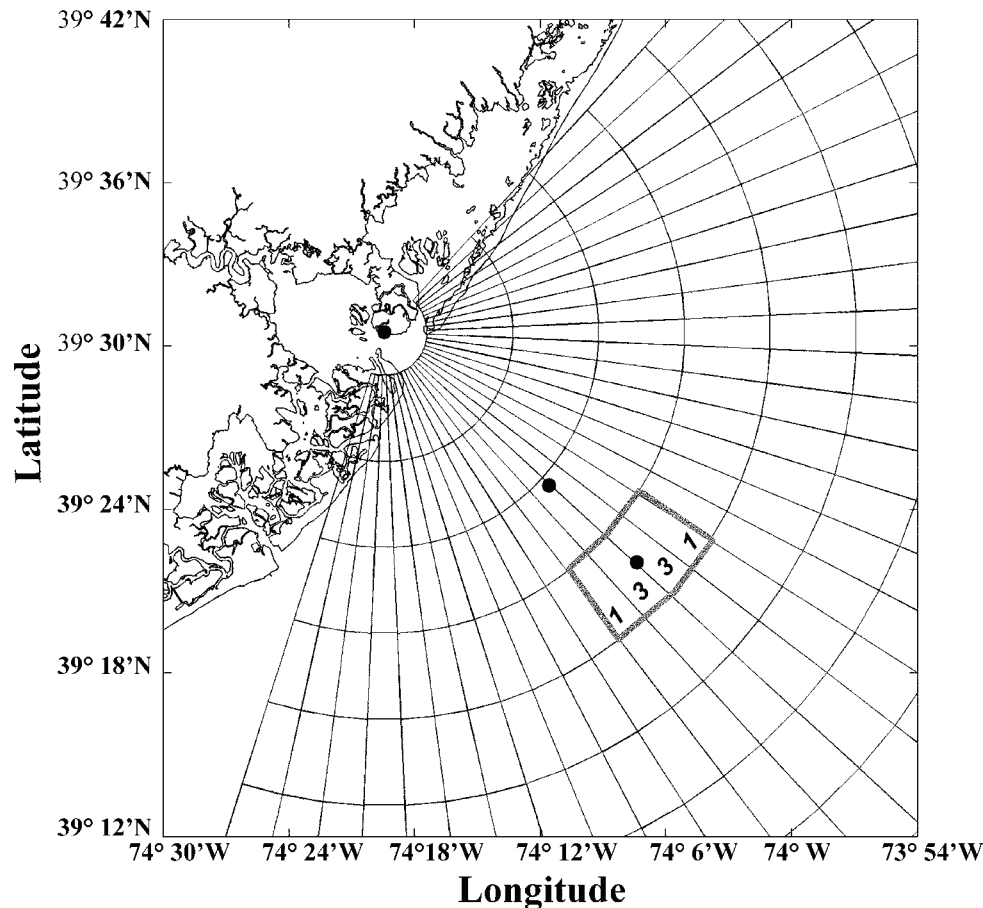


Fig. 3. Four cells used in the interpolation. Their relative weights are indicated within each cell.

in 22 m of water. In addition to the current profile data, there was a string of thermistors running the entire water column at each ADCP, sampling every 10 min through the study period. The ADCPs operated at 600 KHz with a bin resolution of 1 m. Each continuously sampled with 5-s ensembles in mode-1. Sidelobe contamination limits the ability of ADCPs to measure the currents up to the surface. For typical Janus configuration, this is usually 10% of the water depth, which in this case is 1.8 and 2.2 m. Thus, a bin centered at 2.5 m below the surface is expected to be contaminated, and a 1-m bin centered at 3.5 m below the surface is expected to be good. This was checked against the percent good data return calculated with the RD software package. For both ADCPs, the bin 3.5 m below the surface had over 98% good data return. The ADCP data was averaged to exactly match the CODAR processing. For the long-range site comparisons, the ADCP was first averaged into hourly files generated every half hour, and then these hourly files were averaged into 4-h files generated every 3 h. For the standard-site comparison, the ADCP data was first averaged into 15-min files generated every 10 min. These 10-min files were then averaged into 1.25-h files generated every hour. Both data sets were rotated into a radial and cross-radial coordinate system to match the CODAR data. Both the CODAR and ADCP data were detided using a least-squared fit of the dominant constituent  $M_2$  to the raw data. Only concurrent ADCP and CODAR data were used in the least-squares fit.

Since the COOL5 ADCP is not centered directly in any of the long-range radar cells (Fig. 2), the radial data was spatially interpolated to the ADCP. The CODAR processing treats each range bin separately. For each range bin, spectra are run through the MUSIC algorithm to calculate the bearing of each radial velocity within the first-order Bragg region. The number of radial vectors in any given range cell depends on 1) the current resolution determined by the FFT length, operating frequency, and sweep rate and 2) the number of antenna elements in the receive array. The current resolution controls how many radial velocity vectors are available, and the number of antenna elements determines the number of possible MUSIC solutions for each radial velocity. For our setup with three receive antenna elements, a radial velocity every 3.22 cm/s (2.31 cm/s) for the long-range (standard-range) system can be placed in up to two angular bins. If, at the end of the processing, more than one radial velocity is placed in a given angular bin, the vectors are averaged. Consequently, if there are more than two angles with a given radial velocity or periods of weak surface currents, data coverage will be reduced. Based on these constraints, the interpolation was done in angle, not range. This is consistent with previous interpolation techniques used on the standard-range data set [12], [19]. The following interpolation technique was applied to the long-range radial vectors. Using the four bins surrounding the ADCP, two on either side, the radial data were averaged with weights chosen based on the distance of each bin from the ADCP. The center

TABLE II  
rms DIFFERENCE BETWEEN THE COMPLETE ADCP RECORD AT THE COOL5  
TOP BIN AND ADCP TIME SERIES WITH VARYING NUMBER OF POINTS  
GOING INTO EACH 4-h AVERAGE AT THE TOP BIN AT COOL5  
(COLUMN 2) AND COOL3 (COLUMN 3)

# pts	Cool 5 Bin 17 (cm/s)	Cool 3 Bin 15 (cm/s)
1	4.27	7.00
2	2.82	5.55
3	1.86	5.49
4	1.47	5.49
5	1.04	5.34
6	0.70	5.32
7	0.00	5.22

of the two closest bins is three times closer to the ADCP than the center of the two outermost bins, so the two bins adjacent to the ADCP were weighted three times the two bins further away (Fig. 3). For each 4-h file, a value was calculated only if at least two of the four angular CODAR bins contained data. Comparisons of the ADCP were produced with both the noninterpolated and interpolated data. Since most of the previous validation studies have focused on the standard-range systems and the orientation of the long-range bins better match the ADCP locations (Fig 2), the majority of the analysis focuses on the long-range data.

#### IV. CONTRIBUTION OF TIME SAMPLING AND ENVIRONMENTAL VARIABILITY

##### A. Time Averaging

Doppler processing identifies a number of radial current velocities observed in the Bragg peaks of the  $N$  antennas in the compact array. A direction finding algorithm then places each of the observed radial velocities in at most  $N-1$  directions. The effect of varying data coverage is seen when the hourly files (generated every half hour) are averaged over 4 h. If the data were complete, seven vectors would go into the average for each of the gridpoints in the field. Reduced data coverage will lead to less hourly vectors used in the final average. To simulate this, the continuous ADCP record was compared to the same ADCP data with random hourly vectors missing in the 4-h averages. Different time series were constructed with different minimum requirements of vectors going into the 4-h average. The minimum number ranged from one to seven vectors, where seven vectors would be a complete record. This was done for two cases. One compared the complete record of the top ADCP bin at COOL5 to the incomplete records at the same location. The second compared the complete record of the top ADCP bin at COOL5 with incomplete records at the top bin at COOL3. For case one, as the number of hourly data used in the average increases, the rms difference between the complete and incomplete data set decreases (Table II). When the minimum requirement was set to one, the rms difference was 4.27 cm/s. When the minimum requirement was increased to two vectors, the

rms difference reduced to 2.82 cm/s. Increasing the minimum requirement from one vector to two decreased the rms difference by almost half. Above two, the rms difference slowly decreased with larger minimum requirements, eventually reaching 0. This decrease approximately follows the expected  $1/\sqrt{n}$ , where  $\sqrt{n}$  is the square root of the number of samples ( $n$ ), decrease with increased samples. For case two, the rms difference dropped from 7.00 cm/s with one vector to 5.55 cm/s with two vectors. As the number of vectors increased from two to seven, the rms difference gradually decreases to 5.22 cm/s. Unlike the  $1/\sqrt{n}$  decrease seen in case 1, the case 2 data shows no significant decrease in rms difference when the number of vectors increases from two to seven. This suggests that with at least two vectors in the average, the rms difference is based more on the spatial variability than the number of samples. Case 2 is a comparison of data over similar spatial scales of the HF radar range cell. The comparison shows that largest improvement occurred when the minimum requirement was increased from one vector to two vectors. In addition, the requirement of two or more vectors going into the average for case one lowers the rms difference to the current resolution of the standard-range site and below the current resolution of the long-range site. Based on these data, the CODAR data were further sorted to have at least two hourly vectors in each 4-h average to be included in the validation. For the remainder of this analysis, the vertical and horizontal variability refer to the velocity difference of the radial velocity vector in the vertical and horizontal directions, respectively.

##### B. Observed Environmental Variability

Throughout the ADCP deployment, the water column was typically stratified with a strong thermocline at mid-depth with predominantly baroclinic cross-shelf flows [3]. The scale of the vertical variability, defined by the depth of the thermocline, varied between about 8 and 16 m, depending on the local forcing. The horizontal scale of the variability is on the order of 100 km for the tidal and 10–20 km for the subtidal flow [3], [7], [17]. The observed cross-shore standard deviation measured at the surface bin of COOL5, COOL3, and the closest HF radar cell is 10.26, 9.06, and 9.88 cm/s, respectively. Using the two ADCPs, the horizontal and vertical variability during the study period was quantified across the scales relevant to the comparison discussed here. In the vertical, the long-range and standard-range CODAR are measuring the velocity within the upper 2.4 to 0.48 m of the water column while the closest ADCP bin is 3.5 m below the surface. In the horizontal, the ADCP is sampling at a point while the standard- and long-range sites were sampling across a length scale of 1.5 and 6 km, respectively.

In the vertical, the top ADCP bin at COOL5, 3.5 m below the surface, was compared to another bin of the same ADCP, 6.5 m below the surface [Fig. 4(a)]. The rms difference between these two bins over the study period was 6.25 cm/s for the raw currents and 0.63 cm/s for the  $M_2$  tidal fit (Table III). These two bins were chosen because the vertical separation was on the same order as that between the surface CODAR measurement and the top bin of the ADCP. The  $M_2$  tidal velocities on the inner New Jersey shelf are predominately rectilinear in the cross-shelf

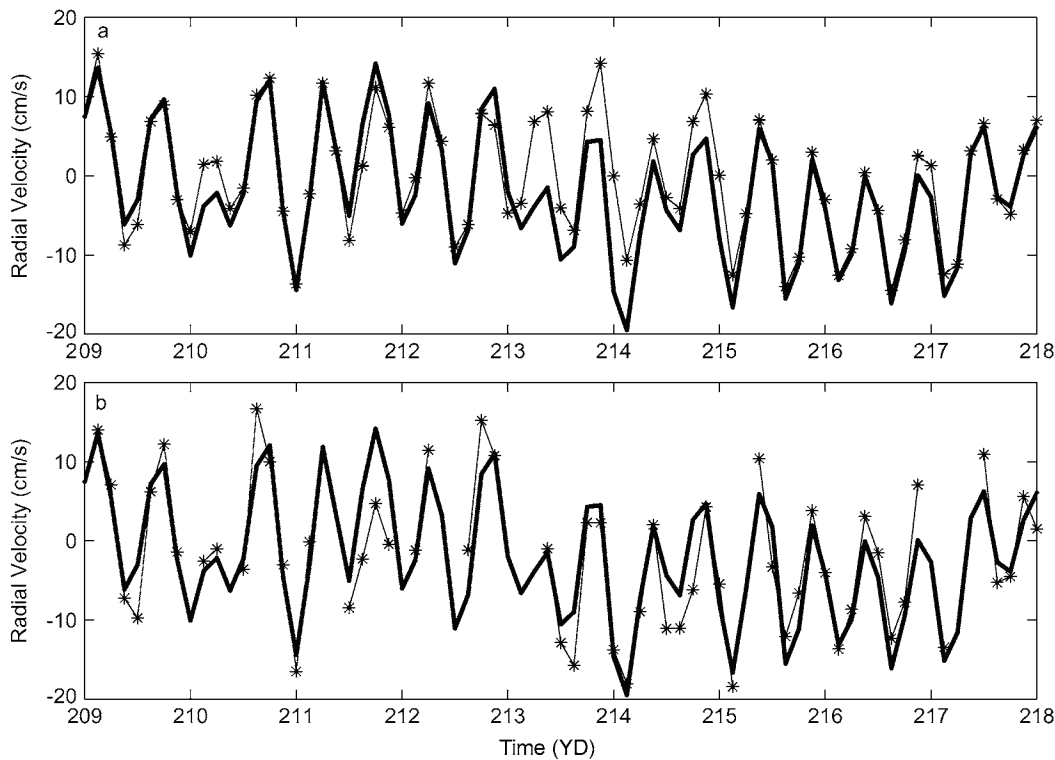


Fig. 4. (a) Time series of the cross-shore velocity of the ADCP5 bin at 3.5-m depth (thick) and the ADCP bin at 6.5-m depth (thin). (b) Time series of the cross-shore velocity of the ADCP5 bin at 3.5-m depth (thick) and the CODAR at the surface (thin).

TABLE III  
rms DIFFERENCE STATISTICS

			Raw Velocity (cm/s)	Tidal Velocity (cm/s)
COOL5 ADCP (3.5 m)	versus	COOL5 ADCP (6.5 m)	6.25	0.63
COOL5 ADCP (3.5 m)	versus	COOL3 ADCP (3.5 m)	5.22	1.22
CODAR	versus	COOL5 ADCP (3.5 m)	5.86	0.71
CODAR	versus	COOL3 ADCP (3.5 m)	6.30	2.22
CODAR (Interpolated)	versus	COOL5 ADCP (3.5 m)	4.98	0.18
CODAR (Standard Range)	versus	COOL5 ADCP (3.5 m)	6.40	0.97

direction with length scales of 100 km, significantly greater than the dimension of the HF radar cell [17]. Since the tides in this region also vary much less over the depth scales discussed here, the  $M_2$  velocity difference in the vertical is much less than that seen in the raw currents.

In the horizontal, the surface bin at COOL5 was compared to the surface bin of COOL3, 8 km away. 8 km is similar to the horizontal length scale of the long-range measurement. During this particular study period, the observed rms difference was

5.22 cm/s for the raw data and 1.22 cm/s for the tidal data (Table III). Once again the difference in the  $M_2$  tide was much less than that seen in the raw currents. Over the study period, both the horizontal and vertical differences were on the order of 5–6 cm/s for the raw velocity fields, and 1.0 cm/s for the  $M_2$  tidal fields. Weaker tidal velocities and larger horizontal and vertical scales of the variability drive the lower rms difference in the  $M_2$  tidal comparisons.

The estimated contribution of the environmental variability to the observed differences between the long-range CODAR site and the top bin of the ADCP were on the order of 5 cm/s. Additionally, data dropouts could contribute differences on the same order intermittently through the study period. Comparisons between the ADCPs and the long-range and standard-range CODAR sites were analyzed in the context of the scale of these contributions.

V. HF RADAR/ADCP COMPARISONS

A. Vertical Difference

Radial current time series of the COOL5 ADCP bin closest to the surface was compared to the radial data of the CODAR range and angular bin closest to the ADCP [Fig. 4(b)]. The rms difference over the study period for the raw radial velocity was 5.86 cm/s and reduced to 4.32 cm/s for the long-range CODAR data interpolated to the ADCP location (Table III). This difference was of the same order as the vertical variability measured with the ADCP alone. The tidal velocity comparison significantly improved with an rms difference of 0.71 and 0.18 cm/s



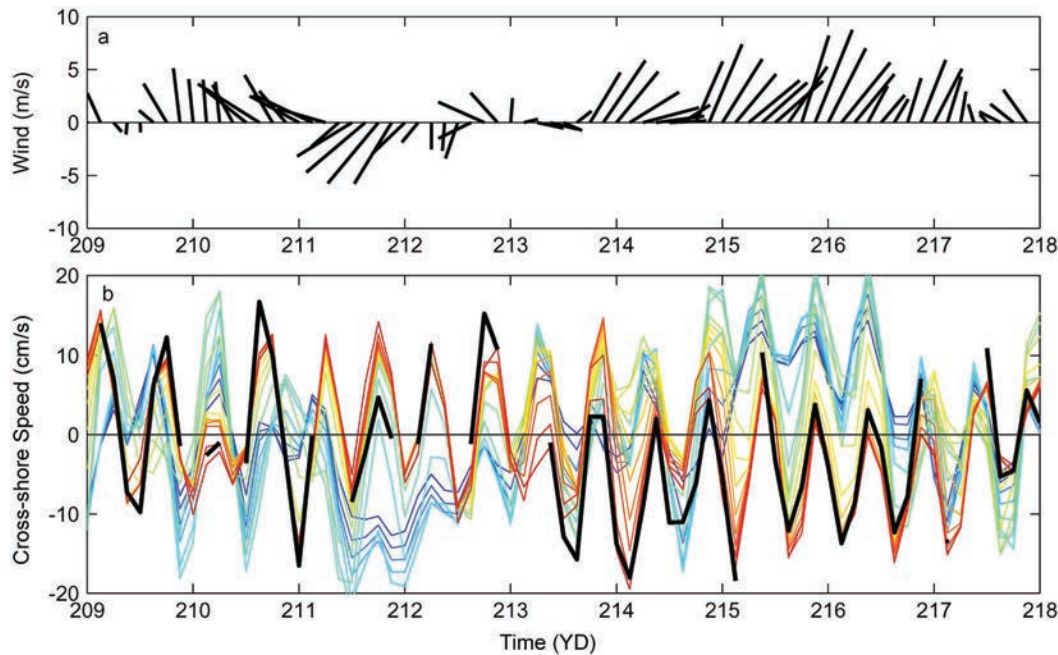


Fig. 5. (a) Time series of the local winds. (b) Time series of the cross-shore velocity measured at each ADCP bin at COOL5 and the interpolated HF radar velocity (black). The ADCP depth scale in meters is shown in the colorbar.

for the closest bin and interpolated data, respectively. These differences were consistent with the observed vertical variability in the tidal velocity at COOL5.

### B. Horizontal Difference

The rms difference between the CODAR bin closest to the ADCP at COOL5 and the top bin of the ADCP at COOL3 was 6.3 cm/s for the raw velocity and 2.22 cm/s for the  $M_2$  tidal velocity (Table III). The horizontal difference measured between COOL3 and COOL5 was 5.22 cm/s for the raw velocity and 1.22 cm/s for the tidal velocity. Once again the HF radar/ADCP difference was on the same order as the observed variability measured between the two ADCPs.

The rms difference was also calculated between the ADCP and the standard-range system. Recall that the standard system sampled across a smaller spatial area and closer to the ocean surface than the long-range system. Therefore, the standard-site velocity was further (closer to the surface) from the top bin of the ADCP than the deeper long-range measurement and closer in spatial scale to the ADCP than the larger long-range cell (Fig. 2). When we compare the standard system to the ADCP, the raw velocity rms difference was 6.4 cm/s. This was on the same order as the long-range comparison but slightly larger. The larger difference could be due to the shallower measurement, further from the top bin of the ADCP. When looking at the standard-range, long-range, and spatially separated ADCPs, the significance of the environmental variability was clear. The velocity differences in both the horizontal and vertical direction must be considered when comparing HF radar data to *in situ* current measurements.

For both the vertical and horizontal direction, the observed differences between the ADCPs and CODAR were of the same order as the differences observed between the two ADCPs over

the same scales. When the environmental variability is as large as the difference between two different current measurements with observations sampling over the same scales, it is difficult to determine exactly what is due to the local environment. These results suggest that the difference observed between the ADCP and CODAR were more representative of the environment, than the accuracy of either instrument. If the contribution from the environment can be removed from the rms differences, we will be able to better understand the instrument uncertainty, both random error and bias.

Since the environmental variability had significant influence on the observed shear, we used the rms difference as a tool to characterize the variability in the upper water column. To analyze the influence of the observed velocity differences separately, the ADCPs were used to identify two specific events, one with high vertical variability and one with low vertical variability relative to the measured horizontal variability.

## VI. INFLUENCE OF ENVIRONMENTAL VARIABILITY

During the study period there were events in which the vertical difference exceeded the observed horizontal difference, and events in which the horizontal difference exceeded the vertical difference. Within a subset of the data between yearday (YD) 209 and YD 214 (July 28, 2001 to August 2, 2001), both cases occur within a few days of each other. YD 209 and 210 are characterized by a relatively strong thermocline and weak upwelling winds [Figs. 5(a) and 6(a)]. The winds change to a downwelling favorable direction on YD 211, deepening the thermocline and weakening the stratification [Figs. 5(a) and 6(b)]. After this mixing event, the wind returns to the upwelling favorable direction and the weaker thermocline shallows. The downwelling event mixes the water column and reduces the stratification.

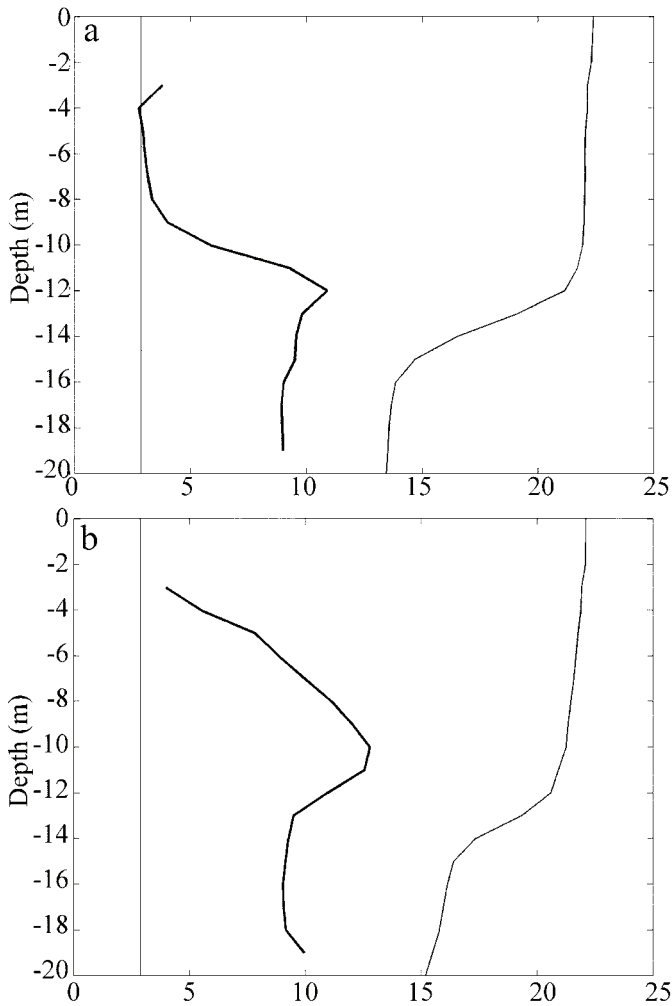


Fig. 6. Depth profile of the mean temperature (degree Celsius) (thin) and rms difference (centimeter per second) between the CODAR surface measurement and each bin of the ADCP at COOL5 (thick) for (a) low-variability case (YD 209–210) and (b) high-variability case (YD 213 and 214). The thin black lines at (a) 2.82 and (b) 2.88 are the rms difference between the surface bin at COOL5 and the surface bin at COOL3 over the respective time period.

#### A. Low Vertical Difference Event (Vertical Component < Horizontal Component)

From YD 209 to YD 211, the rms difference between the 3.5 and 6.5 m bin of the ADCP at COOL5 was 2.22 cm/s. During this two-day period a very strong thermocline separated the surface layer from the effects of bottom friction, resulting in a 10-m deep surface layer with very low vertical variability [Fig. 6(a)]. The temperature profile at COOL5 averaged over these two days showed a surface layer at 22 °C that extends down to 10 m [Fig. 6(a)]. Below this layer the temperature quickly changes to 14 °C. The rms difference between the interpolated CODAR and the top bin at COOL5 is 3.80 cm/s. This comparison was extended throughout the water column with each bin of the ADCP. The rms profile in the surface layer was relatively constant, around 2.80 cm/s with a minimum of 2.50 cm/s at 4.5 m [Fig. 6(a)]. There was a strong correlation between the location of the thermocline and the depth at which the ADCP velocity begins to differ significantly from the CODAR measurement. The peak in the rms difference fell right in the middle of the thermo-

cline. The vertical line in Fig. 6(a) is the rms difference between the top bins at COOL5 and COOL3 over this two-day subset and indicates an estimate of the magnitude of the rms difference due to horizontal variability of 2.82 cm/s. This value was nearly the same as the rms difference between CODAR and the entire surface layer measured by the ADCP. For this low vertical variability case, observed rms differences in the upper water column indicate a relatively constant difference with a near-zero vertical contribution and a horizontal contribution on the order of 3 cm/s.

#### B. High Vertical Difference Example (Vertical Component > Horizontal Component)

Following the downwelling event, the rms difference between the top (3.5 m) bin and the 6.5 m bin of the ADCP at COOL5 increased from 2.22 to 6.86 cm/s while the magnitude of the horizontal difference remained fairly steady, increasing from 2.82 to 2.88 cm/s. Even though there is still a thermocline separating the surface layer from the effects of bottom friction, the profile of the rms difference looked significantly different [Fig. 6(b)]. No longer was the rms constant through the surface layer with a peak at the thermocline. In this higher vertical gradient period, the rms difference increased linearly throughout the surface layer and remained relatively constant through the bottom layer [Fig. 6(b)]. The CODAR comparison starts at 3.98 cm/s at the top bin (3.5 m) and increases to 12.79 cm/s at the thermocline 10 m down. In the high vertical variability event, the vertical component of the velocity difference dominates the observed difference. The linear dependence of the difference with depth indicates that the magnitude of the vertical gradient of velocity in the upper water column was relatively constant. Assuming this and extrapolating the trend upward, the 2.5-m ADCP bin, if uncontaminated by sidelobes, would likely have reached the point where the CODAR/ADCP rms difference was similar to the horizontal COOL5/COOL3 ADCP rms difference.

In both the high and low vertical difference examples, the environment significantly influenced the rms difference. In the low variability case, the horizontal component dominated the rms difference as indicated by a constant magnitude in the upper water column equal the horizontal difference. When the vertical component of the velocity difference increased to almost double that of the horizontal, the profile of the rms difference became depth-dependent in the surface layer, increasing linearly to the thermocline. Here, the velocity variability in the upper water column was again relatively constant from the thermocline to the surface, but now the vertical component had the larger influence on the rms difference.

## VII. SUMMARY AND CONCLUSION

HF radar surface current maps are an important component of regional observing systems. As these systems become more prevalent and utilized, it is necessary to quantify and lower uncertainties at both the radial and total vector level. When time averaging of the ADCP was precisely matched to the time averaging interval of the CODAR, rms differences between the CODAR radial velocity and the nearest ADCP top bin were comparable to the ADCP/ADCP rms difference due to environmental variability. When the vertical difference was reduced, the minimum CODAR/ADCP rms difference was 2.5 cm/s, less

than the ADCP/ADCP rms difference of 2.82 cm/s. In this case, the real environment contributed more to the observed difference than observational uncertainties of either the ADCP or CODAR.

Since the environment dominated the rms difference, it could be used as a tool to characterize the magnitude of the current variability in the upper water column. For the two cases examined here, when the vertical difference was less than the horizontal difference (case 1), the magnitude of the total velocity variability was constant through the surface layer, on the order of the measured horizontal variability. When the vertical difference was larger than the horizontal (case 2), the total velocity variability was once again constant in the surface layer, dominated by the vertical component. In both events, the magnitude of the velocity difference remains relatively steady from the surface to the thermocline. As the range cell size increases with the long-range systems, the instances where the vertical and horizontal components of the velocity gradient are comparable increases. For these systems, both vertical and horizontal components must be considered when quantifying the uncertainties of the observations. Once this environmental variability is quantified and separated from the observed rms differences, we can better understand the details of the HF radar uncertainty, both random error and instrument bias.

The next step in lowering the HF radar uncertainties is to develop new methodologies to fill in the data gaps at the radial level. The present operational processing procedure is only one of the vast number of processing routes that can lead to total vector fields. With rms differences between CODAR and ADCP on the order of a few centimeters per second, consistent with the observed shear, another step is longer FFT lengths to produce finer current resolution. We have already demonstrated that interpolation in direction both fills in coverage and improves comparisons with ADCP data. A systematic comparison of interpolation possibilities in range, bearing, and time is required to fully resolve this issue.

#### REFERENCES

- [1] P. R. Oke, J. S. Allen, R. N. Miller, G. D. Egbert, and P. M. Kosro, "Assimilation of surface velocity data into a primitive equation coastal ocean model," *J. Geophys. Res.*, vol. 107, no. C9, 2002, doi: 10.1029/2000JC000511.
- [2] J. D. Paduan and I. Shulman, "HF radar data assimilation in the Monterey Bay area," *J. Geophys. Res.*, vol. 109, no. C07S09, 2004, doi: 10.1029/2003JC001949.
- [3] J. L. Wilkin, H. G. Arango, D. B. Haidvogel, C. S. Lichtenwalner, S. M. Glenn, and K. S. Hedström, "A regional ocean modeling system for the long-term ecosystem observatory," *J. Geophys. Res.*, 2005, doi: 10.1029/2003JC002218, accepted for publication.
- [4] R. D. Chapman and H. C. Graber, "Validation of HF radar measurements," *Oceanography*, vol. 10, pp. 76–79, 1997.
- [5] H. C. Graber, B. K. Haus, L. K. Shay, and R. D. Chapman, "HF radar comparisons with moored estimates of current speed and direction: Expected differences and implications," *J. Geophys. Res.*, vol. 102, pp. 18 749–18 766, 1997.
- [6] D. Prandle, "The fine-structure of nearshore tidal and residual circulations revealed by HF radar surface current measurements," *J. Phys. Oceanogr.*, vol. 17, pp. 231–245, 1987.
- [7] J. T. Kohut, S. M. Glenn, and R. J. Chant, "Seasonal current variability on the New Jersey inner shelf," *J. Geophys. Res.*, vol. 109, no. C07S07, 2004, doi: 10.1029/2003JC001963.
- [8] D. E. Barrick, M. W. Evens, and B. L. Weber, "Ocean surface currents mapped by radar," *Science*, vol. 198, pp. 138–144, 1977.
- [9] B. J. Lipa and D. E. Barrick, "Least-squares methods for the extraction of surface currents from CODAR cross-loop data: Application at ARSLOE," *IEEE J. Ocean. Eng.*, vol. OE-8, no. 4, pp. 226–253, Oct. 1983.
- [10] B. J. Lipa and D. E. Barrick, "Extraction of sea state from HF-radar sea echo: Mathematical theory and modeling," *Radio Sci.*, vol. 21, pp. 81–100, 1986.
- [11] R. H. Stewart and J. W. Joy, "HF radio measurement of surface currents," *Deep-Sea Res.*, vol. 21, pp. 1039–1049, 1974.
- [12] J. T. Kohut and S. M. Glenn, "Calibration of HF radar surface current measurements using measured antenna beam patterns," *J. Atmos. Ocean. Technol.*, pp. 1303–1316, 2003.
- [13] R. D. Chapman, L. K. Shay, H. C. Graber, J. B. Edson, A. Karachintsev, C. L. Trump, and D. B. Ross, "On the accuracy of HF radar surface current measurements: Intercomparisons with ship-based sensors," *J. Geophys. Res.*, vol. 102, pp. 18 737–18 748, 1997.
- [14] D. E. Barrick and B. J. Lipa, "Radar Angle Determination with MUSIC Direction Finding," United States Patent 5 990 834, 1999.
- [15] R. O. Schmidt, "Multiple emitter location and signal parameter estimation," *IEEE Trans. Antennas Propag.*, vol. AP-34, no. 3, pp. 276–280, Mar., 1986.
- [16] D. E. Barrick and B. J. Lipa, "Correcting for distorted antenna patterns in CODAR ocean surface measurements," *IEEE J. Ocean. Eng.*, vol. OE-11, no. 2, pp. 304–309, Apr. 1986.
- [17] R. J. Chant, S. Glenn, and J. Kohut, "Flow reversals during upwelling conditions on the New Jersey inner shelf," *J. Geophys. Res.*, vol. 109, no. C12S03, 2004, doi: 10.1029/2003JC001941.
- [18] S. M. Glenn, R. Arnone, T. Bergmann, W. P. Bissett, M. Crowley, J. Cullen, J. Gryzmski, D. Haidvogel, J. Kohut, M. A. Moline, M. Oliver, C. Orrico, R. Sherrell, T. Song, A. Weidemann, R. Chant, and O. Schofield, "The Biogeochemical impact of summertime coastal upwelling in the Mid-Atlantic Bight," *J. Geophys. Res.*, vol. 109, no. C12S02, 2004, doi: 10.1029/2003JC002265.
- [19] J. D. Paduan, D. E. Barrick, D. M. Fernandez, Z. Hallock, and C. C. Teague, "Improving the accuracy of coastal HF radar current mapping," *Hydro Int.*, vol. 5, pp. 26–29, 2001.



**Josh T. Kohut** received the Ph.D. degree in oceanography from Rutgers, The State University of New Jersey, New Brunswick, in 2002.

He develops and applies new robotic, radar, cable, and remote sensing technologies to real-time ocean monitoring. He is currently the Director of the Coastal Ocean Observation Lab (COOL), Rutgers.



**Hugh J. Roarty** received the Ph.D. degree in ocean engineering from Stevens Institute of Technology, Hoboken, NJ, in 2001.

He joined the Coastal Oceanographic Observation Lab (COOL), Rutgers, The State University of New Jersey, New Brunswick, in 2002. He was responsible for the maintenance and performance of their high-frequency (HF) radar network. In 2005, he was named Director of Hardware for the operations center, which includes HF radar and Slocum gliders.



**Scott M. Glenn** received the Sc.D. degree in ocean engineering from the Massachusetts Institute of Technology (MIT) and Woods Hole Oceanographic Institution (WHOI) Joint Program, Cambridge, in 1983.

He has worked on the development of new ocean observation and forecasting systems at Shell Oil Company and Harvard University for the U.S. Navy. Currently, he is a Professor of Marine and Coastal Science, Rutgers, The State University of New Jersey, New Brunswick.





# Spatial and temporal variability of diurnal wind forcing in the coastal ocean

Eli Hunter,<sup>1</sup> Robert Chant,<sup>1</sup> Louis Bowers,<sup>1</sup> Scott Glenn,<sup>1</sup> and Josh Kohut<sup>1</sup>

Received 29 November 2006; revised 22 December 2006; accepted 3 January 2007; published 7 February 2007.

[1] Spatial and temporal variability of diurnal wind forcing and the coastal response is characterized for the New York Bight from February through May, 2005. This analysis demonstrates that diurnal wind forced motions are significant in the coastal ocean during the spring and summer months, near shore and as far as 100 km offshore. A doubling of diurnal current amplitudes is common in the spring compared to the winter months, associated with an increase in sea/land breeze days. Diurnal fluid motions due to sea/land breeze events can account for up to 50% of the total kinetic energy during the spring. **Citation:** Hunter, E., R. Chant, L. Bowers, S. Glenn, and J. Kohut (2007), Spatial and temporal variability of diurnal wind forcing in the coastal ocean, *Geophys. Res. Lett.*, 34, L03607, doi:10.1029/2006GL028945.

## 1. Introduction

[2] A commonly occurring and well documented meteorological feature of the coastal zone is the diurnal sea/land breeze system (SLBS) [Miller *et al.*, 2003]. A phenomenon which occurs along the majority of the earth's coastline [Simpson, 1994; Gille *et al.*, 2003], the SLBS is driven by differential heating of adjacent land and water masses. The land mass heats up more rapidly than the water during the day and cools off more rapidly at night. The resulting cross-coastline thermal pressure gradient sets up a circulation cell that propagates both onshore and offshore as a gravity current [Simpson, 1994, Miller *et al.*, 2003]. Although the idealized model of the SLBS is characterized by a reversal of flow in the cross-coastline direction, a variety of factors can influence the strength and orientation of the diurnal variability of the SLBS as well as its inland and offshore extent. Synoptic weather patterns, land-sea temperature difference, coastline shape and topography are important controls on the initiation, intensity and spatial scale of the SLBS [Simpson, 1994, Miller *et al.*, 2003].

[3] While the SLBS is well studied, the importance of the spatial and temporal variability of diurnal wind forcing in the coastal ocean due to the thermal pressure gradient is lesser known. Long term meteorological observations of the coastal ocean are sparse, so detailed knowledge of the seaward structure of the SLBS is limited to numerical weather models. Recently, however, analysis of Quikscat scatterometry demonstrated that sea-breezes occur along most of the world's coastline and can extend 100's of km offshore [Gille *et al.*, 2003, Aparna *et al.*, 2005]. Furthermore, studies have documented aspects of the response of

the ocean to diurnal wind forcing. Doppler current meter data from a single mooring 170 km off the Namibian coast revealed a resonant interaction between internal waves and diurnal wind forcing [Simpson *et al.*, 2002]. Hyder *et al.* [2002] observed diurnal currents of up to  $40 \text{ cm s}^{-1}$  over the upper 3 m of the water column in the Thermaikos Gulf consistent with SLBS forcing. Pattiaratchi *et al.* [1997] related increased wave energy, sediment transport and beach erosion to SLBS forcing off the coast of Australia. Finally, Gibbs [2000] analyzed 3–5 day periods of SLBS activity on the New South Wales coast finding motions associated with the sea breeze that account for one quarter of the variance in diurnal currents.

[4] While these studies highlight the significant role of the SLBS in the coastal ocean, they do not provide a detailed description of the spatial extent of the SLBS induced motion in the coastal ocean nor of the spatial distribution of the diurnal motion. The expanding international array of surface current radar systems provides an opportunity to observe the response of the coastal ocean to SLBS forcing and characterize its spatial distribution.

[5] The motivation for this work is a result of observations made during the Lagrangian Transport and Transformation Experiment in April, 2005, which recorded observations of the evolution of the Hudson River outflow. Diurnal motions 4–5 times stronger than the K1 or O1 tidal constituents are observed as the plume intrudes onto the New York Bight, coincident with a  $5\text{--}7 \text{ m s}^{-1}$  diurnal wind during the course of the experiment. The diurnal wind is identified as a sea breeze, a phenomenon that is well documented and common during the spring and summer months along the New York/New Jersey Coast [Frizzola and Fisher, 1963; Angell and Pack, 1965; Bowers, 2004; Childs and Raman, 2005].

[6] Wind forcing is an important component to buoyant coastal plume dynamics and several studies have examined the response of buoyant coastal discharge to steady wind forcing [Whitney and Garvine, 2005, Fong and Geyer, 2001]. The role of variable winds in the coastal ocean, particularly in the diurnal band is less understood. Pinones *et al.* [2005] found a strong diurnal signal in the Maipo River plume associated with SLBS forcing. Simpson *et al.* [2002] and Rippeth *et al.* [2002] found that a horizontal pressure gradient set up by wind forcing drives diurnal motions in a coastal two layer regime.

[7] Continental margins are among the most productive ecosystems on earth [Field *et al.*, 1998] and this productivity is strongly controlled by physical processes [Mann and Lazier, 2006]. In this paper we demonstrate that the SLBS can be a dominate force that drives circulation over the majority of the shelf. Therefore, quantifying the role of the SLBS in New York Bight circulation has wide implications

<sup>1</sup>Institute for Marine and Coastal Sciences, Rutgers University, New Brunswick, New Jersey, USA.

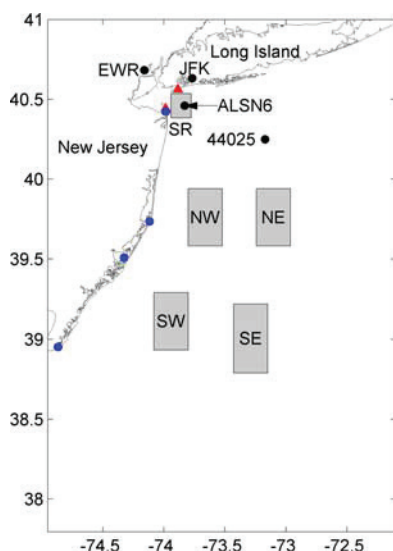


**Figure 1.** Map of the study area showing the New Jersey coastline to the west and the Long Island coastline to the north. Surface current data are averaged over the five grey regions labeled SR, NW, NE, SW and SE for standard range, long range northwest, long range northeast, long range southwest, and long range southeast, respectively. Meteorological stations are shown as black circles, SR HF radar installations are shown as red triangles, and LR HF radar installations are shown as blue circles.

for physical, biological and chemical processes in the coastal ocean, including vertical mixing, primary production and air-sea gas exchange. Assessing the importance of the SLBS in coastal circulation potentially improves our understanding of these transport processes, and consequently our ability to model and predict changes in global biogeochemical cycles.

## 2. Data and Methods

[8] The study area (Figure 1) is within the domain of the Rutgers University Coastal Ocean Observation Lab (COOL). The observatory consists of a nested system of HF radar systems, satellite X-Band and L-Band receivers, and a fleet of autonomous underwater vehicles for measuring subsurface parameters. The HF radar installations, in particular, provide a unique opportunity to characterize the temporal and spatial variability of New Jersey Shelf circulation [Kohut *et al.*, 2004]. Surface current data collected via the COOL 25 MHz Short Range (SR) and 5 MHz Long Range (LR) HF radar systems are used in this study.

[9] The SR system provides a grid of surface current vectors every 0.5 hours with a horizontal resolution of 1.0 km at the mouth of the Hudson River (Figure 1). The gridded field is subsequently averaged over the entire domain at each time step. Only those grid points with low percentages of missing data (<5%) throughout the study period (February 2005–May 2005) are included in averaging.

[10] The LR system collects data every 1.0 hours with a horizontal grid resolution of 6 km. The LR domain is divided

into 4 different sub regions designated northeast (NE), southeast (SE), northwest (NW) and southwest (SW) (Figure 1), each of which is spatially averaged after omitting data at grid-points with less than 80% temporal coverage.

[11] Meteorological data sources for this study are the National Data Buoy Center stations at Ambrose Tower (ALSN6) and buoy 44025, and National Climatic Data Center land based stations at John F. Kennedy airport (JFK) and Newark Airport (EWR). Wind and temperature data are all hourly measurements.

[12] Following Simpson *et al.* [2002] and Rippeth *et al.* [2002], harmonic analysis is applied to the gridded surface current data, the five spatially averaged surface current time series and the two marine (ALSN6 and 44025) wind time series using a harmonic period of 24 hours. The gridded surface current fields are divided into two time periods, February–March, 2005 and April–May, 2005, for which diurnal variance ellipse parameters are calculated. A 4 day running harmonic fit is also applied to the wind and surface current time series from February through May 2005. This time series of harmonic coefficients is used to calculate diurnal kinetic energy in the atmosphere and the ocean.

[13] While the presence of diurnal period energy is a reasonable assumption for the SLBS [Rotunno, 1983] and is used in part to identify SLBS regimes [O'Brien and Pillsbury, 1974; Masselink and Pattiaratchi, 2001; Hyder *et al.*, 2002], synoptic wind variability can contribute to the diurnal band as well. Consequently a method of objectively identifying days where the SLBS develops is required. The dominant factors considered when filtering sea breeze days from synoptic days are the strength of the synoptic wind, the land-sea thermal pressure gradient, and a diurnal change in wind direction. [Biggs and Graves, 1962, Borne *et al.*, 1998, Furberg *et al.*, 2002].

[14] The method of Furberg *et al.* [2002] is applied here, as it is a more conservative estimate of sea breeze frequency, requiring a reversal of wind in the cross-coastline direction, not simply a diurnal change in wind direction. It is a four step conditional filter, almost identical to that outlined by Furberg *et al.* [2002]: (a) A majority of the hourly winds at ALSN6 must be offshore (or calm) during the hours from (sunrise – 6 h) to (sunrise + 2 h). (b) The wind at ALSN6 must blow onshore for at least two consecutive hours during the hours from (sunrise + 2 h) to (sunset + 2 h). (c) A majority of the hourly winds at ALSN6 must be non-onshore (or calm) during the hours from (sunset + 2 h) to (sunset + 8 h). (d)  $T_{\text{land}} - T_{\text{sea}} > 0^{\circ}\text{C}$ .  $T_{\text{land}}$  is the daily averaged (sunrise-sunset) air temperature at a National Climatic Data Center station and  $T_{\text{sea}}$  is the daily averaged (sunrise-sunset) sea surface temperature at buoy 44025.

[15] The local coastline in the New York Bight Apex is unlike most SLBS studies as there are land masses due north and due west of ALSN6, allowing for multiple SLBS boundaries [Novak and Colle, 2006; Colle *et al.*, 2003]. Consequently, the simple filter of Furberg *et al.* [2002] is applied in two directions. The north-south wind at ALSN6 identifies SLBS days along the Long Island (LI) coast and the east-west wind at ALSN6 identifies SLBS days along the New Jersey (NJ) coast. The total diurnal kinetic energy calculated in this study does not distinguish between LI and



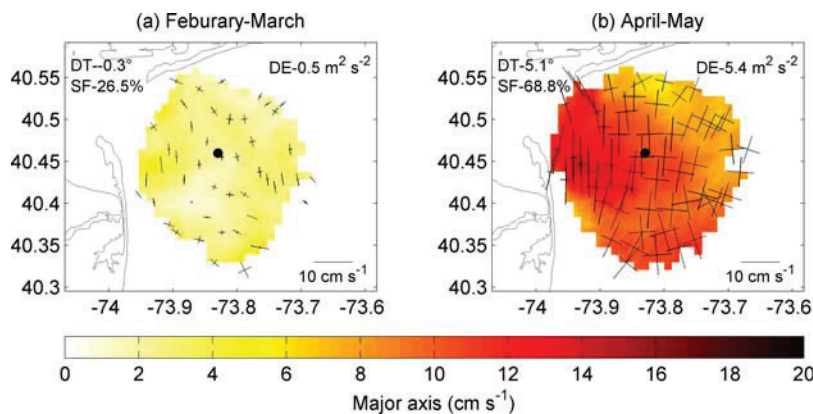


**Figure 2.** Maps showing diurnal variance ellipses (black crosses) and the major axis (color) of diurnal variability calculated from the SR HF radar system for (a) February–March 2005 and (b) April–May 2005. Also noted are the SLBS frequency (SF), ALSN6 diurnal wind energy (DE) and  $T_{\text{land}} - T_{\text{sea}}$  (DT).

NJ SLBS. Consequently, SLBS days are simply identified and not given any directionality.

### 3. Seasonal Variability

[16] Climatology of SLBS frequency indicate the majority of SLBS days occur during the hot summer months, with few in the wintertime and transitional periods in the spring and fall [Prezerakos, 1986; Masselink and Pattiaratchi, 2001; Furberg *et al.*, 2002]. Applying the filter described in section 2, the percentage of SLBS days for the spring transition is calculated. The SLBS frequency (SF) is 26.5% for February–March, increasing to 68.8% in April–May. There is a corresponding increase in diurnal energy (DE) at both ALSN6 and 44025, with clockwise rotating diurnal wind observed at both stations during both time periods. DE at ALSN6 increases by an order of magnitude from the February–March period ( $0.5 \text{ m}^2 \text{ s}^{-2}$ ) to the April–May period ( $5.4 \text{ m}^2 \text{ s}^{-2}$ ). DE increases at 44025 from  $0.7 \text{ m}^2 \text{ s}^{-2}$  to  $2.2 \text{ m}^2 \text{ s}^{-2}$  during the same period.

[17] The results of the diurnal harmonic analysis on the gridded SR HF radar data in Figure 2 are striking. Diurnal variance ellipses have a clockwise sense of rotation for both time periods, consistent with diurnal wind variability. There is more variability in ellipse orientation observed in February–March (Figure 2a), compared to the April–May period (Figure 2b) which are oriented generally North–South. The magnitude of the major axis during February–March is on average  $2\text{--}3 \text{ cm s}^{-1}$ , with maxima of  $\sim 5 \text{ cm s}^{-1}$  near the Hudson River mouth. There is a substantial increase in diurnal energy for the April–May period, with typical values of  $\sim 10 \text{ cm s}^{-1}$  for the major axis and a maximum of  $17 \text{ cm s}^{-1}$ . There is clearly enhanced diurnal energy in the New York Bight apex in April–May not associated with tides.

[18] The harmonic analysis of the LR gridded data is similar to the SR results, particularly in the New York Bight Apex (Figure 3). There are, however, some notable exceptions. Like the SR data, the LR data show an increase in diurnal energy during the April–May period albeit the increase is not as pronounced as in the SR data. Nevertheless, the LR data reveal that the spatial extent of sea-breeze forcing extends across most of the shelf with typical amplitudes of  $\sim 5 \text{ cm s}^{-1}$  during the April–May period

compared to  $2\text{--}3 \text{ cm s}^{-1}$  during February–March (Figures 3a and 3b). In addition to increases in energy, variance ellipse orientation in the diurnal band shifts from generally along shore to cross shore during the enhanced diurnal energy period, an indication the increase in diurnal energy is not due to tides.

### 4. Spatial and Temporal Variability

[19] Time series of diurnal wind energy from ALSN6 and 44025 are presented in Figure 4a with SLBS days highlighted in grey. While there is clearly a net increase in diurnal wind energy in April–May compared with February–March, it is a result of relatively intense, episodic events (in the diurnal energy sense) associated with SLBS days. The strongest events during the study period occur during runs of SLBS days around April 8–April 23 (event A), May 4 (event B), and May 18 (event C) (Figure 4).

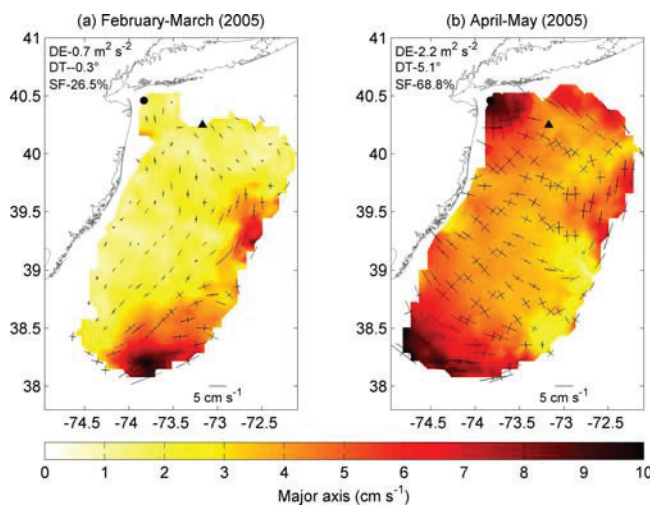


**Figure 3.** Maps showing diurnal variance ellipses (black crosses) and the major axis (color) of diurnal variability calculated from the LR HF radar system for (a) February–March 2005 and (b) April–May 2005. Also noted are the SLBS frequency (SF), 44025 diurnal wind energy (DE) and  $T_{\text{land}} - T_{\text{sea}}$  (DT).

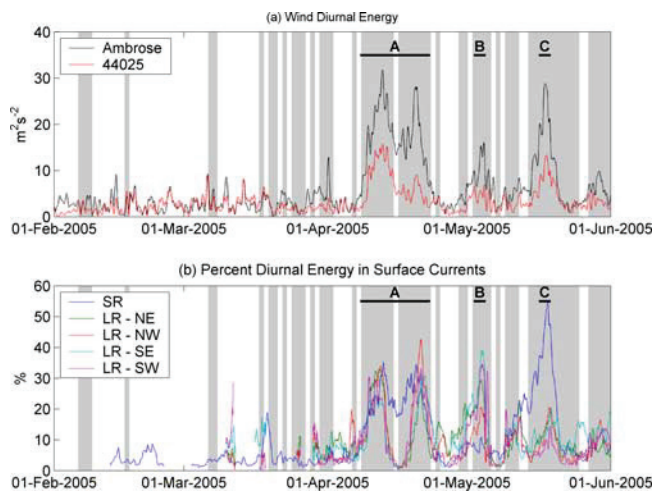


**Figure 4.** Time series of diurnal energy showing SLBS days highlighted in grey. (a) Wind diurnal energy ( $\text{m}^2 \text{s}^{-2}$ ) for buoys ALSN6 and 44025 (red). (b) Percent of the total energy in the diurnal band for the five surface current regions. Events A, B and C are highlighted.

[20] The percent of energy in the diurnal band (PDE) over the study period is reported in Figure 4b for the 1 SR and 5 LR regions. During February–March PDE tends to be very low in the SR data (generally  $<5\%$ ), consistent with an absence of forcing mechanisms other than tidal. In contrast, during Event a 30–35% of the total kinetic energy is contained in the diurnal band, increasing to 50% during event C. However, during event B only  $\sim 10\%$  of the total kinetic energy is diurnal, perhaps due to spatial variability of the SLBS. Diurnal energy in the SR data is clearly correlated with diurnal wind energy at ALSN6 on SLBS days ( $r = 0.85$  with 95% confidence). Significant (95%) correlations are also found at all 4 LR regions when compared with the diurnal wind energy at 44025, with the lowest at LR-SE ( $r = 0.33$ ) and LR-SW ( $r = 0.38$ ) and highest at LR-NE ( $r = 0.52$ ) and LR-NW ( $r = 0.59$ ).

[21] During event A diurnal energy at all 4 LR regions reached 30%, as it did in the SR data, suggesting the SLBS event was not only intense but widespread on the shelf, forcing diurnal circulation offshore. Events B and C in the LR data are quite different from the SR data. Event B reaches 20–40% at all regions in the LR field, while in the SR data it was  $<10\%$ . Event C, which was  $>50\%$  in the SR field is  $\sim 15\text{--}20\%$  in the LR data.

## 5. Summary and Discussion

[22] Using local wind measurements, sea surface temperature, air temperature and coastal HF radar installations, diurnal wind and diurnally forced current variability is characterized for the New York Bight from February through May 2005. The New Jersey/Long Island SLBS tends to be episodic in nature, but can be quite intense and widespread as seen from April 8–April 23, around May 4, and around May 18.

[23] The increased sea breeze activity in April–May drives diurnal current motions throughout the New York Bight. The major axis of diurnal currents in the New York Bight apex increased to  $10\text{--}15 \text{ cm s}^{-1}$  over the two-month

period, with a maximum of  $30 \text{ cm s}^{-1}$  during event A, compared with  $2\text{--}5 \text{ cm s}^{-1}$  during February–March.

[24] Long range HF radar analysis indicates that diurnal motion, correlated with diurnal wind energy on SLBS days, is evident across the entire shelf. Up to 100 km offshore, there is a doubling of the major axis of diurnal ocean currents during April–May when diurnal surface currents are typically  $5 \text{ cm s}^{-1}$  compared to  $2\text{--}3 \text{ cm s}^{-1}$  during February–March. Coincident with the increase in major axis magnitude, associated with the increased occurrence of the SLBS, the orientation of the variance ellipses shift from dominantly along-shore to cross-shore. Spatially, the region of influence of the SLBS during April–May 2005 is from the south shore of Long Island to Cape May and out to 100 km offshore.

[25] SLBS forced ocean current is, as expected, as episodic as the SLBS, yet is an energetic feature during SLBS events. For example, in all 5 CODAR sub-domains 30–40% of the total kinetic energy was contained in the diurnal band during event A, including the SE region that lies  $\sim 100 \text{ km}$  offshore, while during the February–March period only 5% of the total KE is contained in the diurnal band.

[26] Contrast this result with that during B and C. These events, while strong, did not affect the shelf as uniformly as event A. During event B there was little diurnal energy in the New York Bight Apex, yet in the LR sub regions as much as 39% diurnal energy was observed. During event C up to 50% of energy in the New York Bight Apex was diurnal, while the LR sub regions showed 15–20%. Spatial variability in the SLBS could account for these differences, but further study is required.

[27] In summary, these results demonstrate that intermittent sea-breeze forcing can extend over a large fraction of the 150 km wide New York bight shelf. The effect of sea-breeze forcing was shown, at times, to dominate not only the K1 and O1 tidal period motion but also the total kinetic energy in hourly averaged surface current measurements. While the imprint of the SLBS on the coastal ocean has a large spatial scale, its structure varies from event-to-event and appears to be related to synoptic-scale meteorological features. While the objective of this paper was to demonstrate the prominence and spatial scale of SLBS forcing, the fact that at times it dominates surface current kinetic energy suggests that it likely impacts vertical shear and thus vertical mixing. Moreover, spatial gradients in diurnal period motion at the surface would lead to convergences that would drive internal-wave motion that may resonate with the effective inertial period [Lerczak *et al.*, 2001; Simpson *et al.*, 2002]. While these issues are beyond the scope of this paper, insofar as the SLBS is important in driving coastal circulation and mixing, we feel that circulation models may require accurate representation of the SLBS in their atmospheric forcing. Consequently, a corresponding improvement in our understanding of the transport processes which impact broader biogeochemical cycling in the global ocean is expected.

[28] **Acknowledgment.** This study was supported by the National Science Foundation's COastal Ocean Program (CoOP) through grant OCE-028957.

## References

- Angell, J. K., and D. H. Pack (1965), A study of the sea breeze at Atlantic City, New Jersey using tetrons as Lagrangian tracers, *Mon. Weather Rev.*, 93, 475–493.

- Aparna, M., S. R. Shetye, D. Shankar, S. S. C. Shenoi, P. Mehra, and R. G. P. Desai (2005), Estimating the seaward extent of sea breeze from QuikSCAT scatterometry, *Geophys. Res. Lett.*, **32**, L13601, doi:10.1029/2005GL023107.
- Biggs, W. G., and M. E. Graves (1962), A lake breeze index, *J. Appl. Meteorol.*, **1**, 474–480.
- Borne, K., D. Chen, and M. Nunez (1998), A method for finding sea breeze days under stable synoptic conditions and its application to the Swedish west coast, *Int. J. Climatol.*, **18**, 901–914.
- Bowers, L. (2004), The effect of sea surface temperature on sea breeze dynamics along the coast of New Jersey, M.S. thesis, Rutgers Univ., New Brunswick, N. J.
- Childs, P. P., and S. Raman (2005), Observations and numerical simulations of urban heat island and sea breeze circulations over New York City, *Pure Appl. Geophys.*, **162**, 1955–1980.
- Colle, B. A., J. B. Olson, and J. S. Tongue (2003), Multiseason verification of the MM5. part I: Comparison with the Eta model over the central and eastern United States and impact of MM5 resolution, *Weather Forecasting*, **18**, 431–457.
- Field, C. B., M. J. Behrenfeld, J. T. Randerson, and P. Falkowski (1998), Primary production of the biosphere: Integrating terrestrial and oceanic components, *Science*, **281**, 237–241.
- Fong, D. A., and W. R. Geyer (2001), Response of a river plume during an upwelling favorable wind event, *J. Geophys. Res.*, **106**, 1067–1072.
- Frizzola, J. A., and E. L. Fisher (1963), A series of sea breeze observations in the New York City area, *J. Appl. Meteorol.*, **2**, 722–739.
- Furberg, M., D. G. Steyn, and M. Baldi (2002), The climatology of sea breezes on Sardinia, *Int. J. Climatol.*, **22**, 917–932.
- Gibbs, M. T. (2000), Detecting a response to weak sea breezes in the New South Wales coastal ocean, *N. Z. J. Mar. Freshwater Res.*, **34**, 669–680.
- Gille, S. T., S. G. Llewellyn Smith, and S. M. Lee (2003), Measuring the sea breeze from QuikSCAT scatterometry, *Geophys. Res. Lett.*, **30**(3), 1114, doi:10.1029/2002GL016230.
- Hyder, P., J. H. Simpson, and S. Christopoulos (2002), Sea-breeze forced diurnal surface currents in the Thermaikos Gulf, north-west Aegean, *Cont. Shelf Res.*, **22**, 585–601.
- Kohut, J. T., S. M. Glenn, and R. J. Chant (2004), Seasonal current variability on the New Jersey inner shelf, *J. Geophys. Res.*, **109**, C07S07, doi:10.1029/2003JC001963.
- Lerczak, J. A., M. C. Hemdeshot, and C. D. Winant (2001), Observations and modeling of coastal internal waves driven by a diurnal sea breeze, *J. Geophys. Res.*, **106**, 19,715–19,729.
- Mann, K. H., and J. Lazier (2006), *Dynamics of Marine Ecosystems: Biological-Physical Interactions in the Ocean*, 3rd ed., 496 pp., Blackwell, Malden, Mass.
- Masselink, G., and C. B. Pattiaratchi (2001), Characteristics of the sea breeze system in Perth, Western Australia, and its effect on the nearshore wave climate, *J. Coastal Res.*, **17**, 173–187.
- Miller, S. T. K., B. D. Keim, R. W. Talbot, and H. Mao (2003), Sea breeze: Structure, forecasting, and impacts, *Rev. Geophys.*, **41**(3), 1011, doi:10.1029/2003RG000124.
- Novak, D. R., and B. A. Colle (2006), Observations of multiple sea breeze boundaries during an unseasonably warm day in metropolitan New York City, *Bull. Am. Meteorol. Soc.*, **87**, 169–174.
- O'Brien, J. J., and R. D. Pillsbury (1974), Rotary wind spectra in a sea breeze regime, *J. Appl. Meteorol.*, **13**, 820–825.
- Pattiaratchi, C., B. Hegge, J. Gould, and E. Eliot (1997), Impact of sea-breeze activity on nearshore and foreshore processes in southwestern Australia, *Cont. Shelf Res.*, **17**, 1539–1560.
- Pinones, A., A. Valle-Levinson, D. A. Narvaez, C. A. Vargas, S. A. Navarette, G. Yuras, and J. C. Castilla (2005), Wind-induced diurnal variability in river plume motion, *Estuarine Coastal Shelf Sci.*, **65**, 513–525.
- Prezerakos, N. (1986), Characteristics of the sea breeze in Attica, Greece, *Boundary Layer Meteorol.*, **36**, 245–266.
- Rippeth, T. P., J. H. Simpson, R. J. Player, and M. Garcia (2002), Current oscillations in the diurnal-inertial band on the Catalaninan shelf in spring, *Cont. Shelf Res.*, **22**, 247–265.
- Rotunno, R. (1983), On the linear theory of the land and sea breeze, *J. Atmos. Sci.*, **40**, 1999–2009.
- Simpson, J. E. (1994), *Sea Breeze and Local Wind*, Cambridge Univ. Press, New York.
- Simpson, J. H., T. P. Rippeth, P. Hyder, and I. M. Lucas (2002), Forced oscillations near the critical latitude for diurnal-inertial resonance, *Cont. Shelf Res.*, **22**, 177–187.
- Whitney, M. M., and R. W. Garvine (2005), Wind influence on a coastal buoyant outflow, *J. Geophys. Res.*, **110**, C03014, doi:10.1029/2003JC002261.

L. Bowers, R. Chant, S. Glenn, E. Hunter, and J. Kohut, Institute for Marine and Coastal Sciences, Rutgers University, 71 Dudley Road, New Brunswick, NJ 08901, USA. (hunter@marine.rutgers.edu)







## Wind-Driven Response of the Hudson River Plume and its Effect on Dissolved Oxygen Concentrations

**Scott Glenn, Oscar Schofield, Robert Chant, Josh Kohut, Hugh Roarty, Jennifer Bosch, Louis Bowers, Donglai Gong and John Kerfoot**

*Rutgers University, Institute of Marine and Coastal Sciences, USA*

*(received in June, 2006; accepted in March, 2007)*

The Lagrangian Transport and Transformation Experiment (LaTTE) study of the Hudson River Plume has now completed 2 of its 3 field seasons. The interdisciplinary study is being conducted in a sustained coastal research observatory that provides a spatial and temporal context for adaptive shipboard sampling. Observations from the second LaTTE field season are used here to describe the processes responsible for a previously unexplained recurrent hypoxia region along the New Jersey coast.

Key words: *dissolved oxygen, river plume, hypoxia*

### 1. Introduction

Hypoxia and anoxia in marine environments refer to the conditions occurring when the concentration of Dissolved Oxygen (DO) in seawater is reduced to the point that it negatively impacts marine organisms. In some cases, widespread fishkills are reported. In New Jersey, the most significant hypoxia/anoxia event occurred in 1976 when a combination of a prolonged hot summer with few mixing storms produced low DO conditions over much of the New Jersey continental shelf, resulting in 100s of thousands of 1976 dollars of damage to the shellfishing industry. Since the 1976 event, DO concentrations on the New Jersey shelf have been monitored on a regular basis by federal and state managers. NOAA measurements from the 1970s and 1980s (Warsh 1987) were used to identify four regions of recurrent hypoxia along the New Jersey shelf (Fig. 1). Early speculation was that the recurrent hypoxia zones were associated with riverine inputs of nutrients. However, as Fig. 1 indicates, some rivers with similar watersheds do not have hypoxic zones, and some hypoxic zones do not have rivers.

Through a series of individual science experiments in the early 1990's followed by integrated ocean modeling and observation Coastal Predictive Skill Experiments from 1998-2001, the processes responsible for the formation of the three

recurrent hypoxia zones off southern New Jersey were identified (Schofield and Glenn 2004). The processes involve the interaction of coastal upwelling jets with bottom topography (Song 2001), resulting in the formation of a recirculating eddy on the downstream side of a series of topographic highs associated with ancient river deltas (Fig. 2). Sampling of actual upwelling eddies (Fig. 3) indicates that the eddies concentrate phytoplankton in these three regions, depleting the bottom DO concentrations as the phytoplankton die and are decayed by bacteria. (Glenn, Schofield et al. 2004). But what about the fourth region of recurrent hypoxia off of the northern New Jersey coast where bottom topography is quite different? Except for the speculation that this region is likely associated with the Hudson River, the processes responsible for this fourth northern hypoxic zone remained relatively unknown.

### 2. A Process Study in Research Observatory

The National Science Foundation (NSF) has sponsored Lagrangian Transport and Transformation Experiment (LaTTE) which is an interdisciplinary, multi-institutional study of the Hudson River Plume conducted within the footprint of a sustained coastal

research observatory. The LaTTE Principle Investigators and their home Institutions are listed in Table 1. The experiment features two coordinated ships, one to conduct a dye release to tag and track a Hudson Plume water mass as it mixes with the shelf water as the transport component, and a second to observe the chemical and biological transformations that occur within that water mass.

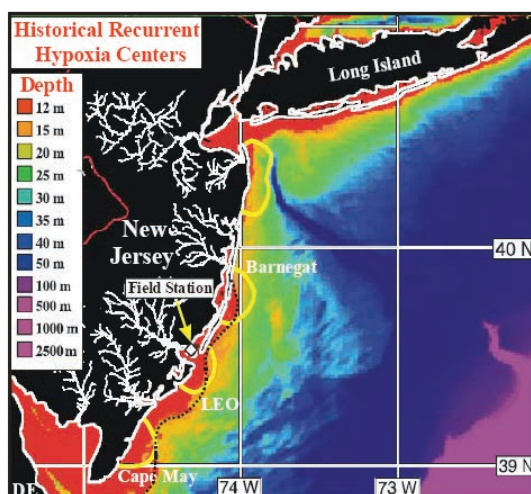


Fig. 1. Regions of recurrent hypoxia on the New Jersey Shelf (Warsh, 1987).

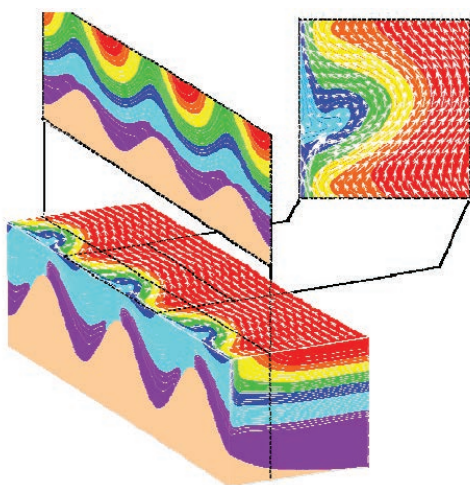


Fig. 2. Mechanisms for the development of upwelling centers along the southern New Jersey coast were identified in idealized models (Glenn 1996).

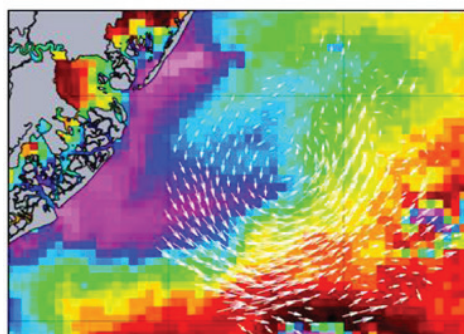


Fig. 3. Coastal Observatory identified upwelling centers in real-time for shipboard sampling (Glenn & Schofield, 2004).

Table 1. LaTTE Principal Investigators

<b>Physics</b>
Bob Chant (Rutgers U.)
Bernie Gardner (U. Massachusetts)
Scott Glenn (Rutgers U.)
Bob Houghton (Lamont)
John Wilkin (Rutgers U.)
<b>Chemistry</b>
John Reinfelder (Rutgers U.)
Bob Chen (U. Mass)
<b>Biology</b>
Paul Bissett (FERI)
Tom Frazer (U. Florida)
Mark Moline (Cal-Poly)
Oscar Schofield (Rutgers U.)
Meng Zhou (U. Mass)
<b>Plus Many Others</b>

The sustained observatory is the New Jersey Shelf Observing System (NJSOS), operated by the Rutgers University (R.U.) Coastal Ocean Observation Lab's (COOL) Operations Center. The regional footprint of NJSOS provides a spatial and temporal context for shipboard-based process studies such as LaTTE. The R.U. COOL Operations Center includes two-way voice, video and data communications with the LaTTE research vessels so that all the information and guidance available from the observatory can be provided to the vessels sampling at sea.

### 3. LaTTE Results

LaTTE provides the first detailed look at the processes responsible for the northern New Jersey recurrent hypoxia center. LaTTE data collected during the field season from April 2005 are used to illustrate these processes. The time period corresponds to high flow conditions during rainy spring. Satellite ocean color imagery (Fig. 4) of the Hudson plume during this time indicates that water from the Raritan River is distinct from the Hudson River. A strong front between the two river waters is often observed in the lower Harbor. Shipboard sampling across the front reveals that the Raritan has a significantly higher organic content than the Hudson, an observation consistent with the more organic sediments in the geologic record. The combined sediment laden flows are then observed to exit the Harbor and flow out onto the continental shelf.

The high-resolution inner nest of the NJSOS CODAR network provides more details on the outflow. The plume exits the estuary not as a steady flow, but as a series of ebb tide pulses (Fig. 5). With each ebb tide, a layer of fresh water squirts out onto the New Jersey shelf, forming a strong front that in



the absence of wind would propagate down the New Jersey coast as a coastal plume. However, because each squirt is a layer of new fresh water, it is very buoyant and susceptible to wind forcing.

Springtime synoptic winds in the New York Bight Apex usually blow from either the northeast or southwest. During strong downwelling favorable winds from the northeast, the plume flows to the south along the New Jersey coast as a coastal current. During strong upwelling winds from the southeast, the plume responds by flowing to the east along the Long Island coast. During weaker winds, a seabreeze often develops in the New York Bight Apex. The offshore extent to the seabreeze is enhanced in the Bight Apex by the coastal geometry (Fig. 6). In this case, the synoptic flow from the north and northeast is blocked by a pair of sea breeze fronts over Long Island and Connecticut, resulting in a relatively stationary seabreeze front. The seabreeze over New Jersey, however, is able to propagate farther inland perpendicular to the synoptic flow. An enlarged area of low winds over the New York Bight Apex results, indicating that the offshore extent of the seabreeze circulation cell is enhanced by the Bight Apex geometry over that expected from a simple two-dimensional seabreeze model. The result is an enhanced seabreeze over the same area in which the buoyant Hudson plume is flowing onto the shelf



Fig. 4. Mixing of the Hudson River (tan) and the Raritan River (brown) in New York Harbor and the flow of the sediment laden plume onto the shelf is illustrated in this RGB ocean color image from India's Oceansat.

Seabreeze has been observed to have a profound effect on the plume. In the case of synoptic winds from the north, the morning ebb tidal pulse is observed to flow along New Jersey with the synoptic winds. As afternoon approaches, the seabreeze kicks in and reverses the wind direction in the Bight Apex. The afternoon ebb tidal pulse is observed to flow along Long Island forced by the afternoon seabreeze. As a result, the sediment and organic laden plume water can be spread over a wide area of the Apex.

The seabreeze also tends to reinforce the recirculation zone observed in the outflow bulge observed in the Bight Apex of Fig. 7. The bulge formation is predicted by some steady outflow models for coastal plumes. The Hudson River Plume was observed to form a persistent bulge with an embedded

recirculating eddy during a series of seabreeze events in April of 2005. The recirculation zone remained intact for several days.

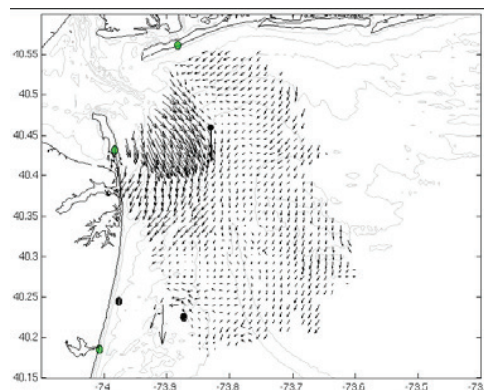


Fig. 5. Flow exiting the Hudson-Raritan Estuary as determined from the CODAR HF Radar network showing a tidal pulse exiting the harbor.

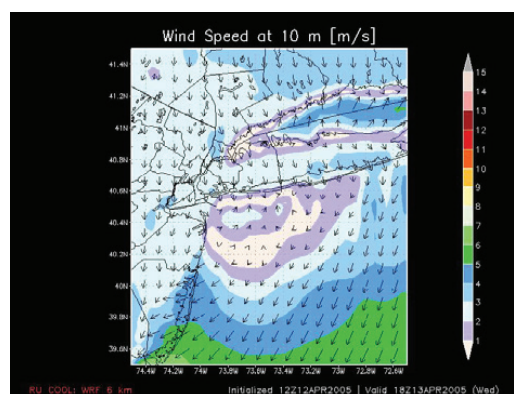


Fig. 6. Offshore extend of the sea breeze cell enhanced by the three-dimensional coastal geometry of the NY Bight Apex.

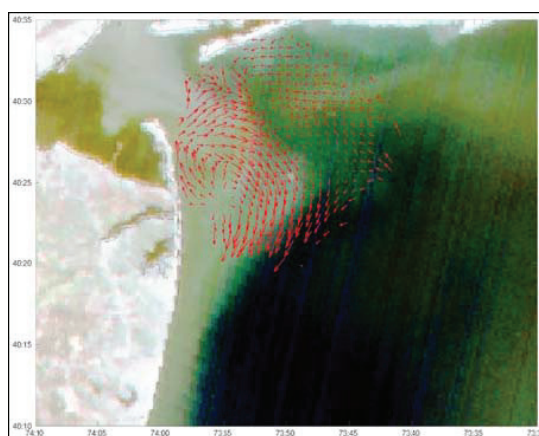


Fig. 7. RGB Ocean color image from Oceansat illustrating the plume bulge formation as the Hudson River Plume exits the estuary. The overlaid CODAR current vectors identify the recirculation zone within the bulge.

The persistent eddy that formed within the bulge acted as an incubator for large phytoplankton that were too big to be grazed by the prevalent zooplankton. The resulting rapid phytoplankton growth followed by the death and decay processes depleted oxygen within the bulge (Fig. 8). The saltiest

water in the picture is the bottom water under the plume with the lowest DO values. Dissolved oxygen values continued to drop well below their historical typical values for several days until a strong storm passed through the area, mixing the waters and returning oxygen values to their normal spring high.

But what happens to the plume water deposited in the Bight Apex? During LaTTE, several pathways out of the Bight Apex were identified. The most intriguing and previously unknown pathway is the cross-shelf transport route along the axis of the Hudson Shelf Valley. Virtual drifter studies in the CODAR surface current fields (Fig. 9) indicate that the transport pathways out for the Bight Apex are related to the wind forcing. Some exit to the south during strong downwelling winds, and some to the east during strong upwelling winds. Some of the virtual drifters flowing along the HSV are observed to flow all the way across the shelf to join the alongshore flows of the Shelf Slope Front. Others are found to only make it as far as midshelf, joining the alongshore flows of the Midshelf Front.

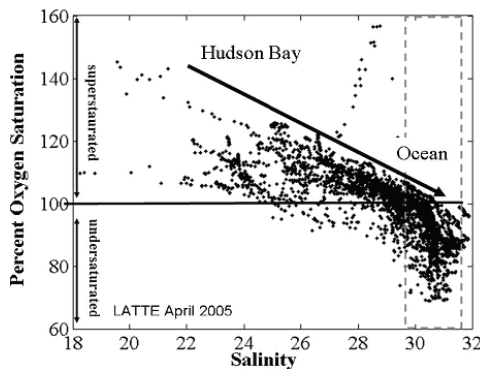


Fig. 8. Dissolved oxygen concentrations plotted as a function of salinity the Hudson River and Plume during the April 2005 LaTTE.

#### 4. Summary and Conclusions

Long-term government monitoring has identified four regions of recurrent hypoxia along the New Jersey coast. A series of coast predictive skill experiments from 1998-2001 determined that the three southern low dissolved oxygen regions were caused by coastal upwelling jets interacting with three topographic highs in the alongshore direction, resulting in recirculating eddies that concentrated phytoplankton in these regions and depleting the oxygen as the dying phytoplankton decayed. The LaTTE experiment in a sustained coastal observatory has determined the fourth hypoxia center is also related to a recirculating eddy that collects phytoplankton, but that the eddy is caused by the recirculated bulge of the Hudson River plume that is enhanced by seabreeze. Knowledge of these processes and demonstration of new observing technologies have led to the collaborative design of more effective and cost efficient dissolved oxygen monitoring networks for federal and state managers.

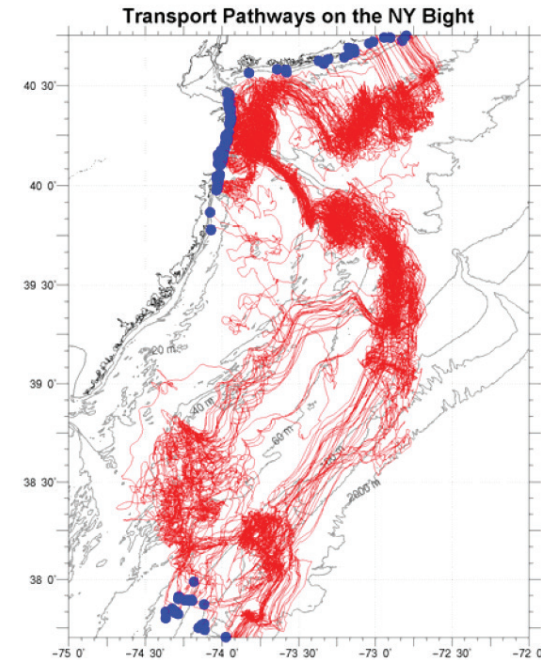


Fig. 9. Virtual tracer release study during the 2005 LaTTE Hudson River Plume Experiment based on the CODAR HF Radar data. Drifters were deployed in the Hudson Plume in the Bight Apex every day during LaTTE and were tracked for an additional 40 days.

#### 5. Acknowledgements

The Lagrangian Transport and Transformation Experiment is supported by the NSF Coastal Oceans Program (CoOP) Buoyant River Plume Initiative. Rutgers Coastal Research Observatory is sustained through grant support from U.S. government agencies (ONR, NSF, NOAA, NOPP, DHS, DoD, & EPA), the power industry (PSE&G), the country of Norway, and the Great State of New Jersey.

#### References

1. Glenn, S. M., M.F. Crowley, D.B. Haidvogel and Y.T. Song (1996). "Underwater observatory captures coastal upwelling events off New Jersey." *EOS* 77: 233, 236p.
2. Glenn, S. M., O. Schofield, et al. (2004). "The expanding role of ocean color and optics in the changing field of operational oceanography." *Oceanography* 107:p.p. 89-95.
3. Schofield, O. M. E. and S. M. Glenn (2004). "Introduction to special section: Coastal Ocean Observatories." *J. Geophys. Res.* 109: 10.1029/2004JC002577.
4. Song, T., D.B. Haidvogel and S.M. Glenn (2001). "Effects of topography variability on the formation of upwelling centers off New Jersey: A simple theoretical model." *Journal of Geophysical Research* 106(C5): p.p.9223-9240.
5. Warsh, C. (1987). "NOAA's northeast monitoring program (NEMP): A report on progress of the first five years (1979-84) and a plan for the future." NOAA Technical Memorandum NMFS-F/NEC-44: Northeast Fisheries Center, Woods Hole.

**Scott Glenn**, Institute of Marine and Coastal Sciences, Rutgers University, New Brunswick.  
Address: 71 Dudley Road  
New Brunswick, NJ 08901, USA  
E-mail: [glenn@marine.rutgers.edu](mailto:glenn@marine.rutgers.edu)

**Oscar Schofield**, Associate Professor at Coastal Ocean Observation Lab, at the Institute of Marine and Coastal sciences, Rutgers University.  
Main research areas: Environmental Regulation of Primary Productivity in Aquatic Ecosystems, Physiological Ecology of Phytoplankton, Hydrological Optics, Integrated Ocean Observatories  
Address: New Brunswick,  
NJ 08903-0231, USA  
Tel.: +1 732 932 6555 548  
E-mail.: [oscar@imcs.rutgers.edu](mailto:oscar@imcs.rutgers.edu)

**PhD. Robert Chant**, Assistant Professor at Coastal Ocean Observation Lab, at the Institute of Marine and Coastal sciences, Rutgers University.  
Main research areas: Physical oceanography and estuarine dynamics  
Address: 71 Dudley Road  
New Brunswick, NJ 08901  
USA  
Tel.: +1 732 932 6555 544  
E-mail.: [chant@imcs.rutgers.edu](mailto:chant@imcs.rutgers.edu)

**Josh Kohut**, Director of the Center of Advanced & Sustained Technology; Institute of Marine and Coastal Sciences, Rutgers University.  
Main research areas: dynamics of the coastal ocean, development of a coastal network of surface wave radars to continuously sample movement of the ocean surface.  
Address: 71 Dudley Road  
New Brunswick, NJ 08901, USA  
Tel.: +1 732 932 6555 542  
E-mail.: [kohut@arctic.rutgers.edu](mailto:kohut@arctic.rutgers.edu)

**Hugh J. Roarty**, coastal engineer at the Coastal Ocean Observation Lab., Institute of Marine and Coastal Sciences, Rutgers University.  
Main research areas: monitoring and hydrographic effectiveness of the Jersey shore.  
Address: New Brunswick, NJ 08903, USA  
Tel.: +1 732 932 6555 543  
E-mail.: [hroarty@imcs.rutgers.edu](mailto:hroarty@imcs.rutgers.edu)

**Jennifer Bosch**, Coastal Ocean Observation Lab., Institute of Marine and Coastal Sciences, Rutgers University.  
Main research areas: Biological/Physical interactions, upwelling systems, larval transport, estuarine ecology, ocean ecology, phytoplankton ecology, satellite oceanography, remote sensing of aquatic environments.  
Address: New Brunswick, NJ 08903, USA  
Tel.: +1 732 932 6555 532  
E-mail.: [bosch@imcs.rutgers.edu](mailto:bosch@imcs.rutgers.edu)

**Louis Bowers**, Staff Meteorologist at the Institute of Marine and Coastal Sciences, Rutgers University.  
Main research areas: validation of mesoscale atmospheric numerical weather prediction models from HYCODE 2002 and continuing work on the NJ sea breeze phenomenon.  
Address: New Brunswick, NJ 08901-8521, USA  
Tel.: +1 732 932 6555  
E-mail.: [bowers@imcs.rutgers.edu](mailto:bowers@imcs.rutgers.edu)

**Donglai Gong**, Graduate Student at the Institute of Marine and Coastal Sciences, Rutgers University.  
Main research areas: ocean circulation and biogeochemical cycling on the continental shelves.  
Address: New Brunswick, NJ 08901, USA  
Tel.: +1 732 887 3514  
E-mail.: [donglai@marine.rutgers.edu](mailto:donglai@marine.rutgers.edu)

**John Kerfoot**, Marine Scientist at the Institute of Marine and Coastal Sciences, Rutgers University.  
Main research areas: using autonomous underwater vehicles (AUVs) in a sustained effort to maintain a continuous subsurface presence in the coastal oceans around the world.  
Address: New Brunswick, NJ 08901, USA  
Tel.: +1 732 932-6555 527  
E-mail.: [kerfoot@imcs.rutgers.edu](mailto:kerfoot@imcs.rutgers.edu)

## Vėjo įtaka Hudsono upės nuotėkio sklaidai ir ištirpusio deguonies koncentracijai jūroje

**Scott Glenn, Oscar Schofield, Robert Chant, Josh Kohut, Hugh Roarty, Jennifer Bosch, Louis Bowers, Donglai Gong, John Kerfoot**

*Rutgers universitetas, Jūros ir pakrantės mokslų institutas*

*(gauta 2006 m. birželio mėn.; atiduota spaudai 2007 m. kovo mėn.)*

Šiuo metu yra baigtos nagrinėti dvi iš trijų Lagranžo transporto ir transformacijos procesų Hudsono upėje, tyrimo stadijos. Tarpdalykinė studija atliekama kranto mokslinių tyrimų observatorijoje, kuri teikia erdvės ir laiko situacijos duomenis, pritaikytus laivo bandinio ėminiams. Antrojo LaTTE tyrimų laikotarpio stebėjimai naudojami procesams, sąlygojantiems anksčiau nepaaiškintą hipoksijos zoną, besidriekiančią išilgai Niu Džersio kranto.





## Bulge Formation of a Buoyant River Outflow

Robert J. Chant,<sup>1</sup> Scott M. Glenn,<sup>1</sup> Elias Hunter,<sup>1</sup> Josh Kohut,<sup>1</sup> Robert F. Chen,<sup>2</sup>  
Robert W. Houghton,<sup>3</sup> Jen Bosch,<sup>1</sup> and Oscar Schofield<sup>1</sup>

Received 10 January 2007; revised 1 June 2007; accepted 28 September 2007; published 24 January 2008.

[1] Observations taken during the Lagrangian Transport and Transformation Experiment (LaTTE) in 2005 indicated that the Hudson's river outflow formed a bulge of recirculating fluid that limits the volume of fresh water that is advected away in a coastal current. Focusing on an event that began with downwelling winds we made estimates of the fresh-water flux in the coastal current and the fresh water inventory of the bulge. The coastal current was characterized by a surface advected plume in thermal wind balance. However, the freshwater transport in the coastal current was less than 1/2 of the total freshwater outflow. The bulge extended 30 km from the coast and 40 km in the along-shore direction and was evident in ocean color imagery. Recirculation in the bulge region was also apparent in daily averaged surface current radar data, but this flow pattern was obscured in the hourly data by tidal and wind-forcing even in the diurnal band. Nevertheless, many aspects of the Hudson's outflow are consistent with recent laboratory experiments and numerical simulations of buoyant discharges. The growing bulge transports the river's outflow to the head of the Hudson shelf valley where it crosses the 50 m isobath. Previous work in this region indicates that frontal features reside along this isobath. We observed fresh water being transported along this isobath and is suggestive of a rapid cross-shelf transport pathway for fresh water. Both the bulge formation and cross-shelf transport have significant biogeochemical implications.

**Citation:** Chant, R. J., S. M. Glenn, E. Hunter, J. Kohut, R. F. Chen, R. W. Houghton, J. Bosch, and O. Schofield (2008), Bulge Formation of a Buoyant River Outflow, *J. Geophys. Res.*, 113, C01017, doi:10.1029/2007JC004100.

### 1. Introduction

[2] The classic model of fresh water debouching into the ocean has the outflow deflected to the right (in the northern hemisphere) and forming a narrow coastal current that is trapped within a few internal Rossby radii of the coast [Garvine, 1999]. The coastal current can be either surface advected or bottom attached [Yankovsky and Chapman, 1997]. In the absence of wind and wave forcing (Fewings et al., Observations of Cross-Shore flow driven by cross-shore winds on the inner continental shelf, submitted to Journal of Physical Oceanography). Cross-shelf transport in bottom attached coastal currents is primarily contained in a bottom Ekman layer [Chapman and Lentz, 1994]. However, at a critical depth the offshore Ekman transport is shut down by baroclinic forcing and the plume is trapped to an isobath [Chapman and Lentz, 1994; Yankovsky and Chapman, 1997]. For surface advected plumes the width is set by the internal Rossby Radius [Lentz and Helfrich, 2002] which is typically on the order of a few km in the coastal

ocean. In general, these models emphasize that in the absence of winds coastal current dynamics severely limit cross-shelf transport of buoyant water on continental shelves.

[3] Buoyant outflows may also contain a bulge-like region in the vicinity of the outflow, and the cross-shelf extent of these bulges can be many times the width of the down stream coastal current. Yankovsky and Chapman [1997] incorporated a bulge in a steady state model which they closed by equating the buoyancy flux in the coastal current to the buoyancy flux exiting the estuary. With this steady state assumption they developed an elegant theory that related coastal current structure to estuarine discharge rate and the cross-shore bathymetric slope.

[4] Recent modeling and laboratory studies of buoyant outflows have provided a more detailed characterization of bulge structure [Avicola and Huq, 2003a; Fong and Geyer, 2002; Horner-Devine et al., 2006] and emphasize that a bulge may be *unsteady* and grow in time. Consequently, the fresh water flux out of the estuary ( $Q$ ) is greater than the fresh water flux in the coastal current ( $Q_{cc}$ ). In a series of numerical experiments Fong and Geyer [2002] found that  $Q_{cc}/Q$  was inversely proportional to a Rossby number with  $Q_{cc}/Q$  dropping from 0.65 to 0.4 as the Rossby number increased from 0.1 to 1. In the laboratory Avicola and Huq [2003b] reported that only approximately 1/3 of the outflow became incorporated in the coastal current, with the rest of the outflow going into bulge formation. Fong and Geyer

<sup>1</sup>Institute of Marine and Coastal Studies, Rutgers University, New Brunswick, New Jersey, USA.

<sup>2</sup>University of Massachusetts Boston, Massachusetts, USA.

<sup>3</sup>Lamont-Doherty Earth Observatory, Columbia University, Palisades, New York, USA.

[2002] discussed the mechanisms by which the bulge feeds the coastal current by invoking a model by *Nof and Pichevin* [1988] where the amount of fresh water entering the coastal current is determined by the amount of the eddy (bulge) pinched off at the coastal wall. As the Rossby numbers increases the eddy's center moves increasingly further from the coastal wall and reduces the fraction of the eddy that is pinched off and thus diminishes the freshwater transport into the coastal current.

[5] *Avicola and Huq* [2003a, 2003b] discuss bulge formation in terms of the angle that the outflow makes with the coastal wall (outflow angle) and the angle that the discharge impacts the coast (impact angle). They note that these two angles are related, with oblique outflow angles corresponding to oblique impact angles while outflows that normal to the coast lead to flows that impact the coastal wall at right angle. *Avicola and Huq* suggest that the physics of bulge formation is determined by the angle that the outflow impacts the coast, and that this impact angle is determined by the outflow angle. For oblique impact angles a coastal current forms. Bulge recirculation increases as the impact angle approaches 90 degrees. Laboratory experiments by *Horner-Devine et al.* [2006] show even more dramatic shunting of coastal current by bulge formation as the recirculation completely pinches off the coastal current and the entire outflow goes into bulge formation.

[6] Wind-forcing also plays a critical role in the cross-shelf transport of river plumes [*Whitney and Garvine*, 2005]. Modeling studies [*Fong and Geyer*, 2002] reveal that upwelling winds are effective both in transporting river plumes offshore and in entraining the plume into the coastal ocean. Observational studies of coastal currents reveal that the structure of the flow and salt field [*Rennie and Lentz*, 1999] and diapycnal fluxes [*Houghton et al.*, 2004] appear to be consistent with numerical studies [*Fong and Geyer*, 2001]. Despite this there has been little research on the effect of wind-forcing on bulge dynamics with the notable exception of *Choi and Wilkin* [2007].

[7] In this study we present data from the Hudson River plume that was collected as part of the LaTTE '05 (Lagrangian Transport and Transformation Experiment) field effort between March and May 2005. LaTTE is focused on the transport and transformation of dissolved and suspended materials such as nutrients, contaminant metals, Colored Dissolved Organic Matter (CDOM) and carbon from this highly urbanized estuary. The Hudson's outflow mixes with the outflow from the Passaic and Raritan River (Figure 1) plus an additional 100 m<sup>3</sup>/s of treated sewage and enters the coastal ocean near Sandy Hook. Once beyond Sandy Hook there is no clear channel to steer the plume. However, 10 km to the east resides the head of the Hudson Shelf Valley (Figure 1) which bisects the entire 150 km wide New York Bight Shelf. The Hudson Shelf Valley was formed by the ancestral Hudson River and its formation may have been augmented by catastrophic flooding following the drainage of the late Wisconsin glacial lakes [*Newman et al.*, 1969]. Recent analysis of near-bottom currents meter data in the shelf valley suggests that it may provide an important conduit for cross-shelf exchange [*Harris et al.*, 2003].

[8] The first order fate and transport of dissolved and suspended material in the Hudson Plume depends on the transport pathway of the fresh water. If the outflow forms a

coastal current, transport pathways will be limited in the cross-shelf direction. However, if bulge formation dominates, both the ballooning of the outflow and the limited down-shelf advection would radically alter transport pathways. Furthermore, if bulge formation brings the outflow into the vicinity of the Hudson shelf valley ambient circulation associated with the shelf valley [*Harris et al.*, 2003] could significantly drive cross-shelf transport pathways. In this paper we demonstrate that the Hudson's outflow is in fact highly susceptible to bulge formation and that this allows the outflow to rapidly mix across the 100 km wide New York Bight.

## 2. 2005 Field Effort

[9] The LaTTE program is an interdisciplinary process study of the Hudson River plume conducted within a sustained coastal ocean observatory. The observatory was designed, built and operated by the Rutgers University Coastal Ocean Observation Lab [*Glenn and Schofield*, 2004]. Observational components include a pair of satellite direct-broadcast data acquisition systems for tracking the international constellation of ocean color and thermal infrared imaging satellites, a triple-nested multistatic CODAR High Frequency (HF) Radar network for surface current mapping, and a fleet of autonomous underwater gliders for subsurface mapping of water properties. An operations center controls the observatory data acquisition, aggregates the data, and produces data products and forecasts to provide a spatial and temporal context for process studies and adaptive sampling. The LaTTE 2005 study included a mooring array that was deployed for approximately 2 months and shipboard surveys.

[10] The shipboard surveys occurred between 9 April and 22 April 2005 with the R/V Cape Hatteras and R/V Oceanus. The cruise featured two Rhodamine dye studies with dye injected on 11 April and 18 April in the surface layer in the vicinity of Sandy Hook. The Cape Hatteras was used to track the dye which was done with a towed undulating vehicle and an instrument package located 1–2 m below the surface that was mounted to a pole over the starboard side of the ship. Instrumentation aboard the undulating vehicle and on the over-the-side mount included a CTD, OBS and fluorometers for Rhodamine dye, Chlorophyll-a and CDOM. In addition the over-the-side mount included a 1200 kHz RDI ADCP. During the dye injection a pair of surface drifters with drogues covering the top two meters of the water column was deployed. The Oceanus was used primarily for biological sampling. During the cruise broadband and cell phone Internet connectivity aboard the two research vessels enabled communications between the ships and the operations center for coordinated adaptive sampling with the research vessels and gliders.

[11] Satellite data from the U.S. (AVHRR, MODIS), India (Oceansat) and China (FY1-D) acquired by the two ground stations was processed using both SeaSpace and NRL algorithms [*Lee et al.*, 2002]. The nested CODAR HF Radar networks are operated at 25 MHz, 13 MHz, and 5 MHz. Radial current data from each site is processed as described by [*Kohut and Barrick*, 2001]. Radial data from the 25 MHz sites is combined into total vector maps using the algorithm described by *Kohut et al.* [2006] and includes



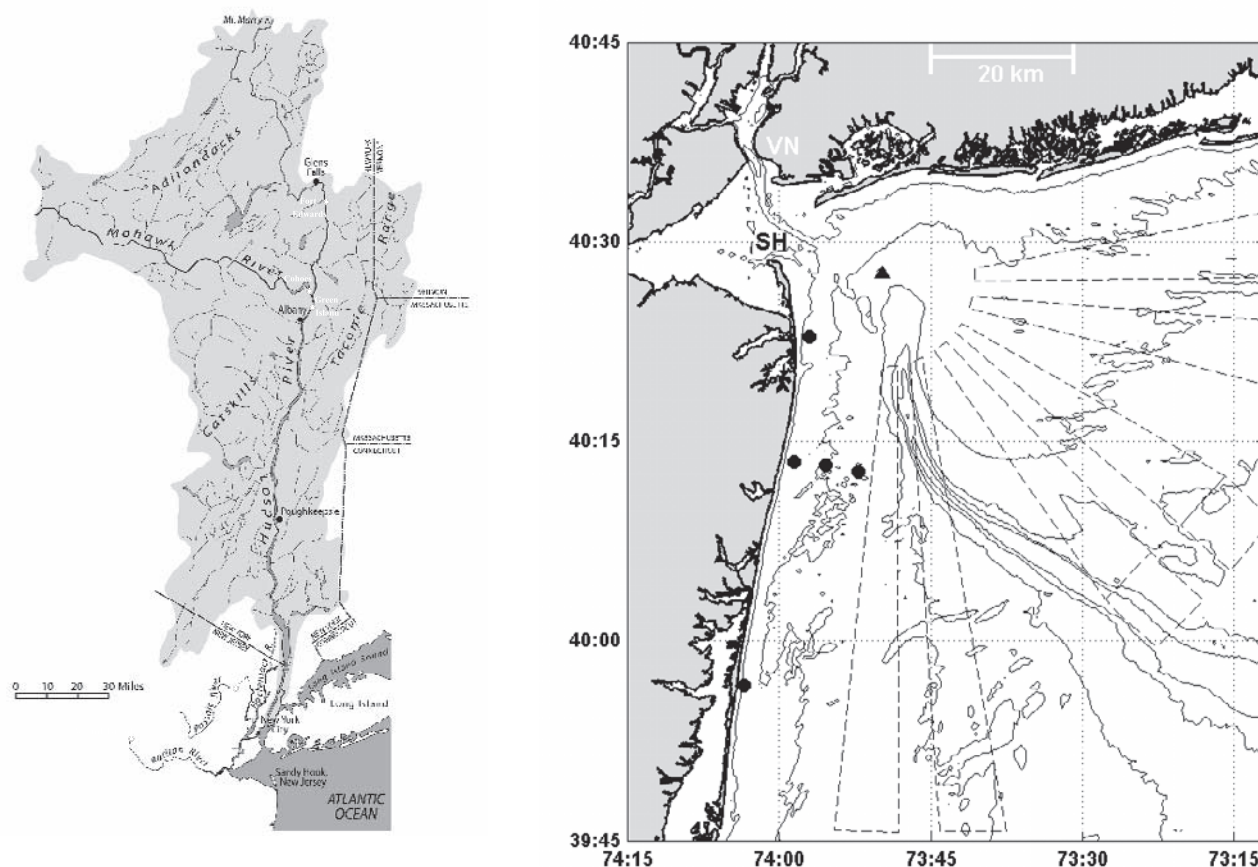


**Figure 1.** Study area. Left panel shows water shed and USGS gauging stations at Bound Brook, Little Falls, Cohoes, Fort Edwards and Green Island and location of USGS ADCP in Poughkeepsie. Right panel depict mooring locations as filled black circles. Contours are at 10 meter intervals. Black triangle shows location of Ambrose light tower. The straight to the west of VN is the Verrazano Narrows, and the peninsula immediately east of SH is Sand Hook. The deep channel cutting across shelf is the Hudson shelf valley.

the calculation of the Geometric Dilution of Precision (GDOP) criteria based on the actual radial data used in each individual map. The resulting quality controlled maps are produced every half hour with a spatial resolution of 1.5 km. Glider data is acquired every time the glider surfaces, which in LaTTE was typically every 3 h. The CTD on the glider operates at 0.5 Hz and yields a vertical resolution of 0.25 m. The glider's SeaBird CTD data is processed using the correction for the response time of both the temperature sensor and conductivity sensor and the thermal lag associated with flushing of conductivity cell [Morison *et al.*, 1994] with the coefficients set by minimizing the upcast/downcast salinity profile differences from summertime data collected on the New Jersey continental shelf.

[12] The moorings consisted of a five element array deployed from 18 March to 19 May 2005 (Figure 1), each containing a Doppler current meter and Conductivity/Temperature (CT) sensors. The four northern moorings were outfitted with CT sensors 50 cm above the bottom (mab) and at 1 and 7 m below the surface (mbs). The southern mooring had surface and bottom CT sensor. The central mooring was damaged, likely due to barge traffic, causing the complete loss of data from the surface and middle CT

sensor. We also utilized Doppler current profile data from a NOAA's PORTS mooring in the Verrazano Narrows and from a USGS mooring in the Hudson River at Poughkeepsie, New York (Figure 1). During this experiment the Poughkeepsie ADCP was in the fresh-water part of the river. The Poughkeepsie Doppler data was calibrated by USGS so that the data could be used to estimate volume transport. Wind data was obtained from the NOAA station at Ambrose Light, and river discharge data was obtained from USGS gauges in the Mohawk River in Cohoes, the Hudson at Fort Edwards, the Passaic at Little Falls and the Raritan at Bound Brook (Figure 1). Throughout the manuscript we use the orientation of the New Jersey coast to characterize winds as upwelling (winds from the south) or downwelling (winds from the north).

### 3. River Discharge

[13] Essential to the analysis in this paper is an estimate of the discharge of fresh-water into the coastal ocean which requires estimates of fresh water fluxes from the ungauged portions of the watershed. The Hudson dominates the fresh water fluxes and has a mean April discharge of 1100 m<sup>3</sup>/s

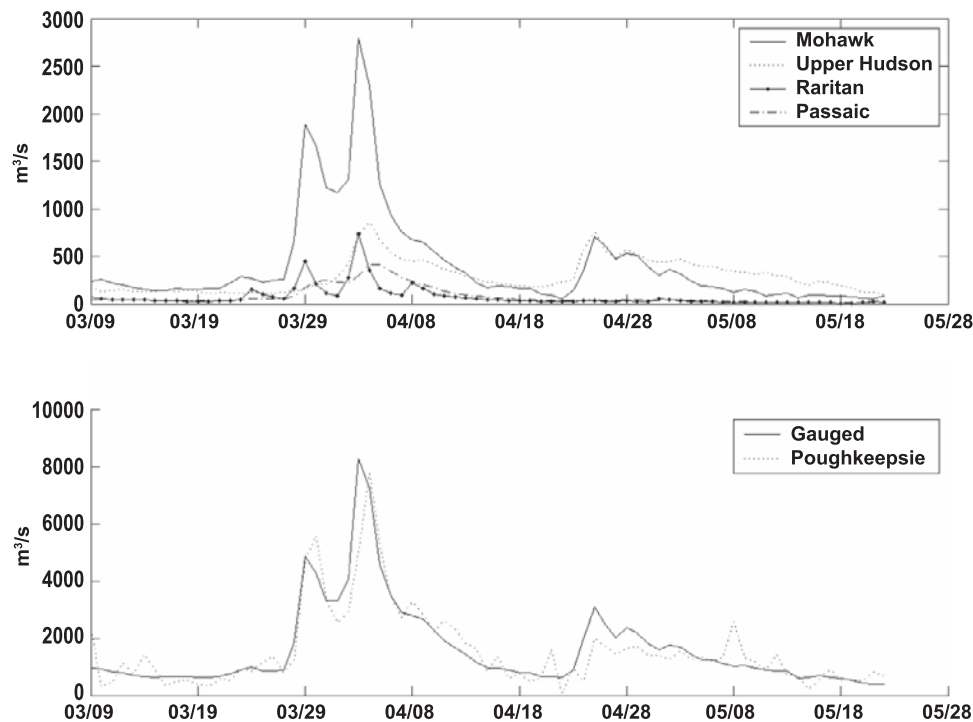


**Figure 2.** Upper panel shows discharge from USGS gauging stations. Lower panel shows two estimates of total discharge as discussed in text.

based on a 47-a record at Green Island. The Passaic and Raritan rivers mean April flows are  $57 \text{ m}^3/\text{s}$  and  $49 \text{ m}^3/\text{s}$  respectively based on nearly 100 a of discharge data. Unfortunately the Green Island gauge is no longer operational and discharge must now be estimated by the sum of upstream gauges in the Mohawk at Cohoes and upper Hudson at Fort Edwards. The watershed area at Green Island is 1.3 times the combined area of the Cohoes and Fort Edwards watershed so we assume that discharge rate at Green Island is equal to 1.3 times the sum of Cohoes and Fort Edwards. The 1.3 factor is also found in a regression of overlapping discharge records that extend from 1979–1998 (not shown). Downstream of Green Island the additional watershed increases discharge by another 60% [Abood, 1977; Lerczak et al., 2006]. Thus we estimate the total Hudson's discharge as twice the sum (i.e.,  $1.3 * 1.6$ ) of Cohoes and Fort Edwards plus the measured discharge from the Passaic and Raritan rivers. We refer to this estimate as the “gauged” estimate of river discharge. Discharge from sewage outflows were not included in this estimate because some fraction of the regions water supply is drawn from the river down stream of the USGS gauges.

[14] The hourly transport estimates at Poughkeepsie were filtered with a Lancocz filter with a cut-off period of 32 h to remove tidal period variability. We note that in addition to river discharge this record also contains additional transport associated with local and remote meteorological forcing [Lerczak et al., 2006]. This is apparent in the noisier nature of the Poughkeepsie data relative to the gauged data. However, this additional transport is relatively small and its value diminishes over longer averaging periods. The watershed upstream of Poughkeepsie contains 89% of the Hudson's total water and thus our “Poughkeepsie” estimate of river discharge is 1.12 times the filtered Poughkeepsie

transport estimate plus the gauged measurements in the Passaic and Raritan Rivers. Figure 2 compares our “gauged” discharge estimate with the “Poughkeepsie” estimate. In general the estimates agree well, with the Poughkeepsie estimate generally slightly lower than the gauged estimate, though not always. Between 1 March and 1 June the mean from the gauged estimate was  $1524 \text{ m}^3/\text{s}$  while the mean value of the Poughkeepsie estimate was  $1466 \text{ m}^3/\text{s}$ . The Poughkeepsie estimate was even higher during the time period that this paper focuses on. Between April 8th and 14th the mean flow using the gauged data was  $1981 \text{ m}^3/\text{s}$ , while using estimates using the Poughkeepsie data was  $2385 \text{ m}^3/\text{s}$ . Some of this discrepancy may be due to variations in the distribution of snow cover and precipitation across the watershed during this time, which if true implies that the Poughkeepsie measurement would be more accurate. However, the difference may also reflect uncertainties in the USGS calibration. Thus we will use these two values as bounds for the estimates the total river discharge. The gauged discharge estimate peaked on 3 April at  $8290 \text{ m}^3/\text{s}$  while the Poughkeepsie estimate peaked on 4 April at  $7825 \text{ m}^3/\text{s}$ . Also during the peak flows the estimate at Poughkeepsie lags the gauged estimate by one day. We note that peak discharge in all of the gauged rivers in the system were significantly above typical peak flows. For example, the discharge at Cohoes, the gauge with the largest flow, peaked at  $2789 \text{ m}^3/\text{s}$  and represents the 8th largest discharge to date in the 88-a record.

#### 4. Estuarine Outflows

[15] Filtered depth averaged velocities from the ADCP at the Verrazano Narrows increase within a few days of the discharge peaks (Figure 3). However, the lag time between

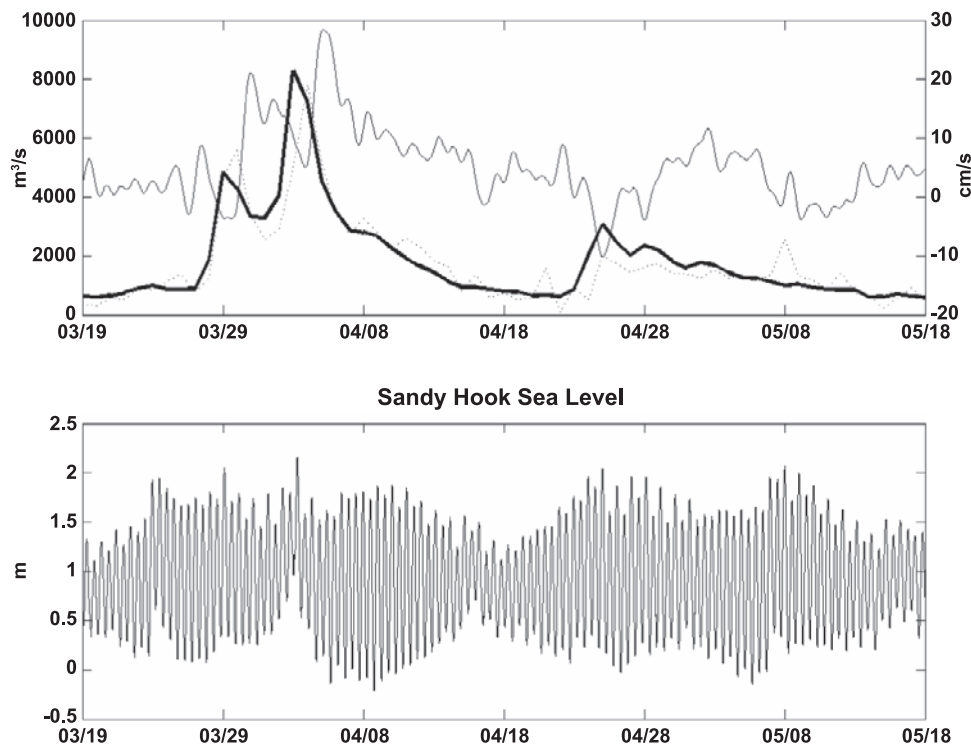


**Figure 3.** Upper panel shows “Gauged” estimate of total discharge (thick line), “Poughkeepsie” discharge estimate (dotted line), low-pass filtered depth averaged flow from Verrazano Narrows (thin line). Lower panel depicts sea level at the Battery as recorded by NOAA tide gauge.

discharge at the upstream gauges and the outflow at the Narrows is variable and is impacted by wind-forcing and the spring neap cycle. It should be noted that the mooring at the Verrazano is on the flank and likely is a better reflection of the upper layer transports than barotropic flows. Filtered velocity at the Narrows lagged the two large peaks in discharge in late March and early April by 2 days. A longer lag time of nearly 1-week was evident following the smaller peak in late April. Here the river peaked on 25 April while the outflow at the Narrows peaked during the neap tide around 2 May. The correlation between the gauged data and the outflow at the Verrazano narrows had a peak value of 0.75 at a two day lag.

[16] During the peak discharge in early April upwelling favorable winds (Figure 4) between 6–8 April drove the plume to the east along the Long Island coast and drove upwelling along the New Jersey Shelf. The eastward transport of the plume is clearly evident in numerous satellite imagery, such as absorption at 448 nm [Lee *et al.*, 2002] (Figure 5). During this period surface salinities at the moorings are low, but begin to rise as the upwelling winds persist. By the end of this upwelling event on April 8th surface salinities at all of the mooring sites increased to over 30 psu (Figure 6).

[17] On 8 April winds shifted to downwelling favorable and were modulated significantly by diurnal variability. Following the shift to downwelling winds a frontal passage was evident in the surface salinity on 8 April at N1 and C1 and 9 April at S1 (Figure 6a). On the basis of the timing of the frontal passage past C1 and S1 the front propagates down-shelf at 0.69 m/s which is faster than estimates of the

internal wave speed ( $g'h$ )<sup>1/2</sup> of 0.50 m/s, suggesting that the downwelling favorable winds increased the down-shelf propagation. However, while rapid down shelf currents were evident at C1 and S1, currents at N1 were weak and generally upshelf (Figure 6b). Furthermore, currents near the surface (the top ADCP bin) at C2 and C3 were weak and the salinity (at C3) was high suggestive that these moorings were seaward of the coastal current. There was, however, a slight freshening on 4/11 and 4/12 in the surface at the C3 in response to the diurnal wind variability.

[18] Images obtained from nearly simultaneous passages of Oceansat (17:09 GMT) and MODIS (17:13 GMT) on 4/9 revealed that the coastal current width diminishes as it propagated south. At the central mooring array it is approximately 3 km wide while at S1 its width is closer to 2 km. Strong down-shelf currents were apparent in low-pass filtered currents at inner moorings at S1 and C1, while the two offshore moorings along the C-line were seaward of the plume and currents were weak. Currents were also weak at N1, despite the relatively fresh and buoyant water at the surface. The bulge was also evident in the satellite imagery and surface currents from CODAR showed enhanced currents along its seaward edge. Furthermore, the data shown in Figure 7 suggests a region of recirculation centered approximately halfway across the bulge, unfortunately, because of the geometry of the CODAR array we cannot obtain surface current vectors on the shoreward side of the bulge. On the basis of the radius of flow curvature ( $\sim 7$ –10 km) and filtered surface current speeds (30 cm/s) the Rossby number is in the range of 0.3–0.5.



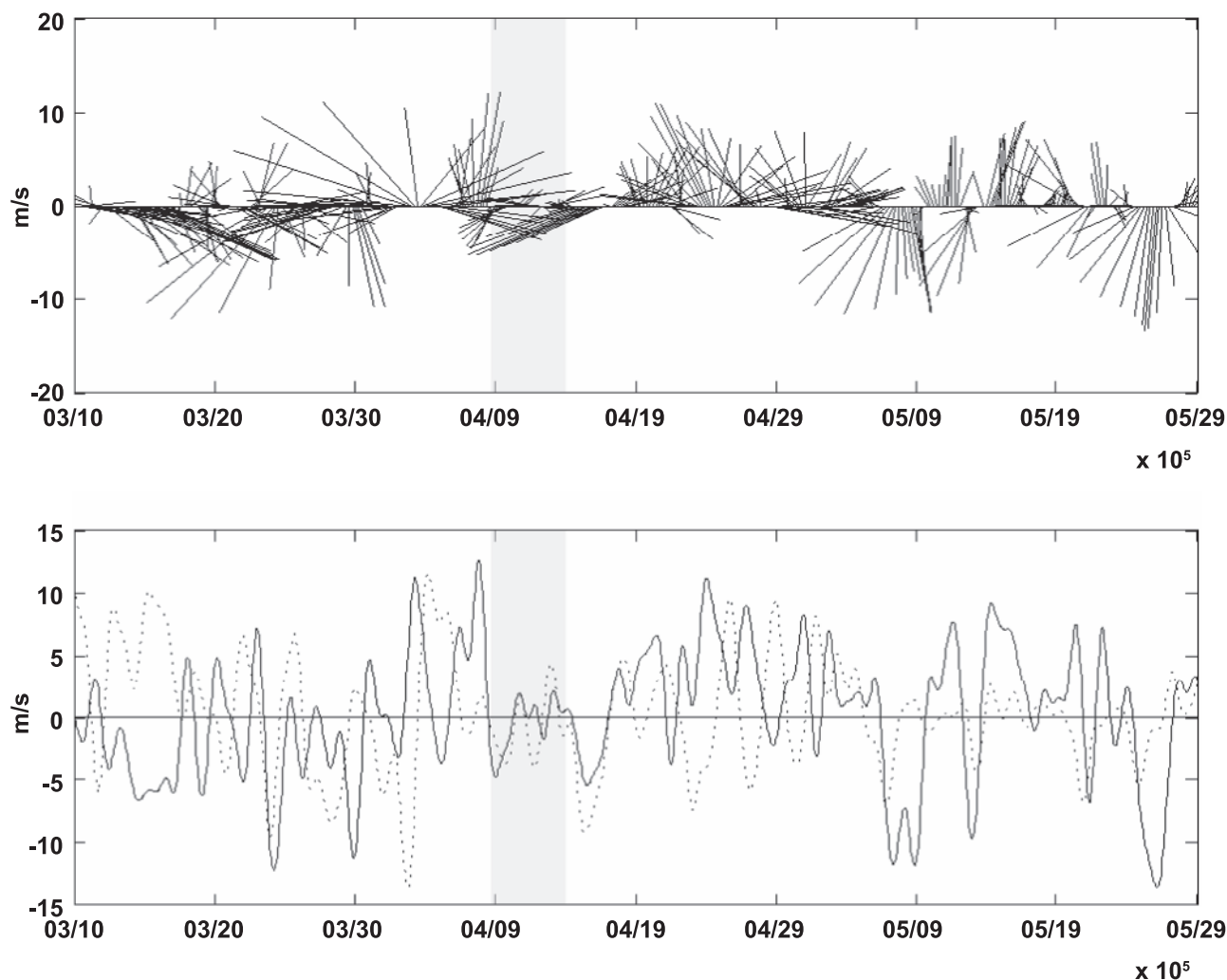


**Figure 4.** Low-pass filtered winds from Ambrose tower. Wind sticks (upper panel) and north(+)/south(−) (solid) and east(+)/west(−) (dashed) winds (lower panel). Gray area in both panels indicate time period of bulge growth focused on in this paper.

[19] Satellite images (Figure 7) resolved the remains of the earlier plume that was transported to the east along the LI coast on 6–8 April by winds from the south. This remnant plume was evident as a broad region of enhanced absorption that extended 60–70 km east of Sandy Hook and 50 km offshore. Shipboard survey confirmed that this region was indeed associated with a fresh water plume and that it was isolated from the newly formed coastal current by the saline surface waters over the Hudson shelf valley.

[20] Following the initial pulse of downwelling favorable winds on 8–9 April a strong sea-breeze developed with peak upwelling favorable winds occurring late each day. The amplitude of the diurnal wind-forcing was approximately 10 m/s. The strong sea-breeze forcing persisted though 4/14. Despite the strong diurnal variability filtered winds have a near zero average between 10 April and 14 April (Figure 6c). Current speeds in the coastal current generally decreased during this time and began to oscillate with the sea-breeze forcing by 4/11. By 4/13 the coastal current was shut down despite the presence of significant buoyancy and the lack of persistent upwelling winds.

During this period of weak low-frequency winds (4/10–4/14) the outflow ballooned into a large bulge of fluid of 20–25 psu and 5–7 m thick that remained in the vicinity of the New York Bight Apex. To determine the fraction of fresh water that goes in to bulge formation and the fraction that is advected away in the coastal current we compare both estimates of river discharge to estimates of fresh-water flux in the coastal current and the fresh water content of the bulge.

## 5. Coastal Current Fresh Water Transport

[21] With the moored, shipboard and satellite imagery we made estimates of the fresh water transport of fresh water in the coastal current. Salinity data from the 3 CT sensors at C1 were linearly interpolated in the vertical to coincide with each of the ADCP bins. Salinity above the surface CT sensor was assumed to be constant. Missing velocity data in the top ~1.5 m of the water column, due to acoustic sidelobe interference with the surface, were filled by extrapolating the profile to the surface. The extrapolation first calculates the vertical shear in the top 1 m of the profile and

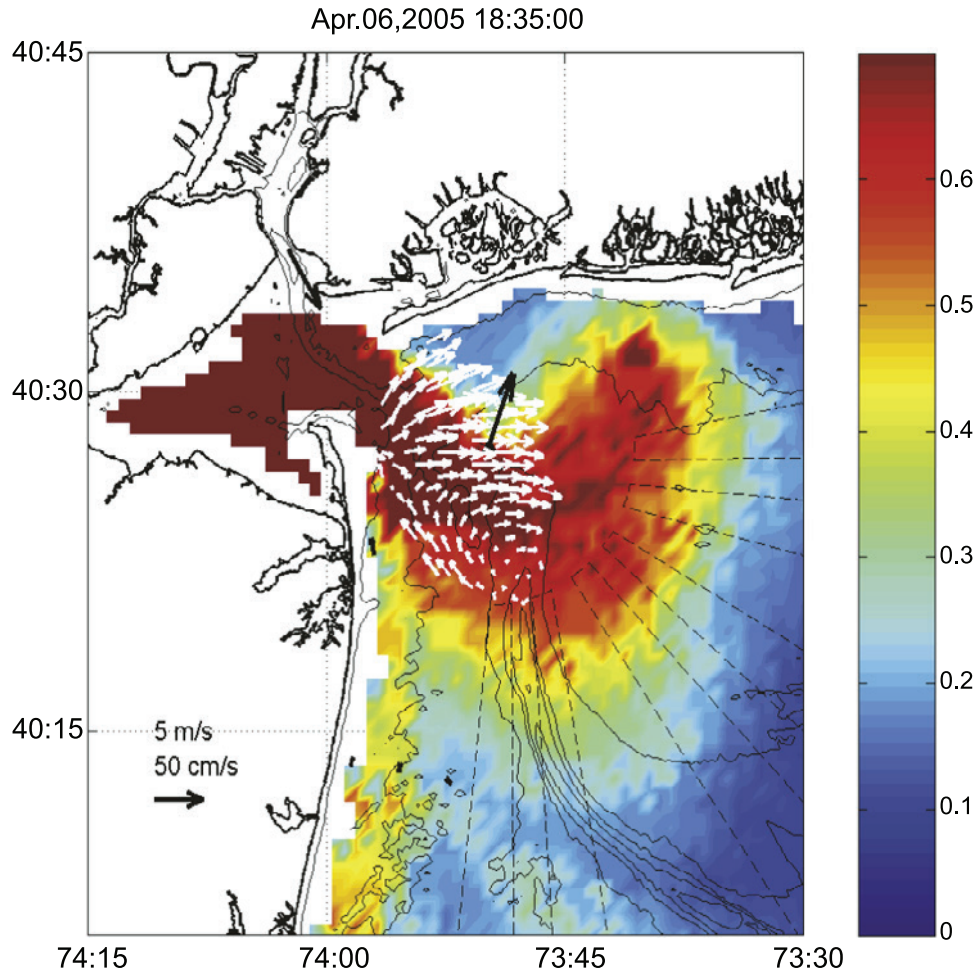


**Figure 5.** Color shows absorption at 488 nm from MODIS using algorithm from *Lee et al.* [2002]. Red indicates high absorption, blue is low absorption. White vectors show CODAR low-pass filtered currents. Filtered winds from Ambrose light tower is represented by black vector in middle of CODAR field. Black arrow depicts the filtered surface currents from moored ADCP's. Isobaths are contoured at 10m intervals. The scale arrow is for current speed (50 cm/s) and wind speed (5 m/s).

assumed that this shear decreases linearly to zero at the surface. With the extrapolated velocity ( $v$ ) and interpolated salinity profile ( $s$ ) the fresh water flux of the coastal current per unit width ( $FW_{cc}$ ) was estimated as

$$FW_{cc} = \int_{z_1}^{\eta} v(z) \times (S_a - s(z)/S_a) dz$$

where  $z_1$  is the depth of the first ADCP bin,  $\eta$  is the sea surface elevation and  $S_a$  is the ambient salinity on the inner shelf, which we set to equal to the salinity at C1 prior to the frontal passage on 8 April (30.6 psu). We note that the bottom salinity sensor had serious fouling and experienced significant drift over the 2 months deployment. While this drift was probably not constant we attempted to correct for it by removing the mean drift. Nevertheless salinities appear to remain erroneously low as evidenced by the salinity (and density) inversions that occurred between the bottom and mid-depth CT sensors during this record (not shown). While this error tended to produce an overestimate of the freshwater flux, down-shelf velocities tended to be weak below 7 m depth and thus this error is likely to be small.

[22] Estimates of fresh-water flux per unit width are shown in Figure 8. Fresh water flux peaked after the passage of the evening pulse on the 9th at slightly over  $0.6 \text{ m}^2/\text{s}$ , and was followed by a series of pulses. The initial pulses occur at the semi-diurnal period but become significantly modified by wind-forcing that is predominantly at the diurnal period. During the first 48 h after the passage of the coastal current fresh water flux is between 0.2 and  $0.6 \text{ m}^2/\text{s}$  with oscillations at both diurnal and semi-diurnal periods. After 4/11 the sea breeze forcing intensifies and the down-shelf transport of fresh water is shutoff on the mornings on 4/11 and 4/12. During this time diurnal fluctuations in the wind lead those in the fresh water flux by about 8 h. Between 4/13 and 4/15 the coastal current stalls and fresh water flux goes to zero, despite the fact that winds have a near zero daily mean. Finally on 4/15–16 an east-northeasterly wind dramatically increased fresh water fluxes to over  $0.8 \text{ m}^2/\text{s}$ .

[23] Fresh water flux in the coastal current,  $Q_{cc}$ , is estimated by multiplying  $FW_{cc}$  by the width of the plume. Both satellite imagery (Figure 7) and shipboard observations (Figure 9) indicate that the plume's width is approx-

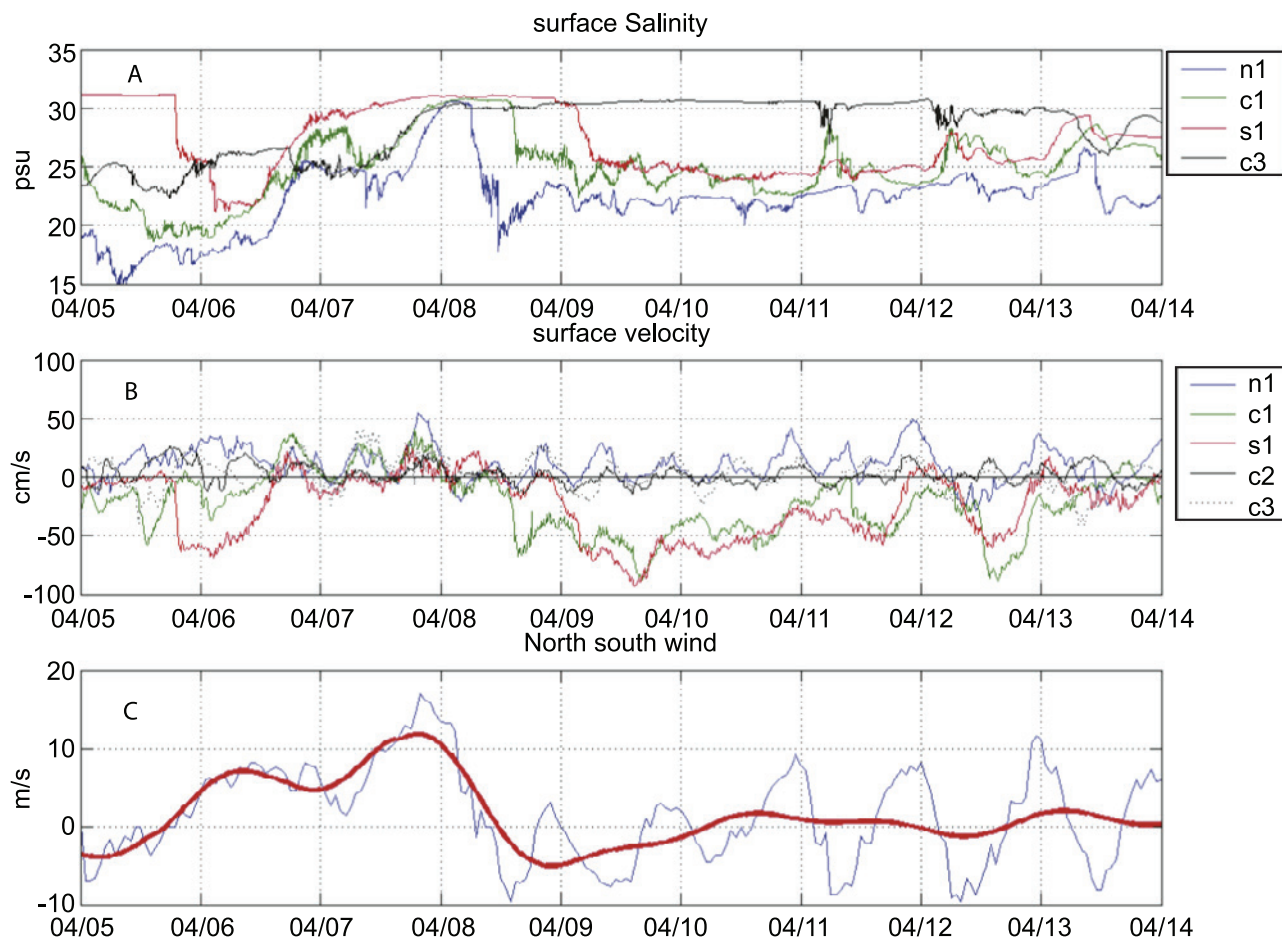


**Figure 6.** Surface salinity from mooring array (upper panel). Hourly surface along shore currents from mooring array (middle panel). Hourly (blue) and low-pass filtered (red) North/south winds from Ambrose light tower (lower panel).

imately 3 km and yields a water flux of  $\sim 800 \text{ m}^3/\text{s}$  which is significantly smaller than the mean discharge out of the estuary. A plume with a width of 3 km is also consistent with the lack of any significant down-shelf flows during this time period from the ADCP mooring at C2 that lies 4 km from the coast. We also estimated  $Q_{cc}$  assuming that the vertical shear remained constant above the top good ADCP bin. These results were nearly identical to those presented above.

[24] A nearly identical estimate of fresh water flux was obtained with a crossing of the coastal current around 1200 GMT on 10 April. The timing of this transect is indicated by the vertical line in Figure 8, while the location of the transect is shown in Figure 7. During this crossing the estimate of the fresh water from the moorings was  $0.29 \text{ m}^2/\text{s}$ , corresponding to a fresh water transport of approximately  $1000 \text{ m}^3/\text{s}$ . Like the moored data the shipboard data needed to be extrapolated to the surface, which we did assuming the shear remained constant to the surface. This extrapolation method differs than the one we applied on the moored velocity data, where we let the shear go to zero at the surface, because the shipboard data is missing the top 3.0 m of the water column and the moored data suggests that the shear remains relatively constant between 3.0 mbs and 1.0 mbs. While vertical shear may weaken near the surface, assuming

it to be constant yields an *overestimate* of the fresh-water flux. The shipboard data clearly shows that the plume is surface advected and 3–4 km wide (Figure 9a) and  $\sim 5 \text{ m}$  thick. Freshwater transport per unit width exceeds  $0.3 \text{ m}^2/\text{s}$  about 1 km from the shore and decreases both landward and seaward of this point and the total freshwater flux is approximately  $780 \text{ m}^3/\text{s}$ .

[25] Finally a third estimate of the fresh water flux was obtained using the density field and following the geostrophic arguments of *Fong and Geyer* [2002]. *Fong and Geyer* [2002] found that the fresh water transport in their modeled coastal current was linearly proportional to  $(g'h)^2$  where  $g'$  is estimated with the mean density in the plume and  $h$  the mean thickness. They found that freshwater transport was equal to  $\gamma \frac{\rho(g'h)^2}{g\beta S_0 f}$ , where  $\beta$  is saline expansivity ( $\beta = 0.8$ ),  $F$  the Coriolis frequency ( $f = 9.2 \times 10^{-5} \text{ s}^{-1}$ ) and  $\gamma$  a constant = 0.377 that they empirically derived from a series of numerical experiments. With data shown in Figure 9 we estimate  $(g'h)^2 = 0.055 \text{ m}^2/\text{s}^2$  from which the *Fong and Geyer* [2002] regression yields a fresh water transport of  $925 \text{ m}^3/\text{s}$  and similar to the transport estimates from both the moored and the shipboard data.

[26] In conclusion, three estimates of the fresh water flux in the coastal current place it in the range of  $800\text{--}1000 \text{ m}^2/\text{s}$



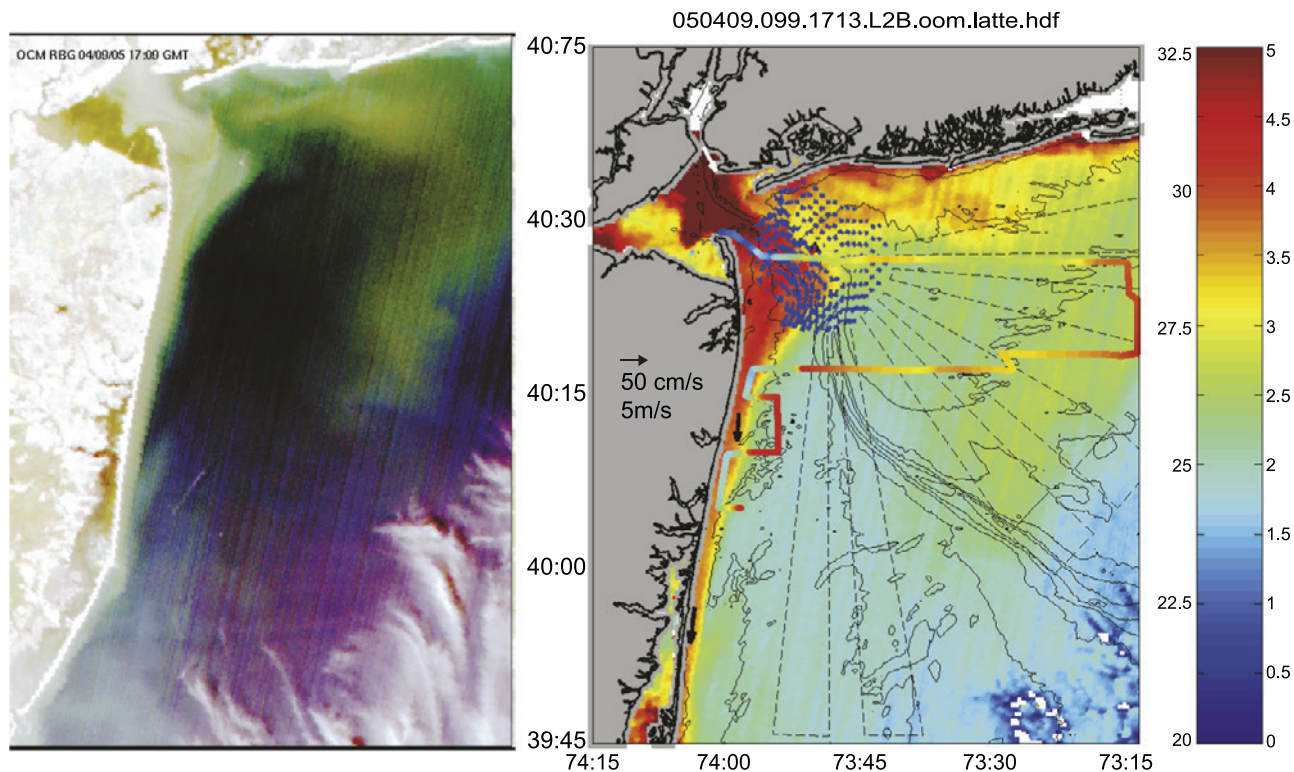


**Figure 7.** Left Panel: RGB image from Ocean sat passage on April 9th 2005 at 17:09 GMT. Right Panel: Image obtained from MODIS at 17:13 GMT. Blue arrows show CODAR field, black from shelf moorings, white from NOAA mooring at the Narrows and red vector represents winds from Ambrose. Color bar is for surface salinity from shiptrack shown in figure. Data from the transect just south of the central mooring array is used to estimate fresh water flux and shown in Figure 10. All current data has been lowpass filtered. Color map on left panel shows absorption at 488 nm and the color scale is relative with red representing high absorption and blue low absorption.

and significantly less than both the gauged fresh-water flux estimates ( $2000 \text{ m}^3/\text{s}$ ) and the Poughkeepsie estimates ( $2300 \text{ m}^3/\text{s}$ ). Consequently, the fraction of fresh water entering the coastal current appears to be only 40–50% of the fresh water that exits the estuary and the remaining freshwater goes into bulge formation. Given the estimate of the Rossby number of the outflow (0.3–0.5) our estimate of the fraction of fresh water that enters the coastal current is consistent with Figure 7 in *Fong and Geyer* [2002] that indicates that for a Rossby number of 0.5 approximately  $1/2$  of the estuarine fresh-water discharge enters the coastal current and the remaining half goes into bulge growth. Furthermore, since fresh water flux in the coastal current ceased after 13 April an even larger fraction of the estuarine outflow must have ultimately gone into bulge formation. Indeed integrating the fresh water flux estimated from the mooring deployment over the entire event (8 April–15 April), and assuming a constant plume width of 4 km we estimated that  $4 \times 10^8 \text{ m}^3$  of fresh water was transported down-shelf in the coastal current. In contrast, the total fresh water discharged into the coastal ocean during this time period was  $1.3 \times 10^9 \text{ m}^3$  based on the gauged estimate and  $1.5 \times 10^9 \text{ m}^3$  using the Poughkeepsie estimate. Thus the bulk of the fresh water that exited the estuary appears not to have gone into the coastal current, but rather into formation of a bulge.

[27] Finally, we note that the rapid increase in fresh-water flux apparent in the moored data on 15–16 April, occurred in response to a predominately east wind. We suggest that the east wind drove the bulge toward the New Jersey coast and this fed the rapid increase in down-shelf fresh water flux. This is consistent both with numerical simulations [*Choi and Wilkin*, 2007] and with theoretical arguments of bulge dynamics interacting a coastal wall [*Nof and Pichevin*, 1988].

## 6. The Bulge

[28] Many aspects of the near-field structure of Hudson's outflow that we observed in April 2005 were consistent with bulge phenomenology described in laboratory experiments [*Avicola and Huq*, 2003a; *Horner-Devine et al.*, 2006]. While details of the circulation are often obscured by wind-forcing and tidal dynamics (processes not included in the laboratory experiments) the outflow tended to form a recirculation that limited the transport into the coastal currents. We note that the formation of a bulge may be influenced by both tidal and wind-forcing. For example, tides will increase the Rossby number of the outflow favoring bulge formation, and tidally driven eddies may further augment bulge formation. However, tidal mixing will also deepen the outflow and alter both the Froude and Burger numbers which are also important parameters gov-

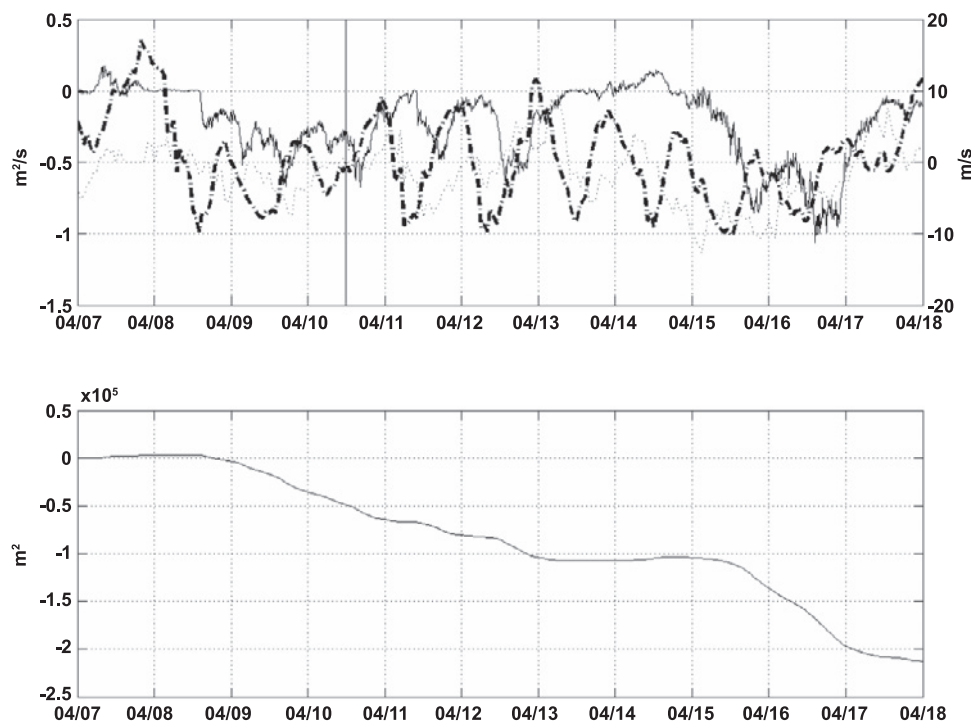


**Figure 8.** Upper panel shows fresh water flux ( $\text{m}^2/\text{s}$ ) from mooring at C1 (solid line), hourly north south (thick dashed) and east/west (thin dotted) winds from Ambrose light tower. Vertical line on 4/10 indicates time that fresh water flux was estimated with shipboard survey. Lower panel shows time integral of fresh water flux beginning on 4/7. Negative values indicate down-shelf transport.

erning bulge formation. The outflow angle which *Avicola and Huq* [2003a] suggest is the factor that determines bulge formation is strongly impacted by wind-forcing, even at the diurnal period. For example the early morning ebb at 0800 on 11 April occurred in the presence of northerly winds and drove the outflow to the south (it was into this ebb that dye was injected following the passage of the new plume) (Figure 10). In contrast the late afternoon ebb occurred in the presence of the southerly sea-breeze and deflected the outflow to the left and significantly increased the angle of the outflow. The outflow in the morning makes an angle approximately 30 degrees with the New Jersey Coast, while the late afternoon ebb makes an angle closer to 60 degrees with the coast. *Avicola and Huq* [2003a] suggested that when the outflow angle exceeded 60 degrees bulge formation was evident in their laboratory experiments.

[29] While the results of *Avicola and Huq* [2003a] suggest that the morning ebb, with its oblique outflow angle, should feed a coastal current the trajectory of drifters and dye suggested otherwise (Figure 11). Dye and drifters were released following the passage of this ebb's tidal bore. The bore was evident by a rapid increase in the velocity, deepening of the surface layer and the surface signature of trains of internal waves. Both the drifters and the dye initially headed west-southwest and veered consistently to the right. Between 2 and 3 h after release their trajectories were normal to the coast and on approaching the coast the remaining drifter (one of the drifters was removed after 3 h) and dye began to move northward. As the dye approached the coast it rapidly spread both north and south, however it

tended to move to the north over the next 48 h (Figure 11) consistent with the mean surface velocity at N1. Yet, despite the recirculation in the bulge a coastal current persisted, apparent by down-shelf currents at C1, and indicated that some of the bulge is leaking out into the coastal current. In general many aspects of the feature depicted in Figure 11 are similar to the conceptual model drawn by *Avicola and Huq* [2003a, Figure 2c]. In particular both the data and their model show a strong divergence in the along channel flow in the region between the bulge and the coastal current and this along shore divergence is maintained by a converging onshore flow.

[30] Surface chlorophyll-a maps from MODIS along with surface salinity maps and equivalent depth of fresh water maps from an 13–15 April survey show clear evidence the ballooning bulge (Figure 12). The surface map on 4/9–10 (Figure 7) shows both the old plume to the east and the development of the new plume that includes waters less than 25 psu both in the bulge and in the coastal current. While the 4/9–10 survey was too crude to estimate the fresh water volume of the bulge region we were able to estimate the fresh-water volume of the bulge region on the 4/13–15 survey.

[31] Of the 11 cross-shelf lines shown in Figure 12, we were able to estimate fresh water volume per meter of coast line for the 7 of the 8 southern lines. (The towed vehicle had to be pulled while on line 8 after its cable was snagged by fishing gear). Line 7 has the highest fresh water content with over  $6 \times 10^4 \text{ m}^2$  of fresh water per unit meter of coast line, and presumably the fresh water content increases

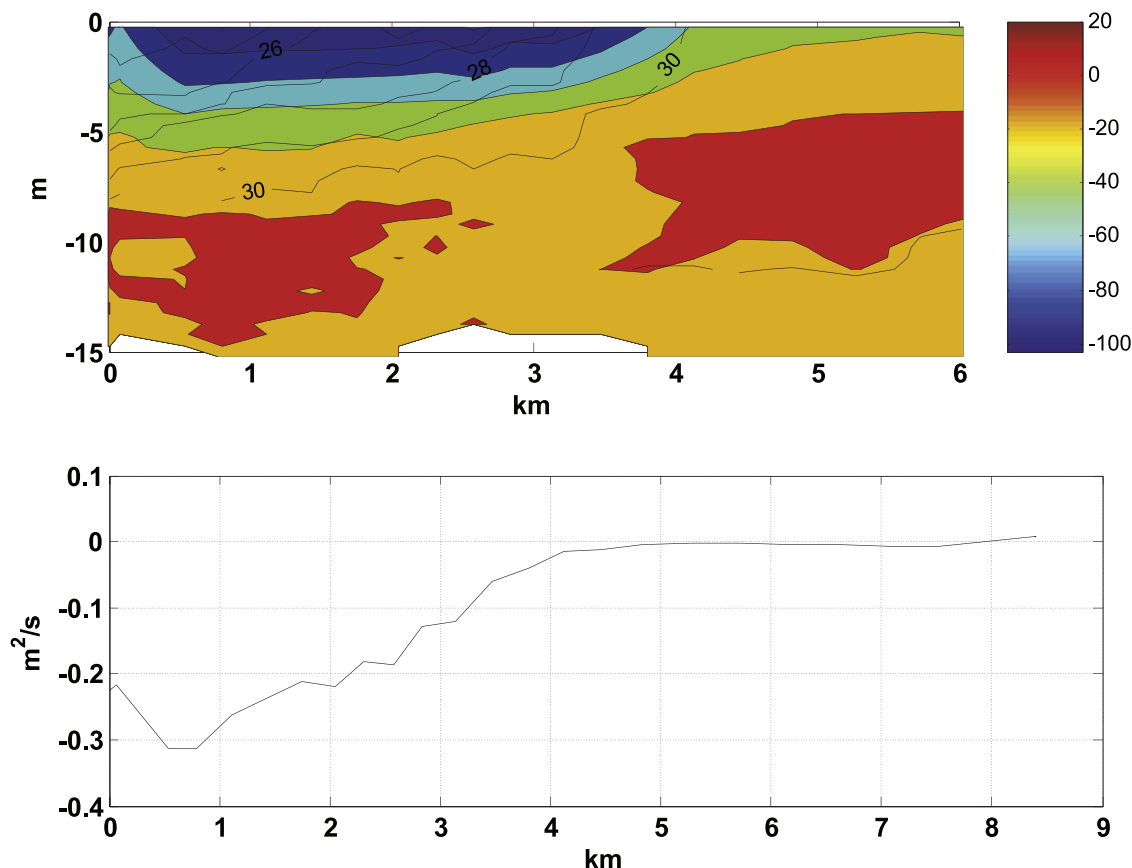


**Figure 9.** Upper panel: along shore velocity (color) and salinity (contour) from crossing of plume on April 10th just south of mooring array (ship track shown in Figure 7). Negative currents are down shelf. Currents above 3 meter below the surface are linearly extrapolated. Lower panel: Fresh water flux per meter based on data shown in upper panel.

moving northward. Fresh-water volumes reduced to  $4\text{--}5 \times 10^4 \text{ m}^3$  per unit meter of coast line on the southern 4 lines. On the 3 northern lines the bulk of the fresh water is incorporated in the bulge region, while for the southern 4 lines fresh water is evenly split between the fresh water along the coast, and the old plume in the vicinity of the shelf valley. Using a value of  $5 \times 10^4 \text{ m}^3$  to represent the fresh water per meter content of the bulge suggests that the 40 km long bulge contains  $2 \times 10^9 \text{ m}^3$  of fresh water. Note that this fresh water inventory exceeds both the gauged and Poughkeepsie estimate of the total fresh water supplied by the rivers between April 8th, when this bulge was formed and 15 April when we completed our survey. While the fresh water inventory in the bulge must be less than what was discharged because a portion was advected away in the coastal current we also recognize the estimate of fresh water volume in the bulge is crude. However, the lag between upland discharge of fresh water into the river at the gauges and outflow flow at the Narrows suggests that the fresh-water content of the bulge should be compared to a discharge record that is lagged by a few days, and since the discharge was rapidly dropping during this event this would increase the amount of fresh water delivered to the coastal ocean during this event. In fact a 3 day lag yields the volume of fresh water delivered to the ocean during this event of  $1.9 \times 10^9 \text{ m}^3$  based on the gauged data and  $2.1 \times 10^9 \text{ m}^3$  based

on the Poughkeepsie data. Regardless of the details, however, it is clear that the bulk of the freshwater discharged into the coastal ocean during this event went into bulge formation rather than the coastal current.

## 7. Shelf Wide Implications

[32] The tendency for the Hudson's outflow to form a bulge has important implications on cross-shelf transport processes because once the fresh water is away from the coast its fate is determined by wind-forcing and ambient shelf circulation, rather than being self-advected away in a narrow coastal current. The bulge formation tends to place water in the vicinity of the shelf-valley and over the 40–50 m deep isobath. It is between these isobaths where the fresh water moving offshore in Figure 12 resides. While details of the ambient shelf flows are beyond the scope of this paper, several other studies have suggested that frontal systems reside between the 40–60 m isobaths in the New York Bight [Biscaye *et al.*, 1994; Bumpus, 1973; Ullman and Cornillon, 1999]. Frontal structure along this isobath appears to be associated with a surface convergence in the vicinity of the 50 m isobath associated with an mean cross-shelf flow characterized by upwelling inshore of this isobath with a downwelling circulation seaward. Cross-shelf transport pathways along the 40–50 m isobath, just west of the



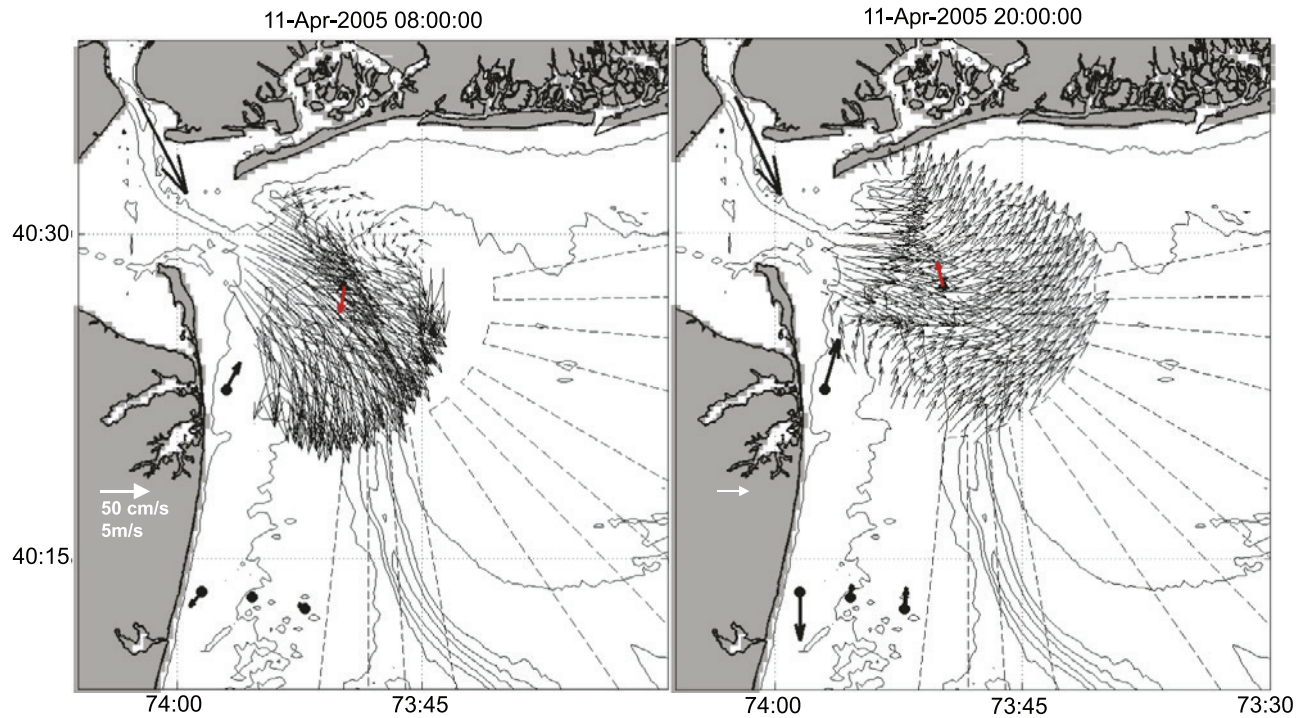


**Figure 10.** Surface currents (black vectors) and winds (red) during subsequent ebb tides on April 11th. Isobaths are contoured at 10 m intervals.

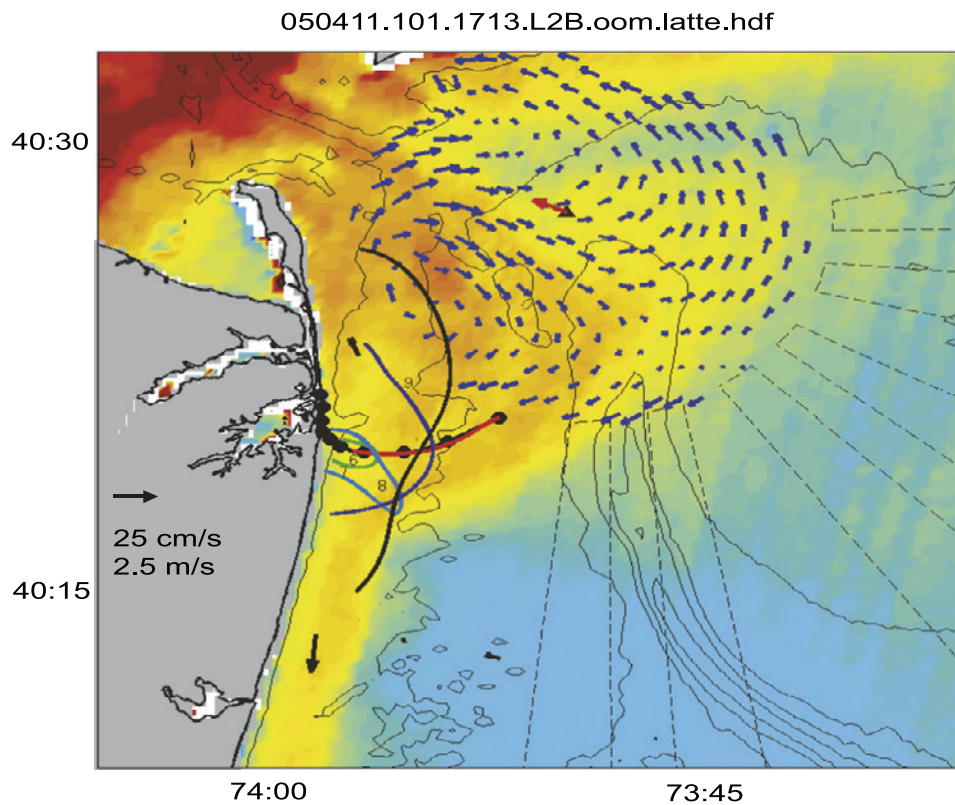


**Figure 11.** Ocean color from OCM, low-pass filtered surface currents from CODAR and mooring array. Red line shows drifter trajectory with black dots plotted each hour. The drifter was deployed during the time of the dye injection. Numbers indicate approximate location of center of dye patch and lines the approximate extent of the patch for surveys 6–9. These surveys occurred 4.3, 8.4, 12.2 and 18 hours after injection respectively.

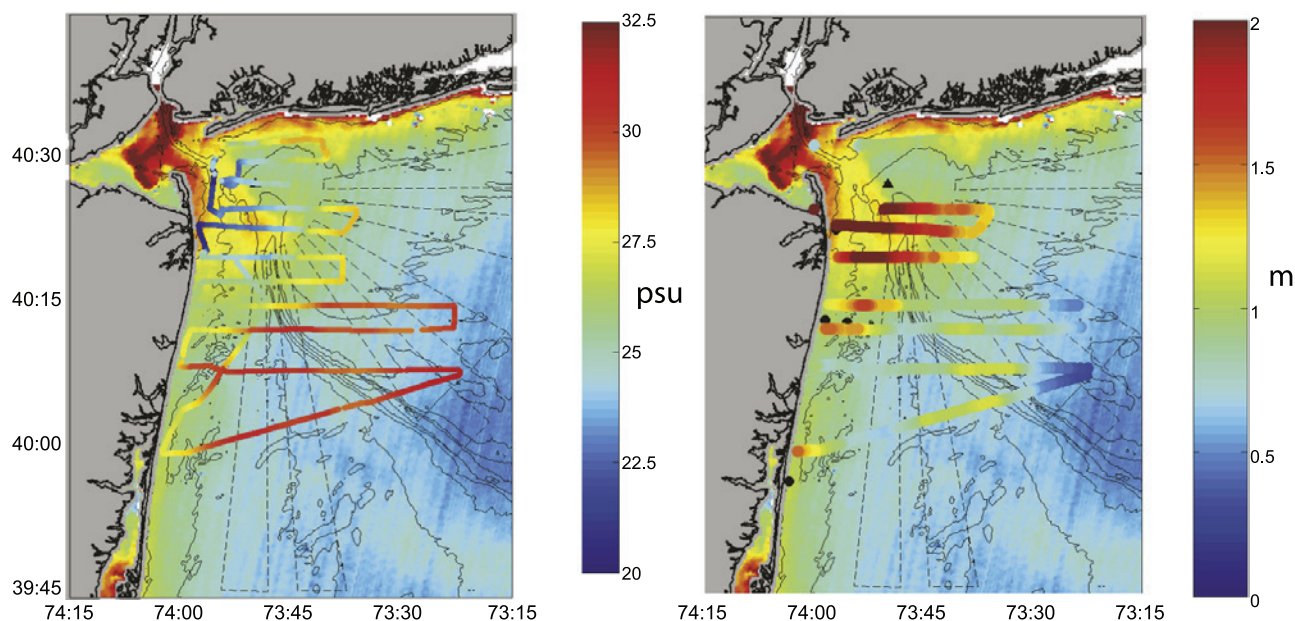


**Figure 12.** Both panels show OCM derived chlorophyll-a surface concentration from April 13th 17:13 GMT. In both panels the color scale for chlorophyll-a is relative with red representing high concentrations and blue low concentrations. The right panel shows surface salinity and the left panel shows equivalent fresh water in meters based on a reference salinity of 32 psu. The color bar is scaled to these variables shown on the shiptrack. The survey began on April 13th at 10:45 GMT and ended April 15th at 0500 GMT. Ship traces that show surface salinity but not equivalent fresh water are during times that the towed vehicle was either out of the water or held at the surface.

shelf valley, are evident in long term mean surface currents from long range CODAR data (personnel communications Scott Glenn, Josh Kohut) and appear to be correlated with upwelling winds that persists for one week or more (Castelao et al., Cross-shelf transport of fresh water in the New Jersey Shelf during Spring and Summer 2006, submitted to *Journal of Geophysical Research*). It was over these isobaths that we observed significant fresh-water on the south-eastern reaches of the survey shown in Figure 12. We note that this fresh water exited the estuary around 6 April was driven along the Long Island Coast by upwelling favorable winds on 6–8 April and subsequently drifted south during the next 5 days when winds were dominated by strong diurnal variability but weak daily means (Figure 6).

[33] Evidence of rapid cross-shelf transport of fresh water is apparent in Glider data obtained along the Rutgers University’s Endurance line that lies approximately 100 km south of the Hudson’s outflow (Figure 13–Figure 14). Comparison between a section run before the freshet (10–16 March) and one run 6 weeks after the freshet (17–24 May) shows significant freshening across the entire 150 km wide shelf (Figure 13). The May section shows that, with the exception of the intrusion of warm/saline slope waters at the end of the section, the entire shelf has freshening by approximately 1psu or more. We note that the surface salinity front located near 74°35′W coincides with a temperature front that AVHRR imagery reveals extends along much of the 100 km long NJ shelf (Figure 14). Estimates of the fresh water content based on the May glider section are  $1.2 \times 10^5 \text{ m}^2$  of fresh water per meter of coast line. Assuming that the along shore extent of this

feature is 100 km the fresh water content on the shelf is  $12 \times 10^9 \text{ m}^3$  and approximately equal to our estimates of the total fresh water discharged into the coastal ocean since the onset of the freshet between 1 March and 15 May, with the both the “gauged” and “Poughkeepsie” estimates of total discharge over this period equal to  $10 \times 10^9 \text{ m}^3$ .

[34] The cross-shelf mixing of the spring freshet by early summer is consistent with results of Mountain [2003] who analyzed two decades of hydrographic data along from Cape Hatteras, North Carolina to Nantucket Shoals. Mountain noted that while there was a strong seasonal signal to mean shelf salinity in the New York Bight Apex, seasonal variability in salinity was not detectable to the south off of Delaware and Chesapeake Bays. We suggest that because these latter two systems form coastal currents fresh water tends to be trapped along the coast and was not resolved by the spatially coarse surveys they analyzed. In contrast, the rapid cross-shelf mixing of the Hudson plume would have been more readily resolved by those surveys.

## 8. Conclusions

[35] A suite of observations indicate that the Hudson’s outflow is susceptible to bulge formation under high discharge conditions. This tends to limit fresh water transport in the nearshore coastal current and enhance cross-shelf transport to mid-shelf. Even during a period of downwelling favorable winds the fresh-water transport in the coastal current was less than 1/2 of the estuarine freshwater outflow. The tendency for a major fraction of the outflow to go into unsteady bulge formation, rather than coastal



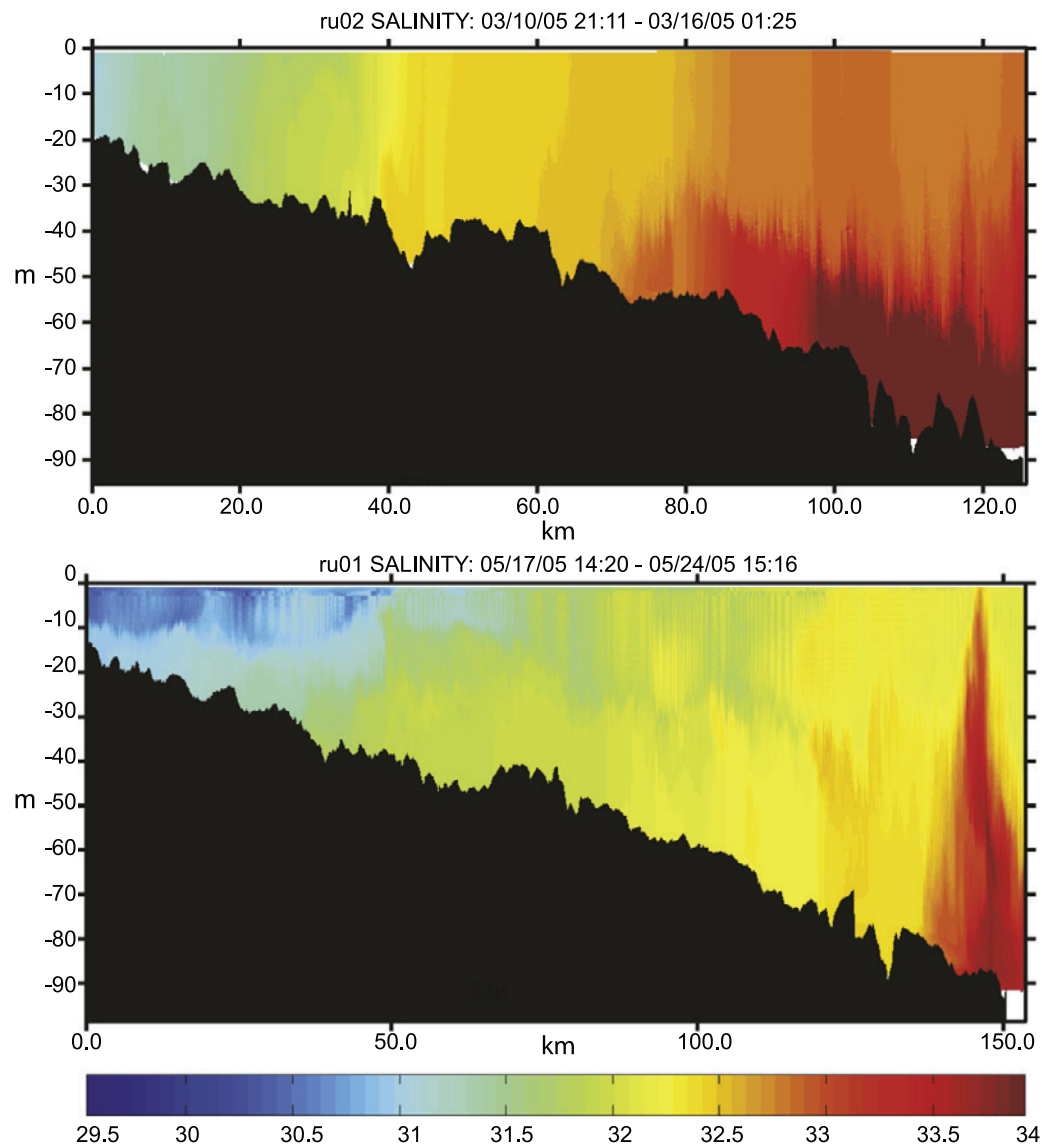


**Figure 13.** Cross-shelf sections of salinity from glider sections run on March 10–16, 2005 (upper panel) and May 17–24, 2005 (lower panel). The colorbar is practical salinity units. The glider transect is shown in Figure 14.

current is consistent with theoretical [Nof and Pichevin, 1988], laboratory [Avicola and Huq, 2003b; Horner-Devine *et al.*, 2006] and numerical studies [Fong and Geyer, 2002] of buoyant discharges. The outflow's trajectory was also highly sensitive to wind-forcing even in the diurnal band and this may have enhanced bulge recirculation as suggested by mechanism proposed by Avicola and Huq [2003b]. Transport in the coastal current is suggestive of a geostrophic cross-shore momentum balance, similar to other coastal sites [Lentz *et al.*, 1999] and modeling studies [Fong and Geyer, 2002].

[36] The tendency for the Hudson's outflow to generate a bulge may be due to several factors. First, there is a tendency for the outflow to make a large angle with the coast line, which laboratory experiments by [Avicola and Huq, 2003a; Horner-Devine *et al.*, 2006] suggest will favor bulge formation. Secondly, unlike the Chesapeake and Delaware the Hudson's outflow is not along a straight

coastline but rather into an Apex. The mean down-shelf circulation probably does not extend into this corner and thus there is not an ambient flow that tends to pin the outflow to the coast. Thirdly, there is no bathymetric channel to steer Hudson's outflow toward the coast, as there is in the Chesapeake's outflow [Valle-Levinson *et al.*, 2007]. Finally, the observations presented in this paper occurred following a large discharge event which may favor bulge formation as suggested by Choi and Wilkin [2007] relative to times of lower discharge events where presumably, in the absence of winds, a larger fraction of the outflow would go into the coastal current.

[37] Finally the tendency for the Hudson's outflow to form a bulge during times of high river discharge has significant implications for biogeochemical pathways. Rather than material being rapidly advected away in a coastal current material in the estuarine discharge, tends to be trapped near the outflow. Nutrient uptake and primary



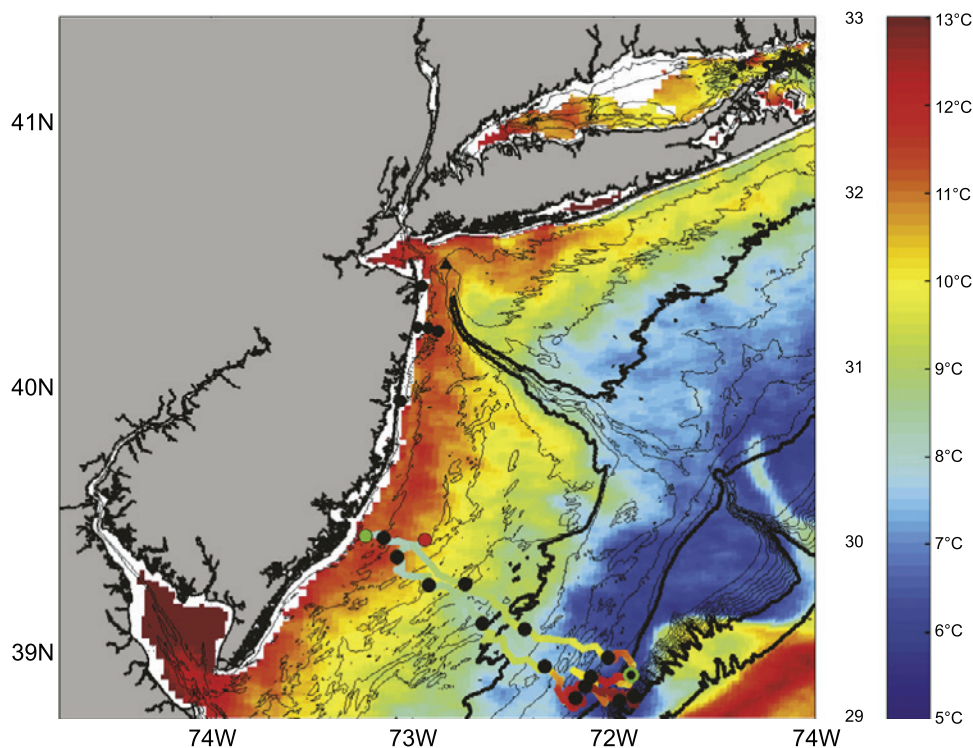


**Figure 14.** Sea Surface temperature from AVHRR at 14:55 on May 29th 2005 along with surface salinity from glider deployment from May 17th–June 11th. Colorbar is labeled for temperature (on the right) and salinity (on the left). Thick contours are used for the 50, 100, 1000 and 2000 meter isobath. Green and red dots mark the beginning and end of the glider deployment on May 17th 14:20 and June 11th 14:50 respectively. Solid black dots on glider track mark two day intervals. Black dot with green circle marks glider location at the time of the satellite pass.

production was so rapid in this region (Schofield et al., “The Hudson River Plume and its role in low dissolved Oxygen in the Mid-Atlantic Bight” submitted to *Journal of Geophysical Research*) that by the time the outflow reached the coastal current primary production was nutrient limited and rapid blooms in the bulge quickly crashed and settled to the bottom and lowered dissolved oxygen levels in the lower layer. Furthermore, the temporary retention of material in the apex region also appears to impact the fate and transport of contaminant metals (Reinfelder et al., in prep). Thus material that is rapidly cycled in the plume may quickly settle out into the lower layer where it may be transported back into the estuary by the landward flowing lower layer and increase the trapping efficiency of the estuary. On the other hand, material that remains dissolved in the plume for weeks appears to be rapidly mixed across the shelf. Details on the biogeochemical implications of the results presented in this paper will be featured in a series of interdisciplinary papers based on the LaTTE program.

[38] **Acknowledgments.** We thank two anonymous reviewers for their comments. We thank the Crew and Captains of the Cape Hatteras and the Oceanus for their efforts and the crew at Millers Launch. We also thank the dedicated members of RU COOL, with particular gratitude to Chip Haldeman who led the mooring deployment and served many roles on the Oceanus. The Observatory was supported by the Office of Naval Research, The National Science Foundation, the National Ocean Partner Program, the National Oceanic and Atmospheric Administration, the Department of Homeland Security, the Department of Defense, the Envi-

ronmental Protection Agency and the National Aeronautic and Space Administration. This study was supported by the National Science Foundation through grant OCE-0238957.

## References

- Abood, K. A. (1977), Evaluation of the circulation in partially stratified estuaries as typified by the Hudson River, Ph. D. Thesis, Rutgers University.
- Avicola, G., and P. Huq (2003a), The characteristics of recirculating bulge region in coastal buoyant outflows, *J. Mar. Res.*, **61**, 435–463.
- Avicola, G., and P. Huq (2003b), The role of outflow geometry in the formation of the recirculating bulge region in coastal buoyant outflows, *J. Mar. Res.*, **61**(4), 411–434.
- Biscaye, P. C., C. N. Flagg, and P. G. Falkowski (1994), The Shelf Edge Exchange Processes experiment, SEEP-II: An introduction to hypotheses, results and conclusions, *Deep-Sea Res.*, **41**, 231–252.
- Bumpus, D. F. (1973), A description of the circulation on the continental shelf of the east coast of the United States, *Progr. Oceanogr.*, **6**, 111–157.
- Chapman, D. C., and S. J. Lentz (1994), Trapping of a coastal density front by the bottom boundary layer, *J. Phys. Oceanogr.*, **24**, 1464–1479.
- Choi, B. J., and J. L. Wilkin (2007), The effect of wind on the dispersal of the Hudson River plume, *J. Phys. Oceanogr.*, **37**(7), 1878–1897.
- Fong, D. A., and W. R. Geyer (2001), Response of a river plume during an upwelling favorable wind event, *J. Geophys. Res.*, **106**, 1067–1084.
- Fong, D., and W. R. Geyer (2002), The alongshore transport of freshwater in a surface-trapped river plume, *J. Phys. Oceanogr.*, **32**, 957–972.
- Garvine, R. (1999), Penetration of buoyant coastal discharge onto the continental shelf: A numerical model experiment, *J. Physical*, **29**, 1892–1909.
- Glenn, S. M., and O. Schofield (2004), Observing the oceans from the COOLroom: Our history, experience, *Oceanography*, **16**.
- Harris, C. K., B. Butman, and P. Traykovski (2003), Winter-time circulation and sediment transport in the Hudson Shelf Valley, *Cont. Shelf Res.*, **23**, 801–820.
- Horner-Devine, A. R., D. A. Fong, S. G. Monismith, and T. Maxworthy (2006), Laboratory experiments simulating a coastal river outflow, *J. Fluid*, 203–232.

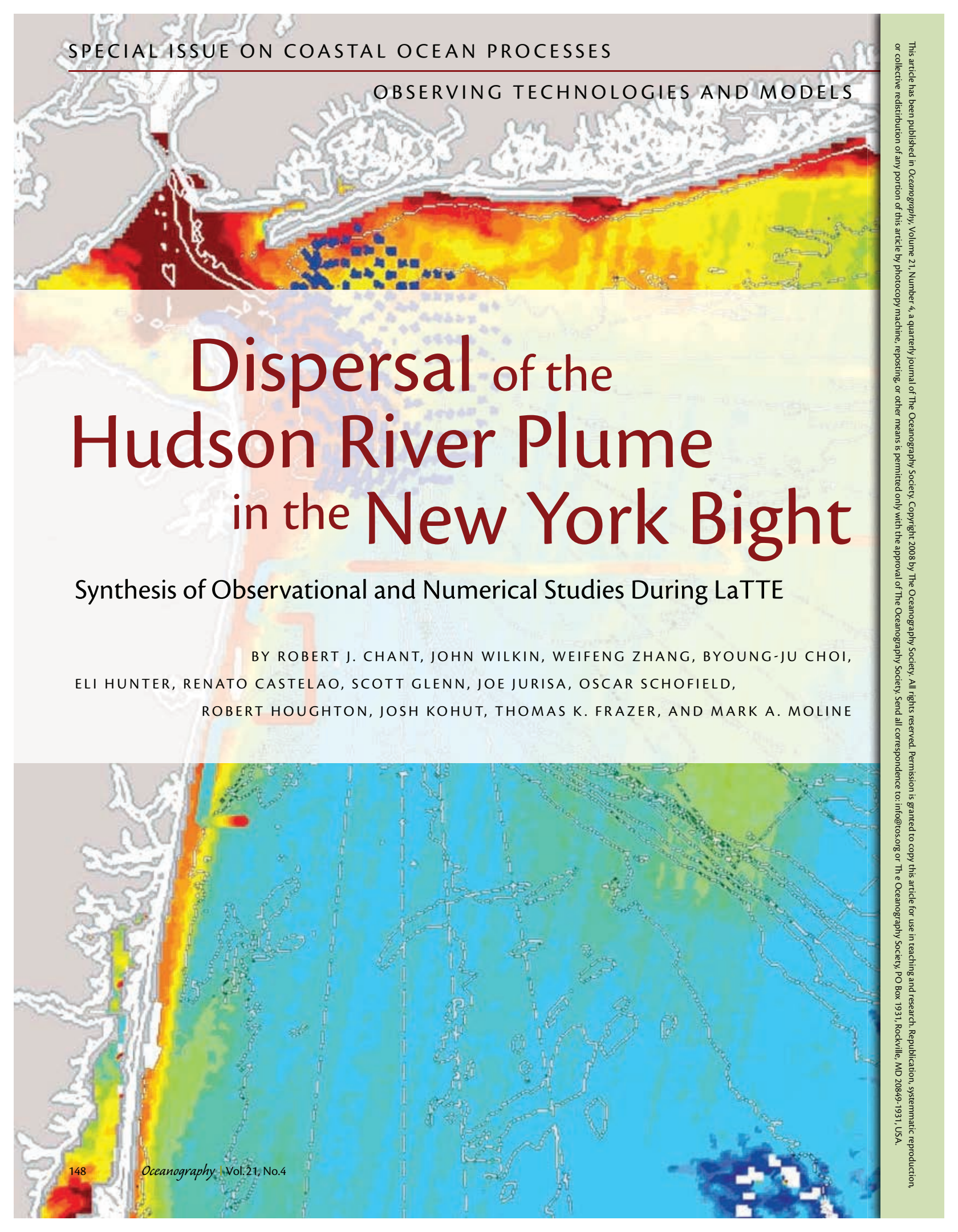
- Houghton, R. W., C. E. Tilburg, and R. W. G. a. A. Fong (2004), Delaware River plume response to a strong upwelling favorable wind event, *Geophys. Res.*, *31*.
- Kohut, J. G. S. M., and D. Barrick (2001), Multiple HF-Radar system development for a regional Longterm Ecosystem Observatory in the New York Big, *American Meteorological Society: Fifth Symposium on Integrated Observing Systems*, 4–7.
- Kohut, J., S. Glenn, and J. Paduan (2006), The inner-shelf response to tropical storm Floyd, *J. Geophys. Res.*, *111*, C09S91, doi:10.1029/2003JC002173.
- Lee, Z., K. L. Carder, and R. A. Arnone (2002), Deriving inherent optical properties from water color: A multiband quasi-analytical algorithm for optically deep waters, *Appl. Opt.*, *41*, 5755–5772.
- Lentz, S. J., and K. R. Helfrich (2002), Buoyant gravity currents along a sloping bottom in a rotating fluid, *J. Fluid Mech.*, *464*, 251–278.
- Lentz, S., R. T. Guza, S. Elgar, and F. F. a. T. H. C. Herbers (1999), Momentum balances on the North Carolina inner Shelf, *J. Geophys. Res.*, *104*, 18,205–18,226.
- Lerczak, J. A., W. R. Geyer, and R. J. Chant (2006), Mechanisms driving the time-dependent salt flux in partially stratified estuary, *J. Phys. Oceanogr.*, *36*, 2283–2298.
- Morison, J., R. Anderson, N. Larson, E. D'Asaro, and T. Boyd (1994), The correction for thermal-lag effects in sea-bird CTD data, *J. Atmos. Oceanic Technol.*, *11*, 1151–1162.
- Mountain, D. G. (2003), Variability in the properties of Shelf Water in the Middle Atlantic Bight, 1977–1999, *J. Geophys. Res.*, *108*(C1), 3014, doi:10.1029/2001JC001044.
- Newman, W. S., D. L. Thurber, H. S. Awiss, A. Rokach, and L. Musich (1969), Late Quaternary geology of the Hudson River estuary: a preliminary report, *31*, 548–570.
- Nof, D., and T. Pichevin (1988), The ballooning of outflows, *J. Phys. Oceanogr.*, *31*, 3045–3048.
- Rennie, S. E., and S. Lentz (1999), Observations of a pulsed buoyance current downstream of Chesapeake Bay, *J. Geophys. Res.*, *104*, 18,228–18,240.
- Ullman, D., and P. Cornillon (1999), Satellite-derived sea surface temperature fronts on the continental shelf off the northeast U.S. coast, *J. Geophys. Res.*, *104*.
- Valle-Levinson, A., K. Holderied, and C. L. a. R. J. Chant (2007), Subtidal flow structure at the turning region of a wide outflow plume, *J. Geophys. Res.*, *112*, C04004, doi:10.1029/2006JC003746.
- Whitney, M. M., and R. W. Garvine (2005), Wind influences on a coastal buoyant outflow, *J. Geophys. Res.*, *110*, C03014, doi:10.1029/2003JC002261.
- Yankovsky, A., and D. C. Chapman (1997), A simple theory for the fate of buoyant coastal discharges, *J. Phys. Oceanogr.*, *27*, 1386–1401.

J. Bosch, R. J. Chant, S. M. Glenn, E. Hunter, J. Kohut, and O. Schofield, Institute of Marine and Coastal Studies, Rutgers University, New Brunswick, NJ, USA. (chant@marine.rutgers.edu)

R. F. Chen, University of Massachusetts Boston, MA, USA.

R. W. Houghton, Lamont-Doherty Earth Observatory, Columbia University, Palisades, NY, USA.





# Dispersal of the Hudson River Plume in the New York Bight

Synthesis of Observational and Numerical Studies During LaTTE

BY ROBERT J. CHANT, JOHN WILKIN, WEIFENG ZHANG, BYOUNG-JU CHOI,  
ELI HUNTER, RENATO CASTELAO, SCOTT GLENN, JOE JURISA, OSCAR SCHOFIELD,  
ROBERT HOUGHTON, JOSH KOHUT, THOMAS K. FRAZER, AND MARK A. MOLINE



**ABSTRACT.** Observations and modeling during the Lagrangian Transport and Transformation Experiment (LaTTE) characterized the variability of the Hudson River discharge and identified several freshwater transport pathways that lead to cross-shelf mixing of the Hudson plume. The plume's variability is comprised of several different outflow configurations that are related to wind forcing, river discharge, and shelf circulation. The modes are characterized by coastal current formation and unsteady bulge recirculation. Coastal currents are favored during low-discharge conditions and downwelling winds, and represent a rapid downshelf transport pathway. Bulge formation is favored during high-discharge conditions and upwelling winds. The bulge is characterized by clockwise rotating fluid and results in freshwater transport that is to the left of the outflow and opposed to classical coastal current theory. Upwelling winds augment this eastward flow and rapidly drive the freshwater along the Long Island coast. Upwelling winds also favor a midshelf transport pathway that advects fluid from the bulge region rapidly across the shelf on the inshore side of the Hudson Shelf Valley. A clockwise bulgelike recirculation also occurs along the New Jersey coast, to the south of the river mouth, and is characterized by an offshore veering of the coastal current. Modeling results indicate that the coastal transport pathways dominate during the winter months while the midshelf transport pathway dominates during summer months. Finally, because the time scales of biogeochemical transformations in the plume range from hours to weeks or longer, the details of both the near- and far-field plume dynamics play a central role in the fate of material transported from terrestrial to marine ecosystems.

## INTRODUCTION

River discharge into the coastal ocean represents a major link between terrestrial and marine systems. Moreover, with over half of the world's human population located within coastal watersheds, this discharge is an important pathway that extends anthropogenic impacts into the ocean. Although biogeochemical processes can significantly modify this transport pathway, understanding the processes that determine freshwater transport pathways is essential in determining the fate and transport of material fluxing across the land-sea interface. River outflows are less dense than the

saline ocean waters and this density difference produces a buoyancy force that drives the plume's circulation. The classic model of plume dynamics balances this buoyancy force with the Coriolis force that causes the outflow to turn to the right (in the northern hemisphere) and form a narrow coastal current trapped within a few internal Rossby radii (the ratio of internal wave speed to the local Coriolis frequency) of the coast (Garvine, 1987, 1999). The coastal current may be confined to a thin surface layer or may be attached to the bottom (Yankovsky and Chapman, 1997). In general, the classic model emphasizes

that, in the absence of winds, coastal current dynamics severely limit the cross-shelf transport of river plumes.

Buoyant outflows may also contain a bulge-like region in the vicinity of the outflow, and the cross-shelf extent of these bulges can be many times the width of the downstream coastal current. Yankovsky and Chapman (1997) incorporated a bulge in a steady-state model that they closed by equating the freshwater flux in the coastal current to the freshwater flux exiting the estuary. With this steady-state assumption, they developed an elegant theory that related coastal current structure to the

estuarine discharge and the cross-shore slope of the seafloor.

Recent modeling and laboratory studies of buoyant outflows provide a more detailed characterization of bulge structure (Fong and Geyer, 2002; Avicola and Huq, 2003; Horner-Devine et al., 2006) and emphasize that a bulge may be *unsteady* and grow in time. Consequently, the freshwater flux out of the estuary may be greater than the freshwater flux in the coastal current, with the remainder going into bulge formation. Based on laboratory experiments in a rotating tank, Avicola and Huq (2003) reported that approximately one-third of the outflow became incorporated in a coastal current. More detailed analysis afforded by numerical modeling indicated that the fraction of freshwater from the river that is incorporated in the coastal current depends on the outflow parameters. Specifically, as the flow becomes increasingly nonlinear,

less of the discharge goes into the coastal current and more into bulge growth.

The nonlinearity is characterized by the Rossby number, which is the ratio of inertial to rotational forces. Fong and Geyer (2002) discuss the mechanisms by which the bulge feeds the coastal current by invoking a model by Nof (1988), whereby the amount of freshwater entering the coastal current is determined by the amount of the eddy (bulge) pinched off at the coastal wall. As the Rossby number increases, the eddy's center moves increasingly further from the coastal wall and reduces the fraction of the eddy that is pinched off, thus diminishing the freshwater transport into the coastal current. Laboratory experiments by Horner-Devine et al. (2006) show even more dramatic shunting of the coastal current by bulge formation as the recirculation completely pinches off the coastal current, and the entire outflow goes into bulge formation. Note that

although laboratory and modeling studies often produced such bulges, the lack of observational evidence caused some to suggest that bulge formation may in fact be an artifact of models. Indeed, Fong and Geyer (2002) note that bulge formation in models is more pronounced than in nature.

Wind forcing also plays a critical role in the cross-shelf transport of river plumes (Whitney and Garvine, 2005). Modeling studies reveal that upwelling winds are effective in both transporting river plumes offshore and mixing the plume with the coastal ocean (Fong and Geyer, 2001). Observational studies of coastal currents reveal that the structure of the flow and salt fields (Rennie and Lentz, 1999) and of the diapycnal fluxes (Houghton et al., 2004) appear to be consistent with numerical studies (Fong and Geyer, 2001). Despite this consistency, there has been little research on the effect of wind forcing on bulge dynamics, with the notable exception of Choi and Wilkin (2007).

In this paper, we discuss the character of the Hudson River's discharge into the coastal ocean based on observations and modeling efforts during the Lagrangian Transport and Transformation Experiment (LaTTE). The major objective of LaTTE was to elucidate the transport and transformation of dissolved and suspended material as it exits New York Harbor onto the continental shelf of the Middle Atlantic Bight; hence, it was imperative to characterize freshwater transport pathways. This highly urbanized watershed (Figure 1) is among the most industrialized in the world; thus, our objectives included tracking contaminant metals along with nutrients and organic matter, as well as aspects of the

---

**Robert J. Chant** ([chant@marine.rutgers.edu](mailto:chant@marine.rutgers.edu)) is Assistant Professor, Institute of Marine and Coastal Sciences, Rutgers University, New Brunswick, NJ, USA. **John Wilkin** is Associate Professor, Institute of Marine and Coastal Sciences, Rutgers University, New Brunswick, NJ, USA. **Weifeng Zhang** is PhD Candidate, Institute of Marine and Coastal Sciences, Rutgers University, New Brunswick, NJ, USA. **Byoung-Ju Choi** is Professor, Department of Oceanography, College of Ocean Science and Technology, Kunsan National University, Korea. **Eli Hunter** is Research Programmer, Institute of Marine and Coastal Sciences, Rutgers University, New Brunswick, NJ, USA. **Renato Castelao** is Postdoctoral Scientist, Institute of Marine and Coastal Sciences, Rutgers University, New Brunswick, NJ, USA. **Scott Glenn** is Professor, Institute of Marine and Coastal Sciences, Rutgers University, New Brunswick, NJ, USA. **Joe Jurisa** is PhD Candidate, Institute of Marine and Coastal Sciences, Rutgers University, New Brunswick, NJ, USA. **Oscar Schofield** is Professor, Institute of Marine and Coastal Sciences, Rutgers University, New Brunswick, NJ, USA. **Robert Houghton** is Senior Staff Associate, Lamont-Doherty Earth Observatory, Columbia University, Palisades, NY, USA. **Josh Kohut** is Assistant Professor, Institute of Marine and Coastal Sciences, Rutgers University, New Brunswick, NJ, USA. **Thomas K. Frazer** is Research Foundation Professor, Department of Fisheries and Aquatic Sciences, University of Florida, Gainesville, FL, USA. **Mark A. Moline** is Professor, Biological Science Department, California Polytechnic State University, San Luis Obispo, CA, USA.

phytoplankton and zooplankton assemblages. A project emphasis was to investigate interactions between the plume's physical structure and biogeochemical processes. For example, we hypothesized that biogeochemical processes that are mediated by photochemistry, such as primary production, colored dissolved organic matter (CDOM) degradation, and production of dissolved gaseous mercury, would fundamentally differ between upwelling and downwelling events because light levels in a thin upwelling plume would be elevated relative to light fields in a thick, and potentially more turbid (if bottom attached), downwelling plume.

These objectives were founded on a classic view of a buoyant discharge (i.e., coastal current formation and the response of the coastal current to along-shore wind stress). Results from LaTTE revealed, however, a much more complex

plume structure not adequately captured by the classic model. In particular, results emphasized that the plume's outflow was in fact susceptible to bulge formation, that the outflow was highly sensitive to meteorological forcing, and that the plume, even though it was surface advected, appeared to be influenced by the underlying topography. The major topographic feature on the shelf, the Hudson Shelf Valley (HSV) bisects the entire 150-km-wide shelf from near the shelf break to within 10 km of the Hudson outflow (Figure 1). The HSV, the ancestral channel of the Hudson, is ~ 50–70 meters deep. Together, coastal currents, bulge formation, sensitivity to wind forcing, and interaction with shelf topography and circulation produce distinct “modes” of freshwater transport that in aggregate drive a rapid cross-shelf mixing of freshwater (Castelao et al., 2008a; Zhang et al., in review–a).

Because the biogeochemical transformations of interest in LaTTE occur over a range of time scales (Moline et al., this issue), describing the details of both the near-field plume dynamics and broader shelfwide dispersal of freshwater are critical to understanding the fate and transport of riverborne materials.

## FIELD OBSERVATIONS

The LaTTE field effort included a series of 2004–2006 cruises and mooring deployments in the New York Bight (Figure 1). Each field campaign featured dye studies whereby rhodamine dye was injected into plume water to provide a Lagrangian framework from which to interpret physical, biological, and chemical data. Drifters were deployed with the dye to guide in tracking the dye and provided additional Lagrangian data to characterize plume trajectories. Details of the dye studies can be found in

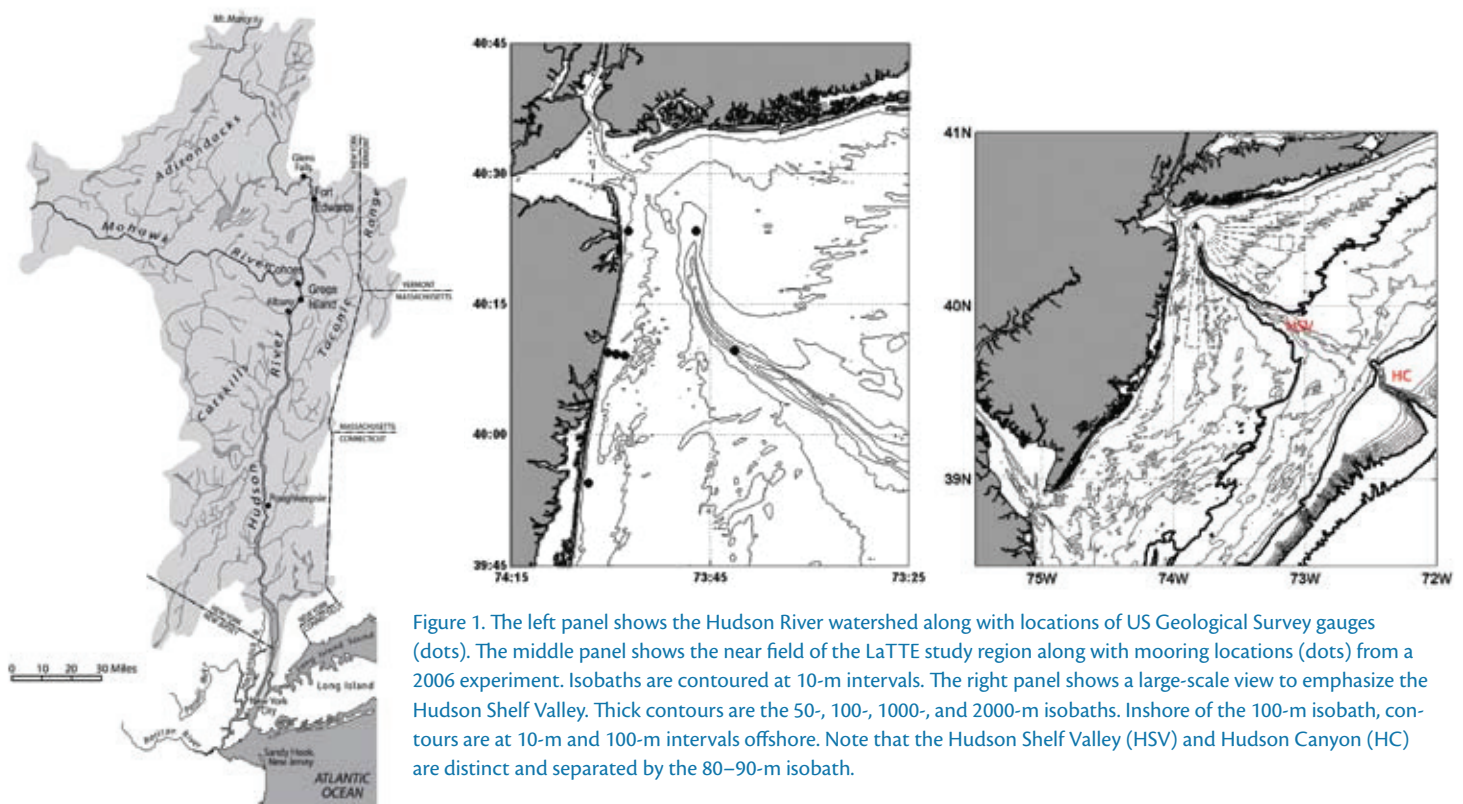


Figure 1. The left panel shows the Hudson River watershed along with locations of US Geological Survey gauges (dots). The middle panel shows the near field of the LaTTE study region along with mooring locations (dots) from a 2006 experiment. Isobaths are contoured at 10-m intervals. The right panel shows a large-scale view to emphasize the Hudson Shelf Valley. Thick contours are the 50-, 100-, 1000-, and 2000-m isobaths. Inshore of the 100-m isobath, contours are at 10-m and 100-m intervals offshore. Note that the Hudson Shelf Valley (HSV) and Hudson Canyon (HC) are distinct and separated by the 80–90-m isobath.



Houghton et al. (in review). All observations were conducted within the Rutgers University Coastal Ocean Observing Laboratory (RU COOL), which facilitated the field effort by providing real-time data from gliders, Coastal Ocean Dynamics Applications Radar (or CODAR, a high-frequency radar system used to measure the surface currents of the coastal ocean), and satellite imagery to guide ship operations. The observatory also provided large-scale context to interpret the shipboard and moored observations by extending the observations in both space and time, such as described in Castelao et al. (2008a, b). Finally, LaTTE included physical and biogeochemical modeling (Choi and Wilkin, 2007; Cahill et al., 2008; Zhang et al., in review-a, b), which was essential in providing a coherent framework to characterize annual variability in the plume's structure and transport pathways. Modeling efforts used the Regional Ocean Modeling System (ROMS; [http://](http://www.myroms.org)

[www.myroms.org](http://www.myroms.org)) that was forced by tides, winds, and remotely forced flows at the offshore boundaries as specified by Lentz (2008). Horizontal resolution in the model was approximately 1 km and covers the New Jersey coastal area from eastern Long Island south to Delaware Bay, and offshore to approximately the 70-m isobath. Details of the model setup and numerics within can be found in Zhang et al. (in review-a, b) and Choi and Wilkin (2007).

The three-year field effort emphasized significant yet coherent variability of the structure and trajectory of the Hudson outflow. Variability was characterized by various modes of the plume's structure that were comprised of a blend of surface-advected coastal currents, bulge formation, and the response of these features to wind forcing.

In 2004, we conducted two dye studies. In one of the studies, we injected dye in a surface-advected coastal current that formed along the New Jersey

coast (Figure 2a). The behavior of this current was largely consistent with classic theory. The downshelf speed of the current, drifter, and dye was close to the internal wave speed,  $c = \sqrt{g'h}$ , where  $h$  is the thickness of the coastal current and  $g'$  is reduced gravity and equal to  $g\Delta\rho/\rho$ , where  $g$  is gravity,  $\Delta\rho$  is the density difference between the plume and ambient shelf waters, and  $\rho$  is the density of the shelf waters. Also consistent with theory, the plume's width was approximately one internal Rossby ( $R=c/f$ ) radius wide, where  $f$  is the local Coriolis frequency. The coastal current formed in response to downwelling-favorable winds. During subsequent upwelling winds, the plume was arrested, advected offshore, and eventually mixed away into the coastal ocean. This reversal is evident in the drifter trajectory (Figure 2a). Note that discontinuity in drifter trajectory occurred because we moved the drifter back toward the center of the dye. In general, the response of

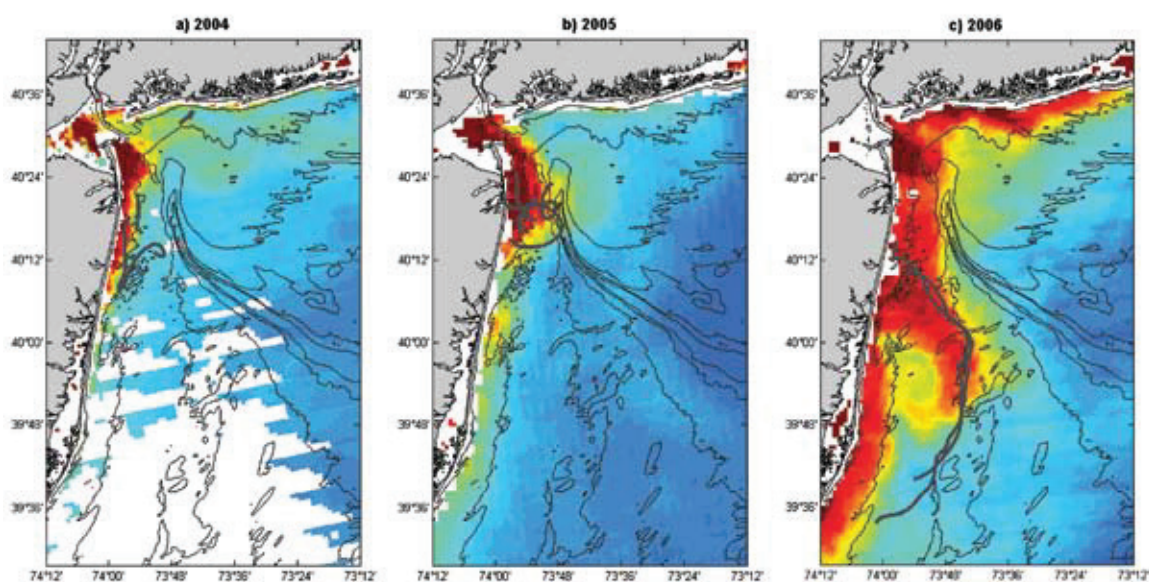


Figure 2. Sea-surface temperature (SST) images from each of the three LaTTE field seasons along with drifter trajectories (thick dark lines). Plume water is warmer (red) relative to cool (blue) offshore waters. Isobaths (thin contours) are at 10-m intervals.

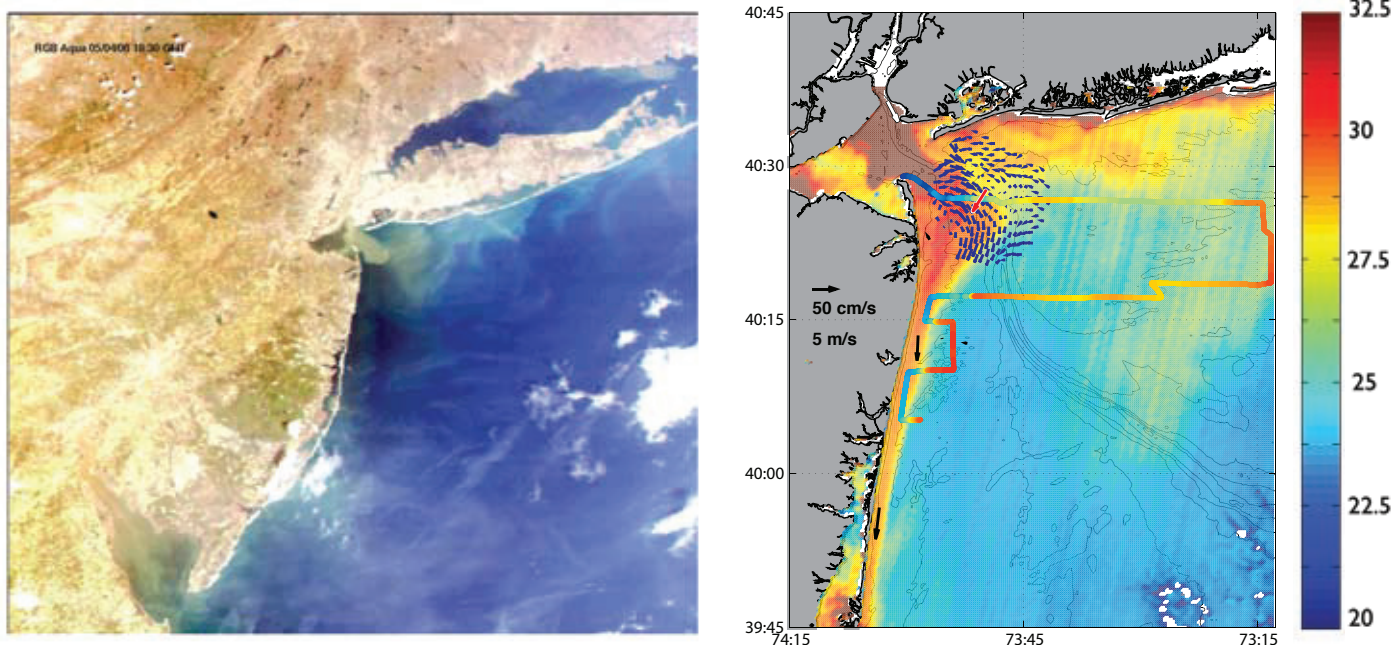


Figure 3. (Left panel) RGB (red-green-blue) image from April 5, 2005, during peak river discharge. Note that the plume is exiting the estuary and heading to the east toward Long Island. (Right panel) Image obtained from the Moderate Resolution Imaging Spectroradiometer (MODIS) on April 9 for absorption at 448 nm; the color scale is relative, with red representing high absorption and blue representing low absorption. Blue arrows (top left in colored area) show the Coastal Ocean Dynamics Applications Radar (CODAR) field, black arrows (near coast) from shelf moorings, white arrow (in outflow region) from NOAA mooring at the Narrows; the red vector (roughly middle of blue arrows) represents winds from Ambrose. The color bar is for surface salinity from the ship track shown in the figure. All current data have been low-pass filtered.

the plume to upwelling winds was consistent with Fong and Geyer (2001) and is discussed in more detail in Houghton et al. (in review).

In 2005, we conducted a field effort immediately following a 10-year flood in the Hudson River Basin, with shipboard surveys commencing four days after the peak in river discharge on April 5 at just under  $8000 \text{ m}^3 \text{ s}^{-1}$ . The plume's behavior during the 2005 field effort was radically different than in 2004 and was characterized primarily by bulge formation, although both coastal currents and plumes driven eastward by wind along the Long Island shore were also evident. For example, immediately following the peak discharge on April 5, 2005, winds were strongly upwelling favorable and the plume was advected eastward and

toward the Long Island coast (Figure 3a). A CTD survey on April 9 revealed that a lens of brackish water extended 70 km east of the outflow and along Long Island's south shore; the lens is also evident in satellite imagery (Figure 3b). A series of satellite images and shipboard surveys indicated that this plume eventually moved south and was found to reside along the western side of the HSV on April 13 (Figure 4). The April 9–10 survey also revealed that a bolus of freshwater extended out of the Hudson and that a surface-advected coastal current emanated from it and flowed along the New Jersey coast (Figure 3b). As was the case in 2004, the downshelf propagation speed of the front, as inferred from consecutive satellite imagery and moored data, was close to the internal

wave speed. Moreover, the cross-shore dynamics were largely geostrophic, which implies that the freshwater transport is proportional to  $(g'h)^2$  (Fong and Geyer, 2002).

The transport of freshwater in the coastal current, however, was only one-third to one-half of the transport of freshwater to the coastal ocean (Chant et al., 2008). Subsequently, most of the freshwater entering the coastal ocean recirculated in a growing bulge at the mouth of the estuary. The retention of estuarine fluid in the bulge region was confirmed by dye releases and drifters that were deployed in new plume water and remained in the vicinity of the outflow for approximately one week (Figure 2b). The growth of this bulge was apparent in the April 13–14



survey, which showed a thin bolus of chlorophyll-rich brackish water extending eastward (Figure 4). Estimates of the freshwater volume of this bolus indicate that most of the discharge that had occurred since its inception on April 9 remained in the bulge with only a small fraction transported away in the coastal current (Chant et al., 2008). Moreover, chemical tracers suggest that the fluid in the coastal current is fed by aged fluid in the bulge that has undergone significant biogeochemical processing. For example, while nitrate levels remained elevated in the outflow during this event, nitrate levels quickly fell to less than  $2\ \mu\text{M}$  in the coastal current. Moline et al. (this issue) discuss the biological and chemical consequences of this bolus and conceptualize the bulge as a chemostat fed by estuarine waters that in turn feed biogeochemically processed waters to the coastal current.

The bulge's structure was also modified by shelf circulation as suggested by

Fong and Geyer (2002). In particular, during upwelling-favorable winds, a jet develops that transfers freshwater from the bulge toward the shelf break along the inshore side of the HSV. This rapid cross-shelf advection of the plume was documented following a second "10-year flood event" during summer 2006 (Castelao et al., 2008a). Glider data revealed that following the flood event, freshwater was transported over 100 km from the coast in fewer than two weeks. Analysis of surface current data revealed a transport pathway that advected the outflow cross-shelf. This pathway was associated with a cross-shelf jet that resides along the 40–50-m isobath on the inshore side of the HSV. The timing of this jet was correlated with persistent upwelling winds and was evident in overlaid surface velocity data, satellite imagery, and drifter trajectories (Figure 5) that show cool water from the Long Island coast extending offshore in a jet

that resides along the 40–50-m isobath (Figure 5, left panel). Note that the drifter trajectory was from July 26–30 while the satellite and CODAR images are from August 11. Nevertheless, both show the jet originates along the 40–50-m isobath on the inshore side of the HSV. Chlorophyll-*a* imagery suggests that the jet entrained biomass from the bulge region and advected it cross shelf along the inshore side of the jet (Figure 5b). Late spring/early summer shelfwide freshening was also observed in glider data from previous years (Castelao et al., 2008a; Chant et al., 2008); this seasonal shelfwide freshening is driven by the seasonal transition from downwelling- to upwelling-favorable winds (Castelao et al., 2008b) associated with springtime development of the Bermuda high. These springtime southerly winds warm the continent and melt the watershed's snow-pack; thus, the seasonal wind reversal tends to coincide with the spring freshet.

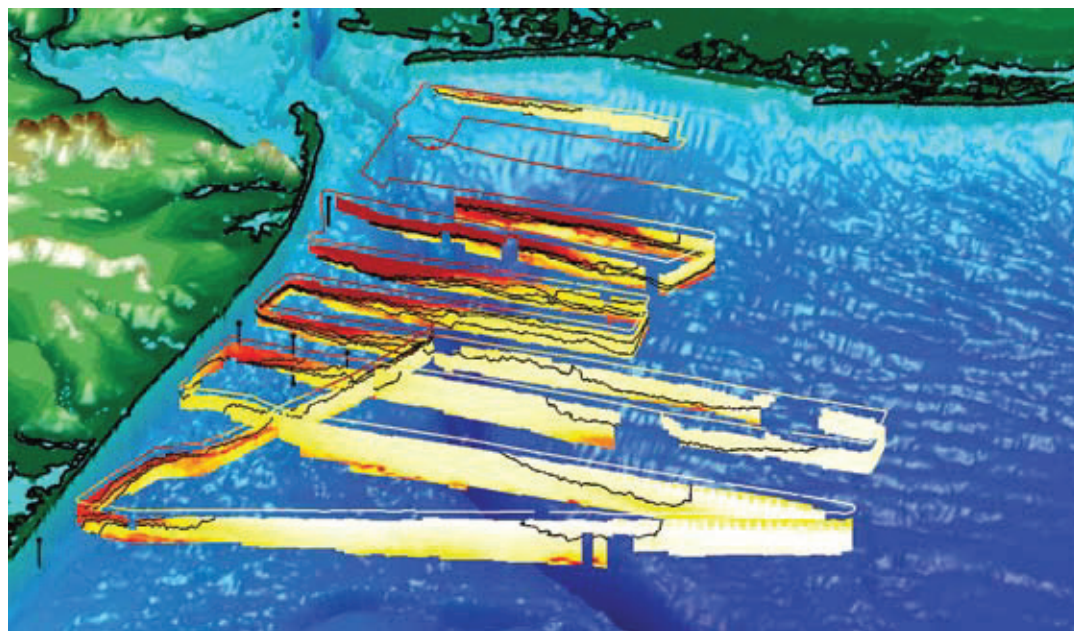


Figure 4. Contours are the 27, 28, and 29 isohalines. Color is chlorophyll *a* on a relative scale, with red representing high values; the bulge is characterized by high chlorophyll *a* values. The old plume over the Hudson Shelf Valley is devoid of plankton but less than 29. Note that the single isohaline on the offshore side of the last four sections is the 29 isohaline.



Consequently, the midshelf freshwater pathway likely represents a robust mechanism that rapidly transports the spring freshet water across the continental shelf to the shelfbreak. We note that climate models are sensitive to the details of how freshwater mixes into the deep ocean (Garvine and Whitney, 2006); the timing between a watershed's freshet and seasonal wind patterns likely plays an important role in this process.

Although the summer 2006 event described above occurred during a high-discharge event, the major LaTTE field efforts in 2006 followed a moderate-discharge event, with flows peaking at  $1500 \text{ m}^3 \text{ s}^{-1}$ . The plume structure was again different from previous years and characterized by a remarkably steady feature that consisted of a coastal current extending from Sandy Hook approximately 30 km south. However, this coastal current veered offshore (bypassing our central mooring array!)

and flowed downshelf as a detached jet of freshwater (Figure 2c). Mean current velocities in the jet were to the south at  $25\text{--}30 \text{ cm s}^{-1}$ , while surface currents at the inshore mooring were to the north at speeds up to  $\sim 20 \text{ cm s}^{-1}$  and salinities of 28–29 (Figure 6c). A more detailed view of the flow structure is apparent in shipboard ADCP data (Figure 6a) and satellite imagery (Figure 2c), which indicated that the flow structure involved recirculation of plume water. This feature's stability was apparent in a suite of satellite imagery and shipboard surveys. For example, the satellite image in Figure 2c taken on April 28 shows a clear separation of plume waters (red in the image) just north of the mooring array and a recirculation to the south and offshore. An ADCP survey on May 2–3 (Figure 6a) picked up this jet, and indicated that its offshore veering was in approximately the same location as the satellite imagery four days earlier.

Moreover, the drifter trajectories between May 4 and 8 closely followed this jet, further emphasizing its steadiness. Although current speed in the jet, as indicated by the speed of the drifters, modulated with wind forcing (Figure 6c), the offshore jet remained evident in a final ADCP survey on May 10 (not shown).

In summary, the LaTTE field studies revealed significant variability in the structure of the Hudson outflow. We classify this variability into three distinct modes. The first mode is the classic surface-advected coastal current that propagated down the New Jersey coast at the internal wave speed. The coastal-current mode tends to occur during low to moderate discharge with downwelling-favorable winds. Although we never observed a bottom-attached coastal current, we suspect that one would develop under strong northerly winds. Upwelling winds of  $5 \text{ m s}^{-1}$  easily arrested this plume, advected it offshore, and mixed

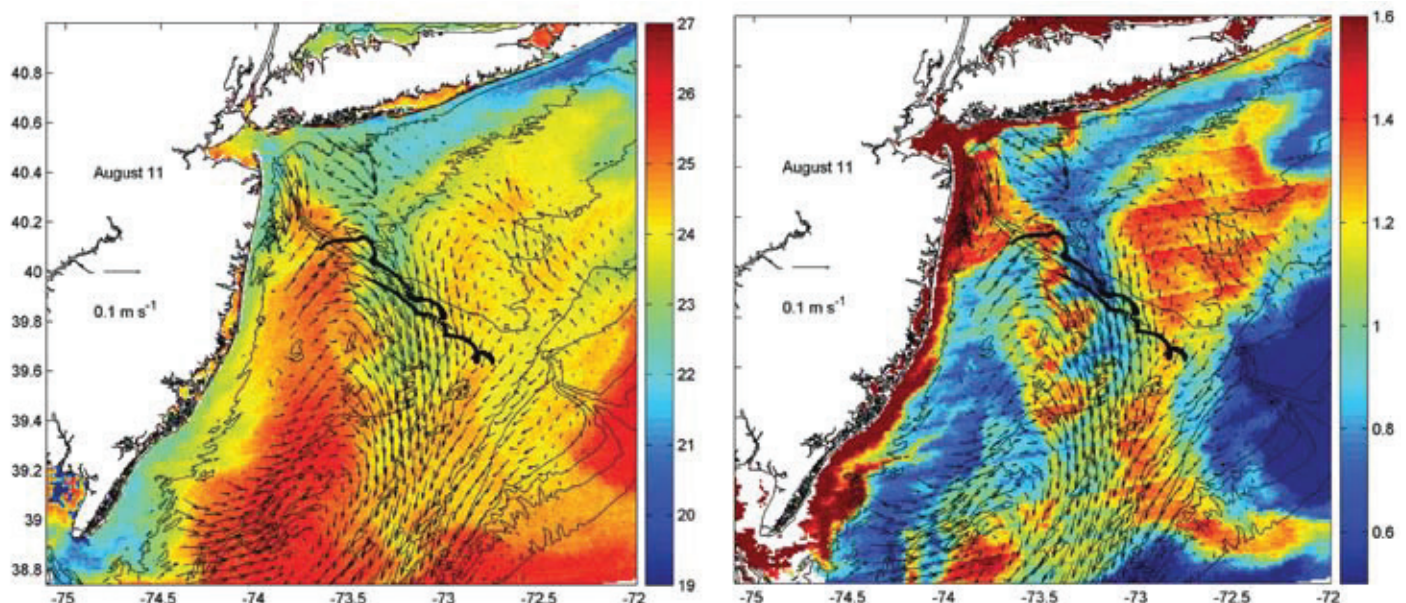


Figure 5. Both panels show surface currents weighted with a one-sided exponential filter as described in Castelao et al. (2008a). Left panel shows SST while the right panel shows chlorophyll *a* ( $\text{gm C m}^{-3}$ ). Both images are from August 11, 2006. Also shown are drifter trajectories from July 26–28, 2006. Together, the images suggest an offshore transport of cold water and high chlorophyll *a* by the midshelf jet just inshore of the Hudson Shelf Valley.

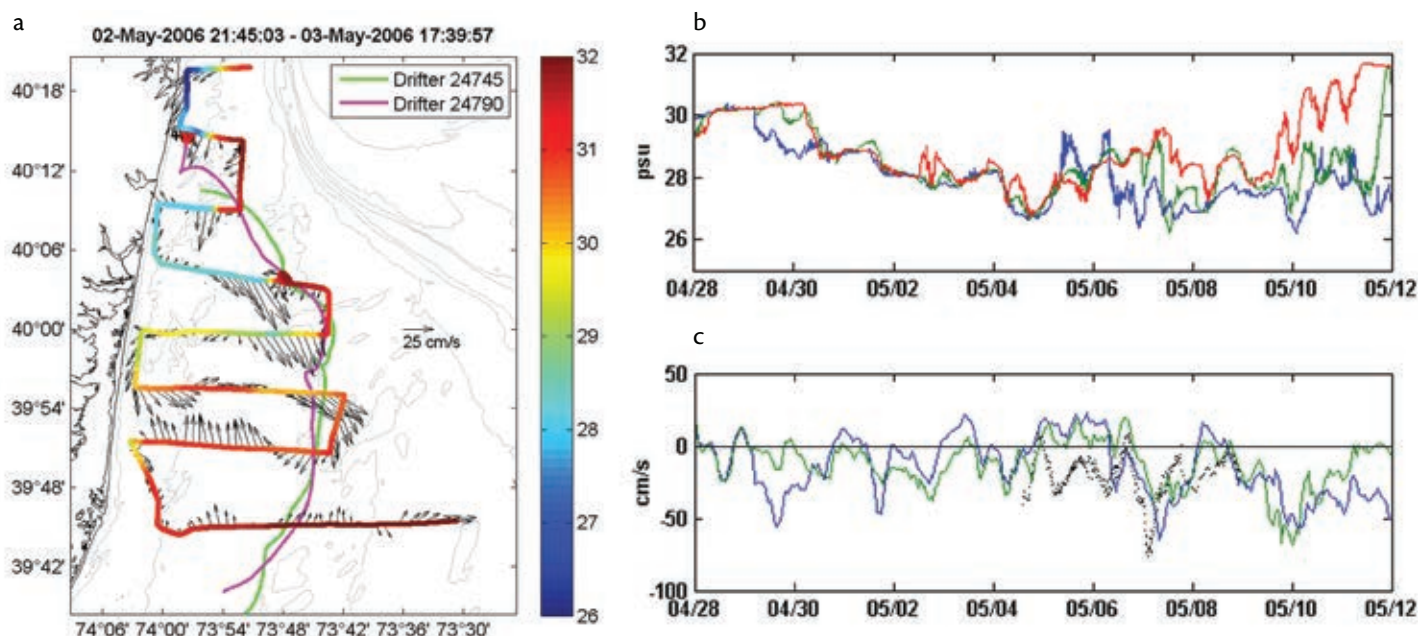


Figure 6. (a) Currents 3.5 m below surface from the May 2–3 shipboard survey along with a drifter trajectory between May 4–8. Note that the drifter track is the same as shown in Figure 2c. (b) Surface salinity from the central mooring array. Top surface salinity from inshore (blue), middle (green), offshore (red). (c) Alongshore surface velocities from inshore (blue) and offshore moorings (green) and alongshore velocity of drifters (dashed). Positive velocities are to the north.

it into the coastal ocean as suggested by the modeling studies of Fong and Geyer (2001) and Choi and Wilkin (2007). A second mode of outflow was characterized by bulge formation, which occurred during moderate to high discharge and weak or upwelling-favorable wind forcing. With upwelling winds, the bulge became compressed along the Long Island coast and extended eastward. Once formed, the bulge's structure was strongly modified by wind forcing and shelf circulation with a particularly rapid cross-shelf transport pathway associated with a midshelf jet. Finally, a third mode was observed that consisted of a coastal current with a downstream recirculating region. Next, we present numerical simulations of the Hudson outflow to provide a more detailed characterization of the spatial and temporal structure of the plume, of the processes that control this structure, and ultimately the freshwater transport pathways.

## NUMERICAL MODELING OF THE PLUME

The variability we observed in the plume's structure raises the following questions: To what extent is the observed variability representative of its typical behavior? Alternatively expressed: What is the relative importance of each "mode" of outflow and what is the seasonal variability of these modes and of these transport pathways? To address these questions in greater detail, we ran numerical simulations, first in a process study (Choi and Wilkin, 2007) and later with realistic forcings (Zhang et al., in review–a, b). The process study related variability in the model plume's structure to variations in river discharge and wind forcing and focused on the near-field plume dynamics while the realistic simulations characterized the plume's seasonal climatology based on a three-year simulation.

Choi and Wilkin (2007) explored

the sensitivity of the plume structure to variations in river discharge with a set of simulations with low ( $500 \text{ m}^3 \text{ s}^{-1}$ ) and high ( $3000 \text{ m}^3 \text{ s}^{-1}$ ) river discharge. Sensitivity to winds was assessed by forcing each of the discharge cases with constant winds from each of the four compass directions. Details of the forcing and model setup can be found in Choi and Wilkin (2007). In general, these simulations emphasized the tendency for bulge formation to occur under high discharge, and the tendency for sensitivity of the plume to wind forcing under both high and low flow conditions. Moreover, the simulations revealed that in addition to the direct action of the wind on the plume, the ability of the estuary to store and release freshwater under variable wind forcing modified plume structure. For example, for the low (and constant) river discharge case, more freshwater exited the estuary when winds blew from the west



than from the east for several days after the onset of steady winds. Although the estuary's outflow must eventually match the prescribed freshwater fluxes on a 2–5-day time scale, there can be significant mismatch because the estuary tends to store water while winds blow from the east and release water when winds blow from the west. This was noted by Lerczak et al. (2006), who found that freshwater flux measured by a mooring array in the lower Hudson River varied between  $200 \text{ m}^3 \text{ s}^{-1}$  upstream and  $2000 \text{ m}^3 \text{ s}^{-1}$  downstream during a time period when river flow was relatively constant at  $\sim 500 \text{ m}^3 \text{ s}^{-1}$ . Subsequently, the transport of freshwater from the estuary to the coastal ocean is strongly modified by meteorological forcing, and has two implications. First, because bulge formation tends to increase with discharge, pumping of the outflow by meteorological forcing will augment bulge formation. Second, it emphasizes

the necessity for models to resolve both estuarine and coastal geometry in modeling river plumes because the ability of the estuary to store freshwater is a function of the estuary's geometry.

Choi and Wilkin's (2007) model results emphasized that bulge formation became more prominent during high-discharge events as anticipated by Fong and Geyer (2002). Choi and Wilkin (2007) also demonstrated the sensitivity of the plume to winds under high-discharge events. Moreover, the modeled plume structure was similar to the outflow structure we observed in 2005. For example, upwelling winds transport freshwater along the Long Island coast while onshore and/or downwelling winds compress the bulge against the New Jersey coast, causing a coastal current to leak out. Choi and Wilkin's (2007) simulations also show the estuarine outflow forming a clockwise jet around the outer edge of the bulge (Figure 7).

When the jet reaches the coastal wall, it bifurcates, with a fraction of the jet feeding the coastal current and the remaining fluid feeding bulge formation. Implications of the model predictions are that in the absence of variable wind forcing, the coastal current would be essentially fed with new estuarine waters while the bulge would contain a mixture of new and old estuarine waters.

The aforementioned model runs were forced with steady winds; thus, while the bulge may be unsteady (i.e., growing in time), its growth is monotonic. In contrast, variable wind forcing would cause the bulge's structure to fluctuate, moving to the east during upwelling and/or eastward winds, and then compressing it along the New Jersey coast during downwelling and/or westward winds. As this fluctuation occurs, the bulge would be filled with fluid during its eastward expansion in response to upwelling winds, while downwelling winds would

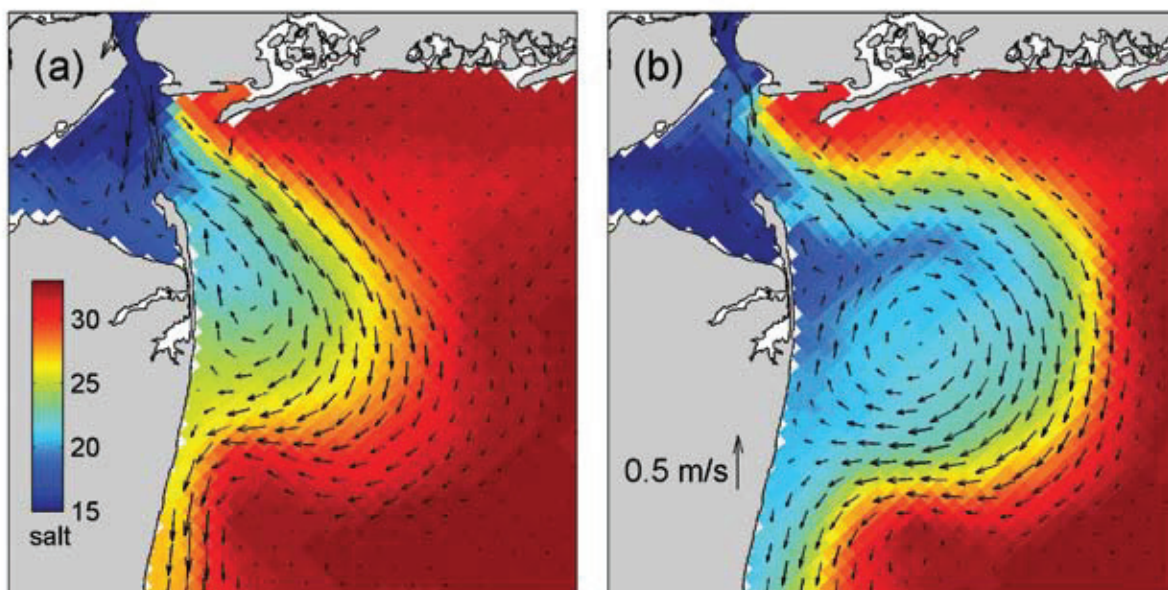


Figure 7. Surface salinity (color) and velocity from a model run without wind forcing and a discharge at  $3000 \text{ m}^3 \text{ s}^{-1}$ . Panel (a) is at model day 13, and panel (b) is day 20.



compress the bulge against the coast causing a coastal current to leak out of it. Chant et al. (2008) clearly identified such fluctuations in coastal current transport in moored data both at the 2–5-day time scale and at the diurnal frequency. Therefore, this variable wind forcing, and thus bulge structure, will supply the coastal current with biogeochemically processed water from the bulge rather than new estuarine waters that circulate around the bulge's perimeter. The tendency for the coastal current to be supplied by aged bulge water was apparent in biogeochemical data as noted by Moline et al. (this issue).

Multiyear numerical simulations by Zhang et al. (in review–a, b) characterized both shelfwide and seasonal freshwater transport pathways. These simulations also captured the modes of plume structure that we observed in the field and in observatory data (i.e., coastal current formation and unsteady bulge formation). Moreover, these model runs characterized the modes' seasonal variability and placed them in context with the shelfwide dispersal of freshwater that is accomplished by the three freshwater transport pathways: the New Jersey coastal current pathway, the Long Island upwelling/bulge pathway, and the

midshelf pathway. These results are concisely described by Figure 8a–c, which depicts the freshwater transport during model year 2005 and 2006 across an arc 100 km south of the Hudson outflow that runs between the New Jersey (km 0) and the Long Island (km 200) coasts (arc 5 on Figure 8d and e). A clear seasonality to the pathway is evident, with freshwater pathways largely confined to the New Jersey coast during the winter months, and with a smaller pathway along the Long Island coast. In contrast, during the summer months, freshwater transport is focused along the midshelf pathway westward of the HSV. This temporal

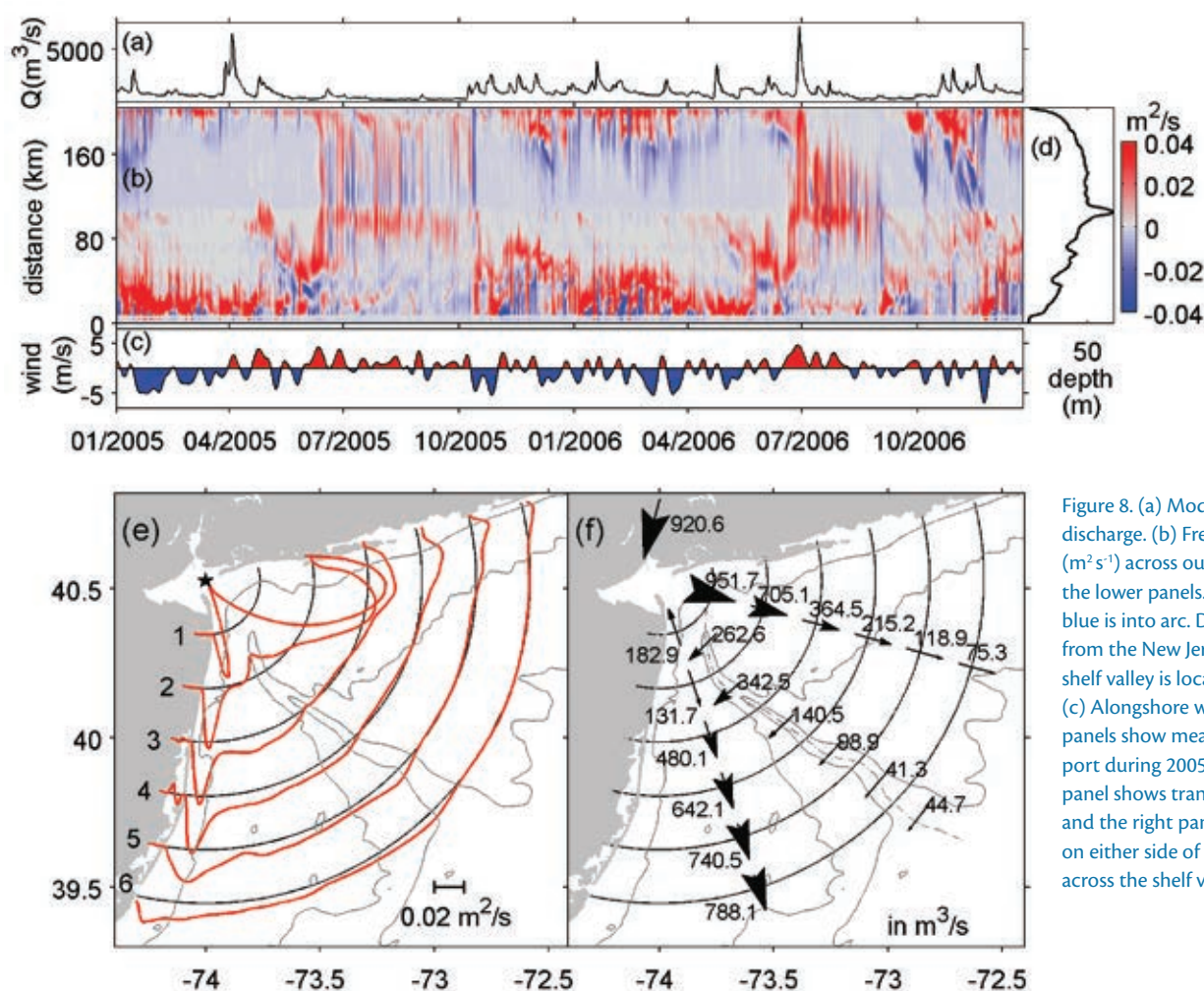


Figure 8. (a) Model-prescribed river discharge. (b) Freshwater transport ( $\text{m}^2/\text{s}$ ) across outer arc 5 shown in the lower panels. Red is out of arc and blue is into arc. Distance is kilometers from the New Jersey shore. The shelf valley is located around km 90. (c) Alongshore winds. The lower two panels show mean freshwater transport during 2005 and 2006. The left panel shows transport per unit width, and the right panel shows transport on either side of the shelf valley and across the shelf valley.

transition between the coastal pathways and the midshelf pathway coincides with the seasonal change in wind from downwelling favorable during the winter months to upwelling favorable during the summer months, and is similar to results obtained from observatory data described in Castelao et al. (2008a).

In addition, the modeled Long Island and New Jersey coastal currents are frequently associated with both upshelf and downshelf freshwater fluxes, as indicated by the red/blue banding in Figure 8b, such as along the New Jersey coastline (km 0–20) early in 2006. These fluxes are indicative of a clockwise recirculation of freshwater along both coasts. Along the New Jersey coast, this recirculation is consistent with observations, such as the quasi-stationary eddy we observed in 2006 (Figures 2c and 6a), with freshwater moving downshelf on the offshore side and freshwater moving upshelf on the inshore side.

Recirculation along the Long Island coast transports freshwater to the east at the coast and recirculates it back to the west offshore. Although this recirculation is consistent with bulge formation, it is also related to an interaction of the bulge with remotely forced downshelf flows on the shelf that increase in strength with distance from the bight apex (Zhang, et al., in review–a, b). The mechanism driving recirculation along the New Jersey coast is unclear and is currently under investigation. However, one important consequence of New Jersey coastal recirculation is that it appears to significantly reduce the speed of freshwater transport downshelf, which, when coupled to a range of time scales associated with biogeochemical processing of material in the plume, is

likely to impact the fate and transport of riverborne material. This slow downshelf propagation of the recirculation may explain the 40-day lag observed by Yankovsky and Garvine (1998) between river discharge and the appearance of freshwater 100 km to the south because coastal currents, traveling at the internal wave speed, would arrive in a few days. We further note that while many of these recirculation events along the New Jersey coast appear to be initiated by upwelling, some of them are not. For example, the New Jersey recirculation event that we observed in 2006 (Figure 6) occurred during persistent downwelling winds and did not appear to be initiated by upwelling winds. It may be related to impulsive discharge (Yankovsky et al., 2004) or associated with lateral shears that develop across the HSV (Harris, et al., 2003).

Together, these transport pathways disperse freshwater across the New York Bight. This dispersal is characterized by model estimates of the mean freshwater flux across a series of concentric arcs centered at Sandy Hook (Figure 8d, e). The mean freshwater transport structure emphasizes the importance of bulge formation. For example, the time-mean freshwater transport along the New Jersey coast at Sandy Hook is actually upshelf and opposed to the expected downshelf transport (Figure 8e). Model simulations indicate that while tides augment this recirculation, recirculation persists even in the absence of tides. To the east, the freshwater flux along the Long Island coast weakens and recirculates back westward and over the shelf valley before heading cross-shelf along the 40–50-m isobath. Freshwater transport along the New Jersey coast occurs

through a rapid jet; however, the maximum value is distinctly off the coast due to the frequent coastal recirculation that drives upshelf freshwater transport near the coast. Freshwater transport across the outer arcs is relatively evenly distributed west of the HSV. However, this distribution is likely due to ensemble averaging rather than a blending of coastal and midshelf pathways. Interestingly, the freshwater transport is sharply cut off at the shelf valley and appears to be related to remotely forced flows (Zhang et al., in review–a, b). This cutoff also suggests that dissolved material exiting the Hudson River, with reactive time scales of a week or longer, will be distributed primarily to the west of the HSV.

## SUMMARY

There were several surprising physical results from the LaTTE field and modeling efforts. First, although coastal currents were frequently observed in the near field, freshwater dispersal was largely accomplished through bulge formation. Indeed, modeling efforts revealed that freshwater transport in a section ~ 10 km from the mouth was *toward* the estuary and fed a mean freshwater recirculation that takes place over a 50–100 km region near the mouth. This recirculation tends to drive the new estuarine discharge toward Long Island and thus water quality in these inland bays may frequently be more impacted by the harbor's discharge, perhaps even more so than the communities along New Jersey's northern shore. We also found that the outflow appeared to be influenced by the underlying bathymetry, which is dominated by the HSV. This interaction is not direct, but rather the plume is interacting with barotropic shelf flows that are

directly steered by bathymetry, such as strong lateral shears that develop across the HSV (Harris et al., 2003).


Although many of the aspects of the Hudson's outflow are consistent with modeling investigations (Fong and Geyer, 2002; Choi and Wilkin, 2007), results from this study together with recent results from the River Influences on Shelf Ecosystems (RISE) project (Kudela et al., this issue; Hickey et al., this issue; Samelson et al., this issue) provide perhaps the most direct observational evidence of bulge formation that heretofore was studied primarily with numerical models and laboratory experiments. Results also emphasized the important role of bulge formation in driving cross-shelf transport of freshwater. We note that in the far field, plume structure appears as a wide coastal current. Indeed, the distribution of freshwater transport in the outer arc in Figure 8d is characterized by broad features as is the cross-shore structure of the annual mean salinity based on glider data (Castelao et al., 2008b). However, the freshwater pathway that produced the broadly distributed freshwater transport pathway was not solely the result of upwelling winds acting on a coastal current but also was significantly influenced by bulge formation and rapid cross-shelf advection associated with a cross-shelf jet along the 40–50-m isobath (Castelao et al., 2008a). Although the dynamics that underlie this cross-shelf jet remain elusive, it appears to be initiated by persistent upwelling winds (Castelao et al., 2008a). Several other studies have noted frontal systems in this region (Bumpus, 1973; Biscaye et al., 1994; Ullman and Cornillon, 1999), and analysis of long-term hydrographic data from the Mid-

Atlantic Bight also revealed a shelfwide freshening that was localized in the New York Bight region (Mountain, 2003).

Finally, the tendency for the Hudson's outflow to recirculate near the apex rather than rapidly advect away in a coastal current has significant implications for biogeochemical pathways. For example, nutrient uptake and primary production was so rapid in this region (Moline et al., this issue) that by the time the outflow reached the coastal current, primary production was nutrient limited, and high phytoplankton biomass in the bulge crashed and settled to the bottom. Furthermore, temporary retention of material in the apex region also appears to impact the fate and transport of contaminant metals (Moline, this issue). Thus, material that is rapidly cycled in the plume may quickly settle out into the landward-flowing lower layer where it may be transported back into the estuary, increasing the estuary's trapping efficiency of both terrestrial and biogenic particulate matter. On the other hand, material that remains dissolved in the plume for weeks will be rapidly mixed across the shelf.

## ACKNOWLEDGEMENTS

We thank two anonymous reviewers for their comments. This study was supported by the National Science Foundation through grant OCE-0238957. We thank the crew and captains of R/V *Cape Hatteras* and R/V *Oceanus* for their efforts and also the crew at Millers Launch. We also thank the dedicated members of RU COOL, with particular gratitude to Chip Haldeman, who led the mooring deployment and served many roles aboard R/V *Oceanus*. The observatory was supported

by the Office of Naval Research, National Science Foundation, National Oceanographic Partnership Program, National Oceanic and Atmospheric Administration, Department of Homeland Security, Department of Defense, Environmental Protection Agency, and National Aeronautics and Space Administration. 

## REFERENCES

*Editor's Note: Oceanography does not usually permit citation of articles that are in review; however, because of the rapidly advancing nature of this issue's topics, we are making an exception. Updates on the status of manuscripts cited as in review here will be posted on the CoOP Web site (<http://www.skio.usg.edu/coop>).*

- Avicola, G., and P. Huq. 2003. The characteristics of recirculating bulge region in coastal buoyant outflows. *Journal of Marine Research* 61:435–463.
- Biscaye, P.E., C.N. Flagg, and P.G. Falkowski. 1994. The Shelf Edge Exchange Processes experiment, SEEP-II: An introduction to hypotheses, results and conclusions. *Deep Sea Research Part II* 41:231–252, doi:10.1016/0967-0645(94)90022-1.
- Bumpus, D.F. 1973. A description of the circulation on the continental shelf of the east coast of the United States. *Progress in Oceanography* 6:111–157.
- Cahill, B., O. Schofield, R. Chant, J. Wilkin, E. Hunter, S. Glenn, and P. Bissett. 2008. Dynamics of turbid buoyant plumes and the feedbacks on near-shore biogeochemistry and physics. *Geophysical Research Letters* 35(L10605), doi:10.1029/2008GL033595.
- Castelao, R., O. Schofield, R.J. Chant, and J. Kohut. 2008a. Cross-shelf transport of freshwater on the New Jersey Shelf. *Journal of Geophysical Research* 113(C07017), doi:10.1029/2007JC004241.
- Castelao, R., O. Schofield, S. Glenn, R. Chant, J. Wilkin, and J. Kohut. 2008b. Seasonal evolution of hydrographic fields in the Central Middle Atlantic Bight. *Geophysical Research Letters* 35(L03617), doi:10.1029/2007GL032335.
- Chant, R.J., S.M. Glenn, E. Hunter, J. Kohut, R.F. Chen, R. Houghton, J. Bosch, and O.M. Schofield. 2008. Bulge formation of a buoyant river outflow. *Journal of Geophysical Research* 113(C01017), doi:10.1029/2007JC004100.
- Choi, B.J., and J.L. Wilkin. 2007. The effect of wind on the dispersal of the Hudson River Plume. *Journal of Physical Oceanography* 37:1,878–1,888.
- Fong, D.A., and W.R. Geyer. 2001. Response of a river plume during an upwelling favorable wind event.



- Journal of Geophysical Research* 106:1,067–1,084.
- Fong, D.A., and W.R. Geyer. 2002. The alongshore transport of freshwater in a surface-trapped river plume. *Journal of Physical Oceanography* 32:957–972.
- Garvine, R. 1987. Estuary plumes and fronts in shelf waters: A layer model. *Journal of Physical Oceanography* 17:1,877–1,896.
- Garvine, R. 1999. Penetration of buoyant coastal discharge onto the continental shelf: A numerical model experiment. *Journal of Physical Oceanography* 29:1,892–1,909.
- Garvine, R.W., and M.M. Whitney. 2006. An estuarine box model of freshwater delivery to the coastal ocean for use in climate models. *Journal Of Marine Research* 64:173–194.
- Harris, C.K., B. Butman, and P. Traykovski. 2003. Winter-time circulation and sediment transport in the Hudson Shelf Valley. *Continental Shelf Research* 23:801–820.
- Horner-Devine, A.R., D.A. Fong, S.G. Monismith, and T. Maxworthy. 2006. Laboratory experiments simulating a coastal river outflow. *Journal of Fluid Mechanics* 555:203–232.
- Houghton, R.W., C.E. Tilburg, R.W. Garvine, and A. Fong. 2004. Delaware River plume response to a strong upwelling-favorable wind event. *Geophysical Research Letters* 31(L07302), doi:10.1029/2003GL018988.
- Houghton, R.W., R.J. Chant, A. Rice, and C. Tilburg. In review. Salt flux into coastal river plumes: Dye studies in the Delaware and Hudson River outflows.
- Lentz, S.J. 2008. Observations of the mean circulation over the middle Atlantic Bight continental shelf. *Journal of Physical Oceanography* 38:1,486–1,500.
- Lerczak, J., W.R. Geyer, and R.J. Chant. 2006. Mechanisms driving the time-dependent salt flux in partially stratified estuary. *Journal of Physical Oceanography* 36(12):2,283–2,298.
- Mountain, D. 2003. Variability in the properties of shelf water in the Middle Atlantic Bight 1977–1999. *Journal of Geophysical Research* 108(C1), 3014, doi:10.1029/2001JC001044.
- Nof, D. 1988. Eddy-wall interactions. *Journal of Marine Research* 46:527–555.
- Rennie, S.E., and S. Lentz. 1999. Observations of a pulsed buoyancy current downstream of Chesapeake Bay. *Journal of Geophysical Research* 104:18,228–18,240.
- Ullman, D., and P. Cornillon. 1999. Satellite-derived sea surface temperature fronts on the continental shelf off the northeast US coast. *Journal of Geophysical Research* 104(C10):23,459–23,478.
- Whitney, M.M., and R.W. Garvine. 2005. Wind influences on a coastal buoyant outflow. *Journal of Geophysical Research* 110(C0314), doi:10.1029/2003JC002261.
- Yankovsky, A., and D.C. Chapman. 1997. A simple theory for the fate of buoyant coastal discharges. *Journal of Physical Oceanography* 27:1,386–1,401.
- Yankovsky, A., and R.W. Garvine. 1998. Subinertial dynamics on the inner New Jersey Shelf during the upwelling season. *Journal of Physical Oceanography* 28:2,444–2,458.
- Yankovsky, A.E., B.M. Hickey, and A.K. Munchow. 2004. The cyclonic turning and propagation of buoyant coastal discharge along the shelf. *Journal of Marine Research* 33:1,954–1,966.
- Zhang, G., J. Wilkin, and R.J. Chant. In review-a. Modeling mean dynamics and freshwater pathways in the New York Bight.
- Zhang, W.G., J.L. Wilkin, J.C. Levin, and H.G. Arango. In review-b. An adjoint sensitivity study of buoyancy and wind-driven circulation on the New Jersey inner shelf.

*Article*

# HF Radar Sea-echo from Shallow Water

**Belinda Lipa** <sup>1,\*</sup>, **Bruce Nyden** <sup>2</sup>, **Don Barrick** <sup>2</sup> and **Josh Kohut** <sup>3</sup>

1 Codar Ocean Sensors, 125 La Sandra Way, Portola Valley, CA 94028 USA

2 Codar Ocean Sensors, 1914 Plymouth Street, Mountain View, CA 94043 USA;

E-mail: bruce@codar.com; don@codar.com

3 Coastal Ocean Observation Lab., Rutgers University, New Brunswick, NJ 08901 USA; E-mail:

kohut@marine.rutgers.edu

\* Author to whom correspondence should be addressed; E-mail: blipa@bayarea.net;

Tel. +011-1-650-851-5517 Fax: +011-1-650-851-5184.

*Received: 4 June 2008; in revised form: 21 July 2008 / Accepted: 23 July 2008 /*

*Published: 6 August 2008*

---

**Abstract:** HF radar systems are widely and routinely used for the measurement of ocean surface currents and waves. Analysis methods presently in use are based on the assumption of infinite water depth, and may therefore be inadequate close to shore where the radar echo is strongest. In this paper, we treat the situation when the radar echo is returned from ocean waves that interact with the ocean floor. Simulations are described which demonstrate the effect of shallow water on radar sea-echo. These are used to investigate limits on the existing theory and to define water depths at which shallow-water effects become significant. The second-order spectral energy increases relative to the first-order as the water depth decreases, resulting in spectral saturation when the waveheight exceeds a limit defined by the radar transmit frequency. This effect is particularly marked for lower radar transmit frequencies. The saturation limit on waveheight is less for shallow water. Shallow water affects second-order spectra (which gives wave information) far more than first-order (which gives information on current velocities), the latter being significantly affected only for the lowest radar transmit frequencies for extremely shallow water. We describe analysis of radar echo from shallow water measured by a Rutgers University HF radar system to give ocean wave spectral estimates. Radar-derived wave height, period and direction are compared with simultaneous shallow-water in-situ measurements.

**Keywords:** HF radar oceanography, wave measurement, remote sensing.

## 1. Introduction

HF radar systems are widely used internationally to provide continuous monitoring of ocean waves and currents for a large range of environmental conditions.

Within the US, coastal ocean current mapping with HF radar has matured to the point where it is now considered an important component of regional ocean observing systems. A mid-Atlantic HF radar network now provides high resolution coverage within five localized networks, which are linked together to cover the full range of the mid-Atlantic coastal ecosystem. Similar regional networks around the US coastline are being formed into a national HF radar network.

While much of the focus of these networks until now has been on offshore current mapping observations, a longer-term objective is to develop and evaluate near-shore measures of waves and currents. These investigations aim to understand the interaction of waves in the shallow coastal waters and how energy is transformed into the creation of dangerous rip currents along the New-Jersey/Long-Island shorelines. Rutgers University radars cover these coastal regions at multiple frequencies from 4.5 to 25 MHz. Their echoes contain information on both currents and waves from deep water up into the shallow coastal zone, providing an excellent archive for such studies. This paper describes the analysis of both simulated and measured radar echo to demonstrate the effect of shallow water on radar observations and their interpretation.

Radar sea-echo spectra consist of dominant first-order peaks surrounded with lower-energy second-order structure. Analysis methods presently in use assume that the waves do not interact with the ocean floor, see [1, 2, 3] for phased-array-antenna beam-forming systems; and [4] for systems with compact crossed-loop direction-finding antennas, such as the SeaSonde.

The assumption of deep water is often invalid close to the coast and for broad continental shelves, and is particularly inadequate to describe the second-order sea-echo used to give information on ocean waves., as second-order echo is often visible above the noise only for close ranges. To interpret this echo correctly, we show that the effects of shallow water must be taken into consideration.

In Section 2, we give the basic equations describing radar echo from shallow water, expanding on the previous description given in [5]. In Section 3, simulations are used to illustrate the effects of shallow water on waveheight, Doppler shifts and spectral amplitudes in radar sea-echo spectra, to investigate limits on the existing theory and to define depth limits at which shallow-water effects must be included in the analysis. The effects of shallow water on the radar spectrum are illustrated using measured spectra. In Section 4, methods are applied to the interpretation of measured radar echo from a Rutgers University radar to produce wave directional spectral estimates, which are compared with wave observations from a bottom-mounted Acoustic Doppler Current Profiler (ADCP) moored in the second radar range cell.

## 2. Radar spectral theory

It follows from the solution of the equations of motion and continuity that long ocean waves are more affected by shallow water. We define the depth at which waves interact with the ocean floor by the approximate relation:



$$d/L \leq 1/8 \quad (1)$$

where  $d$  is the water depth and  $L$  is the dominant ocean wavelength. The deep-water analysis must be modified to allow for shallow-water effects in the coupling coefficients, the dispersion equation refractive effects on wave direction, and the directional ocean wave spectrum itself. We only consider water of sufficient depth that effects of wave energy dissipation such as breaking and bottom friction may be ignored; thus we operate in the linear wave transformation regime. As a general rule, this assumption is valid when the water depth is greater than 5% of the deep-water wavelength.

Applying the lowest-order shallow-water dispersion equation to first-order backscatter from the sea gives the following equations for  $\tilde{k}_s^1$ , the first-order spatial wave vector and  $\omega_s^1$ , the temporal wavenumber of the ocean waves in shallow water producing the backscatter. In this document, a subscript or superscript  $s$  indicates a shallow-water variable; its absence indicates a deep-water variable.

$$\begin{aligned} \tilde{k}_s^1 &= -2\tilde{k}_0 \\ \omega_s^1 &= m'\omega_B \end{aligned} \quad (2)$$

where  $\tilde{k}_0$  is the radar wave vector, of magnitude  $k_0$ , and  $\omega_B$  is the Bragg resonant frequency in shallow water which is given by:

$$\omega_B = \sqrt{2gk_0 \tanh(2k_0 d)} \quad (3)$$

with  $g$  the gravitational constant. The analogous relations for second-order backscatter are:

$$\begin{aligned} \tilde{k}_s + \tilde{k}_s' &= -2\tilde{k}_0 \\ \omega_s^2 &= m\sqrt{gk_s \tanh(k_s d)} - m'\sqrt{gk_s' \tanh(k_s' d)} \end{aligned} \quad (4)$$

where  $\tilde{k}_s, \tilde{k}_s'$  are the spatial wavevectors (with magnitudes  $k_s, k_s'$ ) of the two shallow-water, first-order ocean waves interacting to produce the second-order backscatter.  $m, m'$  are equal to +1, -1 for waves moving toward, away from the radar respectively.

The electromagnetic coupling coefficient has the same form as for deep water [5] but with shallow-water wavevectors:

$$\Gamma_{EM}^s = 0.5 \left[ \frac{(\tilde{k}_s \cdot \tilde{k}_0)(\tilde{k}_s' \cdot \tilde{k}_0) / k_0^2 - 2\tilde{k}_s \cdot \tilde{k}_s'}{\sqrt{\tilde{k}_s \cdot \tilde{k}_s'} - k_0 \Delta} \right] \quad (5)$$

where  $\Delta$  is the normalized surface impedance. The hydrodynamic coupling coefficient, derived by Barrick and Lipa [6] through solution of the equations of motion and continuity, is a function of water depth:

$$\Gamma_H^s = -\frac{i}{2} \left[ k + k' - \frac{(kk' - \tilde{k}_s \tilde{k}'_s)}{mm' \sqrt{kk'}} \left( \frac{\omega^2 + \omega_B^2}{\omega^2 - \omega_B^2} \right) + \frac{\omega \left\{ (m\sqrt{gk_s})^3 \operatorname{csch}^2(k_s d) + (m'\sqrt{gk'_s})^3 \operatorname{csch}^2(k'_s d) \right\}}{g(\omega^2 - \omega_B^2)} \right] \quad (6)$$

where  $k$  and  $k'$  are the spatial wavenumbers of the scattering waves in deep water. The deep- and shallow-water spatial wavenumbers are related as follows:

$$k = k_s \tanh(k_s d) \quad k' = k'_s \tanh(k'_s d) \quad (7)$$

The total radar coupling coefficient  $\Gamma^s$  is the coherent sum of the hydrodynamic and electromagnetic terms

$$\Gamma^s = \Gamma_{EM}^s + \Gamma_H^s \quad (8)$$

It can be shown from these equations that at constant wavenumber, the coupling coefficient increases as the water depth decreases, resulting in an increasing ratio of second- to first-order energy as the depth decreases.

In the following analysis, we assume that the deep-water directional wave spectrum is spatially homogeneous and that any inhomogeneity in shallow water arises from wave refraction. When energy dissipation can be neglected, it follows from linear wave theory that since the total energy of the wavefield, is conserved, the shallow-water wave spectrum expressed in the appropriate variables is equal to the deep-water spectrum [7]:

$$S_s(\tilde{k}_s) = S(\tilde{k}) \quad (9)$$

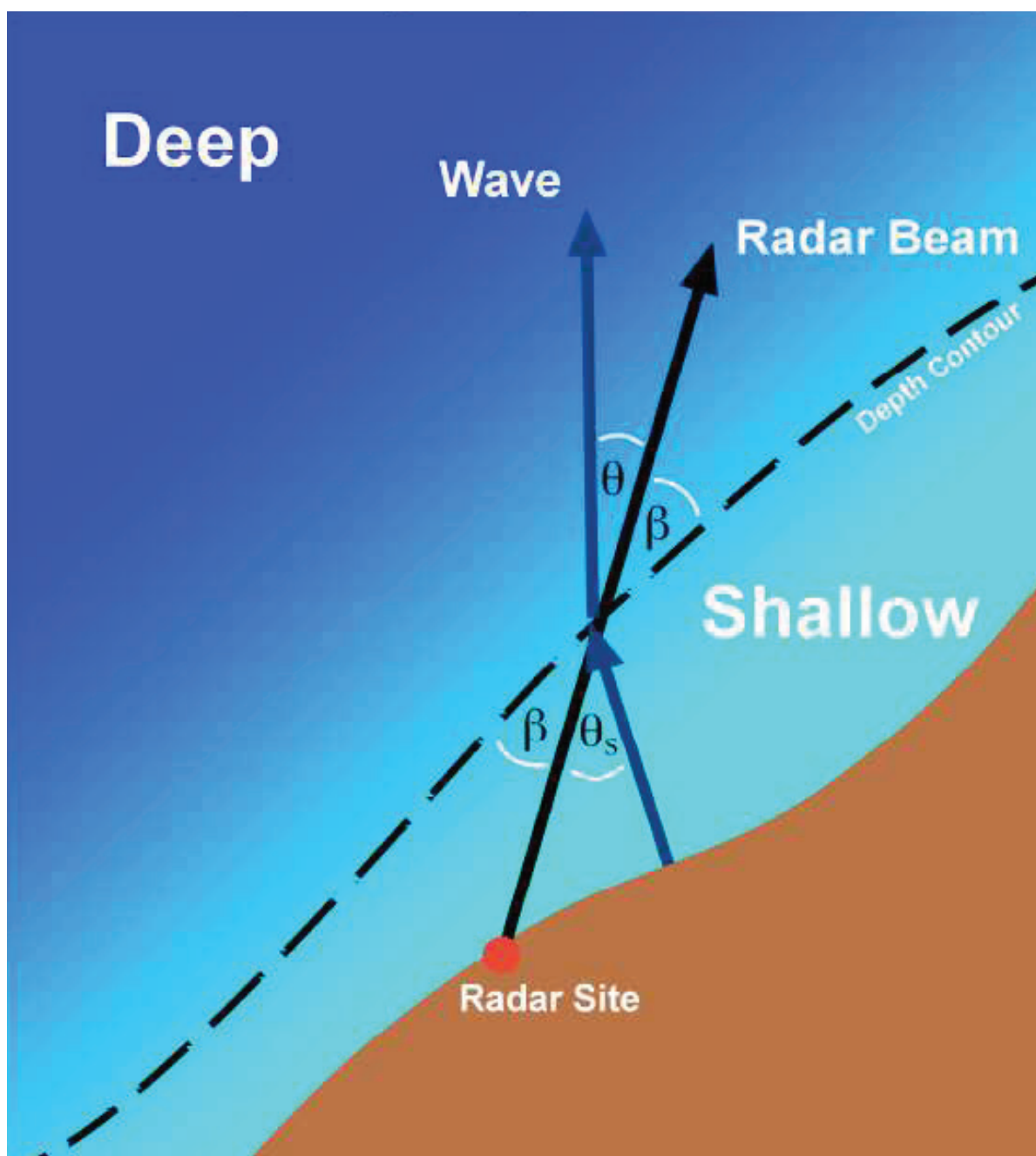
where the deep- and shallow-water wave vectors are related by Snell's law and the dispersion equation:

$$k \cos(\theta + \beta) = k_s \cos(\theta_s + \beta) \quad (10)$$

$$k = k_s \tanh(k_s d) \quad (11)$$

Here  $\beta$  is the angle between the radar beam and the depth contour and  $\theta_s, \theta$  are the angles between the radar beam and the shallow-, deep-water ocean waves respectively. Figure 1 illustrates refraction at a contour between regions of differing depth.

**Figure 1.** Schematic geometry of the radar beam and an ocean wave train at a depth contour, denoted by the dashed line. Wave angles are measured counter-clockwise from the radar beam to the direction the wave is moving. Increasing  $\theta_s, \theta$  by  $180^\circ$  would define an incoming wave.



The shallow- and deep-water rms waveheights are given by:



$$H^2 = \int_0^\infty \int_0^{2\pi} S(k, \theta) k dk d\theta \quad H_s^2 = \int_0^\infty \int_0^{2\pi} S_s(k_s, \theta_s) k_s dk_s d\theta_s \quad (12)$$

Substituting (10) and (11) into (12) gives the following relations which are useful for deriving the shallow- from the deep-water wave spectrum and vice versa:

$$H^2 = \int_0^\infty \int_0^{2\pi} S_s(k_s, \theta_s) J(k_s, \theta_s) k dk_s d\theta_s \quad H_s^2 = \int_0^\infty \int_0^{2\pi} S(k, \theta) J^{-1}(k_s, \theta_s) k_s dk d\theta \quad (13)$$

where the Jacobian  $J(k_s, \theta_s)$  is given by:

$$J(k_s, \theta_s) = \begin{vmatrix} \left( \frac{\partial k}{\partial k_s} \right)_\theta & \left( \frac{\partial \theta}{\partial k_s} \right)_k \\ \left( \frac{\partial k}{\partial \theta_s} \right)_\theta & \left( \frac{\partial \theta}{\partial \theta_s} \right)_k \end{vmatrix} = \left( \frac{\partial k}{\partial k_s} \right)_\theta \left( \frac{\partial \theta}{\partial \theta_s} \right)_k = \left[ 1 + \frac{k_s d \sec^2 h^2(k_s d)}{\tanh(k_s d)} \right] \left[ \frac{\sin(\theta_s + \beta)}{\sin(\theta + \beta)} \right] \quad (14)$$

The first- and second-order radar cross sections in shallow water at frequency  $\omega$  and azimuth angle  $\varphi$  are given by:

$$\sigma_s^1(\omega, \varphi) = k_0^4 \sum_{m'=\pm 1} S_s(2k_0 \varphi + (m'+1)\frac{\pi}{2}) \delta(\omega - m' \omega_B) \quad (15)$$

where  $S_s(k, \alpha)$  is the directional ocean wave spectrum for wavenumber  $k$  and direction  $\alpha$ .

$$\sigma_s^2(\omega, \varphi) = k_0^4 \sum_{m, m'=\pm 1} \int_0^{2\pi} \int_{-\infty}^{\infty} |\Gamma_s|^2 S_s(k_s \theta_s + \varphi + m\pi) \cdot S_s(k'_s \theta_s + \varphi + m'\pi) \delta\left(\omega - m\sqrt{gk_s \tanh(k_s d)} - m'\sqrt{gk'_s \tanh(k'_s d)}\right) k_s dk_s d\theta_s \quad (16)$$

where the coupling coefficient  $\Gamma_s$  is given by (8). The values of  $m$  and  $m'$  in (16) define the four possible combinations of direction of the two scattering waves. Common numerical multiplicative constants in (15) and (16) have been omitted. It can be shown from (4) that the wavenumbers of the scattering waves are related as follows:

$$k'_s = \sqrt{k_s^2 + 2k_s \cos(\theta_s) + 1} \quad (17)$$

To compute the second-order integral in (16), we choose as integration variables  $k_s$  and the deep-water angle  $\theta$ . In terms of these variables (16) becomes

$$\sigma_s^2(\omega, \varphi) = k_0^4 \sum_{m, m' = \pm 1} \int_0^{2\pi} \int_{-\infty}^{\infty} I(k_s, \theta) \delta(\omega - h(k, \theta)) \left| \left( \frac{\partial k_s}{\partial h} \right)_{\theta} \right| dh d\theta \quad (18)$$

where

$$h(k, \theta) = m\sqrt{gk} - m'\sqrt{gk' \tanh(k'd)} \quad (19)$$

and

$$I(k_s, \theta) = \left| \Gamma_s^2 \right| S(k, \theta + \varphi + m\pi) S(k', \theta + \varphi + m'\pi) k_s \left( \frac{\partial \theta_s}{\partial \theta_s'} \right)_k \quad (20)$$

and where we have substituted (9) for the shallow water directional spectra. The factors  $\left( \frac{\partial \theta_s}{\partial \theta_s'} \right)_k$  and  $\left( \frac{\partial k_s}{\partial h} \right)_{\theta}$  are obtained by differentiation using (10), (11) and (19).

To calculate the integral in (18), it is first reduced to a single-dimensioned integral using the delta function constraint. The remaining integral is computed numerically.

Frequency contours are defined by:

$$\omega - h(k, \theta) = 0 \quad (21)$$

which is solved for  $k$  as a function of  $\theta$  for a given value of  $\omega$ . Due to wave refraction, the shallow water angle and wavenumber have discontinuities when the deep-water wave moves parallel to the depth contour, i.e. when

$$\theta = -\beta, \quad \pi - \beta \quad (22)$$

where  $\beta$  is the angle between the radar beam and the depth contour.

Frequency contours are hence also discontinuous due to this effect at deep-water wave angles defined by (22). Examples of frequency contours for deep- and shallow-water are shown in Figure 2, plotted in normalized deep-water spatial wavevector space  $\tilde{k} / (2k_0)$ . Normalized components  $p, q$  are defined so that  $p$  is along the radar beam and  $q$  perpendicular:

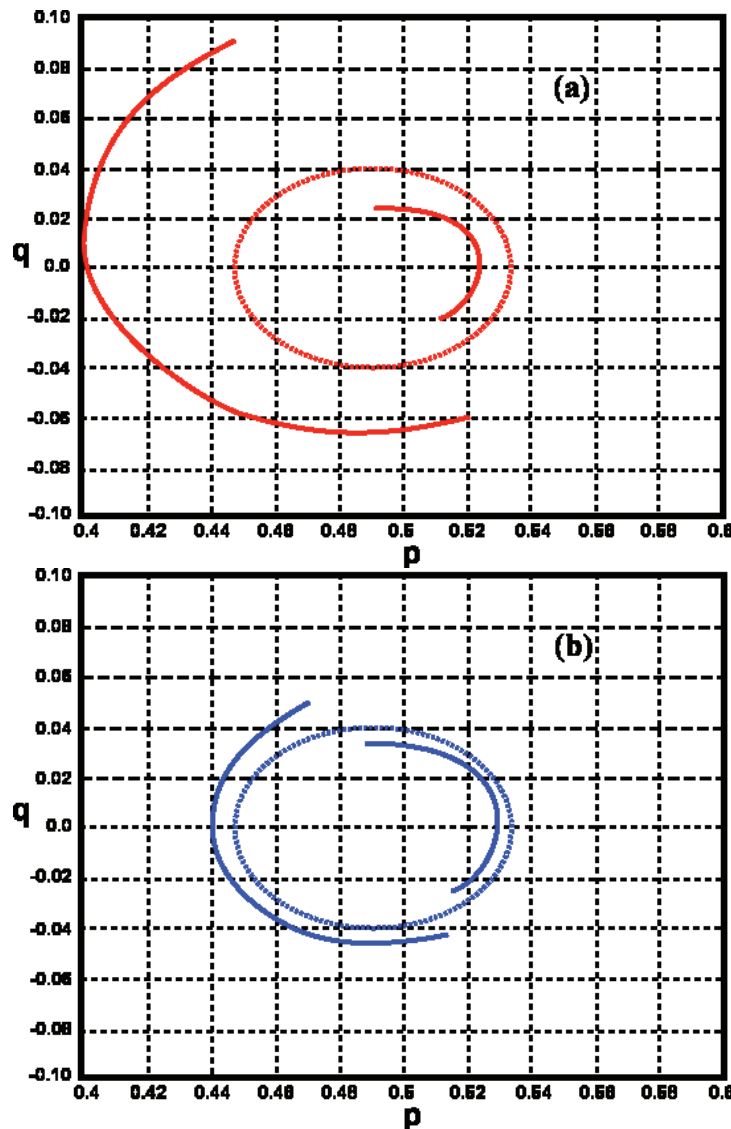
$$\begin{aligned} p &= (k_0 + k \cos(\theta)) / (2k_0) \\ q &= k \sin(\theta) / (2k_0) \end{aligned} \quad (23)$$

The discontinuities in the frequency contours are more pronounced when the contour is drawn in shallow-water wavenumber space, as it follows from (10), (11) that there are discontinuities in the shallow-water wave angle due to wave refraction.

**Figure 2.** Examples of frequency contours for water of depth 10m (continuous lines) compared with the corresponding contours for deep water (dashed lines).

Normalized frequency:  $\omega / \omega_B = 1.2$ ,  $\beta = 60^\circ$ .

Radar frequency: (a) 5Mhz , (b) 25Mhz

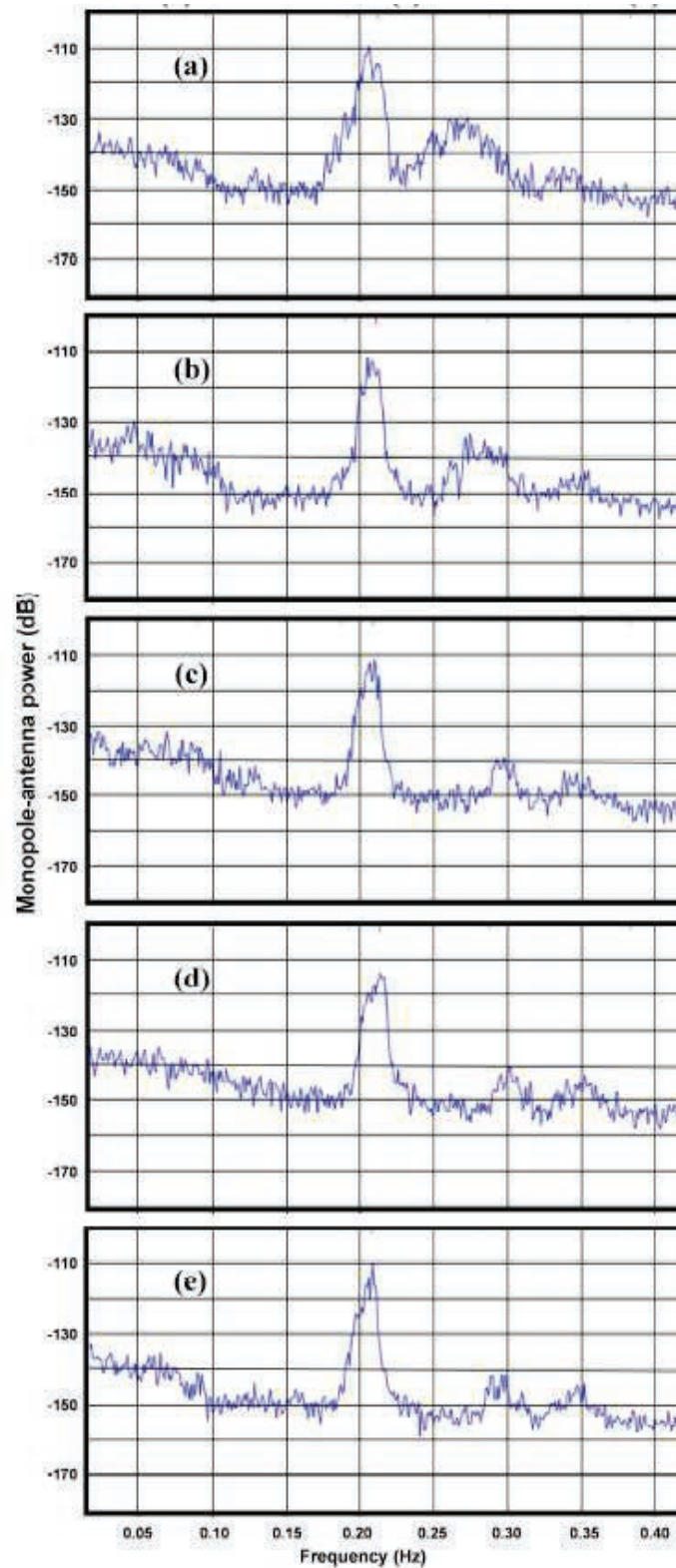


It can be seen from Figure 2 that the deep-water ocean wave numbers corresponding to a given radar spectral frequency change with depth: they become either greater or smaller than the deep-water values, depending on the wave direction. This results in the frequency of second-order peaks in the radar spectrum changing with water depth.

The effects of shallow-water on measured radar spectra are illustrated in Figure 3, which shows measured spectra from a 5 MHz radar in five radar range cells, with distances ranging from 18km to 60km. As the water depth decreases, the second-order energy increases relative to the first-order and the frequency displacement between the first- and second-order peaks decreases. In the outer ranges, the second-order structure is almost the same from range cell to range cell, as the water is effectively infinitely deep.



**Figure 3.** Spectra from a 5MHz SeaSonde monopole antenna. Range/ Water depth:  
 (a) 18km/ 5 -20m (b) 30km/10-50m (c) 42km/ 20-70m (d) 48km/ 35-80m (e) 54km/  
 40-100m



### 3. Narrow-beam radar spectral simulations

To gain insight into the effects of shallow water, simulated radar echo spectra were calculated for a narrow-beam radar, using the model directional wave spectrum defined in [8] which consists of the

sum of two terms: a continuous high-frequency wind wave spectrum and a swell component that is an impulse function in both wavenumber and direction. The swell component is defined by

$$S_s(k_s, \theta_s) = H_s^{*2} \delta(\theta_s - \theta_s^*) \delta(k_s - k_s^*) \quad (24)$$

where  $H_s^*$ ,  $\theta_s^*$ ,  $k_s^*$  are the specified rms waveheight, direction and wavenumber. For this model, four sharp spikes occur in the radar spectrum. Here we consider only the second-order sideband for which  $m=1$ ,  $m'=1$ , and assume water depths in the range 5-100m and radar transmit frequencies of 5Mhz and 25Mhz. For these values, it can be shown numerically that Doppler frequencies are always greater than the positive Bragg frequency. The radar beam is taken to be pointing perpendicular to parallel depth contours (i.e.  $\beta = 90^\circ$  in Figure 1)

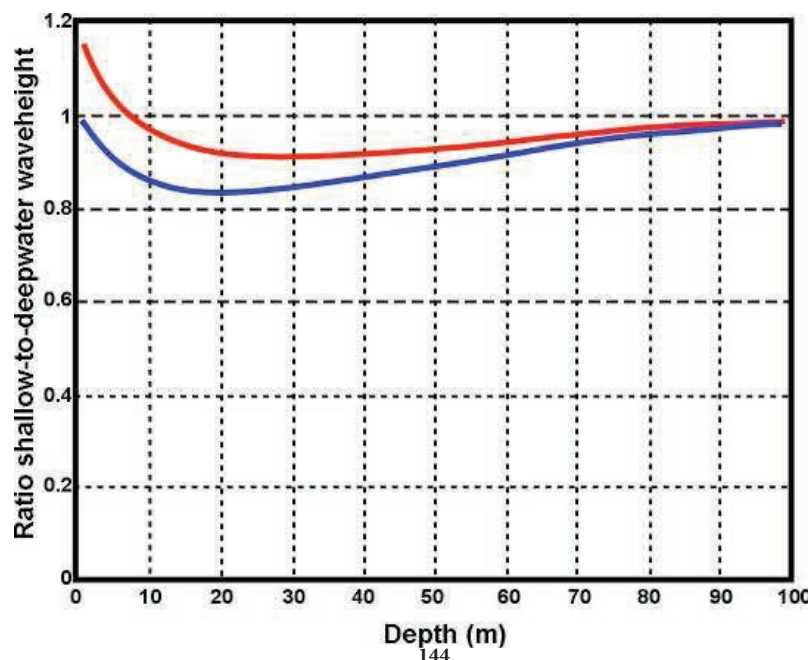
### 3.1 Effect of water depth on waveheight

For our model it follows from (13) that the relationship between the shallow- and deep-water rms waveheights is given by:

$$H_s^* = H^* \sqrt{\frac{\sin(\theta^* + \beta) / \sin(\theta_s^* + \beta)}{\left[ \tanh(k_s^* d) + k_s^* d \operatorname{sech}^2(k_s^* d) \right]}} \quad (25)$$

This relationship is of course independent of radar frequency and has many angle symmetries. Figure 4 shows the ratio plotted as a function of depth for different wave directions.

**Figure 4.** The ratio of shallow- to deepwater waveheight plotted vs. depth for a 12 s wave. Wave direction in deep water relative to the radar beam: Red  $180^\circ$ , Blue  $135^\circ$



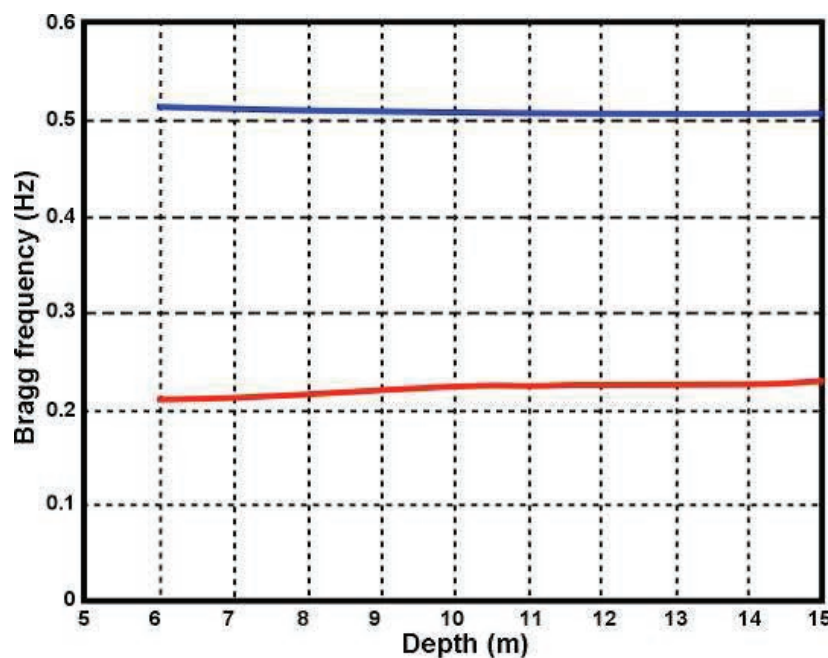
It can be seen from Figure 4 that the waveheight initially decreases with decreasing depth as the wave enters shallow water but increases at depths below about 20m, which agrees with [7].

### 3.2 Effect of water depth on Doppler shifts

It follows from (3) that for a given radar frequency, the Bragg frequency decreases with depth, causing the Bragg peaks to move slightly closer together. Figure 5 shows the Bragg frequency plotted as a function of depth.

**Figure 5.** Bragg frequency plotted as a function of depth.

Radar transmit frequency: Red 5Mhz, Blue 25Mhz



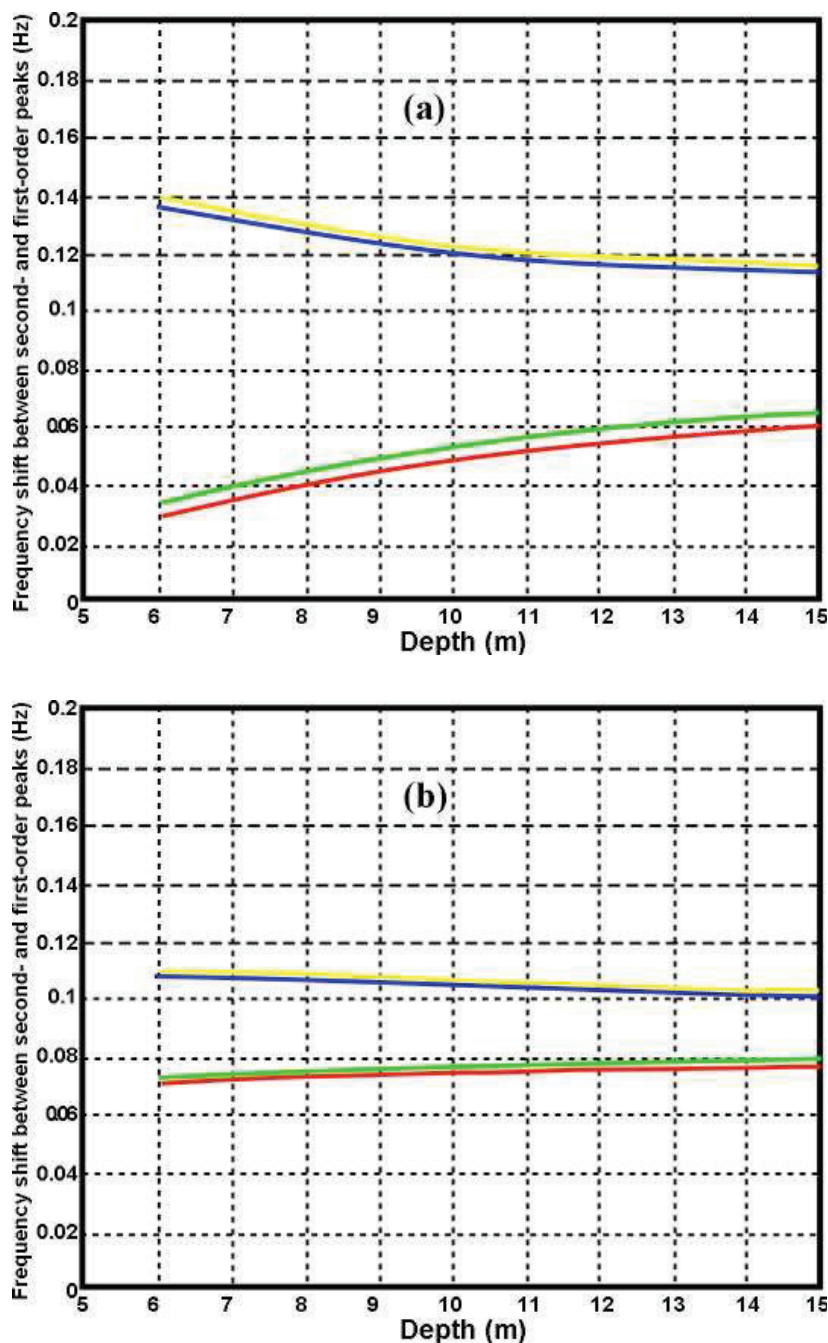
It can be seen from Figure 5 that the change in the Bragg frequency with depth is small.

Figure 6 shows the displacement of the second-order peak from the Bragg frequency plotted as a function of depth for an 11s wave moving at different angles with respect to the radar beam.

It can be seen from Figure 6 that as the water depth decreases, the second-order peak shifts toward the Bragg frequency for waves moving toward the radar, and further away for waves moving away from the radar. This is consistent with the two branches of the contour plot as shown in Figure 2. This effect is more marked for lower radar frequencies and can be seen in the measured spectra shown in Figure 3 in which the second-order peak moves closer to the first-order as the range from the radar and water depth decrease, with waves moving toward the radar.



**Figure 6.** The frequency shift of the second-order peak from the Bragg frequency for an 11s wave. (a) 5Mhz (b) 25Mhz. Angle between wave and radar beam: Yellow 0°, Blue 45°, Green 135°, Red 180°



### 3.3 Effect of water depth on radar spectral amplitudes

It is shown in [8] that for the impulse-function model defined by (24), the ratio  $R$  of the second-order to first-order energy is given by:

$$R = 2H_s^{*2} |\Gamma_s^2| \quad (26)$$

where the coupling coefficient  $\Gamma_s$  is evaluated at wavevectors defined by  $\theta_s^*, k_s^*$ .  $\Gamma_s$  increases with decreasing depth and increasing wave period at a given radar frequency as illustrated in Figures 7 and 8, which also show that shallow water has a greater effect as the radar transmit frequency decreases.

**Figure 7.** The absolute value of the coupling coefficient  $\Gamma_s$  vs. depth for a 9 sec wave. Radar frequency: Red: 5Mhz, Blue: 25Mhz.

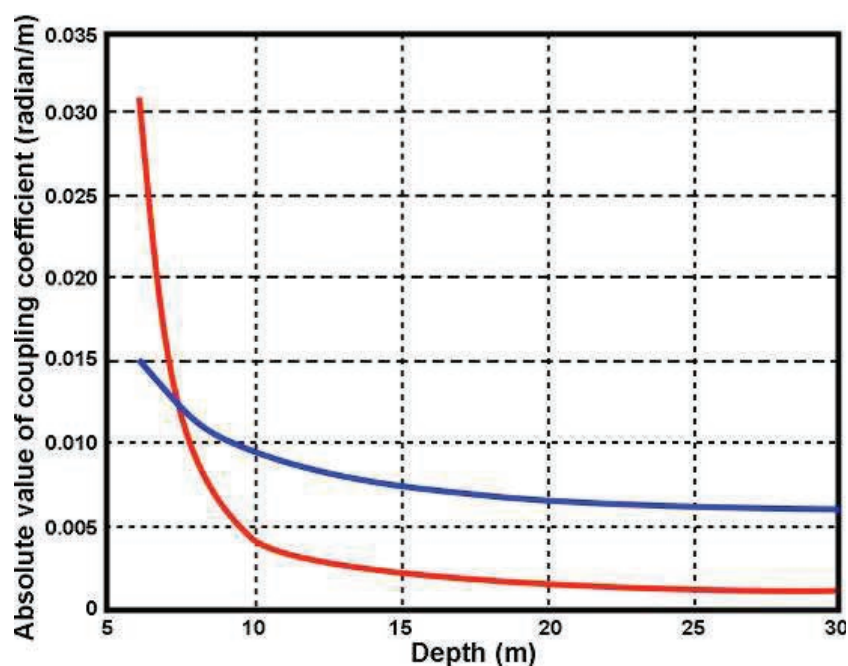
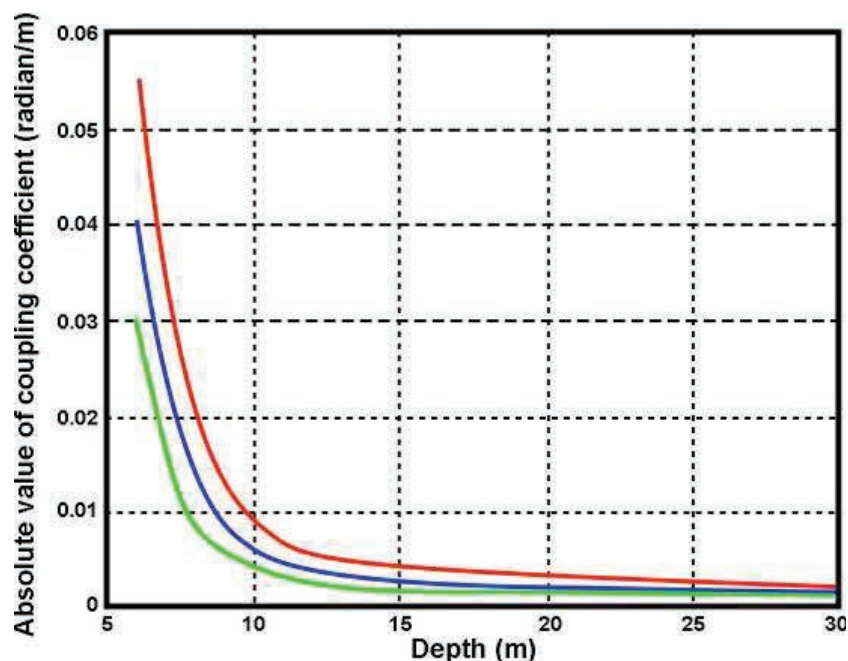
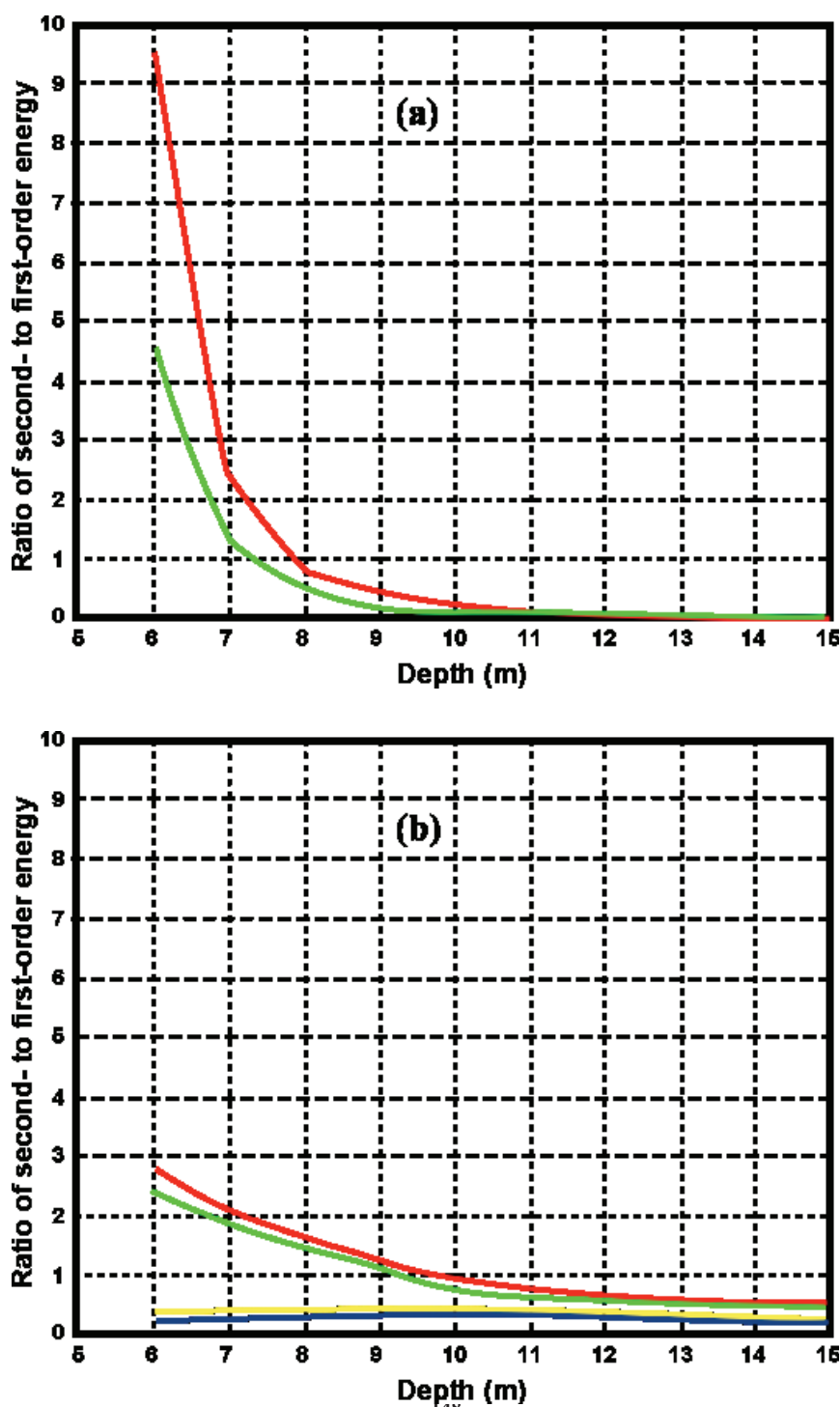


**Figure 8.** The absolute value of the coupling coefficient vs. depth for waves of different period. Radar transmit frequency: 5Mhz. Wave period: Red 15s, Blue 12s, Green 9s.



Since the coupling coefficient increases as the depth decreases, it follows from (26) that the second-order energy will increase with respect to the first-order. This effect can be seen in the measured radar spectra shown in Figure 3. Figure 9 shows the theoretical ratio of the second- to the first-order energy obtained from (26) using our model for an 11s wave.

**Figure 9.** Ratio of second - to first-order energy for an 11s wave. Significant waveheight: 2.4m. Radar transmit frequency: (a) 5 Mhz, (b) 25 Mhz. Angle between wave and radar beam: Yellow 0°, Blue 45°, Green 135°, Red 180°





It can be seen from Figure 9 that the ratio of the second- to the first-order energy exceeds unity (i.e. the calculated second-order energy exceeds the first-order energy) for depths less than about 8 m for a 5MHz transmit frequency and for depths less than about 10m for a 25 MHz transmit frequency.

This subsection demonstrates an important point. Since we have shown that the waveheight itself actually decreases slightly upon moving into shallow water, while the second-order echo increases significantly due to the rapid growth of the coupling coefficient, wrongly using deep-water inversion theory to estimate waveheight will overestimate this important quantity. We note that all previous treatments and demonstrations of wave extraction have been based on deep-water theory, even when in fact many of the radar observations have been made in shallow water.

### 3.4 Effect of water depth on breakdown of theoretical model

When the magnitude of the second-order energy approaches that of the first-order, it is apparent that the perturbation expansions on which (15) and (16) are based are failing to converge and they therefore cannot provide an adequate description of the radar echo. This effect is similar to the well known radar spectral saturation occurring when the waveheight exceeds a limit defined by the radar transmit frequency. Above this waveheight limit, the radar spectrum loses its definitive shape and the perturbation expansions fail to converge. The deep-water saturation limit on the significant waveheight  $W_{Sat}$  (defined to be four times the rms waveheight) is given approximately by the relation:

$$W_{Sat} = 2 / k \quad (27)$$

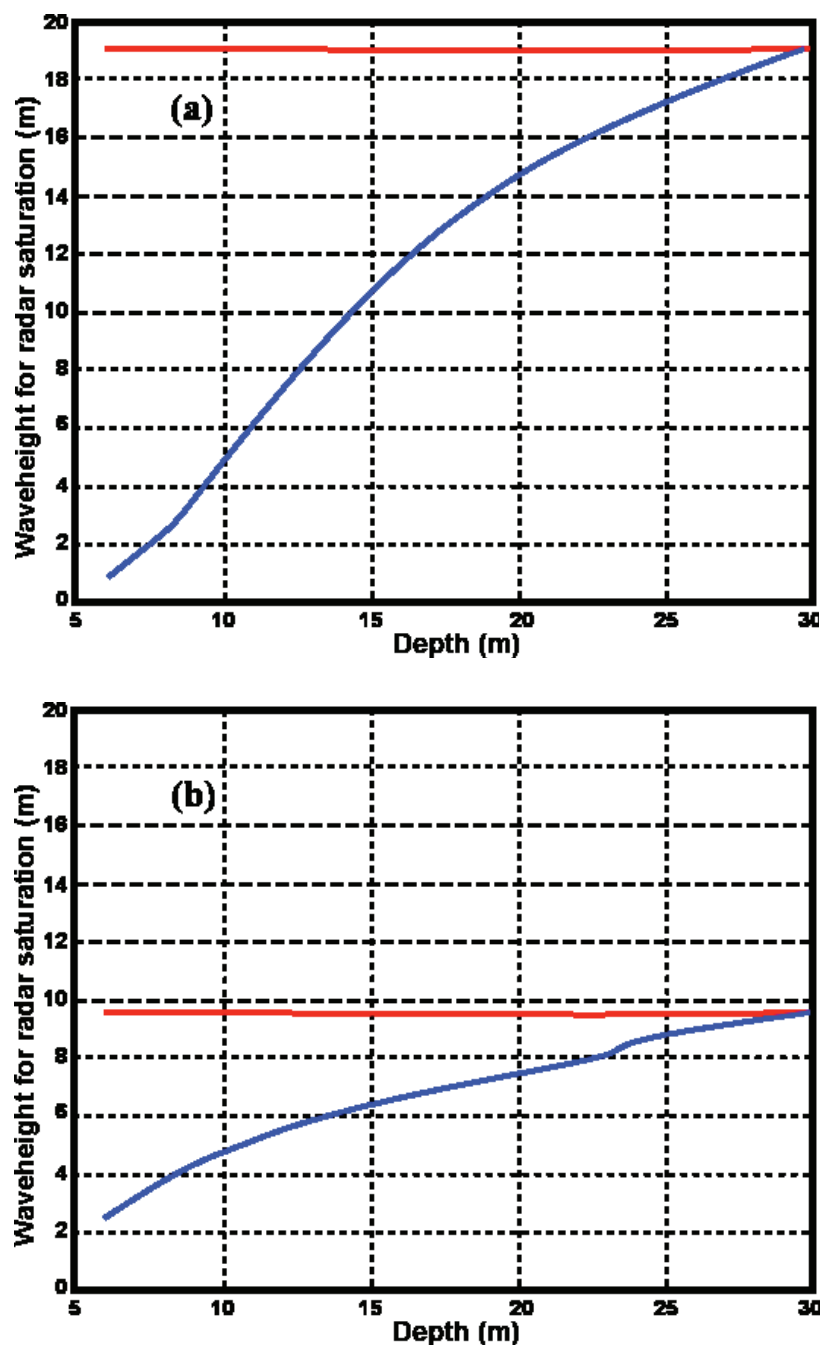
For shallow-water, the saturation of the radar spectrum is exacerbated by the increase of the coupling coefficient and the radar spectrum saturates for waveheights less than that defined by (27). We here define the shallow-water saturation limit  $W_{Sat}^s$  for the model to be that waveheight for which the second-order energy equals the first-order, and the ratio  $R$  is given by:

$$R = 1 \quad (28)$$

In practice the theory may fail before this limit is reached.  $W_{Sat}$  and  $W_{Sat}^s$  are plotted vs. depth in Figure 10 for two different radar frequencies. At depths of 30m the saturation limits are approximately equal. At depths less than 30m, the shallow-water limit drops off sharply, particularly for the lower transmit frequency. Thus the radar spectrum can be expected to saturate at lower values of waveheight in shallow water.

For waveheights above the saturation limit, the waveheight predicted by the theory will be too high. However the theory cannot be applied at all when the second-order spectrum merges with the first, as then separation is not possible.

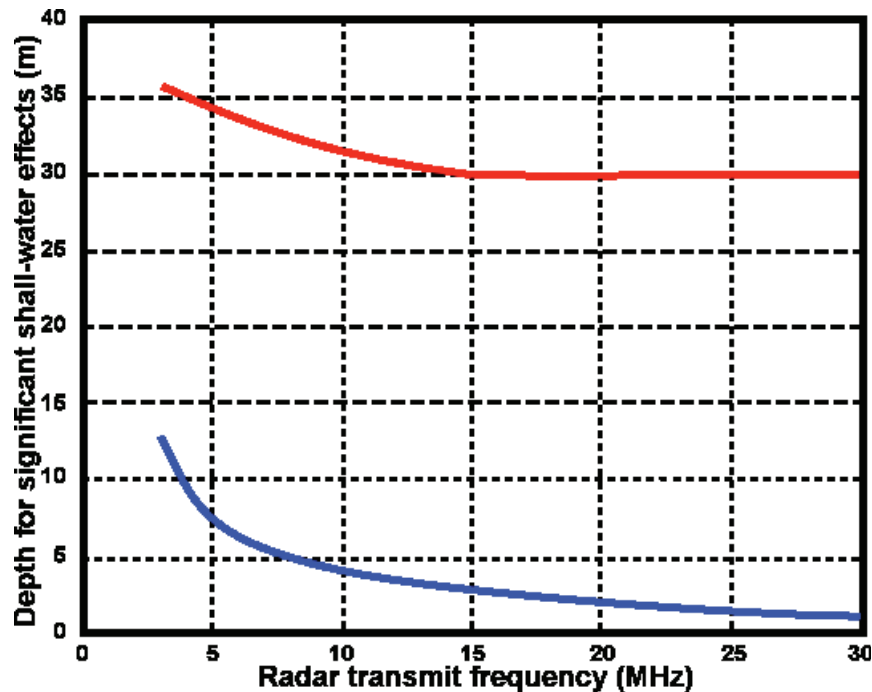
**Figure 10.** Significant waveheight saturation limits for an 11-second wave coming straight down the radar beam. Radar transmit frequency: (a) 5 Mhz , (b) 25 Mhz  
Red: deep-water saturation limit  $W_{Sat}$  , Blue: shallow-water saturation limit  $W_{Sat}^s$



### 3.5 Depth limits for significant shallow-water effects

We estimate depths for which shallow-water effects become significant as follows: For first-order echo, the depth limit is defined by equality in (1). At this depth, the Bragg frequency defined by (3) is 96% of its deep-water value. For second-order echo, we define the depth limit  $D^s$  at which shallow-water effects become significant as the value at which the coupling coefficient defined by (8) exceeds 1.25 times the deep-water value. Figure 11 plots the depths  $D^s$  vs radar transmit frequency for an 11s wave.

**Figure 11.** Depths at which shallow-water effects become significant vs. radar transmit frequency. Red: second-order echo. Blue: First-order echo.



Figures 10 and 11 help in assessing the validity of the existing deep-water methods. However they are based on a wave model (24), which is quite restrictive: waves of a single wavelength are assumed to come down the radar beam. Also Figure 11 applies only to an 11s wave. Performing similar studies for more general wave spectral models is beyond the scope of this paper. However, we observe that: (a) Shallow water effects are stronger for longer ocean wavelengths (b) Second-order radar spectra for  $m=1, m'=1$  are strongest for waves down the radar beam. (c) The stronger the second-order energy for a given waveheight, the sooner the radar spectrum will saturate as waveheight increases. Therefore shallow-water effects will be more marked at a given waveheight for a broad nondirectional spectrum that includes longer wavelengths e.g. the Pierson Moskowitz model (32). These differences would probably not be large however, due to the sharp cutoff of wave-spectral models for long wavelengths. The opposite effects would be expected for spectra that include wave directions not directly down the radar beam e.g. a cardioid directional distribution. To summarize these effects:  $W_{Sat}^s$  will be less and  $D^s$  will be greater than the values shown in Figs. 10 and 11 for the following changes from the wave spectrum (24): broad nondirectional spectrum, wave period  $> 11s$ .  $W_{Sat}^s$  will be greater and  $D^s$  will be less for broad directional distributions, waves nonparallel to radar beam, wave period  $< 11s$ .



## 4. Application to measured data

### 4.1 Data set

The results presented here are based on analysis of 10-minute radar spectra measured by a 25MHz SeaSonde located at Breezy Point, NJ. The time period from December 29 to 30, 2005, was chosen because simultaneous coverage provided by the SeaSonde and a bottom-mounted ADCP allowed a direct comparison to be made between results from the two sensors. The ADCP was located in the second radar range cell in water of depth 8m. The bathymetry in the area and the locations of the two sensors are shown in Figure 12.

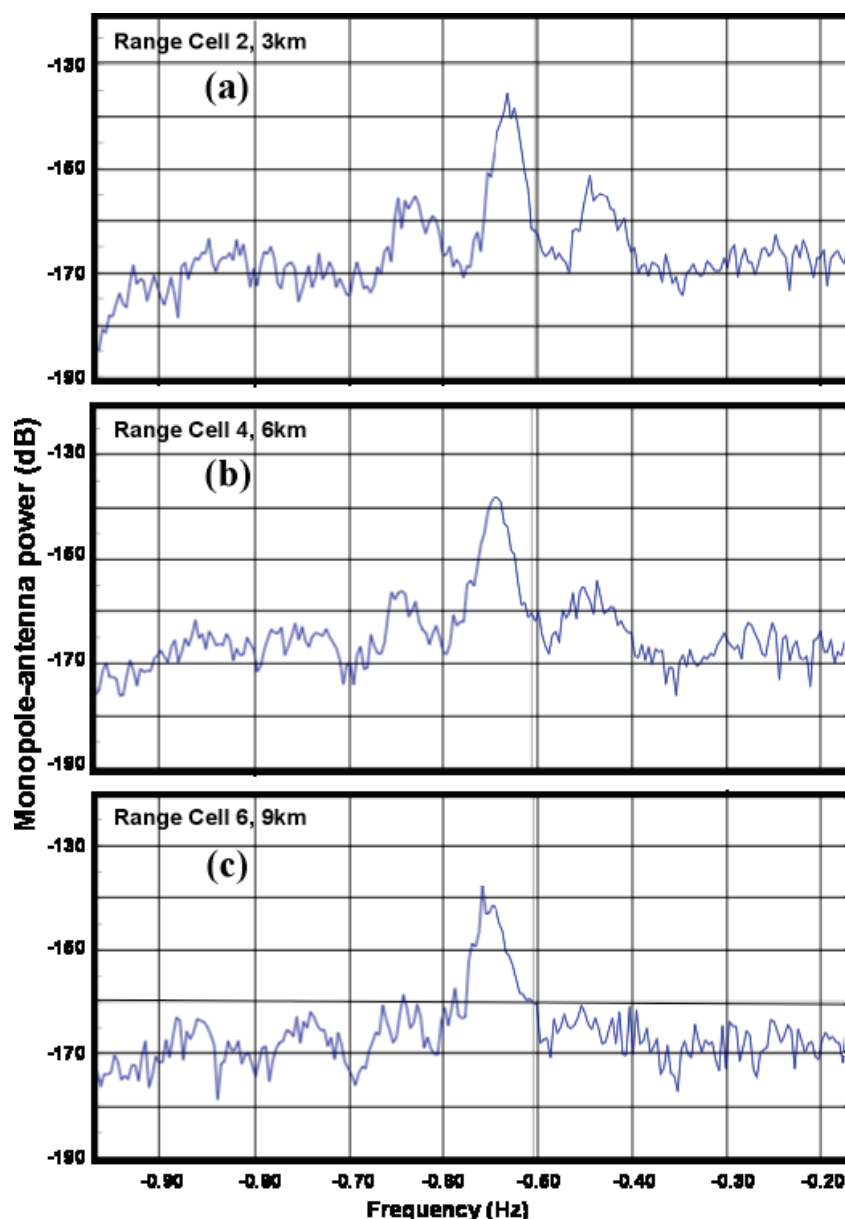
**Figure 12.** The coastline and bathymetry (contours in meters) around Breezy Point, New Jersey, showing the positions of the SeaSonde and the bottom-mounted ADCP.



In our analysis, depth contours near the radar are assumed to be parallel to shore and the depth profile is obtained from Figure 12.

Figure 13 shows measured spectra from the Breezy Point SeaSonde at three ranges: the second-order energy can be seen to increase relative to the first-order as the water depth decreases.

**Figure 13.** (a) Spectra measured by the 25MHz SeaSonde at Breezy Point. at 1:00pm 12/30/2005. Range: (a) 3 km (b) 6 km (c) 9 km.



#### 4.2 Interpretation of the radar spectra

Lipa and Barrick [5] describe the extension of the narrow-beam theory described in Section 2 to apply to a broad antenna system such as the SeaSonde, assuming ideal antenna patterns. From the antenna voltage cross spectra, we form as intermediate data products the first five Fourier angular coefficients of the broad-beam return over a selected range ring surrounding the radar. These coefficients, designated by the index  $n = -2, -1, 0, 1, 2$ , are defined in terms of the narrow-beam first and second-order return through the relation:

$$b_n^{1,2}(\omega) = \int \sigma_s^{1,2}(\omega, \varphi) t f_n(\varphi) d\varphi \quad (29)$$

where the integration over azimuth angle  $\varphi$  is performed over open water around the radar range cell and the superscripts refer to first- and second-order respectively. The narrow-beam radar cross sections  $\sigma_s^{1,2}(\omega, \varphi)$  are defined in terms of the ocean wave spectrum by (15), (16). Following the notation in [5], the trigonometric functions  $t f_n(\varphi)$  are given by

$$\begin{aligned} t f_n(\varphi) &= \sin(n\varphi) \quad n < 0 \\ &= \cos(n\varphi) \quad n \geq 0 \end{aligned} \quad (30)$$

As described in [4], there are three steps in the interpretation of the radar spectrum to give deep-water wave information.

a) The first- and second-order regions are separated.

b) The first order region is analyzed to give the ocean wave spectrum at the Bragg wavenumber. It is assumed that deep-water theory is adequate for this step, as Bragg waves are short and hence insensitive to the effects of shallow water, see Figure 5.

c) Second-order radar spectral data is collected from the four second-order sidebands of 10-minute averaged cross spectra and fit to a model of the deep-water ocean wave spectrum. Least-squares fitting to the radar Fourier coefficients is used to derive estimates of the significant wave height, centroid period and direction. During this step, the second-order spectrum is effectively normalized by the first-order, eliminating unknown multiplicative factors produced by antenna gains, path losses etc.

Shallow-water analysis requires a further step:

d) The shallow-water wave spectrum is calculated from the deep-water spectrum using (9)–(11).

#### 4.3 Model ocean wave spectrum

For our analysis, we define a model for the deep-water ocean wave spectrum as the product of directional and nondirectional factors:

$$S(k, \varphi) = Z(k) \cos^4 \left( \frac{\varphi - \varphi^*}{2} \right) \quad (31)$$

The directional factor in (31) has a cardioid distribution around the dominant direction  $\varphi^*$ . For describing the second-order spectrum,  $\varphi^*$  is taken to be the dominant long-wave direction. For describing the first-order spectrum,  $\varphi^*$  is the short-wave direction, which is assumed to be the same as the wind direction. For the nondirectional spectrum we use the Pierson-Moskowitz model  $Z(k)$ :

$$Z(k) = \frac{A e^{-0.74(k_c/k)^2}}{k^4} \quad (32)$$

whose parameters are the cutoff wavenumber  $k_c$  and a multiplicative constant A. The waveheight, centroid period and direction can be defined in terms of the model parameters. The significant waveheight follows from the directional spectrum through the relation:

$$W = 4 \left( \int_0^{2\pi} \int_0^\infty S(k, \varphi) dk d\varphi \right)^{1/2} \quad (33)$$

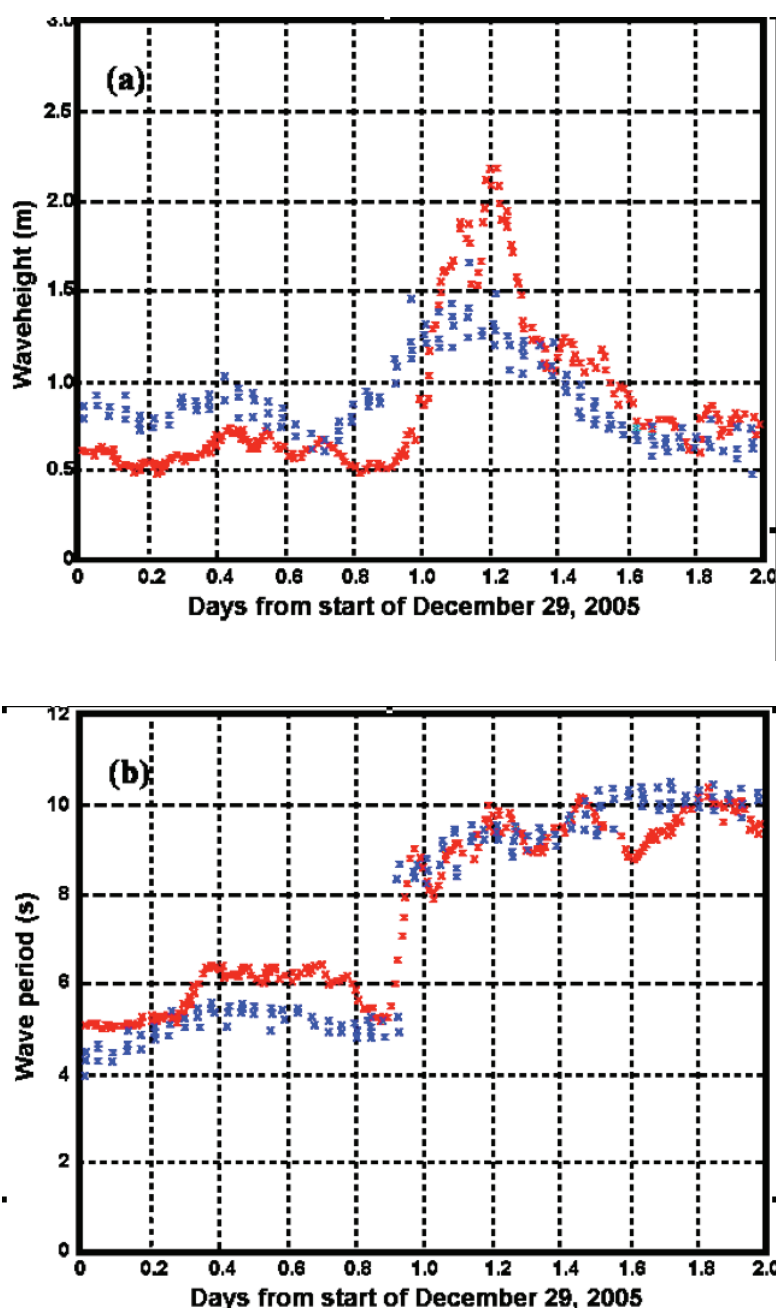


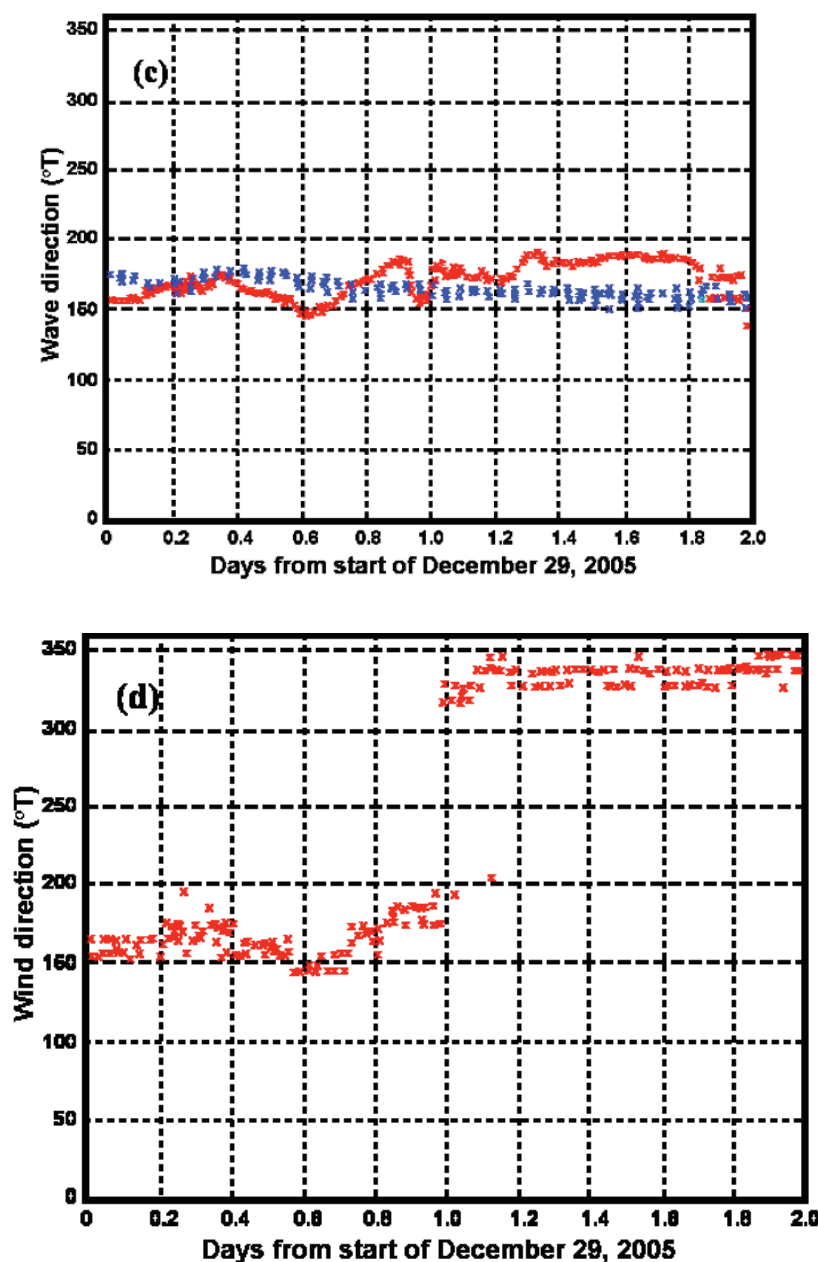
This model has proven satisfactory for use in deep-water wave extraction software that produces waveheight, period, and direction. It has been used for real-time SeaSonde systems for many years, providing good agreement with in-situ measurements e.g. as shown in [4].

#### 4.4 Results

Figure 14 shows SeaSonde results in the second radar range cell calculated using the shallow-water theory described above, together with the ADCP results.

**Figure 14.** SeaSonde (red) and ADCP (blue) results for (a) Significant waveheight (b) Wave period (c) Wave direction (d) Wind direction.





It can be seen from Figure 14 that southerly winds veer to the northwest after the passage of a storm front. Subsequently the wave height and period increase suddenly. Spectral saturation may be occurring at the peak of the storm, causing overestimates in the waveheight. Wave direction remains about the same, as due to wave refraction, wave directions in very shallow water are nearly perpendicular to the depth contours. Both radar and ADCP are observing directions in shallow water, hence this perpendicular condition is being enforced on the longer waves, although the wind direction driving short waves is seen to change significantly over this storm period.

Table 1 gives the bias and standard deviation between the SeaSonde and ADCP measurements of waveheight, wave period and direction, for the short-period waves before the storm and the longer-period waves afterwards.

**Table 1.** Comparison statistics, radar vs. ADCP.

	Before storm	After storm
<b><u>Waveheight</u></b>		
Standard deviation	0.25m	0.35m
Bias	-0.23m	0.17m
<b><u>Wave Period</u></b>		
Standard deviation	0.76s	0.60s
Bias	0.70s	-0.27s
<b><u>Wave Direction</u></b>		
Standard deviation	13.8°	19.7°
Bias	-9.5°	17.0°

To emphasize the necessity of taking shallow water into account for this location, we estimated the waveheight assuming infinitely deep water. Figure 15 shows the SeaSonde results together with the ADCP waveheight. Clearly waveheight is overestimated with this assumption. The simulations described in Section 3 indicate that the cause of this overestimate is the failure to account for the increase of the coupling coefficient in shallow water.

**Figure 15.** Significant waveheight:

Red: SeaSonde calculated assuming infinite water depth. Blue: ADCP.

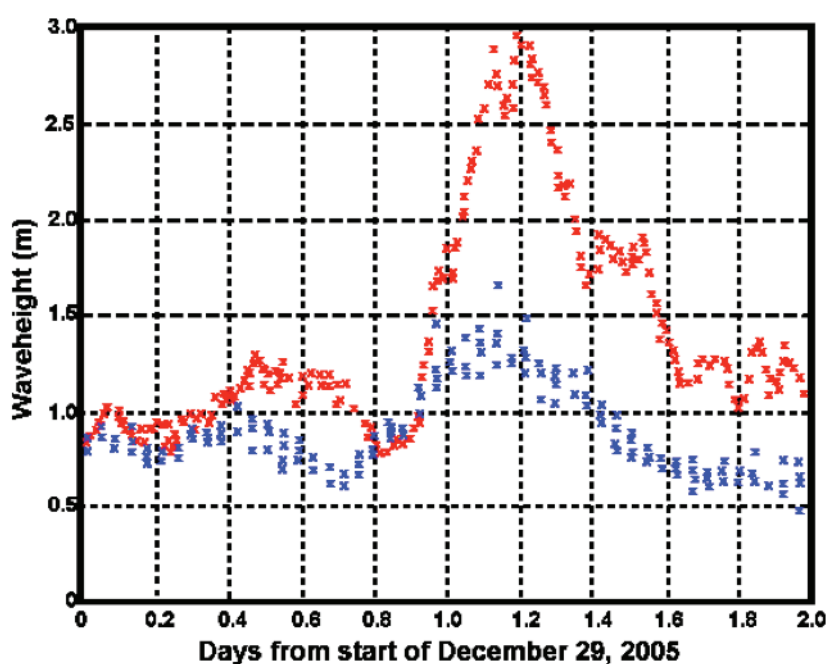




Table 2 gives the bias and standard deviation between the SeaSonde and ADCP waveheight measurements, with the former calculated assuming infinitely deep water.

**Table 2.** Comparison statistics, radar vs. ADCP assuming deep water.

	Before storm	After storm
<b><u>Waveheight</u></b>		
Standard deviation	0.25m	0.95m
Bias	0.19m	0.90m

## 5. Conclusion

We have presented the theory of narrow-beam HF radar sea-echo from shallow water and illustrated the effect of decreasing water depth using simulations for a simple swell model of the ocean wave spectrum. The second-order spectral energy increases relative to the first-order as the water depth decreases, resulting in spectral saturation when the waveheight exceeds a limit defined by the radar transmit frequency. This effect is particularly marked for lower radar transmit frequencies. For waveheights above the saturation limit, the perturbation expansions on which Barrick's equations (15), (16) are based fail to converge. The saturation limit on waveheight is less for shallow water. Shallow water affects second-order spectra (which gives wave information) far more than first-order (which gives information on current velocities). Figure 11 shows the depths at which shallow-water effects become significant plotted as a function of radar frequency for an 11s wave. We discuss how the waveheight and depth limits would change for a more general model.

The shallow-water theory was then extended to apply to broad-beam systems such as the SeaSonde and applied to the interpretation of two days of radar data measured by a 25Mhz SeaSonde located on the New Jersey shore. During the measurement period, a storm passed over the area. An ADCP was operated in the second radar range cell in water 8m deep. Radar results were compared with simultaneous ADCP measurements. The comparison confirms aspects of the theory presented in Section 3. For the longer period waves occurring after the passage of the storm front, the standard deviation between SeaSonde and ADCP waveheight measurements decreased by a factor of three when the effects of shallow water were included in the analysis, and the bias decreased by a factor of five. Possible explanations for the remaining discrepancies are (a) the assumption of parallel depth contours (b) the assumption that the wave spectrum is homogeneous in the circular radar range cell (c) saturation in the radar spectrum around the peak of the storm, which, as discussed in Section 3, leads to the over-prediction of the waveheight.

## Acknowledgements

Measured radar and buoy wave data from New Jersey as well as its analysis were funded through the New Jersey NOAA Sea Grant program.

## References

1. Lipa, B.J. Derivation of directional ocean-wave spectra by integral inversion of the second-order radar echoes. *Radio Sci.* **1977**, *12*, 425-434.
2. Lipa, B.J.; Barrick, D.E. Analysis methods for narrow-beam high frequency radar sea echo, **1982**, NOAA Tech. Report ERL 420-WPL 56.
3. Wyatt, L.R.; Green, J.J.; Gurgel, K.W.; Nieto Borge, J.C.; Reichert, K.; Hessner, K.; Gunther, H.; Rosenthal, W.; Saetra, O.; Reistad, M. Validation and intercomparison of wave measurements and models during the EuroROSE experiments. *Coastal Engineering* **2003**, *48*, 1-28.
4. Lipa, B.J.; Nyden B.B. Directional Wave Information from the SeaSonde. *IEEE Jour. Ocean. Eng.* **2005**, *30* (1), 221-231.
5. Lipa, B.J.; Barrick, D.E. Extraction of sea state from HF radar sea echo: Mathematical theory and modeling. *Radio Sci.* **1986**, *21*, 81-100.
6. Barrick, D.E.; Lipa, B.J. The second-order shallow water hydrodynamic coupling coefficient in interpretation of HF radar sea echo. *IEEE J. of Oceanic Engr.* **1986**, *11*, 310 - 315.
7. Kinsman, B. "Wind Waves", chap. 7.5, 676 pp, Prentice-Hall, New York
8. Lipa, B.J.; Barrick, D.E. Methods for the extraction of long-period ocean-wave parameters from narrow-beam HF radar sea echo. *Radio Sci.* **1980**, *15*, 843-853.

© 2008 by the authors; licensee Molecular Diversity Preservation International, Basel, Switzerland. This article is an open-access article distributed under the terms and conditions of the Creative Commons Attribution license (<http://creativecommons.org/licenses/by/3.0/>).





# Ocean Surface Currents From AVHRR Imagery: Comparison With Land-Based HF Radar Measurements

Scott R. Chubb, Richard P. Mied, Colin Y. Shen, Wei Chen, Thomas E. Evans, and Josh Kohut

**Abstract**—We focus on inverting the surface temperature (or heat) equation to obtain the surface velocity field in the coastal ocean and compare the results with those from the maximum cross correlation (MCC) technique and with the *in situ* velocity fields measured by the Rutgers University Coastal Ocean Dynamics Radar (CODAR). When compared with CODAR fields, velocities from the heat equation and MCC have comparable accuracies, but the heat equation technique better resolves the finer scale flow features. We use the results to directly calculate the surface divergence and vorticity. This is possible because we convert the traditionally underdetermined heat inversion problem to an overdetermined one without constraining the velocity field with divergence, vorticity, or energy statements. Because no *a priori* assumptions are made about the vorticity, it can be calculated directly from the velocity results. The derived vorticity field has typical open-ocean magnitudes ( $\sim 5 \times 10^{-5}/s$ ) and exhibits several structures (a warm core ring, Gulf Stream filament, and a diverging flow) consistent with the types of flows required to kinematically deform the sea surface temperature patterns into the observed configurations.

**Index Terms**—Geophysical measurements, HF radar, infrared (IR) imaging, remote sensing, satellite applications, sea coast, sea surface.

## I. INTRODUCTION

SATELLITE imaging of the ocean affords us the opportunity to image synoptically large areas and offers significant possibilities for understanding the dynamics of the ocean. The allure of obtaining sea surface velocities from sequential views of the ocean has been a powerful incentive to spur the processing of these image sequences to obtain the velocity maps. This paper is concerned with inverting the heat (or temperature) equation in the near-surface ocean to obtain synoptic velocity vector fields.

Researchers have used a number of techniques to obtain these vector fields, but two procedures have achieved prominence over the last few decades. The first is the maximum cross cor-

relation (MCC) algorithm [1], [2], which is a feature-tracking technique used extensively by oceanographers to process satellite data for surface velocities.

In the original work [1], [2] and in most of the many studies in which surface velocities have been extracted by using this procedure, the images are constructed using infrared (IR) data from Advanced Very High Resolution Radiometer (AVHRR) images. However, it is known [3] that phytoplankton act as tracers of currents under certain circumstances [3]. In [4], the MCC is used to obtain currents from a single pair of coastal zone color scanner images. Crocker *et al.* [5] extend this by including additional IR and ocean color information. They derive surface velocities at different times with the MCC procedure from AVHRR IR data and ocean color data from the Moderate Resolution Imaging Spectrometer and the sea-viewing wide field-of-view sensor.

In addition to inferring ocean surface currents through the MCC procedure, the technique has also been used to find surface velocities in such diverse applications as ice motion [6], snow in avalanches [7], beach swash zone flows [8], atmospheric ozone motion [9], and surface velocities on a ground-water stream [10].

Another important, although less extensively used technique, is the inversion of the heat (or temperature) equation for the velocity vector. Two seminal works have laid the foundation for this. Using the 2-D nondiffusive heat equation, Kelly and Strub [11], [12] invert sequential AVHRR fields from early National Oceanographic and Atmospheric Administration (NOAA) imagers to obtain the surface velocity field and compare the results of their inverse (INV) technique with surface velocity fields from acoustic Doppler current profilers (ADCPs), near-surface drifters, geostrophic velocity profiles from Geosat, and the MCC technique.

The INV technique has also been employed to infer the properties of the ocean surface mixed layer [13], [14] as well as vertical mixed layer entrainment velocity and horizontal diffusivity. Using model-generated data, Vigan *et al.* [15], [16] demonstrate the utility of the method for the Brazil–Malvinas confluence region, whereas Zavialov *et al.* [17] perform a similar calculation for the same region using sea surface temperature (SST) data mapped from *in situ* measurements.

An important point, however, is that with the exception of two early applications [11], [12] of the technique, temporal averaging has been performed to obtain average current fields over longer periods of time (weeks and even months). In these

Manuscript received October 1, 2007; revised January 4, 2008. Current version published October 30, 2008.

S. R. Chubb, R. P. Mied, C. Y. Shen, W. Chen, and T. E. Evans are with the Remote Sensing Division, Naval Research Laboratory, Washington, DC 20375 USA.

J. Kohut is with the Center for Advanced and Sustained Technologies, Coastal Ocean Observation Laboratory, Institute of Marine and Coastal Sciences, Rutgers University, New Brunswick, NJ 08901 USA.

Color versions of one or more of the figures in this paper are available online at <http://ieeexplore.ieee.org>.

Digital Object Identifier 10.1109/TGRS.2008.923321

two early efforts [11], [12], constraints were imposed in order to make the problem tractable because the equations that are used are underdetermined. In response to a comment made by Walker [18], Kelly [19] pointed out that these constraints could explain the apparent differences in the magnitudes and directions of the INV and MCC velocity fields with each other and with *in situ* ADCP measurements and modeled currents. However, because of the coarseness of the spatial resolution of the *in situ* measurements, the potential for cloud contamination, and the use of only one AVHRR channel to infer SST, it has never been entirely clear how significantly the INV and MCC velocity fields differ from one another and from *in situ* measurements.

In this paper, we also explore the use of the INV and MCC methods to invert a sequence of AVHRR images to determine ocean surface velocities but focus on much finer temporal and spatial resolution scales than were employed in the earlier papers cited previously. We find that the verifiable accuracy obtained is much better than previously reported for several reasons. First, we do not impose the constraints used in the INV method [11], [12]. Second, we do not smooth the data but remove only broad-area trends. All of the finer scale surface isotherm structure is thus retained, and this structure provides unambiguous features for tracking and inversion.

Bowen *et al.* [20] found that surface velocity fields derived from AVHRR channel 4 ( $10.8 \mu\text{m}$ ) brightness temperature (BT) images appear to be more robust than comparable fields derived from SST. They suggested a plausible reason for this: SST images probably have more noise than BT ones because SST information is inferred from the difference between data from channels 4 and 5. Although the surface velocities are more robust when they are derived by using channel 4 images, surface velocities inferred from INV calculations are most accurate and meaningful when derived by using SST images (because they are derived by inverting the heat equation). For these reasons, we have used SST (as opposed to BT) images in both sets (INV and MCC) of calculations. Although channel 4 images are not used, the SST images that we have used have been processed in a more sophisticated way than the comparable images used in the previous comparable [11], [12] applications of the INV method.

Instead of only the raw irradiance channels available to Kelly and Strub [11], [12], we can now use level 2 SST data, which have been processed to remove sun glint, atmospheric aberrations, and geometric anomalies. An additional important improvement is our use of dense high-resolution surface current maps available from the Rutgers University Coastal Ocean Observing Laboratory Coastal Ocean Radar (CODAR) network. This provides ocean surface current velocity fields with finer spatial and temporal resolution over an ample area of several hundred square kilometers with which to compare velocities from the INV and MCC analyses.

This paper is not the first paper in which a comparison has been made between values of surface currents from MCC calculations and comparable values inferred from ground truth information provided by Rutgers University CODAR measurements. Moulin *et al.* [21], [22] made the first comparison between CODAR measurements and MCC currents. She compared

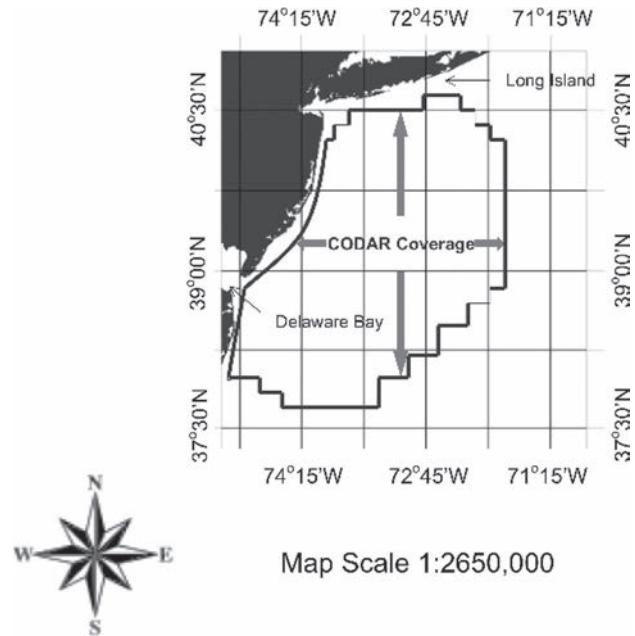


Fig. 1. Schematic diagram showing the approximate region and location of HF radar velocity field measurements used in our study.

four-month time-averaged CODAR current measurements with results inferred from MCC calculations compiled by the Colorado Center for Astrodynamics Research. Results showed a root-mean-square (rms) deviation of  $\sim 0.15$  m/s between each current component and an overall rms magnitude deviation of  $\sim 0.20$  m/s. The time interval employed (months) is substantially longer than the focus of this paper, which deals with time separations of a few hours. In addition, our concentration is on using the INV and MCC techniques and comparing the results obtained with those from the direct measurement of the surface current by CODAR.

This paper is organized as follows. Section II describes the properties of the AVHRR image sets and the current maps from the CODAR arrays. In Section III, the procedures for constructing vector fields from the INV and MCC techniques are discussed, whereas Section IV deals with detailed statistical comparisons among the current fields obtained by the two different procedures and CODAR. There, we compare our modeled velocity magnitude and direction relative to observed HF radar-derived current maps. In Section V, we use our INV modeled results to calculate the surface vorticity. We find that the resulting surface vorticity distribution reveals several identifiable dynamical structures (i.e., a warm core ring (WCR), a Gulf Stream (GS) filament, and a diverging surface flow) with appropriate order-of-magnitude vorticities collocated with their IR signatures. Moreover, finally, Section VI summarizes the important results of this paper.

## II. DATA SOURCES

### A. Overview

Fig. 1 is a schematic diagram showing our study region and the location of the CODAR velocity field measurements within it. The AVHRR images provide an SST field that extends over a rectangular area oriented with the  $y$ -axis pointing north,

$x$ -axis pointing east, and centered at  $38^{\circ} 29' 42.04''$  N,  $71^{\circ} 55' 7.61''$  W. Five successive CoastWatch AVHRR images [23]<sup>1</sup> of this region were collected at  $\sim 3$ -h intervals [23] on February 28, 2004 and obtained from the NOAA's web site [23]. Because these images have been processed by using NASA Level 2 software, they are all georeferenced (based on a Mercator projection and a cubic convolution algorithm within the ENVI software package [24]) relative to each other and have a common (North–South, East–West) orientation. Although each initial image is of the same size ( $1301$  longitude  $\times$   $1402$  latitude pixels) and has a common equatorial pixel resolution ( $1469$  m), the images were derived by using sensors on different satellites with different orbits; therefore, the image boundaries are not identical. For this reason, we choose a smaller subset ( $500 \times 500$  pixels) of each image. The actual resolution (in both the  $x$ - and  $y$ -directions) is thus  $1.469 \text{ km} \times \cos(38.495^{\circ}) = 1.15 \text{ km}$ .

The AVHRR data were all collected on a nearly cloud-free day during a time of high pressure (inferred from NOAA buoy data) and strong evaporative cooling. The buoy is located in the northern portion of the image with water temperatures  $< 3^{\circ}\text{C}$ , but we assume that the local behavior discerned from the records is suggestive of the broader synoptic-scale air–sea interaction physics over the entire image.

From 12:00 A.M. [Eastern Standard Time (EST)] until late morning, during the late afternoon, and through the evening hours, measurements of barometric pressure, sea surface temperature ( $T_{\text{sea}}$ ), and air temperature ( $T_{\text{air}}$ ) appear to confirm this.<sup>2</sup> In particular, between 0:00 and 10:00 EST [5:00 and 15:00 Universal Time (UT)],  $T_{\text{sea}}$  was constant ( $2.4^{\circ}\text{C}$ ), whereas  $T_{\text{air}}$  dropped from  $3.2^{\circ}\text{C}$  to  $1.6^{\circ}\text{C}$ . From 11:00 EST (16:00 UT) to sunset (at  $\sim 17:00$  EST), a period of solar diurnal heating occurred, in which  $T_{\text{sea}}$  rose from  $2.4^{\circ}\text{C}$  to  $2.8^{\circ}\text{C}$  and  $T_{\text{air}}$  rose from  $2.3^{\circ}\text{C}$  to  $4.0^{\circ}\text{C}$ . Between 17:00 and 22:00 EST, evaporative ocean cooling decreased  $T_{\text{sea}}$  from  $2.8^{\circ}\text{C}$  to  $2.5^{\circ}\text{C}$ , whereas  $T_{\text{air}}$  rose from  $4.0^{\circ}\text{C}$  to  $5.4^{\circ}\text{C}$ . During the remaining two hours,  $T_{\text{air}}$  first dropped by  $0.7^{\circ}\text{C}$  and then rose by  $0.1^{\circ}\text{C}$ . Throughout the day and night, the barometric pressure was reasonably high ( $\sim 1024$  mb) and remained nearly constant. As a consequence, the dominant contributions to the variations in heat flux across the air–sea interface for this day are expected to have resulted from the latent heat of vaporization ( $\approx 540 \text{ cal}/(\text{gm H}_2\text{O})$ ). Also, one would expect that because the upper ocean was well mixed vertically in the CODAR region, possible subsurface heat sources and sinks would not play an important role in heat flux variations across the interface. As we will show, this intuitive picture of heat flux across the air–sea interface, through evaporation, is consistent with a situation in which subsurface sources or sinks of heat flux

and thermal gradients are inconsequential. Consequently, we may approximate SST in the region as a conserved quantity, and variations in the SST from one image to the next may be assumed to be due to the advection of fluid particles by the near-surface velocity field.

### B. AVHRR Imagery

Fig. 2 shows the five AVHRR images we have used to infer values of the currents. The images in Fig. 2(a)–(e) were constructed from data collected at 11:13, 14:36, 16:15, 19:02, and 22:32 UT, respectively, on February 28, 2004. In each of these figures, there are four distinctive features marked with arrows and labeled in the image from 16:15 [shown in Fig. 2(c)]. Here, “Warm Core Ring” refers to the circular feature near the northern boundary of the GS. “Dipole Vortices” are the circularly shaped features near the center of the image. We may plausibly hypothesize that these features are eddies resulting from instabilities in the vicinity of the GS. The appearance of the tracer in both of these dipole structures gives the impression that fluid is being advected around the periphery of a counter-rotating vortex pair.

The examination of the frame-to-frame differences of the region between the “Coastal Current Region” and the vortices over time indicates that the water does have a larger scale clockwise (anticyclonic) flow toward the northeast. It seems logical to us to infer that the fourth feature (labeled “Atmospheric Convective Cells/Clouds”) is associated with variations in heat flux to the atmosphere because of the size, shape, and location of the features within the GS. Similar features have been observed in radar images [25] and subsequently modeled [26] by using information obtained during the “Naval Research Laboratory/NASA Gulf Stream, Shuttle Imaging Radar-C Experiment” [27].

### C. CODAR

Maps of surface currents were provided by an array of CODAR HF surface current mappers [28] consisting of four long-range and two high-resolution backscatter systems located along the New York Bight from Long Island to Delaware Bay. Using the Doppler shifted radio signal scattered off the ocean surface, shore stations remotely measure surface current vector maps [29] for most of the New Jersey shelf. These maps have  $\sim 6$ -km resolution across the shelf with increased resolution near the Hudson River mouth. These systems have been operated continuously since 1998 to support validation [30], [31] and process studies across the shelf [32]–[37].

## III. PROCEDURES FOR EXTRACTING SURFACE CURRENTS FROM AVHRR IMAGERY

### A. MCC Method

In this paper, we use the MCC method to compute the velocity vector field between two image scenes by incrementally passing a subset ( $g$ ) from the later scene over a subset ( $f$ ) from the earlier scene and calculating a correlation coefficient between the two. The normalized correlation coefficient  $C_{fg}$  [38]

<sup>1</sup>The first and last (fifth) images (taken at 11:13 and 22:32 UT, respectively) were constructed from data collected by NOAA satellite N15. The second and third images (at 14:36 and 16:15 UT, respectively) were constructed by using data from NOAA satellite N16. The remaining (fourth) image was constructed from data collected from NOAA satellite N17.

<sup>2</sup>Data archived from the National Data Buoy Center includes meteorological measurements at station 44025 (located south of Islip, NY) of  $T_{\text{sea}}$ ,  $T_{\text{air}}$ , atmospheric pressure ( $P_{\text{atmos}}$ ), and wind speed and direction. This information is also available online: [http://www.ndbc.noaa.gov/view\\_text\\_file.php?filename=44025h2004.txt.gz&dir=data/historical/stdmet/](http://www.ndbc.noaa.gov/view_text_file.php?filename=44025h2004.txt.gz&dir=data/historical/stdmet/).



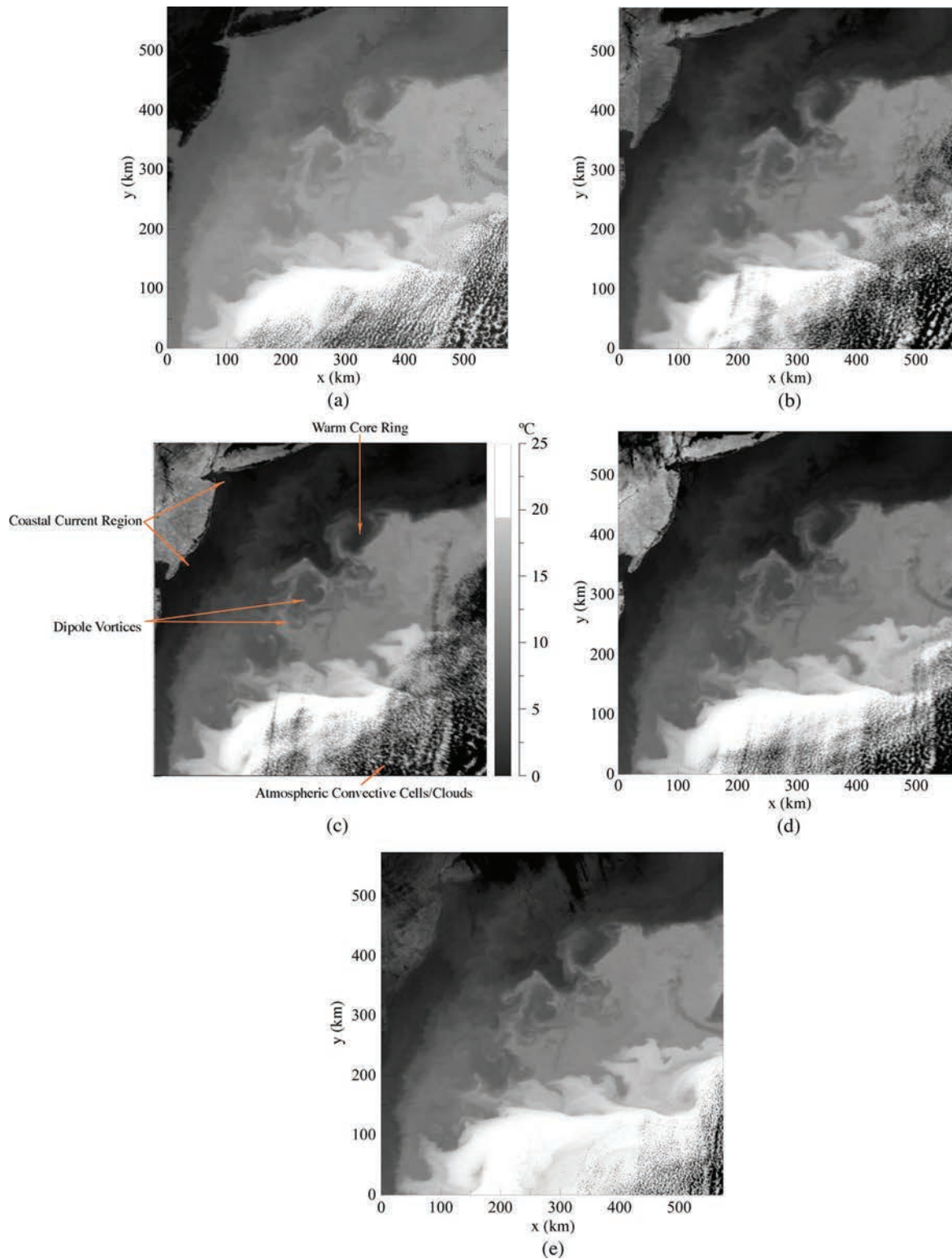


Fig. 2. AVHRR images from February 28, 2004 of the region shown in Fig. 1, derived from data collected at 11:13, 14:36, 16:15, 19:02, and 22:32 UT. We discuss the details of image processing, resolution size, and the precise location and orientation of each image in the text.

is specified in terms of pixels as shown at the bottom of the next page, where  $m$  is the pixel displacement in the  $x$ -direction,  $n$  is the  $y$ -direction pixel displacement, and  $\bar{f}_{00}$  is the average value over all  $f$  pixel values in the  $N \times N$  window. Similarly,  $\bar{g}_{mn}$  is the average over all pixels within an  $N \times N$  window centered over the pixel in the larger (later)  $g$  matrix but located

at  $(k + m, l + n)$ . We require that the smaller window be at least as large as the autocorrelation length scale so that the smaller window can meaningfully capture features within it. This smaller window is shifted one pixel at a time, and a correlation is computed. Moreover, the  $N \times N$  size used for  $f$  must be sufficiently large that the features we are tracking from



the early  $f$  window are identifiable in the later  $g$  window. We do not attempt a correlation in cloudy areas such as the cloud streaks over the GS.

Stated another way, the window size must be large enough so that the feature is not advected out of the  $N \times N$  window in the time interval between the two images. A simple way to do this is to move the  $N \times N$  window over a region, which is defined by an outer window that includes a sufficiently large number ( $N_D$ ) of additional pixels in each direction. This larger window is thus comprised of the original  $N \times N$  picture with an additional border of width  $N_D$  pixels on all four sides; therefore, this larger box has pixel dimensions of  $(N + 2N_D) \times (N + 2N_D)$ .

In order to resolve velocities of fluid particles in the  $N \times N$  window, its largest velocities ( $U_{\text{MAX}}$ ) must be incapable of advecting fluid during a time  $\Delta t$  farther than  $N_D \cdot \Delta x$ , where  $\Delta x$  is the pixel size. That is

$$U_{\text{MAX}} \cdot \Delta t < N_D \cdot \Delta x.$$

When analyzing a new image pair, we have no *a priori* knowledge of either the maximum velocity ( $U_{\text{MAX}}$ ), which will emerge, or the number of pixels ( $N_D$ ) needed to satisfactorily resolve it. To start, we choose  $N_D = 10$  and calculate the maximum resolvable velocities. For the four time intervals  $\Delta t_i \equiv t_{i+1} - t_i = 3.383, 1.650, 2.783$ , and  $3.500$  h. With these time intervals and  $N_D = 10$ , we calculate the maximum resolvable velocities for each of the intervals to be 0.95, 1.95, 1.15, and 0.92 m/s. Typical observed velocities are  $\sim 0.3$ – $0.5$  m/s; therefore, we have confidence in the MCC technique to correctly yield the surface velocities with  $N_D = 10$ .

For the purposes of this study, we have found that images in the North Atlantic are best treated by specifying the size of each ( $x$  and  $y$ ) side of the window as  $N = 40$  (corresponding to 46 km in each  $x$ - and  $y$ -direction). In fact, the autocorrelation length at half the autocorrelation amplitude is  $\sim 11$  pixels; therefore, the smaller window size of  $N = 40$  captures the significant variability in this field. Image separation times are as small as 1.7 h and as large as 3.4 h. During these longer intervals, temperature distributions can become very distorted on the smaller feature-tracking scales we employ, which compromises the correlation between two contiguous images. Nevertheless, minimum acceptable cross correlations of 0.5 have proven to give reliable results.

### B. INV Method

The heat conservation equation in the presence of negligible sources and sinks is

$$\partial T / \partial t + u \partial T / \partial x + v \partial T / \partial y = 0 \quad (2)$$

which relates the temporal rate of temperature change  $\partial T / \partial t$  at a point to the rate of temperature advection by the current velocities  $u$  and  $v$ , expressed here in the rectangular coordinates  $x$  (positive to the east) and  $y$  (positive to the north), respectively. This equation is underdetermined with respect to the two velocity components  $u$  and  $v$ . That is, this single equation for  $T$  cannot be solved for  $u$  and  $v$  uniquely at a point  $(x, y)$ . It is understood, however, that when two SST images are separated in time by  $\Delta t$ , the spatial scales  $L$  of temperature variation that can be accounted for by (2) are necessarily much larger than  $U_{\text{MAX}} \cdot \Delta t$ . Therefore, in effect, the current velocities that can be estimated from (2) have scales of order  $L$ . Current velocities may thus be considered approximately uniform on the grid scales of several  $\Delta x$ 's and  $\Delta y$ 's. As long as the velocity is not directed along the isotherms (so that  $(u, v) \cdot \nabla T \neq 0$ ), an assemblage of relationships of (2) from all points within the grid scales can be considered an overdetermined system of equations for  $u$  and  $v$ . For example, if one limits oneself to two grid scales, (i.e., a  $2\Delta x$  by  $2\Delta y$  area composed of nine grid points) and assumes  $u$  and  $v$  constants over these points, then there are nine equations of (2) for only two local unknowns ( $u$  and  $v$ ), which can be determined uniquely in the least squares sense. For further details associated with the implementation of the INV method and for the possibility of using dynamics in the implementation of this method, see Shen *et al.* [37].

For our computation of  $u$  and  $v$  from (2), the SST images are bandpass filtered to remove small-scale fluctuations of  $< 20$  km and large-scale variations of  $> 60$  km. The small-scale cutoff eliminates signals that cannot be accounted for by (2) based on the  $U_{\text{MAX}} \cdot \Delta t$  criterion discussed previously. The large-scale cutoff is intended to remove broad-scale variations typically associated with the near-surface vertical heat transfer processes unrelated to currents. To invert (2) for  $u$  and  $v$ , we use an array of nine points with three on each side. Before inverting the nine equations, the ratio  $(\partial T / \partial t) / |\nabla T|$  is tested for each equation. If the ratio is larger than what is acceptable ( $> 1$  m/s in the present case), a weight of  $10^{-4}$  is given to that equation. Furthermore, to filter out possibly unreliable data, the difference in the vector angle of  $\nabla T$  between the two images is checked at each grid point (pixel). If the difference is greater than  $90^\circ$ , the point is not used in inversion.

## IV. DETAILED COMPARISONS

Surface velocity maps from the four time intervals discussed previously have been obtained by using the MCC and INV methods, and it is very informative to compare these velocities with those from the CODAR array. To obtain a meaningful comparison, it is necessary to use the actual CODAR velocities, which include advective effects from all physical processes, i.e.,

$$C_{fg}(m, n) = \frac{\sum_{k=1}^N \sum_{l=1}^N [f(k, l) - \bar{f}_{00}] [g(k + m, l + n) - \bar{g}_{mn}]}{\sqrt{\sum_{k=1}^N \sum_{l=1}^N [f(k, l) - \bar{f}_{00}]^2} \sqrt{\sum_{k=1}^N \sum_{l=1}^N [g(k + m, l + n) - \bar{g}_{mn}]^2}} \quad (1)$$

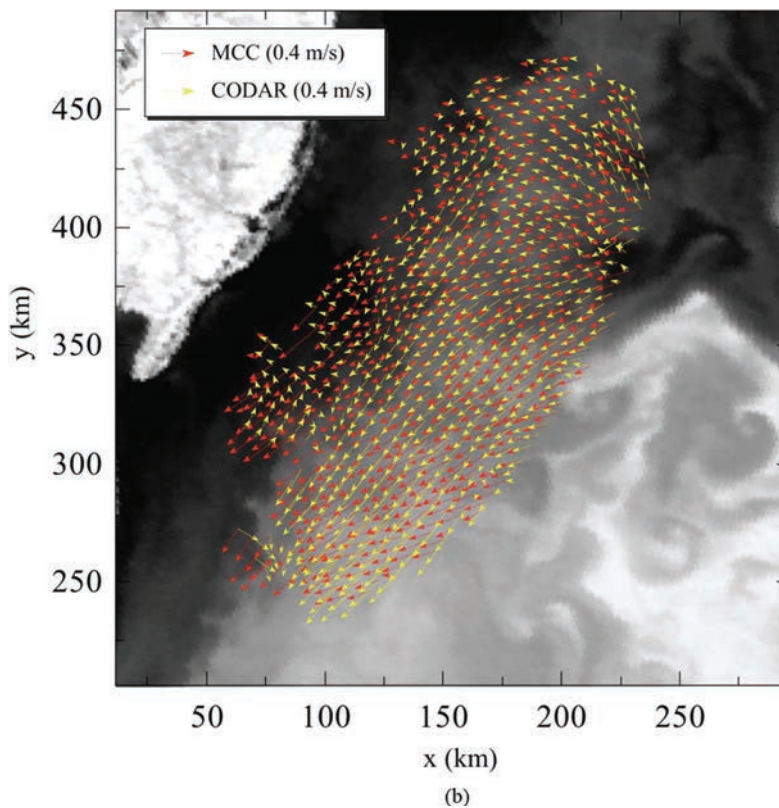
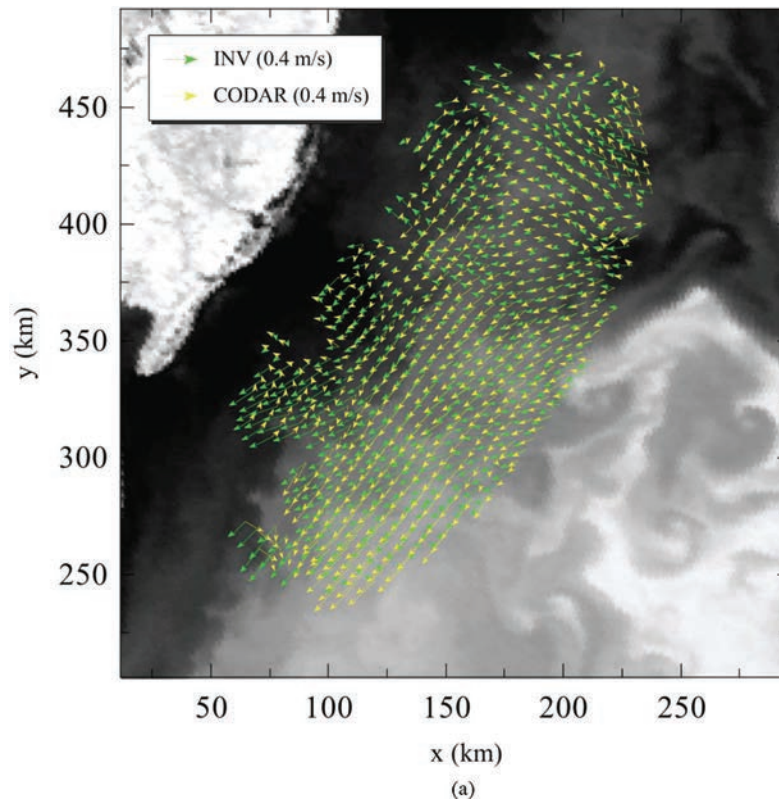


Fig. 3. CODAR current vectors at 12:55 UT, calculated by forming a linearly weighted sum of CODAR data at 12:00 and 13:00 UT, are shown in yellow; see text for details. Currents from (top) (green arrows) INV technique at 12:55 UT (midway between 11:13 and 14:36 UT) are each overlaid on the 11:13 UT AVHRR image in Fig. 2(a). Currents from (bottom) (red arrows) MCC method at 12:55 UT (midway between 11:13 and 14:36 UT) are each overlaid on the 11:13 UT AVHRR image in Fig. 2(a). The same velocity scale is used for all vectors, and the SST gray scale palette is the same as in Fig. 2.

tides and wind drift, as well as mesoscale motion. The CODAR grid has a data point every 6 km, whereas the MCC and INV data spacing is only 1.15 km. These INV/MCC points are never farther than 20% of the CODAR grid spacing from a CODAR data point. For comparison between the two, therefore, we do not interpolate but choose the computed point closest to the CODAR measurement.

We must take additional care when comparing derived velocity fields (either MCC or INV) with CODAR velocities because the two records are not contemporaneous. The available AVHRR images are at times  $t_1 = 11:13$ ,  $t_2 = 14:36$ ,  $t_3 = 16:15$ ,  $t_4 = 19:02$ , and  $t_5 = 22:32$  (all times in UT). Because velocities are derived from contiguous image pairs, the velocity fields occur at times  $\tau_i = (t_{i+1} + t_i)/2$ , ( $i = 1, \dots, 4$ ). In contrast, CODAR records occur on the hour and are transformed to derived-image times  $\tau_i$  by a linearly weighted sum. For example,  $\tau_1 = 12:55$  UT, and CODAR velocities at an equivalent time are obtained by defining

$$\begin{aligned} \vec{u}_{\text{CODAR}}(t = 12:55) = & \frac{(13:00 - 12:55)}{60} \\ & \times \vec{u}_{\text{CODAR}}(t = 12:00) \\ & + \frac{(12:55 - 12:00)}{60} \\ & \times \vec{u}_{\text{CODAR}}(t = 13:00). \end{aligned}$$

A CODAR record is thus more heavily weighted if it is closer to the desired time  $\tau_i$ .

In Fig. 3(a), we show results from applying the INV method (green arrows) at approximately 12:55 UT and the comparable CODAR measurements (yellow arrows) overlaid on the AVHRR image at 11:13 UT from Fig. 2(a). (Note that the regions shown in images in Figs. 2 and 3(a) are different. Fig. 3 shows a smaller region in order to provide a more finely resolved image of the measured values of the currents.) Both fields have the same qualitative behavior. Water in the northeast part of the CODAR footprint flows westward and curves toward the southwest. Except at the edges of the CODAR footprint, the overall visual impression is that the two velocity fields correlate well. The INV vectors appear generally slightly larger (longer) than the CODAR vectors, and the INV velocities are generally rotated clockwise relative to the CODAR. The precise amount by which the INV vectors lead the CODAR vectors varies across the footprint, but a visual impression seems to be approximately  $10^\circ$ .

Fig. 3(b) shows the results when the MCC method is used, and red arrows designate these results. The MCC velocity vectors are also generally oriented clockwise by about  $10^\circ$  with respect to the CODAR vectors and are somewhat larger than them. Although the CODAR field is regularly distributed over the region with a resolution of  $\approx 6$  km, the derived fields (INV and MCC) can exhibit data gaps or “holes” in the results because of a local absence of trackable SST features required to infer current values.

To quantify how well either method (INV or MCC) and the CODAR currents agree, we compute a complex correlation

coefficient [39]

$$\rho = \frac{\langle \omega \cdot \omega_{\text{CODAR}}^* \rangle}{[\langle \omega \cdot \omega^* \rangle \langle \omega_{\text{CODAR}} \cdot \omega_{\text{CODAR}}^* \rangle]^{1/2}} \equiv |\rho| e^{i\phi} \quad (3)$$

where the 2-D velocity field  $(u, v)$  (for either the INV or MCC result) is represented as a complex number  $\omega$  defined by

$$\begin{aligned} \omega &= u + i \cdot v \\ \omega^* &= u - i \cdot v \end{aligned} \quad (4)$$

and  $\omega_{\text{CODAR}}$  is defined similarly for the CODAR field. From (3), we may define an average magnitude correlation coefficient  $|\rho|$  using

$$|\rho| = \left[ (\text{Re}(\rho))^2 + (\text{Im}(\rho))^2 \right]^{1/2} \quad (5)$$

and an average angular phase difference between the derived (INV or MCC) velocity field and the CODAR field. The phase is defined as

$$\phi \equiv \tan^{-1} [\text{Im}(\rho)/\text{Re}(\rho)]. \quad (6)$$

The phase of  $\rho$  [(3) and (6)] indicates that  $\phi$  is defined, effectively, as an average angular difference between the derived and CODAR velocities. Because anticlockwise angles are positive, a negative  $\phi$  represents a situation in which the derived velocities are oriented clockwise relative to the CODAR vectors, which is consistent with the visual impression that one obtains from Fig. 3(a) and (b).

In Table I, we show all of the values of  $\phi$  and  $|\rho|$  (labeled with the appropriate subscripts) for all of the intervals of time. With the exception of 17:39 UT, where the average MCC magnitude is smallest,  $\phi < 0$  in both calculations. This indicates that, on the average, the calculations provide currents that are rotated clockwise relative to the CODAR-derived currents. The correlation coefficient magnitudes are comparable in the INV and MCC calculations, although, with the exception of the correlation values that apply at 17:39 UT, the MCC calculations appear to be slightly better. The range of values for the correlation coefficient magnitude in the MCC case ( $|\rho_{\text{MCC}}|$ ) is

$$0.541 < |\rho_{\text{MCC}}| < 0.806 \quad (7)$$

whereas the comparable range of values for the INV case is

$$0.565 < |\rho_{\text{INV}}| < 0.732. \quad (8)$$

The ranges of variation in the angular correlation coefficients for the two cases are

$$-25.3^\circ < \phi_{\text{MCC}} < 7.0^\circ \quad (9)$$

and

$$-29.2^\circ < \phi_{\text{INV}} < 16.9^\circ. \quad (10)$$

Despite the variation in  $|\rho|$  and  $\phi$ , the average values are remarkably close. As displayed in Table I, the average  $|\rho|$  for MCC and INV are 0.663 and 0.637, respectively. The average  $\phi$ 's for MCC and INV are  $-10.2^\circ$  and  $-9.7^\circ$ , respectively. Together, both magnitudes and angles indicate that the INV and



TABLE I

VALUES OF THE CORRELATION COEFFICIENTS [DEFINED BY (5) AND (6)] DEFINED BY THE AVERAGE ANGLE ( $\phi$ ) AND MAGNITUDE ( $|\rho|$ ) BETWEEN VELOCITIES INFERRED BY THE MCC AND INV METHODS AND MEASURED VALUES (CODAR). THE TIMES ARE DEFINED BY THE AVERAGE VALUE OF EACH TIME  $\tau_i = (t_{i+1} + t_i)/2$  WHEN AVHRR DATA WERE COLLECTED ( $t_1 = 11:13$ ,  $t_2 = 14:36$ ,  $t_3 = 16:15$ ,  $t_4 = 19:02$ ,  $t_5 = 22:32$ )

$\tau_i$	$\phi_{MCC}$	$\phi_{INV}$	$ \rho_{MCC} $	$ \rho_{INV} $
12:55 UT	-9.4°	-14.5°	0.806	0.732
15:26 UT	-25.3°	-29.2°	0.593	0.565
17:39 UT	7.0°	16.9°	0.541	0.676
20:47 UT	-13.2°	-12.0°	0.711	0.574
Average (All times)	-10.2°	-9.7°	0.663	0.637

MCC techniques have the same degree of correspondence with the CODAR measurements.

The data in Fig. 3(a) and (b) are presented in histogram form in Fig. 4. Here, Fig. 4(a) shows the frequency of particular values of the difference between the relative directions  $\Delta\theta = \theta_{INV} - \theta_{CODAR}$  and speeds  $\Delta V = V_{INV} - V_{CODAR}$  for the INV results. Similar results appear in Fig. 4(b) for the MCC. All results are for the time  $\tau_1 = 12:55$  when the currents had their greatest average correlation coefficients. The locations of the histogram peaks in both the INV [Fig. 4(a)] and MCC [Fig. 4(b)] cases indicate that  $\Delta\theta$  is slightly less than zero, which is consistent with the location of the average value of the angular correlation coefficient. The positive current speed difference ( $\Delta V > 0$ ) indicates that the derived speed exceeds the CODAR-derived current speed. The magnitude and direction information in the histograms is thus consistent with our observation of the trends in Fig. 3.

In the previous comparisons, we focus on a complex correlation between the inferred velocities (INV and MCC) and the *in situ* ones (CODAR). However, Kelly and Strub [12] calculate the rms deviation of their velocities from the measured ones as an indicator of the agreement. In order to compare the relative accuracy of our results with theirs, we also calculate the equivalent rms statistics.

Our results are comprised of velocity maps at four time intervals (listed in Table I). We calculate the differences in angular orientation between the inferred and measured values of the current ( $\Delta\phi_{MCC}$  and  $\Delta\phi_{INV}$ ) as well as the ratio of the inferred current magnitudes to the measured ones ( $r_{MCC}$  and  $r_{INV}$ ). We summarize this information in Table II for the same times as in Table I. The rms deviations listed are spatial averages over the entire CODAR footprint for both the MCC and INV procedures. We attempt a meaningful comparison with the results in [12] by calculating a temporal angular average defined as  $\langle\Delta\phi_{INV}\rangle_\tau = (1/4) \sum_{i=1}^4 \Delta\phi_{INV}(\tau_i)$  and similarly for  $\Delta\phi_{MCC}$ ,  $\langle r_{INV}\rangle_\tau$ , and  $\langle r_{MCC}\rangle_\tau$ . Each is listed in Table II. By averaging each column in Table II, we obtain the average rms deviation between the inferred values of the

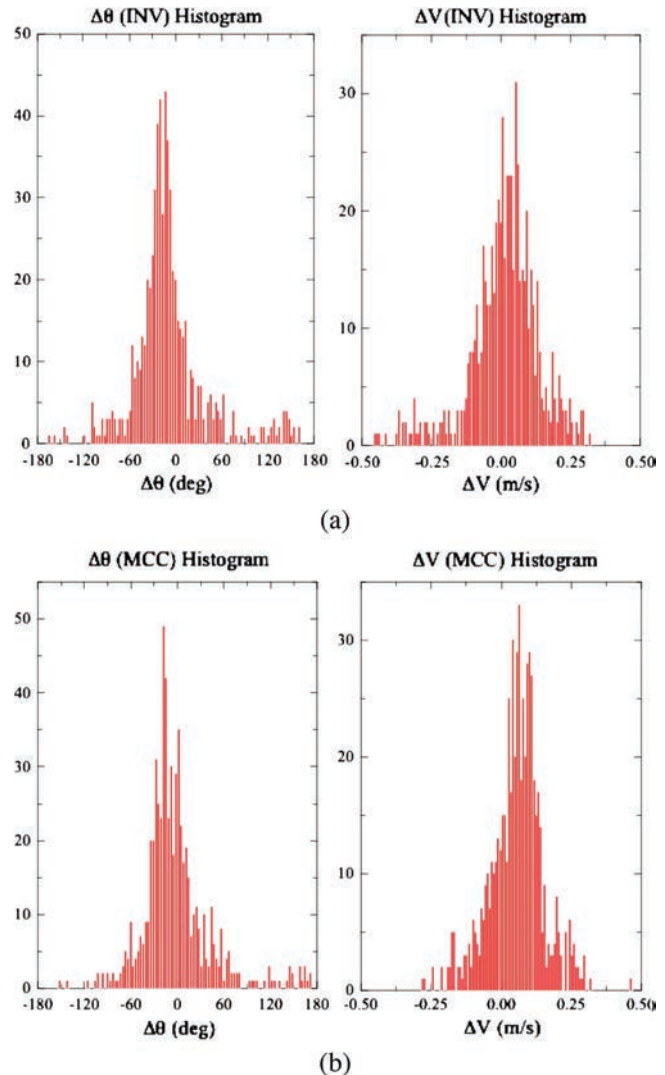


Fig. 4. Histograms of the frequency of current value differences (angle and magnitude) between inferred (a) INV and (b) MCC methods and CODAR at 12:55 UT. Plots in (a) and (b) were constructed by using the linear averaging procedure described for CODAR in Fig. 3(a) and (b).



TABLE II  
RMS DEVIATIONS  $\Delta\phi_{MCC}$  AND  $\Delta\phi_{INV}$  BETWEEN THE ANGLE OF THE CODAR SURFACE CURRENT AND THE SURFACE CURRENTS FROM THE MCC AND INV PROCEDURES. THE RATIOS ( $r_{MCC}$  AND  $r_{INV}$ ) OF THE CALCULATED TO MEASURED VALUE OF THE MAGNITUDE OF THE SURFACE CURRENTS ARE DEFINED AT THE SAME TIMES AS IN TABLE I

$\tau_i$	$\Delta\phi_{INV}$	$\Delta\phi_{MCC}$	$r_{INV}$	$r_{MCC}$
12:55 UT	49°	44°	1.07	1.18
15:26 UT	79°	90°	1.01	0.56
17:39 UT	72°	74°	1.16	1.04
20:47 UT	54°	51°	0.80	0.91
Average (All times)	63°	65°	1.01	0.92

MCC (INV) currents and the CODAR values over the entire footprint for all times. These angular deviations for our MCC (INV) are 65° (63°). The ADCP/image calculations of Kelly and Strub [12] yield MCC (INV) values of 73° (64°). Whereas our MCC calculation reduces the angular difference error in the MCC/CODAR difference by only 8°, the INV direction error is unimproved. Interestingly, though, the ratios of the magnitudes of both the average MCC and INV inferred currents and the measured values exhibit substantial improvement. When the inferred values are derived from our MCC method, the associated ratio is  $\langle r_{MCC} \rangle_\tau = 0.92$ , whereas our INV method yields  $\langle r_{INV} \rangle_\tau = 1.01$ . These are much improved over the previous [12] values for MCC (INV) of 0.58 (0.51).

The INV and MCC image techniques described in this paper use the same data to achieve their results; therefore, it is of interest to compare how well the two sets of results agree with one another. We test this by adopting the complex correlation coefficient from (3) and define

$$\rho = \frac{\langle \omega_{INV} \cdot \omega_{MCC}^* \rangle}{[\langle \omega_{INV} \cdot \omega_{INV}^* \rangle \langle \omega_{MCC} \cdot \omega_{MCC}^* \rangle]^{1/2}} \equiv |\rho| e^{i\phi}.$$

As can be seen from Table III, there is relatively good agreement between the correlation in magnitude (which varies between 0.58 and 0.90) and angular correlation (which varies between  $-1.08^\circ$  and  $+11.2^\circ$ ). We tabulate an average over all data sets as well, and the values for the correlation magnitudes and angles are 0.73 and  $1.31^\circ$ , respectively. The two data-retrieval techniques yield results, which agree quite closely. Moreover, the range over which the velocity angles are distributed is rather small and displays little variation.

## V. SURFACE VORTICITY

At any point, the INV method computes a velocity component pair ( $u$  and  $v$ ) from only nine points. On the other hand, MCC derives results based on a correlation between pixel blocks with side dimensions of  $N = 40$ . One expects that because of the disparity in sample sizes, the INV yields finer spatial resolution than the comparable MCC result and

TABLE III  
AVERAGE ANGULAR ( $\phi$ ) AND MAGNITUDE ( $|\rho|$ ) CORRELATIONS BETWEEN THE INV AND MCC CALCULATIONS AT THE TIMES DEFINED BY THE AVERAGE VALUE OF EACH TIME  $\tau_i = (t_{i+1} + t_i)/2$  AT WHICH THE AVHRR DATA WERE COLLECTED ( $t_1 = 11:13$ ,  $t_2 = 14:36$ ,  $t_3 = 16:15$ ,  $t_4 = 19:02$ ,  $t_5 = 22:32$ ). A POSITIVE (NEGATIVE) ANGLE INDICATES AN INV VECTOR ORIENTED ANTICLOCKWISE (CLOCKWISE) TO THE MCC ONE

$\tau_i$	$\phi$	$ \rho $
12:55 UT	$-6.27^\circ$	0.90
15:26 UT	$1.38^\circ$	0.58
17:39 UT	$11.2^\circ$	0.70
20:47 UT	$-1.08^\circ$	0.75
Average (All times)	$1.31^\circ$	0.73

may be better suited for extracting computed quantities such as the vorticity and divergence. Because the MCC method uses a statistical procedure with a much larger footprint, the technique effectively introduces an averaging that bears the effect of velocities at distant pixels. In contrast, INV operates locally by deriving results from locations no more than one pixel away. For this reason, we calculate these quantities solely with the INV method.

For this purpose, it is useful to define the 3-D current vector  $\vec{C} = (u, v, w)$  so that the vertical component of the vorticity may be written as

$$\xi \equiv \hat{z} \cdot (\nabla \times \vec{C}) = \frac{\partial v}{\partial x} - \frac{\partial u}{\partial y}. \quad (11)$$

We expect that there will be some noise in the retrieved velocity fields, and taking derivatives for the divergence and vorticity can only compound this problem; smoothing is required. Therefore, we fit a general second-order polynomial of the form

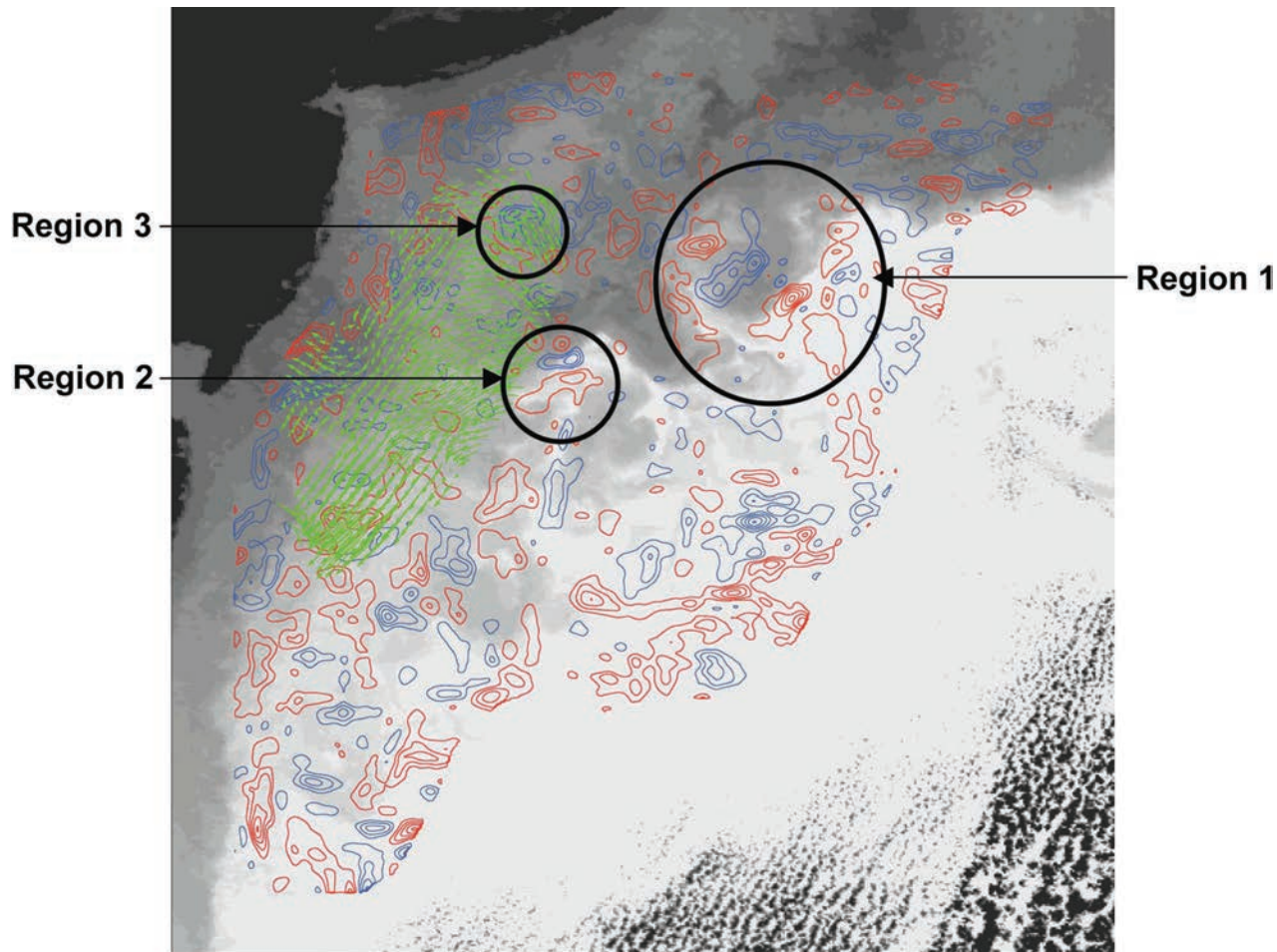


Fig. 5. Contour plots of the calculated vorticity  $\zeta = (\partial v / \partial x) - (\partial u / \partial y)$  (red when  $\zeta > 0$  and blue for  $\zeta < 0$ ) at time 12:55 UT, overlaid on the AVHRR image from 11:13 UT. In these plots,  $\zeta$  varies between  $\zeta_{\min} = -6.67 \times 10^{-5} \text{ s}^{-1}$  and  $\zeta_{\max} = 5.29 \times 10^{-5} \text{ s}^{-1}$ ; the contour increment is  $1 \times 10^{-5} \text{ s}^{-1}$ . INV currents at the location of the CODAR footprint are shown in green. Three regions with interesting collocated IR and vorticity structures are delineated and discussed in the text.

$ax^2 + by^2 + cxy + dx + ey + f$  to both  $u$  and  $v$  components at each pixel location and the surrounding eight points using a least squares fit over the nine points.

In Fig. 5, we show contour plots of the calculated vorticity  $\zeta = (\partial v / \partial x) - (\partial u / \partial y)$ , overlaid on the AVHRR image from 11:13 UT, with  $u$  and  $v$  inferred from the INV procedure. Red contours are used for values of  $\zeta$  that are positive (which are associated with cyclonic or counterclockwise vorticity). Blue is used for values that are negative (and are associated with clockwise vorticity). The contour increment is  $10^{-5} \text{ s}^{-1}$ , and the interval represented is  $-6.67 \cdot 10^{-5} \text{ s}^{-1} < \zeta < +5.29 \cdot 10^{-5} \text{ s}^{-1}$ , which are on the order of the Coriolis frequency (and are typical vorticity magnitudes for this region).

There are three regions shown in Fig. 5, for which there is a strong visual correspondence between the computed vorticity distributions and the shape of the SST distribution. In each of these three locations, we see that the vorticity distribution is consistent with the sense of tracer advection of the SST field.

Fig. 6(a) shows an enlargement of Region 1 and the vorticity contours and a representative anticyclonic swirl distribution [40], [41]. The details of the velocity distribution are not critical for this illustration, and we have sketched this example (and

those below) only to capture the typical properties of the expected flow field. The velocity in the center of the ring increases from zero to an anticyclonic maximum at a finite radius and then decreases at larger radii. The consequences of this typical velocity distribution are that the vorticity is negative near the ring center and positive away from it. Moreover, indeed, we see that the contours in Fig. 6(a) are blue ( $\zeta < 0$ ) for small radii and red ( $\zeta > 0$ ) in an annulus surrounding the negative-vorticity core. The northern portion of the ring appears to possess no vorticity only because of the absence of trackable features there. The negative vorticity core is not circular, which may suggest the presence of azimuthal perturbations from the assumed axisymmetric shape.

Region 2 [Fig. 6(b)] shows a retrograde filament of warmer water being advected from the GS. As in Fig. 6(a), we show a superposition of the SST, surface vorticity, and a notional profile of a velocity distribution consistent with the observed SST deformation. We see that the northern and southern flanks of both the SST and vorticity distribution are consistent with the assumption of a rudimentary jet structure. Specifically, we note  $\zeta < 0$  (blue contours) at this location. Conversely, the southern flank of the jet associated with the filament exhibits a region of red vorticity isopleths, corresponding to  $\zeta > 0$  there.

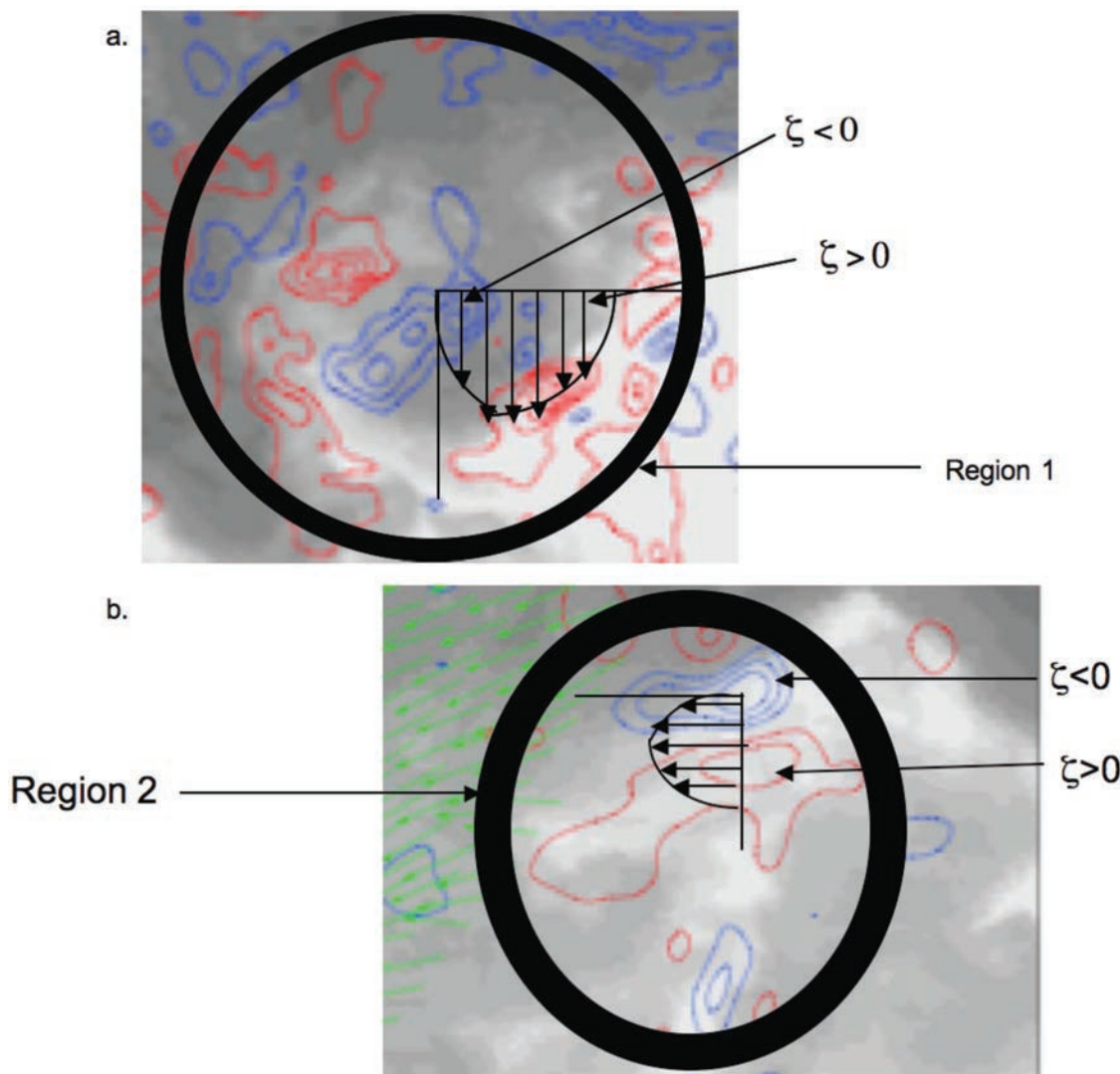


Fig. 6. (a) Enlargement of the WCR in Region 1 (Fig. 5) showing isopleths of vorticity; color code and contour level are as in Fig. 6. A notional velocity profile, typical of WCRs, is superimposed. (b) A retrograde jet from Region 2 is revealed in the AVHRR pattern. The vorticity contours and a typical jet profile are also shown.

The vorticity, SST deformation pattern, and assumed velocity profile are thus all mutually consistent with that of an energetic jet advecting fluid from the GS.

The portion of the ocean shown in Region 3 [Fig. 6(c)] is unique among the three areas shown in Fig. 5, because it also contains some velocity vectors measured by CODAR. Region 3 is centered over the site, where the velocity field is diverging. The CODAR vectors are rotating clockwise in the northern part of the delineated circle, whereas the vectors just south of them exhibit an anticlockwise swirl. The associated vorticity is compatible with this surface velocity structure. In particular, cyclonic ( $\zeta > 0$  or red) contours lie to the south of anticyclonic ( $\zeta < 0$ , blue) ones. In this case, the CODAR velocities provide a direct and independent corroboration of the sense of the vorticities derived from the INV technique.

## VI. CONCLUSION

In this paper, we have used the heat equation INV and MCC methods to invert a sequence of AVHRR images to estimate

ocean surface velocities. The focus for the INV has been on much smaller temporal and spatial resolutions than has been commonly used previously. We have found that the verifiable accuracy obtained is much better than reported previously for several reasons. 1) We have been able to make use of ground truth (CODAR) that provides considerably more current information than was possible in either of the two earlier studies [11], [12], where current information was provided by ADCP measurements. 2) The techniques in this paper do not require the assumption of divergence and vorticity constraints used in these earlier studies. 3) We have not smoothed the data. 4) We have greatly benefited from NASA's Level 2 SST product, which is derived by using a model that removes sun glint, atmospheric aberrations, and geometric anomalies known to be present in the raw irradiance channel data used in the earlier studies.

Five AVHRR images were all collected on a relatively cloud-free day during a time of high pressure and strong evaporative cooling. We infer this fact from temporally resolved buoy measurements<sup>2</sup> of sea temperature ( $T_{\text{sea}}$ ), air temperature



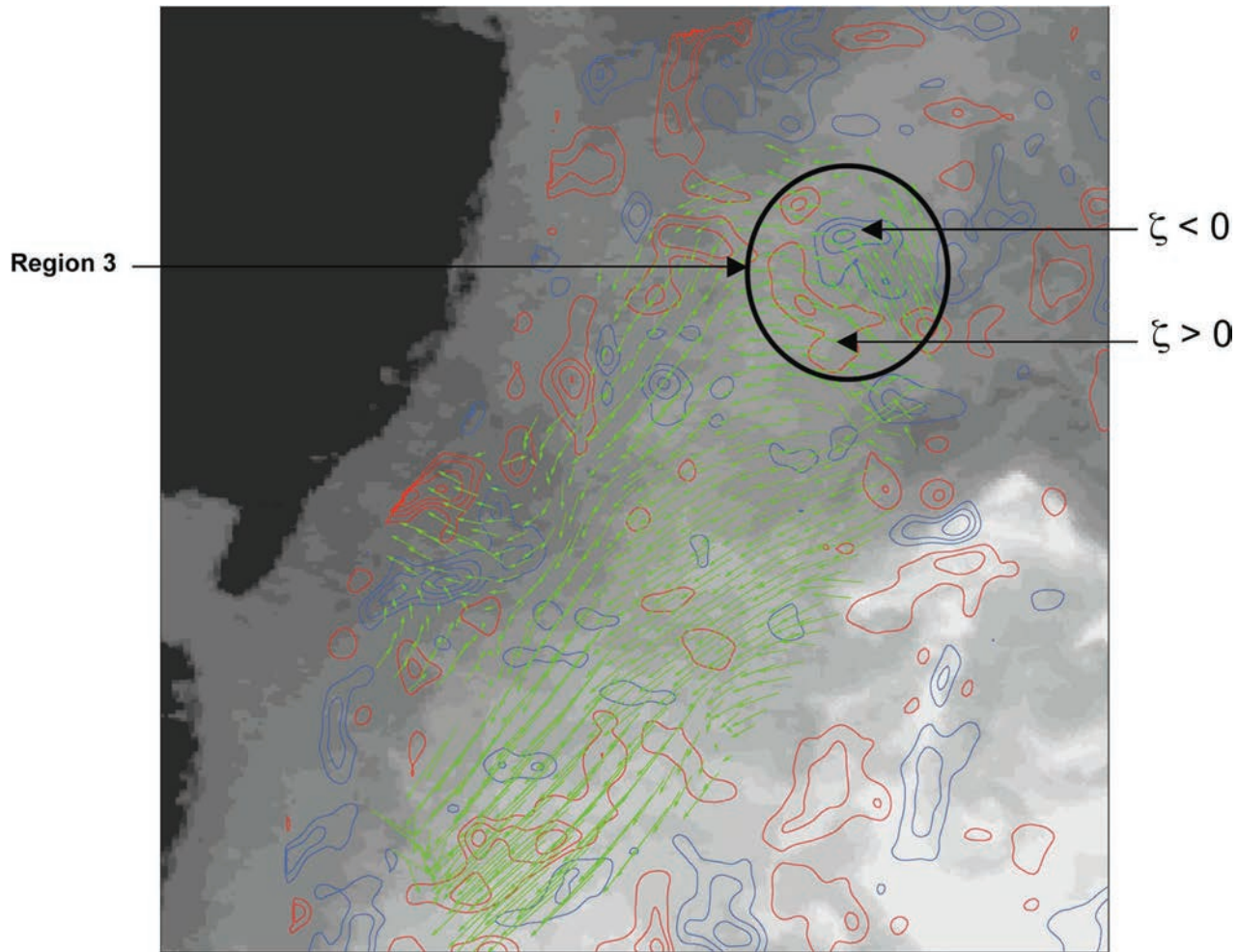


Fig. 6. (Continued.) (c) A region of diverging velocity, as revealed in the INV velocity field, is shown with the computed vorticity contours. A larger region (which includes all of the CODAR measurements) is shown in (c) than in (a) and (b).

( $T_{\text{air}}$ ), and atmospheric pressure. This intuitive picture associated with a dominant source of evaporative heat flux across the air–sea interface is consistent with a situation in which subsurface sources or sinks of heat flux and thermal gradients are inconsequential. Consequently, changes in the SST fields associated with the AVHRR images should closely track variations in the sea surface currents, and this intuitive picture of the dynamics seems valid.

Because of the large amount of available CODAR data, it has been possible to examine quantitatively the deviation between the current speeds and directions of the AVHRR-derived results relative to those values inferred from the CODAR measurements. In Kelly and Strub's seminal studies [11], [12], ground truth velocity information was provided through Doppler acoustic log surveys, ADCP measurements, and drifter tracks at a small number of locations; quantitative comparisons were possible only with approximate temporal averaging. In this paper, CODAR measurements have been performed continuously in time and on a grid comprising hundreds of locations, so that a rich, temporally, and spatially resolved (1 h and 6 km) current data set is available for a more detailed comparison with the image-derived results. These rms angular deviations

for our MCC (INV) are  $65^\circ$  ( $63^\circ$ ), which correspond to the ADCP/image calculations by Kelly and Strub [12] of  $73^\circ$  ( $64^\circ$ ). Whereas our MCC calculation shows an improvement in the MCC–CODAR angular difference error of only  $8^\circ$ , the INV direction error is unimproved. However, the ratios of the magnitudes of both the average MCC and INV inferred currents and CODAR values are improved significantly. For our MCC method, the average ratio is  $\langle r_{\text{MCC}} \rangle_\tau = 0.92$ , and our INV method yields  $\langle r_{\text{INV}} \rangle_\tau = 1.01$ . Compared with previous [12] values for MCC (INV) of 0.58 (0.51), these are much improved, which is likely due to our ability to make detailed comparisons through the densely populated CODAR fields. The agreement between the inferred current speed and direction from the INV and MCC is generally excellent both for the average magnitude of the correlation (0.73) and the angular correlation ( $1.31^\circ$ ) between the inferred values of the currents.

These numerical results have provided an important test of the reliability of our calculations. In order to gain a further understanding of the usefulness of the INV method and to see if further insight could be obtained into the underlying dynamics, we fit a 2-D quadratic expression to the horizontal velocity components to infer values of the local surface vorticity. We find



that at least three interesting examples of vorticity structures emerge: a WCR, a GS filament, and a divergent region. This last scenario is located in the northern part of the region covered by CODAR. In all these cases, the computed vorticity distributions are consistent with the inferred velocity patterns required for the observed kinematic distortions of the tracer.

The resulting calculations have provided quantitative information about local dynamics in the New York Bight and allow a picture of the local smaller scale flow structures. Our hope is that the high-resolution remote measurements made possible by using spaceborne/airborne imagery and the INV technique will allow surface dynamics to be discerned at greater ranges than those for which land-based CODAR measurements are possible.

## REFERENCES

- [1] J. A. Leese and C. S. Novak, "An automated technique for obtaining cloud motion from geosynchronous satellite data using cross correlation," *J. Appl. Meteorol.*, vol. 10, no. 1, pp. 118–132, Feb. 1971.
- [2] W. J. Emery, A. C. Thomas, M. J. Collins, W. R. Crawford, and D. L. Mackas, "An objective method for computing advective surface velocities from sequential infrared satellite images," *J. Geophys. Res.*, vol. 91, no. C11, pp. 12 865–12 878, 1986.
- [3] J. F. R. Gower, K. L. Denman, and R. J. Holyer, "Phytoplankton patchiness indicates the fluctuation spectrum of mesoscale oceanic structure," *Nature*, vol. 288, no. 5787, pp. 157–159, 1980.
- [4] C. A. E. Garcia and I. S. Robinson, "Sea surface velocities in shallow seas extracted from sequential coastal zone color scanner satellite data," *J. Geophys. Res.*, vol. 94, no. C9, pp. 12 681–12 692, 1989.
- [5] R. I. Crocker, W. J. Emery, D. K. Matthews, and D. J. Baldwin, "Computing coastal ocean surface currents from infrared and ocean color satellite imagery," *IEEE Trans. Geosci. Remote Sens.*, vol. 45, no. 2, pp. 435–447, Feb. 2007.
- [6] R. M. Ninnis, W. J. Emery, and M. J. Collins, "Automated extraction of pack ice motion from advanced very high resolution radiometer imagery," *J. Geophys. Res.*, vol. 91, no. C9, pp. 10 725–10 734, Sep. 1986.
- [7] F. Granada, O. Marco, and P. Villemain, "Use of imaging techniques for velocity mapping on the surface of a dense avalanche," *Houille Blanche-Revue Internationale de Eau*, vol. 50, pp. 69–75, 1995.
- [8] K. T. Holland, J. A. Puleo, and T. N. Kooney, "Quantification of swash flows using video-based particle image velocimetry," *Coast. Eng.*, vol. 44, no. 2, pp. 65–77, Dec. 2001.
- [9] V. Gelpke and H. R. Kunsch, "Estimation of motion from sequences of images: Daily variability of total ozone mapping spectrometer ozone data," *J. Geophys. Res.*, vol. 106, no. D11, pp. 11 825–11 834, 2001.
- [10] A. A. Bradley, A. Kruger, E. A. Meselhe, and M. V. I. Muste, "Flow measurement in streams using video imagery," *Water Resour. Res.*, vol. 38, no. 12, pp. 1315–1326, 2002.
- [11] K. A. Kelly, "An inverse model for near-surface velocity from infrared images," *J. Phys. Oceanogr.*, vol. 19, no. 12, pp. 1845–1864, Dec. 1989.
- [12] K. A. Kelly and P. T. Strub, "Comparison of velocity estimates from advanced very high-resolution radiometer in the coastal transition zone," *J. Geophys. Res.*, vol. 97, no. C6, pp. 9653–9668, 1992.
- [13] A. Ostrovskii and L. Piterburg, "Inversion for heat anomaly transport from sea surface temperature time series in the northwest Pacific," *J. Geophys. Res.*, vol. 100, no. C3, pp. 4845–4865, 1995.
- [14] A. G. Ostrovskii and L. I. Piterburg, "Inversion of upper ocean temperature time series for entrainment, advection, and diffusivity," *J. Phys. Oceanogr.*, vol. 30, no. 1, pp. 201–204, Jan. 2000.
- [15] X. Vigan, C. Provost, R. Bleck, and P. Courtier, "Sea surface velocities from sea surface temperature image sequences 1. Method and validation using primitive equation model output," *J. Geophys. Res.*, vol. 105, no. C8, pp. 19 499–19 514, 2000.
- [16] X. Vigan, C. Provost, and G. Podesta, "Sea surface velocities from sea surface temperature image sequences 2. Application to the Brazil–Malvinas confluence area," *J. Geophys. Res.*, vol. 105, no. 8, pp. 19 515–19 534, 2000.
- [17] P. O. Zavialov, R. D. Ghisolfi, and C. A. E. Garcia, "An inverse model for seasonal circulation over the southern Brazilian shelf: Near-surface velocity from the heat budget," *J. Phys. Oceanogr.*, vol. 28, no. 4, pp. 545–562, Apr. 1998.
- [18] S. J. Walker, "Comment on 'Comparison of velocity estimates from advanced very high resolution radiometer in the coastal transition zone' by K. A. Kelly and P. T. Strub," *J. Geophys. Res.*, vol. 99, no. C5, pp. 10 297–10 299, 1994.
- [19] K. A. Kelly, "Reply," *J. Geophys. Res.*, vol. 99, no. C5, p. 10 301, 1994.
- [20] M. B. Bowen, W. J. Emery, J. I. Wilkin, P. C. Tildesley, I. J. Barton, and R. Knewton, "Extracting multiyear surface currents from sequential thermal imagery using the maximum cross-correlation technique," *J. Atmos. Ocean. Technol.*, vol. 19, no. 10, pp. 1665–1676, Oct. 2002.
- [21] A. Moulin, J. R. Moisan, W. J. Emery, and J. Kohut, "A comparison of two methods measuring surface coastal circulation: CODAR versus satellite estimation using the maximum cross-correlation technique," *Florida Scientist*, vol. 68, p. 18, 2005. Supplement 1.
- [22] A. Moulin, *Circulation: CODAR versus satellite estimation using the maximum cross-correlation technique*, 2005, Melbourne, FL: Florida Inst. Technol. unpublished. [Online]. Available: [http://gest.umbc.edu/student\\_opp/2004\\_gssp\\_reports/AurelieMoulin.pdf](http://gest.umbc.edu/student_opp/2004_gssp_reports/AurelieMoulin.pdf)
- [23] [Online]. Available: <http://www.class.noaa.gov/nsaa/products/welcome>
- [24] *Commercial Software, Available Through ITT Visualization Information Systems (IITVIS)*. [Online]. Available: <http://www.itvis.com/envi/index.asp>
- [25] S. R. Chubb, F. Askari, T. F. Donato, R. Romeiser, S. Ufermann, A. L. Cooper, W. Alpers, S. A. Mango, and J.-S. Lee, "Study of Gulf Stream features with a multifrequency polarimetric SAR from the space shuttle," *IEEE Trans. Geosci. Remote Sens.*, vol. 37, no. 5, pp. 2495–2507, Sep. 1999.
- [26] S. Ufermann and R. Romeiser, "Numerical study on signatures of atmospheric convective cells in radar images of the ocean," *J. Geophys. Res.*, vol. 104, no. C11, p. 25 707, 1999.
- [27] S. A. Mango, S. R. Chubb, F. Askari, J. S. Lee, G. R. Valenzuela, R. W. Jansen, R. A. Fusina, B. Holt, R. M. Goldstein, W. Alpers, T. F. Donato, M. R. Grunes, H. H. Shih, J. Verdi, J. C. Church, and L. K. Shay, "Remote sensing of current-wave interactions with SIR-C/X-SAR during SRL-1 and SRL-2 at the Gulf Stream supersite," in *Proc. IGARSS*, vol. 2, 1995, pp. 1325–1327.
- [28] D. E. Barrick, M. W. Evans, and B. L. Weber, "Ocean surface currents mapped by radar," *Science*, vol. 198, no. 4313, p. 138, Oct. 1977.
- [29] B. J. Lipa and D. E. Barrick, "Extraction of sea state from HF radar sea echo: Mathematical theory and modeling," *Radio Sci.*, vol. 21, no. 1, p. 81, 1986.
- [30] J. T. Kohut and S. M. Glenn, "Improving HF radar surface current measurements with measured antenna beam patterns," *J. Atmos. Ocean. Technol.*, vol. 20, no. 9, pp. 1303–1316, Sep. 2003.
- [31] R. J. Chant, S. M. Glenn, and J. T. Kohut, "Flow reversals during upwelling conditions on the New Jersey inner shelf," *J. Geophys. Res.—Oceans*, vol. 109, no. C12, p. C12 S03, 2004.
- [32] J. T. Kohut, H. J. Roarty, and S. M. Glenn, "Characterizing observed environmental variability with HF Doppler radar surface current mappers and acoustic Doppler current profilers: Environmental variability in the coastal ocean," *IEEE J. Ocean. Eng.*, vol. 31, no. 4, pp. 876–884, Oct. 2006.
- [33] J. T. Kohut, S. M. Glenn, and R. J. Chant, "Seasonal current variability on the New Jersey inner shelf," *J. Geophys. Res.—Oceans*, vol. 109, no. C7, p. C07 S07, Jul. 2004.
- [34] M. J. Oliver, S. Glenn, J. T. Kohut, A. J. Irwin, O. M. Schofield, M. A. Moline, and W. P. Bissett, "Bioinformatic approaches for objective detection of water masses on continental shelves," *J. Geophys. Res.—Oceans*, vol. 109, no. C7, p. C07 S04, Jul. 2004.
- [35] J. T. Kohut, S. M. Glenn, and J. D. Paduan, "Inner shelf response to Tropical Storm Floyd," *J. Geophys. Res.—Oceans*, vol. 111, no. C9, p. C09 S91, Sep. 2006.
- [36] D. S. Ullman, J. O'Donnell, J. Kohut, T. Fake, and A. Allen, "Trajectory prediction using HF radar surface currents: Monte Carlo simulations of prediction uncertainties," *J. Geophys. Res.—Oceans*, vol. 111, no. C12, p. C12 005, 2006.
- [37] C. Y. Shen, T. E. Evans, R. P. Mied, and S. R. Chubb, "A velocity projection framework for inferring shallow water currents from surface tracer fields," *Cont. Shelf Res.*, vol. 28, no. 2, pp. 849–864, 2008.
- [38] W. H. Press, S. A. Teukosky, W. T. Vetterling, and B. P. Flannery, *Numerical Recipes in C, the Art of Scientific Computing*. Cambridge, U.K.: Cambridge Univ. Press, 1992, p. 636.
- [39] P. K. Kundu, "Ekman veering observed near the ocean bottom," *J. Phys. Oceanogr.*, vol. 6, no. 2, pp. 238–242, Mar. 1976.
- [40] G. R. Flierl and R. P. Mied, "Frictionally induced circulations and spin down of a warm-core ring," *J. Geophys. Res.—Oceans*, vol. 90, no. C5, pp. 8917–8927, 1985.
- [41] T. A. Joyce and M. A. Kennelly, "Upper-ocean velocity structure of Gulf Stream Warm-Core Ring 82B," *J. Geophys. Res.*, vol. 90, no. C5, pp. 8839–8844, 1985.



**Scott R. Chubb** received the B.A. degree from Princeton University, Princeton, NJ, in 1975 and the M.A. and Ph.D. degrees from the State University of New York, Stony Brook, in 1978 and 1982, respectively, all in physics.

Since 1989, he has been a Research Physicist with the Remote Sensing Division, Naval Research Laboratory, Washington, DC, where he has worked on precision measurements of time, electromagnetic scattering, nonlinear wave dynamics, statistical physics, and remote sensing of the ocean from air-

borne and spaceborne platforms.



**Wei Chen** received the B.S. degree in physics from Nankai University, Tianjin, China, in 1982 and the Ph.D. degree in physics from Brigham Young University, Provo, UT, in 1991.

He held a postdoctoral position at the National Institute of Standards and Technology, Gaithersburg, MD, and has been a Research Scientist with the Remote Sensing Division, Naval Research Laboratory, Washington, DC, since 1999. His areas of research include solid state physics, computer science, computer graphics, image processing, and remote

sensing applications in oceanography.



**Richard P. Mied** received the B.E.S. degree from the Department of Mechanics in 1968 and the Ph.D. degree from the Department of Earth and Planetary Sciences in 1972, both in Johns Hopkins University, Baltimore, MD.

He is a Supervisory Research Physicist with the Remote Sensing Division, Naval Research Laboratory, Washington, DC, where he has performed research on internal-inertial waves, mesoscale eddies, tidal plumes, river flows using remote sensing, and analytical and numerical modeling.



**Thomas E. Evans** received the B.S. and M.S. degrees in mathematics from the Virginia Institute of Technology, Montgomery, WV, in 1985 and 1987, respectively.

He has been with the Remote Sensing Division, Naval Research Laboratory, Washington, DC, in 1998 and has developed a number of numerical modeling codes. His current projects include a 3-D parallel nonhydrostatic coastal model.



**Colin Y. Shen** received the B.S. degree in physics from the University of Massachusetts, Amherst, MA, in 1971 and the Ph.D. degree in physical oceanography from the University of Rhode Island, Narragansett, RI, in 1977.

He has been a Research Scientist with the Remote Sensing Division, Naval Research Laboratory, Washington, DC, since 1984. He has published in the area of double-diffusive convection, internal waves, eddy dynamics, remote sensing hydrodynamics, and nonhydrostatic model formulation.



**Josh Kohut** received the B.S. degree in physics in 1997 and the Ph.D. degree from Rutgers University, Camden, NJ, in 2002.

He is currently an Assistant Professor of Oceanography with the Advanced and Sustained Technologies, Coastal Ocean Observation Laboratory, Institute of Marine and Coastal Sciences, Rutgers University. His research interests include biophysical interactions in the world's oceans, circulation processes on continental shelves, and the impact of these processes on marine resource management.

His research utilizes ocean observing technologies including satellites, high-frequency radar, and underwater robots.

# Seasonal differences in wind-driven across-shelf forcing and response relationships in the shelf surface layer of the central Mid-Atlantic Bight

Brian Dzwonkowski,<sup>1</sup> Josh T. Kohut,<sup>2</sup> and Xiao-Hai Yan<sup>1,3</sup>

Received 23 April 2008; revised 8 June 2009; accepted 16 June 2009; published 27 August 2009.

[1] Observations of surface currents, wind stress, and adjusted sea level from August 2002 to January 2004 were used to study across-shelf forcing and response relationships in the central Mid-Atlantic Bight (MAB). A commonly observed shelf wide offshore flow pattern was associated with distinctly different wind stress magnitudes and directions during mixed and stratified seasons. During the stratified period, the offshore current flow pattern was associated with relatively weak winds out of the Southwest (upwelling favorable), while the mixed period events were associated with relatively strong across-shelf winds from the Northwest. To quantify these observations, time series of the spatial mean surface current, wind stress, and coastal sea level were analyzed using several types of correlation analyses. Seasonal vector correlations between the surface current and wind stress revealed very high correlations but distinctly different phase angles and transfer coefficients. The stratified (mixed) period current veered to the right of the wind by 30–40° (6–8°) and had a higher (lower) transfer coefficient. Scalar correlations between across-shelf wind stress and across-shelf current showed higher  $r$  values than with the along-shelf wind stress during the mixed period. While this pattern did not hold between wind stress and sea level, the correlations did show a stronger (weaker) relationship with across-shelf (along-shelf) wind stress than what was observed in the stratified season. However, conditional sampling of shelf wide events during the weaker stratified periods did show stronger relationships between both across-shelf wind/across-shelf current and across-shelf wind/sea level than with the along-shelf wind stress.

**Citation:** Dzwonkowski, B., J. T. Kohut, and X.-H. Yan (2009), Seasonal differences in wind-driven across-shelf forcing and response relationships in the shelf surface layer of the central Mid-Atlantic Bight, *J. Geophys. Res.*, 114, C08018, doi:10.1029/2008JC004888.

## 1. Introduction

[2] While there is a sophisticated understanding of several aspects of shelf processes, many questions still remain related to across-shelf transport. As *Lentz* [2001] states, wind-driven across-shelf circulation and its dependence on stratification, bathymetry, and forcing are poorly understood, partly due to a lack of observations. Typically, across-shelf currents have weaker magnitudes and smaller spatial scales than along-shelf flows [*Lentz*, 1994]. However, the tendency for across-shelf gradients of mass properties (temperature and salinity), nutrients, sediments, pollutants, and other constituent components to be stronger than along-shelf gradients can lead to significant exchanges of these properties and material via

across-shelf flows [*Lentz*, 1995a; *Austin and Lentz*, 2002]. The most basic explanation typically assumes along-shelf invariance and appeals to Ekman dynamics, in which along-shelf wind drives across-shelf advection of surface waters. As surface waters are advected offshore, bottom water moves onshore and up-wells to replace the surface waters. This explanation works very well in many cases as previous studies have shown [*Winant et al.*, 1987; *Lentz*, 1992; *Wang*, 1997]. In response to changes in the mean across-shelf flow in the surface layer, coastal sea level will fluctuate resulting in coastal setup or set down, depending whether the wind is upwelling favorable or downwelling favorable. Thus changes in coastal sea level are linked to along-shelf wind stress, which can be seen from several previous studies on the response of adjusted sea level to wind-forcing in the MAB [*Noble and Butman*, 1979; *Wang*, 1979].

[3] This simple description of wind driven circulation neglects many important processes that contribute and complicate across-shelf transport. As discussed by *Yankovsky* [2003], the across-shelf flow structure can be affected by many factors, such as along-shelf invariance, lack of steady state, presence of buoyancy forcing/

<sup>1</sup>College of Marine and Earth Studies, University of Delaware, Newark, Delaware, USA.

<sup>2</sup>Institute of Marine and Coastal Sciences, Rutgers-State University of New Jersey, New Brunswick, New Jersey, USA.

<sup>3</sup>Also at State Key Laboratory of Marine Environment, Xiamen University, Xiamen, China.



stratification, and/or strong bottom friction. In particular, much work has been done on the influence of stratification on wind driven across-shelf circulation. Work by *Mitchum and Clarke* [1986], *Lentz* [1995b], and *Tilburg* [2003] have discussed a view of shelf dynamics in which the surface and bottom boundary layers thicken and potential overlap as the coast is approached. However, this notion of merging surface and bottom boundary layers can be arrested in the presence of stratification. *Weisberg et al.* [2001] found that under stratified conditions, the inner shelf supports well separated surface and bottom Ekman layers which are linked through across-shelf divergence. *Garvine* [2004] also found that strong stratification, resulting from buoyant coastal discharges, allows boundary layer separation in water as shallow as 12 m.

[4] Not unrelated, numerous studies [*Allen et al.*, 1995; *Allen and Newberger*, 1996; *Lentz*, 2001; *Weisberg et al.*, 2001; *Austin and Lentz*, 2002; *Tilburg*, 2003; *Kirincich et al.*, 2005, etc.] have noted the influence of stratification on across-shelf transport. While some of the details and conclusions of these studies vary, which is not surprising given the individualized features and processes impacting inner shelf regions [*Weisberg et al.*, 2001], the general link between stratification and across-shelf transport is consistent with reductions in transport being associated with decreases in stratification. Basically, stratification reduces the nearshore turbulence field which retards the growth of the boundary layers as the coast is approached [*Weisberg et al.*, 2001; *Garvine*, 2004]. As pointed out by *Weisberg et al.* [2001] and *Kirincich et al.* [2005], this suppression of the boundary layers allows for increased veering of the velocity vectors which increases across-shelf transport. These results are consistent with the earlier findings of *Li and Weisberg* [1999a, 1999b], who noted that changes in the eddy viscosity and implied turbulence level (via changes in wind stress) in a barotropic model of the West Florida Shelf directly affected interaction between the surface and bottom Ekman boundary layers. The interconnected nature of the inner shelf presents a situation such that the impediment or facilitation of surface pressure gradient setup by surface Ekman layer divergence, the geostrophic interior flow adjustment to the pressure gradient and/or the bottom Ekman layer reaction to the interior flow can alter the system response to wind-forcing [*Weisberg et al.*, 2001] and consequently transport. As a result, stratification also generates asymmetric responses in the flow field [*Weisberg et al.*, 2001]. The details of asymmetric responses have been reported and studied in a number of works [*Weatherly and Martin*, 1978; *Lentz and Trowbridge*, 1991; *Trowbridge and Lentz*, 1991; *MacCready and Rhines*, 1991; *Garrett et al.*, 1993; *Weisberg et al.*, 2001; *Garvine*, 2004; *Liu and Weisberg*, 2005a, 2005b, 2007, etc.].

[5] As many as previous studies have noted, along-shelf wind is not the only mechanism that can drive across-shelf circulation. The ability of across-shelf wind to drive across-shelf flow in shallow water was shown by Ekman as early as 1905. More recently, modeling studies by *Li and Weisberg* [1999a, 1999b] showed that across-shelf wind stress can be an important factor in driving across-shelf circulation on the West Florida shelf using a barotropic three-dimensional numerical model. Similarly, *in situ* observations on the West Florida shelf by *Liu and Weisberg* [2005a, 2007] have also

found that although the across-shelf momentum balance on the inner shelf is primarily geostrophic, across-shelf wind stress plays a secondary role. *Yankovsky and Garvine* [1998] concluded that transient wind-driven events, not associated with upwelling favorable winds, are at least partial responsible for enhancing across-shelf transport of buoyant waters. Bathymetric features have been shown to contribute to the formation of upwelling centers along the NJ coast [*Song et al.*, 2001]. *Pringle and Riser* [2003] have shown evidence of remotely forced coastal trapped waves causing across-shelf transport on the west coast of the US. However, most of these studies were largely focused on the nearshore region of the coastal zone. *Tilburg* [2003] used a numerical model to show that across-shelf winds can account for significant amounts of on and offshore transport in the surface layer within a stratified outer shelf, away from the frictionally dominated inner shelf. In addition, coastal sea level fluctuations, estimated using time series of the across-shelf flow structures, hydrographic transects, and across-shelf wind stress, have been related to other factors including the offshore sea surface height and the dynamical responses of the inner shelf circulation to meteorological forcing [*Liu and Weisberg*, 2007]. As these studies show, along-shelf wind stress may not always be the dominating force that drives across-shelf transport and the resulting coastal sea level, and that other means of driving across-shelf surface flow may play a role advecting material across the shelf.

[6] This paper will examine the wind driven forcing that affects across-shelf surface flows in the central MAB, with a particular emphasis on across-shelf wind. In addition, a previous study on the midshelf off the coast of NJ identified two dominate across-shelf surface flow patterns, shelf wide and point flows [*Dzwonkowski*, 2009]. While this previous study characterizes the temporal and spatial variability of these across-shelf flow events, this study investigates their forcing and response relationships with wind stress and adjusted sea level. The focus of this study is to examine the extent to which wind-forcing is responsible for the observed surface flows and to determine their impact on coastal sea level. In addition, this study attempts to provide observational evidence for *Tilburg's* [2003] recent model results suggesting that across-shelf wind can drive offshore transport in the surface layer on a stratified outer shelf. The remainder of this manuscript is presented as follows. The data used in this investigation are described in section 2. Section 3 presents the spatial and temporal characteristics of the dominant offshore flow events. The effects of wind-forcing over the study region and the response of sea level are contained in section 4. While a discussion and summary of the results are presented in sections 5 and 6.

## 2. Data

### 2.1. High Frequency Radar Data

[7] This study uses HF-radar based surface velocity data derived from four long range mode radar sites in New Jersey (Figure 1). The radars, operating at a frequency of 4.55 MHz, provide continuous radial vectors at an effective depth of 2.4m [*Stewart and Joy*, 1974]. The radial vectors collected by the HF radar array are averaged and geometrically combined into a grid of uv velocity vectors every



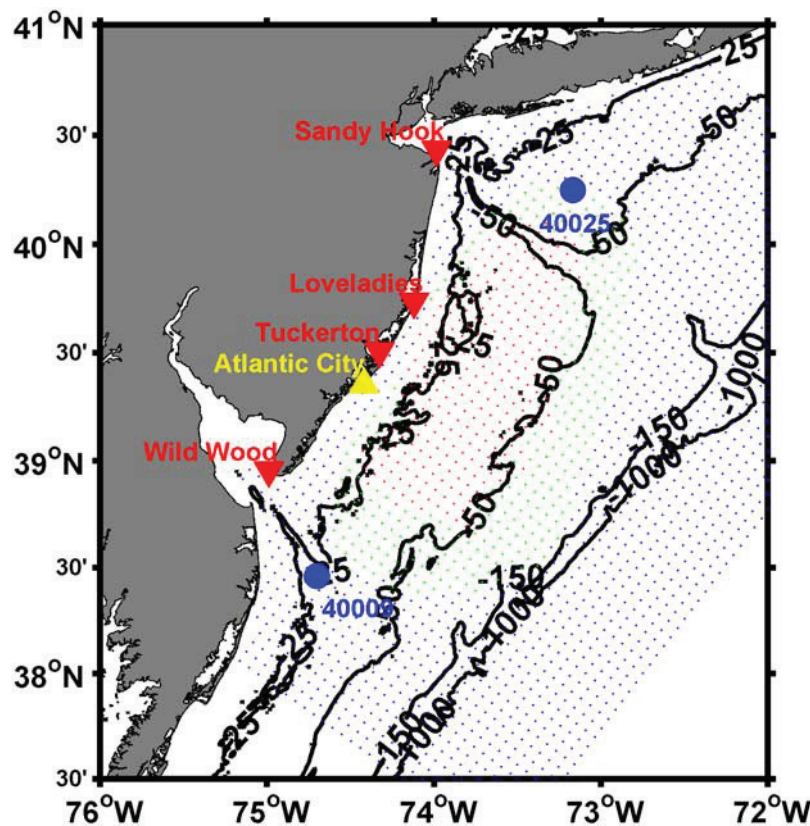


**Figure 1.** Map of the study site showing bathymetry (black lines), HF radar locations (red triangles), HF radar grid (colored dots), coastal tide gauge at Atlantic City, and NOAA buoys (blue circles). The coloration of the dot indicate the grouping bin of the temporal percentage coverage of the data (magenta 94–100%, red 86–93%, green 80–86%, and blue <80%). The temporal percentage coverage is the percentage of good data at a given grid point over the course of the study.

three hours following *Kohut et al.* [2006]. The collection grid (colored dots in Figure 1) covers an area approximately 240km by 115km, with the distance between grid points on the order of 6km. An 18 month period (15 August 2002 to 6 February 2004) was used in this study, as this time period was subjectively determined to have the maximum spatial coverage with minimal temporal gaps. Only grid points with 80% coverage or greater (temporal percent coverage) were used in the study. The spatial distribution of temporal percent coverage is shown in Figure 1 with dot coloration representing a percent bin (magenta 93–100%, red 86–93%, green 80–86%, and blue <80%).

[8] As this study is focused on low frequency events, the temporal gaps in the velocity time series at the individual grid points were linearly interpolated through as the majority of gaps were less than 12 hours. The resulting time series were low-pass filtered with a 40 hour Lanczos filter to remove any tidal effects and other high frequency components from the velocity data. Furthermore, the velocity vectors were rotated into along and across-shelf components with an along-shore angle of  $54^\circ$  counterclockwise from east determined by the orientation of the coastline [*Chant et al.*, 2004]. This analysis focuses on the spatial times series generated by computing a mean vector over the CODAR footprint at each time step.

## 2.2. Wind Data

[9] Wind data from a number of regional sources were collected over the same time period as the current data. The primary wind data used in this study were collected from NOAA buoy #44025 (Long Island (LI)) and NOAA buoy #44009 (Delaware Bay (DB)), at the northern and southern regions of the HF radar footprint. In general, the data were continuous over the 18 month period; however, the LI wind had a considerable gap during May/June of 2003. As several analysis methods used required a gap free data set, the gaps in these records were filled using linear interpolation when gap lengths were less than 12 hours. For the large gap in May/June in LI wind, data from NOAA buoy #40017 (Montauk Point) was used. The replacement data were lagged at the highest correlation value (correlation determined over 9 months of data) and its amplitudes adjusted by an appropriate coefficient determined from linear regression. The lag time was only a few hours and exhibited very high correlations ( $r > .9$ ). The wind data used in this study can be found at the (<http://www.ndbc.noaa.gov/>).

[10] As the NOAA buoys border the north and south boundaries of the study region, a mean wind velocity time series for the study was created by vector averaging the LI and DE buoy wind data. In general, the wind data at the two sites were very similar, particularly after applying the 40 hour low-pass filter, therefore the mean wind data has

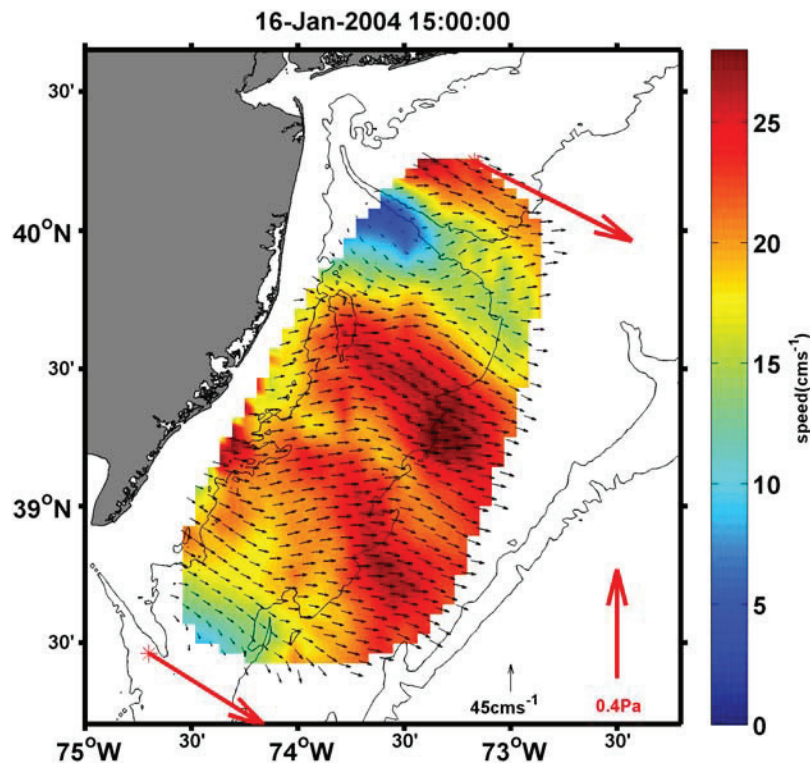


**Figure 2a.** Snapshots of the two most prominent episodic across-shelf flow patterns that were most commonly seen during the course of the study. The black arrows are HF surface velocity measurements (cm/s), the red arrows are wind stress at the NOAA buoys (Pa), and the coloration under the current vector is the magnitude of the current (cm/s). The snapshot is from well-developed stage of the event a shelf wide flow.

only minor deviations from the original two time series. From this wind data, surface wind stress was estimated following *Large and Pond* [1981].

### 2.3. Sea Level Data

[11] Sea level data were collected from the NOAA Center for Operational Oceanographic Products and Services (CO-OPS) which provides hourly tidal gauge data at Atlantic City, NJ ([http://tidesandcurrents.noaa.gov/station\\_retrieve.shtml?type=Historic+Tide+Data](http://tidesandcurrents.noaa.gov/station_retrieve.shtml?type=Historic+Tide+Data)). Prior to 40 hour low-pass filtering the tide gage data, the predicted tide at Atlantic City for the study period (also obtained from CO-OPS) was removed to eliminate any long term tidal effects. To remove changes in sea level resulting from atmospheric pressure, an inverse barometer correction (IBC) was calculated using atmospheric pressure from the NOAA environmental buoy #44009. The correction was calculated as follows,  $IBC = -9.948 * (\text{atmospheric pressure} - \text{mean atmospheric pressure})$ , which was obtained from the Physical Oceanography Distributed Active Archive Center ([http://podaac.jpl.nasa.gov/tpssa/doc/ssa\\_manula.html#INV\\_BAR](http://podaac.jpl.nasa.gov/tpssa/doc/ssa_manula.html#INV_BAR)).

### 3. Offshore Flows

[12] As this study examines the forcing mechanisms associated with across-shelf flow, the results from a companion study [Dzwonkowski, 2009], in which two predominant flow structures, shelf wide and “point” flows were identified (Figures 2a, 2b), has direct bearing on this work. Shelf wide flows were characterized as times in which the

surface velocity vectors were generally directed in the offshore direction and had similar magnitudes over most of the HF radar footprint, with occasional exceptions around the Hudson and Delaware Bay canyon regions. While point flows were characterized as times in which there was along-shelf flow near the 25 m isobath that veered offshore where the orientation of the NJ coastline shifts near Barnegat Inlet ( $\sim 39.6^\circ \text{N}$ ). The veering flow can extend across the entire HF footprint and have a relatively wide velocity core (approximately 12–24 km). The study found that the magnitude and duration of shelf wide flows were stronger and shorter during nonsummer months of the year. As this study is primarily focused on the potential forcing mechanisms of these types of events, Figure 3 shows the temporal distribution of the shelf wide (blue and red circles in the top plot) and point flow (green circles in bottom plot) events with the wind vector (black arrows) at the onset of these events. The red circles distinguish the summer events from the nonsummer events in the top plot, as the events appear to be associated with different wind conditions. During the nonsummer (summer) period, the wind vector appears to be much stronger (weaker) and out of the northwest (south or southwest) during the shelf wide events. As southwest wind is approximately upwelling favorable in this region, the summer shelf wide events fit the typical Ekman dynamical explanation of offshore flow. However, during the nonsummer months the shelf wide events appear to be associated with across-shelf wind. For point flow events, there does not appear to be any strong seasonal wind patterns. The wind conditions during these events tended to be out of

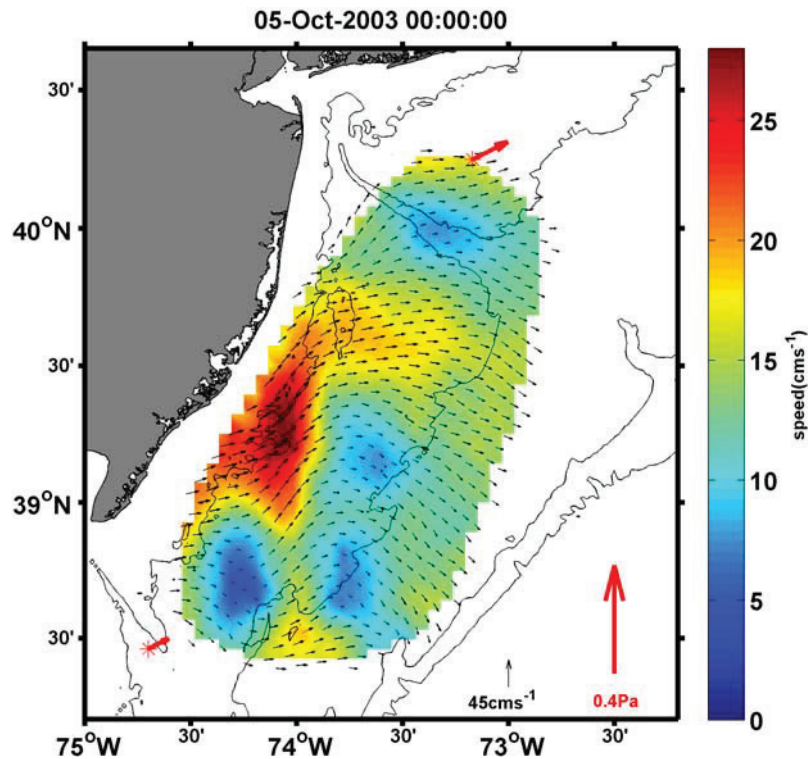
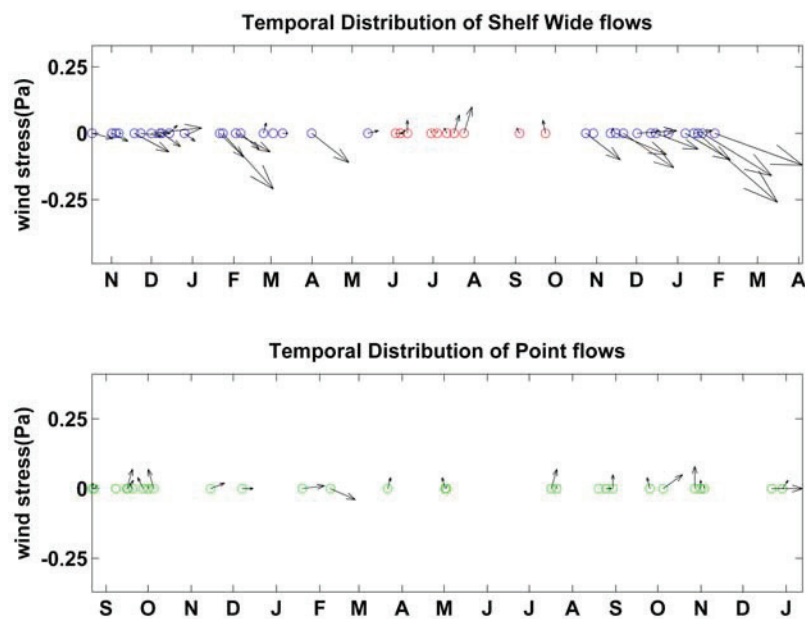


Figure 2b. Same as in Figure 2a, except for a point flow.

the south or southwest (upwelling favorable) with varying levels of magnitude.

[13] As these observations suggest, there appears to be a seasonal difference in the wind current relationship during

shelf wide flow events. To address this issue, the data were divided into time periods reflecting the approximate time period of the stratified (June, July, August, September) and mixed (December, January, February, March) regimes. This



**Figure 3.** The temporal distribution of the two predominate across-shelf offshore flow events: (top) shelf wide and (bottom) point. Circles represent the onset of an across-shelf flow event with the coloration indicating the type of across-shelf flow event, wherein the blue (red) are weakly stratified/mixed (stratified) shelf wide events and the green are point flow events. The black arrows are wind stress vectors (Pa) at the onset of the across-shelf flow event.



**Table 1.** Summary of the Vector Correlation Results Between the Spatial Mean of the HF Radar Surface Currents and the Wind Stress<sup>a</sup>

	<i>r</i>	Lag	Phase	Transfer Coefficient
Total	0.72	3	8	0.75
strat1 (August 2002–September 2002)	0.84	0	32	1.21
strat2 (June 2003–September 2003)	0.82	0	39	1.33
mixed1 (December 2002–March 2003)	0.75	3	4	0.75
mixed2 (December 2003–January 2004)	0.7	3	6	0.65

<sup>a</sup>The result of the entire 18-month time period (Total) and the individual seasonal periods (Mixed1, Mixed2, Strat1, and Strat2). The correlation coefficient is given by the *r* value, the lag is in hours, the phase is in degrees wherein positive values are to the right of the wind, and the transfer coefficient is in (m/s)/(N/m<sup>2</sup>).

division is based on previous studies in and near this region [Lentz *et al.*, 2003; Kohut *et al.*, 2004; Rasmussen *et al.*, 2005; Castelao *et al.*, 2008], and AUV measured across-shelf sections of temperature and salinity (October 2003–October 2004).

#### 4. Force-Response Observations

[14] Many previous studies have shown that wind is a primary forcing mechanism in the MAB region [Beardsley *et al.*, 1976; Ou *et al.*, 1981; Noble *et al.*, 1983, etc.], so it is not surprising that there is a relationship between wind stress and the observed surface velocities and coastal sea level. However, the wind/current and wind/sea level analysis did reveal some interesting results in regards to the strength of its influence, the dominant forcing direction, and its spatial variability. Throughout the following section a number of correlation analyses are conducted whose results are significant at the 95% confidence level unless stated otherwise.

##### 4.1. Wind/Current Relationship

[15] As a first order estimate of the relationship between wind stress and current, the spatial mean current vector was correlated to the wind stress using a lagged vector correlation. The lagged vector correlation, put forth by Kundu [1976], was used to quantify the differences. This correlation provided a correlation coefficient (*r* value), a phase difference (veering angle between vectors), and a transfer function coefficient (magnitude difference between vectors expressed as (m/s)/(N/m<sup>2</sup>) in this study). The correlations were also computed over approximate seasonal periods as stratification can affect the water column dynamics. The temporal breakdown of the data follows the seasonal periods stated above, with the total period being all 18 months, stratified period 1 (strat1) being 19 August 2002–September 2002, mixed period 1 (mixed1) being December 2002–March 2003, stratified period 2 (strat2) being June 2003–September 2003, and mixed period 2 (mixed2) being December 2003–January 2004. The results are shown in Table 1. These temporal divisions impact the correlation analysis by affecting the degrees of freedom (DOF) used in determining the significance of the correlation coefficient. A decorrelation timescale of two days was used to determine the DOF for each period. This is an overly conservative value as most of the time series in the HF radar grid have decorrelation timescales of 1–1.25 days. Consequently, the DOF for each time period are 265 for the total, 22 and 61 for strat1 and strat2, and 60 and 30 for mixed1 and mixed 2. As all the lagged correlations occur at timescales shorter

than a day, no adjustments to the DOFs were made for calculations.

[16] In general, the correlations are very high with *r* values equal to 0.72 for the total data set, and three of the seasonal periods being higher with values of 0.84, 0.82, and 0.75 for strat1, strat2, and mixed1, respectively. The phase difference of 8° during the total time period reflects a blending of the seasonal phase differences where the stratified season which veers to the right of the wind stress to a greater degree (32° and 39° for strat1 and strat2 versus 4° and 6° for mixed1 and mixed2). The fact that the total period results are similar to the mixed suggests that the weakly stratified periods of October–November and April–May behave more like the mixed period. This was confirmed by vector correlations for these time periods. In addition, the lag time is minimal, with lags ranging from 0 to 3 hours. From the seasonal separation, it can be seen that the mixed period has a slower wind response time than the stratified period. The zero lag during the stratified period indicates that the response time of the surface layer currents is less than the three hour sample interval of the HF radar. This near immediate response of the surface currents to wind-forcing was similar to that found during the summer stratified season on the inner shelf of LEO-15 region by Münchow and Chant [2000]. There is also a notable difference in the transfer coefficient between seasons with the mixed period being less than one and the stratified period being greater than one. Since momentum is more easily transferred vertically during mixed conditions it is likely that a given wind stress will produce a smaller surface current, but a deeper overall current, than under stratified conditions. This is consistent with the observations that for a given wind stress, smaller surface currents are produced per unit of wind stress during periods of mixed conditions.

[17] The vector correlations show that the surface current was highly correlated to wind stress, but that there was a seasonal difference in the response. To further explore the seasonal difference, the across-shelf currents are plotted along with across-shelf and along-shelf components of the wind stress, which are shown in Figure 4 for the stratified period (strat2) and Figure 5 for the mixed period (mixed1). In both figures, the spatial mean across-shelf current (red dashed line) is plotted against the along-shelf and across-shelf wind stress (blue) in the top and bottom plots, respectively. Note that in the case of the along-shelf component, the negative of the component is plotted and correlated for visually comparison purposes (i.e. negative along-shelf stress in Figures 4 and 5 corresponded to up-shelf or upwelling favorable wind stress). Figures 4 and 5 also contain the maximum correlation coefficient between

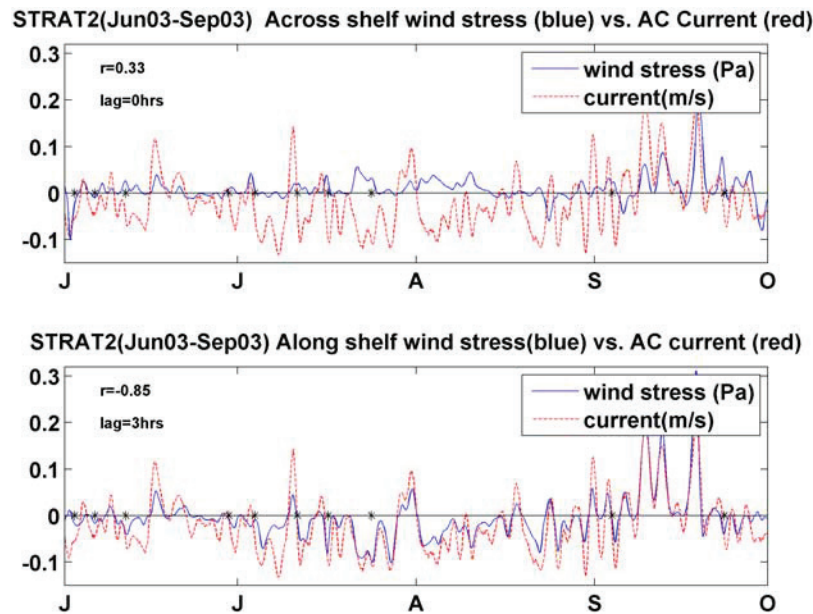


**Figure 4.** Comparison of the (top) across-shelf (blue line) and (bottom) along-shelf (blue line) components of MAB wind vector with the across-shelf (AC) component of the spatial mean current vector (red dashed line) during the stratified period (June–September). The black stars along the zero line (black line) represent the shelf wide. In the top left corner of each plot are the correlation coefficient ( $r$ ) and its lag, wherein any lag indicates the current follows the wind. In the top plot, positive values indicate the onshore direction and negative values indicate the offshore direction. This is the same for the current in the bottom plot, but for the wind stress, the positive values indicate the down shelf direction and the negative direction indicates the up shelf direction.

the wind component and the across-shelf current, its associated lag, and the starting point of shelf wide events (black stars along the zero line) in the given period. During the stratified period, the top plot of Figure 4 shows that the across-shelf current is not well correlated with across-shelf

wind as shown by the low correlation coefficient of 0.33, whereas there is a high correlation between the along-shelf wind stress and across-shelf current with an  $r$  value of  $-0.85$  at a 3 hour lag. A similar relationship occurs during the strat1 period with the along-shelf wind stress and across-

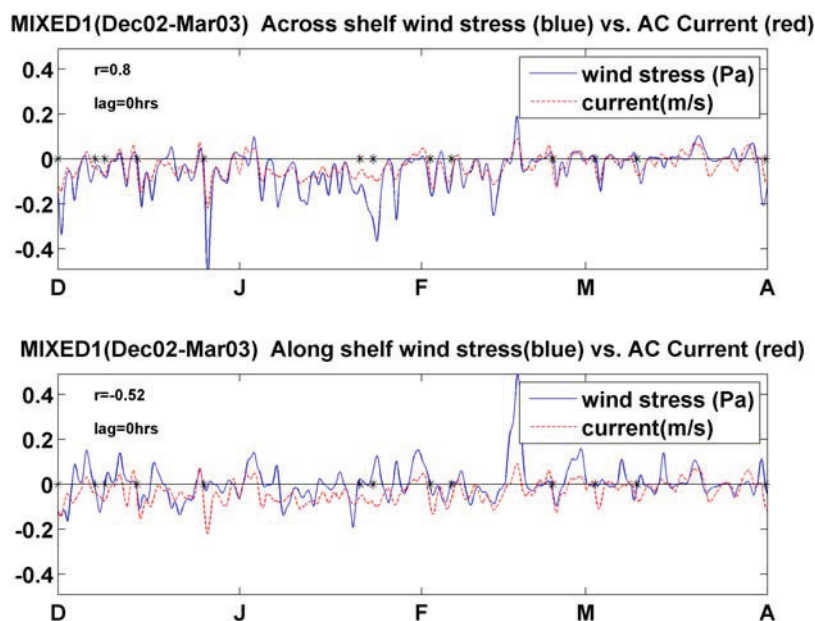


**Figure 5.** Similar to Figure 4, except the comparison is during the mixed period (mixed1 December 2002–March 2004).

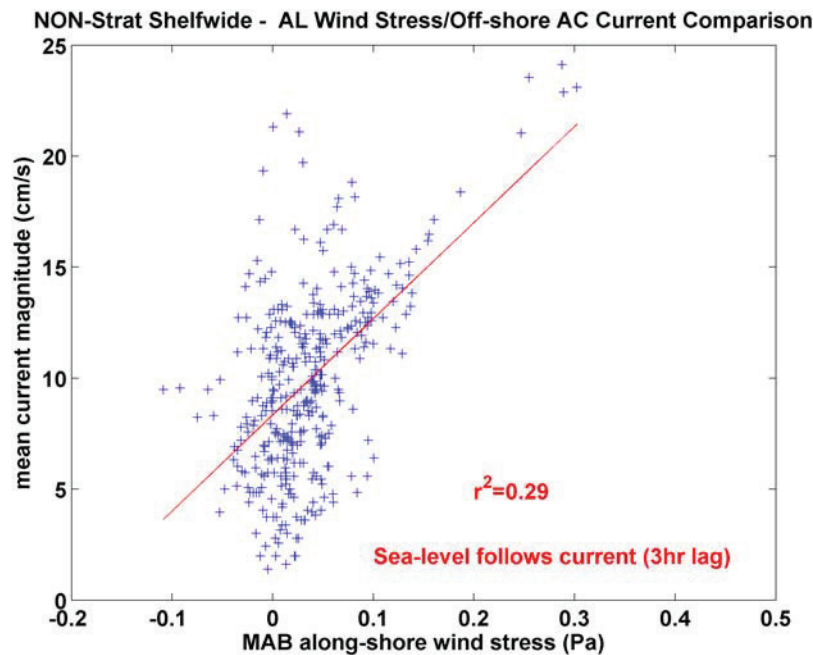


**Figure 6a.** Scatterplot comparison between the across-shelf component of spatial mean current vector and the directional wind components during the conditionally sampled shelf wide offshore flow events in the nonstratified periods. Comparison of the along-shelf current and along-shelf wind. The blue plus signs are the data points, the red line is the linear regression line, and the  $r^2$  value is shown in red.

shelf current being strongly correlated ( $r$  value = 0.83 at 0 hour lag). In addition, nearly all the shelf wide flow events are associated with times of predominately upwelling winds. The one exception occurs in early June where the first event is preceded by a large impulse of across-shelf wind stress (0.1 Pa). However, the along-shelf wind stress begins increasing in strength as the across-shelf component is decreasing just prior to the event.

[18] Figure 5 shows that the current/wind relationship during the mixed period is different from the stratified period. The across-shelf (along-shelf) wind stress appears more (less) in phase with across-shelf current than during the stratified period. This is reflected in the correlation coefficients, where the  $r$  value for the across-shelf wind stress and across-shelf current increased to 0.8 at a zero hour lag, and the  $r$  value for the along-shelf wind stress and across-shelf current decreased to  $-0.52$  at zero hour lag. This increased correlation between across-shelf wind stress and the across-shelf current shows up even stronger in the mixed2 period, which has an  $r$  value of 0.83 with a zero hour lag. This point is further emphasized by examining the fluctuations in across-shelf current and both wind components in conjunction with the shelf wide flow events. There are several shelf wide flow events that occur at times of strong across-shelf wind stress, while the along-shelf wind stress is very weak and/or downwelling favorable (25 December, 22 January, 2 February, 2 March, etc.). This is well illustrated by the 25 December event, in which an extremely strong across-shelf wind stress of approximate 0.5 Pa is well correlated with a 24 cm/s pulse of across-shelf velocity. During the same time, the along-shelf wind stress is only around 0.01 Pa. In contrast, under stratified conditions a similar along-shelf wind stress was observed in

conjunction with offshore flow, however, they were not nearly as large in magnitude as this event.

[19] The across-shelf flow events under mixed conditions support the notion that across-shelf wind can drive across-shelf flow under appropriate conditions. For each shelf wide event, the across-shelf current component was compared to the corresponding along and across-shelf wind stresses, with the lag of the best results shown. These data were compared using scatterplots as a way to identify trends with the results shown in (Figures 6a, 6b). The scatterplot of the across-shelf wind compared to the across-shelf current (Figure 6a) shows a strong linear relationship with an  $r^2$  value of 0.68; as compared to the scatterplot with along-shelf shelf wind stress (Figure 6b), which only had an  $r^2$  value of 0.29. There was no similar relationship between stratified shelf wide across-shelf flows and across-shelf wind. Hence the mixed/less stratified conditional events represent a notably different relationship with wind stress than those in stratified periods.

#### 4.2. Wind/Sea Level Relationship

[20] In addition to the association of across-shelf wind and currents, examining the relationship of across-shelf winds on adjusted sea level could provide evidence of their dynamical importance in forcing coastal set down. Similar to the plots above, adjusted sea level was compared to the along and across-shelf components of the wind stress. During the stratified period (not shown), the fluctuations in adjusted sea level were well correlated ( $r$  value =  $-0.81$  with 6 hour lag) with along-shelf wind stress where upwelling (downwelling) winds were associated with a decrease (increase) in coastal sea level. The correlation with across-shelf wind stress was much weaker ( $r$  value = 0.34 with 0 hour lag). Comparison with the strat1 period was



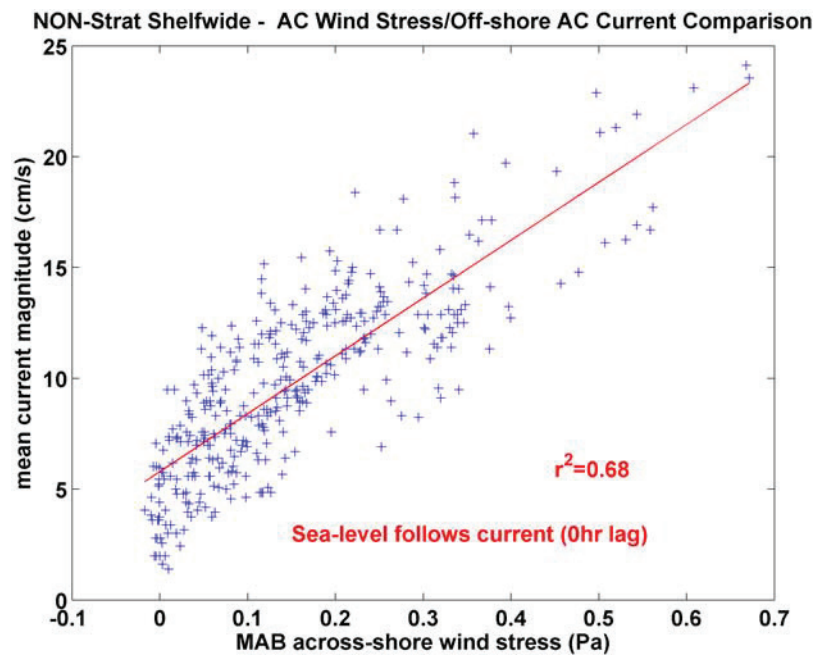


**Figure 6b.** Same as in Figure 6a, except the comparison is of the across-shelf current and across-shelf wind.

avoided because of gaps in the adjusted sea level data during this time period.

[21] The relationship with adjusted sea level and wind stress components becomes more complicated during the mixed season. Figure 7 is similar to Figures 4 and 5 with the exception of the blue line being adjusted sea level in both the top and bottom plots and the red dashed line being the across (along) shelf wind stress in the top (bottom) plot.

From Figure 7, both along and across shelf wind components appear to be correlated with sea level variations. While still strong, the along-shelf wind stress correlation with adjusted sea level weakened ( $r = 0.69$  with a 12 hour lag) and the across-shelf correlation coefficient increased ( $r = 0.42$  with a 3 hour lag) from the strat2 period. The pattern gets stronger in the mixed2 period with the across (along)-shelf stress correlation increasing (remained approximately

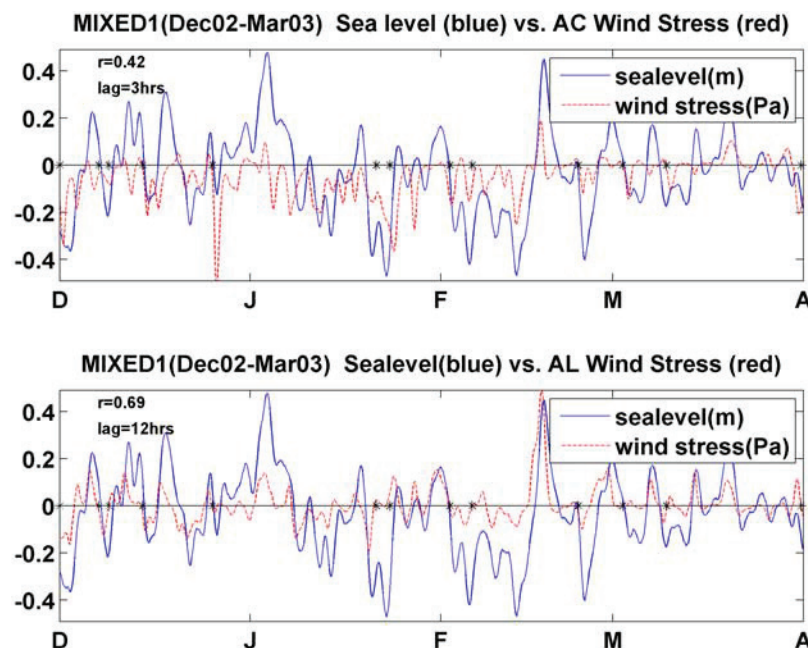


**Figure 7.** Similar to Figures 4 and 5 with the exception of the blue line being sea level in both the top and bottom plots and the red dashed line being the across (along)-shelf wind stress in the top (bottom) plot.

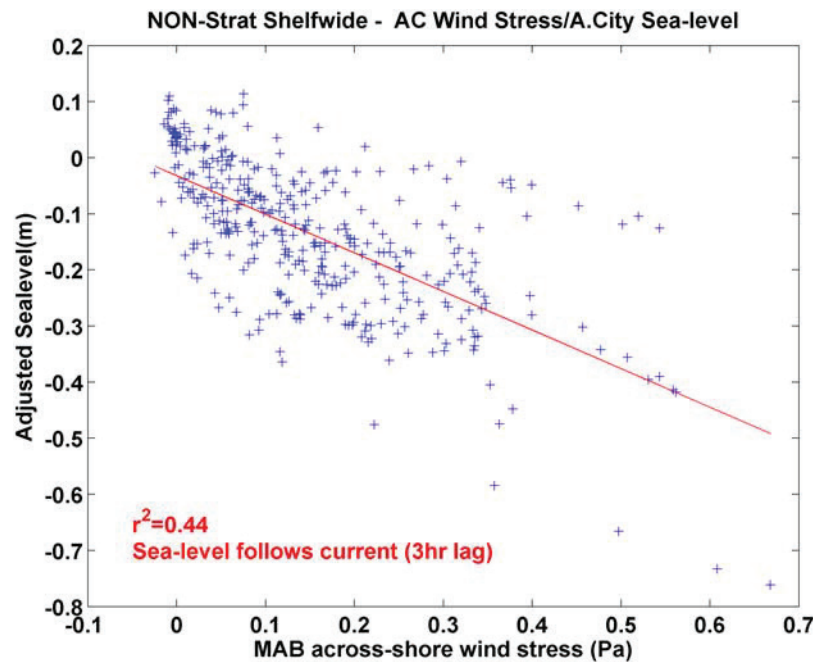


**Figure 8.** Scatterplot comparison between the across-shelf component of wind stress and adjusted sea level during the conditionally sampled shelf wide offshore flow events in the nonstratified periods. The blue plus signs are the data points, the red line is the linear regression line, and the  $r^2$  value is shown in red.

equal) to 0.57 (0.68). Again, similar to the wind stress/ across-shelf current plots, there are several periods of decreasing adjusted sea level when along-shelf wind stress was very small or downwelling favorable, which typically coincided with shelf wide events. Thus the adjusted sea level and wind stress components are conditionally sampled during the shelf wide flows in the nonstratified study period. Scatterplots of along-shelf wind stress showed no significant relationship to adjusted sea level with an  $r^2$  value of 0.09. However, the scatterplot of the across-shelf wind stress and adjusted sea level showed a relationship ( $r^2 = -0.44$ ) with adjusted sea level decreasing with increasing offshore across-shelf wind stress (Figure 8).

#### 4.3. Current/Sea Level Relationship

[22] As a connection between the wind stress/current correlation and the wind stress/sea level correlation, it would be expected that the surface layer across-shelf current should lead to sea level set up and set down. There is generally reasonable agreement between onshore (offshore) flow and adjusted sea level increase (decrease) with an  $r$ -value for the stratified (mixed) period of 0.78 (0.56) with a 6(9) hour lag. Furthermore, the mixed period relationship strengthens during the mixed2 period where the  $r$  value increases to 0.79 at 3 hour lag.

#### 4.4. Spatial Variability of Wind/Current Relationship

[23] As the study area covers a large region of the continental shelf, with depth ranging from less than 25 m to greater than 100 m, the relationship between wind stress and the current would be expected to change as the effects of bottom friction decrease with increasing depth. Here we utilize the spatial time series of the HF radar sampling to describe the variability in the surface current response to

wind-forcing over shelf scales. This was done by grouping the lower portion of the study region, where the relative angle of the isobaths do not change significantly, into three subregion; inside ( $\cong 23$ –28 m isobath), middle ( $\cong 33$ –48 m isobath), and outside ( $\cong 55$ –95 m isobath). The HF radar grid points used in the subregions are shown in Figure 9 with the inside region marked by red “+,” middle region marked by green, and the outside region marked by blue. Each of the subregions is separated by approximated 12 km with regional grouping limiting the potential effects of gaps and reducing the noisiness typically associated individual points.

[24] The time series of the spatial mean current of these subregions was vector correlated with the wind stress and the results are shown in Table 2. All the subregions and temporal periods showed good correlations between the current and wind stress with mixed (stratified) periods having correlations greater than 0.65 (0.7). The veering angle for the mixed periods did not show a consistent relationship with distance from the coast with the mixed1 (mixed2) period showing little change (an increase) in veering angle with distance from the coast. However, the veering angle in both stratified time periods increased consistently with distance from the coast. For stratified conditions in the inside subregion, currents are approximately  $15$ – $20^\circ$  to the right of the wind, but further offshore in the outside subregion, the current/wind veering angle increases by approximately  $25^\circ$  so that the current is  $45$ – $50^\circ$  to the right of the wind.

## 5. Discussion

[25] The results of the correlation analyses identified several important relationships between surface current,

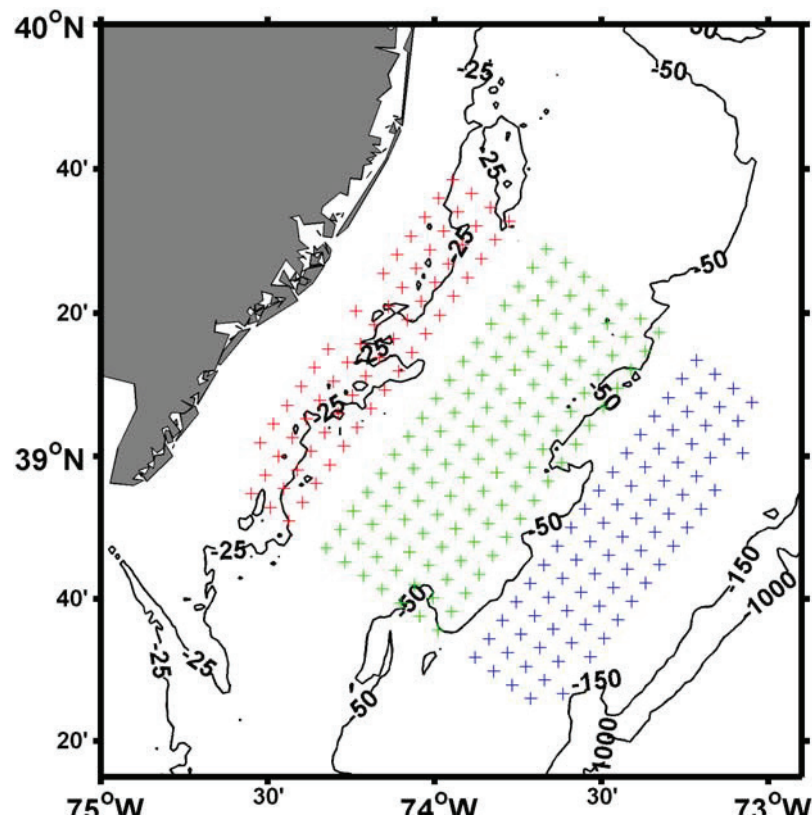


**Figure 9.** Lower portion of the study region showing the HF radar grid points used in the subregions with the inside region marked by red plus signs, middle region is marked in green, and the outside region is marked in blue.

wind stress, and adjusted sea level. During the stratified period, the current appears to exhibit flow behavior consistent with the development of an Ekman spiral in the surface boundary layer as the vector correlation between the wind stress and current indicates that the two are highly correlated with the current veering between  $30^\circ$  and  $40^\circ$  to the right of the wind. Furthermore, the along-shelf wind stress component is highly correlated with across-shelf current and adjusted sea level variability with down (up) shelf wind causing onshore (offshore) current flow and sea level set up (down). These results are consistent with several other studies inner shelf of the NJ coast [Yankovsky and Garvine, 1998; Kohut *et al.*, 2004]. However, Yankovsky and Garvine [1998] observed summer time upwelling events that typically lasted 8–10 days on the inner shelf of the LEO-15 region, which is longer than the duration of events in this study. This difference could result from the quick response times of the surface currents to wind-forcing as mentioned in the vector correlation results (virtually 0 hour lag over the HF grid). For example, two separate offshore flow events were observed during 19–28 August (9 days). However, a one day shift in the wind led to a brief break in the offshore flow and thus resulted in the 9 day period to be considered two separate events. Another interesting result stemming from the regional vector correlations is the reduced correlation in the inner and outer regions during the stratified period. These reductions may be associated with baroclinic processes. The lower correlation on the inside region could be effected by buoyancy intrusions which are known to

impact the inner shelf along the NJ coast during the stratified period [Yankovsky and Garvine, 1998]. While the outside region may be impacted by shelf break processes, such as the shelf break front jet. Liu and Weisberg [2005a, 2005b] found that baroclinicity played an increasingly im-

**Table 2.** Summary of the Subregion Vector Correlation Results Between the Spatial Mean of the HF Radar Surface Currents of Each Subregion (Inside, Middle, Outside) and Wind Stress<sup>a</sup>

	<i>r</i>	Lag	Phase	Transfer Coefficient
<i>Mixed1</i>				
Inside	0.70	3	7	0.81
Middle	0.73	3	3	0.90
Outside	0.69	6	2	0.89
<i>Mixed2</i>				
Inside	0.65	3	0	0.74
Middle	0.68	3	3	0.75
Outside	0.69	3	10	0.70
<i>Stratified1</i>				
Inside	0.78	0	16	1.68
Middle	0.84	0	26	1.55
Outside	0.73	0	43	1.06
<i>Stratified2</i>				
Inside	0.76	0	22	1.47
Middle	0.83	0	34	1.45
Outside	0.70	0	51	1.28

<sup>a</sup>The result of the individual seasonal periods (Mixed1, Mixed2, Strat1, and Strat2). The units are the same as in Table 1.



portant role as the depth and stratification increased on the similarly, gentle sloping West Florida shelf. Using ship-board ADCP transects near the northeast edge of the study region, *Flagg et al.* [2006] has plots of a frontal jet feature impacting near surface currents well within the 150 m isobath. While the climatology of this feature is strongest during fall and winter, there are well illustrated examples of its impact during summer months [*Flagg et al.*, 2006, Figures 4 and 6]. To further explore this possibility, the HF radar data was examined for direct evidence of an offshore jet. However, the approximately 0.1 difference in the correlation coefficient between the outer and middle regions, results in only an approximate 20% difference in the variance explained by the wind/current correlation. Thus the effects of a shelf break jet in the outer region would be expected to be subtle. That being said, surface currents do show some limited evidence of down-shelf flow in the outer region that are counter to what would be expected given the wind-forcing. Whether this is evidence of the shelf break frontal jet can only be speculated as no temperature or salinity data for the water column were available.

[26] The mixed period results suggest a different response to the wind stress, at least at times. While the vector correlation is slightly weaker than the stratified period, it is still high,  $O(0.70)$ , but the slight phase angle implies that the current follows the direction of the wind. This observation, in conjunction with the climatological predominance of northwest winds during this time period, suggest that there could be significant offshore across-shelf flow attributed to across-shelf winds during the mixed period. Supporting this notion is the analysis of the wind stress components and the across-shelf current, which showed strong correlations with across-shelf wind that were significantly higher than the along-shelf wind stress correlations. In addition, a climatologically study of six years of HF radar data showed that these results are constant with longer timescale observations (D. Gong et al., Seasonal climatology of wind-driven circulation on the New Jersey shelf, submitted to *Journal of Geophysical Research*, 2009). While the relationship between wind stress and adjusted sea level was less clear, it does suggest that across-shelf wind stress can be a player in adjusted sea level as previous studies have noted [*Li and Weisberg*, 1999a, 1999b, 2007, etc.]. This was especially notable during specific shelf wide offshore flow events, where conditional sampling showed these events were strongly associated with across-shelf wind stress and well correlated with decreased adjusted sea level. Furthermore, as can be seen from the scatterplots and wind stress/current/sea level plots, the shelf wide events during the mixed periods were often associated with very strong wind stress and depressed adjusted sea level, which supports the notion that the importance of across-shelf wind stress increases significantly during severe weather events as noted by *Trasviña et al.* [1995] and *Liu and Weisberg* [2005a].

[27] In addition, the correlations between wind stress and adjusted sea level are lower than the correlations between wind stress and current. While a definitive explanation is difficult to determine with the given data set, there are several potential factors that could contribute to these results. This is a region of complex geography and bathymetry which has been shown to be significantly impacted by

remotely forced waves. *Ou et al.* [1981] found that wind-forcing and southward propagating free waves in the MAB are equal in magnitude and accounted for 80% of the total energy in the along-shelf direction [*Noble et al.*, 1983]. Thus these continental shelf waves could reduce the correlation between local wind stress and sea level. Furthermore, as one reviewer pointed out, the correlation between the wind stress and sea level compares a spatial mean wind with a point measurement of sea level. A spatially averaged sea level from additional tide gages around the study area could result in higher correlations between the wind and sea level. This could be important, as the geographic complexity of the regional coastline could allow for local winds, as opposed to a regional mean representation thereof, to have a significant impact on the local sea level changes. Another, possible factor is the known three-dimensional nature of shelf circulation. As stated by *Weisberg et al.* [2001], differences between vertically integrated across-shelf volume transport and the volumetric rate of sea level change can only occur in a three-dimensional flow. Thus inner shelf along-shelf divergence could result in across-shelf current without strong changes in sea level. While no comparison to sea level was made, *Tilburg and Garvine* [2003] did demonstrate that along-shelf divergence does occur at the coastal edge of the study region during the stratified time period and would be expected to affect across-shelf transport.

[28] The observed seasonal differences in the vector correlations are supported by a study by *Weisberg et al.* [2001]. The study primarily examined the effects of stratification on upwelling and downwelling events generated by along-shelf wind using a twin model experiment, one model with and without stratification. However, the study did show that current veering in the boundary layer is significantly influenced by stratification. Without stratification very little turning in the surface boundary layer was observed, which is inline with this study's observations.

[29] Both seasonal results can be explained in a manner consistent with Ekman dynamics. During the stratified period, a strong thermocline across the shelf would inhibit the growth of the surface boundary layer, which would consequently extend the timescale for the transfer of momentum from the surface to the bottom. This in effect allows the rotational timescale of  $1/f$  to play a role in the system dynamics [*Lentz*, 2001], which explains the  $30\text{--}40^\circ$  veering of the current to the right of the wind. While in the mixed period the surface boundary layer is often of  $O(h)$ , which causes transport, or in this study's observations, surface flow, to travel in the direction of the wind. As evidence of this, the Ekman surface layer depth was calculate using simple theory,  $\delta_{ek} = \kappa u_* / f$  where  $\kappa$  is von Karman's constant (0.4),  $f$  is the Coriolis parameter, and  $u_*$  is  $\sqrt{\tau / \rho_0}$  where  $\tau$  is the wind stress, and  $\rho_0$  is a reference density (assumed  $1030 \text{ kg/m}^3$ ) [*Ekman*, 1905; *Lentz*, 1995b]. During the mixed1 and mixed2 periods of the study, the mean  $\delta_{ek}$  was 37 m and 46 m, respectively. At these depths, most of the shelf would be considered of the order of  $\delta_{ek}$ , which is similar to what *Lentz* [2001] suggested from his work off the North Carolina shelf. This expectation is consistent with the observed seasonal differences in the transfer coefficient of the vector correlation. The lower transfer coefficient during the mixed period means that

stronger winds are associated with surface current velocity which suggests that since momentum is more easily transferred vertically during mixed conditions, the additional momentum associated with the stronger wind would be transferred to a larger depth, hence a deeper  $\delta_{ek}$ . Furthermore, some additional evidence of this can be found in the spatial relationship between wind stress and current. As shallower water would be proportionally more affected by bottom friction, the expectation is that deeper water, in the presence of weak stratification, would be more likely to allow the formation of  $\delta_{ek}$ . The notion can be indirectly tested in a rather limited way by comparing the veering angle between the wind stress and the current with depth. Unfortunately, the results from the subregion correlations (Table 2) are inconclusive during the mixed periods, with the mixed2 period having only a minor increase in veering angle with depth, while there was actually a decrease, albeit smaller, in the veering angle over subregions during the mixed1 period. However, the stratified period was consistent and had a strong change in the veering angle with distance from the coast. This suggests that water column depth affects coastal dynamics over a large portion of the shelf even during periods associated with strong stratification when the surface boundary layer should be insulated from bottom friction effects.

[30] While the HF radar measures the spatial variability of surface currents as they respond to forcing across the shelf, it only samples near the surface. Attempting to fully describe shelf circulation, an inherently three-dimensional flow field, with only surface currents can lead to interpretation difficulties as pointed out by *Liu et al.* [2007]. As such, it should be re-emphasized that the relationships examined are between *surface* currents, wind stress and sea level. As such, whether there is significant transport associated with the across-shelf flows discussed above is another question that cannot be addressed without further observations and/or modeling. *Lentz* [2001] found that unstratified conditions on the North Carolina coast were associated with transport much lower than that estimated by across-shelf Ekman transport, which lead to the suggestion that strong wind-forcing may not be a very effective mechanism for across-shelf movement of organisms, nutrients, or sediments during the fall and winter. Similarly, the twin model study by *Weisberg et al.* [2001] mentioned above, showed that the constant density case had reduced transports in the boundary layers when compared to the stratified case. The data in this study were similar in that during the mixed period, the along-shelf wind stress was not well correlated with across-shelf flow in the surface layer.

[31] However, the across-shelf surface velocities, and thus possibly surface transport, were episodically quite high ( $>15$  cm/s at times) and were well correlated with across-shelf wind stress during the mixed period as mentioned above. The notion that offshore wind can in fact drive across-shelf transport under constant density conditions was shown by *Li and Weisberg* [1999a, 1999b] with a three-dimensional numerical model. Their modeling results for the West Florida Shelf showed that offshore wind-forcing results in fully three-dimensional flow with opposing surface and bottom boundary layers which account for the across-shelf transports. Furthermore, the contribution of across-shelf wind stress to the across-shelf momentum

balance was confirmed by in situ studies on West Florida Shelf by *Liu and Weisberg* [2005a, 2007], where they showed that across-shelf wind did contribute significantly but in a secondary way to the across-shelf momentum balance on the inner shelf. Thus these studies would suggest that significant across-shelf transport driven by across-shelf wind stress could be occurring during the mixed conditions in the MAB.

[32] On the other hand, the data in this study do not show evidence of across-shelf wind stress driving large amounts of surface transport within a stratified outer shelf as shown in a modeling study by *Tilburg* [2003]. As stated above, this study cannot address the issue of transport, however the surface currents during the stratified period were not correlated with across-shelf wind which would suggest that large amounts of transport in the surface layer were not likely during times of across-shelf wind in the stratified periods observed. Thus there remain some unresolved questions as to the importance of across-shelf wind in across-shelf transport during mixed and stratified periods in the MAB.

## 6. Summary

[33] Seasonal differences in the forcing and response relationships of surface currents, wind stress, and adjusted sea level were observed in 18 months of data in the central MAB. Seasonal vector correlations between the surface current and wind stress revealed very high correlations but distinctly different phase angles and transfer coefficients. The stratified (mixed) period current veered to the right of the wind by  $30\text{--}40^\circ$  ( $6\text{--}8^\circ$ ) and had a higher (lower) transfer coefficient. Scalar correlations between across-shelf wind stress and across-shelf current showed higher  $r$  values than with the along-shelf wind stress during the mixed period. While this pattern did not hold between wind stress and sea level, the correlations did show a stronger (weaker) relationship with across-shelf (along-shelf) wind stress than what was observed in the stratified season. These relationships were particularly notable during commonly observed surface shelf wide offshore flow patterns which were associated with distinctly different wind stress magnitudes and directions during mixed and stratified seasons. Conditional sampling of shelf wide events during the mixed/weaker stratified periods did show stronger relationships between both across-shelf wind/across-shelf current and across-shelf wind/sea level than with the along-shelf wind stress. Furthermore, regionally comparing subsectional current averages of the HF radar footprint with wind stress showed increased current veering to the right of the wind with increased offshore distance during the stratified periods, while the mixed time periods showed little or no current veering to the right of the wind with increased depth.

[34] It was speculated that these seasonal differences resulted from a larger Ekman surface boundary layer depth during the mixed period which suggests that there is a significant seasonal change in the size of the inner shelf, the area of shelf most sensitive to across-shelf wind stress. Thus during the mixed period across-shelf wind stress could be an important factor in driving across-shelf circulation over a much large portion of the central MAB then presumed. However, additional studies in the central MAB during the

mixed period are needed to confirm this. Furthermore, this study presents additional evidence of the episodic importance of across-shelf wind stress during severe wind events, as well as little evidence of significant across-shelf transport being driven by across-shelf wind over a stratified outer shelf. While the analysis relies on correlations with surface currents, which can be difficult to interpret without vertical water column measurements, the results of this study dovetailed well with previous studies of across-shelf circulation in other locations, reinforcing the results analysis in this study.

[35] **Acknowledgments.** This work would not have been possible without collecting, processing, and archiving the HF radar velocity maps by Coastal Ocean Observation Lab at Rutgers University, including Hugh Roarty and Scott Glenn. We also need to thank Bruce Liphardt, Rich W. Garvine, Kuo Wong, and John T. Reager for advice and technical assistance. In addition, we would like to thank the two anonymous reviewers for their comments, as they significantly improved this work. This work was supported by the National Atmospheric and Oceanographic Administration through grant NA17EC2449 and NASA-Space grant NNG05G092H and is a part of the lead author's Ph.D. dissertation at the University of Delaware. This work was partially supported by NOAA-SG through grant NA09OAR4170070, and by NASA through grant NNX08AW02A, NNX09AF33G, and NNG05G092H.

## References

- Allen, J. S., and P. A. Newberger (1996), Downwelling circulation on the Oregon continental shelf: Part I. Response to idealized forcing, *J. Phys. Oceanogr.*, **26**, 2011–2035.
- Allen, J. S., P. A. Newberger, and J. Federiuk (1995), Upwelling circulation on the Oregon continental shelf: Part I. Response to idealized forcing, *J. Phys. Oceanogr.*, **25**, 1843–1866.
- Austin, J. A., and S. J. Lentz (2002), The inner response to wind-driven upwelling and downwelling, *J. Phys. Oceanogr.*, **32**, 2171–2193.
- Beardsley, R. C., W. C. Boicourt, and D. V. Hansen (1976), Circulation on the Atlantic continental shelf of United States, Cape May to Cape Hatteras, *Mem. Soc. R. Sci. Liege*, **6**(10), 187–200.
- Castelao, R., S. Glenn, O. Schofield, R. Chant, J. Wilkin, and J. Kohut (2008), Seasonal evolution of hydrographic fields in the central Middle Atlantic Bight from glider observations, *Geophys. Res. Lett.*, **35**, L03617, doi:10.1029/2007GL032335.
- Chant, R. J., S. M. Glenn, and J. T. Kohut (2004), Flow reversals during upwelling conditions on the New Jersey inner shelf, *J. Geophys. Res.*, **109**, C12S03, doi:10.1029/2003JC001941.
- Dzwonkowski, B. (2009), Surface current analysis of shelf water in the central Mid-Atlantic Bight, Ph.D. thesis, Univ. of Delaware, Newark, Del.
- Ekman, V. W. (1905), On the influence of the earth's rotation on ocean currents, *Ark. Mat., Astron. Fys.*, **2**, 1–53.
- Flagg, C. N., M. Dunn, D. P. Wang, H. T. Rossby, and R. L. Benway (2006), A study of the currents of the outer shelf and upper slope from a decade of shipboard ADCP observations in the Middle Atlantic Bight, *J. Geophys. Res.*, **111**, C06003, doi:10.1029/2005JC003116.
- Garrett, C., P. MacCready, and P. Rhines (1993), Boundary mixing and arrested Ekman layers: Rotating stratified flow near a sloping boundary, *Annu. Rev. Fluid Mech.*, **25**, 291–323.
- Garvine, R. W. (2004), The vertical structure and subtidal dynamics of the inner shelf off New Jersey, *J. Mar. Res.*, **62**, 337–371.
- Kirincich, A. R., J. A. Barth, B. A. Grantham, B. A. Menge, and J. Lubchenco (2005), Wind-driven inner-shelf circulation off central Oregon during summer, *J. Geophys. Res.*, **110**, C10S03, doi:10.1029/2004JC002611.
- Kohut, J. T., S. M. Glenn, and R. J. Chant (2004), Seasonal Current variability on the New Jersey inner shelf, *J. Geophys. Res.*, **109**, C07S07, doi:10.1029/2003JC001963.
- Kohut, J. T., H. J. Roarty, and S. M. Glenn (2006), Characterizing observed environmental variability with HF doppler radar surface current mappers and acoustic doppler current profilers: Environmental variability in the coastal ocean, *IEEE J. Ocean. Eng.*, **31**(4), 876–884.
- Kundu, P. K. (1976), An analysis of inertial oscillations observed near Oregon coast, *J. Phys. Oceanogr.*, **6**, 879–893.
- Large, W. G., and S. Pond (1981), Open ocean momentum flux measurements in moderate to strong winds, *J. Phys. Oceanogr.*, **11**, 324–336.
- Lentz, S. J. (1992), The surface boundary layer in coastal upwelling regions, *J. Phys. Oceanogr.*, **22**, 1517–1539.
- Lentz, S. J. (1994), Current dynamics over the northern California inner shelf, *J. Phys. Oceanogr.*, **24**, 2461–2478.
- Lentz, S. J. (1995a), U. S. contributions to the physical oceanography of continental shelves in the early 1990s, National Report to International Union of Geodesy and Geophysics 1991–1994, *Rev. Geophys., Suppl.*, available at [www.agu.org/journals/rg/rg9504S/95RG00177/index.html](http://www.agu.org/journals/rg/rg9504S/95RG00177/index.html).
- Lentz, S. J. (1995b), Sensitivity of the inner-shelf circulation to the form of the eddy viscosity profile, *J. Phys. Oceanogr.*, **25**, 19–28.
- Lentz, S. J. (2001), The influence of stratification on the wind-driven cross-shelf circulation over the North Carolina shelf, *J. Phys. Oceanogr.*, **31**, 2749–2760.
- Lentz, S. J., and J. H. Trowbridge (1991), The bottom boundary layer over the northern California shelf, *J. Phys. Oceanogr.*, **21**, 1186–1202.
- Lentz, S. J., K. Shearman, S. Anderson, A. Plueddemann, and J. Edson (2003), Evolution of stratification over the New England shelf during the Coastal Mixing and Optics study, August 1996–June 1997, *J. Geophys. Res.*, **108**(C1), 3008, doi:10.1029/2001JC001121.
- Li, Z., and R. H. Weisberg (1999a), West Florida Shelf response to upwelling favorable wind-forcing: Kinematics, *J. Geophys. Res.*, **104**, 13,507–13,527.
- Li, Z., and R. H. Weisberg (1999b), West Florida continental shelf response to upwelling favorable wind forcing: 2. Dynamics, *J. Geophys. Res.*, **104**, 23,427–23,442.
- Liu, Y., and R. H. Weisberg (2005a), Momentum balance diagnoses for the West Florida Shelf, *Cont. Shelf Res.*, **25**, 2054–2074.
- Liu, Y., and R. H. Weisberg (2005b), Patterns of ocean current variability on the West Florida Shelf using the self-organizing map, *J. Geophys. Res.*, **110**, C06003, doi:10.1029/2004JC002786.
- Liu, Y., and R. H. Weisberg (2007), Ocean currents and sea surface heights estimated across the West Florida Shelf, *J. Phys. Oceanogr.*, **37**(6), 1697–1713.
- Liu, Y., R. H. Weisberg, and L. K. Shay (2007), Current patterns on the West Florida Shelf from joint self-organizing map analyses of HF radar and ADCP data, *J. Atmos. Oceanic Technol.*, **24**(4), 702–712.
- MacCready, P., and P. B. Rhines (1991), Bouyant inhibition of Ekman transport on a slope and its effect on stratified spring-up, *J. Fluid Mech.*, **223**, 631–661.
- Mitchum, G. T., and A. J. Clarke (1986), The frictional nearshore response to forcing by synoptic scale winds, *J. Phys. Oceanogr.*, **16**, 934–946.
- Münchow, A., and R. J. Chant (2000), Kinematics of inner shelf motions during the summer stratified season off New Jersey, *J. Phys. Oceanogr.*, **30**, 247–268.
- Noble, M., and B. Butman (1979), Low frequency wind-induced sea level oscillations along the east coast of North America, *J. Geophys. Res.*, **84**, 3227–3236.
- Noble, M., B. Butman, and E. Williams (1983), On the longshelf structure and dynamics of subtidal currents on the Eastern United States continental shelf, *J. Phys. Oceanogr.*, **13**, 2125–2147.
- Ou, H. W., R. C. Beardsley, D. Mayer, W. C. Boicourt, and B. Butman (1981), An analysis of subtidal current fluctuations in the Middle Atlantic Bight, *J. Phys. Oceanogr.*, **11**, 1382–1392.
- Pringle, J. M., and K. Riser (2003), Remotely forced nearshore upwelling in Southern California, *J. Geophys. Res.*, **108**(C4), 3131, doi:10.1029/2002JC001447.
- Rasmussen, L. L., G. Gawarkiewicz, W. B. Owens, and M. S. Lozier (2005), Slope water, gulf stream, and seasonal influences on southern Mid-Atlantic Bight circulation during the fall-winter transition, *J. Geophys. Res.*, **110**, C02009, doi:10.1029/2004JC002311.
- Song, T. Y., D. B. Haidvogel, and S. M. Glenn (2001), Effects of topographic variability on the formation of upwelling centers off New Jersey: A theoretical model, *J. Geophys. Res.*, **106**, 9223–9240.
- Stewart, R. H., and J. W. Joy (1974), HF radio measurements of surface currents, *Deep-Sea Res.*, **21**, 1039–1049.
- Tilburg, C. E. (2003), Across-shelf transport on a continental shelf: Do across-shelf winds matter?, *J. Phys. Oceanogr.*, **33**, 2675–2688.
- Tilburg, C. E., and R. W. Garvine (2003), Three-dimensional flow in a shallow coastal upwelling zone: Alongshore convergence and divergence on the New Jersey shelf, *J. Phys. Oceanogr.*, **33**, 2113–2125.
- Trasviña, A., E. D. Barton, J. Brown, H. S. Velez, P. M. Kosro, and R. L. Smith (1995), Offshore wind forcing in the Gulf of Tehuantepec, Mexico: The asymmetric circulation, *J. Geophys. Res.*, **100**, 20,649–20,664.
- Trowbridge, J. H., and S. J. Lentz (1991), Asymmetric behavior of an oceanic boundary layer above a sloping bottom, *J. Phys. Oceanogr.*, **21**, 1171–1185.
- Wang, D. P. (1979), Low frequency sea level variability on the Middle Atlantic Bight, *J. Mar. Res.*, **37**, 683–697.



- Wang, D. P. (1997), Effects of small-scale wind on coastal upwelling with application to Point Conception, *J. Geophys. Res.*, *102*, 15,555–15,570.
- Weatherly, G. L., and P. J. Martin (1978), On the structure and dynamics of the oceanic bottom boundary layer, *J. Phys. Oceanogr.*, *8*, 557–570.
- Weisberg, R. H., Z. Li, and F. E. Muller-Karger (2001), West Florida shelf response to local wind forcing: April 1998, *J. Geophys. Res.*, *106*, 31,239–31,262.
- Winant, C. D., R. C. Beardsley, and R. E. Davis (1987), Moored wind, temperature and current observations made during Coastal Ocean Dynamics Experiments 1 and 2 over the northern California continental shelf and upper slope, *J. Geophys. Res.*, *92*, 1569–1604.
- Yankovsky, A. E. (2003), The cold-water pathway during an upwelling event on the New Jersey shelf, *J. Phys. Oceanogr.*, *33*, 1954–1966.
- Yankovsky, A. E., and R. W. Garvine (1998), Subinertial dynamics on the inner New Jersey shelf during the upwelling season, *J. Phys. Oceanogr.*, *28*, 2444–2458.
- 
- B. Dzwonkowski, College of Marine and Earth Studies, University of Delaware, 215 Robinson Hall, Newark, DE 19716, USA. (briandz@udel.edu)
- J. T. Kohut, Institute of Marine and Coastal Sciences, Rutgers-State University of New Jersey, 71 Dudley Road, New Brunswick, NJ 08901-8521, USA.
- X.-H. Yan, College of Earth, Ocean and Environment, University of Delaware, 209 Robinson Hall, Newark, DE 19716, USA.





# Sub-inertial characteristics of the surface flow field over the shelf of the central Mid-Atlantic Bight

Brian Dzwonkowski<sup>a,\*</sup>, Josh T. Kohut<sup>b</sup>, Xiao-Hai Yan<sup>a,c</sup>

<sup>a</sup> College of Marine and Earth Studies, University of Delaware, Newark, DE, USA

<sup>b</sup> Institute of Marine and Coastal Sciences, Rutgers State University of New Jersey, New Brunswick, NJ, USA

<sup>c</sup> State Key Lab of Marine Environment, Xiamen University, Xiamen, China

## ARTICLE INFO

### Article history:

Received 14 October 2008

Received in revised form

23 March 2009

Accepted 7 July 2009

Available online 15 July 2009

### Keywords:

Surface currents

Correlation scales

HF radar

Mid-Atlantic Bight

Surface velocity

## ABSTRACT

Observations of surface velocity data from August 2002 to February 2004 were collected by a series of four long-range high-frequency (HF) radars along the coast of New Jersey. The shelf observations of the central Mid-Atlantic Bight (MAB) were compared to historical observations of surface flow characteristics in the area. The time-averaged spatial mean velocity of 4 cm/s in the down-shelf along-shelf direction and 3 cm/s in the offshore across-shelf direction compared very well to historical surface measurements in the study region. However, as the spatial resolution of the data set revealed, this simple measure masked significant spatial variations in the overall and seasonal mean flow structures. Three regions – the south bank of the Hudson Shelf Valley, the southern New Jersey inner shelf (LEO-15) region, and the region offshore of the Delaware Bay mouth (southwest corner) – had mean flows that favor offshore transport of surface water. In terms of temporal variability, maps of the principle axes showed that the across-shelf (minor) axis contribution was not insignificant in the surface layer ranging from 0.3 to 0.9 of along-shelf (major) axis and that there were seasonal differences in orientation and ellipticity. Analysis of the spatial changes in the temporal and spatial correlation scales over the shelf showed that shelf position, in addition to site separation, contributed to the differences in these properties. Furthermore, observations over the Hudson Shelf Valley region suggested that this was a region of transition in which the orientation of along- and across-shelf components begin to change.

© 2009 Elsevier Ltd. All rights reserved.

## 1. Introduction

While there have been many studies on the hydrography of Mid-Atlantic Bight (MAB) dating back to at least the 1930s (Bigelow, 1933; Bigelow and Sears, 1935), the work over the last 30–40 years has lead to a well accepted general circulation pattern. This circulation is well summarized in a recent paper by Lentz (2008) which re-examines past observations and presents a modified theoretical model. The MAB region is dominated by a mean depth-averaged flow in the southwestward direction (down-shelf) of 5–10 cm/s with the mean vertical structure peaking at or near the surface and decreasing with depth (Bumpus, 1973; Beardsley et al., 1976; Shearman and Lentz, 2003; Rasmussen et al., 2005; Flagg et al., 2006; Lentz, 2008; among others). The observations of the across-shelf circulation are described using a layered structure, in which the surface boundary layer flows offshore and a divergence zone in the

bottom boundary layer near the mid to outer shelf separates onshore flow shoreward of the divergence from offshore flow seaward of the divergence (Csanady, 1976; Lentz, 2008). Time-averaged depth-dependent profiles of many previous long-term studies shown by Lentz (2008) indicates mean across-shelf flow is weaker than along-shelf flow, with the across-shelf magnitudes ranging from 1.5 to 4 cm/s depending of the location in the water column. Peak offshore flow occurs in the surface layer, while peak onshore flow occurs in the geostrophic layer and decreases near the bottom. More specifically in the central MAB, measurements indicate along (across)-shelf flow in the *surface* layer of the mid-shelf, between 25 and 60 m isobaths, to be 4 (1.6) cm/s in the down-shelf (offshore) direction. While this general circulation pattern does explain the overarching characteristics in the MAB, the large extent of the area inevitably leads to a synoptic under sampling with numerous experiments having been conducted in limited regions and for limited durations.

In recent years, high-frequency (HF) radar along sections of the MAB coast provides an opportunity to examine smaller-scale surface flow characteristics and variability over intra-annual to inter-annual time scales. The purpose of this study is to examine

\* Corresponding author.

E-mail address: [briandz@udel.edu](mailto:briandz@udel.edu) (B. Dzwonkowski).



the surface flow structure over the shelf of the central MAB at a spatial level unresolved with traditional ship-based cruises or moorings. The study focuses on an 18 month HF radar dataset, examining spatial flow structure across the MAB in the context of historical ship and mooring studies. This new dataset affords us the opportunity to examine surface current variability not previously examined in the MAB. The high resolution HF radar dataset includes time periods of high and low stratification and regions of distinct topographic features. Section 2 describes the study area and the data used. The reader is referred to Dzwonkowski et al. (2009); and Kohut et al. 2006; for additional background information on the HF radar data. Section 3 presents analysis of the structure and variability of the overall and seasonal mean fields, while Section 4 describes along- and across-shelf variability using the velocity time series and the spatial and temporal correlation scales of the surface flow for individual grid points in several key regions of the shelf. A discussion of the results in light of previous studies as well as this study's conclusions are presented in Sections 5 and 6.

## 2. Site and data

### 2.1. Study region

While the focus of this study is the central MAB off the coast of New Jersey, a broader view of the surrounding region reveals several notable features that complicate the flow structure. Two major geographic/bathymetric features of the region are the Hudson shelf valley/Hudson Canyon and the change in coastline orientation at Long Island (Fig. 1). The Hudson shelf valley/Hudson Canyon extends across the entire shelf dramatically warping the bathymetric contours as the mouth of the Hudson River is

approached. This coincides with a shift in coastline orientation from approximately  $54^\circ$  (counter clockwise from east) along the New Jersey coast to approximately  $10^\circ$  along the Long Island coast. This change in orientation impacts the flow and presents difficulties in determining along- and across-shelf coordinates over the northern section of the study area. In addition to these geographic and bathymetric features, the effects of buoyancy discharge from the Hudson River estuary have been shown to be unusually extensive throughout the study region (Yankowsky and Garvine, 1998; Tilburg and Garvine, 2003; Chant et al., 2008a, b; Castelao et al. 2008).

Over the years, there have been a number of experiments conducted in this region with many of the historic works summarized by Beardsley and Boicourt (1981) and Lentz (2008). In addition, there have been several recent programs that are relevant to this study. The majority of recent work has focused on the inner shelf starting with the NJUP experiment in the summer of 1996 and several other studies centered on the Long-term Ecosystem Observatory at 15 m (LEO-15). In late 2003, a Rutgers University autonomous underwater vehicle project began collecting temperature, salinity, and optical data along a regular transect known as the Endurance Line (Fig. 1, blue dashed line) which starts in the inner shelf and extends to the shelf break. Furthermore, the Langrangian Transport and Transformation Experiment (LaTTE), a multiple year project from 2004–2006, examined physical, chemical, and biological dynamics of the Hudson River outflow. This work complements these previous studies by providing surface current information further offshore with long-term coverage not previous available.

### 2.2. HF radar surface currents

This study used 4.55 MHz long-range, HF radar data from a region of the central MAB off the coast of New Jersey (Fig. 2). The

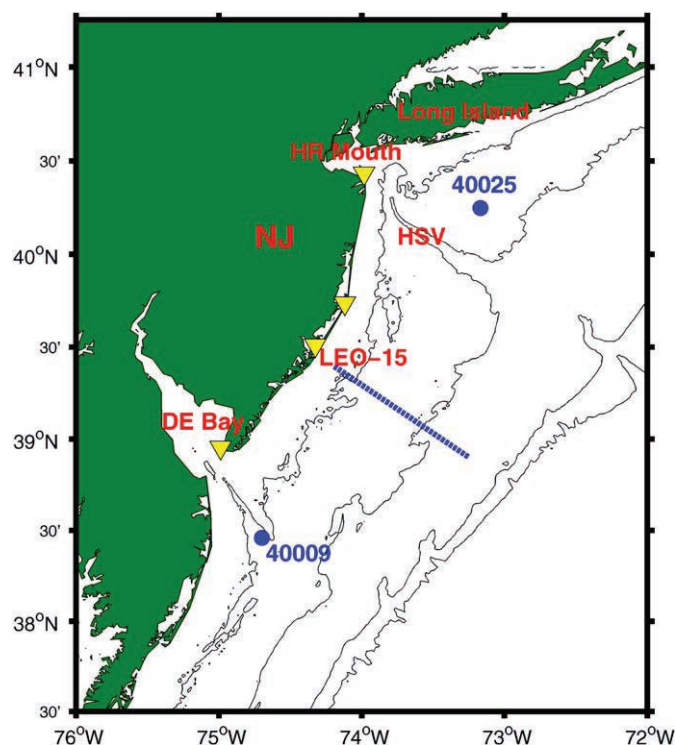


**Fig. 1.** Map of the central MAB showing bathymetry (black lines), HF radar sites (yellow triangles), NOAA buoys (blue circles) and the Endurance line (blue dotted line). In addition, several regions of reference are labeled, where HR Mouth is the Hudson River Mouth, HSV is the Hudson Shelf Valley, LEO-15 is the Long-term Ecosystem Observatory at 15 m, NJ is New Jersey, and DE Bay is the Delaware Bay

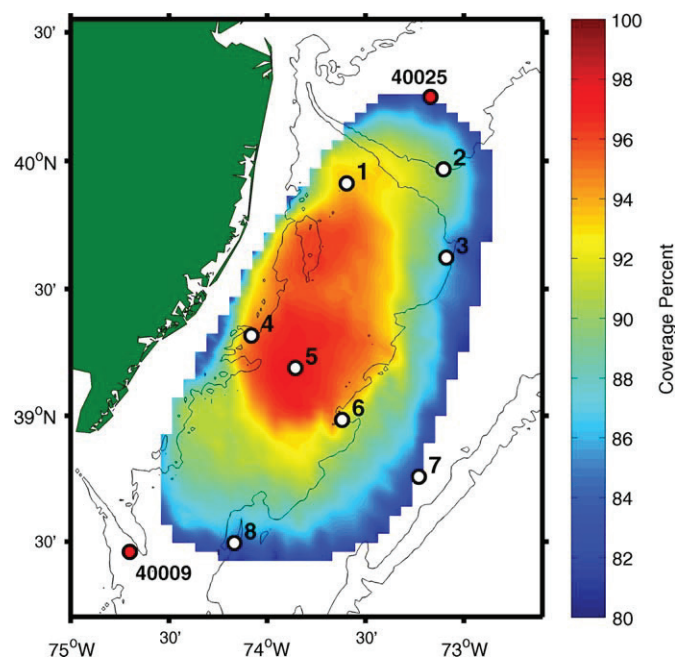


**Fig. 2.** The percent coverage of the HF radar network and the locations of 8 individual study sites. The percent coverage (coloration plot) is percent of valid velocity data contained in the 18 month long time series at each grid point in the coverage areas of 80% or greater. The eight study sites are individual HF radar grid points indicated by the white circles with the black outlines labeled one through eight. Wind data from NOAA environment buoys are shown as red circles with black outlines and labeled in black.

radial vectors collected by the HF radar array were averaged and geometrically combined onto a grid of UV component velocity vectors produced every 3 h following Kohut et al. (2006) and Gong et al. (2009). With an operating frequency of 4.55 MHz, the effective depth of the surface velocity measurement is approximately 2.4 m (Stewart and Joy, 1974) and the distance between grid points was in the order of 6 km. The surface current data was processed and operated in accordance with community recommendations. In particular, any data with geometric dilution of precision (GDOP) values greater than 1.5 were removed. Based on comparisons between radial current vectors from the HF radar and in situ ADCP and drifters (Kohut et al., 2006; O'donnell et al., 2005; Ullman et al., 2006), these data have an expected uncertainty on the order of 5–10 cm/s.

### 2.3. Surface winds

Wind data from a number of regional sources were collected over the same time period as the current data. The primary wind data used in this study were collected from NOAA buoy #44025 (Long Island (LI) wind) and NOAA buoy #44009 (Delaware Bay (DB) wind), at the northern and southern regions of the HF radar data (<http://www.ndbc.noaa.gov/>) (Fig. 2). In general, the hourly data were continuous over the 18 month period; however the LI wind had a considerable gap during May/June of 2003. This gap was filled using data from NOAA buoy #44017 (Montauk Point) with an appropriate transfer coefficient and lag applied to each component. In addition, the wind data was subsampled to match the 3 h HF radar data after the low-pass filtering discussed in the next section. As the NOAA buoys border the study region, a mean wind velocity time series for the study was created by vector averaging the LI and DE buoy wind data. Only minor deviations from the original two time series were present (low-frequency vector correlation between buoy sites:  $r = 0.88$ ,  $\theta = 5^\circ$ , transfer coefficient = 0.84, and lag = 0 h). From this mean wind vector, surface wind stress was estimated following Large and Pond (1981).

### 2.4. Data analysis

As this study focuses on the mean flow patterns and low-frequency characteristics of the surface layer currents, the mean and standard deviation (std.) are calculated only when the time series have 80% data coverage. Fig. 2 shows the 80% coverage area of the HF radar network for the 18 month time period of this study (August 15 2002–February 5 2004). The study uses several mean calculations with the time-averaged mean being the mean over the stated period at each HF radar grid point, the spatial mean being the mean over the HF radar footprint, and the time-averaged spatial mean being the time average of the spatial means. The means were computed as vector averages (mean of each component then combined), and the complex std. is computed as  $\sigma = \sqrt{\sigma_u^2 + \sigma_v^2}$  where  $\sigma$  is the std. of each component.

To isolate the low-frequency signal in the HF radar data, a 40 h low pass Lanczos filter was used to remove tidal and near-inertial signals. Prior to filtering, any gaps in the data were filled using temporal-linear interpolation. This scheme is adequate since the study was concerned with the low-frequency characteristics; and on average only 6% the temporal gaps in the time series were longer than 12 h. This is similar in concept to a study of low-frequency coastal processes by Dever et al. (2006), which interpolated through gaps in ADCP data of 19 h or less.

Using the filtered data, several characteristics of the low-frequency flow were examined. Principle axes were calculated at

each HF radar grid point to determine the primary direction and orientation that maximized the temporal variability at each grid point. Following Chant et al. (2004), the current vectors were rotated  $54^\circ$  counterclockwise from east so that along- and across-shelf components can be analyzed separately. In addition, time series from several individual grid points, discussed below, were used to determine temporal scales, velocity component correlations, and spatial scales. The decorrelation time scale was defined to be the time that the correlation function takes to drop below  $1/e$  ( $e$ -folding time scale) with the correlation function being the time lagged autocorrelation of the time series. Thus, the correlation function is simply the correlation coefficient plotted as a function of time, where time reflects the lag in autocorrelation calculation. Spatial correlations were determined using set points and calculating the correlation coefficient with the other HF radar grid points resulting in distributions of  $r$ -values over the HF radar footprint.

The specified grid points examined in this study were selected so that along- and across-shelf variability of key regions of the shelf could be investigated. The sites are shown in Fig. 2 with Sites 1–3 lying in the direct vicinity of the Hudson Shelf Valley, Site 4–7 lying along the 'Endurance line' (a region of uniformly orientated isobath that Rutgers University regularly runs AUV's along), and Site 8, which is at the base at the southern edge of the HF radar footprint. It should be noted that Sites 2, 3, 6, and 8 approximately follow the 50 m isobath, forming an along-shelf transect and that the Endurance line sites form an across-shelf transect. These stations will be referred to throughout the following sections as they were used to look at some of the spatial and temporal variability in more detail.

In addition to the total 18 month data set (August 15 2002–February 5 2004), two seasonal periods were examined. The results of previous studies in and near this region (Lentz, 2001; Kohut et al., 2004; Rasmussen et al., 2005; Castelao et al., 2008), and AUV measured across-shelf sections of temperature and salinity (October 2003–October 2004) showed that the water is typically strongly stratified during the summer months (June, July, August, September) and relatively well mixed during the winter months (December, January, February, March). Thus, the data were divided into a stratified (June 2003–September 2003) and mixed period (December 2002–March 2003) reflecting these observations. These temporal divisions affect the degrees-of-freedom (DOF) used in determining the significance of the correlation coefficient. A decorrelation time scale of two days was used to determine the DOF for each period. This is an overly conservative value as most of the time series in the HF radar grid have decorrelation time scales of 1–1.25 days as discussed below. Consequently, the DOF for each time period are 265 for the total, 61 for the stratified period, and 60 for the mixed period. The correlations reported in the following were significant at the 95% confidence level unless stated otherwise.

It should be pointed out that analyzing a data set of this size has a several caveats. First, there is some difficulties in establishing the 'along' and 'across' orientation of the surface vectors. Given the complex bathymetry, sharp changes in coastline orientation, and seasonal variability in the principle axes in the northern portion of the HF radar footprint (shown below), there are potential arguments against any of the typical means of objectively selecting the 'along' and 'across' shelf directions. Thus, an orientation as determined by Chant et al. (2004) ( $54^\circ$  counterclockwise from east) that is reasonable for the bulk of the HF radar footprint was used from which changes observed in the assumed orientations are noted and discussed.

In an attempt to avoid 'along' and 'across' shelf terminology, both the temporal and spatial complex correlations were examined. However, when compared to the component

correlations, the complex correlations were typically dominated by the ‘along-shelf’ component in nearly all cases. The complex correlation generally appeared to be a slight modulation of the ‘along-shelf’ correlation which largely masked the variability seen in the ‘across-shelf’ component, even at the sites around the Hudson Shelf Valley. The dominance of the along-shelf component in a coastal region is not unexpected as several studies (Pettigrew, 1981; Dever, 1997; Dever et al. (2006), etc.) have commented the along-shelf component can overwhelm the relatively weaker across-shelf component when analyzed in vector form. However, it is somewhat surprising that in the orientationally ambiguous northern region, the ‘along-shelf’ component still largely dominates the complex spatial correlation. That being said, the rotational component provided by vector analysis was well captured by the rotation observed in the principle component analysis (discussed below). Consequently, the component analyses combined with the principal axis analysis provided the necessary information in the most succinct manner.

In addition, since the HF radar data is a geometric combination of radial component vectors from 4 sites along the coast (red triangles; Fig. 1), the resolution of the radial currents vary from the inner shelf to the outer shelf. When these radials are combined to totals, the grid points further offshore are based on fewer vectors with lower spatial resolution than the higher resolution radials near-shore. Across the grid the resolution of a given vector is therefore at least the scale of the diameter of the search radius in the combination step (20 km in our case) with the potential for slightly larger scales near the offshore edges of the coverage. Consequently, the spatial correlation maps resulting from this study should be viewed in this context from which descriptive differences can be attributed to separation distance and/or position differences. That being said, this study focuses on changes in regions of high correlation, arbitrarily chosen as  $r$ -values greater than 0.75. This was done because the spatial scales defined by the  $1/e$  cutoff are larger than the study region in several cases, particularly in the along-shelf direction. Furthermore, the spatial averaging involved in the processing of the HF radar data has potential for smearing smaller-scale velocity shears, a feature observed in previous studies in the Hudson Shelf Valley (Harris et al., 2003).

### 3. General and seasonal surface patterns

To establish a general sense of the overall flow structure in the study area a few basic statistics were examined. Table 1 shows the time-averaged spatial mean of the current and time-averaged

**Table 1**

Magnitude and direction of the wind stress and the time averaged spatial mean over the HF radar grid during the total (August 15 2002–February 5 2004), mixed (December 02–March 03) and stratified (June 03–September 03) periods.

Total	Magnitude	Direction (deg.)
Current (cm/s)	5	179
Wind stress (Pa)	0.03	131
Mixed		
Current (cm/s)	5	168
Wind stress (Pa)	0.05	132
Stratified		
Current (cm/s)	3	175
Wind stress (Pa)	0.01	340

The direction is in compass degrees with the along-shelf axis being  $36^\circ/216^\circ$  and the offshore direction being  $-126^\circ$ .

wind for the total time period and the mixed and stratified periods. During the total and mixed periods, the wind was from the northwest and strong ( $>0.03$  Pa), while the surface current tended to be southward, with the mixed period being more south-southeastward. The stratified period had weak south winds, but southward current similar to the mixed period despite the change in wind conditions. While these results were not surprising, the HF radar data allows for a much more detailed view of the mean and variability of the surface currents.

The spatial variability in the time-averaged mean flow structure is shown in Fig. 3 with the time-averaged mean of each grid point (Fig. 3a) and their complex std. (Fig. 3b). The mean velocity plot shows that the flow structure had regions of south/southwest flow between 4–7 cm/s, largely in the southern region of the HF radar footprint beyond the 25 m isobath. However, the flow structure was not always parallel with local isobaths as there was a slight offshore veering of the vectors. Furthermore, there was a north to south trend of gradually increasing velocity in the flow field with mean velocity values of 2–3 cm/s in the north and 5–7 cm/s in the south. More importantly, the spatial resolution of the observations revealed several distinct flow structures, one just south of Hudson Shelf Valley, previously identified by a Rutgers University (RU) team (Chant et al., 2008a, b; Castelao et al., 2008) and another at the southern edge of the study region. In addition, the outer edges of the Long-term Ecosystem Observatory at 15 m (LEO-15) study area ( $39^\circ 25'N$ ,  $74^\circ 15'W$ ) appeared to have a significant across-shelf component in the time-averaged mean velocity. While the plot for the time-averaged mean velocity provided a general picture of the surface flow, the std. illustrates that most of the surface current energy is in the variability about that mean. In Fig. 3b, the std. was three to four times the magnitude of the mean velocity and generally increased with distance offshore. The northeast region of the HF radar footprint had the lowest std. values and again, similar to the mean plot, there was a general increase in the std. in the southward direction. However, this increase in value was not as smooth as in the mean plot.

#### 3.1. Mixed response

The time-averaged mean flow structure for the mixed period is in Fig. 4a. The mixed period time-averaged mean structure looked very similar to the total time-averaged mean structure with the velocity magnitudes being somewhat stronger than the total period and the vectors in the southern region tending to veer more offshore. Hence, the general flow direction was more southward, rather than the south-southwestward of the total period.

As more information about flow variance can be obtained from the principle axes, the temporal variability at each grid point was summarized in this way for the two seasonal periods (Fig. 4). During the mixed period (Fig. 5a), the major axes had magnitudes of around 10–16 cm/s and were generally stronger than the minor axes ( $\approx 6$  cm/s), which gave the flow variance a relatively rectilinear appearance. The major axes were orientated in the along-shelf direction with most axis orientations lying between  $40^\circ$  and  $60^\circ$  (along-shelf angle  $54^\circ$ ). Thus, while the time-averaged mean of the grid point was not along isobaths, the variability (principle axes) was largely oriented along the isobaths. Only in the northwest corner (between the 25 and 50 m isobaths) of the study region were the major and minor axes nearly equal. In addition, the effects of the corner geometry of the study area were seen in the region north of the Hudson Shelf Valley where the axis orientation rotated around by  $30^\circ$ – $50^\circ$ . This is more in line with the east–west coast of Long Island.



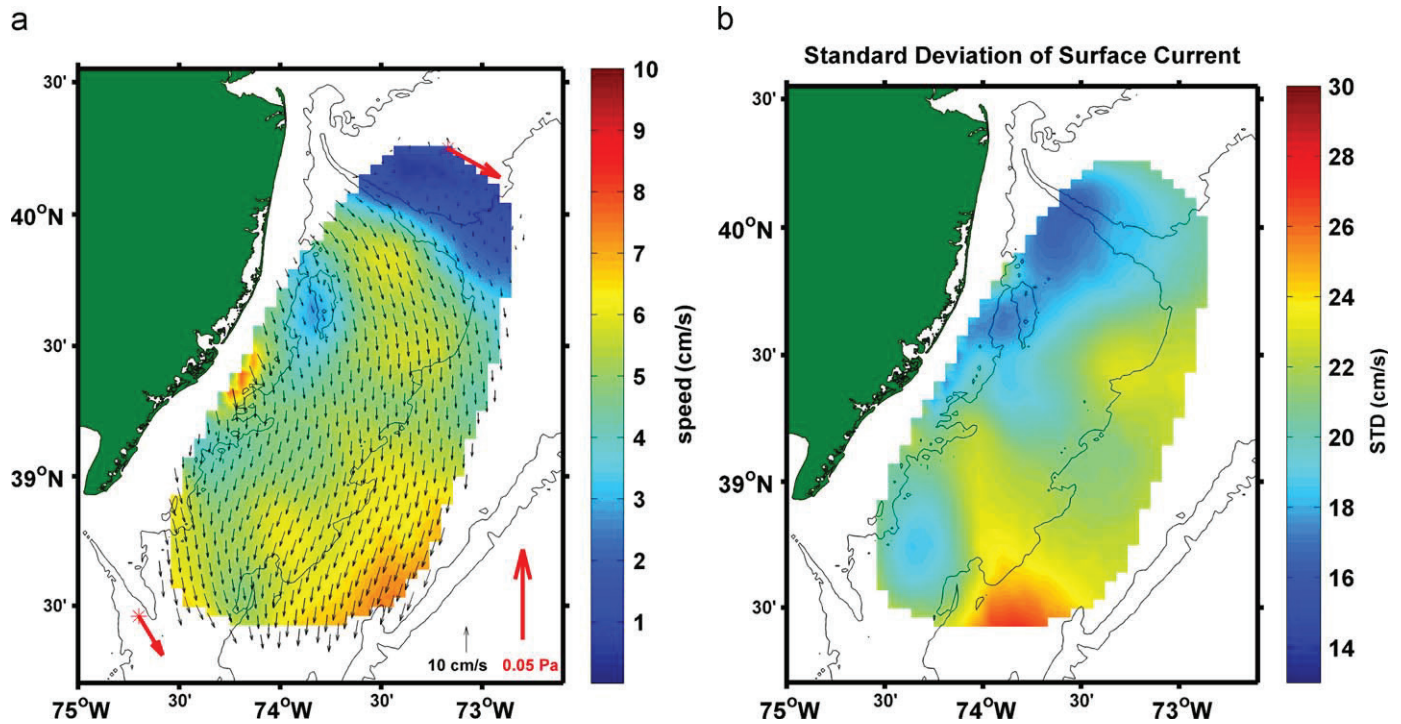


Fig. 3. (a) and (b) The time-averaged mean of each grid point (a) and their stand deviation (std.) (b) over the total period in the study area. In the mean plot, the black arrows are current velocities and the coloration is current magnitude (cm/s). The coloration in the right plot is the complex std. in cm/s. The red arrows are the mean wind stress at the NOAA environment buoys used in the study region.

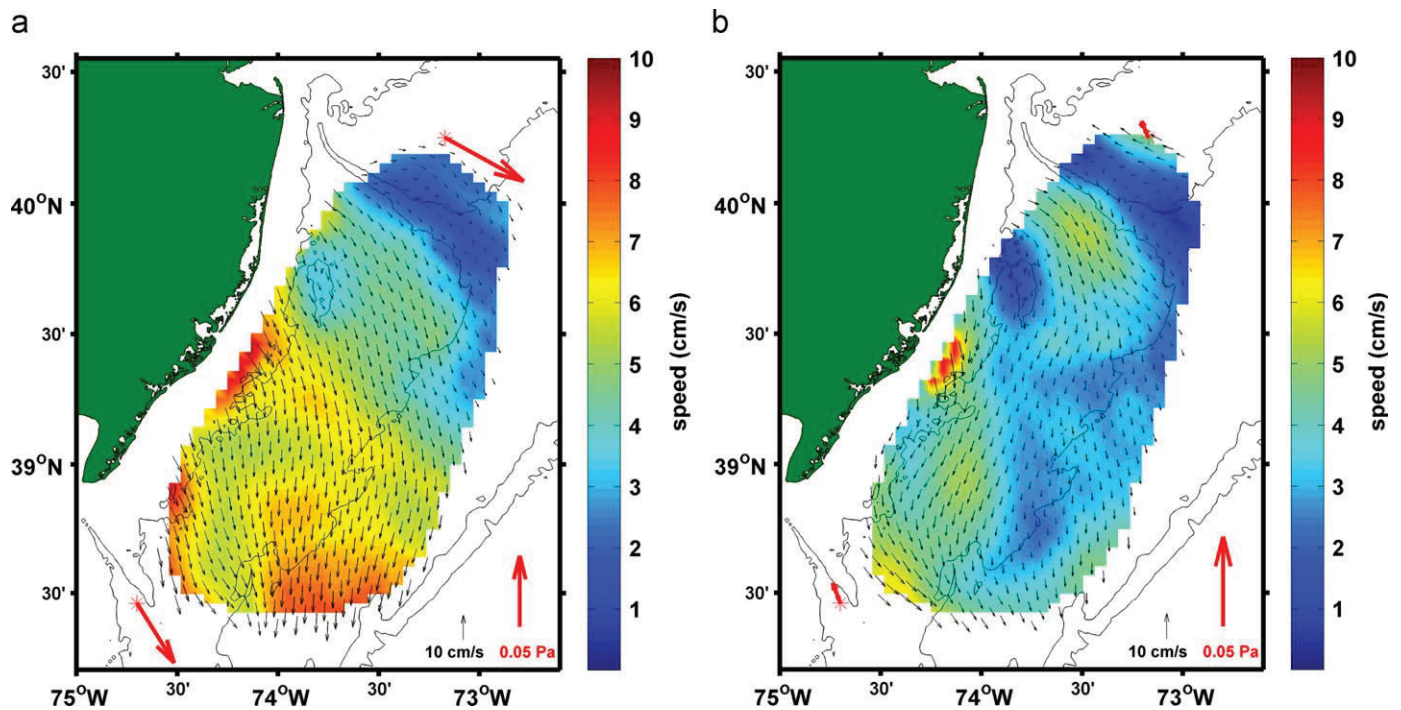
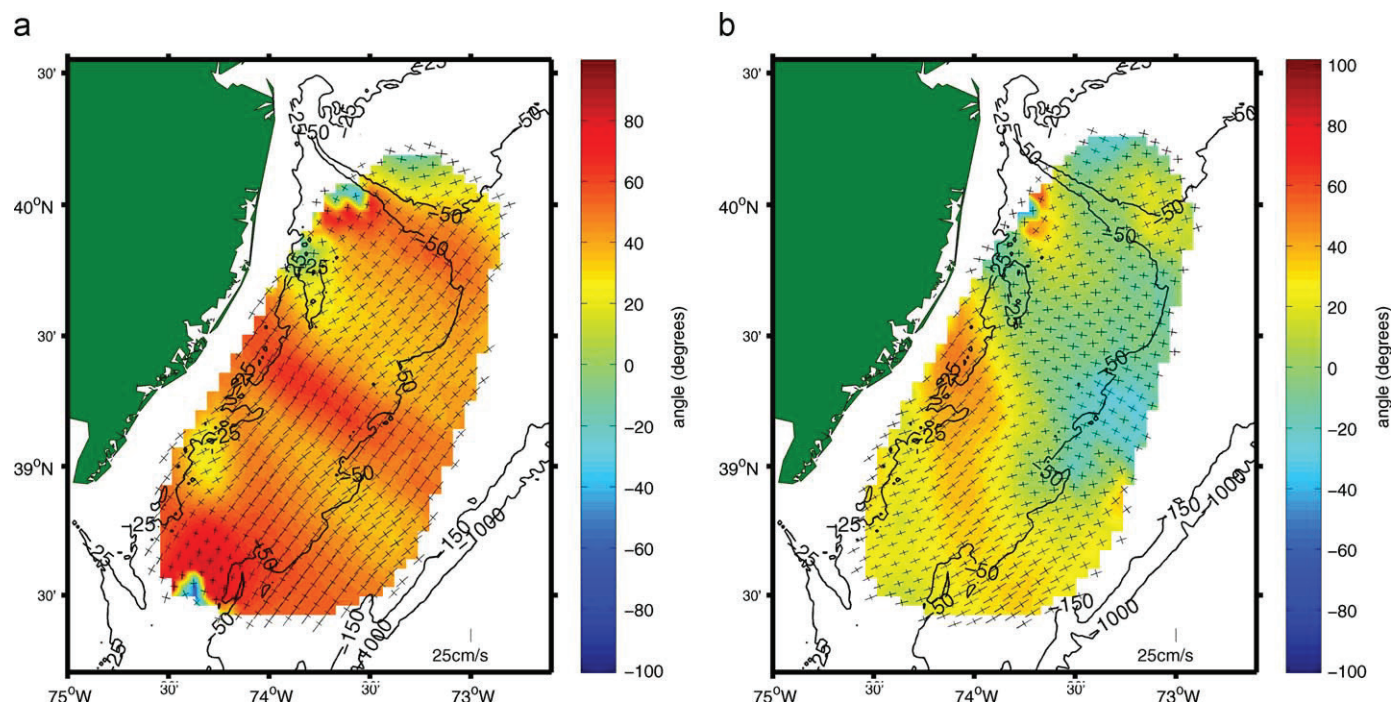


Fig. 4. (a) and (b) The time-averaged mean during the mixed and stratified periods temporal (a) and (b), respectively. The black arrows are current velocities and the coloration is current magnitude (cm/s). The red arrows are the mean wind stress during the respective time period at the NOAA environment buoys used in the study region.

### 3.2. Stratified response

The time-averaged mean flow structure for the stratified period is in Fig. 4b. The flow magnitudes tended to be between

1–5 cm/s. Again, there were three regions of distinct flow similar to those of the total period description mentioned above. However, the velocity differences between these regions and the surrounding grid points were larger, making these features more



**Fig. 5.** (a) and (b) The principle axis at each grid point for the mixed and stratified seasonal periods (a and b, respectively). The principle axes of the low-frequency velocity of the HF radar data (after temporal linear interpolation) are shown with the black crosses being the major and minor axis and the coloration representing the angle orientation of the major axis counterclockwise from east.

notable. In addition, outside of this LEO-15 and southwestern flow regions, the mean current direction tended to be parallel to local isobaths.

The principle axes during the stratified period are shown in Fig. 5b. The major (minor) axes magnitudes were approximately 8–12 cm/s (4–7 cm/s), with the southwest half of the study region favoring the major axis and the northeast half of the study region having a much more circular structure. In addition, the principle axes experienced a gradual rotation with the southwest region having an orientation of 25–45° and the northeast region being 10° to –15°.

#### 4. Along- and across-shelf variability

The spatial differences over the HF radar footprint were further compared using the eight site locations mentioned above to determine the temporal scales, velocity fluctuations, and spatial scales of along- and across-shelf velocity components. While the design of the site locations allowed for observations of specific areas of interest, such as the Hudson Shelf Valley, it was also useful in observing the changes of these properties in along- and across-shelf directions.

##### 4.1. Temporal correlation scales

Before the individual velocity time series were examined, the temporal decorrelation scales were determined as these were important for obtaining the degrees-of-freedom in the scalar correlations mentioned above. Fig. 6 shows the temporal correlation functions of along- and across-shelf components of the current at the eight site locations and the corresponding wind stress (Figs. 6a and b, respectively). The temporal correlation functions showed some expected patterns for along- and across-shelf components of the current velocity and wind stress with the pattern generally following a cosine-shaped monotonic decline

through the decorrelation level (thin horizontal black line). While the temporal correlation for the wind stress components were similar (29–30 h), along-shelf current velocity tended to have a larger decorrelation time and a larger temporal range than the across-shelf current velocity. Furthermore, the sites along the Endurance line (Sites 4–7) showed an increase in the temporal scale from 22 h near-shore to 30 h offshore. This was also seen further north relative to Sites 1 and 3. The time scales in the along-shelf direction as indicated by points along the 50 m isobath (excluding Site 8) showed consistent along-shelf current scales of 27–28 h. The temporal decorrelation scales in the across-shelf velocity component, however, were less consistent with values ranging from 18 to 28 h.

A further investigation of these scales over the full grid revealed a complex and detailed picture of the surface flow characteristics over the shelf. The spatial structure for both along- and across-shelf velocity components over the entire HF radar grid are shown in Figs. 7a and b, respectively. As seen in the individual site analysis, the decorrelation scales of the along-shelf component generally increase with distance offshore over the entire grid. The inner shelf area (around the 25 m isobaths) tended to have values of 20–24 h, the mid-shelf (25–50 m) tended to have values of 24–28 h, and the middle to outer shelf (50–100 m) tended to be 28–32 h. However, there were some exceptions, particularly along the Hudson Shelf Valley, which had longer decorrelation time scales closer to shore as can be seen by the yellow/orange coloration along its path.

The apparent relationship between depth and temporal decorrelation time did not appear to hold for the across-shelf component. In Fig. 7b, in general, the across-shelf temporal decorrelation times were shorter than those seen in the along-shelf component with the longest just north of the Hudson Shelf Valley. This is likely due in part to the changing orientation of the coastline in this location, making our cross-shelf component more consistent with the along-shelf analysis further south along the New Jersey coast.



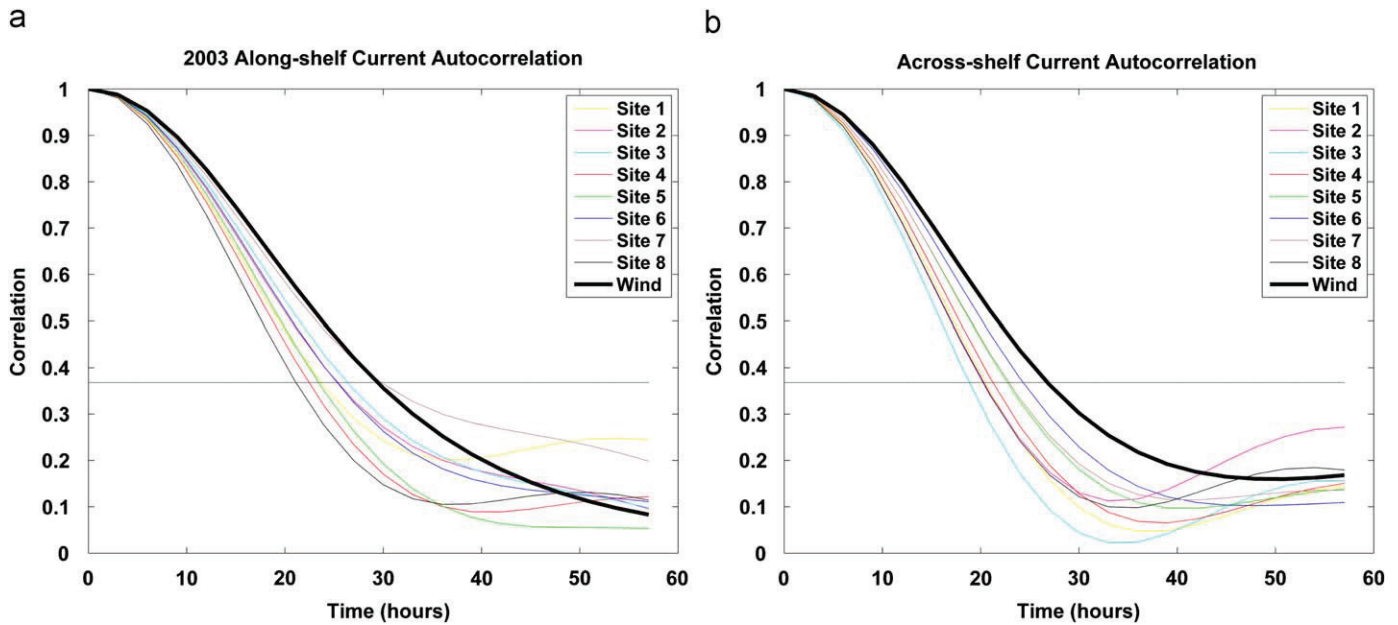


**Fig. 6.** (a) and (b) The temporal correlation functions from along- and across-shelf components of the current at the eight site locations and from the wind stress (a and b, respectively). The thin horizontal black line indicates the  $r$ -value below which the correlation is considered un-correlated. The individual sites and wind stress are shown by the various colors.

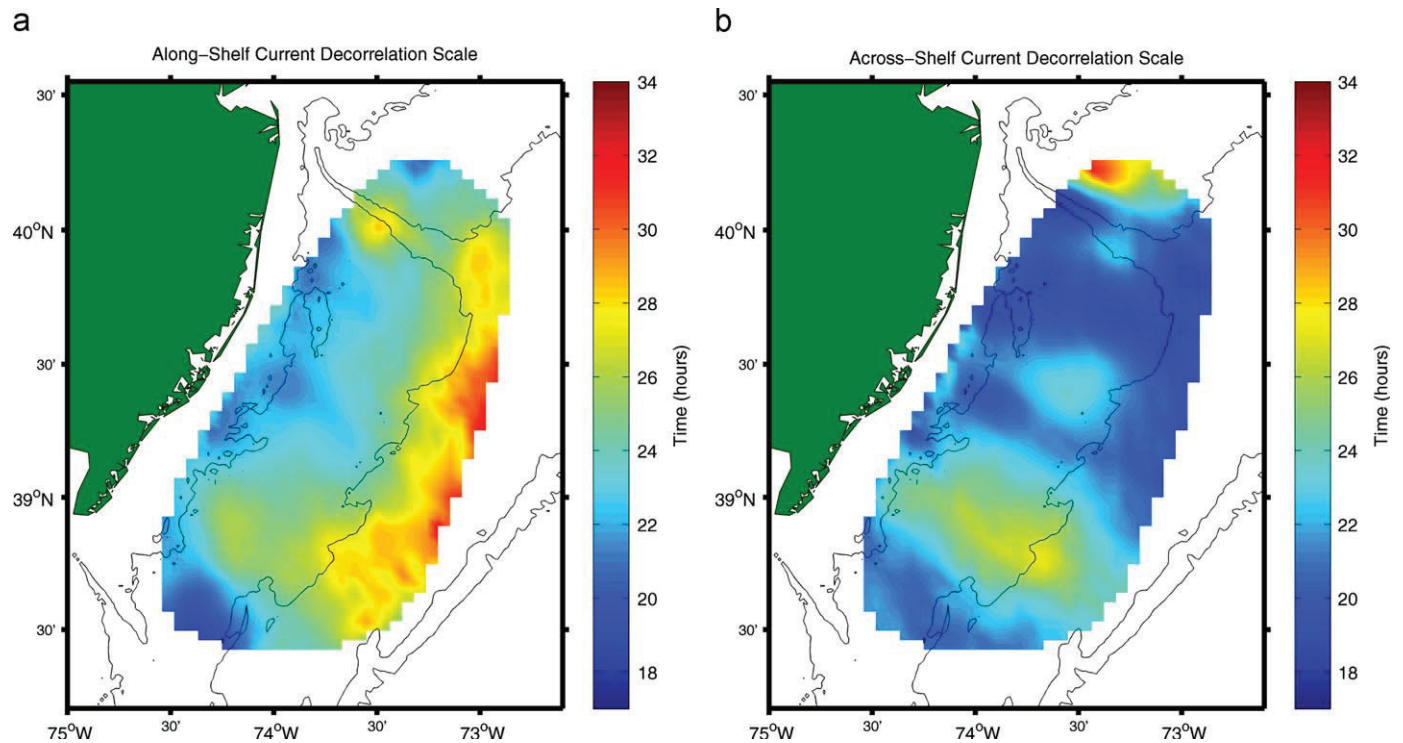


**Fig. 7.** (a) and (b) The decorrelation timescale over the HF radar grid for along- and across-shelf velocity (a and b, respectively). The coloration indicates the length of the decorrelation timescale.

#### 4.2. Velocity time series

The time series of along- and across-shelf components over the entire study period (August 02–January 04) for Site 4 and 6 are shown in Figs. 7 and 8, respectively. The positive (negative) values in Fig. 8 correspond to up-shelf (down-shelf) flow and the onshore and offshore current in Fig. 9, respectively. In general, the along-shelf (across-shelf) components experienced fluctuations of

O(40 cm/s) (O(20 cm/s)), but were well correlated at the two sites. The along (across)-shelf velocity at Sites 4 and 6 had a correlation coefficient of 0.76 (0.78) with Site 4 leading Site 6 by 3 h (0 h). There were some differences in the component magnitudes between the two sites; with Site 4 (Site 6) typically having stronger peaks in the along-shelf (across-shelf) flow. This difference was captured by their component std. While the complex sub-inertial stds. were similar, 16.7 cm/s (Site 4) and



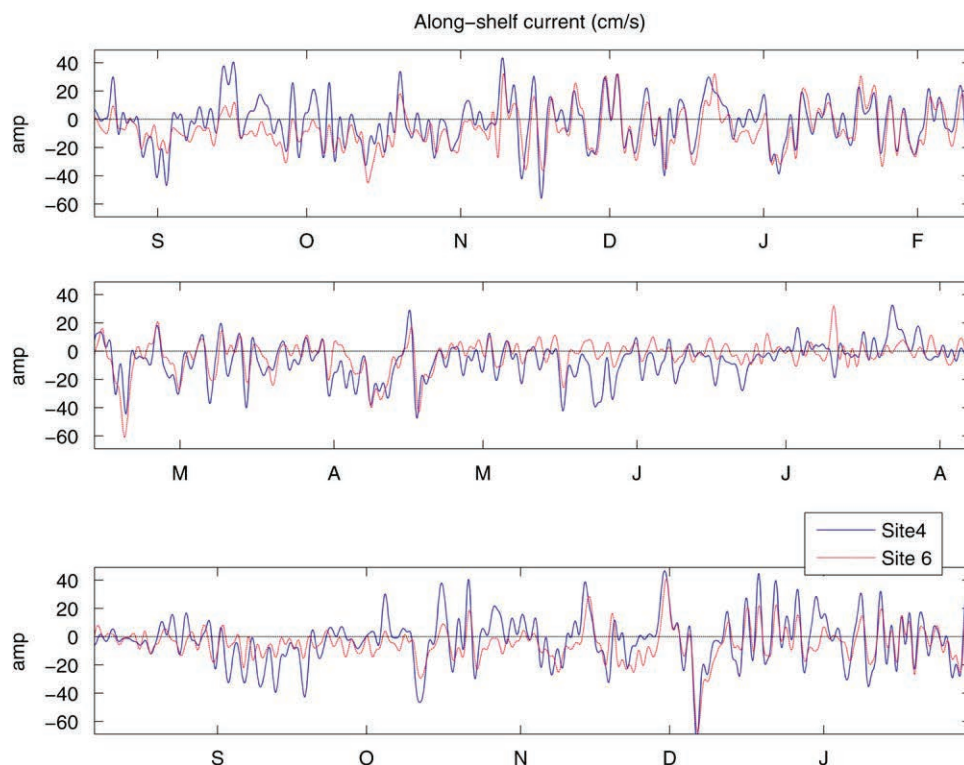


**Fig. 8.** Time series of the sub-inertial along-shelf component for Site 4 (blue) and 6 (red dash) over the duration of the study period (August 02–January 04). The positive (negative) values correspond to up-shelf (down-shelf) flow. The black dashed line is the zero line.

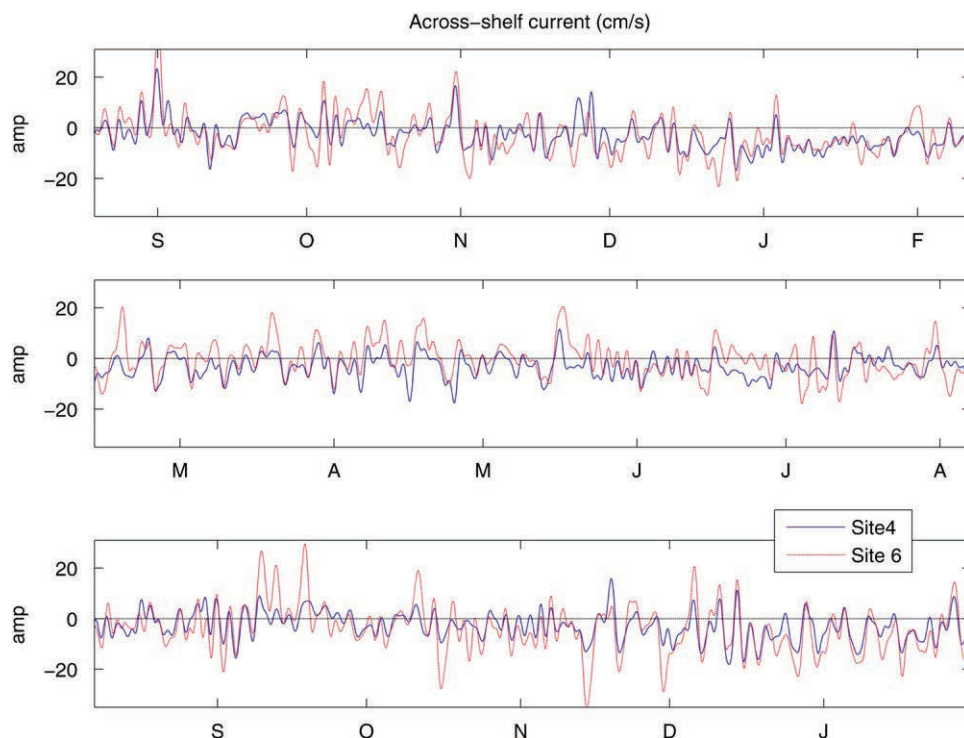


**Fig. 9.** Time series of the sub-inertial across-shelf component, similar to Fig. 8. The positive (negative) values correspond to onshore (offshore) current.

14.4 cm/s (Site 6), the individual components showed that the along-shelf std. is higher at Site 4 (16 cm/s compared to 12 cm/s) and the across-shelf std. was higher at Site 6 (8 compared to 5 cm/s). In addition, there were periods when the across-shelf current underwent periods of consecutive offshore bursts with zero to small onshore velocities separating them (December 02,

January 03, Mid-October 03–Mid-November 03, Mid-December 03–January 04).

Interestingly, there appeared to be a relationship between the across-shelf flow at Site 6 and the along-shelf flow at Site 4 ( $r$ -value =  $-0.71$ ). A good example of this occurred in September 2003, where three large pulses of onshore flow at Site 6 were

associated with strong pulses of down-shelf flow at Site 4. During these pulses, the across-shelf flow between Site 6 and 4 was dramatically reduced, dropping from peaks of 20–30 cm/s at Site 6 to peaks of 5–8 cm/s at Site 4, suggesting strong convergence in this area, with the converging water possibly flowing south at Site 4 as opposed to subducting. As illustrated in that example, there were occurrences of very strong across-shelf currents (20–35 cm/s) which were of the order of the along-shelf currents.

Further north closer to the Hudson Shelf Valley, Sites 1 and 3 showed similar but slightly less consistent relationships in the respective along- and across-shelf comparisons (not shown). The  $r$ -values for the along (across)-shelf current correlation between sites was 0.69 (0.65). However, these sites did not have a high correlation between along- and across-shelf currents as seen between Sites 4 and 6.

#### 4.3. Spatial correlation scales

Maps of spatial correlations were grouped in two ways to illustrate the differences observed throughout the HF radar footprint. Sites 4–6, along the Endurance line, is a region with

relatively uniform isobaths that parallel the coast (Figs. 10 and 12). In contrast, Sites 1–3 surround the Hudson Shelf Valley, a region of more complex bathymetry (Figs. 11 and 13).

##### 4.3.1. Along-shelf velocity correlations

In general, the spatial scales of the along-shelf velocity extend over a large portion of the HF radar footprint with the along-shelf correlation length scale being longer than the across-shelf scale. Across the endurance line (Fig. 10), there were relatively minor changes in the width, length, and magnitude of the regions of high correlations ( $r$ -value  $> 0.75$ , yellow to red color), which suggest that along-shelf velocity correlations are a function of separation rather than position. However, in the area around the Hudson Shelf Valley, the structure of the spatial correlations was less uniform (Fig. 11). The spatial correlations of the seaward locations (Site 2 and 3) were similar, covering a large section of the HF footprint. The structures were less uniform and weaker in magnitude when compared to the Endurance line stations. The shoreward location (Site 1) had a much smaller region of high correlation, confined to a circular region bounded by the 25 and 50 isobath. However, it was still well correlated (0.6–0.75) over a

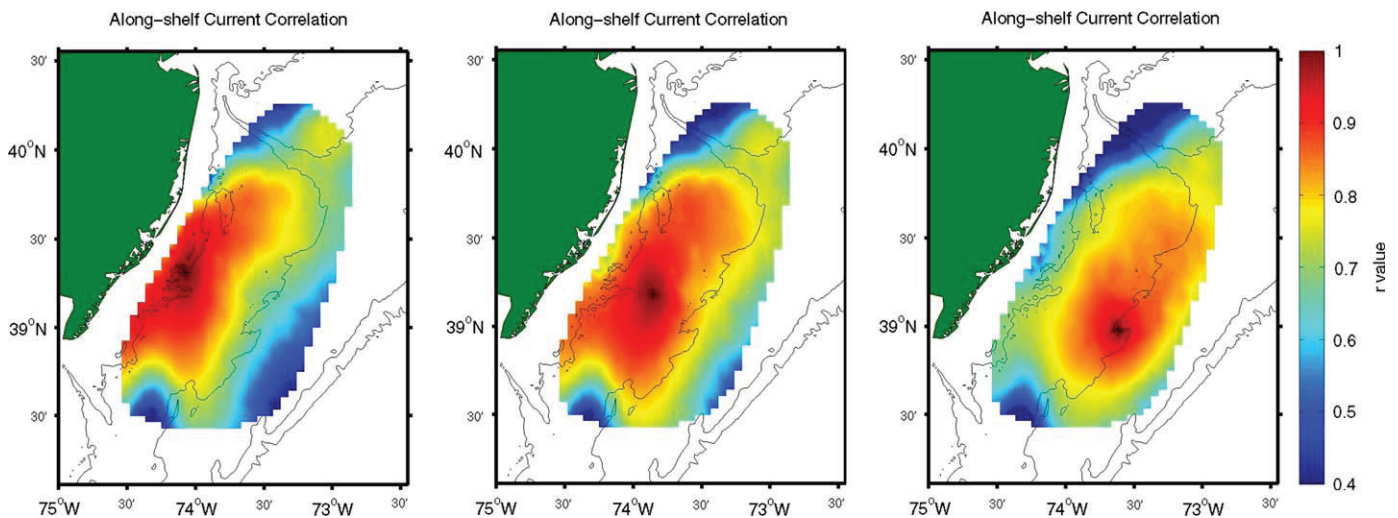


**Fig. 10.** The maps of the spatial correlation for the along-shelf velocities from three points (Sites 4–6) along the Endurance line with the coloration being the correlation coefficient ( $r$ -value) and the black star indicating the site location. The site plots are shown from the nearest to shore in the left plot (Site 4) to furthest offshore in the right plot (Site 6).

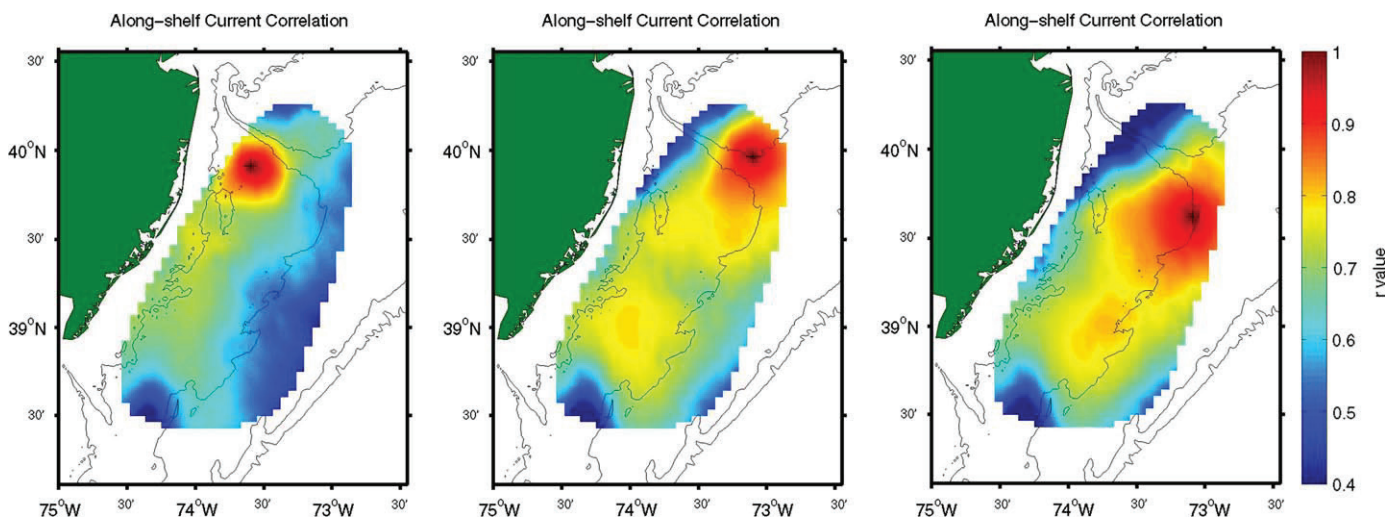


**Fig. 11.** Same as Fig. 10, except the along-shelf velocity correlation maps are shown for Sites 1, 3, and 2, respectively.

large portion of the shelf. These differences in structure around the Hudson Shelf Valley suggest the spatial correlation were functions of position rather separation. The points at the outer edge of the HF radar footprint (Sites 7 and 8, not shown) were somewhat more limited in their spatial scales, which could be due to their association with the study region boundary or regional processes such as the shelf break front, in the case of Site 7. This is further discussed in Section 5.

#### 4.3.2. Across-shelf velocity correlations

The general patterns of the spatial correlations of the across-shelf velocity were smaller and increased with distance offshore. Fig. 12 shows the spatial correlations of the across-shelf velocity from the same sites shown in Fig. 10. At the 25 m isobath (Site 4, left most plot), the region of high correlation was centered closely around the site location with an approximate diameter of 24–30 km. While moving 24 km offshore of Site 5 the scale nearly doubled to approximately 54–60 km (78–84 km) in the along-shelf (across-shelf) direction. This scale continued to increase further offshore at Site 6 on the 50 m isobath with the along-shelf width of the high correlation region being approximately 90 km and the across-shelf width being greater than 96 km (limited by the study boundary). In addition, the spatial correlation structure at Site 7

(not shown) was very similar to Site 6 with slightly reduced along- and across-shelf widths from what can be determined given the site proximity to the edge of the HF radar footprint. It is worth noting that there was a low correlation band over the Hudson Shelf Valley region at all the sites in Fig. 12 which suggest the Hudson Shelf Valley does exert some influence over the surface flow. Further evidence of the Hudson Shelf Valley's influence appeared in two of the sites around the Hudson Shelf Valley. Both Sites 1 and 2 have a very similar spatial structure that appeared partially constrained on their north and south sides, respectively, by the southern 50 m isobath of the canyon. However, the correlation pattern around Site 3 appeared similar to Site 5, rather than Sites 2 and 6 (which are also on the 50 m isobath), with little apparent influence by the Hudson Shelf Valley. Comparing Figs. 12 and 13, the shoreward sites (Sites 1 and 4) had slightly longer across-shelf correlation scales and relatively sharp boundaries. While further offshore the spatial scales increased in length, and more gradually decreased away from the site location. These differences suggest that, in addition to site separation, the shelf position also influences the spatial correlation patterns of the across-shelf velocity, even in regions of simple bathymetry such as the endurance line. This is reasonable since it would be expected that the spatial scales would change as the forcing dynamics change moving from the inner to outer shelf.

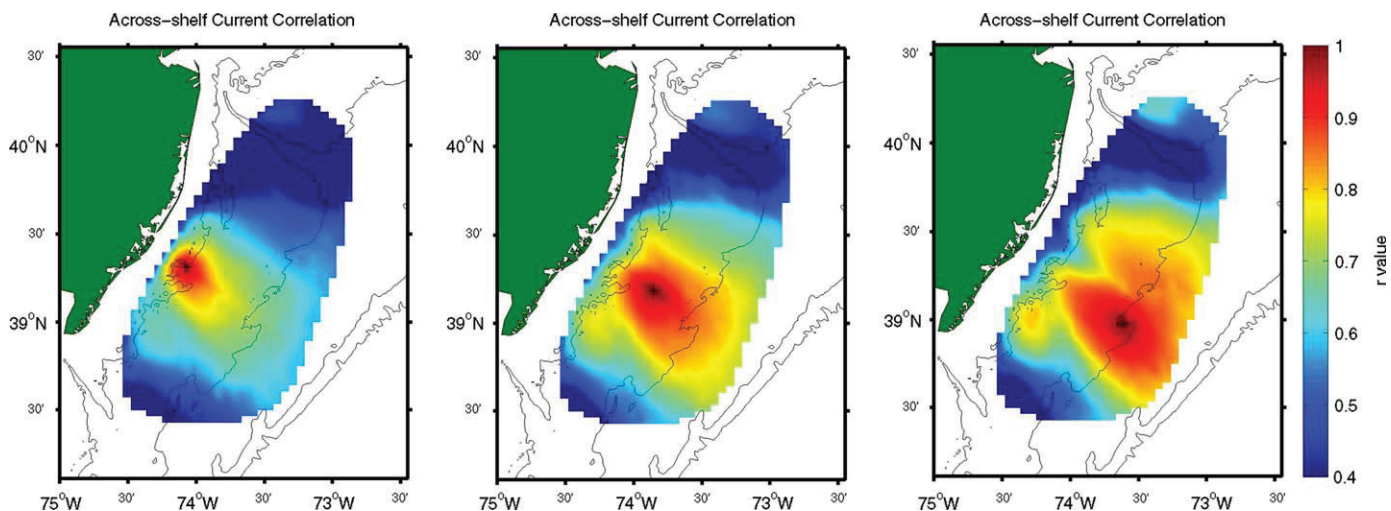


Fig. 12. Same as Fig. 10, except the across-shelf velocity correlation maps are shown.

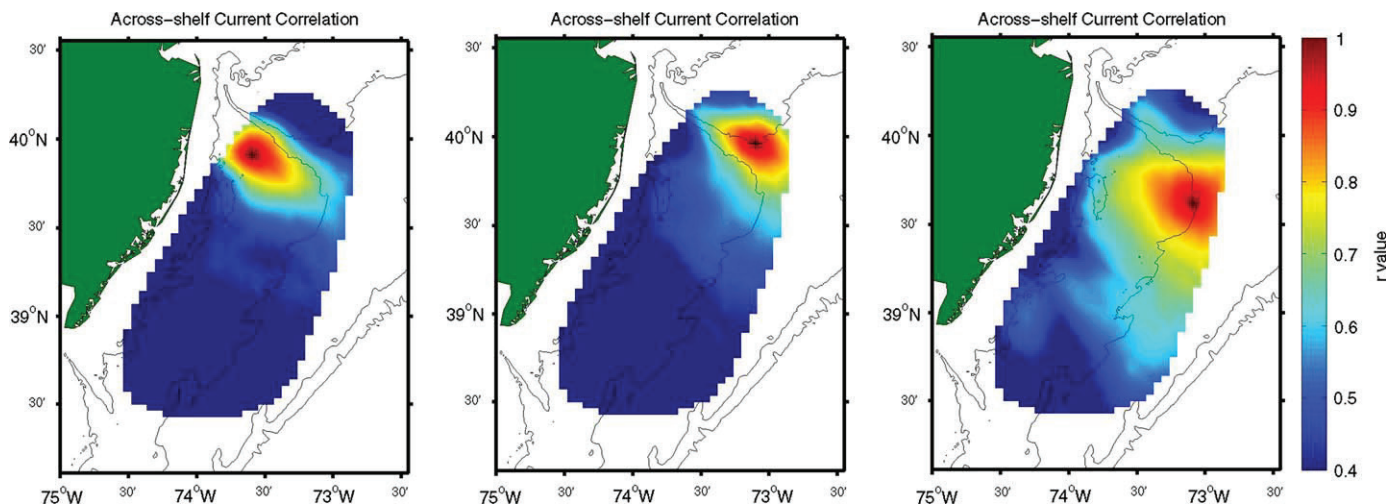


Fig. 13. Same as Fig. 11, except the across-shelf velocity correlation maps are shown.



## 5. Discussion

### 5.1. Mean and seasonal considerations

The various analyses over the HF radar footprint showed the importance of the across-shelf velocity in the surface layer. In terms of components, along- and across-shelf components of the time-averaged spatial mean are  $-4$  and  $-3$  cm/s, respectively, similar to long-term means previously published for the MAB (Lentz, 2008). The strong offshore component in the mean surface flow is consistent with Lentz (2008) and Csanady (1976) idealized 2-D model for mean shelf circulation. However, the spatial plot of the time-averaged velocities showed that the velocity vectors in the study region varied in magnitude and direction with the southern region of the Hudson Shelf Valley, the LEO-15 study area, and the southwest corner displaying stronger offshore flow than along-shelf flow. These features would be difficult to capture in a model that assumes along-shelf invariance. Furthermore, the std. and principle components (not shown for the total period) of the HF radar demonstrated that there were large variation around this mean flow pattern and that the across-shelf contribution was not insignificant in the surface layer. A comparison of the magnitude of the major and minor axis showed that the minor axis (across-shelf) ranged from 0.3 to 0.9 of major axis (along-shelf) depending on season and location.

Dividing the data set into mixed and stratified periods revealed notable differences. The mixed period time-averaged mean currents tended to be similar to the total period in both the magnitude and principle axes, with the vectors tending to have a stronger across-shelf component. The stratified period had weaker time-averaged mean currents, generally in the along-shelf direction with the Hudson Shelf Valley flow being more distinct. This seasonal difference in current magnitude is likely due to differences in wind stress with mean wind during the winter (0.05 Pa) significantly stronger than observed in the summer (0.01 Pa), Table 1. In addition, moving northeastward over the study area, the principle axes of the velocity grid points showed a distinct modulation, becoming less rectilinear and rotating axis orientation.

The observed variability of the principal components within and between different periods is unexpected; however, there is some limited historical evidence that agrees with the HF radar observations. Using several days to many months of surface current meter data from five mooring sites on the shelf to the south of the Hudson Shelf Valley, primarily during the fall and winter months, Mayer (1982b) observed principal component magnitudes of 13–24 cm/s (7–9 cm/s) in the major (minor) axis and variability in the orientation ranging from  $32^\circ$  to  $51^\circ$  counter clockwise from east. This is similar to the variability observed in the mixed period principal axes (Fig. 5b). These results are similar to what would be expected of depth-averaged current (i.e., along-shelf dominated with orientation following local isobaths), and Mayer (1982b) speculated that observed variability was associated with surface wind effects. Wind forcing was also seen to significantly influence the spatial flow patterns across the bight over multi-year climatologies (Gong et al., 2009).

The stratified period has more significant changes throughout the HF radar footprint. Münchow and Chant (2000) showed that surface current data during the stratified period from several moorings along the 20 m isobath in the LEO-15 study region had orientation angles of  $20$ – $30^\circ$ , which agrees well with the HF radar data in that region. In addition, it is speculated that the transition of the principal axes going northward across the HF radar footprint could be related to buoyant outflow from the Hudson River as recent studies have shown the presence of its discharge over a significant portion of the shelf at times (Chant et al., 2008a,

b; Castelao et al., 2008). This in conjunction with seasonal upwelling winds (Southwest winds), which Dzwonkowski et al. (2009) showed are significantly correlated to across-shelf HF radar currents and sea-level fluctuations during the stratified period ( $r = 0.81$  and  $0.85$ , respectively), could lead to the preferential change in the axis ratio (becomes more circular) and the rotation of the orientation as the across-shelf component becomes stronger relative to the along-shelf component. In addition, buoyancy outflow during the summer months may enhance stratification in the north/northwest region, which is known to play a critical role in the surface currents response to forcing mechanisms. In particular, seasonal differences in the surface current response to wind forcing on the inner shelf and shelf has been presented by Kohut et al. (2004) and Dzwonkowski et al. (2009), respectively. Several studies (Münchow and Chant, 2000; Sanders and Garvine, 2001; Garvine, 2004) in the LEO-15 region during the stratified summer season suggest/found that interior currents were in wind thermal wind balance over the shallow inner shelf (10–20 m) which suggests that stratification limits the effects of bottom friction in the water column during this time period. Along similar lines, Lentz (2001), and several others (Kirincich et al., 2005; Gutierrez et al., 2006) have stated that stratification and its relationship to eddy viscosity explain the differences observed in coastal circulation during different water column states. Thus, the observed seasonal differences in the surface current principal axes are reasonable.

Observations in the area of the Hudson Shelf Valley are particularly interesting as they add a new level of detail to the relatively complex flow region. As pointed out by Lentz (2008), there have been several previous studies examining currents in the Hudson Shelf Valley (Nelsen et al., 1978; Mayer, 1982a; Manning et al., 1994; Harris et al., 2003). However, the bulk of these studies examine bottom and/or depth-averaged currents with only very limited measurements of the surface currents. While most of these studies show mean flow (bottom and/or depth-averaged) going up-valley, the surface flow in the area around the Hudson Shelf Valley was observed to be complex, with Mayer (1982a) noting that surface velocities between two moorings, one in and the other adjacent to the Hudson Shelf Valley, could vary in direction by nearly  $180^\circ$  on time scales of 30 days. Since the bottom and depth-average mean current is in the up-valley direction, it should not be unexpected that there is mean surface flow down-valley in its vicinity. That being said, several recent studies (Chant et al., 2008a, b; Castelao, 2008), and several more in preparation, which have examined estuary outflow and consequently surface flow in much more detail around the mouth of the Hudson estuary and along the Hudson Shelf Valley region. These studies provide support for the strong down-valley mean flow observed on the southern edge of the Hudson Valley Shelf, which is related to buoyancy discharge.

While the total period and seasonally averaged velocities are important for understanding the general circulation, they understate the episodic nature of the surface shelf flow. This is well illustrated in the velocity plots for Sites 4 and 6. Of particular interest is the across-shelf component of Sites 4 and 6, which showed strong and frequent across-shelf flow events,  $O(30$  cm/s). These strong, episodic across-shelf flows have the potential to transport nutrients, fresh water, and plankton significant distances offshore. Even more interesting was the increase in the along-shelf current with decreasing distance toward the coast in conjunction with a highly correlated decrease in across-shelf velocity. This relationship in the surface currents at these two sites suggest that across-shelf divergence could result in along-shelf acceleration near-shore in the area around the Endurance line. This could suggest that across-shelf convergences and

divergences in this region may not always result in conventional upwelling or downwelling.

While small scale convergences and divergences have been observed on the inner shelf of the LEO-15 region (Tilburg and Garvine, 2003; Yankovsky et al., 2000), the occurrences noted in the HF radar data appear to have a larger scale. Examining a snapshot of the low pass HF radar velocities during one of the onshore events provides additional information about the spatial extent and variability in the flow field (Fig. 14). The snapshot is preceded by a relative strong northeast wind at both NOAA National Data Buoy Center (NDBC) buoys, however the current response is quite variable with minimum (maximum) velocities in the northern (central and southern) section of the HF radar footprint and some patchiness in terms of magnitude variability. As noted in the site data, the region around the Endurance line experiences strong onshore flow in the outer region of the shelf with increasing along-shelf current closer to the coast. The region over the Hudson Shelf Valley is largely in the down-shelf direction. To the first order, the flow in the central and southern regions appears consistent with the surface Ekman response to downwelling favorable wind stress with the mid/outer shelf surface current being approximately  $45^\circ$  to the right of the wind. The onshore flow converges at the coast causing an amplification of the along-shelf current. The wind forced component of these flows seen over multi-year time scales is further discussed by Gong et al. (2009). In addition to the convergence observed in the individual sites, the lagged along-shelf velocity component correlations between sites revealed that the highest  $r$ -values occurred when the inner shelf led the outer shelf by approximately 3 h. These results agreed with previous observations that along-shelf surface current fluctuations do not vary significantly in the across-shelf direction and that shallow water responds faster to the forcing mechanisms in this region (approximately 6 h response difference) (Chuang et al., 1979; Beardsley and Haidvogel, 1981). However, the same effect was not present in the across-shelf velocity component, where lagged time series did not improve the correlations along the Endurance line.

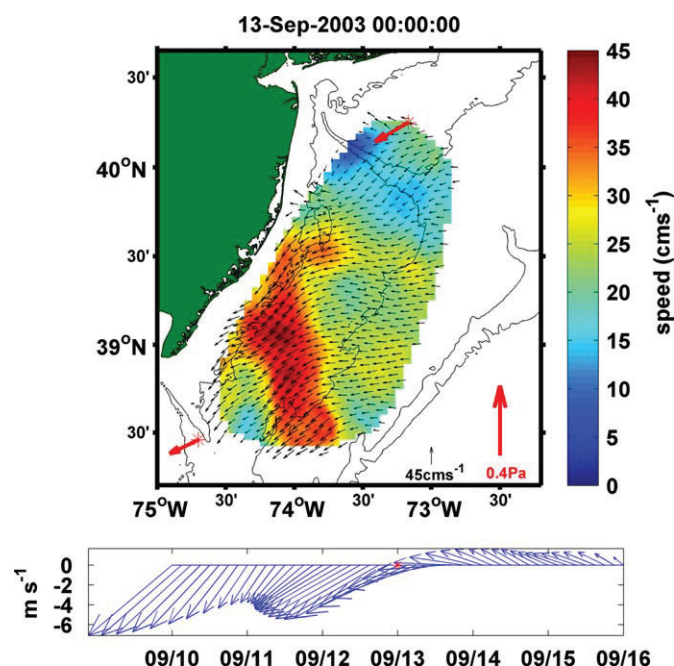


Fig. 14. Surface velocities from low-passed HF radar data for September 13 2003 00:00 UTC. Color contours of current speed (cm/s) and wind stress (red vector) are also shown. Wind vector time series for the six day interval centered on the time of the surface current map are also shown at bottom of the plot.

## 5.2. Characteristic of correlation scales

The temporal decorrelation scales exhibited some expected patterns over the study area. Along the Endurance line and over the shelf in general, the along-shelf decorrelation timescales increased with distance offshore, ranging from 20 to 32 h. The increased temporal decorrelation scales agreed with the notion that deep water has longer timescales. In addition, the results were similar to that of Münchow and Chant (2000) who obtained values in the surface layer of the inner shelf (20 m isobath) of the LEO-15 study area during the NJUP field experiments.

Much of the previous observational work explicitly stating the spatial scales of along- and across-shelf flow have been conducted on the west coast of the US, which has distinctly different shelf morphology than the MAB (Kundu and Allen, 1976; Winant et al., 1987; Dever 1997). As such, some differences were expected. In addition, the values used to determine spatial scales in the various studies differ to some degree, thus, the comparison between studies is qualitative. That being said, some of spatial correlations of the across-shelf currents from this study were larger than expected. Along the Endurance line and over the shelf in general, along-shelf correlation of along-shelf current were the largest,  $O(100 \text{ km})$ , which is in line with theory (100–200 km; Brink et al., 1987, 1994) and observations ( $>60 \text{ km}$ ; Dever, 1997). There was some variability in the structure and magnitude in the Hudson Shelf Valley region as mentioned above. However, across-shelf correlation scales of the along-shelf velocity remained highly correlated for lengths of approximately 20–40 km, larger than those observed on the US west coast (10–15 km, Dever 1997). In regards to the across-shelf component, these scales showed much more site to site variability with spatial scales that were again typically larger than values on the west coast. The observed across-shelf current scales in northern California of 15–20 km (10 km) in the along-shelf (across-shelf) direction (Dever, 1997) were small compared to this studies scales of 15–50 km depending on location and when only considering the region of high correlation. Another novel observation of this study was the rapid increase in the across-shelf velocity spatial correlation over the shelf with the region of high correlation in Fig. 11 nearly tripling in width from Site 4 (25 m isobath) to Site 6 (50 m isobath).

With the exception of the along-shelf velocity along the Endurance line, the position of the various sites appeared to have a significant impact on the spatial correlations. More data is needed to link specific forcing to the detailed variability revealed in the HF radar data including, mass field measurements, high resolution sea-level and wind field data. As mentioned in Section 4.3, it was speculated that the complex bathymetry had an effect on the spatial correlations, however other processes, such as shelf break variability and buoyancy outflow, may also play a role of the positional differences in the spatial correlations. It is likely that the reduced spatial correlations at Site 7 (not shown) on the outer edge of the HF radar footprint was affected by shelf break processes. This is a plausible assumption as a recent paper by Flagg et al. (2006) showed that the along-shelf jet associated with the shelf break can impinge on the outer edges of the shelf. In fact, the reduction in correlation at the outer edges of the shelf was similarly observed off northern California, in which the reduced correlation lengths at the outmost site (130 m) compare to inner sites (60 and 90 m) were attributed to offshore mesoscale activity (Dever, 1997). In addition, the short spatial scales associated with Site 1 were possibly due to localized buoyancy outflow as this region has recently been identified as a transport pathway for the Hudson River outflow (Chant et al., 2008a, b).

Furthermore, this work suggests that the Hudson Shelf Valley represents a transition region over which the orientation of along-

and across-shelf components begin to respond to the changes in coastline orientation. The analysis of the temporal decorrelation scales showed that north of the Hudson Shelf Valley the ‘across-shelf’ component becomes the ‘along-shelf’ component as the across-shelf component has similar time scales as the along-shelf component in the southern region of the HF radar footprint. Additional evidence of this was seen in the principle axes analysis in which the orientation shifted from 40–60° to –10° to 20° and in spatial vector correlation phase plots which showed a similar rotational relationship (not shown). However, the ratio of major to minor axes in the principle components were close to one in this region indicating that a well defined along-shelf/across-shelf orientation is not present.

### 5.3. Forcing mechanisms

The ability of this data to determine dynamical forcing mechanisms is limited by the lack of mass field measurements and high resolution sea-level and wind field data. However, as suggested above, there are a number of likely candidate mechanisms which can be discussed. When compared to depth-averaged currents, the shallow nature of the current measurements and the spatial and temporal variability observed suggest that the measurements are sensitive to temporal and small scale spatial variability in typical forcing mechanisms. It should also be expected that these surface current measurements will be more sensitive to surface forcing such as wind stress and buoyancy discharge.

While the long-term currents are not forced by climatological winds, the low-frequency variability in the time-averaged spatial mean of the HF radar current has been shown to be highly correlated with regional wind stress ( $r = 0.65–0.85$ ) (Dzwonkowski et al. 2009). Furthermore, as suggested by Dever (1997), the relative large correlations in the across-shelf component suggest that the surface currents are correlated with the large-scale wind. However, in terms of smaller-scale variability, one study on the West coast of the US found that using a high resolution atmospheric model (9 km grid) revealed 10–50 km bands of strong wind stress and wind stress curl adjacent to coastal promontories, which had major impacts on the cause of offshore transport along the California coast (Pickett and Paudan, 2003). Given the relative sparse coverage of meteorological measurement stations in or around the HF radar footprint, this is an interest topic for future research that could be investigated with scatterometer data or a high resolution atmospheric model.

As stated and cited above, buoyancy forcing can also play a dynamical role over a significant portion of the shelf in this region by increasing stratification over the shelf (Castelao et al., 2008). But, it can also have significant localized impacts such as those found by Chant et al. (2008a, b) in the Hudson Shelf Valley region and by several studies in the LEO-15 region (Münchow, 1992; Yankowsky and Garvine, 1998; Tilburg and Garvine, 2003). Both of these regions have notable current patterns in the time-averaged mean figures (Figs. 3a and 4).

In addition, bathymetry also appears to contribute to localize flow variability in the flow field, with many notable studies in this region suggesting such. Song et al. (2001) showed that localized upwelling regions off the New Jersey coast could be explained using idealized bathymetry in a numerical model. Kohut et al. (2004) showed that standard range HF radar surface currents were impacted by subtle changes in bathymetry in the LEO-15 region study. In addition, several studies mentioned above indicate that the Hudson Shelf Valley also has a major impact on the shelf currents.

## 6. Conclusions

The overall time-averaged spatial mean is similar to previous mooring-based studies in this area, but there is significant change in the time-averaged means over the footprint of the HF radar data. In particular, there were three notable regions (the southern edge of the Hudson Shelf Valley, the LEO-15 region, and the southwest corner) that favored offshore movement of surface water, which were apparent to varying degrees in the total, mixed, and stratified periods. In addition, there were seasonal differences in the variability of the HF radar data where the principle axes rotated orientation and became more elliptical over the HF radar footprint during the stratified period. Temporal scales in the surface layer for the along (across)-shelf current ranged from 20–32 (18–28)h and appeared to be consistent with previous point measurements near the study region. The spatial scales of the along-shelf velocity were generally well correlated over the study region, consistent with studies that suggest large along-shelf spatial scales. While spatial scales of across-shelf velocity varied with location, but generally increased offshore until the outer shelf. In particular, there was a near tripling of the along-shelf width of high correlation region of across-shelf velocity moving from the 25 to 50 m isobath along the Endurance line. However, regional geography appeared to reduce the spatial correlations as seen around the Hudson Shelf Valley region, which limited the spatial scales of surface velocity. These observations, in addition to the principle component analysis suggested that the Hudson Shelf Valley region appeared to be a transition region over which the orientation of along- and across-shelf components began to respond to the changes in coastline orientation.

On the whole, three potential forcing mechanisms are speculated to be responsible for the observed small scale variability observed: buoyancy discharge; topography irregularities, both in bathymetry and in coastline orientation; and spatial wind stress variability. Adding to the challenge of dynamically analyzing high-resolution surface currents is the fact that these forcing mechanisms may not operate independently which presents the possibility of non-linear interactions. While there have been numerous studies on various continental shelves analyzing these more subtle aspects of shelf forcing, open questions remain and represent a key avenue of future research as high resolution forcing data becomes more readily available. Furthermore, these forcing mechanisms are not unique to this area which suggest that the small scale features and variability observed in this region are likely common in other shelf regions.

Consequently, this study identifies significant seasonal and regional differences observed across the shelf by the time series of well resolved spatially mapped data. From the surface velocity data, several regions in the study showed characteristics consistent with the previous observations, however the level of detail provided by the HF radar data showed areas and time periods of exception. This study serves as a baseline of information for surface currents in terms of mean flow, limited seasonal variability, and temporal and spatial decorrelation scales, for which there is only limited historical data for the surface layer of this duration and spatial coverage. As such, little has been presented in terms of the spatial correlation of the across-shelf component over such an extended portion of the shelf, so the across-shelf spatial scales represent a contribution to the general oceanographic properties on continental shelves. In addition, while these spatial correlations apply to the near-surface, this work may have bearing on other levels of the water column as a study by Dever (1997) off the coast of California suggested that the correlation scales of near-surface across-shelf velocity may be applicable to interior and bottom across-shelf velocity. Finally, the regions of anomalous offshore surface flow identified in this study



have the potential of being areas of net offshore transport. These regions could play an important role in exporting material and fresh water across the continental shelf, however, as this study only had surface layer data, further investigation of these regions is needed.

## Acknowledgments

This work would not have been possible without collecting, processing, and archiving the HF radar velocity maps by Coastal Ocean Observation Lab at Rutgers University, including Hugh Roarty and Scott Glenn. We also need to thank Bruce Lipphardt, Rich W. Garvine, Kuo Wong, and John T. Reager for advice and technical assistance. In addition, the two anonymous reviewers should be thanked for their valuable comments and suggestions, which have greatly improved this manuscript. This work was supported by the National Atmospheric and Oceanographic Administration through Grant #NA17EC2449 and NASA-Space Grant #NNG05G092H.

## References

- Beardsley, R.C., Boicourt, W.C., Hansen, D.V., 1976. Physical oceanography of the Middle Atlantic Bight. In: Gross, M.G. (Ed.), *Middle Atlantic Continental Shelf and the New York Bight*. American Society of Limnology and Oceanography, Special Symposium, vol. 2. pp. 20–34.
- Beardsley, R.C., Boicourt, W.C., 1981. On estuarine and continental-shelf circulation in the Middle Atlantic Bight. In: Warren, B.A., Wunsch, C. (Eds.), *Evolution of Physical Oceanography, Scientific Surveys in Honor of Henry Stommel*. MIT Press, pp. 198–233.
- Beardsley, R.C., Haidvogel, D.B., 1981. Model studies of the wind-driven transient circulation in the Middle Atlantic Bight. Part 1: Adiabatic boundary conditions. *Journal of Physical Oceanography* 11, 355–375.
- Bigelow, H.B., 1933. Studies of the waters on the continental shelf, Cod to Chesapeake Bay. I. the cycle of temperature. *Papers on Physical Oceanography and Meteorology* 2, 135.
- Bigelow, H.B., Sears, M., 1935. Studies of the waters on the continental shelf, Cod to Chesapeake Bay. II. Salinity. *Papers on Physical Oceanography and Meteorology* 4, 94.
- Brink, K.H., Chapman, D.C., Halliwell, G.R., 1987. A stochastic model for wind-driven currents over the continental shelf. *Journal of Geophysical Research* 92, 1783–1797.
- Brink, K.H., LaCasce, J.J., Irish, J.D., 1994. The effect of short-scale wind variations on shelf currents. *Journal of Geophysical Research* 99, 3305–3314.
- Bumpus, D.F., 1973. A description of the circulation on the continental shelf of the east coast of the United States. In: Warren, B.A. (Ed.), *Progress in Oceanography*. Pergamon Press, pp. 111–157.
- Castelao, R., Glenn, S., Schofield, O., Chant, R., Wilkin, J., Kohut, J., 2008. Seasonal evolution of hydrographic fields in the Middle Atlantic Bight from glider observations. *Geophysical Research Letters*. doi:10.1029/2007GL032335.
- Chant, R.J., Glenn, S.M., Kohut, J.T., 2004. Flow reversals during upwelling conditions on the New Jersey inner shelf. *Journal of Geophysical Research* 109, C12S03, doi:10.1029/2003JC001941.
- Chant, R.J., Glenn, S.M., Hunter, E., Kohut, J., Chen, R.F., Houghton, R.W., Bosch, J., Schofield, O., 2008a. Bulge formation of a buoyant river outflow. *Journal of Geophysical Research* 113101029/2007JC004100.
- Chant, R.J., Wilkin, J.J., Weifeng, Z., Choi, B., Hunter, E., Castelao, R., Glenn, S., Jurisa, J., Schofield, O., Houghton, R., Kohut, J., Frazer, T.K., Moline, M.A., 2008b. Dispersal of the Hudson River Plume on the New York Bight. *Oceanography* 21 (4), 149–162.
- Chuang, W.-S., Wang, D.-P., Boicourt, W.C., 1979. Low-frequency current variabilities on the southern Mid-Atlantic Bight. *Journal of Physical Oceanography* 9, 1144–1154.
- Csanady, G.T., 1976. Mean circulation in shallow seas. *Journal of Geophysical Research* 81, 5389–5399.
- Dever, E.P., 1997. Subtidal velocity correlation scales on the northern California shelf. *Journal of Geophysical Research* 102, 8555–8571.
- Dever, E.P., Dorman, C.E., Largier, J.L., 2006. Surface boundary-layer variability off Northern California, USA, during upwelling. *Deep-Sea Research* 53, 2887–2905.
- Dzwonkowski B., Kohut, J.T., Yan, X.H., 2009. Seasonal differences in wind-driven across-shelf forcing and response relationships in the shelf surface layer of the central Mid-Atlantic Bight. *Journal of Geophysical Research*, accepted.
- Flagg, C.N., Dunn, M., Wang, D.P., Rossby, H.T., Benway, R.L., 2006. A study of the currents of the outer shelf and upper slope from a decade of shipboard ADCP observations in the Middle Atlantic Bight. *Journal of Geophysical Research* 111101029/2005JC003116.
- Garvine, R.W., 2004. The vertical structure and subtidal dynamics of the inner shelf off New Jersey. *Journal of Marine Research* 62, 337–371.
- Gong, G., Kohut, J.T., Glenn, S.M., 2009. Seasonal climatology of wind-driven circulation on the New Jersey Shelf. *Journal of Geophysical Research*, submitted.
- Gutierrez, B.T., Voulgaris, G., Work, P.A., 2006. Cross-shore variation of wind-driven flows on the inner shelf in Long Bay, South Carolina, United States. *Journal of Geophysical Research* 111, C03015, doi:10.1029/2005JC003121.
- Harris, C.K., Butman, B., Traykovski, P., 2003. Winter-time circulation and sediment transport in the Hudson Shelf Valley. *Continental Shelf Research* 23, 801–820.
- Kirincich, A.R., Barth, J.A., Grantham, B.A., Menge, B.A., Lubchenco, J., 2005. Wind-driven inner-shelf circulation off central Oregon during summer. *Journal of Geophysical Research* 110, C10S03, doi:10.1029/2004JC002611.
- Kohut, J.T., Glenn, S.M., Chant, R.J., 2004. Seasonal current variability on the New Jersey inner shelf. *Journal of Geophysical Research* 109, C07S07, doi:10.1029/2003JC001963.
- Kohut, J.T., Roarty, H.J., Glenn, S.M., 2006. Characterizing observed environmental variability with HF doppler radar surface current mappers and acoustic doppler current profilers: environmental variability in the Coastal Ocean. *IEEE Journal of Oceanic Engineering* 31 (4), 876–884.
- Kundu, P.K., Allen, J.S., 1976. Some three-dimensional characteristics of low-frequency current fluctuations near the Oregon coast. *Journal of Physical Oceanography* 6, 181–199.
- Large, W.G., Pond, S., 1981. Open ocean momentum flux measurements in moderate to strong winds. *Journal of Physical Oceanography* 11, 324–336.
- Lentz, S.J., 2001. The influence of stratification on the wind-driven cross-shelf circulation over the North Carolina shelf. *Journal of Physical Oceanography* 31, 2749–2760.
- Lentz, S.J., 2008. Observations and a mode 1 of the mean circulation over the Middle Atlantic Bight Continental Shelf. *Journal of Physical Oceanography* 38101175/2007JP03768.1.
- Manning, J.P., Oey, L.Y., Packer, D., Vitaliano, J., Finneran, T.W., You, K.W., Fromm, S., 1994. Observations of bottom currents and estimates of resuspended sediment transport at the New York 12-mile dumpsite. *Journal of Geophysical Research* 99, 10221–10239.
- Mayer, D.A., 1982a. Circulation in the Hudson Shelf Valley: MESA physical oceanographic studies in New York Bight, 1. *Journal of Geophysical Research* 87, 9563–9578.
- Mayer, D.A., 1982b. The structure of circulation: MESA physical oceanographic studies in New York Bight, 2. *Journal of Geophysical Research* 87, 9579–9588.
- Münchow, A., 1992. The formation of a buoyancy driven coastal current. Ph.D dissertation, University of Delaware, Newark, DE, 205.
- Münchow, A., Chant, R.J., 2000. Kinematics of inner shelf motions during the summer stratified season off New Jersey. *Journal of Physical Oceanography* 30, 247–268.
- Nelsen, T.A., Gadd, P.E., Clarke, T.L., 1978. Wind-induced current flow in the upper Hudson Shelf Valley. *Journal of Geophysical Research* 83, 6073–6081.
- O'Donnell, J., Ullman, D., Spaulding, M., Howlett, E., Fake, T., Hall, P., Isaji, T., Edwards, C., Anderson, E., McClay, T., Kohut, J., Allen, A., Lester, S., Turner, C., Lewandowski, M., 2005. Intergration of Coastal Ocean Dynamics Application Radar (CODAR) and Short-Term Predictive System (STPS) Surface Currents into the Search and Rescue Optimal Planning System (SAROPS). CG-D-01-2006.
- Pettigrew, N.R., 1981. The dynamics and kinematics of the coastal boundary layer off Long Island. Ph.D Thesis, Massachusetts Institute of Technology/Woods Hole Oceanographic Institute, Woods Hole, MA.
- Pickett, M.H., Paduan, J.D., 2003. Ekman transport and pumping in the California current base on the US Navy's high-resolution atmospheric model (COAMPS). *Journal of Geophysical Research* 108 (C10), 3327, doi:10.1029/2003JC0019092.
- Rasmussen, L.L., Gawarkiewicz, G., Owens, W.B., Lozier, M.S., 2005. Slope water, Gulf Stream, and seasonal influences on the southern Mid-Atlantic Bight circulation during the fall-winter transition. *Journal of Geophysical Research* 110101029/2004JC002311.
- Sanders, T.M., Garvine, R.W., 2001. Fresh water delivery to the continental shelf and subsequent mixing: an observational study. *Journal of Geophysical Research* 106 (C11), 27087–27102.
- Shearman, R.K., Lentz, S.J., 2003. Dynamics of mean and subtidal flow on the New England shelf. *Journal of Geophysical Research* 108, 3281, doi:10.1029/2002JC001.
- Song, Y.T., Haidvogel, D.B., Glenn, S.M., 2001. Effects of topographic variability on the formation of upwelling centers off New Jersey: a theoretical model. *Journal of Geophysical Research* 106, 9223–9240.
- Stewart, R.H., Joy, J.W., 1974. HF radio measurements of surface currents. *Deep-Sea Research* 21, 1039–1049.
- Tilburg, C.E., Garvine, R.W., 2003. Three-dimensional flow in a shallow coastal upwelling zone: alongshore convergence and divergence on the New Jersey shelf. *Journal of Physical Oceanography* 33, 2113–2125.
- Ullman, D.S., O'Donnell, J., Kohut, J., Fake, T., Allen, A., 2006. Trajectory prediction using HF radar surface currents: Monte Carlo simulations of prediction uncertainties. *Journal of Geophysical Research* 111, C12005, doi:10.1029/2006JC003715.
- Winant, C.D., Beardsley, R.C., Davis, R.E., 1987. Moored wind, temperature, and current observations made during Coastal Ocean dynamics experiments 1 and 2 over the northern California shelf and upper slope. *Journal of Geophysical Research* 92, 1569–1604.
- Yankovsky, A.E., Garvine, R.W., 1998. Subinertial dynamics on the inner New Jersey shelf during the upwelling season. *Journal of Physical Oceanography* 28, 2444–2458.
- Yankovsky, A.E., Garvine, R.W., Münchow, A., 2000. Mesoscale currents on the inner New Jersey shelf driven by the interaction of buoyancy and wind forcing. *Journal of Physical Oceanography* 30, 2214–2230.

## Seasonal climatology of wind-driven circulation on the New Jersey Shelf

D. Gong,<sup>1</sup> J. T. Kohut,<sup>1</sup> and S. M. Glenn<sup>1</sup>

Received 15 May 2009; revised 24 September 2009; accepted 2 October 2009; published 3 April 2010.

[1] The spatial structure of the mean and seasonal surface circulation in the central region of the Mid-Atlantic Bight (New Jersey Shelf) are characterized using 6 years of CODAR long-range HF radar data (2002–2007). The mean surface flow over the New Jersey Shelf is 2–12 cm/s down shelf and offshore to the south. The detided root-mean-square (RMS) velocity variability ranges from 11 to 20 cm/s. The variability is on the order of the mean current offshore and several times that of the mean current nearshore. The Hudson Shelf Valley and the shelf break act as dynamical boundaries that define the New Jersey Shelf. The surface flow on the New Jersey Shelf depends on topography, seasonal stratification, and wind forcing. The flow is in the approximate direction of the wind during the unstratified season and more to the right of the wind during the stratified season. During the stratified summer season, the dominant along-shore upwelling favorable winds from the SW drive cross-shelf offshore flow. During the unstratified/well-mixed winter season, the dominant cross-shore NW winds drive cross-shelf offshore flows. During the transition seasons of spring and autumn, along-shore NE winds, often associated with storm events, drive energetic down-shelf, along-shelf flows. The surface transport pathways are either cross-shelf dominated during summer and winter or along-shelf dominated during the transition seasons. The residence time of surface Lagrangian drifters on the New Jersey Shelf ranged from 1 to 7 weeks with summer and autumn showing faster transport than winter and spring.

**Citation:** Gong, D., J. T. Kohut, and S. M. Glenn (2010), Seasonal climatology of wind-driven circulation on the New Jersey Shelf, *J. Geophys. Res.*, 115, C04006, doi:10.1029/2009JC005520.

### 1. Introduction

[2] The Middle Atlantic Bight (MAB), a shallow and wide continental shelf located off the east coast of the United States, is bounded by Cape Cod to the northeast and Cape Hatteras to the southwest (Figure 1). It is a highly productive shelf that exhibits strong seasonal cycles in both physical and biological processes [Bigelow, 1933; Bigelow and Sears, 1935; Beardsley and Boicourt, 1981; Yoder *et al.*, 2002]. Several major urban estuaries such as the Connecticut River, the Hudson River, the Delaware River and the Susquahana River discharge into the bays and sounds connected to the MAB, delivering fresh and nutrient rich water onto the shelf. Transport of nutrients and organic material can determine the timing and distribution of shelf primary production and the subsequent response in the higher trophic levels [Yoder *et al.*, 2002; Schofield *et al.*, 2008]. An important objective of recent research projects is to characterize and quantify the cross-shelf exchange mechanisms and transport pathways on the

MAB [Biscaye *et al.*, 1994; Castelao *et al.*, 2008a; Chant *et al.*, 2008; Zhang *et al.*, 2009]. This transport is critical to the understanding of shelf marine ecosystem dynamics. The dynamics of shelf circulation are governed by the combined interactive forcing of many factors such as stratification [Lentz, 2001; Flagg *et al.*, 2002; Castelao *et al.*, 2008b], winds [Allen, 1980; Beardsley *et al.*, 1985; Lentz, 2001; Whitney and Garvine, 2005], storms [Keen and Glenn, 1995; Kohut *et al.*, 2006a; Glenn *et al.*, 2008], river discharge [Fong and Geyer, 2001; Byoung-Ju and Wilkin, 2007; Chant *et al.*, 2008], topography [Harris *et al.*, 2003; Zhang *et al.*, 2009], bottom boundary layers [Gawarkiewicz and Chapman, 1992; Chapman and Lentz, 1994; Keen and Glenn, 1994; Garvine, 2004], upstream forcing [Mountain, 2003], and offshore forcing [Gawarkiewicz *et al.*, 1996; Linder and Gawarkiewicz, 1998; Churchill *et al.*, 2003; Lentz, 2003]. The seasonal variability of the dominant processes impacts the coupled seasonal biological response. The set of forcing factors driving the dynamics of the midshelf or the outer shelf is often different from that of the inner shelf. Whereas buoyancy forcing and bottom friction play major roles in the inner shelf dynamics, winds and changing stratification are the major drivers of the dynamics at the mid to outer shelf. In this study, a 6 year time series of HF Radar surface current data from Rutgers University Coastal Ocean

<sup>1</sup>Institute of Marine and Coastal Sciences, Rutgers-State University of New Jersey, New Brunswick, New Jersey, USA.

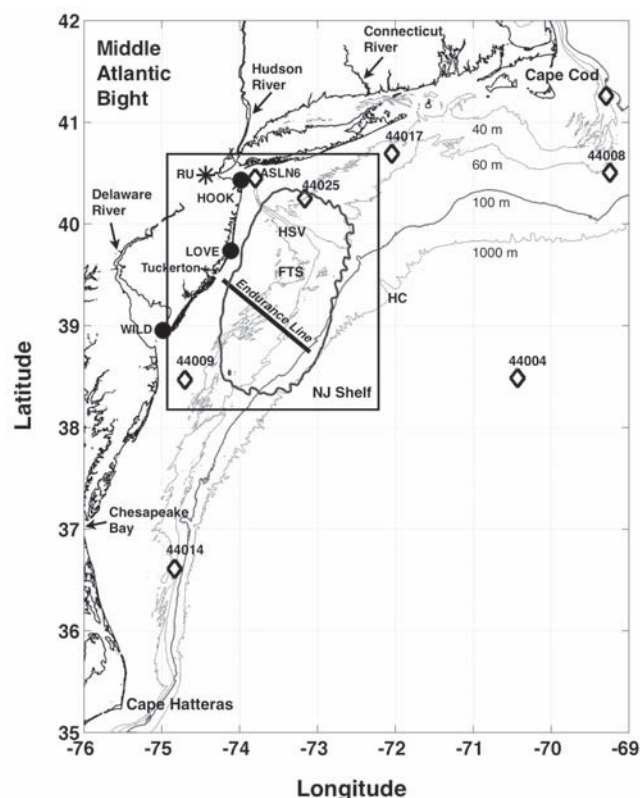


**Figure 1.** Middle Atlantic Bight from Cape Hatteras up to Cape Cod. The 40, 60, 100, and 1000 m isobaths are marked. HSV, Hudson Shelf Valley; HC, Hudson Canyon; FTS, Fortune Tiger Shore; RU, Rutgers University; HOOK, Sandy Hook CODAR site; LOVE, Loveladies CODAR site; WILD, Wildwood CODAR site. The 50% CODAR coverage area for the New Jersey Shelf is outlined. NOAA NDBC buoys are marked as diamonds and are labeled.

Observation Lab [Glenn and Schofield, 2009] is used to characterize the effect of topography, seasonal stratification and wind forcing on the surface subtidal circulation and transport at the mid to outer portion of the New Jersey Shelf. In particular, the surface flows during the transition seasons of spring and autumn are characterized and compared with the stratified summer as well as the unstratified winter. A seasonal climatology of the wind-driven surface current response is constructed and the seasonal transport patterns and residence times are examined.

[3] This paper is structured as follows. In section 2, we review the relevant physical processes affecting circulation and transport on the New Jersey Shelf. In section 3, we describe the 6 year Rutgers HF Radar and National Oceanic and Atmospheric Administration (NOAA) National Data Buoy Center (NDBC) weather buoy data set used in this analysis. In section 4.1, we characterize the mean and the subtidal variability of surface flow. In section 4.2, we characterize the low-wind background flow and effect of topographic features such as the Hudson Shelf Valley (HSV) and the Fortune/Tiger Shore (FTS). In section 4.3, we discuss the effect of seasonal variability in stratification and wind on the mean flow over seasonal time scales. In

section 4.4, we discuss the response of surface flow to seasonal wind forcing. In section 4.5, we present the seasonal climatology of the wind-current correlation. In section 4.7, we calculate the seasonal cross-shelf transport pathways and shelf residence time. Finally in section 4.6, we explore the interannual variability of the current response to changes in seasonal forcing. The results are discussed in section 5 and summarized in section 6.

## 2. Background

### 2.1. Mean Flow and Upstream Sources

[4] Studies using geochemical tracers have shown that the upstream source of MAB shelf water originates from southern Greenland with a volume flux of 4–5 Sverdrups [Chapman and Beardsley, 1989]. Most of this water exits the shelf as it travels down shelf. By the time the coastal current enters the MAB, the mean volume flux drops to approximately 0.4 Sverdrups [Beardsley et al., 1985]. Historically, the depth-averaged mean flow on the MAB is shown to be 3–7 cm/s down shelf toward the southeast based on current meter moorings [Beardsley and Boicourt, 1981]. A recent study using an expanded data set of current meter measurements shows that the mean depth-averaged along-shore flow on the shelf is constant along-isobath and is linearly correlated with the depths of the isobaths, decreasing toward shore [Lentz, 2008a]. This along-shelf flow has been largely attributed to a basin-scale along-shelf pressure gradient [Beardsley and Winant, 1979; Lentz, 2008a]. A climatological study of MAB hydrography found that shelf water volume (characterized by salinity <34) on the New Jersey Shelf varied seasonally with a magnitude on the order of the mean shelf water volume [Mountain, 2003]. Variability about the mean shelf flow is significant on various temporal and spatial scales ranging from tidal to interannual and from internal Rossby radius to shelf-wide length scales [Beardsley et al., 1985; Lentz, 2008b; Dzwonkowski et al., 2009a].

### 2.2. Topography

[5] Topographic variations on the shelf-wide scale can play an important role on along-shelf and cross-shelf transport. The Hudson Shelf Valley (HSV) is the only remaining submarine shelf valley that cuts perpendicularly across the entire width of the MAB shelf. The Fortune/Tiger Shore (FTS) [Knebel and Spiker, 1977; Thiel et al., 2007], an ancient shoreline to the south of the HSV, is outlined by the 40 m isobath (Figure 1). The steep topography between the 40 and 60 m isobaths at the outer shelf edge of this shoreline makes the FTS one of the most prominent features on the shelf besides the HSV. The HSV/FTS system has significant influence on the cross-shelf transport. The HSV acts both as a conduit for cross-shelf flow as well as a dynamical boundary for along-shelf flow. Winds from the NW can drive a strong up valley return flow along the HSV during the winter mixed season [Harris et al., 2003]. Analysis of CODAR surface current and ADCP mooring data deployed in the HSV during the Langrangian Transport and Transformation Experiment (LaTTE) showed a clear two layer exchange flow during the spring time [Chant et al., 2008]. During the Shallow Water 2006 (SW06) experiment [Tang et al., 2009], satellite Sea Surface Temperature (SST), surface drifters and CODAR surface currents showed that a significant quantity of fresh



riverine water was transported rapidly offshore from the inner shelf to the outer shelf along a pathway south of the HSV [Castelao *et al.*, 2008a]. All of this evidence suggests that the flow in the HSV/FTS region can deviate from the long-term mean shelf-wide flow, depending on the wind and stratification regimes.

### 2.3. Wind Forcing

[6] Wind forcing has long been recognized as an important driver of circulation and transport on continental shelves [Allen and Smith, 1981; Winant, 1980]. Studies of the wind-driven response at the inner shelf have shown that the surface flow is highly correlated with the wind during the stratified season, consistent with an Ekman-type response, and less correlated with the wind when the water column is mixed [Kohut *et al.*, 2004; Dzwonkowski *et al.*, 2009a]. Alongshore winds drive significant cross-shelf transport during the stratified seasons on the North Carolina Shelf [Lentz, 2001] while cross-shore wind is found to be the main driver of surface cross-shelf flow on the inner New England Shelf [Fewings *et al.*, 2008]. Idealized modeling exercises have also shown that cross-shore wind is a significant driver of cross-shelf flow in a weakly stratified water column [Tilburg, 2003]. The different depths and external forcing at the inner and outer shelf result in different dynamical balances reflected in the cross-shelf variability of the shelf flow. Prior studies have focused on the circulation and dynamics at the inner shelf and the outer shelf.

### 2.4. Inner Shelf

[7] The inner shelf dynamics are dominated by buoyancy driven river plumes for most of the year while coastal upwelling becomes more important during the summer time [Song *et al.*, 2001]. Coastal river plumes can carry a high concentration of nutrients and pollutants. The response of a buoyancy trapped river plume, such as the Hudson River Plume, to wind forcing, topography and background flow determines both its initial development [Chant *et al.*, 2008] and downstream evolution [Yankovsky and Garvine, 1998; Yankovsky *et al.*, 2000], which can then affect the whole shelf ecosystem [Schofield *et al.*, 2008]. Extensive research efforts have focused on the effect of upwelling and downwelling favorable alongshore winds on coastal plume dynamics and plume transport [Fong and Geyer, 2001; Chant *et al.*, 2008]. A springtime CODAR virtual drifter study during the Lagrangian Transport and Transformation Experiment (LaTTE) 2005 experiment revealed multiple pathways for Hudson River water leaving the inner shelf Bight apex, either along the Long Island coast, the New Jersey coast, or a cross-shelf pathway south of the HSV [Gong *et al.*, 2006; Zhang *et al.*, 2009]. Coastal upwelling driven by winds from the southwest brings nutrient rich water near the surface, driving summer time primary production at the inner shelf [Glenn *et al.*, 2004]. Alongshore downwelling favorable winds, on the other hand, are associated with development of an alongshore coastal plume [Chant *et al.*, 2008]. Wind-driven Ekman transport associated with coastal upwelling has been proposed as a dominant mechanism for cross-shelf transport from the inner shelf to the outer shelf during the stratified season, with much less influence in the mixed season. [Lentz, 2001].

### 2.5. Outer Shelf

[8] At the outer shelf, the dynamics are dominated by the shelf-slope frontal interactions. The interface between the shelf water and the slope water on the MAB is porous and highly dynamic. A shelf break frontal jet exists at the interface throughout the year, although its structure varies seasonally with changing hydrography [Linder and Gawarkiewicz, 1998]. The equatorward along-shelf transport associated with the shelf break jet is on the order of the shelf-wide transport for the MAB, with stronger summer transport than winter transport observed [Linder and Gawarkiewicz, 1998]. Cross-shelf exchange of shelf and slope water at the shelf break is enhanced during the stratified season when the isopycnals are nearly horizontal from the midshelf to the shelf break. Offshore features such as eddies and Warm Core Rings in the slope sea can modify the velocity structure of the shelf break jet [Gawarkiewicz *et al.*, 2001] and enhance the cross-frontal exchange by pulling surface shelf water offshore and/or bring slope water onshore via subsurface intrusions [Flagg *et al.*, 1994; Hare *et al.*, 2002].

[9] Although there have been case studies of cross-shelf transport pathways on shorter time intervals [Castelao *et al.*, 2008a; Dzwonkowski *et al.*, 2009b], the spatial and temporal variability of the shelf flow is not well known on the seasonal to interannual time scales. The midshelf region and the vicinity of a cross-shelf valley such as the HSV are also much less studied. Furthermore, most previous studies of shelf circulation have divided the shelf into a stratified regime and a mixed regime. That approach misses the flow response to winds and changing stratification during the crucial transition seasons. The transition between the stratified and the well-mixed water column is not instantaneous across the entire shelf, but progresses from shallow to deep water over several weeks or months. A complete seasonal climatology of surface circulation for all four seasons over the full shelf is needed to understand the temporal and spatial variability of shelf-scale transports and their impact on the observed variability in the shelf ecosystem (Y. Xu *et al.*, manuscript in preparation, 2009).

## 3. Methods and Data

### 3.1. Surface Current

[10] The New Jersey Shelf has a cross-shelf distance of 90 to 130 km from the inner shelf to the shelf break and an along-shelf distance of approximately 300 km from the tip of Long Island to Delaware Bay (Figure 1). Surface current data were collected on the New Jersey Shelf from the start of 2002 to the end of 2007 using radial data from three 5 MHz long-range CODAR (Codar Ocean Sensors SeaSonde HF Radar system) sites along the New Jersey coast: Sandy Hook (HOOK), Loveladies (LOVE), and Wildwood (WILD) (Figure 1, black dots). HF Radar uses the Doppler Shift of a radio signal backscattered off the ocean surface to measure the component of the flow in the direction of the antenna [Barrick, 1971a, 1971b; Teague, 1971]. These systems have supported various studies on the New Jersey Shelf including nearshore studies using a 25 MHz standard range system consisting of two shore stations with a coverage area of approximately 30 by 40 km and a resolution of 1.5 km [Kohut *et al.*, 2004, 2006a]. Shelf-wide studies have been

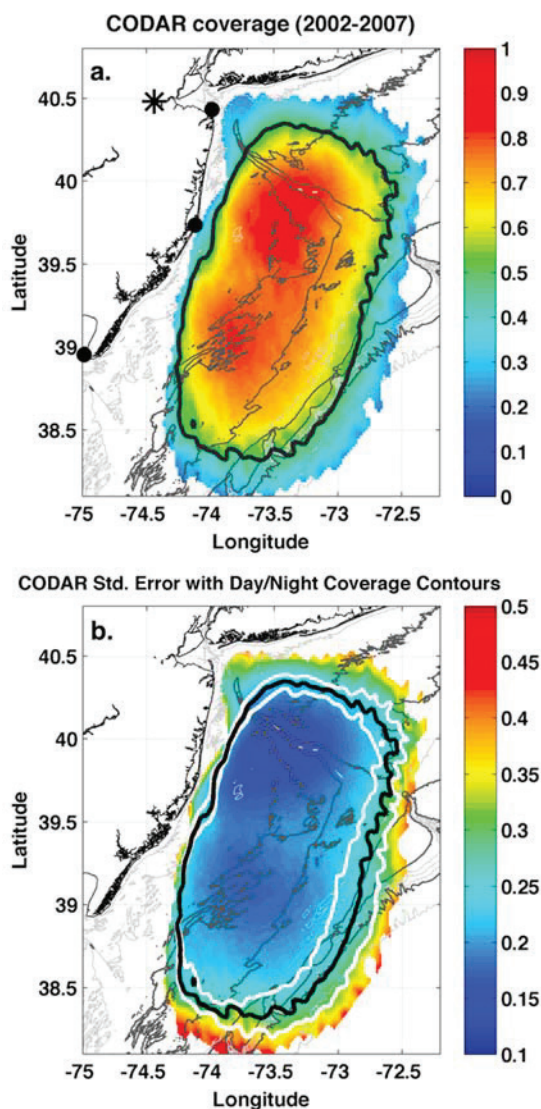


**Figure 2.** (a) Long-range CODAR data coverage for the New Jersey Shelf from 2002 to 2007. The 50% contour is drawn in black. (b) The standard error of the mean current (in cm/s) with day (outer white) and night (inner white) coverage contours.

done using the long-range 5 MHz system consisting of three shore stations with an approximate coverage area of 250 km by 160 km and a resolution of 6 km [Ullman *et al.*, 2006; Hunter *et al.*, 2007; Castelao *et al.*, 2008a; Dzwonkowski *et al.*, 2009a, 2009b].

[11] Hourly radial data from each station are transferred to the Coastal Ocean Observation Lab at Rutgers University, where the radial vector maps (radials) are combined to make 2-D current maps (totals) every 3 hours. Potential ionospheric contamination is eliminated using the manufacturer (CODAR Ocean Sensors) supplied filter applied to each individual Doppler spectra. If ionospheric characteristics are found, data from the entire range cell are removed. Our approach is consistent with the data processing procedures used in previous studies of the New Jersey Shelf [Kohut *et al.*, 2006b; Ullman *et al.*, 2006; Hunter *et al.*, 2007;

Dzwonkowski *et al.*, 2009b]. The resolution of the CODAR radial spectra is dependent on the operating frequency, sweep rate, and FFT length used in processing. Using a standard 1 Hz sweep rate, an operating frequency of 4.55 MHz, and a 1024 point FFT gives a radial velocity resolution of 3.22 cm/s. This operating frequency implies an effective depth of the surface velocity of 2.4 m [Stewart and Joy, 1974]. When radial data from several sites are combined to estimate a total vector, any nonorthogonal angles would introduce some geometric uncertainty. To eliminate less reliable Totals due to poor radial site geometry, we set a threshold for the estimated Geometric Dilution of Precision (GDOP) [Chapman and Graber, 1997]. For this analysis we adopt a community recommended geometric mapping error value of 1.5 or less to identify the vectors with acceptable GDOP [Dzwonkowski *et al.*, 2009a]. This value is chosen based on current comparison studies using CODAR and ADCPs [Kohut *et al.*, 2006a] and CODAR and drifters [Ohlmann *et al.*, 2007]. These studies show that when subgrid-scale spatial variability is accounted for, the adjustable CODAR current resolution is matched to the uncertainty level in the observed currents. The spatial resolution of the final total vector current maps is 6 km with a cross-shelf range of 150 km. The averaged current fields are constructed using the 3 hourly total vector maps. A minimum of 50% temporal coverage over the entire 6 year record is required to be included in the following analysis (Figure 2a).

[12] Diurnal differences in the CODAR coverage area do occur due to the increase in the background noise levels at night. To assess their potential impact, the standard error of the mean flow was calculated for the full field. The 50% coverage line for the larger day time and smaller nighttime fields are added to the standard error plot in Figure 2b. In all cases, the standard error remains in the range of 0.25 to 0.35 cm/s with little difference from the intermediate value chosen for this study. The HF Radar coverage area is also affected by the roughness of the sea state, which has been shown to increase with larger wind waves [Barrick, 1971a]. The theoretical study of Barrick [1971a] showed that the returned signal is enhanced in stronger winds up to 15 knots for HF Radar systems operating below 10 MHz. On average, persistent NW winds during winter are stronger than SW winds during summer [Mooers *et al.*, 1976]. As a result the CODAR coverage area is often increased during the windy winter compared to the calmer summer.

[13] All CODAR surface currents are detided using the T\_TIDE Matlab package [Pawlowicz *et al.*, 2002] before further analysis is performed. Since the outer shelf is least affected by the diurnal variations of sea/land breeze due to its distance from shore [Hunter *et al.*, 2007], and the time scale of our study is from monthly to interannual averaging over many tidal, diurnal and inertial cycles, we believe that the higher-frequency effects of diurnal coverage difference, sea/land breeze, and tidal/inertial influences will not measurably bias the result of our present study.

### 3.2. Winds

[14] Wind data from five NOAA NDBC buoys (ASLN6, 44025, 44009, 44017, 44004) including four on the New Jersey Shelf and one offshore in the slope sea (44004) are used for the wind analysis (Figure 1, open diamonds). Cross correlations of the 5 buoys are performed on low-pass filtered (Hamming filter with a 33 hour window) hourly wind



**Table 1.** NDBC Buoy Wind Cross-Correlation Magnitudes

Wind Cross Correlation	ASLN6	44025	44009	44017	44004
ASLN6	1.00	0.82	0.72	0.84	0.56
44025		1.00	0.80	0.82	0.64
44009			1.00	0.79	0.70
44017				1.00	0.51
44004					1.00

data over the 6 years from 2002 to 2007. The cross-correlation coefficients and the temporal lags of the wind velocity among the five buoys are tabulated in Tables 1 and 2, respectively. Over the length scale of the New Jersey Shelf, winds are highly correlated ( $>0.7$ ) at subtidal time scales among all four sites on the shelf (Table 1). The southern buoys lead the northern buoys and the inshore buoys lead the offshore buoys in time on the order a few hours (Table 2). The observed temporal lag is consistent with the fact that most frontal systems propagate northeastward on the MAB shelf. The velocity correlation of shelf wind buoys with the offshore wind buoy are weaker, but are still greater than 0.5 between all sites. The correlation analysis suggests that under many conditions, the wind field of the Mid-Atlantic Bight region had a correlation scale at least the size of the New Jersey Shelf. For the analysis presented in sections 4.1–4.7, we will be focusing on wind data from NOAA NDBC Buoy 44009 (38.46 N 74.70 W) due to its good temporal coverage and proximity to the center of the study region near the Tuckerton Endurance Line.

## 4. Results

### 4.1. Mean Current and Variability

#### 4.1.1. Mean

[15] The mean surface flow on the New Jersey Shelf over a period of 6 years (2002–2007), as measured by the Rutgers long-range CODAR network, is generally offshore and down shelf with a speed of 3–12 cm/s (Figure 3a). The mean surface flow contained along-shelf and cross-shelf flow structures with velocity ranges from 2 cm/s at the inner shelf, to 6 cm/s at the midshelf, to 12 cm/s at the shelf break. The weakest flow regions, with a speed of 3 cm/s or less, are observed at the inner to midshelf south of the Hudson Shelf Valley (HSV) and in an area north of the HSV. A band of higher-velocity flow 30 to 50 km wide, with an average current speed of 5–7 cm/s, is seen just to the south of the HSV. The fastest surface flow is seen offshore of the 80 meter isobath near the shelf break (8–12 cm/s). Just north of the HSV, the flow is weakly down shelf toward the SW. South of the HSV at the inner shelf, the flow is offshore, directed toward the SE. At the outer shelf, the flow veered clockwise heading down shelf toward the SW. The mean surface flow is largely consistent with the along-isobath, equatorward depth-averaged flow as measured by current meter moorings [Beardsley and Boicourt, 1981; Lentz, 2008a].

[16] The HSV appears to separate the flow regimes geographically and exert topographic control over local circulation. There is a clear difference in the surface current velocities between regions to the north and to the south of the HSV, with enhanced flow velocity observed to the south compared to the north (Figure 3a). A divergence map of the

mean surface flow illustrates that the 6 year mean flow is divergent over the HSV and north near the midshelf and convergent south of the HSV (Figure 3b). The persistent divergence zone suggests an enhanced upwelling of sub-surface material. In regions away from the influence of the HSV, the along-shelf component of the flow velocity increases linearly with the water column depth, a result consistent with a simple 2-D shelf model assuming geostrophic balance plus wind forcing for the along-shelf direction [Csanady, 1976; Lentz, 2008a]. The flow in these regions shows no coherent structure in the divergence, though the amplitude of the divergence fluctuations is of the same order of magnitude as the HSV region.

#### 4.1.2. Variability

[17] Consistent with historical current meter analysis [Beardsley and Boicourt, 1981], the variability in the surface current is significant compared to the mean. The root mean square (RMS) of the detided surface current ranges from 11 cm/s at the upper portion of the HSV to 17 cm/s at midshelf regions to the south of the HSV (Figure 3c). Two regions of high variability are noted, one centered along the 40 m isobath near 39.5 N, 73.5 W just south of the HSV, and the other located further to the south near latitude 38.5 N, with RMS of 17 to 20 cm/s. Near the HSV, on the other hand, the RMS speed has much lower values of 12 to 15 cm/s. The average RMS for the whole field is 15.5 cm/s.

[18] Different forcing mechanisms can affect the spatial variability at different scales. Earlier analyses of the spatial correlation of winds and different seasonal stratification suggest that coherent wind forcing and stratification operate at shelf-wide scales while the shelf topography can vary on scales of a few kilometer to tens of kilometers, a fraction of the shelf size. For temporal variability, we hypothesize that wind forcing is the dominant factor after the tidal contribution has been removed. The RMS current speed for the low-wind conditions from 2002 to 2007 with an average value of 12.2 cm/s (Figure 3d) is significantly lower than the total RMS (Figure 3c). In sections 4.3–4.5 we examine how different wind conditions and changing stratification affect the temporal and spatial variability of the surface circulation in the New Jersey Shelf. The first step is to determine the topographically modulated background flow in the absence of winds so that the effect of large-scale forcing can be separated from that of the winds and stratification.

### 4.2. Background Flow and Topography

[19] The large-scale along-shelf flow over the length of the MAB has long been observed [Bumpus, 1973; Beardsley et al., 1976]. Since the very early studies of the MAB shelf, the along-shelf flow has been hypothesized to be driven by a large-scale along-shelf pressure gradient imposed at the shelf break [Csanady, 1976] setup by the large-scale circulation in

**Table 2.** NDBC Buoy Wind Cross-Correlation Time Lags<sup>a</sup>

Wind t Lag (days)	ASLN6	44025	44009	44017	44004
ASLN6	0	−1	1	−3	−5
44025		0	2	−2	−4
44009			0	−4	−6
44017				0	−2
44004					0

<sup>a</sup>Time lag is given in hours.



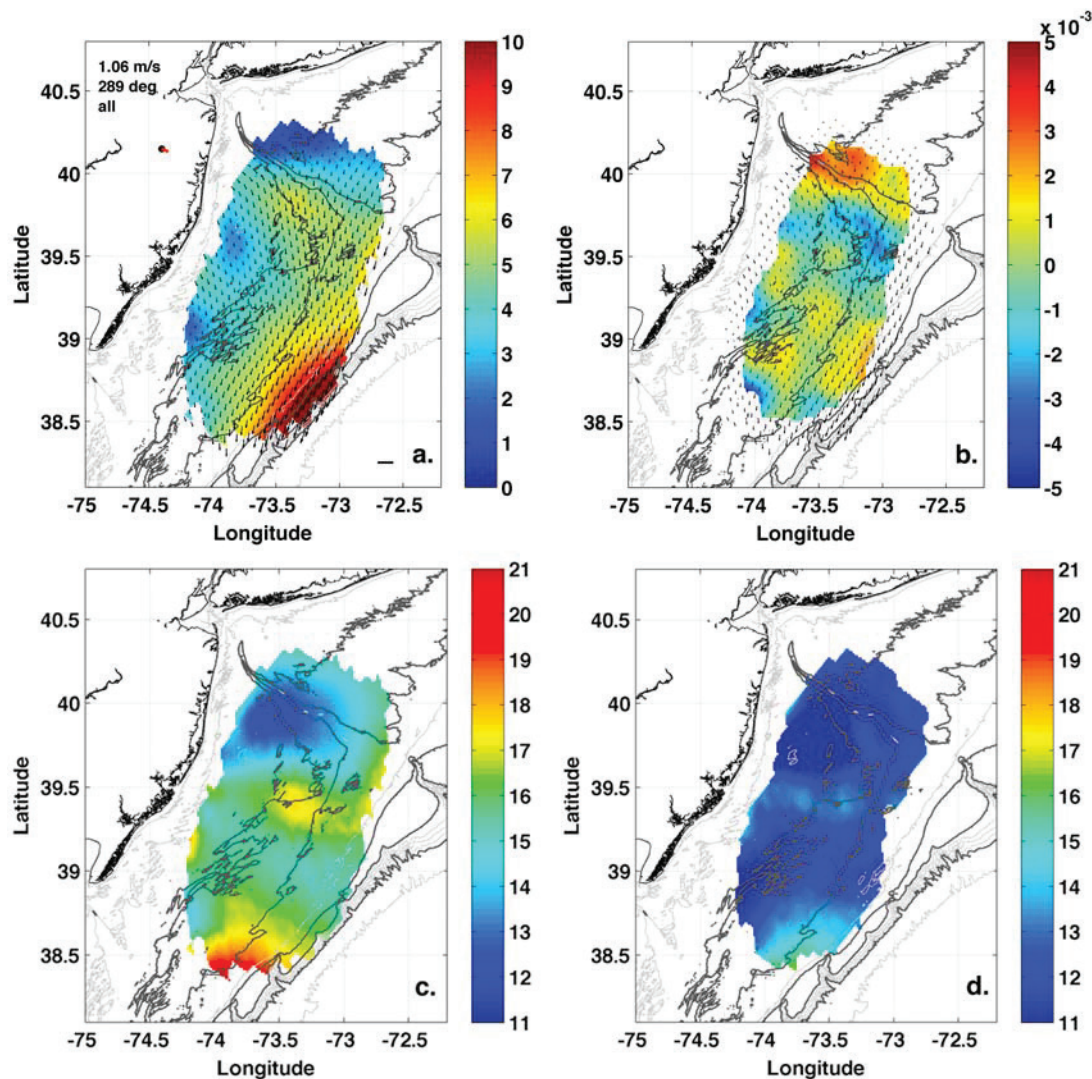


**Figure 3.** (a) Mean surface current for New Jersey Shelf (2002–2007) in cm/s. Average wind speed (m/s) and direction (degrees from true north) measured by NOAA NDBC Buoy 44009 is given. (b) Divergence map of the CODAR mean surface current (2002–2007) in  $10^{-3}$ . (c) RMS of the detided surface current from 2002–2007. Color bar indicates current speed in cm/s. (d) RMS current speed for weak wind conditions when winds were less than 2 m/s.

the western North Atlantic [Beardsley and Winant, 1979]. Such a background flow would exist on the shelf in the absence of wind and other local forcing such as river discharge. To calculate an estimate of the background shelf surface flow due to the large-scale along-shelf pressure gradient, the 2002–2007 surface current data was averaged conditionally for winds less than 2 m/s (Figure 4a). The directional distribution of the winds in this weak wind regime is approximately uniform for all seasons with a mean wind speed of 0.1 m/s. The effect of the sloping cross-shelf topography is clearly seen in the background surface flow, away from the HSV/FTS. The along-shelf flow speed increases from 2–4 cm/s at the inner shelf to 6–10 cm/s at the outer shelf. Compared to the 6 year mean field (Figure 3a), the low-wind flow field has a weaker offshore flow component at the inner to midshelf.

[20] Assuming maximum velocities of 6–10 cm/s (Figure 4a),  $f = 10^{-4} \text{ s}^{-1}$  and a curvature length scale of  $L \sim 50 \text{ km}$  derived from the maximum curvature of the flow along the axis of the HSV, the Rossby number of the flow is  $Ro = U/fL = 0.025$  or less. This indicates a geostrophic balance dominating these low-wind regimes. Even for the larger flow speeds of 30 cm/s occasionally observed on the shelf under strong wind conditions, the Rossby number remains small and less than 0.1, indicating that the nonlinear advective terms in the momentum equation do not contribute significantly to the momentum balance over the seasonal time scale.

[21] A two-dimensional model for the mean circulation on the MAB that assumed a geostrophic balance in the cross-shelf direction and an Ekman balance in the along-shelf direction produced a depth-averaged along-shelf velocity

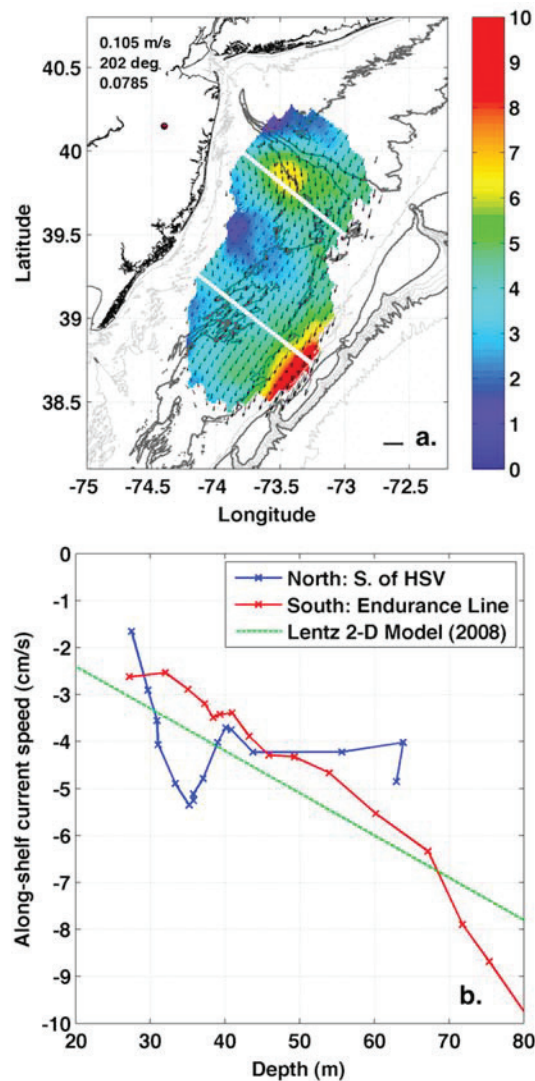


**Figure 4.** (a) Mean surface current field for weak wind conditions (<2 m/s) for 2002–2007 in cm/s. The mean wind speed, direction, and fraction of the total time are listed. (b) Comparison of along-shelf velocity for a cross-shelf section just south of HSV (blue) and another south of the Tuckerton Endurance Line (red). The depth-averaged along-shelf flow velocity given by a 2-D shelf model is shown in green.

that is a linear function of the depths of the isobaths [Csanady, 1976; Lentz, 2008a]. To evaluate the dynamical importance of winds below 2 m/s, we compare the contributions to the momentum equation by the large scale pressure gradient ( $g\theta$ ) and by the mean wind stress ( $\tau/\rho_0 h$ ) for winds below 2 m/s, where  $\theta = \Delta\eta/\Delta y$  is the slope of sea surface,  $\tau$  is the wind stress and  $h$  is the depth of the surface mixed layer. Using a mean along-shelf sea surface slope of  $3.7 \times 10^{-8}$  as estimated by Lentz [2008a], a mean wind stress of  $1.5 \times 10^{-5}$  N/m<sup>2</sup> (corresponding to a mean wind speed of 0.1 m/s) and a surface mixing layer thickness of  $h = 15$  m, the pressure gradient contribution to the momentum equation of  $3.6 \times 10^{-7}$  m/s<sup>2</sup> is over 2 orders of magnitude larger than the wind stress contribution of  $10^{-9}$  m/s<sup>2</sup>, suggesting that the uniformly distrib-

uted winds below 2 m/s do not significantly affect the shelf momentum balance.

[22] Topographic features such as the HSV and FTS can modify the shelf flow by introducing along-shelf variability. In the low-wind background current field, the flow velocity is enhanced at the midshelf just to the south of the HSV and FTS (Figure 4a). The surface along-shelf velocity for two cross-shelf transects is calculated from the low-wind background mean field described above. One transect is just south of the HSV and the other transect is further south near the Tuckerton Endurance Line. The cross-shelf velocity profiles as a function of depth for the two transects are compared with the 2-D model result of Lentz [2008a] (Figure 4b). The linear 2-D model (green line) has a slope of  $-0.09$  cm s<sup>-1</sup> m<sup>-1</sup> and an intercept of  $-0.6$  cm/s, within the range of parameter uncertainty provided by Lentz [2008a]. The different flow dependence on water depth is noted for the two transects with different cross-shelf topography. The along-shelf flow across the northern HSV transect (blue), is significantly different from the linear 2-D model (green). The observed flow exhibits a nonmonotonic dependence on the depth of the isobath with a maximum in along-shelf velocity observed at the midshelf just to the south of the HSV. The southern transect, on the other hand, has an along-shelf current speed that is nearly a linear function of depth out to the 70 m isobath (red). Offshore of the 70 m isobath, the linear relationship still holds but the flow speed's dependence on depth has a steeper slope. This increase in along-shelf speed seaward of the 70 m isobath is likely due to the effect of the shelf slope frontal jet meandering onto the outer shelf near the edge of the CODAR coverage. The shelf-slope frontal jet is not included in the model of Lentz [2008a].

[23] The direction and the general features associated with this background flow do not change with the seasons, although the magnitude of the flow in the seasonal low-wind field can vary up to 3 cm/s compared to the multiyear mean. Specifically there is enhanced down-shelf flow at the outer shelf in the autumn and just south of the HSV in the winter. For the majority of the shelf and for most of the year, the variability in the low-wind background flow is less than 2 cm/s. The weak winds condition is not common on the shelf, occurring on average 8% of the time. Over the seasonal time scale, the weak wind condition is more frequent in the summer occurring 10% of the time and significantly less frequent in the winter occurring only 4% of the time. Over the interannual time scale, the annual average of the low-wind condition ranges between 6% of the time and 12% of the time over a 20 year period from 1987 to 2007.

[24] Before investigating the surface flow response to winds and stratification on the New Jersey Shelf, we want to remove the effect of the topographically modulated pressure gradient driven background flow using the calculated low-wind mean surface current as a representation of the surface response to the large-scale along-shelf forcing. The multi-year averaged low-wind mean is used as the background field because the observed seasonal variability of the low-wind current is relatively small and the enhanced coverage gained by combining the limited amount of low-wind data is significant. The calculated background field is then subtracted from the surface current data in our Eulerian analysis



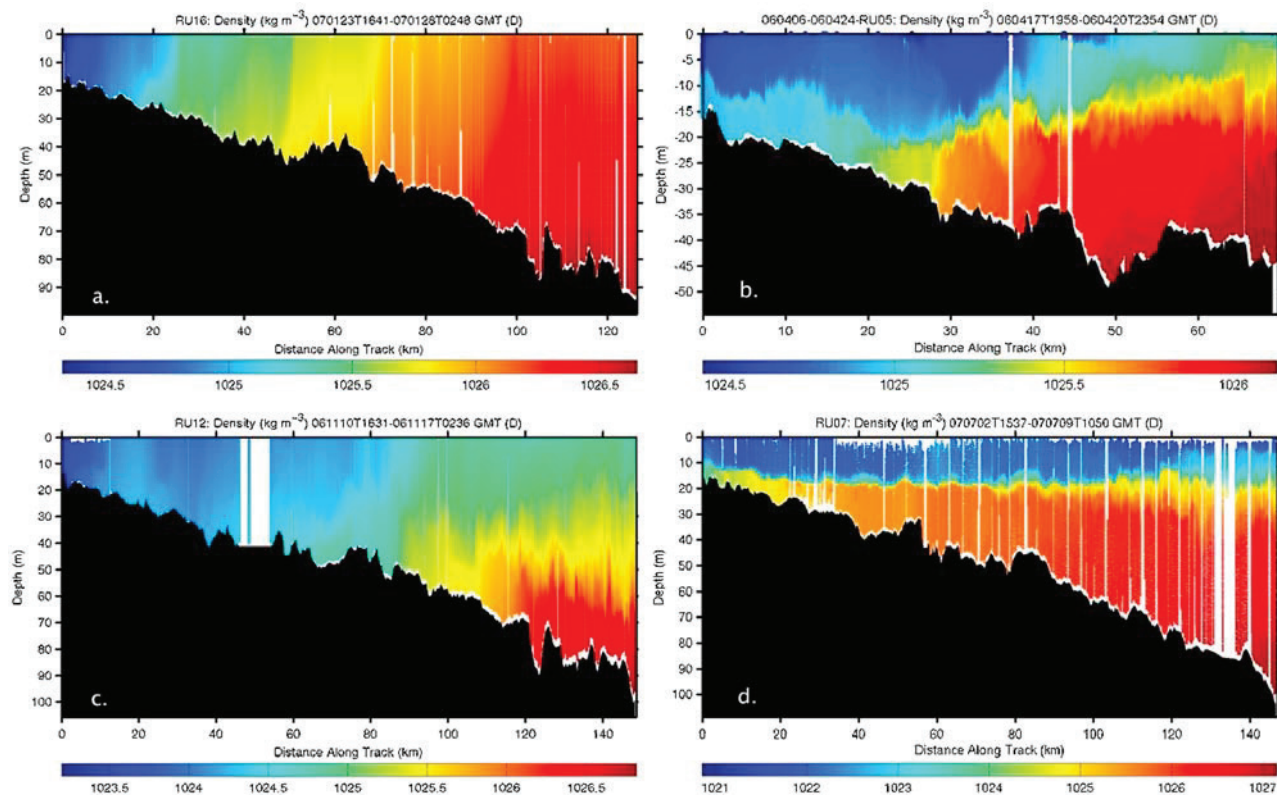


**Figure 5.** New Jersey Shelf seasonal density sections along the Tuckerton Endurance Line ( $\text{kg/m}^3$ ): (a) unstratified winter (December–February), (b) stratifying spring (March–May), (c) destratifying autumn (September–November), and (d) stratified summer (June–August).

of seasonal wind-driven circulation (section 4.4 and 4.5). This approach enables us to look more directly at the spatial and temporal structure of the flow response associated with the surface wind forcing from various directions and under different stratification regimes.

### 4.3. Stratification, Wind, and Seasonal Flow

[25] While many factors contribute to the variability of the surface currents, two significant forcing factors are stratification and wind [Beardsley and Boicourt, 1981; Kohut *et al.*, 2004; Lentz, 2001; Dzwonkowski *et al.*, 2009b]. The New Jersey Shelf undergoes an annual cycle ranging from intense stratification in the summer to mixed conditions in the winter [Bigelow, 1933; Bigelow and Sears, 1935; Castelao *et al.*, 2008b; Schofield *et al.*, 2008]. The changes in the water column's density structure can affect the vertical transfer of momentum, which in turn can affect the current's response to wind forcing. Wind stress is highly variable on the shelf in the synoptic band (2–10 days) due to broadband atmospheric transients [Beardsley and Boicourt, 1981]. Seasonal variability of stratification and wind forcing can have significant effect on the seasonal flow, which is characterized by calculating the mean surface current for each of the seasons for the six years from 2002 to 2007.

[26] Representative hydrographic sections from the Tuckerton Endurance Line [Castelao *et al.*, 2008b] for each of the four seasons are shown in Figure 5. The summer months are highly stratified, characterized by a strong thermocline at middepth. In the cooler, windy winters the water

column is well mixed. For the transition seasons, the water column is stratifying in the spring from seasonal heating and increased river runoff and destratifying in autumn due to seasonal cooling and storm-induced mixing. The four seasons are defined as by Flagg *et al.*'s [2006] climatological analysis of the outer shelf currents, a reasonable choice based on our historic knowledge of the MAB [e.g., Bigelow, 1933], recent analysis of the seasonal variability in the New Jersey Shelf hydrography [Castelao *et al.*, 2008b], and our own climatological analysis of winds from NOAA NDBC Buoy 44009 (1987–2007, outside Delaware Bay; Figures 6 and 7).

[27] Winter, from December to February, is characterized by a well-mixed water column [Castelao *et al.*, 2008b] and the prevalence of NW winds blowing across the shelf [Mooers *et al.*, 1976]. A sample glider cross-shelf density transect during the month of January shows the typical winter time New Jersey Shelf density structure (Figure 5a). The 2-D histogram of wind speed and wind direction for 2002–2007 indicates that the frequency of NW winds was highest during the winter season, occurring on average 41% of the time (Figure 6a). Over the period from 1987 to 2007, the relative frequency of NW winds varies from 30% in 1998 to 53% in 2007 (Figure 7a). For all years except 1990 when SW winds were dominant, NW is the dominant wind direction for the winter mixed season. The wintertime mean surface flow has three notable characteristics (Figure 8a). First, in the region south of the HSV, the southward flow is nearly spatially uniform and directed offshore and down shelf. The flow velocity is  $\sim 6$  cm/s for most of the shelf except at the outer



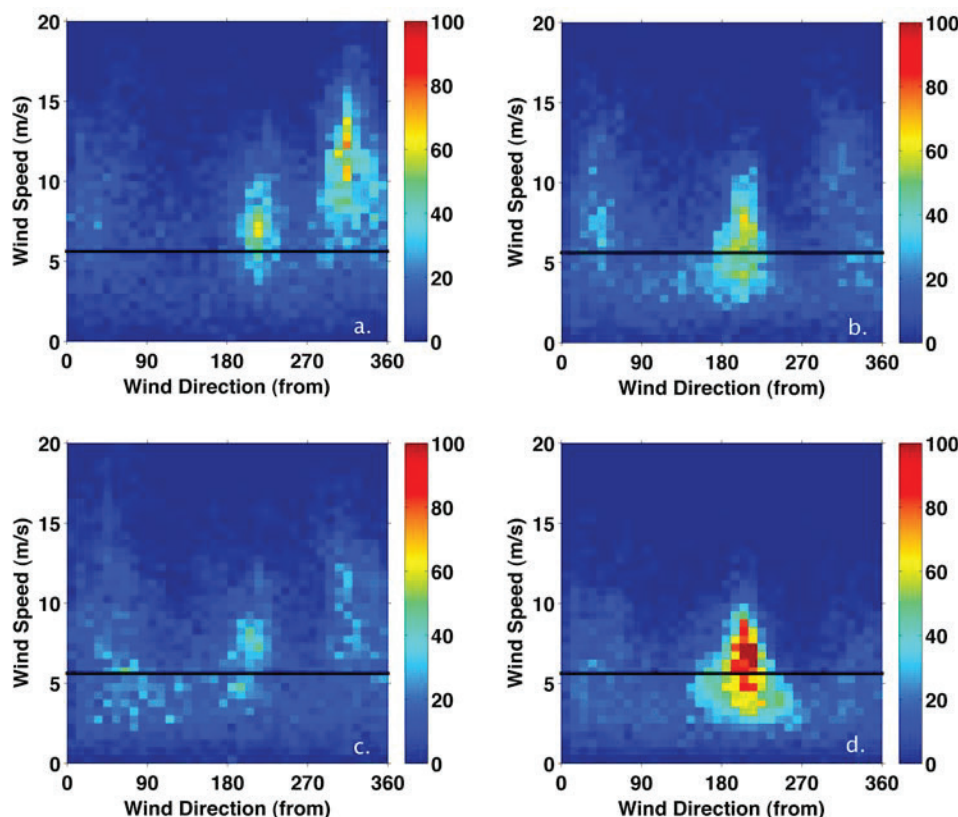


**Figure 6.** Histogram of hourly winds by season with color bar indicating number of occurrences. The black lines represent a wind stress of  $0.05 \text{ N/m}^2$ : (a) winter (December–February), (b) spring (March–May), (c) autumn (September–November), and (d) summer (June–August).

shelf region. Second, along the outer shelf seaward of the 80 m isobath at the shelf break, the surface flow speed increases to greater than  $13 \text{ cm/s}$  while the flow direction turns along shelf. Third, in the region north of the HSV, the current velocity is very weak ( $<3 \text{ cm/s}$ ). Over most of the shelf, the surface flow over seasonal scales is wind-driven except for the area near the HSV and the shelf break where topographic steering effects become important and baroclinic forcing drives a shelf-slope frontal jet. Compared to the long-term mean (Figure 3a), the wintertime flow has a significantly higher cross-shelf flow for most of the shelf except for the region near the HSV and just to the south where it was similar to the mean.

[28] Spring, from March to May, is characterized by the transition from a well-mixed water column to a more stratified water column. During most years the highest freshwater river discharge onto the shelf also occurs during the spring season [Chant *et al.*, 2008]. A sample glider cross-shelf transect from April shows a partially stratified water column with significantly more of the lower-density riverine water appearing on the shelf (Figure 5b). During spring, the wind pattern is less stable than either the stratified or the mixed season. The weakening NW winds give way to more frequent but lower-energy along-shore NE and SW winds (Figure 6b), occurring on average 21 and 32% of the time, respectively. The spring wind pattern can vary significantly on the inter-annual time scale. NW winds can occur 8% (1991) to 28% (1997) of the time, NE winds can occur 10% (1997) to 38% (1987) of the time, while SW winds can occur 17% (1992)

to 44% (1991) of the time (Figure 7b). The causes of such interannual variability are likely associated with variability in the large-scale atmospheric circulation pattern and the frequency of storms. NE winds tend to drive along-shelf, down-shelf flow. The 6 year climatology of seasonal flow on the shelf during the spring is directed mostly down shelf toward the southwest with a speed of  $3$  to  $7 \text{ cm/s}$  (Figure 8b). A large portion of the area to the south of the HSV has a velocity of less than  $5 \text{ cm/s}$ . Near the shelf break, offshore of the 100 m isobath, the current velocity increases significantly to over  $15 \text{ cm/s}$ . The increased alongshore wind forcing combined with buoyancy forcing due to increased river discharge results in favorable conditions for along-shelf transport during the spring. Compared to the long-term mean, springtime flow has weaker offshore flow, especially in the region south of the HSV and inshore of the 40 m isobath.

[29] Summer, from June to August, is characterized by a highly stratified water column. As shown in the sample cross-shelf density section (Figure 5d), the stratified surface layer is 10 to 25 meters thick. The density difference between the surface and bottom layers could be as large as  $6 \text{ kg/m}^3$ , sometimes higher. The overall wind strength for the summer season is weaker than all the other seasons. The wind direction is predominately along-shore from the upwelling favorable SW, occurring 48% of the time (Figure 6d). This SW wind pattern varies little interannually ranging from 30% in 1998 to 55% in 1988 (Figure 7d). NE winds are the second most common direction during the summer, with occurrences ranging from 7% (1994) to 22% (1995) of the time, and

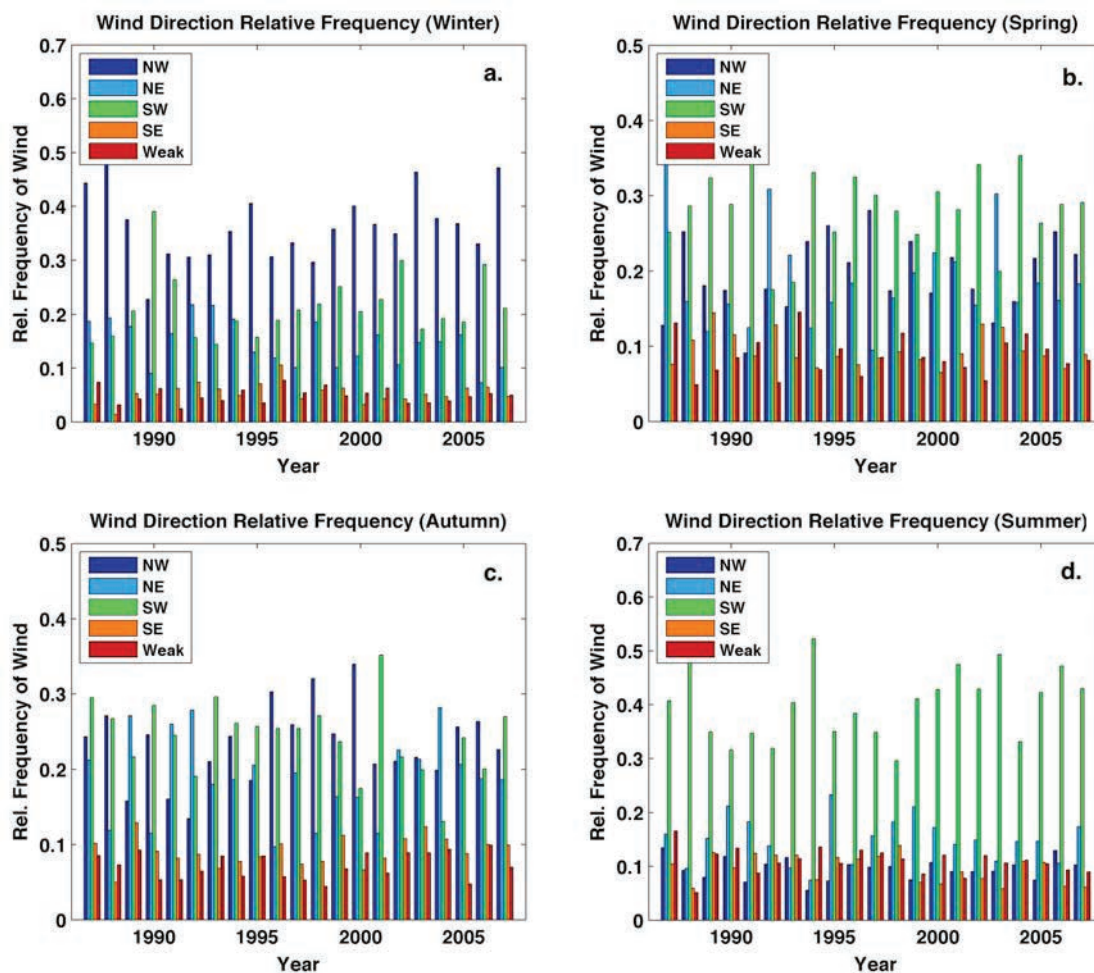


**Figure 7.** Interannual variability of the relative frequency of NW, NE, SW, SE, and weak (less than 2 m/s) winds for NOAA NDBC Buoy 44009: (a) winter (December–February), (b) spring (March–May), (c) autumn (September–November), and (d) summer (June–August).

averaging 15% of the time between 2002 and 2007. The climatology of mean surface currents for the summer season from 2002 to 2007 includes a continuous band of stronger flow on the shelf (Figure 8d), starting with the region just south of the Hudson Shelf Valley stretching from the inner shelf to the outer shelf with the flow directed mostly cross shelf. This cross-shelf flow connects with faster offshore flows seaward of the 60 m isobath, where the flow is directed more along-shelf with a velocity of 7–9 cm/s. The surrounding regions, in particular the region north of the HSV and the region in between the 40 and 60 m isobath to the south, has down-shelf surface current speeds weaker than 5 cm/s, directed down shelf to the SW. Shoreward of the 40 m isobath, the current velocity drops to nearly zero. The increased offshore flow is qualitatively consistent with a SW wind driving a coastal upwelling system on the shelf. The summertime flow structure over the HSV and offshore is similar to that of the long-term mean, but the flow at the inner shelf has a weaker along-shelf component compared to the overall mean.

[30] Autumn, from September to November, is characterized by frequent storms that break down the summer stratification. The cooling of the surface layer preconditions

the water column for storm mixing. A warm and salty surface layer tends to overlay a cold and fresher bottom layer during autumn on the New Jersey Shelf. Eventually increased storm activity mixes away the remaining stratification. A sample density cross-shelf section from November shows that the stratification of the water column had already broken down at the inner shelf and is reduced at the mid- to outer shelf (Figure 6c). During this time, the winds shift from the weaker SW winds of the summer (23% of the time between 2002 and 2007) to the stronger and more frequent NE and NW winds associated with passing fronts and storms occurring 24% and 25% of the time (between 2002 and 2007), respectively (Figure 6c). There is significant variability in their relative frequency over the interannual time scale. Over the twenty year time period from 1987 to 2007, the occurrence of autumn SW winds ranged from 13% (2004) to 35% (2001), the occurrence of NW winds ranged from 13% (1992) to 34% (2000), and the occurrence of NE winds ranged from 10% (1996) to 28% (1992 and 2004) (Figure 7c). The frequent NE winds drive energetic along-shelf and onshore flow. The seasonal mean surface current map shows three distinct flow regions (Figure 8c). North of the HSV, there is weak flow with



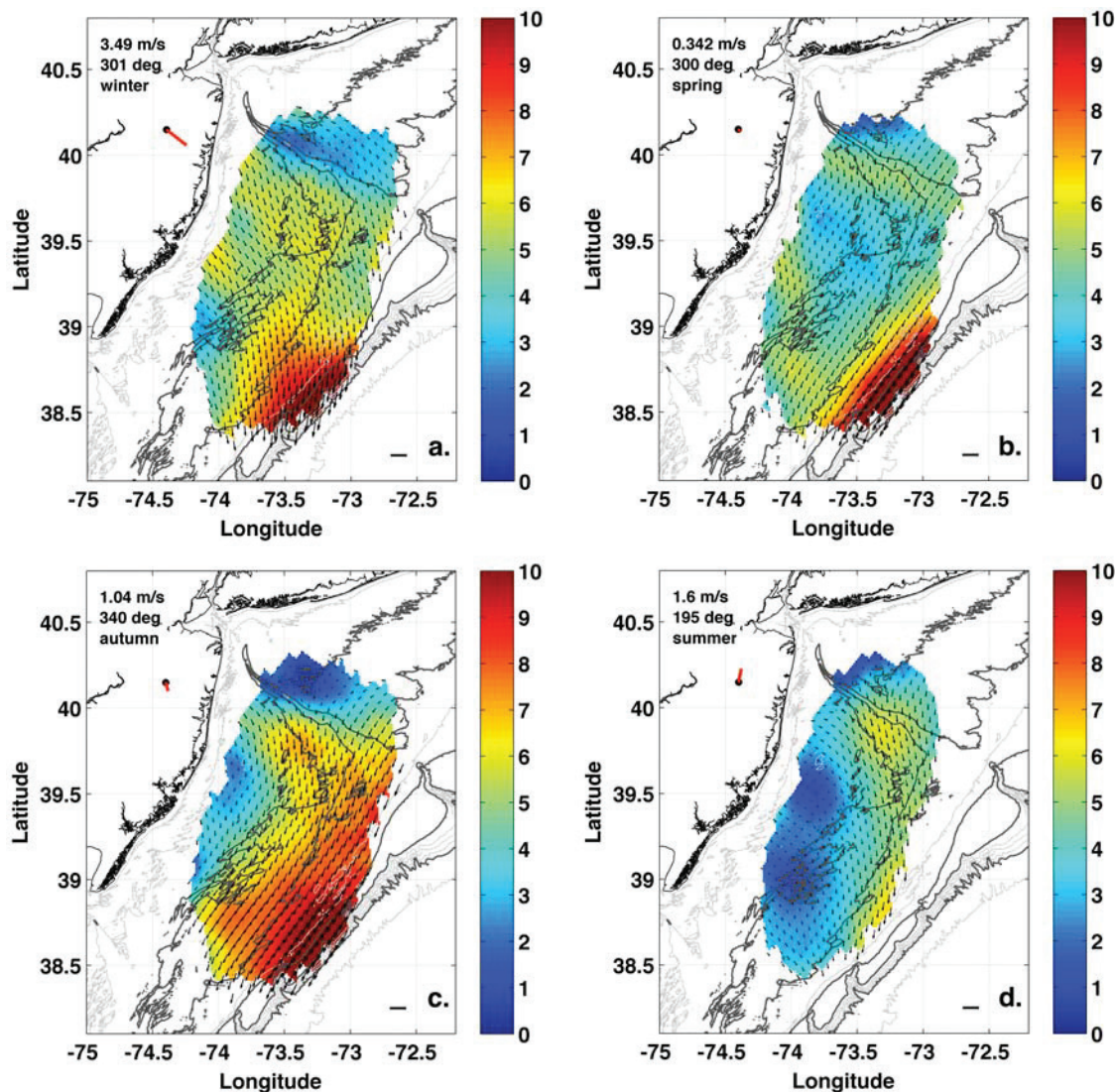


**Figure 8.** Seasonal surface current on the New Jersey Shelf (cm/s): (a) winter (December–February), (b) spring (March–May), (c) autumn (September–November), and (d) summer (June–August).

speeds less than 3 cm/s. The mid to outer portion of the shelf south of the HSV includes a broad band of strong along-shore, down-shelf flow with the highest seasonal mean velocity of any of the seasons, averaging 8–10 cm/s. The current at the inner shelf region south of the HSV is weak with velocities less than 5 cm/s. Compared to the long-term mean, the autumn down-shelf flow is significantly higher at the mid and outer shelf in the region south of the HSV.

#### 4.4. Wind-Driven Circulation

[31] We next calculate the mean spatial response of the surface circulation on the New Jersey Shelf to wind forcing and seasonal changes. The low-wind mean is used as an estimate of the nonwind driven background component of the surface circulation, which is then subtracted from the conditionally averaged fields to obtain the wind-only component of the surface flow for different wind regimes. The response of the ocean surface to each wind regime for the different seasons with the background low-wind mean

removed are shown in Figures 9–12. At a first glance, the surface flow is largely in the direction of the wind during the winter when the water column is well mixed and more to the right of the wind during the summer when the water column is highly stratified. For the transition seasons of spring and autumn, the wind driven response of surface flow is in between the angular range of the winter and summer scenarios. To characterize the effect of wind forcing on the current variability for all the seasons, the spatially averaged RMS/Mean for each case of the wind-based conditionally averaged flow are computed and presented in Table 3. The total RMS/Mean for all seasons and all wind directions is 3.3. In general the variability of the current compared to the mean is much lower for wind-driven flows with RMS/Mean ranging from 1.1 under NE winds to 1.8 under SW with the exception of SE winds (with a value of 3.5) because the average flow is very weak under those conditions. In some cases such as under NE winds during winter and spring, the RMS/Mean is less than 1. This result confirms that wind



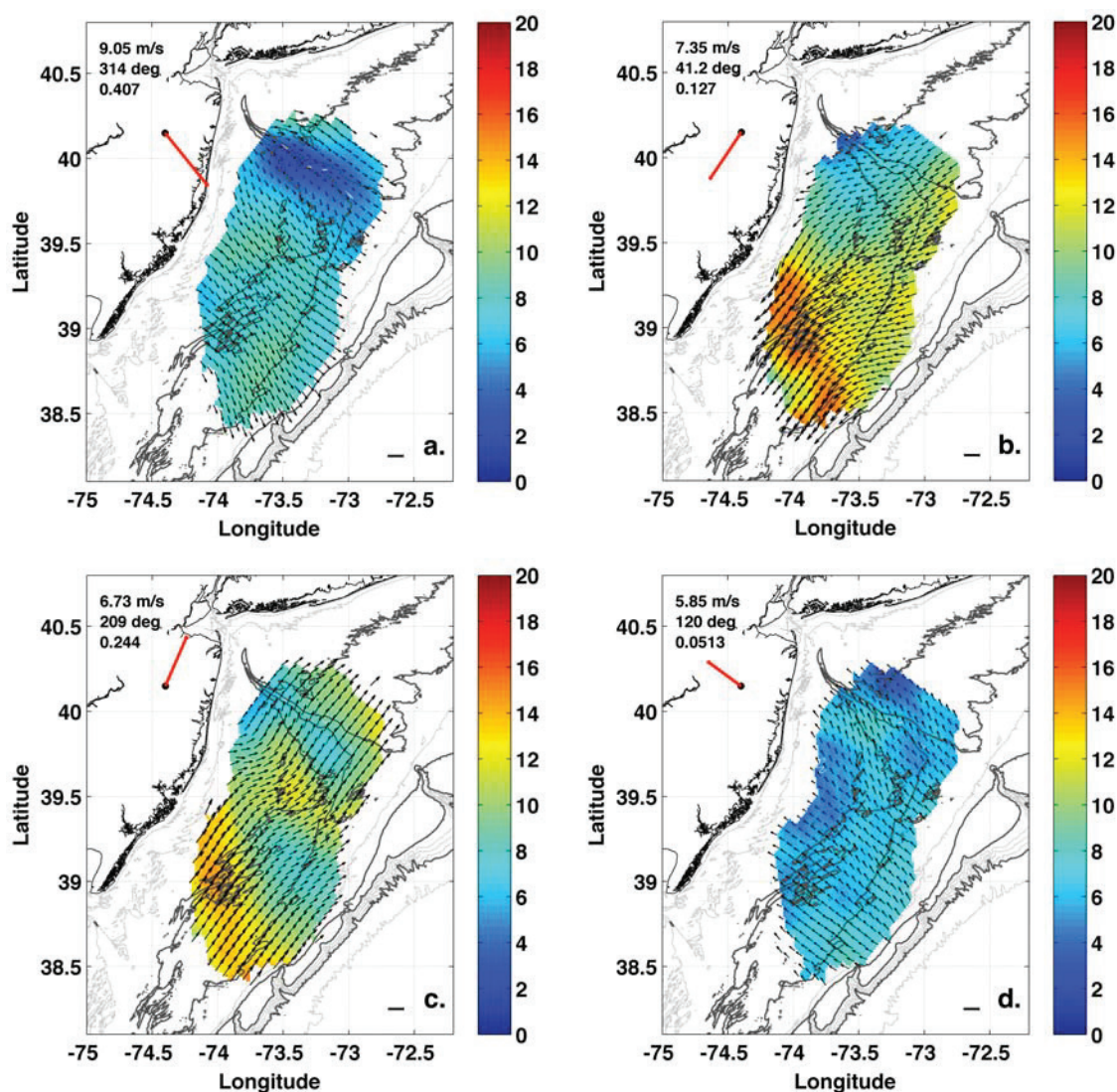


**Figure 9.** Winter mean current based on wind (cm/s): (a) northwest winds, (b) northeast winds, (c) southwest winds, and (d) southeast winds.

forcing variability is the dominant source of subtidal temporal variability for the shelf surface flow.

[32] The surface flow responses to winter wind forcing are shown in Figure 9. Winter is characterized by strong NW winds, which occur 41% of the time with a mean velocity of 9.1 m/s ( $0.13 \text{ N/m}^2$ ), followed by SW winds which occur 24% of the time with a mean velocity of 6.73 m/s ( $0.072 \text{ N/m}^2$ ). Under the cross-shore NW winds, the surface flow is cross shelf in the offshore direction (Figure 9a). However, despite the strong wind forcing, the flow velocity over the HSV and the nearby region remain weak with mean current speeds of less than 5 cm/s. Nevertheless, winter can be a season of significant cross-shelf transport due to frequent NW winds driving cross-shelf flow. Southward of the offshore tip of the FTS, the flow velocity increases to 8 cm/s. The shelf-wide offshore flow south of the HSV has little cross-shelf variability, suggesting a depth-independent wind-driven response of the unstratified water column. Under wintertime SW winds, the surface flow is essentially up shelf toward the NE with a speed of 8–14 cm/s (Figure 9c). An offshore veering is

observed as the flow reaches the southern side of the FTS. For the two less common wind regimes, NE winds (13% of the time) drive along-shore, down-shelf flow with speeds of 7–16 cm/s (Figure 9b), and SE winds (5% of the time) drive onshore, up-shelf flow with speeds of 3–7 cm/s for most of the shelf (Figure 9d).

[33] The surface flow responses to different spring wind forcing regimes are shown in Figure 10. Spring is characterized by the weakening of NW winds and a corresponding increase in the frequency of NE and SW winds. NW winds, common in the early part of spring, occur 21 percent of the time with a mean wind speed of 7.2 m/s. Under such wind forcing, the surface flow is largely cross shelf for the southern portion of the New Jersey Shelf. The flow is similar to what was observed during the winter but with an expanded low-speed zone that includes the whole HSV and FTS area. The combination of the weakening of the cross-shelf NW wind and shrinking area of the cross-shelf flow suggest less offshore transport during the spring. SW winds, more common in late spring, occur 32% of the time with a mean speed of

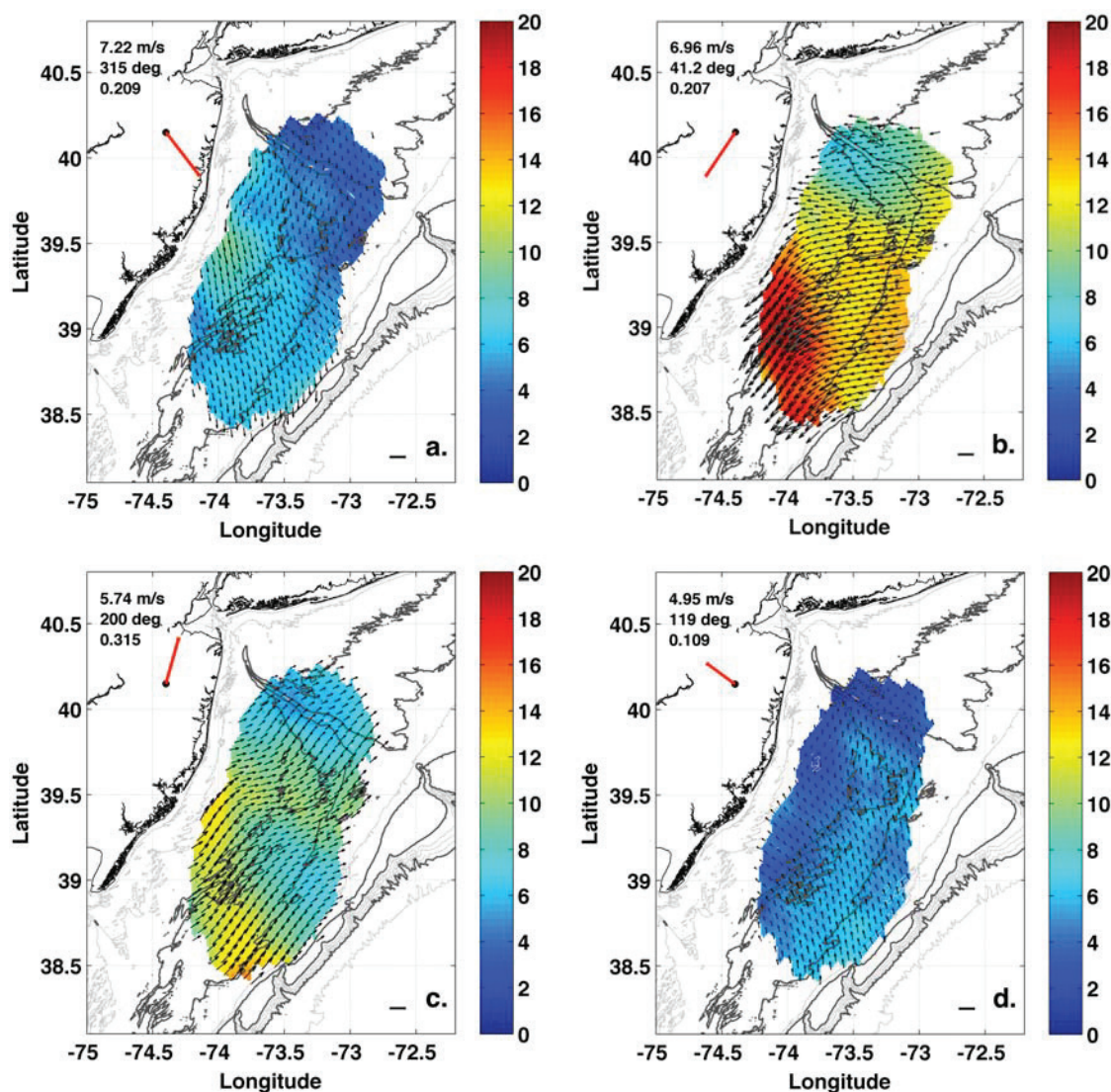


**Figure 10.** Spring mean current based on wind (cm/s): (a) northwest winds, (b) northeast winds, (c) southwest winds, and (d) southeast winds.

5.7 m/s (Figure 10c). It generates an along-shore up-shelf flow pattern that is largely similar to that of the wintertime case. The alongshore NE winds, which occur 21% of the time with a mean velocity of 6.96 m/s, generate the most energetic flow response of the spring. The surface current speeds range from 8 cm/s near the HSV to over 20 cm/s near the Tuckerton Endurance Line (Figure 10b). Just south of the HSV, over the FTS region, the flow is mostly onshore. Further south near the Tuckerton Endurance Line, the flow turns alongshore at the inner shelf (Figure 10b). The counterclockwise veering of the flow under NE winds is observed for much of the southern region approaching the inner shelf from offshore.

[34] The surface flow responses to different summer wind forcing regimes are shown in Figure 11. The summer stratified season is the least energetic of all the seasons. Nearly 48% of all winds are along-shore SW winds with a mean speed of 5.3 m/s. SW winds tend to drive up-shelf flow at the inner shelf and cross-shelf offshore flow at the mid to outer shelf (Figure 11c). The flow over the HSV is

the weakest with a speed of 7 cm/s, while the flow at the inner shelf and over the FTS south of the HSV is the strongest with a speed of 10–12 cm/s. Of the three other wind regimes during the summer, NE winds, occurring 15% of the time with a mean speed of 5.5 m/s, drive a nearly on-shore flow with a slight down-shelf component (Figure 11b). NW winds, occurring 11% of the time with a mean speed of 4.57 m/s, drive a down-shelf flow of 5 to 10 cm/s. SE winds, occurring 9% of the time with a mean speed of 4.4 m/s, interestingly stop nearly all wind-driven components of the surface flow on the shelf (Figure 11d).

[35] The surface flow response to autumn wind forcing regimes are shown in Figure 12. Surface flow during autumn is the most energetic of all the seasons. With the arrival of autumn, decreasing surface temperature and increased storm frequency enhance the vertical mixing of the water column. The wind regime undergoes a transitional phase from weak SW winds to strong NE winds often generated by storms. Winds from all three principal directions, NW, SW, and NE,



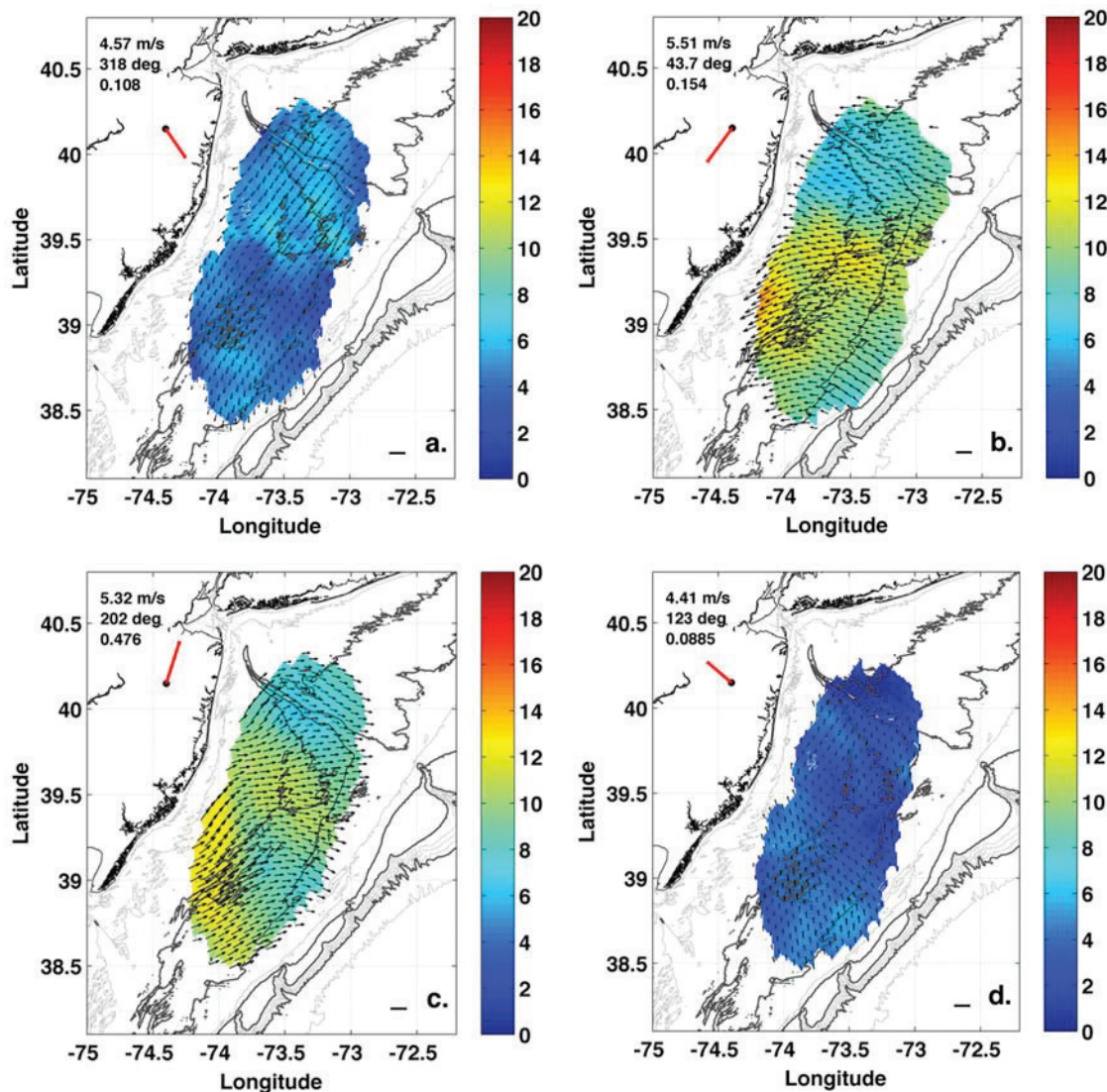


**Figure 11.** Summer mean current based on wind (cm/s): (a) northwest winds, (b) northeast winds, (c) southwest winds, and (d) southeast winds.

are significant contributors during the autumn, each account for 25, 23, and 24% of the total winds, respectively. The response of the shelf flow under NW winds is offshore and down shelf with a flow velocity of 8 to 12 cm/s south of the HSV (Figure 12a). Under SW winds the flow is offshore and up shelf, similar to the summer scenario but more intense with flows of 8 to 16 cm/s (Figure 12c). NE winds generate the most intense flow, mostly down shelf and onshore with velocities in excess of 14 cm/s for nearly the entire shelf south of the HSV with peak currents of over 20 cm/s near the Endurance Line (Figure 12b). Near the HSV, the flow is 6 to 10 cm/s. Lastly, under the onshore SE winds, the flow is weakly inshore and up shelf with a speed of 2 to 6 cm/s (Figure 12d).

[36] The response of the surface currents to the different wind forcing regimes show clear seasonal differences. The surface flow is to the right of the wind during the summer stratified season and largely in the direction of the wind during the winter mixed season. The spatial maps exhibit along-shelf variability and weak cross-shelf variability.

Flow near the Hudson Shelf Valley has a persistently weaker response to wind forcing compared to regions down shelf to the south. SW winds are most common for summer, and NW winds are most common for winter. All three major wind directions (SW, NW and NE) are significant during the transition seasons of spring and autumn. During the transition seasons, NE winds in particular generate strong down shelf and onshore flow, the most energetic surface current response to wind forcing observed on the New Jersey shelf.

#### 4.5. Wind Current Correlation

[37] The 2-D maps of surface flow from section 4.4 show that surface currents have a strong seasonal variability in response to wind forcing. This is consistent with modeling results showing the wind-driven MAB shelf flow is strongly dependent on the stratification [Keen and Glenn, 1994]. The structure of the surface and bottom boundary layers determine the vertical mixing of momentum, which is reflected observationally in the seasonal differences in the wind-current correlation angle. Weak winds and strong stratifi-



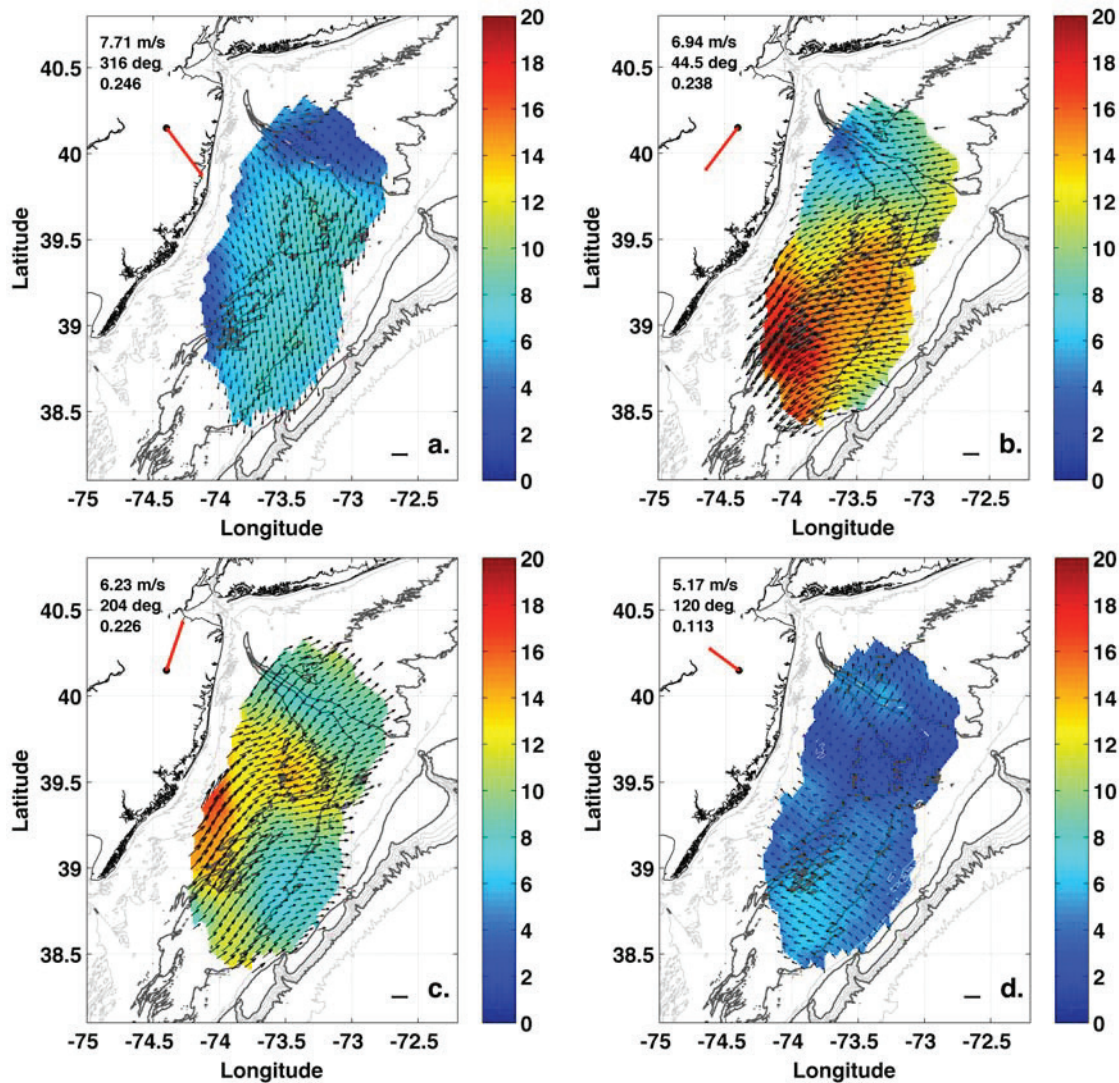


**Figure 12.** Autumn mean current based on wind (cm/s): (a) northwest winds, (b) northeast winds, (c) southwest winds, and (d) southeast winds.

cation (i.e., summer) result in separate surface and bottom layers across the shelf except at the coastal upwelling zone [Keen and Glenn, 1994]. The strong summer stratification tends to constrain the surface mixed layer to the upper 10–12 m, above the season pycnocline [Castelao *et al.*, 2008b]. On the other hand, strong winds and moderate stratification (i.e., spring and autumn) can result in interacting boundary layers at the inner shelf [Glenn *et al.*, 2008] and separate boundary layers over the outer shelf. Finally strong winds and weak stratification (winter) can result in interacting boundary layers across the entire shelf. One can estimate the depth of the surface Ekman layer [Csanady, 1976; Lentz, 2001] for an unstratified water column

$$\delta_s = \frac{\kappa}{f} \sqrt{\frac{\tau^s}{\rho}},$$

where  $u^* = \sqrt{\frac{\tau^s}{\rho}}$  is the shear velocity and  $\kappa = 0.4$  is von Kármán constant. Let  $f = 9 \times 10^{-5} \text{ s}^{-1}$  at latitude 39°N, and assume  $\tau = 0.1 \text{ N/m}^2$  (corresponding to 8 m/s wind at

5 meters above sea level), the surface Ekman layer depth is 43 m. If the wind stress increases to  $0.35 \text{ N/m}^2$ , as was occasionally seen on the New Jersey Shelf during the winter, the estimated surface Ekman layer would extend over 80 m. The bottom mixed layer typically has a height of less than 10 m during the stratified season but can also exceed 20 m on the MAB [Perlin *et al.*, 2005; Lentz and Trowbridge, 1991; Glenn *et al.*, 2008]. Solutions to the classic Ekman problem using different vertical eddy viscosities exhibit significant differences in the wind-current angle depending on

**Table 3.** Relative Variability of Detided CODAR Currents: RMS/Mean

	Summer	Winter	Spring	Autumn	All Seasons
All Directions	4.9	2.6	3.0	3.0	3.3
NW	1.9	1.4	1.4	1.6	1.6
NE	1.3	0.9	0.9	1.1	1.1
SW	1.7	1.7	1.8	1.8	1.8
SE	6.8	1.8	3.7	3.0	3.5

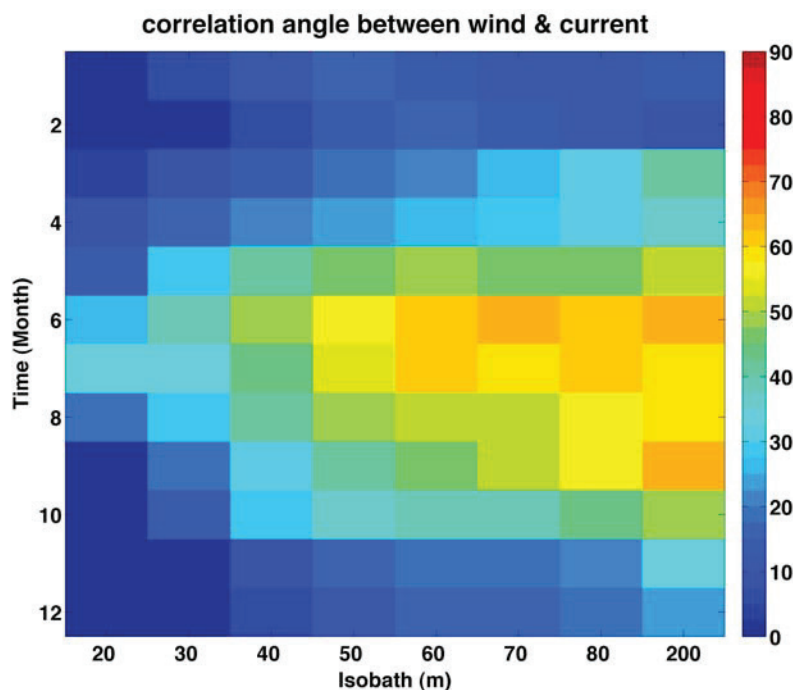


**Figure 13.** Correlation angle between wind and current along a cross-shelf transect just south of the Tuckerton Endurance Line (2002–2007).

the structure of the vertical eddy viscosity [Ekman, 1905; Madsen, 1977; Trowbridge and Lentz, 1991].

[38] It is therefore worthwhile to quantify the wind-current correlation as a function of time and space over the New Jersey Shelf. A small correlation angle would be consistent with an eddy viscosity profile of a water column with interacting boundary layers and a large angle would be consistent with a shallow surface Ekman layer and separate boundary layers. The monthly climatology of the complex cross correlation between lowpassed wind velocity and subtidal surface current velocity are calculated for eight cross-shelf stations just south of the Tuckerton Endurance Line using the 6 year CODAR data set and the NOAA wind data set from NDBC buoy 44009 (Figure 13). For this analysis, the low-wind background mean is removed from the surface current velocities. The color of each pixel indicates the angle of the complex correlation between wind and current. A correlation angle of zero (blue) signifies flow exactly in the direction of the wind and a correlation angle of 90 (red) signifies perpendicular flow to the right of the wind. The magnitude of the complex correlations range between 0.5 and 0.8 with the lower values seen at the outermost station near the 200 m isobath for this set of eight stations. For the New Jersey Shelf, the angle between the wind and the surface currents is larger during the stratified summer ( $>45^\circ$ ) and smaller during the unstratified winter ( $<20^\circ$ ) (Figure 13). In particular, during the summer months of June–August, the mid to outer shelf stations (deeper than the 50 m isobath) show a correlation angle of 60 to  $70^\circ$  while the same stations during the winter months December–February show a correlation angle of 10 to  $20^\circ$ . The inshore stations also show a seasonal difference but with less variability. At the inner most station on the 20 m isobath, for example, the wind-current correlation angle is less than  $20^\circ$  for most months of

the year except during the summer months when the angle increases to  $35^\circ$  in July. Simple Ekman theory predicts a maximum deflection angle of  $45^\circ$  between the wind and surface current when the vertical eddy viscosity is constant [Ekman, 1905]. The fact that correlation angles of greater than  $45^\circ$  are observed suggests that the non-Ekman component of the background down-shelf flow is not completely removed. Processes such as the interaction of the wind and the shelf-slope frontal jet could be a contributing factor. The correlation angle increases from the inner shelf to the midshelf near the 50 m isobath, and beyond that there is little cross-shelf variation. The transition seasons are more dynamic in nature. At each cross-shelf location, the wind-current correlation angles change rapidly during spring (increasing from April to May) and autumn (decreasing from October to November). These results suggest that the seasonal change in stratification exerts a strong influence on the response of surface flow to wind forcing on the New Jersey Shelf.

[39] To visualize the effect of wind-driven circulation in the context of along-shelf and cross-shelf transport, wind-current cross correlations along the natural geographic axes of the shelf are also calculated (Figure 14). The along-shore and cross-shore axes on the New Jersey Shelf are rotated  $35^\circ$  clockwise from true north. The cross correlation between the winds and currents are calculated for the along- and cross-shore wind and along- and cross-shelf currents for each month of the year along the same cross-shelf transect south of the Endurance Line noted earlier. The along-shore winds are correlated with along-shelf currents for all months of the year shoreward of the 40 m isobath (Figure 14a). The shallow inner shelf has an unstratified water column most months of the year. The overlapping bottom and surface Ekman layers would cause wind driven flow to be in the direction of the

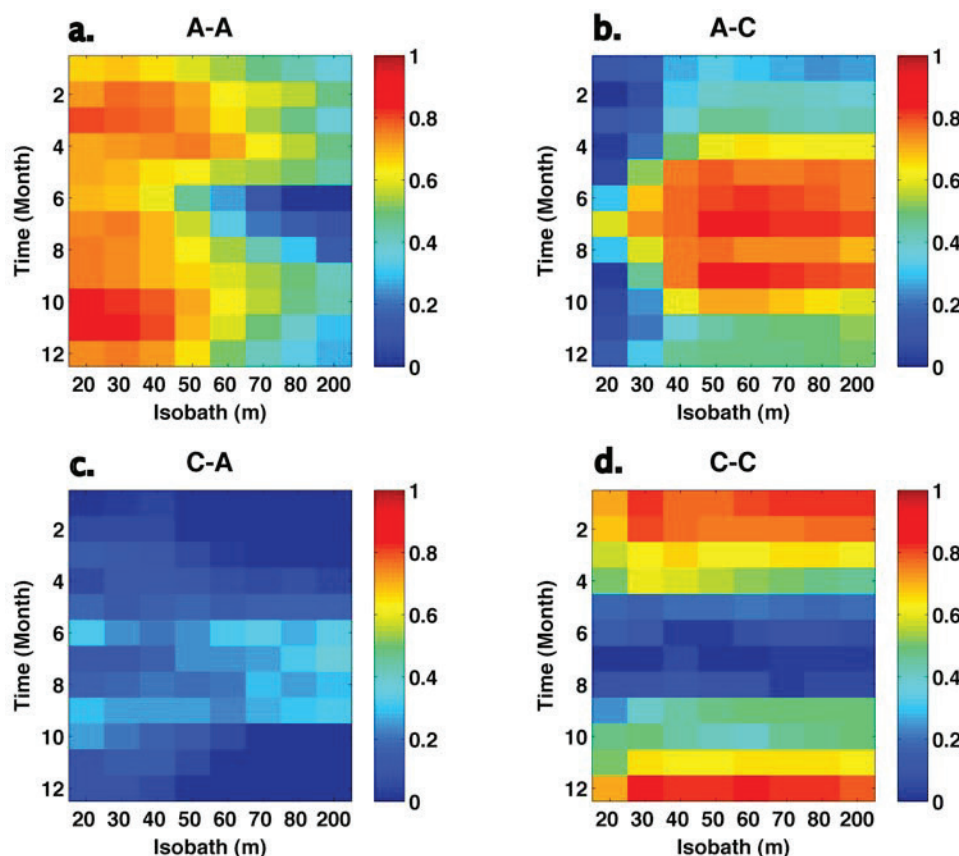


**Figure 14.** Cross correlation along geographic axes between wind and current (2002–2007): (a) along-shore winds and along-shelf current, (b) along-shore winds and cross-shelf current, (c) cross-shore winds and along-shelf current, and (d) cross-shore winds and cross-shelf current.

wind. The winds and currents are especially well correlated with each other ( $>0.7$ ) shoreward of the 50 m isobath during the spring and autumn months (Figure 14a). This could be due to the frequent occurrence of energetic along-shelf wind during the transition seasons which tend to drive along-shelf, down-shelf flow. Offshore of the 50 m isobath, the correlation decreases between the along-shore winds and the along-shelf currents. During the summer months of June, July, and August, the correlation is less than 0.3, indicating the along-shore wind is not a significant factor driving along-shelf flow at the outer shelf.

[40] The along-shelf wind is highly correlated with cross-shelf current at the mid to outer shelf from late spring to early autumn with a correlation coefficient of  $>0.8$  from May to September (Figure 14b). A linear fit between the summer along-shore winds and cross-shelf flow at the 60 m isobath is shown in Figure 15a. The slope for the summer fit is 0.0067 and it has a  $R^2$  of 0.59. This is consistent with the observations of upwelling favorable wind from the SW driving surface flow cross shelf (Figure 11c). Using a subset of the surface current data from 2003 to 2004, [Dzwonkowski *et al.*, 2009b] also finds strong summertime correlations between along-shore winds and the cross-shelf currents. Coastal upwelling due to along-shore winds on the shelf results in the offshore transport of the surface layer seaward of the upwelling region. Shoreward of the 30 m isobath, the correlation is weak, likely due to contributing factors within

the coastal upwelling zone [Glenn *et al.*, 2004]. During the unstratified periods there is a relatively weak correlation between the along-shore wind and cross-shelf current with a correlation coefficient of  $<0.5$  for October–March. This is not surprising since we know from earlier analysis that the along-shelf wind was not dominant and that the flow is in the direction of the wind during the winter season.

[41] Cross-shelf wind and cross-shelf currents have strong correlations ( $>0.7$ ) during the late autumn and winter across the entire New Jersey Shelf (Figure 14c). Since the dominant winds during late autumn and winter are mainly cross-shore, strong cross-shelf flow is observed during these times (Figure 9a). Cross-shelf depth variation does not appear to affect the variability of the cross-shore flow offshore of the 20 m isobath. A linear fit between winter cross-shore winds and cross-shelf transport at the 60 m isobath is shown in Figure 15b. The slope for the winter fit is 0.0096 and it has a  $R^2$  of 0.50, indicating a stronger response of cross-shelf flow to winter wind forcing than summer wind forcing. During the summer stratified season, the correlation between cross-shore winds and cross-shelf current is significantly reduced due to upwelling favorable along-shore winds driving cross-shelf flow.

[42] In summary, cross-shelf flow is driven by different wind patterns during the stratified summer and unstratified winter seasons. It happens that the alongshore wind is dominant during summer and cross-shore wind is dominant



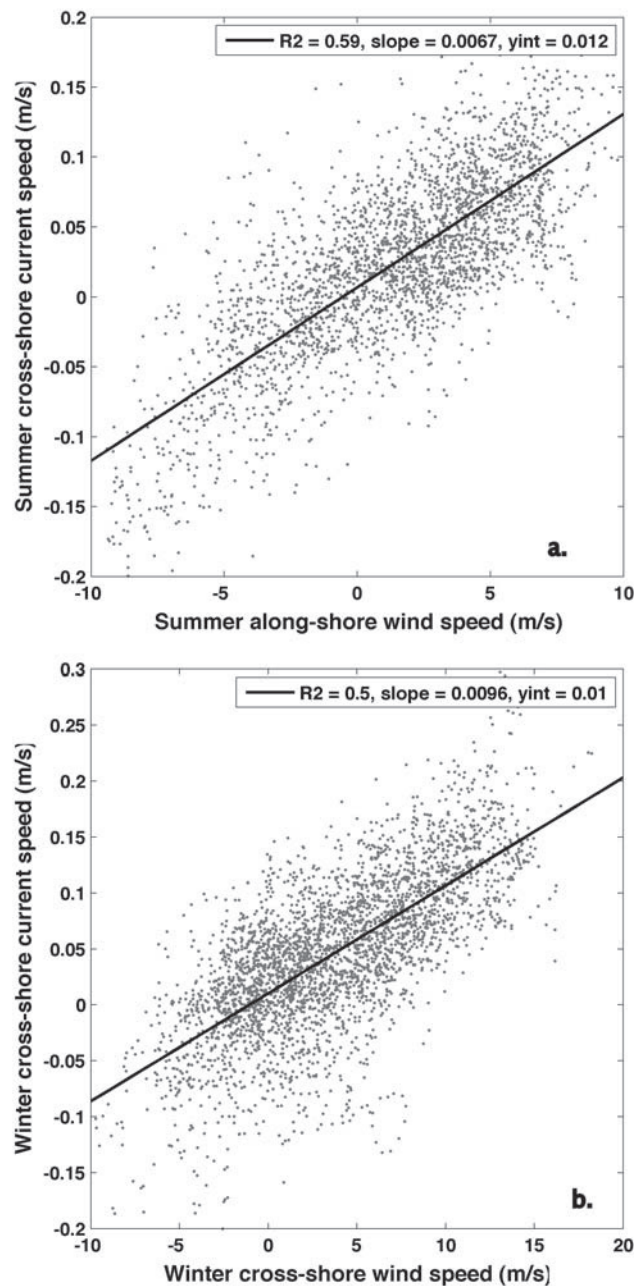


**Figure 15.** Wind-current speed correlation at a 50 m isobath site: (a) summer correlation between along-shore wind speed and cross-shore current speed and (b) winter correlation between cross-shore wind speed and cross-shore current speed.

during winter. The large wind-current correlation angle at mid to outer shelf during the summer is consistent with a shallow Ekman layer and separate boundary layers, with alongshore SW wind driving offshore flow. The small wind-current correlation angle shelf-wide during the winter is consistent with an eddy viscosity profile reflecting interacting boundary layers and cross-shore NW winds driving offshore flow. During the transition seasons of spring and autumn, boundary layer interactions are complicated by

changing stratification and frequent storms. During this time along-shelf flow is mainly driven by along-shore winds, especially at the inner to midshelf.

#### 4.6. Interannual Variability

[43] Both the magnitude and the sign of the seasonal along-shelf and cross-shelf surface flow can vary on the interannual time scale. The analysis in sections 4.3–4.5 showed that changing winds and changing water column stratification are major drivers of the seasonal and annual variability of the shelf flow. To examine the interannual variability, potential forcing functions including the Hudson River discharge (Figure 16a), New Jersey statewide average air temperatures (not shown), and along-shelf and cross-shelf winds from NDBC Buoy 44009 (Figure 16b) were seasonally averaged for each year. The along-shelf and cross-shelf current response are similarly averaged at several locations across the shelf. At each site, current vectors within a 10 km radius are averaged for each time step before being seasonally averaged. The 10 km radius was chosen to be consistent with the averaging radius used to construct CODAR vector field. Selected seasonal time series at the inner shelf (39.4 N, 73.9 W) and the outer shelf (38.95 N, 73.3 W) sites along the Tuckerton Endurance Line [Castelao *et al.*, 2008b], as well as a midshelf (39.5N, 73.3W) location to the north of the line are plotted in Figures 16c and 16d. The inner shelf site is located on the 30 m isobath near the inshore edge of the coverage area. The midshelf site is located right over the FTS near the 40 m isobath. The outer shelf site is located in between the 60 and 70 m isobaths, inshore of the shelf-slope frontal jet. The sites are chosen to highlight the interannual variability of cross-shelf flow differences.

[44] Both the summer stratified season (red) as well as the winter mixed season (blue) are characterized by consistently offshore flow across the entire shelf with low interannual variability (Figures 16c–16e, solid lines). Despite the large injection of freshwater by the Hudson River during the summer of 2006, the shelf circulation as indicated by the time series in Figure 16 is similar to the other years. For the spring (green), the cross-shelf flow also is usually offshore except for 2003. The anomalous spring of 2003 exhibited colder air temperatures (not shown), higher river discharge, and strong alongshore winds from the NE. It is the only spring with a strong onshore wind (green lines, Figure 16b), and it is the only spring in which a reversal of the cross-shelf flow to onshore at the mid and outer shelf is observed. Cross-shelf flow during autumn (purple) is largest at midshelf and is offshore, with fluctuating weak flows observed at the inshore and offshore sites.

[45] For the alongshore flow during the summer, despite the consistent upwelling favorable winds, the current is usually down shelf at the mid to outer shelf (Figures 16d and 16e, red dashed line). The only flow reversal occurs in 2003 at the midshelf when the summer upwelling wind is strongest (Figure 16b, red dashed line). In contrast to the mid and outer shelf, the summer inner shelf current oscillates around zero (Figure 16c), possibly due to the nearly equal influences of the wind-driven, up-shelf transport and the diminishing shoreward effect of the large-scale along-shelf pressure gradient. In winter, the pattern of alongshore currents on the inner shelf (Figure 16c, blue dashed line) is highly correlated with the pattern of alongshore winds

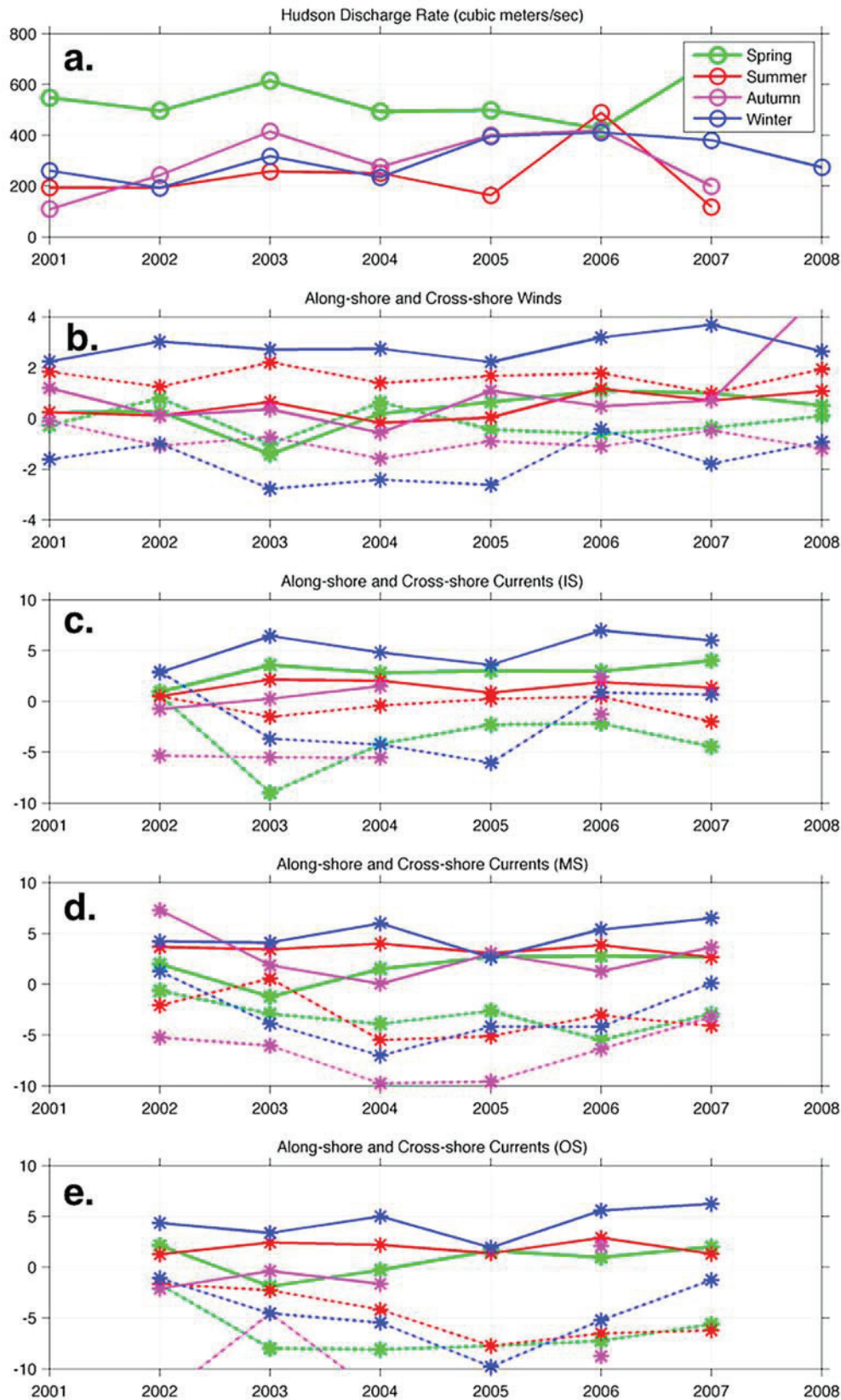


**Figure 16.** (a) Seasonal time series of Hudson River discharge; (b) along-shelf and cross-shelf winds; and mean along-shelf and cross-shelf surface current at the (c) inner shelf, (d) midshelf, and (e) outer shelf. Solid lines are cross-shore (positive is offshore), and dashed lines are along-shore (positive is up shelf). Red is summer, blue is winter, green is spring, and purple is autumn.

**Table 4.** Cross-Shelf Drifter Time, Speed, and Fraction Reaching 60 m Isobath<sup>a</sup>

	Jun 2006	Sep 2006	Dec 2006	Mar 2007	Distance to 60 m
<i>Drifter Time</i>					
Site N	13.6	30.7	23.9	36.1	97
Site C	13.3	20.5	17.4	24.8	82
Site S	12.9	13.1	14.9	27.6	67
<i>Drifter Speed</i>					
Site N	49.9	22.1	28.4	18.8	97
Site C	43.2	28.0	33.0	23.1	82
Site S	36.4	35.8	31.5	21.4	67
<i>Fraction Reaching 60 m</i>					
Site N	0.27	0.09	0.73	0.39	97
Site C	0.68	0.17	0.99	0.71	82
Site S	0.77	0.25	1.00	0.45	67

<sup>a</sup>Time in days, speed in km/week, and distance in km.

(Figure 16b, blue dashed line). A reversal in the winter alongshore current to up shelf at the inner shelf location in 2002, 2006 and 2007 is observed when the alongshore NE winter winds weaken below 2 m/s. At the midshelf, the alongshore current reverses to up shelf in only winter 2002 and summer 2003. Spring along-shelf flow is persistently down shelf. The anomalous 2003 experienced the strongest down-shelf flow at the inner shelf site, consistent with a buoyant river plume driven by high river discharge, the only onshore spring winds, and strong downwelling favorable winds from the NE (Figure 16c). Along-shelf flow is strongest and down shelf in autumn, especially at the midshelf where 2004 and 2005 were especially intense.

#### 4.7. Transport and Residence Time

[46] Understanding the transport pathways and residence time of material is important for addressing many biogeochemical questions on continental shelves. The MAB is highly productive and its biological activity exhibits strong seasonal cycles [Schofield *et al.*, 2008]. Analysis of Eulerian surface current data in sections 4.3–4.5 have shown that circulation on the shelf also has strong seasonal cycles driven by seasonal wind forcing and changing stratification. Given the potential influence of shelf circulation on biogeochemical activities, we want to examine the potential transport pathways and estimate the residence time on the New Jersey Shelf from a Lagrangian perspective. The large spatial coverage area of the CODAR fields, the high temporal resolution, and the long observation duration allow us to capture the advective state of the ocean and use it in a numerical Lagrangian drifter study. To visualize the transport pathways, virtual drifters are deployed in the CODAR fields at various locations on the New Jersey Shelf. The Lagrangian virtual drifter study focuses on the long-range CODAR data from June 2006 to May 2007. This time period has excellent data coverage and as the previous interannual study indicates, does not exhibit anomalous seasonal circulation patterns compared to the other years.

[47] The effect of dispersion in the virtual drifter advection scheme associated the instrument uncertainty and the subgrid-scale variability is estimated using a Markovian random flight model [Griffa, 1996]. Prior applications of this type of drifter dispersion model include the U. S. Coast Guard Search and Rescue (SAR) comparison study of CODAR virtual drifters and actual Self-Locating Datum

Marker Buoys (SLDMB) [Ullman *et al.*, 2006]. The random flight method they used provided search areas that enclose the real drifter approximately 90% of the time in this same CODAR current field. A set of best fit parameters for the U and V components of the turbulent velocity dispersion on the New Jersey Shelf are derived by minimizing the least squared difference between the actual drifters and the virtual drifters. The same methodology and the same set of best fit turbulence parameters from Table 2 of Ullman *et al.* [2006] are used to estimate the combined instrument uncertainty and the subgrid-scale dispersion. The U component of the velocity dispersion  $\sigma_u$  is 11 cm/s and the V component  $\sigma_v$  is 12 cm/s, with the turbulent time scales  $T_u = 3.3$  hours and  $T_v = 3.1$  hours.

[48] The integration of the drifter velocities is formulated using a first-order scheme. The error associated with the first-order integration is the highest for a circular flow field such as that of an eddy. Persistent eddy fields on the shelf, however, are rare. We estimate the advective error for a typical situation and compare with the dispersion error associated with uncertainty in the velocity field. Assuming a current speed of 30 cm/s, a radius of curvature of 50 km as discussed before, and an integration step of 3 hours, the maximum advective error from using a first-order integration scheme for each time step is 0.1 km. On the other hand, assuming a velocity dispersion of 11 cm/s, the random distance per time step of integration (3 hours) is 1.2 km. The numerical error introduced by using a first-order advection scheme is an order of magnitude smaller than the uncertainty associated with subgrid-scale variability for typical flow conditions, justifying its usage.

[49] Two sets of virtual drifter experiments are performed. The first set deploys virtual drifters at three inshore sites to determine the cross-shelf transport pathways and residence times during all four seasons. The amount of time it takes each of the drifters to reach the 60 m isobath is calculated. The three deployment sites are chosen to capture the cross-shelf transport for different parts of the New Jersey Shelf while maximizing the drifters exposure to the high data coverage areas. These locations are consistent with regions of offshore flow seen in the HF Radar data between 2003 and 2004 [Dzwonkowski *et al.*, 2009a]. The northern release site (N) is located on the HSV at (73.66 W, 40.18 N), the central release site (C) is located 20 km offshore of Loveladies, New Jersey (73.85 W, 39.70 N), and the southern release site (S) is situated 30 km offshore of Tuckerton, New Jersey (74.00 W, 39.30 N). The sites are located 97 km, 82 km and 67 km from the 60 m isobath, respectively. One drifter is deployed every 3 hours at each location for 30 days and is then allowed to drift for up to 90 days. Occasional missing CODAR grid points are filled in with the mean current from each 90 day interval. Drifters are stopped once they reach the boundary of the CODAR coverage or the 60 m isobath line. The mean travel time, the cross-shore speed, and the fraction of drifters reaching the 60 m isobath from their release locations are listed in Table 4. Example transport pathways for drifters released at Site C, offshore of Loveladies, are shown for the summer 2006 (Figure 17d) and the winter 2006 (Figure 17a).

[50] For the study period from June 2006 to May 2007, drifters deployed at the inner shelf that reached the outer shelf 60 m isobath took 2 to 5 weeks, traveling at speeds of



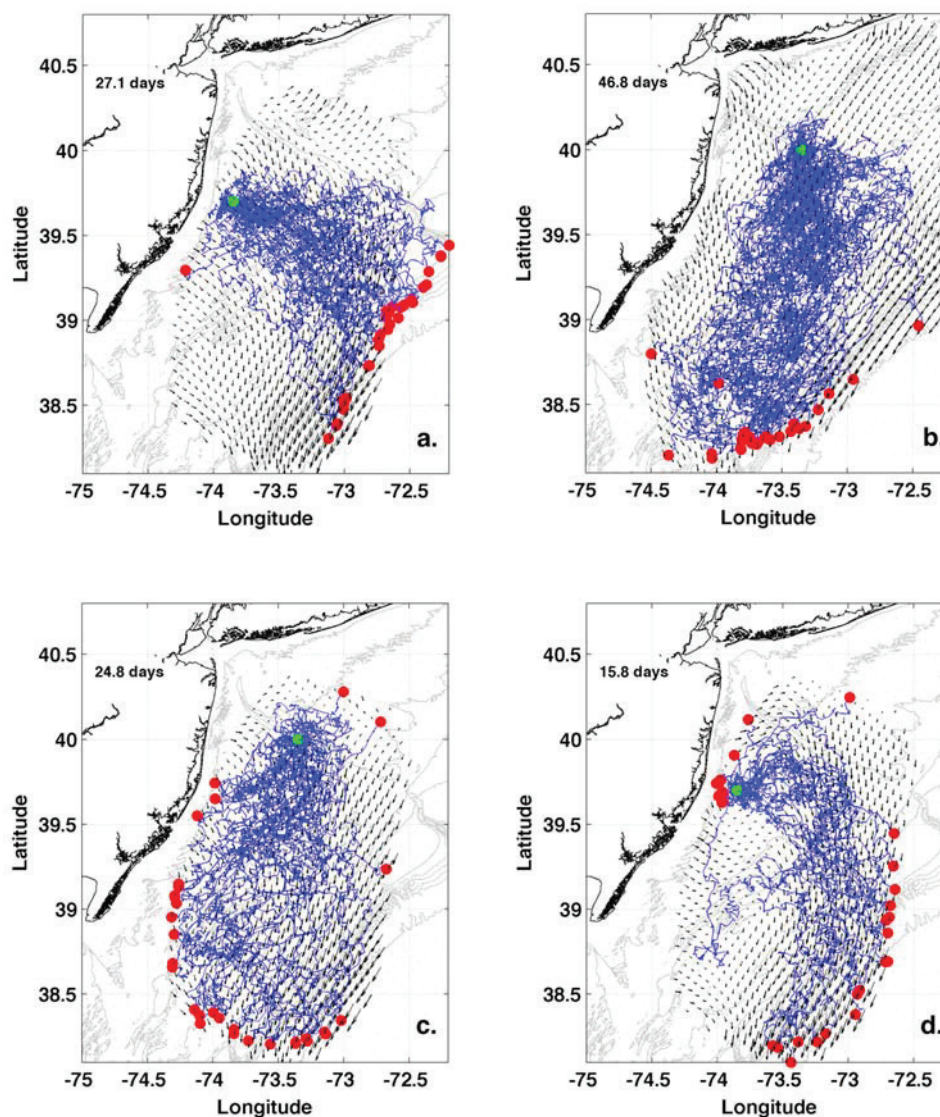


**Figure 17.** Virtual drifter transport study; green dot is deployment location, and red dots are end locations. Mean transport times are printed. (a) Winter (December 2006), (b) spring (March 2007), (c) autumn (September 2006), and (d) summer (June 2006).

19 to 50 km/week. Summer experienced the fastest cross-shelf flow and spring exhibited the slowest (Table 4). Summertime upwelling favorable winds and the winter offshore winds result in the persistent offshore advection of the surface drifters. The majority of the drifters deployed during the stratified summer and well-mixed winter reach the 60 m isobath boundary. During the transition seasons of spring and autumn, a significant fraction of the drifters do not reach the 60 m isobath, instead they exit through the inshore/down-shelf pathway. A particularly interesting feature of summer drifters is that they are often advected up shelf along the inner shelf before moving cross-shelf at the midshelf and eventually veer down shelf near the shelf break. This inverted U-shaped pattern south of the HSV (Figure 17d) is a persistent circulation feature of summer 2006. The average cross-shelf speed of the drifters is 43 km/week, significantly faster than the average winter cross-shelf speed of 31 km/week. The average cross-shelf speed for the

minor fraction of drifters released in spring 2007 and autumn 2006 that do make it across to the 60 m isobath are 21 km/week and 29 km/week, respectively. There is large scatter in the actual traversal time of individual drifters. Some of the virtual drifters can cross the shelf in a week whereas others can take over a month. The summer drifter paths show less spatial scatter compared to the paths of the winter drifters.

[51] The second set of drifter experiments focuses on illustrating the residence time and transport pathways during the transition seasons of spring and autumn. Spring and autumn mean fields are generally dominated by along-shelf flow on the New Jersey Shelf. Drifters are released at a site situated over the HSV (73.35 W, 40.00 N) for two seasons at the beginning of spring (March 2007; Figure 17b) and the beginning of autumn (September 2006; Figure 17c). The drifter deployment location is chosen to maximize their data exposure in the along-shelf direction. The spring drifters take an average of a month and half to travel the length of

the New Jersey Shelf with relatively little scatter despite the month long release schedule (Figure 17b). The average along-shelf velocity for the spring drifters is approximately 25 km/week. Recall that NE winds become more frequent during the spring time. When the wind is from the NE, the surface flow is predominantly down shelf and alongshore. For autumn, winds from the SW, NW and NE all occur about the same percentage of time although NE winds generate the most energetic flows. While the different wind conditions of autumn likely cause the drifters to follow more scattered paths, the drifters still exhibit a clear alongshore down-shelf movement (Figure 17c). Drifters deployed during the month of September 2006, for example, show a variety of down-shelf transport pathways, some exit the study region at the inner shelf, some head down at midshelf while others are exported toward the shelf break. Despite the more scattered drift paths, however, the autumn drifters move at a significantly faster speed down the shelf, taking approximately 3–4 weeks at an average speed of 44 km/week, nearly twice as fast compared to the spring season. On average the along-shelf transport time scale for the transition seasons is the same as the cross-shelf transport time scale for the stratified and mixed seasons on the New Jersey Shelf.

## 5. Discussion

[52] Large-scale background flow, local shelf topography, changes in stratification and wind forcing influence the spatial and temporal transport patterns on the New Jersey shelf. The surface flow under various wind and stratification regimes display both coherent large-scale patterns as well as small-scale variability. Shelf-scale wind forcing and background flow determines the large-scale patterns of along-shelf or cross-shelf transport while local topography modulates the direction and magnitude of the flow near the HSV/FTS region. The different forcing mechanisms come together such that during the transition seasons of spring and autumn, the surface transport on the shelf is primarily alongshore and down shelf while during the stratified summer and mixed winter seasons the surface transport on the shelf is primarily cross-shelf and offshore. Through the annual cycle the location of the down-shelf transport shifts. During the transition seasons of the autumn and spring down-shelf flow stretches across the entire shelf. During the winter and summer seasons, the down-shelf flow is pushed offshore along the shelf break, fed by the flow of the inner and midshelf.

[53] Such seasonal shift in circulation pattern could affect the rate of volume transport on the shelf. Previous studies of MAB watermasses showed that the volume of the shelf water can vary seasonally with a magnitude on the order of the mean volume [Manning, 1991; Mountain, 2003]. Shelf water, defined to be water with salinity less than 34, reaches a maximum southwestward extent during the summer and retreats to a minimum volume during the winter [Mountain, 2003]. We observed that the seasons of maximum and minimum shelf water volume are characterized by mainly cross-shelf transport, whereas seasons with the maximum change in the shelf water volume are characterized by mainly along-shelf transport. The seasonal cycle of shelf water volume was attributed to a change in the influx of the Scotian Shelf Water [Manning, 1991]. A study by [Lentz, 2008b]

using moored current meter data from the central MAB found that the magnitude of the seasonal variability of the along-shelf depth-averaged flow to be comparable to the mean, on the order of 4–6 cm/s. He attributed such variability to wind forcing, river discharge and the seasonal cycle of the cross-shelf density gradient over the shelf. We note that during the transition seasons of spring and autumn, when the maximum change in the shelf water volume in the central MAB occurs, alongshore NE winds also become more common (Figures 10b and 12b) and they appear to drive strong along-shelf surface flow and transport (Figures 8b, 8c, 17b, and 17c). During the summer stratified season and the winter mixed season, the New Jersey Shelf switches from an along-shelf flow regime to a cross-shelf flow regime. The cross-shelf surface flow, evident in both the seasonal mean fields (Figures 8a and 8d) and the Lagrangian drifter maps (Figures 17a and 17d), suggests a surface export from the shelf which must be balanced by a return onshore flow at depth as is the case with the inner shelf [Fewings *et al.*, 2008]. Such cross-shelf circulation patterns would imply that cross-shore shelf-slope exchange is enhanced during the winter and summer periods.

[54] Over the interannual time scale, the seasonal mean along-shelf and cross-shelf flow for each year closely follows the 6 year mean from 2002 to 2007. No long-term trends in the transport were observed at various cross-shelf locations. However, there are anomalous seasons for some of the years. For example, the spring of 2003 had higher Hudson River discharge, colder air temperature, more frequent NE winds and bigger down-shelf, inner shelf flow than the other years. This was a particularly stormy spring that could have delayed the onset of seasonal stratification and the timing of the spring bloom. The summer of 2006 had very high seasonal Hudson River discharge but the flow velocity at the inner, mid and outer shelf are not significantly different from the other years. Shifts in the seasonal wind pattern over the longer time scale, such as those associated with the Atlantic Multi-decadal Oscillation (AMO) [Delworth and Mann, 2000; Kerr, 2000], could affect the seasonal shelf circulation as well as the biological response. A shift in the phase of the AMO from negative to positive took place in the mid-1990s [Schofield *et al.*, 2008]. Analysis of the decadal pattern in wind variability and changes in biological productivity have shown that the negative phase of the AMO is associated with weaker winter winds and higher productivity whereas positive phase of the AMO is associated with stronger winter winds and lower productivity [Schofield *et al.*, 2008]. Cross-shelf flow is significantly correlated with cross-shore and along-shore wind forcing at the midshelf during winter and summer, respectively (Figure 14). We therefore expect that during the years when the seasonal winter wind forcing is weak, there will be a weaker cross-shelf surface transport over the New Jersey Shelf. On the decadal time scale, we expect to see stronger wintertime cross-shelf transport during the present positive phase of the AMO and weaker wintertime cross-shelf transport during the negative phase of the AMO.

[55] The different flow patterns for each of the seasons on the New Jersey Shelf are likely to have important implications for physical transport-dependent biological processes such as shelf primary production [Schofield *et al.*, 2008; Y. Xu *et al.*, manuscript in preparation, 2009] and recruitment



dynamics of key shelf fish species [Nelson *et al.*, 1977; Werner *et al.*, 1997; Hare *et al.*, 1999; Quinlan *et al.*, 1999].

## 6. Summary

[56] Here we study the spatial and temporal variability of the surface flow on the New Jersey Shelf over a six year period from 2002 to 2007. The mean surface flow on the New Jersey Shelf is equatorward and offshore toward the south. The flow is significantly affected by bottom topography, stratification and wind forcing on the monthly to annual time scales. A band of higher-velocity cross-shelf flow exists in the mean field just south of the Hudson Shelf Valley, indicating that the valley exerts a dynamical influence on the surface flow at the longest time scales. Furthermore, the HSV acts as a dynamical boundary between flow to the north and flow to the south. Divergent flow is observed over the HSV and to the north whereas convergent flow is observed just to the south. The shelf undergoes large changes in stratification from well mixed during the winter to highly stratified during the summer. The response of the surface flow is characterized for the dominant wind conditions of the different seasons. The angle between wind stress and surface current is larger when the water column is more stratified and it exceeds Ekman theory at the mid to outer shelf. The angle is small ( $<25^\circ$ ) when the water column is well mixed. On the seasonal time scale, the surface flow oscillates between being along-shelf dominated during the transition seasons of spring and autumn and cross-shelf dominated during the stratified and well-mixed seasons of winter and summer. Cross correlation of winds and currents along a cross-shelf transect south of the Tuckerton Endurance Line show that the winter cross-shelf flow is highly correlated with cross-shore winds dominated by the NW winds, and the summer cross-shelf flow is highly correlated with along-shore winds dominated by the SW winds. Flows during the transition seasons are mainly along-shelf and they are correlated with the along-shore NE winds. From a Lagrangian perspective, the summer and winter drifters move predominantly cross-shelf. They make their way across the shelf over the period of 2 to 5 weeks. Spring drifters travel mainly alongshore and take 4–7 weeks to travel the along-shore distance of the New Jersey Shelf. Autumn drifters move and scatter on the shelf rapidly due to the energetic surface flow often driven by storms; their paths can scatter over the whole shelf and the drifters can exit the New Jersey Shelf via a variety of pathways at the inner, mid and outer shelf in a month or less. Physical transport can affect shelf biology over temporal scales from days to decades. Changes in wind strength associated with decadal shift in climate pattern can drive changes in the cross-shelf and along-shelf transport which can potentially affect shelf primary production and recruitment dynamics of key MAB fish species.

[57] **Acknowledgments.** The authors are thankful for helpful comments and suggestions from Renato Castelao, Robert Chant, Glen Gawarkiewicz, Elias Hunter, John Manderson, Patricia Ramey, Oscar Schofield, and John Wilkin. The authors would especially like to thank the RUCOOL operational team led by Hugh Roarty who has worked extremely hard to keep the HF Radar network up and running during the long study period. The HF Radar network used in this study was supported by the Office of Naval Research (ONR), the National Oceanic and Atmospheric Administration (NOAA), the Department of Homeland

Security (DHS), the National Science Foundation (NSF), the Department of Defense (DoD), and the National Oceanographic Partnership Program (NOPP). The research was supported by the Office of Naval Research grants Shallow Water 2006 N00014-06-1-0283 and Nonlinear Internal Wave Initiative N00014-08-1-0373.

## References

- Allen, J. S. (1980), Models of wind-driven currents on the continental shelf, *Annu. Rev. Fluid Mech.*, 12(1), 389–433, doi:10.1146/annurev.fl.12.010180.002133.
- Allen, J. S., and R. L. Smith (1981), On the dynamics of wind-driven shelf currents, *Philos. Trans. R. Soc. London Ser. A*, 302(1472), 617–634.
- Barrick, D. E. (1971a), Theory of HF/VHF propagation across the rough sea: 1. The effective surface impedance for a slightly rough highly conducting medium at grazing incidence, *Radio Sci.*, 6, 517–526.
- Barrick, D. E. (1971b), Theory of HF/VHF propagation across the rough sea: 2. Application to HF/VHF propagation above the sea, *Radio Sci.*, 6, 527–533.
- Beardsley, R. C., and W. C. Boicourt (1981), On estuarine and continental-shelf circulation in the Middle Atlantic Bight, in *Evolution of Physical Oceanography: Scientific Surveys in Honor of Henry Stommel*, edited by B. A. Warren and C. Wunsch, pp. 198–235, MIT Press, Cambridge, Mass.
- Beardsley, R. C., and C. D. Winant (1979), On the mean circulation in the Mid-Atlantic Bight, *J. Phys. Oceanogr.*, 9(3), 612–619.
- Beardsley, R. C., W. C. Boicourt, and D. Hanson (1976), Physical oceanography of the Mid-Atlantic Bight, *Spec. Symp. Am. Soc. Limnol. Oceanogr.*, 2, 20–34.
- Beardsley, R. C., D. C. Chapman, K. H. Brink, S. R. Ramp, and R. Schlitz (1985), The Nantucket Shoals Flux Experiment (NSFE79). Part I: A basic description of the current and temperature variability, *J. Phys. Oceanogr.*, 15(6), 713–748.
- Bigelow, H. B. (1933), Studies of the waters on the continental shelf, Cape Cod to Chesapeake Bay. I. The cycle of temperature, *Pap. Phys. Oceanogr. Meteorol.*, 2(4), 1–135.
- Bigelow, H. B., and M. Sears (1935), Studies of the waters on the continental shelf, Cape Cod to Chesapeake Bay. II. Salinity, *Pap. Phys. Oceanogr. Meteorol.*, 4(1), 1–94.
- Biscaye, P. E., C. N. Flagg, and P. G. Falkowski (1994), The shelf edge exchange processes experiment, Seep-II: An introduction to hypotheses, results and conclusions, *Cont. Shelf Res.*, 41(2–3), 231–252.
- Bumpus, D. F. (1973), A description of the circulation on the continental shelf of the east coast of the United States, *Prog. Oceanogr.*, 6, 111–157.
- Byoung-Ju, C., and J. L. Wilkin (2007), The effect of wind on the dispersal of the Hudson River Plume, *J. Phys. Oceanogr.*, 37(7), 1878–1897.
- Castelao, R., O. Schofield, S. Glenn, R. Chant, and J. Kohut (2008a), Cross-shelf transport of freshwater on the New Jersey Shelf, *J. Geophys. Res.*, 113, C07017, doi:10.1029/2007JC004241.
- Castelao, R., S. Glenn, O. Schofield, R. Chant, J. Wilkin, and J. Kohut (2008b), Seasonal evolution of hydrographic fields in the central Middle Atlantic Bight from glider observations, *Geophys. Res. Lett.*, 35, L03617, doi:10.1029/2007GL032335.
- Chant, R. J., S. M. Glenn, E. Hunter, J. Kohut, R. F. Chen, R. W. Houghton, J. Bosch, and O. Schofield (2008), Bulge formation of a buoyant river outflow, *J. Geophys. Res.*, 113, C01017, doi:10.1029/2007JC004100.
- Chapman, D. C., and R. C. Beardsley (1989), On the origin of shelf water in the Middle Atlantic Bight, *J. Phys. Oceanogr.*, 19(3), 384–391.
- Chapman, D. C., and H. C. Graber (1997), Validation of HF radar measurements, *Oceanography*, 10, 76–79.
- Chapman, D. C., and S. J. Lentz (1994), Trapping of a coastal density front by the bottom boundary-layer, *J. Phys. Oceanogr.*, 24(7), 1464–1479.
- Churchill, J. H., J. P. Manning, and R. C. Beardsley (2003), Slope water intrusions onto Georges Bank, *J. Geophys. Res.*, 108(C11), 8012, doi:10.1029/2002JC001400.
- Csanady, G. T. (1976), Mean circulation in shallow seas, *J. Geophys. Res.*, 81(6), 5389–5399.
- Delworth, T. L., and M. E. Mann (2000), Observed and simulated multidecadal variability in the Northern Hemisphere, *Clim. Dyn.*, 16(9), 661–676, doi:10.1007/s003820000075.
- Dzwonkowski, B., J. T. Kohut, and X. H. Yan (2009a), Sub-inertial characteristics of the surface flow field over the shelf of the central Mid-Atlantic Bight, *Cont. Shelf Res.*, 29, 1873–1886.
- Dzwonkowski, B., J. T. Kohut, and X. H. Yan (2009b), Seasonal differences in wind-driven across-shelf forcing and response relationships in the shelf surface layer of the central Mid-Atlantic Bight, *J. Geophys. Res.*, 114, C08018, doi:10.1029/2008JC004888.
- Ekman, V. W. (1905), On the influence of the Earth's rotation on ocean current, *Ark. Mat. Astron. Fys.*, 2, 1–53.



- Fewings, M., S. J. Lentz, and J. Fredericks (2008), Observations of cross-shelf flow driven by cross-shelf winds on the inner continental shelf, *J. Phys. Oceanogr.*, **38**(11), 2358–2378.
- Flagg, C. N., R. W. Houghton, and L. J. Pietrafesa (1994), Summertime thermocline salinity maximum intrusions in the Mid-Atlantic Bight, *Deep Sea Res. Part II*, **41**(2–3), 325–340.
- Flagg, C. N., L. J. Pietrafesa, and G. L. Weatherly (2002), Springtime hydrography of the southern Middle Atlantic Bight and the onset of seasonal stratification, *Deep Sea Res. Part II*, **49**(20), 4297–4329.
- Flagg, C. N., M. Dunn, D. P. Wang, H. T. Rossby, and R. L. Benway (2006), A study of the currents of the outer shelf and upper slope from a decade of shipboard ADCP observations in the Middle Atlantic Bight, *J. Geophys. Res.*, **111**, C06003, doi:10.1029/2005JC003116.
- Fong, D. A., and W. R. Geyer (2001), Response of a river plume during an upwelling favorable wind event, *J. Geophys. Res.*, **106**, 1067–1084.
- Garvine, R. W. (2004), The vertical structure and subtidal dynamics of the inner shelf off New Jersey, *J. Mar. Res.*, **62**(3), 337–371.
- Gawarkiewicz, G., and D. C. Chapman (1992), The role of stratification in the formation and maintenance of shelf-break fronts, *J. Phys. Oceanogr.*, **22**(7), 753–772.
- Gawarkiewicz, G., T. G. Ferdelman, T. M. Church, and G. W. Luther (1996), Shelfbreak frontal structure on the continental shelf north of Cape Hatteras, *Cont. Shelf Res.*, **16**(14), 1751–1773.
- Gawarkiewicz, G., F. Bahr, R. C. Beardsley, and K. H. Brink (2001), Interaction of a slope eddy with the shelf break front in the Middle Atlantic Bight, *J. Phys. Oceanogr.*, **31**(9), 2783–2796.
- Glenn, S., and O. Schofield (2009), Growing a distributed ocean observatory: Our view from the COOLroom, *Oceanography*, **22**(2), 112–129.
- Glenn, S., et al. (2004), Biogeochemical impact of summertime coastal upwelling on the New Jersey Shelf, *J. Geophys. Res.*, **109**, C12S02, doi:10.1029/2003JC002265.
- Glenn, S., C. Jones, M. Twardowski, L. Bowers, J. Kerfoot, J. Kohut, D. Webb, and O. Schofield (2008), Glider observations of sediment resuspension in a Middle Atlantic Bight fall transition storm, *Limnol. Oceanogr.*, **53**(5), 2180–2196.
- Gong, D., S. Glenn, R. Chant, J. Wilkin, and J. Kohut (2006), NJ Turnpike—Dynamics of the Hudson Shelf Valley, *Eos Trans. AGU*, **87**(36), Ocean Sci. Meet. Suppl., Abstract OS34I-05.
- Griffa, A. (1996), Applications of stochastic particle models to oceanographic problems, in *Stochastic Modelling in Physical Oceanography*, vol. 113, edited by R. J. Adler, P. Muller, and B. Rozovskii, Birkhauser, Boston.
- Hare, J. A., J. A. Quinlan, F. E. Werner, B. O. Blanton, J. J. Govoni, R. B. Forward, L. R. Settle, and D. E. Hoss (1999), Larval transport during winter in the SABRE study area: Results of a coupled vertical larval behaviour—three-dimensional circulation model, *Fish. Oceanogr.*, **8**, 57–76.
- Hare, J. A., J. H. Churchill, R. K. Cowen, T. J. Berger, P. C. Cornillon, P. Dragos, S. M. Glenn, J. J. Govoni, and T. N. Lee (2002), Routes and rates of larval fish transport from the southeast to the northeast United States continental shelf, *Limnol. Oceanogr.*, **47**(6), 1774–1789.
- Harris, C. K., B. Butman, and P. Traykovski (2003), Winter-time circulation and sediment transport in the Hudson Shelf Valley, *Cont. Shelf Res.*, **23**(8), 801–820.
- Hunter, E., R. Chant, L. Bowers, S. Glenn, and J. Kohut (2007), Spatial and temporal variability of diurnal wind forcing in the coastal ocean, *Geophys. Res. Lett.*, **34**, L03607, doi:10.1029/2006GL028945.
- Keen, T. R., and S. M. Glenn (1994), A coupled hydrodynamic-bottom boundary layer model of Ekman flow on stratified continental shelves, *J. Phys. Oceanogr.*, **24**(8), 1732–1749.
- Keen, T. R., and S. M. Glenn (1995), A coupled hydrodynamic-bottom boundary layer model of storm and tidal flow in the Middle Atlantic Bight of North America, *J. Phys. Oceanogr.*, **25**(3), 391–406.
- Kerr, R. A. (2000), A North Atlantic climate pacemaker for the centuries, *Science*, **288**(5473), 1984–1985, doi:10.1126/science.288.5473.1984.
- Knebel, H. J., and E. C. Spiker (1977), Thickness and age of surficial sand sheet, Baltimore Canyon Trough area, *Am. Assoc. Pet. Geol. Bull.*, **61**, 861–871.
- Kohut, J. T., S. M. Glenn, and R. J. Chant (2004), Seasonal current variability on the New Jersey inner shelf, *J. Geophys. Res.*, **109**, C07S07, doi:10.1029/2003JC001963.
- Kohut, J. T., S. M. Glenn, and J. D. Paduan (2006a), Inner shelf response to Tropical Storm Floyd, *J. Geophys. Res.*, **111**, C09S91, doi:10.1029/2003JC002173.
- Kohut, J. T., H. J. Roarty, and S. M. Glenn (2006b), Characterizing observed environmental variability with HF Doppler radar surface current mappers and acoustic Doppler current profilers: Environmental variability in the coastal ocean, *IEEE J. Oceanic Eng.*, **31**(4), 876–884.
- Lentz, S. J. (2001), The influence of stratification on the wind-driven cross-shelf circulation over the North Carolina Shelf, *J. Phys. Oceanogr.*, **31**(9), 2749–2760.
- Lentz, S. J. (2003), A climatology of salty intrusions over the continental shelf from Georges Bank to Cape Hatteras, *J. Geophys. Res.*, **108**(C10), 3326, doi:10.1029/2003JC001859.
- Lentz, S. J. (2008a), Observations and a model of the mean circulation over the Middle Atlantic Bight continental shelf, *J. Phys. Oceanogr.*, **38**(6), 1203–1221.
- Lentz, S. J. (2008b), Seasonal variations in the circulation over the Middle Atlantic Bight continental shelf, *J. Phys. Oceanogr.*, **38**(7), 1486–1500.
- Lentz, S. J., and J. H. Trowbridge (1991), The bottom boundary layer over the northern California Shelf, *J. Phys. Oceanogr.*, **21**(8), 1186–1201.
- Linder, C. A., and G. Gawarkiewicz (1998), A climatology of the shelf break front in the Middle Atlantic Bight, *J. Geophys. Res.*, **103**(C9), 18,405–18,423.
- Madsen, O. S. (1977), A realistic model of the wind-induced Ekman boundary layer, *J. Phys. Oceanogr.*, **7**(2), 248–255.
- Manning, J. (1991), Middle Atlantic Bight salinity: Interannual variability, *Cont. Shelf Res.*, **11**(2), 123–137.
- Mooers, C. N. K., J. Fernandez-Partagas, and J. F. Price (1976), Meteorological forcing fields of the New York Bight (first year's progress report), technical report, Univ. of Miami, Coral Gables, Fla.
- Mountain, D. G. (2003), Variability in the properties of shelf water in the Middle Atlantic Bight, 1977–1999, *J. Geophys. Res.*, **108**(C1), 3014, doi:10.1029/2001JC001044.
- Nelson, W. R., M. C. Ingham, and W. E. Schaaf (1977), Larval transport and year-class strength of Atlantic menhaden, *Brevoortia tyrannus*, *U.S. Natl. Mar. Fish. Serv. Fish. Bull.*, **75**, 23–41.
- Ohlmann, C., P. White, L. Washburn, E. J. Terrill, B. Emery, and M. P. Otero (2007), Interpretation of coastal HF radar-derived surface currents with high-resolution drifter data, *J. Atmos. Oceanic Technol.*, **24**, 666–680, doi:10.1175/JTECH1998.1.
- Pawlowicz, R., R. C. Beardsley, and S. J. Lentz (2002), Classical tidal harmonic analysis including error estimates in MATLAB using T\_TIDE, *Comput. Geosci.*, **28**, 929–937.
- Perlin, A., J. N. Moum, and J. M. Klymak (2005), Response of the bottom boundary layer over a sloping shelf to variations in alongshore wind, *J. Geophys. Res.*, **110**, C10S09, doi:10.1029/2004JC002500.
- Quinlan, J. A., B. O. Blanton, T. J. Miller, and F. E. Werner (1999), From spawning grounds to the estuary: Using linked individual-based and hydrodynamic models to interpret patterns and processes in the oceanic phase of Atlantic menhaden *Brevoortia tyrannus* life history, *Fish. Oceanogr.*, **8**, 224–246.
- Schofield, O., et al. (2008), The decadal view of the Mid-Atlantic Bight from the COOLroom: Is our coastal system changing?, *Oceanography*, **23**(4), 108–117.
- Song, T., D. B. Haidvogel, and S. M. Glenn (2001), Effects of topographic variability on the formation of upwelling centers off New Jersey: A theoretical model, *J. Geophys. Res.*, **106**(C5), 9223–9240.
- Stewart, R. H., and J. W. Joy (1974), HF radio measurements of surface currents, *Deep Sea Res. Part I*, **21**, 1039–1049.
- Tang, D., et al. (2009), Shallow Water '06—A joint acoustic propagation/nonlinear internal wave physics experiment, *Oceanography*, **20**(4), 156–167.
- Teague, C. C. (1971), High frequency resonant scattering techniques for the observation of directional ocean-wave spectra, Ph.D. thesis, Stanford Univ., Palo Alto, Calif.
- Thieler, E. R., B. Butman, W. C. Schwab, M. A. Allison, N. W. Driscoll, J. P. Donnelly, and E. Uchupi (2007), A catastrophic meltwater flood event and the formation of the Hudson Shelf Valley, *Palaeogeogr. Palaeoclim. Palaeoecol.*, **246**(1), 120–136, doi:10.1016/j.palaeo.2006.10.030.
- Tilburg, C. E. (2003), Across-shelf transport on a continental shelf: Do across-shelf winds matter?, *J. Phys. Oceanogr.*, **33**(12), 2675–2688.
- Trowbridge, J., and S. Lentz (1991), Asymmetric behavior of an oceanic boundary layer above a sloping bottom, *J. Phys. Oceanogr.*, **21**(8), 1171–1185.
- Ullman, D. S., J. O'Donnell, J. Kohut, T. Fake, and A. Allen (2006), Trajectory prediction using HF radar surface currents: Monte Carlo simulations of prediction uncertainties, *J. Geophys. Res.*, **111**, C12005, doi:10.1029/2006JC003715.
- Werner, F. E., J. A. Quinlan, B. O. Blanton, and R. A. Luetich (1997), The role of hydrodynamics in explaining variability in fish populations, *J. Sea Res.*, **37**(3–4), 195–212, doi:10.1016/S1385-1101(97)00024-5.
- Whitney, M. M., and R. W. Garvine (2005), Wind influence on a coastal buoyant outflow, *J. Geophys. Res.*, **110**, C03014, doi:10.1029/2003JC002261.
- Winant, C. D. (1980), Coastal circulation and wind-induced currents, *Annu. Rev. Fluid Mech.*, **12**(1), 271–301, doi:10.1146/annurev.fl.12.010180.001415.

- Yankovsky, A. E., and R. W. Garvine (1998), Subinertial dynamics on the inner New Jersey Shelf during the upwelling season, *J. Phys. Oceanogr.*, 28(12), 2444–2458.
- Yankovsky, A. E., R. W. Garvine, and A. Münchow (2000), Mesoscale currents on the inner New Jersey Shelf driven by the interaction of buoyancy and wind forcing, *J. Phys. Oceanogr.*, 30(9), 2214–2230.
- Yoder, J. A., S. E. Schollaert, and J. E. O'Reilly (2002), Climatological phytoplankton chlorophyll and sea surface temperature patterns in continental shelf and slope waters off the northeast US coast, *Limnol. Oceanogr.*, 47(3), 672–682.
- Zhang, W. G., J. L. Wilkin, and R. J. Chant (2009), Modeling the pathways and mean dynamics of river plume dispersal in the New York Bight, *J. Phys. Oceanogr.*, 39, 1167–1183.

---

S. M. Glenn, D. Gong, and J. T. Kohut, Institute of Marine and Coastal Sciences, Rutgers-State University of New Jersey, 71 Dudley Rd., New Brunswick, NJ 08901, USA. (glenn@marine.rutgers.edu; donglai@marine.rutgers.edu; kohut@marine.rutgers.edu)





# High-frequency forcing and subtidal response of the Hudson River plume

Elias J. Hunter,<sup>1</sup> Robert J. Chant,<sup>1</sup> John L. Wilkin,<sup>1</sup> and Josh Kohut<sup>1</sup>

Received 6 July 2009; revised 5 February 2010; accepted 8 March 2010; published 21 July 2010.

[1] The Lagrangian Transport and Transformation Experiments (LaTTE) document the physical, biological, and chemical evolution of the Hudson River plume during the spring seasons of 2004, 2005, and 2006. While plume variability due to river discharge, subinertial frequency variability in winds, and ambient shelf circulation are important, the observations show that the plume reacts directly to higher-frequency forcing as well. Mooring records during 2005 and 2006 show that fortnightly variability in tidal mixing is manifested as fortnightly changes in plume stratification. Diurnal variability related to forcing by the sea-land breeze system (SLBS) is apparent in the Hudson River plume during the 2005 experiment. The SLBS, while episodic, accounts for ~15% of the kinetic energy in surface currents in the New York Bight apex during the summer months with individual SLBS events providing up to 50% of the total kinetic energy. Simulations of the plume, using the Regional Ocean Modeling System (ROMS), demonstrate there is a subtidal response to high-frequency forcing. Spring-neap variability in tidal mixing modifies the estuary outflow Rossby and Froude numbers, resulting in increased transport (80% of river discharge) in the New Jersey coastal current during spring tides with lower transport (60% of river discharge) during neap tides. SLBS variability results in greater storage of river discharge water in the recirculating bulge region and increases the net transport of freshwater along the Long Island coast while significantly reducing freshwater supplied to the New Jersey coastal current to as little as 30% of the total river discharge.

**Citation:** Hunter, E. J., R. J. Chant, J. L. Wilkin, and J. Kohut (2010), High-frequency forcing and subtidal response of the Hudson River plume, *J. Geophys. Res.*, *115*, C07012, doi:10.1029/2009JC005620.

## 1. Introduction

[2] River discharge to the inner continental shelf influences variability across a range of time scales in many coastal ocean regions worldwide. The large freshwater flux associated with rivers (particularly during the spring freshet) leads to the development of well-documented hydrographic features such as fronts, jets, and recirculating eddies on the inner shelf [Castelao *et al.*, 2008; Orton and Jay, 2005]. In addition, river plumes can play a first-order role in the transport and dispersal of sediment, biota, nutrients, and anthropogenic contamination in the coastal zone. This has implications for coastal biological and chemical processes and is particularly relevant in a highly urbanized estuary such as the Hudson River [Levinton and Waldman, 2006].

[3] These buoyant river plumes are often classified according to their dominant dynamical balance and divided into two groups depending on their interaction with the

ocean bottom [Avicola and Huq, 2002; Lentz and Helfrich, 2002; Yankovsky and Chapman, 1997]. The “bottom-advected” plume has low-salinity water extending from the surface to the bottom. The plumes momentum drives an offshore buoyancy flux in the bottom Ekman layer that produces a well-defined bottom-attached front that isolates the inshore plume from the offshore waters. The offshore location of this front and the isobath that it resides on is often well predicted by theory [Chapman and Lentz, 1994]. The “surface-advected” plume, on the other hand, is a shallow buoyant layer overlaying a more dense background fluid and has little or no direct interaction with the seafloor. For the purposes of this study, we restrict discussion to surface-advected plumes, which typically characterizes the Hudson River plume [Avicola and Huq, 2002; Chant *et al.*, 2008; Yankovsky and Chapman, 1997].

[4] Numerical modeling studies and laboratory tank experiments demonstrate that the idealized surface-advected plume has two distinct dynamic regions: a coastal gravity current that propagates down shelf (in the Kelvin wave sense) and a recirculating low-salinity “bulge” near the river outflow [Avicola and Huq, 2003a, 2003b; Chao and Boiucourt, 1986; Chapman and Lentz, 1994; Fong and Geyer, 2002; Nof and Pichevin, 2001]. The cross-shore dynamics of the coastal current are primarily geostrophic, while those of the

<sup>1</sup>Institute for Marine and Coastal Sciences, Rutgers, State University of New Jersey, New Brunswick, New Jersey, USA.

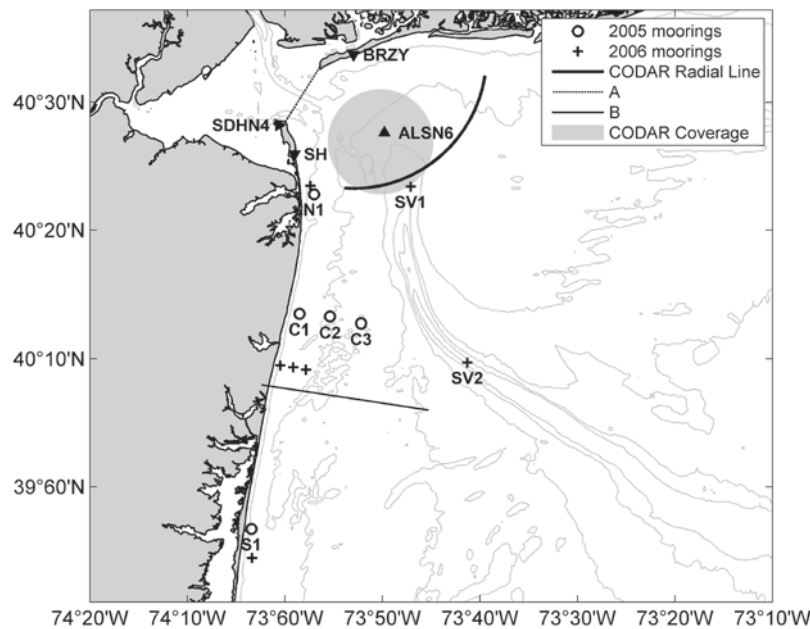


**Figure 1.** The above map shows the locations of observational data stations in the LaTTE study area. Included are the CODAR installations at Sandy Hook (SH) and Breezy Point (BRZY), NBDC stations at Sandy Hook (SDHN4) and Ambrose Tower (ALSN6), and the mooring locations during LaTTE 2005 and 2006. Also noted are a CODAR radial arc from BRZY and the approximate footprint of CODAR coverage for BRZY and SH. Lines A and B are the locations of cross sections extracted from ROMS simulations.

anticyclonically rotating bulge are weakly cyclostrophic, whereby the cross-stream pressure gradient is balanced by the sum of Coriolis and centrifugal accelerations.

[5] The extensive literature on buoyant river plumes identify, through characteristic length scales and nondimensional numbers, regimes describing plume spatial and temporal variability and highlight the important dynamical balances of the river outflow. *Garvine* [1995] classifies buoyant plumes according to a Kelvin number, which is the ratio of the cross-shore length scale of the coastal current to the baroclinic Rossby radius. Coastal currents with small Kelvin number are dominated by nonlinear momentum advection terms with little contribution from the Coriolis effect, while large Kelvin number flows are associated with weak advection and relatively strong Coriolis terms. *Yankovsky and Chapman* [1997] derived length scales (plume width and depth) from the basic dynamics of surface-advected and bottom-advected plumes and further framed these scales as Froude ( $F_i$ ), Rossby ( $R_o$ ), and Rossby ( $S$ ) numbers, defined as

$$F_i = v_i / (g'_i h_o)^{1/2}, \quad (1)$$

$$R_o = v_i / fL, \quad (2)$$

$$S = R_o / F_i, \quad (3)$$

where  $v_i$  is the mean outflow velocity,  $g'_i$  is reduced gravity ( $g'_i = g\Delta\rho/\rho_o$ ),  $f$  is the Coriolis parameter, and  $L$  is the width of the outflow.

[6] The resulting parameter space is useful in determining whether a plume is surface or bottom advected based on inflow properties and bottom slope. *Yankovsky and Chapman* [1997] applied the scaling framework to a series of numerical model runs and observational data, noting that the Hudson River plume is surface advected, as did *Avicola and Huq* [2002].

[7] The recirculating bulge region of a surface-advected plume is documented in many laboratory experiments and numerical simulations of buoyant river plumes [*Avicola and Huq*, 2003a, 2003b; *Fong and Geyer*, 2002; *Horner-Devine et al.*, 2006; *Nof and Pichevin*, 2001; *Yankovsky and Chapman*, 1997; *Garvine*, 2001]. While the underlying dynamics that govern the rate of bulge growth remains elusive, both *Avicola and Huq* [2003a, 2003b] and *Horner-Devine et al.* [2006] suggest that outflow geometry plays a central role in bulge formation. There is, however, little observational evidence. While the recirculating bulge region of a river plume is more difficult to observe fully in nature, there is ample evidence of the feature in the Hudson River plume [*Chant et al.*, 2008], the Columbia River plume [*Horner-Devine*, 2008; *Hickey et al.*, 1998] and the Niagara River plume [*Masse and Murthy*, 1990, 1992; *Horner-Devine et al.*, 2008]. The Hudson River mouth has a particularly complicated coastal geometry (Figure 1), which has been shown should favor bulge formation [*Avicola and Huq*, 2003b].

[8] The theory of *Yankovsky and Chapman* [1997] assumes a steady state bulge, but both laboratory and numerical simulations suggest that bulges are unsteady features and that the volume of fluid in the recirculating bulge can continue to

grow over a long time scale in the absence of any remotely forced processes [Avicola and Huq, 2003a; Fong and Geyer, 2002; Horner-Devine et al., 2006; Nof and Pichevin, 2001]. Hence, with a portion of the estuarine outflow going to bulge formation, freshwater transport in the coastal current is less than the river discharge. Fong and Geyer [2002] found that the fraction of river discharge transported by the coastal current decreases with increasing Rossby number, from 60% to 30% as the Rossby number increased from  $\sim 0.13$  to  $\sim 3.7$ . In addition to outflow geometry, bulge formation and structure are modified by remotely forced shelf-wide circulation, winds, tides [Fong and Geyer, 2002; Valle-Levinson et al., 1996; Yankovsky and Chapman, 1997; Guo and Valle-Levinson, 2007; Choi and Wilkin, 2007] and variations in river discharge [Yankovsky et al., 2001].

[9] Tidal mixing in the estuary is a dominant process controlling outflow stratification [Lerczak et al., 2006] and consequently plumes stratification. Numerical simulations of Chesapeake Bay by Guo and Valle-Levinson [2007] yields a bottom-advected plume when tides are included, while the plume becomes surface advected in simulations without tidal forcing. The spring/neap cycle in the Hudson River and the associated variations in mixing are well documented [Chant et al., 2007; Lerczak et al., 2006; Peters, 1997] and contribute to a fortnightly cycle in the buoyant discharge. While the fortnightly response of estuarine stratification is well known, less is documented about the corresponding plume response, although Wong [1998] notes variability in the Delaware River plume associated with spring-neap variability. Local tidal mixing in the near-field plume [MacDonald et al., 2007; Whitney and Garvine, 2007] is a possible mechanism controlling plume stratification, although its importance relative to estuarine mixing is unknown. Moreover, wind mixing in the plume may obscure the spring/nearest-variability down coast.

[10] There are numerous studies of the wind forcing of river plumes that address steady wind regimes [Choi and Wilkin, 2007; Fong and Geyer, 2001; Geyer et al., 2004; Houghton et al., 2004; Whitney and Garvine, 2005] but rather few that consider highly variable forcing such as the sea/land breeze system (SLBS) [Miller et al., 2003]. This despite the SLBS being a feature of coastal zone meteorology along many of the world's coastlines [Gille et al., 2003; Simpson, 1994]. SLBS events are common along the coastline of New Jersey and Long Island [Bowers, 2004] during spring and summer. While most coastal studies of the sea breeze are focused on shelf waters [Lerczak et al., 2001; Simpson et al., 2002; Hyder et al., 2002; Hunter et al., 2007], we note that Pinones et al. [2005], in a study of the Maipo river in central Chile, found evidence of SLBS forcing of a river plume.

[11] The study presented here is motivated by observations made during the three field seasons of the Lagrangian Transport and Transformation Experiment (LaTTE) in 2004, 2005, and 2006, showing significant variability in the plumes structure at diurnal and fortnightly time periods. In particular, Chant et al. [2008] show evidence that the outflow trajectory alters with SLBS forcing, and this in turn may play a significant role in bulge formation and, ultimately, in the dispersal of the estuarine discharge across the shelf. These dispersal processes play a significant role in the evolution of physical, chemical, and biological properties of the Hudson River

plume, the documentation of which is a primary objective of the LaTTE program. Here we focus on quantifying the effect that tides and SLBS forcing have on bulge formation and transport in the coastal current. We note that coastal currents and bulges represent two radically different transport pathways. In coastal currents, freshwater and material are rapidly transported down shelf, while bulge formation represents both cross-shelf transport pathway and also a mechanism to retain suspended material near the estuarine mouth. In this study we refer to the bulge region as a region of freshwater retention near the source of a buoyant outflow. This is more general than the commonly used definition of an anticyclonic eddy in cyclostrophic balance but appropriate due to the complicated nature of the dynamics involved.

[12] This article is organized as follows. Section 2 describes the study area and the observational data. Section 3 contains examples of observations showing spring/nearest variability and SLBS forcing of the river plume. The Regional Ocean Modeling System (ROMS) configuration for this application is described in section 4, and the simulation results are presented in section 5. Section 6 summarizes the results and conclusions.

## 2. Study Area and Measurements

[13] The LaTTE study area extends from the south shore of Long Island, New York to Atlantic City, New Jersey and approximately 80 km offshore of Sandy Hook, New Jersey (Figure 1). Field efforts in May 2004, April 2005, and May 2006 include mooring deployments and shipboard surveys carried out within a sustained coastal ocean observatory. The observatory is designed, built, and operated by the Rutgers University Coastal Ocean Observation Lab (RUCOOL) and described in detail in the study of Glenn and Schofield [2004]. While there are myriad data sets available, the RUCOOL data sets used in this study include the Moderate Resolution Imaging Spectroradiometer (MODIS) chlorophyll *a* satellite data product as well as the Coastal Ocean Dynamic Applications Radar (CODAR) surface ocean current data. CODAR data used in this study is limited to the RUCOOL standard range system, which is limited in spatial extent to a region near the mouth of the Hudson River (Figure 1). The MODIS spatial coverage encompasses the entire LaTTE domain.

[14] Mooring data used here are from the inner shelf in 2005 and 2006. These include surface, middepth, and bottom salinity sensors as well as an Acoustic Doppler Current Profiler (ADCP) at each site. The moorings are located off Sandy Hook (N1), a three mooring line off of Belmar NJ (C1, C2, C3), and a southern mooring (S1) (Figure 1). Note that the C1–C3 mooring line changes from 2005 to 2006. Data archived by the National Data Buoy Center (NDBC) for stations at Sandy Hook (SDHN4) and Ambrose Light (ALSN6) are used for sea level and wind data, respectively. Discharge data for the Hudson River is provided by the USGS National Water Information System (<http://waterdata.usgs.gov>).

[15] In addition to the observational data, a modeling effort using the Regional Ocean Modeling System (ROMS) is a component of the LaTTE program [Choi and Wilkin, 2007; Zhang et al., 2009a, 2009b]. We have adapted the model (section 4) in this study to consider and quantify the



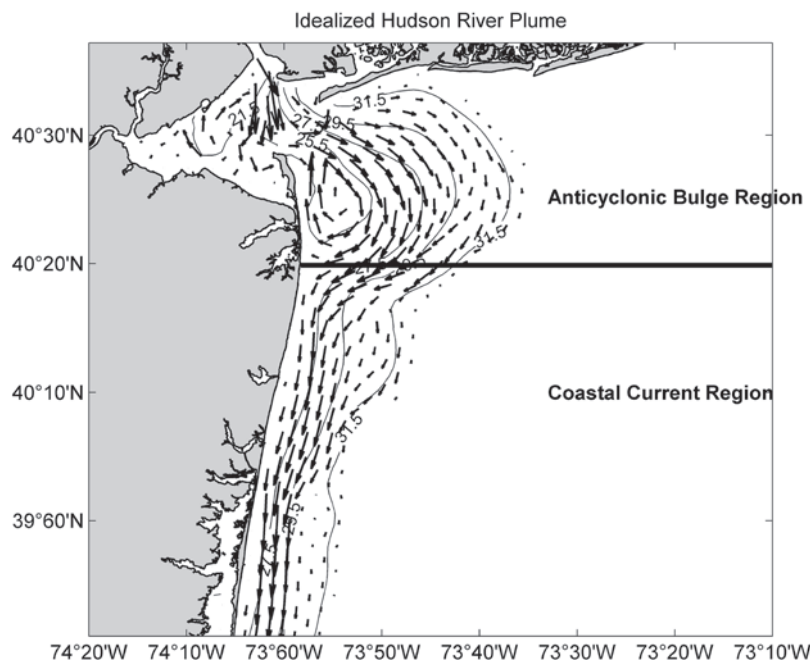


**Figure 2.** Idealized ROMS output showing the isohalines and current vectors of the surface signature of a surface-advected river plume.

impact of tides and SLBS forcing on the plume's transport pathways.

### 3. Observations

[16] The classic conceptual model (recirculating bulge and coastal current) of a surface-advected river plume is well established and illustrated in the idealized ROMS output (see section 4) in Figure 2. However, comparable field observations have proven somewhat elusive as this structure is often obscured by variability associated with tidal and wind forcing or remotely forced shelf-wide circulation, all of which can disrupt the pattern.

[17] Figure 3 depicts the surface signature of the plume using MODIS chlorophyll *a* images from an April climatology (Figure 3a) and snapshots from the 2004 (Figure 3b), 2005 (Figure 3c), and 2006 (Figure 3d) field seasons. The climatology resembles the classic picture in Figure 2 with a clearly defined bulge and coastal current. There is, however, significant interannual variability. In 2004, during low river flow conditions, the plume also resembles the classic picture, with a bulge and coastal current (Figure 3b). A drifter deployed in the coastal current traveled southward at ~55 cm/s with the coastal current until the flow was arrested by upwelling winds. During the 2005 field study, which followed immediately after a near record river discharge [Chant *et al.*, 2008], the plume forms a large recirculating bulge with little or no coastal current (Figure 3c). Drifters deployed in 2005 move anticyclonically throughout the duration of the experiment, remaining in the bulge region. We note that during the 2005 field study, there is a strong and persistent SLBS and a near-zero mean wind [Chant *et al.*, 2008]. Oceanic conditions during the 2006 experiment were distinguished from both preceding years by the appearance of a relatively steady anticyclonic feature positioned downstream

of the river outflow (Figure 3d). The narrow coastal current, evident in the drifter tracks, satellite imagery, and shipboard data (not shown), detached from the coast carrying flow offshore that subsequently recirculated back toward the coast. The drifters followed this offshore jet along the outside of the anticyclonic flow region (centered at approximately 40°N). The feature was not related to the low-salinity bulge that forms at the river mouth.

[18] Within each field season, the plume exhibits spring/neap variability in stratification as characterized by the surface-bottom salinity difference measured at the moorings (Figure 4). This effect is more evident in 2006 than in 2005 because the near record river discharge event in early April 2005 obscured the spring/neap variability of the outflow. However, during the second half of the 2005 record spring/neap variability in stratification is evident with increased stratification following neap tides on 3 and 17 May. In 2006 spring/neap variability in stratification is evident throughout the deployment with the strongest stratification following each neap tide at the beginning of May and June.

[19] The structure of the Hudson River outflow was also modified by diurnal forcing associated with the SLBS, particularly in 2005. Figure 5 illustrates the modification of the river outflow for two tidal cycles during an SLBS event in 2005. The offshore wind (toward the south) complements the ebb tide to drive the river outflow south (Figure 5a), presumably into the coastal current. The subsequent ebb (Figure 5c), responding to the onshore SLBS wind, is directed along the Long Island coast. This response is not limited to a single day. A time series of CODAR radial velocities (normal to the arc in Figure 1) over a 5 day period during the 2005 LaTTE experiment shows significant diurnal variability in the region of the river plume (Figure 6). The radial angles in Figure 6 are divided into 5° intervals of azimuth with respect to north, from 180° (southward) to 90° (eastward). Positive

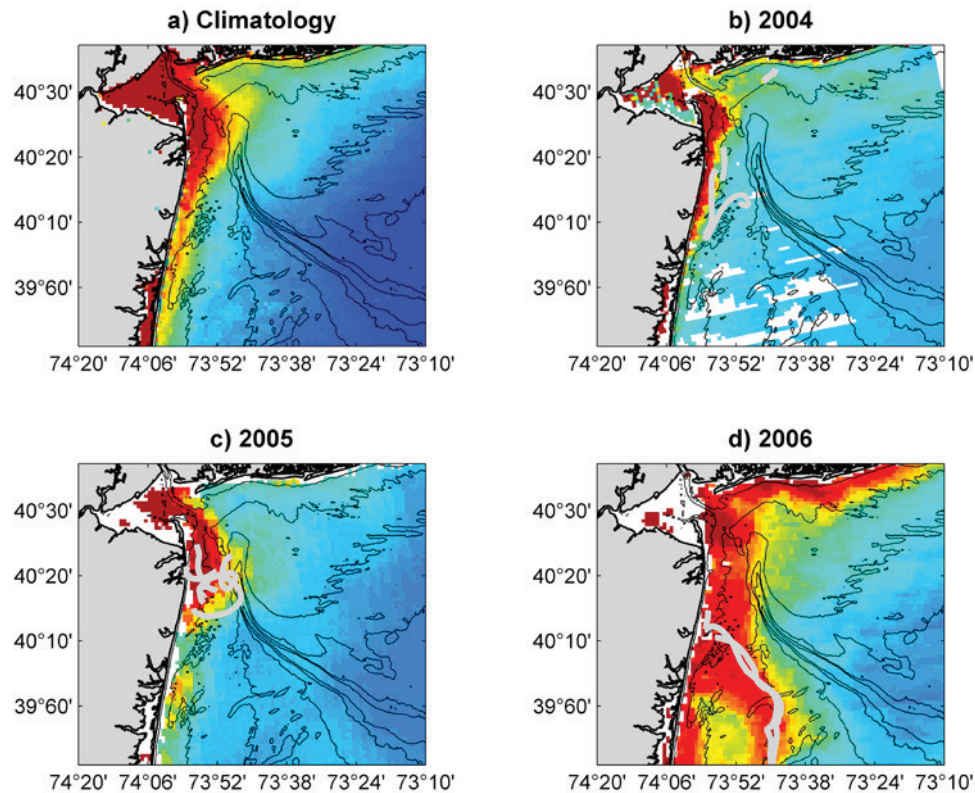


**Figure 3.** Moderate Resolution Imaging Spectroradiometer (MODIS) chlorophyll *a* images of the LaTTE study area for (a) April climatology (2004–2008), (b) 5 May 2004, (c) 4 April 2005, and (d) 28 April 2006. Higher chlorophyll concentrations (in red) are indicative of the presence of the Hudson River plume. Drifter deployments during the LaTTE experiments are shown in gray.

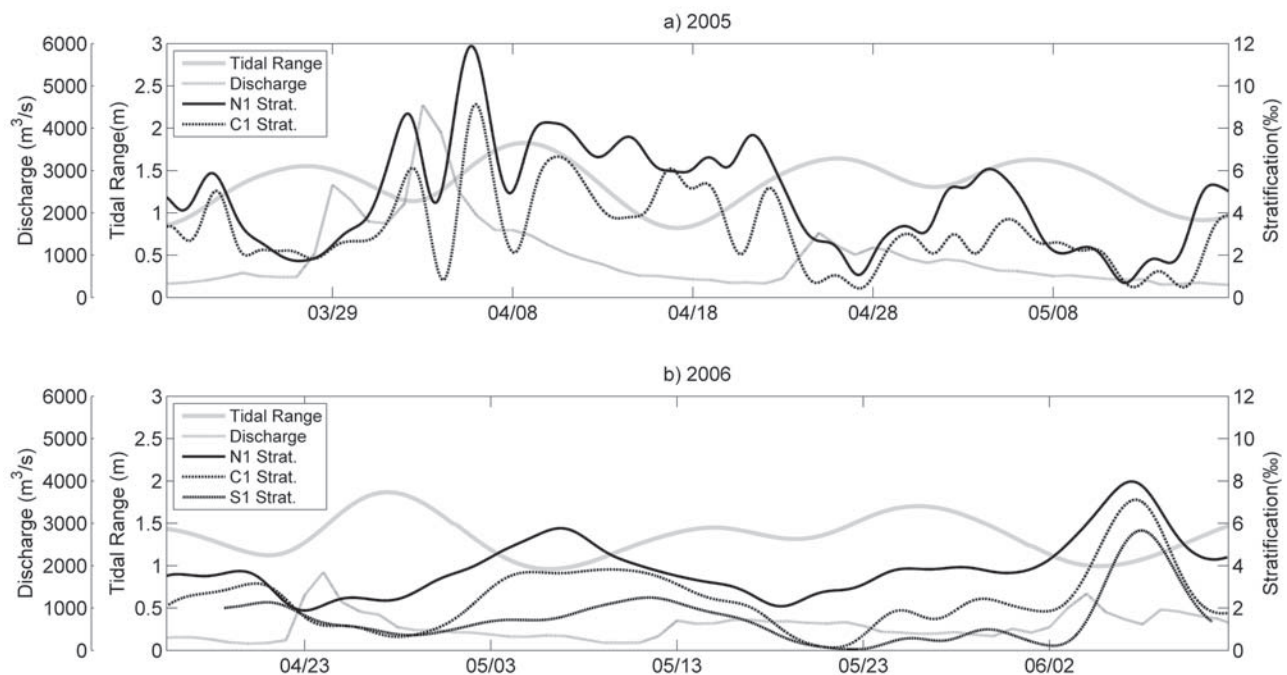


**Figure 4.** Time series of tidal range, stratification, and river discharge for the LaTTE mooring deployments in (a) 2005 and (b) 2006. Stratification is calculated as the top to bottom salinity difference at moorings N1, C1, and S1, low-pass filtered with a 72 h cutoff. The tidal range is the demodulated semidiurnal sea level at the Sandy Hook NDBC site.

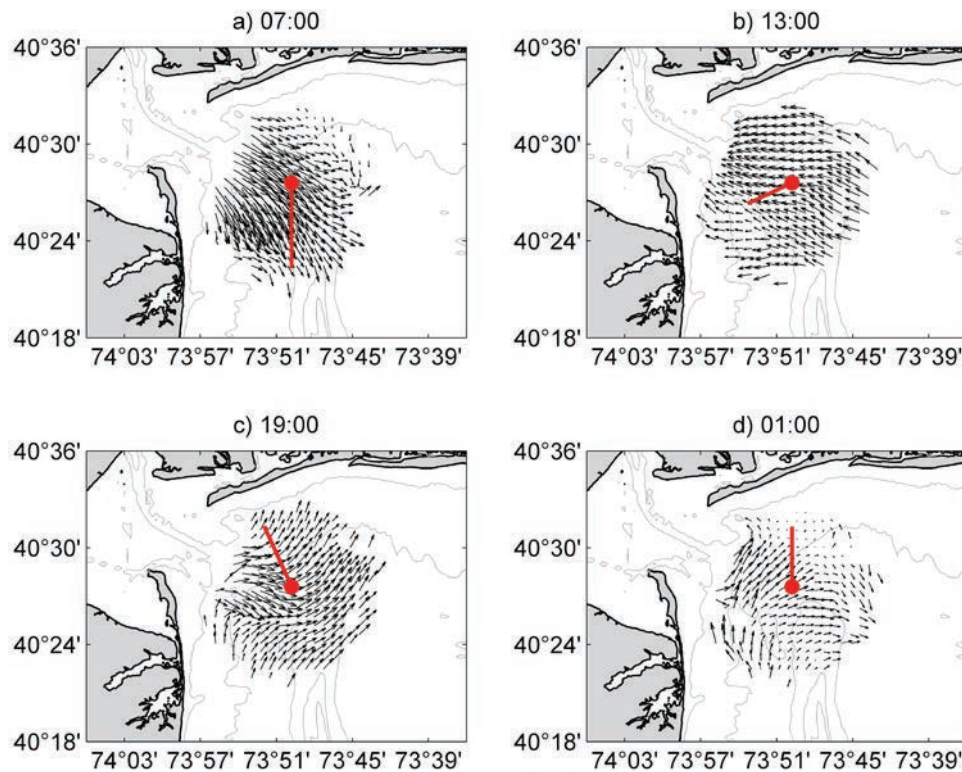


**Figure 5.** CODAR near-surface currents in 2005 showing (a) ebb tide with offshore wind, (b) flood tide during SLBS transition, (c) ebb tide with onshore sea breeze, and (d) end of ebb with onshore sea breeze.

values are directed away from the Hudson River mouth. Also shown on Figure 6 is the north-south component (positive to the north) of the wind at ALSN6, in which the SLBS manifests as a strong diurnal signal with a near-zero mean wind. During the nighttime, northerly wind phase of the SLBS

radial velocities are positive in the southern part of the arc and negative in the north, indicating the current is to the west along Long Island and to the south along New Jersey. This phase of the SLBS should therefore favor coastal current formation. In contrast, during the afternoon southerly wind

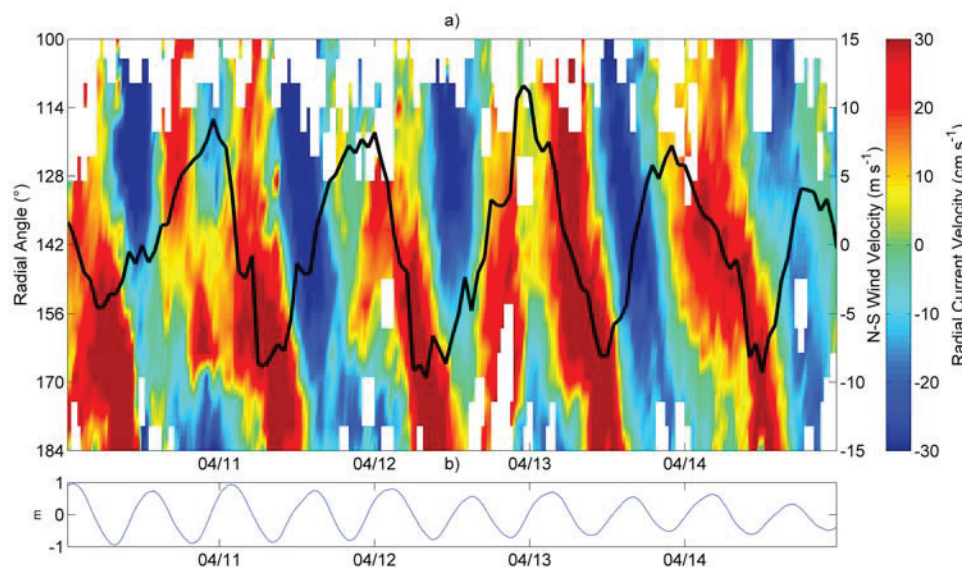


**Figure 6.** (a) CODAR radial velocity and north-south component (black line) of the wind (positive is to the north) at ALSN6. Radial velocity measurements are along the arc shown in Figure 1. 180° is south, and 90° is east. Positive values are away from the Hudson River mouth. (b) The water level at Sandy Hook (NDBC station SDHN4).



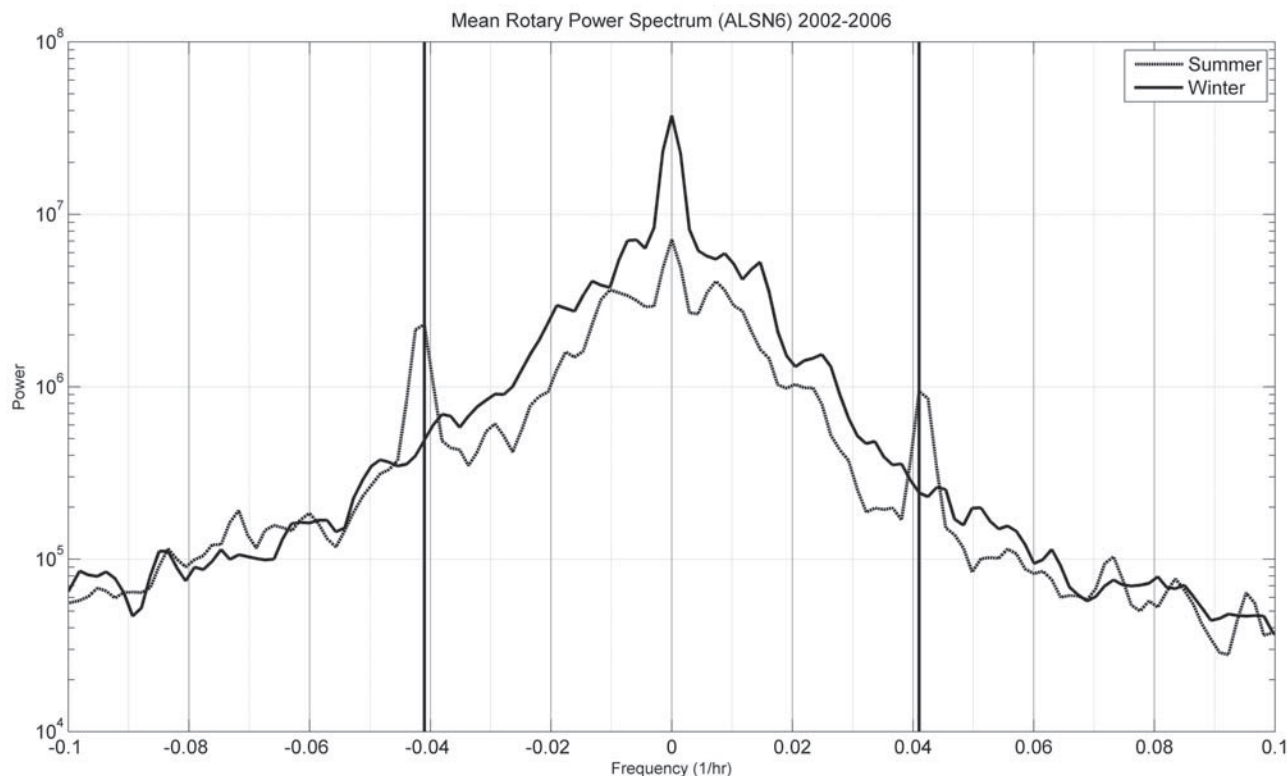


**Figure 7.** Mean rotary power spectrum of winds at ALSN6 for 2002–2006. The solid line is the winter spectrum, and the dashed line is the summer spectrum.

phase of the SLBS, the radial velocities are positive in the northern part of the arc and negative in the southern part; flow is to the north along New Jersey and to the east along Long Island. This phase of the SLBS directs freshwater away from the New Jersey coast and thus tends to reduce coastal current formation [Chant *et al.*, 2008].

[20] The SLBS is a well-known feature of New York/New Jersey coastal meteorology during the spring and summer months [Hunter *et al.*, 2007; Pullen *et al.*, 2007; Colle *et al.*, 2003]. Figure 7 shows the wind mean rotary power spectrum at ALSN6 for the winter and summer months from 2002 to 2006. There is a sharp increase in diurnal band energy in the summer consistent with the SLBS and accompanied by a decrease in subinertial energy. Individual SLBS days are identified using the method described in the study of Furberg *et al.* [2002]. A day is identified as an SLBS day if there is a sufficient land-sea temperature gradient, and there is an offshore wind in the morning, followed by an onshore wind for at least 2 h, followed by an offshore wind. The percentage of SLBS days for each month from 2002 to 2006 is calculated and shown in Figure 8. The SLBS activity picks up sharply in April, which coincides with the spring freshet. Indeed, during the freshet, diurnal winds associated with the SLBS occur approximately 50% of the time. The freshet leads to a highly stratified plume in the New York Bight apex at a time of increased SLBS activity. The coincidence of sea breeze activity and the spring freshet occurs because they are both driven by the same seasonal change in heating; the freshet by the melting of winter snows in upstate New York and the SLBS by developing land/sea thermal gradients that are most pronounced in early spring.

[21] During this time of higher stratification, increased occurrence of SLBS, and decreased mean/low frequency wind magnitude (Figures 7, 8), the diurnal energy in the coastal ocean increases. Hunter *et al.* [2007] documented increased diurnal energy due to the SLBS in the New York Bight apex during 2005. The kinetic energy of the diurnal wind at Ambrose increases (Figure 9) in April and remains high until September. Also in Figure 9 is the percentage of total kinetic energy in the diurnal band of the CODAR record for each month. The diurnal energy increases from ~1%–2% in the winter to 10%–15% in the summer. While 10%–15% is a modest increase, the SLBS events and the ocean response are episodic in nature. The increase in percentage of diurnal kinetic energy is due in large part to the absolute increase in diurnal energy of the surface current rather than a decrease in total kinetic energy. Wavelet transforms are presented in Figure 10 of the spatially averaged CODAR data and the ALSN6 wind data in 2007. While 2007 is not a LaTTE field year, it has the most complete record for winds and CODAR. The diurnal band power time series for the winds and CODAR show little variability or intensity in the winter months. Toward the end of March, the diurnal power increases and is highly variable in both the CODAR and wind records, suggesting times when the ocean diurnal energy is a significant percentage of the total energy. In fact, Hunter *et al.* [2007] identified time periods where the diurnal energy was as much as 50% of the total energy.

[22] In summary, observations show evidence of a subtidal response in plume stratification to fluctuations in tidal range over the spring/neap cycle. The observations also show diurnal energy in the coastal ocean responding to the

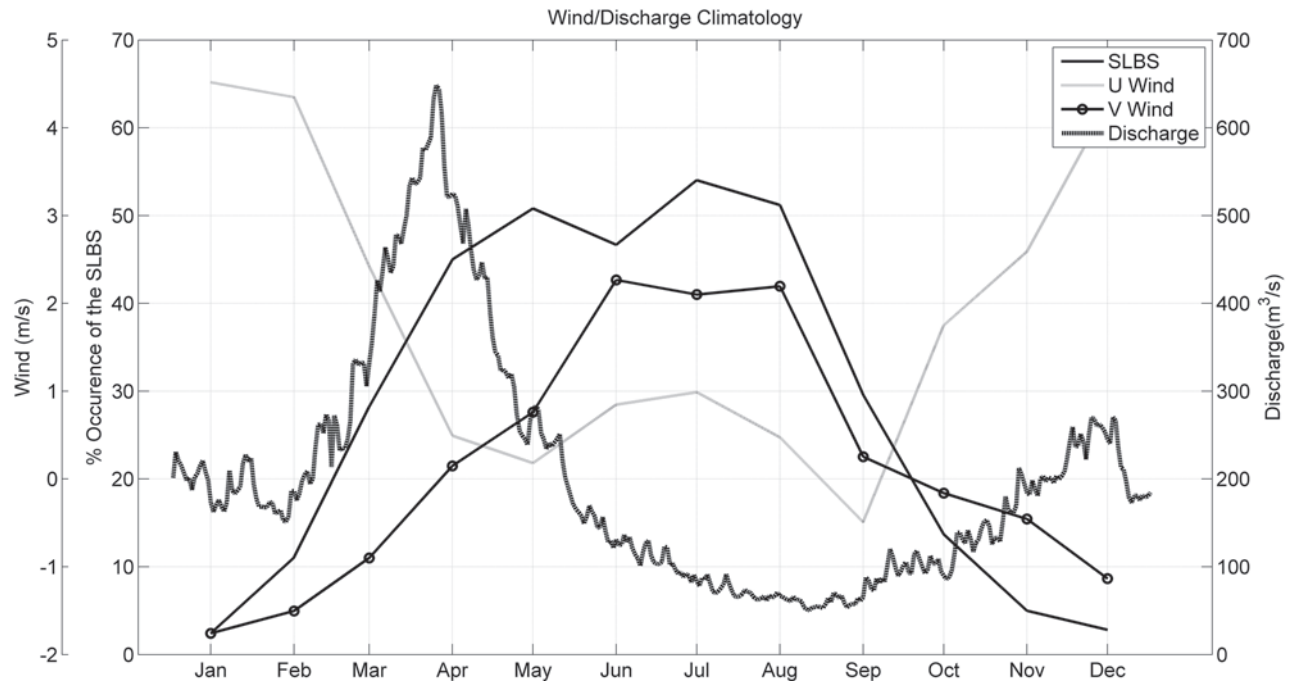


**Figure 8.** Climatology of Hudson River discharge, N-S (V) wind at ALSN6, E-W (U) wind at ALSN6 and SLBS occurrence [following *Furberg et al.*, 2002].

SLBS on seasonal and multiple-day time scales. It is further demonstrated that the diurnal energy in the region of the Hudson River plume represents a significant portion of the total kinetic energy. We suggest that the spring/neap variability could impact the dynamics of the plume by altering

the Rossby and Froude numbers, which are set in part by stratification and are known to be important in determining many features of the plume [*Fong and Geyer*, 2002; *Horner-Devine et al.*, 2006; *Yankovsky and Chapman*, 1997]. We also suggest that the SLBS forcing may also

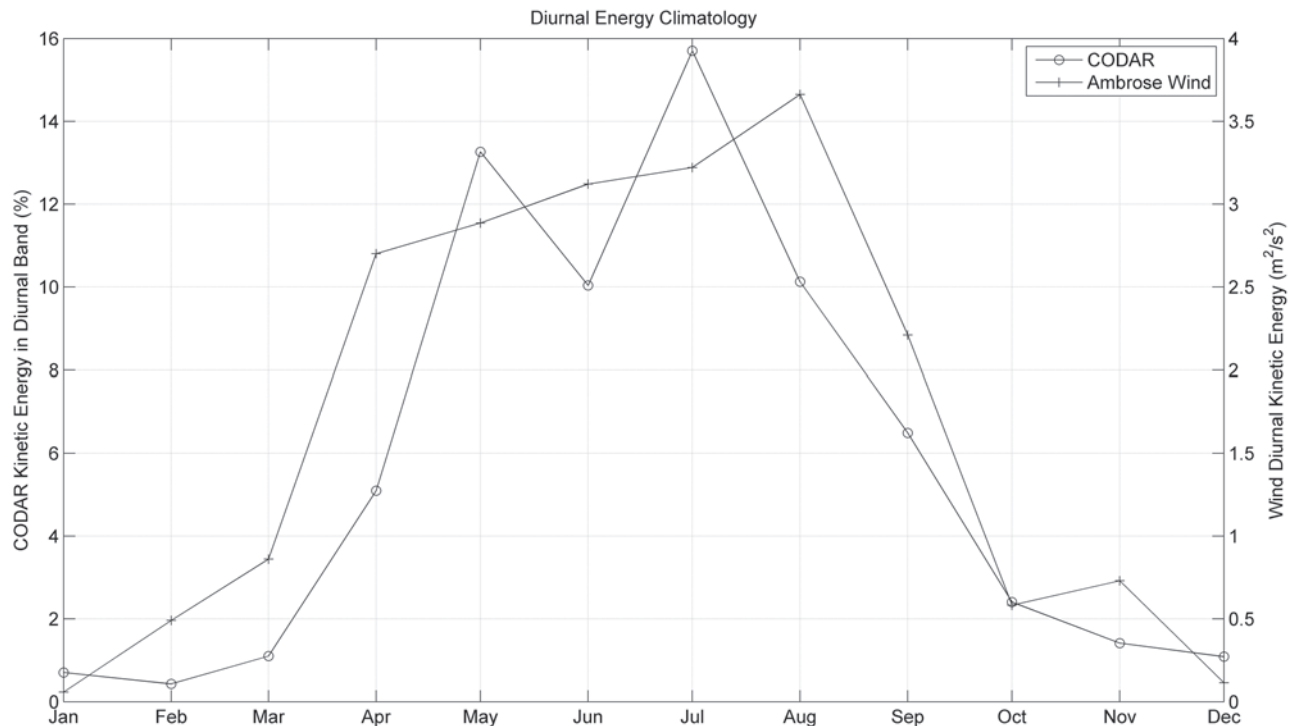


**Figure 9.** Climatology of the diurnal kinetic energy of the wind at ALSN6 (solid) and the percentage of total kinetic energy in the diurnal band (dashed) in the CODAR record for 2004–2007.

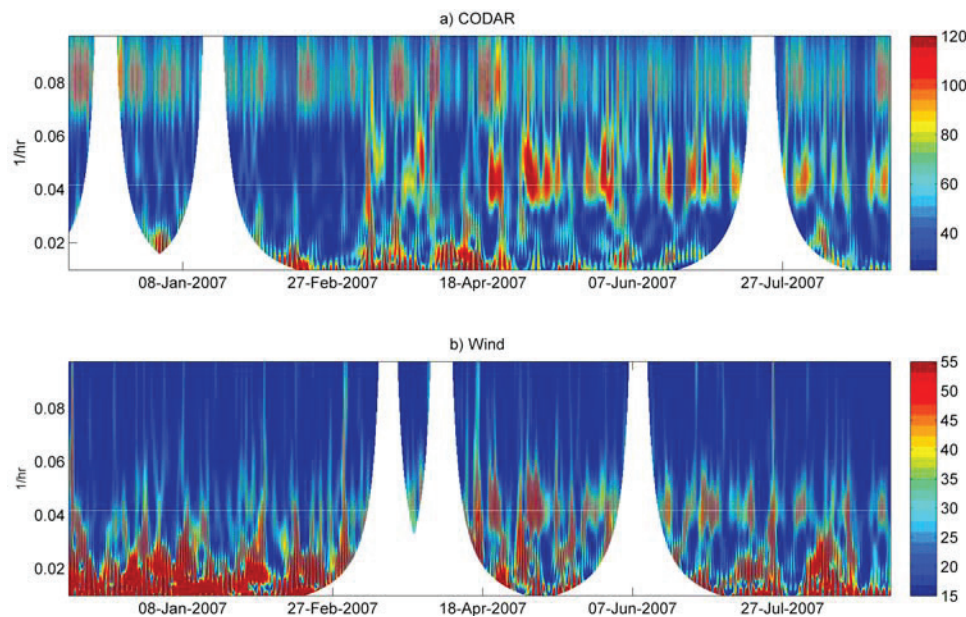


**Figure 10.** Time series of the magnitude of complex wavelet coefficients for (a) the CODAR surface current record and (b) the ALSN6 wind record. The diurnal frequency is the white dashed line.

play an important role by impacting the outflow angle, which it has been suggested plays a central role in bulge formation [Avicola and Huq, 2003b] and, subsequently, plume dispersion. To test these conjectures, we have conducted a set of ROMS model simulations to elucidate the effect of tides and diurnal wind variability on freshwater transport pathways.

#### 4. Model Description

[23] The Regional Ocean Modeling System (ROMS; <http://myroms.org>) is a three-dimensional, free-surface, hydrostatic, split-explicit, primitive-equation ocean model that has been applied to numerous studies of regional ocean dynamics including estuaries, river plumes, and inner shelf circulation [Hetland, 2005; MacCready and Geyer, 2001; Warner *et al.*, 2005; Wilkin, 2006]. Details of the ROMS algorithms are described in the study of Shchepetkin and McWilliams [2005] and other model features have been summarized by Haidvogel *et al.* [2008].

[24] The model grid used here is identical to that used by Choi and Wilkin [2007]. The computational domain is rectangular, rotated from north/east to align approximately with the shelf break, and extends well beyond the region shown in Figure 1. The horizontal grid resolution is 1 km, and there are 30 levels in a vertically stretched terrain following coordinate system. Following Choi and Wilkin [2007], we apply the Mellor and Yamada [1982] level 2.5 vertical turbulence closure scheme, and at the open boundaries Orlanski-type radiation conditions on three-dimensional variables (tracers and velocity) augmented with tidal harmonic variability in depth-averaged velocity and sea level. Unlike Choi and Wilkin [2007], the only atmospheric forcing variable here is an idealized wind stress, with no imposed air-sea heat fluxes. A constant Hudson River discharge of  $500 \text{ m}^3 \text{ s}^{-1}$  is used in all model runs, which is approximately

the annual mean discharge. Each model run is initialized with constant salinity of 32‰.

[25] The tidal forcing applied at the open boundaries uses harmonics from the ADCIRC model derived tidal constituent data base of Mukai *et al.* [2002]. Three sets of simulations were run that forced the model with a single tidal constituent at the  $M_2$  tidal frequency to investigate the role of tidal amplitude on bulge formation. The first set forced the model with the ADCIRC model mean tidal range in the New York Bight (0.74 m), a second forced the model with an increased  $M_2$  tidal range (amplitude 0.97 m), while the third applied a decreased  $M_2$  tidal range (0.36 m). These three runs represent typical average, spring, and neap tidal range conditions. Simulations were also forced with the set of constituents ( $M_2$ ,  $S_2$ ,  $N_2$ ,  $O_1$ ,  $K_1$ ,  $M_4$ ,  $M_6$ ) to model actual spring/neap variability.

[26] The SLBS is simulated by applying a spatially uniform diurnally varying wind stress derived from the wind record at ALSN6 during the LaTTE 2005 field experiment. Using harmonic analysis, the diurnal wind during this period was determined to be a clockwise rotary wind with a major axis of  $\sim 6 \text{ m s}^{-1}$ . Wind stress was subsequently estimated using a quadratic drag law with a drag coefficient of  $\sim 1.0 \times 10^{-3}$ . The New York Bight apex has coastlines to the north and west, each of which has the potential to generate an SLBS front, and this is apparent in the variable orientation of the major diurnal wind ellipse at Ambrose and captured by high-resolution regional meteorological models [Pullen *et al.*, 2007; Colle *et al.*, 2003]. Therefore, two SLBS wind forcing cases were examined: one with the ellipse major axis in the north-south (NS) direction and a second case with the major axis in the east-west (EW) direction. In the following section, we focus on results for the NS case. Results for the EW case are similar unless otherwise noted.

[27] In total, we present seven model runs. The three tidal ranges (neap, average, and spring) are each run without wind stress and also with SLBS wind stress yielding six simula-



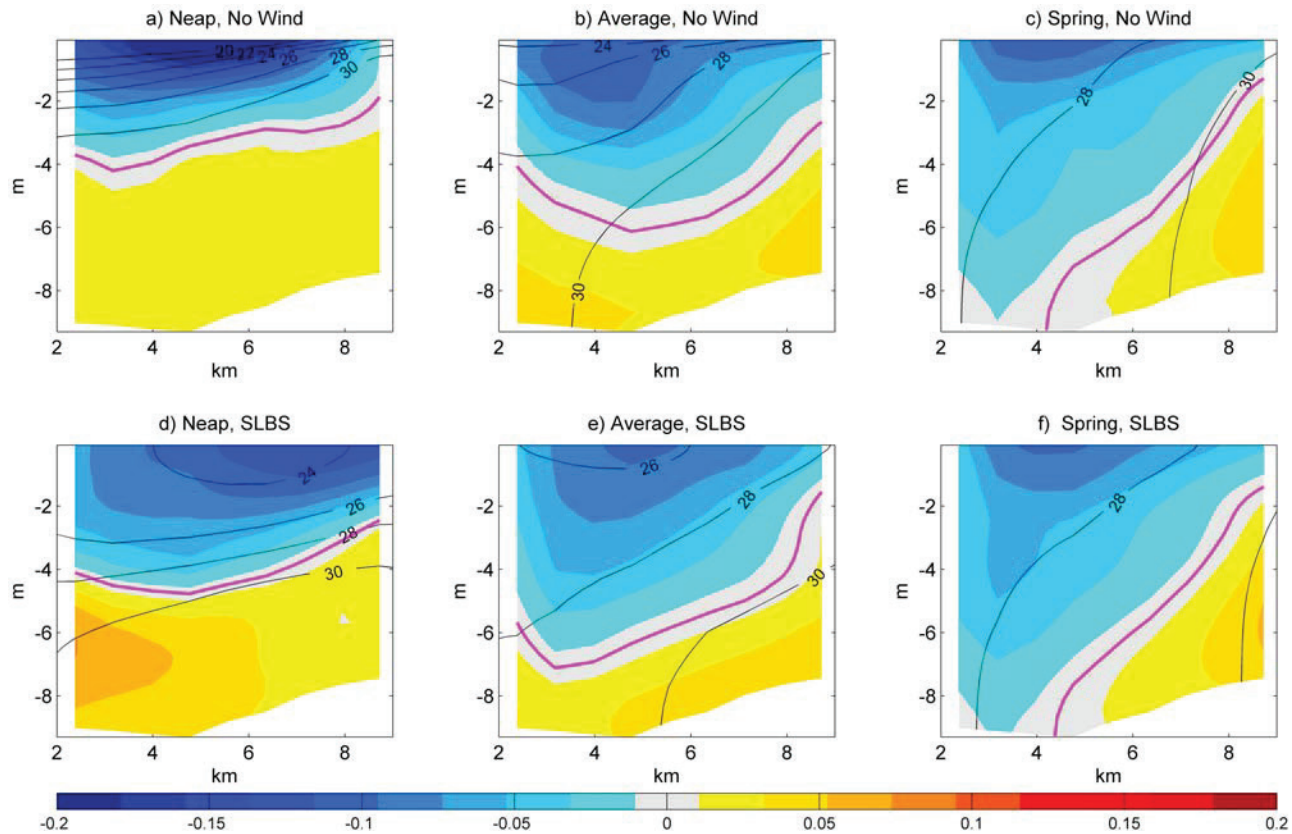


**Figure 11.** Cross section of the Hudson River outflow (transect A in Figure 1) with salinity contours (black) overlaid along channel velocity (m/s). Negative velocity is out of the estuary, and the zero velocity contour is shown in magenta. Model runs included are (a) neap tidal range/no wind, (b) average tidal range/no wind, (c) spring tidal range/no wind, (d) neap tidal range/SLBS, (e) average tidal range/SLBS, and (f) spring tidal range/SLBS.

tions. The seventh run was forced with the full complement of tidal constituents without wind to assess the time/scale of adjustment of the plume dynamics to fortnightly and monthly tidal variability. The results presented have been low-pass filtered so that we can assess the extent to which high-frequency forcing produces low-frequency response in the plume variability.

## 5. Model Results

[28] Each simulation was run for 60 days to allow freshwater transport in the coastal current to reach a quasi-steady, slowly varying state. (True steady state conditions were not a characteristic of any of the numerous studies of river plumes noted in section 1.) Figure 2 is an example of such a state, for the no wind, average tidal range case. The mean circulation in the model outside the plume region is negligible for all model runs presented in this study, suggesting little or no rectified flow through the interaction of tides, SLBS, bathymetry, and coastal shape.

[29] In order to characterize the nature of the surface-advected plume in a manner similar to the studies of *Avicola and Huq* [2003a, 2003b] and *Yankovsky and Chapman* [1997], we estimate outflow parameters for a section from Sandy Hook to Rockaway Point (line A in Figure 1). Figure 11 shows salinity contours and velocity normal (along

channel) to this transect on model day 30. The greatest differences between the six cases are associated with varying tidal range and the variability over the spring/neap cycle is consistent with the mechanism described by *Lerczak et al.* [2006]. The neap tidal range/no-wind case (Figure 11a) has the thinnest, freshest outflow and is completely detached from the bottom. This case exhibits a fairly symmetric cross section with some cross-channel tilting of isohalines. The neap tidal range/NS SLBS case (Figure 11d) is similar, although mixing due to the diurnal winds has deepened the buoyant outflow by 1–2 m.

[30] The average tidal range model runs (Figures 11b and 11e) have a deeper halocline and outflow compared to the corresponding neap tide cases. For all tidal regimes, the surface salinity is lower for the no-wind case compared to the corresponding SLBS case. Increased tidal range is accompanied by increased tilting of isohalines and a developing asymmetry in the outflow with the center moving toward the Sandy Hook side of the channel. The spring tidal range case exhibits further deepening of the buoyant outflow layer (Figures 11c and 11f) and enhanced asymmetry across the section. The buoyant outflow intersects the bottom at the south side of the channel. The depth of the outflow is a critical parameter in defining the structure of the plume [*Yankovsky and Chapman*, 1997], and thus, we next look at its dependence on tidal and wind forcing.

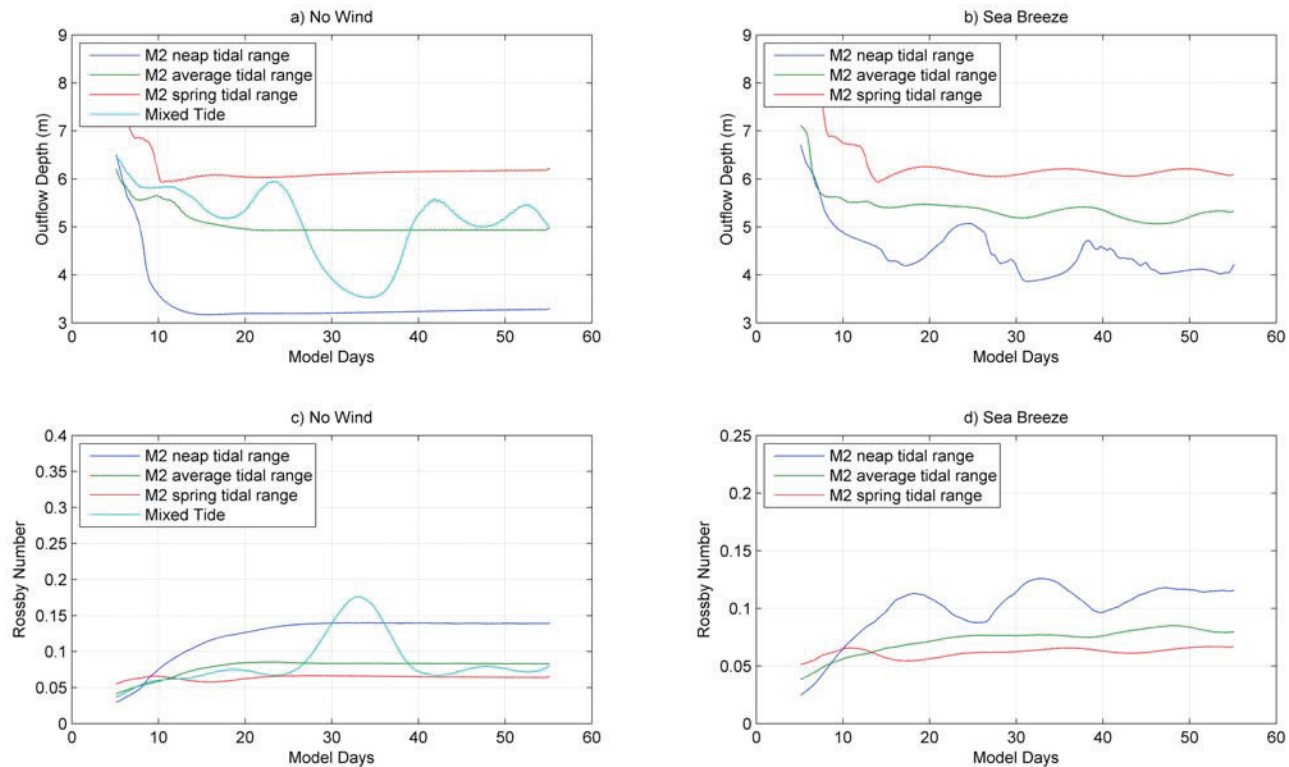


**Figure 12.** Time series of (a, b) outflow depth and (c, d) Rossby number for the Hudson River outflow calculated at transect A in Figure 1. (a) Outflow depth for the no-wind case. (b) Outflow depth for the SLBS case. (c) Rossby number for the no-wind case. (d) Rossby number for the SLBS case.

[31] We define the outflow depth  $h_o$  as the cross-channel average of the depth of the zero velocity isotach (magenta line in Figure 11) and plot the result in Figures 12a and 12b for each of the simulations. The outflow depth is generally stable throughout the model runs, equilibrating by about model day 10. The outflow depth in the average tidal range case is  $\sim 5.0$  m for both wind regimes and  $\sim 6.1$  m in the spring tidal range case, again for both wind regimes. In contrast, during the neap tide conditions, a thin ( $\sim 3.3$  m) outflow occurs in the absence of wind compared to  $\sim 4.2$  m in the SLBS case. The outflow depth for the no-wind run with multiple tidal constituents modulates between 3.4 and 6.0 m from neap to spring tidal conditions, respectively, which is very close to the response to the idealized  $M_2$  amplitudes we characterize as *neap* and *spring*. In summary, the outflow depth generally increases with increased tidal range with little variability due to wind regime except during times of decreased tidal range suggestive that wind mixing becomes less efficient as mixed layer depth increases.

[32] In a manner similar to *Yankovsky and Chapman* [1997], we use nondimensional Froude (1) and Rossby (2) numbers to characterize the buoyant plume. The outflow velocity ( $v_i$ ) in (1) and (2) is defined as the mean velocity above the zero isotach and the width of the outflow ( $L$ ) is 7 km. Reduced gravity in (1) is a layer reduced gravity, with the outflow density calculated as the mean density above the zero isotach. Variability in  $F_i$  and  $R_o$  across model runs is dominated by  $v_i$ , while variations in  $(g'h_o)^{-1}$  are small by comparison. Time series of  $R_o$  are shown in Figures 12c and 12d. The relevant features of the  $F_i$  time series (not shown)

are identical to that of  $R_o$ . Thus, variability that we ascribed to changes in the Rossby number may be dependent on the Froude number instead. Unfortunately given the constraints of the realistic grid, we were unable to separate Froude number dependence from Rossby number dependence in these runs. We note that for all model runs the magnitudes of  $F_i$  and  $R_o$  are similar, indicating buoyancy and Coriolis forces are comparable and suggesting a Burger number ( $S = R_o/F_i$ ) near unity. The Burger number, a measure of the relative importance of stratification to rotation and is also the ratio of the inertial period (rotation) to the time scale associated with internal gravity wave propagating across the plume (stratification), maintains a magnitude from 0.6 to 0.75 for all cases.

[33] According to *Yankovsky and Chapman* [1997], a plume whose outflow satisfies the inequality  $S > (2R_o)^{1/2}$  should be surface advected. Such a scaling is used to classify observed river plumes, despite the steady state nature of the theory. This condition is satisfied for all model runs in this study in agreement with previous modeling studies and shipboard observations during LaTTE, indicating the Hudson River plume is surface advected. There is also what appears to be a fortnightly variability (Figure 12d) in  $F_i$  and  $R_o$  in the decreased tidal range/SLBS model runs due to the beating between the diurnal SLBS and the semidiurnal tide.

[34] Cross sections of the coastal current are shown in Figure 13 corresponding to line B in Figure 1. Negative values are down shelf (in the Kelvin wave sense), and salinity contours are overlaid. Note that the salinity contour interval for Figures a13–13c is 1 ppt while for Figures 13d–

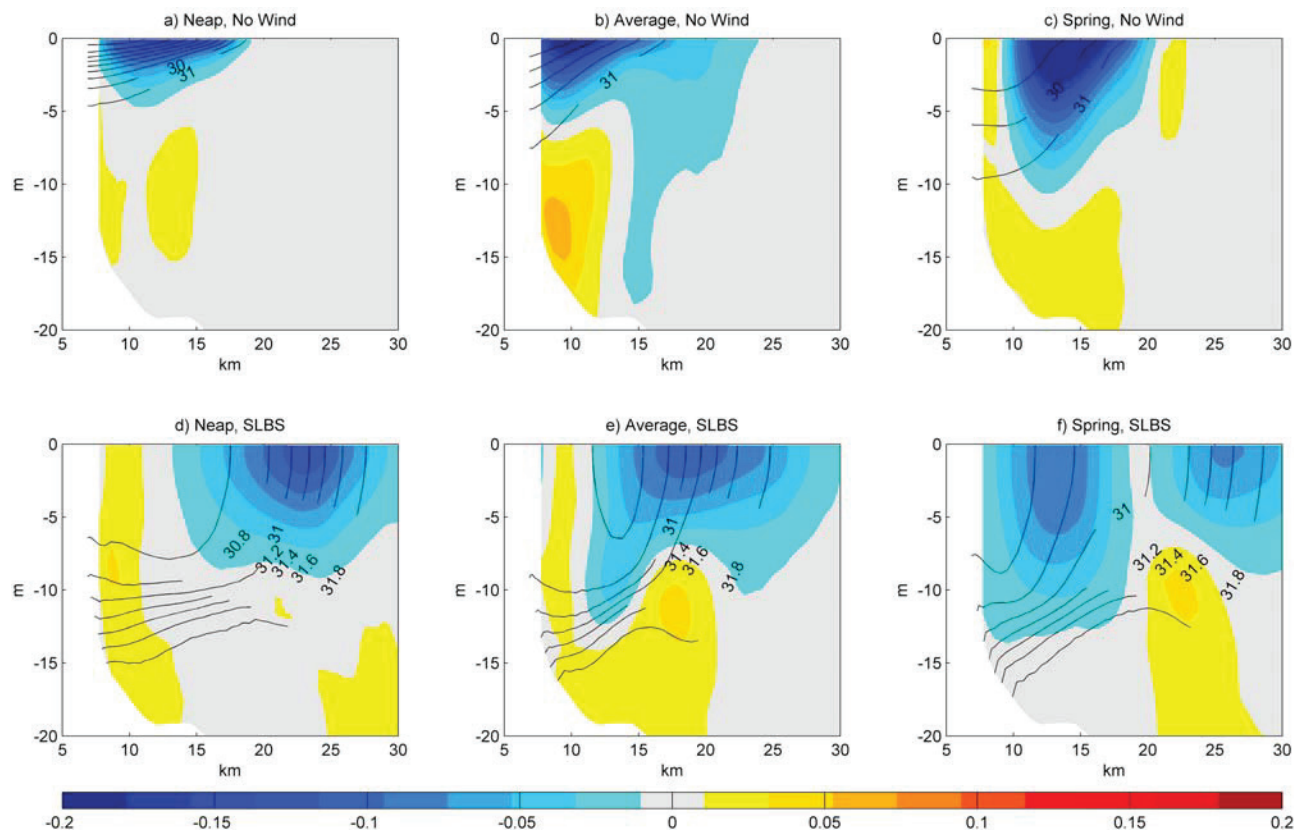


**Figure 13.** ROMS Salinity and current velocity (m/s) cross sections for transect B in Figure 1. Positive velocity is along shelf in the Kelvin wave sense (in blue). Please note the contour interval in Figures 13a–13c is 1 ppt and in Figures 13d–13f is 0.2 ppt. (a–c) The neap tidal range/no-wind, average tidal range/no-wind, and spring tidal range/no-wind cases, respectively. (d–f) The neap tidal range/SLBS, average tidal range/SLBS, and spring tidal range/SLBS cases, respectively.

13f is 0.2 ppt. Figures 13a–13c are the no-wind model runs for neap, average, and spring tidal ranges, respectively. As tidal range increases, stratification in the coastal current decreases and the depth of the coastal current increases. There is also little evidence of local tidal mixing in the plume when compared to the outflow cross sections in Figures 11a–11c. Figures 13d–13f show the corresponding SLBS results. Coastal current depths are similar for these three cases and much deeper (~10–15 m) than in the no-wind model runs. The deeper, wider halocline in these cases is evidence of enhanced local mixing due to the SLBS. The effect of spring/neap variability becomes less pronounced with wind forcing applied.

[35] Figure 14 shows time series of freshwater flux at line B expressed as a fraction of the river discharge ( $500 \text{ m}^3 \text{ s}^{-1}$ ). Freshwater flux in the coastal current ( $Q_{cc}$ ) is calculated as

$$Q_{cc} = \iint v \frac{s_o - s}{s_o} dA, \quad (4)$$

where  $v$  is along shelf velocity,  $s$  is salinity in the coastal current,  $s_o$  is the ambient shelf salinity (32‰), and  $A$  is the cross-sectional area.

[36] Figure 14a shows the no-wind cases. Low-pass filtered coastal current freshwater flux values are 0.5–0.9 of

the river discharge for all cases, with the largest transport occurring for the spring tidal range. It is notable that for the spin-up period (~10–30 days) under neap tidal range conditions, the freshwater flux at line B increases much faster than in the average or spring tidal range cases. This corresponds to higher Rossby numbers and subsequently a tendency to favor bulge formation and a reduction of freshwater transport in the coastal current.

[37] Freshwater flux in the coastal current is further reduced by the introduction of SLBS forcing (Figure 14b), with the transport falling to approximately 1/2 of the river discharge for the case with spring tidal range and to less than 1/3 of river discharge for the neap tide case. While Figure 14b shows only the NS SLBS model runs, the freshwater flux in the EW SLBS model runs was even lower (~0.14–0.35 of river discharge). We note that while the SLBS forcing decreased the freshwater flux in the coastal current, the outflow Rossby number either decreased (neap tide case) or changed minimally (average or spring tide cases). This is in contrast to *Fong and Geyer's* [2002] inverse relationship between  $Q_{cc}$  and  $R_o$ , suggesting that SLBS modification of the river outflow is less important than the plumes response to advective processes associated with SLBS. The SLBS forcing enhances bulge formation near the river mouth, thereby inhibiting freshwater transport in the coastal current.



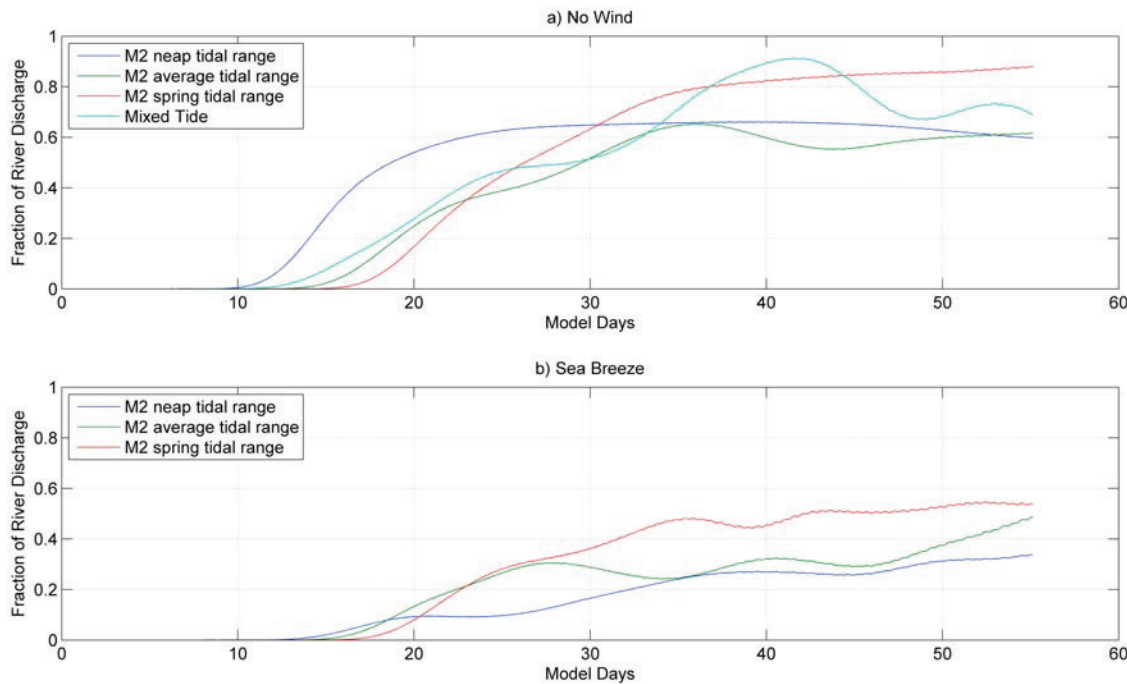


**Figure 14.** ROMS freshwater flux in the coastal current (transect B in Figure 1) for (a) the no-wind case and (b) the SLBS case. Flux values are expressed as a fraction of the constant river discharge of  $500 \text{ m}^3 \text{ s}^{-1}$ . The SLBS wind forcing reduces freshwater flux in the coastal current by  $\sim 50\%$ . The largest coastal current transport occurs during the strongest tidal range case for both the no-wind and SLBS regimes.

This accumulation of freshwater near the river mouth is due to the southerly phase of the SLBS that steers the outflow to the east and increases the outflow angle [Chant *et al.*, 2008], which favors bulge formation [Avicola and Huq, 2003b]. We note that in all tidal forcing cases the transport in the coastal current is decreased by 50% when sea breeze is added, which is consistent with the outflow being directed to the east and away from the New Jersey coast during the southerly phase of the SLBS. This scenario is also consistent with arguments by Nof [1988], who suggests that coastal current formation is inhibited when the recirculating bulge moves away from the coastal wall, which occurs 50% of the time when SLBS forcing is added. Thus, with SLBS forcing, we expect increased bulge formation which appears to be driven primarily by advective processes associated with the transport of freshwater to the east along Long Island's south shore.

[38] An example of the ocean response (average tidal range/SLBS model run) to the SLBS cycle during subsequent tidal cycles is shown in Figure 15. The result is similar to the CODAR example in Figure 5, i.e., subsequent ebbs interact with different phases of the SLBS. The first ebb (Figure 15a) during the offshore phase of the SLBS encourages transport into the coastal current, while the onshore phase of the SLBS forces the next ebb along the coast of Long Island. Over many SLBS cycles, the bulge region expands along the coast of Long Island, resulting in a net transport of freshwater to the east. Note, however, that in reality SLBS would be interrupted by cold fronts and storms that will radically modify the plume structure and potentially promote coastal current formation [Choi and Wilkin, 2007; Zhang *et al.*, 2009b].

[39] In order to illustrate the influence of SLBS on freshwater transport pathways, we calculate the equivalent depth of freshwater  $\delta_{\text{fw}}$  [following Choi and Wilkin, 2007]

$$\delta_{\text{fw}} = \int_{-h}^{\eta} \frac{S_a - S(z)}{S_a} dz, \quad (5)$$

where  $S_a$  is the ambient shelf salinity (here  $S_a = 32.0$ ),  $S(z)$  is the salinity of the water column,  $\eta$  is the sea level, and  $h$  is the water depth.

[40] Examples of the development of the plume are shown in Figures 16a–16f. The outer edge of the plume is defined as the 0.25 m contour of  $\delta_{\text{fw}}$ . Figures 16a–16c show the plume surface on model day 12 for decreased, normal, and increased tidal ranges, respectively. Figures 16d–16f is the same except for model day 40. The no-wind model runs are the solid contours, and the SLBS cases are the dashed contours. The plume structure is more responsive to SLBS forcing in the cases with neap tidal range when the plume is shallow and highly stratified. Under these conditions, the down-shelf penetration of the coastal current is significantly reduced and bulge formation significantly increased. Conversely, the response of the plume to SLBS forcing (relative to the no-wind case) becomes less pronounced as tidal range increases, although there is still a substantial decrease in freshwater transport. However, we note that during high-flow events, such as the 2005 freshet [Chant *et al.*, 2008], the plume can remain strongly stratified throughout the entire spring/neap cycle and be highly responsive to sea breeze forcing. Therefore, we suggest that SLBS forcing has a larger impact on freshwater dispersal during the spring freshet when discharge is high than during the summer months with low

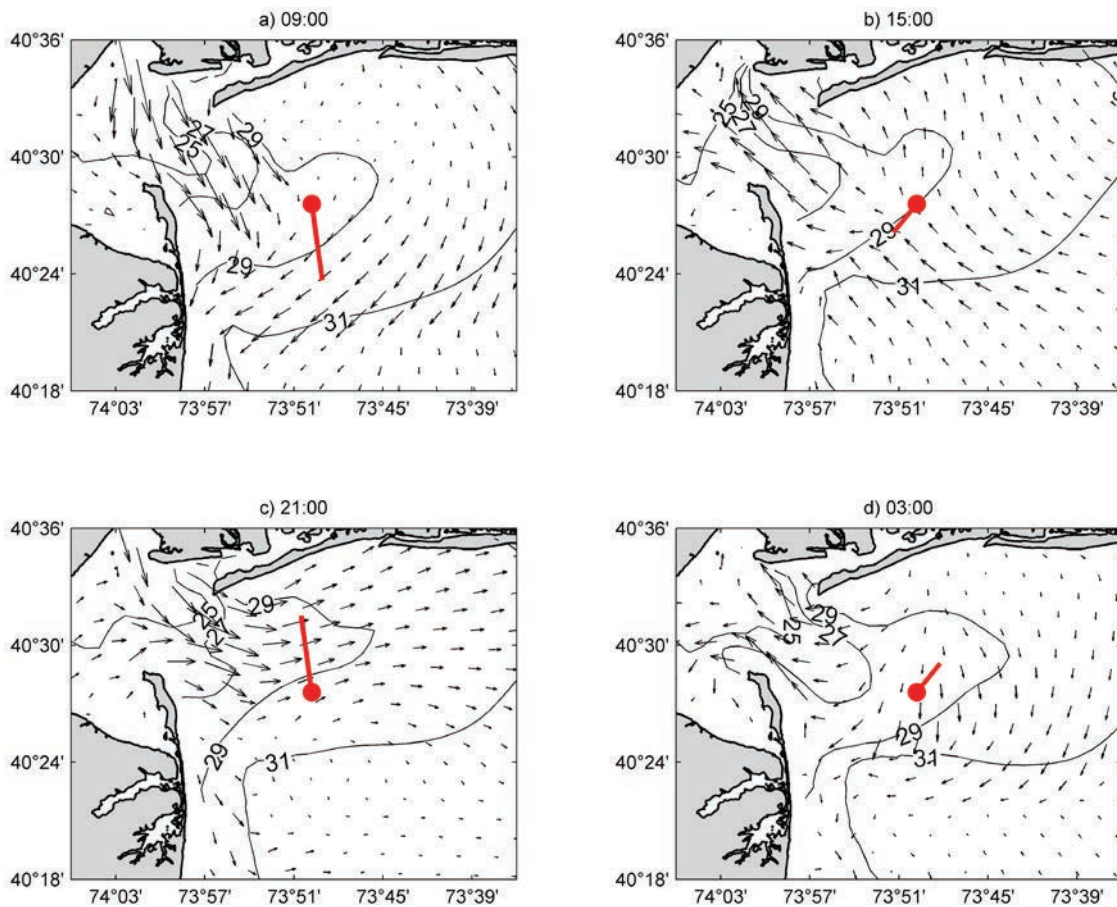


**Figure 15.** ROMS average tidal range/SLBS case showing near-surface currents for the (a) ebb tide with offshore wind, (b) flood tide during the SLBS transition, (c) ebb tide with onshore sea breeze, and (d) flood tide at the end of the SLBS cycle.

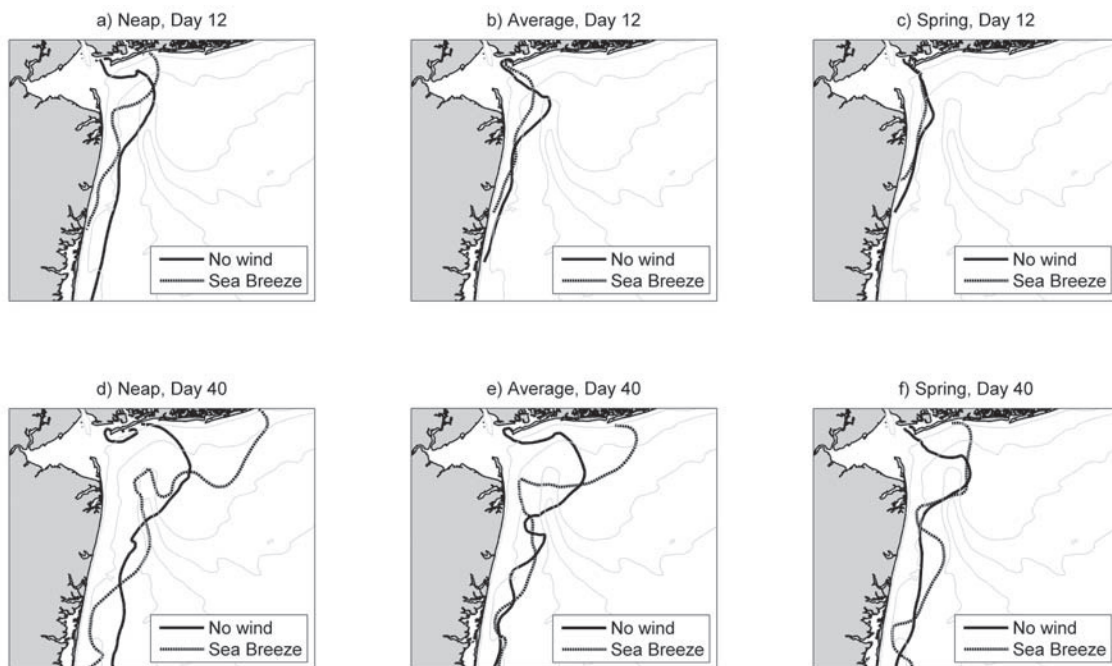


**Figure 16.** Equivalent depth of freshwater contour (0.25 m) for (top) day 12 and (bottom) day 40 for cases (a, d) neap tidal range, (b, e) average tidal range, and (c, f) spring tidal range.

discharge. More generally, these simulations indicate that the impact of SLBS forcing on river plumes diminishes with increased plume thickness.

[41] In Figure 16, there is also a notable transport of freshwater toward the east along Long Island during SLBS cases, contrary to accepted coastal current theory. This is particularly evident during the neap tidal range case, suggesting a net freshwater transport pathway assisted by variable winds in the New York Bight apex. Eventually the freshwater along Long Island's shore does turn south. These transport pathways, for simulations using observed winds and remote forcing, are discussed by Zhang *et al.* [2009a].

## 6. Summary

[42] Observations during the LaTTE 2004, 2005, and 2006 field seasons show that the structure of the Hudson River's outflow exhibits significant variability on a range of time scales. While much of this can be explained by variability in river discharge and the synoptic wind band, high-frequency forcing associated with tides and SLBS events also plays a significant role in shaping the structure of the plume. Stratification in the coastal current shows clear spring/neap tidal variability associated with variation in mixing within the Hudson River estuary as local tidal mixing in the plume is negligible. While the spring tide produces a less stratified coastal current, it also enhances coastal current transport. We suggest this latter result occurs for two reasons. First, while tidal currents are stronger during spring tide conditions the tidal mean velocities (i.e., that of the plume) are swifter during neap tides, and this increased horizontal advection increases the outflow Rossby number, which favors bulge formation, thus robbing the coastal current of transport [Fong and Geyer, 2002]. Second, during spring tides the spatial structure of the estuarine exchange flow becomes more laterally sheared with the outflow concentrated along the New Jersey coast, while during neap tides the exchange is more vertically sheared and the outflow is displaced from the coast. The spring tide lateral shear results in a river plume favoring coastal current formation, as evidenced by increased freshwater transport in the coastal current at these times. Conversely, during neap tides, the outflow is vertically sheared and more jet-like with the outflow swiftest away from the coast, which tends to favor bulge formation.

[43] The more significant result is that plume response to SLBS forcing is not only detectable but is a major mechanism determining the structure of the Hudson River plume during the spring and summer months. However, the outflow Rossby number argument, which fits the plume structure over the spring/neap cycle, is not consistent with the variation in coastal current for the SLBS results. The SLBS modifies the plume structure via a combination of advective and mixing processes outside the estuary, with advective processes seemingly dominating the transport pathways by sending 1/2 the outflow to the east along Long Island's south shore.

[44] This advective response is more pronounced when stratification is intensified during neap tides or when river discharge is high, i.e., there is a greater response to the SLBS in shallow, highly stratified plumes. The SLBS-dominated wind regime during the 2005 LaTTE field season coincided with a large recirculating bulge and limited freshwater transport in the coastal current. In particular, the phasing of

the tides with respect to the SLBS is documented. CODAR radial velocities showed the outflow trajectory was strongly modified by SLBS forcing with the outflow directed to the east along the Long Island coast during the northward phase (sea breeze) of the SLBS and directed to the south along the New Jersey coast during the southward (land breeze) phase. We suggest that this essentially cuts the transport of the coastal current in half because the outflow during the northward phase is incorporated in the bulge. Numerical simulations suggest that the combination of neap tide conditions and SLBS winds reduces the transport of freshwater in the coastal current to less than 1/3 of the estuarine outflow, with the balance of the transport driving bulge formation. The resulting plume evolution provides a freshwater transport pathway along Long Island.

[45] The mixing response is clear in model cross sections of the coastal current. There is a deepening and vertical spreading of the halocline, coupled with the horizontal spreading of the plume. Although both mixing and advection are significant, we suggest that the plume's inviscid response to the SLBS plays the central role in reducing freshwater transport in the coastal current.

[46] Finally, SLBS conditions occur along many coastlines [Gille *et al.*, 2003] during spring and summer. It is likely then that coincidence of the spring freshet and SLBS activity is not unusual in temperate regions where the winter-time watershed stores precipitation as snowpack. Therefore, the results here suggesting that high-frequency variability and, in particular, the SLBS play a role in explaining lower-frequency variability in the Hudson River plume are likely to be echoed in other river plume systems globally.

[47] **Acknowledgments.** We thank the dedicated members of the Rutgers University Coastal Ocean Observing Lab, invaluable as sources of observatory data used in this study. We also thank Chip Haldeman for leading the mooring deployment and Gordon Zhang for providing support in the operation of ROMS. This study was supported by the National Science Foundation grant OCE-0238957.

## References

- Avicola, G., and P. Huq (2002), Scaling analysis for the interaction between a buoyant coastal current and the continental shelf: Experiments and observations, *J. Phys. Oceanogr.*, **32**(11), 3233–3248.
- Avicola, G., and P. Huq (2003a), The characteristics of the recirculating bulge region in coastal buoyant outflows, *J. Mar. Res.*, **61**, 435.
- Avicola, G., and P. Huq (2003b), The role of outflow geometry in the formation of the recirculating bulge region in coastal buoyant outflows, *J. Mar. Res.*, **61**, 411.
- Bowers, L. A. (2004), The effect of sea surface temperature on sea breeze dynamics along the coast of New Jersey, M.S. thesis, 139 pp., Rutgers Univ., New Brunswick, N. J.
- Castelao, R., O. Schofield, S. Glenn, R. Chant, and J. Kohut (2008), Cross-shelf transport of freshwater on the New Jersey shelf, *J. Geophys. Res.*, **113**, C07017, doi:10.1029/2007JC004241.
- Chant, R. J., W. R. Geyer, R. Houghton, E. Hunter, and J. Lerczak (2007), Estuarine boundary layer mixing processes: Insights from dye experiments, *J. Phys. Oceanogr.*, **37**, 1859.
- Chant, R. J., S. M. Glenn, E. Hunter, J. Kohut, R. F. Chen, R. W. Houghton, J. Bosch, and O. Schofield (2008), Bulge formation of a buoyant river outflow, *J. Geophys. Res.*, **113**, C01017, doi:10.1029/2007JC004100.
- Chao, S.-Y., and W. C. Boicourt (1986), Onset of estuarine plumes, *J. Phys. Oceanogr.*, **16**, 2137–2149.
- Chapman, D. C., and S. J. Lentz (1994), Trapping of a coastal density front by the bottom boundary-layer, *J. Phys. Oceanogr.*, **24**, 1464–1479.
- Choi, B.-J., and J. L. Wilkin (2007), The effect of wind on the dispersal of the Hudson River plume, *J. Phys. Oceanogr.*, **37**, 1878–1897.
- Colle, B. A., J. B. Olson, and J. S. Tongue (2003), Multiseason verification of the MM5: Part I. Comparison with the eta model over the central and



- eastern United States and impact of MM5 resolution, *Weather Forecasting*, 18, 431–457.
- Fong, D. A., and W. R. Geyer (2001), Response of a river plume during an upwelling favorable wind event, *J. Geophys. Res.*, 106, 1067–1084, doi:10.1029/2000JC900134.
- Fong, D. A., and W. R. Geyer (2002), The alongshore transport of freshwater in a surface-trapped river plume, *J. Phys. Oceanogr.*, 32(3), 957.
- Furberg, M., D. G. Steyn, and M. Baldi (2002), The climatology of sea breezes on Sardinia, *Int. J. Climatol.*, 22(8), 917–932.
- Garvine, R. W. (1995), A dynamical system for classifying buoyant coastal discharges, *Cont. Shelf Res.*, 15, 1585–1596.
- Garvine, R. W. (2001), The impact of model configuration in studies of buoyant coastal discharge, *J. Mar. Res.*, 59, 193–225.
- Geyer, W. R., R. P. Signell, D. A. Fong, J. Wang, D. M. Anderson, and B. A. Keafer (2004), The freshwater transport and dynamics of the western Maine coastal current, *Cont. Shelf Res.*, 24, 1339.
- Gille, S. T., S. G. Llewellyn Smith, and S. M. Lee (2003), Measuring the sea breeze from QuikSCAT Scatterometry, *Geophys. Res. Lett.*, 30(3), 1114, doi:10.1029/2002GL016230.
- Glenn, S. M., and O. Schofield (2004), Observing the oceans from the COOLroom: Our history, experience, and opinions, *Oceanography*, 16.
- Guo, X. Y., and A. Valle-Levinson (2007), Tidal effects on estuarine circulation and outflow plume in the Chesapeake Bay, *Cont. Shelf Res.*, 27, 20–42.
- Haidvogel, D. B., et al. (2008), Ocean forecasting in terrain-following coordinates: Formulation and skill assessment of the Regional Ocean Modeling System, *J. Comput. Phys.*, 227(7), 3595–3624.
- Hetland, R. D. (2005), Relating river plume structure to vertical mixing, *J. Phys. Oceanogr.*, 35, 1667–1688.
- Hickey, B. M., L. J. Pietrafesa, D. A. Jay, and W. C. Boicourt (1998), The Columbia River Plume Study: Subtidal variability in the velocity and salinity fields, *J. Geophys. Res.*, 103(C5), 10,339–10,368, doi:10.1029/97JC03290.
- Horner-Devine, A. R. (2008), The bulge circulation in the Columbia River plume, *Cont. Shelf Res.*, 29, 234–251, doi:10.1016/j.csr.2007.12.012.
- Horner-Devine, A. R., D. A. Fong, S. G. Monismith, and T. Maxworthy (2006), Laboratory experiments simulating a coastal river inflow, *J. Fluid Mech.*, 555, 203–232.
- Horner-Devine, A. R., D. A. Fong, and S. G. Monismith (2008), Evidence for the inherent unsteadiness of a river plume: Satellite observations of the Niagara River discharge, *Limnol. Oceanogr.*, 53, 2731–2737.
- Houghton, R. W., C. E. Tilburg, R. W. Garvine, and A. Fong (2004), Delaware River plume response to a strong upwelling-favorable wind event, *Geophys. Res. Lett.*, 31, L07302, doi:10.1029/2003GL018988.
- Hunter, E., R. Chant, L. Bowers, S. Glenn, and J. Kohut (2007), Spatial and temporal variability of diurnal wind forcing in the coastal ocean, *Geophys. Res. Lett.*, 34, L03607, doi:10.1029/2006GL028945.
- Hyder, P., J. H. Simpson, and S. Christopoulos (2002), Sea-breeze forced diurnal surface currents in the Thermaikos Gulf, north-west Aegean, *Cont. Shelf Res.*, 22(4), 585–601.
- Lentz, S. J., and K. R. Helfrich (2002), Buoyant gravity currents along a sloping bottom in a rotating fluid, *J. Fluid Mech.*, 464, 251–278.
- Lerczak, J. A., M. C. Hendershott, and C. D. Winant (2001), Observations and modeling of coastal internal waves driven by a diurnal sea breeze, *J. Geophys. Res.*, 106, 19,715–19,729, doi:10.1029/2001JC000811.
- Lerczak, J. A., W. R. Geyer, and R. J. Chant (2006), Mechanisms driving the time-dependent salt flux in a partially stratified estuary, *J. Phys. Oceanogr.*, 36, 2296–2311.
- Levinton, J. S., and J. R. Waldman, (2006), The Hudson River Estuary, Cambridge University Press, New York, 417 pp.
- MacCready, P., and W. R. Geyer (2001), Estuarine salt flux through an isohaline surface, *J. Geophys. Res.-Oceans*, 106, 11629–11637.
- MacDonald, D. G., L. Goodman, and R. D. Hetland (2007), Turbulent dissipation in a near-field river plume: A comparison of control volume and microstructure observations with a numerical model, *J. Geophys. Res.*, 112, C07026, doi:10.1029/2006JC004075.
- Masse, A. K., and C. R. Murthy (1990), Observations of the Niagara River thermal plume (Lake Ontario, North America), *J. Geophys. Res.*, 95(C9), 16,097–16,109.
- Masse, A. K., and C. R. Murthy (1992), Analysis of the Niagara River Plume Dynamics, *J. Geophys. Res.*, 97(C2), 2403–2420.
- Mellor, G. L., and T. Yamada (1982), Development of a turbulence closure model for geophysical fluid applications, *Rev. Geophys. Space Phys.*, 20, 851–875.
- Miller, S. T. K., B. D. Keim, R. W. Talbot, and H. Mao (2003), Sea breeze: Structure, forecasting, and impacts, *Rev. Geophys.*, 41(3), 1011, doi:10.1029/2003RG000124.
- Mukai, A. Y., J. J. Westerink, R. A. Luettich, and D. J. Mark (2002), East-coast 2001, A tidal constituent data base for the western North Atlantic, Gulf of Mexico and Caribbean Sea. Engineer Research and Development Center/Coastal and Hydraulics Laboratory, *Tech. Rep. TR-02-24*, 196 pp.
- Nof, D. (1988), Eddy-wall interactions, *J. Mar. Res.*, 46, 527–555.
- Nof, D., and T. Pichevin (2001), The ballooning of outflows, *J. Phys. Oceanogr.*, 31, 3045–3058.
- Orton, P. M., and D. A. Jay (2005), Observations at the tidal plume front of a high-volume river outflow, *Geophys. Res. Lett.*, 32, L11605, doi:10.1029/2005GL022372.
- Peters, H. (1997), Observations of stratified turbulent mixing in an estuary: Neap-to-spring variations during high river flow, *Estuar. Coast. Shelf S.*, 45, 69–88.
- Pinones, A., A. Valle-Levinson, D. A. Narvaez, C. A. Vargas, S. A. Navarrete, G. Yuras, and J. C. Castilla (2005), Wind-induced diurnal variability in river plume motion, *Estuar. Coast. Shelf S.*, 65, 513–525.
- Pullen, J., T. Holt, A. F. Blumberg, and R. D. Bornstein, (2007), Atmospheric response to local upwelling in the vicinity of New York–New Jersey harbor, *J. Appl. Meteorol. Climatol.*, 46, 1031–1052.
- Shepetchkin, A. F., and J. C. McWilliams (2005), The regional oceanic modeling system (ROMS): A split-explicit, free-surface, topography-following-coordinate oceanic model, *Ocean Model.*, 9, 347–404.
- Simpson, J. E. (1994), *Sea breeze and local winds*, Cambridge Univ. Press, Cambridge, New York, 234 pp.
- Simpson, J. H., P. Hyder, T. P. Rippeth, and I. M. Lucas (2002), Forced oscillations near the critical latitude for diurnal-inertial resonance, *J. Phys. Oceanogr.*, 32, 177–187.
- Valle-Levinson, A., J. M. Klinck, and G. H. Wheless (1996), Inflows/outflows at the transition between a coastal plain estuary and the coastal ocean, *Cont. Shelf Res.*, 16, 1819–1847.
- Warner, J. C., W. R. Geyer, and J. A. Lerczak (2005), Numerical modeling of an estuary: A comprehensive skill assessment, *J. Geophys. Res.*, 110, C05001, doi:10.1029/2004JC002691.
- Whitney, M. M., and R. W. Garvine (2005), Wind influence on a coastal buoyant outflow, *J. Geophys. Res.*, 110, C03014, doi:10.1029/2003JC002261.
- Whitney, M. M., and R. W. Garvine (2007), Estimating tidal current amplitudes outside estuaries and characterizing the zone of estuarine tidal influence, *J. Continent. Res.*, 28, 280–290.
- Wilkin, J. L. (2006), The summertime heat budget and circulation of southeast New England shelf waters, *J. Phys. Oceanogr.*, 36, 1997–2011.
- Wong, K. C. (1998), On the variability in the vertical structure of the Delaware coastal current, *Cont. Shelf Res.*, 18, 929–940.
- Yankovsky, A. E., and D. C. Chapman (1997), A simple theory for the fate of buoyant coastal discharges, *J. Phys. Oceanogr.*, 27, 1386–1401.
- Yankovsky, A. E., B. M. Hickey, and A. K. Munchow (2001), Impact of variable inflow on the dynamics of a coastal buoyant plume, *J. Geophys. Res.-Oceans*, 106, 19809–19824.
- Zhang, W. G., J. L. Wilkin, and R. J. Chant (2009a), Modeling the pathways and mean dynamics of river plume dispersal in the New York Bight, *J. Phys. Oceanogr.*, 39, 1167–1183.
- Zhang, W. G., J. L. Wilkin, J. C. Levinand, and H. G. Arango (2009b), An adjoint sensitivity study of buoyancy- and wind-driven circulation on the New Jersey inner shelf, *J. Phys. Oceanogr.*, 39, 1652–1668.

R. J. Chant, E. J. Hunter, J. Kohut, and J. L. Wilkin, Institute for Marine and Coastal Sciences, Rutgers, State University of New Jersey, New Brunswick, New Jersey 08901-8521, USA. (hunter@marine.rutgers.edu)

# Dual-use of compact HF radars for the detection of mid- and large-size vessels

Hugh J. ROARTY<sup>1</sup>, Don E. BARRICK<sup>2</sup>, Josh T. KOHUT<sup>1</sup>, Scott M. GLENN<sup>1</sup>

<sup>1</sup>*The Coastal Ocean Observation Laboratory, Institute of Marine and Coastal Sciences Rutgers,  
The State University of New Jersey, New Brunswick, NJ 08901 USA*

*e-mail: hroarty@marine.rutgers.edu*

<sup>2</sup>*CODAR Ocean Sensors, Ltd., 1914 Plymouth Street Mountain View, CA 94043 USA*

## Abstract

*This paper describes the development of the SeaSonde High Frequency Radar system into a dual-use application for the mapping of ocean surface currents and detection of ships at sea. This development entailed the creation of a new radar waveform that would permit this dual-use as well as a detection algorithm to identify the ships in the radar spectra. The detection algorithm utilizes two methods for calculating a background signal level: an infinite impulse response (IIR) filter and a two-dimensional median filter. These two methods are employed simultaneously with multiple length averaging times to maximize the number of detections. The initial phase of development focused on improving the radar waveform to maximize the results for ship detection while still retaining the ability to measure surface currents. The latter phase of the development concentrated on testing the detection algorithm on a known vessel in different environmental conditions.*

**Key Words:** *HF radar, object detection, networks, ocean currents, remote sensing.*

## 1. Introduction

High Frequency Surface Wave Radars (HFSWRs) are proliferating as backbone instrumentation within the United States Integrated Ocean Observing System (IOOS). The main purpose of these radars is for environmental mapping of sea conditions such as surface currents, sea state and wind direction [1]. Figure 1 shows a recent map of ocean surface currents off the eastern United States from Cape Cod to Cape Hatteras. This map was created from the radial vectors generated by thirteen long-range (5 MHz) HFSWRs. The inset of Figure 1 shows wave height, period and direction data from one of those radars. However, another application for these radars is for the detection of vessels at sea [2]. Typical ship velocities fall in the same span as the Bragg waves from which currents and waves are derived. Echoes from ships are therefore frequently seen, and are considered clutter in the processing of sea echo to measure sea conditions. However, radar signal and processing parameters for measuring surface currents do not always match the best settings for detection of hard targets. Different

signal transmission and processing options were tested to determine the optimal settings for a dual-use radar (simultaneous current mapping and vessel detection). With these “optimal” settings, the radars collected echo time series vs. range data. These range data were processed into Doppler spectra using multiple-length fast Fourier transforms (FFTs) developed for this application. The Doppler spectral data were then run through a detection algorithm to pick out the vessel targets.

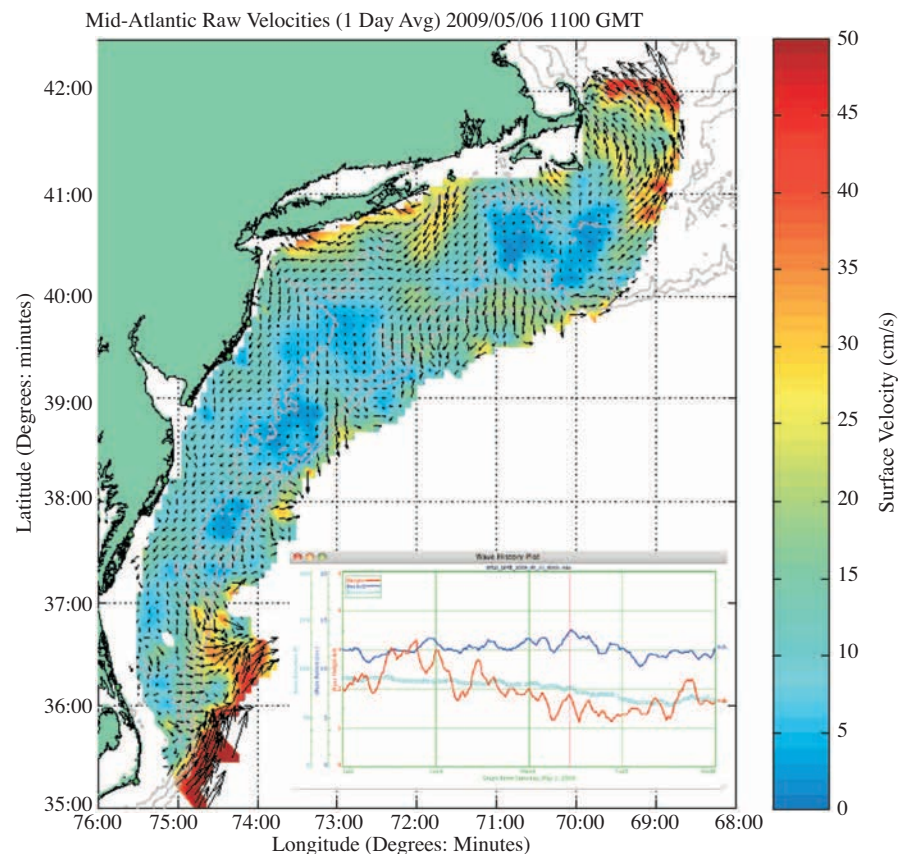


**Figure 1.** Map of surface currents from Mid Atlantic High Frequency Radar Systems. There are a total of 27 HF radars in the Mid Atlantic that are operational for environmental monitoring. The speed of the currents are displayed from the color bar on the right with the arrows indicating direction. Wave height (red), period (blue) and direction (aqua) from one of the radar systems is shown in the inset.

The detection algorithm consists of:

1. Calculating a background level of the Doppler spectrum by two different methods
2. Setting a threshold (typically 6-9 dB) above the background
3. Any signal above the threshold is considered a detection—the classic Constant False Alarm Rate (CFAR) detection algorithm.

A Global Positioning System (GPS) track record from the vessel was used as ground truth for the potential detections and served to optimize the algorithms.



## 2. A different approach—network coverage and multi-statics

This section introduces and discusses a departure of our approach from conventional radar ship surveillance—both High Frequency (HF) and microwave. HFSWRs [3] and sky wave radars [4] have been utilized for the detection of ships at sea. In the conventional approach, a single radar operates as a stand-alone system. Transmitter and receiver are collocated, and the radar is called backscatter or monostatic. If a target is successfully detected above the background, its position is given in polar coordinates, i.e., range and bearing from the radar. At HF, these single backscatter systems have weaknesses. Because target Doppler measurement is an accurate and critical HF observable, the vessel must compete with sea clutter, whose speed-induced Doppler causes it to fall in same velocity span as the targets being detected. The dominant sea echo is the first-order Bragg scatter that comes from ocean waves of half the radar wavelength; this echo is generally larger than the echo from even the largest supertanker. Surrounding the Bragg peaks are second-order sea echoes that lay 15 - 40 dB lower, but usually well above the background noise. Taken together, these sea echoes can mask and/or hinder detection of perhaps 40% of candidate ships. Sometimes a ship may be seen, but as it changes course or speed, it will enter a region of high sea clutter and disappear from radar view. As a countermeasure, it is trivial for a ship navigator to determine the frequency of the HF radar, and in order to evade detection, adjust speed/course so that it will be masked by the strong sea-clutter spectral background. Conceptually, if the radar could change operating frequency by a significant increment (e.g., factor of two), a ship hidden by a Bragg peak would be unmasked. Such complexity drives up the cost of the radar significantly.

The build-up of coastal HF radar networks in the U.S. and elsewhere for IOOS-related current and wave monitoring offers an opportunity to conceive of a different approach to ship surveillance with the conventional single backscatter radar scenario described above. The backscatter radars of these distributed networks are spaced sufficiently close together that the same spot on the sea is observed by at least two radars. When applied to ship detection, this means that the same vessel will be viewed from two or more different angles leading to several advantages. First, in the distributed network if the target's radial velocity with respect to one radar is masked by a sea-echo spectral peak, a second radar or a third—seeing a different radial velocity from that target—will uncover the target. Second, if the transmitter of one radar (or a transmitter on a buoy) serves as the target illuminator, then the echo seen by a second receiver (the multi-static configuration) cannot also be masked. In other words, different simultaneous observing geometries have the advantage of unmasking a target hidden in the clutter of a single radar. Third, external noise bursts—that can cause loss of detection at one radar receiver—rarely occur at the same range/Doppler for two or more radar receivers. Fourth, even if the masking is not a problem, multiple solid observations of the same target increase the probability of detection and reduce false alarm rate.

Multiple observations of the same target entail another algorithmic function that must be added to the detection-tracking process. This function is the association task: which detection seen by one radar observation is the same as one seen by another radar? Or, is one seeing a new target that is close to the first? The development of this association algorithm can also aid in target identification / classification. It improves the tracking accuracy significantly: bearing accuracy, which is the weakest observable at HF, is mitigated by the triangulation offered by multiple observations of the same target. In addition, it can feed back information to the detection process of radars that may have lost the target as it moved into sea-echo peaks: i.e., one radar can inform another radar where to look for the target as it emerges from the sea clutter. We will examine the

ramifications of this multi-observation system enabled by the network approach to HF radar configuration that is being put into place for other purposes.

### 3. Network operation and data collection

The HFSWR used for these experiments was the SeaSonde developed by CODAR Ocean Sensors. The SeaSonde has been in use for the past two decades for the mapping of ocean surface currents [5]. This paper explores the dual-use aspect of the SeaSonde for measuring surface currents as well as detection of hard targets (ships). Signals from ships were seen in the data from the outset of the development process for current and wave monitoring. Since the SeaSonde was designed to extract information from the sea echo, algorithms were developed to remove the ship echo from the data. The algorithms that have been specifically developed to extract the ship information from the data will be explained later.

The SeaSonde is capable of operating monostatically, where the transmit and receive antennas are colocated, as well as bistatically, where the recorded signal originates from a transmitter some distance from the location of the receiver. The radars are capable of operating bistatically by using GPS synchronization timing [6]. A network of radars is then capable of operating multi-statically where the individual radars are observing simultaneously in monostatic and several bistatic modes. The Rutgers HF Radar Network was operated multi-statically for the tests discussed here.

The first pair of these radars was installed at Brigantine and Brant Beach, NJ in 1998, followed in 2000 by long-range versions at Loveladies, Wildwood, Sandy Hook, and Tuckerton, NJ. A map showing the location of the four long-range SeaSonde units is shown in Figure 2a. Each radar site consists of a Codar SeaSonde system housed in a climate controlled enclosure with cables leading to the transmitter and receiver antennas typically deployed on the beach near the dune line. Figure 2b shows the radial vector density for 2003, the second year of the study. The radial vectors from each site were produced every three hours. The long-range transmit antenna is a monopole with height of a quarter wave length (15 m) of the transmitted signal, nominally 5 MHz. The receive antenna consists of an omnidirectional monopole and two directional crossed loops [7], [8]. A picture of one of the compact radar installations is shown in Figure 3. The spacing between the antennas is approximately one wavelength, 60 m in this case for a 5 MHz system. The radars have been in constant operation since their installation.

The SeaSonde is a direction-finding HF radar system. A direction finding system measures the returned signal over all directions on the three receive antennas. These signals are then passed through the multiple signal classification (MUSIC) algorithm to determine bearing of the incoming signal [9].

The antenna pattern is a measure of the response of each element to incoming signals. The ideal loop pattern free of any distortion is a sinusoid; two crossed loops have a sine and cosine pattern over bearing angle. When the antenna is placed in the field, objects in the near field (within one wave length) can couple with the antenna and distort the ideal pattern. That is why it is important to always measure the antenna pattern when the system is first installed to quantify and correct for any possible distortion [10]. Any distortion will impact the bearing determination of the incoming signal. The antenna patterns of all systems were measured and used by the detection algorithm.

The nature of the vessel tracking tests varied in the initial stages. Vessel detection tests used multiple ships (dedicated vessels as well as ships of opportunity), of various sizes, to test different signal transmis-

sion/processing options, in order to optimize the SeaSondes for dual use (simultaneous current mapping and vessel detection). Examples of associated GPS tracks for each test are plotted as the aqua lines in Figure 2A. At the conclusion of this initial set of tests, the Rutgers network was modified based on lessons learned in Year 1. The best dual-use waveform, which will be explained later, was installed on all systems. GPS timing was adjusted for multi-static data collection from all four New Jersey long-range sites. Data archiving was done for range files, which are a collection of consecutive time sweeps consisting of received signal power versus range. The data processing paths for ship detection and current mapping diverge after the range file creation. Archiving these

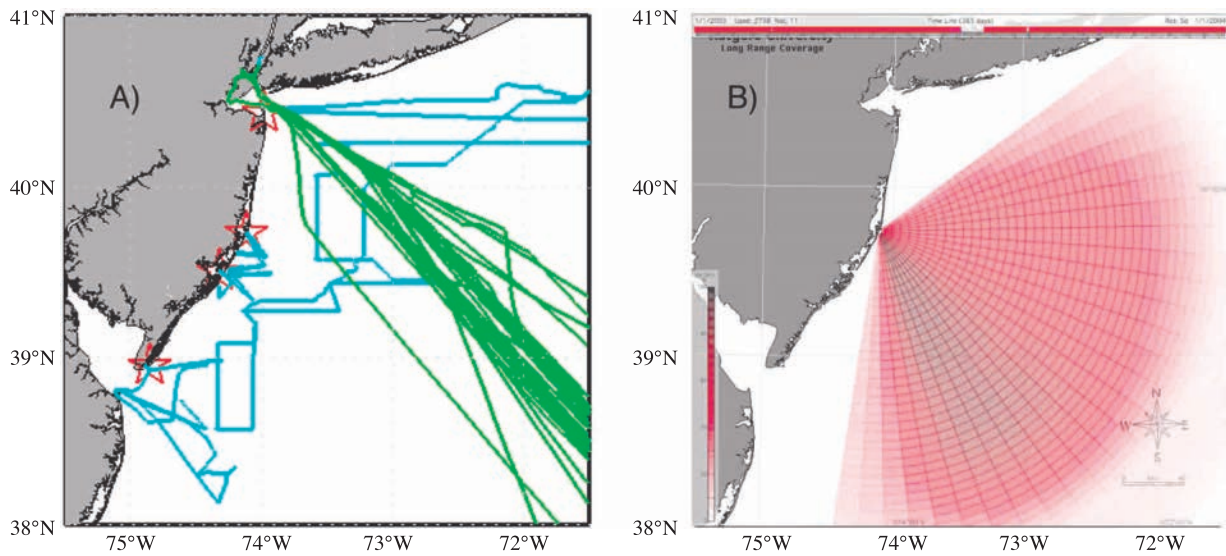


**Figure 2.** (A) Study area off the coast of New Jersey showing the location of the four long-range SeaSonde units as red stars. The tracks of the vessels in year 1 (aqua) and year 2 (green) used for the study. (B) The radial vector density from the Loveladies SeaSonde site for year 2. The polar grid delineates the angular and range bins of the radar. The color bar is on the lower left hand side to illustrate spatial coverage and the timeline along the top shows temporal coverage.



**Figure 3.** Picture of 5 MHz long-range SeaSonde. The receive antenna is shown in the foreground on the right. The transmit antenna is shown in the background on the left. Technicians installing the radar are shown for scale.



range files enables use of multiple-length FFT post-processing for vessel tracking that was not necessary for current mapping. The radar sites were able to measure currents during this entire time period [11] when the ship detection capability of the radar was being developed.

A long-term test of the multi-static network was begun using a single known ship, the M.V. Oleander ..[12], as a known, reliable test target that could be examined under a variety of environmental conditions. The Oleander is a container ship that maintains a weekly schedule of transits between New York and Bermuda. GPS tracks obtained from the University of Rhode Island (green lines in Figure 2A) indicate that the Oleander usually approaches and departs New York Harbor along the Hudson Canyon traffic lane and only once used the north-south Barnegat traffic lane. Over 7 months of multi-static SeaSonde data at the range file level were collected and archived at the four long-range radars. The GPS data were used to identify times when the Oleander was within 200 km of Sandy Hook for detection processing.

## 4. HF radar target observables

HF radar ship (or hard target) detection and processing is much different from standard microwave radar target detection, because the HF radar signals and processing, including use of direction finding instead of beam scanning for bearing determination, are significantly different. The HF ship-detection observables listed in order of accuracy and importance are:

1) **Echo Doppler shift, and thence radial velocity.** This is the most accurate and meaningful parameter from an HF radar. It is usually nonexistent in conventional microwave target detection. The equation used to calculate radial velocity is given as

$$v_r = \frac{f_d \lambda}{2},$$

where  $v_r$  is the radial velocity (m/s),  $f_d$  is the Doppler frequency( $s^{-1}$ ),  $\lambda$  is the radar wave length (m). The sign convention here is positive for targets approaching the radar and negative for targets receding from the radar. The velocity resolution for the SeaSonde system operating at the nominal 5 MHz is 3 cm/s with a maximum velocity of 15 m/s before aliasing within the Doppler window for each range cell.

2) **Target range.** This is also quite precise, but is quantized based on the bin size (e.g., 1.5 km, 3 km or 6 km, depending on the signal bandwidth). The range to target for any radar depends on the time delay of the scattered signal after transmission. The SeaSonde employs a unique, patented method of determining the range from this time delay. By modulating the transmitted signal with a swept-frequency signal and demodulating it properly in the receiver, the time delay is converted to a large-scale frequency shift in the echo signal. The frequency shift is used to calculate distance to target. The detection algorithm does a fit to range bins in order to narrow the range more precisely. This fit uses a centroid calculation of the sum of the product of the signal range and power divided by the sum of the signal power. This range measurement is quite accurate, depending on the Signal to Noise ratio (SNR).

3) **Target bearing.** This is calculated for the echo at each spectral point (range and speed) by using simultaneous data collected from the three collocated directional receive antennas (two crossed loops and a monopole). The complex voltages from these three antennas are put through a ‘direction-finding’ (DF) algorithm to get the bearing. The particular, patented algorithm adapted and perfected for the SeaSonde is referred to

as MUSIC [13]. Bearing is the poorest observable, and is usually noisy. This is the nature of working with compact antennas designed for frequencies 1000 times lower than microwave. With microwave radars, range and bearing are quite accurate observables while range rate is not directly observed.

4) **Target echo amplitude** (from the signal strength). As with microwave radars, this echo amplitude is a fluctuating quantity, depending on ship aspect, sea state, and other environmental factors. Target amplitude can be used to calculate the target radar cross section (RCS). The RCS is a very good identifier of the nature of the target, i.e., its size and sometimes its shape.

5) **Uncertainties** in the first three quantities are calculated and included in the detection file for a suspected target. These are estimated based on resolution, SNR and other considerations.

## 5. Waveform

The SeaSonde is unique from most microwave radars in the fact that it does not use pulsing to determine range to the target. Range is determined by using a waveform with a repeating linear frequency sweep. However, unlike time-domain pulse compression used with chirp waveforms for microwave radars, the echo time delay shows up as a frequency offset between the presently transmitted signal and the received target signal. Pulsing is used by the SeaSonde only so that the receiver and its incoming signal integrity will not be damaged nor limited by swallowing an intense transmit signal while receiving the weaker target echoes. Thus, we consider the pulsing only as a means for turning the transmitter and receiver on and off at complementary times, to preserve this integrity. In the case where transmitter and receiver are separated (called a bistatic radar), pulsing is not necessary and not used by the SeaSonde, because the separation between the two prevents damage to receiver and signal integrity.

The signal-to-noise ratio, SNR, in any optimized receiver (referred to as a “matched-filter receiver”) is proportional to the average power, not the peak power. By pulsing, for a given maximum peak power, the average power—and hence the SNR—is reduced. If one must pulse so that transmitter and receiver are not on at the same time, the best one can do in maximizing average power is a 50% duty-factor signal. This happens when the receiver/transmit on/off patterns are identical. The simplest way to do this is a square wave. All SeaSonde waveforms were invented to employ this maximum 50% duty factor pulsed waveform, but to do so in a manner that optimizes the SNR over the coverage region of interest [14]. In addition, the square-wave edges of the transmit signal are tapered slightly. This goes a long way to reducing spectral harmonics of the pulsing that cause slower roll-off of the signal away from the edges of the sweep, thereby mitigating interference possibilities to others. The pulse tapering that was used reduces the duty factor only slightly, i.e., to about 48%.

For current mapping from the sea echo, pulsing/gating has another advantage. Sea echo is a strong signal that appears in every range cell. Echoes, however, fall off very rapidly with distance from the radar. Hence, strong echoes in early range cells must be suppressed so their range-processing side lobes don’t overwhelm the weaker echoes further out, mitigating this dynamic range constraint. This is achieved for microwave radars by using sensitivity-time control circuitry. Square wave pulsing meets this requirement by reducing echoes from early range cells at no expense to weak echoes from distant ones.

All standard SeaSonde systems are designed to operate optimally for sea echo, i.e., current mapping. However this waveform is not optimal for detection of smaller vessels in close range cells. It was the aim of the research done here to optimize the radar wave form for both current mapping as well as target detection. This entails optimizing the waveform to identify small targets closer to the radar where their echo SNR is much

weaker than that of the sea echo, rendering the signals too weak to be detected. This waveform was designed to increase the SNR of signals close to the radar while not compromising the SNR at distant ranges from the radar. To illustrate this design progression see Figure 4 which details three types of square wave pulsing with different lengths. The longer curve shown in red has a pulse length optimized for measuring surface currents using the 5 MHz long-range SeaSonde, about 2000 microseconds long. Two other pulsing options are shown in the middle panels. The one on the left uses mixed length pulsing and is used for calibrating the radar. The one on the right is a combination of the one optimized for currents and the one used for calibration which is given the name enhanced. The waveform duty factors for the three wave forms are shown and compared in the bottom panels. The duty factor is the fraction of signal that is available for use in the detection process. In the case of the wave form designed for currents measurements (red), 100% (0 dB) of the signal scattered off a target (waves or ships) at a range 190 km are available for reception at the receiver. Whereas, the signal scattered off a target at a range of 10 km is only visible to the receiver 0.1% (-30 dB) of the time. When the pulse is scattering off these close targets the receiver is off most of the time. Only at the end of the pulse does the receiver turn on and is able to receive signals from close targets. The receiver is on the entire time and is able to receive the full scattering signal from targets at a range of 190 km.

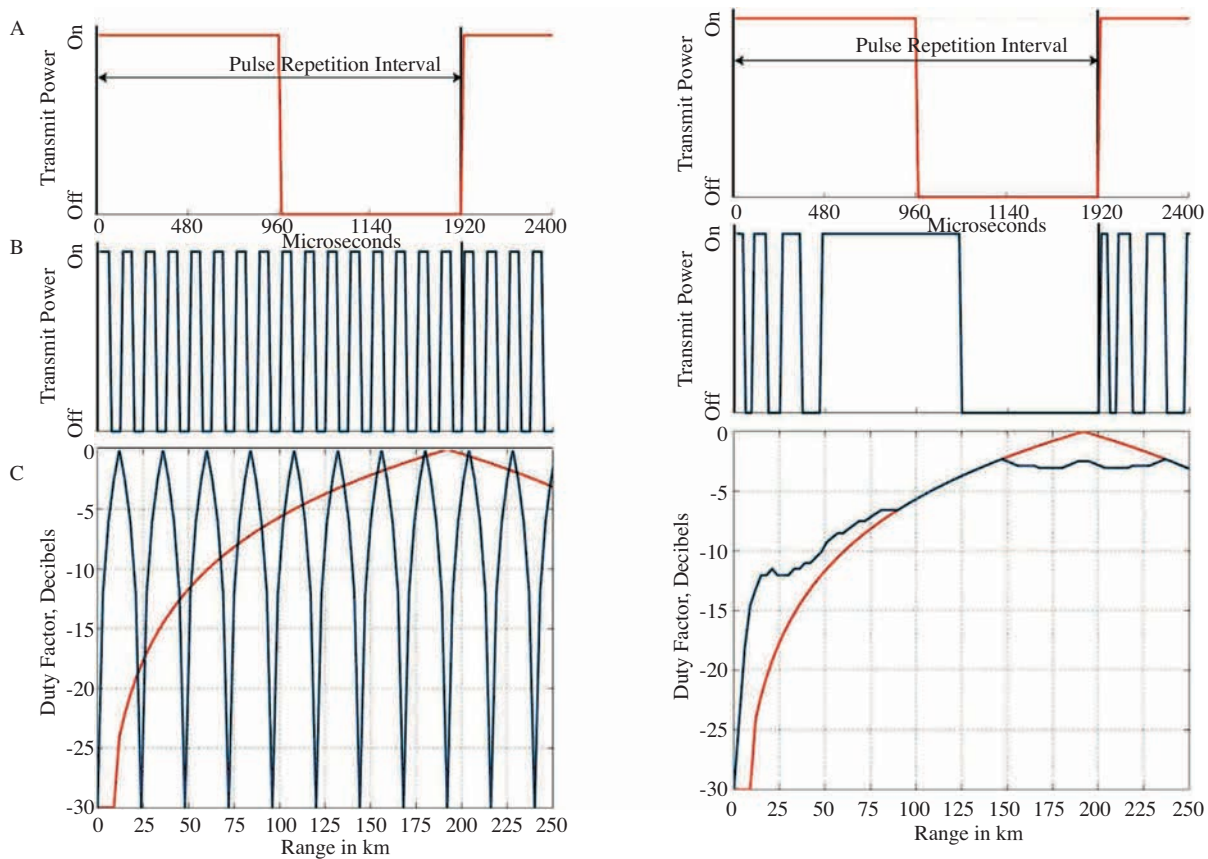


**Figure 4.** (A) Square-wave pulsing (red line) suitable for long-range current mapping. (B) Mixed length pulsing (left) used for calibration measurements of the radar. Enhanced pulsing (right) increases signal strength on targets close in, while minimizing loss at greatest range. (C) Duty factor vs. range for the three pulsed waveforms, square (red), mixed (blue, left) and enhanced (blue, right).



Figure 4 shows the standard square-wave pulsing installed on any standard Long-Range SeaSonde systems for current mapping, as the red upper curve. Its duty factor for target echo strength maximizes near 200 km, as shown in the lower panel. The blue curve in the middle left represents a very short-pulsed square waves that has been used for antenna pattern calibrations. This simple waveform offers much greater echo power close in, out to  $\sim 11$  km; it can be greater by nearly 30 dB from the long-pulse red duty factor, seen from the lower panel. However, it has blind zones at 25 km, 50 km, etc.

The waveform shown in Figure 4 on the middle right shows the compromise developed for dual use. Here, a 50% duty factor is achieved, the best that can be done. At close in ranges, power is higher by 13 dB from that of the default long square wave (compare the difference between red and blue curves in the lower panel at 25 km). On the other hand, there are no blind zones in the coverage area. Furthermore, the power at maximum range (200 km) is only down by 2.5 dB. This waveform was set at the beginning of Year 2 and is currently being used on all Rutgers long-range SeaSonde systems. In addition to being beneficial for hard target detection this wave form is also useful in increasing weaker close-in signals from the second-order sea echo which are utilized for wave parameter (height, period, direction) estimates.

## 6. Ship detection algorithm

The ship detection algorithm uses a straightforward thresholding scheme, which is known in the microwave radar community as constant false alarm rate CFAR. After a peak (local maximum) in the spectral domain (range-Doppler space) is identified, its SNR, which is the signal power divided by the noise floor or background power, has to be above a preset threshold for antenna 3 (monopole) and at least one of the two loops (antenna 1 or 2). Usually a threshold of six to ten dB gives good detection rates at HF without too many false positives. The thresholding is excluded for regions around the zero-Doppler position and sea-echo Bragg peaks. Both regions produce strong signal returns that would make detecting a ship nearby very difficult. The zero-Doppler is from signals returned from any stationary object while the sea-echo Bragg peaks are due to signal returns off ocean waves with half the wavelength of the transmitted radio signal [15]. Currently two bins on each side of zero Doppler and Bragg peaks are excluded.

Two types of background calculations were used to identify the noise floor: a 2-D median filter that averages by finding the median in Doppler space and range, which was based upon an image processing algorithm [16], and an Infinite Impulse Response (IIR) filter that averages in time, also known as an exponential smoother [17]. An example of the two background calculations is shown in Figure 5. Panel 5A shows the power spectrum with the IIR background. Panel 5B shows the power spectrum and the median background. The peak that represents a ship (marked by the arrow) can be identified above the background plus threshold in both cases. The two backgrounds produce a different SNR for this vessel, 15.0 dB for the IIR background and 11.3 dB for the median background. Note that the zero-Doppler and Bragg peaks in the IIR background are thicker due to lower resolution. Hence the median background has the potential to detect targets closer to these regions. The pros and cons of the two methods are discussed in Table 1.

Since these two methods complement each other, it was decided that the best strategy is to employ both at the same time. Also built into the detection algorithm is the ability to use simultaneous different-length, multiple sliding window FFTs in the Doppler processing. Typical FFT lengths range from 8 to 1024 points.

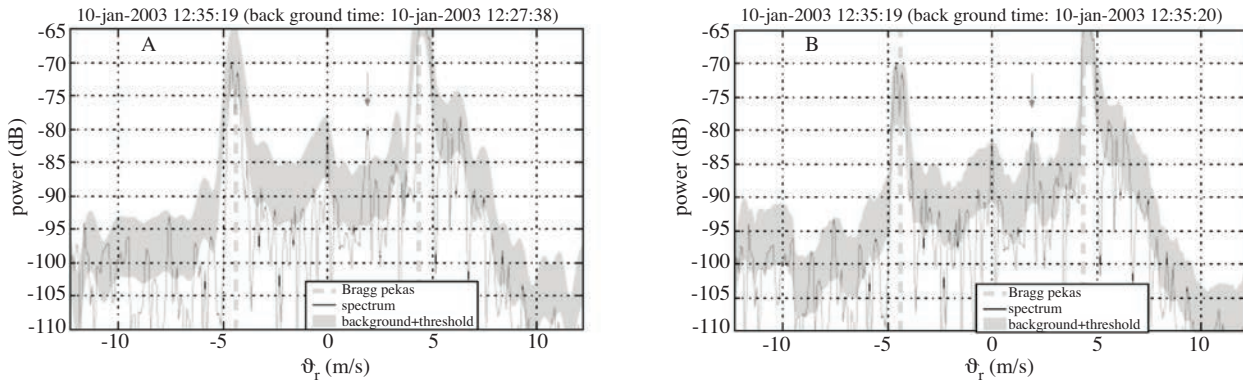


**Figure 5.** Power spectrum compared with two types of background (a) Infinite Impulse Response and (b) Median. The FFT length is 256 and the IIR background length is 64. The threshold is 7 dB for both. The ship is marked by the arrow between zero Doppler and 5 m/s radial velocity.

**Table 1.** Pros and Cons of IIR Background versus median background.

	IIR Background	Median Background
Pros	<ul style="list-style-type: none"> <li>• Fast for multiple FFTs</li> <li>• Smoother variation in time</li> <li>• More consistent results during calm ocean</li> </ul>	<ul style="list-style-type: none"> <li>• Fast for short FFTs</li> <li>• Faster response</li> <li>• Possible detection closer to zero-Doppler and Bragg peaks</li> </ul>
Cons	<ul style="list-style-type: none"> <li>• Have to wait for onset of detection (edge effect)</li> <li>• Slower response time</li> <li>• More prone to false positives during times of interference</li> </ul>	<ul style="list-style-type: none"> <li>• Slower for multiple FFTs</li> <li>• Less consistent tracks during calm ocean</li> <li>• Detection at edge range bins less reliable</li> </ul>

## 7. Test results

One case study is presented here to display the current capability of the detection system. This example is for the transit of the vessel Oleander out of New York Harbor on February 21, 2004. The center transmit frequency of the radar was set to 4.55 MHz with a bandwidth of 25 kHz, which results in a range cell size of 5.85 km. The range data from the radar was passed onto the detection algorithm. The detection algorithm was run using six parallel processes: three using the median background with 64, 128 and 256 point FFTs and three using the IIR background with 128, 256 and 512 point FFTs. All six processes used a 32 second update interval. The Oleander became visible to the radar at approximately 0030 GMT and was 150 km from the radar at 0600 GMT. The thresholds that were used with each FFT length are given in Table 2. The threshold used in the SeaSonde processing for currents is 6 dB, so that was used as the starting point. The threshold was increased

by 1 dB for each doubling of the FFT length because it was learned through previous runs of the algorithm that the average SNR increased by 1 dB with each doubling of the FFT. This trend is generally expected as the SNR should increase by 3 dB for a constant Doppler target when doubling the FFT length. The fact that average SNR only increased by 1 dB reveals the inconsistency of the target velocity/Doppler over the time intervals. The matrix shown in Table 2 is only one of several possible permutations for the FFT length and threshold level. The authors will explore the optimal settings in different environmental conditions for future work.

**Table 2.** Parameters used for one execution of the detection algorithm.

Nfft	Threshold Using Median Background (dB)	Threshold Using IIR Background (dB)
64	6	NA
128	7	6
256	8	7
512	NA	8

An example of the file output from the detection algorithm is shown as Table 3. This is the output using the median background with an FFT length of 512 points and a threshold of 8 dB. Each line represents one detection by the radar at one instance in time. The metadata is shown at the top of the file, preceded by percent symbols so they will be considered comments by programs that would be used to read the data. The columns of data reading from left to right for each detection are range cell number, Doppler velocity in spectral bins from the center, range (km), range uncertainty (km), radial velocity (m/s), radial velocity uncertainty (m/s), bearing of the target in degrees clockwise from north ( $^{\circ}$  CWN), bearing uncertainty ( $^{\circ}$ ), longitude ( $^{\circ}$ ), latitude ( $^{\circ}$ ), east distance from the radar (km), north distance from the radar (km), signal to noise ratio for loops 1, 2 and 3 (dB), spectral power of the monopole (dB) and the radar cross section of the target (dB). A detection file is generated at every update interval.

A plot of all the detection files using the median filter with an FFT length of 256/8 dB threshold is shown in Figure 6. There are five other plots like this one corresponding to the five other detection methods, but they are not shown here to conserve space. The top panel shows detected points in range as a function of time over a four hour period. The second panel is the detected-peak Doppler shift, converted to range rate. The two yellow lines are the position of the Bragg sea echo. These regions constitute intense clutter peaks at and near which ship detection is difficult. Lastly, the bottom panel shows the bearing of the detected points. The solid yellow regions are bearing sectors over which it was not expected for the radar to make measurements (i.e. in back of the radar on land). The solid aqua line in all three panels is the ground truth data of the Oleander as derived from the GPS record of the vessel.

This detection process identifies many signals that exceed the threshold of 8 dB that was set. These are all candidate ships. Some are real vessels and some are false alarms. When one plots these points in range, range rate, and bearing as a function of time, patterns quickly emerge. A real vessel becomes obvious, as one will see a continuous trail of concatenated points as time marches forward as seen in the top panel of Figure 6. Many other points appear only once at or near any position in 4D space (range, range rate, bearing, and time). These are false alarms. They may be due to random atmospheric noise (e.g., near and distant thunderstorms) or radio interference. When all of these detection candidate points are plotted, their unique appearance has given rise to the descriptive term “pepper plots.”



**Table 3.** Output of detection algorithm. The columns of data reading from left to right for each detection are range cell number, Doppler velocity in spectral bins from the center, range (km), range uncertainty (km), radial velocity (m/s), radial velocity uncertainty (m/s), bearing of the target in degrees clockwise from north ( $^{\circ}$  CWN), bearing uncertainty ( $^{\circ}$ ), longitude ( $^{\circ}$ ), latitude ( $^{\circ}$ ), east distance from the radar (km), north distance from the radar (km), signal to noise ratio for loops 1, 2 and 3 (dB), spectral power of the monopole (dB) and the radar cross section of the target (dB).

%ship_detect ver.: 3.1 %Rx(SEAB): 73.9728 40.3617 %TransmitCenterFreqHz: 1.346000e+07 %TransmitBandwidthHz: -4.943848e+04 %TransmitSweepRateHz: 2.000000 %lobe1_bearing(deg CWN): 130 %use measured pattern %azLimit(deg cwn): -50 305 %Possible Targets: 14 %SNRThreshold(dB): 8 %Nfft: 512 %Rmax(km): 103.037 %TimeStamp: 2009 2 26 0 15 21 %timeConstforIIRfilterSec: 1800 %NfftBckGnd: 128 %bck_gnd_time_sec_ago: 416 %bck_gnd_time: 2009 2 26 0 8 25 %bin sizes(km, m/s): 3.03049 0.0435016																
%nr	nv	R	sigR	-Vr	sigVr	az(CWN)	sigAz	longi	latitude	x(E)	y(N)	snr1	snr2	snr3	P3	RCS
%(0-based)	(DC-ctr)	(km)	(km)	(m/s)	(m/s)	(deg)	(deg)	(deg)	(deg)	(km)	(km)	(dB)	(dB)	(dB)	(dB)	(dBsm)
0	-142	2.08	1.05	-6.18	0.015	285	14.02	73.949	40.367	-2	0.54	8.2	2.98	9.21	-106.5	-8.3
0	-41	1.26	0.49	-1.78	0.007	63	6.58	73.986	40.367	1.12	0.57	9.47	18.95	15.79	-101.7	-8
0	-38	1.21	0.52	-1.65	0.007	56	6.94	73.985	40.368	1	0.67	6.88	19.67	15.33	-102	-8.8
2	103	6.07	1.08	4.5	0.015	68	14.42	74.039	40.382	5.63	2.27	8.51	11.17	8.97	-82.8	26
3	-41	8.13	0.07	-1.78	0.001	61	0.95	74.057	40.397	7.12	3.94	24.02	32.18	32.62	-82	30
5	57	14.86	1.04	2.48	0.015	52	13.87	74.111	40.444	11.73	9.14	7.28	9.85	9.31	-92.3	27.2
7	-168	22.23	0.84	-7.32	0.012	259	11.27	73.715	40.323	-21.81	-4.27	7.86	8.03	11.12	-107.5	18.1
8	-80	23.88	1.18	-3.49	0.017	10	15.81	74.022	40.573	4.16	23.51	5.96	9.01	8.17	-104.3	22.5
11	236	32.02	1.09	10.26	0.016	305	14.62	73.662	40.526	-26.3	18.32	10.3	3.07	8.85	-107.5	24.8
14	120	41.08	1.09	5.22	0.016	300	14.59	73.552	40.546	-35.68	20.46	10.55	-0.19	8.87	-105.4	34.8
15	-211	45.7	1.15	-9.17	0.016	-40	15.36	73.624	40.676	-29.52	34.95	9.47	-5.18	8.42	-107.4	37.7
15	-180	47.66	1.06	-7.83	0.015	-48	14.17	73.553	40.648	-35.57	31.81	9.52	-16.77	9.12	-108.6	38.6
19	207	56.01	1.16	8.99	0.017	294	15.45	73.367	40.565	-51.32	22.61	9.4	-2.05	8.37	-108.1	48.5
30	71	89.8	1.16	3.07	0.017	304	15.57	73.088	40.81	-74.95	49.84	9.14	-5.94	8.31	-108.8	66.1

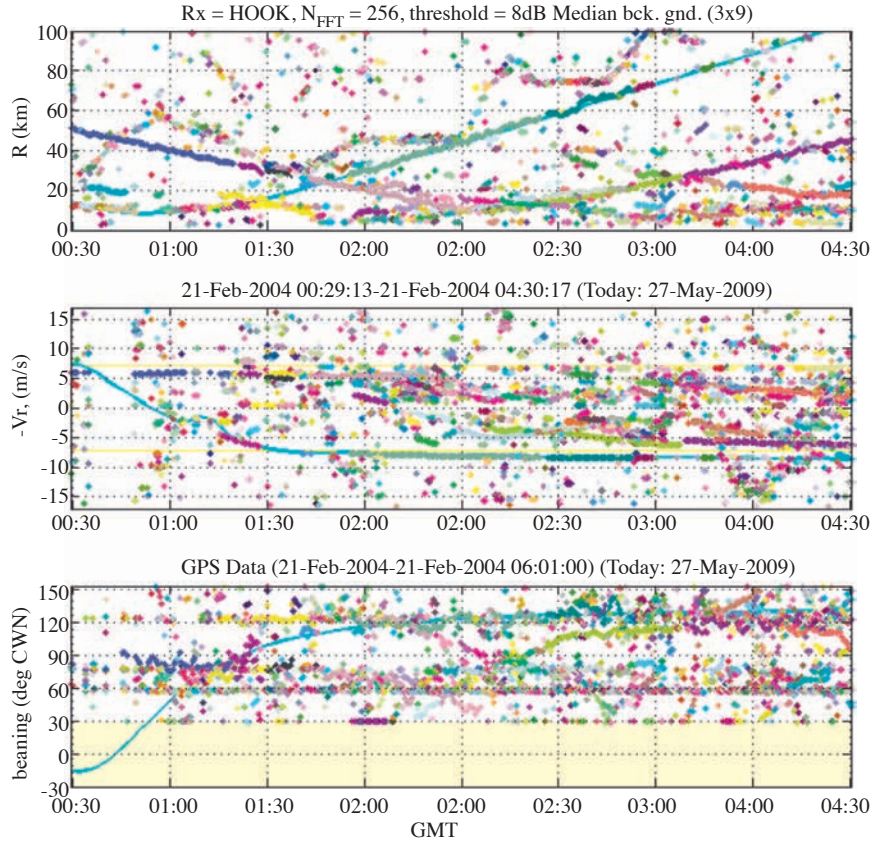


**Figure 6.** Detection results using the Median background with a 256 point FFT/8 dB threshold from the Sandy Hook radar site, February 21, 2004. The GPS track of the Oleander is shown as the solid aqua line. The algorithm is able to mark detections that are close in range or range rate with the same color.

Much of the volume of the pepper, i.e., point scatter, is controllable by the threshold that is set. The lower the threshold, the more pepper is admitted, becoming dominated by false alarms. The “false alarm rate” (FAR) is related to the threshold above the noise. For illustration we have included the results from another execution of the detection algorithm Figure 7. This shows the results of the detection algorithm using the Median filter with a threshold of 11 dB. Much of the pepper has been removed. The higher the threshold, the fewer false alarms, but then legitimate targets are missed (probability of detection, PD, goes down). FAR is exponentially (i.e., very strongly) related to threshold level, while PD varies much more slowly with threshold level. The philosophy we are exploring is that a higher FAR for dual-use HF radars is acceptable, because observation in 4D space and by multiple radars (overlapping backscatter and multi-static) will allow one to filter for the true ship target trails. This increases PD at lower SNR thresholds.

The valid detections on the Oleander for all six detection processes are shown in Figure 8. A detection is counted as valid when the calculated range is within half the width of a range bin and within two Doppler bins for speed. If the ship is seen by more than one detection scheme, the algorithm chooses the one with the largest SNR on the monopole. Figure 8 again shows range, range rate and bearing detections of the Oleander over a six hour period. The detections are represented by a square (error box) with half the height as on standard deviation and the width is the length of the FFT window. The solid aqua line in all three panels is the ground

truth data of the Oleander as derived from the GPS track record of the vessel. The six colors represent the six detection processes IIR-128 (blue), IIR-256 (red), IIR-256 (magenta), Median-64 (dark brown), Median-128 (brown), Median-256 (dark green). As the Oleander is departing NY Harbor and sailing past the Sandy Hook SeaSonde site, the radial velocity is changing. Over this section the shorter FFTs do a better job for the detections. As the Oleander reaches its cruising speed the longest FFT of the median background does the best for detecting the vessel. As noted in the radar observables the error bars for range and range rate are quite small while those for the bearing are the largest. The Oleander remained visible to the radar to a range of approximately 100 km and was seen 42% of the time. Including multiple length FFTs optimizes ship detection for the vessel type and velocity parameters: longer FFTs for larger vessels and shorter FFTs for smaller faster vessels. The advantages of calculating multiple length FFTs have been identified as a key design aspect of this detection scheme.

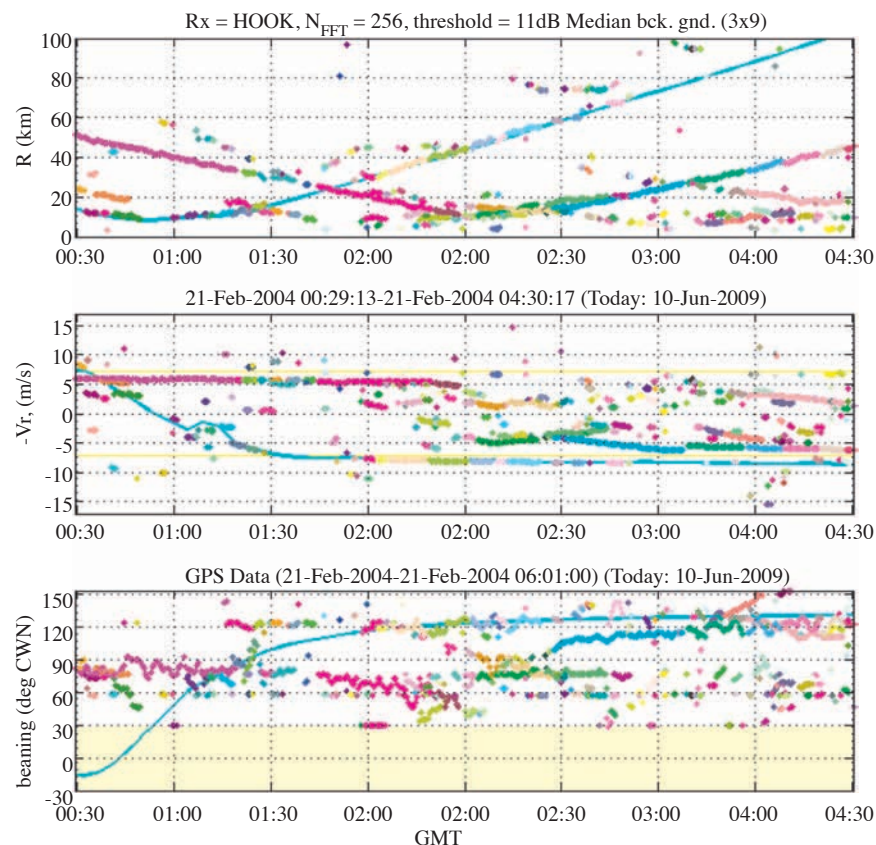


**Figure 7.** Detection results using the Median background with a 512 point FFT/11 dB threshold from the Sandy Hook radar site, February 21, 2004. The GPS track of the Oleander is shown as the solid aqua line. The algorithm is able to mark detections that are close in range or range rate with the same color.

## 8. Conclusions

As the number of HFSWRs for environmental monitoring increase, the potential exists to simultaneously use these instruments for detection of hard targets—a dual-use capability. This data stream can serve as an



additional layer for Maritime Domain Awareness (MDA). The radar waveform was modified from the form that was optimized for current measurements to one that will allow for a dual-use: mapping currents and detection of ships. The data stream was therefore split to generate two products, radial maps of currents and target files of possible detections. This proposed system is robust in that it can illuminate a single target from multiple sites monostatically, which were presented here, as well as bistatically, which will be presented in future work. This design prevents a vessel from hiding in the intense Bragg sea echo. The detection algorithm currently uses the GPS recorded on the vessel and/or the position information broadcast over the Automatic Identification System (AIS) to separate good detections from the false alarms. The AIS data will be utilized to refine the algorithm in a multi-ship environment. The authors also envision passing the detections onto an association and tracking algorithms to refine the position and filter out the false alarms.

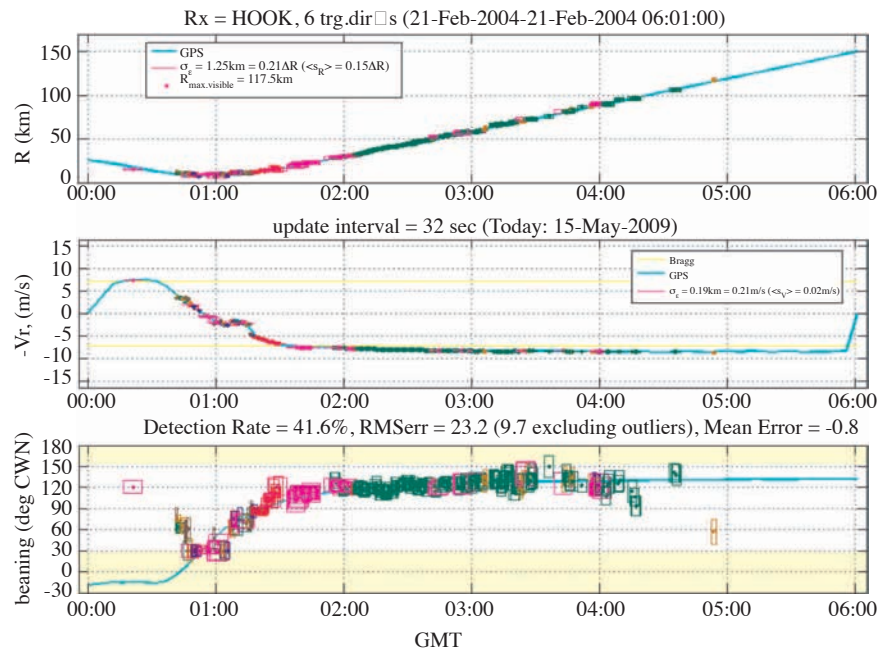


**Figure 8.** Valid detection results for all six processes of the Oleander from the Sandy Hook radar site, February 21, 2004. The error bars are for the six detection processes IIR-128 (blue), IIR-256 (red), IIR-256 (magenta), Median-64 (dark brown), Median-128 (brown), Median-256 (dark green).

## Acknowledgements

This work was funded by the United States Office of Naval Research (N00014-02-10917), the United States Department of Homeland Security (N00014-06-1-0177) and the United States Department of Defense (NO 03-5412). The authors would like to acknowledge Dr. Bill Browning of Applied Mathematics, Inc. for his contribution to the detection algorithm development. The authors would also like to thank Erick Rivera Lemus for helpful comments and Igor Heifetz for help with figures.

## References

- [1] D.E. Barrick, J.M. Headrick, R.W. Bogle, D.D. Crombie, "Sea backscatter at HF: Interpretation and utilization of the echo", Proc. IEEE, Vol. 62(6): pp. 673-680, 1974.
- [2] D.M. Fernandez, J.F. Vesecky, C.C. Teague, J.D. Paduan, K.E. Laws. "Ship detection with high-frequency phased-array and direction-finding radar systems", Geoscience and Remote Sensing Symposium Proceedings, 1998. IGARSS '98. 1998 IEEE International, 1998.
- [3] R. Khan, B. Gamberg, D. Power, J. Walsh, B. Dawe, W. Pearson, D. Millan, "Target detection and tracking with a high frequency ground wave radar", Oceanic Engineering, IEEE Journal of, Vol. 19(4): pp. 540-548, 1994.
- [4] J. Barnum, "Ship detection with high-resolution HF skywave radar", Oceanic Engineering, IEEE Journal of, Vol. 11(2): pp. 196-209, 1986.
- [5] J.D. Paduan, L.K. Rosenfeld, "Remotely sensed surface currents in Monterey Bay from shore-based HF-radar (CODAR)", Journal of Geophysical Research, Vol. 101: pp. 20669-20686, 1996.
- [6] D.E. Barrick, P.M. Lilleboe, C.C. Teague, "Multi-station HF FMCW radar frequency sharing with GPS time modulation multiplexing", U.S. Patent SN 10/109,769.
- [7] B.J. Lipa, D.E. Barrick, "Least-squares methods for the extraction of surface currents from CODAR cross-loop data: application at ARSLOE", IEEE Journal of Oceanic Engineering, Vol. OE-8: pp. 226-253, 1983.
- [8] D.E. Barrick, B.J. Lipa, "Comparison of direction-finding and beam-forming in hf radar ocean surface current mapping", Phase 1 SBIR final report, Contract No. 50-DKNA-5-00092, 1996.
- [9] D.E. Barrick, B.J. Lipa, "Radar angle determination with MUSIC direction finding", U.S. Patent 5,990,834.
- [10] J.T. Kohut, S.M. Glenn, "Improving HF Radar Surface Current Measurements with Measured Antenna Beam Patterns", Vol. 20(9): pp. 1303-1316, 2003.
- [11] D. Gong, J.T. Kohut, S.M. Glenn, "Seasonal Climatology of Wind-Driven Circulation on the New Jersey Shelf", Journal of Geophysical Research, Vol., 2009.
- [12] T. Rossby, E. Gottlieb, "The Oleander Project: Monitoring the variability of the Gulf Stream and adjacent waters between New Jersey and Bermuda." Bulletin of American Meteorology Society, Vol. 79: pp. 5-18, 1998.
- [13] R.O. Schmidt, "Multiple Emitter Location and Signal Parameter Estimation", IEEE Trans. Antennas Propaga, Vol. AP-34: pp. 276-280, 1986.
- [14] D.E. Barrick, Belinda J. Lipa, P.M. Lilleboe, J. Isaacson, "Gated FMCW DF Radar and signal processing for range/Doppler/angle determination", U.S. Patent 5,361,072.
- [15] D.D. Crombie, "Doppler spectrum of sea echo at 13.56 Mc./s", Nature, Vol. 175: pp. 681-682, 1955.
- [16] M.A. Sid-Ahmed, Image Processing: Theory, Algorithms and Architectures: McGraw Hill. 1994.
- [17] S.J. Orfanidis, Introduction to Signal Processing. 4th ed: Prentice-Hall. 1996.

# Operation and Application of a Regional High-Frequency Radar Network in the Mid-Atlantic Bight

## AUTHORS

**Hugh Roarty**  
**Scott Glenn**  
**Josh Kohut**  
**Donglai Gong**  
**Ethan Handel**  
**Erick Rivera**  
 Coastal Ocean Observation  
 Laboratory, Rutgers University

**Teresa Garner**  
**Larry Atkinson**  
 Center for Coastal  
 Physical Oceanography,  
 Old Dominion University

**Wendell Brown**  
**Chris Jakubiak**  
 School for Marine Science  
 and Technology, University  
 of Massachusetts Dartmouth

**Mike Muglia**  
**Sara Haines**  
**Harvey Seim**  
 University of North Carolina  
 at Chapel Hill

## 1. Introduction

Insights arising from a deeper understanding of surface currents can be valuable when one seeks to characterize and quantify the transport of plankton and anthropogenic material in the coastal ocean. The Mid-Atlantic Bight High-Frequency (HF) Radar Network, which is comprised of 13 long-range sites, two medium-range sites, and 12 standard-range sites, is operated as part of the Inte-

## ABSTRACT

The Mid-Atlantic Regional Coastal Ocean Observing System (MARCOOS) High-Frequency Radar Network, which comprises 13 long-range sites, 2 medium-range sites, and 12 standard-range sites, is operated as part of the Integrated Ocean Observing System. This regional implementation of the network has been operational for 2 years and has matured to the point where the radars provide consistent coverage from Cape Cod to Cape Hatteras. A concerted effort was made in the MARCOOS project to increase the resiliency of the radar stations from the elements, power issues, and other issues that can disable the hardware of the system. The quality control and assurance activities in the Mid-Atlantic Bight have been guided by the needs of the Coast Guard Search and Rescue Office. As of May 4, 2009, these quality-controlled MARCOOS High-Frequency Radar totals are being served through the Coast Guard's Environmental Data Server to the Coast Guard Search and Rescue Optimal Planning System. In addition to the service to U.S. Coast Guard Search and Rescue Operations, these data support water quality, physical oceanographic, and fisheries research throughout the Mid-Atlantic Bight.

Keywords: HF radar, Networks, Ocean currents, Remote sensing

grated Ocean Observing System. This regional implementation of the network has been operational for 2 years and has matured to the point where the radars provide consistent coverage from Cape Cod to Cape Hatteras. This is based on a significant effort to ensure hardware and software resiliency, quality control, and quality assurance (QA). Spatial coverage has been observed to vary on daily and seasonal scales because of ionospheric interference at the lower end of the HF radio spectrum and variable sea state conditions (Liu et al., 2010). Through a partnership with the U.S. Coast Guard Research and Development Center and Office of Search and Rescue, Mid-Atlantic Regional Coastal Ocean Observing System (MARCOOS)

partners have worked to advance this network to provide consistent and accurate surface current information to search and rescue operations. As a result of this partnership, surface currents are automatically delivered to the Coast Guard with improved quality control of the data and dissemination of typical current patterns and anomalous conditions to search and rescue personnel. In turn, the improved system quality has supported basic oceanographic research, water quality applications, numerical and statistical model assimilation, and environmental monitoring associated with offshore energy development throughout the Mid-Atlantic Bight. In this article, we will describe the network as it operates today, giving special



attention to the resiliency of the hardware and the flow of data from the sites on shore to regional and national data networks (Section 2). In Section 3, we describe the data processing at the radial and total level. The quality control, assurance, and data evaluation are summarized in Section 4. Finally in Section 5, we present some of the regional applications of the network.

## 2. The Network

### 2.1. Hardware

The MARCOOS HF Radar Network consists of 27 SeaSonde-type radars, 13 of which are long range (Figure 1), 12 of which are standard range, and 2 of which are medium range. Table 1 provides the typical characteristics of the different types of systems. Each site consists of two categories of hardware: the radar

TABLE 1

Typical characteristics of long-, medium-, and standard-range HF radar systems.

System Type	Radio Frequency (MHz)	Range (km)	Resolution (km)
Long range	4–6	200	6.0
Medium range	12–14	90	3.0
Standard range	24–26	40	1.5

equipment purchased directly from CODAR Ocean Sensors and the ancillary site-specific hardware required for communications, power, backup power, temperature control, weather proofing, security, and antenna foundations.

A typical HF radar system purchased from CODAR Ocean Sensors includes a transmitter, receiver, transmit antenna, receive antenna, Apple Computer, cabling, and a GPS antenna. In addition, a CODAR Ocean Sensors transponder unit is required for site calibration. A few vendor hardware op-

tions are available such as different computer types (laptop, desktop, or compact) and combined transmit and receive antennas for all but the long-range systems. The transmit and receive units are rack-mounted units approximately the size of a home stereo receiver. Transmit antenna sizes vary with the frequency of the system, from 4 m (25 MHz) to 10 m (5 MHz). Three RG-58 cables connect the SeaSonde Receiver to the receive antenna. A single RG-8 cable connects the SeaSonde Transmitter to the transmit antenna. Typical cable runs are up to 100 m to each antenna.

The site-specific hardware varies widely on the basis of site requirements and the operator’s experience. Typical considerations include power (both primary and backup), communications, climate control, security and vandalism, consideration for erosion, and antenna foundations. Communication for data transmission in near real time can be done with a phone line, but higher bandwidths are preferable for remote computer control and trouble shooting applications where available. A secondary communication option is encouraged. The number of sites with two lines of communication increased from three to nine from 2007 to 2009.

Communications sources in our region include cable Internet, DSL, telephone, satellite Internet, cellular modems, radio frequency communications, and short-range wireless

FIGURE 1

Location of the long-range HF radar locations (circles) within the MARCOOS region with four-letter site code next to station location.

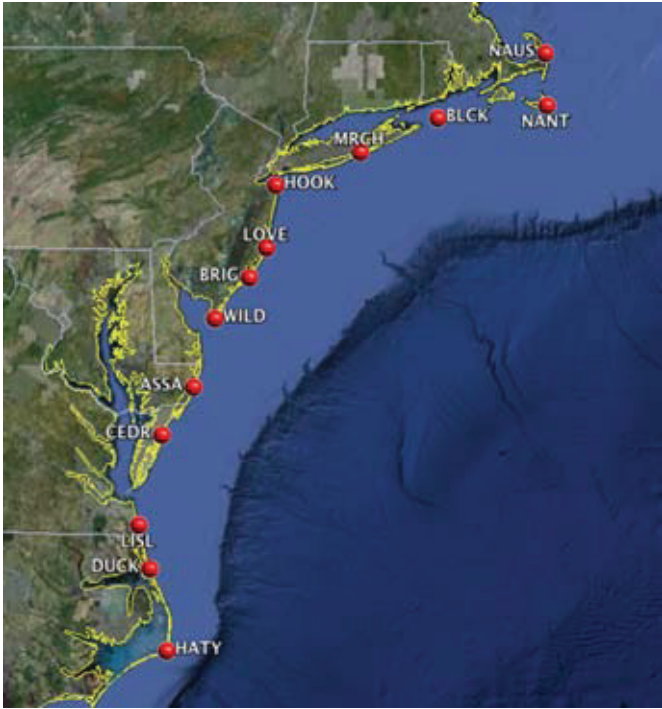


**TABLE 2**

Primary communication modes for network in years 2007 through 2009.

	2007	2008	2009
Phone	8	2	0
Cell modem	8	9	13
DSL	0	5	5
Cable modem	9	9	9
Number of sites with two lines of communication	3	9	9

telemetry from an Internet source. Communication preference is given to the most robust connection and to a redundant communication source. Table 2 provides a history of the primary communication methods used in the network. The phone line, which has been phased out as the primary communication method, has been kept at all sites to serve as a secondary line of communication. This line can be used for data transfer when the primary method fails and can also be used to control power cycling devices that restore the primary communication method in the event of an outage. Having a fixed Internet Protocol address at a site allows for more robust diagnostic capabilities.

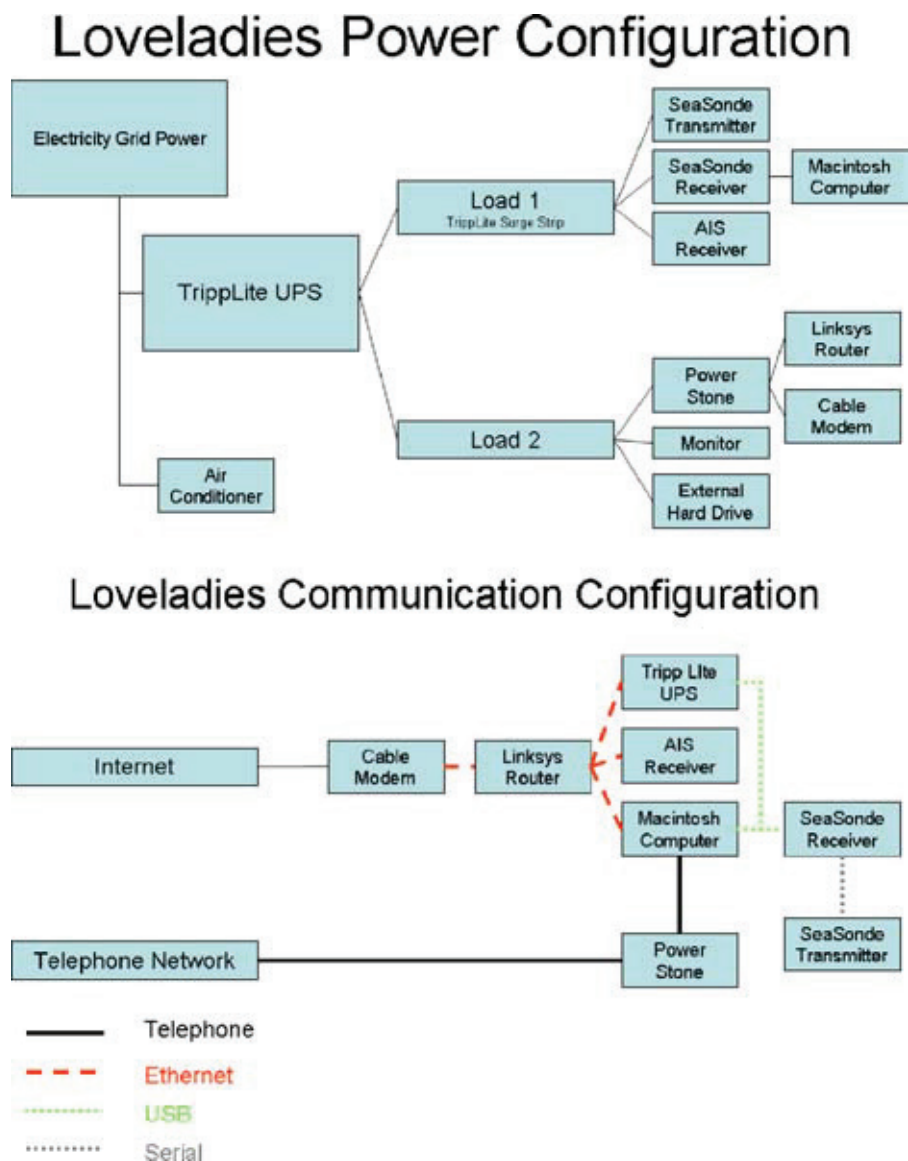
All sites in the network have access to the power grid. All sites use of an uninterrupted power supply (UPS) to provide a “cleaner” source of power as well as to eliminate power loss during outages of less than 30 min. In addition, some sites use backup power such as a propane generator and transfer switch to eliminate outages during inclement weather like tropical storms to maintain the data time series through these significant oceanographic events. Remote control devices such as the Powerstone, iBoot, and Web Power Switch are used for toggling power to separate components

for automated toggling of components that are not functioning properly.

A concerted effort was made in the MARCOOS project to increase the resiliency of the radar stations from the elements, power issues, and other issues that can disable a system. The optimal configuration of the shore station is shown in Figure 2. The site uses a TrippLite UPS with optional Web card as recommended in the Southern California Coastal Ocean Observing

**FIGURE 2**

Power (top) and communication (below) configuration for resilient HF radar station.



System Best Practices Document. This UPS has two power loads that can cycle power remotely to the devices on each load. This Web card will log power interruptions, send notifications of the power interruption, and allow for remote cycling of power to individual components of the system. Electrical power to the router and cable modem is directed through the Power Stone so that if either device freezes, the secondary telephone line can be used to cycle power to these components. Environmental events in our region like coastal storms and associated lightning can cause prolonged outages because of hardware damage. To counter one of the more common events in our region, lightning, we are testing a protection device that is designed to protect the transmitter and receiver from direct lightning strikes to the antennas. In addition, we are continually monitoring the local environments of the antennas to ensure that the sites are operating optimally. Since the 2007, three sites were relocated with the specific objective to improve the data quality provided by the site. One site had poor coverage because of a long cable run (150 m), so this site was moved so the cable run would be the standard length of 100 m. The other two sites that were moved had distorted antenna patterns because of the presence of a large structures in the vicinity of the receive antenna. These sites were moved to a “clear environment” (Kohut and Glenn, 2003) free of known conductors. All moves resulted in improved radial coverage and hence improved total coverage.

## 2.2. Data Flow

Each site described above collects hourly measurements of the radial surface currents and wave conditions within a footprint local to the antenna.

For surface currents this footprint can be as large as 200 km from the site with 6-km resolution for the 5-MHz systems to higher resolution 25 MHz systems that stretch 50 km with a spatial resolution of 1 km. These data are first collected at the local central computer sites for each of the eight operators in the region (Rutgers University, University of Massachusetts, University of Rhode Island, University of Connecticut, Stevens Institute of Technology, University of Delaware, Old Dominion University, and University of North Carolina). The radial data are then aggregated at Rutgers as part of the National HF Radar data server supported by the National Oceanic and Atmospheric Administration. The radial data from the long-range sites is combined into total vectors on a low-resolution 6-km regional scale grid that covers coastal waters from Cape Cod to Cape Hatteras. The total vector fields are made available via Open-source Project for a Network Data Access Protocol (OPeNDAP) for assimilation into the University of Connecticut’s Short Term Prediction

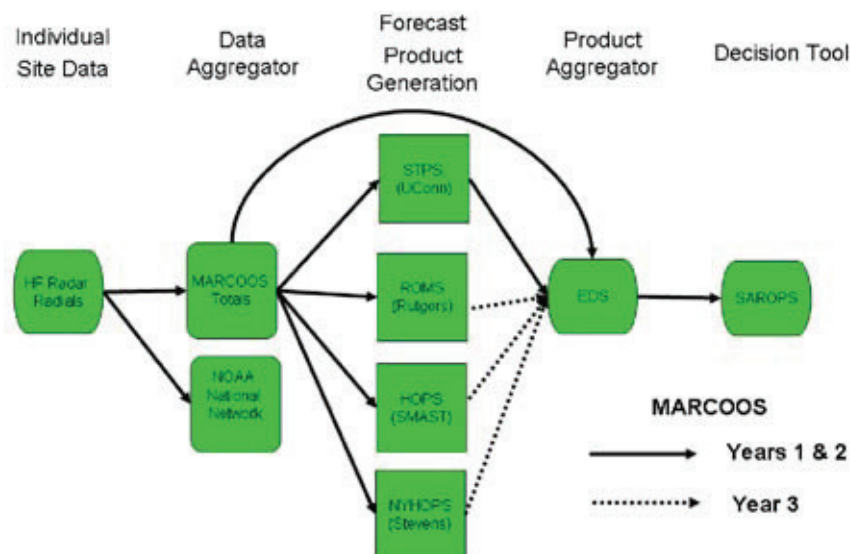
System (STPS) and an ensemble of three dynamical forecast models run by Rutgers, Stevens Institute of Technology, and University of Massachusetts, Dartmouth. The total vector fields and statistical forecasts are then transferred to the US Coast Guards Environmental Data Server (EDS), which is managed by Applied Science Associates. Once in EDS, the data and the forecasts underwent a year-long test phase within the Coast Guard’s new Search and Rescue Optimal Planning System (SAROPS). This data flow is summarized in Figure 3. After the test phase at the Coast Guard office of Search and Rescue, the accepted data and model forecasts are available in the field offices that have access to SAROPS. In May 2009, the data met that criteria and became an operational data stream of the U.S. Coast Guard Office of Search and Rescue.

## 2.3. Operation and Maintenance

At the beginning of the MARCOOS effort, several steps were taken to standardize the practices of the individual operators and subregional networks

**FIGURE 3**

Schematic showing the data flow from individual radar sites to the Coast Guard SAROPS.





already in place. An operator working group was formed, and conference calls were held every 2 weeks to discuss the progress of the project. The existing sites in the region were inventoried, and an online database of hardware and software was developed. On the basis of this inventory, software versions were standardized throughout the network. All sites running CODAR software were updated to Release 5 Update 3. The current version of CODAR software is Release 6 Update 2, and all operators were encouraged to upgrade to the latest release. Three QA settings were implemented on all sites as of April 1, 2008:

- The “Minimum Radial Vector Filter” was set to 2. This is the second parameter on line 1 of the AnalysisOptions.txt file
- The “Radial Factor Above Noise” was set to 5. This is the second parameter on line 15 of the Header.txt file
- The measured antenna phases were checked against those set in the SeaSonde Radial Setup application. If there was a difference of more than 15°, the set phases were changed to match the measured phases.

These settings were established on the basis of data evaluation (Section 4 of this article) to ensure real-time QA of the radial data. Computer scripts to monitor these and other site settings and data quality were developed, and a network-wide diagnostic monitoring Website was developed and installed. In addition to the Websites, an e-mail is sent daily to the operators reporting on the radial file size and latency of each radial file on the National Network.

All HF radar sites in the Mid-Atlantic were set up to report their data to the National Oceanic and Atmospheric Administration National

Network Server at Rutgers. HF radar operations were sustained at a rate consistent with Phase 2 of the Mid-Atlantic HF Radar Consortium’s three-phase implementation plan. Phase 2 includes three full-time HF radar technicians distributed across the northern, central, and southern subregions of the Mid-Atlantic with a part time regional coordinator managing the technicians and network. A week-long advanced training session was held in February 2008. The three full-time technicians as well as technicians from seven of the eight operators in the region attended this training. At this meeting, it was decided that the regional HF radar network would adopt a distributed technician approach, with one operator responsible for the systems in each of the three regions (north, central, and south). This work force was able to achieve an 89% operating time for the long-range systems from December 1, 2008, to November 30, 2009 (Table 3).

### 3. Data Processing

#### 3.1. Radial Processing

A suite of CODAR software programs processes the received radar signals to generate the hourly radial current files at each site. Further processing combines the radials from two or more sites to produce total current velocity vector maps. The radar system determines wave speed by measuring the Doppler shift between a transmitted radio signal and its return signal reflected off of ocean waves (Barrick et al., 1977). The CODAR radar software empirically isolates the strongest sea echo returns because of Bragg scattering and uses these to calculate radial current velocity. According to the Bragg principle, these strong reflections, referred to as first-order sea echo, come from waves of a

**TABLE 3**

Radar operational time as a percentage of the time from December 1, 2008, till November 30, 2009.

Four-Letter Site Code	Operating Time (% year)
NAUS	93
NANT	92
BLCK	90
MRCH	97
HOOK	98
LOVE	98
BRIG	99
WILD	69
ASSA	92
CEDR	59
LISL	71
DUCK	100
HATY	100
Network average	89

known wavelength, half that of the transmitted electromagnetic wave (Crombie, 1955). The Doppler shift of these waves in the absence of ocean current is proportional to the phase velocity given by the deep water dispersion equation for gravity waves. The difference between the observed first-order Doppler shift and the shift due to wave speed represents the speed of the surface current underlying the wave (Lipa and Barrick, 1983).

Each 5-MHz Mid-Atlantic radar site measures these one-dimensional radial current velocities, directed toward or away from the antenna, in 6-km-range bins and in 5° directional bins. To do this, two spectral analyses are performed within the software. The first separates the incoming raw voltage time series into different range bins, whereas the second transforms the range-dependent time series,

resulting from the first into Doppler spectra binned by range. These spectra contain the first-order Bragg scatter used to extract the radial currents. Because SeaSondes are direction-finding systems, the bearing of the radial vectors is determined from the signal received from three separate antennas using the MUSIC algorithm (Lipa et al., 2006). Using a transponder, the angular-dependent response of each antenna can be incorporated into the processing as a way to calibrate the system for distortions to the antenna pattern (Barrick and Lipa, 1986; Kohut and Glenn, 2003). The operational time from each of the long-range sites is given in Table 3.

### 3.2. Total Vector Processing

During the extension of the network to the regional footprint, we have processed radials to totals using two algorithms, unweighted least squares (UWLS; Lipa and Barrick, 1983) and Optimal Interpolation (Kim et al., 2008). The first approach merges radial vectors located within a search radius around each grid point using a UWLS fitting method (Lipa and Barrick, 1983). The CODAR combine software uses this method as well as the community Matlab toolbox, HFR\_Progs. The regional radial-to-total processing is accomplished within Matlab. In the Mid-Atlantic, the search radius for the UWLS method is 10 km, and the spacing for the grid is 8 km. A minimum of three radials from at least two sites are required to calculate a total and the geometric dilution of precision uncertainty estimate for the vector must be less than 1.25 to pass quality control checks. The second technique for computing totals uses optimal interpolation (OI) adaptation developed by Kim et al. (2008). For this method, we used an asymmetric search area

stretch in the along-isobath direction and consistent with the length scales of the currents in the region. For QA, we require that both the *u* and *v* component uncertainty be less than 60% the expected variance. The MARCOOS real-time processing scripts output results using both methods. Through the evaluation discussed later in this article, the total vector product delivered operationally is based on the OI.

## 4. Surface Current Evaluation

### 4.1. Quality Control and QA

The quality control and assurance activities in the Mid-Atlantic Bight have been guided by the needs of the Coast Guard Search and Rescue Office. QA is a set of procedures done to instrumentation and a system of processing that ensure quality and measure uncertainties. Quality control is the activity of testing the data against defined standards or measured uncertainties to ensure quality. QA includes following the manufacture's installation guidelines of hardware and sighting of systems to avoid known interference. Toward this end and because all the systems in the region are CODAR systems, MARCOOS developed a set of recommendations to follow in hardware setup (Roarty, 2009) and radial vector processing software (Kohut, 2008) that ensures that all new sites are configured properly and in a consistent manner across the region. QA also includes understanding the environment of HF distortions and minimizing interferences to the return signal, which can vary dramatically from site to site. Each site in the region ensures their radial quality by measuring the HFR receive antenna pattern once it is located and set up (Kohut, 2008) and then using the measured

pattern in the software. This measured pattern serves to calibrate the software with the actual antennas response in the field. In addition, a collaborative effort between all sites using the same frequency was conducted to ensure no one site causes contamination at a neighboring site or sites. This is performed using the GPS synchronization capability (Barrick et al., 2001) of the SeaSonde. Finally, each group monitors a site's health, raw spectra, and radial output by manual or automated means and ensures that the site is operating within its hardware specifications and that data are delivered in a timely fashion. As part of the MARCOOS effort and the delivery of regional and subregional HF radar data, there is a need to define the uncertainty bounds of the data for effective utility in SAROPS (Roarty, 2009). The UWLS geometric dilution of precision uncertainty estimate must be less than 1.25 to pass quality control checks (see Software Section). With OI, normalized velocity uncertainty of velocity components is determined. A threshold of 60% of the error variance for either the *u* or *v* component was chosen to remove any grid points in real-time data on the basis of this uncertainty threshold to maximize data coverage while preserving data quality (Kohut et al., 2009).

### 4.2. Integration with SAROPS

Quality-controlled MARCOOS HF Radar totals are being served through the Coast Guard's EDS to the Coast Guard SAROPS as of May 4, 2009. Before the introduction of the HF radar product to the Coast Guard decision tool, an extensive validation and evaluation was done. A focus of this evaluation was to determine the most accurate algorithm for combining radial vectors into totals that

would provide consistent accurate coverage.

Using a test period in the winter to spring of 2007, totals generated with both the existing UWLS and the new OI algorithms were compared with four moored acoustic Doppler current profilers (ADCPs) and seven surface drifters. The analysis included sensitivity to input parameters to OI, including expected variances and spatial decorrelation scales. The specific sites used include Sandy Hook, NJ (HOOK), Loveladies, NJ (LOVE), Wildwood, NJ (WILD), and Assateague, MD (ASSA). Each site was operated with the QA/QC recommendations from the regional operators and the Radiowave Operators Working Group community providing radial data to these standards.

**ADCP:** Four ADCPs were deployed off the coast of New Jersey as part of the National Science Foundation supported Mid-Shelf Front Experiment. Three of the moorings were oriented in a cross-shelf line approximately 10 km apart. The shallowest mooring, deployed in 45 m of water, was a 300-kHz unit. The mid-point mooring in 53 m of water was a 600-kHz unit, and the offshore 600-kHz unit was in approximately 54 m of water. A third 600-kHz unit mooring deployed 11 km upshelf of the midpoint mooring was deployed in 50 m of water. All units were configured with 2-m bins in the vertical. Sampling was configured to collect a 10-min ensemble each hour. These data were then averaged to match the sampling of the HF radar.

**Drifters:** The Self-Locating Data Marker Buoy (SLDMB) position data were used to evaluate the CODAR observations. The SLDMB drifters were provided by the U.S. Coast Guard. They had exceeded their shelf life for

use in life saving operations but remained excellent platforms to evaluate the performance of the two combination algorithms. The drifters were drogued to 1-m depth. Throughout the deployment, velocities on the basis of two drifter positions 1 h apart were calculated every half hour. These surface velocity estimates were compared with the radial and total vector estimates of the long-range CODAR network off the New Jersey coast. For the total vector comparisons, the velocity average was set to match the sampling of the CODAR. The SLDMB data discussed here are from two deployments in the winter and spring of 2007. The first deployment included two drifters deployed on February 24, 2007. Since the one deployed inside the mid-shelf front spent more time within the coverage of the radar, it was used in the analysis. The second deployment began April 3, 2007, and included six drifters. Although this second group of drifters did not overlap with the ADCP deployments, the larger cluster of drifters provides an extended data set to explore the impact of spatial variability on the comparisons. All of the deployments together allow us to explore spatial dependency in the evaluation particularly close to the offshore edge of the coverage. A more thorough

explanation of the evaluation is given by Kohut et al. (in preparation). An example of one ADCP and one drifter comparison is provided in Table 4.

Comparisons between both the UWLS and the OI total vector solutions showed significant agreement with the in situ measurements of both the ADCPs and the drifters. Root mean square (RMS) differences ranged from 7.5 to 11.8 cm/s over the study period (Chapman and Graber, 1997). It is important to note that the ADCPs were deployed in a region of very good geometric coverage of the radial sites used in the total vector combination, whereas the drifters spent time in regions of good and poor coverage and geometry. Using both sources of in situ data gives us the opportunity to compare the OI and UWLS algorithms across ranges of coverage and geometric quality within the CODAR domain. Both the OI and the UWLS algorithms had similar skill in areas of good system geometry and consistent coverage with RMS differences of 8 cm/s and  $R^2$  of 0.7 and provided consistent coverage on the order of 94%. However, in regions of inconsistent coverage like the offshore edge of the CODAR domain, the OI improved coverage from 53% to 65% over the UWLS method while only increasing

**TABLE 4**

Summary table of ADCP and drifter comparison with the Optimal Interpolation (OI) and UWLS vector combining method.

	ADCP Comparison		Drifter Comparison	
	UWLS	OI	UWLS	OI
Temporal Coverage (%)	93	95	53	65
RMS u (cm/s)	8.3	8.7	7.4	8.4
RMS v (cm/s)	7.9	7.5	9.8	11.8
$R^2$ u	0.75	0.73	0.83	0.81
$R^2$ v	0.63	0.65	0.58	0.44



the uncertainty approximately 1–2 cm/s (RMS). On the basis of these results and the criteria set by the Coast Guard for consistent coverage with known uncertainties, the OI algorithm was selected as the best algorithm for inclusion in the SAROPS tool.

## 5. Network Applications

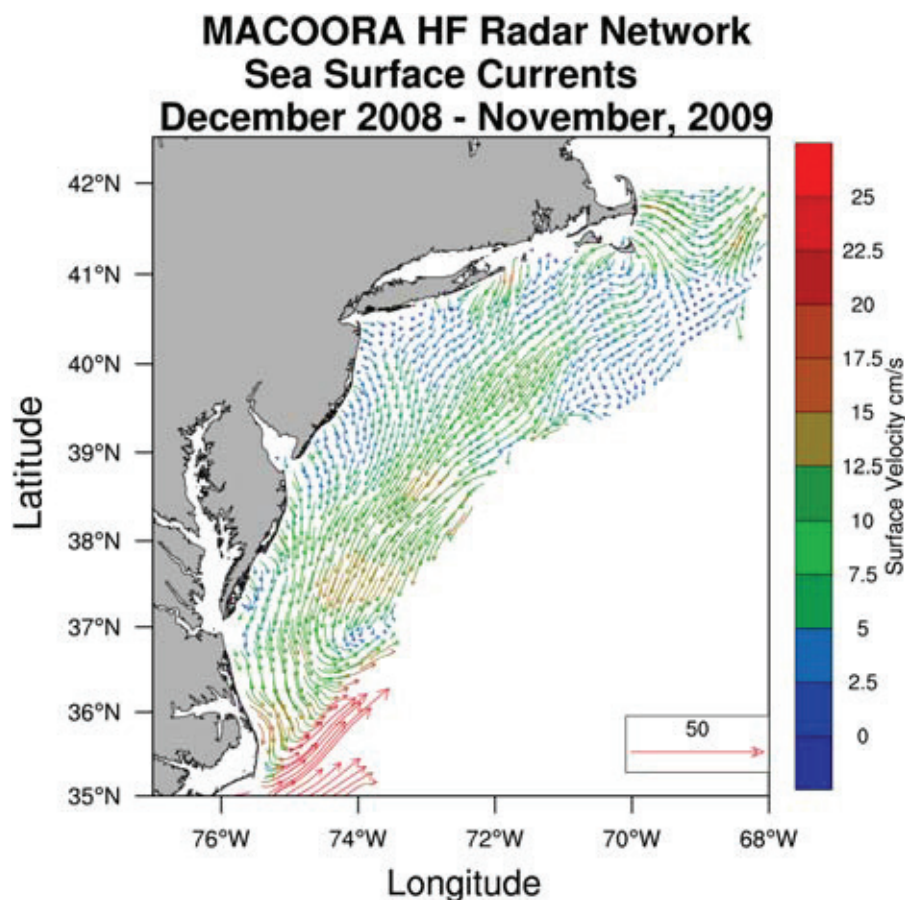
HF radar has supported a variety of applications in the Mid-Atlantic Bight over the past decade. These applications include basic research on the dynamics of the coastal ocean (Kohut et al., 2004; Dzwonkowski et al., 2009; Dzwonkowski et al., 2010; Shay et al., 2008; Ullman and Codiga, 2004; Kohut et al., 2006; Gong et al., 2010; Hunter et al., 2007) to applications centered around Coast Guard Search and Rescue (O'Donnell et al., 2005; Ullman et al., 2006) and water quality associated with floatable tracking along the New Jersey Coast. Below we highlight three applications of the integrated regional network.

### 5.1. Regional Results

The Mid-Atlantic Bight 1-year average surface currents calculated from the 2009 MARCOOS data are plotted in Figure 4. The annual average flow is generally along shelf to the southwest, with mid-shelf surface current speeds in the 5- to 10-cm/s range. Faster currents between 10 and 17.5 cm/s are found east of Cape Cod running offshore, along the shelf break running alongshore over the central region, and along the narrower shelf of North Carolina running across isobaths into the Gulf Stream, the strongest currents observed on the southern edge. Inshore flows are generally lower than those at mid-shelf, with increased cross-shelf flow noted at the outflow

**FIGURE 4**

Mid-Atlantic Bight 1-year average surface currents calculated for seasonal year 2009. Only the vectors where there was 50% data coverage are plotted. (Color versions of figures available online at: <http://www.ingentaconnect.com/content/mts/mts/2010/00000044/00000006>.)



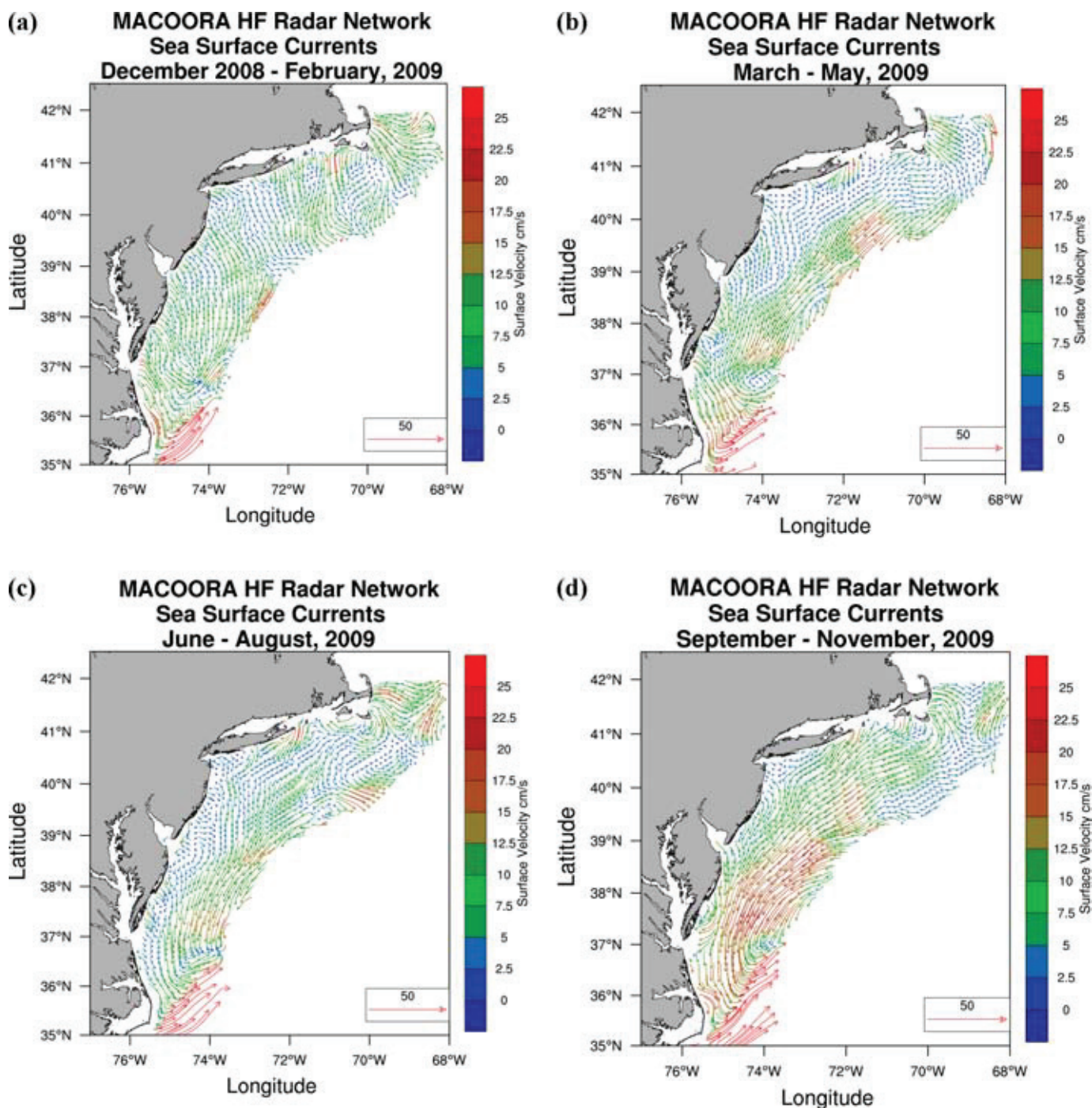
locations of the major bays that then joins the along shelf flow at the outer shelf.

Three CODAR HF Radar systems were used to study the annual and seasonal response of the New Jersey shelf currents (Gong et al., 2010). The seasonal results for the New Jersey shelf can be extended to the full Mid-Atlantic Bight for 1 year using the 2009 MARCOOS data set. Adopting the same seasonal definitions used by Gong et al. (2010) on the basis of their analysis of the water column stratification, winter of 2009 begins in December of 2008. As noted by Gong et al. (2010) and others, winter winds are predominately from the northwest. Average

surface flow during the three winter months for the full Mid-Atlantic Bight (Figure 5a) is generally cross-shelf in the offshore direction. Stronger cross shelf flows are again observed offshore the major outflows of Long Island Sound, New York Harbor, and Delaware Bay. The MAB spring currents (Figure 5b) are generally alongshore, with stronger alongshore currents in deeper water near the shelf break, and on the southern side of the coverage over the narrower North Carolina shelf. Currents east of Cape Cod are persistently offshore to the east. Summer currents are generally the weakest, with reduced range reflecting the lower wave environment of the summer. The inner to

**FIGURE 5**

Seasonal means for surface currents in the Mid-Atlantic (a) winter, (b) spring, (c) summer, and (d) fall.



mid-shelf flows have a stronger cross-shelf component than the yearly average. East of Cape Cod, some of the strongest cross-shelf flows are observed. Conversely, some of the weakest currents of the year are found on the narrow

shelf east of North Carolina. As in the results of Gong et al. (2010) for the New Jersey shelf, offshore cross-shelf flows are more common in the summer and winter months over most of the Mid-Atlantic Bight. Fall

has the strongest surface currents, mostly along shelf and with increasing intensity as flow heads south. Except in the Bight Apex offshore Long Island and New Jersey, the alongshore flow extends across the entire shelf. This is



the only season where the alongshore response is not blocked by an offshore flow on the inner shelf. This has important implications for the fall season and fish larvae.

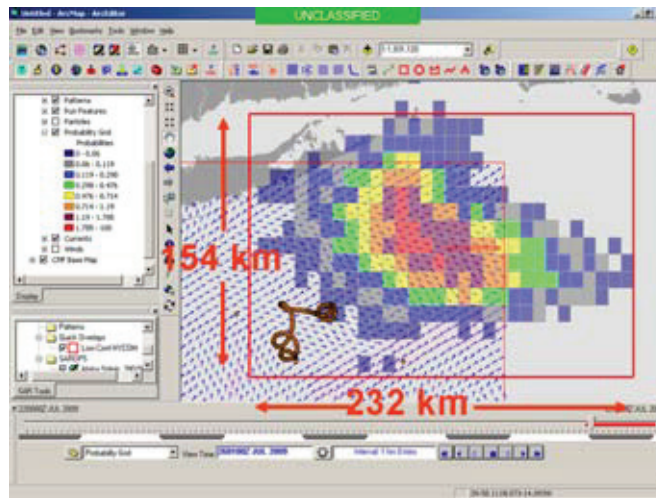
## 5.2. U.S. Coast Guard Search and Rescue

MACOORA has five regional priorities supported by the 10 MARCOOS regional observing and forecasting capabilities. MACOORA's first regional priority is supporting Safety at Sea by providing improved data sets and forecast models for the U.S. Coast Guard's operational SAROPS. One primary function of SAROPS is to predict the trajectories of a large cloud (typically 5000) of simulated drifters using real-time surface current data sets and forecasts accessed via the EDS and a random flight dispersion model with pre-calculated coefficients to simulate dispersion. The random flight model coefficients, a standard deviation and half-life time scale, are precalculated on the basis of comparisons of the various surface current products with actual SLDMBs trajectories. On the basis of these historical comparisons, various current products are designated as high confidence, with a standard deviation of 0.22 knots or low confidence, with a standard deviation of 0.37 knots. In each of these standard designators, the half life time scale is set at 264 min. New validation case studies are then generated each time a new SLDMB is deployed.

One case study was created to analyze the impact of HF radar data on the efficacy of SAROPS. The actual path of an SLDMB over 4 days (July 22, 2009–July 26, 2009) was compared with predicted path of the buoy using four data sources (STPS, NCOM, HYCOM, and HF Radar). The pre-

**FIGURE 6**

Screen shot of the SAROPS user interface showing the predicted dispersion of the 5,000 simulated drifters using the HYCOM data source (cloud) and path of SLDMB (line in lower left-hand corner of search area). Coast Guard search area is shown as the red box.



dicted dispersion of the 5000 simulated drifters using the HYCOM data source is shown in Figure 6. The search area using the HYCOM data equates to 36,000 km<sup>2</sup>. The predicted dispersion after 4 days of the 5000 simulated drifters using the HF radar data source is shown in Figure 7. The search area using the HF radar data equates to

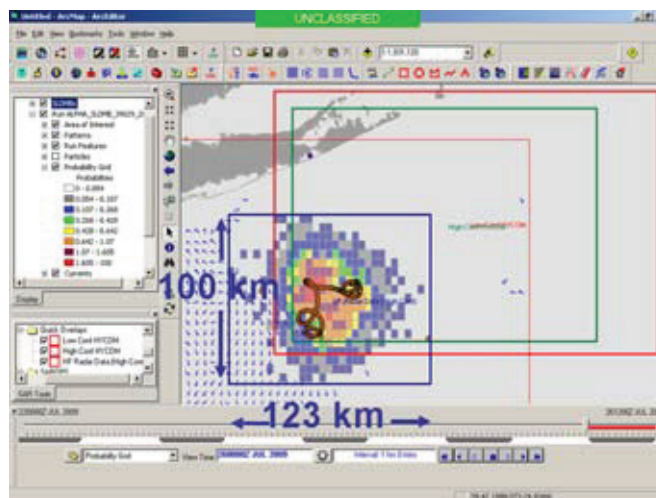
12,000 km<sup>2</sup>, a marked improvement over the HYCOM data source. In this test case, the HF radar was shown to provide a smaller search area centered on the actual drifter location.

## 5.3. Fisheries

MACOORA's second regional priority is Ecosystem Decision Support,

**FIGURE 7**

Screen shot of the SAROPS user interface showing the predicted dispersion of the 5,000 simulated drifters using the HF radar data source (cloud) and path of SLDMB (line in center of the cloud). Coast Guard search area is shown as the blue box.





initially focusing on applications to fisheries. An application of the MAB HF Radar network is to study the larval dispersal pattern of key marine species such as summer flounder (*Paralichthys dentatus*). Adult summer flounders spawn during fall, winter, or spring on the shelf when temperature is between 12°C and 19°C (Smith, 1973). Survey of the monthly abundance of summer flounder eggs from 1978 to 1987 showed that the peak spawning season of *P. dentatus* is in the autumn (Packer et al., 1999). Three regions of high egg concentrations are identified ranging from Georges Bank down to Cape Hatteras. The northern population, residing mostly north of the Hudson Shelf Valley, spawns in October. The central population, near the Hudson Shelf Valley, and the southern population, south of Delaware Bay, spawns about a month later (Packer et al., 1999). The early life history stages of *P. dentatus* are pelagic, and the com-

bined egg and early larvae stages are temperature dependent and can last 2 weeks (Manderson, personal communication). During this time, their movement is very limited, and dispersal is likely mainly driven by the prevailing ocean currents. On the basis of these facts, a CODAR-based virtual drifter experiment is performed on the MAB for fall 2009. Three groups of virtual drifters were deployed at the known *P. dentatus* spawning grounds during the month of October 2009. These drifters were deployed twice daily, and each group is tracked for up to 10 weeks. When a drifter reached the edge of the CODAR coverage, it was stopped, and the position was marked (Figure 8). The drifter advection algorithm includes the same random flight dispersion algorithm (Ullman et al., 2006) as used in SAROPS.

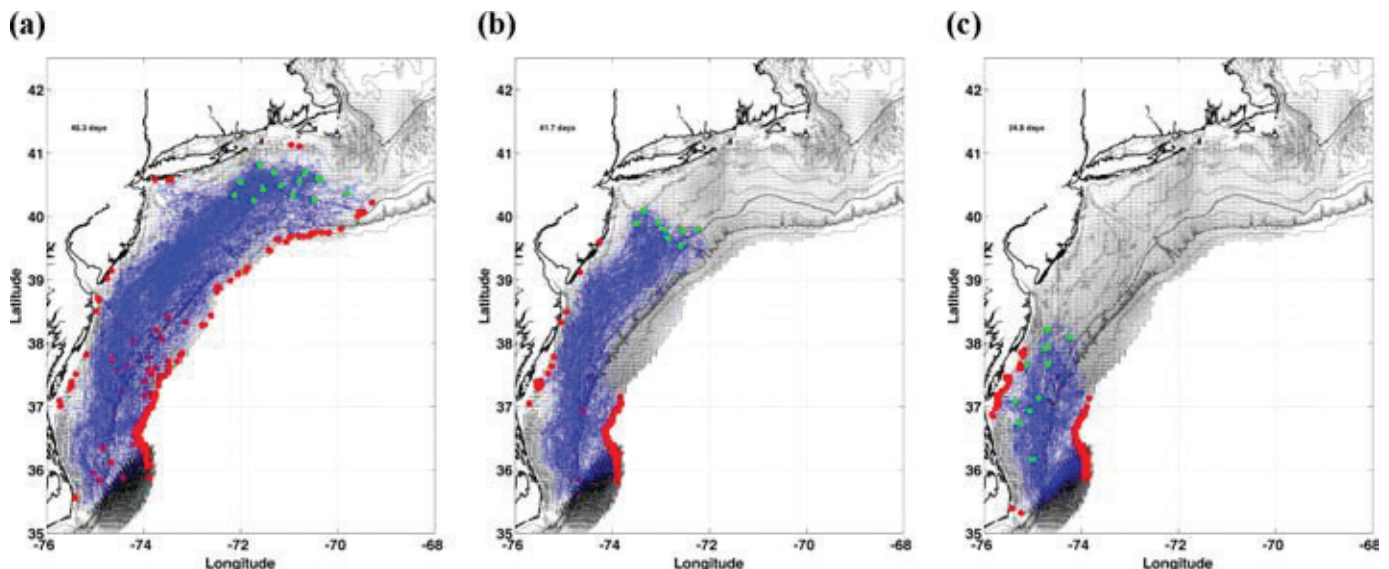
The drifter study provides us the following scientific results:

1. Surface transport in autumn is mainly downshelf.
2. Despite significant offshore loss, shoreward transport toward the major estuaries is observed. Study of Gong et al. (2010) on the central MAB showed that this only happens in the autumn season.
3. The end locations for all three spawning locations are remarkably similar, suggesting population connectivity linking the three spawning grounds.
4. The time scale of drifter transport is on the order 3–5 weeks, consistent with the time scale of the early life stages of *P. dentatus*.

The drifter study also illustrates the MACOORA development strategy. MACOORA, through its user meetings, has identified five regional priorities: (1) safety at sea, (2) ecosystem decision support, (3) water quality, (4) coastal inundation, and (5) energy. MARCOOS is the operating arm of MACOORA, responsible for installing and maintaining the 10 regional observing capabilities. Once an operational

## FIGURE 8

Virtual drifter study showing the release points (green circles), path (blue lines), and exit point (red triangles) for known *Paralichthys dentatus* spawning grounds during the month of October, 2009, in the (a) northern, (b) central, and (c) southern sections of the MARCOOS domain. (Color versions of figures available online at: <http://www.ingentaconnect.com/content/mts/mts/2010/00000044/00000006>.)



capability is developed and validated for one of the regional priorities, that capability is then available for application to the other four priorities.

## 6. Conclusions

The evolution of HF radar in the Mid-Atlantic bight has progressed from distinct subregional systems to an integrated regional network. The application of this network ranges from basic research to support of operational search and rescue. This range of application has required a very systematic approach to operation and maintenance of the hardware and software. Through this approach, we have defined QA and control measures to ensure that quality data with consistent coverage is delivered to the user groups working in the region. The approach has relied heavily on regional partners and distributed expertise working through a coordinated center.

HF radar networks like that in the Mid-Atlantic are being constructed around the country with high-resolution standard-range systems nested within lower-resolution, long-range systems. With Integrated Ocean Observing System support, these regional networks are part of a coordinated national network. As we move toward products in support of national applications, like the Coast Guard Search and Rescue, there is a need for coordination and communication of all regional and subregional groups. Through a national system, lessons learned from the Mid-Atlantic and other regions around the country can drive a national resource that can support a variety of applications, as it has done in the Mid-Atlantic for the past decade.

## Lead Author:

Hugh Roarty  
Coastal Ocean Observation  
Laboratory, Rutgers University  
Email: hroarty@marine.rutgers.edu

## References

- Barrick, D.E., Evens, M.W., Weber, B.L.** 1977. Ocean surface currents mapped by radar. *Science*. 198:138-144. doi:10.1126/science.198.4313.138.
- Barrick, D.E., Lilleboe, P.M., Teague, C.C.** 2001. Multi-station HF FMCW radar frequency sharing with GPS time modulation multiplexing, US Patent SN 10/109, 769.
- Barrick, D.E., Lipa, B.J.** 1986. Correcting for distorted antenna patterns in CODAR ocean surface measurements. *IEEE J Ocean Eng.* OE-11:304-309. doi:10.1109/JOE.1986.1145158.
- Chapman, R.D., Graber, H.C.** 1997. Validation of HF radar measurements. *Oceanography*. 10:76-79.
- Crombie, D.D.** 1955. Doppler spectrum of sea echo at 13.56 Mc/s. *Nature*. 175:681-682. doi:10.1038/175681a0.
- Dzwonkowski, B., Kohut, J.T., Yan, X.-H.** 2009. Seasonal differences in wind-driven across-shelf forcing and response relationships in the shelf surface layer of the central Mid-Atlantic Bight. *J Geophys Res.* 114(C8): C08018. doi:10.1029/2008JC004888.
- Dzwonkowski, B., Lipphardt, B.L., Jr, Kohut, J.T., Yan, X.-H., Garvine, R.W.** 2010. Synoptic measurements of episodic offshore flow events in the central Mid-Atlantic Bight. *Cont Shelf Res.* 30(12):1373-1386. doi:10.1016/j.csr.2010.05.004.
- Gong, D., Kohut, J.T., Glenn, S.M.** 2010. Seasonal climatology of wind-driven circulation on the New Jersey Shelf. *J Geophys Res.* 115(C4):C04006. doi:10.1029/2009JC005520.
- Hunter, E., Chant, R., Bowers, L., Glenn, S., Kohut, J.** 2007. Spatial and temporal variability of diurnal wind forcing in the coastal ocean. *Geophys Res Lett.* 34(3):L03607. doi:10.1029/2006GL028945.
- Kim, S.Y., Terrill, E.J., Cornuelle, B.D.** 2008. Mapping surface currents from HF radar radial velocity measurements using optimal interpolation. *J Geophys Res.* 113(C10): C10023. doi:10.1029/2007JC004244.
- Kohut, J.** 2008. MARCOOS HF Radar Quality Control/Quality Assurance Document. Available from: [http://www.marcoos.us/downloads/data/MARCOOSHF RadarQualityControl\\_04182008.pdf](http://www.marcoos.us/downloads/data/MARCOOSHF RadarQualityControl_04182008.pdf).
- Kohut, J., Roarty, H.J., Rivera Lemus, E.** 2009. Optimizing HF radar for SAR using USCG surface drifters and moored ADCPs. The 4th Radiowave Operators Working Group (ROWG) Meeting, Norfolk, VA.
- Kohut, J.T., Glenn, S.M.** 2003. Improving HF radar surface current measurements with measured antenna beam patterns. *J Atmos Oceanic Tech.* 20(9):1303-1316. doi:10.1175/1520-0426(2003)020<1303:IHRSCM>2.0.CO;2.
- Kohut, J.T., Glenn, S.M., Chant, R.J.** 2004. Seasonal current variability on the New Jersey inner shelf. *J Geophys Res.* 109(C7):C07S07. doi:10.1029/2003JC001963.
- Kohut, J.T., Randall-Goodwin, E., Roarty, H.J., Glenn, S.M.** in preparation. Evaluation of an optimal interpolation technique for combining HF radar radial vectors to totals. *J Atmos Oceanic Tech.*
- Kohut, J.T., Roarty, H.J., Glenn, S.M.** 2006. Characterizing observed environmental variability with HF Doppler radar surface current mappers and acoustic Doppler current profilers: environmental variability in the coastal ocean. *IEEE J Ocean Eng.* 31(4):876-884. doi:10.1109/JOE.2006.886095.
- Lipa, B.J., Barrick, D.E.** 1983. Least-squares methods for the extraction of surface currents from CODAR cross-loop data: application at ARSLOE. *IEEE J Ocean Eng.* OE-8: 226-253. doi:10.1109/JOE.1983.1145578.

- Lipa**, B.J., Nyden, B., Ullman, D.S., Terrill, E.J. 2006. SeaSonde Radial Velocities: derivation and internal consistency. IEEE J Ocean Eng. 31(4):850-861. doi:10.1109/JOE.2006.886104.
- Liu**, Y., Weisberg, R.H., Merz, C.R., Lichtenwalner, S., Kirkpatrick, G.J. 2010. HF radar performance in a low energy environment: CODAR SeaSonde experience on the West Florida shelf. J Atmos Oceanic Tech. 27(10):1689-1710.
- O'Donnell**, J., Ullman, D.S., Spaulding, M., Howlett, E., Fake, T., Hall, P., Isaji, T., Edwards, C., Anderson, E., McClay, T., Kohut, J.T., Allen, A., Lester, S., Lewandowski, M. 2005. Integration of Coastal Ocean Dynamics Application Radar (CODAR) and Short-Term Predictive System (STPS) Surface Current Estimates into the Search and Rescue Optimal Planning System (SAROPS). New London, CT: U.S. Coast Guard Research & Development Center.
- Packer**, D.B., Griesbach, S.J., Berrien, P.L., Zetlin, C.A., Johnson, D.L., Morse, W.W. 1999. Summer Flounder, *Paralichthys dentatus*, Life History and Habitat Characteristics. Washington, DC: NOAA.
- Roarty**, H.J. 2009. Standard Operating Procedure for Adding a New Long Range (5 MHz) HF Radar Site to the Mid-Atlantic Regional Coastal Ocean Observing System (MARCOOS). Available from: [http://www.marcoos.us/downloads/data/SOP\\_MARCOOS\\_Long\\_Range\\_Radar.doc](http://www.marcoos.us/downloads/data/SOP_MARCOOS_Long_Range_Radar.doc).
- Shay**, L.K., Seim, H., Savidge, D., Styles, R., Weisberg, R.H. 2008. High frequency radar observing systems in SEACOOS. Mar Technol Soc J. 42(3):55-67. doi:10.4031/002533208786842435.
- Smith**, W.G. 1973. The distribution of summer flounder, *Paralichthys dentatus*, eggs and larvae on the continental shelf between Cape Cod and Cape Lookout. Fish Bull. 71(2):527-48.
- Ullman**, D.S., Codiga, D.L. 2004. Seasonal variation of a coastal jet in the Long Island Sound outflow region based on HF radar and Doppler current observations. J Geophys Res. 109(C7):C07S06. doi:10.1029/2002JC001660.
- Ullman**, D.S., O'Donnell, J., Kohut, J., Fake, T., Allen, A. 2006. Trajectory prediction using HF radar surface currents: Monte Carlo simulations of prediction uncertainties. J Geophys Res. 111(C12):C12005. doi:10.1029/2006JC003715.





# The Integrated Ocean Observing System High-Frequency Radar Network: Status and Local, Regional, and National Applications

## AUTHORS

**Jack Harlan**  
NOAA IOOS® Program

**Eric Terrill**

**Lisa Hazard**  
Scripps Institution of Oceanography,  
Coastal Observing R&D Center

**Carolyn Keen**  
Scripps Institution of Oceanography,  
Institute of Geophysics and  
Planetary Physics

**Donald Barrick**  
**Chad Whelan**  
CODAR Ocean Sensors, Ltd.

**Stephan Howden**  
Stennis Space Center, University  
of Southern Mississippi

**Josh Kohut**  
Rutgers University

## History and Technical Background for HF Radar History

The present state of the U.S. national high-frequency (HF) radar network has resulted from nearly 40 years of research and applications. HF radar observations of the ocean surface truly began with Crombie's (1955) experimental discovery of the mechanism behind his puzzling analog sea-echo spectral plots. Don Barrick (1968, 1972) theoretically derived the model that indeed showed that this resonant scatter was in fact "Bragg scatter" and related the echo strength to the ocean

## ABSTRACT

A national high-frequency radar network has been created over the past 20 years or so that provides hourly 2-D ocean surface current velocity fields in near real time from a few kilometers offshore out to approximately 200 km. This preoperational network is made up of more than 100 radars from 30 different institutions. The Integrated Ocean Observing System efforts have supported the standards-based ingest and delivery of these velocity fields to a number of applications such as coastal search and rescue, oil spill response, water quality monitoring, and safe and efficient marine navigation. Thus, regardless of the operating institution or location of the radar systems, emergency response managers, and other users, can rely on a common source and means of obtaining and using the data. Details of the history, the physics, and the application of high-frequency radar are discussed with successes of the integrated network highlighted.

wave height spectrum at the Bragg wave number. Barrick was invited to present his results at seminars in Boulder, Colorado, as the National Oceanic and Atmospheric Administration (NOAA), and its Boulder laboratories were being formed in 1970. A group was formed within NOAA's new Environmental Research Laboratories to build a compact antenna system to be used for coastal ocean surface current mapping. This was the Coastal Ocean Dynamics Applications Radar (CODAR) program. After demonstrating its effectiveness, the NOAA/National Ocean Service formed a Transitional Engineering Program in 1978 to encourage development of a commercial version of CODAR. With only a small potential market, no existing radar companies were interested in commercializing CODAR so a small group left NOAA to start CODAR Ocean Sensors, Ltd. in the early 1980s.

In the 1990s, the Office of Naval Research and the National Science Foundation funds were used to acquire radars at several universities including the Oregon State University, the Rutgers University, the University of California-Santa Barbara, the Naval Postgraduate School, the University of Rhode Island, and the University of Connecticut. This was followed by a surge in acquisition because of the National Oceanographic Partnership Program, an NOAA/Office of Naval Research/National Science Foundation program that funded coastal oceanographic research at many of these same universities.

In 2002, California voters approved funds that led to a program called the Coastal Ocean Currents Monitoring Program, which allowed for the investment of \$21 million to create a California network of HF radars to measure ocean surface

currents to ensure the monitoring of coastal water quality. The acquisition began in 2005 with 40 CODAR radars eventually being integrated with the then-existing 14 CODARs in California.

On a national scale, the Integrated Ocean Observing System (IOOS®) Program has been facilitating the development of a national data management and distribution system for all U.S. HF radars as well as radars operated by the Canadian Coast Guard in Nova Scotia. Presently, more than 100 HF radars and 30 institutions are part of the network, and their data are delivered by IOOS national data servers. The development server and data display are provided by Scripps Institution of Oceanography's Coastal Observing Research and Development Center (<http://cordc.ucsd.edu/projects/mapping/>), and its mirror is at the NOAA National

Data Buoy Center (<http://hfradar.ndbc.noaa.gov/>) while data failover redundancy is also provided at Rutgers University. Data file management and distribution follow internationally accepted standards, for example, netCDF-CF file and metadata formats and OpenGIS® *Web Coverage Service* Interface Standard for interoperable delivery of gridded data. Nationally, an additional focus has been the effort to acquire primary radio frequency licenses. To form an operational network, the radars need to operate at dedicated radio frequencies, which requires the approval of the International Telecommunications Union as well as U.S. agencies. The process to acquire those frequencies has been supported by NOAA IOOS for nearly 5 years, with the expectation that the final approvals will be given at the World Radiocommu-

nications Conference in January 2012 (Figure 1).

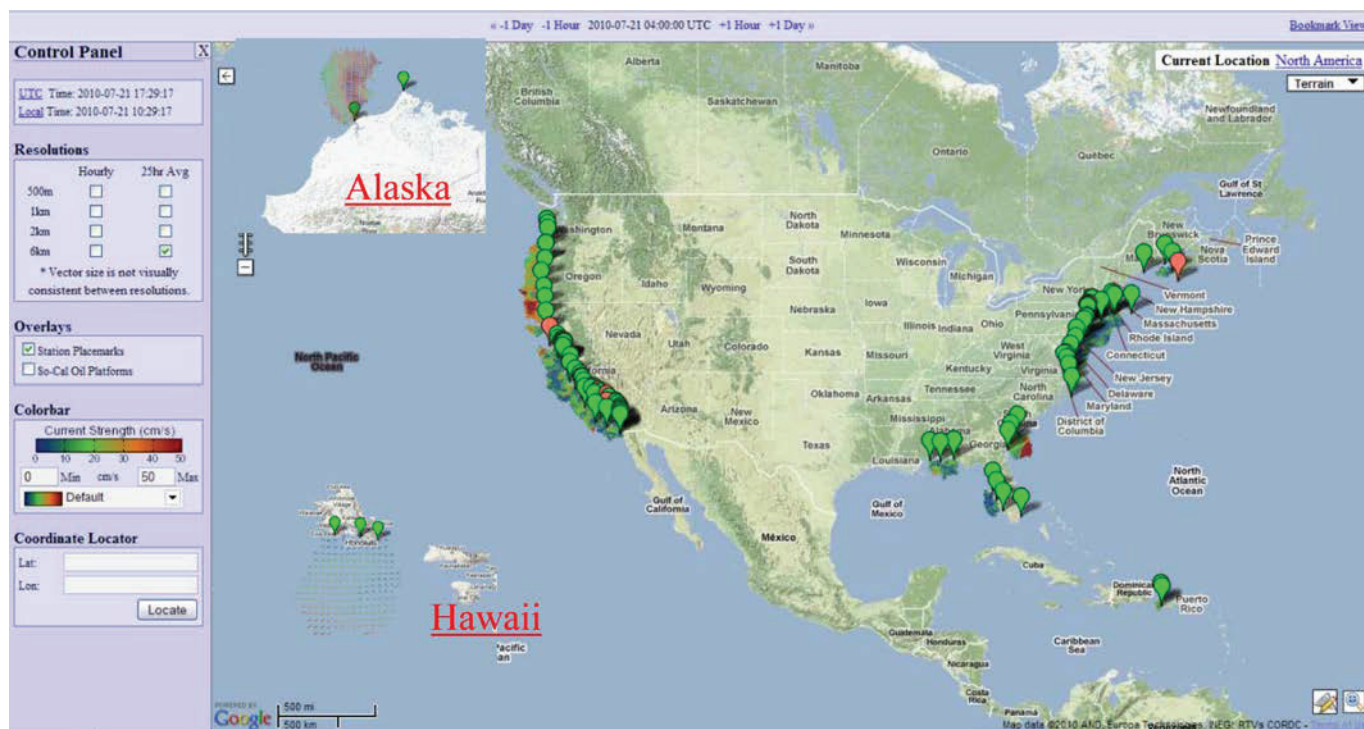
## Physics of HF Radar Current Monitoring

### Why HF radar?

HF denotes that part of the electromagnetic spectrum having frequencies from 3 to 30 MHz, which is equivalent to radio wavelengths of 10 to 100 m. HF radar has been shown to be the optimal method for coastal sea surface current mapping for a number of reasons. First, the targets required to produce coherent sea echo using HF are surface gravity waves, typically of several to a few tens of meters wavelength, which are well understood and nearly always present in the open ocean. Second, vertically polarized HF waves can propagate over conductive seawater via coupling to the mean spherical sea surface, producing measurement ranges

**FIGURE 1**

Montage of U.S. HF radar site locations. Green sites are sending data on schedule. Red sites have delayed data. (Color versions of figures available online at: <http://www.ingentaconnect.com/content/mts/mts/2010/00000044/00000006>.)





beyond line of sight, out to 200 km or more offshore. Third, Doppler sea echo at HF, under most wave conditions, has a well-defined signal from wave–current interactions that is easily distinguishable from wave–wave processes. This allows for robust extraction of current velocities. It is primarily these three features, along with the spatial resolutions that are possible due to the frequency modulation discussed below, which place the HF band in a unique status for coastal current monitoring.

### Physics of HF Sea Scattering

The two environmental conditions necessary for HF current mapping are conductive surface water and the presence of surface gravity waves of sufficient length and height. Conductivity of water is primarily determined by salinity, which is typically 32–37 PSU in the open ocean. As salinity decreases, so does the strength of the sea echo and, therefore, range of measurement. Since freshwater is inherently 5,000 times less conductive than seawater, HF signals do not travel nearly as far (e.g. Fernandez et al., 2000). It has been observed in bays and around river mouths that during times of high freshwater discharge ranges can be significantly reduced (e.g., Long et al., 2006).

The ocean surface, at any given moment, contains a random structure of crests and troughs, the slopes of which scatter radar signals in all directions. However, within the random surface, it is only the periodic structure of surface waves whose wavelength,  $\lambda_o$ , is precisely half the radar wavelength,  $\lambda$ , that will produce coherent backscatter. This is an analytic result known as Bragg scattering. In the case of a standard backscatter (or monostatic) radar, the scattered energy will be shifted in

Doppler proportional to the relative speed of the ocean wave traveling directly toward or away from the radar. The transmit frequency of the radar determines the radar wavelength and, hence, determines the length of ocean waves from which the radar wave will backscatter. Because attenuation increases as frequency increases, the result is that higher frequency radars (shorter radar wavelength) have a shorter maximum range. Approximately one third of the radars in the United States are in the 4- to 5-MHz band, which can achieve 200 km or more, depending on conditions. Another third operates in the 12- to 14-MHz band and can achieve an approximately 90-km range. Approximately one quarter of the radars operate in the 24- to 27-MHz band and achieve ranges of approximately 45 km. At the higher frequencies, it is possible to obtain greater radio spectrum bandwidth that in turn allows for higher range resolution. The resolutions vary from less than 1 km to approximately 6 km. Regardless of the operating frequency, the physics is the same. Assuming a stationary radar, the relative wave speed is comprised of the phase speed of the Bragg wave plus any underlying current. For deep water, the phase speed for surface waves is well known as a function of  $\lambda_o$ :

$$c = \sqrt{\frac{g\lambda_o}{2\pi}}$$

which can be subtracted leaving only the velocity of the current. This velocity is the projection of the actual current along the ray from the radar location to the scattering area and is generally referred to as a *radial velocity*. In water of shallow or intermediate depth, the water depth,  $D$ , must also be known at each measurement location

*a priori* to properly remove the Bragg wave phase speed:

$$c = \sqrt{\frac{g\lambda_o}{2\pi} \tanh\left(\frac{2\pi D}{\lambda_o}\right)}$$

### Range and Velocity Determination

All HF radar systems currently used for ocean measurements use some form of frequency-modulated continuous wave (FMCW) waveform for range determination. FMCW has the benefit of much lower maximum power requirements to achieve the same average power and, therefore, range performance as older time-gated pulsed radars (Barrick, 1973). For closely spaced or colocated transmit and receive antennas, a pulsed and gated FMCW (or FMiCW, “i” = interrupted) waveform is desirable whereby the transmit signal is cycled on and off and radar echo received in opposition over a period determined by the system’s achievable range. This is done to prevent saturation of the electronics as well as the received echo by the much stronger transmit signal. For both cases, the fundamental range determination is the same (Barrick, 1973).

A continuous linear frequency sweep (or chirp) over a fixed bandwidth and pulse repetition frequency is generated in the receiver and amplified for transmit. As scattered energy is received, it is delayed by the two-way travel time and shifted in Doppler on the basis of the target velocity. When mixed with the coherent linear sweep still generated inside the receiver, the time delay of the received echo results in a difference frequency train, which is digitized for range and Doppler processing. By applying a fast Fourier transform to the digitized signal, the data can be sorted into discrete range

bins at each sweep. Application of a second fast Fourier transform at each range bin over multiple sweeps produces a Doppler spectrum at each range.

A typical Doppler spectrum for a single receive antenna is shown in Figure 2. The characteristic Bragg peaks from surface wave echoes are indicated with a positive Doppler shifted peak resulting from waves approaching the radar and negative Doppler shifted peak from waves retreating from the radar. Each peak is further spread because of the underlying current velocities present across the entire arc at the selected range. Also shown is the weaker second-order sea echo, which is a harmonic of the first order, whereby longer waves, not currents, modify the Doppler of the Bragg waves. Wave state information can be extracted from second-order spectra for certain wave conditions that vary by radar frequency (Lipa, 1977) (Figure 3).

**FIGURE 2**

CODAR SeaSonde on San Clemente Island, CA.

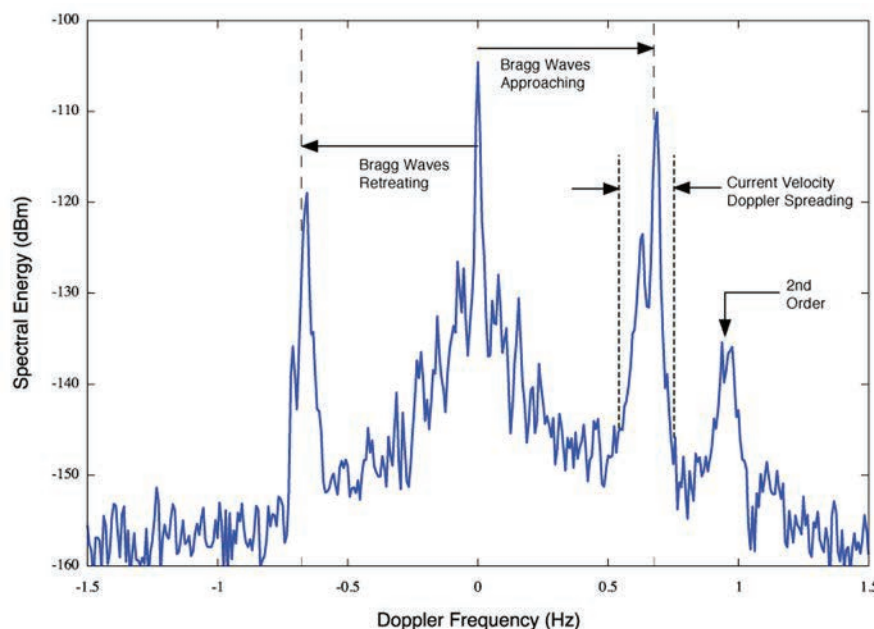


### *Bearing Determination Methods*

The final stage of processing radial vectors is bearing determination. A single antenna can detect all of the current velocities present at a given range, but more information is needed to de-

**FIGURE 3**

Representative HF radar Doppler spectrum.



termine the bearing to which each velocity can be attributed. In general, there are two classifications of bearing determination commonly used for HF radar: beam forming and direction finding.

Direction finding uses the phase and amplitude differences between receive antenna elements, known as the antenna response pattern. These differences are applied to each Doppler bin in the spectra of the individual elements to determine the most likely direction of arrival. Direction finding can be applied to compact directional antennas or to phased array antennas. It is most commonly used with the three colocated elements of the compact cross-loop/monopole configuration (e.g., Miller et al., 1985). Approximately 90% of the HF radars in the United States use a direction finding method.

Beam forming uses an array of receiving antenna elements, typically between 8 and 16 in a linear alignment and spaced about half of the radar

wavelength apart. Phase differences exist between signals received on the array elements that depend on the direction of arrival. When the Doppler spectra of the individual array elements are summed with the proper phase differences applied for a given bearing, a digital narrow beam is formed and a peak-picking algorithm used on the resultant spectrum. The digital beam width depends on the ratio of the wavelength divided by the array length and on the bearing toward which the beam is steered (Skolnik, 1990).

### *Methods for Combining Radial Current Vectors*

Although there are a variety of uses for radial vectors by themselves, most often the radial velocity vectors from two or more sites must be combined to produce a 2-D map of the surface current velocity. The problem inherent in any combining method, however, is that each radar inherently outputs radial vector data in a polar grid centered on the radar location.

Mapping multiple sets of radial vectors from displaced polar grids onto a Cartesian coordinate system results in variations in data density, signal strength, and geometric dilution of statistical accuracy (Chapman et al., 1997) across the field of coverage.

A number of combining methods have been developed including but not limited to simple interpolation with vector addition, least squares methods on vectors falling inside a defined averaging circle, and objective mapping. Recently, efforts have been made both in applying modal analysis to multiple radial data sets (Lekien et al., 2004) as well as assimilating radial velocity data directly into models without performing a separate radial combining step (Shulman et al., 2007).

## IOOS HF Radar: An Exemplary Partnership

In 1999, a number of HF radar researchers gathered informally in Oregon as a side meeting to a National Oceanographic Partnership Program awardees workshop. The clear benefits to everyone from having meetings specifically designed to exchange information and research about HF radar gave birth to the Radiowave Oceanography Workshop (<http://radiowaveoceanography.org/>) series of meetings starting in 2001, which have continued annually ever since. Although completely self-funded, these meetings have been successful in annually bringing together HF radar experts at a dedicated forum in which to share state-of-the-art knowledge. This series of workshops illustrates the level of cooperation and commitment within the HF radar community.

There are presently 30 institutions that contribute their data to the national HF radar network data management system, which is funded by IOOS but relies on the voluntary adherence to data file format standards by the HF radar operators. Users from these institutions also routinely volunteer their time for workshops such as the Radar Operators Working Group (<http://www.rowg.org>), information collection efforts such as the gap analyses, and standards compiled for the creation of the National Surface Current Mapping Plan (<http://www.ioos.gov/hfradar>) and advisory panels such as the National HF Radar Technical Steering Team to help make the transition to an operational national HF radar network.

## National Applications

On a national scale, there are two main applications presently underway: (1) the U.S. Coast Guard (USCG) Search and Rescue (SAR) operations and (2) the NOAA oil spill response operations. These applications use ocean surface current data to track and predict the flow of the uppermost layer of the ocean, and IOOS within NOAA is providing resources to bring new capabilities to both of them.

### USCG SAR Optimal Planning System

Beginning in 2000, the USCG Research and Development Center began a multiyear investigation into the utility of real-time HF radar surface-current measurements for search and rescue (SAR). In collaboration with the University of Connecticut, the University of Rhode Island, and the Rutgers University, these drifter-verified tests were based around the CODAR SeaSonde (CODAR Ocean Sensors,

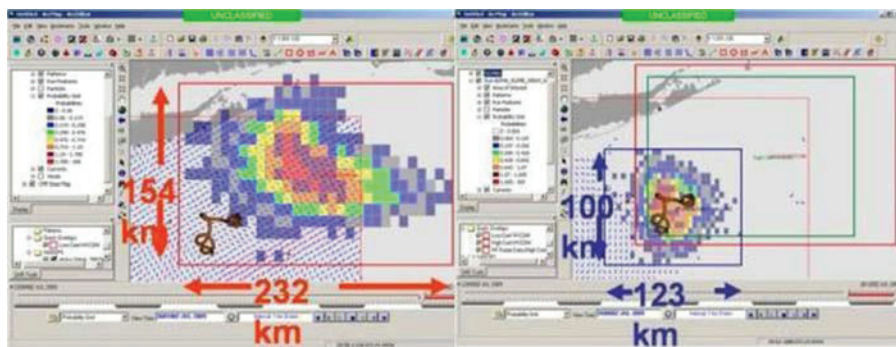
Ltd.) standard-range and long-range HF radar systems operating on the eastern coast of the United States. The USCG assessed the improvement from HF radar data in their SAR planning process (Ullman et al., 2003). This study showed better comparison when CODAR-derived currents were compared against available NOAA tidal current predictions. Along with these key comparisons, an equally important product was developed, the Short-Term Predictive System (STPS), which provides a 24-h forecast of surface currents based on the statistics of the previous 30 days of CODAR surface current data. Following these evaluation studies, available *in situ* data were used to evaluate and define appropriate parameters for inclusion in the USCG search planning tool. In May 2009, the current velocities from the Mid-Atlantic long-range CODAR network and long-range STPS forecasts were included in the operational USCG SAR Optimal Planning System. For SAR cases in the Mid-Atlantic, planners now have access to these data and forecasts within their operational planning tool.

Because SAR is a national mission encompassing all U.S. coastal waters, the IOOS Program in NOAA is extending these Mid-Atlantic data products to all coastal areas where HF radars are located. This is a partnership with the USCG, the Scripps Institution of Oceanography, the University of Connecticut, the Rutgers University, and the Applied Sciences Associates that will extend the STPS and also provide a gap-filled current velocity field using optimal interpolation (e.g., Kim et al., 2008) as input to the STPS. These groups provide expertise from a spectrum of topics that are needed to provide a real-time end-to-end product, including data handling from the



**FIGURE 4**

Screenshots from USCG SAROPS. Left: search area without using HF radar data. Right: search area reduced by 2/3 when HF radar data used. Both after 96 h.



radar site to multiple distributed national servers, intermediate products (STPS and optimal interpolation portions), and finally to the USCG Environmental Data Server (Figure 4).

## Oil Spill Response

Although the main impetus for creating the NOAA CODAR system in the 1970s was for oil spill response, it was not until 2006 HF radar was used by official government spill responders. In August of 2006, the National Ocean Service and the USCG led an interagency field exercise, *Safe Seas 2006*, in the San Francisco Bay area to enhance the preparedness of oil spill responders. As part of that exercise, the IOOS program collaborated with the NOS Office of Response and Restoration (OR&R) to create hourly gap-filled maps of HF radar-derived surface currents. The IOOS partners at the San Francisco State University and the Naval Postgraduate School created new data handling software and implemented a real-time open-boundary modal analysis suite of algorithms (Kaplan and Lekien, 2007). These nowcasts were then formatted into files that were readily ingested by the General NOAA Oil Modeling Environment. Eleven HF

radars, spanning more than 160 km of coastline and having 1- to 2-km resolution, provided continuous coverage during the 5-day exercise. This preparedness exercise provided a foundation for the use of HF radar data by the NOAA OR&R spill response trajectory modeling team (Figure 5).

When the container vessel *Cosco Busan* collided with the base of the Bay Bridge in San Francisco Bay in November of 2007, spilling more than 53,000 gallons of fuel oil, managers used surface current maps from HF radar data to monitor the spill trajectory, predicting movement as far north as Angel Island and westward

along the San Francisco waterfront. This closely matched visual reports of oil on the shorelines of Alcatraz, Angel Island, and San Francisco and on a map produced by the NOAA OR&R. Once the oil moved into the Gulf of the Farallones, the HF radar data accurately predicted that the oil would not beach there. As HF radar capabilities are integrated into California oil spill response, spills like the *Cosco Busan*'s (which occurred in dense fog) can be more effectively tracked, with mitigation efforts unimpeded by lack of visual data.

The earlier *Safe Seas* exercise and use of HF radar data during the *Cosco Busan* spill allowed OR&R to make a seamless transition to utilizing Gulf of Mexico HF Radar data soon after the Deepwater Horizon platform in the northern Gulf of Mexico exploded and sank in April of 2010. As of this writing in August 2010, the HF radar data are still being used daily. Partners from the University of Southern Mississippi and the University of South Florida have monitored their radar systems constantly to ensure that they are operating while the Deepwater Horizon spill continued and that the data were delivered to the IOOS national

**FIGURE 5**

Schematic of data flow for new HF radar SAROPS project.

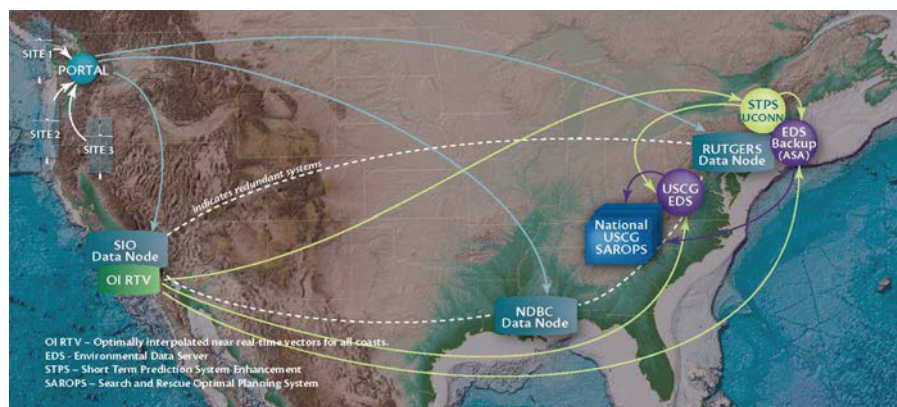
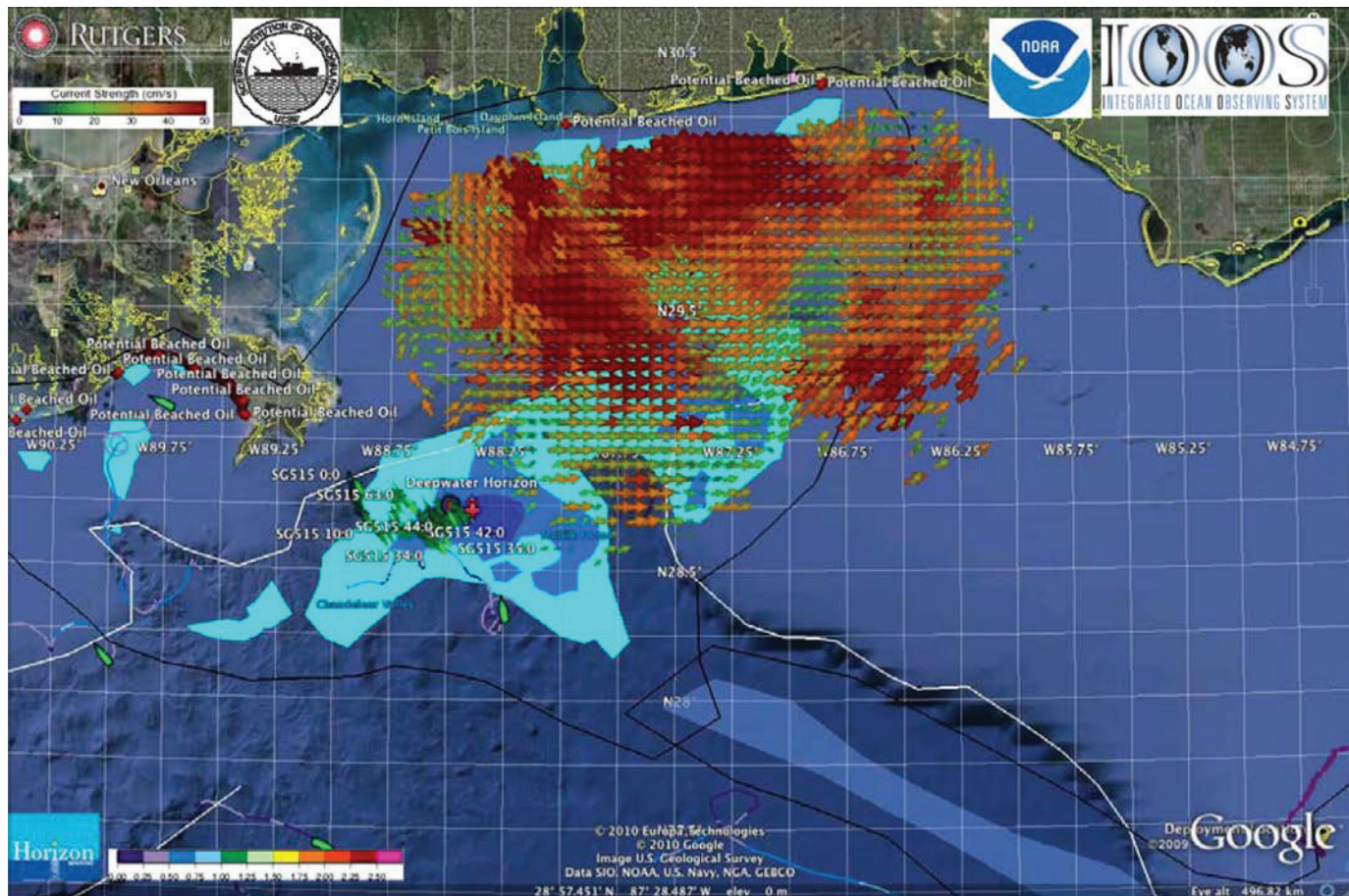


**FIGURE 6**

HF radar currents for June 4, 2010, overlaid with oil coverage in the Deepwater Horizon spill area in the northern Gulf of Mexico, courtesy Rutgers University Coastal Ocean Observation Lab.



HF radar data servers at Scripps Institution of Oceanography and the NOAA National Data Buoy Center. These Gulf of Mexico sites have been particularly valuable since they cover a good portion of the continental shelf in the Mississippi Bight, which is just to the north and northeast of the site where the Deepwater Horizon was located (Figure 6).

Similar to USCG SAR, the optimally interpolated current velocity fields, mentioned earlier, will also provide a product that can be ingested into the NOAA oil spill response team's General NOAA Oil Modeling Environment model for application wherever HF radars operate.

### Regional Applications Tracking Impacts on Marine Populations

Ocean conditions change from year to year and the ongoing measurements of surface currents made by HF radar are a crucial backbone for ocean observations along the coast. Unlike buoys and ships, which collect information at single points and times, HF radar provides full, archived mapping, day and night, of our coastal waters to 150 km offshore. Long-term monitoring of surface currents is used to track impacts on marine populations. Off Bodega Bay, California researchers are using HF radar-derived surface current data to obtain seasonal to annual infor-

mation on ocean conditions that likely influence the survival rate of young salmon when they first enter the ocean. As smolts exit estuaries like the Russian River in early spring, strong northerly winds and southward-moving currents can carry weakly swimming small fish south to the predator-rich Gulf of Farallones in some years or alongshore to the north in others. Preliminary evidence suggests that surface flows in the months leading up to the spring emigration period may be important for the survival of salmon smolts and returns to the Russian River system years later (W.J. Sydeman/Farallon Institute and J.L. Largier/Bodega Marine Laboratory, unpublished data).



Reversing the collapse of the California salmon fishery requires an understanding of the migratory paths of young salmon as well as knowledge of the movement of nearshore surface currents and upwelling events that comprise their ocean going habitat.

Coastal surface currents can also provide important input to establishing and evaluating marine protected areas (MPAs); it provides the only multiyear data with enough spatial coverage to assess how larvae of marine populations are dispersed from the location where they originate to where they settle and grow to maturity. HF radar data from a regional network in California have demonstrated the connectivity between central California marine protected areas (MPAs) by back-projecting trajectories from 10 MPAs more than a 40-day period. Clarifying this connectivity is an important step toward understanding the movement of invertebrate and fish larvae (Zelenke et al, 2009) (Figure 7).

HF radar data are also being used to identify and track large eddy features (tens of kilometers wide) off Cape Mendocino, Point Arena, and in the Santa Barbara Channel. These eddies play a critical role in connecting or disrupting marine populations that live along the coast of California. The

California coast is experiencing an increasing frequency and toxicity of harmful algal blooms (HABs), exacting serious economic, human, and marine wildlife costs. Surface current mapping has proven to be an essential tool for managers and scientists to assess and respond to HABs and will be instrumental in developing the ability to predict these events. Like all food chain components, HABs are part of a larger marine ecosystem driven by the physics of winds, waves, and currents. HF radar has become a core technology for understanding these ecosystem processes.

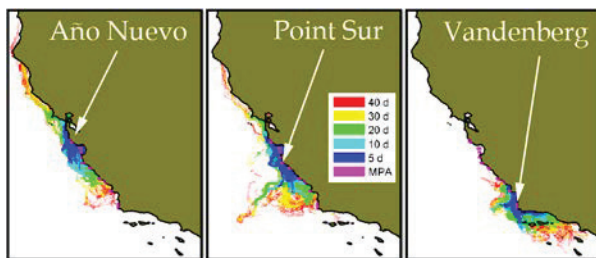
A California statewide Harmful Algal Bloom Monitoring and Alert Program that was initiated by the NOAA, the California Ocean Science Trust, and the Southern California Coastal Water Research Project is supported through the Ocean Observing Regional Associations. Weekly bottle samples measure chlorophyll, nutrients, domoic acid, and harmful algal species. Data are posted to the Web and distributed via the California Harmful Algal Bloom Monitoring and Alert Program Listserv. When HABs are detected, opportunistic sampling from additional shore sites, HF radar-derived surface currents, gliders, and boats determines their extent and severity.

Within the Northwest Association of Networked Ocean Observing Systems region, the Pacific Northwest Harmful Algal Bloom Bulletin has been developed by the NOAA and the University of Washington to provide a comprehensive early warning information system for Washington coast razor clam toxicity and amnesic shellfish poisoning events. The bulletin builds upon the Olympic Region HAB monitoring program and Ecology and Oceanography of Harmful Algal Blooms in the Pacific Northwest research by automating the aggregation of data into a single location on a Web-based information dashboard. Among the array of chemical and biological information included are currents from HF radars that operate within Northwest Association of Networked Ocean Observing Systems (Trainer and Hickey, 2010).

The goal of assimilating HF radar-derived currents into numerical circulation models has for a number of years remained a priority within the modeling and HF radar research communities. Generally, these models are developed for areas that scale to approximately that of an IOOS regional coastal ocean observing system. A number of successful modeling projects are described in the National Surface Current Mapping Plan (<http://ioos.gov/hfradar>), and a recent American Geophysical Union Meeting of the Americas 2010 (Foz do Iguaçu, Brazil, program available [here](#)) held a session on *Application of HF Radar Networks to Ocean Forecasts*. In addition, as part of the recently established National HF Radar Technical Steering Team, the IOOS HF radar community is presently undertaking a comprehensive review of the many modeling efforts that use HF radar data throughout the globe.

## FIGURE 7

Color map: location of waters 40 days ago (red), 30 days ago (yellow), 20 days ago (green), 10 days ago (cyan), and 5 days ago (blue) before reaching the labeled MPA (magenta). Connectivity maps on the basis of measured surface currents show what waters are influencing MPAs and the potential extent of surface water larval transport.





## Local Applications

### Coastal Water Quality

In southern California, HF radar-derived surface currents has allowed managers to track the movement of planned and unplanned discharges in our coastal waters, enabling more precise and timely management decisions. An Orange County Environmental Health Engineering Specialist, familiar with the Tijuana River outflow issues, wrote that “this real-time surface currents monitoring system has allowed the San Diego County Environmental Health Agency to predict when contaminated water from the Tijuana River will impact the southern beaches of San Diego County.” In November of 2006, the City of Los Angeles diverted the flow from Hyperion—its oldest and largest wastewater treatment plant—from an outfall 5 miles from the shoreline to a rarely used pipe 1 mile offshore to allow inspection of the 5-mile pipe. The diversion lasted 3 days, and approximately 800 million gallons of secondary-treated wastewater was released 1 mile off the coast of Santa Monica. A division manager for the City of Los Angeles, Bureau of Sanitation’s Environmental Monitoring Division writes that the city’s monitoring effort greatly benefited from information provided through the HF radar system and that “the real-time current information provided through [the program] enabled us to adaptively modify our sampling grid to better track the discharge plume and to predict the dispersion of the plume.”

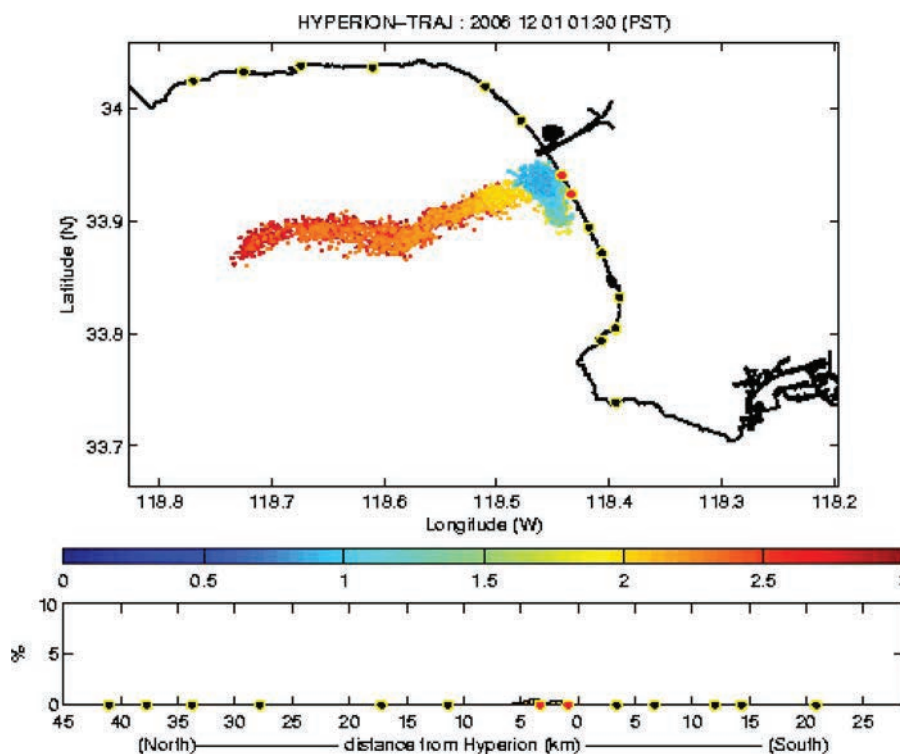
In October of 2007, the end gate to the Southwest Ocean Outfall offshore Ocean Beach in San Francisco was lost; a buoyant mixture was released from the pipe 6.5 km offshore and rose to the surface. At the request of the San Francisco Public Utilities Commission,

HF radar data were used to track movement of the effluents based on real-time observations of ocean surface currents from the HF radar network. “[A scientist] was able to rapidly provide daily and cumulative modeling of effluent trajectories that really demonstrated the immediate value of the existing program,” said Michael Kellogg of the San Francisco Public Utilities Commission. This information significantly improved the decision-making and response capabilities of the utilities commission. The trajectories showed a weak onshore flow, indicating that the discharge would not move toward beaches by the time the rupture could be repaired; this allowed responding agencies to better manage beach closures, offshore and onshore water quality monitoring, and outfall repairs (Figure 8).

Since 2008, several floatable events along the New Jersey coast have prompted investigations on possible sources and ultimate fate of debris that has washed up on local beaches. For example, in August 2008, medical waste washed up on the shores near Avalon, New Jersey. The New Jersey Department of Environmental Protection asked the mid-Atlantic HF radar network managers at Rutgers University to provide information on the possible source. Using the location and the time of the initial beach location of the debris, Rutgers radar scientists were able to trace back its probable location several days before the washup. The weak currents indicated that if the debris were put into the ocean within several days of the initial siting, it had to be a local source. Consistent with the

**FIGURE 8**

Upper panel: shows the near real-time Hyperion Outfall plume trajectory color coded based on particle age (dark blue—0 days; red—3 days). The color coding is based on approximate life cycle of bacteria. Lower panel: distance along the coastline from the Hyperion Outfall with Los Angeles County sampling locations red if there is plume potential.



guidance from the HF radar data, the investigation determined that the source was in fact a dentist who dropped the waste from a boat just off the beaches of Avalon the day before. This result, along with other events in the region, has highlighted the need to extend the regional coverage of the present HF radar network closer to the coast. These local enhancements are being initiated in the Mid-Atlantic Bight with leveraged state agency resources to build out nested high-resolution HF radar sites and assimilation of these data into coastal models tuned to track particles along the coast.

## Marine Navigation

HF radar data are a core component of a simple but very effective near real time, customized, interactive Website displaying environmental conditions at the entrance to the Ports of Los Angeles and Long Beach Harbor: <http://www.sccoos.org/data/harbors/lalb>. This Website could serve as a template for ports throughout the United States. This application is discussed more fully in a companion article by Thomas et al. in this issue.

Integrating HF radar data with existing conventional in situ sensors will also occur in an upcoming demonstration project in Mobile Bay, Alabama, involving Mobile's NOAA Physical Oceanographic Real-Time System (PORTS®) and two CODAR systems, operated by the University of Southern Mississippi. This project may provide a basis for consideration of a Gulfport, Mississippi HF radar-PORTS® equivalent.

## Offshore Wind Energy

Rutgers University has been funded by the New Jersey Board of Public Util-

ities to develop a 3-D wind resource map to support the offshore wind energy community. The work will use available forecast models and a new deployment of a radar subnetwork (four sites) along the southern New Jersey coast. This is a 2-year grant that leverages IOOS infrastructure and creates a higher resolution HF radar coverage area within the Mid-Atlantic Bight.

## Summary

HF radar as a tool for ocean surface current mapping has been in existence for more than 30 years. It has proven itself in a number of applications of national, regional, and local significance, especially during the last 10 years or so. The physics of the measurement and the technology that delivers the measured ocean current velocities provides a robust method for coastal monitoring from nearshore to more than 200 km offshore. Through an integrated network of radars distributed throughout U.S. coastal waters, data are delivered in near real time for use in a number of applications that are critical to the health, safety, ecology, and economies of coastal areas.

## Lead Author:

Jack Harlan  
NOAA IOOS® Program,  
Silver Spring, MD  
Email: [jack.harlan@noaa.gov](mailto:jack.harlan@noaa.gov)

## References

- Barrick, D.E.** 1968. A review of scattering from surfaces with different roughness scales. *Radio Sci.* 3:865-68.
- Barrick, D.E.** 1972. First-order theory and analysis of MF/HF/VHF scatter from the sea. *IEEE Trans Antennas and Propag.* AP-20(1): 2-10. doi:10.1109/TAP.1972.1140123.

**Barrick, D.E.** 1973. FM/CW Radar signals and digital processing. NOAA Technical Report ERL 283-WPL 26, July 1973.

**Chapman, R.D.,** Shay, L.K., Graber, H.C., Edson, J.B., Karachintsev, A., Trump, C.L., Ross, D.B. 1997. Intercomparison of HF radar and ship-based current measurements. *J Geophys Res.* 102:18,737-48. doi: 10.1029/97JC00049.

**Crombie, D.D.** 1955. Doppler spectrum of sea echo at 13.56 mc/s. *Nature.* 175:681-2. doi:10.1038/175681a0.

**Fernandez, D.M.,** Meadows, L.A., Vesecky, J.F., Teague, C.C., Paduan, J.D., Hansen, P. 2000. Surface current measurements by HF radar in freshwater lakes. *IEEE J Oceanic Eng.* 25(4):458-71.

**Kaplan, D.M.,** Lekien, F. 2007. Spatial interpolation and filtering of surface current data based on open-boundary modal analysis. *J Geophys Res.* 112:C12007, doi:10.1029/2006JC003984.

**Kim, S.Y.,** Terrill, E.J., Cornuelle, B.D. 2008. Mapping surface currents from HF radar radial velocity measurements using optimal interpolation. *J Geophys Res.* 113:C10023, doi:10.1029/2007JC004244.

**Lekien, F.,** Coulliette, C., Bank, R., Marsden, J.E. 2004. Open-boundary modal analysis: interpolation, extrapolation, and filtering. *J Geophys Res.* 109:C12004. doi:10.1029/2004JC002323.

**Lipa, B.J.** 1977. Derivation of directional ocean-wave spectra by integral inversion of the second-order radar echoes. *Radio Sci.* 12:425-34. doi:10.1029/RS012i003p00425.

**Long, R.,** Garfield, N., D. Barrick, D.E. 2006. The effect of salinity on monitoring San Francisco Bay surface currents using Surface Current Monitoring Instruments (SMCI). Presentation at the California and the World Ocean '06 Conference, September 17-20, Long Beach, California.

**Miller, P.A.,** Lyons, R.S., Weber, B.L. 1985. A compact direction-finding antenna for HF remote sensing. *IEEE Trans Geosci*

Remote Sens. GE-23:18-24. doi:10.1109/  
TGRS.1985.289496.

**Shulman**, I., Kindle, J., Martin, P., deRada, S.,  
Doyle, J., Penta, B., Anderson, S., Chavez, F.,  
Paduan, J., Ramp, S. 2007. Modeling of  
upwelling/relaxation events with the Navy  
Coastal Ocean Model. J Geophys Res.  
112:C06023. doi:10.1029/2006JC003946.

**Skolnik**, M. 1990. Radar Handbook. 2nd ed.  
New York: McGraw-Hill, Inc.

**Trainer**, V., Hickey, B.M. 2010. A Forecasting  
Bulletin for Harmful Algal Blooms in the  
Pacific Northwest, Eos Trans. AGU, 91(26),  
Ocean Sci. Meet. Suppl., Abstract IT33B-06.

**Ullman**, D., O'Donnell, J., Edwards, C.,  
Fake, T., Morschauser, D., Sprague, M.,  
Allen, A., LCDR B, Krenzien. 2003. Use of  
Coastal Ocean Dynamics Application Radar  
(CODAR) Technology in U.S. Coast Guard  
Search and Rescue Planning. US Coast Guard  
Report No. CG-D-09-03.

**Zelenke**, B., Moline, M.A., Crawford, G.B.,  
Garfield, N., Jones, B.H., Largier, J.L.,  
Paduan, J.D., Ramp, S.R., Terrill, E.J.,  
Washburn, L. 2009. Evaluating connectivity  
between marine protected areas using  
CODAR high-frequency radar. In: OCEANS  
2009 MTS/IEEE Conference, Biloxi, MS.







FEATURE ARTICLE

# Ocean observatory data are useful for regional habitat modeling of species with different vertical habitat preferences

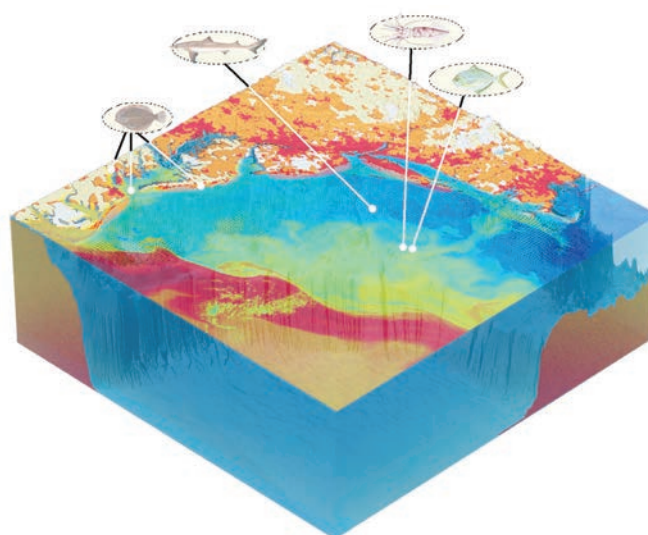
John Manderson<sup>1,\*</sup>, Laura Palamara<sup>2</sup>, Josh Kohut<sup>2</sup>, Matthew J. Oliver<sup>3</sup>

<sup>1</sup>Ecosystems Processes Division, NEFSC/NMFS/NOAA, James J. Howard Marine Highlands, New Jersey 07732, USA

<sup>2</sup>Institute of Marine and Coastal Science, Rutgers University, New Brunswick, New Jersey 08901, USA

<sup>3</sup>College of Earth, Ocean and Environment, University of Delaware, Lewes, Delaware 19958, USA

**ABSTRACT:** Ocean Observing Systems (OOS) now provide comprehensive descriptions of the physical forcing, circulation, primary productivity and water column properties that subsidize and structure habitats in the coastal ocean. We used generalized additive models (GAM) to evaluate the power of OOS remotely sensed ocean data along with *in situ* hydrographic and bottom data to explain distributions of 4 species important in the Mid-Atlantic Bight, USA, ecosystem that have different vertical habitat preferences. Our GAMs explained more abundance variation for pelagic species (longfin inshore squid and butterfish) than demersal species (spiny dogfish and summer flounder). Surface fronts and circulation patterns measured with OOS remote sensing as well as the rugosity and depth of the bottom were important for all species. *In situ* measurements of water column stability and structure were more useful for modeling pelagic species. Regardless of vertical habitat preference, the species were associated with vertical and horizontal current flows, and/or surface fronts, indicating that pelagic processes affecting movement costs, prey production and aggregation influenced distributions. Habitat-specific trends in abundance of 3 of the 4 species were well described by our OOS-informed GAMs based upon cross validation tests. Our analyses demonstrate that OOS are operationally useful for regional scale habitat modeling. Regional scale OOS-informed statistical habitat models could serve as bases for tactical ecosystem management and for the development of more sophisticated spatially explicit mechanistic models that couple ontogenetic habitats and life history processes to simulate recruitment of organisms important to maintaining the resilience of coastal ecosystems.



Data and models integrated in Ocean Observing Systems capture ocean dynamics at scales required for regional habitat modeling and management.

Image: Igor Heifetz

**KEY WORDS:** Ocean observing · Pelagic habitat · Remote sensing · Generalized Additive Modeling

Resale or republication not permitted without written consent of the publisher

## INTRODUCTION

Species distributions reflect the habitat selection decisions individual animals make to maximize fitness under constraints imposed by their perceptual and movement capabilities. Variations in survival and reproduction are the consequences of con-

\*Email: john.manderson@noaa.gov

strained habitat selection and the mechanistic underpinnings of spatial population dynamics. The diversity of habitats used by species, and effects of habitat variation on vital rates, including movements, determine the productivity, stability and resilience of regional populations (Secor et al. 2009, Tian et al. 2009, Kerr et al. 2010). Furthermore, the effects of habitat diversity and its loss on the resilience and stability of populations that serve as ecosystem keystones should be translated across a level of ecological organization to affect ecosystem productivity, resilience, and stability. Understanding the ways habitat effects on recruitment are translated into the emergent dynamics of regional populations important in maintaining the resilience of large marine ecosystems is crucial for the development of effective space-based ecosystem management, particularly in the face of rapid climate change (Mora et al. 2007, Hsieh et al. 2010). The development of statistical habitat models that are broad in scope and explicitly consider bottom features as well as the dynamic properties and processes of the water column (e.g. temperature, primary productivity, advection) known to regulate critical physiological, behavioral and demographic rates is a necessary first step toward this end.

Regional scale habitat models have been difficult to develop for coastal species, in part because data describing habitat variation at broad spatial but fine time scales have been unavailable. Ocean Observing Systems (OOS) now provide spatially and temporally comprehensive regional scale descriptions of pelagic features and processes required to understand the ways in which dynamic features of the ocean fluid affect the distribution and recruitment of fish living in it. Ocean Observing data include sea surface temperature and ocean color measured with satellite sensors, surface currents measured with networks of high-frequency (HF) radars deployed along the shore, and physical and optical properties measured by fleets of robots gliding beneath the ocean surface. The data describe the physical forcing, current flows, and sources and transport of detritus, primary and secondary productivity which structure, couple and fuel coastal ocean habitats and thus regulate the recruitment of animals using them. Remotely sensed data have been used to construct habitat models for open ocean pelagic predators, but are not commonly used for coastal species (Valavanis et al. 2008, Zainuddin et al. 2008, Becker et al. 2010, Mugo et al. 2010, Zydels et al. 2011).

Presently, Ocean Observing data with the broadest spatial coverage are satellite measurements of ocean temperature and color, and HF radar measurements

of surface currents. These data can be processed to describe upwelling and downwelling centers and the spatial dynamics of surface fronts where high primary productivity occurs or is concentrated. These products may therefore be most useful for identifying habitat associations of pelagic species. While surface data collected directly overhead of trawl samples may be less useful for describing habitats of demersal animals, particularly in deep water, the vital rates of demersal species are also regulated by surface processes, although effects may be downstream and delayed in time. Distributions of large demersal animals may be influenced to a greater degree by pelagic processes regulating movement costs and prey production, than by structural features of the bottom that may provide smaller and younger stages with predation refugia. Finally, surface features can serve as proxies for important subsurface properties and processes (Castelao et al. 2008).

We used generalized additive modeling to evaluate the power of Ocean Observing data, as well as *in situ* pelagic data and benthic data, to describe the distributions of 4 trophically important interacting species with different vertical habitat preferences in the Mid-Atlantic Bight US coastal ocean. We quantified the strength of species associations with mesoscale pelagic features described by OOS, as well as pelagic and benthic features measured with shipboard CTDs, acoustics and bottom grabs, emphasizing habitat characteristics likely to influence growth, dispersal, survival or reproduction. Finally, we discuss the potential value of current and future Ocean Observing assets and research for the development of regional scale habitat models that could serve as fundamental tools for understanding the role of marine habitat dynamics in ecosystem dynamics and the development of more effective space- and time-based ecosystem management strategies.

## MATERIALS AND METHODS

### Study area

Our study area was the Mid-Atlantic Bight (MAB), USA, where the dynamics of the coastal ocean are continuously monitored at broad spatial scales but fine time scales by the Mid-Atlantic Regional Association Coastal Ocean Observing System (MARACOOS: <http://maracoos.org>; Fig. 1). The oceanography of the MAB is described in detail elsewhere (Beardsley & Boicourt 1981, Epifanio & Garvine 2001, Lentz 2008). Briefly, the broad, gently sloping continental shelf in



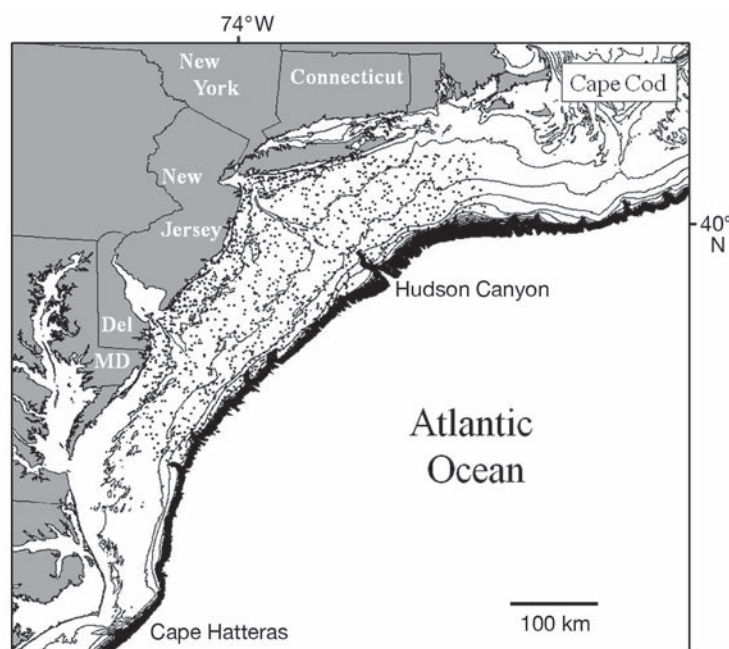


Fig. 1. Locations on the Mid-Atlantic Bight continental shelf, USA, of stations sampled during North East Fisheries Science Center fishery-independent bottom trawl surveys and considered in our analysis of longfin inshore squid, butterfish, spiny dogfish and summer flounder habitat

the MAB is incised by canyons and drowned river valleys that serve as important cross shelf transport pathways. Mean current flow is southwestward and driven by cold buoyant water derived from the northeast. Biological productivity is strongly seasonal. However, air and ocean temperatures, stratification, and wind and buoyancy forcing are extremely variable and superimpose complex, ecologically important variation on mean patterns. Mean southwestward current flows can be intensified by southward, downwelling favorable winds and estuarine discharge, or steered offshore by northward, upwelling favorable winds associated with approaching atmospheric fronts and summer sea breezes. Wind forcing results in sea surface set up and set down along the coast that produces cross-shelf, subsurface counter flows that are strongest along drowned river valleys. During the summer, areas of high primary productivity occur in estuaries and nearshore upwelling centers. During the spring, meanders in the shelf slope front produce upwelling of deep nutrient-rich oceanic waters that, with increasing solar radiation, promote an early bloom in the shelf slope sea (Marra et al. 1990, Ryan et al. 1999). Spring blooms fueled by nutrients supplied by winter water column overturning occur with the onset of stratification closer to shore, while blooms also occur on the shelf when stratifica-

tion breaks down in the autumn. Organisms occupying the MAB exhibit complex seasonal cycles of reproduction and habitat use in response to the complex seasonal dynamics of ocean climate, circulation and primary productivity.

### Species abundance data

We selected longfin inshore squid *Loligo pealeii*, butterfish *Peprilus triacanthus*, spiny dogfish *Squalus acanthias* and summer flounder *Paralichthys dentatus* for analysis because they exhibit differences in vertical habitat preference, are abundant in fishery-independent bottom trawl surveys and are trophically important interacting species in the MAB (Link et al. 2008). Butterfish and longfin squid are small pelagic species important in the transfer of energy from lower trophic levels to apex predators (Link et al. 2008). Both species reach maturity at a year or less of age and have very high reproductive rates (Hatfield & Cadrin 2002, Collette & Klein MacPhee 2002). Butterfish feed primarily upon zooplankton. Squid feed on small pelagic animals including butterfish.

Spiny dogfish and summer flounder feed upon squid and butterfish but generally spend more time deeper in the water column (Packer & Hoff 1999, Moustahfid et al. 2010, Staudinger 2006, Stehlik 2007). Spiny dogfish are not as surface oriented as squid and butterfish but still spend considerable amounts of time in the water column. They exert strong top down effects on the MAB food web. Summer flounder are subtropical flatfish more strongly associated with the seabed in the ocean and estuaries.

All 4 species migrate between lower latitude and/or offshore overwintering habitats to higher latitude, inshore habitats where they spend the summer. Longfin inshore squid, butterfish and summer flounder are abundant in the MAB throughout the year while spiny dogfish are more abundant in cooler waters to the northeast during the summer (Stehlik 2007).

We used collections of the 4 species made by National Marine Fisheries Service, Northeast Fisheries Science Center's (NMFS-NEFSC) autumn, winter, and spring fisheries independent bottom trawl survey (Fig. 1; [www.nefsc.noaa.gov/epd/ocean/MainPage/ioos.html](http://www.nefsc.noaa.gov/epd/ocean/MainPage/ioos.html)) in our statistical habitat modeling. Azarovitz (1981) described the design of the stratified random survey in detail. Winter surveys occurred in February, spring surveys from March to early May,

and autumn surveys in September and October. Survey tows were made with a #36 Yankee trawl with a 10.4 m wide × 3.2 m high opening and rollers (12.7 cm stretched mesh [SM] opening, 11.4 cm SM cod end, 1.25 cm SM lining in the cod end and upper belly). The net was towed over the bottom at ~3.5 knots for 30 min. Distances the net was towed on the bottom averaged 3.5 km (95% confidence limits 3.2 to 3.7 km). Tows were made throughout the 24 h day. Consecutive samples were collected approximately every 2 h (50th, 5th, and 95th quantiles: 2.07, 1.38, 3.53 h respectively) and 19 km apart (50th, 5th, and 95th quantiles: 19.02, 4.80, 41.88 km respectively) on each survey. Examination of available length and age frequencies confirmed that large age 1+ juveniles and adults dominated collections because the trawl mesh was relatively coarse and shallow coastal and estuarine nursery habitats were not sampled.

We selected the analysis domain for this study based upon the availability of remotely sensed data from the OOS. Bottom trawl samples collected from February 2003 through October 2007 between latitudes 37.14° and 40.85° N and longitudes 70.83° and 75.16° W fit within the domain (Fig. 1). An average of 101 stations was sampled during spring and autumn. An average of 70 stations was sampled during the winter.

### Habitat data

For bottom data, we computed topographic characteristics of the bottom from the 3-arc-second NGDC Coastal Relief Model ([www.ngdc.noaa.gov/mgg/coastal/coastal.html](http://www.ngdc.noaa.gov/mgg/coastal/coastal.html); cell size = 93 m; Table 1). We used circular moving window analysis in GRASS GIS to calculate median and standard deviations of bot-

Table 1. Data sources and potential ecological effects of environmental variables considered in generalized additive model (GAM) habitat models for longfin inshore squid, butterflyfish, spiny dogfish and summer flounder. Squid and butterflyfish were considered prey in auxiliary models for spiny dogfish and summer flounder predators. na = not applicable, " : same data as given in the line above

Variables	Spatial grain	Possible ecological effect	Data source
Sun's elevation	na	Vertical migration/catchability	Calculated for trawl locations & times
Geographic coordinates	2 km	Unknown spatial process	NEFSC bottom trawl survey
<b><u>Benthic data</u></b>			
Depth (μ, SD)	1.95 km (93 m)	Structural/spatial refuge	NGDC 93 m grid <sup>a</sup>
Slope (μ, SD) <sup>d</sup>	"	"	"
Aspect (SD) <sup>d</sup>	"	"	"
Profile curvature (μ, SD) <sup>d</sup>	"	"	"
Sediment grain size (μ)	2 km	Structural/spatial refuge/enrichment	US seabed data base <sup>b</sup>
<b><u>Pelagic data</u></b>			
<b><u>In situ CTD measurements</u></b>			
Bottom temperature	1 m	Metabolic rate	NEFSC bottom trawl survey
Bottom salinity <sup>d</sup>	"	Alias proximity to freshwater source	"
Mixed layer depth	"	Mixing/1° productivity	"
Stratification index <sup>d</sup>	"	"	"
Simpson's PE (30 m)	"	"	"
<b><u>OOS remote sensing</u></b>			
<b><u>High-frequency radar</u></b>			
Cross shelf velocity	10 km	Advection/movement cost/mixing	MARACOOS HF radar <sup>c</sup>
Along shelf velocity	"	"	"
Variance in velocity	"	Tidal mixing/episodic forcing	"
Divergence potential	"	Upwelling/downwelling & mixing	"
Vorticity potential <sup>d</sup>	"	Eddy development/retention	"
<b><u>Satellites</u></b>			
Sea surface temperature	10 km	Metabolic rate/other seasonal factors	MODIS through MARACOOS <sup>c</sup>
Chlorophyll <i>a</i>	"	Primary production/organic matter	"
Normalized water leaving radiances (412, 443, 488, 531, 551, 667 nm) <sup>d</sup>	"	Surface organic matter	"
Water mass class	"	Various	"
Frontal index (distance to & strength of gradient between water masses)	"	Concentration/enrichment	"
<b><u>Prey abundance</u></b>			
Squid	2 km	Prey	NEFSC bottom trawl survey
Butterfish	"	"	"

<sup>a</sup>[www.ngdc.noaa.gov/mgg/coastal/coastal.html](http://www.ngdc.noaa.gov/mgg/coastal/coastal.html); <sup>b</sup><http://walrus.wr.usgs.gov/usseabed/>; <sup>c</sup><http://maracoos.org/data/>;

<sup>d</sup>variables that were redundant or not ecologically meaningful and therefore excluded in the final analysis

tom depth, aspect, slope, and curvature from the relief model (e.g. see Fig. 3; Neteler & Mitasova 2008). The window diameter was 2 km. Profile and tangential curvature measured the concavity (negative values indicate valleys) and convexity of the bottom (positive values indicate ridges) parallel and tangential to major axes of the bottom slope. Sediment grain sizes were selected from a map interpolated from the usSEABED data base (Reid et al. 2005). The sediment map had a spatial resolution of 2 km and was constructed using sample bias correction, maximum *a posteriori* resampling, and a spline-in-tension algorithm (Goff et al. 2006, 2008).

For pelagic data, we used conductivity, temperature and depth (CTD) profiles collected during each NEFSC trawl survey to describe bottom temperature and salinity, water column structure and stability (Table 1; [www.nefsc.noaa.gov/epd/ocean/MainPage/ioos.html](http://www.nefsc.noaa.gov/epd/ocean/MainPage/ioos.html)). We considered the ‘mixed layer’ depth at which density was  $0.125 \text{ kg m}^{-3}$  higher than the surface (Levitus 1982), a stratification index calculated as the difference in seawater density between the surface and 50 m, and Simpson’s potential energy anomaly (PE; Simpson 1981, Simpson & Bowers 1981). We calculated Simpson’s PE within the upper 30 m of the water column because the stability index calculated for the entire water column was correlated with bottom depth.

A network of HF radar provided remotely sensed measurements of surface currents (Table 1; <http://maracoos.org>; frequency = 5 MHz; Barrick et al. 1977). Radial current vectors from the network were combined to produce hourly surface current maps (resolution = 6 km). We de-tided the raw time series at each HF radar grid point using a least-squares fit of the 5 strongest principal body tide constituents (M2, S2, N2, K1, and O1). These data were then low pass filtered with a cutoff period of 30 h. We only used data for grid points with signal returns of  $>25\% \text{ yr}^{-1}$ . We calculated 8 d average cross-shore and along-shore velocity, variance in velocity, divergence (vertical velocity) and vorticity within 10 km of each trawl. Divergence and vorticity were calculated using finite difference. Divergence was calculated as the vertical current velocity in  $\text{m d}^{-1}$  at a depth of 1 m. Vorticity was normalized by the local Coriolis parameter. We also calculated indices describing seasonal trends in divergence and vorticity. Instantaneous divergence values were assigned a new value of  $-1$  if values were  $<-0.1 \text{ m d}^{-1}$ ,  $0$ , if between  $-0.1$  and  $+0.1 \text{ m d}^{-1}$ , or  $+1$  if values were  $>+0.1 \text{ m d}^{-1}$ . These new values were averaged for each grid point to produce a mapped index of upwelling and downwelling potential for each sea-

son and year (e.g. see Fig. 3). Seasonal trends in vorticity were calculated similarly using threshold values of  $\pm 0.02$ . Values for the trawl samples were extracted from the grids.

Satellite remote sensing provided surface temperature, chlorophyll *a* (chl *a*), raw light absorption and backscatter within 10 km of each trawl tow (Table 1). Moderate Resolution Imaging Spectrometer (<http://oceancolor.gsfc.nasa.gov>) data were binned to 1 km resolution using standard data quality flags. We considered measurements of sea surface temperature, chlorophyll ( $\text{mg m}^{-3}$ ; e.g. see Fig. 3), and normalized water-leaving radiance ( $\text{W m}^{-2} \text{ sr}^{-1} \mu\text{m}^{-1}$ ) at 412, 443, 488, 531, 551, and 667 nm in our analysis.

Ensemble clustering was applied to satellite sea surface temperature and normalized water-leaving radiance at 443 and 555 nm to classify water masses using the methods of Oliver et al. (2004) and Oliver & Irwin (2008). Clustering identified 27 water masses within the study domain. We made time series maps of the strengths of gradients along frontal boundaries between these water masses (e.g. see Fig. 3) and used them to compute distance ( $d_{\text{km}}$ ) to, and gradient strength ( $G$ ) of the nearest front for each trawl sample. We then calculated a frontal index (FI) for each station using the equation:

$$\text{FI} = \ln(G/d_{\text{km}} + 1) \quad (1)$$

Values for the frontal index were therefore higher for samples nearer to stronger fronts.

Many of 27 water masses identified with ensemble clustering contained 5 or fewer trawl samples. Thus, before final assignment of the samples to water masses, we used *k*-means clustering of the original satellite data to reduce the number of water masses from 27 to 8. Following this clustering, each of the 8 water masses contained at least 20 bottom trawl samples.

## Analysis

### GAMs

We developed our statistical habitat models for large juvenile and adult stage squid, butterfish, dogfish and summer flounder, using generalized additive models (GAM) implemented with the *mgcv* package in R software (Wood 2006). GAM is a nonparametric multiple regression technique that does not require shapes of abundance responses to habitat variables to be specified *a priori*. It has been used to statistically model ecological relationships, including habitat associations, and performs well in comparison



with other methods (Pearce & Ferrier 2000, Ciannelli et al. 2007, Ficetola & Denoël 2009). Like all regressions, GAMs constructed with collinear independent variables perform poorly. We therefore eliminated intercorrelated variables prior to modeling, retaining those most likely to affect important physiological or behavioral processes (Table 1).

We standardized species abundances by trawl tow distances and found they were best modeled using an over-dispersed Poisson distribution. Using this distribution required that we round abundances to the nearest integer. Abundance in bottom trawls can vary with time of sampling if animals exhibit diel behavioral cycles, especially vertical migration (e.g. Brodziak & Hendrickson 1999). As a result, we considered solar elevation at trawl locations and times as a covariate in GAMs.

To construct GAMs we used a backward stepwise procedure to select habitat covariates that minimized the generalized cross validation statistic (GCV, Wood 2006). We set gamma to 1.4, which increased the penalty for models of greater complexity (higher degrees of freedom). We set the maximum basis dimension of smoothers (k) to 4, which limited the complexity of the response functions to the nonparametric equivalent of a 3rd degree polynomial, and thus a Gaussian-like response. These conservative settings reduced our chances of over fitting the models. We used smoothing splines to model single term covariates which we eliminated beginning with those with the highest p-values in approximate *F*-tests. We retained only those habitat covariates producing lower GCV and significant reduction in residual deviance at the  $p < 0.05$  level in analysis of deviance of nested models, which were also likely to affect the animals through mechanisms we understood. We examined residual and convergence diagnostics throughout the modeling process.

Following the construction of single term models, we evaluated first order interactions among retained covariates using tensor product smooths (Wood 2006). We found that nearly all significant first order interactions included sea surface temperature (SST), which was seasonally discontinuous between the autumn (warm SST  $> 17^{\circ}\text{C}$ ) and the winter and spring (SST  $< 15^{\circ}\text{C}$ ) surveys. As a result, we constructed a factor for season based upon SSTs (warm [autumn] vs. cold [winter & spring]), and determined whether abundance responses to the habitat covariates were seasonally dependent. Seasonally dependent habitat responses were retained if they produced lower GCVs and residual deviance in analysis of nested models ( $p < 0.05$ ). Once we formulated

these final models we added spatial co-variables (latitude and longitude) to identify residual spatial variation in abundance that was not well described by retained habitat covariates. We also included log-transformed abundances of squid and butterfish as covariates in spiny dogfish and summer flounder GAMs to evaluate the effects of prey distributions on distributions of the predators.

We used deviance partitioning (~variance partitioning) to quantify the independent and joint effects on species distributions of habitat covariates included in the final models which we organized into 3 sets: meso-scale pelagic features described by OOS; pelagic features based on CTD casts and benthic features measured with acoustics or bottom grabs (Borcard & Legendre 1994, Cushman & McGarigal 2002). We used partial GAM regression and nested analysis of deviance to compute independent and intercorrelated effects of the 3 variable sets on abundance patterns.

#### Model evaluation

We evaluated our GAMs using a cross validation out-of-sample prediction procedure that bootstrapped Spearman correlations between standardized abundance and abundance predicted with habitat covariates in the final GAMs. In each of 1000 iterations, 10% of the observations were randomly selected using a uniform distribution and set aside as test data. The remaining training observations were used to fit abundance to the habitat covariates included in the final GAMs. At each iteration the trained GAM was used to predict the relationship between habitat covariates and abundance in the test data. Predicted abundances were then compared with measured abundances in the test data using Spearman's rho. We calculated 50th, 5th, and 95th quantiles to estimate median and 95% confidence intervals for the bootstrapped rhos.

#### Demonstration projection of a habitat model

We modified the final summer flounder habitat GAM to accept available raster data layers for the autumn of 2008, and qualitatively compared this model projection with animal collections made from September 3 through November 13 during the NEFSC bottom trawl survey. We selected autumn 2008 for the demonstration because it was nearest in time to surveys used to train the habitat model (2003 to 2007) and because 2008 was the first year the

MARACOOS HF radar network continuously monitored surface currents throughout the MAB coastal ocean from Cape Hatteras to Cape Cod. The October 1, 2008 model projection used 8 d averaged satellite data and a 32 d rolling 'seasonal' trend in divergence (see Fig. 3). In the demonstration, we eliminated subsurface measures of water column properties because estimates are not currently accessible in near real time using operational remote sensing assets or models.

## RESULTS

The explanatory power of GAMs made for the 2 pelagic species, squid and butterfish, was higher than for models made for spiny dogfish and summer flounder (Table 2, Fig. 2). Our models accounted for 73 % of abundance variation for pelagic species, and ~50 % of the variation for the demersal species. Models for pelagic species incorporated more pelagic habitat covariates measured with *in situ* CTD sampling. Models for demersal species did not, however, accept more of the benthic habitat covariates measured at relatively coarse spatial grains. Benthic covariates did not have greater explanatory power in demersal species models. Responses of the animals to many of the habitat covariates were seasonally dependent, and habitat distributions were better described during the winter and early spring than during the autumn when surface waters were stratified and animals were migrating, or soon to migrate, to overwintering habitats.

Bottom depth and variations in bottom depth (SD depth) met selection criteria in GAMs for all 4 species, and associations with seabed characteristics were seasonally dependent in every case (Table 2; see the Supplement at [www.int-res.com/articles/suppl/m438p001\\_suppl.pdf](http://www.int-res.com/articles/suppl/m438p001_suppl.pdf)). During winter and early spring when temperatures were cold, the animals were abundant in deeper, offshore waters. Squid, butterfish, and summer flounder were most abundant over bottoms with depths ranging from 50 to 150 m. Spiny dogfish were more abundant in shallower habitats (<75 m). Deep overwintering habitats for squid and summer flounder were topographically complex (high STD depth) and located in the outer Hudson shelf valley and along the edge of the continental shelf. During winter, dogfish were also abundant over complex bottoms. Butterfish were more common over smooth bottoms. During autumn, abundance varied with depth only for butterfish which were rare over bottoms deeper than 150 m. Butterfish

preferred complex bottoms in the nearshore during the autumn.

Bottom water temperature met selection criteria in GAMs for all 4 species (Table 2, see Supplement). Temperature responses of longfin squid, butterfish, and summer flounder were not seasonally dependent. All 3 species were rare where bottom temperatures were <6.5°C. Summer flounder, butterfish and squid were also uncommon on the continental shelf where bottom temperatures were warmer than 12.5°C, 16°C, and 20°C, respectively. In contrast, the temperature response of spiny dogfish was seasonally dependent. The sharks overwintered where bottom water temperatures were warmer than 7°C. During the autumn, dogfish preferred cool temperatures measured in the northern part of the study area.

Water column stability measured *in situ* and indexed as Simpson's PE anomaly for the upper 30 m of the water column met model selection criteria for squid, butterfish and summer flounder, while the abundance of butterfish also varied with mixed layer depth (Table 2, see Supplement). Summer flounder were consistently more abundant where the water column was stable in the vicinity of estuarine plumes during the autumn and the outer continental shelf during the winter and spring. Both pelagic species were more abundant where the water column was unstable during the autumn. In the winter, butterfish were more abundant where the water column was stable and the mixed layer was deep near the shelf slope front (see below, this section). Water column stability and stratification measured *in situ* varied negatively with surface current velocities and positively with current variances measured with HF radar. This produced relatively high, intercorrelated habitat effects in GAMs for the pelagic species (Table 2, Fig. 2).

Pelagic habitat characteristics measured remotely with satellites and HF radar did not have consistently greater explanatory power in models for the pelagic species than the demersal species (Table 2, Fig. 2). At least one remotely sensed pelagic characteristic met selection criterion for each species and the independent effects of remotely sensed variables were actually slightly higher in the GAM for summer flounder than for the pelagic species (Table 2, Fig. 2, see Supplement).

Summer flounder, butterfish and squid were most abundant in areas where the index of surface current divergence, and thus upwelling potential, was high (Table 2, Fig. 3, see Supplement). This response was seasonally dependent for the 2 pelagic species, but not for summer flounder.

Table 2. Analysis of deviance from generalized additive habitat modeling of longfin inshore squid, butterfish, spiny dogfish and summer flounder abundances in the Mid-Atlantic Bight coastal ocean (see also Fig. 2). Partial deviance is the additional deviance 'explained' by each variable after effects of other variables were removed. Null model is an approximation of the total deviance (~ variance) in abundance data. % of Null expresses the deviance and partial deviance as a percentage of the Null Model for each species. The decrease in the generalized cross validation statistic ( $\Delta GCV$ ) is indicated in the last column. Only variables that resulted in an increase in GCV when they were removed in backward selection were included in the final models and reported here

Species	Habitat variable	Deviance	% of Null	Partial deviance	% of Null	$\Delta GCV$
<b>Longfin inshore squid</b>	Bottom temperatures	260027.0	40.4	50878.0	7.9	150.7
	Cross shelf velocity <sup>a</sup>	24295.0	3.8	24173.0	3.8	62.2
	Watermass	135449.0	21.0	22388.0	3.5	59.6
	Bottom depth <sup>a</sup>	214195.0	33.2	17068.0	2.6	41.7
	STD bottom depth <sup>a</sup>	156599.0	24.3	14255.0	2.2	37.6
	Sun's elevation <sup>a</sup>	59145.0	9.2	13172.0	2.0	22.5
	Simpson's PE (30 m) <sup>a</sup>	77978.0	12.1	10939.0	1.7	21.1
	Divergence index <sup>a</sup>	24633.0	3.8	8038.2	1.2	15.4
	Frontal index <sup>a</sup>	5115.9	0.8	6971.1	1.1	6.3
	Cross shelf variance (vel.)	8614.1	1.3	4051.5	0.6	10.0
	Benthic habitat data			37586.0	5.8	
	Pelagic habitat data ( <i>in situ</i> )			70533.0	10.9	
	Pelagic habitat data (remote)			80824.0	12.5	
	Final model	474644.5	73.7			
	Residual	169746.3	26.3			
	Null model	644390.8				
	Spatial coordinates	206838.0	32.1	66810.0	10.4	171.3
<b>Butterfish</b>	Bottom depth <sup>a</sup>	40207.0	23.6	8846.3	5.2	21.3
	Bottom temperature	27987.0	16.4	8152.1	4.8	23.7
	Cross shelf velocity <sup>a</sup>	6343.5	3.7	8090.8	4.7	22.5
	Sun's elevation	4759.3	2.8	7229.3	4.2	16.5
	STD bottom depth <sup>a</sup>	18282.0	10.7	6948.0	4.1	18.5
	Divergence index <sup>a</sup>	5482.3	3.2	6903.8	4.0	15.2
	Mixed layer depth <sup>a</sup>	873.4	0.5	5490.5	3.2	12.1
	Frontal index <sup>a</sup>	23422.0	13.7	4922.1	2.9	11.8
	Simpson's PE (30 m) <sup>a</sup>	11882.0	7.0	4288.6	2.5	9.6
	Cross shelf variance (vel.)	101.1	0.1	1335.1	0.8	3.2
	Benthic habitat data			21218.0	12.4	
	Pelagic habitat data ( <i>in situ</i> )			23151.0	13.6	
	Pelagic habitat data (remote)			21269.0	12.5	
	Final model	124984.6	73.2			
	Residual	45673.4	26.8			
	Null model	170658.0				
	Spatial coordinates	63635.5	37.3	17360.0	10.2	44.6
<b>Spiny dogfish</b>	Bottom temperature <sup>a</sup>	42380.0	40.0	22554.0	21.3	35.7
	Along shelf variance (vel.) <sup>a</sup>	21770.0	20.6	3938.9	3.7	5.3
	Bottom depth <sup>a</sup>	7090.1	6.7	3409.8	3.2	4.5
	STD bottom depth <sup>a</sup>	4008.4	3.8	2414.9	2.3	3.1
	Sun's elevation	3628.1	3.4	844.0	0.8	0.8
	Benthic habitat data			5913.8	5.6	
	Pelagic habitat data ( <i>in situ</i> )			22554.0	21.3	
	Pelagic habitat data (remote)			3938.9	3.7	
	Final model	53152.6	50.2			
	Residual	52670.0	49.8			
	Null model	105822.6				
	Prey [log(squid)]	29544.0	27.9	2434.2	2.3	3.1
	Spatial coordinates	40954.6	38.7	15075.0	14.2	20.1



Table 2 (continued)

Species	Habitat variable	Deviance % of Null		Partial deviance % of Null		$\Delta$ GCV
Summer flounder	Chlorophyll <i>a</i> <sup>a</sup>	2556.9				
	Bottom depth <sup>a</sup>	2955.5				
	Bottom temperature	1322.6				
	Frontal index <sup>a</sup>	290.3				
	STD bottom depth	214.4				
	Divergence index	161.9				
	Benthic habitat data			1288.8	12.9	
	Pelagic habitat data ( <i>in situ</i> )			676.7	6.8	
	Pelagic habitat data (remote)			1302.3	13.1	
	Final model	5017.8	50.4			
	Residual	4934.5	49.6			
	Null model	9952.3				
	Spatial coordinates	2462.8	24.7	652.3	6.6	1.2
	Prey [log(squid)]	3379.7	34.0	1053.3	10.6	2.7
	Prey [log(butterfish)]	3561.7	35.8	795.7	8.0	2.0
Both prey			1323.5	13.3	3.4	
<sup>a</sup> Response to habitat variable was seasonally dependent and different during cruises conducted when water was warm (autumn) and cold (winter and early spring)						

During autumn, summer flounder was associated with nearshore areas where chl *a* concentrations were relatively high (Fig. 3, see Supplement). These areas were in close proximity to estuarine plumes. The animals were rarely collected where surface chl *a* was highest during winter and spring.

Squid, butterfish and summer flounder abundance varied with proximity to, and the strength of, surface fronts identified with satellites (Table 2, Fig. 3, see Supplement). Associations with fronts were strong during cold seasons but weak or absent during the autumn when the water column was warm and stratified. The pelagic species were associated with fronts on the outer continental shelf during the winter and spring. Summer flounder were rarely collected close to these strong fronts.

Although proximity to fronts between water masses was important in 3 of 4 habitat models, water mass type only met model selection criterion for longfin squid (see Supplement). Squid were slightly more abundant in water masses of moderate temperature, salinity, and primary productivity that occurred over intermediate bottom depths.

Squid and butterfish appeared to respond to cross shelf surface current velocities (see Supplement). During autumn, the animals were common where strong surface currents were directed offshore. They were abundant during winter and spring where high surface current velocities were directed inshore. The pelagic species also preferred areas where surface current velocities were relatively consistent (low variance in velocity). The response of spiny dogfish to variance in velocity was similar.

During the winter and spring, summer flounder and spiny dogfish were associated with the pelagic species they prey upon on the outer continental shelf (Table 2, Fig. 2, see Supplement). Both predators were abundant where squid were abundant, while summer flounder were also associated with butterfish.

Maps of residual spatial variation made by adding spatial covariates indicated that abundances of squid and butterfish were lower in the nearshore off Long Island, New York, than predicted based upon the habitat covariates included in the final models (Table 2, see Supplement). Squid were more abundant during the winter offshore south of Hudson shelf valley, while butterfish abundance was higher than predicted in the autumn just southeast of the Sandy Hook peninsula where the Hudson-Raritan estuary discharges into the coastal ocean. Dogfish abundance was overestimated at the mouth of the Hudson-Raritan estuary and along the continental shelf break based upon retained habitat covariates. Finally, there was a cross shelf gradient in errors in the GAM for summer flounder, which were less abundant than predicted in the nearshore continental shelf, but more abundant offshore north of the Hudson Shelf Valley.

The out-of-sample prediction test indicated that habitat-specific trends in abundances of longfin inshore squid, spiny dogfish and summer flounder were well described by our GAMs (Fig. 4). Bootstrapped rank correlations between predicted and actual catches were >0.7 and confidence intervals were relatively narrow for squid and spiny dogfish. For the butterfish model, correlations between pre-

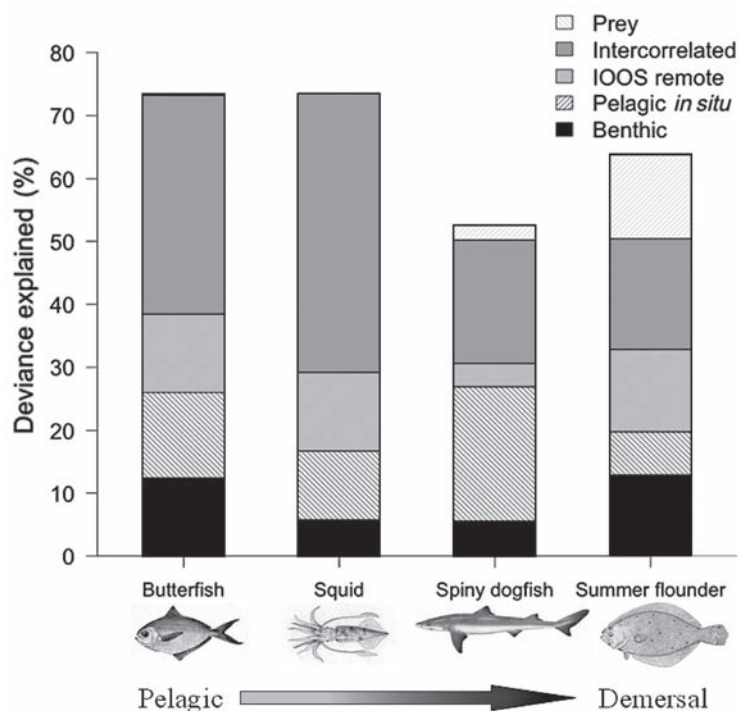


Fig. 2. Partial deviance (~variance) components calculated from generalized additive model (GAM) habitat modeling for 4 species with different vertical habitat preferences in the coastal ocean (see Table 2 and the Supplement available at [www.int-res.com/articles/suppl/m438p001\\_supp.pdf](http://www.int-res.com/articles/suppl/m438p001_supp.pdf)). Less of the abundance variation was 'explained' for demersal than for pelagic species, whose distributions appeared to be more directly affected by water column stability and mixed layer depth measured *in situ*. These variables were correlated with HF radar surface current measurements. Percentages depicted for Prey, IOOS remote, Pelagic *in situ* and Benthic habitat feature groups are partial components after intercorrelated effects (also shown) were removed. Spatial covariates were not included in this analysis

dicted and actual abundances were weaker and confidence intervals were wide.

Actual catches of summer flounder during autumn 2008 generally matched the demonstration projection of the statistical habitat model we modified to accept OOS ocean data for October 1. Catches were relatively high offshore south of Martha's Vineyard, and in shallower water from the mouth of Long Island Sound west to the mouth of the Hudson-Raritan estuary to central New Jersey.

## DISCUSSION

Broad scale dynamic habitat models for species contributing resilience to large marine ecosystems could be useful for space- and time-based ecosystem management. However, operational habitat models require sustained collection of high resolution data

describing pelagic and benthic processes affecting the physiologies, behaviors and ecologies of important species at the scale of large marine ecosystems. These kinds of data are much too expensive and time consuming to collect using traditional shipboard techniques. OOS are designed to measure ocean variability at the space–time scales necessary to describe the fundamental physical and biological processes driving the spatial dynamics of coastal marine ecosystems (Schofield et al. 2008). It is therefore not surprising that OOS satellite and HF radar descriptions of meso-scale oceanographic features and processes were useful for modeling the habitats of several ecologically important species in the Mid-Atlantic Bight.

The availability of high resolution, spatially explicit time series data for the Mid-Atlantic Bight allowed us to build models of greater explanatory power than would have been possible using shipboard data alone. We built our GAMs conservatively, constraining the complexity of smoothers, increasing the penalty for model complexity, and considering only habitat features affecting ecological processes. Nevertheless, our models explained 50 to 70% of the variation in abundance of 4 species with diverse vertical habitat preferences. Furthermore, out-of-sample prediction capabilities of 3 of our 4 models were high. GAM models developed using just shipboard measurements of pelagic and benthic habitat heterogeneity typically explain between 10 to

50% of abundance variation and generally have poorer out-of-sample prediction capabilities than we measured (e.g. Stoner et al. 2001, 2007, Jensen et al. 2005). Becker et al (2010) also demonstrated that habitat models built with remotely sensed ocean data of the proper resolution have predictive capabilities as good or better than those made with analogous shipboard data alone.

As OOS are designed to sample at the space–time scales necessary to describe the physical and primary production dynamics of the coastal ocean, we were able to consider several fundamental processes controlling ecosystem productivity in our statistical habitat models. Measurements of vertical current velocities, and locations and strengths of fronts were the most valuable of these descriptors of processes known to regulate and structure coastal ocean food webs (Olson et al. 1994, Bakun 2010). Measurements of vertical current velocities allowed us to consider

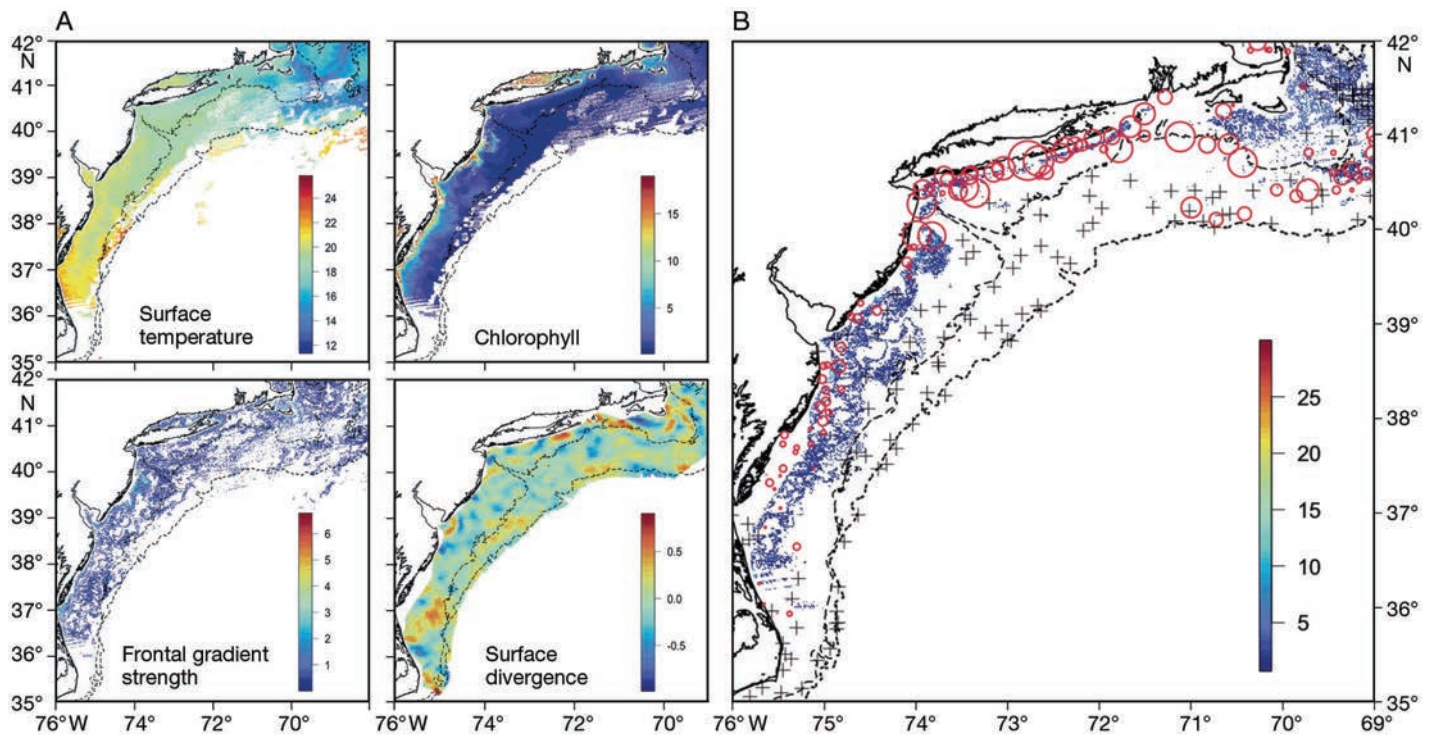


Fig. 3. Pelagic habitat gradients and predicted and realized summer flounder catches during autumn 2008. (A) Pelagic habitat variables (8 d average except for divergence which was 32 d) on October 1, 2008 that were used to project a modified generalized additive model (GAM) habitat model for summer flounder. The modified GAM did not include bottom temperature which was too sparsely measured during autumn 2008, and gradient index was replaced with gradient strength to make 'forecasting' tractable. The modified model included log transformed SD of bottom depth as well as the 4 gradients shown in panel A. (B) Summer flounder abundance projected for October 1, 2008 from the modified GAM habitat model in the color gradient. The open red symbols are scaled to the catch of summer flounder per unit effort (CPUE) in Northeast Fisheries Science Centre bottom trawl tows from September through mid-November 2008. + indicates tows in which fish were absent

spatial and temporal variation in upwelling and downwelling potential in our models. Summer flounder were consistently abundant in areas of the coastal ocean where the potential for upwelling was high, while butterflyfish and squid showed seasonally dependent associations with areas of upwelling. Strong gradients in temperature, salinity, and/or chl *a* are characteristic of ocean fronts where the interaction of circulation with the buoyancies and behaviors of organisms results in the concentration of food web constituents along them (Helfrich & Pineda 2003, Genin et al. 2005, Bakun 2010). Our frontal index, which integrated the strength of, and distance to, the nearest frontal gradient met the selection criterion in 3 of our 4 models. The pelagic species, longfin inshore squid and butterflyfish, were collected near strong surface fronts on the outer continental shelf during winter and early spring. During the same season, summer flounder were more abundant inshore of these strong fronts.

If indices of surface divergence and fronts between water masses referenced physical processes control-

ling the spatial structure and dynamics of coastal ocean food, we might have expected species responses to be similar and stronger, and satellite measurements of primary productivity to meet selection criterion in more than one of our GAMs. However, we modeled secondary and tertiary consumers with trophic positions ranging from 3.5 (butterfish) to 4.5 (summer flounder), using only surface habitat features measured directly overhead of trawl samples (Bowman et al. 2000, Hunsicker & Essington 2006, Smith & Link 2010). As these animals feed at high trophic levels, they may, under many circumstances, be distributed downstream and later in time than the physics and primary productivity that ultimately supports them (Yamamoto & Nishizawa 1986, Olson et al. 1994, Bakun 2010). These sorts of space-time lags are highly likely for demersal species like summer flounder and spiny dogfish in deep overwintering habitats that are linked by advection and prey behavior to primary production at the surface along the shelf slope front (Linder et al. 2004, Johnson et al. 2007). Demersal predators at high trophic levels



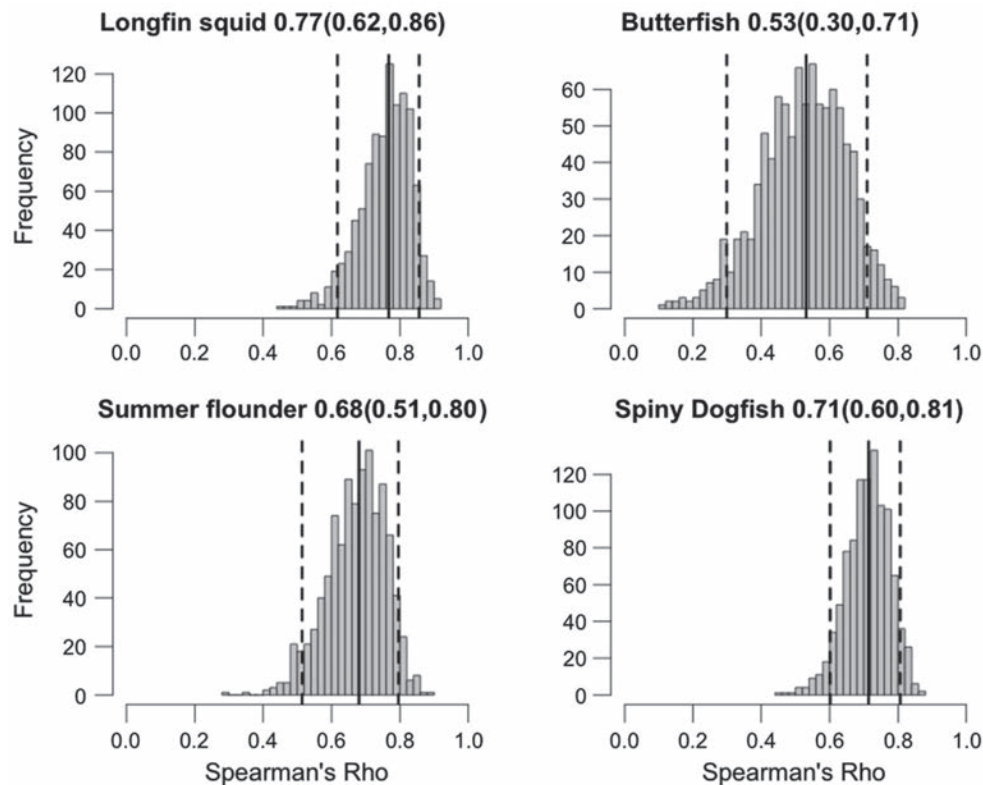


Fig. 4. Bootstrapped (1000 iterations) Spearman correlations ( $\rho$ ) between actual abundances and abundances predicted using habitat covariates in final generalized additive models (GAMs) for each of the 4 species generated with the cross validation out-of-sample prediction procedure (see 'Materials and methods'). Solid lines indicate median correlation while dashed lines are 5th and 95th quantiles for the bootstrapped  $\rho$  values

should be more strongly associated in space and time with the prey they directly consume than with lower trophic levels. We found spiny dogfish and summer flounder to be strongly associated with the squid and butterfish they feed upon during the winter and spring (Torres et al. 2008, Moustahfid et al. 2009, Smith & Link 2010, Staudinger & Juanes 2010). In our analyses, the predators were not associated with these prey during autumn. However, during warmer months, including the autumn, spiny dogfish are more abundant north of our study domain, while estuaries are important nurseries and summer feeding habitats for summer flounder that are not sampled in the NEFSC fishery independent bottom trawl surveys (Packer et al. 1999, Stehlik 2009). Thus seasonal changes in the importance of prey in our statistical models for the demersal predators were probably related simultaneously to limitations of the data we analyzed and to seasonal changes in habitat overlap between the specific predators and prey.

Primary productivity as indexed by satellite estimates of chl *a* only met selection criteria in the model for summer flounder during the autumn migration and spawning period. (Fig. 3, see Supplement). Abundance of the flatfish increased with increases in chl *a* to a threshold, and the animals were associated with plumes of moderately high chl *a* occurring outside the mouths of several large MAB estuaries where up-

welling potential was also high (Fig. 3). Areas of coastal ocean impacted by estuarine plumes are optically complex, but the high concentrations of colored dissolved organic matter and detritus that confound satellite-based estimates of phytoplankton production also contribute to high productivity (Moline et al. 2008, Pan et al. 2010). The association of summer flounder with estuarine plumes may be purely coincident with migratory pathways between shallow estuarine and coastal feeding habitats and overwintering habitats offshore. However, Berrien & Sibunka (1999) reported high densities of summer flounder eggs that have stage durations of 48 to 72 h in these same locations (Johns et al. 1981). We speculate that coastal ocean areas impacted by estuarine plumes where upwelling occurs and productivity is high could serve as high quality spawning grounds that place eggs in close proximity to optimal feeding habitats for larvae which are at a lower trophic level of ~3 (Grimes & Kingsford 1996). These same areas also have physical transport mechanisms likely to deliver larvae south and west to important estuarine nurseries (Epifanio & Garvine 2001, Lentz 2008, Tilburg et al. 2009, Zhang et al. 2009, Gong et al. 2010). Spawning habitat selection and suitability should be largely defined by conditions promoting the development, survival and successful transport of early life stages to juvenile nurseries rather than by the immediate requirements of adults.

Distributions of the 2 pelagic species were related to horizontal surface currents in our statistical habitat models. During autumn migration, squid and butterflyfish were more abundant in areas where higher velocity surface flows (and low variance) were directed offshore, while the species were associated with high velocity (low velocity variance) onshore surface flows during the spring. Most swimming and flying animals exploit complex 3-dimensional flows to conserve energy, particularly during long-distance migrations (Liao 2007, Mandel et al. 2008, Mansfield et al. 2009, Stehlik 2009). Associations of the pelagic species with specific surface flows in our models may have reflected the efficient use of cross shelf transport pathways during seasonal migrations. However, the animals were collected in trawls on the bottom where current flows can be different to seasonally complex surface flows (Lentz 2008, Gong et al. 2010). Furthermore, areas with higher velocity, low variance surface flows also tended to have weakly stratified water columns with shallow mixed layers. These are also characteristics of productive habitats (Mann & Lazier 2006, Bakun 2010). The inverse relationship between horizontal surface currents and water column stratification and stability was largely responsible for the inter-correlated habitat effects and the large amount of deviance explained in our models for pelagic species (Fig. 2). Mechanistic studies are therefore required to determine whether responses of the 2 pelagic species captured by our models reflected preferences for cross shelf transport pathways useful for energy efficient migration, physical conditions promoting high primary productivity, or for areas where both processes occur simultaneously.

The habitat associations of all 4 species, regardless of vertical preference, were better described by the pelagic than the benthic data available to us. Sediment grain sizes estimated at a spatial resolution of 2000 m did not meet selection criterion in any of our GAMs and species associations with bottom depths and seabed complexity measured at a grain of 93 m and resolution of 2 km were seasonally dependent in nearly every case. The interactions between bottom depth and season captured inshore–offshore migrations that were probably more directly related to the seasonal dynamics of temperature and the temperature preferences of the animals than to depth preferences. All of the species except spiny dogfish showed a seasonally independent response to bottom water temperature with a minimum threshold of  $\sim 6.5^{\circ}\text{C}$ . The animals were concentrated in deep water near the edge of the continental shelf during the winter and early spring when water temperatures are gen-

erally warmer and less variable offshore than inshore. Abundance relationships with bottom habitat complexity could have reflected species associations with refuges from predation or current flow if our coarser grained index served as a proxy for bottom complexity at scales of tens of centimeters to tens of meters. However, responses to bottom habitat complexity were also seasonally dependent and complex for 3 of the 4 species, and therefore probably aliased other characteristics of overwintering habitats along submarine valleys and canyons on the outer continental shelf. Animals respond to centimeter to 100 m scale variability in bottom characteristics, and the data available to us were just too coarse to describe benthic habitat heterogeneity that might have directly affected the survival and energy budgets of the animals (Abookire et al. 2007, Liao 2007, Stoner et al. 2007, Gray & Elliott 2009). Centimeter to meter scale descriptions of the structural complexity of the seabed have been shown to increase the fit of habitat models (Abookire et al. 2007, Stoner et al. 2007) and the predictive capability of several of our models might have increased if data describing bottom habitat heterogeneity at finer, ecologically relevant scales had been available for our study domain (e.g. Harris & Stokesbury 2010). Higher resolution bottom data might have improved our model for longfin inshore squid, which deposit egg masses on hard structures located on sand and muddy substrata (Jacobson 2005). However, it is also true that bottom characteristics may be less important to large animals even when they are strongly demersal. Habitat associations of age 1+ summer flounder on the continental shelf are poorly described by fine scale characteristics of the seabed identified with side scan sonar or underwater video (Lathrop et al. 2006, Slacum et al. 2008). Our results are consistent with speculation that distributions of the flatfish on the continental shelf are determined primarily by mesoscale oceanographic features controlling patterns of productivity and prey distributions rather than by fine-scale seabed characteristics (Slacum et al. 2008).

## CONCLUSIONS

Resource managers are turning increasingly to spatial management as a tool for conserving marine populations and ecosystems (Pérez-Ruzafa et al. 2008, Worm et al. 2009, Edwards & Plagányi 2011). Regional scale habitat modeling could serve as the foundation for tactical decisions as to where and when to site marine protected and closed areas

designed to conserve species that provide essential ecosystem services. While much of the seabed remains unmapped, variability in the physical structure, dynamics and productivity of the water column is being measured and mapped at ecologically relevant space/time scales with remote sensing technology integrated into OOS. Furthermore, all OOS are actively developing ensembles of oceanographic models that assimilate data from sensors on satellite, HF radar, underwater robot, and fixed mooring platforms to make spatially and temporally explicit hindcasts and forecasts of the structure and dynamics of the coastal ocean including subsurface features (e.g. Zhang et al. 2010a,b,c). Many of the pelagic features and processes currently measured and modeled by OOS determine patterns of habitat suitability for species and their life stages and could be considered in spatial management (Game et al. 2009, Watson et al. 2011).

In our view, several avenues of research need to be pursued in order to develop habitat models useful for spatial management. These include investigation of the resolution and ranges of habitat variability measured with OOS resulting in biological responses, including the identification of space–time lags between variability in physical and primary production dynamics and responses of important upper level consumers, particularly those associated with the bottom. There is also a need for biological data, in addition to trawl net surveys, to be integrated into OOS (e.g. Kloser et al. 2009, Żydelis et al. 2011). Currently, the data available for broad scale habitat modeling are fisheries-independent surveys designed for stock assessment, not habitat assessment. These surveys are highly selective with respect to season and organism size and often do not sample habitats used during important periods in the life history of many species. Infrequent traditional net surveys cannot be used to distinguish dispersal corridors that many animals move through quickly from areas in which fewer individuals take up longer term residency because habitat resources meet the requirements of particular life history stages. Finally, habitat models based on abundance assume that organisms evaluate habitat quality accurately, without perceptual and movement constraints, and therefore reach abundances at equilibrium with habitat carrying capacity without time delays. This is probably rarely the case, particularly in regions like the Mid-Atlantic Bight where important habitat dimensions are highly dynamic in time and space and many animals are highly migratory. Integration of telemetry and fishery hydroacoustics data into regional OOS (e.g. Kloser et

al. 2009, Żydelis et al. 2011) would be useful for addressing some of the sampling biases and assumptions inherent in habitat models based upon traditional fisheries survey data.

We view statistical habitat models informed by OOS, such as those we have developed here, as a first step toward the development of operational mechanistic habitat models: As hypothesis-generating tools that can be coupled with OOS products to perform mechanistic studies of the effects of pelagic, as well as benthic, habitat heterogeneity on the processes of growth, survival, dispersal and reproduction that underlie spatial population dynamics (Kritzer & Sale 2006, Buckley et al. 2010). This type of adaptive, iterative approach could be a cost-effective way to develop mechanistic models with scopes broad enough to meet the requirements of spatial resource management in the sea.

**Acknowledgements.** We thank S. Lucey, M. Taylor and J. Goff for generously providing us with the data used in our analysis, and S. Gray for his contributions to stimulating discussions about the role of the Integrated Ocean Observing System (IOOS) in fisheries science and management. B. Phelan also provided much needed support. We thank A. Stoner and 3 anonymous reviewers whose comments helped us to improve the manuscript. The NOAA Fisheries and the Environment Program (NA08NMF450626) provided primary support for this research. The authors also thank the following agencies for additional support during this project: NASA Biodiversity NNG06GH75G1/3, NASA New Investigator Program NNH07ZDA001N, NOAA IOOS Office (MARACOS Grant NA01NOS4730014 and NA07NOS 4730221) and Delaware Sea Grant (NA10OAR4170084).

#### LITERATURE CITED

- Abookire AA, Duffy-Anderson JT, Jump CM (2007) Habitat associations and diet of young-of-the-year Pacific cod (*Gadus macrocephalus*) near Kodiak, Alaska. *Mar Biol* 150:713–726
- Azarovitz T (1981) A brief historical review of the Woods Hole Laboratory trawl survey time series. In: Doubleday WG, Rivard D (eds) *Bottom trawl surveys*. *Can Spec Publ Fish Aquat Sci* 58:62–67
- Bakun A (2010) Linking climate to population variability in marine ecosystems characterized by non-simple dynamics: Conceptual templates and schematic constructs. *J Mar Syst* 79:361–373
- Barrick DE, Evens MW, Weber BL (1977) Ocean surface currents mapped by radar. *Science* 198:138–144
- Beardsley RC, Boicourt WC (1981) On estuarine and continental-shelf circulation in the Middle Atlantic Bight. In: Warren BA, Wunsch C (eds) *Evolution of physical oceanography*. MIT Press, Boston, p 198–235
- Becker EA, Forney KA, Ferguson MC, Foley DG, Smith RC, Barlow J, Redfern JV (2010) Comparing California Current cetacean–habitat models developed using *in situ* and remotely sensed sea surface temperature data. *Mar*



- Ecol Prog Ser 413:163–183
- Berrien P, Sibunka J (1999) Distribution patterns of fish eggs in the U.S. Northeast Continental Shelf Ecosystem, 1977–1987. NOAA Tech Rep NMFS 145:310
- Borcard D, Legendre P (1994) Environmental control and spatial structure in ecological communities: an example using oribatid mites (Acari, Oribatei). *Environ Ecol Stat* 1:37–53
- Bowman RE, Stillwell CE, Micheals WL, Grosslein MD (2000) Food of Northeast Atlantic fishes and two common species of squid. NOAA Tech Rep NMFS-F/ME-155
- Brodziak JKT, Hendrickson LC (1999) An analysis of environmental effects on survey catches of squids, *Loligo pealeii* and *Illex illecebrosus* in the northwest Atlantic. *Fish Bull* 97:9–24
- Buckley LB, Urban MC, Angilletta MJ, Crozier LG, Rissler LJ, Sears MW (2010) Can mechanism inform species' distribution models? *Ecol Lett* 13:1041–1054
- Castelao R, Glenn S, Schofield O, Chant R, Wilkin J, Kohut J (2008) Seasonal evolution of hydrographic fields in the central Middle Atlantic Bight from glider observations. *Geophys Res Lett* 35; L03617 doi:10.1029/2007GL032335
- Ciannelli L, Dingsør GE, Bogstad B, Ottersen G and others (2007) Spatial anatomy of species survival: effects of predation and climate driven environmental variability. *Ecology* 88:635–646
- Collette BG, Klein-MacPhee G (2002) Bigelow and Schroeder's fishes of the Gulf of Maine, xxi. Smithsonian Institution Press, Washington, DC
- Cushman SA, McGarigal K (2002) Hierarchical, multi-scale decomposition of species–environment relationships. *Landsc Ecol* 17:637–646
- Edwards CTT, Plagányi EE (2011) Protecting old fish through spatial management: is there a benefit for sustainable exploitation? *J Appl Ecol* 48:853–863
- Epifanio CE, Garvine RW (2001) Larval transport on the Atlantic continental shelf of North America: a review. *Estuar Coast Shelf Sci* 52:51–77
- Ficetola GF, Denoël M (2009) Ecological thresholds: an assessment of methods to identify abrupt changes in species habitat relationships. *Ecography* 32:1075–1084
- Game ET, Grantham HS, Hobday AJ, Pressey RL and others (2009) Pelagic protected areas: the missing dimension in ocean conservation. *Trends Ecol Evol* 24:360–369
- Genin A, Jaffe JS, Reef R, Richter C, Franks PJS (2005) Swimming against the flow: a mechanism of zooplankton aggregation. *Science* 308:860–862
- Goff JA, Jenkins C, Calder B (2006) Maximum a posteriori resampling of noisy, spatially correlated data. *Geochem Geophys Geosys* 7, Q08003 doi:10.1029/2006GC001297
- Goff JA, Jenkins CJ, Williams SJ (2008) Seabed mapping and characterization of sediment variability using the usSEABED data base. *Cont Shelf Res* 28:614–633
- Gong D, Kohut JT, Glenn SM (2010) Seasonal climatology of wind-driven circulation on the New Jersey Shelf. *J Geophys Res* 115:C04006 doi:10.1029/JC005520
- Gray JS, Elliott M (2009) *Ecology of marine sediments*. Oxford University Press, Oxford
- Grimes C, Kingsford M (1996) How do riverine plumes of different sizes influence fish larvae: Do they enhance recruitment? *Mar Freshw Res* 47:191–208
- Harris BP, Stokesbury KDE (2010) The spatial structure of local surficial sediment characteristics on Georges Bank, USA. *Cont Shelf Res* 30:1840–1853
- Hatfield EMC, Cadrin SX (2002) Geographic and temporal patterns in size and maturity of the longfin inshore squid (*Loligo pealeii*) off the northeastern United States. *Fish Bull* 100:200–213
- Helfrich KR, Pineda J (2003) Accumulation of particles in propagating fronts. *Limnol Oceanogr* 48:1509–1520
- Hsieh CH, Yamauchi A, Nakazawa T, Wang WF (2010) Fishing effects on age and spatial structures undermine population stability of fishes. *Aquat Sci* 72:165–178
- Hunsicker ME, Essington TE (2006) Size-structured patterns of piscivory of the longfin inshore squid (*Loligo pealeii*) in the mid-Atlantic continental shelf ecosystem. *Can J Fish Aquat Sci* 63:754–765
- Jacobson LD (2005) Essential fish habitat source document: Longfin inshore squid, *Loligo pealeii*, life history and habitat characteristics. NOAA Tech Memo NMFS-NE-193
- Jensen OP, Seppelt R, Miller TJ, Bauer LJ (2005) Winter distribution of blue crab *Callinectes sapidus* in Chesapeake Bay: application and cross-validation of a two-stage generalized additive model. *Mar Ecol Prog Ser* 299:239–255
- Johns DM, Howell WH, Klein-MacPhee G (1981) Yolk utilization and growth to yolk-sac absorption in summer flounder (*Paralichthys dentatus*) larvae at constant and cyclic temperatures. *Mar Biol* 63:301–308
- Johnson NA, Campbell JW, Moore TS, Rex MA, Etter RJ, McClain CR, Dowell MD (2007) The relationship between the standing stock of deep-sea macrobenthos and surface production in the western North Atlantic. *Deep-Sea Res I* 54:1350–1360
- Kerr LA, Cadrin SX, Secor DH (2010) The role of spatial dynamics in the stability, resilience, and productivity of an estuarine fish population. *Ecol Appl* 20:497–507
- Kloser RJ, Ryan TE, Young JW, Lewis ME (2009) Acoustic observations of micronekton fish on the scale of an ocean basin: potential and challenges. *ICES J Mar Sci* 66: 998–1006
- Kritzer JP, Sale PF (2006) *Marine metapopulations*. Academic Press, Amsterdam
- Lathrop RG, Cole M, Senyk N, Butman B (2006) Seafloor habitat mapping of the New York Bight incorporating sidescan sonar data. *Estuar Coast Shelf Sci* 68:221–230
- Lentz SJ (2008) Observations and a model of mean circulation over the Middle Atlantic Bight continental shelf. *J Phys Oceanogr* 38:1203–1220
- Levitus S (1982) *Climatological atlas of the world's oceans*. NOAA Professional Paper 13:173
- Liao JC (2007) A review of fish swimming mechanics and behaviour in altered flows. *Philos Trans R Soc B* 362: 1973–1993
- Linder CA, Gawarkiewicz GG, Pickart RS (2004) Seasonal characteristics of bottom boundary layer detachment at the shelfbreak front in the Middle Atlantic Bight. *J Geophys Res* 109:C03049 doi:10.1029/U2003JC002032
- Link J, Overholtz W, O'Reilly J, Green J and others (2008) The Northeast U.S. continental shelf Energy Modeling and Analysis exercise (EMAX): ecological network model development and basic ecosystem metrics. *J Mar Syst* 74:453–474
- Mandel JT, Bildstein KL, Bohrer G, Winkler DW (2008) Movement ecology of migration in turkey vultures. *Proc Natl Acad Sci USA* 105:19102–19107
- Mann K, Lazier J (2006) *Dynamics of marine ecosystems: biological–physical interactions in the oceans*, 3rd edn. Blackwell Publishing, Oxford
- Mansfield K, Saba V, Keinath J, Musick J (2009) Satellite tracking reveals a dichotomy in migration strategies

- among juvenile loggerhead turtles in the Northwest Atlantic. *Mar Biol* 156:2555–2570
- Marra J, Houghton RW, Garside C (1990) Phytoplankton growth at the shelf-break front in the Middle Atlantic Bight. *J Mar Res* 48:851–868
- Moline MA, Frazer TK, Chant R, Glenn S and others (2008) Biological responses in a dynamic buoyant river plume. *Oceanography* 21:70–89
- Mora C, Metzger R, Rollo A, Myers RA (2007) Experimental simulations about the effects of overexploitation and habitat fragmentation on populations facing environmental warming. *Proc R Soc B* 274:1023–1028
- Moustahfid H, Tyrrell MC, Link JS (2009) Accounting explicitly for predation mortality in surplus production models: an application to longfin inshore squid. *North Am J Fish Manage* 29:1555–1566
- Moustahfid H, Tyrrell MC, Link JS, Nye JA, Smith BE, Gamble RJ (2010) Functional feeding responses of piscivorous fishes from the northeast US continental shelf. *Oecologia* 163:1059–1067
- Mugo R, Saitoh SI, Nihira A, Kuroyama T (2010) Habitat characteristics of skipjack tuna (*Katsuwonus pelamis*) in the western North Pacific: a remote sensing perspective. *Fish Oceanogr* 19:382–396
- Neteler M, Mitasova H (2008) Open source GIS: A GRASS GIS approach. Springer, New York, NY
- Oliver MJ, Irwin AJ (2008) Objective global ocean biogeographic provinces. *Geophys Res Lett* 35:L15601 doi: 10.1029/2008GL034238
- Oliver MJ, Glenn SM, Kohut JT, Irwin AJ, Schofield OM, Moline MA, Bissett WP (2004) Bioinformatic approaches for objective detection of water masses on continental shelves. *J Geophys Res* 109:C07S04 doi:10.1029/2003JC002072
- Olson DB, Hitchcock GL, Mariano AJ, Ashjian CJ, Peng G, Nero RW, Podestá GP (1994) Life on the edge: marine life and fronts. *Oceanography* 7:52–60
- Packer DB, Hoff T (1999) Life history, habitat parameters, and essential habitat of Mid-Atlantic summer flounder. *Am Fish Soc Symp* 22:76–92
- Packer DB, Griesbach S, Berrien PL, Zetlin C, Johnson DL, Morse WW (1999) Essential fish habitat source document: summer flounder, *Paralichthys dentatus*, life history and habitat characteristics. NOAA Tech Memo NMFS-NE-151
- Pan X, Mannino A, Russ ME, Hooker SB, Harding LW Jr (2010) Remote sensing of phytoplankton pigment distribution in the United States northeast coast. *Remote Sens Environ* 114:2403–2416
- Pérez-Ruzafa A, Martín E, Marcos C, Miguel Zamarro J and others (2008) Modeling spatial and temporal scales for spill-over and biomass exportation from MPAs and their potential for fisheries enhancement. *J Nat Conserv* 16: 234–255
- Pearce J, Ferrier S (2000) An evaluation of alternative algorithms for fitting species distribution models using logistic regression. *Ecol Model* 128:127–147
- Reid JM, Reid JA, Jenkins CJ, Hastings ME, Williams SJ, Poppe LJ (2005) usSEABED: Atlantic coast offshore surficial sediment data release: U.S. Geological Survey Data Series 118, version 1.0. Online at <http://pubs.usgs.gov/ds/2005/118/>
- Ryan JP, Yoder JA, Cornillon PC (1999) Enhanced chlorophyll at the shelfbreak of the Mid-Atlantic Bight and Georges Bank during the spring transition. *Limnol Oceanogr* 44:1–11
- Schofield O, Chant RB, Cahill RC, Gong D and others (2008) The decadal view of the Mid-Atlantic Bight from the COOLroom: Is our coastal system changing? *Oceanography* 21:108–117
- Secor DH, Kerr LA, Cadrin SX (2009) Connectivity effects on productivity, stability, and persistence in a herring metapopulation model. *ICES J Mar Sci* 66:1726–1732
- Simpson JH (1981) The shelf fronts: implications of their existence and behaviour. *Philos Trans R Soc A* 302: 531–546
- Simpson JH, Bowers D (1981) Models of stratification and frontal movement in shelf seas. *Deep-Sea Res A* 28: 727–738
- Slacum HW, Istad JH, Weber ED, Richkus WA, Diaz RJ, Tallent CO (2008) The value of applying commercial fishers experience to designed surveys for identifying characteristics of essential fish habitat for adult summer flounder. *North Am J Fish Manage* 28:710–721
- Smith B, Link J (2010) The trophic dynamics of 50 finfish and 2 squid species on the Northeast US continental shelf. NOAA Tech Memo NMFS-NE-216
- Staudinger MD (2006) Seasonal and size-based predation on two species of squid by four fish predators on the Northwest Atlantic continental shelf. *Fish Bull* 104: 605–615
- Staudinger MD, Juanes F (2010) A size-based approach to quantifying predation on longfin inshore squid *Loligo pealeii* in the northwest Atlantic. *Mar Ecol Prog Ser* 399: 225–241
- Stehlik LL (2007) Essential fish habitat source document: Spiny dogfish, *Squalus acanthias*, life history and habitat characteristics, 2nd edn. NOAA Tech Mem NMFS-NE-203
- Stehlik LL (2009) Effects of seasonal change on activity rhythms and swimming behavior of age-0 bluefish (*Pomatomus saltatrix*) and a description of gliding behavior. *Fish Bull* 107:1–12
- Stoner AW, Manderson JP, Pessutti J (2001) Spatially-explicit analysis of estuarine habitat for juvenile winter flounder (*Pseudopleuronectes americanus*): combining generalized additive models and geographic information systems. *Mar Ecol Prog Ser* 213:253–271
- Stoner AW, Spencer ML, Ryer CH (2007) Flatfish-habitat associations in Alaska nursery grounds: use of continuous video records for multi-scale spatial analysis. *J Sea Res* 57:137–150
- Tian RC, Chen C, Stokesbury KDE, Rothschild B and others (2009) Modeling the connectivity between sea scallop populations in the Middle Atlantic Bight and over Georges Bank. *Mar Ecol Prog Ser* 380:147–160
- Tilburg CE, Dittel AI, Epifanio CE (2009) High concentrations of blue crab (*Callinectes sapidus*) larvae along the offshore edge of a coastal current: effects of convergent circulation. *Fish Oceanogr* 18:135–146
- Torres LG, Read AJ, Halpin P (2008) Fine-scale habitat modeling of a top marine predator: Do prey data improve predictive capacity? *Ecol Appl* 18:1702–1717
- Valavanis V, Pierce G, Zuur A, Paliallexis A, Saveliev A, Katara I, Wang J (2008) Modeling of essential fish habitat based on remote sensing, spatial analysis and GIS. *Hydrobiologia* 612:5–20
- Watson JR, Hays CG, Raimondi PT, Mitarai S and others (2011) Currents connecting communities: nearshore community similarity and ocean circulation. *Ecology* 92:

- 1193–1200
- Wood S (2006) Generalized Additive Models: an introduction with R. Chapman & Hall, Boca Raton, FL
- Worm B, Hilborn R, Baum JK, Branch TA and others (2009) Rebuilding global fisheries. *Science* 325:578–585
- Yamamoto T, Nishizawa S (1986) Small-scale zooplankton aggregations at the front of a Kuroshio warm-core ring. *Deep-Sea Res A* 33:1729–1740
- Zainuddin M, Katsuya S, Saitoh SI (2008) Albacore (*Thunnus alalunga*) fishing ground in relation to oceanographic conditions in the western North Pacific Ocean using remotely sensed satellite data. *Fish Oceanogr* 17: 61–73
- Zhang W, Wilkin JL, Chant RJ (2009) Modeling the pathways and mean dynamics of river plume dispersal in the New York Bight. *J Phys Oceanogr* 39:1167–1183
- Zhang WG, Wilkin JL, Arango HG (2010a) Towards an integrated observation and modeling system in the New York Bight using variational methods. Part I: 4DVAR data assimilation. *Ocean Model* 35:119–133
- Zhang WG, Wilkin JL, Levin JC (2010b) Towards an integrated observation and modeling system in the New York Bight using variational methods. Part II: Representer-based observing strategy evaluation. *Ocean Model* 35:134–145
- Zhang WG, Wilkin JL, Schofield OM (2010c) Simulation of water age and residence time in New York Bight. *J Phys Oceanogr* 40:965–982
- Žydelis R, Lewison, RL, Shaffer SA, Moore JE and others (2011) Dynamic habitat models: using telemetry data to project fisheries bycatch. *Proc R Soc B* doi:10.1098/rspb.2011.0330

*Editorial responsibility: Kenneth Sherman,  
Narragansett, Rhode Island, USA*

*Submitted: January 17, 2011; Accepted: July 19, 2011  
Proofs received from author(s): September 15, 2011*





# Optimizing and Validating High-Frequency Radar Surface Current Measurements in the Mona Passage

## AUTHORS

Jorge E. Corredor  
 Andre Amador  
 Miguel Canals  
 Samuel Rivera  
 Jorge E. Capella  
 Julio M. Morell  
 Department of Marine Sciences,  
 University of Puerto Rico,  
 Mayagüez

Scott Glenn  
 Hugh Roarty  
 Ethan Handel  
 Erick Rivera Lemus  
 Coastal Ocean Observation  
 Laboratory, Rutgers the State  
 University of New Jersey

## Introduction

The Mona Passage, one of the main passages between the Atlantic Ocean and the Caribbean Sea, is a key shipping lane to the Panama Canal and one of the main gateways for vessels entering the Caribbean. It is also a route for drug and illegal alien trafficking between the Dominican Republic and Puerto Rico and is consequently heavily patrolled by federal and state enforcement agencies. Intense recreational and commercial traffic, as well as illegal traffic, triggers frequent search and rescue efforts. We have emplaced two high-frequency radar (HFR) stations on the west coast of Puerto Rico to allow mapping of the ocean surface velocity

## ABSTRACT

The Mona Passage is a major shipping lane to the Panama Canal and a key route for illegal traffic into the United States. We have emplaced two high-frequency radar (HFR) stations on the west coast of Puerto Rico intended to allow mapping of the ocean surface velocity field of the eastern Mona Passage and to explore its performance in vessel detection and tracking. The array provides coverage of the southeastern quadrant of the Passage extending west to Mona Island and north to Rincon. Hourly results are posted online in near-real time. To optimize our results, we twice measured the antenna beam patterns and applied these corrections to the resulting radial returns. To assess the basic capability of the Mona Passage HFR array to measure surface currents in this tropical environment, we undertook validation measurements, including repeated deployment of Lagrangian drifters, deployment of an acoustic Doppler current profiler, and comparison with modeled tidal currents. Our experimental measurements showed good agreement to both modeled and *in situ* data lending confidence to the area-wide surface current maps generated by this system. Repeated measurements showed limited temporal variability of antenna distortion patterns, demonstrating that these are in large part the product of the surrounding environment. Comparison between a numerical particle tracking algorithm and experimental Lagrangian trajectories showed mixed results, with better agreement during periods of low intrahour variability in current direction than during periods of rapid tidal reversal.

Keywords: high-frequency radar, Lagrangian, drifters, acoustic Doppler, validation

field of the eastern Mona Passage and explore vessel detection and tracking applications. Operational implementation of these systems is expected to serve other multiple uses including recreational and commercial fishery and search and rescue operations.

HFR, a technology based on Bragg scattering of radio waves off ocean surface waves, affords a practical means of estimating direction and magnitude of surface ocean currents. CODAR SeaSonde® HFR technology (Barrick & Lipa, 1997) makes use of an omnidirectional transmit (Tx) antenna and

a collocated receive (Rx) antenna fitted with an omnidirectional whip antenna and two directional coils. By estimating the Doppler displacement of the frequency band in the backscatter signal from the ocean surface signal, current velocities towards or away from the receive antenna are obtained for an individual Tx/Rx pair. Such partial vectors are referred to as radial components or “radials” for short. Solutions for true current magnitude and direction can be computed using radials obtained from two or more Tx/Rx arrays positioned strategically along the coast.

HFR current measurements can be validated through comparison with *in situ* current measurements using either Lagrangian drifters (Stewart & Joy, 1974; Barrick et al., 1977; Ohlmann et al., 2007) or moored current meters (Holbrook & Frisch, 1981; Emery et al., 2004; Kohut et al., 2006). Computation of total vectors requires measurements from at least two radars; however, this procedure can suffer from errors due to geometric dilution of precision (Chapman et al., 1997). It can also mask errors that may be present in radials, such as biases in bearing estimates (Emery et al., 2004). Thus, validation of radials from a single-radar station is not only possible but is in fact advisable.

Kohut and Glenn (2003) demonstrated that using the measured receiver beam patterns to reconstruct the radial current field from each HFR shore site resulted in better agreement with currents measured by an array of moored acoustic Doppler current profilers (ADCPs). Accordingly, we measured antenna beam patterns and applied the resulting corrections prior to (and subsequent to) the validation exercise.

In addition to the primary design application of surface current visualization and mapping, the HFR array has the added benefit of being able to detect the speed and location of surface vessels (Roarty et al., 2010), to assist in search and rescue operations, and to provide service to fishermen and recreational users. Following antenna installation, our initial concern was to validate current measurements obtained with the HFR arrays. Various validation approaches were used including repeated deployment of Lagrangian drifters, deployment of an ADCP, and comparison with modeled tidal currents. *In situ* observation and model data were compared to radial

returns from the CODAR units. Good agreement was found between the HFR and both the Lagrangian measurements and modeled forecasts. The Eulerian measurements yield good agreement with one station, but not the other. We also compare the drifter trajectories with trajectories resulting from numerical integration using the HFR data and a particle tracking algorithm, finding good agreement in cases with low intrahour variability in current direction. Rapid tidal current reversals, however, led to larger discrepancy between numerical and experimental trajectories.

## Methodology

Two CODAR SeaSonde HFR antenna pairs are currently deployed

along the western coast of Puerto Rico: One at a coastal police station in the municipality of Añasco (site code FURA, 18.2917°N, 67.1986°W) and the second at a private marina in the municipality of Cabo Rojo (site code CDDO, 18.0998°N, 67.1907°W) as shown in Figure 1 and at the center of the radial grids in Figure 2. FURA and CDDO radars operate at 13 and 13.45 MHz, respectively. The CDDO system was installed in February 2009, and the FURA system was installed in September 2009. The distance between stations is approximately 21 km.

In the comparisons reported here, the receiver antenna beam pattern measurement techniques described by Kohut and Glenn (2003) were applied. A transponder tuned to the transmitter frequency was installed

### FIGURE 1

Location of FURA and CDDO antenna emplacements,  $3 \times 3 \text{ km}^2$  experimental Lagrangian deployment box, ADCP mooring, PO virtual tidal current station, and five radial locations along heading 343° selected for comparison to the NOAA tidal current forecasts at PO.

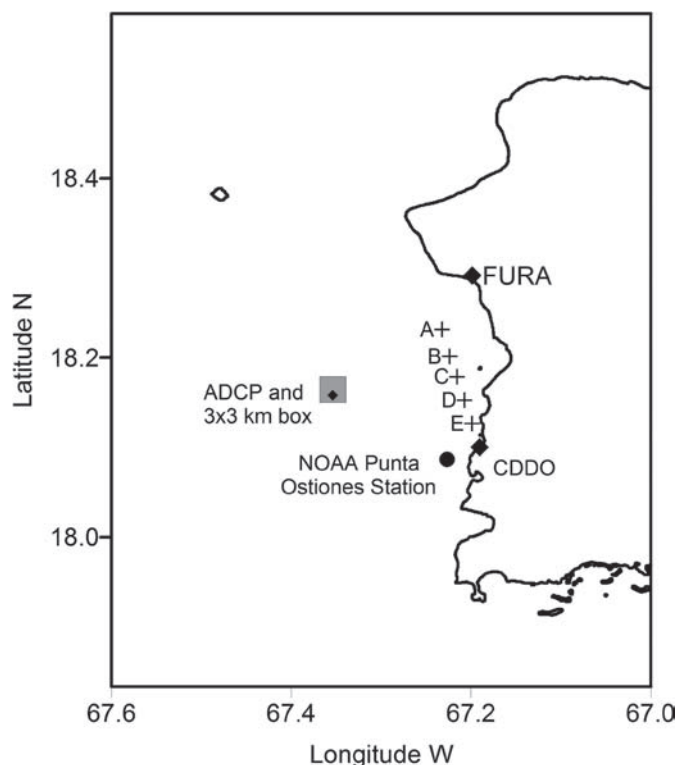
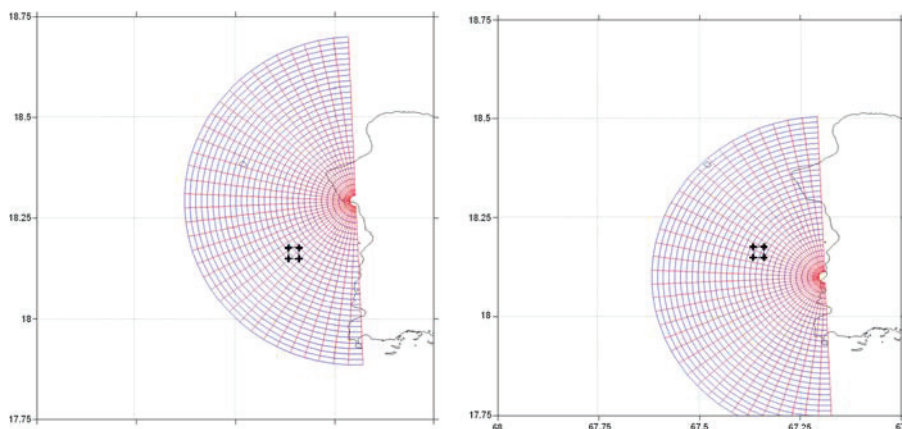




## FIGURE 2

Radial computational grids for FURA (left) and CDDO (right) with overlaid experimental  $3 \times 3$  km grid. (Color versions of figures available online at: <http://www.stevens.edu/csr/>.)



on a boat that then circled the antenna at a constant radial offset ( $<1/2$  km) from shore to shore. The antenna beam patterns were measured in both clockwise and counterclockwise directions of boat travel, and the results were averaged. To investigate receive antenna pattern changes over time, the patterns at FURA and CDDO were measured over a year later by the same technique.

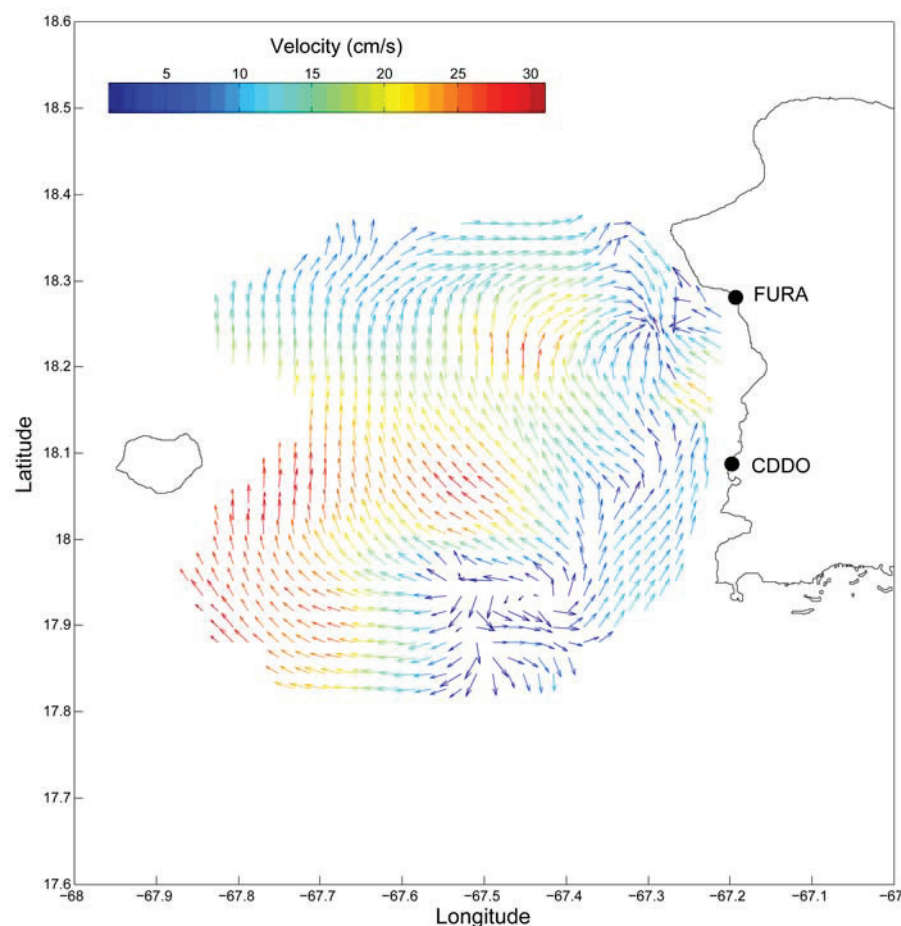
Following implementation of software calibration to compensate for measured distortions, Doppler-derived current totals are computed hourly, stored onsite, and transmitted to the Caribbean Coastal Ocean Observing System (Watlington et al., 2008) data depository at La Parguera in Puerto Rico. A sample velocity field of eastern Mona Passage obtained from the HFR array during July 7, 2010, the day of the validation experiment is portrayed in Figure 3. These data are made available to the general public through the National Oceanic and Atmospheric Administration (NOAA) National Data Buoy Center Web portal and the Coastal Observing Research and Development Center of

the University of California at San Diego Web portal. Measurements at 13 MHz correspond to the average current from the surface to a depth of approximately 1 m (Stewart & Joy, 1974).

Initially, when a single HFR installation was available at CDDO, we compared radial returns at selected sites with predictions at the NOAA tidal current station denoted as Point Ostiones (PO) (Figure 1). Punta Ostiones is a secondary station subject to the reference station of Vieques Passage, Puerto Rico, where harmonic constants are known. Ebb and flood current speeds for PO are forecasted by NOAA only

## FIGURE 3

Sample velocity field of eastern Mona Passage obtained from the HFR array during July 7, 2010, the day of the validation experiment at 17:00 UTC. (Color versions of figures available online at: <http://www.stevens.edu/csr/>.)



in the north-south direction ( $v$ ). These forecast data were obtained from the NOAA Tides and Currents Web page, and radial data were gathered from the CDDO site for the months of April to May 2009. The  $v$  (north-south) current velocity component was extracted from the HFR radial output for comparison with the tidal predictions using the Matlab T\_Tides Harmonic Analysis (Pawlowicz et al., 2002) toolbox and the cptoolbox collection of Matlab functions and scripts for use in basic processing and display of HFR-derived data. The correlation coefficient was computed, taking the covariance of NOAA tidal velocity predictions (variable  $X$ ) and CDDO velocities (variable  $Y$ ) in the north-south direction:

$$R(X, Y) = \frac{C(X, Y)}{\sqrt{\sigma_X \sigma_Y}}$$

where  $C$  is the covariance matrix and  $\sigma$  is the standard deviation of each variable. Hourly NOAA tidal velocities were used in the calculation. HFR output values were not interpolated in this analysis. Each correlation coefficient was obtained using only one data set corresponding to the points (A-E) depicted in Figure 1.

Following installation of the second HFR unit at the Añasco Police Station (FURA), we implemented a validation experiment following the approach of Ohlmann et al. (2007) with Lagrangian drifters repeatedly deployed within a small area. Validation was conducted on July 7, 2010 within a  $3 \times 3$  km box bounded by coordinates  $18.15^\circ\text{N}$  to  $18.18^\circ\text{N}$  and  $67.34^\circ\text{W}$  to  $67.37^\circ\text{W}$ . The  $3 \times 3$  km box was, for convenience, located in the vicinity of a navigation buoy in a position approximately orthogonal to the two HFR arrays (Figures 1 and 2).

A sample of the HFR surface velocity field during the day of the validation experiment is shown in Figure 3. Two types of GPS-equipped drifters were used: A Pacific Gyre Microstar® drifter with satellite telemetry reporting every 10 min and a locally designed coastal drifter with GARMIN ASTRO 220® VHF telemetry reporting every 5 sec, all drogued nominally at 1 m depth. These drifters were deployed using two outboard-powered vessels near the southern boundary of the box at a time close to slack tide and allowed to drift until they exited the box whereupon they were redeployed once again within the box.

Drifter velocity estimates were obtained from differentiation of the GPS position measurements provided by the drifters. To quantify HFR performance, we followed the statistical parameterization of Ohlmann et al. (2007). We compute the HFR bias as

$$\text{bias} = \langle (u_{\text{radial}} - \langle u_{\text{measured}} \rangle) \rangle$$

and the root mean square (RMS) difference

$$\text{RMS} = \sqrt{\langle (u_{\text{radial}} - \langle u_{\text{measured}} \rangle)^2 \rangle}$$

where  $u_{\text{radial}}$  is the hourly averaged HFR radial velocity and  $u_{\text{measured}}$  is the measured radial velocity using either drifter or ADCP data. The angle brackets denote a space and time average. For the measured radial velocities  $u_{\text{measured}}$ , the time averaging of drifter and ADCP data is performed over a 1-h period centered on the hour, e.g., 30 min before and after the hour, to agree with the HFR averaging scheme. Spatial averaging was done by averaging all drifter data within the sample area for a given time step.

In conjunction with the above experiment, we deployed an ADCP unit within the  $3 \times 3$  km box in the vicinity of a coastal navigation buoy for Eulerian validation (Figure 1). A Teledyne Workhorse ADCP operating at 600 kHz was deployed through July 1-15, 2010 at  $18.158^\circ\text{N}$ ,  $67.354^\circ\text{W}$  at a depth of 20 m. The instrument was configured for a sampling bin size of 1 m (this is the vertical resolution of the velocity profile) and a recording time step of 15 min; the recorded vector is an average of 300 pings equally spread over the 15-min time step to reduce aliasing effects. For this analysis, we used data from the top bin centered at 2.2 m below the surface.

Finally, in order to recreate the trajectory of a particle floating at the surface for a specific time period, a particle tracking algorithm was developed using MATLAB code. The algorithm works on the basis of linear interpolation between sea surface velocities for a given time and location inside a sea surface velocity grid. An initial particle location was given as input along with a time step and an integration time span. Two kinds of interpolations are made in the algorithm. The first is performed to obtain the sea surface velocity vector field corresponding to the specific time under analysis. This interpolation is done between the sea surface velocity vector grids, which are the average of the velocity for each point in the grid over the last hour starting at the half hour. The second interpolation is a spatial interpolation using distance-weighted averages, which is necessary to determine the velocity vector at the time-dependent particle position based on the closest HFR grid point velocity estimate. The final result of the algorithm is a track file with the corresponding geographic coordinates for each time specified previously by the user.



## Results

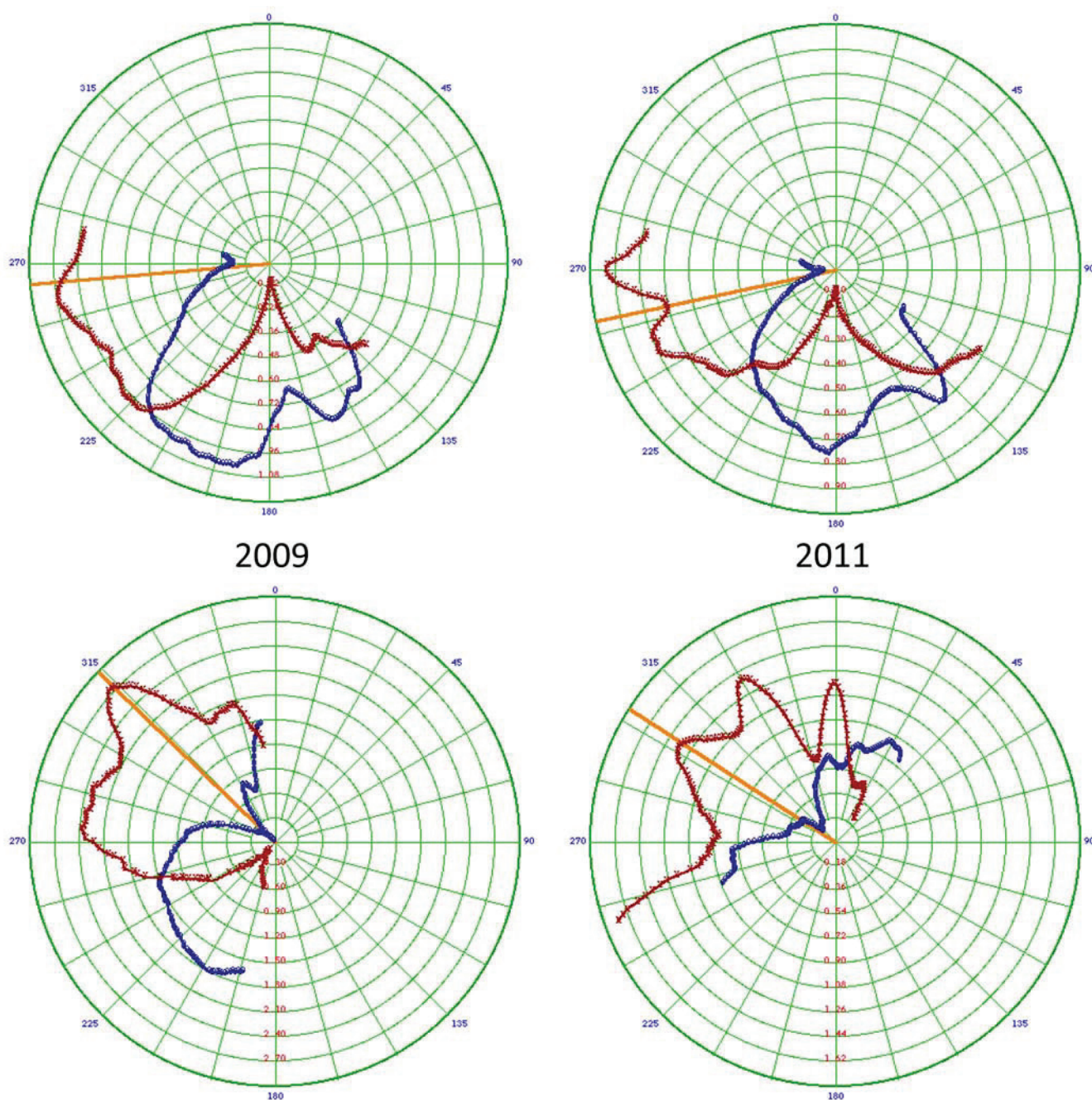
Electrical conducting material in proximity of HFR Rx stations can produce highly distorted patterns with multiple nulls that are difficult to use (Kohut & Glenn, 2003). Conductors

in the near field of the receive antenna cause the antenna patterns to deviate from the ideal cosine response. Thus, in the absence of temporal change of the local electromagnetic environment, antenna patterns are expected

to be stable. We tested this hypothesis by measuring the antenna patterns at stations FURA and CDDO in September 2009 and again in January 2011. The FURA distortion patterns varied only modestly (Figure 4), and

**FIGURE 4**

Antenna test patterns for station FURA (top) and CDDO (bottom) in October 2009 (left) and January 2011 (right). The yellow line in the figures represents the center bearing of loop 1 of the receive antenna. (Color versions of figures available online at: <http://www.stevens.edu/csr/>.)





even though the patterns are distorted from ideal, each measured antenna pattern retains only one null in the proper location. The antenna distortion parameter  $\Gamma$  provided by Laws et al. (2010) was applied to the MeasPattern.txt file and the loop file for the measurements performed in 2009 and 2011.

The distortion is unchanged at the FURA site between the measurements performed in 2009 and 2011. The distortion did increase at the CDDO site between measurements. This site is located at a private marina with sport fishing vessels within one wavelength of the antenna. Any change in the vessel locations between measurements could explain the change. The distortion is lower using the MeasPattern.txt file compared with the loop file. This is expected because a smoothing between 10° and 20° is applied to the pattern across bearing. This test thus constitutes an intermediate level of distortion that can provide other HFR users additional guidance on whether or not to relocate their HFR (Tables 1 and 2).

For comparison of data from the CDDO station to NOAA tidal current forecasts at PO, we selected five locations at increasing distances of 3 km along the most northerly azimuth available, as shown in Figure 1. The figure illustrates a time series of HFR output for this set of five points located near the west coast of Puerto Rico together with hourly NOAA PO tidal

TABLE 1

Schedules of antenna pattern measurements (APM) at FURA and CDDO.

	APM 1	APM 2
FURA	10/20/2009	1/9/2011
CDDO	10/23/2009	1/12/2011

TABLE 2

Antenna pattern distortion for the MeasPattern.txt file and the raw loop file from the antenna pattern measurements performed in 2009 and 2011.

Site		2009	Degrees Smoothing	2011	Degrees Smoothing
FURA	MeasPattern.txt	0.15	10	0.15	10
	Loop file	0.34		0.34	
CDDO	MeasPattern.txt	0.14	10	0.21	20
	Loop file	0.34		0.52	

current forecasts. HFR data exhibit two maximum and two minimum current velocities per day in excellent phase agreement with the NOAA predictions. Radial data from the CDDO station was highly correlated ( $r = 0.89$ ) with NOAA current forecasts at the node closest to the PO station and more modestly ( $r = 0.59 \pm 0.0344$ ) at stations beyond this point. The discrepancy between the NOAA tidal prediction and the CDDO HFR estimate increases at the times of tidal current reversal. Correlation did not further degrade along the radial (Table 3), but amplitude of the HFR estimate decreased significantly with distance relative to the tidal current forecast. NOAA forecasts depict this transition as a sharp current reversal peak in the time series rather than the

TABLE 3

Correlation between HFR observations and NOAA tidal predictions.

Site	Distance to PO Station (nautical miles)	Correlation Coefficient
A	19.1	0.89
B	16.1	0.61
C	13.1	0.54
D	10.3	0.61
E	7.6	0.60

elliptical 180° rotation observed in the radar data. The amplitude decay reflects dilution of precision with distance (Figure 5).

Repeated deployment of GPS-tracked drifters enabled the collection of five Lagrangian trajectories within the experimental box over the period 09:00 to 15:00 local (13:00-19:00 GMT) on July 7, 2010. Initial drifter deployments coincided with tidal reversal and drifter trajectories trended WSW, thereon veering clockwise towards the north. After about 10:00 AM local time, trajectories were towards the west veering to the WNW (Figure 6).

For the CDDO station, HFR data were collected consistently for two sectors within the 3 × 3 km box. However, for the FURA station, only two reports within the box were available; one at 11:00 AM and one at 12 noon. We consequently searched for the nearest reporting sectors outside the box, which resulted at distances of 2.9, 3.5, and 4.4 km from the box borders. Time series of drifter radial velocity components and the corresponding hourly HFR values for stations FURA and CDDO are shown in Figure 7. Our analysis (Table 4) reflects RMS differences of 5.74 cm s<sup>-1</sup> for FURA and 3.96 cm s<sup>-1</sup> for CDDO over a range of observed net

**FIGURE 5**

Observed HFR  $v$  (north-south) components of tidal currents at five locations (top to bottom, A-E; see Figure 1) along heading 343° (green) compared to the NOAA  $v$  tidal current forecast (blue). All values are in  $\text{cm s}^{-1}$ . (Color versions of figures available online at: <http://www.stevens.edu/csr/>.)

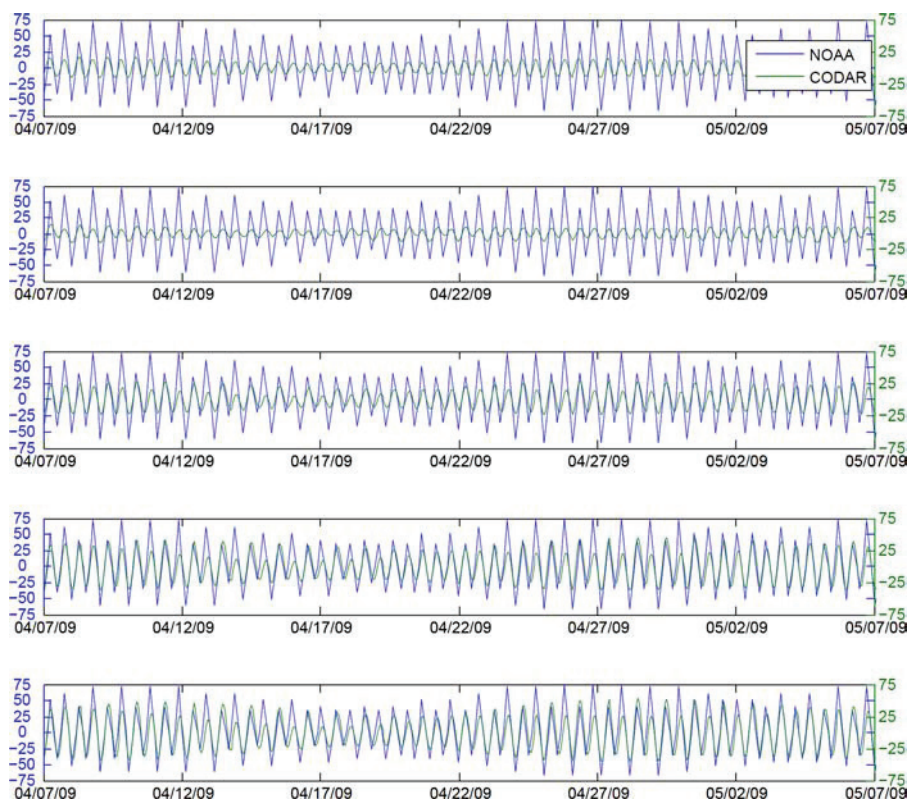
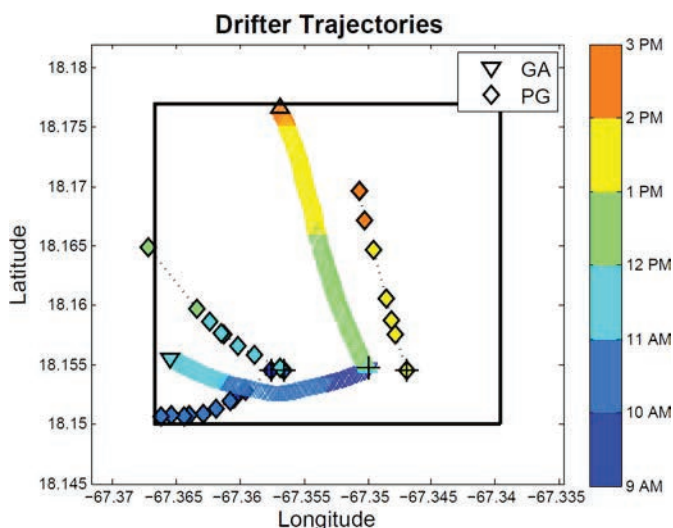


**FIGURE 6**

Lagrangian drifter tracks within the  $3 \times 3$  km box. Data are color coded hourly for July 7, 2010. GA denotes drifters equipped with Garmin Astro telemetry. PG denotes consecutive deployments of the Pacific Gyre drifter. The black crosses denote the drifter release location. (Color versions of figures available online at: <http://www.stevens.edu/csr/>.)



radial velocities between  $-20$  and  $32 \text{ cm s}^{-1}$ .

Comparison of computed ADCP hourly radial components with hourly HFR radials (Figure 8, Table 5) results in good agreement for the FURA station with RMS difference of 1.67 and bias of  $-1.09$ . Corresponding agreement for station CDDO, however, is much poorer with RMS difference and bias, both amounting to about 60% of the observed range of values.

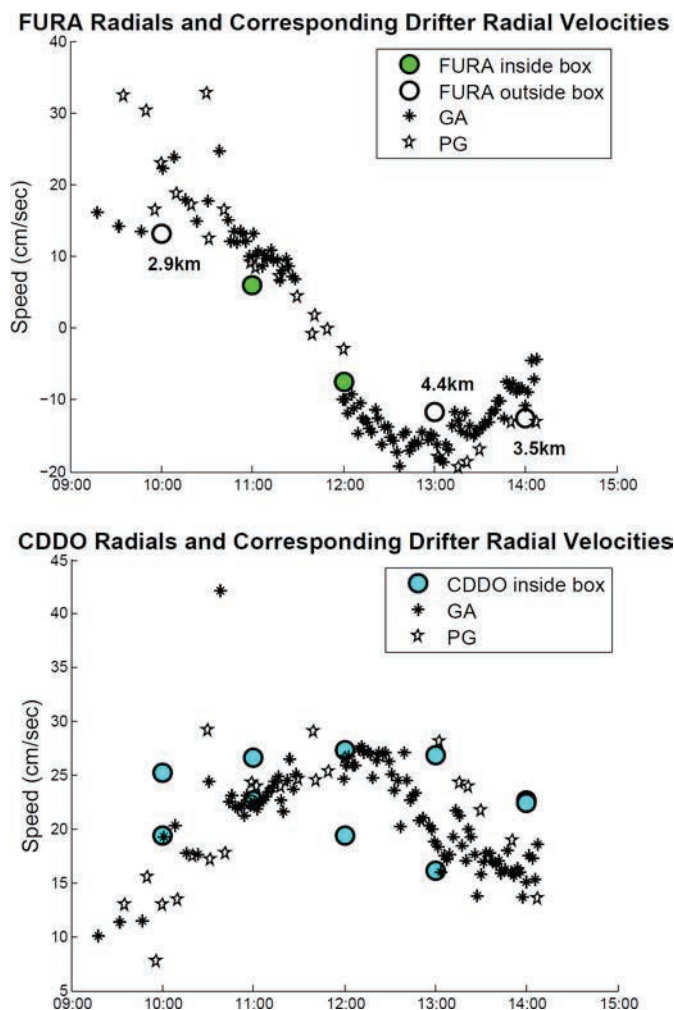
Figure 9 provides comparisons between Lagrangian drifter data and the trajectories obtained from the particle tracking algorithm based on the HFR vector fields. Over the time period from 11:59:20 to 14:09:40, good agreement between the experimental and numerical trajectories is observed but poor agreement is evident over the time period from 9:17:30 to 11:31:50 during which tidal current reversal occurred. We attribute these significant differences to tidal current variability at time scales smaller than the 1-h HFR averaging period.

## Discussion

To test temporal variability, the antenna patterns at FURA and CDDO were remeasured in January 2011 by the same techniques, and the result is plotted in Figure 4. The difference between the 2009 and 2011 patterns is less than the difference between either measured pattern and the ideal cosine (theta), sine (theta) shape. During this time period, the FURA antenna was taken down for servicing and reinstalled twice. While small changes in the local environment or the antenna may have occurred over time, the overall environment and antenna pattern is the same, with similar broad peaks and narrow nulls. This is a welcome result,

**FIGURE 7**

(Top) Time series of instantaneous drifter radial velocity components and the corresponding hourly CODAR values for station FURA. (Bottom) Time series of instantaneous drifter radial velocity components and the corresponding hourly CODAR values for station CDDO.



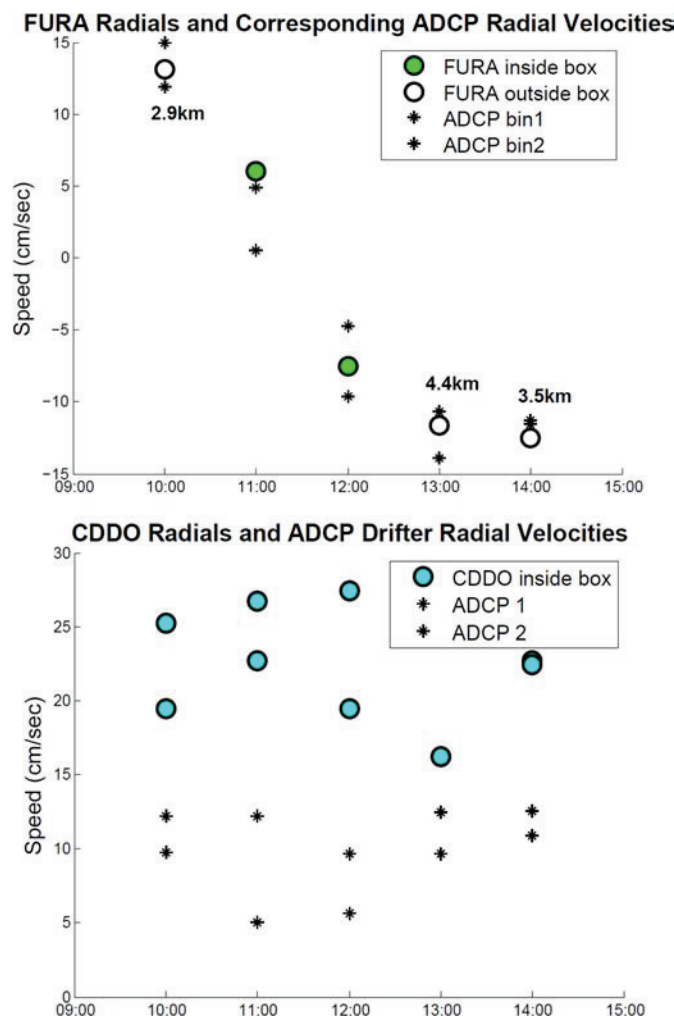
since the sensitivity of the measured pattern to reassembly of the antenna was previously undocumented. The pattern measurements here indicate that the major distortion to the shape

of the pattern is caused with any HFR antenna interacting with the local environment, not a specific one.

A general understanding of coastal circulation off the west coast of Puerto

**FIGURE 8**

(Top) Time series of the near-surface ADCP radial velocity component and corresponding hourly HFR values for station FURA. (Bottom) Time series of ADCP radial velocity components and the corresponding hourly HFR values for station CDDO.



Rico has been made possible by direct current measurement (Morelock et al., 2000; Capella et al., 2003). Extensive studies using moored ADCPs in the Mona Passage indicate net northward

**TABLE 4**

RMS difference and bias between CODAR radials at FURA and CDDO and radial components computed for surface drifters.

	RMS Difference (cm/s)	Bias (cm/s)
FURA	5.74	2.97
CDDO	3.96	1.93

**TABLE 5**

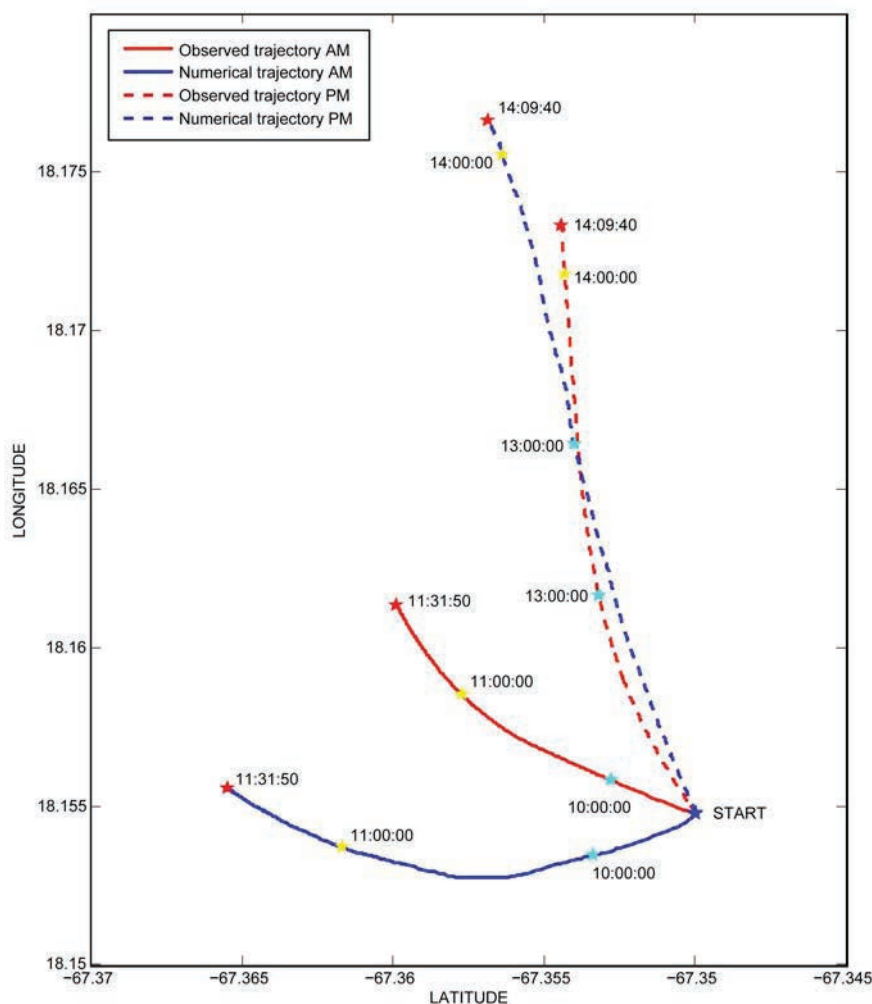
RMS difference and bias between CODAR radials at FURA and CDDO and radial components computed from the top bin of the ADCP data record.

	RMS Difference (cm/s)	Bias (cm/s)
FURA	1.67	-1.09
CDDO	15.10	14.73



## FIGURE 9

Comparison between the Lagrangian drifter trajectory (red) and the trajectory obtained from the particle tracking algorithm (blue) from 9:17:30 to 11:31:50 on July 7, 2010. (b) Same but from 11:59:20 to 14:09:40 on July 7, 2010. (Color versions of figures available online at: <http://www.stevens.edu/csr/>.)



flowing coastal currents superimposed upon semidiurnal tidal ebb and flow. Overall, along-shore currents following the general north-south coastline orientation prevail in the eastern portion of the Passage. Our HFR and drifter observations coincide with these previous studies. Sustained correlation is found between the NOAA PO virtual tidal current station and selected HFR cells north to a distance of 19 km attesting to the homogeneity of the alongshore current pattern. Ohlmann et al. (2007) validated the performance

of HFR systems operating in the 11–13.5 MHz range on the California coast by comparison of Lagrangian *in situ* drifter data with HFR returns. Results in the Mona Passage using similar methodology and radar frequencies compare well with their observations falling within the lower range of their computed RMS differences. Robust agreement is also found between HFR data from station FURA and *in situ* ADCP measurements. The discrepancy between the HFR data from CDDO and *in situ* ADCP measurements may

respond to local flow distortion by abrupt topography at the deployment site.

Comparison between numerically derived Lagrangian trajectories based on the HFR data and experimental drifter trajectories showed mixed results, with good agreement during periods with low intrahour variability in current direction and poor agreement during periods of rapid tidal reversal. A shorter averaging interval for the HFR may improve the comparison with the Lagrangian trajectories but at the expense of degraded radar accuracy.

## Acknowledgments

We thank the Club Deportivo del Oeste and the Puerto Rico Police for hosting the HFR stations, J.S. Bonner of Clarkson University for the loan of the HFR unit emplaced at FURA, and Kenneth Laws for providing the antenna pattern distortion Matlab code. Technical support was provided by the Caribbean Coastal Ocean Observing System (CarICOOS). This work is a contribution of the Center for Secure and Resilient Maritime Commerce (CSR), a Department of Homeland Security Center of Excellence, under Award 2008-ST-061-ML0001. The views and conclusions contained in this document are those of the authors and should not be interpreted as necessarily representing the official policies, either expressed or implied, of the U.S. Department of Homeland Security.

## Lead Author:

Jorge E. Corredor  
Department of Marine Sciences,  
University of Puerto Rico,  
Mayagüez, Puerto Rico  
Email: [jorge.corredor@upr.edu](mailto:jorge.corredor@upr.edu)

## References

- Barrick, D.E., Evans, M.W., & Weber, B.L.** 1977. Ocean surface currents mapped by radar. *Science*. 198:138-44. doi: 10.1126/science.198.4313.138.
- Barrick, D.E., & Lipa, B.J.** 1997. Evolution of bearing determination in HF current mapping radars. *Oceanography*. 10:72-5.
- Capella, J.E., Alston, D.E., Cabarcas-Núñez, A., Quintero-Fonseca, H., & Cortes-Maldonado, R.** 2003. Oceanographic considerations for offshore aquaculture on the Puerto Rico-U.S. Virgin Islands platform. In: *Open Ocean Aquaculture: From Research to Commercial Reality*, eds. Bridger, C.J., & Costa-Pierce, B.A., 247-61. Baton Rouge, LA: The World Aquaculture Society.
- Chapman, R.D., Shay, L.K., Graber, H.C., Edson, J.B., Karachintsev, A., Trump, C.L., & Ross, D.B.** 1997. On the accuracy of HF radar surface current measurements: Intercomparison with ship-based sensors. *J Geophys Res.* 102(C8):18 737-48.
- Emery, B.M., Washburn, L., & Harlan, J.A.** 2004. Evaluating radial current measurements from CODAR high-frequency radars with moored current meters. *J Atmos Oceanic Technol.* 21:1259-71.
- Holbrook, J.R., & Frisch, A.S.** 1981. A Comparison of near-surface CODAR and CACAM measurements in the Strait of Juan De Fuca, August 1978. *J Geophys Res.* 86(C11):10 908-12.
- Kohut, J.T., & Glenn, S.M.** 2003. Improving HF radar surface current measurements with measured antenna beam patterns. *J Atmos Oceanic Technol.* 20:1303-16.
- Kohut, J.T., Roarty, H.J., & Glenn, S.M.** 2006. Characterizing observed environmental variability with HF Doppler radar surface current mappers and acoustic Doppler current profilers: environmental variability in the coastal ocean. *IEEE J Ocean Eng.* 31(4): 876-84. doi: 10.1109/JOE.2006.886095.
- Laws, K., Paduan, J.D., & Vesecky, J.** 2010. Estimation and assessment of errors related to antenna pattern distortion in CODAR SeaSonde high-frequency radar ocean current measurements. *J Atmos Oceanic Technol.* 27:1029-43. doi: 10.1175/2009JTECHO658.1.
- Morelock, J., Capella, J., Garcia, J., & Barreto, M.** 2000. Puerto Rico. In: *Seas at the Millenium: An Environmental Evaluation*, Volume I, Chapter 36, ed. Sheppard, C., 539-49. Oxford: Pergamon Press, ISBN: 0-08-043207-7.
- Ohlmann, C., White, P., Washburn, L., Terril, E., Emery, B., & Otero, M.** 2007. Interpretation of coastal HF radar-derived surface currents with high-resolution drifter data. *J Atmos Oceanic Technol.* 24:666-80. doi: 10.1175/JTECH1998.1.
- Pawlowicz, R., Beardsley, B., & Lentz, S.** 2002. Classical tidal harmonic analysis including error estimates in MATLAB using T\_TIDE. *Comput Geosci.* 28:929-37. doi: 10.1016/S0098-3004(02)00013-4.
- Roarty, H.J., Barrick, D.E., Kohut, J.T., & Glenn, S.M.** 2010. Dual-use compact HF radars for the detection of mid- and large-size vessels. *Elektrik: Turk J Electr Eng Comput Sci.* 18(3):373-88.
- Stewart, R.H., & Joy, J.W.** 1974. HF radio measurements of surface currents. *Deep-Sea Res.* 21:1039-49.
- Watlington, R.A., Morell, J.M., & Corredor, J.E.** 2008. Improved understanding of oceanic processes through an Integrated Caribbean Coastal Ocean Observing System. *Rev Biol Trop.* (Int J Trop Biol ISSN-0034-7744). 56(Suppl. 1):89-96.

# Performance Evaluation of SeaSonde High-Frequency Radar for Vessel Detection

## AUTHORS

**Hugh J. Roarty**  
**Erick Rivera Lemus**  
**Ethan Handel**  
**Scott M. Glenn**  
 Coastal Ocean Observation  
 Laboratory, Rutgers University

**Donald E. Barrick**  
**James Isaacson**  
 CODAR Ocean Sensors, Ltd.,  
 Mountain View, CA

## ABSTRACT

High-frequency (HF) surface wave radar has been identified to be a gap-filling technology for Maritime Domain Awareness. Present SeaSonde HF radars have been designed to map surface currents but are able to track surface vessels in a dual-use mode. Rutgers and CODAR Ocean Sensors, Ltd., have collaborated on the development of vessel detection and tracking capabilities from compact HF radars, demonstrating that ships can be detected and tracked by multistatic HF radar in a multiship environment while simultaneously mapping ocean currents. Furthermore, the same vessel is seen simultaneously by the radar based on different processing parameters, mitigating the need to preselect a fixed set and thereby improving detection performance.

Keywords: radar, detections, maritime domain awareness, dual-use

## Introduction

The U.S. Integrated Ocean Observing System (IOOS®) led by the National Oceanic and Atmospheric Administration (NOAA) has designed (Interagency Working Group on Ocean Observation, 2009), is constructing, and has recently begun operating the more advanced portions of a national high-frequency (HF) radar network focused on the real-time mapping of surface currents. The primary operational users of the resulting surface current maps are the U.S. Coast Guard for Search and Rescue and the NOAA HazMat team for ocean spill response. The IOOS Mid-Atlantic Region's CODAR SeaSonde HF Radar Network, led by Rutgers University, is the first region in the United States to achieve operational status by constructing and operating the end-to-end system that produces and links validated real-time surface current maps to the Coast Guard's Search and Rescue Optimal Planning System (Roarty et al., 2010b).

The Department of Homeland Security has called for the development of tools to provide wide-area surveillance from the coast to extend beyond the horizon (Department of Homeland Security Science and Technology, 2009). Rutgers and CODAR Ocean Sensors, an academic-industry partnership established in 1997, have worked together for over a decade to expand the capabilities of compact CODAR HF radars to include the dual-use application of detecting and tracking ships without compromising the network's ability to map surface currents. Initial development focused on the demonstration and evaluation of a non-real-time end-to-end system for dual-use vessel tracking in the New York Bight multifrequency HF radar testbed (Roarty et al., 2010a). Technology demonstrations determined (a) that vessels could be detected, (b) that multilook detections could be associated with a known ship, and (c) that the associated detections could then be input to a range of tracking algorithms

whose output produced tracks and predicted trajectories on a computer screen, providing useful information to operators. Radar hardware development focused on developing network flexibility beyond monostatic backscatter operations, demonstrating (a) that bistatic and multistatic operations were possible with a shore-based network and (b) that buoy-based bistatic transmitters can be operated at all three of the commonly used HF radar frequencies (5-6, 12-13, and 24-25 MHz). The greatest challenge in developing a robust ship surveillance capability for any HF radar is the development of the initial vessel detection algorithm. This conclusion focused the initial research on the mathematical problem of identifying and extracting the radar return of a surface vessel hidden within a highly variable and noisy background, requiring additional detection algorithm development, testing, and sensitivity analysis in a variety of environments with different noise characteristics. It is the aim of this paper to



analyze the parameters and settings of the vessel detection algorithm that are optimal for finding those ship echoes among the other signals that are sent back towards the radar. In Methodology, we describe the HF radar network, the SeaSonde HF radar used in this test, the Automatic Identification System (AIS) network used to ground truth the radar detections, and the ship detection software used to process the radar data for ships. In Results, we discuss the results of the ship detection test that was conducted. Lastly, the performances of the various ship detection processing methods against the available targets are discussed in Discussion.

## Methodology

### HF Radar Network

These experiments were conducted within the New Jersey Shelf Observing System (Glenn & Schofield, 2002). A major component of this observing system is an HF radar network. The network was created in 1998 with the placement of two 25-MHz systems on the southern coastline of New Jersey (Kohut & Glenn, 2003). The network was then expanded with the placement of four 5-MHz systems spanning the New Jersey coastline (Gong et al., 2009). The 25-MHz network was moved north in 2003 in support of the Lagrangian Transport and Transformation Experiment (Chant et al., 2008). The work discussed here utilizes the latest addition to the network: the placement of a 13-MHz system outside the entrance to New York Harbor in Sea Bright, New Jersey. This network also contributes to the Mid-Atlantic Regional Coastal Ocean Observing System (MARCOOS), which has a total of 30 radars from Cape Hatteras to Cape Cod that are operated by eight universities (Roarty et al., 2010b).

### 13-MHz SeaSonde System

The radar was deployed in Sea Bright, New Jersey, 40 km south of the Battery in New York City. The radar was a direction-finding type radar, SeaSonde Remote Unit SSRS-100, manufactured by CODAR Ocean Sensors and was installed in October 2008. The radar's primary function was the measurement of surface currents, which are provided in real time to the NOAA National HF Radar Network (Temll et al., 2006). The radar also has the dual-use capability to detect the location of ships at sea.

The radar consists of a compact receive antenna with three elements: two directional crossed loops and an omnidirectional monopole, a monopole transmit antenna, and a hardware housed within a climate-controlled enclosure (Figure 1). The radar transmits a radio wave with a center frequency of 13.46 MHz and a bandwidth of 50 kHz. The bandwidth of the radar sets the spatial range resolution of the system, which was about 3 km for this particular bandwidth. The details of the waveform are given in Table 1. Separate transmit and receive antennas were used for this study spaced at least one wavelength apart, which is approximately 23 m at the 13-MHz radio band. A ship with a vertical structure of a quarter wavelength (6 m) is the minimum-sized optimal reflector (Ruck et al., 1970).

Figure 2 shows the spatial and temporal radial vector coverage for ocean currents of the radar over a 1-week period, which coincided with the ship detection exercise. The radar collected range data, which are a time series of the complex echo signal voltages before Doppler processing, from 00:00 GMT to 01:00 GMT on February 26, 2009. These range files are the result of the first fast Fourier transform

**FIGURE 1**

Picture of the (A) transmit antenna, (B) receive antenna, and (C) equipment enclosure for the SeaSonde 13-MHz radar.



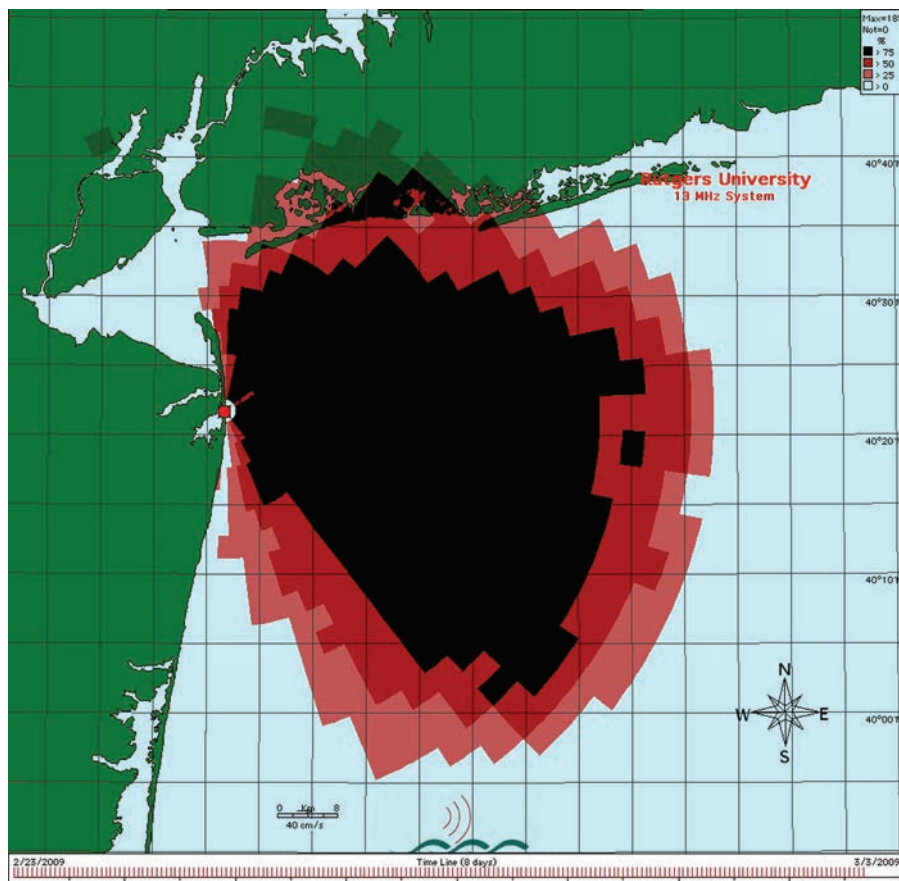
**TABLE 1**

Characteristics of the radar waveform used in the study.

Waveform Characteristic	Value
Center frequency	13.46 MHz
Bandwidth	50 kHz
Blank	668.8 $\mu$ s
Blank delay	8.55 $\mu$ s
Sweep rate	2 Hz
Pulse shaping	On

## FIGURE 2

Radial coverage map of the SeaSonde at Sea Bright, New Jersey, over a 1-week period. The color map illustrates the temporal coverage along the radial grid (black = 75%, red = 50%, pink = 25%). (Color versions of figures available online at: <http://www.ingentaconnect.com/content/mts/mtsj/2011/00000045/00000003>.)



(FFT) of the frequency-modulated continuous wave received signal. The range data were collected using an FFT length of 512 points. With a 2-Hz sweep of the radar, each range file encompasses 256 s of coherent integration time. There were a total of 15 range files over the hour-long period. The time on the computer and all the subsequent files it generates are synchronized to atomic time via GPS by the Macintosh operating system.

### AIS Receivers

Rutgers also operates an AIS receiver network, which was utilized in this study; this allows transponders on

vessels to broadcast the ship's position and identification. When earlier work was performed (Roarty et al., 2010a), the authors were limited to verifying detections of vessels where a self-recording GPS could be placed on a vessel by the researchers or when the GPS information could be provided by other researchers (Rossby & Gottlieb, 1998). The ability of the researchers to obtain AIS position data on the vast majority of ships at sea has greatly accelerated the research. The Rutgers AIS network has receivers, which are manufactured by Shine Micro, Inc., located at its field station in Tuckerton, Sandy Hook, and Loveladies, New Jersey, as shown in

Figure 3. The AIS transmissions are used as ground truth for the HF radar ship detections. The range of the shore-received AIS signal is typically 30 nautical miles, but under certain atmospheric conditions, range can be upwards of hundreds of nautical miles (International Maritime Organization, 2006). Data from the individual AIS receivers were sent back to the Rutgers Coastal Ocean Observation Laboratory (Glenn & Schofield, 2009), where it was archived using the Coast Guard software 'AIS Source.' The data were then time stamped using the clock on the computer. The computer kept time with a software tool to synchronize with the National Institute of Standards and Technology Internet Time Service. Figure 4 shows the tracks of vessels sent via AIS over a 3-week period, indicating that this is a target-rich environment and that vessels do not always stay in the shipping lanes.

### Detection Software

The ship detection algorithm is explained in Roarty et al. (2010a). The ship detection code is written in the MATLAB programming language and is designed to run offline in a batch-processing mode. The range data that were collected by the radar were read by the software to process for the hard targets. The ship detection code utilizes a constant false alarm rate (CFAR) to find targets. A signal that is above the background by some threshold on the monopole and at least one of the two loops is considered a possible detection. Figure 5 shows the spectra from the monopole of the Sea Bright radar site at 00:15:21 GMT on February 26, 2009. The  $x$  axis denotes Doppler shift, the  $y$  axis shows signal strength, and the  $z$  axis denotes

### FIGURE 3

Location of the three AIS receivers operated by Rutgers University shown as green circles. (Color versions of figures available online at: <http://www.ingentaconnect.com/content/mts/mts/2011/00000045/00000003>.)

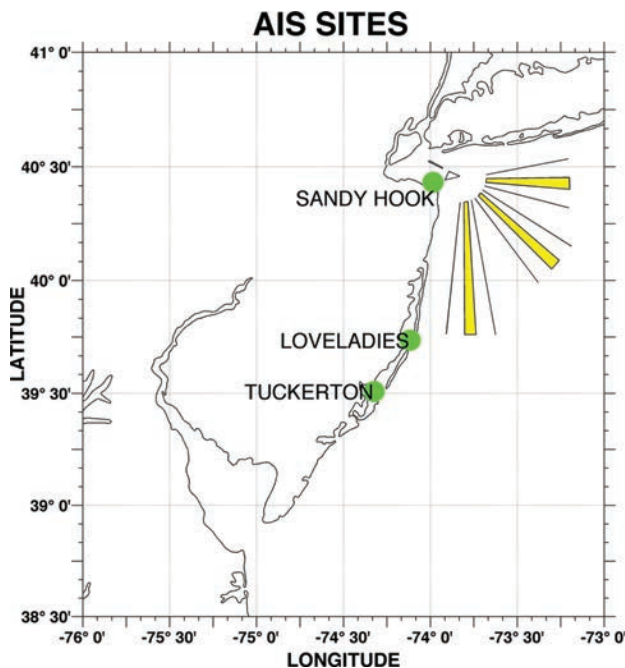
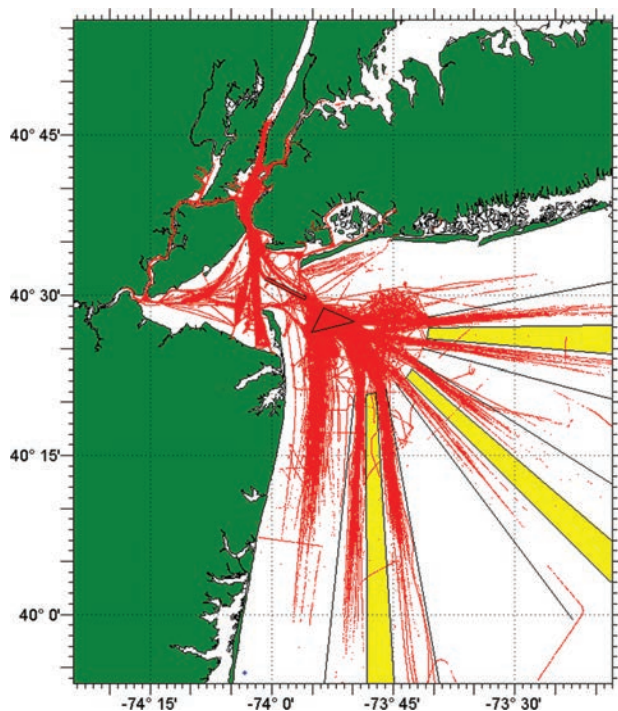


### FIGURE 4

Map of the study area showing tracks of vessels (red lines) sent via AIS over a 3-week period. The Nantucket, Hudson Canyon and Barnegat (clockwise from right) shipping lanes are shown in the bottom right.



the radar range cell, which was 3 km for these spectra. The Bragg peaks from which surface currents are derived (Barrick, 1972) are shown  $\pm 0.4$  Hz. The large signals at zero Doppler are signals returned to the radar from stationary objects. Ship signals can be seen between the Bragg peaks and the zero Doppler signals, with positive Doppler shift denoting a ship moving towards the radar and the corollary with a signal on the negative Doppler measuring a ship moving away from the radar. The ship detection code is designed to identify these signals. The code utilizes two schemes as the basis for thresholding in its CFAR peak-picking, where one averages in time, infinite impulse response (IIR), and the other averages in Doppler and range space using a median to create the signal background. In its current form, the code is able to process the data using three combinations of threshold and integration time for each background simultaneously. This results in a set of six detection packages after each software run. The detection code performs a sliding FFT on the range data so a new detection file is output every 32 s. This setting is adjustable so that the user can input the desired update rate for the detections. The output of the detection code is a series of files that contain range, range rate, and bearing of possible detections from the radar. The files also include the uncertainties in the above quantities, the signal-to-noise ratio for each antenna, and an estimate of the radar cross section of the possible target.

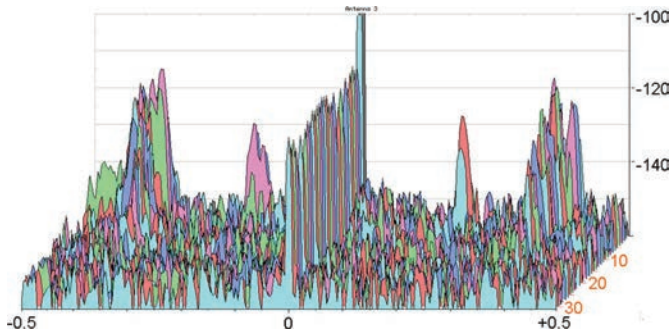
### Results

The range data that were collected at the radar site were transported back



## FIGURE 5

Picture of power spectra for Antenna 3 of the SeaSonde at 00:15 GMT on February 26, 2009. The x-axis is Doppler shift (Hz), the y-axis is signal strength (dB), and the z-axis denotes the range bin from the radar (scalar). Vessel echoes are observed between the two sea-echo Bragg peaks at approximately  $\pm 0.4$  Hz.

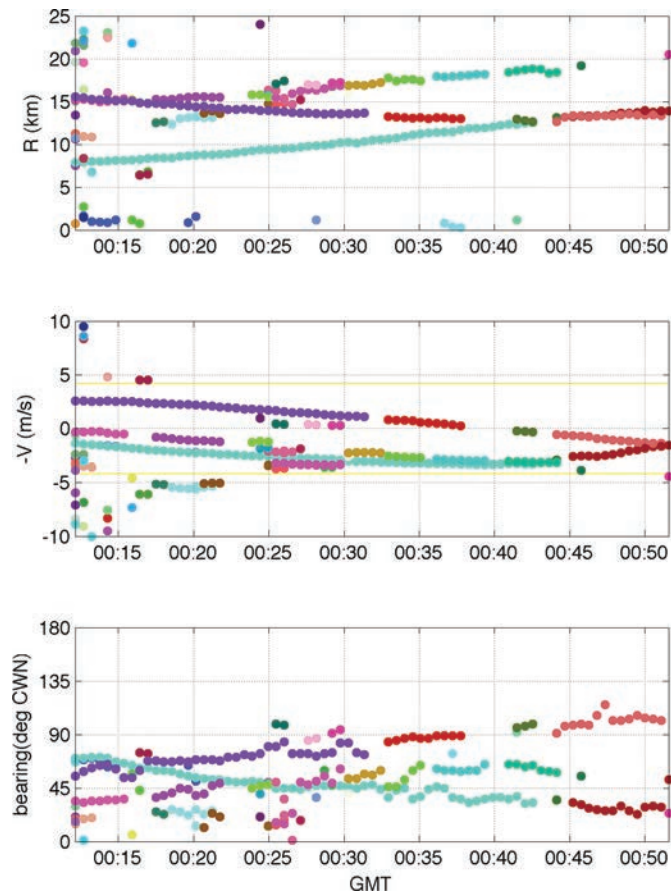


to the laboratory for offline processing. The user sets three combinations of integration time and threshold for each of the two backgrounds. Hence, the output of one run of the range data through the ship detection code results in six concurrent data streams of possible ship detections. Because the ship detection code only outputs six packages (three for the IIR method and three for the Median method) for each software run, the software is run several times to fill out our desired processing matrix. The threshold (dB)/FFT points that were initially tried using the IIR background were 6/16, 7/32, 8/64, 9/128, 10/256, and 11/512. The threshold (dB)/FFT points that were tried using the Median background were 8/32, 9/64, 10/128, 11/256, 12/512, and 13/1024. The threshold was increased because the average of signal to noise increased by  $\sim 1$  dB for each doubling of the FFT length (Roarty et al., 2010a). A plot of range (km), range rate (m/s), and bearing (degrees clockwise from north) of possible detections using the IIR background, 256-point FFT, and 10-dB threshold is shown in Figure 6. The trails of vessels can be seen in the range and range rate subplots. There are also false positives in the data

stream as noted by the single detections with no adjacent detections in space or time.

## FIGURE 6

Plot of target detections from 00:10 to 00:55 GMT on February 26, 2009. Panels from top to bottom are range, range rate, and bearing. The yellow horizontal lines in the middle are the expected positions of the very strong Bragg sea clutter echoes that would mask vessel detection.



The AIS data were then used to see how the radar was performing when it came to detecting the speed and location of vessels at sea. The AIS data were first filtered by time to coincide with the measurements, then geographic proximity to the radar site (a 60-km threshold was used) and then binned by ship identification. Eighteen ships passed this first stage of filtering. Then any ship that was located on the bay side of the radar or had zero radial velocity was removed. This left four ships for possible detection, one tug boat (the *Dolphin*), two cargo containers (the *Maas Trader* and the *MOL Efficiency*), and a tanker (the *Joelmare*). The latitude, longitude, and time

reports of these four ships were used to calculate the ship range, radial velocity, and bearing relative to the radar at Sea Bright, New Jersey. A text file of ship position and time was processed using the program 'GPSTracker', which is part of the SeaSonde detection software package. This software is normally used to perform the same task when measuring the antenna pattern of the receive antenna with a transponder on a vessel. This software generates a file for each vessel that contained the range, radial velocity, and bearing of that particular vessel as shown in Figure 7. These data were then used for comparison with the range, radial velocity, and bearing calculations from the radar.

The next step was to compare the data from the radar with data obtained via AIS. If the calculated range is within half the width of a range bin (1.5 km in this case) and within two Doppler bins (varied between 0.02 and 1.4 m/s, depending on the length of the FFT window) of the actual vessel, then the detection is considered a hit. A detection rate is then calculated as the number of times the radar detected the target divided by the total number of time sample possibilities, which was every 32 s for this experiment. The detection rates for *Joelmare* using the IIR and Median background are shown in Tables 2 and 3, respectively. The detection rates for *Maas Trader* using the IIR and Median background are shown in Tables 4 and 5, respectively. The detection rates for the *Dolphin* using the IIR and Median background are given in Tables 6 and 7, respectively. In the case of the *Maas Trader*, once the highest detection rate was found for the initial runs, then the thresholds were varied along the FFT length with the highest detection rate. The detection

**FIGURE 7**

Range, range rate, and bearing plot of four vessels in the vicinity of the Sea Bright HF radar station on February 26, 2009 as measured by AIS.

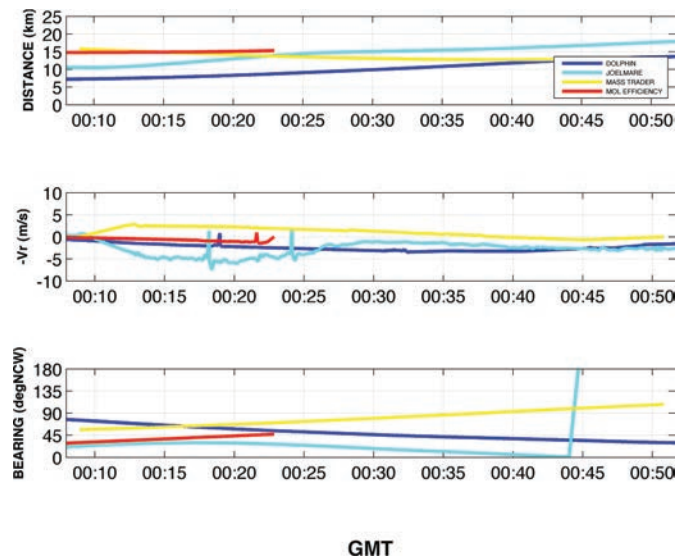


**TABLE 2**

Detection rate in percent for the *Joelmare* with different combinations of threshold (columns) and FFT points (rows) using the IIR background.

	6 dB	7 dB	8 dB	9 dB	10 dB	11 dB
16	NSD					
32		NSD				
64			0.6			
128				15.6		
256					13.2	
512						10.8

NSD stands for "no ship detected."

**TABLE 3**

Detection rate for the *Joelmare* with different combinations of threshold (columns) and FFT points (rows) using the Median background.

	8 dB	9 dB	10 dB	11 dB	12 dB	13 dB
32	0.2					
64		3.3				
128			34.0			
256				33.3		
512					12.5	
1024						7.6

**TABLE 4**

Detection rate in percent for the *Maas Trader* with different combinations of threshold (columns) and FFT points (rows) using the IIR background.

	6 dB	7 dB	8 dB	9 dB	10 dB	11 dB
16	NSD					
32		NSD				
64			NSD			
128				58.7		
256	70.3	70.3	68.9	66.2	64.9	64.9
512						38.5

NSD stands for “no ship detected.”

**TABLE 5**

Detection rate for the *Maas Trader* with different combinations of threshold (columns) and FFT points (rows) using the Median background.

	8 dB	9 dB	10 dB	11 dB	12 dB	13 dB
32	13.8					
64		23.6				
128			55.0			
256	65.0	65.0	62.5	61.3	58.8	58.8
512					46.5	
1024						30.8

**TABLE 6**

Detection rate for the Tugboat *Dolphin* with different combinations of threshold (columns) and FFT points (rows) using the IIR background.

	6 dB	7 dB	8 dB	9 dB	10 dB	11 dB
16	NSD					
32		0.5				
64			5.4			
128				92.4		
256					73.1	
512						60.0

NSD stands for “no ship detected.”

rate for the *MOL Efficiency* was not calculated due to a short AIS record, but there are results that will be discussed in the next section.

An example of the “association” of the detections with the ground truth data is shown in Figure 8. This figure shows the detections made by the radar associated with the GPS position of the cargo ship the *Maas Trader* from Figure 6. The detections are shown as blue diamonds with error boxes around the detection, with half the height signifying the uncertainty of the measurement and the width of the box denoting the length of the FFT window. The uncertainty  $\sigma$  is given by the equation

$$\sigma = \frac{\Delta}{\sqrt{\text{SNR}_3}},$$

where  $\Delta$  is the range, range rate, or bearing bin size and  $\text{SNR}_3$  is the signal-to-noise ratio on Antenna 3 (the monopole). This figure is characteristic of the uncertainty provided by the SeaSonde HF radar that determines bearing using direction finding, i.e., low uncertainty in range and range rate measurements and higher uncertainty for the bearing estimate.

## Discussion

We will now discuss detection results of the radar with four vessels that passed in front of the radar during the test period.

### Cargo Container *MOL Efficiency*

The *MOL Efficiency*, International Maritime Organization (IMO) Ship No. 9251365, is a cargo container with a length of 294 m and a beam of 32 m. The vessel was exiting New York Harbor on a southeast course



**TABLE 7**

Detection rate for the Tugboat *Dolphin* with different combinations of threshold (columns) and FFT points (rows) using the Median background.

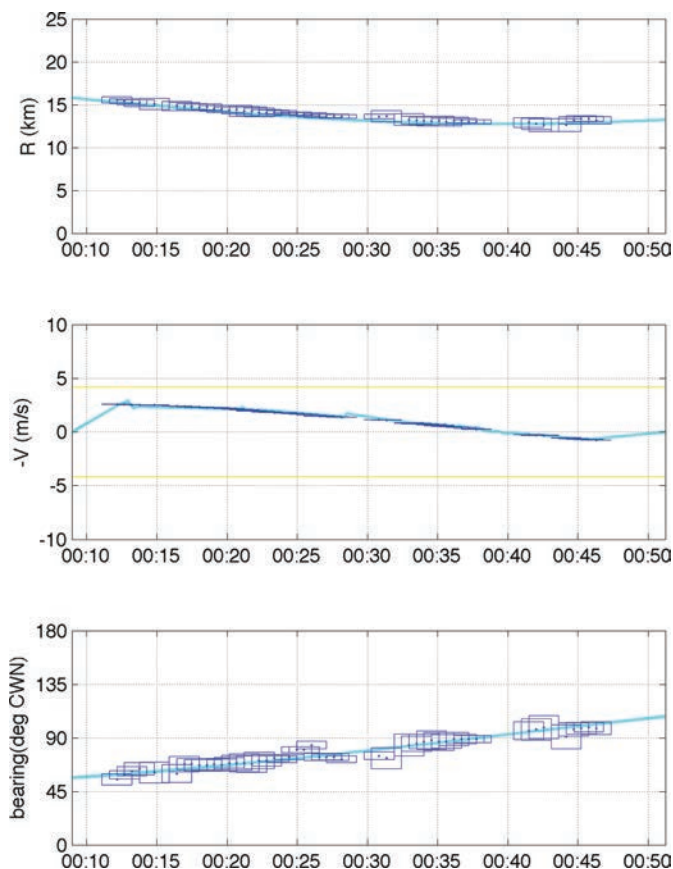
	8 dB	9 dB	10 dB	11 dB	12 dB	13 dB
32	10.8					
64		31.0				
128			93.2			
256				78.6		
512					56.2	
1024						32.8

and was approximately 15 km from the radar. The AIS record of the *MOL Efficiency* only spans from

00:00 to 00:23 GMT on February 26, 2009. It is unclear to the authors as to why the AIS record terminated.

**FIGURE 8**

Plot of target detections (blue dots) and corresponding uncertainty values (blue squares) associated with GPS track of the *Maas Trader* (solid aqua line). The panels from top to bottom are range (km), radial velocity (m/s), and bearing (degrees clockwise north). The uncertainty values for each measurement are shown as the height of each blue box; the length of the FFT is the width of the box. (Color versions of figures available online at: <http://www.ingentaconnect.com/content/mts/mts/2011/00000045/00000003>.)



Did the operators of the vessel stop transmitting the signal, or were the receivers unable to record the signal? The radar was able to make detections on the vessel coincidental with the AIS data. If we assume that the vessel maintained its course and the radial velocity maintained its rate of change, then the radar did indeed make the additional detections of the vessel as clearly shown in Figure 9.

### Tanker *Joelmare*

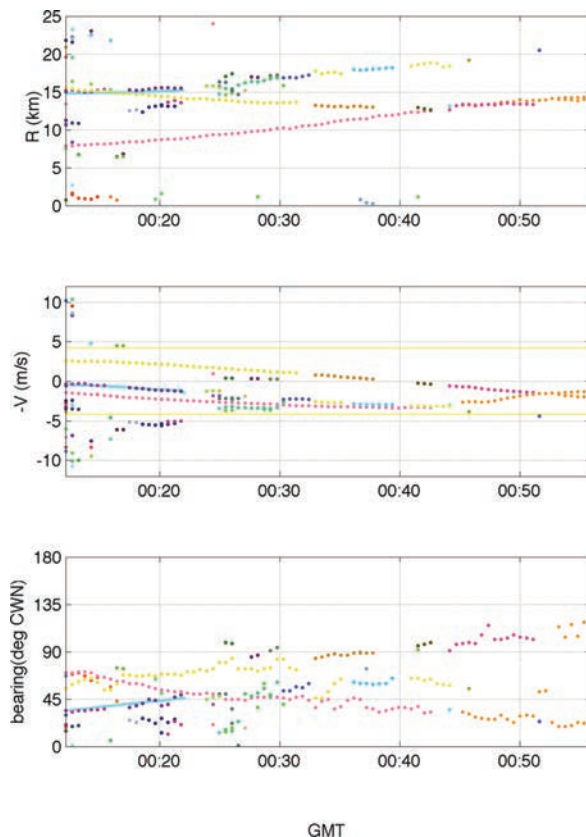
The *Joelmare*, IMO Ship No. 9288019, is a tanker with a length of 228 m and a beam of 32 m. The tanker *Joelmare* was exiting New York Harbor but then turned around and headed back into the harbor. The radar was able to detect the vessel 34% of the time with the Median background and 16% of the time using the IIR background. We propose two explanations as to why the radar did not detect this vessel very well. First, from Figure 7: The radial velocity of the vessel was noisiest of all the vessels. This lack of a constant radial velocity would spread the energy of the returned signal over several Doppler bins. This would cause the signal to not be detected, because its amplitude falls below the threshold set in the software. The second reason as to why the radar did not detect this vessel was that the vessel was north-northeast of the radar site, and the signal had to propagate over large sections of land that attenuated the signal in those directions.

### Cargo Container *Maas Trader*

The *Maas Trader*, IMO Ship No. 9308625, has a length of 139 m, a beam of 23 m, and a gross tonnage of 9981. More particulars on this vessel as well as the *Dolphin* are given in Table 8.

**FIGURE 9**

Plot of target detections for range, range rate, and bearing. The solid aqua line from 00:10 to 00:23 GMT shows the path of the *MOL Efficiency* from the AIS signal. There are additional detections past 00:23 on the figure, but the AIS data were not available to compare with the radar detections. (Color versions of figures available online at: <http://www.ingentaconnect.com/content/mts/mts/2011/00000045/00000003>.)

**TABLE 8**

Characteristics of vessels detected in this study.

Vessel Characteristic	<i>Maas Trader</i>	<i>Dolphin</i>	<i>MOL Efficiency</i>	<i>Joelmare</i>
MMSI No.	237956000	366920980	351166000	477738400
IMO No.	9308625	7319010	9251365	9288019
Type	Cargo	Tug	Cargo	Tanker
Length (m)	139	41	294	228
Beam (m)	23	6	32	32
Hull type	Single	Single	NA	NA
Gross tonnage	9981	198	NA	NA
Depth (m)	11.8	5	NA	NA
Draught (m)	8	4.25	12.1	6.6
Freeboard (m)	3	0.75	NA	NA
Hull material	Steel	Steel	NA	NA

NA stands for "not available."

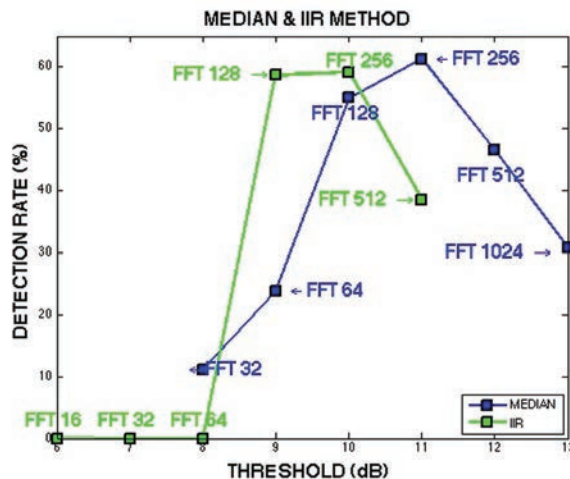
The authors were unable to find the height above the water for any of the vessels detected. The cargo container *Maas Trader* was heading south in the Barnegat shipping lane for this test. The radar at Sea Bright had the best detection rate of 70% using the IIR background and 65% with the Median background. Both of these cases occurred with the lowest threshold and yielded the highest number of false positives. It would be up to a potential user of the detection files to determine where the threshold should be set. If the detection files were to be passed on to a tracker, the performance of the data in the tracker could help determine what the threshold level should be. Another option is to run all combinations of FFT length and threshold and let a tracker determine which detections are authentic and which ones are false. The radar was not able to detect the vessel at 00:40. This was due to the fact that the vessel was crossing through the zero Doppler area, where there are large echoes from stationary objects. A plot of the FFT length and threshold combinations versus detection rate, which is a summary of Tables 4 and 5 for the *Maas Trader* test case, is given in Figure 10. A peak in the detection rate is found between the 128- and 256-point FFT. With a 2-Hz sweep, this converts to a 1- to 2-min averaging period as optimal for the detection of these vessels with the HF radar.

### Tugboat *Dolphin*

The *Dolphin*, IMO Ship No. 7319010, has a length of 41 m, a beam of 10 m, and a gross tonnage of 198. The tugboat *Dolphin* was heading north into New York Harbor inside of the Barnegat shipping lane. Figure 4 shows that this is a heavily transited

**FIGURE 10**

Response of detection rate to the variance of FFT length and threshold level.



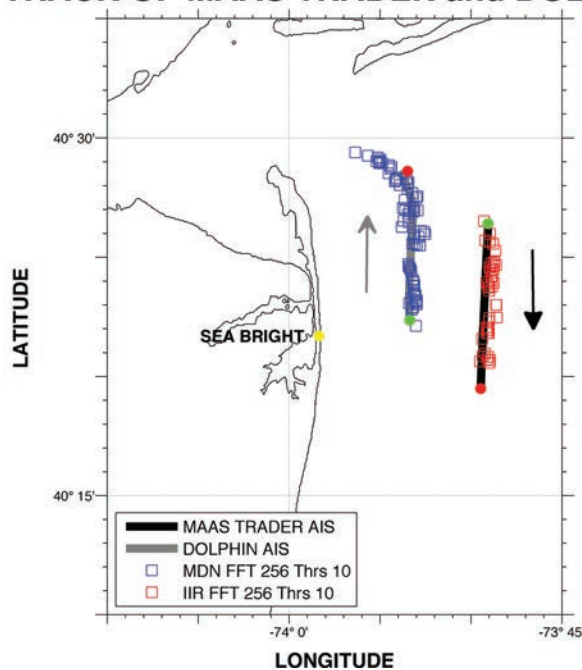
route as well. The Sea Bright radar had the highest detection rate on this vessel with a 92% using the IIR background and 93% using the Median background. The vessel had a large

superstructure, which made it an ideal target for the radar. The best case detections from the *Dolphin* and *Maas Trader* were placed on a map in Figure 11.

**FIGURE 11**

Detections of the *Maas Trader* (IIR background, 256-point FFT, and 10-dB threshold) and *Dolphin* (median background, 256-point FFT, and 10-dB threshold) overlaid on the path of the vessel from GPS/AIS.

**TRACK OF MAAS TRADER and DOLPHIN**



## Summary

A case study has been performed using a SeaSonde HF radar to detect vessels at sea in a dual-use mode. The selected 13-MHz HF radar that operates within the MARCOOS and provides radial current data to the NOAA National HF Radar Network simultaneously detected the speed and location of several ships at sea. The detections made with the HF radar were checked against the GPS position of the target sent via the AIS system. An optimal integration time for this type of radar with this class of vessel is between 1 and 2 min. The detection rates for some vessels were above 90%. Lower thresholds resulted in higher detection rates but also led to higher false alarm rates. Overall, the median background performed better than the IIR background, but there were instances where the IIR background was the best.

One benefit of HF systems for vessel detection/tracking is that they provide over-the-horizon detection capability (Khan et al., 1994). The systems being developed and evaluated within the 5-MHz and 13-MHz bands regularly see vessels between 50 and 110 km. However, the focus of this paper was on the optimal processing parameters that would enable the best detections. Because of this, the authors focused on vessels that were close to shore and would provide the most signal to test these parameters without introducing other parameters from the radar equation. The authors will, in future work, use these optimal parameters to test the range limits of the vessel detection system as a separate study.

A significant finding was that the same targets were seen by the detection algorithm simultaneously, at different



FFT/coherent-integration times, with different thresholding and back-grounds. Thus, one is not forced to preselect a fixed processing parameter suite. A properly optimized association algorithm (which is under development) would search for detections of the same vessel among all of the output combinations and thereby yield a much improved detection. This would increase the detection rate seen by an individual look of 90%, for example, to perhaps 98%, while reducing the overall false alarm rate.

This offers the opportunity to convert the National HF Radar Network into a dual-use system that would provide surface currents to the U.S. Coast Guard as well as provide wide area surveillance in the maritime domain to the Department of Homeland Security.

## Acknowledgment

This material is based on work supported by the U.S. Department of Homeland Security under Award No. 2008-ST-061-ML0001.

The views and conclusions contained in this document are those of the authors and should not be interpreted as necessarily representing the official policies, either expressed or implied, of the U.S. Department of Homeland Security.

## Lead Author:

Hugh J. Roarty  
Coastal Ocean  
Observation Laboratory  
Institute of Marine and  
Coastal Sciences  
Rutgers University  
New Brunswick, NJ 08901  
Email: hroarty@marine.rutgers.edu

## References

**Barrick, D.** 1972. First-order theory and analysis of MF/HF/VHF scatter from the sea. *IEEE Trans Antennas Propag.* 20(1):2-10. doi: 10.1109/TAP.1972.1140123.

**Chant, R.J., Glenn, S.M., Hunter, E., Kohut, J., Chen, R.F., Houghton, R.W., ... Schofield, O.** 2008. Bulge formation of a buoyant river outflow. *J Geophys Res.* 113(C1):C01017.

**Department of Homeland Security Science and Technology.** 2009. High-Priority Technology Needs. Washington, D.C. 24 pp. Available at: [http://www.dhs.gov/xlibrary/assets/st\\_high\\_priority\\_technology\\_needs.pdf](http://www.dhs.gov/xlibrary/assets/st_high_priority_technology_needs.pdf).

**Glenn, S.M., & Schofield, O.** 2009. Growing a distributed ocean observatory: Our view from the COOL room. *Oceanography.* 22(2):128-45.

**Glenn, S.M., & Schofield, O.M.E.** 2002. The New Jersey shelf observing system. *OCEANS '02 MTS/IEEE.* 3:1680-7.

**Gong, D., Kohut, J.T., & Glenn, S.M.** 2009. Seasonal climatology of wind-driven circulation on the New Jersey shelf. *J Geophys Res.* 109(C7):C07S07.

**Interagency Working Group on Ocean Observation.** 2009. A Plan to Meet the Nation's Needs for Surface Current Mapping. Washington, D.C. 64 pp.

**International Maritime Organization.** 2006. Automatic Identification Systems. London: IMO Publishing. 102 pp. Available at: [http://www.ioos.gov/library/surfacecurrentplan9\\_3lowres.pdf](http://www.ioos.gov/library/surfacecurrentplan9_3lowres.pdf).

**Khan, R., Gamberg, B., Power, D., Walsh, J., Dawe, B., Pearson, W., & Millan, D.** 1994. Target detection and tracking with a high frequency ground wave radar. *Journal of Oceanic Engineering.* 19(4):540-8.

**Kohut, J.T., & Glenn, S.M.** 2003. Improving HF radar surface current measurements with measured antenna beam patterns. *J Atmos Oceanic Technol.* 20(9):1303-16. doi: 10.1175/1520-0426(2003)020<1303:IHRSCM>2.0.CO;2.

**Roarty, H.J., Barrick, D.E., Kohut, J.T., & Glenn, S.M.** 2010a. Dual-use compact HF radars for the detection of mid- and large-size vessels. *Turk J Electr Eng Comput Sci.* 18(3):373-88.

**Roarty, H.J., Glenn, S.M., Kohut, J.T., Gong, D., Handel, E., Rivera Lemus, E., ... Seim, H.** 2010b. Operation and application of a regional high-frequency radar network in the Mid-Atlantic Bight. *Mar Technol Soc J.* 44(6):133-45.

**Rossby, T., & Gottlieb, E.** 1998. The Oleander Project: Monitoring the variability of the gulf stream and adjacent waters between New Jersey and Bermuda. *Bull Am Meteorol Soc.* 79:5-18. doi: 10.1175/1520-0477(1998)079<0005:TOPMTV>2.0.CO;2.

**Ruck, G.T., Barrick, D.E., Stuart, W.D., & Krichbaum, C.K.** 1970. Radar Cross Section Handbook. New York: Plenum Press. 949 pp.

**Temll, E., Otero, M., Hazard, L., Conlee, D., Harlan, J., Kohut, J., ... Lindquist, K.** 2006. Data management and real-time distribution in the HF-radar national network. In: *OCEANS 2006 MTS/IEEE Proceedings*, pp. 1-6. Boston, MA. doi: 10.1109/OCEANS.2006.306883.



# Evaluation of two algorithms for a network of coastal HF radars in the Mid-Atlantic Bight

Josh Kohut · Hugh Roarty · Evan Randall-Goodwin ·  
Scott Glenn · C. Sage Lichtenwalner

Received: 19 September 2011 / Accepted: 2 March 2012 / Published online: 29 April 2012  
© The Author(s) 2012. This article is published with open access at Springerlink.com

**Abstract** The National High Frequency (HF) Surface Current Mapping Radar Network is being developed as a backbone system within the U.S. Integrated Ocean Observing System. This paper focuses on the application of HF radar-derived surface current maps to U.S. Coast Guard Search and Rescue operations along the Mid-Atlantic coast of the USA. In that context, we evaluated two algorithms used to combine maps of radial currents into a single map of total vector currents. In situ data provided by seven drifter deployments and four bottom-mounted current meters were used to (1) evaluate the well-established unweighted least squares (UWLS) and the more recently adapted optimal interpolation (OI) algorithms and (2) quantify the sensitivity of the OI algorithm to varying decorrelation scales and error thresholds. Results with both algorithms were shown to depend on the location within the HF radar data footprint. The comparisons near the center of the HF radar coverage showed no significant difference between the two algorithms. The most significant distinction between the two was seen in the drifter trajectories. With these simulations, the weighting of radial velocities by distance in the OI implementation was very effective at reducing both the distance between the actual drifter and the cluster of simulated particles as well as the scale of the search area that encompasses them. In this study, the OI further reduced the

already improved UWLS-based search areas by an additional factor of 2. The results also indicated that the OI output was relatively insensitive to the varying decorrelation scales and error thresholds tested.

**Keywords** Coastal ocean processes · HF radar · Ocean observing systems · Remote sensing

## 1 Introduction

Saving lives at sea and on beaches is a United States Integrated Ocean Observing System (IOOS) priority that is supported by a Memorandum of Understanding between the National Oceanic and Atmospheric Administration (NOAA) and the United States Coast Guard (USCG). Nationally, the Coast Guard saves an average of 14 lives each day. Unfortunately, another three lives a day are lost ([http://www.uscg.mil/hq/cg5/cg534/sarfactsinfo/USCG\\_SAR\\_Stats.asp](http://www.uscg.mil/hq/cg5/cg534/sarfactsinfo/USCG_SAR_Stats.asp)). To reduce the lives lost, the critical USCG need is to optimize search and rescue (SAR) operations to minimize search time (Arthur Allen, personal communication). The USCG decision support tool for search and rescue cases is the Search and Rescue Optimal Planning System (SAROPS). SAROPS uses observed or predicted surface wind and surface current fields from the USCG's Environmental Data Server (EDS) to predict the trajectories of floating objects. During an actual event, a cluster of typically 5,000 virtual objects is deployed in the EDS provided surface wind and current fields and allowed to drift over time (Spaulding et al. 2006). Based on the distribution of the predicted cluster, the tool helps search planners coordinate the appropriate search strategy given available assets. Environmental input fields include in situ and remote observations and numerical and statistical forecasts.

---

Responsible Editor: Oyvind Breivik

This article is part of the Topical Collection on *Advances in Search and Rescue at Sea*

---

J. Kohut (✉) · H. Roarty · S. Glenn · C. S. Lichtenwalner  
Rutgers, The State University of New Jersey,  
New Brunswick, NJ, USA  
e-mail: kohut@marine.rutgers.edu

E. Randall-Goodwin  
University of California Santa Cruz,  
Santa Cruz, CA, USA



The USCG and the ocean observing community have worked to evaluate the value of high frequency (HF) radar-derived surface currents within SAROPS. These studies have shown that the time series of mapped surface currents provided by regional scale HF radar networks reduce search areas by a factor of 3 (O'Donnell et al. 2005; Ullman et al. 2003; Roarty et al. 2010). If these surface currents have lower uncertainties, there is less dispersion in the cluster, a smaller more accurate search area, and greater likelihood for success.

Coordinated through the U.S. IOOS, the Mid-Atlantic Regional Association Coastal Ocean Observing System (MARACOOS) has evaluated the application of these data and provided estimates of uncertainty for incorporation into SAROPS (O'Donnell et al. 2005; Roarty et al. 2010; Ullman et al. 2003). The 35-site MARACOOS network is a triple-nested HF radar network that covers the continental shelf between Cape Hatteras, NC and Cape Cod, MA with higher resolution coverage nearshore and into the estuaries. Since the first sites were deployed in 1998, there have been evaluations to determine the optimal system configuration and associated vector uncertainty in the 5-, 13-, and 25-MHz bands (Kohut and Glenn 2003; Kohut et al. 2006; O'Donnell et al. 2005; Roarty et al. 2010). These frequencies cover the scales of the mid and outer shelf, inner shelf, and harbors/estuaries, respectively. Based on this work, in May of 2009, the MARACOOS HF radar network became the first to support the operational SAROPS decision support tool. To maintain this operational status within SAROPS, the surface current data and associated forecasts must continue to meet quality standards defined by the Coast Guard.

In the USA, there is now an effort to expand the operational support of SAROPS beyond the Mid-Atlantic Bight to the national scale (Harlan et al. 2010). In that process, there is currently an evaluation to determine the optimal processing suite to maintain a national surface current mapping product that meets USCG quality standards. In this context, we use the HF radar network in the Mid-Atlantic Bight (MAB) to evaluate two different algorithms that both combine radial component vectors from an array of coastal stations into hourly total vector surface current maps. This evaluation is enabled through a partnership between the USCG Research and Development Center, the USCG Office of Search and Rescue, and MARACOOS. It is based on two available combination algorithms, the established unweighted least squares (UWLS) (Lipa and Barrick 1983) already providing surface currents to the EDS to support operational SAR in the MAB and the more recently adapted optimal interpolation (OI) (Bretherton et al. 1976; Kim et al. 2007). There are two main objectives of this study. The first is to evaluate the recently adapted OI-derived surface current maps with parameter inputs consistent with the existing UWLS implementation. The control for this evaluation will be the already implemented UWLS product. Since the OI implementation is new to the HF radar community, the

second objective is to quantify the sensitivities of the OI-derived surface current maps to varying parameter inputs. For this objective, the base OI solution evaluated in objective 1 will serve as the control and be compared to other OI solutions with varying spatial decorrelation scales and error thresholds. Both objectives will be discussed in the context of USCG search and rescue using in situ current estimates and drifter trajectories. Background information and specific methods used are discussed in Sections 2 and 3. Expected differences due to known environmental variability in the surface current fields and evaluation results are presented in Sections 4 and 5. Finally, Sections 6 and 7 discuss the results and general conclusions.

## 2 HF radar processing

### 2.1 HF radar surface current processing

HF radar systems, typically deployed along the coast, use Bragg peaks within a transmitted signal (3–42 MHz) scattered off the ocean surface to calculate radial components of the total surface velocity at a given location (Barrick et al. 1977). Peaks in the backscattered signal are the result of an amplification of a transmitted wave, at grazing incidence, by surface gravity waves with a wavelength equal to half that of the transmitted signal (Crombie 1955). The frequency of the backscattered signal will be Doppler-shifted depending on the velocity of the scattering surface. Using the linear wave theory, the phase speed of the surface waves can be separated from the total frequency shift, leaving only that shift due to the surface current component in the direction of the antenna. Over a given time period, sites along the coast generate radial maps of these component vectors with typical resolutions on the order of 1–6 km in range and 5° in azimuth. The HF radar sites in the MARACOOS network are all SeaSonde direction finding systems manufactured by Codar Ocean Sensors (Barrick 2008). The direction finding radars use a three element receive antenna mounted on a single post to determine the direction of the incoming signals. The angular resolution, set in the processing, is 5° (Barrick and Lipa 1996; Teague et al. 1997). Since the Doppler shift can only resolve the component of the current moving toward or away from the site, information from at least two sites must be geometrically combined to generate total surface current maps.

The main source of error in the geometric combination from radials to totals is based on the geometry of the network (Chapman et al. 1997). The contribution of the geometric error is based on the relative angles between the radial component vectors at the total grid point, commonly referred to as the geometric dilution of precision (GDOP). The geometric error increases as the angle between radials from contributing sites moves away from orthogonality.

In HF radar networks operating around the world for the past few decades, the most commonly used algorithm to combine maps of radial velocities into total vector currents is UWLS (Lipa and Barrick 1983). The coverage of the UWLS surface current maps is dependent on the density of available radial components measured at each site. Due to variations in signal-to-noise based on either the electromagnetic interference or sea state conditions, the available radial data can vary in both space and time. To overcome these data gaps, various interpolation techniques have been applied to HF radar total vector fields. These algorithms that include 2DVAR (Yaremchuk and Sentchev 2009), normal modes (Lipphardt et al. 2000), open modal analysis (Kaplan and Lekien 2007), and statistical mapping (Barrick et al. 2012; O'Donnell et al. 2005) have largely been applied to the UWLS surface current maps after the UWLS combination. Recently, Kim et al. (2007) introduced a method that interpolates data as part of the combination step from radial component vectors to total vector maps. This approach weights radials based on the decorrelation scale of the observed current fields. Details on both the UWLS and OI algorithms as implemented in this study are described in Sections 2.2 and 2.3.

## 2.2 Unweighted least squares

UWLS is the most commonly used algorithm to combine fields of radial surface current components from a network of shore sites into a total vector map over a fixed grid (Lipa and Barrick 1983). The UWLS calculation provides a total current vector that minimizes the error between the radial components of the calculated total vector and the measured radial velocities. The algorithm assumes that all vectors within a defined area relative to the grid point have an equal weight in the calculation. The UWLS makes no assumption on the signal variance of the surface currents and assumes that the correlation function of the surface currents within this radius is unity and zero outside. The contribution to the GDOP error in the implementation of the UWLS is quantified as a mapping error (Gurgel 1994). For each total vector estimate, there is an associated mapping error value that is scaled based on the contribution to GDOP. The larger the mapping error value, the more significant the error due to geometry is in the resulting total vector. For this study, and consistent with the UWLS implementation in the national network for the 5-MHz radial data, total vectors were calculated with radial components that were within a radius of 10 km from each grid point and a mapping error threshold of 1.5. If any UWLS-derived total vector had an error threshold above 1.5, it was not considered in the analysis. This is consistent with quality standards already governing the data going to the EDS and SAROPS and the national network (Harlan et al. 2010; Roarty et al. 2010).

## 2.3 Optimal interpolation

The technique for the optimal interpolation of oceanographic data was derived from the Gauss–Markov theorem (Bretherton et al. 1976). This technique was more recently adapted to calculate total vector surface currents from available HF radar radial component observations (Kim et al. 2007). The OI requires a quantification of the surface current signal variance and error measurement variance. For our study, the signal variance is the expected variance of the observed surface current field and the error measurement variance is the uncertainty assigned to the input radial velocities. It also requires a decorrelation length scale in the east and north direction to define the correlation function of the surface currents. We define a base OI run for this study that uses a defined decorrelation scale of 10 km. This is consistent with the scale of the radius used as a community standard in the UWLS algorithm.

Radial velocities are weighted based on an exponential decay defined by the decorrelation scales in the north ( $S_y$ ) and east ( $S_x$ ) directions. Vectors closer to the grid point are weighted more than those further away.  $S_x$  and  $S_y$  set the length scale of the decay in this weight. Radials that fall outside this scale are weighted much less than those closer to the grid point. Unlike the UWLS in which all radials within the radius are weighted 1 and included in the calculation, the OI can use vectors outside the defined length scale. For example, if a radial vector were 10 km from the grid point, it would be weighted as 1 for the UWLS and 0.37 for the OI. Another vector 20 km from the grid point would be weighted 0 for the UWLS and 0.14 for the OI. Therefore, the OI will use radial data from further away than the UWLS, but these vectors will be weighted significantly less. The other input parameters for the OI algorithm are (1) the signal variance of the surface current fields and (2) the data error variance of the input radial velocities. The signal variance for all OI solutions was set to  $420 \text{ cm}^2/\text{s}^2$  for all grid points in the domain;  $420 \text{ cm}^2/\text{s}^2$  is representative of the typical conditions in the MAB with surface currents on the order of 20 cm/s (Beardsley and Boicourt 1981; Dzwonkowski et al. 2009, 2010; Gong et al. 2010; Kohut et al. 2004). The data error variance is defined by Kim et al. (2007) as the sum of the average measurement uncertainty and the average standard error of the radial currents (Eq. 17, Kim et al. 2007). These two values are calculated from the input radials. The average measurement uncertainty is the mean of the uncertainty values reported with each radial velocity and the average standard error is calculated from radial velocities themselves. Applying Eq. 17 from Kim et al. (2007) to the radial data and associated uncertainties from each of the four sites considered in this study, the data error variance is  $66 \text{ cm}^2/\text{s}^2$  and held constant across the field. All OI solution sets evaluated in this study use a constant 420 and  $66 \text{ cm}^2/\text{s}^2$  for the signal variance and data error variance, respectively.

To test the sensitivity of the OI solution to varying decorrelation scales, we considered a second parameter set that stretched  $S_y$  along the isobaths. In the MAB, the decorrelation scales tend to be longer along the isobaths (Beardsley and Boicourt 1981; Kohut et al. 2004). Therefore, the decorrelation scale for the second run was elongated by a factor of 2.5 and rotated along the isobaths ( $S_x=10$ ;  $S_y=25$ ). To do this, we rotated the coordinate system that defines  $S_x$  and  $S_y$  in the along-isobath direction and assigned the along-isobath component ( $S_y$ ) a value of 2.5 times larger than  $S_x$ . The algorithm uses these parameters to determine the weight of the individual radials going into the combination. So the result is a weight based on decorrelation scales oriented along isobaths. The along-isobath direction was defined as  $31^\circ$  clockwise from true north, consistent with previous generalizations of the topography of the central MAB (Kohut et al. 2004).

With the OI algorithm, the geometric contribution to the error of the total vector estimate is quantified as individual error estimates for each component. For each component of the total current vector, there is an associated normalized uncertainty. The threshold for the base OI run was set to 0.95. This threshold was selected to be consistent with the implementation of the OI algorithm in the Southern California Bight (Sung Yong Kim, personal communication). The Southern California system was the only known real-time implementation of the OI algorithm at the time of our study. If any total vector had an uncertainty greater than 0.95 in either the east or north component, it was not considered in the evaluation. The sensitivity of the OI results to this threshold was tested with a lower value of 0.6. This second value was selected based on the balance between data quality and data coverage (Section 5.2 of this manuscript). In summary, there will be four OI runs tested. The first with a decorrelation defined as  $S_x=S_y=10$  and an error threshold of 0.95 will be compared to the UWLS solution with a radius of 10 km and a mapping error threshold of 1.5 to meet our stated objective 1. For objective 2, an additional three OI runs with varying decorrelation scales ( $S_x=10$ ;  $S_y=10$ ; and  $S_x=10$ ,  $S_y=25$ ) and error thresholds (0.95 and 0.6) will quantify the sensitivity of this recently implemented combination algorithm to these settings.

### 3 Data

#### 3.1 HF radar

The HF radar data were provided by the MARACOOS network, a nested array of 5 MHz long range systems, 13 MHz standard range systems, and 25 MHz high resolution systems (Roarty et al. 2010). The nested coverage stretches across the shelf from Cape Cod, MA to Cape Hatteras, NC with higher

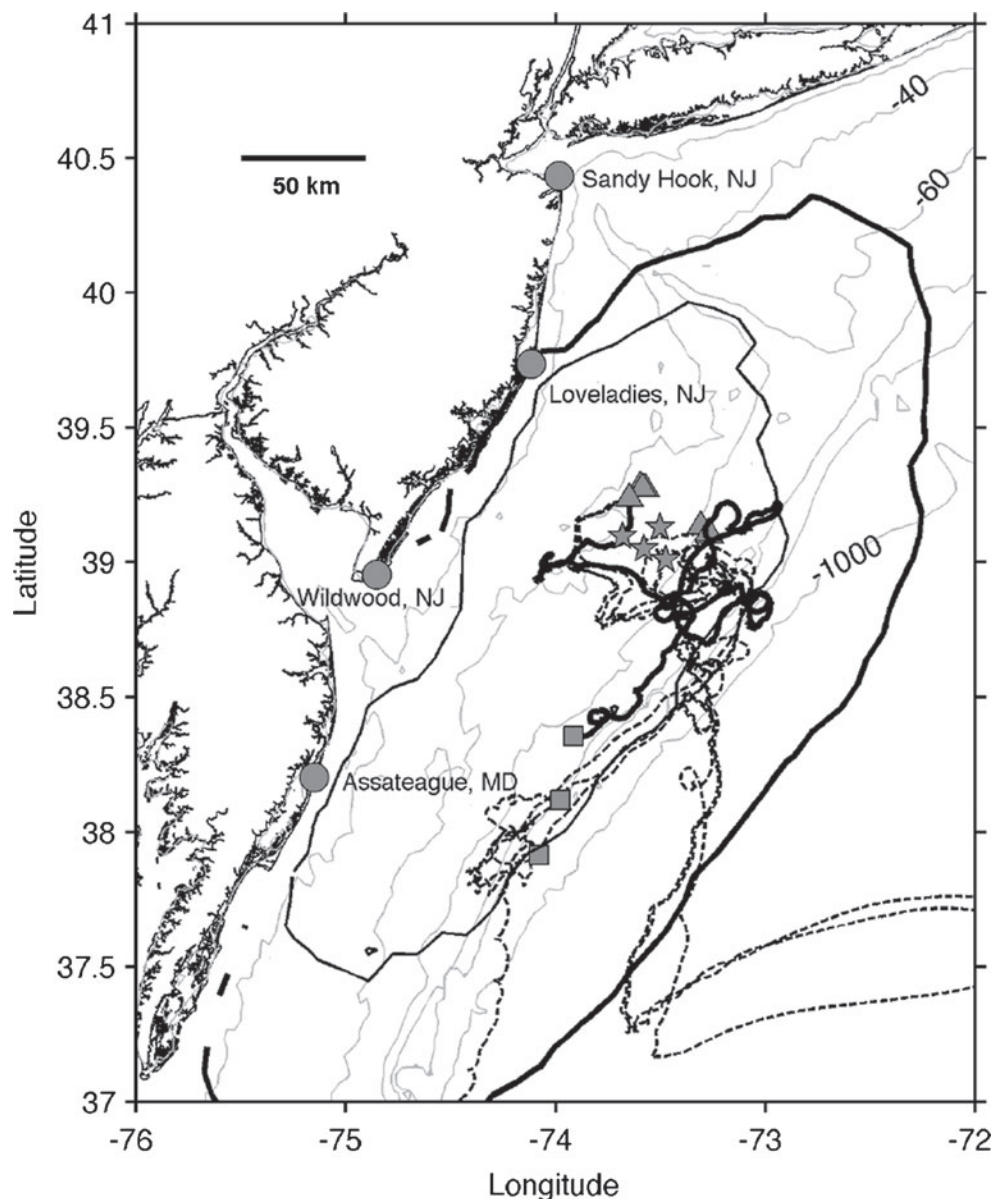
resolution into the estuaries. This study focuses on the radial data from four 5 MHz sites in the central MAB in Sandy Hook, NJ; Loveladies, NJ; Wildwood, NJ; and Assateague, MD between February 20, 2007 and April 30, 2007 (Fig. 1). Each remote site was operated with the Quality Assurance/Quality Control recommendations from the MARACOOS operators and the Radiowave Operators Working Group community. These are the same data provided to the national HF radar server at the NOAA National Data Buoy Center (<http://hfradar.ndbc.noaa.gov/>). Every hour, the available radial velocities are combined into a single total vector map on the national network 6-km grid (Temll et al. 2006). A total vector was only generated if at least three radial velocities from at least two remote sites were available to the combination algorithm. For each grid point, the available radial velocities within the defined area were combined into a single total vector with both the UWLS and OI algorithms described in Section 2. For the comparison to the acoustic Doppler current profiler (ADCP) moorings, the UWLS and OI totals were calculated on a grid that exactly matched the mooring locations. For drifter estimated current and trajectory comparisons, the OI and UWLS totals calculated on the national 6-km grid were spatially interpolated to each drifter position at each time step.

#### 3.2 Acoustic Doppler current profilers

Four ADCPs were deployed off the coast of New Jersey as part of the National Science Foundation supported Mid-Shelf Front Experiment (Ullman et al. 2012). They were deployed on January 13, 2007 and recovered 83 days later on April 6, 2007. Three of the moorings were deployed in a cross-shelf line approximately 10 km apart (Fig. 1). A fourth mooring was deployed 11 km upshelf of this cross-shelf array. Since the offshore mooring was recovered from a different location than the original deployment, special processing steps were taken with the current profile time series. The data record for this mooring indicated that on February 12th, about 32 days into the deployment, there was an hour of bad data. This was followed by 53 days of good data. Scrapes on the unit seen after recovery indicate a likely strike, staying upward looking throughout the event. Based on the deployment and recovery locations, it is estimated that the ADCP moved approximately 2.4 km. Since this is within the approximate 20-km scale of the HF radar measurement cell, these data were merged and treated as one time series. The position was the duration-weighted mean of the deployment and recovery locations. All units were configured with 1-m bins in the vertical. Sampling was set to collect a 10-min ensemble each hour (Codiga 2007). These hourly data were averaged into 3-h files outputted every hour to be consistent with the sampling and averaging of the HF radar processing.



**Fig. 1** Map of the study area showing the location of the HF radar stations (circles), the ADCPs (stars), and track of the February–March drifter (thick black line) and April drifters (dashed lines). The isobaths (meters) are shown as faint gray lines. All drifter tracks start at the triangles and end at the squares. The total vector coverage for the UWLS solutions is shown for the 50 % (thick black) and 90 % (thin black) contours



### 3.3 Drifters

All drifters used in this evaluation were self-locating data marker buoys (SLDMBs) provided by the USCG Research and Development Center. These drifters are drogued to 1-m depth with minimal surface expression to minimize wind drift (Allen 1996). The first deployment included two drifters released on February 24, 2007. Of the two drifters deployed, only drifter 43484, deployed inshore of the Mid-Shelf front (Ullman and Cornillon 1999), remained in the HF radar coverage (Fig. 1). This winter deployment overlaps the ADCP deployments providing a contrasting Eulerian and Lagrangian evaluation in regions of the HF radar footprint beyond the reach of the ADCP array. The second deployment of six

drifters began April 3, 2007. These six drifters remained primarily in the HF radar data footprint through the end of April (Fig. 1). While this second group of drifters did not overlap with the ADCP deployment, the larger cluster of drifters provided simultaneous observations across different regions of the HF radar data footprint. Throughout the deployment, velocities based on two drifter positions 1 h apart were calculated every half hour. Drifter-derived currents estimated every 30 min were averaged into 3-h files outputted every hour to be consistent with the sampling and averaging of the HF radar processing. Three of the drifters entered the Gulf-stream toward the end of the time series (43266, 43271, and 43325). For these three drifters, only the position data over the shelf were included in the evaluation.

### 3.4 Drifter trajectories

Drifter tracks were used to evaluate particle trajectories estimated from each algorithm. Each hour, we took the actual position of drifter #43484 as the initial condition for the particle release. This drifter was selected because most of its path is within the 90 % coverage contour of the HF radar data giving a longer time period with which to evaluate the trajectories (Fig. 1). The entire track of the drifter was split into 713 forty-eight-hour segments each beginning 1 h after the last. For each segment, we released 1,000 particles into the HF radar fields at the location of the actual drifter at time 0. The particles trajectories were then compared to the actual drifter track for the 48-h segment.

The motion of a particle in a two-dimensional velocity field is described by:

$$\frac{dr}{dt} = u(t, r) \quad (1)$$

Where  $r(x, y)$  is the position of the particle and  $u = (u, v)$  is the Eulerian velocity at position  $r$  and time  $t$ . The prediction of the particle trajectory was done by integrating Eq. (1) using a predictor-corrector scheme with the velocity given by:

$$u = U + u' \quad (2)$$

Where  $U$  was the spatially interpolated radar velocity derived from either the UWLS or OI algorithms to the particle location and  $u'$  is the contribution of the sub-grid scale variability and the measurement uncertainty. The model used to determine  $u'$  in this study was based on a random flight model (Ullman et al. 2006; Griffa 1996). The random flight turbulent parameters that we used to determine  $u'$  are shown in Table 1. The parameters are consistent with those calculated by Ullman et al. 2006 and used in the present application in SAROPS by the USCG. At each hour of each simulation, we calculated the location of the centroid of the particle cluster and the 95th percentile confidence region (Fig. 2). This confidence region was calculated by rank ordering the spatial bins, by frequency, of a two-dimensional frequency histogram of the final simulated particle locations (Ullman et al. 2006). In addition to the drifter trajectories, we also calculated the mean separation and 95th percentile separation of the actual drifter position relative to the initial drifter position for each 48-h segment. This position persistence scenario represents a search based on the last known position in the absence of surface current data.

**Table 1** Parameters used in the random flight model to determine particle trajectories

$\sigma_u$ (m/s)	$T_u$ (h)	$K_x$ (m <sup>2</sup> /s)	$\sigma_v$ (m/s)	$T_v$ (h)	$K_y$ (m <sup>2</sup> /s)
0.11	3.3	144	0.12	3.1	161

The processing and analysis metrics are consistent with those introduced in Ullman et al. (2006) and applied in Gong et al. (2010).

## 4 Expected differences between HF radar and in situ data

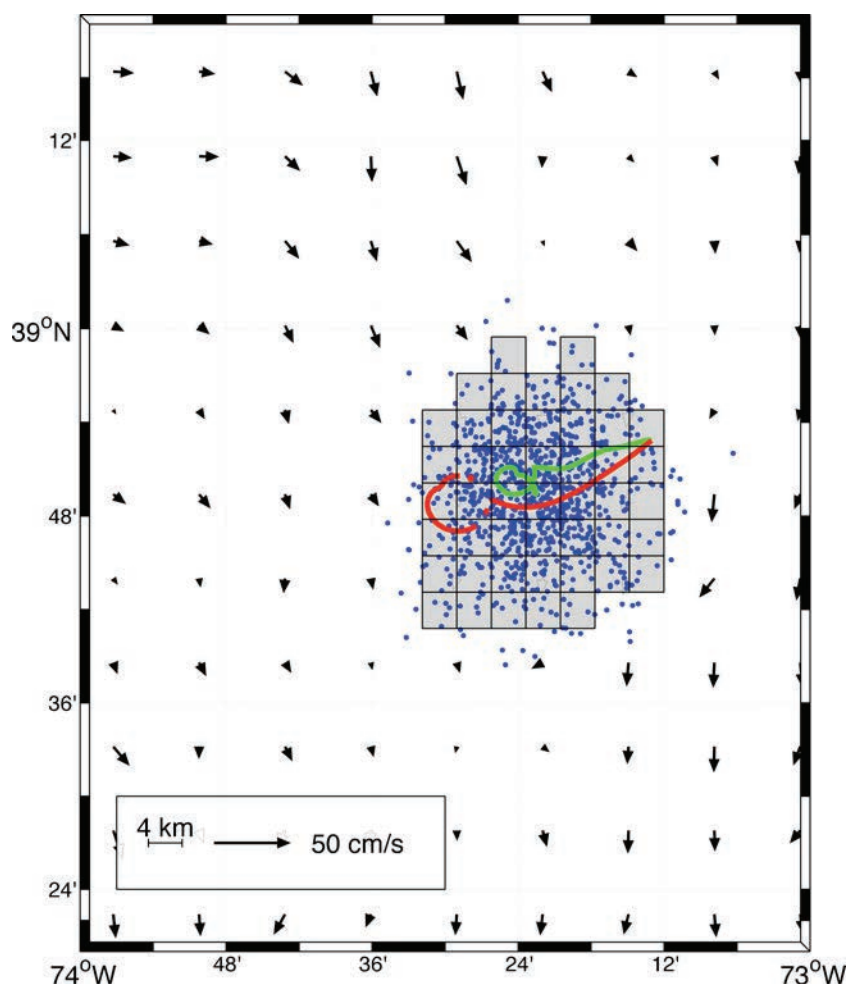
HF radar provides a unique measure of the surface current. Before any evaluation can be done to assess the quality of HF radar surface current estimates, the expected differences due to environmental variability must be quantified (Graber et al. 1997; Kohut et al. 2006; Ohlmann et al. 2007; Paduan et al. 2006). The temporal averaging of the drifter and ADCP velocities was consistent with the HF radar processing to remove bias from different temporal sampling and averaging. Due to significant differences in the HF radar, drifter, and ADCP sampling in the horizontal and vertical, the same cannot be accomplished through spatial averaging.

### 4.1 Vertical differences

Since the HF radar currents are based on the signal scatter off the surface gravity wave field, the measurement is limited to the upper portion of the water column influenced by the waves. Depending on the assumed velocity shear profile, the effective depth of the 5-MHz system is approximately 2.4 m (Stewart and Joy 1974). The moored ADCPs sampled a bin approximately 2.0 to 3.2 m deeper than this effective depth. The expected difference between the HF radar and ADCP observations will scale with the magnitude of the vertical shear between the effective depth and the depth of the ADCP measurement bin. Since the drifters are drogued to 1-m depth within the range of the HF radar measurement, the contribution of vertical shear to the observed differences is expected to be small.

The best measure of the vertical velocity shear that will contribute to observed differences between the ADCP surface bins and the HF radar observations at the time of this study were from the four moored ADCPs. For each ADCP, the velocity estimates from the bin closest to the surface were compared with the bin 3 m deeper. This depth range most closely matches the approximate distance from the surface HF radar measurement and the uppermost uncontaminated ADCP bin. This shallowest uncontaminated bin is defined as the shallowest bin without contamination from interaction with the surface. Given the ADCP frequencies and water depths, this bin was between 4.39 and 5.59 m below the surface for the four ADCPs. The root mean square (RMS) difference between these surface bins and the bins 3 m deeper was on average 2.1 cm/s in the east direction and 2.4 cm/s in the north direction. All values were between 1.9 and 2.9 cm/s with the square of the sample correlation coefficients ( $r^2$ ) all greater

**Fig. 2** Predicted particle locations (*blue dots*) using the OI currents 48 h after the start of the segment. The track of the centroid of the particles (*green*) and the actual drifter, SLDMB 43484 (*red*), is also shown. For reference, an instantaneous HF radar vector map is shown as overlaid black vectors



than 0.96. The complex correlation indicates that not only are the velocities through the upper water column correlated (correlation coefficients of 0.97–0.99), but for each mooring the deeper current direction most correlated with the surface was offset by less than  $1^\circ$ . These comparisons indicate that the contribution of vertical shear to the measured difference between HF radar and the moored ADCPs is 2–3 cm/s.

#### 4.2 Horizontal differences

Velocity shear in the horizontal contributes to the observed differences between HF radar and both the ADCP and drifter velocities. Again, the HF radar measurement is unique relative to the available in situ data in that it samples a spatial cell much larger than both the ADCP and individual drifters (Fig. 3). Given our range resolution of 5.85 km and azimuthal resolution of  $5^\circ$ , the spatial area of each radial velocity average scales with the range from the remote site. Ten kilometers from the site this area is approximately  $7 \text{ km}^2$  and grows to  $54 \text{ km}^2$  100 km from the site. In addition, both combination

algorithms use the spatially averaged radial velocities within a radius on the order of 10 km in the total vector calculation. Shear in the flow across the scales sampled by the HF radar, drifters, and ADCPs will contribute to the observed differences between their current observations. These shears have been shown to vary significantly in time and space and contribute to the observed differences between HF radar and in situ sensors (Kohut et al. 2006; Ohlmann et al. 2007).

Both the spatially separated array of ADCPs and clusters of drifters were used to quantify the horizontal shear in the surface velocity fields. There were three moorings deployed 10 km apart along a line perpendicular to the coast between the 40- and 60-m isobaths (Fig. 3). A fourth mooring was located 11 km upshelf along the same isobath as the center mooring in the cross-shelf line. The surfacemost bin of each mooring was compared to all other ADCPs to quantify horizontal differences across the scale of the array. For reference, the 10-km spacing is on the same order as the distance across adjacent range cells of the HF radar grid. The RMS differences between the surface bins of each ADCP were on the order of



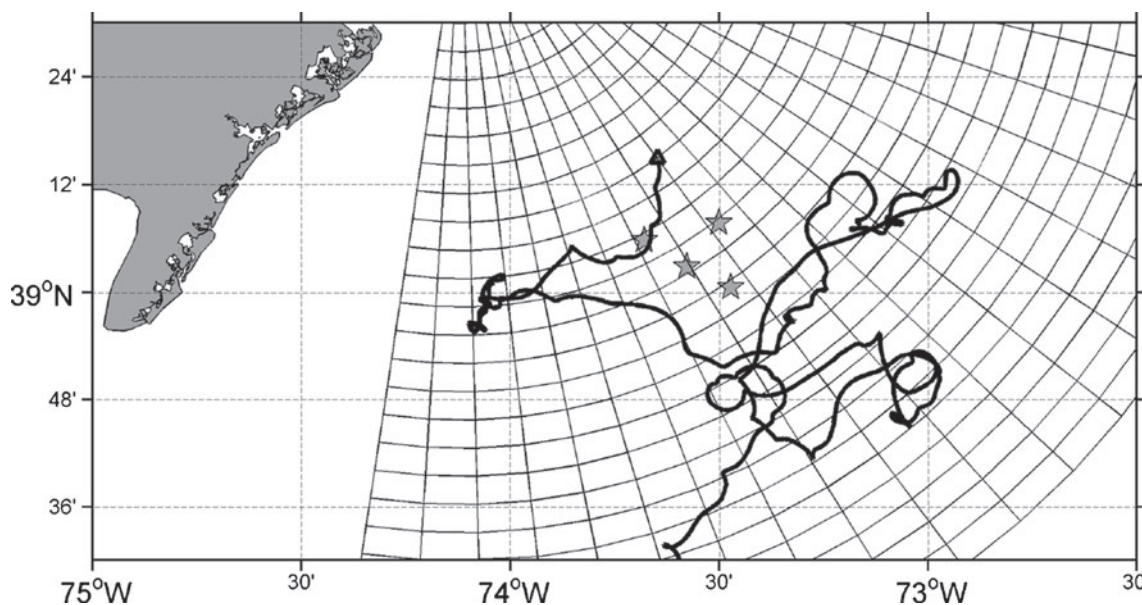


**Fig. 3** An expansion of the study site showing the location of the ADCPs (stars), the track of the February–March drifter (thick black lines), and the radial grid from the Loveladies, NJ HF radar coastal

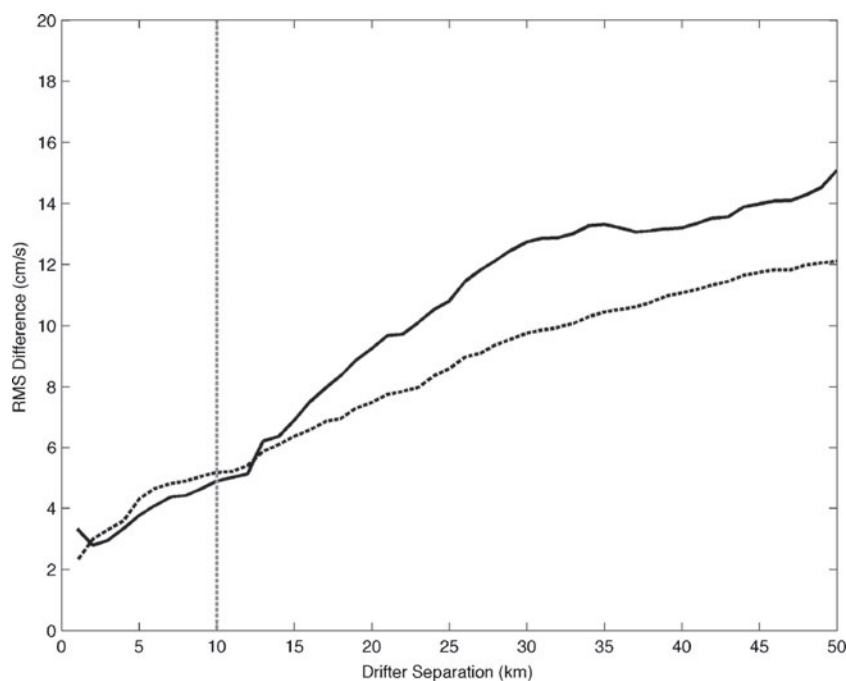
station (thin black lines). The triangle marks the deployment location of drifter #43484. For scale, the grid resolution is 5.8 km in range and 5° in azimuth

5–7 cm/s in the east direction and 8–10 cm/s in the north direction. The complex correlation shows that there is a strong correlation ( $r^2$  between 0.82 to 0.87) with angle offsets ranging from  $-5.9$  to  $4.4^\circ$ .

The cluster of drifters deployed in April of 2007 was also used to provide an estimate of the horizontal shear. Unlike the ADCPs, the drifters move throughout the footprint of the HF radar network and the separation between them varies throughout the deployment. In the April deployment, the

drifter separation ranged from 100 m to 100 km. At each 30-min time step, the current was estimated for each drifter in the cluster. From these time series of velocities, we calculated the RMS difference between drifters binned by range (Fig. 4). The RMS difference for a drifter separation of 10 km is based on all estimated velocity pairs from drifters between 0 and 10 km apart. As the distance between drifters increases so does the RMS difference. At the scale of the HF radar observation, the RMS difference in both the north and east velocity

**Fig. 4** RMS difference of the east (solid) and north (dashed) components of the estimated velocities for the drifters released in April 2007. All data between drifters within the distance plotted on the x-axis were used to determine the RMS difference



components is approximately 5 cm/s. This is consistent with the RMS difference determined from the ADCPs over a similar scale. As the distance between drifters grows toward 50 km, the RMS difference in each component reaches its maximum at 12–15 cm/s (Fig. 4).

The spatial contribution of known environmental variability is 5–10 cm/s based on the ADCP and drifter inter-comparison. This gives us a measured quantity for the horizontal shears as they impact the evaluation and the application of each algorithm. These expected differences indicate that the environmental shears, particularly in the horizontal, can be a significant contributor to observed differences in the comparisons between HF radar and the available in situ currents and should be considered in this evaluation.

## 5 Results

### 5.1 UWLS and OI comparisons

The ADCPs were deployed in a region of greater than 90 % HF radar coverage with good remote site geometry. A scatter plot of the velocities between the center ADCP (MSF-C) compared to the UWLS and the OI base run 1 is shown in Fig. 5. The statistics between the surface bin of the four ADCPs and the UWLS vectors had RMS differences that ranged between 6.9 and 8.5 cm/s in the *u* component and 7.6 cm/s and 8.8 cm/s in the *v* component (Table 2). These statistics are meant to summarize the comparison between the in situ and remote currents and do not themselves reveal the episodic nature of the data mismatches. The data coverage for all comparisons is referenced to a complete in situ time series so that 100 % coverage means that all in situ observations have a concurrent HF radar observation. The data coverage for each ADCP/UWLS comparison time series was between 82.7 % for the offshore ADCP and 92.9 % for the inshore ADCP with at least 764 data pairs in each evaluation series. The OI run compared to the UWLS is run 1 with  $S_x=S_y=10$  and an error threshold of 0.95. For these OI total vectors, both the *u* and *v* components are consistent with the UWLS with slightly higher RMS differences from 7.6 to 8.8 cm/s and from 7.6 to 9.4 cm/s, respectively (Table 2, runs 1 and 5). All of these evaluations were based on at least 839 comparison pairs with a higher data coverage compared to the UWLS runs ranging between 98.3 % for the offshore ADCP and 99.6 % for the central ADCP.

The drifter tracks crossed the 90 % coverage contours into regions of reduced HF radar coverage (Fig. 1). Scatter plots between drifter 43484 estimated currents and the UWLS and OI (run 1) currents are shown in Fig. 6. The comparison between this drifter and the UWLS totals was

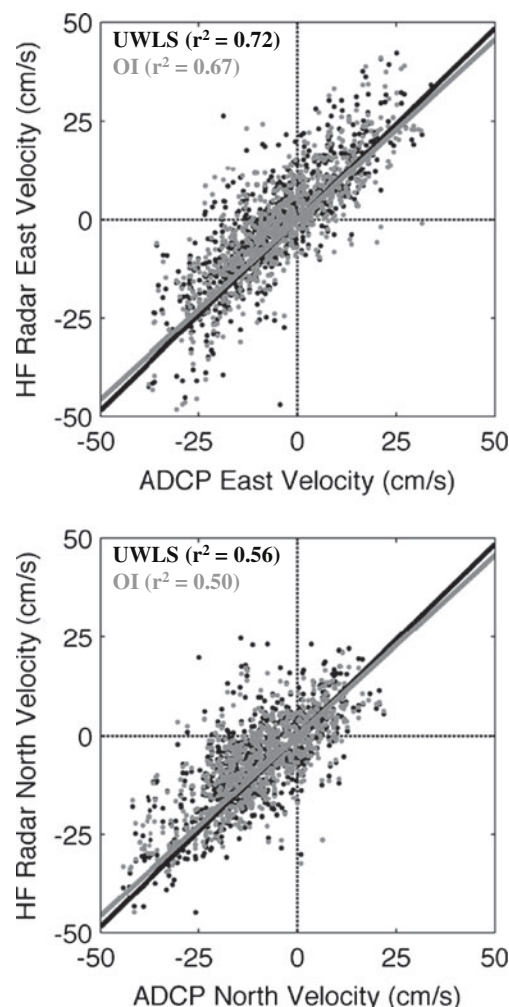


**Fig. 5** Scatter plots of the UWLS (black) and OI (gray) compared to ADCP MSF-C for the east (top panel) and north components (bottom panel)

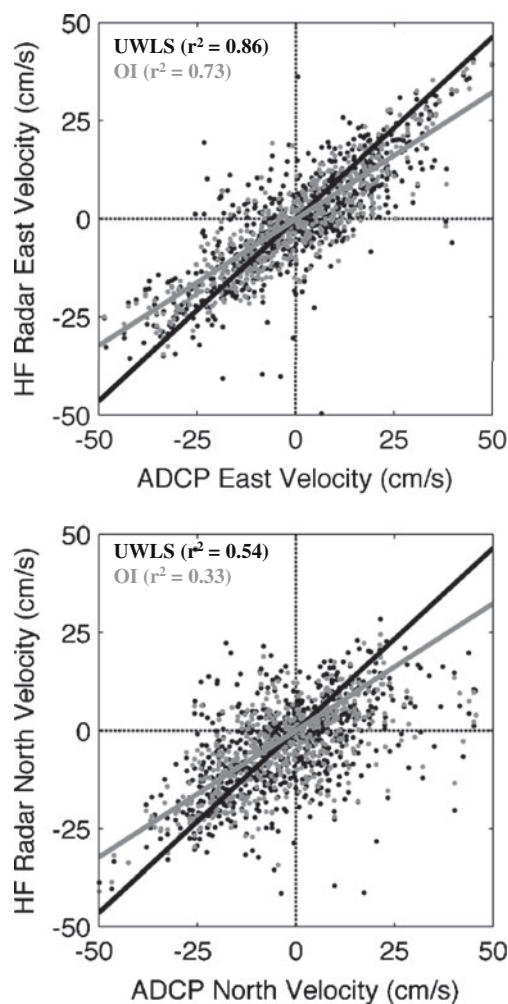
consistent with the ADCP evaluation with RMS differences of 7.2 and 9.7 cm/s in the *u* and *v* components, respectively. The coverage of the UWLS total vectors with the drifter, however, was significantly less with 418 data pairs (49.9 %). The OI total vectors compared to the same drifter had higher RMS differences of 9.3 and 12.6 cm/s in the *u* and *v* components, respectively. The coverage with the OI total vectors was significantly higher than the UWLS with 823 comparison pairs giving a data coverage of 98.3 %.

The April drifter tracks spent more time in regions of less than 90 % HF radar coverage. The spread in these tracks led to a significant variation in the comparison statistics. For the UWLS totals, the RMS difference ranged from 7.3 to 12.5 cm/s in the *u* component and 11.1 to 12.4 cm/s in the *v* component. The data coverage varied significantly between each drifter from 37.2 to 73.4 %. For the OI base run, the RMS differences were higher with a range of 9.4 to 12.4 cm/s in the *u* component and 11.6 to 14.4 cm/s in the *v* component. Like the February drifter, the percent coverage with the OI totals

**Table 2** Summary of error statistics between HF radar and the moored current meters

Run	$S_x$	$S_y$	Error criterion	MSF-I	MSF-C	MSF-O	MSF-U	MSF-I	MSF-C	MSF-O	MSF-U	MSF-I	MSF-C	MSF-O	MSF-U
				RMS-u				$r^2$ -u				%Cov			
1	10	10	0.95	8.70	8.77	8.01	7.58	0.72	0.67	0.67	0.71	98.6	99.6	98.3	98.6
2	10	25	0.95	8.68	8.53	8.03	7.52	0.72	0.69	0.67	0.72	98.7	99.8	98.7	98.7
3	10	10	0.6	8.63	8.79	7.66	7.54	0.73	0.67	0.70	0.72	94.7	93.5	91.3	93.1
4	10	25	0.6	8.63	8.53	7.96	7.50	0.72	0.69	0.68	0.72	96.9	97.3	95.4	96.9
5	UWLS		1.5	8.59	8.39	7.85	6.92	0.73	0.72	0.70	0.76	92.9	91.8	82.7	87.5
				RMS-v				$r^2$ -v				Num points			
1	10	10	0.95	7.57	9.41	9.04	8.83	0.64	0.50	0.55	0.52	911	910	908	911
2	10	25	0.95	7.45	9.31	9.14	8.69	0.65	0.51	0.55	0.53	912	912	912	912
3	10	10	0.6	7.46	8.89	8.46	8.37	0.65	0.54	0.61	0.56	875	855	844	860
4	10	25	0.6	7.42	8.97	8.91	8.58	0.65	0.53	0.57	0.54	895	889	881	895
5	UWLS		1.5	7.63	8.84	8.74	8.44	0.64	0.56	0.60	0.56	858	839	764	808

was significantly higher than the UWLS with a range across all April drifters between 55.7 and 96.7 %.

**Fig. 6** Scatter plots of the UWLS (black) and OI (gray) compared to drifter 43484 for the east (top panel) and north components (bottom panel)

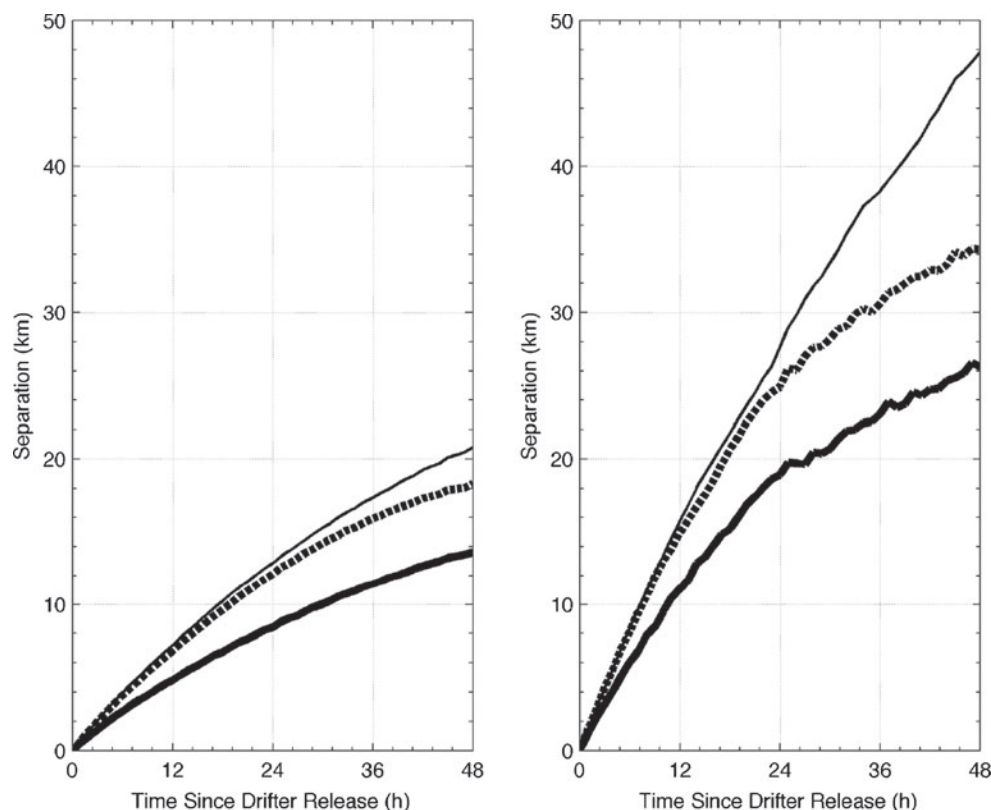
Drifter trajectories based on both the UWLS and OI base run solutions were compared to the actual track of drifter 43484. For each simulation up to 48 h, the distance between the centroid of the 1,000 simulated particles and the actual drifter location was calculated each hour (Fig. 7). The UWLS-based trajectories show a mean distance steadily increasing toward 12 km at 24 h and 18 km at 48 h after the start of each segment. The 95th percentile separation is a measure of the scale of the area encompassing 95 % of the released particles each hour. For the UWLS, this separation grows steadily with a maximum of 34 km at 48 h. The OI base run trajectories are shorter for all times with a mean distance of 9 km at 24 h and 14 km at 48 h. Similarly, the 95th percentile separation is consistently less than the UWLS solution with a maximum of 26 km at 48 h (Fig. 7). Both the UWLS and OI results fall below the drifter persistence values assuming a search based on the last known position alone.

## 5.2 OI sensitivities

**Decorrelation scales** The decorrelation scale used to determine the weights for the input radials to the OI algorithm is defined as a distance east and north from the grid point. For our base run, this area was scaled as a circle with a radius of 10 km ( $S_x=S_y=10$ ). For the OI algorithm, a radial within and a little beyond this area are weighted based on an exponential decay with distance from the grid point. The rate of this decay is a function of  $S_x$  and  $S_y$ . As a variation to this base setting, we added asymmetry to the scale and oriented it to match the local topography. For this run,  $S_y$  was rotated along the isobaths and stretched 2.5 times  $S_x$  ( $S_x=10$ ,  $S_y=25$  and orientation= $31^\circ$  CW from true north). For both the ADCP and drifter estimated currents, the comparison between runs 1 and 2 are very similar (Tables 2 and 3). The RMS difference and data coverage for all in situ observations are within 0.5 cm/s and 0.5 %, respectively (Tables 2 and 3, runs 1 and 2). Similarly, the drifter trajectories



**Fig. 7** Mean separation between the particle centroid and actual drifter (left) and the 95th percentile separation (right) for the UWLS (*thick dashed*) and OI (*thick solid*) simulations. For reference, we show the same statistics for the persistence simulation based on a static last known position (*thin*)



show very little sensitivity to the decorrelation scales. The mean separation between the centroid of the simulated particles and the 95th percentile separation follows similar trajectories to the base run with a separation of 9 km 24 h out and 14 km 48 h out (Fig. 8, top panels).

**Error thresholds** For each of the OI runs described above, a lower threshold of 0.6 was applied in runs 3 and 4. We selected this lower threshold of 0.6 to optimize the quality of the data without significantly impacting coverage (Fig. 9). While there is an increase in the correlation with in situ observations, these lower thresholds come at a significant cost to data coverage. We selected 0.6 as a second error threshold to test the sensitivities because it has higher correlation than the 0.95 values and it falls just above the sharp decline in data coverage seen in values less than 0.5 (Fig. 9). The comparison with the ADCPs for these second set of runs showed a slight reduction in the RMS difference on the order of 0 to 0.5 cm/s with a nominal loss in coverage on the order of 5–8 % compared to runs 1 and 2 with a threshold of 0.95. As with the decorrelation scales, the error thresholds had a minimal impact on the drifter trajectory results (Fig. 8, bottom panels). In both runs 3 and 4, the lower threshold did not significantly change the mean of the distance between the actual drifter and the particle centroid or the 95th percentile separation seen in run 1. In each case, the mean gradually increases over the 48-h simulation to a centroid distance of about 14 km with similar 95th percentile separation.

## 6 Discussion

### 6.1 UWLS and OI comparisons

The in situ ADCP array was centered in a region of greater than 90 % HF radar data coverage and good geometry. In this region, the comparison between the OI and UWLS algorithms was very similar in both RMS and percent coverage. All RMS difference and correlation ( $r^2$ ) statistics were within 0.7 cm/s and 0.06, respectively with a slight increase in data coverage with the OI currents (Table 2, runs 1 and 5). Based on the ADCP comparison, the two algorithms can be interchanged with little impact on the resulting total vector quality. The location of the ADCPs in the center of the HF radar footprint ensured that there was consistent radial vector coverage at nearly orthogonal angles at every time step so that the total vector calculations will be based mostly on radials very close to the total vector grid point. Given these conditions, the mathematics associated with either algorithm gives very similar results. It is not until the comparison data move away from this optimal location that the strengths of each algorithm become more evident.

The drifter tracks took the in situ observations throughout the coverage, from regions above and below the 90 % contour and regions of good and bad radial site geometry. Across these regions of the HF radar footprint, the UWLS- and OI-derived velocity fields were more distinct. The UWLS algorithm had consistently lower RMS difference, typically 1–3 cm/s

**Table 3** Summary of error statistics between the HF radar and drifters

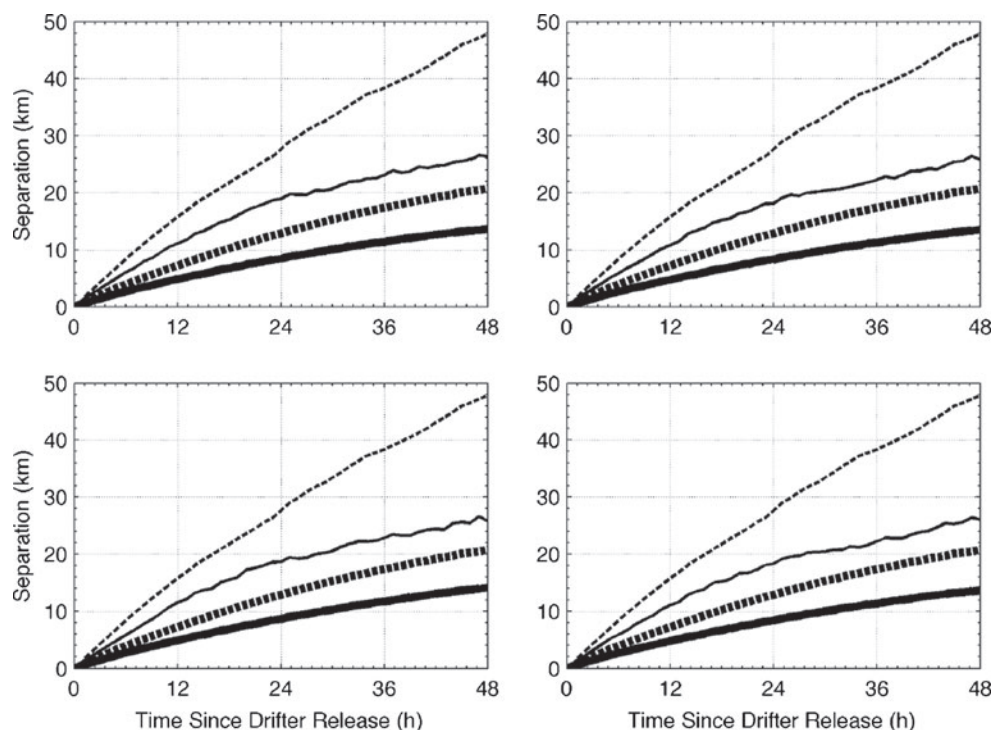
Run	$S_x$	$S_y$	Error criterion	Drifter 43484	Drifter 38940	Drifter 43198	Drifter 43266	Drifter 43271	Drifter 43324	Drifter 43325	Drifter 43484	Drifter 38940	Drifter 43198	Drifter 43266	Drifter 43271	Drifter 43324	Drifter 43325	Drifter 43484	Drifter 38940	Drifter 43198	Drifter 43266	Drifter 43271	Drifter 43324	Drifter 43325	Drifter 43484	Drifter 38940	Drifter 43198	Drifter 43266	Drifter 43271	Drifter 43324	Drifter 43325	Drifter 43484	Drifter 38940	Drifter 43198	Drifter 43266	Drifter 43271	Drifter 43324	Drifter 43325	Drifter 43484	Drifter 38940	Drifter 43198	Drifter 43266	Drifter 43271	Drifter 43324	Drifter 43325	Drifter 43484	Drifter 38940	Drifter 43198	Drifter 43266	Drifter 43271	Drifter 43324	Drifter 43325	Drifter 43484	Drifter 38940	Drifter 43198	Drifter 43266	Drifter 43271	Drifter 43324	Drifter 43325	Drifter 43484	Drifter 38940	Drifter 43198	Drifter 43266	Drifter 43271	Drifter 43324	Drifter 43325	Drifter 43484	Drifter 38940	Drifter 43198	Drifter 43266	Drifter 43271	Drifter 43324	Drifter 43325	Drifter 43484	Drifter 38940	Drifter 43198	Drifter 43266	Drifter 43271	Drifter 43324	Drifter 43325	Drifter 43484	Drifter 38940	Drifter 43198	Drifter 43266	Drifter 43271	Drifter 43324	Drifter 43325	Drifter 43484	Drifter 38940	Drifter 43198	Drifter 43266	Drifter 43271	Drifter 43324	Drifter 43325	Drifter 43484	Drifter 38940	Drifter 43198	Drifter 43266	Drifter 43271	Drifter 43324	Drifter 43325	Drifter 43484	Drifter 38940	Drifter 43198	Drifter 43266	Drifter 43271	Drifter 43324	Drifter 43325	Drifter 43484	Drifter 38940	Drifter 43198	Drifter 43266	Drifter 43271	Drifter 43324	Drifter 43325	Drifter 43484	Drifter 38940	Drifter 43198	Drifter 43266	Drifter 43271	Drifter 43324	Drifter 43325	Drifter 43484	Drifter 38940	Drifter 43198	Drifter 43266	Drifter 43271	Drifter 43324	Drifter 43325	Drifter 43484	Drifter 38940	Drifter 43198	Drifter 43266	Drifter 43271	Drifter 43324	Drifter 43325	Drifter 43484	Drifter 38940	Drifter 43198	Drifter 43266	Drifter 43271	Drifter 43324	Drifter 43325	Drifter 43484	Drifter 38940	Drifter 43198	Drifter 43266	Drifter 43271	Drifter 43324	Drifter 43325	Drifter 43484	Drifter 38940	Drifter 43198	Drifter 43266	Drifter 43271	Drifter 43324	Drifter 43325	Drifter 43484	Drifter 38940	Drifter 43198	Drifter 43266	Drifter 43271	Drifter 43324	Drifter 43325	Drifter 43484	Drifter 38940	Drifter 43198	Drifter 43266	Drifter 43271	Drifter 43324	Drifter 43325	Drifter 43484	Drifter 38940	Drifter 43198	Drifter 43266	Drifter 43271	Drifter 43324	Drifter 43325	Drifter 43484	Drifter 38940	Drifter 43198	Drifter 43266	Drifter 43271	Drifter 43324	Drifter 43325	Drifter 43484	Drifter 38940	Drifter 43198	Drifter 43266	Drifter 43271	Drifter 43324	Drifter 43325	Drifter 43484	Drifter 38940	Drifter 43198	Drifter 43266	Drifter 43271	Drifter 43324	Drifter 43325	Drifter 43484	Drifter 38940	Drifter 43198	Drifter 43266	Drifter 43271	Drifter 43324	Drifter 43325	Drifter 43484	Drifter 38940	Drifter 43198	Drifter 43266	Drifter 43271	Drifter 43324	Drifter 43325	Drifter 43484	Drifter 38940	Drifter 43198	Drifter 43266	Drifter 43271	Drifter 43324	Drifter 43325	Drifter 43484	Drifter 38940	Drifter 43198	Drifter 43266	Drifter 43271	Drifter 43324	Drifter 43325	Drifter 43484	Drifter 38940	Drifter 43198	Drifter 43266	Drifter 43271	Drifter 43324	Drifter 43325	Drifter 43484	Drifter 38940	Drifter 43198	Drifter 43266	Drifter 43271	Drifter 43324	Drifter 43325	Drifter 43484	Drifter 38940	Drifter 43198	Drifter 43266	Drifter 43271	Drifter 43324	Drifter 43325	Drifter 43484	Drifter 38940	Drifter 43198	Drifter 43266	Drifter 43271	Drifter 43324	Drifter 43325	Drifter 43484	Drifter 38940	Drifter 43198	Drifter 43266	Drifter 43271	Drifter 43324	Drifter 43325	Drifter 43484	Drifter 38940	Drifter 43198	Drifter 43266	Drifter 43271	Drifter 43324	Drifter 43325	Drifter 43484	Drifter 38940	Drifter 43198	Drifter 43266	Drifter 43271	Drifter 43324	Drifter 43325	Drifter 43484	Drifter 38940	Drifter 43198	Drifter 43266	Drifter 43271	Drifter 43324	Drifter 43325	Drifter 43484	Drifter 38940	Drifter 43198	Drifter 43266	Drifter 43271	Drifter 43324	Drifter 43325	Drifter 43484	Drifter 38940	Drifter 43198	Drifter 43266	Drifter 43271	Drifter 43324	Drifter 43325	Drifter 43484	Drifter 38940	Drifter 43198	Drifter 43266	Drifter 43271	Drifter 43324	Drifter 43325	Drifter 43484	Drifter 38940	Drifter 43198	Drifter 43266	Drifter 43271	Drifter 43324	Drifter 43325	Drifter 43484	Drifter 38940	Drifter 43198	Drifter 43266	Drifter 43271	Drifter 43324	Drifter 43325	Drifter 43484	Drifter 38940	Drifter 43198	Drifter 43266	Drifter 43271	Drifter 43324	Drifter 43325	Drifter 43484	Drifter 38940	Drifter 43198	Drifter 43266	Drifter 43271	Drifter 43324	Drifter 43325	Drifter 43484	Drifter 38940	Drifter 43198	Drifter 43266	Drifter 43271	Drifter 43324	Drifter 43325	Drifter 43484	Drifter 38940	Drifter 43198	Drifter 43266	Drifter 43271	Drifter 43324	Drifter 43325	Drifter 43484	Drifter 38940	Drifter 43198	Drifter 43266	Drifter 43271	Drifter 43324	Drifter 43325	Drifter 43484	Drifter 38940	Drifter 43198	Drifter 43266	Drifter 43271	Drifter 43324	Drifter 43325	Drifter 43484	Drifter 38940	Drifter 43198	Drifter 43266	Drifter 43271	Drifter 43324	Drifter 43325	Drifter 43484	Drifter 38940	Drifter 43198	Drifter 43266	Drifter 43271	Drifter 43324	Drifter 43325	Drifter 43484	Drifter 38940	Drifter 43198	Drifter 43266	Drifter 43271	Drifter 43324	Drifter 43325	Drifter 43484	Drifter 38940	Drifter 43198	Drifter 43266	Drifter 43271	Drifter 43324	Drifter 43325	Drifter 43484	Drifter 38940	Drifter 43198	Drifter 43266	Drifter 43271	Drifter 43324	Drifter 43325	Drifter 43484	Drifter 38940	Drifter 43198	Drifter 43266	Drifter 43271	Drifter 43324	Drifter 43325	Drifter 43484	Drifter 38940	Drifter 43198	Drifter 43266	Drifter 43271	Drifter 43324	Drifter 43325	Drifter 43484	Drifter 38940	Drifter 43198	Drifter 43266	Drifter 43271	Drifter 43324	Drifter 43325	Drifter 43484	Drifter 38940	Drifter 43198	Drifter 43266	Drifter 43271	Drifter 43324	Drifter 43325	Drifter 43484	Drifter 38940	Drifter 43198	Drifter 43266	Drifter 43271	Drifter 43324	Drifter 43325	Drifter 43484	Drifter 38940	Drifter 43198	Drifter 43266	Drifter 43271	Drifter 43324	Drifter 43325	Drifter 43484	Drifter 38940	Drifter 43198	Drifter 43266	Drifter 43271	Drifter 43324	Drifter 43325	Drifter 43484	Drifter 38940	Drifter 43198	Drifter 43266	Drifter 43271	Drifter 43324	Drifter 43325	Drifter 43484	Drifter 38940	Drifter 43198	Drifter 43266	Drifter 43271	Drifter 43324	Drifter 43325	Drifter 43484	Drifter 38940	Drifter 43198	Drifter 43266	Drifter 43271	Drifter 43324	Drifter 43325	Drifter 43484	Drifter 38940	Drifter 43198	Drifter 43266	Drifter 43271	Drifter 43324	Drifter 43325	Drifter 43484	Drifter 38940	Drifter 43198	Drifter 43266	Drifter 43271	Drifter 43324	Drifter 43325	Drifter 43484	Drifter 38940	Drifter 43198	Drifter 43266	Drifter 43271	Drifter 43324	Drifter 43325	Drifter 43484	Drifter 38940	Drifter 43198	Drifter 43266	Drifter 43271	Drifter 43324	Drifter 43325	Drifter 43484	Drifter 38940	Drifter 43198	Drifter 43266	Drifter 43271	Drifter 43324	Drifter 43325	Drifter 43484	Drifter 38940	Drifter 43198	Drifter 43266	Drifter 43271	Drifter 43324	Drifter 43325	Drifter 43484	Drifter 38940	Drifter 43198	Drifter 43266	Drifter 43271	Drifter 43324	Drifter 43325	Drifter 43484	Drifter 38940	Drifter 43198	Drifter 43266	Drifter 43271	Drifter 43324	Drifter 43325	Drifter 43484	Drifter 38940	Drifter 43198	Drifter 43266	Drifter 43271	Drifter 43324	Drifter 43325	Drifter 43484	Drifter 38940	Drifter 43198	Drifter 43266	Drifter 43271	Drifter 43324	Drifter 43325	Drifter 43484	Drifter 38940	Drifter 43198	Drifter 43266	Drifter 43271	Drifter 43324	Drifter 43325	Drifter 43484	Drifter 38940	Drifter 43198	Drifter 43266	Drifter 43271	Drifter 43324	Drifter 43325	Drifter 43484	Drifter 38940	Drifter 43198	Drifter 43266	Drifter 43271	Drifter 43324	Drifter 43325	Drifter 43484	Drifter 38940	Drifter 43198	Drifter 43266	Drifter 43271	Drifter 43324	Drifter 43325	Drifter 43484	Drifter 38940	Drifter 43198	Drifter 43266	Drifter 43271	Drifter 43324	Drifter 43325	Drifter 43484	Drifter 38940	Drifter 43198	Drifter 43266	Drifter 43271	Drifter 43324
-----	-------	-------	-----------------	---------------	---------------	---------------	---------------	---------------	---------------	---------------	---------------	---------------	---------------	---------------	---------------	---------------	---------------	---------------	---------------	---------------	---------------	---------------	---------------	---------------	---------------	---------------	---------------	---------------	---------------	---------------	---------------	---------------	---------------	---------------	---------------	---------------	---------------	---------------	---------------	---------------	---------------	---------------	---------------	---------------	---------------	---------------	---------------	---------------	---------------	---------------	---------------	---------------	---------------	---------------	---------------	---------------	---------------	---------------	---------------	---------------	---------------	---------------	---------------	---------------	---------------	---------------	---------------	---------------	---------------	---------------	---------------	---------------	---------------	---------------	---------------	---------------	---------------	---------------	---------------	---------------	---------------	---------------	---------------	---------------	---------------	---------------	---------------	---------------	---------------	---------------	---------------	---------------	---------------	---------------	---------------	---------------	---------------	---------------	---------------	---------------	---------------	---------------	---------------	---------------	---------------	---------------	---------------	---------------	---------------	---------------	---------------	---------------	---------------	---------------	---------------	---------------	---------------	---------------	---------------	---------------	---------------	---------------	---------------	---------------	---------------	---------------	---------------	---------------	---------------	---------------	---------------	---------------	---------------	---------------	---------------	---------------	---------------	---------------	---------------	---------------	---------------	---------------	---------------	---------------	---------------	---------------	---------------	---------------	---------------	---------------	---------------	---------------	---------------	---------------	---------------	---------------	---------------	---------------	---------------	---------------	---------------	---------------	---------------	---------------	---------------	---------------	---------------	---------------	---------------	---------------	---------------	---------------	---------------	---------------	---------------	---------------	---------------	---------------	---------------	---------------	---------------	---------------	---------------	---------------	---------------	---------------	---------------	---------------	---------------	---------------	---------------	---------------	---------------	---------------	---------------	---------------	---------------	---------------	---------------	---------------	---------------	---------------	---------------	---------------	---------------	---------------	---------------	---------------	---------------	---------------	---------------	---------------	---------------	---------------	---------------	---------------	---------------	---------------	---------------	---------------	---------------	---------------	---------------	---------------	---------------	---------------	---------------	---------------	---------------	---------------	---------------	---------------	---------------	---------------	---------------	---------------	---------------	---------------	---------------	---------------	---------------	---------------	---------------	---------------	---------------	---------------	---------------	---------------	---------------	---------------	---------------	---------------	---------------	---------------	---------------	---------------	---------------	---------------	---------------	---------------	---------------	---------------	---------------	---------------	---------------	---------------	---------------	---------------	---------------	---------------	---------------	---------------	---------------	---------------	---------------	---------------	---------------	---------------	---------------	---------------	---------------	---------------	---------------	---------------	---------------	---------------	---------------	---------------	---------------	---------------	---------------	---------------	---------------	---------------	---------------	---------------	---------------	---------------	---------------	---------------	---------------	---------------	---------------	---------------	---------------	---------------	---------------	---------------	---------------	---------------	---------------	---------------	---------------	---------------	---------------	---------------	---------------	---------------	---------------	---------------	---------------	---------------	---------------	---------------	---------------	---------------	---------------	---------------	---------------	---------------	---------------	---------------	---------------	---------------	---------------	---------------	---------------	---------------	---------------	---------------	---------------	---------------	---------------	---------------	---------------	---------------	---------------	---------------	---------------	---------------	---------------	---------------	---------------	---------------	---------------	---------------	---------------	---------------	---------------	---------------	---------------	---------------	---------------	---------------	---------------	---------------	---------------	---------------	---------------	---------------	---------------	---------------	---------------	---------------	---------------	---------------	---------------	---------------	---------------	---------------	---------------	---------------	---------------	---------------	---------------	---------------	---------------	---------------	---------------	---------------	---------------	---------------	---------------	---------------	---------------	---------------	---------------	---------------	---------------	---------------	---------------	---------------	---------------	---------------	---------------	---------------	---------------	---------------	---------------	---------------	---------------	---------------	---------------	---------------	---------------	---------------	---------------	---------------	---------------	---------------	---------------	---------------	---------------	---------------	---------------	---------------	---------------	---------------	---------------	---------------	---------------	---------------	---------------	---------------	---------------	---------------	---------------	---------------	---------------	---------------	---------------	---------------	---------------	---------------	---------------	---------------	---------------	---------------	---------------	---------------	---------------	---------------	---------------	---------------	---------------	---------------	---------------	---------------	---------------	---------------	---------------	---------------	---------------	---------------	---------------	---------------	---------------	---------------	---------------	---------------	---------------	---------------	---------------	---------------	---------------	---------------	---------------	---------------	---------------	---------------	---------------	---------------	---------------	---------------	---------------	---------------	---------------	---------------	---------------	---------------	---------------	---------------	---------------	---------------	---------------	---------------	---------------	---------------	---------------	---------------	---------------	---------------	---------------	---------------	---------------	---------------	---------------	---------------	---------------	---------------	---------------	---------------	---------------	---------------	---------------	---------------	---------------	---------------	---------------	---------------	---------------	---------------	---------------	---------------	---------------	---------------	---------------	---------------	---------------	---------------	---------------	---------------	---------------	---------------	---------------	---------------	---------------	---------------	---------------	---------------	---------------	---------------	---------------	---------------	---------------	---------------	---------------	---------------	---------------	---------------	---------------	---------------	---------------	---------------	---------------	---------------	---------------	---------------	---------------	---------------	---------------	---------------	---------------	---------------	---------------	---------------	---------------	---------------	---------------	---------------	---------------	---------------	---------------	---------------	---------------	---------------

compared to the OI total vectors. While these OI-derived vectors were typically associated with lower uncertainty, the data coverage of the UWLS fields was significantly lower. The OI algorithm did fill the gaps seen around the edges of the coverage more effectively with data returns for the drifters on the order of 10–30 % greater than the UWLS total vectors.

The drifter estimated current comparisons highlight the distinction between the two algorithms. The UWLS, as it is configured for this study and consistent with the operation in the present national network implementation, will scale all vectors within the 10-km radius with an equal weight of 1. Any radial vector falling outside of that radius will have an equal weight of 0 and will therefore not be included in the current vector estimate. The OI implementation as tested here weights each radial vector based on its distance from the grid point. So a vector located 10 km away will have a weight of 0.37. All vectors inside of this distance will be weighted higher, and vectors that fall beyond will be weighted less. Unlike the UWLS implementation, these far field vectors will get included in the vector estimate, but will be weighted far less than the vectors that fall inside the decorrelation scale set by  $S_x$  and  $S_y$ . Given this, the UWLS implementation will only have a vector to compare to the drifter if there are radial velocities within 10 km of the grid point closest to the drifter. At those times, the OI will weight these velocities much higher than those that fall beyond 10 km. For the times when there is no UWLS solution but there is an OI solution, there cannot be radial velocities within 10 km of the closest grid point to the drifter. Therefore, the velocities that are included in the OI solution must fall outside the decorrelation scale of 10 km. The result is a total vector to compare with the drifter velocity that is based only on radial velocities more than 10 km from the grid point. The larger the horizontal shear between the grid point location and the input radial velocities, the greater the difference with the drifter velocity. If the shears are small over these scales, than a radial vector weighted relatively high, but further away from the grid point, will provide a representative velocity component for the estimated total vector. The 5–7-cm/s RMS difference observed across a similar scale in the ADCP array and April drifter cluster reinforces the significance of the observed shears in our study region and helps explain the issues that arise when weighting radials further away from the grid point too high.

As an example, we look at the comparison with drifter 43484. When we constrain the comparison to those times when there is a current estimate from the drifter, UWLS, and OI, we are limiting the HF radar solution to those times when there are radial velocities inside the 10-km radius set by the UWLS settings. In this case, the RMS difference between the UWLS and OI results compared to the drifter is 7.19 and 7.85 cm/s in the east direction and 9.70 and 9.12 cm/s in the north direction, respectively. In both the north and east directions, the OI results have come down to the lower uncertainties

**Fig. 8** Mean separation between the particle centroid and actual drifter (*thick solid*) and the 95th percentile separation (*thin solid*) for the OI simulations listed in Tables 2 and 3 for run 1 (*upper left*), run 2 (*upper right*), run 3 (*lower left*), and run 4 (*lower right*). For reference, the mean separation (*thick dashed*) and the 95th percentile separation (*thin dashed*) for the persistence simulation based on a static last known position are shown in each panel

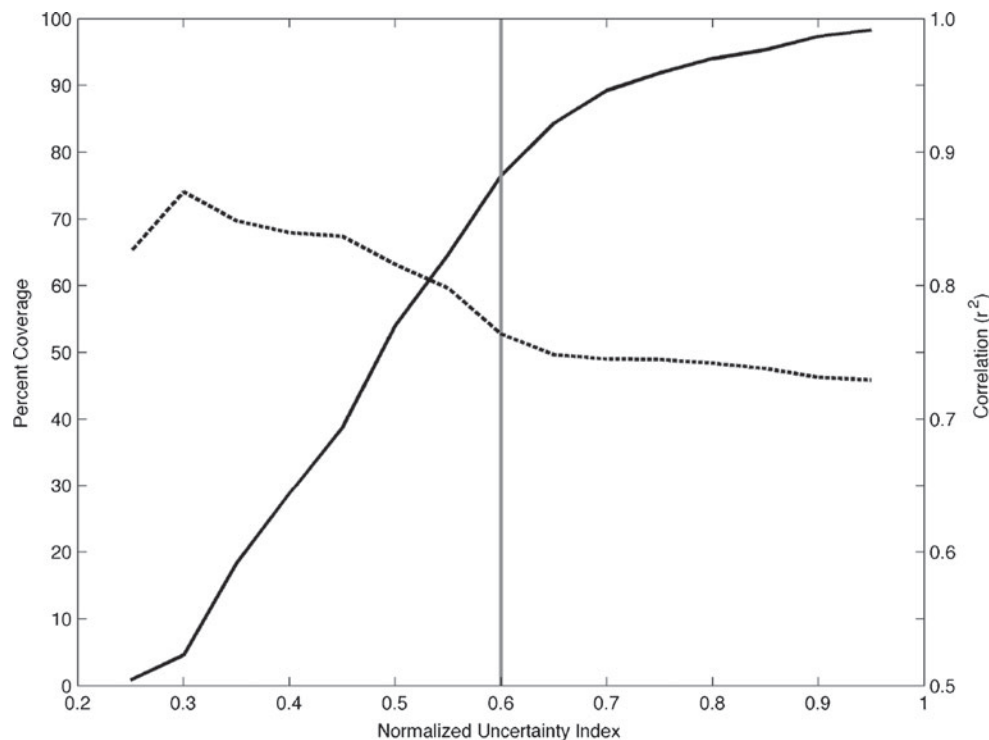


seen in the UWLS comparisons reported in Table 3. This shows a reduction in the RMS difference with the OI solutions of about 2–3 cm/s. So if there are radial vectors within the decorrelation scale of 10 km, the results from each algorithm are consistent. However, in those instances when there are no vectors within the 10-km scale, as is the case with the additional vectors seen in the higher data coverage of the original

evaluation, the OI implementation will weight these far field vectors relatively higher and base the total vector calculation only on them. The result is a more filled in field with higher uncertainty.

The most striking difference between the two algorithms as implemented in this study was seen in the drifter trajectories. The UWLS simulations were consistent with those reported

**Fig. 9** Correlation (*dashed*) and data coverage (*solid*) for the comparison between the OI algorithm and drifter 43484 based on the normalized uncertainty of the total vector components. The threshold of 0.6 for runs 3 through 4 is shown as a gray line





by Ullman et al. (2006) using data collected over the same area of the shelf 3 years before our study period. In both studies, the drifter mean separation was on the order of 10–12 km at the end of the 24-h segment. This is an improvement over the persistence solution in which we assume a search based on a static last known position (shown in Fig. 7). It is this improvement and the associated statistics that drove the inclusion of UWLS-derived total vectors into the first operational application of HF radar in SAROPS. It has been shown that this improvement with the UWLS can reduce search areas by a factor of 3 (Roarty et al. 2010).

For the OI simulations, the metrics for both the mean drifter separation with the particle centroid and the 95th percentile separation are better than those of the UWLS. The smaller 95th percentile separation across all hours of the simulation leads to a smaller search area, reducing search times and increasing the likelihood for a successful rescue. The OI-based trajectories have a mean separation of about 12 km 48 h into the simulation. This is of the same order as the UWLS results at 24 h into the simulation (Fig. 7). This improvement is based on the varying weights applied in the combination. The variable weight based on the distance from the grid point assures that radial velocities closer to the SLDMB location will be weighted more than those further away. The result is a more representative total vector to drive the virtual drifter trajectories. Based on both the intercomparison of the ADCPs and the drifter clusters, we quantify significant variation in the surface velocity over the decorrelation scales used in the OI. In the case of the UWLS, the vectors within 10 km of the actual drifter are all weighted the same, leading to radial velocities as far as 10 km away contributing equally to the resulting total vector calculation as those within 1 km. In the context of the observed shears, this will lead to a total vector less representative of the velocity at that grid point compared to the weighted OI results. The impact of weighted radials on the particle trajectories will scale based on the magnitude of the horizontal shears over the scales of the processing. Our objective in this study was to evaluate the two algorithms as they have been implemented in existing HF radar networks. There are of course opportunities to weight the radials vectors within a least squares approach. Based on this evaluation, this would likely move the weighted least squares estimated trajectories closer to the observed drifter track in a similar way as that seen in the OI results.

The UWLS solutions currently feeding the operational SAROPS tool for cases in the Mid-Atlantic Bight was shown to reduce search areas by a factor of 3 over other available data and forecasts (Roarty et al. 2010). These OI simulations indicate that 24 h from the initialization of these segments, the search area is reduced by an additional factor of 2. Smaller, more accurate particle trajectories led to smaller more accurate search areas that lower search times and increase likelihood of a successful search.

## 6.2 OI sensitivities

The UWLS algorithm has been applied to HF radar total vector calculations for at least 30 years. Since the implementation of the OI to calculate HF radar total vectors has only recently been introduced to the field, we tested some of the algorithm's sensitivities to help determine the optimal application of the algorithm. The two categories of parameters we tested were the decorrelation scales ( $S_x$  and  $S_y$ ) and the threshold for the reported uncertainties in the east and north directions.

The impact of the selection of decorrelation scale was tested with both the ADCP and drifter estimated currents.  $S_x=S_y=10$  was our base run to be consistent with scales currently used in the UWLS implementation and a second parameter set ( $S_x=10$ ,  $S_y=25$ ) with an elongated scale oriented in the direction of the isobaths. This second parameter set incorporated the characteristics of the local dynamics into the calculation of the total vector. The ADCP comparisons showed very little sensitivity between the two runs (Table 2). In all the comparisons, the RMS differences were within 0.24 cm/s. Once again, the ADCPs are located in a region of HF radar data coverage greater than 90 %. In this region, the estimated totals will be based on vectors close to the grid point that are weighted much higher than those further away. So the sensitivity of the estimated total to the decorrelation scale is minimized. The fact that this high density region showed little sensitivity is a validation that the larger scale we chose was dynamically consistent. Care was taken in the selection of the parameters to define the asymmetry and orientation of the larger search area. Both the orientation and asymmetry were based on the dynamics of the region. The velocity fields of the MAB tend to have longer correlation scales along the isobaths compared to across the isobaths. The larger number of radial vectors included in the along isobath direction did not introduce more uncertainty into the estimated total vector because they still represent the velocity over the grid point.

The component-based normalized uncertainty reported in the OI algorithm is potentially very useful in not only assessing the quality of each total vector, but also in considering the component-based uncertainty in the application of the data. As part of the sensitivity tests, we evaluated the impact of different error thresholds on both the RMS difference and data coverage. While there was slight improvement seen in most of the runs, the sensitivity of the total vector field resulting from the higher or lower error threshold was minimal. In some cases, the RMS difference was slightly higher with the lower threshold. It is not until the thresholds fall below 0.5 that there is a sharper increase in correlation (Fig. 9). This of course comes at a much more significant reduction in data coverage.

The sensitivity of the different OI parameter sets was also small in the 48-h particle trajectory simulations. All four runs had a steady increase in distance between the actual drifter and the centroid of the simulated particles over time with a

maximum of about 14 km at the end of the 48-h segments (Fig. 8). The larger decorrelation scale stretched in the direction of the isobaths slightly lengthened the region of the highest weighted radials around the drifter. This nominal change had little impact on the drifter trajectories. Consistent with the Eulerian results, the lower error threshold of 0.6 did not eliminate a large portion of the original data. Operators of regional and national networks must balance the improved RMS difference and reduced coverage to determine an appropriate error criterion (Fig. 9). At a value of 0.6, we saw some improved RMS difference with minimal impact on the data coverage. If a lower criterion were selected, we would expect a large drop-off in data coverage with a measured improvement in RMS difference.

## 7 Conclusions

Regional scale HF radar networks are developing into coordinated national systems to support a variety of coastal applications, from search and rescue and spill response to oceanographic research. For each application, it is important to understand and quantify the uncertainty of each total vector included in a given surface current map. Based on the evaluations conducted here, we identified the strengths of two existing algorithms to combine radial velocities to maps of total vector currents. Both the UWLS and OI algorithms produced surface current vectors that compared well with in situ sensors in the context of known sampling bias due to environmental variability. In regions of good geometry and greater than 90 % data coverage, they produced similar results with no significant difference between the two. The difference in the total vector solutions from the two algorithms was much more evident with the drifter comparisons where in situ observations moved throughout the HF radar data footprint. The largest contributing factor to the observed differences between the two algorithms is based on the known horizontal shears in the study region and how these particular algorithms weighted radial velocities. Given the significant shear, the evaluation highlighted the importance of weighting radials closer to the grid point higher than those that fall further away. It also showed the risk in estimating total vectors beyond the decorrelation scale in the absence of vectors closer to the grid point. In these cases, the OI algorithm filled gaps, but the interpolated data carried with it higher uncertainty. The most significant distinction between the two was seen in the drifter trajectories. With these simulations, the weighted radial approach of the OI was very effective at reducing both the distance between the actual drifter track and the scale of the search area. In this study, the OI further reduced the already improved UWLS-based search areas by an additional factor of 2. The results indicated that the OI output was relatively insensitive to the varying

decorrelation scales and error thresholds tested here. In regions like the Mid-Atlantic Bight off the east coast of the USA with significant horizontal shears, we are able to quantify the importance of weighting radial velocities when combining into maps of total vectors. Operators of the large regional and national networks will need to decide on what processing algorithm and parameter sets should be used to ensure quality data output that will support activities like search and rescue and oil spill response.

**Acknowledgments** This work was supported with data provided from the IOOS regional association in the Mid-Atlantic Bight, MARACOOS (NA07NOS4730221), and a National Science Foundation grant focused on the mid-shelf front of the MAB (OCE-0550770). We would like to specifically thank Nancy Vorona of CIT and Larry Atkinson and Teresa Gardner of Old Dominion University for the radial data from the Assateague, MD HF radar site. Dave Ullman and Daniel Codiga at the University of Rhode Island provided the ADCP data and Arthur Allen from the U.S. Coast Guard Office of Search and Rescue provided the seven SLDMBs used in the study. We would also like to thank Sung Yong Kim for his insights in applying the optimal interpolation algorithm to the radial data in the Mid-Atlantic Bight and two anonymous reviewers for their constructive comments that helped shape the final form of the manuscript.

**Open Access** This article is distributed under the terms of the Creative Commons Attribution License which permits any use, distribution, and reproduction in any medium, provided the original author(s) and the source are credited.

## References

- Allen A (1996) Performance of GPS/Argos self-locating datum marker buoys (SLDMBs). In: OCEANS '96. MTS/IEEE. 'Prospects for the 21st century'. Conference Proceedings, 23–26 Sep 1996. pp 857–861. doi:10.1109/OCEANS.1996.568341
- Barrick DE (2008) 30 Years of CMTC and CODAR. In: Current measurement technology (2008). CMTC 2008. IEEE/OES 9th Working Conference on, Charleston, SC, 17–19 March 2008. pp 131–136. doi:10.1109/CCM.2008.4480856
- Barrick DE, Lipa BJ (1996) Comparison of direction-finding and beam-forming in HF radar ocean surface current mapping. Phase 1 SBIR final report. National Oceanic and Atmospheric Administration, Rockville
- Barrick DE, Evans MW, Weber BL (1977) Ocean surface currents mapped by radar. *Science* 198(4313):138–144. doi:10.1126/science.198.4313.138
- Barrick D, Fernandez V, Ferrer M, Whelan C, Breivik O (2012) A short-term predictive system for surface currents from a rapidly deployed coastal HF radar network. *Ocean Dyn*. doi:10.1007/s10236-012-0521-0
- Beardsley RC, Boicourt WC (1981) On estuarine and continental-shelf circulation in the Middle Atlantic Bight. In: Warren BA, Wunsch C (eds) *Evolution of physical oceanography*. MIT, Cambridge, pp 198–233
- Bretherton FP, Davis RE, Fandry CB (1976) A technique for objective analysis and design of oceanographic experiment applied to MODE-73. *Deep-Sea Res* 23:559–582
- Chapman RD, Shay LK, Graber HC, Edson JB, Karachintsev A, Trump CL, Ross DB (1997) On the accuracy of HF radar surface

- current measurements: intercomparisons with ship-based sensors. *J Geophys Res* 102:18737–18748
- Codiga DL (2007) Moored ADCP records from the Winter/Spring 2007 mid-shelf fronts experiment: data report and preliminary description of tidal and subtidal flow. Graduate School of Oceanography, University of Rhode Island, Narragansett
- Crombie DD (1955) Doppler spectrum of sea echo at 13.56 Mc/s. *Nature* 175:681–682
- Dzwonkowski B, Kohut JT, Yan X-H (2009) Seasonal differences in wind-driven across-shelf forcing and response relationships in the shelf surface layer of the central Mid-Atlantic Bight. *J Geophys Res* 114(C8):C08018. doi:10.1029/2008JC004888
- Dzwonkowski B, Lipphardt BL Jr, Kohut JT, Yan X-H, Garvine RW (2010) Synoptic measurements of episodic offshore flow events in the central mid-Atlantic Bight. *Cont Shelf Res* 30(12):1373–1386
- Gong D, Kohut JT, Glenn SM (2010) Seasonal climatology of wind-driven circulation on the New Jersey Shelf. *J Geophys Res* 115(C4):C04006. doi:10.1029/2009JC005520
- Graber HC, Haus BK, Shay LK, Chapman RD (1997) HF radar comparisons with moored estimates of current speed and direction: expected differences and implications. *J Geophys Res* 102:18749–18766
- Griffa A (1996) Applications of stochastic particle models to oceanographic problems. In: Adler RJ, Müller P, Rozovskii BL (eds) *Stochastic modelling in physical oceanography*. Birkhäuser, Boston
- Gurgel KW (1994) Shipborne measurement of surface current fields by HF radar. *L'Onde Electrique* 74:54–59
- Harlan J, Terrill E, Hazard L, Keen C, Barrick D, Whelan C, Howden S, Kohut J (2010) The integrated ocean observing system high frequency radar network: status and local, regional and national applications. *Mar Technol Soc J* 44(6):122–132
- Kaplan D, Lekien F (2007) Spatial interpolation and filtering of surface current data based on open-boundary modal analysis. *J Geophys Res* 112(C12):C12007
- Kim SY, Terrill E, Cornuelle B (2007) Objectively mapping HF radar-derived surface current data using measured and idealized data covariance matrices. *J Geophys Res* 112(C6):C06021
- Kohut JT, Glenn SM (2003) Improving HF radar surface current measurements with measured antenna beam patterns. *J Atmos Ocean Technol* 20(9):1303–1316
- Kohut JT, Glenn SM, Chant RJ (2004) Seasonal current variability on the New Jersey inner shelf. *J Geophys Res* 109(C7):C07S07. doi:10.1029/2003JC001963
- Kohut JT, Roarty HJ, Glenn SM (2006) Characterizing observed environmental variability with HF Doppler radar surface current mappers and acoustic Doppler current profilers: environmental variability in the coastal ocean. *IEEE J Ocean Eng* 31(4):876–884
- Lipa BJ, Barrick DE (1983) Least-squares methods for the extraction of surface currents from CODAR cross-loop data: application at ARSLOE. *IEEE J Ocean Eng* 8(4):226–253
- Lipphardt BL Jr, Kirwan AD Jr, Grosch CE, Lewis JK, Paduan JD (2000) Blending HF radar and model velocities in Monterey Bay through normal mode analysis. *J Geophys Res* 105:3425–3450
- O'Donnell J, Ullman DS, Spaulding M, Howlett E, Fake T, Hall P, Isaji T, Edwards C, Anderson E, McClay T, Kohut JT, Allen A, Lester S, Lewandowski M (2005) Integration of Coastal Ocean Dynamics Application Radar (CODAR) and Short-Term Predictive System (STPS) surface current estimates into the Search and Rescue Optimal Planning System (SAROPS). U.S. Coast Guard Research and Development Center, Washington
- Ohlmann C, White P, Washburn L, Emery B, Terrill E, Otero M (2007) Interpretation of coastal HF radar derived surface currents with high-resolution drifter data. *J Atmos Ocean Technol* 24(4):666–680
- Paduan JD, Kim KC, Cook MS, Chavez FP (2006) Calibration and validation of direction-finding high frequency radar ocean surface current observations. *IEEE J Ocean Eng* 31(4):862–875. doi:10.1109/JOE.2006.886195
- Roarty HJ, Glenn SM, Kohut JT, Gong D, Handel E, Rivera Lemus E, Garner T, Atkinson L, Jakubiak C, Brown W, Muglia M, Haines S, Seim H (2010) Operation and application of a regional high frequency radar network in the Mid Atlantic Bight. *Mar Technol Soc J* 44(6):133–145
- Spaulding M, Isaji T, Hall P, Allen A (2006) A hierarchy of stochastic particle models for Search and Rescue (SAR): application to predict surface drifter trajectories using HF radar current forcing. *J Mar Environ Eng* 8(3):181–214
- Stewart RH, Joy JW (1974) HF radio measurements of surface currents. *Deep-Sea Res* 21:1039–1049
- Teague CC, Vesecky JF, Fernandez DM (1997) HF radar instruments, past to present. *Oceanography* 10(2):40–43
- Temll E, Otero M, Hazard L, Conlee D, Harlan J, Kohut J, Reuter P, Cook T, Harris T, Lindquist K (2006) Data management and real-time distribution in the HF-radar national network. In: *OCEANS 18–21 September 2006*. pp 1–6
- Ullman DS, Cornillon PC (1999) Satellite-derived sea surface temperature fronts on the continental shelf off the northeast U.S. coast. *J Geophys Res* 104(C10):23459–23478. doi:10.1029/1999JC900133
- Ullman DS, O'Donnell J, Edwards C, Fake T, Morschauser D, Sprague M, Allen A, Krenzien LB (2003) Use of Coastal Ocean Dynamics Application Radar (CODAR) technology in U.S. Coast Guard Search and Rescue Planning. U.S. Coast Guard Research and Development Center, Washington
- Ullman DS, O'Donnell J, Kohut J, Fake T, Allen A (2006) Trajectory prediction using HF radar surface currents: Monte Carlo simulations of prediction uncertainties. *J Geophys Res* 111:C12005. doi:10.1029/2006JC003715
- Ullman DS, Codiga DL, Hebert DL, Decker LB, Kincaid CR (2012) Structure and dynamics of the mid-shelf front in the New York Bight. *J Geophys Res*. doi:10.1029/2011JC007553
- Yaremchuk M, Sentchev A (2009) Mapping radar-derived sea surface currents with a variational method. *Cont Shelf Res* 29(14):1711–1722. doi:10.1016/j.csr.2009.05.016



# Improving habitat models by incorporating pelagic measurements from coastal ocean observatories

Laura Palamara<sup>1,\*</sup>, John Manderson<sup>2</sup>, Josh Kohut<sup>1</sup>, Matthew J. Oliver<sup>3</sup>,  
Steven Gray<sup>4</sup>, John Goff<sup>5</sup>

<sup>1</sup>Institute of Marine and Coastal Sciences, Rutgers University, New Brunswick, New Jersey 08901, USA

<sup>2</sup>NOAA, National Marine Fisheries Service, Northeast Fisheries Science Center, Ecosystems Processes Division,  
James J. Howard Marine Sciences Laboratory, Highlands, New Jersey 07732, USA

<sup>3</sup>College of Earth, Ocean and Environment, University of Delaware, Lewes, Delaware 19958, USA

<sup>4</sup>Department of Natural Resources and Environmental Management, University of Hawaii,  
Honolulu, Hawaii 96822, USA

<sup>5</sup>Institute for Geophysics, Jackson School of Geosciences, University of Texas at Austin, Austin, Texas 78758, USA

**ABSTRACT:** As in all temperate coastal seas, habitats in the Mid-Atlantic Bight are spatially and temporally dynamic. Understanding how species respond to the dynamics of their environment is important for developing effective management strategies. In this study, we used canonical correspondence analysis (CCA) to determine habitat variables most important in explaining variation in fish and invertebrate communities sampled with bottom trawls. We also quantified the relative explanatory power of seabed habitat features, pelagic features measured *in situ* and pelagic features measured remotely, all of which can be used to explain species variability. Pelagic habitat features, most notably surface and bottom temperature and stratification, explained 76 % of the community variation observed, compared with 40.9 % explained by seabed features, mainly depth. Remotely sensed pelagic characteristics explained 46.9 % of the variation that was accounted for and were redundant for features measured *in situ*; this suggests that remotely sensed features are representative of features measured *in situ* including certain subsurface features. Cross-shelf and seasonal variation in environmental variables were the major predictors of species distributions and accounted for 71.3 % of the total explained community variation. We described the seasonal dynamics of important habitat gradients and the responses of species with different habitat requirements and geographic range distributions to those gradients. We argue that consideration of dynamic pelagic features in addition to slowly changing features is important. Dynamic approaches are necessary for effective management and ocean observing systems can be used to develop dynamic space-based management strategies.

**KEY WORDS:** Habitat characteristics · Pelagic · Remote sensing · Spatial fisheries management · Canonical correspondence analysis · CCA · Mid-Atlantic Bight

Resale or republication not permitted without written consent of the publisher

## INTRODUCTION

Spatial distributions of many species are largely a result of behavioral habitat selection along environmental gradients that are variable in both space and time. The factors that define habitat for mobile marine ectotherms, including circulation, temperature, primary and secondary productivity and seabed habitat structure, regulate growth, dispersal, survival and re-

productive success. These habitat effects on the vital rates of individuals influence the productivity and stability of regional populations and communities (Fry 1971, Yamashita et al. 2001). In temperate areas like the Mid-Atlantic Bight (MAB), off the Atlantic coast of the USA, important habitat characteristics vary in space at daily, monthly, seasonal, annual and decadal time scales. Many species in this temperate region are highly migratory at different life stages in response to

\*Email: palamara@marine.rutgers.edu

frequent and dramatic changes in the environment. In the short term the animals move to optimal habitats in new areas rather than remaining in the same location and adapting to new environmental conditions (Nye et al. 2009, Lucey & Nye 2010). They use a variety of habitats at different times in their life cycles and at different times of year. To develop effective space- and time-based conservation strategies, it is important to understand how animal populations respond to changing habitat components like temperature (Yamashita et al. 2001), circulation (Bakun 2010) and primary production (Yamashita et al. 2001).

There is a tendency to concentrate on seabed characteristics when describing habitats selected by marine species. However, characteristics of ocean habitats are strongly defined by the pelagic environment for both bottom-dwelling and pelagic species (Manderson et al. 2011). Many species spend at least part of their life cycle in the water column—often during the most sensitive early stages, when they suffer the highest mortality rates (Houde 2009)—and/or have prey that rely on water column characteristics (Yamashita et al. 2001). Even benthic species, which are also nearly neutrally buoyant, are strongly linked to many pelagic habitat features and processes that affect both intrinsic (e.g. temperature, form drag) and extrinsic (prey distribution) bioenergetic processes. Marine species are directly affected by pelagic characteristics in all life history stages; their metabolism depends largely on temperature, the transport of individuals (especially during early life stages) can be aided by currents and the productivity of the system can be affected by many pelagic factors including the mixing of the water column. Because of this, seascapes and the habitats that comprise them need to be evaluated in 3 dimensions. Inclusion of variables that describe water column processes, properties and structures in addition to seabed variables in habitat models should give more complete descriptions of marine species–environment relationships, which are useful for ecosystem analysis and development of space-based management strategies.

It has been difficult to measure water column habitat factors over ecologically relevant large spatial but fine time scales because of the difficulty and cost in regularly sampling the ocean at synoptic scales. The implementation of ocean observation systems, such as the Integrated Ocean Observing System (IOOS), overcomes this difficulty by sampling many important habitat variables on the required scales. For example, Bakun (2010) described 3 major classes of physical processes important for yielding ideal reproductive habitat for coastal fishes: processes of en-

richment (i.e. upwelling and mixing), concentration (i.e. convergence and formation of fronts) and retention within or advection toward nursery grounds, each of which involves several pelagic features and processes best described by remotely sensed currents and fronts. IOOS can also be used to describe what is in the water and can sometimes be used to estimate the amount of food (primary productivity) in the area. By considering dynamic water column features and processes that can be measured both *in situ* and remotely with comparatively stable seabed features, we can more precisely describe the 3-dimensional structure of the environment to which marine species respond (Game et al. 2009).

The technology that IOOS uses to detect these pelagic variables remotely includes satellites (i.e. sea surface temperature and ocean color), high frequency (HF) radar (i.e. sea surface currents) and gliders (i.e. water column temperature, salinity, optical backscatter). These data streams are analyzed to produce derived variables such as chlorophyll, water mass boundaries and surface divergence. Satellites and HF radar provide the greatest amount of spatial coverage and include synoptic maps of surface currents, temperature and chlorophyll. These fields can be combined to map the location and relative strength of water mass boundaries (Oliver et al. 2004, Oliver & Irwin 2008). While these observations are confined to the near-surface of the ocean, they are often indicative of the subsurface environment, especially during the winter and spring when the water column is well mixed in the MAB (Castelao et al. 2008). The increasing availability and coverage of various types of remotely sensed data in the MAB allow us to examine the relationships between fish and the pelagic environment that until now could not be studied in the region.

In the present study we combined measurements of habitat features on the bottom and in the water column to identify important species–habitat relationships in the MAB coastal ocean. We built statistical relationships between fish abundances and habitat characteristics likely to affect the growth, survival, dispersal and reproduction of marine species. Abundances were measured by the National Marine Fisheries Service, Northeast Fisheries Science Center's (NMFS-NEFSC) bottom trawl surveys, and habitat characteristics were measured with remote sensing and *in situ* technologies. Remotely sensed data were provided by the Mid-Atlantic Regional Association Coastal Ocean Observing System (MARACOOS) ([www.maracoos.org](http://www.maracoos.org)), a regional association of IOOS. This study consisted of 3 major components: (1) a determination of the environmen-

tal variables most strongly correlated with variations in fish and invertebrate abundance; (2) a quantification of the independent and joint effects on fish and invertebrate community structure of environmental variables in 3 categories—seabed variables, pelagic variables measured *in situ* (from conductivity, temperature and depth profiles) and pelagic variables measured with remote sensing technology; and (3) a description of the spatial structure of environmental gradients and responses of species with northern and southern species ranges and associations with the seabed or water column. Our goals were to identify habitat-defining environmental characteristics in the MAB, examine the effectiveness of remote sensing technology for measuring those characteristics and provide baseline information for IOOS-informed space-based ecosystem management.

## MATERIALS AND METHODS

### Study area

The MAB extends from Cape Cod, Massachusetts, USA, to Cape Hatteras, North Carolina, USA. Physical variation between seasons in this area is among the most dramatic in the global ocean and this highly dynamic environment makes it an important location to study the effects of changes in pelagic features on fish and invertebrate distributions. Many of the fish and invertebrates in the MAB have evolved to be highly migratory and should respond to the dynamic water column features, which include gradients in temperature, stratification and surface currents (Gong et al. 2010, Shearman & Lentz 2010). Many of these species are also of great interest to both commercial and recreational fisheries. Though there is high benthic biomass, pelagic species are still very important (Link et al. 2008). The region has a well-developed ocean observation system that integrates data describing these features and, thus, is well suited for this type of research.

### Species abundance data

Abundance estimates for fish and invertebrate species were determined

from fall, winter and spring fisheries-independent bottom trawl surveys conducted by NMFS-NEFSC (Table 1, Fig. 1). The survey design and trawl characteristics are described in detail by Azarovitz (1981). Winter cruises occurred in February, spring cruises between March and the beginning of May and fall cruises from the beginning of September through late October. The winter and spring surveys were undertaken when the water column was relatively well mixed compared with fall cruises (Gong et al. 2010). Survey tows were made with a #36 Yankee trawl (12.7 cm stretched mesh opening, 11.4 cm stretched mesh cod end, 1.25 cm stretched mesh lining in cod end and upper belly) equipped with rollers and a 10.4 m wide  $\times$  3.2 m high opening. The net was towed at  $\sim$ 3.5 knots over the bottom for 30 min. The distance a net was towed at each station averaged 1.9 nautical miles (95 % confidence limits, 1.75 to 2.01 nautical miles). Trawls occurred throughout the 24 h day. We selected a spatial and temporal domain for analysis based upon the availability of remotely sensed data collected by MARACOOS. NEFSC bottom trawl samples collected from February 2003 through October 2007 in the central MAB between the Delmarva Peninsula and the eastern end of Long Island between latitudes 37.14 to 40.85°N and longitudes 70.83 to 75.16°W (Fig. 1) fit within the domain. Only samples with the full complement of important

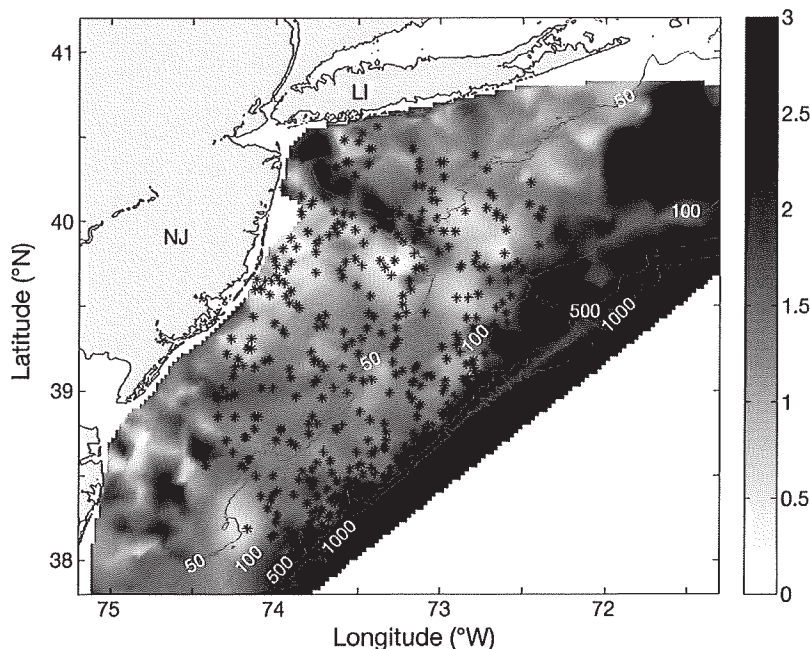


Fig. 1. Locations of sample sites in the Mid-Atlantic Bight (NJ: New Jersey; LI: Long Island) off the Atlantic coast of the USA. The locations of the trawls included in the analysis are shown overlapping a map of sediment grain size on a phi scale, where grain size in mm =  $2^{(-\phi)}$



Table 1. Common and scientific names (listed alphabetically by the latter) of the 65 species included in the multivariate analysis. Species included were those observed in at least 10 of the trawls used in the analysis

Common name	Scientific name	Common name	Scientific name
Blueback herring	<i>Alosa aestivalis</i>	Haddock	<i>Melanogrammus aeglefinus</i>
Alewife	<i>Alosa pseudoharengus</i>	Atlantic silverside	<i>Menidia menidia</i>
American shad	<i>Alosa sapidissima</i>	Offshore hake	<i>Merluccius albidus</i>
Northern sand lance	<i>Ammodytes dubius</i>	Silver hake	<i>Merluccius bilinearis</i>
Deepbody boarfish	<i>Antigonia capros</i>	Smooth dogfish	<i>Mustelus canis</i>
Striated argentine	<i>Argentina striata</i>	Lanternfish, unclassified	Myctophidae
Jonah crab	<i>Cancer borealis</i>	Bullnose ray	<i>Myliobatis freminvillei</i>
Atlantic rock crab	<i>Cancer irroratus</i>	Longhorn sculpin	<i>Myoxocephalus octodecemspinosus</i>
Black sea bass	<i>Centropristis striata</i>	Atlantic hagfish	<i>Myxine glutinosa</i>
Shortnose greeneye	<i>Chlorophthalmus agassizi</i>	Snake eel, unclassified	Ophichthidae
Gulf stream flounder	<i>Citharichthys arctifrons</i>	Summer flounder	<i>Paralichthys dentatus</i>
Atlantic herring	<i>Clupea harengus</i>	Fourspot flounder	<i>Paralichthys oblongus</i>
Conger eel, unclassified	Congridae	Butterfish	<i>Peprilus triacanthus</i>
Barndoor skate	<i>Dipturus laevis</i>	Armored searobin	<i>Peristedion miniatum</i>
Smallmouth flounder	<i>Etropus microstomus</i>	Sea lamprey	<i>Petromyzon marinus</i>
Red deepsea crab	<i>Geryon quinquedens</i>	Sea scallop	<i>Placopecten magellanicus</i>
Witch flounder	<i>Glyptocephalus cynoglossus</i>	Bluefish	<i>Pomatomus saltatrix</i>
Blackbelly rosefish	<i>Helicolenus dactylopterus</i>	Northern searobin	<i>Prionotus carolinus</i>
Sea raven	<i>Hemitripterus americanus</i>	Striped searobin	<i>Prionotus evolans</i>
American lobster	<i>Homarus americanus</i>	Winter flounder	<i>Pseudopleuronectes americanus</i>
Northern shortfin squid	<i>Illex illecebrosus</i>	Clearnose skate	<i>Raja eglanteria</i>
Fawn cusk-eel	<i>Lepophidium profundorum</i>	Windowpane	<i>Scophthalmus aquosus</i>
Little skate	<i>Leucoraja erinacea</i>	Atlantic mackerel	<i>Scomber scombrus</i>
Rosette skate	<i>Leucoraja garmani</i>	Chain dogfish	<i>Scyliorhinus rotifer</i>
Winter skate	<i>Leucoraja ocellata</i>	Bobtail, unclassified	Sepiolidae
Yellowtail flounder	<i>Limanda ferruginea</i>	Spiny dogfish	<i>Squalus acanthias</i>
Atlantic seasnail	<i>Liparis atlanticus</i>	Scup	<i>Stenotomus chrysops</i>
Longfin squid	<i>Loligo paeleii</i>	Tonguefish	<i>Symphurus</i> sp.
Goosefish	<i>Lophius americanus</i>	Red hake	<i>Urophycis chuss</i>
Ocean pout	<i>Macrozoarces americanus</i>	Spotted hake	<i>Urophycis regia</i>
Longspine snipefish	<i>Macrorhamphosus scolopax</i>	White hake	<i>Urophycis tenuis</i>
Grenadier, unclassified	Macrouridae	Buckler dory	<i>Zenopsis conchifera</i>
Spider crab, unclassified	Majidae		

environmental variables were considered in the final model: an average of 26 samples each winter, 33 each spring and 20 each fall. The 65 species we used for this analysis were observed in at least 10 of the bottom trawls included in the final model (Table 1). Species abundance was normalized to the trawl distance and log transformed for analysis.

### Habitat data

#### Seabed data

For the purposes of this study we considered 'seabed' features to be seafloor characteristics, such as topography and sediment grain size, that remain relatively stable over time. We computed topographic seabed habitat characteristics from the 3-arc-second Coastal Relief Model available from the

National Geophysical Data Center (93 m cell size; [www.ngdc.noaa.gov/mgg/coastal/coastal.html](http://www.ngdc.noaa.gov/mgg/coastal/coastal.html)) (Table 2). We used circular-moving window analysis in Geographic Resources Analysis Support System Geographic Information System (GRASS GIS) software to calculate median and SD values of bottom depth, aspect, slope and curvature from the relief model (Neteler & Mitasova 2008), with a window diameter of 2 km. Profile bottom curvature measured the concavity and convexity of the surface parallel to major axes of slope (Neteler & Mitasova 2008). Sediment grain sizes (phi) for the trawl samples were selected from a map interpolated from records in the usSEABED data base (Reid et al. 2005). The map of sediment grain size had a spatial resolution of 2.0 km and was constructed by using sampling bias correction, maximum *a posteriori* resampling and a spline-in-tension algorithm described in Goff et al. (2006, 2008).

Table 2. Data sources and possible ecological effects of environmental variables considered in the CCA. Unless otherwise noted, the source of seabed variables is [www.ngdc.noaa.gov/mgg/coastal/coastal.html](http://www.ngdc.noaa.gov/mgg/coastal/coastal.html), the source of CTD variables is the shipboard CTD and the sources of remotely sensed data are HF radar for surface current data and Moderate Resolution Imaging Spectrometer (MODIS) for satellite data. Geographic coordinates were recorded at the time of the trawl, and solar elevation was calculated with the maptools library in R.  $\mu$ : mean value; PE: potential energy; HF: high frequency; na: not applicable; MAB: Mid-Atlantic Bright

Habitat variable	Spatial resolution	Effect or process
Solar elevation	na	Vertical migration/catchability
Seasonality	na	Various
<b>Seabed data</b>		
Depth ( $\mu^a$ and SD)	1.95 km	Structural/spatial refuge
Slope ( $\mu^b$ and SD)	1.95 km	Structural/spatial refuge
Aspect (SD)	1.95 km	Structural/spatial refuge
Profile curvature ( $\mu$ and SD)	1.95 km	Structural/spatial refuge
Sediment grain size ( $\mu^a$ , from usSEABED)	2 km	Structural/spatial refuge/enrichment
<b>Pelagic data: CTD</b>		
Bottom temperature <sup>a</sup>	na	Metabolic rate
Bottom salinity	na	Proximity to freshwater source
Surface salinity <sup>b</sup>	na	Proximity to freshwater source
Mixed-layer depth	na	Mixing/primary productivity
Stratification <sup>a</sup>	na	Mixing/primary productivity
Simpson's PE (upper 30 m)	na	Mixing/primary productivity
<b>Pelagic data: remotely sensed (HF radar)</b>		
Cross-shelf velocity (raw $\mu$ and SD, de-tided $\mu$ and SD, filtered $\mu^a$ and SD)	10 km radius	Advection/movement cost/mixing
Along-shelf velocity (raw $\mu$ and SD, de-tided $\mu$ and SD, filtered $\mu$ and SD)	10 km radius	Advection/movement cost/mixing
Variance in raw velocities (cross-shelf <sup>a</sup> and along shelf)	10 km radius	Tidal mixing/episodic forcing
Divergence/convergence ( $\mu$ and SD)	10 km radius	Upwelling/water column mixing
Divergence/convergence tendency <sup>a</sup>	10 km radius	Upwelling/water column mixing
Vorticity ( $\mu$ and SD)	10 km radius	Eddy development/retention
Vorticity tendency	10 km radius	Eddy development/retention
<b>Pelagic data: remotely sensed (satellite)</b>		
SST ( $\mu^c$ and SD)	10 km radius	Metabolic rate/seasonality
Chl <i>a</i> ( $\mu$ and SD)	10 km radius	Primary productivity/organic matter
Water-leaving radiances at 412, 443, 488, 531, 551 and 667 nm ( $\mu$ and SD)	10 km radius	Water clarity and brightness/organic matter
Water-leaving radiance divided by the maximum at each trawl: 412, 443, 488 <sup>a</sup> , 531, 551 <sup>b</sup> and 667 nm	10 km radius	Water clarity/organic matter
Water mass class	na	Various
Gradient strength and distance to gradient (frontal index)	na	Enrichment/concentration

<sup>a</sup>Variable is included in the final CCA model  
<sup>b</sup>Residuals of a GAM with log-transformed depth are included in the final CCA model  
<sup>c</sup>Anomalies from MAB 7 yr monthly averages are included in the final CCA model

### Pelagic data

We considered all characteristics of the water column to be 'pelagic', including water temperatures and salinities measured *in situ* near to the substrata. These characteristics and remotely measured features vary over much shorter timescales than do the seabed variables. We used conductivity, temperature, and depth (CTD) profiles collected during NEFSC bottom trawl surveys to describe water column characteristics in-

cluding temperature, salinity and water column structure and stability (Table 2). We considered mixed layer depth (depth at which density was  $0.125 \text{ kg m}^{-3}$  greater than surface density, Levitus 1982), a stratification index (density difference between 50 m and the surface), and Simpson's potential energy (PE) anomaly (Simpson 1981) in our analysis. Because the stability index for the entire water column was positively correlated with bottom depth, we used Simpson's PE calculated within the upper 30 m of the water column.

Surface features were observed remotely with shore-based and space-based sensors. HF radar (Barrick et al. 1977) provided remotely sensed surface current measurements (Table 2). A network of HF radars (frequency = 5 MHz) maintained by MARACOOS measured radial current vectors that were geometrically combined to produce total vector surface current maps each hour with a resolution of 6 km from the shore to the edge of the continental shelf ([www.maracoos.org](http://www.maracoos.org), Roarty et al. 2010). These data have been used to describe seasonal (Gong et al. 2010) and event-scale surface dynamics (Dzwonkowski et al. 2010) in the MAB. The entire raw time series for each HF radar grid point was detided with a least squares fit of the 5 strongest tidal constituents (M2, S2, N2, K1 and O1). These detided data were then lowpass filtered with a cutoff period of 30 h, which left filtered velocity data that only showed variability on time scales longer than 30 h. We only used data for grid points with >25% return over the annual records. Surface divergence (represented as vertical velocity at 1 m depth) and vorticity (normalized by the local Coriolis parameter of the lowpass filtered fields) were calculated using finite difference (Dzwonkowski et al. 2010, Gong et al. 2010). We considered 1 and 8 d mean raw, de-tided and filtered cross-shore and along-shore velocities, as well as divergence, vorticity and the variance of the raw fields within 10 km of each trawl sample in our modeling. To identify species associations with areas where upwelling and downwelling occurred over time scales longer than 8 d we calculated a seasonal 'divergence tendency' for each year by assigning a new value of -1 to instantaneous divergence (vertical velocity) values that were less than  $-0.1 \text{ m d}^{-1}$  (downwelling), 0 to values between  $-0.1$  and  $+0.1 \text{ m d}^{-1}$  (neutral) or +1 to values greater than  $+0.1 \text{ m d}^{-1}$  (upwelling). These new values were averaged for each grid point to produce a mapped index of upwelling and downwelling potential for each season and year. We calculated divergence tendency for each trawl by averaging all seasonal means within 10 km of the trawl location. The same processing was performed to generate vorticity tendencies using threshold values of  $\pm 0.02$ . Thresholds were in approximately the 25th and 75th percentiles of the entire set of values.

Satellite remote sensing provided maps of surface temperature, chlorophyll *a* (chl *a*) and water-leaving radiance within 10 km of each NEFSC trawl tow over the previous 24 h and 8 d before each bottom trawl tow (Table 2), which helped to fill in some of the gaps in coverage. We used data from the Moderate Resolution Imaging Spectrometer (MODIS) binned to

1 km spatial resolution with the standard data quality flags using Seadas v. 5.3 for sea surface temperature (SST) and ocean color (<http://oceancolor.gsfc.nasa.gov>). Since the seasonal signal in SST is so large in the region, ranging from less than  $3^{\circ}\text{C}$  to about  $28^{\circ}\text{C}$ , especially in shallower water (Shearman & Lentz 2010), we removed this seasonal variability to develop spatial SST anomalies independent of the strong seasonal signal. We used anomalies of raw SST from monthly 7 yr composites averaged over the entire study site instead of raw SST data. To account for this adjustment we included season as a factor in the analysis. We considered measurements of chlorophyll ( $\text{mg m}^{-3}$ ) and normalized water-leaving radiance (nlw,  $\text{W m}^{-2} \text{ sr}^{-1} \mu\text{m}^{-1}$ ) at 412, 443, 488, 531, 551 and 667 nm (nlw412, nlw443, ... nlw667). In addition to raw channel values, we also considered each wavelength divided by the maximum radiance measured for each survey as a proxy for spectral shape of the water-leaving radiance. In coastal oceans, there are many other optically active constituents in the water that are not captured and contaminate the chlorophyll estimates from space (Preisendorfer 1976). Spectral shape is another source of information that is correlated with the overall optical load of the coastal ocean. Hereafter, we refer to spectral shape (the wavelengths relative to the maximum for each site) as rnlw412, rnlw443, ... rnlw667.

Ensemble clustering was applied to satellite SST and reflectance measured at 490 and 555 nm to objectively classify water masses. Gradient strengths along frontal boundaries between water masses were determined using the methods described in Oliver et al. (2004) and Oliver & Irwin (2008). We used maps of gradient strength along frontal boundaries of the 27 water masses identified to compute a frontal index equal to the front strength divided by the distance to the front. Because many of the 27 water masses contained fewer than 5 NEFSC trawl samples, we agglomerated the 27 water masses into 8 using k-means clustering and the satellite data used in the original ensemble clustering. Each of the 8 water masses included at least 20 trawl tows.

Since the species selected for analysis can exhibit day–night differences in behavior, including vertical migration, capture efficiencies in bottom trawls can vary with the time of day of the sampling (Powell et al. 2004). We used the maptools library in R (Lewin-Koh & Bivand 2008, R Development Core Team 2008) to calculate solar elevations for the times and locations of each trawl and included these in our model for partial analyses. All of the environmental variables except for season and solar elevation were



divided into one of 3 categories: CTD (*in situ* pelagic), IOOS (remotely sensed pelagic) or seabed (Table 2).

### Statistical model development

We used canonical correspondence analysis (CCA) to describe the environmental gradients most strongly related to community variation in the MAB. Following application of principal component analysis to identify highly intercorrelated variables in each variable set, we performed the analysis described in detail below (Fig. 2). We used backward selection of variables within each category of habitat data and with all habitat categories combined to create the final CCA model. We then used partial CCA to determine the relative explanatory value of each category. Finally we mapped habitat gradients extracted from the full CCA and used generalized additive modeling (GAM) analysis of species responses to these gradients.

All statistical analysis was performed with R, a free software used for statistical computing and graphics (R Development Core Team 2008). CCA and partial CCA were conducted using the *vegan* library, a package with several tools available for various analyses of ecological communities (Oksanen et al. 2008). GAMs identifying nonlinear relationships between intercorrelated environmental variables and between species abundance and environmental gradients were formed

with the *mgcv* library, a package containing routines for GAMs and similar regressions (Wood 2006).

### Variable selection for models

We used CCA because it allowed us to simultaneously ordinate nonlinear species responses to long environmental gradients as opposed to redundancy analysis that assumes linear responses to environmental gradients (McGarigal et al. 2000, Oksanen et al. 2008). This technique identifies environmental variables that can be combined to best explain the total community variation.

We first performed 3 separate CCAs, one for each category of environmental data (seabed, CTD pelagic and remotely sensed pelagic), to identify highly redundant variables and reduce the number of environmental variables in each set. This was followed by a total CCA including season, solar elevation and all significant variables from each initial CCA. We performed backward selection and selected variables with values of  $p < 0.01$  in Monte Carlo permutation tests. We further reduced variables by only including those with possible mechanistic effects on the physiology or behaviors of the animals (Table 2). For variables that were highly intercorrelated and had the same ecological meanings, the least noisy and most ecologically meaningful variable was used. For intercorrelated

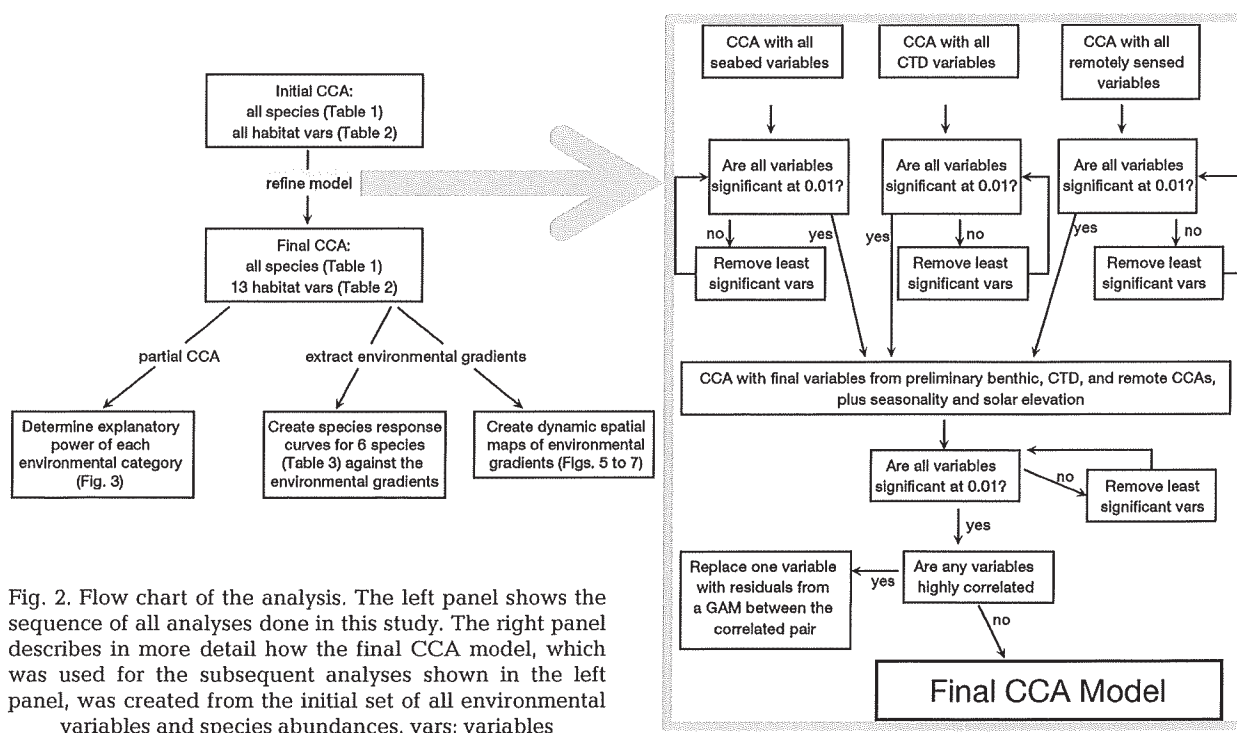


Fig. 2. Flow chart of the analysis. The left panel shows the sequence of all analyses done in this study. The right panel describes in more detail how the final CCA model, which was used for the subsequent analyses shown in the left panel, was created from the initial set of all environmental variables and species abundances. vars: variables

pairs with different implications, one variable in the pair was replaced with residuals from a GAM fit between the intercorrelated pair. Because there was a large skew to the left for depth, we used log-transformed depth in the model. The final CCA model included the 65 species listed in Table 1 and 13 environmental variables — season, 3 seabed variables, 3 CTD variables and 6 remotely sensed variables (Table 2).

### Model partitioning

We determined relative explanatory power of each category of environmental data (seabed, CTD pelagic and remotely sensed pelagic; Table 2) and overlap in explanatory power between categories with partial and constrained CCA using the variables included in the final CCA (Borcard et al. 1992, Cushman & McGarigal 2002).

### Species responses to environmental variability

We used scores for each trawl station along each of the first 3 CCA axes to map the gradients extracted in the ordination and examine the responses of species to them. Color maps of each gradient within each season were derived by applying bilinear interpolation to the station scores on a grid with a cell size of 0.025° latitude (2.8 km) by 0.025° longitude (2.1 km). To describe species responses to the environmental gradients, we chose 6 species from the 65 included in the CCA that were well described by the ordination (Table 3). These species also represented different latitudinal ranges relative to the Northeast US Continental Shelf Large Marine Ecosystem (north and south) and water column preferences (pelagic fish, pelagic squid and benthic flatfish); these included Atlantic herring *Clupea harengus*, witch flounder

*Glyptocephalus cynoglossus*, northern shortfin squid *Illex illecebrosus*, butterfly *Peprilus triacanthus*, summer flounder *Paralichthys dentatus* and longfin squid *Loligo paeleii*. Each of these species is common in the MAB and had relatively high goodness-of-fit scores in the final CCA model. GAM was used to fit a response curve using the relative abundance of each of these 6 species at the trawl stations as the dependent variable against the CCA axis scores for the trawl stations along each of the first 3 gradients derived from the ordination.

## RESULTS

### Variable selection

A total of 13 habitat variables were selected for final analysis based upon correlation structure of the independent variables and the ecological mechanisms they represented. These variables included season, 3 seabed variables (log-transformed depth, bottom slope residuals versus log-transformed depth, sediment grain size), 3 pelagic variables measured *in situ* with CTDs (bottom temperature, surface salinity residuals versus log-transformed depth, stratification) and 6 remotely sensed pelagic variables (8 d mean rnlw488, rnlw551 residuals versus log-transformed depth, SST anomalies and filtered cross-shore velocity, 8 d variance in raw cross-shore velocity and seasonal divergence tendency).

### Community variance partitioning

The 13 variables included in the final CCA model accounted for 26.0% of the community variation. When the effects of season were removed from the model, 23.7% of the community response was explained by the 12 remaining environmental variables.

Each of the 3 categories of environmental data considered (seabed, CTD pelagic, remotely sensed pelagic) individually explained approximately the same proportion of this 23.7% (Fig. 3), but the pelagic characteristics (remotely sensed: 46.9%; CTD: 45.1%) explained slightly more than the seabed characteristics (40.9%). Remotely sensed pelagic variables were redundant with both seabed and pelagic variables measured with CTD

Table 3. The 6 species analyzed in response to the environmental gradients extracted from the CCA

Common name	Scientific name	Latitudinal region	Water column preference
Atlantic herring	<i>Clupea harengus</i>	Northern	Pelagic fish
Witch flounder	<i>Glyptocephalus cynoglossus</i>	Northern	Benthic flatfish
Northern shortfin squid	<i>Illex illecebrosus</i>	Northern	Pelagic squid
Butterfish	<i>Peprilus triacanthus</i>	Southern	Pelagic fish
Summer flounder	<i>Paralichthys dentatus</i>	Southern	Benthic flatfish
Longfin squid	<i>Loligo paeleii</i>	Southern	Pelagic squid

(16.7 and 16.0%, respectively), while there was little correlation between seabed variables and pelagic characteristics measured with CTD (3.0%). Redun-

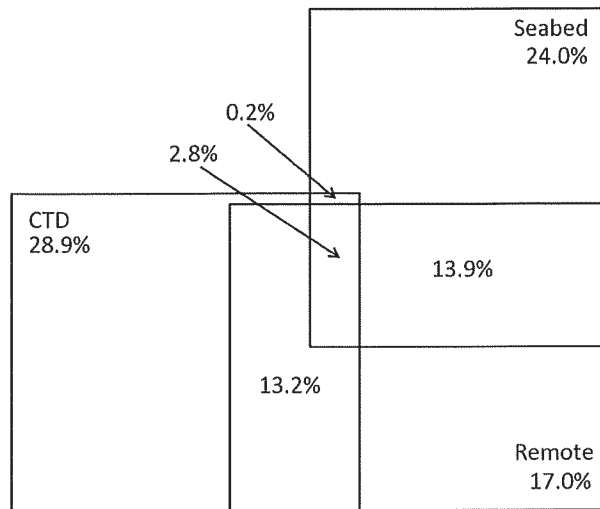


Fig. 3. Relative explanatory power of categories of habitat data. Proportion of the total 23.7% of the community response explained by spatial variation divided into 3 categories (seabed, CTD pelagic, remotely sensed pelagic) is depicted. Overlap between categories indicates redundancy between those categories. Pelagic categories were as effective at explaining community response as the seabed category was. The remotely sensed category showed high redundancy with both other categories

dancy between the remotely sensed category and the seabed category appeared to be primarily due to a correlation between log-transformed depth and the spatial SST anomaly. Redundancy between pelagic habitat measured remotely and *in situ* with CTD profiles was probably due to correlations between the CTD-derived variables of surface salinity residuals and water column stratification and the remotely sensed variables of cross-shore velocity, variance in cross-shore velocity, and *rnw551* residuals (Fig. 4).

### Species response to CCA axes

The first 3 axes of the final CCA model accounted for 71.3% of the explained community variation

Table 4. Amount of variation accounted for by the CCA explained by each of the first 3 axes and the most influential variables on each axis

CCA axis	% explained	Cumulative % explained	Important habitat variables
1	39.3	39.3	SST anomaly Log-transformed depth
2	20.7	60.0	Log-transformed depth Bottom temperature
3	13.1	73.1	Stratification

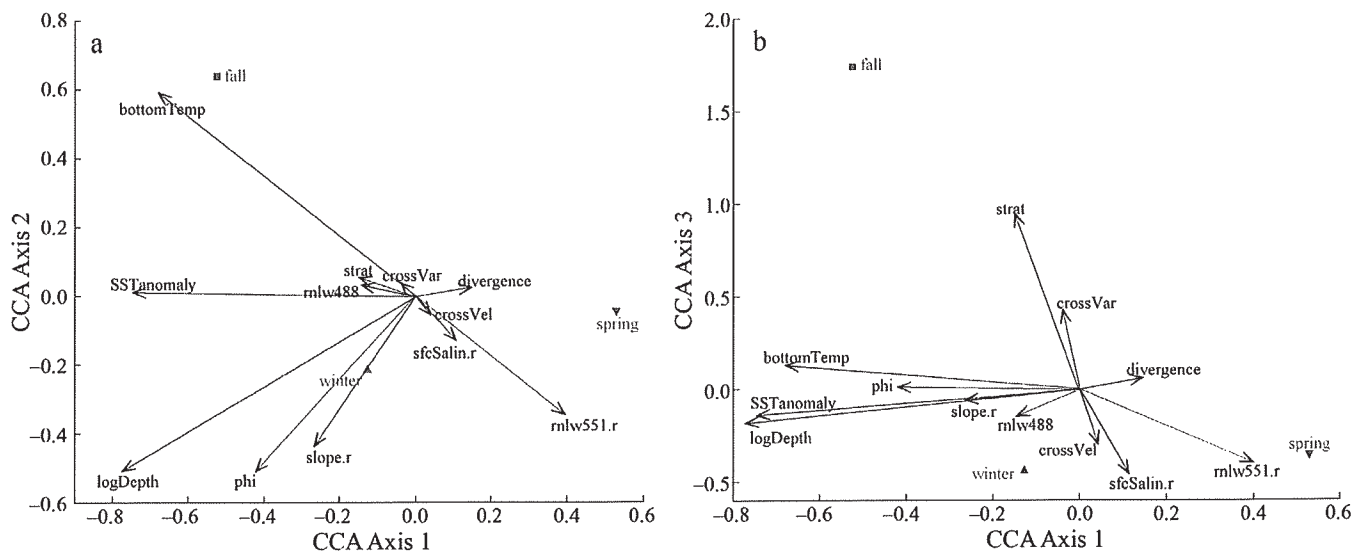


Fig. 4. CCA biplots for the final model. (a) Axes 1 and 2 and (b) Axes 1 and 3 are shown. Points correspond to weighted centroids for each season and arrows correspond to biplot scores for spatial environmental variables (logDepth: log-transformed depth; slope.r: slope residuals versus depth; phi: sediment grain size; bottomTemp: bottom temperature; sfcSalin.r: surface salinity residuals versus depth; strat: stratification; *rnw488*: water-leaving radiance at 488 nm relative to the maximum at a site; *rnw551.r*: *rnw551* residuals versus depth; SSTanomaly: SST anomaly; crossVel: filtered cross-shore velocity; crossVar: variance in raw cross-shore velocity; divergence: divergence tendency). Variables corresponding to arrows reaching far along an axis are important on that axis



(Table 4). The remaining axes had about half the explanatory power (or less) compared with any of these 3 axes (Fig. 4). Maps of environmental gradients derived from the CCA and the species response curves to those gradients indicate areas and times the species were most likely to occur in the study area for winter, spring and fall of 2006 (Figs. 5 to 7).

The first axis was defined by a winter/spring cross-shelf gradient. The most influential variables on the first axis ('+' indicates a positive correlation with axis scores, '-' indicates a negative correlation) were log-transformed depth (-), SST anomaly (-), bottom temperature (-), sediment grain size (phi, -) and rnlw551 residuals (+). Axis scores tended to be

low across the entire shelf during the fall owing to high SST over shallow water inshore and low SST over deep water farther offshore. In the winter and spring, low SST over shallow inshore water and high SST over deeper offshore water created a gradient with high axis scores close to shore that decreased farther offshore. Atlantic herring and summer flounder were most abundant in areas with high scores on this axis and showed an association with shallow, cold areas with coarse-grained sediment and anomalously high rnlw551 (551 nm is in the green range of the spectrum). Witch flounder, northern shortfin squid and longfin squid all tended to be most abundant at very negative axis values

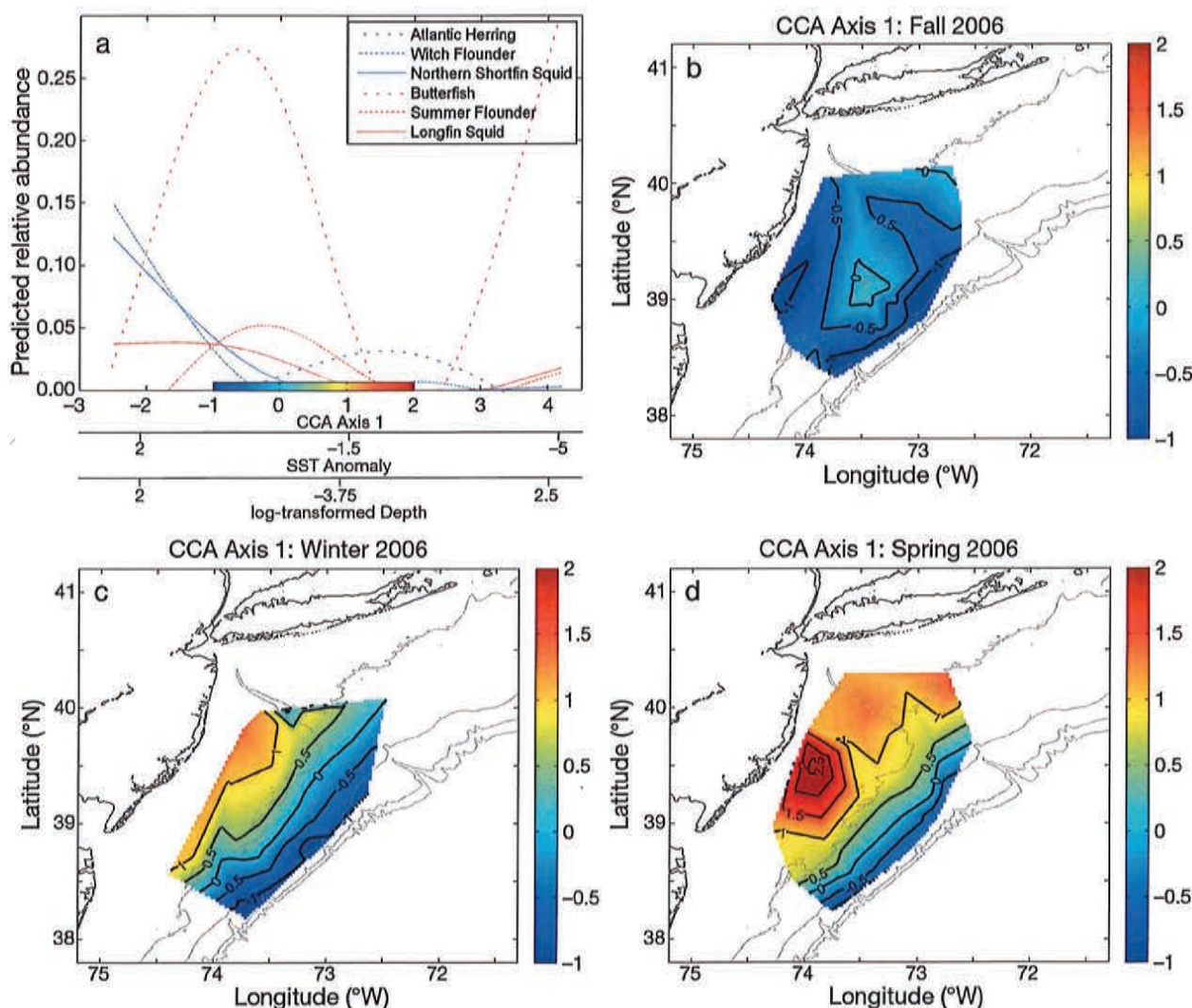


Fig. 5. Response curves and spatial maps for CCA Axis 1. (a) Abundance, relative to the maximum observed abundance, is plotted for 6 species as predicted by a GAM dependent on Axis 1 scores, correlated with SST anomaly and depth (blue: northern; red: southern; solid: pelagic squid; dotted: pelagic fish; dashed: benthic flatfish). Color maps and contours show how Axis 1 scores are distributed spatially for (b) fall, (c) winter and (d) spring of 2006



(Figs. 4 & 5). Butterfish and summer flounder were not well explained on this axis.

The second axis was a cross-shelf gradient that was stronger during the fall and mostly consisted of bottom temperature (+) and seabed variables including log-transformed depth (-), sediment grain size (phi, -) and bottom slope residuals (-). Shallow water with a warm bottom, coarse-grained sediment and an anomalously small slope for that depth produced high scores here. Spatial maps of this axis showed high scores inshore and low scores offshore in the fall (from shallow water with a warm bottom to deep water with a cold bottom). In the winter and spring, bottom temperature and depth balanced each other

on the axis and resulted in maps that were neutral across the entire region. Southern species (butterfish, summer flounder, longfin squid) were most abundant where axis values were very positive, while northern species (Atlantic herring, witch flounder, northern shortfin squid) tended to be most abundant where axis values were more negative (Figs. 4 & 6). Atlantic herring and northern shortfin squid were not well explained on this axis and southern species were better explained than northern species.

The third axis was characterized mostly by stratification (+), but variance in raw cross-shore velocity (+), surface salinity residuals (-), and rnlw551 (-) were also important. Sites with high scores on this axis ex-

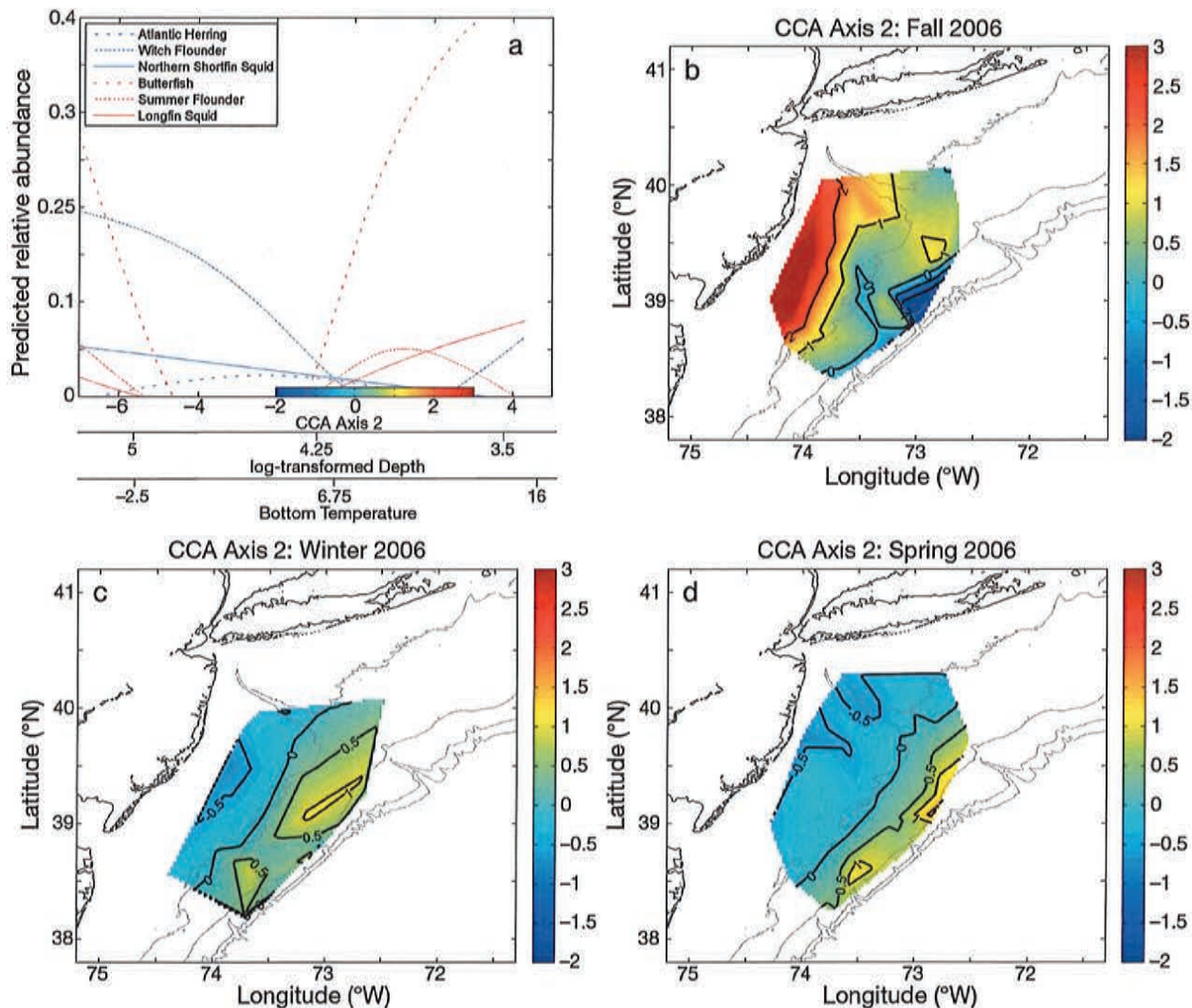


Fig. 6. Response curves and spatial maps for CCA Axis 2. (a) Abundance, relative to the maximum observed abundance, is plotted for 6 species as predicted by a GAM dependent on Axis 2 scores, correlated with depth and bottom temperature (blue: northern; red: southern; solid: pelagic squid; dotted: pelagic fish; dashed: benthic flatfish). Color maps and contours show how Axis 2 scores are distributed spatially for (b) fall, (c) winter and (d) spring of 2006



hibited high stratification, high variance in cross-shore velocity, and low surface salinity and  $\text{rnlw551}$  for that depth. This axis included major environmental factors that all exhibit strong seasonal variation. Fall samples had high values on this axis and were collected in locations where stratification was high, salinity was low, onshore flow was variable and the water was relatively clear. Maps of this gradient in the fall show scores that were low very near the coast but increased rapidly with depth and were high throughout most of the study area. During winter and early spring when the water column was well mixed, scores along this gradient were low throughout the study area. Summer flounder and Atlantic herring were most abundant at

low gradient values, while northern shortfin squid was most abundant at high values (Figs. 4 & 7). Longfin squid, witch flounder, butterfish and Atlantic herring were not well explained on this axis.

## DISCUSSION

We took a community-based multivariate approach to define important environmental gradients in the MAB. We eliminated most of the environmental variables initially considered because they were redundant with other variables or not significant to the model. These factors were further condensed into 2

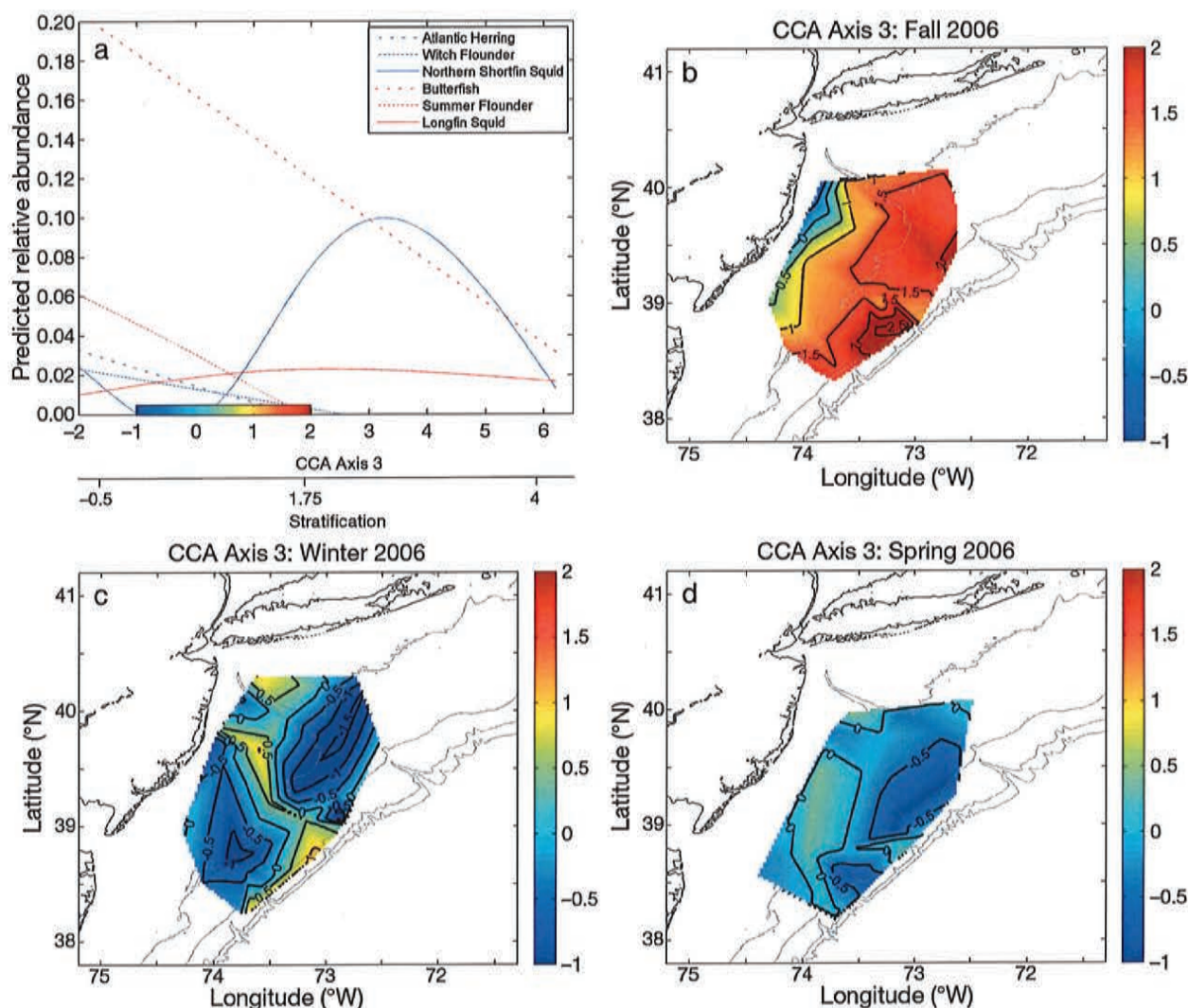


Fig. 7. Response curves and spatial maps for CCA Axis 3. (a) Abundance, relative to the maximum observed abundance, is plotted for 6 species as predicted by a GAM dependent on Axis 3 scores, correlated with stratification (blue: northern; red: southern; solid: pelagic squid; dotted: pelagic fish; dashed: benthic flatfish). Color maps and contours show how Axis 3 scores are distributed spatially for (b) fall, (c) winter and (d) spring of 2006



major gradients (cross-shelf and seasonal) associated with variations in fish and invertebrate community structure in the MAB. These environmental gradients were relatively well described by the seabed and pelagic features we considered in our analysis. Surface pelagic features measured remotely and integrated into ocean observation systems increased the explanatory power of our model beyond what was traditionally used in marine habitat analyses (seabed and pelagic variables measured with CTD). Furthermore, several important habitat features measured by CTD were correlated with remotely sensed features; this indicates that it may be possible to use remote sensing as a proxy without going to sea. These types of analyses make it possible to look at the ecosystem holistically and avoid evaluating each species independently. Identifying environmental features important to large groups of species should lead to more parsimonious descriptions of essential fish habitat and be useful for defining areas for ecosystem process studies.

Though only a seemingly small percentage of community variation was explained by the CCA (26%), several authors argue that total variance explained carries very little meaning in ordinations and that ordinations should be used primarily as graphical tools (Palmer 1993, Oksanen 2011). A multivariate approach used to predict the responses of many species to only a few environmental variables cannot be expected to directly predict species abundances; even a small amount of variance explained still provides valuable information (Palmer 1993, Cushman et al. 2007).

### Importance of pelagic habitat

Current spatial management focuses nearly exclusively on seabed habitat characteristics and features with slow spatial dynamics (Leslie 2005). Bottom structure provides refuge from predators and drag induced by current flow and partially controls the composition and densities of benthic prey. The environmental gradient represented by our second CCA axis was composed almost exclusively of seabed variables; bottom temperature was the only pelagic characteristic important on the axis. Because many species depend on features that vary over scales smaller than the 2 km grid used in this study, these variables may have been even more powerful in the model if data with finer spatial resolution had been available. However, the pelagic habitat is at least as important for describing community structure in the MAB (Nye

et al. 2009), and in our analysis two of the top 3 most explanatory axes of the model were primarily defined by pelagic features. Pelagic features measured *in situ* with CTD and remotely each explained about as much community variation as the seabed category, and only 24 % of the community variation accounted for was unrelated to the pelagic categories measured with the CTD or remote sensing. The dominant environmental gradient (CCA Axis 1) was described by both seabed and pelagic variables, including temperature and *rnw551*. The third axis was defined by a combination of stratification and other processes related to mixing and thus exclusively by pelagic features.

No discernible differences could be distinguished between the responses for benthic flatfish, pelagic fish and pelagic squid to any of the environmental gradients. There may be a northern–southern distinction on the second axis; southern species were more abundant in shallow, warm water ( $>7^{\circ}\text{C}$ ), but it is difficult to draw conclusions from this because two out of the 3 northern species were not well explained on this axis. Species responses to environmental gradients reasonably reflected typical species distributions and seasonal migrations. Witch flounder remains in deep water year-round (Cargnelli et al. 1999). Herring was only well explained on the first axis, as they were caught during winter and spring in cold, shallow, green (possibly due to primary productivity) water. During fall, when the second and third axes are well defined, Atlantic herring migrate into colder waters farther north and outside of our study range (Stevenson & Scott 2005). Northern shortfin squid were most abundant in offshore waters during the winter and spring, and even though they move inshore during the warmer fall months they still remain in relatively deep, stratified waters (Hendrickson & Holmes 2004). Summer flounder, on the other hand, were observed most often during the fall in warm, inshore waters that are shallow enough to be relatively unstratified (Packer et al. 1999). Longfin squid was most common in warm, deep water during the winter and spring, but was found much farther inshore during the fall in shallow, warm water (Jacobson 2005), similar to the distribution of butterfish (Cross et al. 1999).

It is not surprising to find that marine species respond to pelagic features, given how tightly they are coupled with their fluid environment. Because these species are ectothermic, water column characteristics such as temperature have important effects on their metabolism. They also rely heavily on the productivity of the ecosystem, which in turn depends on several factors, including plankton that are af-

ected by currents, primary productivity that is dependent on water column stability and other pelagic features that are often confined to the surface ocean. Our results showed that pelagic features were not merely somewhat important, but in fact explained the majority of community variation accounted for by this model and were major factors in two of the most important CCA axes. This supports the concept that seascapes need to be viewed as 3-dimensional environments in which the entire vertical water column is just as important as seabed features.

### **Ocean observing systems describe pelagic habitat and enhance habitat models**

Remotely sensed variables were important in our model, especially for defining the first and third CCA axes. Axis 1 was heavily weighted with both SST and *rnlw551*, and *rnlw551* and variance in currents were major variables on Axis 3. Remote sensing offers a growing number of possibilities, and several of the other variables that were most important on these axes could potentially be measured and predicted by using remote sensing equipment in the near future.

Many characteristics measured with CTD were well explained by remotely sensed data already available, as evidenced by the high degree of redundancy between remotely sensed surface pelagic features and both seabed and pelagic features measured with CTD; approximately one-third of each of these 2 categories was also described by remotely sensed variables. This suggests that remote-sensing methods for measuring sea surface characteristics are an effective proxy for water column structure, especially during the well-mixed seasons. The redundancy between remotely sensed pelagic features and the seabed features of depth, slope and sediment grain size was most likely due to the inclusion of monthly SST anomalies in the remotely sensed category; SST in deep water is less likely to vary as much as it does in shallow water. Redundancy of remotely sensed surface pelagic features with CTD variables appeared to be due to correlations of cross-shore velocity and variance in velocity, and *rnlw551* residuals with stratification and surface salinity residuals. This may be due to mixing processes in regions where surface current velocities are high and variable, which in turn may relate to surface characteristics like salinity and *rnlw551* (greenness) that are due to river runoff and mixing of the water column. Although we did not consider differences in redundancy between categories within seasons, it is likely that redundancy varies sea-

sonally. In the winter and early spring, surface characteristics are more likely to be similar to bottom characteristics even in relatively deep water because the water column tends to be unstratified. In summer and early fall, however, the water column is highly stratified and surface characteristics are less likely to represent conditions on the bottom (Castelao et al. 2008).

Remotely sensed variables also accounted for an additional 17% of the explained community variation independently of any redundancy with CTD-derived or seabed features. This indicates that ocean observatories not only provide information about habitat features routinely measured *in situ*, but also on features not ordinarily measured *in situ*. Furthermore, 6 habitat variables were included in the remotely sensed category of data: twice as many as in either the CTD or seabed category. While this indicates that there were many remotely sensed variables that contributed important information about habitat, it is important to note that there were also many remotely sensed variables available to be used in this analysis and only a few available in the seabed and CTD categories. The explanatory power of the category was increased simply owing to the number of variables used. The remotely sensed category explained approximately the same amount of community variation as the CTD and seabed categories; even though twice as many variables were included they did not seem to contribute proportionately to the explanation of community variation.

### **Future directions**

We were able to address and mitigate the effects of some common sources of uncertainty in multivariate ecological models (Cushman et al. 2007), but owing to the limited data available several questions are still left unanswered and deserve further study. Seabed variables in this analysis were assumed to be static over time, but in fact they can be very dynamic over our sampled time scales (Glenn et al. 2008, Harris & Stokesbury 2010). In addition, the trawls for winter, spring and fall took place over a limited time period and the entire seasons were not covered; no trawls were performed during the summer. Bottom trawl surveys are limited in their ability to represent the entire water column and therefore may not accurately describe distributions of pelagic species. It is also not safe to assume that fish are in a 'preferred' environment. They may be in transit between habitat patches or, if spawning, in (or moving to or from) an environment that is optimal for their young (Katz et

al. 1994, Terceiro 2007). We only had data available for individuals large enough to be captured in bottom trawls (mostly adults), but to fully understand the ecosystem, information about the abundance and distribution of all life stages is important. Models could also benefit by considering a time lag incorporating past environmental conditions experienced when adults were in younger, more vulnerable life stages. While we believe our major conclusions will hold across all seasons and for the ecosystem as a whole, the more specific details will probably vary depending on the seasons and species in question.

In the future, the ability of remote sensing equipment to augment *in situ* measurements can be increased further by measuring new characteristics, or by using new applications available with present equipment and by increasing the spatial and temporal coverage of the current equipment (between 2007 and 2008, the HF radar network was expanded to cover the entire MAB). Other ocean observing assets not considered in this study, such as gliders, can also provide more continuous measures of pelagic characteristics (including but not limited to those measured with CTDs) remotely at depths spanning the entire water column, and ensembles of dynamical physical models that assimilate these data have recently been implemented to forecast full vertical water column characteristics ([www.maracoos.org/](http://www.maracoos.org/)). There are already a number of great data sources, many of which were used in this study, that are useful resources for fisheries research and management. As technology develops further, the possibilities will expand.

Our study was a useful first step toward providing information required for effective space-based ecosystem management. Similar studies in the region have considered large-scale changes in distributions over relatively long time scales (e.g. Link et al. 2002, Nye et al. 2009), while our study emphasized fine-scale variations in space and time. Further development of our approach can provide techniques for developing dynamic models that describe essential fish habitat for ecologically and economically important species (Manderson et al. 2011) and provide tactical advice for habitat conservation and other important management issues such as by-catch reduction and adaptive management (Kar & Matsuda 2006). The maps and response curves in Figs. 5 to 7 are an example of what can be done with this type of study. If, with the help of remote sensing technology, maps like these can be created and updated frequently and used to predict the locations of groups of species relevant to fisheries, they may be helpful in developing dynamic management strategies (Game et al. 2009).

**Acknowledgements.** The authors thank the following agencies for support during this project: NOAA Fisheries and the Environment (FATE NA08NMF450626) for primary support, as well as NASA Biodiversity (NNG06GH75G1/3), NASA New Investigator Program (NNH07ZDA001N), US IOOS Program (MARACOOS NA07NOS4730221, MARACOOS NA10NOS4730014 and MARACOOS NA11NOS0120038) and Delaware Sea Grant (NA10OAR4170084). RU COOL, usSEABED, National Geophysical Data Center and M. Taylor, B. Phelan and S. Lucey at NOAA-NEFSC provided data used in the analysis. We also thank H. Fuchs, J. Manning and anonymous reviewers for their comments and advice.

#### LITERATURE CITED

- Azarovitz TR (1981) A brief historical review of the Woods Hole Laboratory trawl survey time series. In: Doubleday WG, Rivard D (eds) Bottom trawl surveys. Can Spec Publ Fish Aquat Sci 58:62–67
- Bakun A (2010) Linking climate to population variability in marine ecosystems characterized by non-simple dynamics: conceptual templates and schematic constructs. J Mar Syst 79:361–373
- Barrick DE, Evans MW, Weber BL (1977) Ocean surface currents mapped by radar. Science 198:138–144
- Borcard D, Legendre P, Drapeau P (1992) Partialling out the spatial component of ecological variation. Ecology 73: 1045–1055
- Cargnelli LM, Griesbach SJ, Packer DB, Berrien PL, Morse WW, Johnson DL (1999) Essential fish habitat source document: witch flounder, *Glyptocephalus cynoglossus*, life history and habitat characteristics. NOAA, Natl Mar Fish Serv, NE Fish Sci Cent, Woods Hole, MA. Available at [www.nefsc.noaa.gov/nefsc/publications/tm/tm139/tm139.pdf](http://www.nefsc.noaa.gov/nefsc/publications/tm/tm139/tm139.pdf)
- Castelao R, Glenn S, Schofield O, Chant R, Wilkin J, Kohut J (2008) Seasonal evolution of hydrographic fields in the central Middle Atlantic Bight from glider observations. Geophys Res Lett 35, L03617, doi:10.1029/2007GL032335
- Cross JN, Zetlin CA, Berrien PL, Johnson DL, McBride C (1999) Essential fish habitat source document: butterfly, *Pepilus triacanthus*, life history and habitat characteristics. NOAA, Natl Mar Fish Serv, NE Fish Sci Cent, Woods Hole, MA. Available at [www.nefsc.noaa.gov/publications/tm/tm145/tm145.pdf](http://www.nefsc.noaa.gov/publications/tm/tm145/tm145.pdf)
- Cushman SA, McGarigal K (2002) Hierarchical, multiscale decomposition of species–environment relationships. Landsc Ecol 17:637–646
- Cushman SA, McKenzie D, Peterson DL, Littell J, McKelvey KS (2007) Research agenda for integrated landscape modeling. Gen Tech Rep RMRS-GTR-194. US Department of Agriculture, Forest Service, Rocky Mountain Research Station, Fort Collins, CO
- Dzwonkowski B, Lipphardt BL, Kohut JT, Yan XH, Garvine RW (2010) Synoptic measurements of episodic flow events in the central Mid-Atlantic Bight. Cont Shelf Res 30:1373–1386
- Fry FEJ (1971) The effect of environmental factors on the physiology of fish. In: Hoar WS, Randall DJ (eds) Fish physiology, Vol 6. Academic Press, New York, NY, p 1–98
- Game ET, Grantham HS, Hobday AJ, Pressey RL and others (2009) Pelagic protected areas: the missing dimension in ocean conservation. Trends Ecol Evol 24:360–369
- Glenn SM, Jones C, Tawrdowski M, Bowers L and others



- (2008) Glider observations of sediment resuspension in a Middle Atlantic Bight fall transition storm. *Limnol Oceanogr* 53:2180–2196
- Goff JA, Jenkins C, Calder B (2006) Maximum *a posteriori* resampling of noisy, spatially correlated data. *Geochim Geophys Geosyst* 7:Q08003, doi:10.1029/2006GC001297
- Goff JA, Jenkins CJ, Williams SJ (2008) Seabed mapping and characterization of sediment variability using the usSEABED data base. *Cont Shelf Res* 28:614–633
- Gong D, Kohut JT, Glenn SM (2010) Seasonal climatology of wind-driven circulation on the New Jersey Shelf. *J Geophys Res* 115,C04006, doi:10.1029/2009JC005520
- Harris BP, Stokesbury KDE (2010) The spatial structure of local surficial sediment characteristics on Georges Bank, USA. *Cont Shelf Res* 30:1840–1853
- Hendrickson LC, Holmes EM (2004) Essential fish habitat source document: northern shortfin squid, *Illex illecebrosus*, life history and habitat characteristics, 2nd edn. NOAA Natl Mar Fish Serv, NE Fish Sci Cent, Woods Hole, MA. Available at [www.nefsc.noaa.gov/nefsc/publications/tm/tm191/tm191.pdf](http://www.nefsc.noaa.gov/nefsc/publications/tm/tm191/tm191.pdf)
- Houde ED (2009) Recruitment variability. In: Jakobsen T, Fogarty MJ, Megrey BA, Moksness E (eds) *Fish reproductive biology: implications for assessment and management*. Wiley, Hoboken, NJ, p 91–171
- Jacobson LD (2005) Essential fish habitat source document: longfin inshore squid, *Loligo paeleii*, life history and habitat characteristics, 2nd edn. NOAA Natl Mar Fish Serv, NE Fish Sci Cent, Woods Hole, MA. Available at [www.nefsc.noaa.gov/nefsc/publications/tm/tm193/tm193.pdf](http://www.nefsc.noaa.gov/nefsc/publications/tm/tm193/tm193.pdf)
- Kar TK, Matsuda H (2006) An overview of bioeconomic analysis and management in fisheries. *J Fish Aquat Sci* 1: 218–234
- Katz CH, Cobb JS, Spaulding M (1994) Larval behavior, hydrodynamic transport, and potential offshore-to-inshore recruitment in the American lobster *Homarus americanus*. *Mar Ecol Prog Ser* 103:265–273
- Leslie H (2005) A synthesis of marine conservation planning approaches. *Conserv Biol* 19:1701–1713
- Levitus S (1982) *Climatological atlas of the world ocean*. US Government Printing Office, Washington, DC
- Lewin-Koh NJ, Bivand R, Pebesma EJ, Archer E and others (2008) *Maptools: tools for reading and handling spatial objects*. R package version 0.7-16. R Foundation for Statistical Computing, Vienna
- Link JS, Brodziak JKT, Edwards SF, Overholtz WJ and others (2002) Marine ecosystem assessment in a fisheries management context. *Can J Fish Aquat Sci* 59:1429–1440
- Link J, Overholtz W, O'Reilly J, Green J and others (2008) The northeast U.S. continental shelf energy modeling and analysis exercise (EMAX): ecological network model development and basic ecosystem metrics. *J Mar Syst* 74:453–474
- Lucey SM, Nye JA (2010) Shifting species assemblages in the Northeast US Continental Shelf Large Marine Ecosystem. *Mar Ecol Prog Ser* 415:23–33
- Manderson J, Palamara L, Kohut J, Oliver M (2011) Ocean observatory data is useful for regional habitat modeling of species with different vertical habitat preferences. *Mar Ecol Prog Ser* 438:1–17
- McGarigal K, Cushman S, Stafford S (2000) *Multivariate statistics for wildlife and ecology research*. Springer-Verlag, New York, NY
- Neteler M, Mitasova H (2008) *Open source GIS: a GRASS GIS approach*, 3rd edn. Springer Science and Business Media, New York, NY
- Nye JA, Link JS, Hare JA, Overholtz WJ (2009) Changing spatial distribution of fish stocks in relation to climate and population size on the Northeast United States continental shelf. *Mar Ecol Prog Ser* 393:111–129
- Oksanen J (2011) *Multivariate analysis of ecological communities in R: vegan tutorial*. Available at <http://vegan.r-forge.r-project.org/>
- Oksanen J, Kindt R, Legendre P, O'Hara B and others (2008) *vegan: community ecology package*. R package version 1.15-0. Available at <http://cran.r-project.org/>, <http://vegan.r-forge.r-project.org/>
- Oliver MJ, Irwin AJ (2008) Objective global ocean biogeographic provinces. *Geophys Res Lett* 35,032008, doi: 10.1029/2008GL034238
- Oliver MJ, Glenn SM, Kohut JT, Irwin AJ and others (2004) Bioinformatic approaches for objective detection of water masses on continental shelves. *J Geophys Res* 109, C07S04, doi:10.1029/2003JC002072
- Packer DB, Griesbach SJ, Berrien PL, Zetlin CA, Johnson DL, Morse WW (1999) Essential fish habitat source document: summer flounder, *Paralichthys dentatus*, life history and habitat characteristics. NOAA Natl Mar Fish Serv, NE Fish Sci Cent, Woods Hole, MA. Available at [www.nefsc.noaa.gov/nefsc/publications/tm/tm151/tm151.pdf](http://www.nefsc.noaa.gov/nefsc/publications/tm/tm151/tm151.pdf)
- Palmer MW (1993) Putting things in even better order: the advantages of canonical correspondence analysis. *Ecology* 74:2215–2230
- Powell EN, Bonner AJ, Muller B, Bochenek EA (2004) Assessment of the effectiveness of scup bycatch-reduction regulations in the *Loligo* squid fishery. *J Environ Manag* 71:155–167
- Preisendorfer RW (1976) *Hydrologic optics*. NOAA Pacific Marine Environmental Laboratory, Honolulu, HI
- R Development Core Team (2008) *R: a language and environment for statistical computing*. R Foundation for Statistical Computing, Vienna. Available at [www.R-project.org](http://www.R-project.org)
- Reid JM, Reid JA, Jenkins CJ, Hastings ME and others (2005) usSEABED: Atlantic coast offshore surficial sediment data release. US Geol Surv Data Ser 2005-118, v. 1.0. US Dept Interior, US Geological Survey, Reston, VA
- Roarty H, Glenn S, Kohut J, Gong D and others (2010) Operation and application of a regional high-frequency radar network in the Mid-Atlantic Bight. *Mar Technol Soc J* 44: 133–145
- Shearman RK, Lentz SJ (2010) Long-term sea surface temperature variability along the US east coast. *J Phys Oceanogr* 40:1004–1017
- Simpson J (1981) The shelf–sea fronts: implications of their existence and behaviour. *Philos Trans R Soc Lond A Math Phys Eng Sci* 302:531–546
- Stevenson DK, Scott ML (2005) Essential fish habitat source document: Atlantic herring, *Clupea harengus*, life history and habitat characteristics, 2nd edn. NOAA, Natl Mar Fish Serv, NE Fish Sci Cent, Woods Hole, MA. Available at [www.nefsc.noaa.gov/nefsc/publications/tm/tm192/tm192.pdf](http://www.nefsc.noaa.gov/nefsc/publications/tm/tm192/tm192.pdf)
- Terceiro M (2007) Appendix 6. Modeling environmental factors and summer flounder recruitment success. In: SAW 47 Working Paper 11(TOR 6) — Modeling Environmental Factors. NOAA Fisheries, NE Fish Sci Cent, Woods Hole, MA, p 2068–2085
- Wood SN (2006) *Generalized additive models: an introduction with R*. Chapman & Hall/CRC Press, Boca Raton, FL
- Yamashita Y, Tanaka M, Miller JM (2001) Ecophysiology of juvenile flatfish in nursery grounds. *J Sea Res* 45:205–218

# High-frequency radar observations of the June 2013 US East Coast meteotsunami

Belinda Lipa · Hardik Parikh · Don Barrick · Hugh Roarty · Scott Glenn

Received: 4 October 2013 / Accepted: 4 December 2013 / Published online: 17 December 2013  
© The Author(s) 2013. This article is published with open access at Springerlink.com

**Abstract** We report here on the observation and offline detection of the meteotsunami off the New Jersey coast on June 13, 2013, using coastal radar systems and tide gauges. This work extends the previous observations of tsunamis originating in Japan and Indonesia. The radars observed the meteotsunami 23 km offshore, 47 min before it arrived at the coast. Subsequent observations showed it moving onshore. The neighboring tide gauge height reading provides confirmation of the radar observations near the shore.

**Keywords** Radar oceanography · Remote sensing · Current velocity measurement · Tsunami detection · Meteotsunami

## 1 Introduction

An unusual storm system moved eastward across the country on June 13, 2013, commonly called a “derecho”, and appears to have launched a meteotsunami that impacted the US East Coast. Meteotsunamis occur frequently in the Mediterranean region (Adriatic, Aegean, and Black Seas) (Renault et al. 2011; Vilibić et al. 2008), but are rarely mentioned in the USA. The existence of the meteotsunami was confirmed by several of the 30 tide gauges along the East Coast up through New England and was seen as far away as Puerto Rico and Bermuda. A NOAA DART buoy was triggered by the event, as well as another bottom-pressure sensor-of-opportunity in the region, a Sonardyne bottom-pressure recording (Hammond 2013). All of these outputs give a measure of the meteotsunami height.

---

B. Lipa (✉)  
Codar Ocean Sensors, 125 La Sandra Way, Portola Valley, CA 94028, USA  
e-mail: Belinda@lipa.name

H. Parikh · D. Barrick  
Codar Ocean Sensors, 1914 Plymouth St., Mountain View, CA 94043, USA

H. Roarty · S. Glenn  
Coastal Ocean Observation Laboratory, Rutgers University, 71 Dudley Road, New Brunswick, NJ, USA

The event, which occurred during daylight hours, attracted widespread attention after several media reports were released focusing on local impacts including people being swept off a breakwater at Barnegat Light, NJ, some damage to boat moorings, and minor inundation.

Although the origins of meteotsunamis vis-a-vis seismically generated tsunamis differ, the propagation and evolution of these shallow-water waves are the same, as are the applicable detection and warning methods. In Sect. 3, we describe the general mechanism for the generation of meteotsunamis.

A tsunami is a shallow-water wave, implying that the depth determines its properties and how they evolve. A high-frequency (HF) radar measures its orbital velocity, not its height. The orbital velocity of a single traveling wave at its crest moves in the direction of wave propagation; at its trough, the velocity opposes that direction. The radar maps the velocity with distance from the shore. Most other sensors provide point measurements. The radar mapping distance depends on bathymetry and tsunami strength. For the orbital velocity observed by the radar as a current flow, a single radar is adequate. However, multiple sites producing 2D maps give a complete picture of the near-field dynamics.

Tsunami warning systems presently in place rely primarily on computer models. They provide warning of earthquake-generated tsunami impacts and predict their strength and arrival times versus location based on the earthquake characteristics, subsequent sensor detections, e.g., from DART buoys, and forecast models. Earthquake information and tsunami model predictions are disseminated rapidly after dangerous earthquakes. Operational radar systems with software that can detect an incoming tsunami with a significant warning capability are only now being deployed. Tide gauge sea levels at coastal positions closer to the epicenter can provide useful information on water levels for locations further downstream, if they are able to transmit data after detection. The 2011 Japan tsunami signal was observed by many HF radars (SeaSonde 2013) around the Pacific Rim with clear results from sites in Japan and the USA (Lipa et al. 2011, 2012a). The 2012 Indonesia tsunami was observed by radars (SeaSonde 2013) on the coasts of Sumatra and the Andaman Islands (Lipa et al. 2012b). In addition to their primary operational purpose of observing real-time offshore circulation, radars equipped with tsunami detection software can also provide local quantitative tsunami information and warning as the wave approaches.

We have demonstrated an empirical method for the automatic detection of a tsunami based on pattern recognition in time series of tsunami-generated current velocities, using data measured by seventeen radars (Lipa et al. 2012a, b). Such HF radar systems presently operate continuously from many coastal locations around the globe, monitoring ocean surface currents and waves.

In this paper, we examine June 13, 2013, data from three HF radars on the New Jersey coast and show that the measured current velocities display the characteristic tsunami signature, allowing the detection of the meteotsunami, initially well offshore. For the first time, these data provide detection time as a function of range. Radar-observed detection times are compared with tide gauge observations and with that predicted from the phase speed of the meteotsunami, which depends on depth alone.

## 2 Theoretical analysis

The Navier–Stokes equation and the equation of continuity form the basis for tsunami modeling. Barrick (1979) derived closed-form expressions for tsunami parameters, based



on linear wave theory, assuming piecewise constant depths and a sinusoidal profile for the tsunami. We present some of these equations here.

For shallow-water waves like tsunamis, the phase velocity,  $v_{ph}(d)$ , for depth  $d$  is given by

$$v_{ph}(d) = \sqrt{gd} \quad (1)$$

where  $g$  is the acceleration due to gravity. The height,  $h(d)$ , of the tsunami is expressed in terms of its value in deep water, which was taken to have a depth of 4,000 m:

$$h(d) = h_{4000} (4000/d)^{1/4} \quad (2)$$

where  $h_{4000}$ , the height of the tsunami in deep water, and  $d$  are expressed in meters. The maximum surface orbital or particle velocity is given by

$$v_o(d) = v_{ph}(d)h(d)/d \quad (3)$$

The time for the tsunami to cover a distance  $L$  terminating at the radar site is given in terms of the phase velocity by

$$T = \int_0^L \frac{dx}{v_{ph}(d)} \quad (4)$$

For a tsunami, the phase/group velocity of the wave is much faster than the maximum orbital velocity, but from (1), it slows down in shallow water as  $d^{1/2}$ , increasing the warning available from the time of detection. From (2) and (3), the height increases as  $d^{-1/4}$ , while the maximum particle velocity increases more quickly as  $d^{-3/4}$ , increasing the signal seen by the radar.

### 3 Origin of meteotsunamis and nature of June 13, 2013, event

A meteotsunami is generated by an atmospheric pressure disturbance traveling across the sea (Renault et al. 2011; Vilibić et al. 2008; Monserrat and Thorpe 1996; Rabinovich and Monserrat 1996; Monserrat et al. 2006; Asano et al. 2012). Explained simply, a low-/high-pressure center (or edge) moving at a given velocity attempts to produce a peak/trough under it on the sea traveling at the same speed. This can generate a freely propagating surface gravity wave that increases in amplitude when the speed of the atmospheric anomaly  $v_{aa}$  matches the phase velocity of a shallow-water wave  $v_{ph}(d)$  given by (1). The June 13, 2013, “derecho” event traveled at about 21.1 m/s or 76 km/h (Hammond 2013). As the speed  $v_{aa}$  is equal to  $v_{ph}(d)$ , it follows that the depth  $d$  at which “resonance” or onset of independent wave launching occurs is 45 m. This depth region lies about 60 km off the New Jersey coast (refer to Fig. 1).

Meteotsunamis generally do not have sufficient heights/energies to cause catastrophic loss of life, as do severe seismic tsunamis, although damage to harbors and coastal structures is frequently significant. Few in the USA are even aware of the term “meteotsunami” although these events indeed do occur along our coasts. However, meteotsunamis have been reported for North America in the scientific literature, in particular for the East Coast (Sallenger et al. 1995; Churchill et al. 1995; Mercer et al. 2002; Pasquet and Vilibić 2013; Vilibić et al. 2013).

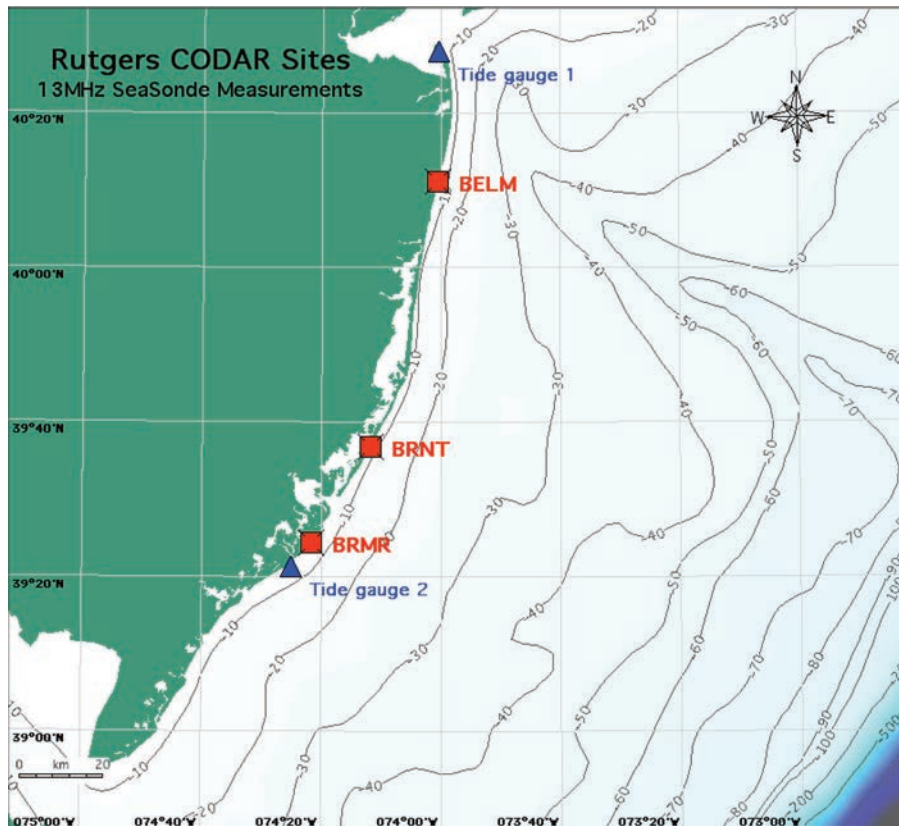


**Fig. 1** The radar stations at Brant Beach (BRNT), Brigantine (BRMR), and Belmar (BELM); the NOAA tide gauges at Sandy Hook (1) and Atlantic City (2), NJ and the offshore bathymetry contours, with depths in meters

This June 13, 2013, event, however, attracted significant attention among many agencies and scientific groups that may have been lacking for prior, more localized incidents. Perhaps this resulted from the fact that it was seen from New England through Southern New Jersey, and as far away as Puerto Rico. A scientific team was convened (Hammond 2013). Their analysis and collaboration are ongoing, this paper being one of several that are in process.

The unique characteristic of this meteotsunami is that it was generated by a frontal pressure anomaly traveling eastward, i.e., offshore. Yet it was seen by coastal sensors including HF radars as approaching the coast. How is this possible? The models reported by Hammond (2013) show that a strong reflection occurs at the edge of the shelf, about 110–120 km offshore. There, the depth drops from about 100–1,200 m over the space of about 20 km. The reflection coefficient is greater when the wave travel approaches a drop-off rather than a step-up with the same slope. Radar data presented here confirm the existence of a wave reflected back toward the New Jersey coast.

We now describe what happens when the tsunami interacts with a hard boundary. Consider a single “soliton” Gaussian pulse of water approaching the coast; it is a traveling

wave, with its forward velocity maximum at the crest. As a wall/hard boundary is approached, the height will double and the velocity must become zero. Then, at some time after the reflection, there is a solitary wave traveling backward again, with the crest velocity maximum in phase with the height crest.

What has happened at the wall? The velocity is zero but height is at a maximum. The velocity must flow toward the wall before mass transport builds up the height of the water. When the water height reaches its maximum at the wall, the velocity becomes zero. Then, gravity forces the water to flow away from the wall and the height begins to decrease, slowly at first, then more rapidly as the relaxation of the water peak accelerates.

In reality, the situation is more complex, but it can be seen that as a result of this boundary effect, the height wave approaching the coast (as seen by a tide gauge) will lag the velocity wave seen by a radar by as much as a quarter cycle.

#### 4 HF radar tsunami detection

For tsunami detection, a transmit frequency >10 MHz is preferred, as having greater time, space, and velocity resolution.

##### 4.1 History

Barrick (1979) originally proposed the use of shore-based HF radar systems for tsunami warning. Lipa et al. (2006) described a simulation that superimposed modeled tsunami-induced currents at the end of the HF radar processing chain and proposed a detection method based on these simulations.

The analysis described by Lipa et al. (2006) was based on simulated tsunami currents, which at that time were the only data available. Since then, we have accumulated a database of actual HF radar tsunami observations from both strong (Japan 2011) and weak (Indonesia 2012) tsunamis that have been used to identify the tsunami signature in current velocities and test automatic detection methods.

##### 4.2 Factors affecting detectability

1. As a traveling tsunami wave approaches the coast over a shelf with decreasing depth, as discussed in Sect. 2, its orbital velocity increases as the  $d^{-3/4}$ , while the amplitude increases as  $d^{-1/4}$ . Thus, the velocity increases more sharply than does the depth, which gives advantage to the radar sensor. At the depth decreases, the orbital velocity exceeds a detection threshold.
2. The orbital velocity and amplitude, being locked together, of course depend on the severity of the tsunami, and this is a second factor determining detectability.
3. Finally, the orbital tsunami current must be detected among the ambient background flow. There are two types of current with which it must contend for detectability:
  - a. A mean flow, for example, due to tides, geostrophic effects. We have considered and employ a variety of means to filter out or mitigate these effects.
  - b. A sub-grid-scale random current variability, seen in the surface currents by the radar as well as drifters. This random variability is the ultimate limitation and cannot be filtered out over the short time scales during which tsunamis must be detected. It is variable depending on location. For example, on the East Coast off



New Jersey, we find it is about 5 cm/s, while in the Pacific off the West Coast, it is approximately 12 cm/s (Hubbard et al. 2013).

Tsunamis with orbital velocity amplitudes of 5 cm/s have been detected (Lipa et al. 2012a, b). Taking the above factors into account, and based on our past cited experience with moderate tsunami heights in deep water, we find the 200-m isobath to be a convenient—albeit approximate—onset demarcation for likely detectability.

## 5 Data sets

We analyzed data sets from three SeaSonde HF radar systems located at Brant Beach (BRNT), Brigantine (BRMR), and Belmar (BELM), New Jersey. These radars stored data in a form suitable for tsunami analysis. Raw radar spectra files for June 13, 2013, with a 2-min time resolution were averaged in pairs, resulting in 4-min temporal outputs. Radar transmit frequencies and range cell widths were approximately 13.5 MHz and 3 km, respectively. Radar system specifications are available online (SeaSonde 2013).

Radar results were compared with data from NOAA tide gauges at Atlantic City and Sandy Hook, NJ. Graphics of the tide gauges were obtained from the file SeaLevel06132013.pdf downloaded from the NOAA website: <http://ntwc.arh.noaa.gov/about/>

Figure 1 shows the locations of the radars and tide gauges, and the offshore bathymetry. The meteotsunami height at the neighboring DART buoy was small (5 cm) (Hammond 2013).

## 6 Methods

In the following text, we use the term “arrival” to signify the first tsunami detection. Methods used to produce velocity components for analysis have been described previously (Lipa et al. 2012a). To summarize, (a) short-term radar cross-spectra (4-min time outputs) are analyzed to give radial velocities; (b) radial velocities in narrow rectangular area bands approximately parallel to the depth contours are resolved parallel and perpendicular to the depth contour; (c) these velocity components are averaged within each band to reduce the noise that is inherent in velocities derived from short 4-min spectra; (d) time series of the average velocity components (termed area-band velocities) are formed.

For tsunami observations, two effects distinguish the area-band velocities from the background: First, after arrival within the area monitored, velocities in neighboring bands are strongly correlated and second, the oscillation magnitudes deviate significantly from background values. We use a pattern detection procedure extended from that developed for the Japan tsunami (Lipa et al. 2012a) to calculate a factor (termed the  $q$ -factor) that signals the tsunami arrival when it exceeds a preset threshold.

An empirical pattern detection procedure has been developed, based on signal characteristics. The following data set is analyzed: Velocity components  $v_b(t)$  at three adjacent times and five area bands,  $b$ , within the coverage area are selected for tsunami detection. At a given time  $t$ , three quantities ( $q_1$ ,  $q_2$ , and  $q_3$ ) are calculated as running sums over different area-band combinations. Initially, they are set to zero. Based on experimentation with measured tsunami data, three augmentation factors  $\Delta q_1$ ,  $\Delta q_2$ , and  $\Delta q_3$  and three limits  $L_1$ ,  $L_2$ , and  $L_3$  on velocity increments have been defined and are preset.

### (1) Calculation of $q_1$

For each band at time  $t$ , the change in velocity  $\Delta v_b(t)$  over two adjacent time intervals is calculated, i.e.,  $\Delta v_b(t) = v_b(t) - v_b(t - 2\delta)$ , where  $\delta$  is the time spacing. If this is less than  $-L_1$  (velocity is decreasing),  $q_1$  is augmented by  $-\Delta q_1$ . If it is greater than  $L_1$  (velocity is increasing),  $q_1$  is augmented by  $+\Delta q_1$ .

### (2) Calculation of $q_2$

The times defining maximum/minimum velocities over a sliding time window are found for each band. If the minimum values for different bands coincide,  $q_2$  is augmented by  $-\Delta q_2$ . If the maximum values for different bands coincide,  $q_2$  is augmented by  $+\Delta q_2$ .

### (3) Calculation of $q_3$

If the velocity increases/decreases with time for three area bands from  $t - 2\delta$  to  $t - \delta$  and from  $t - \delta$  to  $t$ ,  $q_3$  is augmented by  $+\Delta q_3 / -\Delta q_3$ .

The final  $q$ -factor is the product of  $q_1$ ,  $q_2$ , and  $q_3$ ; tsunami arrival is signaled when the value of  $q$  exceeds a preset threshold. Positive/negative values indicate the tsunami is moving toward/away from the radar.

To set the threshold,  $q$ -factors are obtained from an extended data set, in order to determine typical values under normal conditions. There is a trade-off in selecting the threshold value. Too small a value will result in many false alarms. To detect small tsunamis (like this meteotsunami), the threshold is set a factor of 10 higher than typical values. For this study, the threshold was set to 50. For the 2011 Japan tsunami, it was set to 500 (Lipa et al. 2012a). The tsunami signal can be evident for some time after arrival; however, this detection method is optimized to apply to the first arrival. These detection methods were applied offline.

## 7 Results

### 7.1 Tide gauge water levels

Tide gauge data are shown in Fig. 2. Readings at Atlantic City show the maximum negative meteotsunami signal at approximately 18:42 UTC, indicated by the sharp water level decrease. This is followed at approximately 22:00 UTC by a sharp increase in water level and subsequent oscillations. The effects of the meteotsunami on the Sandy Hook water level are much less, with the arrival barely noticeable.

### 7.2 Radar current velocity observations

#### 7.2.1 Unfiltered area-band velocities

As described in Sect. 6, radial velocities in rectangular area bands 2 km wide approximately parallel to the depth contours were resolved along and across the depth contour and averaged within each band. The tsunami arrival is indicated by a marked drop in the perpendicular velocity component and correlation in time between different area bands. No tsunami signature was observed in the parallel component.

Figure 3 shows the BRNT, BRMR perpendicular velocity components at four area bands, and the generated  $q$ -detection factors, which were derived from all the area bands.

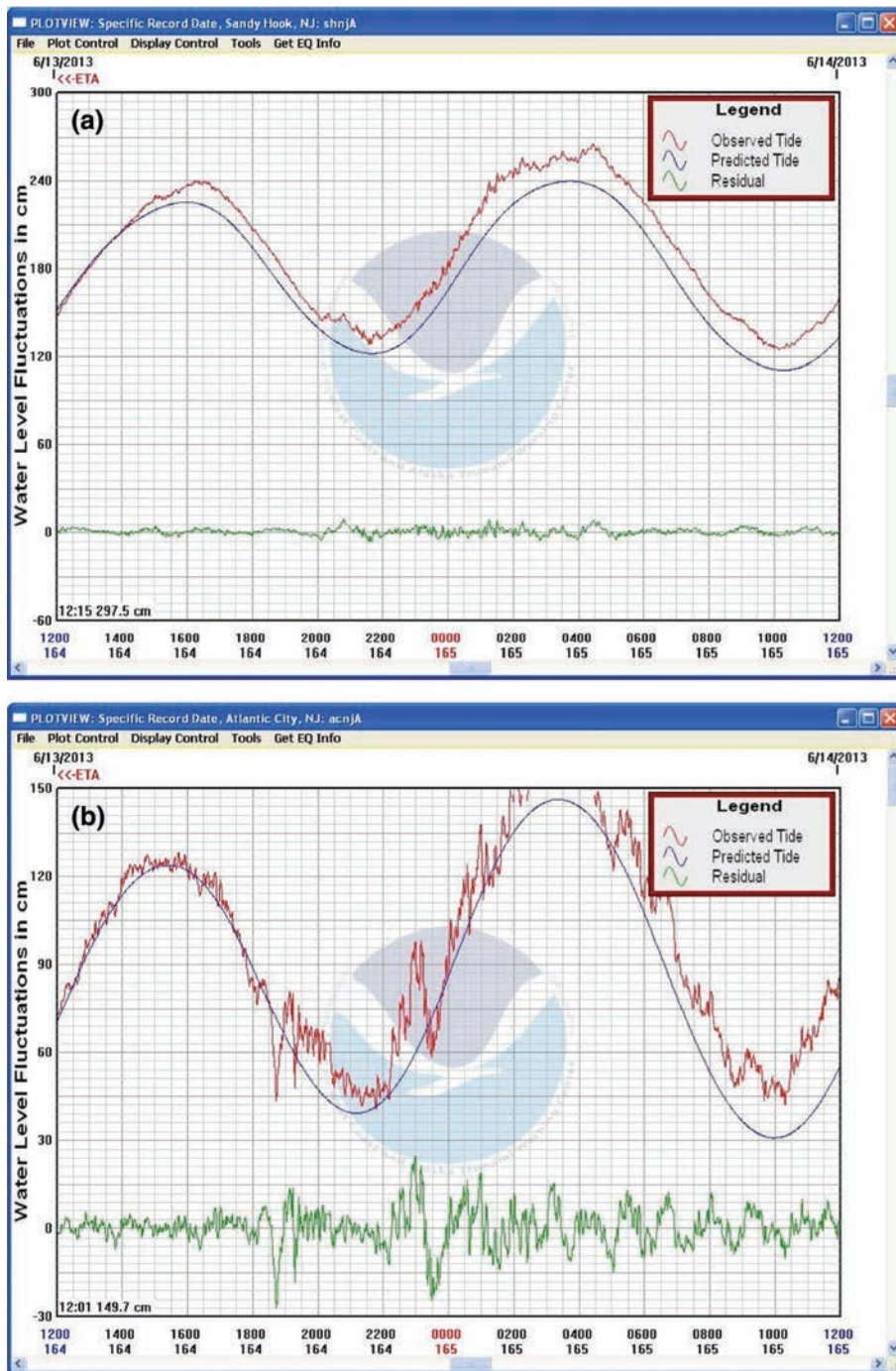


**Fig. 2** NOAA tide gauge observations June 13, 2013, **a** Sandy Hook, NJ. **b** Atlantic City, NJ. Graphics of the tide gauges were obtained from the file SeaLevel06132013.pdf, which was downloaded from the NOAA website: <http://ntwc.arh.noaa.gov/about/>



The velocity decreases at the tsunami arrival (Fig. 3) as is also indicated by the closest tide gauge at Atlantic City.

Velocities at BELM (Fig. 4) show much less tsunami signal, with the weak signal evident in only two area bands. This is consistent with tide gauge measurements at Sandy Hook, 30 km to the North, which barely registered the tsunami arrival. The tsunami signal at BELM was too weak to trigger a tsunami detection.

About 4 h later, after 22:00 UTC, BRNT velocities first increase and then sharply decrease (Fig. 5), as is also shown by the Atlantic City tide gauge. This effect was not seen at BRMR or BELM.

### 7.2.2 Filtered area-band velocities

In order to illustrate more clearly the approach of the first meteotsunami velocity trough onto the coast, the BRNT area-band velocities shown in Fig. 3 were processed as follows:

1. The velocity time series were detrended to remove variations with scales longer than 1.5 h, getting rid of tides and other longer-term slopes. This was done by fitting a constant and linear trend to the data for a 1.5-h time period before the tsunami began and subtracting this from the data that included the tsunami.
2. The data were then low-pass-filtered with a three-point (12-min) non-causal algorithm, in this case, the MATLAB “filtfilt” function. This eliminates the non-symmetric lag inherent in causal filters and minimizes end effects.
3. The resulting time series from two consecutive bathymetry-parallel bands were averaged to further reduce the inherent random signal variations.

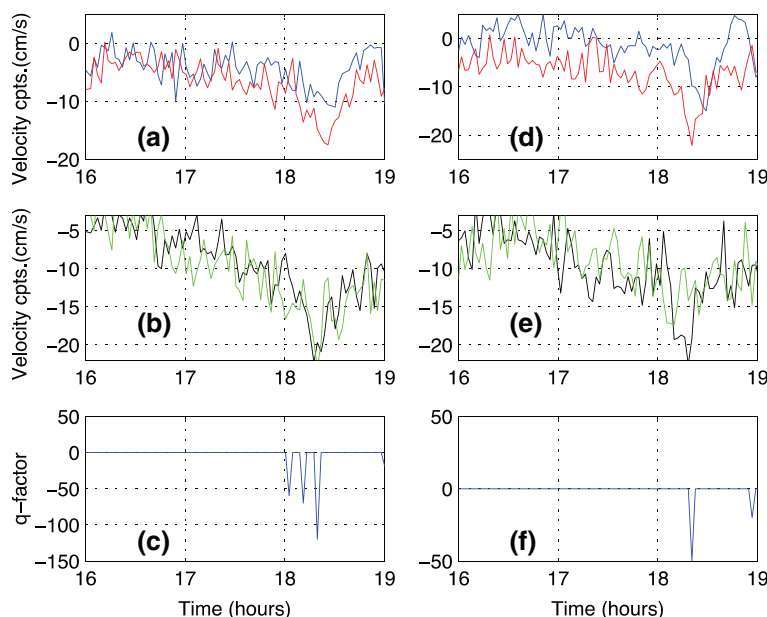


**Fig. 3** Radar observations of the tsunami arrival. Area-band velocity components versus time (hours UTC from June 13, 2013, 00:00) Negative velocity means water is moving offshore: BRNT **a** blue 6–8 km; red 8–10 km; **b** black 10–12 km; green 12–14 km. **c** The q-factor detection. BRMR **d** blue 2–4 km; red 4–6 km; **e** black 6–8 km; green 8–10 km. **f** The q-factor detection

**Fig. 4** BELM radar observations of the tsunami arrival. Area-band velocity component versus time (hours UTC from June 13, 2013, 00:00): **a** blue 10–12 km; red 22–24 km. The weak tsunami signal (too weak to trigger a detection) is evident in only these two area bands at approximately 18:15

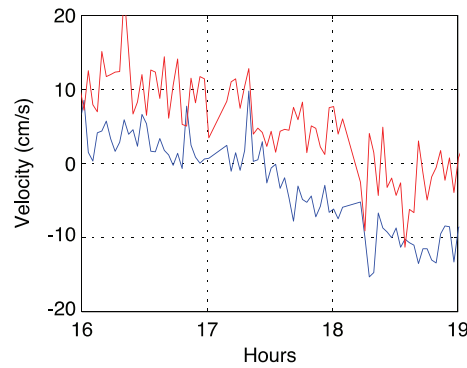
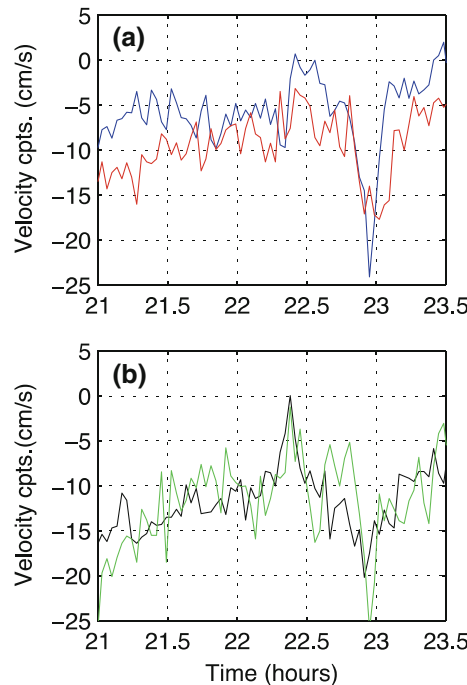


**Fig. 5** BRNT radar observations 3 h after the initial meteotsunami. Area-band velocity versus time (hours UTC from June 13, 2013, 00:00): **a** blue 4–6 km; red 8–10 km; **b** black 10–12 km; green 12–14 km



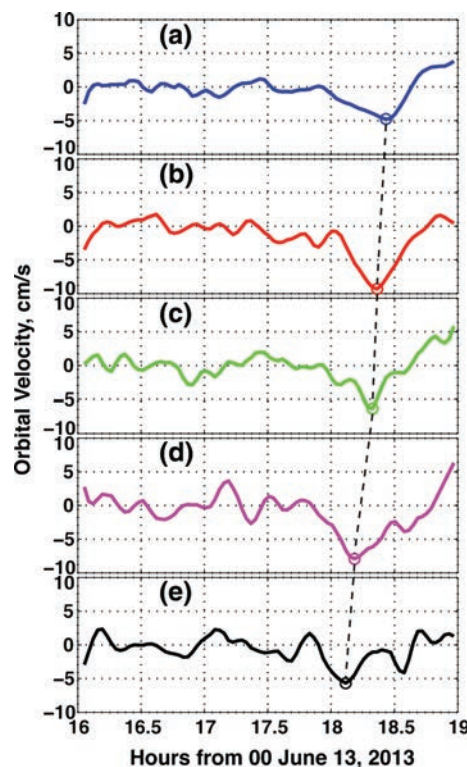
Results are shown in Fig. 6, where the subplots are the smoothed signals as a function of time for different distances from shore. The dashed line illustrates the progression of the first tsunami trough versus time and distance. The time–distance progression of the shoreward-moving event was confirmed by tsunami hindcast modeling discussed and presented by Hammond (2013).

### 7.3 Tsunami arrival times versus distance from shore

#### 7.3.1 Radar-observed arrival times from orbital velocities

The velocity plots in Figs. 3 and 4 indicate that the tsunami arrives earliest in the most distant range cells and later as shore is approached. Fig. 7a shows arrival times versus

**Fig. 6** BRNT area-band orbital velocity versus time (hours UTC from June 13, 2013, 00:00). Data have been detrended and filtered around tsunami bandwidths. The dashed line tracks the first trough minimum of the tsunami. Distance from shore: **a** 6 km; **b** 10 km; **c** 14 km; **d** 18 km; **e** 22 km



distance from shore for the radars (defined to correspond to the minimum velocity value) and the Atlantic City tide gauge (defined to correspond to the minimum water level).

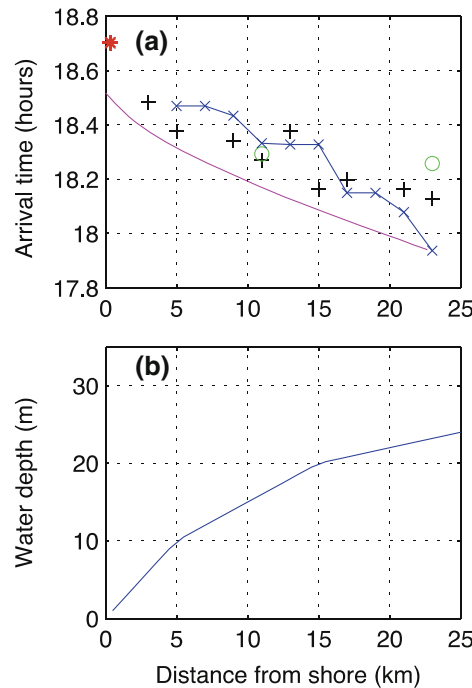
### 7.3.2 Calculated arrival times from the phase speed of the traveling tsunami trough

The arrival time of the minimum wave height trough at BRNT in the absence of a coastal boundary was calculated from (4). In shallow water, this differs from the radar-observed arrival times resulting from the orbital velocity. The depth offshore from BRNT shown in Fig. 1 was approximated by parallel contours, which was considered reasonable given that small-scale depth features are naturally low-pass-filtered on a scale of the tsunami wavelength. The solid curve in Fig. 7a shows the calculated arrival times at BRNT plotted as a function of distance offshore. The approximate depth versus distance from shore is plotted in Fig. 7b.

Figure 7a indicates that the meteotsunami arrived 23 km off BRNT and BRMR at approximately the same time and then moved toward shore at about 30 km/h (average speed over all points). The meteotsunami arrived 23 km off BELM about 14 min later. From the two readings, it appears to move toward shore at a higher speed, probably because the water is deeper close to the Hudson Canyon. The first observation of the tsunami at BRNT occurred 47 min before its arrival at the Atlantic City tide gauge.



**Fig. 7** **a** The radar-observed arrival time (hours UTC from June 13, 2013, 00:00) of the first tsunami trough versus distance from shore. *Red asterisk* Atlantic City tide gauge; Radar: *Blue* BRNT, *Black* BRMR, *Green* BELM, *Magenta* Tsunami arrival time calculated from the phase speed of a traveling tsunami trough, calculated from (4) based on initial detection at 23 km; **b** Approximate depth versus distance from BRNT perpendicular to the shore



## 8 Discussion and conclusions

Sources of uncertainty in the results presented here include noise in radar and tide gauge results, approximations in specifying depths contours, and the fact that the tide gauge is located 35 km from BRNT.

As discussed in Sect. 3, as the coast is approached, the maximum height wave lags the velocity maximum. This time difference is confirmed in Fig. 7: The arrival of the tsunami at the tide gauge lags the radar-observed arrival.

Although the calculated arrival time is set to be the same as the radar-observed time at the distance of 23 km, the curves diverge as the coast is approached, with the radar-observed time lagging (Fig. 7). This is because the calculation assumes a pure traveling wave and no interaction with the coastal boundary, while the radar-observed times are affected by the boundary. The arrival of the tsunami at the tide gauge lags both radar-observed and calculated arrival times close to the coast.

The coastal boundary explains why the trough velocity closest to the shore shown in Fig. 6 is smaller than at greater distances: The hard boundary forces normal velocity to zero while doubling the height at the boundary from that at greater distances from shore, as discussed in Sect. 3.

The first tsunami signal deviation was a “trough”. The SeaSonde-observed velocity was offshore, and the closest tide gauge at Atlantic City also saw a trough (depression). Nonetheless, although the velocity at this trough was flowing offshore, the wave itself was approaching the coast, as confirmed by the wave pattern propagating through the range cells shown in Fig. 6. As discussed in Sect. 3, this is due to a strong reflection occurring at the edge of the shelf, about 110–120 km offshore.

The radars observed the tsunami up to 23 km offshore, 47 min before it arrived at the coast. The tide gauge height reading provides confirmation of the radar observations at the shore and indicates the successful detection of a meteotsunami with a wave height of less than 50 cm. It also suggests that as much as a half hour warning alert can be provided by HF radar under similar tsunami height and bathymetry conditions before the wave strikes the shore.

**Acknowledgments** We thank the New Jersey Board of Public Utilities for the funding used to purchase the 13-MHz radars. This material is based on the work supported by the US Department of Homeland Security under Award No. 2008-ST-061-ML0001. The views and conclusions contained in this document are those of the authors and should not be interpreted as necessarily representing the official policies, either expressed or implied, of the US Department of Homeland Security. This work was partially funded by NOAA Award Number NA11NOS0120038 “Toward a Comprehensive Mid-Atlantic Regional Association Coastal Ocean Observing System (MARACOOS)”. Sponsor: National Ocean Service (NOS), National Oceanic and Atmospheric Administration (NOAA) NOAA-NOS-IOOS-2011-2002515/CFDA: 11.012, Integrated Ocean Observing System Topic Area 1: Continued Development of Regional Coastal Ocean Observing Systems.

**Open Access** This article is distributed under the terms of the Creative Commons Attribution License which permits any use, distribution, and reproduction in any medium, provided the original author(s) and the source are credited.

## References

- Asano T, Yamashiro T, Nishimura N (2012) Field observations of meteotsunami locally called “abiki” in Urauchi Bay, Kami-Koshi Island, Japan. *Nat Hazards* 64:1685–1706
- Barrick D (1979) A coastal radar system for tsunami warning. *Remote Sens Environ* 8:353–358
- Churchill DD, Houston SH, Bond NA (1995) The Daytona Beach wave of 3–4 July 1992: a shallow water gravity wave forced by a propagating squall line. *Bull Am Meteorol Soc* 76:21–32
- Hammond S (2013) Teleconference on Meteotsunami, July 18, Chaired by Steve Hammond, NOAA. <http://nctr.pmel.noaa.gov/eastcoast20130613/>
- Hubbard M, Barrick D, Garfield N, Pettigrew J, Ohlmann C, Gough M (2013) A new method for estimating high-frequency radar error using data from Central San Francisco Bay. *Ocean Sci J* 48(1):105–116
- Lipa B, Barrick D, Bourg J, Nyden B (2006) HF radar detection of tsunamis. *J Oceanogr* 2:705–716
- Lipa B, Barrick D, Saitoh S-I, Ishikawa Y, Awaji T, Largier J, Garfield N (2011) Japan tsunami current flows observed by HF radars on two continents. *Remote Sens* 3:1663–1679
- Lipa B, Isaacson J, Nyden B, Barrick D (2012a) Tsunami arrival detection with high frequency (HF) radar. *Remote Sens* 4:1448–1461
- Lipa B, Barrick D, Diposaptono S, Isaacson J, Jena BK, Nyden B, Rajesh K, Kumar TS (2012b) High Frequency (HF) Radar detection of the weak 2012 Indonesian tsunamis. *Remote Sens* 4:2944–2956
- Mercer D, Sheng J, Greatbatch RJ, Bobanović J (2002) Barotropic waves generated by storms moving rapidly over shallow water. *J Geophys Res* 107(C10):3152. doi:10.1029/2001JC001140
- Monserrat S, Thorpe AJ (1996) Use of ducting theory in an observed case of gravity waves. *J Atmos Sci* 53(12):1724–1736
- Monserrat S, Vilibić I, Rabinovich AB (2006) Meteotsunamis: atmospherically induced destructive ocean waves in the tsunami frequency band. *Nat Hazards* 6:1035–1051
- Pasquet S, Vilibić I (2013) Shelf edge reflection of atmospherically generated long ocean waves along the central US East Coast. *Cont Shelf Res* 66:1–8
- Rabinovich AB, Monserrat S (1996) Meteorological tsunamis near the Balearic and Kuril islands: descriptive and statistical analysis. *Nat Hazards* 13:55–90
- Renault L, Vizoso G, Jansà A, Wilkin J, Tintoré J (2011) Toward the predictability of meteotsunamis in the Balearic Sea using regional nested atmosphere and ocean models. *Geophys Res Lett* 38:L10601
- Sallenger AH Jr, List JH, Gelfenbaum G, Stumpf RP, Hansen M (1995) Large wave at Daytona Beach, Florida, explained as a squall-line surge. *J Coastal Res* 11:1383–1388
- SeaSonde (2013) Codar Ocean Sensors. Available online. <http://www.codar.com/SeaSonde.shtml>

- Vilibić I, Monserrat S, Rabinovich A, Mihanović H (2008) Numerical modeling of a destructive meteotsunami of 15 June, 2006 on the coast of the Balearic Islands. *Pure Appl Geophys* 165:2169–2195
- Vilibić I, Horvath K, Strelec Mahović N, Monserrat S, Marcos M, Amores A, Fine I (2013) Atmospheric processes responsible for generation of the 2008 Boothbay meteotsunami. *Nat Hazards*. doi:[10.1007/s11069-013-0811-y](https://doi.org/10.1007/s11069-013-0811-y)



# Enhancing Arctic Maritime Domain Awareness Through an Off-Grid Multi-sensor Instrument Platform

## AUTHORS

**Hank Statscewich**

Institute of Marine Science,  
University of Alaska

**Hugh Roarty**

**Michael Smith**

Institute of Marine and Coastal  
Sciences, Rutgers University

**Ed Page**

Marine Exchange of Alaska,  
Juneau, Alaska

**Scott Glenn**

Institute of Marine and Coastal  
Sciences, Rutgers University

**Tom Weingartner**

Institute of Marine Science,  
University of Alaska

## Introduction

A network of four high-frequency (HF) radars along Alaska's northwest coast provides hourly maps of ocean surface currents in real time (Figure 1). During the open water periods (July to November) of 2010–2013, the University of Alaska Fairbanks operated an off-grid instrument platform, herein referred to as the remote power module (RPM; Figure 2), at Point Barrow, Alaska (Statscewich et al., 2011). The RPM provided power and communications to a SeaSonde<sup>®</sup> High-Frequency Surface Wave Radar (HFSWR), a meteorological station with data feeds consisting of wind speed, wind direction, air temperature and solar radia-

## ABSTRACT

Surface current mapping high-frequency radars were installed along the northwest corner of Alaska during the open water periods of 2011–2013. A combination of wind and solar renewable energy inputs supplied electricity to a single radar site operating at Point Barrow, Alaska, via an off-grid remote power module (RPM). The radar at Point Barrow was able to simultaneously collect measurements of ocean surface currents, measure the position and velocity of passing vessels, and provide meteorological data in real time. This paper provides a summary of the performance of the power module from 2011 to 2013 and vessel detection results from 2013 with corresponding Automated Identification System (AIS) data. The RPM provided infrastructure to meteorological stations, high-frequency radars, and AIS in a resilient and robust manner and serves as an example of how the multi-use capability of integrated sensor modules can provide enhanced maritime domain awareness and persistent surveillance capabilities in remote Arctic environments. Keywords: geoscience, remote sensing, high frequency, radar, oceans

tion, and an Automated Identification System (AIS) transceiver.

With the increased interest and presence that the U.S. Coast Guard has in the Arctic (USCG Arctic Strategy, 2013), there is also a rising need for increased maritime domain awareness (MDA) from autonomous sensors in this area. To address that need, in 2012 and 2013, the HF radar system at Point Barrow was augmented with software to identify vessels in the radar spectra simultaneous to the surface current measurements. Detection data such as the range, range rate, and bearing of targets relative to the radar station were generated and telemetered in real time to the University of Alaska Fairbanks, Rutgers University, and Naval Research Laboratory.

The Arctic region poses challenges to HF radar operation, including remote locations requiring specialized shelter, power and communications, extreme

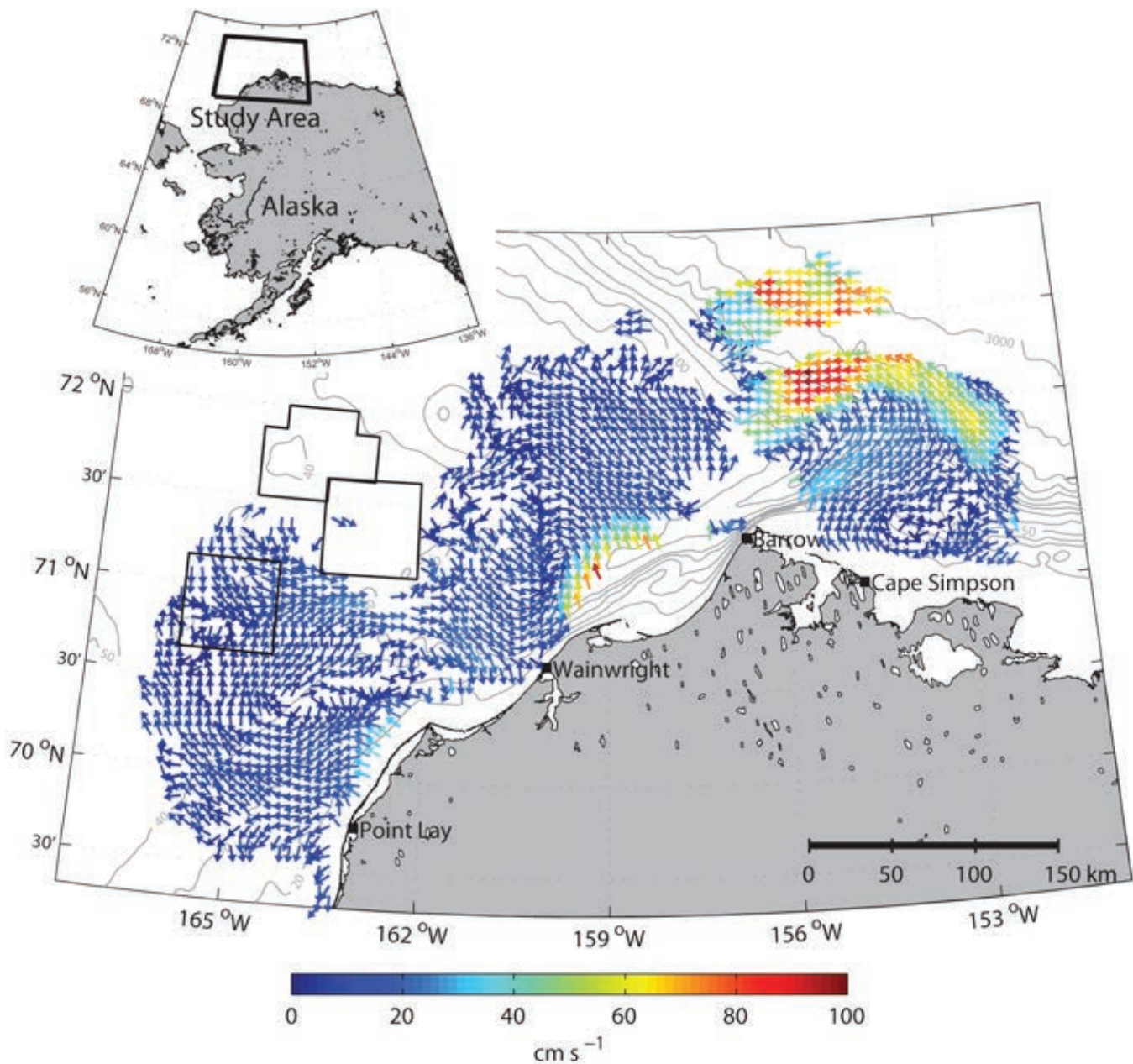
weather, the presence of ice floes, which have their own Doppler echoes in addition to sea clutter, and a complex radio frequency (RF) environment with ionosphere and auroral-based interference (Teague, 2001). This paper provides a summary of the performance of the RPM from 2011 to 2013 and vessel detection results from 2013 with corresponding AIS data. The RPM provided infrastructure to meteorological stations, HF radars, and AIS in a resilient and robust manner and serves as an example of how the multi-use capability of integrated sensor modules can provide enhanced maritime domain awareness in remote Arctic environments.

## Materials and Methods Remote Power Module

The RPM is a standalone device developed to withstand harsh Arctic

**FIGURE 1**

Map of daily mean ocean surface currents from October 2, 2013, derived from the four station high-frequency radar network at Point Lay, Wainwright, Barrow, and Cape Simpson. Arrowheads provide the direction of the current and arrow colors correspond to the current magnitude. The black boxes represent regions of interest for offshore development. (Color versions of figures available online at: <http://www.ingentaconnect.com/content/mts/mts/2014/00000048/00000005>.)



climates, to be rapidly deployed in remote areas, and to minimize impacts on the local environment. It consists of an aluminum foundation, insulated instrument enclosure, four wind turbines, a solar array, backup generator, battery bank, and satellite telemetry

system. Satellite communications are provided through a contract with HughesNet broadband Internet service. Electrical power generated onsite is stored in the battery bank and delivered to communications equipment and scientific instruments. The power

module logs data on battery bank voltage and current at multiple points in the system. Data from these measurements are used to autonomously start the backup generator, ventilate air through exhaust fans, or divert excess electricity to resistive loads. In case of

low-battery voltage, the unit may also turn off power in successive fashion to the instruments housed within the enclosure.

Since there are no sea echo returns from land fast sea ice, the utility of the HF radar is greatly reduced and the RPM is winterized after the onset of the ice cover each year. Winterization consists of topping off the battery bank with the onsite generator, lowering the four wind turbines, dismantling the meteorological station, disassembling the HF radar antennas, removing the data acquisition system, and shutting down all electronics. In the spring of the following year, the process is reversed when the land fast sea ice begins to erode and open water develops, typically by July in the Barrow area (Shirasawa et al., 2009; Zhang et al., 2003).

### High-Frequency Radar

HFR determines surface currents by analyzing and processing the Doppler spectrum of backscattered radar waves (Barrick et al., 1985). The cross-spectra of the backscattered radar waves include dominant first-order peaks, which arise by Bragg scattering from ocean waves at half the wavelength of the radar wave. In the absence of ambient noise and ocean currents, the backscattered signal appears as a delta function in the spectra. Spectral broadening occurs due to currents in the field of view of the radar, which also measures the bearing and range of the sea echo. A single-site HFR obtains radial velocities only, but by combining data from two overlapping radar masks (Lipa & Barrick, 1983; Kohut et al. 2012), horizontal currents are obtained. As an example, Figure 1 is an instantaneous map of surface currents from Alaska's Chukchi Sea as determined by four long-range (~5 MHz) HFRs.

### FIGURE 2

Remote power module deployed at Point Barrow, Alaska.



The HFR systems used in this study were the SeaSonde<sup>®</sup> model manufactured by CODAR Ocean Sensors. The radars, operating at 5 MHz, were located at Point Lay, Wainwright, Barrow, and Cape Simpson (Figure 1). In addition to measuring the surface currents along the north slope of Alaska, the radar at Barrow includes real-time vessel detection software (Roarty et al., 2013a). This software utilizes two backgrounds and three coherent integration times to form six

simultaneous detection outputs with adjustable threshold levels for each detection output (Roarty et al., 2010).

Vessel tracking, in its simplest form, takes place in three steps: (1) detection, (2) association, and (3) tracking. Detection uses different data processing algorithms to define peaks in the radar returns above a highly variable background of noise and clutter. The result is a time series of all the observed peaks (real or false) identified by their range, range rate toward or away from

### FIGURE 3

Battery bank voltage logged at the RPM for 2011 (top), 2012 (middle), and 2013 (bottom).

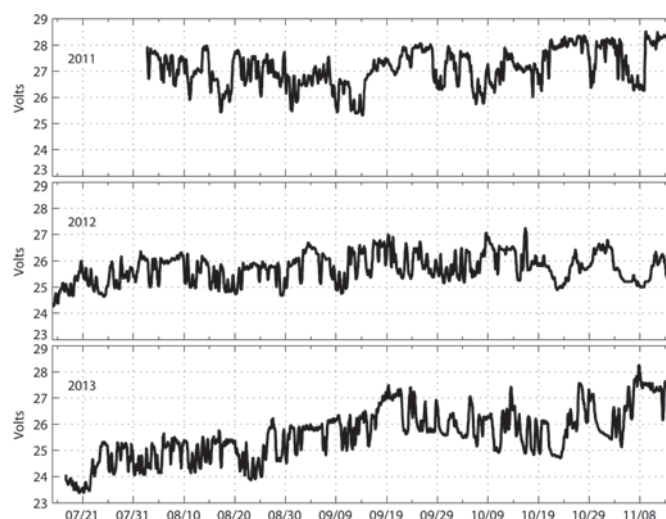
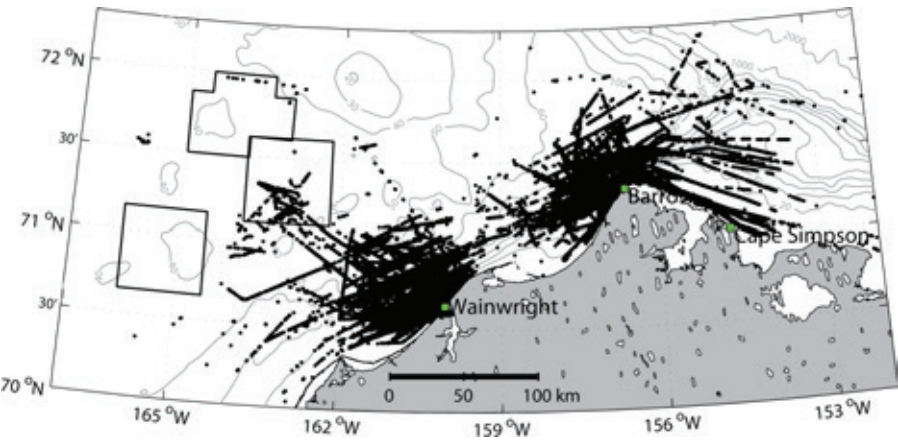




**FIGURE 4**

Map of the AIS traffic (black dots) in the study area for 2013. The locations of the radar stations are shown as green squares. The black polygons represent potential offshore development sites.



the radar, and bearing along with their associated uncertainties. The association process decides which detections are associated with a specific ship (Smith et al., 2013), clustering them for input to a tracker. The tracker then fits specific models for ship behavior (e.g., constant course and speed followed by a turning maneuver to a new constant course and speed) that enables both the past best fit and the projected track to be plotted on a computer screen for an operator to interpret.

Previous studies (Glenn et al., 2004) have confirmed that HFR are capable of detecting ships and that, given a

**TABLE 1**

Summary of the vessels recorded on AIS from the receiver at Point Barrow, Alaska.

#	MMSI	Data Points	Vessel Name	Country	Vessel Type	Length (m)	Beam (m)
1	367064000	29,684	Alaska Knight	USA	Fishing	43	10
2	367562110	144,534	Alulaq	USA	NA	23	9
3	367494000	5,782	Aquila	USA	Pilot boat	50	13
4	441619000	5,891	Arnon	South Korea	Service ship	102	19
5	366898440	514,940	Arctic Hawk	USA	Pilot boat	15	5
6	230049160	2,036	Arktika	Finland	Sailing vessel	15	5
7	366932130	14,874	Barbara Foss	USA	Tug	39	10
8	308429000	4,943	Bremen	Bahamas	Passenger ship	112	18
9	367108560	3,769	Blistol Explorer	USA	Fishing boat	54	12
10	316165000	1,149	Louis St Laurent	Canada	Service ship	120	24
11	316006101	1,939	Cindy Mozel	Canada	Tug	22	7
12	303902000	25,777	Coast Guard Healy	USA	Icebreaker	117	20
13	367576720	12,933	Emmett Foss	USA	Tug	25	10
14	230245000	52,358	Fennica	Finland	Icebreaker	116	26
15	316001821	3,108	Frost	Canada	Fishing boat	40	9
16	273458600	9,229	Geo Arctic	Russia	Research vessel	82	15
17	367438220	112,322	Greta	USA	Other ship	45	13
18	304977000	1,700	Hanse Explorer	Antigua and Barbuda	Pleasure craft	48	10
19	309577000	3,040	Hanseatic	Bahamas	Passenger ship	123	21
20	366927570	35,916	Island Spirit	USA	Tug	NA	NA

continued



**TABLE 1**

Continued

#	MMSI	Data Points	Vessel Name	Country	Vessel Type	Length (m)	Beam (m)
21	316015269	4,746	Island Tugger	Canada	Tug	32	10
22	368637000	10,076	Island Viking	USA	Tug	35	12
23	366888820	279,182	Kavik River	USA	Tug	20	9
24	366889330	211,597	Kuparuk River	USA	Tug	20	9
25	536070743	1,825	Lady M II	Marsahal Islands	Yacht	50	9
26	303350200	16,018	lauren Foss	USA	Tug	46	12
27	576000200	6,415	Le Soleal	France	Passenger ship	142	18
28	269101200	289	Libellule	Switzerland	Sailing vessel	14	6
29	366622140	101,954	Mala H	USA	Tug	26	8
30	233731000	235	Michaela Rose	Unitad Kingdom	Yacht	49	8
31	367484440	11,387	Millie Cruz	USA	Tug	30	10
32	431939000	18,546	Mirai	Japan	Service ship	128	19
33	319866000	1,582	My Octopus	Cayman Islands	Yacht	126	21
34	338117719	23	N2 Tender	USA	NA	NA	NA
35	338160289	569	NA	NA	NA	NA	NA
36	367399170	183,534	Nachik	USA	Tug	23	10
37	367309280	46,901	Nokes	USA	Tug	31	10
38	373437000	1,000	Nordic Qtion	Liberia	Bulk carrier	225	32
39	230275000	23,744	Nordica	Finland	Icebreaker	116	26
40	367061720	23,401	Norseman	USA	Service ship	NA	NA
41	367176270	94,892	Norseman II	USA	Service ship	30	10
42	368197000	197,989	Nunaniq	USA	Other ship	45	15
43	366960160	53,238	Ocean Titan	USA	Tug	37	12
44	367492440	41,882	Old Bull	USA	Tug	12	6
45	367309390	3,777	Pacific Freedom	USA	Tug	37	10
46	366888930	63,248	Pt. Thompson	USA	Tug	27	10
47	366869350	298,672	Sag River	USA	Tug	20	9
48	367182920	10,882	Sam B	USA	Tug	28	12
49	367399110	8,538	Sesok	USA	Tug	23	10
50	386886910	84,752	Siku	USA	Tug	28	9
51	316052000	3,013	Sir Wilfred Laurier	Canada	Service ship	83	16
52	338584000	1	Time Bandit	USA	Cargo	NA	NA
53	367000620	47,801	Westward Wind	USA	Fishing boat	45	10

known ship track for the association process, the resulting time series of range, range rate, and bearing could

be used by a variety of trackers to produce accurate vessel tracks. The results of this paper show that the detection

step can be performed in real time and the data can be telemetered back from a remote location like the Arctic.

## Automated Identification System

A Shine Micro RadarPlus<sup>®</sup> radio receiver collects AIS reports from vessels passing in front of the station. AIS broadcast frequencies are at 161.975 or 162.025 MHz with a data rate of 9,600 bits/s with 12.5 W of transmit power. The AIS reports consist of the vessel name, size, position, and course. The data are telemetered to the Marine Exchange of Alaska headquarters in Juneau, Alaska, in near-real time for incorporation into PacTracs, a statewide vessel-monitoring tool. The International Maritime Organization's International Convention for the Safety of Life at Sea requires AIS to be fitted aboard international voyaging ships with gross tonnage (GT) of 300 or more, domestic cargo ships of 500 GT or more, and all passenger ships regardless of size.

## Meteorological Station

Near-real-time monitoring and remote control of the system is accomplished by integrating a Campbell Scientific CR1000 data logger with a multiplexor and a relay driver. Measurements of power, current, voltage, ambient and indoor temperatures, wind velocity, and solar radiation are logged and then transmitted via satellite communications to Fairbanks for performance evaluations and/or control adjustments. Wind speed and direction are measured by a R.M. Young marine grade anemometer.

## Results

### Power Module

August, September, and October are the target months for ocean circulation studies using HF radar in the Chukchi Sea. In 2011, 2012, and 2013, the RPM delivered 100% of the required power to all of the instrumentation at the site. RPM battery

bank voltages ranged from 24 to 29 V DC (Figure 3), with a 3-year average voltage of 27.1 V DC. This voltage level represents a healthy battery bank that is maintained at a high float voltage. The predominant source of energy input to the system is from the four wind turbines (93%) with the remaining (7%) power provided to the system from the photovoltaic array. The backup generator has never been required to charge batteries in any of the 3 years the RPM has been in service.

Only one significant operational problem occurred in the 3 years of operations. In 2012, electrical wires housed within the wind turbine diversion load controller contacted a hot surface used to divert charging current from the battery bank. During a period of sustained high winds, the insulation on the wires melted, causing a short in the system and a brief power surge.

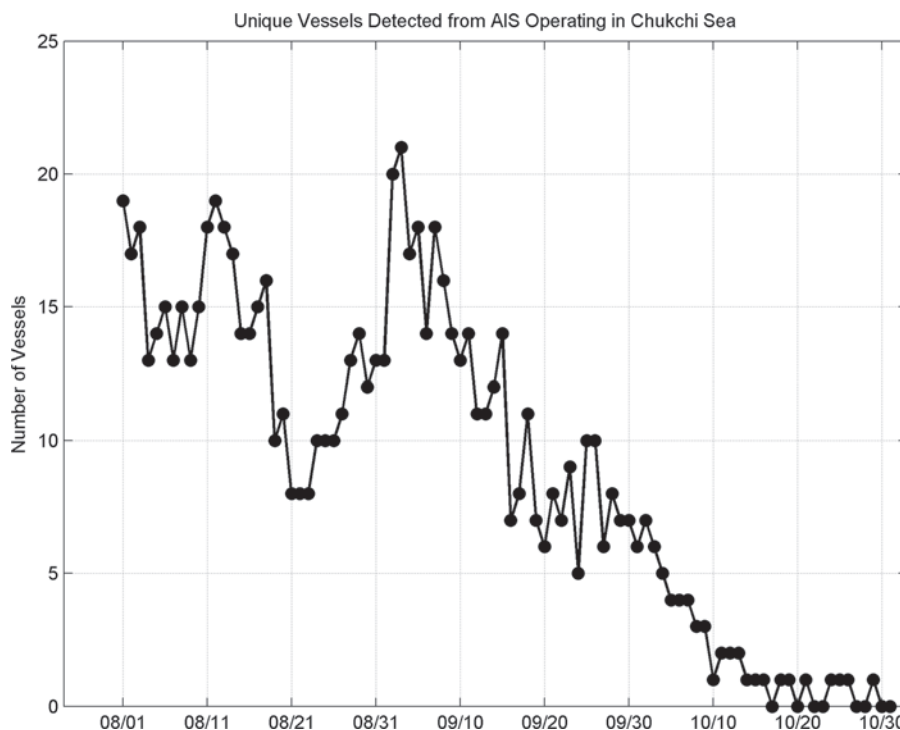
This surge upsets the data logger around October 18, and all system health data for the remainder of the 2012 season were corrupted. None of the other instruments suffered damage from the power surge; the HFR, AIS, and communications equipment all continued to operate collecting data through the middle of November. To ensure this failure mode would not occur again, the wiring to the diversion loads was re-engineered with high temperature-rated, Teflon-treated glass insulation wire, and all cables were re-routed so that unintended contact with hot surfaces is no longer possible.

### AIS Data

The AIS data were recorded from August 1 to November 1, 2013. Figure 4 shows the AIS traffic during the 2013 3-month collection period. A total of 52 unique maritime mobile

**FIGURE 5**

Time series plot of the number of vessels per day recorded by the AIS receiver at Barrow. The record spans from August 1 to November 1, 2013.



service identity numbers (MMSI; and summarized in Table 1) were recorded over the deployment at Point Barrow. The vessels captured on AIS had an average length of 57 m and beam of 13 m. The United States had the largest number of vessels operating in the theater with 32 (60%) followed by Canada with five vessels (9%). The tug and service ship class was the most common vessel type operating in the region. The most common route through the area is a path along the coast approximately 10 km offshore, well within the detection range of the HF radar. Figure 5 shows unique vessel activity as a function of time from August to November. The peak time for vessel activity was in early September with 21 vessels recorded on September 3, 2013.

## HFR Detection Data

Because the SeaSonde HF radar uses a vertically polarized electromagnetic wave, it is the vessel's height that is the critical parameter to determine the radar's ability to detect the vessel. The vessel becomes resonant when the height is a quarter of the transmitted radio wave length. For heights above that value, the echo strength increases slowly; for heights below resonance, the echo decreases precipitously. At 5 MHz, the relationship between radar frequency and vessel height for detection yields an optimal vessel height of 15 m or more. It is difficult to obtain the vessel's height from public databases on vessel particulars so vessel length and beam are used as a proxy for height to aid in the analysis of the vessel detection data. The tests performed here utilized vessels of opportunity that transited through the radar mask. No specific tests were performed using a dedicated vessel in order to minimize costs and

also to allow testing of the system under different environmental conditions. The most important environmental conditions that can affect the performance of the radar are wave height, wave period, and electromagnetic interference produced by atmospheric phenomena (Teague, 2001; Roarty et al., 2013b, 2013c). Increasing wave heights tend to diminish system range due to increased signal scattering. For the 5-MHz system, wave periods of  $\sim 4.6$  s decrease range because the second-order wave energy overlaps within the region of Bragg scattering. Although, these conditions do not necessarily limit vessel detection range, they do increase signal-to-noise ratios

and therefore limit detection sensitivities. In contrast, an extremely calm wave climate can also reduce maximum current-mapping range because of the reduction in Bragg-echo energy. During the time period of August to October 2013, an offshore buoy within the radar mask showed average wave periods of 5.5 s and a mean significant wave height of 1.2 m.

At the Point Barrow radar, there were 134 instances of vessels recorded on AIS that were within 100 km of the radar that had a nonzero radial velocity relative to the radar. Over this same time, 112 vessels were detected by the HF radar, implying an 84% radar detection rate. (We define a successful

## FIGURE 6

Detections (black circles) from the radar at Point Barrow for August 6, 2013, from 0800 to 1800 GMT. The panels from top to bottom represent range (km), radial velocity (m/s), and bearing (degrees from true north). The data from AIS are shown as the colored lines, and the legend denotes the individual vessel. The plot shows the most raw form of the echo output, as such the horizontal strips of detections near  $-7$  m/s represent known detected velocities of sea-echo Bragg peaks and the vertical strips are bursts of interference. These detections are not random false-positive detections and are filtered out during later processing steps.

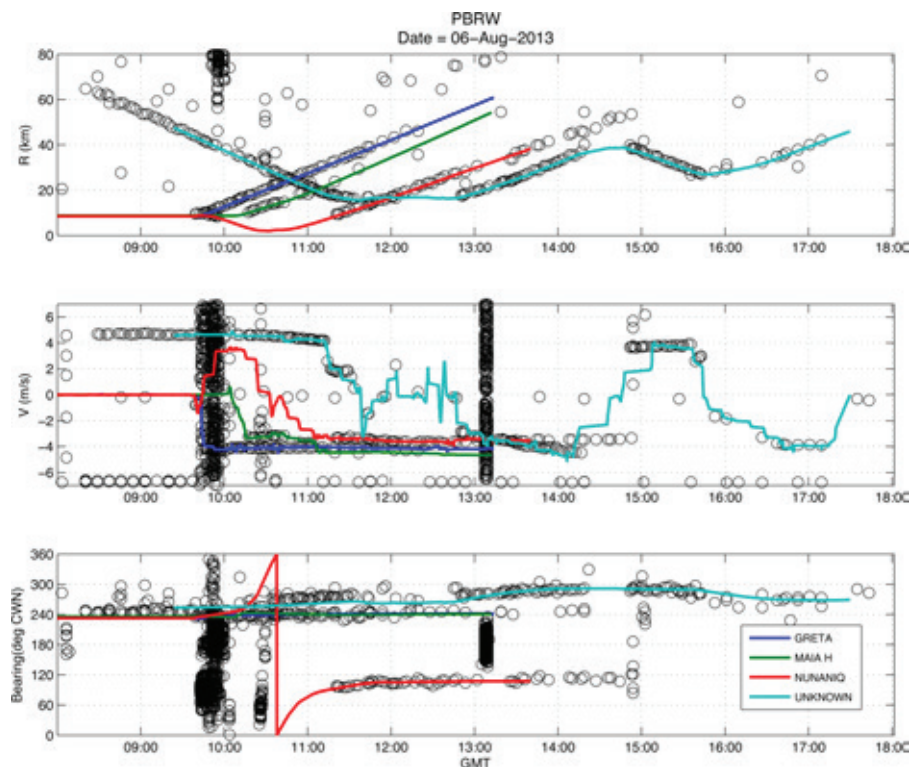
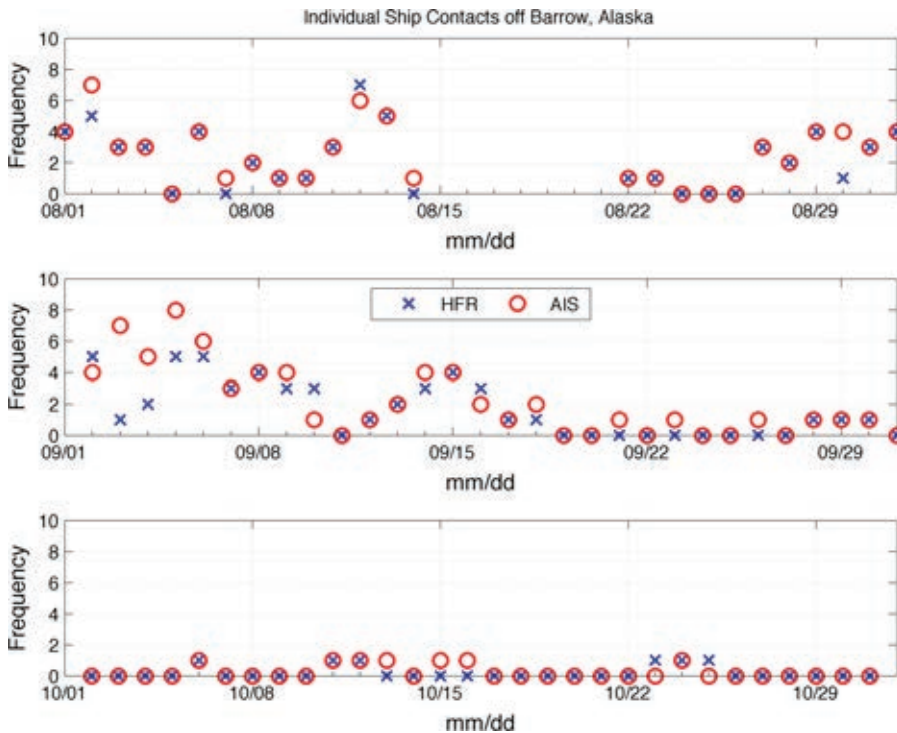


## FIGURE 7

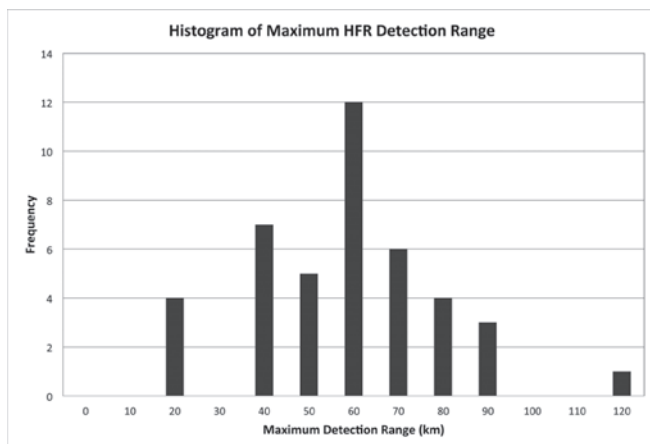
Comparison between detections by the AIS system (red circles) and HF radar system (blue crosses) from August 1 to October 31, 2013.



detection as one in which the range and the range rate of the radar detection coincide with the AIS data of the vessel.) The radar's vessel bearing measurement is the least accurate of the radar vessel detection measurements, so we allow for higher uncertainty in this measurement. Figure 6 shows an individual example of this analysis

## FIGURE 8

Histogram of maximum HF radar detection range during the study. The total sample size is 41.

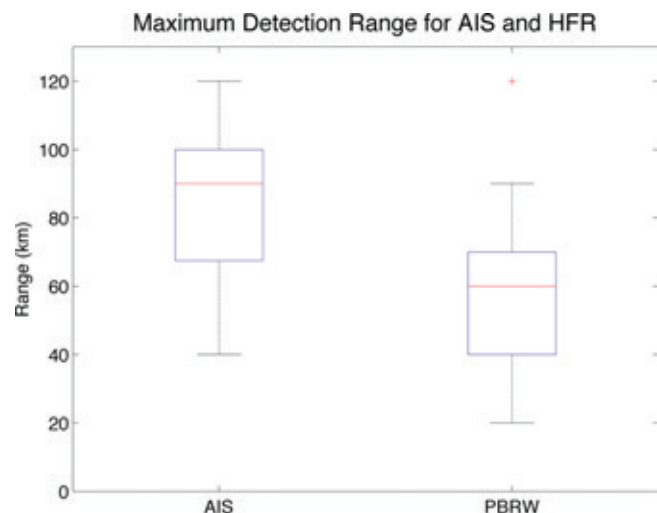


along with radar detections (black circles) at Point Barrow on August 6, 2013. Four vessels were recorded by AIS (colored lines), and the radar detections overlapped with each of the vessels on AIS. While there were a fair number of false alarms over this 24-h period, these were due to a low signal-to-noise ratio threshold, which we had purposely set low to minimize missing potential detections. Also of note is that the HFR detections extend beyond the range of the AIS for the Nunaniq and the "Unknown" vessel. The vessel was marked "Unknown" because the MMSI number that it broadcasts (338160289) could not be identified in any public database.

Figure 7 shows comparisons between the HF radar detections and the AIS detections over the 3-month test period in 2013. As in Figure 5, peak vessel traffic occurred in early September and diminished to zero detection by late October. There were several instances in October when the

## FIGURE 9

Box plot of maximum detection rang for AIS (left) and HF radar (right). The central mark is the median, the edges of the box are the 25th and 75th percentiles, the whiskers extend to the most extreme data points the algorithm considers to be not outliers, and the outliers are plotted individually.





radar and the AIS did not detect a single vessel within a 24-h period. This is an important result relevant to USCG planning with respect to maritime domain awareness in the Arctic, for it implies that vessels of this size are not operating in the region at this time.

Figure 8 is a histogram of the maximum detection range for the radar during the study. Determination of maximum detection range is made by visually inspecting the range panel of the daily plot as in Figure 6 and noting where vessel detections ceased. The mean of the maximum radar range is 59 km, and the median was 60 km. There were 3 days when the radar saw vessels at 90-km range. The 95% confidence maximum radar detection range over the study period was between 52 and 65 km. In addition to the vessels on AIS, the radar was able to detect four vessels when there was no AIS record available. These detections occurred on August 12, September 8, and September 14.

We then compared the detection range of the radar to AIS. The mean of the maximum detection range for AIS was 86 km, and the median was 90 km. The 95% confidence interval for maximum detection range for the land based AIS was between 79 and 92 km. A box and whisker plot of these data (Figure 9) shows that the AIS detection range was greater than that of the HF radar. We attribute these differences to the one-way transmit and receive path of the AIS radio as compared to the more active transmit-reflect-receive pathway of the HF radar, which is constrained by environmental interference issues discussed earlier in the manuscript.

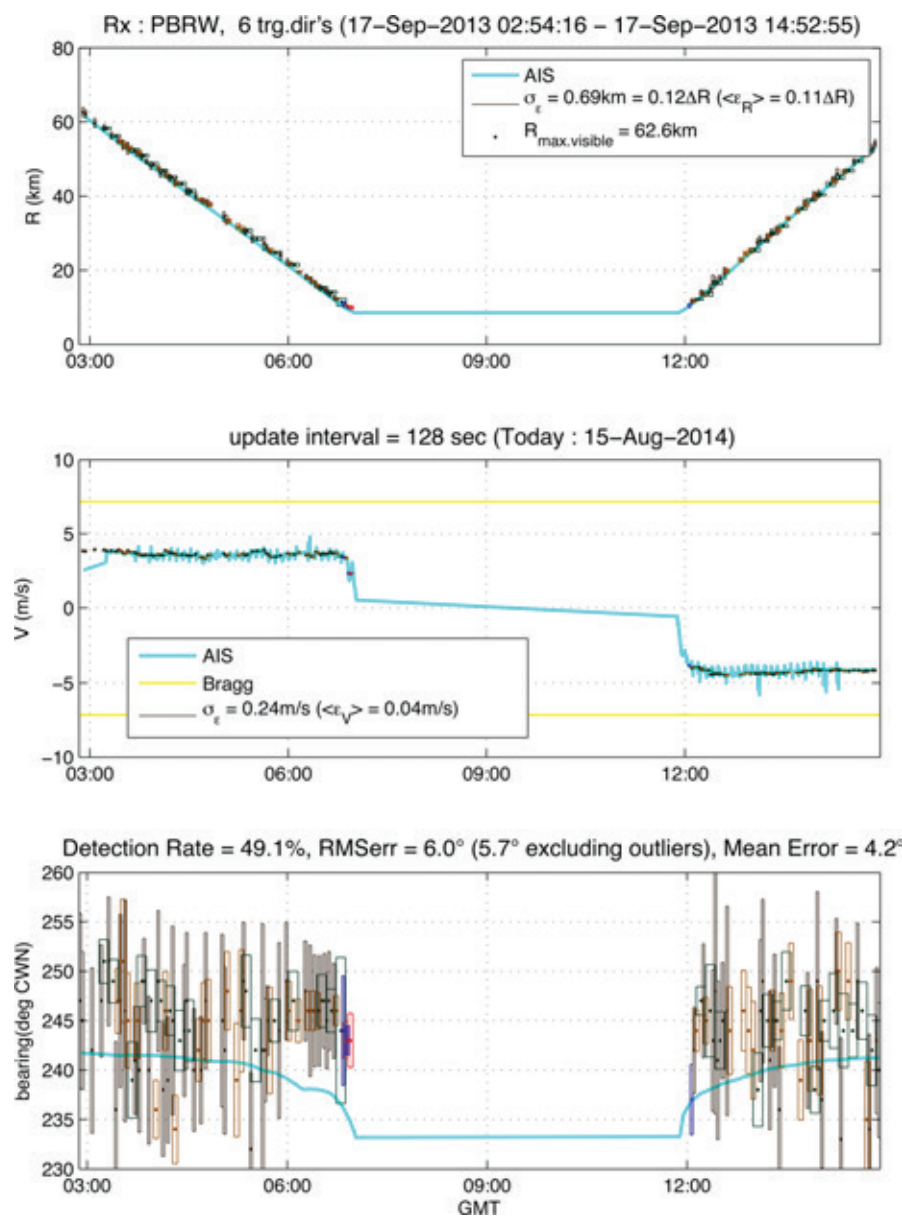
The AIS records that were collected in the first section of this report were utilized to validate the detections by

the radar. Figure 10 shows one example of the validation process in which the AIS track of the 45-m long by 15-m beam tug Nunaniq (aqua line) is superposed on the detections by the HFR (colored dots). Under the assumption that the beam is proportional to the vessel height, then the Nunaniq should be detected by the HFR. Indeed, the radar easily detected

this vessel from 0300 to 0700 as it approached Barrow. The Nunaniq was then stationary for the next 5 h when it anchored and was undetectable by the radar at this time. The tug resumed transit at 1200 and was immediately detected by the radar until 1500 when it left the radar mask. The overall HFR detection rate of 49.1% between 0400 and 1500 includes the time that the

**FIGURE 10**

Association of radar detection data with AIS for tug boat Nunaniq. The panels from top to bottom represent range (km), radial velocity (m/s), and bearing (degrees from true north). The detections by the radar are the different colored dots. The data from AIS are shown as the aqua line.



vessel was on anchor so the actual detection rate is higher than the one presented. The root mean square error  $\sigma_e$  and mean error  $\langle \epsilon \rangle$  are shown in the legend of the range and velocity plot. This vessel was detected to a maximum range of 63 km with a mean bearing error of  $4.2^\circ$ . Another example of using the AIS data to ground truth the radar detections is shown in Figure 11.

This is for the tugboat Nokea. The radar made detections on the Nokea out to 36 km over a period of 20 h.

Figure 12 shows a map of the detections for the Nunaniq. The detections are represented by ellipses where the ellipse axes are the uncertainty in range and bearing. Uncertainties are estimated and outputted

from the detection algorithm based on cell size and the signal-to-noise ratio, using standard radar methods (Roarty et al., 2010). The most accurate radar measurements are of the radial velocity, followed by the range, and lastly, the bearing. By only utilizing range and bearing in mapping the detections, this leads to scatter around the vessel path and a noisy track appearance. The scatter is diminished by first removing the bearing bias of  $4.2^\circ$  and then smoothing the bearing data through a Kalman filter (Mahafza, 2000). The bearing bias was calculated by comparing each bearing measurement of the radar with the bearing of the vessel from AIS. The position was then recalculated with the smoothed and bias-corrected bearing estimate, which significantly improved the position estimates of the vessel (Figure 13). It should be noted that the Kalman filter is the heart of the target tracker, whose purpose is to use all radar observables and their outputted uncertainties as well as their histories to get the best possible track and position. The bearing bias of the three other vessels was found to be relatively constant. The bearing bias was  $3.0^\circ$  for the Norseman II,  $3.8^\circ$  for the Healy, and  $2.7^\circ$  for the Nokea. So our procedure to improve the position estimate by removing the bearing bias and passing the new bearing estimates through the Kalman filter would be valid for these vessels as well. The authors would like to increase the sample size to see if the assumption that bearing bias is constant with azimuth holds, but this analysis is beyond the scope of this paper.

The process of comparing the vessel detections against AIS was repeated for an additional three vessels, the Coast Guard Ice Breaker Healy, research vessel Norseman II, and tugboat

## FIGURE 11

Association of radar detection data with AIS for tug boat Nokea. The panels from top to bottom represent range (km), radial velocity (m/s), and bearing (degrees from true north). The detections by the radar are the different colored dots. The data from AIS are shown as the aqua line.

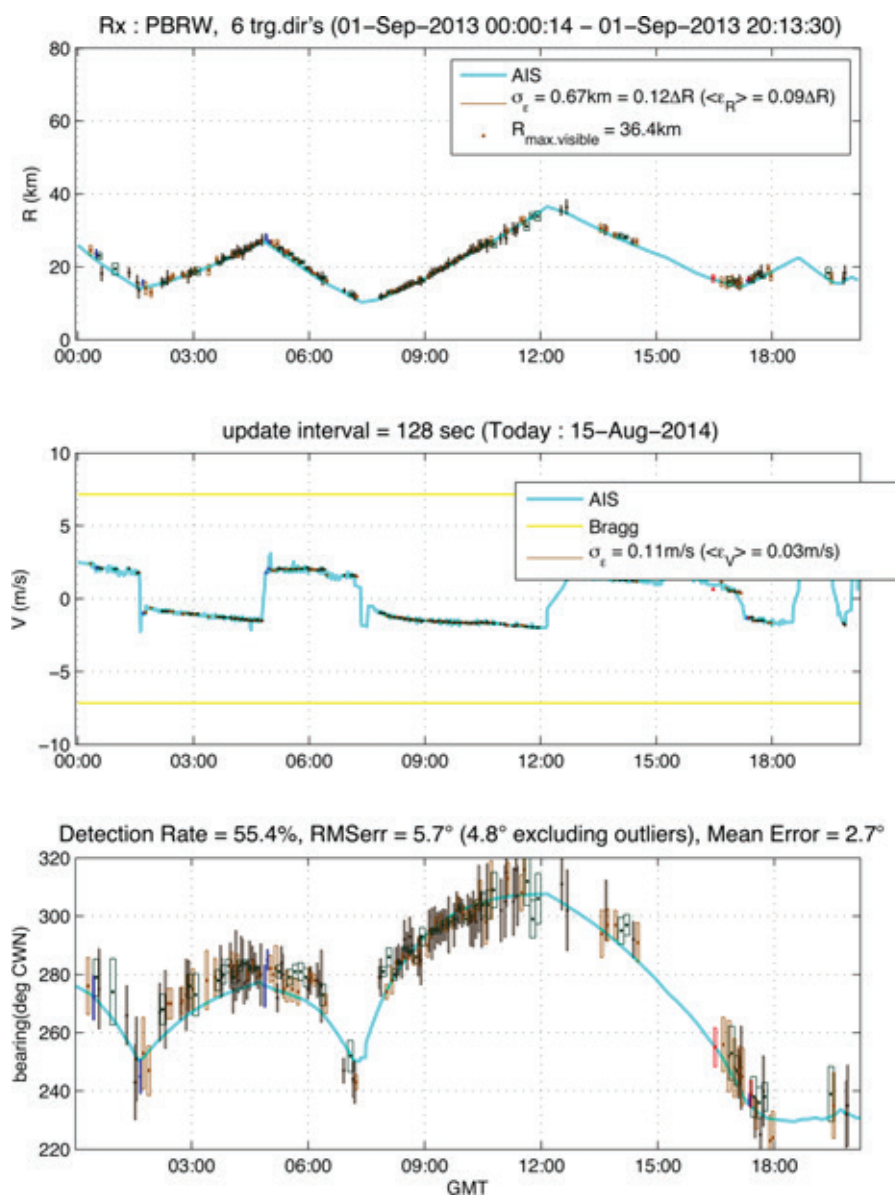
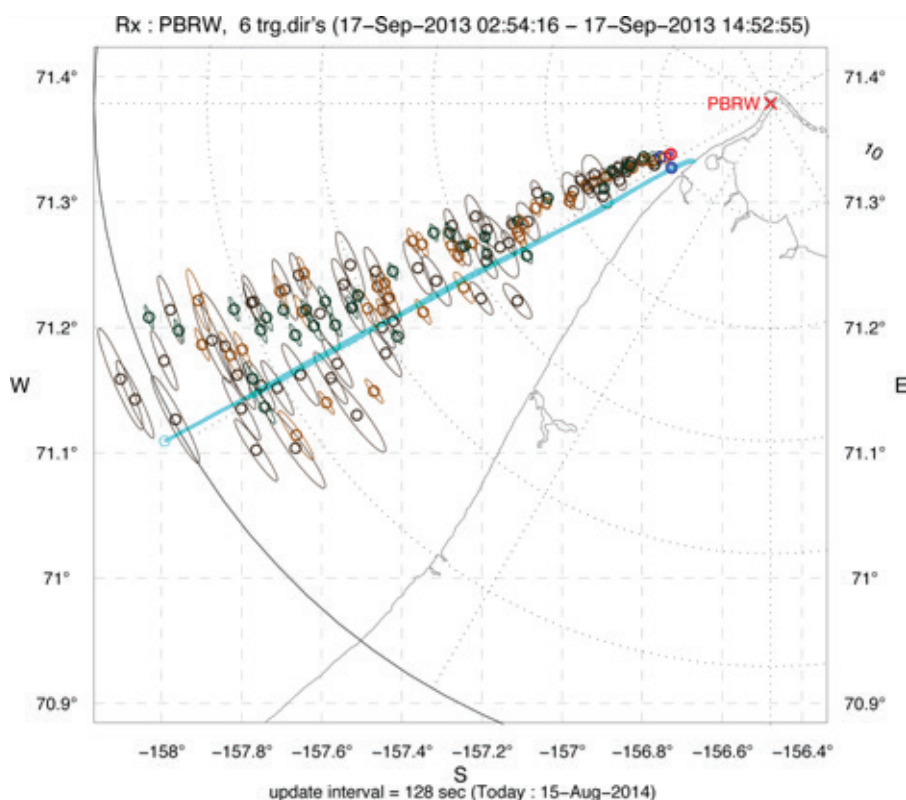


**FIGURE 12**

Detections from Figure 10 placed on a map (colored circles). The major axis of the ellipse is the uncertainty in bearing, and the minor axis is the uncertainty in range.



Nokea. These four test cases were used to determine the optimal settings for vessel detection during this experiment. The radars were run in real time with settings optimized for vessel detections at 13 MHz; these settings were previously verified from an extensive study off the coast of New Jersey (Roarty et al., 2013a). The vessel detection algorithm utilizes two background calculations (median and infinite impulse response) and three fast Fourier transforms (FFTs) for detection (Roarty et al., 2010). Table 2 shows the detection rate for each combination of background and FFT length. In each case, the median background with a 128-point FFT was the optimum choice for vessel detection. The radar at Barrow was operated with a 1-Hz sweep repetition, so the 128-point FFT amounts to slightly more than

2 min of averaging time between position updates. It should be noted that, in different locations under varying environmental conditions, a user does not need to guess at an optimal combination of processing parameters prior to sending them to the association algorithm; one can apply them all (in parallel), and the association algorithm will use all of them from the detection file outputs to get the best estimate of present position and velocity.

## Discussion

SeaSonde<sup>®</sup> HF radars were installed along the north slope of Alaska at an off-grid site. They simultaneously generated measurements of ocean surface currents and vessel detections. The vessel detection data were compared against ground truth data trans-

mitted via AIS. The 5-MHz radar was able to detect vessels to 90 km offshore. In some cases, individual vessels were continuously detected for up to 12 h. Increases in offshore detection range and/or duration of detection would require augmenting the system to transmit more power, which would increase operations and maintenance costs exponentially. For comparison with microwave radar, the line of sight calculation for a range of 90 km would require an antenna height of 640 m, which will be difficult to install and maintain at remote sites in the Arctic. The real-time dual-use capability of the SeaSonde<sup>®</sup> HF radar provides an ability to assess environmental security and shipping activity in a manner that reduces risk and enhances response. It is worth noting that the ranges over which vessels can be detectable by the HFR easily encompass the width of the passages in the Canadian Archipelago and over most of Bering Strait. These two passages or choke points are the principal pathways by which ships are entering and exiting the U.S. Chukchi and Beaufort seas.

Our research suggests the HFR-RPM-AIS system provides a compact, resilient, and energy-redundant package useful for simultaneously maintaining clear maritime domain awareness and conducting persistent surveillance activities over a large area. Our findings are particularly useful to the U.S. Coast Guard, USNORTHCOM, the Alaska state Department of Emergency Management and Military Affairs, the Alaska Department of Environmental Conservation, the Alaska State Department of Natural Resources, and the Alaska North Slope Borough, who all have a stake in keeping commercial activity in the Arctic safe and secure. The technology utilized within the RPM, while



**FIGURE 13**

Detections from Figure 12 (red dots) placed on a map after the bearing bias was removed and the bearing measurement was passed through a Kalman filter for smoothing. The track of the vessel from AIS is the blue line.



developed for the Arctic, is also applicable to remote settings elsewhere, including the tropics. In such settings, some modifications may have to be made such as the addition of solid-state thermo-electric air conditioners in order to cool the electronics. The

RPM is capable of accommodating such cooling devices if sufficient renewable inputs are available.

The Coast Guard has referred to maritime domain awareness as the centerpiece of their maritime security strategy and has advocated inter-

national initiatives that have led to the use of LRIT (Long Range Identification and Tracking) and AIS to track vessels (USCG Arctic Strategy, 2013). The vessels of greatest concern are those that are not adhering to the international treaties regarding the use of

**TABLE 2**

Detection rates, given in units of percent, for the four vessels with the different FFT lengths and background types.

Vessel	Date and Time	Background	FFT Length		
			128	256	512
Norseman II	2-AUG-13 03:00–07:30	IIR	2.4	1.6	0
		Median	54.8	33.1	17.7
Nunaniq	17-SEP-13 03:00–15:00	IIR	4.7	2.1	0.3
		Median	42.6	24.3	12.4
Healy	6-AUG-13 00:00–18:00	IIR	27.5	12.1	2.3
		Median	31.4	18.4	8.8
Nokea	1-SEP-13 00:00–18:00	IIR	2.4	1.4	0
		Median	47.7	32.5	16.4



LRIT and AIS and attempting to avoid detection. Periodic aerial over flights relying on visual observation are used by the Coast Guard to detect such vessels when visibility is good. HF radar can operate in any weather to identify vessels that are not transmitting via LRIT or AIS and provide this information on “suspect vessels” to the Coast Guard and DOT for follow up action as appropriate.

## Acknowledgments

This material is based on work supported by the U.S. Department of Homeland Security under Award No. 2008-ST-061-ML0001. We are thankful for the support provided by the community of Barrow, Alaska, and the North Slope Borough. The logistics involved in deploying and maintaining our equipment are extremely complex, and we are very grateful for the support provided by UMIAQ, LLC. The authors are grateful for the HFR data processing completed by Rachel Potter and Colin Evans. The views and conclusions contained in this document are those of the authors and should not be interpreted as necessarily representing the official policies, either expressed or implied, of the U.S. Department of Homeland Security.

## Corresponding Author:

Hank Statscewich  
Institute of Marine Science, University of Alaska, Fairbanks, AK 99775  
Email: [hank.stats@alaska.edu](mailto:hank.stats@alaska.edu)

## References

- Barrick, D.E., Lipa, B.J., & Crissman, R.D.** 1985. Mapping surface currents with CODAR. *Sea Technol.* 26(10):43-8.
- Glenn, S.M., Barrick, D.E., & Browning, W.J.** 2004. September 30. “Development and Demonstration of Shiptracking Capabilities for a Dual-Use Multi-Static Long-Range HF Radar Network,” Office of Naval Research Final Project Report, Award Number N00014-02-10917. 95 pp.
- Kohut, J., Roarty, H., Randall-Goodwin, E., Glenn, S., & Lichtenwalner, C.** 2012. Evaluation of two algorithms for a network of coastal HF radars in the Mid-Atlantic Bight. *Ocean Dynam.* 62:953-68. <http://dx.doi.org/10.1007/s10236-012-0533-9>.
- Lipa, B.J., & Barrick, D.E.** 1983. Least-squares methods for the extraction of surface currents from CODAR cross-loop data: application at ARSLOE. *IEEE J Ocean Eng.* OE-8:226-53. <http://dx.doi.org/10.1109/JOE.1983.1145578>.
- Mahafza, B.R.** 2000. Radar systems & analysis and design using Matlab. Boca Raton, FL: CRC Press LLC.
- Roarty, H.J., Barrick, D. E., Kohut, J.T., & Glenn, S.M.** 2010. Dual-Use Compact HF Radars for the Detection of Mid- and Large-Size Vessels. *Turk J Electr Eng Co.* 18:373-88.
- Roarty, H.J., Smith, M., Glenn, S.M., & Barrick, D. E.** 2013a. Real-time beyond the horizon vessel detection. *Proc. SPIE* 8714, Radar Sensor Technology XVII. pp. 87140Z.
- Roarty, H.J., Smith, M., Glenn, S. M., Barrick, D. E., Whelan, C., Page, E., ... Weingartner, T.** 2013b. Expanding maritime domain awareness capabilities in the arctic: High frequency radar vessel-tracking, in Radar Conference (RADAR), 2013. Radarcon 2013. pp. 1-5. <http://ieeexplore.ieee.org/xpl/articleDetails.jsp?arnumber=6586136>.
- Roarty, H.J., Smith, M., Glenn, S.M., Whelan, C., Barrick, D. E., Statscewich, H., & Weingartner, T.** 2013c. Multi-use HF radar for arctic maritime domain awareness, in OCEANS - Bergen, 2013. Bergen, Norway: MTS/IEEE. pp. 1-6. <http://ieeexplore.ieee.org/xpl/articleDetails.jsp?arnumber=6608132>.
- Shirasawa, K., Eicken, H., Tateyama, K., Takatsuka, T., & Kawamura, T.** 2009. Sea-ice thickness variability in the Chukchi Sea, spring and summer 2002–2004, *Deep-Sea Res. II.* 56:1182-200. <http://dx.doi.org/10.1016/j.dsr2.2008.10.015>.
- Smith, M., Roarty, H., Glenn, S., Whelan, C., Barrick, D., & Isaacson, J.** 2013. Methods of associating CODAR seasonde vessel detection data into unique tracks, in *Oceans - San Diego*, 2013. pp. 1-5. San Diego, CA: MTS/IEEE.
- Statscewich, H., Weingartner, T., Danielsen, S., Grinau, B., Egan, G., & Timm, J.** 2011. A high-latitude modular autonomous power, control, and communication system for application to high-frequency surface current mapping radars. *Mar Technol Soc J.* 45:59-68. <http://dx.doi.org/10.4031/MTSJ.45.3.7>.
- Teague, C.C.** 2001. Ionospheric effects on coastal radar systems. *Proceedings of the Radiowave Oceanography Workshop.* vol. Timberline, OR.
- U.S. Coast Guard Arctic Strategy.** 2013. Available at: [http://www.uscg.mil/seniorleadership/DOCS/CG\\_Arctic\\_Strategy.pdf](http://www.uscg.mil/seniorleadership/DOCS/CG_Arctic_Strategy.pdf).
- Zhang, X., Ikeda, M., & Walsh, J.E.** 2003. Coordinated changes of sea ice over the Beaufort and Chukchi seas: regional and seasonal perspectives. *Polar Res.* 22: 83-90. <http://dx.doi.org/10.1111/j.1751-8369.2003.tb00099.x>, <http://dx.doi.org/10.3402/polar.v22i1.6447>.



## Gap Filling of the Coastal Ocean Surface Currents from HFR Data: Application to the Mid-Atlantic Bight HFR Network

ERICK FREDJ

*Department of Computer Sciences, Jerusalem College of Technology, Jerusalem, Israel, and Department of Marine and Coastal Sciences, Rutgers, The State University of New Jersey, New Brunswick, New Jersey*

HUGH ROARTY, JOSH KOHUT, MICHAEL SMITH, AND SCOTT GLENN

*Department of Marine and Coastal Sciences, Rutgers, The State University of New Jersey, New Brunswick, New Jersey*

(Manuscript received 25 March 2015, in final form 1 December 2015)

### ABSTRACT

High-frequency radar (HFR) surface current data are an increasingly utilized tool for capturing complex dynamics of coastal ocean systems worldwide. The radar is uniquely capable of sampling relevant temporal and spatial scales of nearshore processes that impact event response activities and basic coastal ocean research. HFR is a shore-based remote sensing system and is therefore subject to data gaps, which are predominately due to environmental effects, like increased external noise or low signal due to ocean surface conditions. Many applications of these surface current data require that these gaps be filled, such as Lagrangian numerical models, to estimate material transport and dispersion. This study introduces a new penalized least squares regression method based on a three-dimensional discrete cosine transform method to reconstruct hourly HFR surface current data with a horizontal resolution of 6 km. The method explicitly uses both time and space variability to predict the missing value. Furthermore, the method is fast, robust, and requires relatively low computer memory storage. This paper evaluates the method against two scenarios of common data gaps found in HFR networks currently deployed around the world. The validation is based on observed surface current maps along the mid-Atlantic coast of the United States with specific vectors removed to replicate these common gap scenarios. The evaluation shows that the new method is robust and particularly well suited to fill a more common scenario with complete data coverage surrounding an isolated data gap. It is shown that the real-time application of the method is suitable for filling data gaps in large oceanography datasets with high accuracy.


### 1. Introduction

The coastal ocean is an intricate system that forms the boundary between the land and the deep ocean. This environment consists of tightly linked chemical and biological processes that coexist in a causal relationship with complicated flow dynamics. As the water depth decreases, physical forcing shifts from density gradients to turbulent mixing and frictional forcing along the

surface, bottom, offshore, and inshore boundaries (Robinson and Glenn 1999). In addition, tidal oscillations interacting with low-frequency features along the offshore boundary contribute to the complexity of the shelf dynamics that govern the exchange between the coast and the deep ocean (Magnell et al. 1980). Wind forcing is a large component in coastal ocean flow and can quickly change the dynamics, resulting in the generation of large wave disturbances greater than or of the same magnitude as the underlying low-frequency current. High-frequency radars (HFRs) are commonly used to observe and classify these complicated processes through hourly two-dimensional maps of surface currents.

HFR systems are one technology deployed along the coast to remotely measure the complex surface current dynamics over these highly variable seas. In the

---

 Denotes Open Access content.

---

*Corresponding author address:* Erick Fredj, Department of Computer Sciences, Jerusalem College of Technology, 21 Havaad Haleumi Street, P.O. Box 16031, 91160 Jerusalem, Israel.  
E-mail: erick.fredj@gmail.com

DOI: 10.1175/JTECH-D-15-0056.1

Mid-Atlantic Bight (MAB), a network of over 40 land-based radar sites provides hourly maps of surface ocean currents in support of oceanographic research and applications ranging from developing offshore wind energy (Seroka et al. 2013), pollution and storm response, and U.S. Coast Guard search and rescue (Roarty et al. 2010). These radars can reliably measure currents from a few kilometers off the coast out to 200 km offshore through a large range of weather and ocean conditions (Fig. 1). The shore-based antenna approach provides continuous temporal and broad spatial surface current observations, enabling the delivery of data in real time. Nearly every application of ocean monitoring requires, to some extent, measurements of surface current velocity maps.

While the coastal deployment of these networks provides some great advantages in setup, maintenance, cost, and access, the remote sensed nature of the measurement leads to sporadic gaps in data coverage in both time and space. Each coastal site within an HFR network uses a radio signal backscattered off the ocean surface to estimate the velocity component in the direction of the antenna. Data from overlapping sites are then geometrically combined to provide a two-dimensional surface current map over time. Throughout the community two primary algorithms are used to combine individual site radial component maps into total vector current maps, unweighted least squares (UWLS; Lipa and Barrick 1983), and optimal interpolation (OI; Kim et al. 2007, 2008). Gaps in the final surface current map are therefore dependent on the coverage of each remote site that feeds the combined product. Many research products and applications require that these data gaps be filled. For example, to predict the material transport, the standard approach is to run a Lagrangian numerical model. Lagrangian applications provide an understanding of transport in complex surface current fields (Peacock and Haller 2013). Traditionally, Lagrangian applications track the trajectories of individual particles determined by time-evolving spatial current fields. Assuming that the velocity field is observed for times  $t$  over a finite interval  $[t_1, t_2]$ , the existence of missing values in HFR observation poses a major obstacle.

Several techniques have been used to fill the gaps in either the UWLS or OI derived total vector maps. These are implemented using covariance derived from normal mode analysis (Lipphardt et al. 2000), open-boundary modal analysis (OMA) (Kaplan and Lekien 2007), and empirical orthogonal function (EOF) analysis (Beckers and Rixen 2003; Alvera-Azcárate et al. 2005); and using idealized or smoothed observed covariance (Davis 1985). A comparison of these methods was given by Yaremchuk and Sentchev (2009), who proposed to

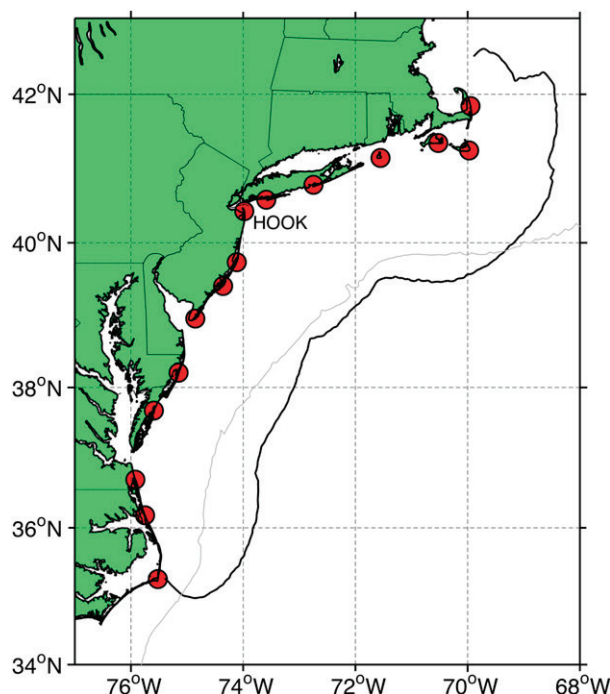


FIG. 1. Map showing the location of the HF radar stations used to construct the MARACOOS surface current maps. The 70% data coverage contour for 2012 (black) marks the best coverage domain that is utilized by the DCT-PLS algorithm to fill data gaps, and the 100-m isobath (gray) are also shown.

add a cost function with the terms penalizing grid-scale variability in the divergence and vorticity fields. However, the mapping methods mentioned above are statistical techniques; therefore, their performance depends on the accuracy of the covariance used for interpolating the HFR data both in space and time. Moreover, present mapping techniques often do not make full use of the dynamical information from the observations.

The goal of the present study is to design an HFR interpolation algorithm capable of filling data gaps in near-real time over the regional scales of a coastal network. To do that we apply a penalized least squares (PLS) regression as a real-time solution to fill gaps in the total vector surface current estimates from an HFR network as a postprocessing step on the derived total vector fields from either the UWLS or OI approach. PLS regression is based on a three-dimensional discrete cosine transform (DCT) (Garcia 2010). The method has been successfully applied to a global soil moisture product derived from Earth observation satellites (Wang et al. 2012). This method is introduced specifically to fill gaps as a required step in many post-processing real-time applications, including particle trajectories, search and rescue, and spill tracking.



In practice, the occurrence of small data gaps due to environmental factors are more frequent than the larger dropouts due to significant hardware failure or power and communication disruptions at individual radar stations. The highly nonrandom occurrence of missing values in HFR observations challenge their interpretation, since the possible causes include—but are not limited to—geometry of antenna setup, sea state, radio frequency interference, and instrumentation failure. This paper introduces the DCT-PLS technique to HFR gap filling and evaluates it against common gap scenarios observed in regional HFR networks. The paper is organized as follows. In the next section we describe the method and the HFR network used in the evaluation. Section 3 describes the gap-filling results and evaluation. We then discuss these results and implications for application of the method across similar regional networks deployed around the world in section 4.

## 2. Methods

### a. DCT-PLS gap-filling method applied to HFR data

According to Ohlmann (2007), a typical 2D instantaneous HFR velocity field can be expressed from HF radar total vectors as

$$\mathbf{V}(t, x) = \mathbf{V}_{\text{total}}(t, x) + \mathbf{V}'(t, x),$$

where  $\mathbf{V}_{\text{total}}(t, x)$  is the total HF radar velocity, which is an average over time ( $t$ ) and space ( $x$ ); and  $\mathbf{V}'(t, x)$  is largely a nondeterministic subgrid-scale velocity component that is not necessarily uniform in space and time.

In the study here, we introduce for the first time a DCT-PLS method applied to HFR data processing. The DCT-PLS method was originally proposed by Garcia (2010, 2011), and we adapt it here for the purpose of filling data gaps of HFR data for real-time and post-processing. We now give an introduction of the DCT-PLS algorithm. For more details on the mathematics of the method, the reader is referred to Garcia (2010).

#### 1) AUTOMATIC SMOOTHING WITH THE DCT-PLS METHOD

The proposed method based on the penalized least squares approach, combined with the DCT, allows for automatic smoothing of multidimensional data that may include outlying and missing data. Let us define the 2D HFR  $m \times n$  velocity field  $\mathbf{V} = (u, v)$  surface current (shown in the equation above), where  $u$  is the zonal (east/west) component and  $v$  is the meridional (north/south) component. First, we assume that the HFR data are corrupted by noise only (no outliers, no missing

data). Following Garcia (2010) the smoothed velocity field  $\hat{\mathbf{V}}$  can be expressed as

$$\hat{\mathbf{V}} = \text{IDCT2}[\mathbf{\Gamma} \circ \text{DCT2}(\mathbf{V})],$$

where DCT2 and IDCT2 denote the type II 2D DCT and its inverse (IDCT), respectively; and  $\circ$  stands for the element-wise product. The filtering matrix  $\mathbf{\Gamma}$  is defined by

$$\Gamma_{kl} = \left\{ 1 + s \left[ 4 - 2 \cos \frac{(k-1)\pi}{m} - 2 \cos \frac{(l-1)\pi}{m} \right] \right\}^{-1},$$

where the subscript  $(k, l)$  refers to the position in the 2D HFR current field and the parameter  $s$  is a positive scalar that controls the degree of smoothing. An unsuitable selection for  $s$  causes under- or oversmoothed velocities; as  $s$  increases, the smoothness of  $\hat{\mathbf{V}}$  also increases. For small values of  $s$ , the value of  $\hat{\mathbf{V}}$  will be dominated by noise. The value of the parameter  $s$  is determined by minimizing the generalized cross validation (GVC) score method introduced by (Craven and Wahba 1978). The GVC criterion makes the DCT-PLS method fully automated.

#### 2) EFFECT OF THE SMOOTHNESS PARAMETER

Our goal is to find the best estimated  $\hat{y}(t)$  from the observed value  $y(t)$  for the  $t = t_1, t_2, \dots, t_n$  predictor, where the index  $n$  refers to the number of predictors.

The technique is to minimize  $F$  to balance the infidelity of the data measured by the residual sum of square  $\text{RSS} = \|y - \hat{y}\|^2$  and a penalty functional  $P(s)$  evaluated by a square second-order difference derivative  $s\|D\hat{y}\|^2$ . The procedure is known as smoothing splines (see Wahba 1990):

$$F(s) = \text{RSS} + P = \|y - \hat{y}\|^2 + s\|D\hat{y}\|.$$

The parameter  $s$  specifies the “constant” number  $s \times n$  of neighboring observation points used to calculate the local fits. Thus, the bandwidth  $s$  determines the degree of smoothness of the fitted data: Choosing too small an  $s$  value leads to undersmoothing, whereas selecting an  $s$  too large may result in oversmoothing of the fitted data that ignores local features of the data, as shown in Fig. 2. In the frequency domain, increasing the smoothness parameter  $s$  reduces the low-pass-filter bandwidth. Extremely large values of  $s$ , which cause the loss of high-frequency components, may happen with turbulence or high shear flow.

The tuning parameter  $s$  controls the amount of regularization, so choosing a good value of the tuning parameter is crucial. We can question what might be considered a good choice of a tuning parameter.

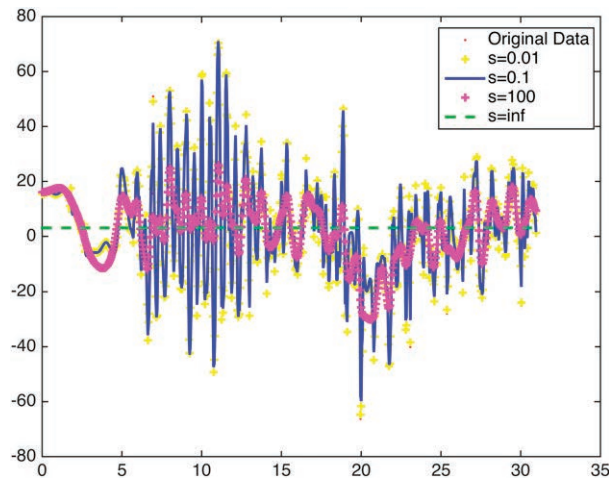


FIG. 2. Smoothness vs original HFR data from 1 Jan 2012 for given  $s$  values 0.01, 0.1, 100, and  $\infty$ . Increasing the smoothness control parameter removes the high frequency. The mean HFR velocity is obtained for  $s \rightarrow \infty$ .

A common solution to select the optimal value of  $s$  is to use the cross-validation (CV) procedure. The classical concept of CV consists of splitting the dataset into a *train set* and a *test set*  $\{t(i), y_i, i = 1, \dots, n\}$ . We fit the model on the train set and test its predictive performance on the test set. By testing the model on a different dataset than the one used for training, we avoid overfitting.

There are many ways to split the initial set dataset into parts like this. One possibility is to remove one sample to form the train set and to put this one sample into the test set. This is called leave-one-out (LOO) cross validation. With  $N$  samples, we obtain  $N$  sets of train and test sets. The cross validated is the average performance on all these set decompositions.

The expected prediction error rate is defined as  $E\{F[y_0, \hat{y}(t_0; s, S_{-1})]\}$ , where the CV score has to be taken with respect to new data  $(t_0, y_0)$  from the same source and all possible subsets minus one  $S_{-1}$ . Those prediction estimators are also linear in the observation  $\hat{y}(t_0; s, S_{-1}) = H(s)y(t_0)$ , where  $H(s)$  provides a measure of leverage. The average leverage is by definition in the range of  $[0, 1]$ ; weak smoothing occurs if the average leverage is close to 1, while oversmoothing appears when the average leverage is 0. A naïve approach of the problem selection of  $s$  is to select  $s$  equal to the value  $s_0$ , thus minimizing the CV score:

$$\min(E\{F[y_0, \hat{y}(t_0; s, S_{-1})]\}) = \min \left\{ \frac{1}{n} \sum_i^n \frac{[y_i - \hat{y}(t_i; s, S_{-1})]^2}{[1 - H_i(s)]^2} \right\}.$$

We note that for each positive  $s \geq 0$ , there exists a *unique*  $P(s)$  that optimizes the normalized mean-square error

(NRMSE), so that the minimum of  $F(s)$  is also the solution to the problem known as fair optimizer.

Craven and Wahba (1978) derived an alternative CV criterion. The idea is to replace the weights factor by their average value. This leads to a GCV criterion, which is quickly calculated using

$$\begin{aligned} \min(E\{F[y_0, \hat{y}(t_0; s, S_{-1})]\}) \\ = \min \left( \frac{\sum_{i=1}^n [y_i - \hat{y}(t_i; s, S_{-1})]^2 / n}{\{1 - \text{Tr}[H(s)]/n\}^2} \right). \end{aligned}$$

Furthermore, Garcia (2010) reduced the computational complexity and increased the speed of the GCV scores by evenly spacing the data.

Thus,  $\hat{y}$  can be expressed by

$$\hat{y} = \text{IDCT}[\Gamma \times \text{DCT}(y)],$$

where  $\Gamma$  is given by  $\Gamma_{i,i} = (1 + s\{2 - 2\cos[(i-1)\pi/n]\})^2$  and  $\Gamma_{i,j} = 0$  if  $i \neq j$ .

However, the smoothing with the minimization of the GVC score has no clear relation to the smoothing parameter and the gap-filling result in time or space. If the variance of the magnitude of the HFR data is great, then an oversmoothing might occur even with an extremely small smoothing parameter (see Fig. 4). Similarly, in Fig. 2, when a smaller smoothing pattern ( $10^{-2}$ ) is used, there is no relation to the gap filling. Both figures demonstrate that there is no correlation between the smoothing parameter and the actual smoothing achieved.

### 3) REPLACEMENT OF THE OUTLYING DATA WITH THE DCT-PLS METHOD

The remote sensed nature of the HFR data can lead to spurious vectors. These outliers are commonly the result of a low signal-to-noise ratio due to either a weak return signal often near the outer edges of the coverage or heightened noise due to external sources. Neglecting these outlying HFR current vectors can affect the smoothed HFR field. To overcome the outlying data, the DCT-PLS method uses a robust procedure that is almost not influenced by the outliers. Garcia (2010) expressed the robust procedure of the DCT-PLS method as

$$\hat{\mathbf{V}} = \text{IDCT2}\{\Gamma \circ \text{DCT2}[\mathbf{W}^{\text{bs}} \circ (\mathbf{V} - \hat{\mathbf{V}}) + \hat{\mathbf{V}}]\}.$$

The method uses the initial current velocity ( $\hat{\mathbf{V}} = \mathbf{V}$ ) to generate successive weights coefficients from bisquare weights ( $\mathbf{W}^{\text{bs}}$ ) of the residual current  $(\mathbf{V} - \hat{\mathbf{V}})$  until  $\hat{\mathbf{V}}$  matches reasonably well  $\mathbf{V}_{\text{total}}$ . We note that the “robust” procedure discussed here avoids the

weakness related to the linear model of the least square techniques.

#### 4) DEALING WITH MISSING VALUES AND MASKS

To utilize the algorithm, we first have to define the best coverage domain. This was defined as the grid points within the 70% data coverage from Fig. 1, which was taken for the year 2012. Seventy percent was chosen, as this was the highest contour that covered the entire domain of the MAB. This best coverage is a compromise of the data. Any data gaps within the best coverage domain will be filled; however, if the real-time measurement extends beyond the best coverage domain, then the algorithm will remove it. So, it is critical that an appropriate domain be chosen as input to the algorithm. In the presence of missing data, the corresponding weights coefficient is zero, while an arbitrary value is assigned to the velocity. The DCT-PLS method easily deals with missing and masked data by introducing a second weight matrix  $\mathbf{W}^m$ , defined by zero if the velocity located in  $(k, l)$  is masked or missing and 1 otherwise,

$$\hat{\mathbf{V}} = \text{IDCT2}\{\Gamma \circ \text{DCT2}[\mathbf{W}^m \circ \mathbf{W}^{\text{bs}} \circ (\mathbf{V} - \hat{\mathbf{V}}) + \hat{\mathbf{V}}]\}.$$

This is the equation of the robust DCT-PLS method used for HFR data.

#### b. HFR

HFR systems deployed along the coast use transmitted radio signals (3–30 MHz) scattered off the ocean surface to calculate radial components of the total surface velocity at a given location (Barrick et al. 1977). Peaks in the backscattered signal are the result of an amplification of a reflected wave, at grazing incidence, by surface gravity waves with a wavelength equal to half that of the transmitted signal (Crombie 1955). The frequency of the backscattered signal will be Doppler shifted depending on the velocity of the scattering surface. Using linear wave theory, the phase speed of the surface waves can be separated from the total frequency shift, leaving only that shift due to the surface current component in the direction of the antenna (Barrick et al. 1977). The radar software isolates the strongest sea echo returns from the Bragg scattering and uses that portion of the radar spectra to calculate radial current velocities.

Over a given time period, sites along the coast generate radial maps of these component vectors with resolutions on the order of 1–6 km in range and 5° in azimuth (Barrick and Lipa 1997; Teague et al. 1997). The HF radar sites in the Mid-Atlantic Regional Association Coastal Ocean Observing System (MARACOOS) network are all

TABLE 1. Typical characteristics of long, medium, and standard range HF radar systems.

System type	Radio frequency (MHz)	Range (km)
Long range	4–6	180
Medium range	12–14	80
Standard range	24–26	30

SeaSonde direction-finding systems manufactured by CODAR Ocean Sensors (Barrick 2008; Roarty et al. 2010). The direction-finding radars use a three-element receive antenna mounted on a single post to determine the direction of the incoming signals. Since the antenna can resolve only the component of the current moving toward or away from the site, information from at least two sites must be geometrically combined to generate total surface current maps.

The MARACOOS HF radar network consists of 43 SeaSonde-type radars (Fig. 1), 17 of which are long range, 18 of which are standard range, and 8 of which are medium range. Table 1 provides the typical characteristics of the different types of systems. For the long-range systems utilized in this study, the radar cell is defined by a range resolution ( $\Delta s$ ) of 6 km and an azimuthal resolution ( $\Delta \theta$ ) of 5°. The maximum range is on the order of 200 km, and the effective bearing angles of individual radars are different due to the coastline geometry. The focus of this study will be the broader coverage provided by the lower-frequency long-range network (Fig. 1).

Each site collects hourly measurements of the radial component of the surface current and wave conditions within a footprint local to the antenna. A suite of CODAR software programs processes the received radar signals to generate the hourly radial current files at each site. Further processing is used to combine the radials from two or more sites to produce total current velocity maps. The existence of a total vector solution depends strongly on the bearing angle diversity of the radial velocities within a search radius at each vector grid point. Since at least two radial velocities from different radar sites are required for a vector solution, the regions with overlapping radar range cells from multiple radar sites have better data coverage through time. The regional radial-to-total processing is accomplished using an OI adaptation developed by Kim et al. (2008) with the MATLAB HFR community toolbox, HFR\_Progs (Kohut et al. 2012; Kim et al. 2008). For this method, we used an asymmetric search area stretched parallel to the isobath direction and consistent with the length scales of the currents in the region (Beardsley and Boicourt 1981; Kohut et al. 2004). For quality assurance (QA), we require that both  $u$  and  $v$  component

uncertainty be less than 60% of the expected variance (Kohut et al. 2012). Each remote site was operated with the quality assurance/quality control (QA/QC) recommendations from the MARACOOS operators and the Radiowave Operators Working Group (ROWG) community (Kohut et al. 2012). These are the same data provided to the national HF radar server at the National Oceanic and Atmospheric Administration (NOAA) National Data Buoy Center (<http://hfradar.ndbc.noaa.gov/>). Every hour the available radial velocities are combined into a single total vector map on the national network 6-km grid (Terrill et al. 2006). A total vector was generated only if at least three radial velocities from at least two remote sites were available to the combination algorithm.

### c. The Mid-Atlantic Bight study site

For our study we used the MAB as a natural laboratory, as it has an extensive coastal HFR network that supports both research and applications that depend on reliable surface current data delivery. The seasonal forcing cycles drive significant variability in the physical environment of the MAB. Water masses originating from the watershed, deep ocean, and northern latitudes collide in the waters off New Jersey. Ocean fronts, relatively narrow zones that separate these different water types, are important both because of the role they play in ocean dynamics and because they mark some water mass boundaries. Their dynamical importance in the coastal ocean stems from their association with strong currents, such as the equatorward jet observed at the shelfbreak front off the east coast of North America (Loder et al. 1998; Ullman and Cornillon 1999), and with the strong vertical velocities that often occur in coastal regions (Barth et al. 2005; Houghton and Visbeck 1998).

From events lasting several hours to days on through interannual and decadal scales, the variability of the currents helps define the structure of the marine ecological system. The physical structures within the MAB are characterized by transport pathways and strong hydrographic and velocity gradients that vary in space and time. On longer scales of seasons to years, circulation patterns drive persistent cross- and along-shelf transport pathways (Kohut et al. 2004; Dzwonkowski et al. 2009; Gong et al. 2010). On shorter scales of days to weeks, upwelling and strong coastal storms can disrupt or enhance these patterns (Kohut et al. 2006; Dzwonkowski 2009).

### d. HFR gap scenarios

The gap-filling method was tested for two scenarios commonly observed in HFR-derived surface current

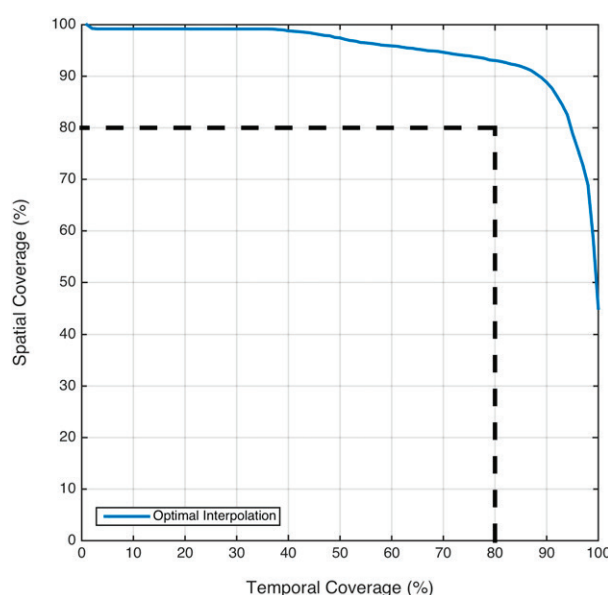


FIG. 3. The ratio of spatial and temporal coverage of the MARACOOS surface current maps for 2012 (blue line). The data delivery target of the network for 80% spatial coverage at least 80% of the time (dashed black line).

maps. Based on a 7-yr dataset (MARACOOS; <http://maracoos.org/>), the hourly coverage of the regional HFR network in the Mid-Atlantic Bight is characterized based on both spatial and temporal coverage. The operational data coverage goal of the network is to provide at least 80% spatial coverage 80% of the time. In this metric, the percentage of spatial coverage is the proportion of grid points within the data footprint beyond the 15-m isobath and within 150 km of the coast with measured data. The measurements within the 15-m isobath are excluded because the deep-water wave assumption that the radar utilizes is no longer valid at our operating frequency of 5 MHz. The points beyond 150 km are excluded, as this is the maximum range of the radar stations during nighttime interference. The temporal coverage can be variable between hours to a time frame of years. This linked spatial temporal metric describes the typical coverage observed across the network over our study period, January–December 2012 (Fig. 3). Figure 3 shows that over much of the year, small spatial gaps of less than 20% of the complete data footprint are more common than larger gaps (>40%) observed during significant hardware or communication disruptions. These smaller data dropouts are isolated areas of the data footprint due to local environmental factors. The larger gaps observed less frequently are due to more significant issues that remove one or more remote sites from the network. In this analysis we define two scenarios that reproduce each of these situations. These



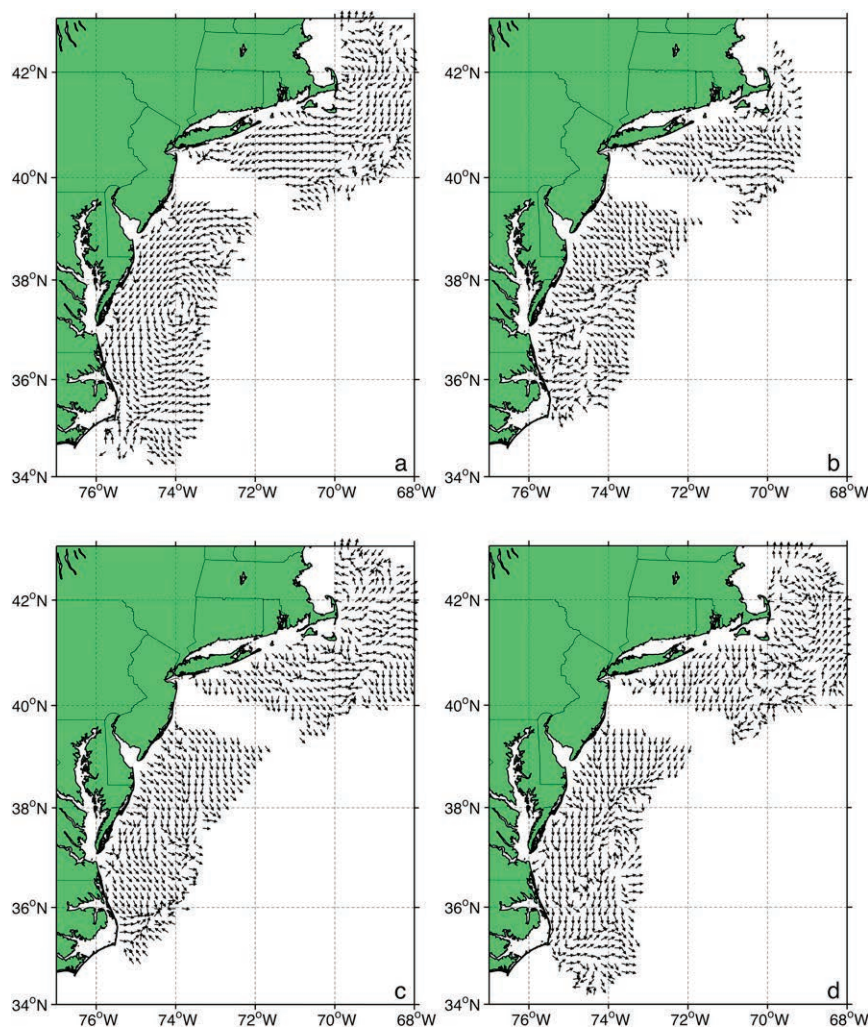


FIG. 4. Surface current maps showing artificial gaps under scenario 1 for the (a) winter, (b) spring, (c) summer, and (d) fall test periods.

more detrimental gaps will typically reduce the coverage by at least 40%.

### 1) SCENARIO 1

The first scenario tested replicates a major hardware or communication disruption that effectively removes at least one site from the network. Observed gaps under this scenario can be best described as a gap that extends along the coast from the shore to the offshore edge of the coverage, effectively splitting a single data footprint into two. This is very uncommon and is primarily due to a disruption in either the real-time communication link or a hardware failure. The result is a gap that stretches from the coast out to the edge of the coverage (Fig. 4). The size of the band with no data depends on the site spacing and the number of sites that are not reporting data. For the purposes of this

analysis, we are simulating a loss in contributing radials from a single site in Sandy Hook, New Jersey, near the apex of the MAB in the vicinity of the approaches to New York Harbor.

### 2) SCENARIO 2

The second gap scenario tested replicates more common situations in which each site is contributing radial vectors, but there is a reduction in the number of radial data from one or more of the sites (Fig. 5). These dropouts could be due to a number of environmental factors. The most common cause is an increase in external noise that lowers the signal-to-noise ratio and therefore limits the range a detectable signal can be used to determine radial velocity (Barrick 1971). For the long-range system, this is more common during local nighttime hours, when the ionosphere effects

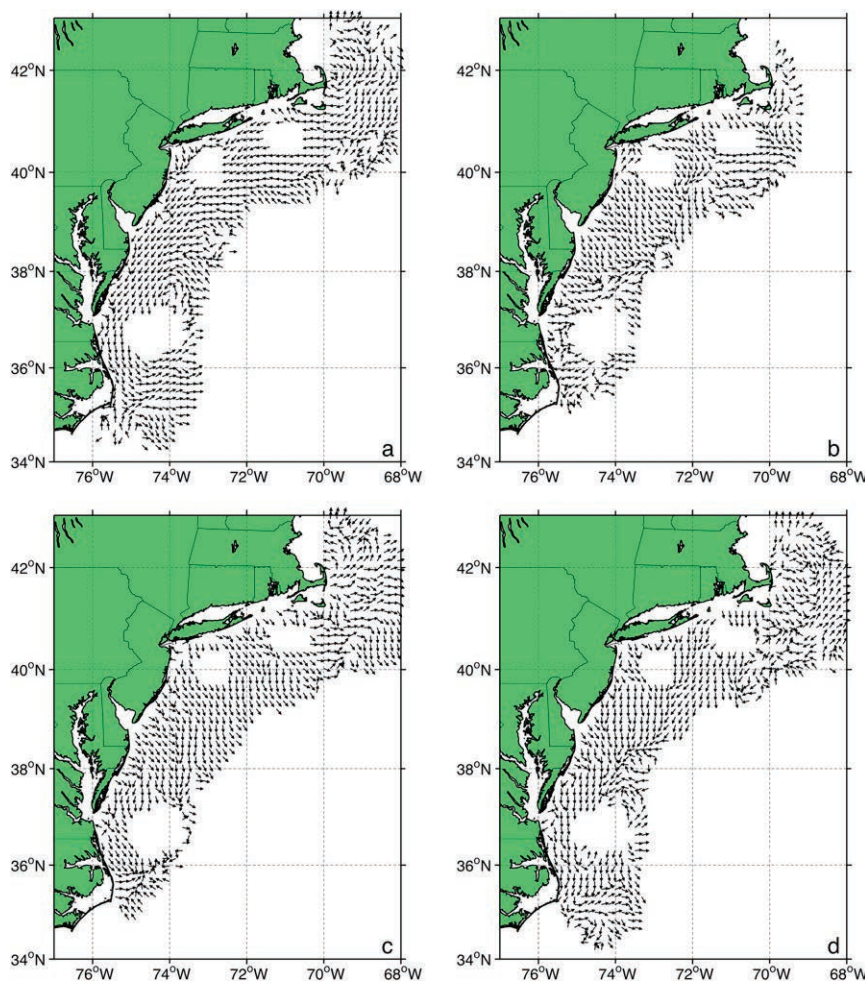


FIG. 5. Surface current maps showing artificial gaps under scenario 2 for the (a) winter, (b) spring, (c) summer, and (d) fall test periods.

increase the range at which a given site receives external noise. Additional environmental factors like local wind and waves could also reduce coverage. These reductions in coverage from sites contributing radials are manifested in the total vector maps as isolated holes in the coverage. The size and location of the gaps depend on the location and magnitude of the reduction of coverage from each individual site. To replicate this in our evaluation, we chose three holes, approximately 30–50 km in diameter, that simulate reduction in coverage from a site in the south, central, and northern regions of the MAB coverage. Based on our analysis of the 7-yr (2007–13) dataset in the MAB coastal radar network, scenario 1 occurs less than 20% of the time with gaps and the smaller, more isolated gaps of scenario 2 represented by any of three gaps shown in Fig. 5 occur 80% of the time with gaps (Fig. 3). This analysis will quantify the accuracy of estimated

vectors from our DCT-PLS method for each of these scenarios.

### 3. Results

#### a. Gap-filling results

First, we verify that the new automatic gap-filling method discussed in this paper is appropriate for HFR data gap filling. To do this the DCT-PLS-filled vectors were evaluated over time at grid points in the northern MAB (Fig. 6a). The data coverage during January 2012 and the location of our two analysis points are shown in Fig. 6a. The coverage shows high data returns over the continental shelf with reduced coverage along the edge of the data footprint well offshore near one of the analysis points. The DCT-PLS algorithm was applied to the entire spatial dataset over the month of January to

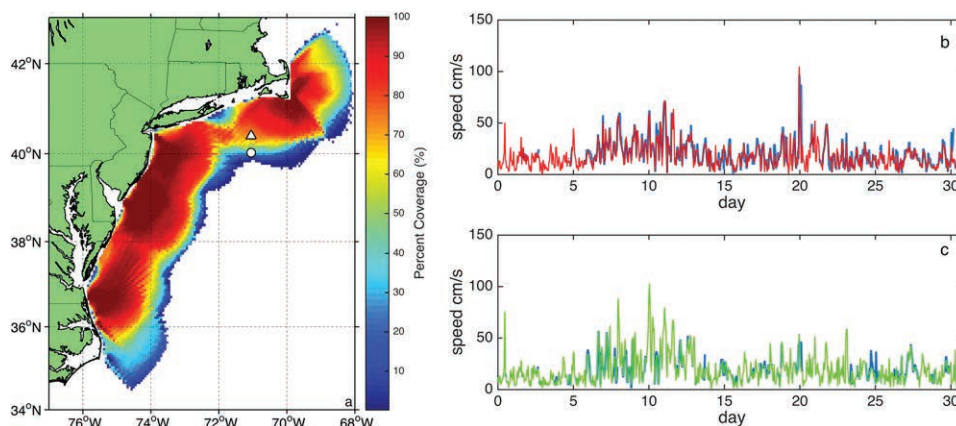


FIG. 6. (a) HFR data coverage over January 2012. The location of our two test sites with 39% (white circle) and 76% (white triangle) are shown. (b) Time series of HFR observations (blue) and the corresponding DCT-PLS model reconstructions (red) for the 76% coverage (white triangle). (c) Time series of HFR observations (blue) and the corresponding DCT-PLS model reconstructions (green) for the 39% coverage.

fill some of these data gaps. The two test sites fall along the same line of longitude and originally possessed 39% and 76% temporal data coverage. We chose these two points to quantify the impact of the gap-filling algorithm over the month. In Figs. 6b and 6c, we show two time series for our selected points in which the algorithm filled the temporal gaps with information from the grid surrounding these locations with higher temporal coverage over the month. The more complete time series of the DCT-PLS-filled values are shown in red and green for the two test sites, respectively. The method does a good job of filling gaps in the time series while retaining the integrity of the data in the surrounding regions without gaps. In a spatiotemporal dataset, the spatially continuous gaps can be temporally intermittent, or vice versa as in shown in Fig. 6. Here the method takes advantage of the spatial and temporal data provided by the HFR to fill gaps in time.

The method was also tested against varied levels of noise in the input data. Specifically, the DCT-PLS method was analyzed on the HFR field with additive Gaussian noise with a variance of  $(0.1 \times V_{\max})^2$ . The results of this test are shown in Fig. 7. An amount of 0%–50% (using an increment of 5%) of clustered missing data were included within the original HFR data field from 1300:00 UTC 8 January 2012 using random Poisson distribution, and 100 Monte Carlo simulations per configuration were performed.

The performance of the methods is evaluated by using the NRMSE. The NRMSE remained relatively low ( $<28\%$ ) even with 50% of additional missing vectors and was mostly influenced by the additive noise.

Although this case represents an artificial HFR velocity field, it clearly illustrates that the DCT-PLS method can efficiently deal with a large percentage of clustered missing data. In conclusion, these results demonstrate that the DCT-PLS method is highly robust to clustered missing data.

#### b. Comparison between DCT-PLS and OMA methods

In practice, hardware and environmental factors lead to gaps in HFR-derived surface current maps. In such cases, local interpolations often fail over gap scenarios highlighted in Figs. 4 and 5. As part of our DCT-PLS evaluation, we computed interpolated vectors across the large data gap due to one or two site outages within the MAB network with both the DCT-PLS and OMA methods during autumn (scenario 1; Fig. 4d). We implemented the OMA in a way that could be run across the entire domain in a real-time mode to address potential gaps across the entire domain.

The OMA was performed with the OpenMA toolbox developed by Kaplan and Lekien (2007). The application of OMA to hourly current data is carried out in several steps. First, modes are generated on a specific domain with a continuous boundary. Next, the modes are typically interpolated on the total current grid. The next step is to fit data to the modes. This can be done with either radial current measurements or total currents. After the fits the OMA currents are ready to be used. We applied the OMA method to the MARACOOS domain hourly sampling on a uniform grid with  $6 \text{ km} \times 6 \text{ km}$  intervals. The fits were performed using minimum spatial scales of 6 km (all modes) on the total current



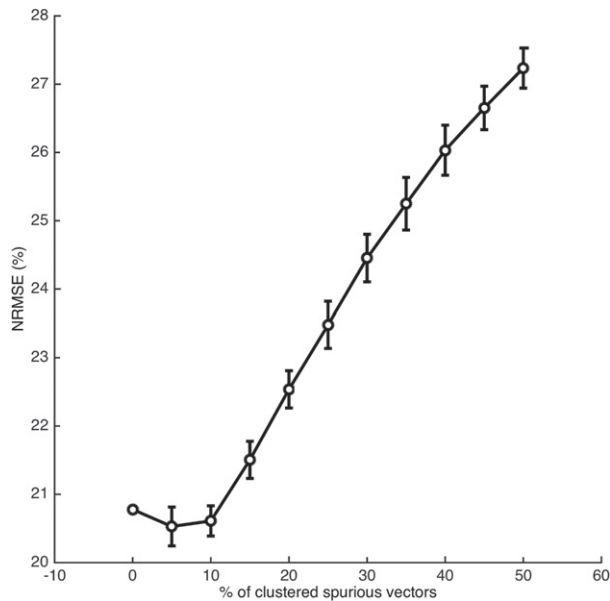


FIG. 7. HFR data postprocessed with the DCT-PLS method: NRMSE (between the postprocessed and original velocities fields) as a function of the percentage of Gaussian noise with a standard deviation of 1% of the maximum velocity.

measurements based on the OpenMA toolbox default value of 200 modes. We acknowledge that the 200 modes fall short of the theoretical  $\sim 6000$  total modes, at least 3000 Dirichlet modes and 3000 Neumann modes, needed resolve features approaching the grid resolution over our domain. Given the computing constraints and our intention to use the OMA as an alternative to benchmark the DCT-PLS method in a real-time data delivery setting, the available OMA tools will fail to produce this large number of modes. So, we had to reduce the number of modes to the toolbox default of 200. The OMA method has two primary input parameters: the spatial length scale  $L$ , which defines the number of modes used for the interpolation; and the diffusion parameter “ $\kappa$ ,” which penalizes the magnitude of the modes. The parameters used in our application of OMA were  $L = 6$  km and  $\kappa = 10^{-4}$ .

We investigated the reconstruction of the missing data performance of both algorithms on the fall scenario 1 and analyzed the reconstruction of the current patterns within the data gap (Fig. 8). A visual comparison showed that for this scenario, the DCT-PLS method performed as well as and across much of the domain better than the OMA interpolated vectors. The velocity pattern of the DCT-PLS interpolated vectors better replicated the patterns of the removed vectors across much of the gap and were more realistic compared to the OMA velocities. Table 2 presents the RMS error statistics for the vector magnitude and direction

comparison between these two methods and the withheld vectors. We caution the reader that the quality of the OMA interpolation is very dependent on the number of modes selected. Our intention in this paper is to see whether the new DCT-PLS application is comparable to the OMA application that has been more widely applied to HFR gap filling over our entire domain as a real-time tool. This required us to reduce the number of modes to the toolbox default value of 200. Therefore, the OMA-derived fields will not be able to resolve the finer spatial scales. In general the DCT-PLS method had smaller RMS errors in both scenarios across our four seasonal test periods. In the OMA formulation, the number of modes is proportional to  $(D/L)^2$  (see Kaplan and Lekien 2007), where  $D$  is the horizontal size of the domain and  $L$  is the spatial length scale introduced previously. To achieve a better reconstruction of the more spatially complex current fields with OMA, we must increase the number of modes by reducing  $L = 2\text{--}3$  km, which will require an increased  $\kappa$ . This optimization of the OMA for our specific region and data gap is beyond the scope of this study. In addition, both the OMA and DCT-PLS methods did not accurately represent the small-scale features of the HFR velocity field, especially in scenario 1.

In conclusion, when a large data gap is present, the DCT-PLS method with RMS differences between 3.5 and  $18.9\text{ cm s}^{-1}$  and  $14.4$  and  $204.3\text{ cm s}^{-1}$  for the vector magnitude and phase, respectively, is better than the OMA with RMS differences between  $8.6$  and  $31.2\text{ cm s}^{-1}$  and  $19.9^\circ$  and  $191^\circ$  for the vector magnitude and phase, respectively. These are lower averages on average because of the robust statistical ability of DCT-PLS to estimate the current within the gap. Based on this basic evaluation, the DCT-PLS method is comparable to the OMA method, and in many regions of our test scenario it produces more realistic interpolated vectors. Since the DCT-PLS method does not require any preprocessing, it is also more computationally efficient to run on large HFR networks like that deployed in the MAB. More work is needed to quantify the differences and similarities of these two methods and others in filling a variety of gaps in HFR networks. The details of the comparison between the DCT-PLS method introduced in this manuscript is discussed in more detail in the following section.

### c. Synthetic data validation of the DCT-PLS method

The evaluation of the interpolated fields is organized into tests that replicate typical gap scenarios observed in the coastal networks deployed around the world (Lipphardt et al. 2000; Paduan and Rosenfeld 1996). The



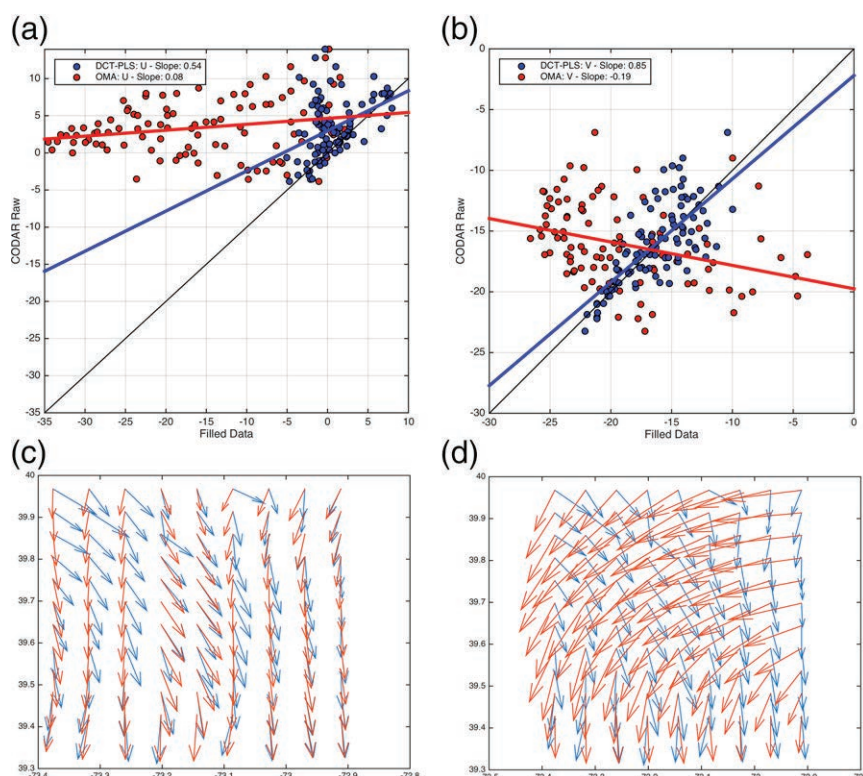


FIG. 8. Scatterplots comparing the estimated velocities with the removed observations for the DCT-PLS (blue) and OMA (red) methods for the (a) east and (b) north velocity components for scenario 1. Vector maps showing the CODAR observations (blue) and the filled values (red) for the (c) DCT-PLS and (d) OMA.

challenge we had in designing the evaluation of the method was to artificially define the gaps so that we could use the withheld data as truth. The size of the gaps in each scenario was chosen based on the analysis described in Fig. 3. Since the gaps represented in our two scenarios do occur in the spatial time series, we could not consistently identify observations to remove and use as truth throughout the entire time series. As an alternative, we identified four maps with complete coverage that represent the range of spatial complexity observed in the maps over our 7-yr time series (Dzwonkowski et al. 2009; Dzwonkowski 2009; Gong et al. 2010). During the windier better mixed months of the fall and winter, the maps tend to be more uniform compared to the shorter decorrelation scales observed during the calmer months of the spring and summer. These hourly current maps sampled in each season provide the consistent ground truth needed for our evaluation and the variability in the flow fields representative of the entire time series.

For scenarios 1 and 2, we evaluated these four velocity fields by comparing the interpolated vectors to those removed within each gap. The comparison between the

removed vectors and the predicted values from our method for each scenario is shown in Fig. 9. The scatter shows a stronger agreement between the predicted currents and the observed under scenario 2 representing the more common occurrence of small isolated data gaps. Under this scenario the method performed well with slopes for all four time periods above 0.7 for both the  $u$  and  $v$  components. The slopes less than one indicate that, on average, the filled-in values were slightly less than the observed velocities. For the less frequent gap scenario 1, the method does not perform as well with slopes below 0.35 and increased variance. The comparison statistics between the removed and predicted vectors across each of these scenarios are shown in Table 2. For scenario 1, the RMS error between the DCT-PLS predicted and removed vector magnitudes across the four time periods range from 3.4 to 18.9  $\text{cm s}^{-1}$ . This variability across the time periods tested is shown in Fig. 10. The four time periods represent a range in the characteristics of the flow surrounding the gap. They were chosen to represent the typical structure observed throughout the year in the MAB (Gong et al. 2010). The lowest correlation in

TABLE 2. RMS error between the DCT-PLS and OMA estimated velocities and the removed observations over each scenario and season.

Scenario 1				
	DCT-PLS magnitude ( $\text{cm s}^{-1}$ )	DCT-PLS direction ( $^{\circ}$ )	OMA magnitude ( $\text{cm s}^{-1}$ )	OMA direction ( $^{\circ}$ )
Winter	18.9	204.3	31.3	191.0
Spring	5.3	41.4	8.7	94.4
Summer	6.1	14.4	8.6	20.0
Fall	3.5	30.8	12.8	104.9
Scenario 2				
	DCT-PLS magnitude ( $\text{cm s}^{-1}$ )	DCT-PLS direction ( $^{\circ}$ )	OMA magnitude ( $\text{cm s}^{-1}$ )	OMA direction ( $^{\circ}$ )
Winter	14.4	105.1	34.5	169.8
Spring	5.2	66.7	11.6	91.5
Summer	8.4	28.5	23.1	35.0
Fall	9.1	76.7	12.2	110.8

the winter is characterized by broad scatter with slopes close to zero for both the  $u$  and  $v$  components (Fig. 10). The highest correlation occurred in the summer with a slope closer to 1, particularly in the north/south component (0.82).

In contrast to the large range of values seen in scenario 1, the correlation of the interpolated vectors in scenario 2 was more consistent. Similarly, the scatterplots all show a more concentrated distribution along a line closer to the target 1:1 line (Fig. 11). The exception was the fall test, when the slopes for both components fell below 0.5. In the winter, the correlation was the highest observed at 0.95 with slopes for both components above 0.7. The relatively high winter RMS differences reported in Table 2 compared to the other seasons tested over scenario 2 are due to the small number of points above the 1:1 line (Fig. 11a). Because of the faster currents in this winter scenario, these points bias the RMS difference statistics high compared to the majority of filled values in this test that fall on the 1:1 line.

#### 4. Discussions and conclusions

In this study we introduced an efficient automated DCT-PLS method for filling data gaps in the HFR ocean spatiotemporal dataset applied to the MARACOOS domain. The procedure explicitly utilizes both spatial and temporal information to derive the statistical model and to predict the missing values.

The evaluation highlights the sensitivity of the gap-filling method to the vectors surrounding the gaps. In our analysis we chose two scenarios to replicate the conditions typically observed in coastal networks operating around the world. The band scenario is a less common occurrence in which either a communication or hardware failure causes a gap in the coverage that stretches from the coast to the outer edge of the coverage. In this scenario we saw a large range in the accuracy of the interpolated vectors. Since this scenario by definition does not have observed vectors surrounding the gap, the quality of the interpolated vectors is dependent

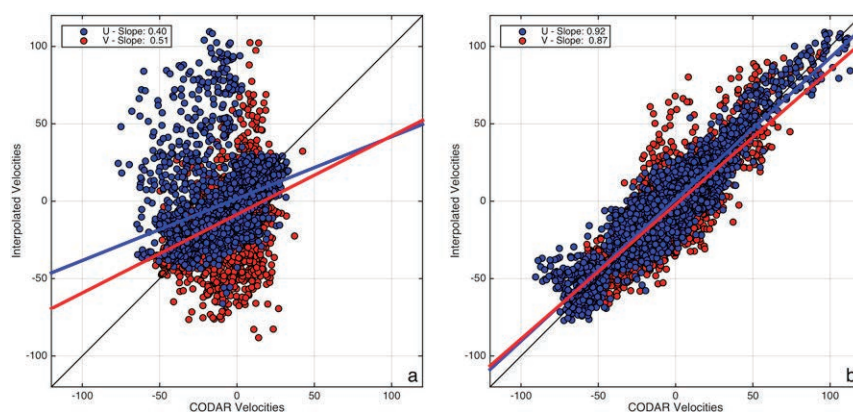


FIG. 9. Scatterplots comparing the estimated velocities with the removed observations for the east (blue) and north (red) components in the gaps under (a) scenario 1 and (b) scenario 2 for all the seasonal tests.

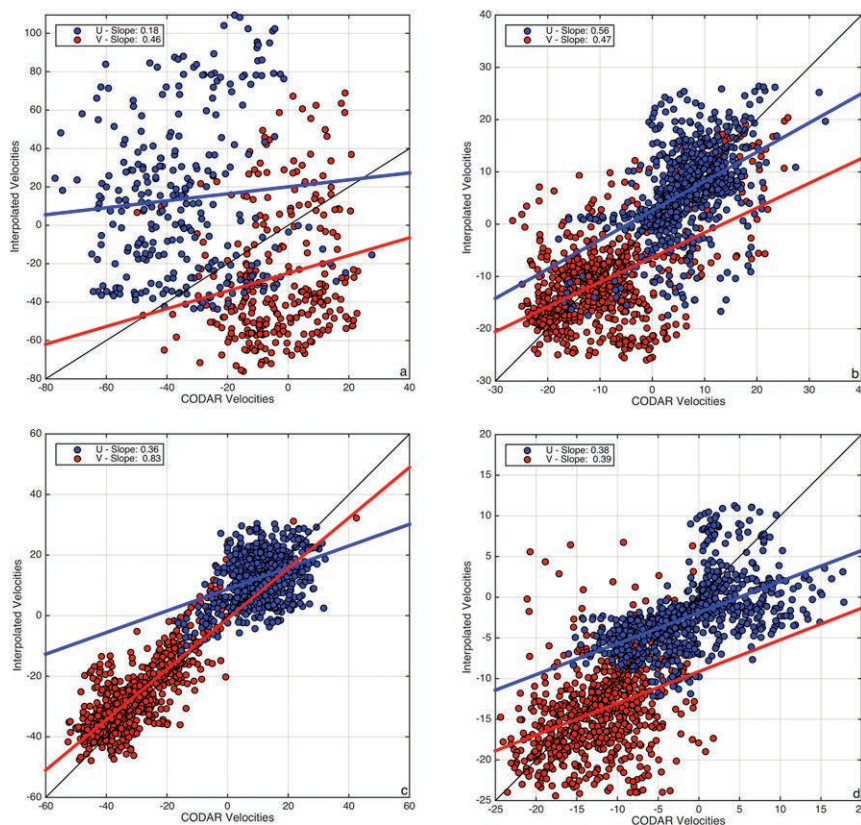


FIG. 10. Scatterplots comparing the estimated velocities with the removed observations for the east (blue) and north (red) components in the gaps under scenario 1 for the (a) winter, (b) spring, (c) summer, and (d) fall test periods. Note that the velocity scales of each panel change as they are optimized for the range of the input data.

on the spatial structure of the flow on either side of the data gap. For those times when the flow was uniform and flowing along the gap, the comparison was quite good with a correlation of 0.7. If the flow was not uniform or flowing mostly across the band, then the lack of vectors nearshore and offshore of the band reduced the quality of the interpolated vectors. This is most evident in the wintertime image with flow around the band moving mostly across the band.

Scenario 2 tested gaps that are much more typical in regional networks. Under this scenario the gaps are smaller and isolated within complete coverage. They occur when environmental conditions reduce the range of individual coastal sites. Under this scenario the comparison on average was much better. Unlike the band scenario, observed currents that informed the interpolation method surrounded these gaps. With information surrounding the gap, the method performed better. The flow characteristics did impact the quality of the interpolated vectors with the highest correlation observed when the flow was largely uniform across the gap. As the complexity of the flow reached scales

equivalent to the size of the gap, the correlation dropped.

The user, however, should be aware of some limitations of the automatic gap-filling procedure. The method was tested as a gap-filling solution to a real-time HFR data stream. Consequently, the GVC criterion was applied for the fully automated smoothing algorithm. Therefore, good results are expected for a Gaussian noise with zero mean and constant variance (scenario 2). [Garcia \(2011\)](#) and [Wahba \(1990\)](#) reported that the GVC criterion is fairly well adapted to non-Gaussian noise and nonhomogeneous variances. Additionally, the GVC criterion may cause problems when the area of missing data size is large with incomplete surrounding data coverage (scenario 1). Under these conditions, the automated application of the method may lead to poorly predicted vectors. In this case, the best smoothing parameter will need to be determined manually based on the specific gap location and size. As a consequence, the efficiency of the automated gap filling depends specifically upon the original data and on the properties of the additive noise, as shown above.



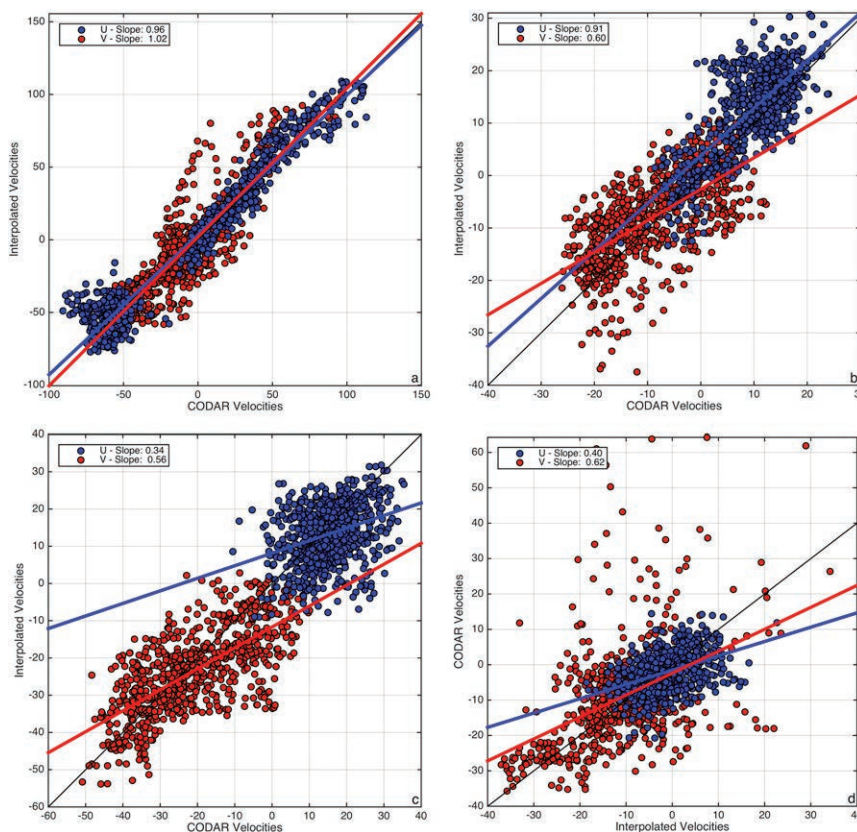


FIG. 11. Scatterplots comparing the estimated velocities with the removed observations for the east (blue) and north (red) components in the gaps under scenario 2 for the (a) winter, (b) spring, (c) summer, and (d) fall test periods. Note that the velocity scales of each panel change as they are optimized for the range of the input data.

We have evaluated the DCT-PLS method for filling gaps inherent in HFR real-time data streams. The method is shown to be a robust solution for the most common gap scenarios characterized as holes, approximately 30–50 km in diameter, in the data coverage with observations completely surrounding the gap. Under the less common scenario in which more significant outages can remove entire sites from a coastal network, the effectiveness of the method depends on the characteristics of the surrounding flow. Individual HFR network operators will need to assess the scales of variability in their operating area to determine the optimal way to apply this method in either a real-time or post-processed application.

**Acknowledgments.** This study was supported by a grant from the Israel Science Foundation and the Taiwan Ministry of Science and Technology (EF). The HFR dataset was supported through NOAA Award NA11NOS0120038, “Towards a Comprehensive Mid-Atlantic Regional Association Coastal Ocean Observing System (MARACOOS),” and the National Ocean Service (NOS), National Oceanic

and Atmospheric Administration (NOAA) NOAA-NOS-IOOS-2011-2002515 / CFDA: 11.012, “Integrated Ocean Observing System Topic Area 1: Continued Development of Regional Coastal Ocean Observing Systems.” We also acknowledge the time and advice provided by Dr. Bruce Lipphardt and three reviewers, all of whom helped to revise the manuscript into its present form.

#### REFERENCES

- Alvera-Azcárate, A., A. Barth, M. Rixen, and J. M. Beckers, 2005: Reconstruction of incomplete oceanographic data sets using empirical orthogonal functions: Application to the Adriatic Sea surface temperature. *Ocean Modell.*, **9**, 325–346, doi:10.1016/j.ocemod.2004.08.001.
- Barrick, D. E., 1971: Theory of HF and VHF propagation across the rough sea: 1. The effective surface impedance for a slightly rough highly conducting medium at grazing incidence. *Radio Sci.*, **6**, 517–526, doi:10.1029/RS006i005p00517.
- , 2008: 30 years of CMTC and CODAR. *CMTC 2008: IEEE/OES 9th Working Conference on Current Measurement Technology*, IEEE, 131–136, doi:10.1109/CCM.2008.4480856.
- , and B. J. Lipa, 1997: Evolution of bearing determination in HF current mapping radars. *Oceanography*, **10**, 72–75, doi:10.5670/oceanog.1997.27.



- , M. W. Evens, and B. L. Weber, 1977: Ocean surface currents mapped by radar. *Science*, **198**, 138–144, doi:10.1126/science.198.4313.138.
- Barth, J. A., S. D. Pierce, and T. J. Cowles, 2005: Mesoscale structure and its seasonal evolution in the northern California Current System. *Deep-Sea Res. II*, **52**, 5–28, doi:10.1016/j.dsr2.2004.09.026.
- Beardsley, R. C., and W. C. Boicourt, 1981: On estuarine and continental-shelf circulation in the Middle Atlantic Bight. *Evolution of Physical Oceanography*, B. A. Warren and C. Wunsch, Eds., MIT, 198–233.
- Beckers, J. M., and M. Rixen, 2003: EOF calculations and data filling from incomplete oceanographic datasets. *J. Atmos. Oceanic Technol.*, **20**, 1839–1856, doi:10.1175/1520-0426(2003)020<1839:ECADFF>2.0.CO;2.
- Craven, P., and G. Wahba, 1978: Smoothing noisy data with spline functions: Estimating the correct degree of smoothing by the method of generalized cross-validation. *Numer. Math.*, **31**, 377–403, doi:10.1007/BF01404567.
- Crombie, D. D., 1955: Doppler spectrum of sea echo at 13.56 Mc/s. *Nature*, **175**, 681–682, doi:10.1038/175681a0.
- Davis, R. E., 1985: Objective mapping by least squares fitting. *J. Geophys. Res.*, **90**, 4773–4778, doi:10.1029/JC090iC03p04773.
- Dzwonkowski, B., 2009: Surface current analysis of shelf water in the central Mid-Atlantic Bight. Ph.D. thesis, University of Delaware, 178 pp.
- , J. T. Kohut, and X.-H. Yan, 2009: Seasonal differences in wind-driven across-shelf forcing and response relationships in the shelf surface layer of the central Mid-Atlantic Bight. *J. Geophys. Res.*, **114**, C08018, doi:10.1029/2008JC004888.
- Garcia, D., 2010: Robust smoothing of gridded data in one and higher dimensions with missing values. *Comput. Stat. Data Anal.*, **54**, 1167–1178, doi:10.1016/j.csda.2009.09.020.
- , 2011: A fast all-in-one method for automated post-processing of PIV data. *Exp. Fluids*, **50**, 1247–1259, doi:10.1007/s00348-010-0985-y.
- Gong, D., J. T. Kohut, and S. M. Glenn, 2010: Seasonal climatology of wind-driven circulation on the New Jersey Shelf. *J. Geophys. Res.*, **115**, C04006, doi:10.1029/2009JC005520.
- Houghton, R. W., and M. Visbeck, 1998: Upwelling and convergence in the Middle Atlantic Bight Shelfbreak Front. *Geophys. Res. Lett.*, **25**, 2765–2768, doi:10.1029/98GL02105.
- Kaplan, D. M., and F. Lekien, 2007: Spatial interpolation and filtering of surface current data based on open-boundary modal analysis. *J. Geophys. Res.*, **112**, C12007, doi:10.1029/2006JC003984.
- Kim, S. Y., E. Terrill, and B. Cornuelle, 2007: Objectively mapping HF radar-derived surface current data using measured and idealized data covariance matrices. *J. Geophys. Res.*, **112**, C06021, doi:10.1029/2006JC003756.
- , —, and —, 2008: Mapping surface currents from HF radar radial velocity measurements using optimal interpolation. *J. Geophys. Res.*, **113**, C10023, doi:10.1029/2007JC004244.
- Kohut, J. T., S. M. Glenn, and R. J. Chant, 2004: Seasonal current variability on the New Jersey inner shelf. *J. Geophys. Res.*, **109**, C07S07, doi:10.1029/2003JC001963.
- , H. J. Roarty, and S. M. Glenn, 2006: Characterizing observed environmental variability with HF Doppler radar surface current mappers and acoustic Doppler current profilers: Environmental variability in the coastal ocean. *IEEE J. Oceanic Eng.*, **31**, 876–884, doi:10.1109/JOE.2006.886095.
- Kohut, J., H. Roarty, E. Randall-Goodwin, S. Glenn, and C. Lichtenwalner, 2012: Evaluation of two algorithms for a network of coastal HF radars in the Mid-Atlantic Bight. *Ocean Dyn.*, **62**, 953–968, doi:10.1007/s10236-012-0533-9.
- Lipa, B. J., and D. E. Barrick, 1983: Least-squares methods for the extraction of surface currents from CODAR cross-loop data: Application at ARSLOE. *IEEE J. Oceanic Eng.*, **OE-8**, 226–253, doi:10.1109/JOE.1983.1145578.
- Lipphardt, B. L., A. D. Kirwan, C. E. Grosch, J. K. Lewis, and J. D. Paduan Jr., 2000: Blending HF radar and model velocities in Monterey Bay through normal mode analysis. *J. Geophys. Res.*, **105**, 3425–3450, doi:10.1029/1999JC900295.
- Loder, J. W., B. Petrie, and G. Gawarkiewicz, 1998: The coastal ocean off northwestern North America: A large-scale view. *The Global Coastal Ocean: Regional Studies and Syntheses*, A. R. Robinson and K. H. Brink, Eds., The Sea—Ideas and Observations on Progress in the Study of the Seas, Vol. 11, John Wiley and Sons, 105–133.
- Magnell, B. A., S. L. Spiegel, R. I. Scarlet, and J. B. Andrews, 1980: The relationship of tidal and low-frequency currents on the north slope of Georges Bank. *J. Phys. Oceanogr.*, **10**, 1200–1212, doi:10.1175/1520-0485(1980)010<1200:TROTAL>2.0.CO;2.
- Ohlmann, C., P. White, L. Washburn, E. Terrill, B. Emery, and M. Otero, 2007: Interpretation of coastal HF radar-derived surface currents with high-resolution drifter data. *J. Atmos. Oceanic Technol.*, **24**, 666–680, doi:10.1175/JTECH1998.1.
- Paduan, J. D., and L. Rosenfeld, 1996: Remotely sensed surface currents in Monterey Bay from shore-based HF radar (Coastal Ocean Dynamics Application Radar). *J. Geophys. Res.*, **101**, 20 669–20 686, doi:10.1029/96JC01663.
- Peacock, T., and G. Haller, 2013: Lagrangian coherent structures: The hidden skeleton of fluid flows. *Phys. Today*, **66**, 41–47, doi:10.1063/PT.3.1886.
- Roarty, H. J., and Coauthors, 2010: Operation and application of a regional high-frequency radar network in the Mid-Atlantic Bight. *Mar. Technol. Soc. J.*, **44**, 133–145, doi:10.4031/MTSJ.44.6.5.
- Robinson, A. R., and S. M. Glenn, 1999: Adaptive sampling for ocean forecasting. *Naval Res. Rev.*, **51**, 28–38.
- Seroka, G., J. Kohut, L. Palamara, S. Glenn, H. Roarty, L. Bowers, and R. Dunk, 2013: Spatial evaluation of high-resolution modeled offshore winds using estimated winds derived from a network of HF radars. *Proc. Oceans—San Diego, 2013*, San Diego, CA, IEEE, 1–5.
- Teague, C. C., J. F. Vesecky, and D. M. Fernandez, 1997: HF radar instruments, past to present. *Oceanography*, **10** (2), 40–43, doi:10.5670/oceanog.1997.19.
- Terrill, E., and Coauthors, 2006: Data management and real-time distribution in the HF-Radar National Network. *OCEANS 2006*, IEEE, 1–6, doi: 10.1109/OCEANS.2006.306883.
- Ullman, D. S., and P. C. Cornillon, 1999: Satellite-derived sea surface temperature fronts on the continental shelf off the northeast U.S. coast. *J. Geophys. Res.*, **104**, 23 459–23 478, doi:10.1029/1999JC900133.
- Wahba, G., 1990: Estimating the smoothing parameter. *Spline Models for Observational Data. Society for Industrial Mathematics*, SIAM, 45–65, doi: 10.1137/1.9781611970128.ch4.
- Wang, G., D. Garcia, Y. Liu, R. de Jeu, and A. J. Dolman, 2012: A three-dimensional gap filling method for large geophysical datasets: Application to global satellite soil moisture observations. *Environ. Modell. Software*, **30**, 139–142, doi:10.1016/j.envsoft.2011.10.015.
- Yaremchuk, M., and A. Sentchev, 2009: Mapping radar-derived sea surface currents with a variational method. *Cont. Shelf Res.*, **29**, 1711–1722, doi:10.1016/j.csr.2009.05.016.



## ARTICLE

Received 21 May 2015 | Accepted 29 Jan 2016 | Published 8 Mar 2016

DOI: 10.1038/ncomms10887

OPEN

# Stratified coastal ocean interactions with tropical cyclones

S.M. Glenn<sup>1</sup>, T.N. Miles<sup>1</sup>, G.N. Seroka<sup>1</sup>, Y. Xu<sup>2</sup>, R.K. Forney<sup>1</sup>, F. Yu<sup>3</sup>, H. Roarty<sup>1</sup>, O. Schofield<sup>1</sup> & J. Kohut<sup>1</sup>

Hurricane-intensity forecast improvements currently lag the progress achieved for hurricane tracks. Integrated ocean observations and simulations during hurricane Irene (2011) reveal that the wind-forced two-layer circulation of the stratified coastal ocean, and resultant shear-induced mixing, led to significant and rapid ahead-of-eye-centre cooling (at least 6 °C and up to 11 °C) over a wide swath of the continental shelf. Atmospheric simulations establish this cooling as the missing contribution required to reproduce Irene's accelerated intensity reduction. Historical buoys from 1985 to 2015 show that ahead-of-eye-centre cooling occurred beneath all 11 tropical cyclones that traversed the Mid-Atlantic Bight continental shelf during stratified summer conditions. A Yellow Sea buoy similarly revealed significant and rapid ahead-of-eye-centre cooling during Typhoon Muifa (2011). These findings establish that including realistic coastal baroclinic processes in forecasts of storm intensity and impacts will be increasingly critical to mid-latitude population centres as sea levels rise and tropical cyclone maximum intensities migrate poleward.

<sup>1</sup>Center for Ocean Observing Leadership, Department of Marine and Coastal Sciences, School of Environmental and Biological Sciences, Rutgers University, 71 Dudley Road, New Brunswick, New Jersey 08901, USA. <sup>2</sup>State Key Laboratory of Estuarine and Coastal Research, East China Normal University, 3663 Zhongshan Road North, Shanghai 200062, China. <sup>3</sup>Institute of Oceanology, Chinese Academy of Sciences, 7 Nanhai Road, Qingdao 266071, China. Correspondence and requests for materials should be addressed to S.G. (email: glenn@marine.rutgers.edu).

**T**ropical cyclones are among the most destructive weather phenomena on Earth<sup>1</sup>. Declines in hurricane related mortalities<sup>2</sup> reflect improvements in global atmospheric and ensemble modelling approaches<sup>3</sup> that have reduced hurricane track forecast errors by factors of 2–3 (ref. 4). Despite two decades of progress in hurricane track prediction, improvements in hurricane-intensity forecast skill have lagged significantly<sup>4</sup>. The predictions, public response and unexpected devastation patterns related to Hurricane Irene exemplify this dichotomy. Accurate track forecasts days in advance provided time for preparations and coastal evacuations, but Irene's official forecast maximum wind speeds along the Mid-Atlantic coast were consistently  $\sim 5 \text{ m s}^{-1}$  too high<sup>5</sup>. Irene instead caused catastrophic inland flooding because of heavy rainfall<sup>5</sup>, making it the eighth costliest cyclone to hit the United States since 1900 (ref. 6), with damages of  $\sim \$16$  billion (ref. 5). These intensity forecast uncertainties have significant negative consequences, ranging from unnecessary preparation costs to future public skepticism<sup>7</sup>.

Improved tropical cyclone intensity predictions include dependencies on the rapid space-time evolution of the atmosphere–ocean responses and feedbacks<sup>8</sup>. Coupled atmosphere–ocean models demonstrate that small shifts in sea surface temperature (SST) and stratification, even on small (100 km) horizontal scales, can have significant impacts on storm intensity<sup>9–11</sup>. Several studies have noted<sup>12–16</sup> the relationship between warm and cold mesoscale features in the deep ocean and rapid changes in intensity, but the coastal ocean has received much less attention.

Here, utilizing an ocean observing network to inform ocean and atmospheric model simulations, the role of baroclinic processes on a stratified coastal ocean and their impact on the intensity of Hurricane Irene was quantified. The high percentage of ahead-of-eye-centre<sup>14,17,18</sup> cooling (76–98%) observed in Irene

is not reproduced by standard open ocean models that exclude these coastal baroclinic processes. Atmospheric model sensitivity studies indicate that intense in-storm sea surface cooling over a strongly stratified coastal regime is the missing contribution required to reproduce the rapid decay of Hurricane Irene's intensity. The 30-year historical buoy record shows an average of 73% of the in-storm cooling occurs ahead-of-eye-centre on the Mid-Atlantic Bight (MAB) in the stratified season. A Yellow Sea buoy observed up to 85% of in-storm cooling ahead-of-eye-centre during Super Typhoon Muifa (2011). The results demonstrate the importance of rapid ahead-of-eye-centre vertical shear-induced mixing processes and the ensuing ocean–atmosphere feedbacks for generating more accurate simulations of storm intensity.

## Results

**Synoptic conditions.** Hurricane Irene formed east of the Caribbean's Windward Islands on 22 August 2011 and made initial United States landfall in North Carolina as a Category 1 hurricane on 27 August. It re-emerged over the ocean in the MAB before a second landfall in New Jersey as a tropical storm on 28 August (ref. 5), closely following the historical northeastward tracks of hurricanes along the northeast United States<sup>19</sup>. Irene accelerated and lost intensity as it crossed the MAB, moving parallel to the coast with the eye over inner-continental shelf waters (Fig. 1a). Propagation was rapid at  $30\text{--}40 \text{ km h}^{-1}$ , requiring only  $\sim 9.5 \text{ h}$  to cross from North Carolina to New Jersey landfall. Cloud bands extended over 600 km from the eye centre, obscuring the ocean from satellite infrared SST sensors during passage. Differencing 3-day composites of cloud-free satellite imagery before (24–26 August) from after (29–31 August) Irene reveals the regional pattern of MAB sea surface cooling (Fig. 1a and Supplementary Fig. 1A,B). The largest

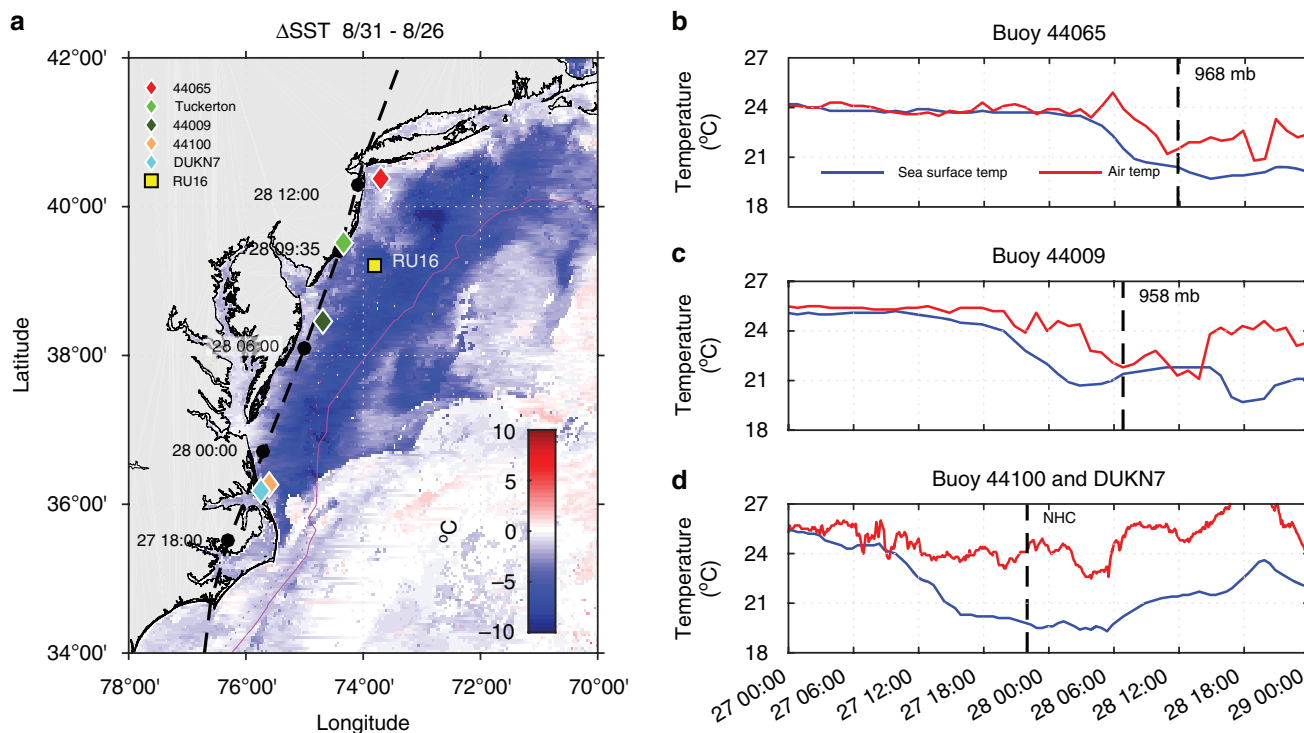


**Figure 1 | Map of the study domain with satellite and buoy data. (a)** SST difference map post-Irene (8/31) minus pre-Irene (8/26) with NHC best track (black dots connected by dashed line labelled with August date and UTC time), weather buoys/stations (coloured diamonds), underwater glider RU16 location during storm (yellow square) and bathymetry at 50 m (dotted magenta) and 200 m (solid magenta). **(b–d)** Buoy/station observed SST (blue) and air temperature (red) with vertical black dashed line/label indicating the time/value of minimum air pressure **(b,c)**, and time of eye passage according to NHC best track data **(d)**. The individual SST three-day composite maps for 24–26 August and 29–31 August are provided in Supplementary Fig. 1A,B.



cooling ( $5\text{--}11\text{ }^{\circ}\text{C}$ ) was observed to the right of the eye centre over the MAB's middle to outer shelf. Inner shelf cooling was slightly less, with averages of  $3\text{--}5\text{ }^{\circ}\text{C}$  of cooling within the  $25\text{-km}$  radius eye wall (Supplementary Fig. 1C). Cooling was much less significant on the shelf seas to the south of the MAB, in the deep ocean to the east and, as previously noted in other hurricanes<sup>20</sup>, along the very shallow unstratified coast, bays and sounds.

**Observations.** National Data Buoy Center (NDBC) buoys 44009 and 44065 recorded peak wind speeds (Supplementary Fig. 2) near  $20\text{ m s}^{-1}$  from offshore as Irene approached. At these NDBC buoys and at 44100, water temperatures dropped rapidly by  $3.8\text{--}6.3\text{ }^{\circ}\text{C}$  ahead of eye centre passage (Fig. 1b–d), representing 82–98% of the in-storm cooling at these locations (Supplementary Fig. 3). At Irene's fast propagation speed, the eye was still  $150\text{--}200\text{ km}$  to the south after the most rapid cooling was complete. As the ocean surface cooled, observed air temperatures were greater than SSTs, indicating air–sea-sensible heat fluxes were from the atmosphere into the ocean.

Atmospheric conditions (Fig. 2a) were recorded just inshore of a Slocum autonomous underwater glider<sup>21,22</sup> measuring subsurface ocean conditions<sup>23</sup> during Irene at the location shown in Fig. 1a (see Supplementary Fig. 4 for a plot of the complete glider track well before, during and after the storm). Winds initially from offshore ( $90^{\circ}$ ), with speeds near  $20\text{ m s}^{-1}$  ahead of the eye, rotated rapidly to blow from onshore ( $270^{\circ}$ ) after the eye passed. Glider-observed subsurface temperatures (Fig. 2b) indicate that initially, typical MAB summer stratification<sup>24</sup> was present, with a seasonally warmed surface layer ( $\sim 24\text{ }^{\circ}\text{C}$ ) above the MAB Cold Pool<sup>25</sup> ( $<10\text{ }^{\circ}\text{C}$ ) separated by a sharp ( $<8\text{ m}$  thick) thermocline. Significant cooling of the surface layer ( $5.1\text{ }^{\circ}\text{C}$ ) and deepening of the thermocline ( $>15\text{ m}$ ) was observed under the leading edge of the storm. Little change in thermocline depth and much less cooling ( $1.6\text{ }^{\circ}\text{C}$ ) of the upper layer was observed after eye passage. Thus, ahead-of-eye-centre cooling represents 76% of in-storm cooling observed at the glider (Fig. 2b). Both the glider and buoy data suggest that much of the satellite observed SST cooling (over  $\sim 100,000\text{ km}^2$  of continental shelf) occurred ahead-of-eye-centre.

Ocean surface currents measured by a CODAR high-frequency (HF) radar<sup>26</sup> network<sup>27</sup> illustrated the rapid response of the thin surface layer (Supplementary Fig. 5) to the changing wind direction (Fig. 2a). Time-series of the cross-shelf components of the currents (Fig. 2c) at the glider location, with positive values towards land, indicate that the onshore surface currents began building before the eye entered the MAB, increasing to a peak value  $>50\text{ cm s}^{-1}$  towards the coast before the eye passage. Along-shelf currents throughout the water column were weak (Fig. 2d). After the eye, the winds changed direction and within a few hours, the cross-shelf surface currents switched to offshore. Despite the strong observed surface currents, the depth-averaged current (Fig. 2c) reported by the glider remained small during the storm's duration, with peaks barely exceeding  $5\text{ cm s}^{-1}$ . As in deep water, the current response is baroclinic<sup>28,29</sup>, but the low depth-averaged current implies a strong offshore flow in the bottom layer. These bottom layer currents were estimated based on the relative layer thicknesses and the requirement that the combined surface and bottom layer-averaged currents matched the glider-observed depth-averaged current. The estimated bottom layer currents accelerated in the offshore direction as the eye approached, causing significant shear between the two layers at the same time the surface layer was deepening and cooling.

**Ocean model simulations.** Coastal ocean three-dimensional (3D) model simulations of Irene using the Regional Ocean Modeling

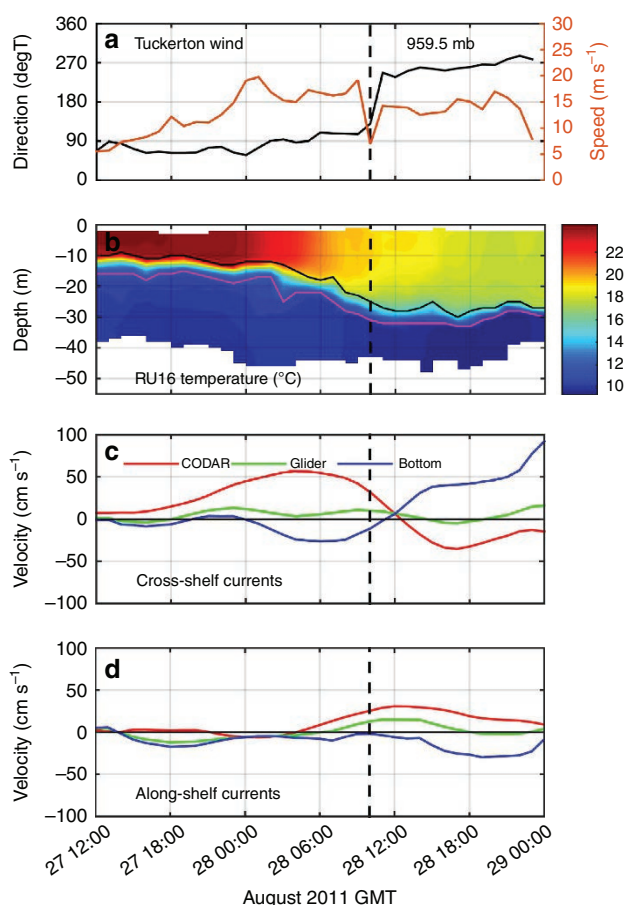


**Figure 2 | Data from a local meteorological station, glider and HF radar.**

(a) Tuckerton WeatherFlow, Inc. station 10 m wind speed (orange) and direction from (black) with vertical black dashed line/label indicating the time/value of the minimum air pressure corresponding to landfall time on 28 August at 935 GMT. (b) Temporal evolution and vertical structure of the glider temperature during storm conditions with lines indicating top (black) and bottom (magenta) of thermocline. (c) Cross-shelf currents (positive onshore, negative offshore) for the surface layer (red) from CODAR HF Radar, depth-averaged (green) from the glider and bottom layer (blue) calculated from the depth-weighted average of the HF radar and glider velocities. (d) Same as c but for along-shelf currents (positive up-shelf northeastward and negative down-shelf southwestward).

System (ROMS) in the MAB<sup>30,31</sup> successfully reproduced the thermocline deepening and surface layer cooling (Fig. 3a) similar to the glider observations (Fig. 2b). The modelled cross-shelf velocity component (Fig. 3b) also has similarities to the combined glider and HF radar data (Fig. 2c). The surface layer flow accelerated shoreward for 12 h until eye passage, while the bottom layer responded more slowly with an offshore counter-flow. A few hours after eye passage, the cross-shelf flows reversed, also consistent with observations. The dominant terms in the cross-shelf momentum balance (Fig. 3g) indicate that the surface wind stress increased as the eye approached and decreased as it receded. Before the eye centre arrival, the presence of a coastline produced an offshore-directed pressure gradient that nearly balanced the wind stress and accelerated the offshore jet in the bottom layer. After the storm passage, the cross-shelf surface current switched to offshore; the cross-shelf pressure gradient also switched sign and was redirected towards the coast. At this point in the storm, the dominant cross-shelf momentum balance was nearly geostrophic (Fig. 3g) with a northward along-shelf surface current (Fig. 3d).

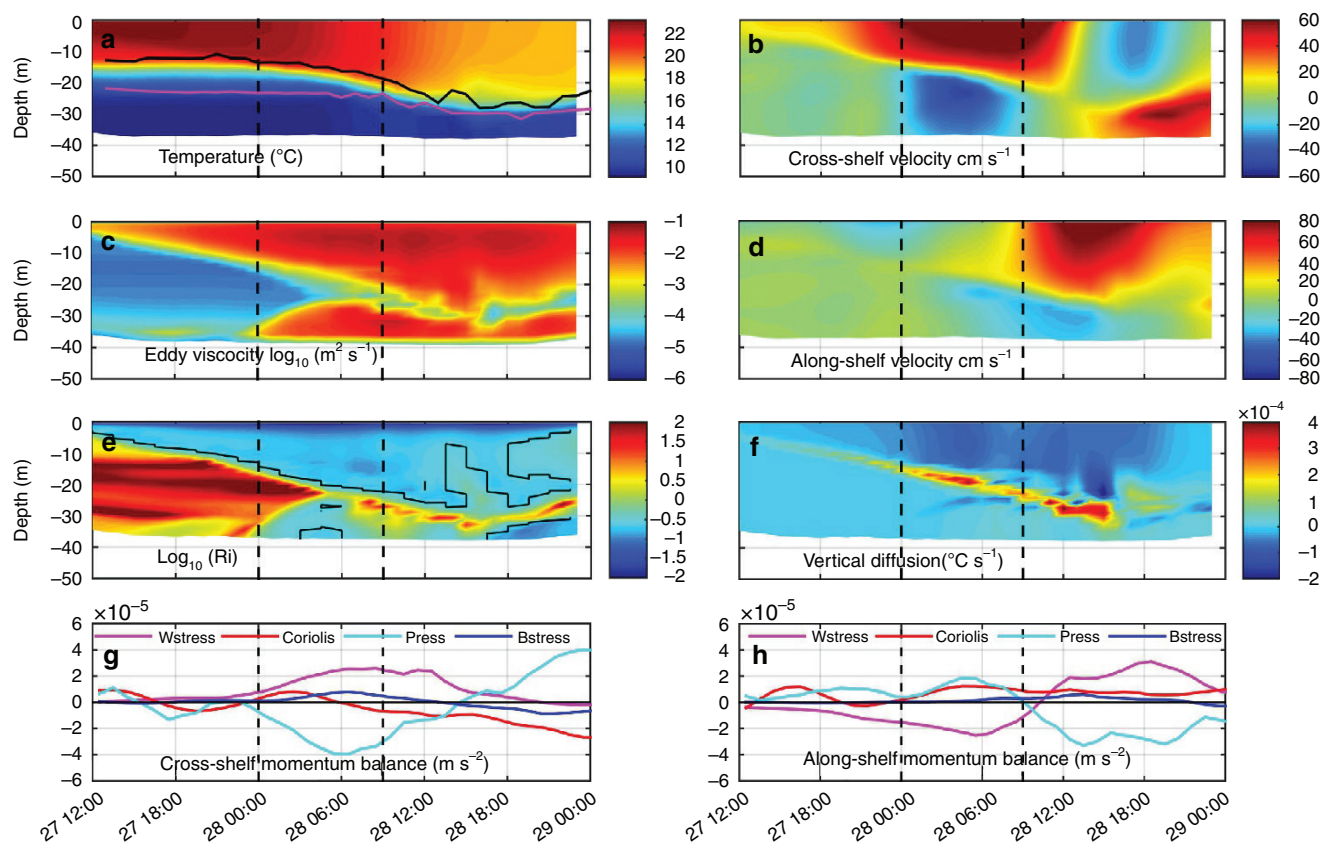


**Figure 3 | ROMS ocean simulation results at the glider location.** ROMS ocean simulation results at the glider location during the storm period, with first vertical black dashed line indicating initiation of the coastal baroclinic response and second vertical black dashed line indicating eye passage. (a) Temperature with top (black) and bottom (magenta) of thermocline as in Fig. 2b. (b) Cross-shelf velocity (red/yellow onshore; blue offshore). (c) Eddy viscosity. (d) Along-shelf velocity (red/yellow northward; blue southward). (e)  $\text{Log}_{10}(\text{Richardson number})$  with black contour indicating Richardson number of 0.25. (f) Vertical diffusion temperature diagnostic equation term, showing warming (positive, red/yellow) and cooling (negative, dark blue). (g) Dominant depth-averaged cross-shelf momentum balance terms (positive onshore and negative offshore) from wind stress (wstress, magenta), Coriolis force (coriolis, red), pressure gradient (press, cyan) and bottom stress (bstress, blue). (h) Same as g but for along-shelf momentum balance terms (positive northward, negative southward).

The subsurface cross-shelf circulation within the two-layer coastal ocean had a significant influence on vertical mixing as illustrated by the Richardson number (Fig. 3e) and the vertical eddy viscosity (Fig. 3c). The Richardson number and the eddy viscosity show that the surface layer deepened to meet the stratification at the top of the thermocline as the surface layer accelerated with the approaching storm. As the offshore counter current accelerated in the bottom boundary layer, the lower layer Richardson number also decreased and eddy viscosity increased until the two layers interacted. The most rapid ahead-of-eye-centre cooling and deepening of the surface layer occurred when the small Richardson numbers and large vertical eddy viscosities from the surface and bottom boundary layers overlapped. The model's temperature diagnostic equation indicates that vertical diffusion (Fig. 3f) was the dominant term (Supplementary Fig. 6) acting to deepen the thermocline and cool the surface layer during the event.

**Atmospheric model simulations.** Atmospheric model simulations of Irene used the Weather Research and Forecasting (WRF)<sup>32</sup> model as applied to the US East Coast for tropical cyclone forecasting<sup>33</sup>. Typical surface boundary approaches in uncoupled atmospheric models use satellite SSTs over water that remain fixed when new data is not available because of cloud cover. A matrix of over 130 simulations revealed ahead-of-eye-centre cooling of the ocean's surface layer has a significant impact

on intensity as reflected in the hurricane pressure (Fig. 4) and wind fields (Supplementary Fig. 7). Examining the ensemble of simulations with track errors less than one eye-wall radius, the largest wind and pressure intensity sensitivities were generated using fixed warm pre-storm and cold post-storm SST boundary conditions (Supplementary Figs 8,9). The sea level pressure (SLP) fields at landfall indicate the warm (Fig. 4a) versus the cold (Fig. 4b) SST changed the centre SLP by 7–8 hPa, with the maximum wind speed reduced by  $>5 \text{ m s}^{-1}$  due to the cooler SST (Supplementary Fig. 7). The minimum SLP time history (Fig. 4c) of selected model runs can be compared with the National Hurricane Center (NHC) best track parameters. The best track central pressure remains constant near 952 hPa until the eye enters the MAB (28 August at about 00 h), followed by a steady increase in the central pressure to 965 hPa 13 h later as the eye leaves the MAB. Once Irene's eye entered the MAB, the cold SST air-sea flux parameterization sensitivities all produce a reduction in intensity that cluster with the best track analysis, while the warm SST air-sea flux parameterization sensitivities maintain a lower minimum SLP with little change nearly until landfall.

The top three model sensitivities are quantified by the envelope width for the minimum SLP (Fig. 4d). For both warm and cold SSTs, sensitivities to the three standard WRF air-sea flux formulations range from 0 to 2 hPa for the 13 h after the eye entered the MAB. The sensitivity to warm and cold SST

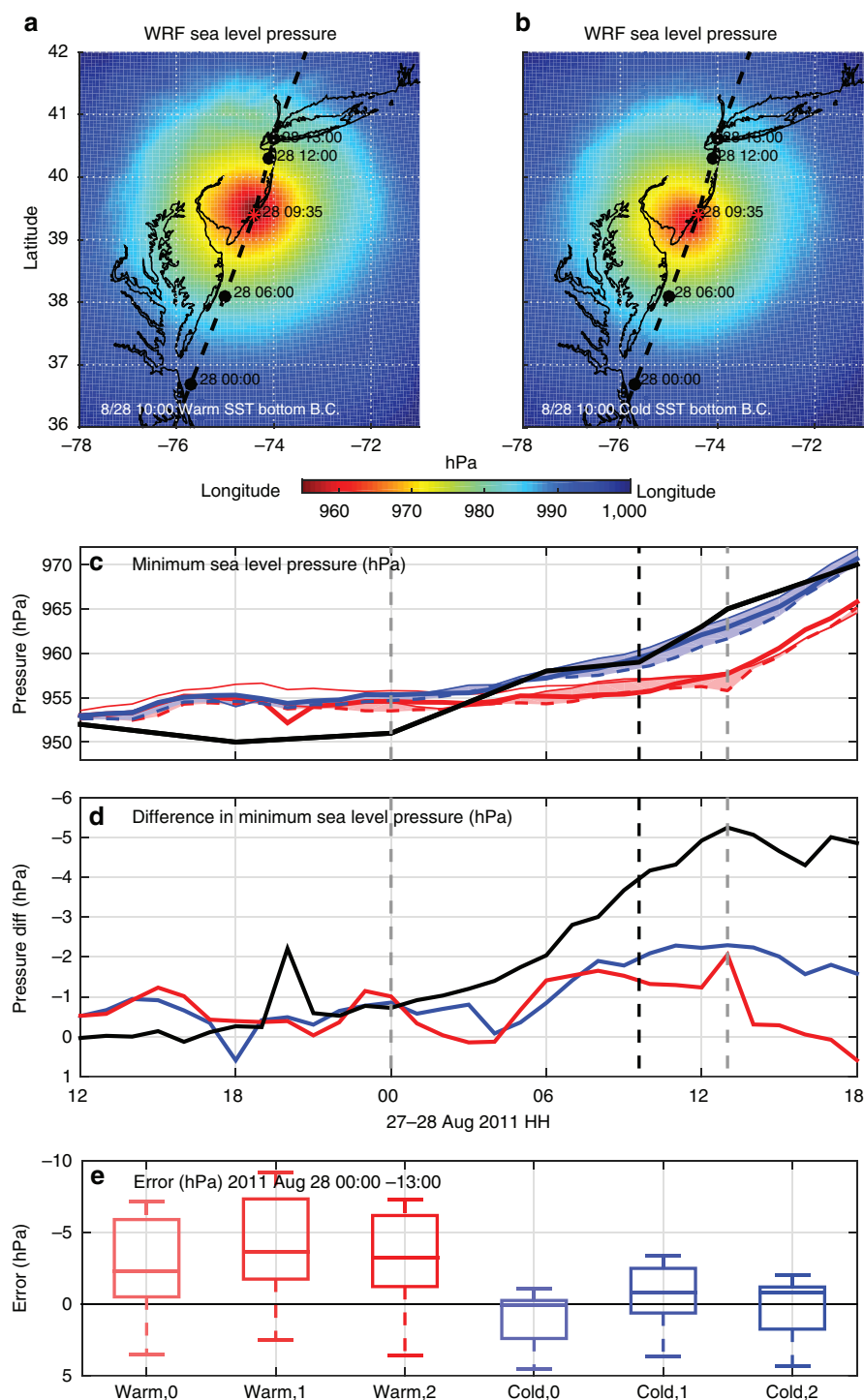


**Figure 4 | WRF atmospheric model simulation results.** (a) WRF model SLP (with surface flux option 2) at landfall (red star) for the warm SST boundary condition with NHC best track drawn as in Fig. 1a. (b) Same as a but for the cold SST. (c) Minimum SLP for NHC best track (black), and WRF's three air-sea flux parameterization options isftcflx = 0 (thin line); 1 (dotted line); and 2 (thick line) for the warm (red) and cold (blue) SST. Vertical grey and black dashed lines indicate eye enters MAB, makes landfall and leaves MAB. (d) Model SLP sensitivity to SST (black, warm minus cold SST for isftcflx = 2), and to flux parameterizations (isftcflx = 1 minus isftcflx = 0) for warm (red) and cold (blue) SST. (e) Box and whisker plots of SLP deviations from NHC best track when eye is over MAB for warm (red) and cold (blue) SST.

begins growing as the storm nears the MAB, climbing steadily to 5 hPa as it leaves the MAB. Statistical comparisons of each model run to the NHC best track over the MAB are quantified by the box and whisker plots (Fig. 4e) showing the median, inter-quartile range and outliers. The three

warm SST air-sea flux sensitivities consistently over-predict the intensity with minimum SLPs that are too low, while the three cold SST air-sea flux sensitivities more accurately reflect the intensity reduction for all of the air-sea flux options.



Table 1   Sea surface temperature cooling in coastal tropical cyclones.					
Storm name	Buoy	Water depth (m)	Ahead-of-eye-centre cooling (°C)	In-storm cooling (°C)	% Ahead-of-eye-centre
Arthur (2014)	44014	48	1.4	2.4	58%
Irene (2011)	44009	26	4.5	5.5	82%
Barry (2007)	ALSN6	29	5.1	5.1	100%
Hermine (2004)	44009	31	0.9	1.1	82%
Allison (2001)	CHLV2	14	2.3	2.6	88%
Bonnie (1998)	CHLV2	14	4.2	4.2	100%
Danny (1997)	44009	31	2.1	3.6	58%
Arthur (1996)	44009	31	2.3	3.5	66%
Emily (1993)	44014	48	2.3	2.8	82%
Bob (1991)	44025	41	2.1	4.6	46%
Charley (1986)	44009	31	2.7	5.4	50%
Average		31	2.7	3.7	73%
Standard deviation		11	1.3	1.4	19%
Irene (2011)	44065	25	3.8	4.2	90%
Irene (2011)	RU16	37–46	5.1	6.7	76%
Irene (2011)	44100	26	6.3	6.4	98%
Muifa (2011)	37.045 N 122.66 E	31	4.1	4.8	85%

Ahead-of-eye-centre cooling (°C), in-storm cooling (°C) and % ahead-of-eye-centre observed at nearshore MAB buoys for 11 tropical cyclones that traversed the MAB continental shelf during summer stratified conditions since 1985, additional data from Hurricane Irene and Super Typhoon Muifa.

**Discussion**

Using Hurricane Irene as a diagnostic case study, a new feedback mechanism on storm intensity in the coastal ocean has been identified. The strong onshore winds occurring ahead-of-eye-centre in tropical cyclones and the coastal wall set up a down-welling circulation that limits the storm surge and results in significant shear across the thermocline. This shear leads to turbulent entrainment of abundant cold bottom water and mixing with warmer surface water. The resulting ocean cooling reduces surface heat fluxes to the atmosphere, weakening the storm.

Rapid tropical cyclone intensity changes over the deep ocean have been correlated with storm passage over warm and cold core eddies<sup>12–16,34</sup>. Also in the deep ocean, SST changes of as little as 1 °C are noted to significantly impact storm intensity<sup>9,35</sup>. During Hurricane Irene, ahead-of-eye-centre cooling of 3.8–6.3 °C was observed with nearshore buoys (Supplementary Fig. 3) and 5.1 °C was observed with a mid-shelf glider (Fig. 2). Storm-induced cooling in deep water is often equally distributed between the front and back half of the storm<sup>36</sup>. Deep ocean simulations of Irene with both a 1D ocean mixed layer model and the 3D Price–Weller–Pinkel<sup>37</sup> model produced 32 and 56% of the in-storm cooling ahead-of-eye-centre, respectively. In Hurricane Irene, 76% (glider) to 98% (buoy 44100) of the in-storm cooling occurred ahead-of-eye-centre, indicating that coastal baroclinic processes are enhancing the percentage of ahead-of-eye-centre cooling in Irene.

To verify that enhanced ahead-of-eye-centre coastal ocean cooling is not unique to Irene, 30 years of historical nearshore buoy data throughout the MAB were investigated. During that time period, ahead-of-eye-centre cooling was observed in all 11 tropical cyclones that tracked northeastward over the MAB continental shelf during the highly stratified summer months (June–August)<sup>24,38</sup> (Table 1 and Supplementary Figs 10–12). The maximum continental shelf buoy observed ahead-of-eye-centre cooling for these 11 storms averages  $2.7 \pm 1.3$  °C, representing an average of 73% of the in-storm cooling.

An 11-year global satellite climatology<sup>39</sup> reveals that the shallow mid-latitude Yellow Sea and northern East China Sea also experience a large 20 °C seasonal SST cycle, similar to the MAB but over three times larger in area. A 1986 Yellow Sea shipboard conductivity temperature and depth survey reports surface to bottom temperature differences approaching 15 °C (ref. 40), also

similar to the stratified summer MAB. Maps of western Pacific typhoon tracks (coast.noaa.gov/hurricanes) indicate 26 typhoons have tracked across the northern East China Sea and Yellow Sea during June–August since 1985. Like Irene, the landfalling intensity of Super Typhoon Muifa (2011) was over-predicted by standard models<sup>41</sup>. Satellite SST maps indicate Muifa caused significant in-storm cooling (up to 7 °C) across ~300,000 km<sup>2</sup> of the continental shelf<sup>41</sup>. Nearshore buoy observations show cooling of 4.1 °C (85% of the in-storm cooling observed at that location) was ahead-of-eye-centre (Table 1, Supplementary Fig. 13).

Globally, over the past 30 years, tropical cyclone maximum intensities have migrated poleward<sup>42</sup>. In the North Atlantic, hurricane intensities have increased since the early 1980s and are projected to continue to increase as the climate warms<sup>43–46</sup>. Combined with rapid sea level rise<sup>47</sup>, mid-latitude population centres will experience heightened vulnerability to storm surge and inundation from increasingly powerful storms. To mitigate these risks, improved forecasting of tropical cyclone intensity over mid-latitude stratified coastal seas is vital, and will require realistic 3D ocean models to forecast enhanced ahead-of-eye-centre cooling.

**Methods**

**Data source.** The Mid-Atlantic Regional Association Coastal Ocean Observing System (MARACOOS) is a sustained regional component of the US Integrated Ocean Observing System (IOOS)<sup>48</sup>. Its integrated observation network of satellites, buoys, coastal meteorological stations, HF radar and autonomous underwater gliders provided the data used in this study<sup>49</sup>.

**Satellite remote sensing.** National Oceanographic and Atmospheric Administration (NOAA) Advanced Very High-Resolution Radiometer (AVHRR) satellite data (Supplementary Fig. 1) were acquired through a SeaSpace TeraScan L-Band satellite ground station at Rutgers University. AVHRR data are converted to SST using the multi-channel SST algorithm<sup>50</sup>. To specifically map areas of rapid cooling, a ‘coldest-dark-pixel’ composite technique is used to identify and remove bright cloud covered pixels while retaining the darker ocean pixels. This is accomplished through the following series of tests performed on AVHRR channels 4 and 2 scans. Pixels are considered contaminated by clouds and removed if (1) AVHRR channel 4 (10.3–11.3 μm) temperatures are <5 °C (3.5 °C) in summer (winter); or (2) near infrared albedo in daytime AVHRR Channel 2 (0.725–1 μm) exceeds 2.3% (an empirically derived threshold specific to the MAB). Further tests are performed on 3 × 3 km grid boxes to account for large changes in temperature over short distances typical of cloud edges. Centre pixels are flagged as potential cloud edges and removed if (1) temperature changes in AVHRR channel 4 scans



are  $>1^{\circ}\text{C}$  across the centre point of each  $3 \times 3$  grid data; or (2) the change in infrared albedo across the centre of each  $3 \times 3$  grid box is  $>0.15\%$ . After declouding is performed, the resulting 3 days of scans between 12:00 to 17:00 GMT are composited with the NASA (National Aeronautics and Space Administration) short-term Prediction Research and Transition centre (SPoRT) 2 km blended 7-day SST product. At each pixel the coldest value is retained between all daytime AVHRR scans for the past 3 days and the SPoRT SST product for that day to ensure retention of coastal upwelling zones and regions that underwent rapid mixing. Consistent with real-time processing protocols, the date assigned to each composite corresponds to the final day of the data window.

**Meteorological observations.** Meteorological observations were obtained from NOAA NDBC buoys, coastal towers and pier stations, and a WeatherFlow Inc. meteorological tower located in Tuckerton, New Jersey (Fig. 1a). Buoys 44009 ( $38.461^{\circ}$  North and  $74.703^{\circ}$  West) and 44065 ( $40.369^{\circ}$  North and  $73.703^{\circ}$  West) included wind speed and direction measured at a height of 5 m, air temperature at a height of 4 m and ocean temperatures at 0.6 m depth. Buoy 44100 ( $36.255^{\circ}$  North and  $75.591^{\circ}$  West) is a Waverider buoy managed by Scripps Institution of Oceanography that measured ocean temperatures at 0.46 m depth. Station DUKN7 ( $36.184^{\circ}$  North and  $75.746^{\circ}$  West) is a coastal station that measures air temperature at 15.68 m above mean sea level. The Tuckerton WeatherFlow Inc. meteorological tower ( $39.52^{\circ}$  North and  $74.32^{\circ}$  West) measured wind speed and direction at 12 m. Meteorological data is plotted at the standard frequencies and averaging intervals reported by these stations.

**High frequency radar.** A network of over 40 CODAR Ocean Sensors SeaSonde HF Radar stations<sup>26</sup> are deployed along the MAB coast by a consortium of institutions coordinated through MARACOOS<sup>27</sup>. The stations transmit HF radio waves that are scattered off the ocean surface waves and then received back on shore. The Doppler shift in the Bragg peaks of the received signal are used to map the radial components of the total surface velocity field in front of each station<sup>51</sup>. Radial components from multiple stations are combined using an optimal interpolation scheme<sup>52</sup> to produce 1 h centre-averaged hourly surface current maps<sup>53</sup> with a nominal 6 km spatial resolution (Supplementary Fig. 5).

**Autonomous underwater gliders.** Teledyne Webb Research Slocum gliders are buoyancy-driven underwater vehicles that act as mobile sensor platforms<sup>22</sup>. These instrument platforms adjust small amounts of buoyancy in order to glide through the water column at  $20\text{--}30\text{ cm s}^{-1}$  in a sawtooth pattern. At pre-programmed intervals the gliders come to the surface and transfer data back to Rutgers University in near real-time. The glider used in this study, RU16, was equipped with an un-pumped Seabird conductivity temperature and depth sensor that logged data every 4 s on downcasts and upcasts. Depth- and time-averaged velocity calculations were performed using a dead-reckoning technique typical for such platforms<sup>22,54,55</sup>. The measured pitch angle, fall velocity and a model of glider flight to estimate angle of attack are used to calculate an underwater horizontal displacement during each dive segment. The difference between the calculated horizontal displacement from the final pre-dive location and the actual surfacing location divided by the time underwater provides an estimate of depth- and time-averaged velocity.

A combination of dead-reckoned depth-averaged glider currents and HF radar surface currents are used to estimate bottom currents along the glider track (Fig. 2c). The following algorithm assumes that the HF radar surface currents are representative of the surface layer above the thermocline (defined as the maximum vertical temperature gradient along each profile) and requires that the depth-weighted average surface and bottom layer currents must equal the total depth-averaged glider current:

$$U_b = \frac{U_g(H_s + H_b)}{H_b} - \frac{U_s H_s}{H_b} \quad (1)$$

$$V_b = \frac{V_g(H_s + H_b)}{H_b} - \frac{V_s H_s}{H_b} \quad (2)$$

where  $H_s$  and  $H_b$  are the layer thicknesses above and below the thermocline, respectively,  $U_g$  and  $V_g$  are along- and cross-shelf depth-averaged currents, respectively, from glider dead-reckoning,  $U_s$  and  $V_s$  are surface layer-averaged currents from HF radar, and  $U_b$  and  $V_b$  are the calculated bottom layer-averaged currents (Fig. 2).

**ROMS model setup.** The numerical simulations were conducted using the ROMS<sup>31</sup>, a free-surface, sigma coordinate, primitive equation ocean model (code available at <http://www.myroms.org>) that has been widely used in a diverse range of coastal applications. The ESPReSSO (Experimental System for Predicting Shelf and Slope Optics) model<sup>56</sup> covers the MAB from the centre of Cape Cod southward to Cape Hatteras, from the coast to beyond the shelf break and shelf/slope front. Gridded bathymetric data is used to construct a model grid with a horizontal resolution of 5 km (Supplementary Fig. 4) and 36 vertical levels in a terrain-following s-coordinate system. The initial conditions were developed from the same domain ROMS run with strong constrained four-dimensional variational (4D-Var) data assimilation<sup>57</sup>. The meteorological forcing is from the North American Mesoscale (NAM) model 12 km 3-hourly forecast data. Reanalyses of surface air temperature, pressure, relative humidity, 10 m vector winds, precipitation, downward longwave radiation and net shortwave radiation were used

to specify the surface fluxes of momentum and buoyancy based on the COARE bulk formulae<sup>58</sup>. Boundary conditions are daily two-dimensional surface elevation, as well as three-dimensional velocity, temperature, and salinity fields from the Hybrid Coordinate Ocean Model Navy Coupled Ocean Data Assimilation forecast system. Inflows for the seven largest rivers are from daily average United States Geological Survey discharge data. Tidal boundary conditions are from the The ADvanced CIRCulation tidal model. The general length scale method k-kl type vertical mixing scheme<sup>59,60</sup> is used to compute vertical turbulence diffusivity.

**ROMS momentum balance analysis.** We extracted depth-averaged momentum balance terms from ROMS (Fig. 3g–h) at the glider sampling location in order to diagnose the dominant forces during the storm, where the acceleration terms are balanced by a combination of horizontal advection, pressure gradient, surface and bottom stresses and the Coriolis force (horizontal diffusion was small and neglected in this case):

$$\underbrace{\frac{\partial u}{\partial t}}_{\text{Acceleration}} = - \underbrace{\frac{\partial(uu)}{\partial x} - \frac{\partial(vu)}{\partial y}}_{\text{Horizontal advection}} - \underbrace{\frac{1}{\rho_0} \frac{\partial P}{\partial x}}_{\text{Pressure gradient}} + \underbrace{\left( \frac{\tau_s^x}{h\rho_0} - \frac{\tau_b^x}{h\rho_0} \right)}_{\text{Stress}} + \underbrace{fv}_{\text{Coriolis}} \quad (3)$$

$$\underbrace{\frac{\partial v}{\partial t}}_{\text{Acceleration}} = - \underbrace{\frac{\partial(uv)}{\partial x} - \frac{\partial(vv)}{\partial y}}_{\text{Horizontal advection}} - \underbrace{\frac{1}{\rho_0} \frac{\partial P}{\partial y}}_{\text{Pressure gradient}} + \underbrace{\left( \frac{\tau_s^y}{h\rho_0} - \frac{\tau_b^y}{h\rho_0} \right)}_{\text{Stress}} - \underbrace{fu}_{\text{Coriolis}} \quad (4)$$

where  $u$  and  $v$  are the along-shelf and cross-shelf components of velocity respectively,  $t$  is time,  $P$  is pressure,  $\rho_0$  is a reference density,  $\tau_s$  and  $\tau_b$  are surface and bottom stresses,  $h$  is water column depth and  $f$  is the latitude-dependent Coriolis frequency.

**ROMS heat balance analysis.** *Heat balance analysis.* The general conservation expression for the temperature budget in ROMS is given by

$$\frac{\partial T}{\partial t} = - \frac{\partial(uT)}{\partial x} - \frac{\partial(vT)}{\partial y} - \frac{\partial(wT)}{\partial z} + \frac{\partial A_{kt} \frac{\partial T}{\partial z}}{\partial z} + D_T + \mathcal{F}_T \quad (5)$$

with the following surface and bottom boundary conditions:

$$\left( A_{kt} \frac{\partial T}{\partial z} \right)_{z=0} = \frac{Q_{\text{net}}}{\rho_0 C_p} \quad (6)$$

$$\left( A_{kt} \frac{\partial T}{\partial z} \right)_{z=-h} = 0 \quad (7)$$

Here,  $T$  is the temperature,  $t$  is time,  $u$ ,  $v$  and  $w$  are the along-shelf, cross-shelf and vertical components of velocity.  $A_{kt}$  is the vertical diffusivity coefficient,  $D_T$  is the horizontal diffusion term and  $\mathcal{F}_T$  is friction.  $Q_{\text{net}}$  is the surface net heat flux,  $\rho_0 = 1025\text{ kg m}^{-3}$  is a reference density,  $C_p = 3985\text{ J (kg }^{\circ}\text{C)}^{-1}$  is the specific heat capacity of seawater and  $h$  is the water depth.

The ROMS conservation of heat equation was used to diagnose the relative contributions of the different terms responsible for the modelled temperature change. Time-series of the vertical temperature diagnostic terms were investigated along the glider track with emphasis on the temperature evolution between the top of the thermocline depth (the shallowest location where the vertical temperature gradient exceeded  $0.4^{\circ}\text{C m}^{-1}$ , black contour in Fig. 3a and Supplementary Fig. 6) and the transition layer depth (the deepest location where the vertical temperature gradient exceeded  $0.7^{\circ}\text{C m}^{-1}$ , magenta contour in Fig. 3a and Supplementary Fig. 6). Term-by-term analysis of equation 5 offered additional insights on the temperature source and sink terms. Supplementary Fig. 6A shows the temperature rate of change, which is the sum of the vertical diffusion term (Supplementary Fig. 6B) and advection term (Supplementary Fig. 6C), in which the advection term is separated into along-shelf advection (Supplementary Fig. 6D), cross-shelf advection (Supplementary Fig. 6E) and vertical advection (Supplementary Fig. 6F). The horizontal diffusion term's order of magnitude is much smaller than other terms and is not plotted. The dominant term influencing the surface mixed layer temperature change was the vertical diffusion, which is plotted in Fig. 3f.

**WRF-ARW model setup.** The Weather Research and Forecasting Advanced Research (WRF-ARW) dynamical core (code available at <http://www.wrf-model.org>)<sup>32</sup>, Version 3.4 was used for the atmospheric simulations in this study. WRF-ARW is a fully compressible, non-hydrostatic, terrain-following coordinate, primitive equation atmospheric model. Our WRF-ARW domain extends from South Florida to Nova Scotia (Supplementary Fig. 14), with grid resolution of 6 km in the horizontal and 35 vertical levels. Lateral boundary conditions used are from the Global Forecast System (GFS)  $0.5^{\circ}$  initialized at 06 UTC on 27 August 2011.

Our simulations begin at 06 UTC on 27 August 2011 when Hurricane Irene was south of North Carolina (NC) over the South-Atlantic Bight (SAB) and end at 18

UTC on 28 August 2011 as the storm moved into New England. Simulation results shown (Fig. 4c,d and Supplementary Fig. 7C,D) begin at 12 UTC on 27 August 2011, at NC landfall time, after the model has 6 h to adjust to vortex initialization. WRF's digital filter initialization (DFI) was run to determine the sensitivities to different realizations of the GFS initializations. DFI deepened the initial vortex central pressure by over 10–960 hPa, which matches GFS initial central pressure (Supplementary Fig. 15). However, downstream sensitivity to DFI beyond 2 h was minimal.

For our control run, the following are used: longwave and shortwave radiation physics were both computed by the Rapid Radiative Transfer Model-Global scheme; the Monin–Obukhov atmospheric layer model and the Noah Land Surface Model were used with the Yonsei University planetary boundary layer scheme; and the WRF Double-Moment 6-class moisture microphysics scheme was used for grid-scale precipitation processes.

**WRF sensitivity to SST.** The model was run over 130 times to compare the sensitivity of certain parameter tuning. All sensitivities were compared to the control run (described above), which for surface boundary conditions over the ocean, that is, SST, used the Real-Time Global High-Resolution (RTG HR) SST analysis from 00 UTC on 27 August 2011 fixed throughout the simulation. This is the warm pre-storm SST, and has temperatures across the model domain similar to the AVHRR coldest-dark-pixel composite a day earlier (Supplementary Fig. 1A). By having the control run use Real-Time Global High-Resolution SST fixed throughout the simulation, we are consistent with what the operational NAM 12 km model used for bottom boundary conditions over the ocean.

To show the maximum impact of the ahead-of-eye-centre SST cooling on storm intensity, we compared our control run with a simulation using observed cold post-storm SST. For this, we used our AVHRR coldest-dark-pixel composite, which includes data from 29 to 31 August 2011 (Supplementary Fig. 1B). According to underwater glider and NDBC buoy observations along Irene's entire MAB track, almost all of the SST cooling occurred ahead of Irene's eye centre (Fig. 1b–d). NDBC buoy observations near Irene's track in the SAB (41013, 41036, 41037) also show ahead-of-eye-centre SST cooling, but values are on the order of 1 °C or less (Fig. 1a). Because our model simulations include only 6 h of storm presence over the SAB before NC landfall, and SST cooling in the SAB was significantly less than observed in the MAB (Fig. 1), we can conclude that the main result from our SST sensitivity is due to the ahead-of-eye-centre cooling in the MAB.

**WRF sensitivity to air-sea flux parameterizations.** The equations for the momentum ( $\tau$ ), sensible ( $H$ ) and latent heat fluxes ( $E$ ) are as follows:

$$\tau = -\rho C_D U^2 \quad (8)$$

$$H = -(\rho c_p) C_H U (\theta_{2m} - \theta_{sfc}) \quad (9)$$

$$E = -(\rho L_v) C_Q U (q_{2m} - q_{sfc}) \quad (10)$$

where  $\rho$  is density of air,  $C_D$  is drag coefficient,  $U$  is 10 m wind speed,  $c_p$  is specific heat capacity of air,  $C_H$  is sensible heat coefficient,  $\theta_{2m}$  is potential temperature at 2 m and  $\theta_{sfc}$  is potential temperature at the surface,  $L_v$  is enthalpy of vaporization,  $C_Q$  is latent heat coefficient,  $q_{2m}$  is specific humidity at 2 m and  $q_{sfc}$  is interfacial specific humidity at the surface.

Three options exist in WRF-ARW Version 3.0 and later for air-sea flux parameterizations (WRF namelist option `isfcflx` = 0, 1, and 2; see (ref. 61) for more details). These parameterization options change the momentum ( $z_0$ ), sensible heat ( $z_T$ ) and latent heat roughness lengths ( $z_Q$ ) in the following equations for drag ( $C_D$ ), sensible heat ( $C_H$ ) and latent heat ( $C_Q$ ) coefficients:

$$C_D = K^2 / [\ln(z_{ref} / z_0)]^2 \quad (11)$$

$$C_H = \left( C_D^{1/2} \right) [K / \ln(z_{ref} / z_T)] \quad (12)$$

$$C_Q = \left( C_D^{1/2} \right) [K / \ln(z_{ref} / z_Q)] \quad (13)$$

where  $K$  is the von Kármán constant and  $z_{ref}$  is a reference height (usually 10 m).

Therefore, our SST sensitivity effectively changes the variables  $\theta_{sfc}$  and  $q_{sfc}$  in equations 8–10 above, while our air-sea flux parameterization sensitivities change the equations for the momentum, sensible heat and latent heat coefficients (equations 11–13) going into the respective flux equations 8–10.

For our air-sea flux parameterization sensitivities in this study, we ran `isfcflx` = 0, 1, and 2 with both the warm (control) and cold SST boundary conditions.

**Additional WRF sensitivities.** We have discussed SST and air-sea flux parameterizations. WRF-ARW was run over 130 times in total, with various model configuration and physics options turned on and off.

We examined the ensemble of simulations with space/time track errors < 25 km (one eye-wall radius) from available NHC best track positional data. Only preserving those simulations with accurate tracks is important because Hurricane Irene tracked close to and parallel to the Mid-Atlantic coast. The remaining sensitivities are shown in central pressure (Supplementary Fig. 8) and maximum winds (Supplementary Fig. 9). These are cumulative hourly sensitivities during

Irene's presence over the MAB and NY Harbor (28 August 00–13 UTC).

Supplementary Table 1 shows a list of these sensitivities, with the WRF namelist option number alongside its name (control run listed last for each sensitivity).

The sensitivity titled 'latent heat flux < 0 over water' requires a brief explanation. In the WRF surface layer scheme code, there is a switch that disallows any latent heat flux less than 0 W m<sup>-2</sup> (similarly, there is a switch that disallows any sensible heat flux less than -250 W m<sup>-2</sup>). WRF convention for negative heat flux is downward, or atmosphere to land/water. We run WRF after removing the line of code disallowing negative latent heat flux, and compare to the control run. This switch removal only changes latent heat flux and allows it to be negative over water, as the subsequent WRF land surface scheme modifies fluxes and allows for negative latent heat flux over land.

**Ahead-of-eye-centre and in-storm cooling calculations.** Ahead-of-eye-centre cooling (Table 1) at NDBC buoys (Supplementary Figs 10–12) and the Yellow Sea buoy (Supplementary Fig. 13) was calculated by taking the difference between the maximum water temperature as the winds increased above 5 m s<sup>-1</sup> and the minimum water temperature before or at the minimum observed SLP. In-storm cooling was determined as the difference between the same maximum water temperature as the winds increased above 5 m s<sup>-1</sup> and the minimum water temperature while winds remained above 5 m s<sup>-1</sup> after the pressure minimum. To calculate the average and standard deviation of cooling for the 11 storms passing through the MAB since 1985, we selected the one buoy on the continental shelf that recorded wind speed, pressure and water temperature and exhibited the greatest ahead-of-eye-centre cooling. For completeness we show Irene cooling statistics (Table 1) and time-series (Supplementary Fig. 3) for buoys 44065 and 44100 used in Fig. 1.

**Data availability.** Buoy meteorological data used in this study are available through the National Data Buoy Center. Glider and HF Radar data can be found through the MARACOOS THREDDS server at <http://maracoos.org/data>. Tuckerton meteorological data are supported by WeatherFlow Inc. and can be made available upon request to the corresponding authors. WRF and ROMS model simulations are stored locally at the Rutgers Department of Marine and Coastal Sciences and will be made available upon request to the corresponding authors. The Yellow Sea buoy data are stored at the Institute of Oceanology, Chinese Academy of Sciences.

## References

- Keim, B. D., Muller, R. A. & Stone, G. W. Spatiotemporal patterns and return periods of tropical storm and hurricane strikes from Texas to Maine. *J. Clim.* **20**, 3498–3509 (2007).
- Walker, N. *et al.* Hurricane prediction a century of advances. *Oceanography* **19**, 24–36 (2006).
- Krishnamurti, T. N. *et al.* Improved weather and seasonal climate forecasts from multimodel superensemble. *Science* **285**, 1548–1550 (1999).
- Cangialosi, J. P. & Franklin, J. L. 2012 *National Hurricane Center Forecast Verification Report* pp. 79 (National Hurricane Center, 2013).
- Avila, L. A. & Cangialosi, J. P. *Tropical Cyclone Report: Hurricane Irene* (2012); pp. 45.
- Blake, E. S., Landsea, C. W. & Gibney, E. J. *The Deadliest, Costliest, and Most Intense United States Tropical Cyclones from 1851 to 2010* (National Weather Service National Hurricane Center, 2011) pp. 47.
- Considine, T. J., Jablonowski, C., Posner, B. & Bishop, C. H. The value of hurricane forecasts to oil and gas producers in the Gulf of Mexico. *J. Appl. Meteorol.* **43**, 1270–1282 (2004).
- Emanuel, K., DesAutels, C., Holloway, C. & Korty, R. Environmental control of tropical cyclone intensity. *J. Atmos. Sci.* **61**, 843–858 (2004).
- Emanuel, K. Tropical cyclones. *Annu. Rev. Earth Planet. Sci.* **31**, 75–104 (2003).
- Schade, L. R. & Emanuel, K. A. The ocean's effect on the intensity of tropical cyclones: results from a simple coupled atmosphere–ocean model. *J. Atmos. Sci.* **56**, 642–651 (1999).
- Jaimes, B. & Shay, L. K. Enthalpy and momentum fluxes during Hurricane Earl relative to underlying ocean features. *Mon. Weather Rev.* **143**, 111–131 (2015).
- Ma, Z., Fei, J., Liu, L., Huang, X. & Cheng, X. Effects of the cold core eddy on tropical cyclone intensity and structure under idealized air–sea interaction conditions. *Mon. Weather Rev.* **141**, 1285–1303 (2012).
- Emanuel, K. A. Thermodynamic control of hurricane intensity. *Nature* **401**, 665–669 (1999).
- Jaimes, B. & Shay, L. K. Mixed layer cooling in mesoscale oceanic eddies during Hurricanes Katrina and Rita. *Mon. Weather Rev.* **137**, 4188–4207 (2009).
- Shay, L. K., Goni, G. J. & Black, P. G. Effects of a warm oceanic feature on Hurricane Opal. *Mon. Weather Rev.* **128**, 1366–1383 (2000).
- Walker, N. D., Leben, R. R. & Balasubramanian, S. Hurricane-forced upwelling and chlorophyll a enhancement within cold-core cyclones in the Gulf of Mexico. *Geophys. Res. Lett.* **32**, 1–5 (2005).

17. Jacob, S. D. & Shay, L. K. The role of oceanic mesoscale features on the tropical cyclone-induced mixed layer response: a case study. *J. Phys. Oceanogr.* **33**, 649–676 (2003).
18. D'Asaro, E. The ocean boundary layer below Hurricane Dennis. *J. Phys. Oceanogr.* **31**, 561–579 (2003).
19. Hall, T. & Yonekura, E. North American tropical cyclone landfall and SST: a statistical model study. *J. Clim.* **26**, 8422–8439 (2013).
20. Cornillon, P., Stramma, L. & Price, J. F. Satellite measurements of sea surface cooling during Hurricane Gloria. *Nature* **326**, 373–375 (1987).
21. Schofield, O. *et al.* A regional Slocum Glider network in the mid-Atlantic bight leverages broad community engagement. *Mar. Technol. Soc. J.* **44**, 185–195 (2010).
22. Schofield, O. *et al.* Slocum gliders: robust and ready. *J. F. Robot.* **24**, 473–485 (2007).
23. Kohut, J. T., Haldeman, C. & Kerfoot, J. *Monitoring Dissolved Oxygen in New Jersey Coastal Waters Using Autonomous Gliders*. EPA/600/R-13/180 (US Environmental Protection Agency, Washington, DC, 2014).
24. Castelao, R., Glenn, S. & Schofield, O. Temperature, salinity, and density variability in the central middle Atlantic Bight. *J. Geophys. Res.* **115**, C10005 (2010).
25. Houghton, R. W., Schlitz, R., Beardsley, R. C., Butman, B. & Chamberlin, J. L. The Middle Atlantic Bight cold pool: evolution of the temperature structure during summer 1979. *J. Phys. Oceanogr.* **12**, 1019–1029 (1982).
26. Barrick, D. E., Evans, M. W. & Weber, B. L. Ocean surface currents mapped by radar. *Science* **198**, 138–144 (1977).
27. Roarty, H. *et al.* Operation and application of a regional high-frequency radar network in the Mid-Atlantic Bight. *Mar. Technol. Soc. J.* **44**, 133–145 (2010).
28. Shay, L. K., Chang, S. W. & Elsberry, R. L. Free surface effects on the near-inertial ocean current response to a hurricane. *J. Phys. Oceanogr.* **20**, 1405–1424 (1990).
29. Teague, W. J., Jarosz, E., Wang, D. W. & Mitchell, D. A. Observed oceanic response over the upper continental slope and outer shelf during Hurricane Ivan. *J. Phys. Oceanogr.* **37**, 2181–2206 (2007).
30. Wilkin, J. L. & Hunter, E. J. An assessment of the skill of real-time models of Mid-Atlantic Bight continental shelf circulation. *J. Geophys. Res. Ocean* **118**, 2919–2933 (2013).
31. Haidvogel, D. B. *et al.* Ocean forecasting in terrain-following coordinates: formulation and skill assessment of the Regional ocean modeling system. *J. Comput. Phys.* **227**, 3595–3624 (2008).
32. Skamarock, W. *et al.* A description of the advanced research WRF version 3, NCAR Technical Note, NCAR/TN-475 + STR (NCAR, Boulder, CO, USA, 2008).
33. Seroke, G. *et al.* in *Proceedings of the OCEANS MTS/IEEE Conference*, 1–4 (Rutgers University Coastal Ocean Observation Laboratory (RU-COOL) Hampton Roads, North Carolina, USA, 2012).
34. Lin, I.-I., Wu, C.-C., Pun, I.-F. & Ko, D.-S. Upper-ocean thermal structure and the Western North Pacific Category 5 Typhoons. Part I: ocean features and the category 5 typhoons' intensification. *Mon. Weather Rev.* **136**, 3288–3306 (2008).
35. Cione, J. J. & Uhlhorn, E. W. Sea surface temperature variability in hurricanes: implications with respect to intensity change. *Mon. Weather Rev.* **131**, 1783–1796 (2003).
36. Price, J. F. Upper ocean response to a hurricane. *J. Phys. Oceanogr.* **11**, 153–175 (1981).
37. Price, J. F. & Weller, R. A. Diurnal cycling: observations and models of the upper ocean response to diurnal heating, cooling, and wind mixing. *J. Geophys. Res.* **91**, 8411–8427 (1986).
38. Gong, D., Kohut, J. & Glenn, S. Seasonal climatology of wind-driven circulation on the New Jersey Shelf. *J. Geophys. Res. Ocean* **115**, 953–968 (2010).
39. Schofield, O. *et al.* The decadal view of the mid-Atlantic Bight from the COOLroom: is our coastal system changing? *Oceanography* **21**, 108–117 (2008).
40. Chen, C., Beardsley, R. C., Limeburner, R. & Kim, K. Comparison of winter and summer hydrographic observations in the Yellow and East China Seas and adjacent Kuroshio during 1986. *Cont. Shelf Res.* **14**, 909–929 (1994).
41. Sun, M. *et al.* Simulation of typhoon Muifa using a mesoscale coupled atmosphere-ocean model. *Acta Oceanol. Sin.* **33**, 123–133 (2014).
42. Kossin, J. P., Emanuel, K. A. & Vecchi, G. A. The poleward migration of the location of tropical cyclone maximum intensity. *Nature* **509**, 349–352 (2014).
43. Walsh, J. *et al.* *Our Changing Climate*. Synopsis of Climate Change Impacts in the United States. The Third National Climate Assessment, Natl Clim. Team Staff (2014).
44. Knutson, T. R. Dynamical downscaling projections of twenty-first-century Atlantic Hurricane activity: CMIP3 and CMIP5 model-based scenarios. *J. Clim.* **26**, 6591–6617 (2013).
45. Knutson, T. R. *et al.* Tropical cyclones and climate change. *Nat. Geosci.* **3**, 157–163 (2010).
46. Seneviratne, S. *et al.* in *Managing the Risk of Extreme Events and Disasters to Advance Climate Change Adaptation* (eds Field, C. *et al.*) 109–230 (Cambridge University Press, 2012).
47. Miller, K. G. *et al.* Sea-level rise in New Jersey over the past 5000 years: Implications to anthropogenic changes. *Glob. Planet. Change* **66**, 10–18 (2009).
48. Briscoe, M. G., Martin, D. L. & Malone, T. C. Evolution of regional efforts in international GOOS and US IOOS. *Mar. Technol. Soc. J.* **42**, 4–9 (2008).
49. Glenn, S. & Schofield, O. Growing a distributed ocean observatory: our view from the COOL Room. *Oceanography* **22**, 128–145 (2009).
50. McClain, E. P., Pichel, W. G., Walton, C. C., Paul, E. & Pichel, G. Comparative performance of AVHRR-based multichannel sea surface temperatures. *J. Geophys. Res. Ocean* **90**, 11587–11601 (1985).
51. Kohut, J. T. & Glenn, S. M. Improving HF Radar surface current measurements with measured antenna beam patterns. *J. Atmos. Ocean. Technol.* **20**, 1303 (2003).
52. Kohut, J., Roarty, H., Randall-Goodwin, E., Glenn, S. & Lichtenwalner, C. S. Evaluation of two algorithms for a network of coastal HF radars in the Mid-Atlantic Bight. *Ocean Dyn.* **62**, 953–968 (2012).
53. Roarty, H., Baskin, C., Smith, M. & Glenn, S. in *Proceedings of the OCEANS MTS/IEEE Conference* (Rutgers University Coastal Ocean Observation Laboratory (RU-COOL) New Brunswick, New Jersey, USA, 2014).
54. Davis, R., Eriksen, C. & Jones, C. in *Technology and Applications of Autonomous Underwater Vehicles* (ed. Griffiths, G.) 37 (Taylor & Francis, 2003).
55. Sherman, J., Davis, R. E., Owens, W. B. & Valdes, J. The autonomous underwater glider 'Spray'. *IEEE J. Ocean. Eng.* **26**, 437–446 (2001).
56. Wilkin, J. & Hunter, E. An assessment of the skill of real-time models of Mid-Atlantic Bight continental shelf circulation. *J. Geophys. Res.* **118**, 2919–2933 (2013).
57. Moore, A. M. *et al.* The Regional Ocean Modeling System (ROMS) 4-dimensional variational data assimilation systems. *Prog. Oceanogr.* **91**, 34–49 (2011).
58. Fairall, C. W., Bradley, E. F., Hare, J. E., Grachev, A. A. & Edson, J. B. Bulk Parameterization of air-sea fluxes: updates and verification for the COARE algorithm. *J. Clim.* **16**, 571 (2003).
59. Warner, J. C., Sherwood, C. R., Arango, H. G. & Signell, R. P. Performance of four turbulence closure models implemented using a generic length scale method. *Ocean Model.* **8**, 81–113 (2005).
60. Umlauf, L. & Burchard, H. A generic length-scale equation for geophysical turbulence models. *J. Mar. Res.* **61**, 235–265 (2003).
61. Green, B. W. & Zhang, F. Impacts of air-sea flux parameterizations on the intensity and structure of tropical cyclones. *Mon. Weather Rev.* **141**, 2308–2324 (2013).

## Acknowledgements

Support was provided by the National Oceanic and Atmospheric Administration (NOAA) led Integrated Ocean Observing System (IOOS) through the Mid-Atlantic Regional Association Coastal Ocean Observing System (MARACOOS, NA11NOS0120038), the Environmental Protection Agency (EP-11-C-000085), the New Jersey Department of Environmental Protection (WM13-019-2013) and Board of Public Utilities (2010RU-COOL) and the NOAA Cooperative Institute for the North Atlantic Region (CINAR, NA13OAR4830233), Disaster Recovery Act. The authors thank Teledyne Webb Research and Rutgers University for student support, and the NOAA National Centers for Environmental Prediction for student engagement. We further thank David Titley, Jim Price and an anonymous reviewer for their useful comments.

## Author contributions

S.M.G. synthesized and analysed the multiple data sets and wrote the manuscript in collaboration with the other authors. T.N.M. assisted in the synthesis of the *in situ* oceanographic data. G.N.S. contributed the atmospheric and storm sensitivity studies. Y.X. contributed the ocean simulations and analysis. R.K.F. performed historical buoy data and storm track analysis. F.Y. provided plots of buoy data beneath Super Typhoon Muifa. H.R. provided the observational data from the HF Radars. O.S. was involved in data collections and involved in analysis and manuscript preparation. J.K. contributed the Slocum data and was involved in analysis and manuscript preparation. All authors reviewed and edited this manuscript.

## Additional information

**Supplementary Information** accompanies this paper at <http://www.nature.com/naturecommunications>

**Competing financial interests:** The authors declare no competing financial interests.

**Reprints and permission** information is available online at <http://npg.nature.com/reprintsandpermissions/>

**How to cite this article:** Glenn, S. M. *et al.* Stratified coastal ocean interactions with tropical cyclones. *Nat. Commun.* 7:10887 doi: 10.1038/ncomms10887 (2016).



This work is licensed under a Creative Commons Attribution 4.0 International License. The images or other third party material in this article are included in the article's Creative Commons license, unless indicated otherwise in the credit line; if the material is not included under the Creative Commons license, users will need to obtain permission from the license holder to reproduce the material. To view a copy of this license, visit <http://creativecommons.org/licenses/by/4.0/>



# Evaluation of the Hf-Radar Network System around Taiwan using Normalized Cumulative Lagrangian Separation

**Erick Fredj<sup>1\*</sup>, Josh Kohut<sup>2</sup>, Hugh Roarty<sup>2</sup> and Jain-Wai Lu<sup>3</sup>**

<sup>1</sup>Department of Computer Sciences, Lev Academic Center, Israel

<sup>2</sup>Department of Marine and Coastal Sciences Rutgers, The State University of New Jersey, USA

<sup>3</sup>Taiwan Ocean Research Institute, National Applied Research Laboratories, Taiwan

**\*Corresponding author:** Erick Fredj, Department of Computer Sciences, Lev Academic Center, 21 Havaad Haleumi Street PO Box 16031, 91160 Jerusalem, Israel, Tel: +972 2 6751018; E-mail: fredj@jct.ac.il

## Research Article

Volume 1 Issue 1

**Received Date:** January 30, 2017

**Published Date:** March 22, 2017

## Abstract

The Lagrangian separation distance between the endpoints of simulated and observed drifter trajectories is often used to assess the performance of numerical particle trajectory models. However, the separation distance fails to indicate relative model performance in weak and strong current regions, such as over continental shelves and the adjacent deep ocean. A skill score described in detail by Lui, et al. was applied to estimate the cumulative Lagrangian separation distances normalized by the associated cumulative trajectory lengths [1]. The proposed dimensionless skill score is particularly useful when the number of drifter trajectories is limited and neither a conventional Eulerian-based velocity nor a Lagrangian based probability density function may be estimated. The skill score assesses The Taiwan Ocean Radar Observing System (TOROS) performance. TOROS consists of 17 SeaSonde type radars around the Taiwan Island. The currents off Taiwan are significantly influenced by the nearby Kuroshio Current. The TOROS High Frequency radars network product is useful for providing essential information on ocean surface currents of use in water property transports, fishing, offshore oil and gas operations, hazardous spill mitigation, search and rescue, etc.

**Keywords:** Lagrangian Skill Score; Altimetry; Drifter; Hf-Radar

## Introduction

Taiwan and its outlying islands' nearly 1,600 kilometers of coastline and 42,000 square kilometers of territorial sea possess rich and diverse coastal features, marine biological resources, and marine ecosystems (Figure 1). The many ecosystems, including coral reefs, wetlands, mangroves, lagoons, algal reefs, estuaries, and beaches/sandbars, provide many forms of "ecosystem services," such as "supporting," "provisioning," "regulating," and "cultural" services, yielding many

benefits and products, including fishery resources, coastal protection, water purification, tourism and recreation opportunities. In addition, the fact that Taiwan is surrounded by sea also supports the development of many industries, including shipping, shipbuilding, coastal engineering, offshore wind power, oil and mineral exploration, biotechnology, and so on. The Taiwanese coastal ocean is a complex system that forms the boundary between the land and the deep ocean. Deeper understanding of surface currents can be extremely valuable when one seeks to characterize and quantify the

transport of plankton and anthropogenic material in the coastal ocean [2]. Many observations such as Glider, ADCP, High Frequency Radar and Altimetry, are required to collect data from both deep and coastal ocean. In particular, accurate prediction of the path of a drifting search target given estimates of an initial location and the evolution of the velocity field is a crucial step. Furthermore, the currents off Taiwan are significantly influenced by the nearby Kuroshio current, as demonstrated in the below diagram.

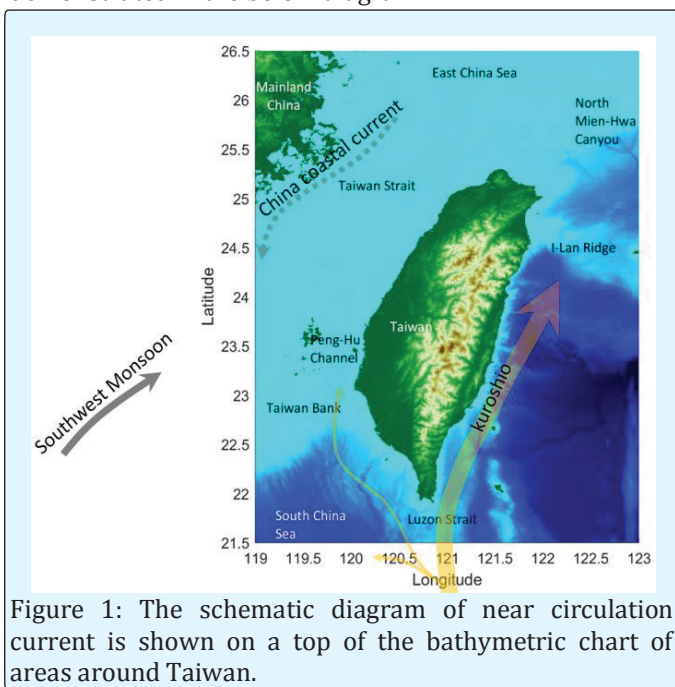


Figure 1: The schematic diagram of near circulation current is shown on a top of the bathymetric chart of areas around Taiwan.

The Kuroshio has two velocity maximum cores southeast of Taiwan, which gradually combine into one as the Kuroshio flowed north. The Kuroshio is deflected by the I-Lan Ridge east of Taiwan and the zonal-running shelf break northeast of Taiwan. At the shelf break, the Kuroshio splits, with one branch intruding onto the shelf. West of the Luzon Strait, the Kuroshio intrudes into the South China Sea. Some water flows northward into the Taiwan Strait and re-joins the Kuroshio. Currents in the Taiwan Strait flow primarily in a northward direction, except for the southward current near the coast of Mainland China. North of the Taiwan Strait, a branch of the northward flow follows the northern coast of Taiwan to join the Kuroshio. The composite current varies consistently from season to season. There is generally poor correlation between currents and local winds, especially in the deep-water regime. Remote forces are important in the currents around Taiwan. The Taiwan Strait (TS), bounded by the mainland to the west and the island of Taiwan to the east, is a narrow passage that connects the East China Sea (ECS) in the north to the

South China Sea (SCS) in the south (see Figure 1). The seasonal circulation in the TS, primarily dominated by monsoons and the bottom topography is regionally important, because the TS is a key path for the exchange of water in the SCS with that in the ECS, the Yellow Sea and even the Sea of Japan [3-5].

Since 2009, the Taiwan Ocean Research Institute (TORI) of the National Applied Research Laboratories (NARLabs) has been providing consistent and accurate hourly surface current information in the seas around Taiwan. This is based on a significant effort to ensure hardware and software resiliency, quality control, and quality assurance. Spatial coverage of High Frequency radar (HF-radar), with a good data percentage of more than 50%, based on the past three years' records (see Figure 2), has been observed to vary on daily and seasonal scales due to ionospheric interference at the lower HF radio spectrum and variable state conditions. This coverage is uniquely capable of sampling relevant temporal and spatial scales of near shore processes that impact event response activities and basic coastal ocean research.

Remote sensing of near-surface currents with HF-radar was demonstrated more than 30 years ago by Stewart and Joy. The measurement is based on the fact that electromagnetic radiation in the 3- to 30-MHz range scatters strongly (Bragg scattering) from ocean surface gravity waves. The returned energy spectrum thus indicates movement of ocean surface gravity waves with a wavelength of half the radar transmitted wavelength in directions either toward or away from the HF radar site (radial directions). Multiple radars are typically deployed so radials have enough angular separation to resolve both the north-south and east-west velocity components (hereafter referred to as totals). TORI employed the Seasonde technology which uses two directional antennas and a monopole antenna [6,7].

HF radar is a shore based remote sensing system, and is therefore subject to data gaps, which are predominately due to environmental effects, like increased external noise or low signal due to surface ocean conditions. Many applications of these surface current data require that these gaps be filled, including Lagrangian numerical models to estimate material transport and dispersion. The validation is based on observed surface current maps around the coast of Taiwan with specific common gap scenarios. Several techniques have been used to fill the gaps in the total vector maps. These are implemented using covariance made from normal mode analysis, open boundary modal analysis (OMA), Empirical Orthogonal Function (EOF) analysis, using idealized or smoothed

observed covariance and the recently developed, Least Square regression method based on the Discrete Cosine Transform (DCT-PLS) algorithm, which has been adapted to the mapping of hourly High Frequency Radar data observation [8-14].

The purpose of this study is to examine the usefulness of both High Frequency Radar data and Altimetry data in providing surface sub-mesoscale, mesoscale ocean circulation properties transport sand to improve our understanding of how physical processes influence coastal ecosystems. The rest of the paper is arranged as follows: Data sets are described in section 2; trajectory model and its evaluation methods are provided in section 3; regional results are reported in section 4, with a summary in section 5.

## Data

The Lagrangian ocean observations were collected from Drifters trajectories, Altimetry product and High Frequency radars during May 2015 from measurements performed by the Taiwan Ocean Research Institute. The data points are reviewed in this section.

### Drifter Trajectories

One drifter was released in the sea around Taiwan by the Taiwan Ocean Research Institute during the spring 2015 with the objective of providing a reference data set to validate trajectory predictions. The drifter was released within the coverage region of the national Taiwan CODAR system operated by TORI. The drifters were self-locating datum marker buoys (SLDMB). The drifter's location was recorded using a Global Positioning System (GPS) fixes at one hour intervals sampling and were transmitted to shore via the Argo communication, with a nominal GPS position uncertainty of 10m. Drifters were deployed in October 2015 both in the South China Sea (SCS) and in the Philippine Sea (PS).

As the drifter is rapidly advected northwards driven by the Kuroshio current after deployment and thus leaving the range of the HF radars, the results discussed in this section are limited to a single drifter experiment entrance to the TOROS domain, which started on 10 May 2015 at 00:00 UTC. Trajectories were run for 5 days. The skill score of data tracking was also evaluated by comparing observed and predicted trajectories. For this comparison, we used the method presented in which not only the end points of the observed and modeled trajectories were compared, but also the entire history of the drifter trajectories (3,6, and 9 hours' waypoints of the drifter trajectory) [1].

### Altimetry Product

The Ocean Surface Current Analysis Real-time (OSCAR) offers gridded surface current data on global coverage, which allows us to extract surface current data in the TOROS domain. The OSCAR product, developed at Earth and Space Research (ESR), provides near real-time ocean surface velocities from satellite fields on global grid of 1/3 resolution with a 5-day interval [15-17]. The spatial coverage of OSCAR has been extended to as close to the coast as 1/3 degrees. This product is a direct computation of global surface currents using satellite SSH, scatter meter winds, and both Advanced Very High Resolution Radiometer (AVHRR) and in situ sea surface temperatures [18]. Currents are calculated using a quasi-steady geostrophic model together with an eddy viscosity based wind-driven a geostrophic component and a thermal wind adjustment. So, the OSCAR sea surface currents are averaged over the top 30 m of the upper ocean. The OSCAR data are also freely available through two data centers operated by NOAA and NASA JPL Physical Oceanography DAAC, respectively.

### The High Frequency Radar Network

The Taiwan Ocean Radar Observing System (TOROS) of TORI consists of 17 SeaSonde type radars around the Taiwan Island (Figure 2), 12 of which are long range, 4 of which are medium range, and 1 of which is standard range. Table 1 provides the typical characteristics of the different types of systems. Each site consists of two categories of hardware: the radar equipment purchased directly from CODAR Ocean Sensors and the ancillary site specific hardware required for communications, power, backup power, temperature control, weather proofing, security, and antenna foundations. High Frequency Radar (HFR) systems are one technology deployed along the coast to remotely measure the complex surface current dynamics over these highly variable seas [19].

System Type	Radio Frequency (MHz)	Range (km)	Resolution (km)
Long Range	4.58	150	3.75
Medium Range	13.4	70	1.5
Standard Range	24.3	40	1.5

Table 1: Characteristic of Toros Long-, Medium-, and Standard Range Hf Radar Systems.

All of the sites are managed by Taiwan Ocean Research Institute (TORI), National Applied Research Laboratories (NARLabs) since 2009 and the primary function of the radars was to map surface currents. The TORI head



quarters in Kaohsiung processed all data, combined to surface current maps, checked for quality control, and saved to the archive. According to the 2014 TOROS annual report, the correlation coefficient of the surface current between HFR observed and 11 drifter-derived current velocities are 0.70 and 0.84 in  $u$  and  $v$  directions, respectively, and the mean differences are 0.019 m/s and -0.033 m/s in  $u$  and  $v$  directions [20].

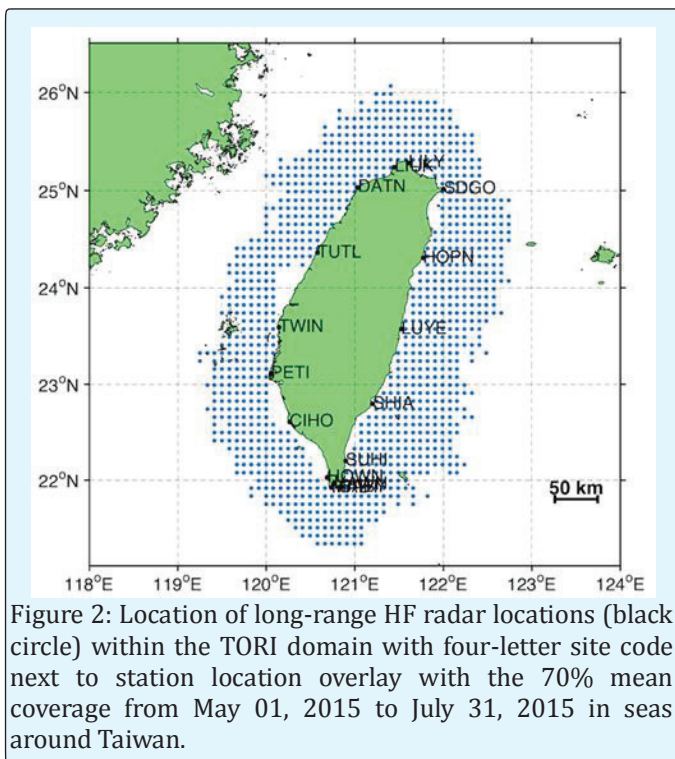


Figure 2: Location of long-range HF radar locations (black circle) within the TORI domain with four-letter site code next to station location overlay with the 70% mean coverage from May 01, 2015 to July 31, 2015 in seas around Taiwan.

## The Gap Filling Method, Lagrangian Trajectory Model and Evaluation

### The Gap Filling Method

Fredj et al. introduced for the first time a DCT-PLS method applied to HFR data processing. We now give a short introduction of the DCT-PLS algorithm. For more details on the mathematics of the method, the reader is referred to [14].

$$F(\hat{X}) = RSS + sP = \left\| W^{1/2} (X - \hat{X}) \right\|^2 + s \left\| \nabla^2 \hat{X} \right\|^2$$

Let  $X$  stand for a spatial-temporal dataset with gaps, and  $W$  a binary array of the same size indicating whether or not the values are missing. The technique consists in minimizing a criterion that balances the fidelity of the data, measured by the residual sum of squares (RSS), and a penalty term ( $P$ ) that reflects the roughness of the smooth data  $\hat{X}$  measured. The DCT-PLS seeks for an  $\hat{X}$  that minimizes the error function.  $\| \cdot \|$  is the Euclidian norm,

$\nabla^2$  and  $\circ$  stand for the Laplace operator and the Schur (element wise) product, respectively. The term  $s$  is a positive scalar that controls the degree of smoothing. As  $s$  increases, the smoothness of  $\hat{X}$  also increases. For small values of  $s$ , the value of  $\hat{X}$  will be dominated by noise. To investigate the best fit of the model coefficients, we apply the Generalized Cross Validation (GCV) score method to find a good compromise between goodness and smoothness of  $\hat{X}$  [21]. In the case of equispaced data, simplified considerably the complexity of the GCV calculation by rewriting the GCV score in terms of the type-2 DCT and its inverse (IDCT), which forms [22]

$$\hat{X} = IDCT (\Gamma \circ DCT(W \circ (X - \hat{X}) + \hat{X}))$$

Where  $\Gamma$  are the components of the diagonal three-dimensional tensor defined by [23]

$$\Gamma_{i_1, i_2, i_3} = [1 + s \left( \sum_{j=1}^3 (2 - 2\cos(i_j - 1)\pi/n_j) \right)^2]^{-1}$$

Where  $i_j$  denotes the  $i$  elements along the direction  $j$ , and  $n_j$  denotes the size of  $X$  along the direction  $j$ . The DCT-PLS technique relies only on the choice of the smoothing parameter  $s$ . In the case of gap filling the parameter  $s$  has an infinitesimal value to reduce the effect of smoothing. A high  $s$  value leads to the loss of high frequency variability in the HFR surface current fields. To avoid any subjectivity in the choice of the smoothing parameter, this parameter is determined by minimizing the GCV score. Minimization of the GCV score helps to optimize the trade-off between bias and variance. The bias measures how well the smoothed velocity field approximates the true velocity field, and the variance measures how well the smoothing velocity field can estimate the original experimental velocity field.

**Lagrangian Trajectory Model:** Lagrangian particle tracking is often found in oceanographic applications. A Lagrangian particle trajectory model, based on the surface velocity fields output from HF-radar corrected using our DCT-PLS algorithm. The Lagrangian trajectories of the “virtual” particles can be solved by the equation:

$$\frac{d\mathbf{r}}{dt} = \mathbf{u}(t, \mathbf{r})$$

Where  $\mathbf{r} = (x, y)$  denotes the position of the particle and  $\mathbf{u} = (u, v)$  is the Eulerian velocity at position  $\mathbf{r}$  and time  $t$ . We hypothesize that the velocity of the particles is identical to that of the water (the virtual particles have no inertia and they do not interact with each other). The trajectories are evaluated using the Matlab Runge-Kutta 4/5th order to solve the Lagrangian trajectories. In addition, a linear interpolation in time and bilinear interpolation in space is performed due to the fact that the



temporal resolution of the velocity field is 30 minutes and the spatial resolution is 9km in the TORI network. Two measures will be used to quantify the trajectory hind cast to evaluate the relative performance of the HF-Radar TORIS: (1) the Lagrangian separation distance ( $d$ ), defined as the separation distance between the end points of the simulated and observed Lagrangian trajectories, and (2) a purely trajectory-based non-dimensional index ( $s$ ) [1].

$$s = \begin{cases} 1 - \frac{c}{n}, & (c \leq n) \\ 0, & (c > n) \end{cases}$$

Following the suggestion of Lui, et. al.,  $n$  is the tolerance threshold  $n = 1$ , and  $c$  is the normalized cumulative Lagrangian separation distance,

$$c = \sum_{i=1}^N d_i / \sum_{i=1}^N l_{oi}$$

Where  $i = 1, 2, \dots, N$  and  $N$  is the total number of time steps, and  $d_i$  is the separation distance between the modeled and observed end points after the initialization of the virtual passive drifter, and  $l_{oi}$  is length of the observed trajectory. This definition is shown in the Figure (3). The smaller the  $s$  value, the worse the performance becomes, where  $s=0$  implies no skill (the worst performance), and  $s=1$  indicating a perfect fit between observation and simulation.

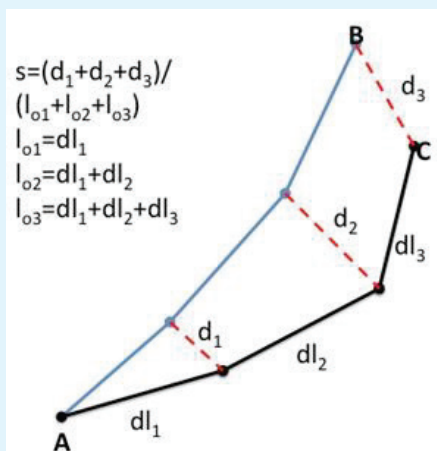


Figure 3: An illustration of the separation distances between the modeled and observed endpoints of Lagrangian trajectories (A-B and A-C, respectively) is shown in red. The lengths of the modeled ( $l_m$ ) and observed trajectories ( $l_o$ ) between the start and end points are shown in blue and in black, respectively. An index  $s$  is defined as an average of the separation distances weighted by the lengths of the observed trajectory.

Extended the non-dimensional skill score used for the skill score in the evaluation of a High Frequency Radar network to derive the performance.

## Regional Results

This section focuses on evaluating the results of several measurements and demonstrating a hindcast system for the sub-mesoscale and mesoscale ocean circulation around Taiwan.

**Dominant Current:** The predominant wind system around Taiwan is the monsoon. The northeasterly monsoon prevails November–March, and the southwesterly monsoons prevail from May–September. April and October are transition months. The monsoon system is the primary force causing current variation around Taiwan [24]. Nitani described surface currents around Taiwan in summer and winter [25]. The Kuroshio flows to the north along the coast of Taiwan and the shelf break of the East China Sea Figure 1. In winter, the Kuroshio intrudes into the South China Sea in the Luzon Strait. In summer, water from the South China Sea enters the western edge of the Kuroshio [26]. East of Taiwan, the width of the Kuroshio is around 100 km, with a maximum speed of around  $100 \text{ cm s}^{-1}$ . The Kuroshio's pathway parallels the shoreline of Taiwan demonstrates no obvious seasonal variation Figure 1. South of Peng-Hu Archipelagos, current in the Taiwan Strait flows predominantly north-eastward regardless of the seasons. North of the Peng-Hu Archipelagos, the current flows north-eastward in summer and southwestward in winter. The seasonal variation is significant only in the Luzon Strait and in the northern Taiwan Strait. Many oceanographers believe that the Kuroshio intrudes into the South China Sea through the Luzon Strait in winter and stops in summer [24].

## Gap-Filling Verification

The gap-filling algorithm was tested for two main scenarios observed in the hourly HFR current data in the seas around Taiwan. Based on the last three-month datasets (Figure 2), the gaps in the hourly maps around Taiwan are characterized with at least 70% spatial coverage, 70% of the time. In this study we defined two scenarios, which reproduce the most common gap situations (Figure 3).

**Scenario 1:** The first scenario mimicked a major hardware failure in July 9, 2015 14:00 with the loss of at least one site from the network. Observed gaps under this scenario extend along the coast from the shore to the offshore edge of the coverage, splitting the TORI HFR

network into two. The width of the gap across the coverage depends on the number of sites that are not reporting data. For this analysis, we are simulating the loss in contributing radials from a single site in HOPN region in the eastern part of Taiwan Island.

**Scenario 2:** The second scenario tested in June 2, 2015 16:00 mimics more common gaps in which each site is contributing radial vectors, but there is a reduction in the number of radial data from one or more sites. The most common cause of the reduced coverage is an increase in external noise that lowers the signal to noise ratio and therefore limits the range of detectable signal used to determine radial velocity. The size and location of the gaps depend on the location and magnitude of the reduction of coverage from each individual site. For long-range SeaSonde HF radar, the interference from the ionosphere effects can increase the noise floor, particularly at night. The impact of this ionospheric interference was observed on June 11, 2015 16:00:00 (Figure 3).

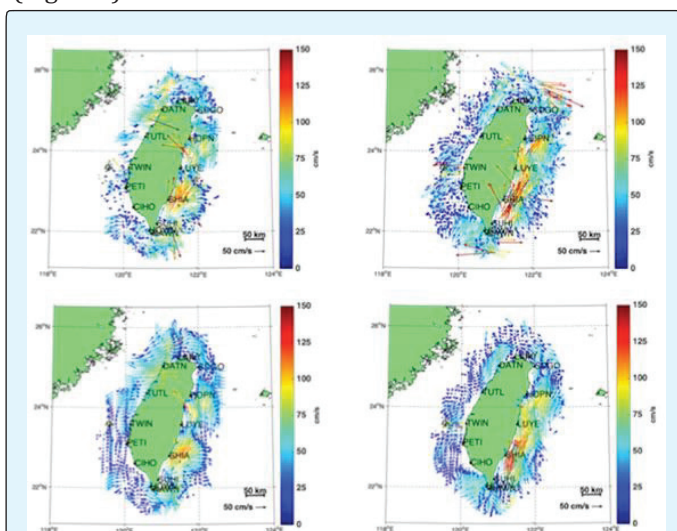


Figure 3: Surface current maps showing Scenario 1 on July 9, 2015 14:00:00 in the right column, and Scenario 2 on June 11, 2015 16:00:00 in the left column. The observed velocity field by TORI HFR is on the top and the smoothed velocity field map with 70% mean coverage is on the bottom.

Based on a 7-year analysis of TORI, from 2009 HFR coastal radar network, Scenario 1 occurs less than 6 % of the time and Scenario 2 occur almost 60 % of the time. For both Scenarios 1 and 2, we estimated the validity DCT-PLS velocity fields by comparing the removed vectors and the predicted vectors. The correlation shows a strong agreement between meridional and zonal velocity components.

## Model Evaluation

The TOROS HF-Radars network validation is based on tracked drifter trajectories around Taiwan. For each drifter trajectory released daily at the observed location, and tracked using the HF-radars model network current velocities, both the Lagrangian separation distance  $d_9$  and skill score  $s_9$  are evaluated after 9 hours' simulations adapted from [1]. Figure 4 shows an example of simulated trajectories and the corresponding model skill scores  $s_9$ . A high skill score  $s_9 \sim 0.8$  corresponding to better correlation between the simulated and observed trajectories is seen during 11-13 May 2015. The lower skill score  $s_9 < 0.2$  is found for 10 May 2015 near the coast where the simulated particle diverges from the observed drifter trajectory. So, the skill score  $s_9$  clearly indicates the poor performance of the TORI HF-Radars network.

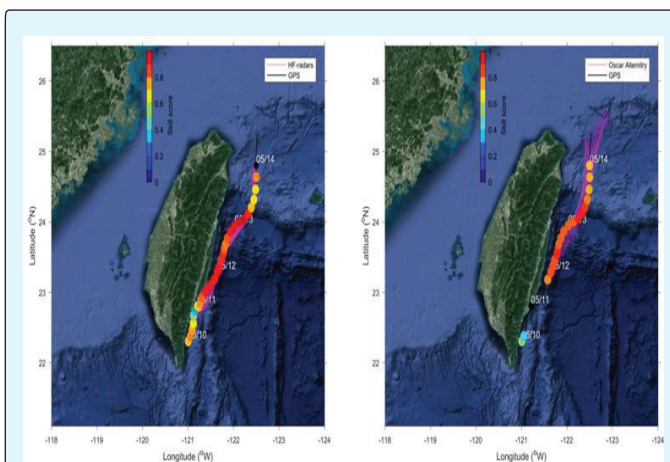


Figure 4: compares the simulated mean drifter trajectories initialized from the actual drifter # 1045 locations with the observed trajectories. The forecast skill score by TORI HF-radars and Oscar Altimetry is on the left and right, respectively. The drifter trajectory is represented by the black line and the predicted is colored red.

The Altimetry and HF-radars forecast skill score is highly dependent on the environmental conditions (see Figure 4). The complex flow structure was observed due to the strong Kuroshio current ( $\sim 1$  m/s) interacting with dramatically changed topography and the eddy transportation from the Pacific Ocean. HF-radars currents now cast provided the most valuable information for understanding of the coastal surface current, with a mean  $s_9$  value of (0.4 – 0.7). In coastal zones (the strip of land within a few tens of kilometers from the coasts of Taiwan) the Oscar data is often contaminated by the land (see Figure 4 right panel in May 11, 2015), making the estimated velocity an extremely challenging task to

perform. The present research paves the way to confirm the reliability of TORI's HF-radars network.

The entire altimetry trajectories model has about the same performance, with mean  $s_0$  value of (1 – 0.8) in the deep ocean and mean  $s_0$  value of (0.6 – 0.7) within the transition zone from the shelf to deep ocean. Particularly within the transition zone from the shelf to the deep ocean, both the HF-Radars and Altimetry based trajectory models have reduced (20% – 30%) the skill score. Thus, comparisons focus mainly on the deep ocean region. Note that the OSCAR altimetry products skill score was not available near the coast, to avoid the problem of degraded performance of altimetry near the coast the comparison is restricted to buoys located in the open ocean no closer than 20 km to the coast.

## Conclusions

In this study, we introduce an efficient automated DCT-PLS method for filling the data gaps in the HF-Radar ocean Spatial-Temporal dataset applied to TOROS domain in the seas around Taiwan. The DCT-PLS approach was demonstrated by reconstructing the hourly HF-Radar observation with a spatial resolution of nine kilometers across the Taiwanese seas. We validated the method during summer 2015 against typical gap scenarios. A major advantage of the approach is the ability to perform fast and robust computation while requiring a small amount of memory storage, demonstrating the feasibility of a real-time application for filling HF-Radar missing data. The user, however, should be aware of some limitations of the automatic gap filling procedure. Under the less common scenario in which more significant outages can remove entire sites from a coastal network, the effectiveness of the method depends on the characteristics of the surrounding flow. Individual HF-Radar network operators will need to assess the scales of variability in their operating area to determine the optimal way to apply this method in either a real-time or post-processed application.

This study has demonstrated a clearly higher skill score of surface data derived from HF-Radar than Oscar altimetry surface current in combination with drifter observations for offshore skill forecast. Furthermore, Oscar altimetry current surface achieves poor skill forecast in the offshore shelf area prediction. Surface currents derived based on both HF-radars and Altimetry affect the forecast skill score, especially in the region where the dramatic change of the bathymetry occurs along the drifter trajectory. However, further investigation is required before concrete conclusions are made.

## Acknowledgment

This study was supported by a grant from the Israel Science Foundation (ISF) and the Taiwan Ministry of Science and Technology. Taiwan Ocean Research Institute (TORI), National Applied Research Laboratories (NARLabs), sponsored the HFR dataset.

## References

1. Liu Y, Robert H, Weisberg (2011) Evaluation of trajectory modeling in the different dynamic region using normalized cumulative Lagrangian separation, *J Geophys Res* 116(C9).
2. Liang W-D, Tang TY, Yang YJ, Ko MT, Chuang W-S (2003) Upper-ocean currents around Taiwan, *Deep-Sea Research II* 50(6-7): 1085-1105.
3. Jan S, Wang J, Chern C-S, Chao SY (2002) Seasonal variation of the circulation in the Taiwan Strait. *J Mar Syst* 35(3-4): 249-268.
4. Kondo M (1985) Oceanographic investigations of fishing grounds in the East China Sea and the Yellow Sea-I. Characteristics of the mean temperature and salinity distributions measured at 50 m and near the bottom. *Bull Seikai Reg Fish Res Lab* 62: 19-66.
5. Isobe A (1999) On the origin of the Tsushima warm current and its seasonality. *Cont Shelf Res* 19(1) 117-133.
6. Stewart RH, JW Joy (1974) HF radio measurements of surface currents. *Deep-Sea Res* 21(12): 1039-1049.
7. Barrick DE, BJ Lipa (1997) Evolution of bearing determination in HF current mapping radars, *Oceanography* 10(2): 72-75.
8. Lipphardt BL, Kirwan AD, Grosch CE, Lewis JK, Paduan JD (2000) Blending HF radar and model velocities in Monterey Bay through normal mode analysis. *J Geophys Res* 105 (C2): 3425-3450.
9. Kaplan DM, Lekein F (2007) Spatial interpolation and filtering of surface current data based on open-boundary modal analysis. *J Geophys Res* 112(C12).
10. Beckers JM, Rixen M (2003) EOF calculations and data filling from incomplete oceanographic data sets. *JTECH* 20(12): 1839-1856.
11. Alvera-Azcarate A, Barth A, Rixen M, Beckers JM (2005) Reconstruction of incomplete oceanographic

- data sets using Empirical Orthogonal Functions: Application to the Adriatic Sea surface temperature. *Ocean Modelling* 9(4): 325-346.
12. Davis RE (1985) Objective mapping by least squares fitting. *J Geophys Res* 90(C3): 4773-4778.
  13. Kim SY, Terrill E, Cornuelle B (2008) Mapping surface currents from HF radar radial velocity measurements using optimal interpolation. *J Geophys Res* 113(C10): 1-16.
  14. Fredj E, Roarty H, Kohut J, Smith M, Gleen S (2016) Gap Filling of the Coastal ocean surface current from HFR data: Application to the Mid Atlantic Bight Network. *JTECH* 33: 1097-1111.
  15. Lagerloef GSE, GT Mitchum, R Lukas, P Niiler (1999) Tropical Pacific near surface currents estimated from altimeter, wind and drifter data. *J Geophys Res* 104(C10): 23313-23326.
  16. Johnson ES, F Bonjean, GSE Lagerloef, JT Gunn, GT Mitchum (2007) Validation and error analysis of OSCAR sea surface current, *J Atmos Oceanic Technol* 24: 688-701.
  17. Dohan K, N Maximenko (2010) Monitoring ocean currents with satellite sensors. *Oceanography* 23(4): 94-103.
  18. Bonjean F, GSE Lagerloef (2002) Diagnostic model and analysis of the surface currents in the Tropical Pacific Ocean. *J Phys Oceanogr* 32(10): 2938-2954.
  19. Kohut J, Roarty H, Randall-Goodwin E, Glenn S, Lichtenwalner C (2012) Evaluation of two algorithms for a network of coastal HF radars in the Mid-Atlantic Bight. *Ocean Dynam* 62(6):953-968.
  20. Lai JW, Lin KI, Yu CM, Hsu TC, Yang YC, et al. (2015) TOROS 2014 Annual Report. TORI Tech Note, p. 443.
  21. Craven P, Wahba G (1978) Smoothing noisy data with spline functions. Estimating the correct degree of smoothing by the method of generalized cross-validation. *Numer Math* 31(4): 377-403.
  22. Strang G (1999) The discrete cosine transform. *SIAM Review* 4(1): 135-147.
  23. Yueh WC (2005) Eigenvalues of several tridiagonal matrices. *Appl Math E-notes* 5: 66-74.
  24. Wirtky K (1961) Physical oceanography of the south east Asia waters. Scripps Institute of Oceanography NAGA Report 2: 195.
  25. Nitani H (1972) Beginning of the Kurishio, In: Stommel H, Yoshida K (eds) *Kurishio: Physical Aspects of the Japan Current*. University of Washington Press, Seattle, pp. 441-500.
  26. Zhang D, Lee TN, Johns WE, Liu C-T, Zantopp R (2001) The Kuroshio east of Taiwan: Modes of variability and relationship to interior ocean mesoscale eddies. *J Physical Oceanography* 31(4): 1054-1074.



# SCIENTIFIC REPORTS

OPEN

## Central place foragers select ocean surface convergent features despite differing foraging strategies

Matthew J. Oliver<sup>1</sup>, Josh T. Kohut<sup>2</sup>, Kim Bernard<sup>3</sup>, William Fraser<sup>4</sup>, Peter Winsor<sup>5</sup>, Hank Statscewich<sup>5</sup>, Erick Fredj<sup>6</sup>, Megan Cimino<sup>7</sup>, Donna Patterson-Fraser<sup>4</sup> & Filipa Carvalho<sup>8</sup>

Discovering the predictors of foraging locations can be challenging, and is often the critical missing piece for interpreting the ecological significance of observed movement patterns of predators. This is especially true in dynamic coastal marine systems, where planktonic food resources are diffuse and must be either physically or biologically concentrated to support upper trophic levels. In the Western Antarctic Peninsula, recent climate change has created new foraging sympatry between Adélie (*Pygoscelis adeliae*) and gentoo (*P. papua*) penguins in a known biological hotspot near Palmer Deep canyon. We used this recent sympatry as an opportunity to investigate how dynamic local oceanographic features affect aspects of the foraging ecology of these two species. Simulated particle trajectories from measured surface currents were used to investigate the co-occurrence of convergent ocean features and penguin foraging locations. Adélie penguin diving activity was restricted to the upper mixed layer, while gentoo penguins often foraged much deeper than the mixed layer, suggesting that Adélie penguins may be more responsive to dynamic surface convergent features compared to gentoo penguins. We found that, despite large differences in diving and foraging behavior, both shallow-diving Adélie and deeper-diving gentoo penguins strongly selected for surface convergent features. Furthermore, there was no difference in selectivity for shallow- versus deep-diving gentoo penguins. Our results suggest that these two mesopredators are selecting surface convergent features, however, how these surface signals are related to subsurface prey fields is unknown.

Optimal foraging theory suggests central place foragers consider external cues like food quality, distance to food patch, and revisit times to food patches to maximize fitness<sup>1</sup>. The end result of the feedback between prey patch characteristics and the desire and ability of the predator to find food is manifested as random walks<sup>2</sup>, Lévy walks<sup>3</sup>, or other diffusive<sup>4</sup> or multi-modal movements. Interpreting the ecological significance of these movement modes necessitates an understanding of the dynamic nature of the available environmental cues, the relative response of predators and prey to these cues, and how organisms remember these cues<sup>5</sup>. For example, many organisms appear to exhibit Lévy walks, which are documented to optimize foraging success of random searchers<sup>6</sup>. However, the selective interactions that lead to the emergence of these patterns are often unknown, hence in the absence of an understanding of selective cues between the environment and the focal individual, alternative movement modes may equally explain observed movement patterns<sup>7,8</sup>. Therefore, it is not enough to only establish a movement mode to understand the ecological significance of foraging behaviors or how these behaviors might change in dynamic environmental conditions. Discovering the environmental predictors of foraging locations is equally important, yet can be challenging and is often the critical missing piece for interpreting the ecological significance of observed movement patterns of predators. It is difficult to map environmental cues at the appropriate scale to

<sup>1</sup>University of Delaware, College of Earth, Ocean and Environment, 700 Pilottown Road, Lewes, DE, 19958, USA.

<sup>2</sup>Rutgers, The State University of New Jersey, Department of Marine and Coastal Sciences, 71 Dudley Road, New Brunswick, NJ, 08901, USA. <sup>3</sup>Oregon State University, College of Earth, Ocean, and Atmospheric Sciences, 104 CEOAS Admin Bldg, Corvallis, OR, 97330, USA. <sup>4</sup>Polar Oceans Research Group, P.O. Box 368, Sheridan, MT, 59749, USA. <sup>5</sup>University of Alaska, Fairbanks, College of Fisheries and Ocean Sciences, 905 Koyukuk Dr. Suite 245 O'Neill Bldg., Fairbanks, AK, 99775–7220, USA. <sup>6</sup>The Jerusalem College of Technology, Computer Science Department, 21 Havaad Haleumi St., P.O. Box 16031, Jerusalem, 91160, Israel. <sup>7</sup>Scripps Institution of Oceanography, University of California, San Diego, Coastal Observing R&D Center, 9500 Gilman Drive #0214, La Jolla, CA, 92093, USA. <sup>8</sup>National Oceanography Centre, European Way, Southampton, SO14 3ZH, United Kingdom. Correspondence and requests for materials should be addressed to J.T.K. (email: [kohut@marine.rutgers.edu](mailto:kohut@marine.rutgers.edu))

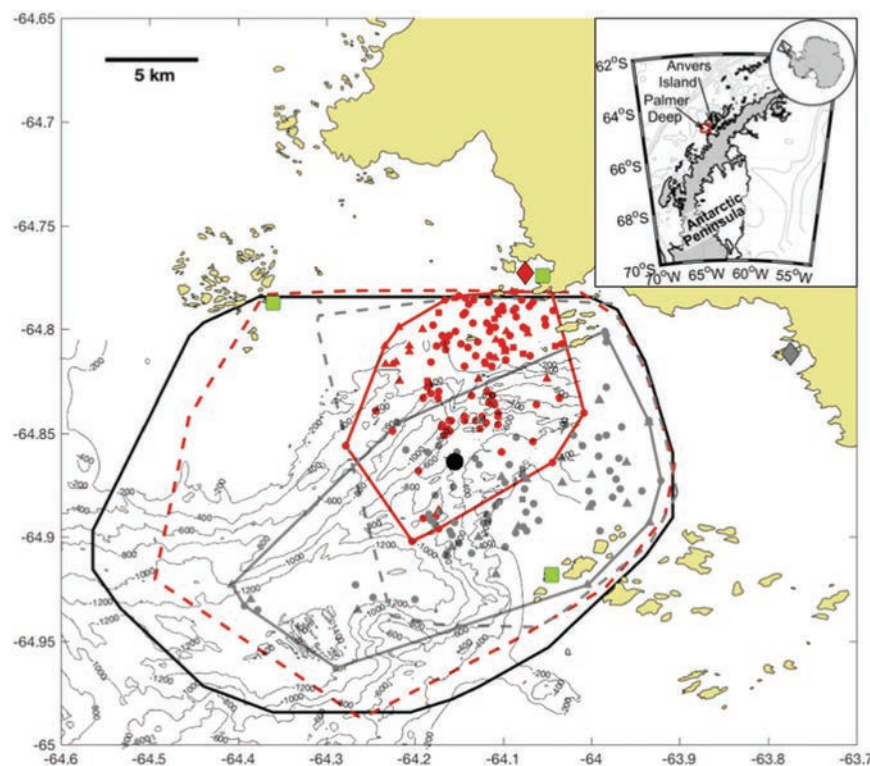


**Figure 1.** Map of the study site over Palmer Deep. Locations of tagged Adélie (red) and Gentoo Penguin (grey) foraging dives (circles), search dives (squares) and transits (triangles) for 2015 study season are shown. The convex spatial hulls are shown for the tagged (thin red) and simulated (red dashed) Adélie and the tagged (thin grey) and simulated (grey dashed) Gentoo Penguins for the 2015 study season. Also shown is the Adélie colony at Torgersen (red diamond) and the gentoo colony at Biscoe Point (grey diamond); the HFR sites (green squares); the HFR data footprint (thin black line); and the glider time series (black circle). The maps were generated by the authors J.K. and H.S. using Matlab version R2016b ([www.mathworks.com](http://www.mathworks.com)).

determine if they are being selected<sup>9,10</sup>, especially in a fluid marine environment. In the coastal Western Antarctic Peninsula (WAP), the food web is short and characterized by intense phytoplankton blooms that are grazed by Antarctic krill (*Euphausia superba*, referred to hereafter as “krill”), a primary prey source for penguins and other predators. Although krill aggregations occur throughout the WAP<sup>11</sup>, their distribution is extremely patchy even on scales less than 1 km<sup>12,13</sup>. Krill have intermediate Reynolds numbers ( $\sim 10^2$ – $10^3$ ), compared to drifting phytoplankton ( $\sim 10^{-2}$ ) and swimming penguins ( $\sim 10^6$ ), which means they can make directed movements, even though they are also heavily influenced by local circulation.

Lagrangian convergent features are representations of time-dependent concentrating ocean dynamics at scales relevant to marine predator foraging ecology. Broadly, they are regions that concentrate neutrally buoyant particles and are often associated with filaments and mesoscale features, such as eddies, jets and fronts. Convergent features, identified by time varying concentrations of buoyant particle densities, may be proxies for the mechanisms by which sparse food resources move through marine trophic levels by collapsing the essential components of the food web in time and space. Realistic particle simulations show that convergent features have much higher concentrations of zooplankton<sup>14</sup>. Seabirds have also been associated with convergent features such as mesoscale eddies<sup>15</sup>, and their flight paths are coherent with dynamic convergent features<sup>16</sup>. Macaroni penguins have been shown to associate with convergent features at relatively large scales (10–100 km), presumably because they concentrate prey resources<sup>17</sup>. These studies have focused on relatively large-scale associations using infrequent satellite composites of ocean features. However, convergent features are dynamic in space and time, and therefore should optimally be examined at space and time scales relevant to predator foraging behaviors.

At our study site, Adélie penguin (*Pygoscelis adeliae*) populations have decreased rapidly over the last three decades, while numbers of gentoo penguins (*P. papua*) have increased<sup>18</sup>. These population changes have resulted in relatively recent sympatry between these two congeneric central place foragers in our study site, where they also exhibit partially overlapping foraging ranges over the Palmer Deep canyon (Fig. 1). In this study, we determine if these two species select convergent features in a similar way to guide their foraging behavior. To do this, we used an integrated ocean observatory (Fig. 1) to estimate the relationship between surface convergent features and the foraging behavior of these two mesopredators.

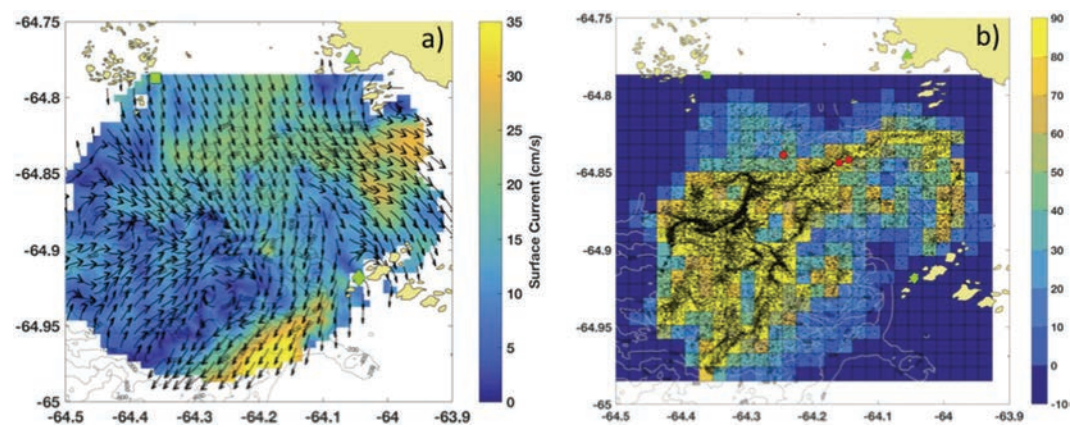


**Figure 2.** Convergent features near penguin foraging. **(a)** Hourly surface current map, January 27, 08:00 GMT 2015. The HFR sites located at Palmer Station (green triangle) and the Wauwermans (green diamond) and Joubin (green square) island groups are also shown. **(b)** Map showing the distribution of particles on January 27, 08:00 GMT (black dots) overlaid on the particle density metric (number of particles within each  $1 \times 1$  km cell minus the median across all cells). The location of penguins is also shown (red circles). The maps were generated by the corresponding author J.K. using Matlab version R2016b ([www.mathworks.com](http://www.mathworks.com)).

Species	Time Window (minutes)	Transiting	Search Diving	Forage Diving
Adélie	1	<b>0.001</b> (N = 32)	<b><math>\leq 0.001</math></b> (N = 18)	<b><math>\leq 0.001</math></b> (N = 74)
	2.5	<b><math>\leq 0.001</math></b> (N = 22)	<b>0.004</b> (N = 8)	<b><math>\leq 0.001</math></b> (N = 94)
	5	<b>0.004</b> (N = 16)	<b>0.004</b> (N = 7)	<b><math>\leq 0.001</math></b> (N = 101)
	15	0.184 (N = 2)	0.307 (N = 4)	<b><math>\leq 0.001</math></b> (N = 118)
Gentoo	1	<b>0.009</b> (N = 49)	0.760 (N = 7)	0.309 (N = 42)
	2.5	0.373 (N = 22)	0.460 (N = 4)	0.063 (N = 72)
	5	0.547 (N = 10)	0.836 (N = 2)	<b>0.007</b> (N = 86)
	15	0.835 (N = 2)	N = 0	<b>0.009</b> (N = 94)

**Table 1.** The p-value and number of observations for KS tests comparing the field RPD to Adélie and gentoo ARGOS locations classified into transiting, search diving and forage diving behavior. The classifications were based on 1, 2.5, 5, and 15 minute windows before and after the ARGOS hit to classify the location. Bold text indicates that ARGOS locations had higher RPD than the field RPD.

Results

**Penguin Locations Relative to Ocean Features.** During the austral summer of 2014–2015, we mapped penguin foraging patterns relative to sea surface currents derived each hour from a High Frequency Radar (HFR) network over Palmer Deep canyon (Fig. 2a)<sup>19</sup>. Simulated passive particles released in the hourly surface current maps were used to identify the location and intensity of convergent features that may locally concentrate prey biomass during penguin foraging days. Maps of Relative Particle Densities (RPD) derived from particles released each hour across the HFR footprint were used to estimate the location of convergent features each hour between January 1<sup>st</sup> and March 1<sup>st</sup> 2015, where higher RPD values were indicative of convergence (Fig. 2b).

For 11 Adélie and 7 gentoo penguins, there was a total of 124 and 98 ARGOS class 1–3 locations representing 27 and 17 foraging trips, respectively. These locations were spatially matched to hourly RPD (Tables 1 and 2). ARGOS locations were classified as transiting, searching or foraging based on their dive profiles within 1, 2.5, 5, and 15 minutes of the ARGOS location (Tables 1 and 2). Adélie penguin dives associated with ARGOS locations had significantly higher RPD values compared to RPD values across the entire HFR field and significantly higher RPD values compared to the RPD values sampled by simulated Adélie penguins ( $p \leq 0.001$  and  $p \leq 0.001$ , two-sample Kolmogorov-Smirnov tests respectively, Fig. 3a). Gentoo penguin locations had higher RPD values compared to RPD values across the entire HFR field but these were weakly significant ( $p = 0.03$ , two-sample Kolmogorov-Smirnov tests respectively, Fig. 3b). However, compared to RPD values sampled by simulated gentoo penguins, tagged gentoo penguins showed a significant selection for higher values as well ( $p \leq 0.001$ , two-sample Kolmogorov-Smirnov tests, Fig. 3b).

Both simulated and tagged penguins covered different areas of the HFR field during our experiment, and therefore experienced different RPD. However, simulated penguins within the convex hull of their tagged counterparts still showed significantly lower RPD values compared to tagged Adélie and gentoo penguins ( $p = 0.02$  and  $p = 0.0005$ , respectively). To test the sensitivity of these results to the effects of individual trips or individual penguins, we resampled these ARGOS locations, systematically leaving out one foraging trip or one penguin (represented by the grey envelope in Fig. 3a,b). In all resampling cases, the Adélie and gentoo ARGOS RPD

Species	Time Window (minutes)	Transiting	Search Diving	Forage Diving
Adélie	1	0.075 (N = 32)	<b>0.001 (N = 18)</b>	<b>&lt;&lt;0.001 (N = 74)</b>
	2.5	<b>0.028 (N = 22)</b>	<b>0.017 (N = 8)</b>	<b>&lt;&lt;0.001 (N = 94)</b>
	5	0.057 (N = 16)	<b>0.021 (N = 7)</b>	<b>&lt;&lt;0.001 (N = 101)</b>
	15	0.294 (N = 2)	0.543 (N = 4)	<b>&lt;&lt;0.001 (N = 118)</b>
Gentoo	1	<b>&lt;&lt;0.001 (N = 49)</b>	0.339 (N = 7)	<b>0.025 (N = 42)</b>
	2.5	0.120 (N = 22)	0.189 (N = 4)	<b>&lt;&lt;0.001 (N = 72)</b>
	5	0.466 (N = 10)	0.821 (N = 2)	<b>&lt;&lt;0.001 (N = 86)</b>
	15	0.874 (N = 2)	N = 0	<b>&lt;&lt;0.001 (N = 94)</b>

**Table 2.** The p-value and number of observations for KS tests comparing the RPD of simulated Adélie or gentoo penguins to Adélie or gentoo ARGOS locations classified into transiting, search diving and forage diving behavior. The classifications were based on 1, 2.5, 5, and 15 minute windows before and after the ARGOS hit to classify the location. Bold text indicates that ARGOS locations had higher RPD than the simulated penguins RPD.

values were significantly higher than both the field and simulated penguin RPD values ( $p < 0.001$ , two-sample Kolmogorov-Smirnov tests). As a result, it is likely that both Adélie and gentoo penguins were systematically selecting for higher RPD.

We partitioned the ARGOS locations by behavior classification within the above mentioned time intervals (Tables 1 and 2). For Adélie penguins, ARGOS locations classified as foraging and search diving behavior occurred in significantly higher RPD compared to both the background RPD and the simulated penguin RPD. The exception was for the search diving behavior classified with a 15 minute time window, likely due to a low sample size ( $n = 4$ ). Adélie penguin ARGOS locations classified as transiting had higher RPD compared to the background RPD, except when using a 15 minute time window due to low sample size ( $n = 2$ ). Furthermore, only RPD for transiting Adélie penguins classified with the 2.5 minute window were significantly higher than the simulated penguins, although it should be noted that for the shorter time window of 1 minute the p-value was 0.075. For the tagged gentoo penguins, only ARGOS locations classified as forage diving had significantly higher RPD compared to the simulated penguin RPD for all time classifications. Search diving behavior had very few samples. The largest sample size for ARGOS locations classified as transiting with a 1 minute time window had significantly higher RPD compared to both background and simulated penguin RPD, while the longer time windows with fewer samples did not have significantly higher RPDs compared to both the background and simulated RPD. Overall, only ARGOS locations classified as forage diving had significantly higher RPD compared to simulated penguin RPD across both species and all time windows (Table 2).

Adélie and gentoo penguins displayed markedly different diving behaviors relative to oceanographic features. Adélie penguins foraged in waters above the mixed layer at depths between 5 and 50 m, where the surface layer is sensitive to atmospheric forcing, while gentoo penguins foraged both above and below the mixed layer, at depths between 5 and 100 m (Fig. 3c,d). The mixed layer depth (MLD), estimated from the maximum buoyancy frequency<sup>20</sup>, was ~30 m during the time period that Adélie penguins were tagged and deepened to ~50 m during the period gentoos were tagged, which accords with natural seasonal changes<sup>21</sup>. We partitioned the gentoo data by dive depth relative to MLD. Gentoo penguins diving shallower than the MLD selected for higher RPD values than the simulated gentoo penguins ( $p = 0.028$ ). Gentoo penguins diving deeper than the MLD also selected for higher RPD values compared to the simulated gentoo penguins ( $p < 0.001$ ). The distributions of RPD targeted by the shallow and deep diving penguins were not significantly different ( $p = 0.1$ ), indicating that gentoo selectivity of surface RPD was not dependent on penguin foraging depth.

**Relative Particle Density Values in Diurnal and Semi-Diurnal Tidal Regimes.** Prior work has shown that local tides are coherent with Adélie penguin ARGOS locations over Palmer Deep<sup>22</sup>. The dominant tidal constituent near Palmer Station is the diurnal  $K_1$  followed closely by another diurnal constituent,  $O_1$ . The two prominent semi-diurnal constituents,  $K_2$  and  $M_2$ , are smaller in magnitude<sup>23</sup>. The interaction of these constituents leads to a unique mixed tide that is slightly diurnal-dominated based on tide gauge data collected at Palmer Station<sup>23</sup>. The result is a tidal forcing and response that transitions from a diurnal to semi-diurnal regime approximately every two weeks. A long-term (2002–2011) record of Adélie penguin foraging distances showed that Adélies foraged at greater distances from shore during semi-diurnal tides, compared to diurnal tides (Fig. 4)<sup>22</sup>. In 2015, Adélie ARGOS locations expanded to the south and east during semi-diurnal tides, while gentoo ARGOS locations translated to the north and west during semi-diurnal tides. During the austral summer of 2014–2015, we mapped the location of strong convergent features based on the hourly RPD maps partitioned by days with semi-diurnal and diurnal tides. The convergent features were defined as grid cells with particle counts, normalized by subtracting the spatial median, greater than 100. The location frequency of these strongest fronts associated with the semi-diurnal and diurnal tidal regimes are shown in Fig. 4. During the semi-diurnal tidal regime, the highest occurrence of convergent features was located offshore over the central canyon (Fig. 4a), consistent with the offshore historic Adélie penguin foraging locations observed during semi-diurnal tides. During the diurnal tidal regime, the location of the highest percentage of convergent features moved south and inshore (Fig. 4b), closer to the penguin colonies. We suggest that the predictability of the locations of convergent features associated



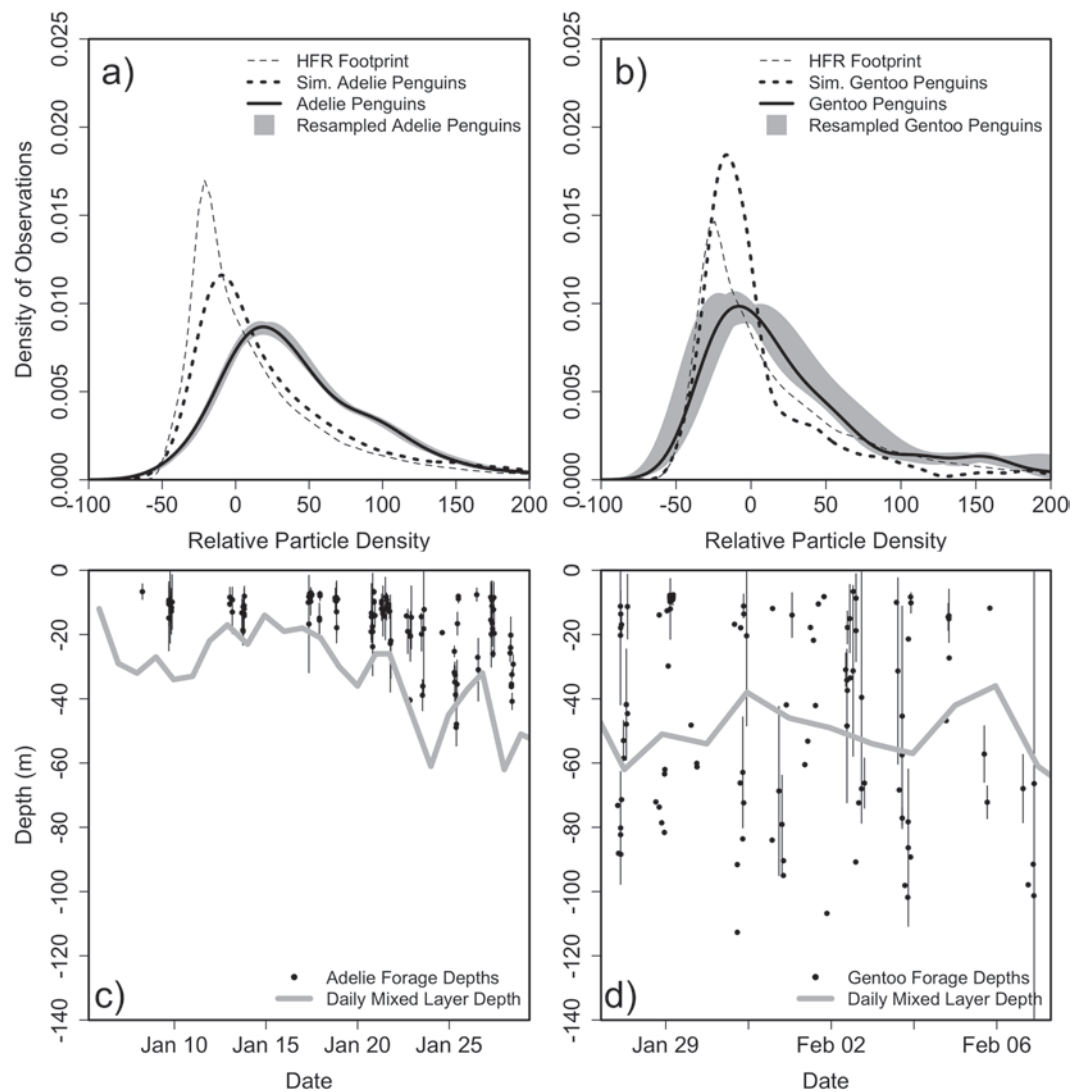


**Figure 3.** Penguin selectivity relative to convergent ocean features. Distribution of observed field PD values available to the penguins (grey dashed) and distribution of PD values at the tagged (solid black) and simulated (black dashed) penguin dive location for the (a) Adélie and (b) Gentoo Penguins. The range of solutions with of the resampled penguins by individual and by foraging trip is shown as a gray shade. Foraging dive depths (black dots) with one standard deviation and daily mixed layer depth determined from the station keeping glider (grey line) for the (c) Adélie and (d) gentoo penguins.

with the changing tidal regimes combined with their selection for these convergent features provides a mechanistic explanation for the variability in historic foraging locations observed in Adélie penguins<sup>22</sup>.

## Discussion

The outer and mid WAP continental shelf is characterized by irregular, episodic intrusions of Upper Circumpolar Deep Water (UCDW)<sup>24,25</sup> that drive intense phytoplankton blooms that may be advected into coastal regions<sup>26,27</sup>. These blooms are fed on by krill, which show a high degree of interannual variability in their abundance<sup>28,29</sup>, both along the shelf and into coastal regions<sup>30–32</sup>. Palmer Deep canyon supports enhanced phytoplankton production<sup>33</sup> and is considered a biological hotspot that is home to Adélie, gentoo and chinstrap penguins<sup>34</sup>. This region is also a common feeding ground for humpback whales (*Megaptera novaeangliae*)<sup>35</sup>, indicating that it is a place where upper trophic levels are persistently linked to primary producers through krill and other zooplankton. What is not known are the specific physical mechanisms that concentrate the various levels of the food web at the scales of the individual predators.

Within the Palmer Deep hotspot, a historical analysis (10 years) of Adélie penguin foraging locations demonstrated a correlation to local tidal regimes, indicating that individual penguins may track tidally-driven features, such as convergent zones, associated with the diurnal and semi-diurnal tides<sup>19,22</sup>. Here we show that as the tidal regime shifts from diurnal to semi-diurnal, the spatial patterns in the occurrence of strong convergent features is matched by similar shifts in penguin foraging locations. While penguin foraging locations and the occurrence

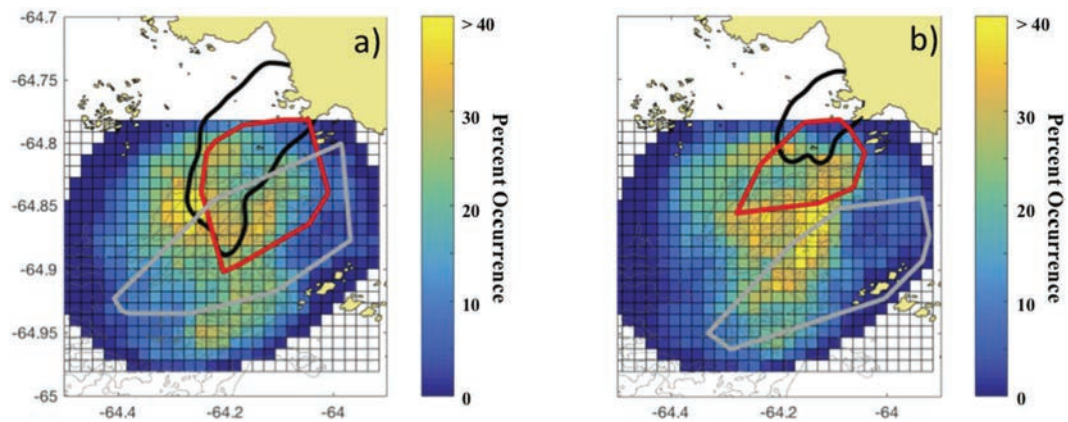


**Figure 4.** Maps of the percent of occurrence of the convergent features based on RPD (number of particles minus median  $> 100$ ) observed during (a) semi-diurnal and (b) diurnal days. The spatial density kernels (black contours) based on 10 years of tagged Adélie data are shown in panel a) for the semi-diurnal days and in panel b) for diurnal days<sup>25</sup>. The convex hulls for the 2015 Adélie (red) and gentoo (grey) ARGOS locations are also shown. In 2015, Adélie penguins also foraged closer to their home colony during diurnal, compared to semi-diurnal tides. The maps were generated by the corresponding author J.K. using Matlab version R2016b ([www.mathworks.com](http://www.mathworks.com)).

of convergent features covaried with tidal regime (Fig. 4), we show that both Adélie and gentoo penguins were specifically selecting for stronger surface convergent zones than were available based on simulations, suggesting the importance of these features at the scale of the individual. Despite the different typical dive depths exhibited by these two species, both the shallow-diving Adélie and deeper-diving gentoo penguins selected for surface convergent features (Fig. 3).

Penguins in the Palmer Deep canyon region travel relatively short distances ( $\sim 8$ – $25$  km) during foraging trips compared to penguins breeding in many other locations, where foraging distances may reach up to  $100$  km<sup>36</sup>. These short foraging distances are also combined with the persistence of foraging locations across both tidal regimes, suggesting that these penguins may not need to use environmental cues to initiate foraging behavior; that is, they are simply returning to the same general location to find prey because the prey field spans the entire area. However, we argue that this is not always the case. Although the prey-scape was not spatially resolved in this study, previous vessel and AUV acoustic surveys in the region report typical krill patch length scales on the order of  $40$  m<sup>12,37</sup>. These patches are dispersed hundreds of meters apart across the  $+20$  km foraging range of the local Adélie and gentoo colonies<sup>12</sup>. This spacing by itself might suggest that both Adélie and gentoo penguins could return to the same foraging ground and be successful, independent of foraging cues. However, measurements of the residence time of this region indicate that the surface layer is replaced on average every two days, and can be as short as  $18$  hours<sup>38</sup>. This leads to a very patchy and rapidly evolving prey environment within the penguin foraging range that is simultaneously targeted by other species including whales and seals. Therefore, the rapid replacement of the surface layer may necessitate individual foraging responses triggered by oceanographic conditions at the scale of the individual, along with memory of recent successful foraging trips, or social cues from other foragers<sup>5</sup>.

At Palmer Station, Adélie penguins are often relatively shallow divers ( $< 50$  m)<sup>39</sup> compared to gentoo penguins that often dive deeper ( $< 100$  m)<sup>37,40</sup>. Gentoo penguins are the larger of the two species and consequently have a greater scope for maximum diving depth, even though Adélie penguins are capable of dives to similar depths<sup>41</sup>. During our study, Adélie penguins not only selected for stronger surface convergent features compared to their availability, but their foraging was also limited to the surface mixed layer. In contrast, gentoo penguins foraged both above and below the surface mixed layer, with some dives as deep as  $150$  m, yet also selected for stronger surface convergent features. We suggest that despite the variable foraging dive depths relative to the mixed layer, both species use surface layer convergent features as foraging cues.

ARGOS locations associated with foraging behavior for both species had consistently higher RPD compared to simulated penguins and background RPD suggesting that convergent features may cue foraging behavior. What is less clear is the impact of higher RPD for transiting Adélie and gentoo penguins. Gentoo penguins showed little selectivity for increased RPD during transiting behavior, with only one exception, suggesting that perhaps gentoo penguins are using past foraging experiences to get to a general foraging region before selecting for higher RPD values at finer spatial scales. Transiting Adélie penguins, however, showed some selectivity for higher RPD compared to background concentrations. As the time window we used to behaviorally classify ARGOS locations widened (Table 1), all but two ARGOS locations were considered to be associated with foraging behavior, suggesting foraging behavior could be interspersed throughout a foraging trip. It has been shown previously that ARGOS locations without diving behavior were strongly coherent with ARGOS locations with diving behavior in this location for Adélie penguins<sup>22</sup>.

The link between the occurrence of strong convergent features and the foraging behavior of satellite-tagged penguins raises important questions about the coupling mechanisms operating throughout the entire food web. These convergent features may coincidentally concentrate or attract krill in the surface layer, and trigger penguin

foraging behavior, irrespective of whether penguins are shallow- or deep-diving. This would be consistent with a penguin that repeatedly dives in the same location once a prey patch is found<sup>5</sup>. Alternatively, there may be different physical mechanisms that concentrate prey above and below the mixed layer. For example, barotropic tides influence the entire water column, while the seasonal surface mixed layer circulation is likely driven by local winds<sup>38</sup> but retains a tidal signal when integrated over the foraging season. Below the mixed layer, circulation is likely driven by the bathymetric steering of density currents along isobaths (i.e. along  $f/H$  contours), suggesting the influence of the Palmer Deep canyon. Critically, these depth-dependent features could be co-located with deeper gentoo prey aggregations, thus explaining why deep-diving penguins appear to be selecting for higher surface convergence, even though they are feeding well below the surface mixed layer. Another speculative possibility that could explain why deep diving penguins selected for higher surface RPD, is that they may select convergent features independently of visual prey detection. Dimethylsulphoniopropionate is released from grazed phytoplankton, which is volatilized in the ocean surface as dimethyl sulphide (DMS)<sup>42</sup>, and is not necessarily correlated to surface phytoplankton concentrations<sup>43</sup>. Krill-consuming chinstrap penguins (*P. antarctica*), for example, have been shown to be attracted to DMS<sup>44</sup>, and African penguins (*Spheniscus demersus*) have been shown to use DMS as a foraging cue<sup>45</sup>. If surface RPD values are a proxy for higher DMS, this may explain why deep diving gentoo penguins select for higher RPD values.

Given our results, we believe that physical factors like surface convergent features are an important mechanism that influences penguin foraging locations, and are therefore a critical feature influencing the maintenance of the Palmer Deep biological hotspot for penguins. Convergent fronts likely concentrate krill, the primary prey of penguins<sup>46</sup> in this region. This example of tight coupling from the hydrography through the lower trophic levels to foraging penguins shows the important role that these physical features may have on the coastal Antarctic food web. If these features are commonly targeted by predators, they may represent a key physical mechanism that is critical for the persistence of the Palmer Deep biological hotspot over the last 1000 years<sup>34</sup>, despite known climate and environmental variability. However, because this study did not simultaneously resolve the distribution of krill and all of their major predators, there is still much work to be done to understand how important prey convergence is relative to other factors affecting prey distributions. Even though both penguin species selected, on average, for higher convergence zones, both also utilized a wide range of particle densities. This suggests to us that there are other important factors, in addition to surface convergence, affecting foraging behavior. One possibility is the top-down impact of other krill predators. For example, Adélie penguins at Cape Crozier in the Ross Sea increased their foraging duration and dove deeper as krill were removed by predation near the colony<sup>47</sup>, suggesting a significant top-down control on penguin foraging location. In our study, we also observed a deepening of forage depths by Adélie penguins (Fig. 3c). Because this study did not resolve the distribution of krill, or account for other krill predators like whales, it is difficult for us to tell if prey depletion was an important factor in this study. One important difference between the colonies at Cape Crozier and those at Palmer Deep is that of colony size; the colonies in the Ross Sea that showed the prey depletion effect are two orders of magnitude larger than those near Palmer Deep. Because of this, we speculate that top-down effects like prey depletion play a relatively smaller role in determining foraging location near Palmer Deep. However, the relative importance of bottom up physical concentration factors and top down biological factors on penguin foraging remains an open and important question for understanding how these ecosystems may change in the future.

## Materials and Methods

**High Frequency Radar (HFR).** HFR systems, typically deployed along the coast use Bragg peaks within a transmitted signal (3–30 MHz) scattered off the ocean surface to calculate radial components of the surface velocity at a given location<sup>48</sup>. Individual sites, composed of electronics, cables and a transmit and receive antenna, generate maps of surface component vectors directed toward the antenna with range resolution of 500 m horizontally and 5 degrees in azimuth. To provide sufficient coverage over the penguin foraging grounds associated with Palmer Deep, a three-site HFR network was deployed in November 2014 (Fig. 2). The first site was deployed at and powered by Palmer Station. The other two sites, deployed at the Joubin and Wauwermans Islands, relied on remote power systems that were constructed on site, lightered to shore via zodiac with ship support. Remote Power Modules (RPMs) generated the required power for the HFRs through a combination of small-scale micro wind turbines and a photovoltaic array with a 96-hour battery backup<sup>19</sup>. The RPMs consisted of a single water-tight enclosure, used to house power distribution equipment, the HFR, and the communication gear. Built-in redundancies within the RPMs, including wind charging/resistive loads, solar energy, and independent battery banks ensured that, should any one component fail, the unit would be able to adjust autonomously. Each site also collected 15-minute meteorological measurements of air temperature, wind, relative humidity, and solar radiation. Communication between the two remote sites and Palmer Station was with line of sight radio modems (Freewave), which enabled remote site diagnostics and maintenance and provided a real-time data link.

The three-site network collected hourly measurements of ocean surface current component vectors throughout the penguin foraging season (November 2014 through March 2015). Every hour, the radial components from each site were combined into two-dimensional vector maps using the optimal interpolation algorithm of<sup>49</sup>. Throughout the time of active penguin foraging, a roughly 1,500 km<sup>2</sup> area of ocean over Palmer Deep was covered greater than 80% of the time with hourly maps of surface ocean circulation. The evolution of these current fields was used to identify convergent features, including fronts and eddies, relative to known penguin foraging.

**Surface Convergent Features.** Various metrics have been used to map ocean convergent features. Maps of Lagrangian Coherent Structures (LCS), specifically Finite-Time Lyapunov Exponent (FTLE) and Finite-Space Lyapunov Exponent (FSLE) have seen greater application to marine ecological studies<sup>14,16,50,51</sup>. While these metrics often delineate boundaries in a fluid that distinguish regions with differing dynamics<sup>52</sup> they are based on an

assumption that the input velocity fields are horizontally non-divergent (i.e. zero vertical velocity). The highly resolved current maps provided by the HFR network deployed over Palmer Deep display complex currents that do not meet this important criterion for both FTLE and FSLE. Consequently, we define a more appropriate metric to map the convergent features within our study site consistent with the dynamics captured by the HFR surface current maps.

To objectively map the time and location of convergent ocean features in the mapped surface current time series, we used a metric derived from simulated particle releases in the HFR surface current fields. Our relative particle density (RPD) metric is calculated based on the movement of simulated particles released in the HFR footprint and tracked over time. Each hour, we released simulated particles over a  $200 \times 200$  m grid over the HFR footprint. The Lagrangian particles were advected in the HFR velocity field with a 4<sup>th</sup>-order Runge-Kutta integration scheme for a period of 48 hours. In our application, we compute hourly maps of RPD from  $t_1$  = December 31, 2014, to  $t_N$  = February 19, 2015 (spanning the date range that penguins were tagged and actively foraging).

The hourly RPD was determined by the number of particles within  $1 \times 1$  km boxes within the overlapping HFR coverage and penguin foraging grounds (Fig. 2b). To minimize the effect of the grid on the particle densities, only particles in the field for at least 6 hours were included in the count. To correct for time varying residence time of particles throughout the study period<sup>38</sup>, each count was normalized by subtracting the median count across all 1 km boxes within the field for each time step (Fig. 2b), termed RPD for the purposes of this analysis.

**Slocum Glider.** Gliders are buoyancy driven vehicles that dive and climb at a nominal 26° angle and travel in a vertical “sawtooth” pattern between predetermined surface events<sup>49</sup>. Glider-based sampling provided a continuous presence, through all weather conditions, over the spatial domain identified by the HFR network. Simultaneous measurements of physical and biological variables from the gliders sampled the spatial and temporal variability over Palmer Deep. A glider was programmed to complete a mission as a virtual mooring between January 5, 2015 to February 26, 2015 (Fig. 1), diving between the surface and 100 m. The glider was equipped with a sensor suite to characterize the ecosystem’s physical structure (Seabird C, T, D). This glider provided the time series of mixed layer depth throughout the penguin foraging time period used in this analysis<sup>20</sup>.

**Penguin Tagging and Dive Analysis.** From January 5 to 28, 2015, we deployed ARGOS satellite transmitters on 12 Adélie penguins (8 female, 4 male) that nested on Torgersen Island (64°46’S, 64°5’W), and from January 27 to February 7, 2015, we deployed satellite transmitters on 7 gentoo penguins (2 female, 5 male) at Biscoe Point (64°49’S, 63°46’W). All protocols were carried out in accordance with the approved guidelines of the Columbia University Institutional Animal Care and Use Committee (Assurance #AAAH8959). Tagged penguins were paired and had brood-stage nests containing two chicks. Penguins were equipped with SPOT 5 satellite transmitters (Wildlife Computers Redmond, WA, USA) and Lotek LAT1400 time-depth recorder (Lotek Wireless, Inc, St. John’s Canada; resolution of 0.05 m, accuracy of 2 m) sampling at 2 Hz. Dive depths less than 5 m were not recorded to save space on the memory cards. Transmitters were attached to the anterior feathers on the lower dorsal region using waterproof tape and small plastic zip ties. Transmitters were removed and rotated to new penguins every 3–5 days dependent on weather conditions. Penguin locations were filtered to remove inaccurate location data due to erroneous terrestrial positions, unreasonable locations based on swimming speed and coastal geometry, following published the data processing methods<sup>37</sup>. We time-matched dive records to location data and the maximum dive depth was determined for each dive. Penguin dives were classified into transit, search and foraging dives, where foraging dives consisted of wiggles, plateaus or bottom time where prey was likely pursued (see<sup>37</sup> for more information). The convex hulls of penguin locations were computed using *chull* in the *grDevices* package<sup>53</sup>.

**Penguin Habitat Selectivity Statistical Tests.** We compared the distribution of penguin ARGOS locations to distributions of available RPD values using two-sided Kolmogorov-Smirnov tests (*ks.test* in the *stats* package)<sup>53</sup> to test for habitat selectivity. Penguin selectivity is inferred from the distributional differences between RPD values at penguin ARGOS locations. Several considerations are needed for comparing penguin ARGOS locations to RPD simulations. For this analysis, we used ARGOS classes 1–3 (estimated accuracy is 350–1000 m, 150–350 m and <150 m, respectively), which have errors similar to, or smaller than the RPD grid cells. Penguins periodically haul-out on sea ice or islands during their foraging trips, so we restricted our analysis to ARGOS locations where the wet sensors were triggered and were within the field of computed RPD values. We used two estimates of available habitat for Adélie and gentoo penguins. The first estimate of available RPD habitat is the entire RPD HFR field over Palmer Deep during the times the penguins were foraging, because both Adélie and gentoo penguins are capable of traversing the entire RPD field in a single foraging trip. The second estimate of available RPD habitat was based on simulated Brownian motion of central place foragers (*simmm.bb* in the *adehabitatLT* R package)<sup>54</sup>, nesting at the Adélie and the gentoo penguin colonies (Fig. 1). We simulated two penguins per day from each colony, which was similar to the tagging effort during the field season. A 10-year analysis of foraging trip duration showed that these penguins take forage trips up to 48 hours, but most are 6–24 hr<sup>22</sup>. Simulated foraging trip duration was limited to 24 hr in one hour time steps, and the simulated penguin speeds were normally distributed around a mean of 4 km hr<sup>−1</sup>, and a maximum of 8 km hr<sup>−1</sup> to mimic Adélie and gentoo penguin swimming speeds<sup>55</sup>. Brownian motion is an uncorrelated movement that represents random foragers not selecting for environmental features, remembering previous feeding locations, or cuing off of other environmental proxies. We used these simulated penguin locations as a null metric of available RPD values by a non-selecting central place forager originating from the Adélie and gentoo penguin nesting sites.

The possibility of individual effects in tagging studies is a persistent problem reflected in their foraging trips or individual behavior. To deal with the possibility of foraging trip level effects driving the results of the of the



Kolmogorov-Smirnov tests, we systematically withheld individual foraging trips and individual penguins from our analysis to test the sensitivity of our results to individuals foraging trips being withheld from the analysis.

## Data Availability

The HFR datasets are archived and accessible through the United States National HF radar archive housed at the National Oceanic and Atmospheric Administration (NOAA) National Data Buoy Center (NDBC): <http://hfradar.ndbc.noaa.gov/>. Additionally, the post-processed raw and de-tided total vector maps can be accessed via the Rutgers HFR Environmental Research Division Data Access Program (ERRDAPP) Service: <http://hfr.marine.rutgers.edu/>. The other datasets including the glider and penguin tagged data are available from the corresponding author on reasonable request, as some of these data are still in use for student dissertations.

## References

- Pyke, G. H. Optimal foraging theory: a critical review. *Annu Rev Ecol Syst* **15**, 523–575 (1984).
- Berg, H. C. *Random Walks in Biology* (Princeton University Press, Princeton, NJ, 1983).
- Klafter, J. & Sokolov, I. M. Anomalous diffusion spreads its wings. *Physics world* **18**, 29 (2005).
- Okubo, A. & Levin, S. A. *Diffusion and ecological problems: modern perspectives* (Springer, New York, 2001).
- Ford, R. G. *et al.* Testing assumptions of central place foraging theory: a study of Adélie penguins *Pygoscelis adeliae* in the Ross Sea. *J Avian Biol* **46**, 193–205 (2015).
- Viswanathan, G. M., Buldyrev, S. V., Havlin, S. & Da Luz, M. G. E. Optimizing the success of random searches. *Nature* **401**, 911 (1999).
- Palyulin, V. V., Chechkin, A. V. & Metzler, R. Lévy flights do not always optimize random blind search for sparse targets. *Proc Natl Acad Sci USA* **111**, 2931–2936 (2014).
- Benhamou, S. How many animals really do the Levy walk. *Ecology* **88**, 1962–1969 (2007).
- Nathan, R. *et al.* A movement ecology paradigm for unifying organismal movement research. *Proc Natl Acad Sci USA* **105**, 19052–19059 (2008).
- Reynolds, A. M. & Rhodes, C. J. The Lévy flight paradigm: random search patterns and mechanisms. *Ecology* **90**, 877–887 (2009).
- Atkinson, A. *et al.* Oceanic circumpolar habitats of Antarctic krill. *Mar Ecol Prog Ser* **362**, 1–23 (2008).
- Bernard, K. S. *et al.* Factors that affect the nearshore aggregations of Antarctic krill in a biological hotspot. *Deep-Sea Res Part I* **126**, 139–147 (2017).
- Bernard, K. S. & Steinberg, D. K. Krill biomass and aggregation structure in relation to tidal cycle in a penguin foraging region off the Western Antarctic Peninsula. *ICES J Mar Sci* **70**, 834–849 (2013).
- Harrison, C. S., Siegel, D. A. & Mitarai, S. Filamentation and eddy— eddy interactions in marine larval accumulation and transport. *Mar Ecol Prog Ser* **472**, 27–44 (2013).
- Hyrenbach, K. D., Veit, R. R., Weimerskirch, H. & Hunt, G. L. Seabird associations with mesoscale eddies: the subtropical Indian Ocean. *Mar Ecol Prog Ser* **324** (2006).
- Kai, E. T. *et al.* Top marine predators track Lagrangian coherent structures. *Proc Natl Acad Sci USA* **106**, 8245–8250 (2009).
- Bon, C. *et al.* Influence of oceanographic structures on foraging strategies: Macaroni penguins at Crozet Islands. *Mov Ecol* **3**, 32 (2015).
- Schofield, O. *et al.* How do polar marine ecosystems respond to rapid climate change? *Science* **328**, 1520 (2010).
- Kohut, J. *et al.* Studying the impacts of local oceanographic processes on Adélie Penguin foraging ecology. *Mar Technol Soc J* **48**, 25–34 (2014).
- Carvalho, F., Kohut, J., Oliver, M. J. & Schofield, O. Defining the ecologically relevant mixed-layer depth for Antarctica's coastal seas. *Geophys Res Lett* **44**, 338–345 (2017).
- Carvalho, F., Kohut, J., Oliver, M. J., Sherrell, R. M. & Schofield, O. Mixing and phytoplankton dynamics in a submarine canyon in the West Antarctic Peninsula. *J Geophys Res C* **121**, 5069–5083 (2016).
- Oliver, M. J. *et al.* Adélie Penguin Foraging Location Predicted by Tidal Regime Switching. *PLoS One* **8**, e55163 (2013).
- Amos, A. F. RACER: the tides at Palmer Station. *Antarct J US* **28**, 162–164 (1993).
- Moffat, C., Owens, B. & Beardsley, R. C. On the characteristics of Circumpolar Deep Water intrusions to the west Antarctic Peninsula continental shelf. *J Geophys Res C* **114** (2009).
- Martinson, D. G. & McKee, D. C. Transport of warm Upper Circumpolar Deep Water onto the western Antarctic Peninsula continental shelf. *Ocean Sci* **8**, 433 (2012).
- Dinniman, M. S. & Klinck, J. M. A model study of circulation and cross-shelf exchange on the west Antarctic Peninsula continental shelf. *Deep Sea Research Part II: Topical Studies in Oceanography* **51**, 2003–2022 (2004).
- Prézelin, B. B., Hofmann, E. E., Moline, M. & Klinck, J. M. Physical forcing of phytoplankton community structure and primary production in continental shelf waters of the Western Antarctic Peninsula. *J Mar Res* **62**, 419–460 (2004).
- Saba, G. K. *et al.* Winter and spring controls on the summer food web of the coastal West Antarctic Peninsula. *Nat Commun* **5**, <https://doi.org/10.1038/ncomms5318> (2014).
- Steinberg, D. K. *et al.* Long-term (1993–2013) changes in macrozooplankton off the Western Antarctic Peninsula. *Deep-Sea Res Part I* **101**, 54–70 (2015).
- Hofmann, E. E., Klinck, J. M., Locarnini, R. A., Fach, B. & Murphy, E. Krill transport in the Scotia Sea and environs. *Antarct Sci* **10**, 406–415 (1998).
- Piñones, A., Hofmann, E. E., Daly, K. L., Dinniman, M. S. & Klinck, J. M. Modeling environmental controls on the transport and fate of early life stages of Antarctic krill (*Euphausia superba*) on the western Antarctic Peninsula continental shelf. *Deep-Sea Res Part I* **82**, 17–31 (2013).
- Piñones, A., Hofmann, E. E., Daly, K. L., Dinniman, M. S. & Klinck, J. M. Modeling the remote and local connectivity of Antarctic krill populations along the western Antarctic Peninsula. *Mar Ecol Prog Ser* **481**, 69–92 (2013).
- Kavanaugh, M. T. *et al.* Effect of continental shelf canyons on phytoplankton biomass and community composition along the western Antarctic Peninsula. *Mar Ecol Prog Ser* **524**, 11–26 (2015).
- Emslie, S. D., Fraser, W., Smith, R. C. & Walker, W. Abandoned penguin colonies and environmental change in the Palmer Station area, Anvers Island, Antarctic Peninsula. *Antarct Sci* **10**, 257–268 (1998).
- Friedlaender, A. S., Fraser, W. R., Patterson-Fraser, D. L., Qian, S. S., & Haplin, P. N. The Effects of Prey Demography on Cetacean Community Structure Around the Western Antarctic Peninsula. *Polar Biol* in press (2008).
- Williams, T. D. *The penguins* (Oxford University Press, 1995).
- Cimino, M. A., Moline, M. A., Fraser, W. R., Patterson-Fraser, D. L. & Oliver, M. J. Climate-driven sympatry may not lead to foraging competition between congeneric top-predators. *Sci Rep* **6**, <https://doi.org/10.1038/srep18820> (2016).
- Kohut, J. T. *et al.* Variability in summer surface residence time within a West Antarctic Peninsula biological hotspot. *Philosophical Transactions of the Royal Society A*, <https://doi.org/10.1098/rsta.2017.0165> (2018).

39. Chappell, M. A., Shoemaker, V. H., Janes, D. N., Bucher, T. L. & Maloney, S. K. Diving behavior during foraging in breeding Adélie penguins. *Ecology* **74**, 1204–1215 (1993).
40. Croxall, J. P., Davis, R. W. & O'Connell, M. J. Diving patterns in relation to diet of gentoo and macaroni penguins at South Georgia. *Condor* **157**–167 (1988).
41. Schreer, J. F. & Kovacs, K. M. Allometry of diving capacity in air-breathing vertebrates. *Can J Zool* **75**, 339–358 (1997).
42. Dacey, J. W. H. & Wakeham, S. G. Oceanic dimethylsulphide: production during zooplankton grazing on phytoplankton. *Science* **233**, 1314–1316 (1986).
43. Kwint, R. L. J. & Kramer, K. J. M. Annual cycle of the production and fate of DMS and DMSP in a marine coastal system. *Mar Ecol Prog Ser* **217**–224 (1996).
44. Amo, L., Rodríguez-Gironés, M. Á. & Barbosa, A. Olfactory detection of dimethyl sulphide in a krill-eating Antarctic penguin. *Mar Ecol Prog Ser* **474**, 277–285 (2013).
45. Wright, K. L. B., Pichegru, L. & Ryan, P. G. Penguins are attracted to dimethyl sulphide at sea. *J Exp Biol* **214**, 2509–2511 (2011).
46. Cimino, M. A., Fraser, W. R., Patterson-Fraser, D. L., Saba, V. S. & Oliver, M. J. Large-scale climate and local weather drive interannual variability in Adélie penguin chick fledging mass. *Mar Ecol Prog Ser* **513**, 253 (2014).
47. Ainley, D. G. *et al.* Trophic cascades in the western Ross Sea, Antarctica: revisited. *Mar Ecol Prog Ser* **534**, 1–16 (2015).
48. Barrick, D. E., Evans, M. W. & Weber, B. L. Ocean surface currents mapped by radar. *Science* **198**, 138–144 (1977).
49. Kim, S. Y., Terrill, E. & Cornuelle, B. Objectively mapping HF radar-derived surface current data using measured and idealized data covariance matrices. *J Geophys Res C* **112** (2007).
50. Della Penna, A., De Monte, S., Kestenare, E., Guinet, C. & d'Ovidio, F. Quasi-planktonic behavior of foraging top marine predators. *Sci Rep* **5** (2015).
51. Maps, F. *et al.* Linking acoustics and finite-time Lyapunov exponents reveals areas and mechanisms of krill aggregation within the Gulf of St. Lawrence, eastern Canada. *Limnol Oceanogr* **60**, 1965–1975 (2015).
52. Haller, G. Lagrangian coherent structures. *Annu Rev Fluid Mech* **47**, 137–162 (2015).
53. R Development Core Team. *R: A language and environment for statistical computing* (R Foundation for Statistical Computing, Vienna, Austria, 2014).
54. Calenge, C. The packaged adehabitat for the R software: a tool for the analysis of space and habitat use by animals. *Ecol Model* **197**, 516–519 (2006).
55. Ainley, D. G. *The Adélie Penguin: Bellwether of Climate Change* (Cambridge University Press, New York, 2002).

## Acknowledgements

This project was funded through the National Science Foundation, award # ANT 1327248, with additional support provided by award # OPP-1440435 to WRF. We are grateful to the Antarctic Support Contractor and their teams, both in Denver, CO, aboard the ARSV Laurence M. Gould, and at Palmer Station, without whom a project such as ours would be impossible. We also thank the students and field assistants for their valued involvement in the CONVERGE project. Finally, we thank the Palmer Antarctica Long-Term Ecological Research team, for their advice, suggestions and collaboration.

## Author Contributions

H.F. radar data collection and analysis was done by J.K., P.W., H.S. and F.C., and E.F. M.O., W.F., D.P.-F., and K.B., and M.C. lead the penguin data analysis relative to the HFR and glider observations. All authors contributed text to and reviewed the complete document.

## Additional Information

**Competing Interests:** The authors declare no competing interests.

**Publisher's note:** Springer Nature remains neutral with regard to jurisdictional claims in published maps and institutional affiliations.



**Open Access** This article is licensed under a Creative Commons Attribution 4.0 International License, which permits use, sharing, adaptation, distribution and reproduction in any medium or format, as long as you give appropriate credit to the original author(s) and the source, provide a link to the Creative Commons license, and indicate if changes were made. The images or other third party material in this article are included in the article's Creative Commons license, unless indicated otherwise in a credit line to the material. If material is not included in the article's Creative Commons license and your intended use is not permitted by statutory regulation or exceeds the permitted use, you will need to obtain permission directly from the copyright holder. To view a copy of this license, visit <http://creativecommons.org/licenses/by/4.0/>.

© The Author(s) 2019

## Chapter 20

# Developments in Compact HF-Radar Ocean Wave Measurement

**Belinda Lipa, Maeve Daugharty, Maria Fernandes,  
Donald Barrick, Andres Alonso-Martirena, Hugh Roarty,  
Jaden Dicopoulos and Chad Whelan**

### 20.1. Introduction

The potential of high frequency (HF) radar devices for the remote measurement of sea-surface parameters has been recognized since Crombie [1] observed and identified the distinctive features of sea-echo Doppler spectra. Barrick [2] modeled the first-order Bragg scatter from waves of half the radar wavelength moving toward and away from the transmitter to obtain data on surface currents. Analysis [3] of the second order spectral echoes that surround these Bragg peaks showed that they contain detailed information on the ocean-wave spectrum, which can be used to monitor sea state. Coastal HF radars that observed sea echo first followed conventional radar practice of forming and scanning a relatively narrow beam in bearing. This involved phased-array receive antennas hundreds of meters long, many dating back 50 years, that were also considered for beyond-the-horizon military target detection. By phasing signals from these antenna elements, a beam was scanned in software. A separate broad-beam transmit antenna usually illuminated the sector seen by the receive array antenna ( $\pm 45^\circ$ ). For example, the British Pisces [4] was demonstrated for sea- surface monitoring.

In many locations it was difficult to obtain permits for the use of large conventional phased arrays, which led to the development of smaller broad-beam systems for use in current velocity mapping [5]. Sea-state extraction from the weaker second-order echo has had a more protracted evolution as this is a more difficult challenge. Numerous research papers document this 40-year history. We here describe two approaches to sea-state extraction and provide our assessment of present operational readiness.

SeaSonde radars are used primarily for surface-current measurement, based on analysis of the first-order radar spectral echo. Wave parameters are derived from the portion of the

---

Belinda Lipa  
Codar Ocean Sensors, Mountain View, CA, USA

weaker second-order radar Doppler echo that lies above the noise floor, meaning that analysis for wave information is restricted to closer ranges than for currents. If a pair of radars were required to map wave information, as is the case for total current vectors, there would be a difficult tradeoff in the spacing of the radars. The smaller, common coverage area for waves demands a smaller spacing that is far from optimal for currents. Thus a radar pair spaced for waves would reduce the effective current-mapping area by a large factor, because of geometrical dilution of precision: measured radial current vectors at a point on the map cannot be too close to parallel, as then robust total vectors cannot be produced. For this reason, the wave extraction methods for the SeaSonde apply to a single radar site, so pair-spacing does not come into consideration.

For compact, crossed-loop antennas, methods were developed over a decade ago to apply where shallow water does not affect wave dispersion and second-order scatter. Only a single radar is needed to give local wave information, allowing operation from an offshore platform or small island. At present, wave information is derived from radar echo from each range cell, assuming ocean wave spectral homogeneity over the area covered. When wave fields are not perfectly homogeneous around more distant semi-circular range cells, the methods produce an average of the output parameters. These could be weighted toward angle sectors where the signal-to-noise ratio is stronger. In practice, checks are done to find the limiting range where the output wave parameters begin to change. This range limit needs to be set using our present method in order to maintain homogeneity. Similarly, the radar spectra at the inner ranges are checked for changes due to shallow water, and the affected range cells are not used for wave analysis. There will be always a need to analyze each station individually before clearing it for operational waves measurement use.

Having derived exact expressions relating the second-order Doppler spectrum to wave spectra 45 years ago [2], it was anticipated that detailed directional sea-state information could be derived at many points on a radar coverage map. Years of mathematical attempts have shown this is not the case: robustness of wave information was consistently lacking. Lipa and Barrick [6] developed simulations to give the wave-height directional spectrum at each grid point by looking with two overlapping radars, just as with current mapping. In practice detailed wave spectral information was not consistently produced; this was found also in [7] for narrower-beam phased arrays. One reason, as we explain in the following section, appears to be current smearing inherent in the second-order echo that is needed for wave extraction. This has led us to seek a simpler model-fit method that seeks considerably less information from the radar echo.

Lipa and Nyden [8] reported on two extraction methods applied to measured broad-beam radar cross spectra, assuming ideal antenna patterns. The first involved deriving a non-directional wave energy spectrum by inversion. This was tried in several locations and radar frequencies. However this was not found to be sufficiently robust in practice, and is not applied in operational use. The second method has proven robust; this involves the fitting of a Pierson-Moskowitz (P/M) wave energy model to the radar echo Doppler spectrum. Wind direction is derived from the first-order Doppler spectrum. Analysis of the weaker second-order spectrum produces estimates of significant waveheight, centroid



period and wave direction. This method has been in operational use for over a decade at several radar sites. Using this method, Long et al. [9] provide favorable comparisons over several years of results from five compact HF radar systems with four buoys. In one sense, this is surprising because the P/M model describes a unimodal energy spectrum derived for fully developed seas, which would seem to be the case a fraction of the time on the ocean. Perhaps it is the simplicity of this model and the small number of parameters involved that has contributed to its success.

New techniques reported here use measured antenna patterns, rather than assuming that the antenna patterns are ideal, when in fact they are always distorted to some degree. Wave parameters are optimized by defining the wave directions for both onshore and offshore wave directions. However, recent testing using this simple model at different sites has uncovered situations where it is inadequate, resulting in significant overestimation of the waveheight. Examination of the second-order Doppler spectral region and energy spectra from wave buoys revealed the reason: the frequency spectrum can be bimodal or multimodal, meaning that it displays two or more distinct peaks, e.g. from swell and wind waves. We are in the process of extending the analysis methods to begin to handle these more complex bimodal scenarios and here present initial results from a radar located at Espichel, Portugal.

Section 20.2 of this chapter describes the theory of HF radar spectra in terms of the P/M ocean wave spectrum and the antenna patterns, first for narrow-beam radars and then for compact broad-beam radars. Methods that involve the use of measured antenna patterns are described in Section 20.3. Section 20.4 describes the analysis methods used to derive ocean wave parameters from the radar spectra and discusses the effects of varying ocean surface currents on the results. Section 20.5 shows results from application of the methods to five radar sites, including comparison with results from neighboring buoys. Section 20.6 describes the extension of analysis methods to use bimodal ocean wave spectral models.

## 20.2. Radar Spectral Theory

We assume that the waves producing the second-order scatter do not interact with the ocean floor. This requires the following approximate condition for water depth over most of the radar range ring [10]:

$$\frac{2\pi d}{L} > 0.8, \quad (20.1)$$

where  $d$  is the water depth and  $L$  is the dominant ocean wavelength.

Broad-beam radars provide robust measurements of ocean surface currents, which are obtained from the dominant first-order peaks in the radar echo spectrum. The derivation of wave information from the second-order radar spectrum is more fragile, partly because the lower-energy second-order spectrum is closer to the additive noise floor. Another source of contamination is the near-surface sub-grid-scale current variability, because this is convolved with the second-order Doppler echo energy. In addition, for the high wave

conditions of greatest interest, the radar spectrum saturates when the waveheight exceeds a limit defined by the radar transmit frequency. Beyond this limit, two problems set in: (i) the first- and second-order regions of the radar echo spectrum can merge together; (ii) the analysis methods described below cease to apply. At present, such saturated radar spectra are not amenable to analysis. When normal interpretation methods are applied to saturated spectra, waveheight can be underestimated, as noted by Lipa and Barrick [6]. The perturbation-theory saturation limit on the significant waveheight is defined approximately by the relation:

$$h_{sat} = \frac{2}{k_0}, \quad (20.2)$$

where  $k_0$  is the radar wavenumber. For a standard-range transmit frequency of 13 MHz, the value of  $h_{sat}$  is 7.4 m; this value increases to 20 m for the long-range transmit frequency of 5 MHz. Hence, the quantitative measurement of extremely high waves requires the use of lower-frequency, long-range systems

### 20.2.1. Narrow-Beam Radar Cross Section

Barrick [2] showed that the narrow-beam first-order radar cross section  $\sigma^1(\omega, \phi)$  at frequency  $\omega$  and azimuthal direction  $\phi$  is defined in terms of the ocean wave spectrum at the Bragg wavenumber by the relation:

$$\sigma^1(\omega, \phi) = k_0^4 \sum_{m'=\pm 1} S\left(2k_0, \phi + (m' + 1)\frac{\pi}{2}\right) \partial(\omega - m'\omega_B - 2k_0 v_r(\phi)), \quad (20.3)$$

where  $S(k, \phi)$  is the directional ocean wave spectrum for wavenumber  $k$  and direction,  $v_r(\phi)$  is the radial current velocity at bearing angle  $\phi$  and  $\omega_B$  is the Bragg frequency given by  $\sqrt{2gk_0}$ , where  $g$  is the gravitational constant.

Barrick [3] gives the narrow-beam second-order radar cross-section as

$$\sigma^2(\omega, \phi) = k_0^4 \sum_{m, m'=\pm 1} \int_0^{2\pi} \int_{-\infty}^{\infty} [\Gamma^2] S(k, \theta + \phi + m\pi) S(k', \theta + \phi + m'\pi) \\ \partial(\omega - m\sqrt{gk} - m'\sqrt{gk'} - 2k_0 v_r(\phi)) k dk d\theta, \quad (20.4)$$

where  $\Gamma$  is the radar coupling coefficient, which is the incoherent sum of hydrodynamic and electromagnetic terms and  $k, k'$  are the wavenumbers of the two scattering ocean waves [3]. The values of  $m$  and  $m'$  in (20.4) define the four possible combinations of direction of the two scattering waves and also the four sidebands that surround the first-order peaks, see Lipa and Barrick, [6]. Using tildes to indicate vector quantities, the two ocean wave vectors obey the constraint:

$$\tilde{k} + \tilde{k}' = -2\tilde{k}_0. \quad (20.5)$$

When the waveheight exceeds the saturation limit, the perturbation expansions on which Barrick's equation (20.4) is based fail to converge.

In this chapter, and in all previous work on the derivation of wave parameters from HF radar sea-echo, the effect of surface current velocities is ignored. It is included in (20.3) and (20.4) for purposes of discussion.

### 20.2.2. Broad-Beam Radar Cross Spectra

In this chapter we focus the analysis on SeaSonde broad beam systems [11], for which data is available from a diverse set of sites. The basic SeaSonde data set consists of complex frequency cross spectra measured by two crossed loop antennas and a monopole antenna, all coaxially collocated. The radar echo spectrum from circular range cells over the coverage area consists of dominant peaks produced by first-order Bragg scatter from waves with one half the radar wavelength, surrounded by lower-energy sidebands produced by second-order scatter, as shown in Fig. 20.1. The first-order peaks at positive/negative Doppler frequencies come from advancing/receding Bragg waves, as seen within a circular range cell.

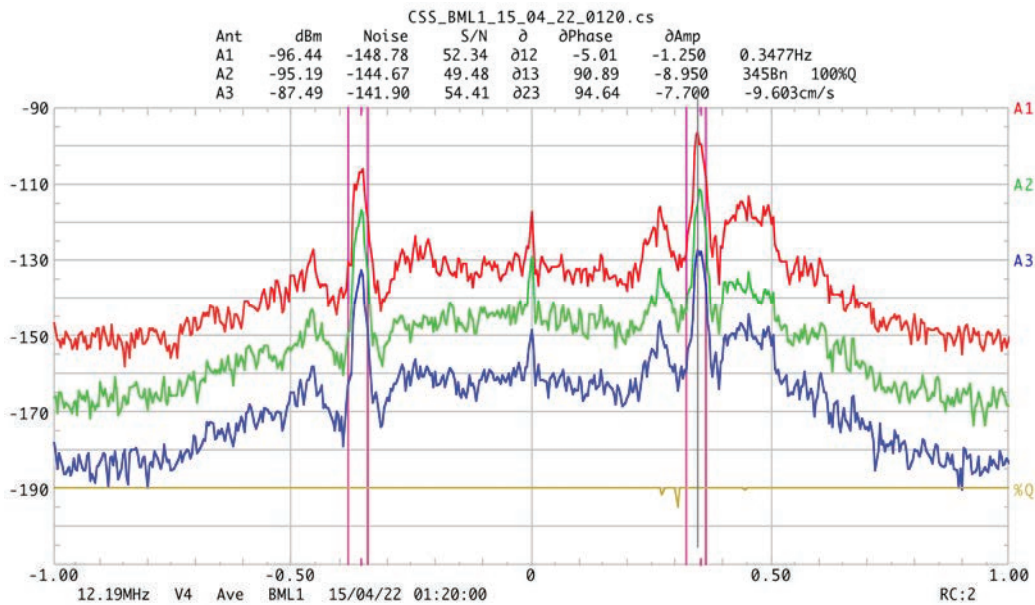


**Fig. 20.1.** An example of broad beam cross spectra obtained from a SeaSonde system, with signal strength (dB) plotted vs. Doppler frequency (Hz) for the Loop 1 antenna (A1, red), the Loop 2 antenna (A2, green) and the monopole (A3, blue). The curves are offset by 20 dB for better visibility. The magenta color tic marks indicate the Bragg frequencies  $\omega_B$  and vertical magenta lines mark the first-order spectral boundaries.

### 20.2.3. The Effects of Varying Ocean Surface Currents

As shown in (20.3) and (20.4), currents transporting the ocean waves induce an added Doppler shift to the radian frequency of the echoes.

Because the broad-beam radar under consideration by its nature integrates vs. bearing angle over the ocean sector, this implies a convolution in the integral (20.4) defining the second-order echo spectrum. Hence a current that varies with bearing angle destroys spectral resolution and inherent information about waves in the inversion process. There are two current effects that contribute to this process:

- a. One might argue that the current can be determined (it is the primary product of HF coastal radars), therefore it should be removable. In practice such "deconvolution" is difficult to execute with noisy data. Indeed, all sea echo (both first and second order) originates from zero-mean Gaussian random processes. The frequency-range of current smearing is as wide as the first-order echo peak itself, covering many Doppler cells.
- b. Drifter comparisons with radar current measurements have revealed another random process: subgrid-scale current variability within the radar cell [12, 13]. This near-surface turbulence is site dependent, varying from 6 to 16 cm/s, thereby contaminating many Doppler spectral bins of the second-order radar echo.

At this point, we have found robust operational extraction of wave parameters to be possible only with the fitting of simple models to the smeared second-order echo available from coastal HF radars.

### 20.3. Using Measured Antenna Patterns in Wave Extraction

Wave parameters from a broad beam radar can be calculated using either ideal or measured antenna patterns. For this chapter, we use measured antenna patterns to reduce bias in the results. To measure the patterns, a transponder can be placed on a boat that traverses an arc at constant range transmitting signals that are picked up by the radar receiver, passing through the three antennas and their respective channels [14]. The received signals are then processed to give the complex antenna voltage patterns to be used in the signal analysis. The pattern can also be measured from ship echoes correlated with ship position information sent via the Automatic Identification System [15] or a signal source carried by an aerial drone [16].

Complex voltage cross spectra from the three antennas  $\langle \tilde{V}_i \tilde{V}_j^* \rangle$  (where  $i, j = 1, 2, 3$ ) can be expressed as follows in terms of the antenna patterns and the radar cross section:

$$\langle |\tilde{V}_1|^2 \rangle = \int_{\phi_1}^{\phi_2} |\tilde{Z}_1|^2 \sigma(\phi) d\phi, \quad (20.6)$$

$$\langle |\tilde{V}_2|^2 \rangle = \int_{\phi_1}^{\phi_2} |\tilde{Z}_2|^2 \sigma(\phi) d\phi, \quad (20.7)$$

$$\langle |\tilde{V}_3|^2 \rangle = \int_{\phi_1}^{\phi_2} \sigma(\phi) d\phi, \quad (20.8)$$



$$\langle \tilde{V}_1 \tilde{V}_3^* \rangle = \int_{\phi_1}^{\phi_2} \tilde{Z}_1(\phi) \sigma(\phi) d\phi, \quad (20.9)$$

$$\langle \tilde{V}_2 \tilde{V}_3^* \rangle = \int_{\phi_1}^{\phi_2} \tilde{Z}_2(\phi) \sigma(\phi) d\phi, \quad (20.10)$$

$$\langle \tilde{V}_1 \tilde{V}_2^* \rangle = \int_{\phi_1}^{\phi_2} \tilde{Z}_1(\phi) \tilde{Z}_2(\phi) \sigma(\phi) d\phi, \quad (20.11)$$

where  $\tilde{Z}_1(\phi)$ ,  $\tilde{Z}_2(\phi)$  are the complex antenna pattern values for Loops 1 and 2, normalized by the Antenna 3 values;  $\phi$  is the bearing angle measured from the loop 1 axis;  $\sigma(\phi)$  is the narrow-beam radar cross section;  $\phi_1$  and  $\phi_2$  are the radar cutoff angles imposed by the coastline, which can be a function of range. Equations (20.3) and (20.4) for the radar cross section are inserted into these equations and the complex voltages are interpreted to give parameters of the ocean wave spectrum.

For ideal patterns, as have been used in the past for wave extraction [8],  $\tilde{Z}_1(\phi)$ ,  $\tilde{Z}_2(\phi)$  are simple sine and cosine functions of bearing angle,  $\phi$ , and the ideal monopole pattern used for normalization was taken to be unity, i.e. an omni-directional pattern. We define the antenna pattern as the ratio of the loop signal amplitudes defined in (20.6), (20.7) to the monopole signal amplitude defined in (20.8). Fig. 20.2 shows measured antenna patterns for a SeaSonde located at Bodega Bay CA and the corresponding ideal patterns, indicating a significant departure of measured patterns from ideal.

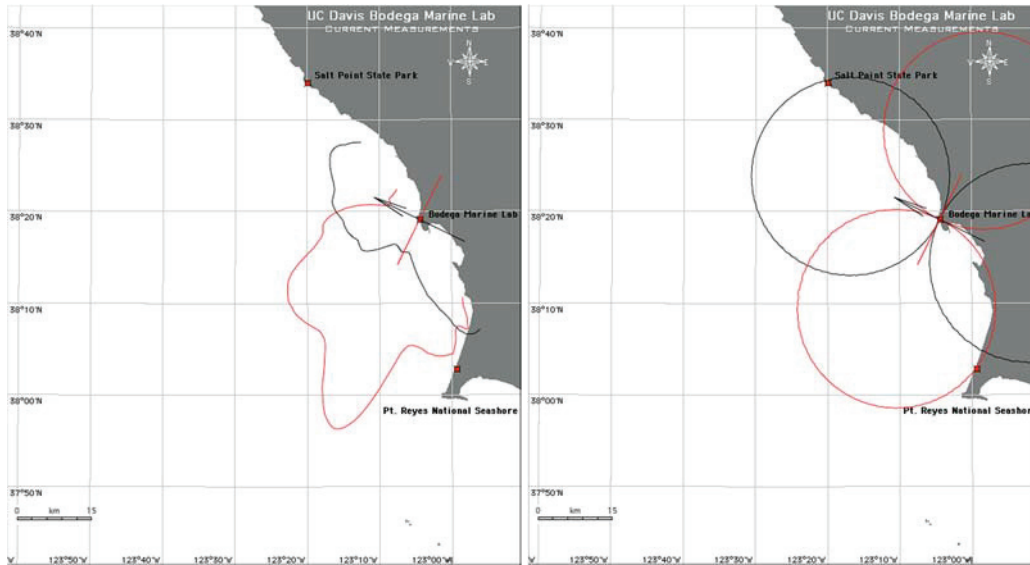


**Fig. 20.2.** Antenna patterns for the Bodega Bay radar. Left: measured. Right: ideal.

## 20.4. Interpretation of the Radar Doppler Spectrum Using the Pierson/Moskowitz Ocean Wave Model

### 20.4.1. Definition of the Ocean Wave Spectral Model

The ocean wave spectral model used in radar wave analysis is defined in terms of the wavenumber  $k$  and wave direction  $\phi$ . We use as a model for the ocean wind-wave spectrum  $S(k, \phi)$  the product of a nondirectional spectrum based on the P/M model and a cardioid directional distribution around the dominant direction  $\phi_{ww}$ , see [8]:

$$S(k, \phi) = \frac{A_{ww} e^{-0.74(k_c/k)^2}}{k^4} \cos^4\left(\frac{\phi - \phi_{ww}}{2}\right), \quad (20.12)$$

with parameters  $k_c$ ,  $\phi_{ww}$  and a multiplicative constant  $A_{ww}$ .

### 20.4.2. Steps in the Analysis Procedure

In this analysis, the effects of radial current velocity in (20.2) and (20.3) are ignored:  $v_r(\phi)$  is set to zero. We assume that the ocean wave spectrum is homogeneous over the radar range cell used for the analysis. Because of this assumption, the smaller close-in radar range cells are used for wave analysis. In this chapter, we consider only deep-water conditions and ignore wave refraction. In practice, this generally excludes only the closest range cell. Shallow-water effects are discussed in [10].

There are four steps in the interpretation of the radar spectrum to give wave information:

*Step 1:* The first- and second-order regions are separated and then the first-order region is analyzed to give the ocean-wave spectrum at the Bragg wavenumber, using the spectral model defined by (20.12). Wind direction is taken to define the peak of the spectrum.

*Step 2:* The second-order radar spectrum is analyzed using the model (20.12), which is assumed to apply throughout the whole radar spectrum. The radar cross spectra are analyzed to indicate if onshore or offshore waves dominate. For onshore waves, the coastline restricts the angle of approach and limits to onshore wave bearings are set by the user; if the second-order echo indicates that waves are moving offshore, they are assumed to follow the wind direction, which is determined in Step 1 from the first-order radar spectrum.

*Step 3:* The optimum values of the model parameters are determined based on the best fit of the theoretically modeled Doppler spectra to the observed radar Doppler spectrum. In this step, the second-order spectrum is effectively normalized by the first-order, which eliminates unknown multiplicative factors produced by antenna gains, path losses etc.

*Step 4:* A running mean over 7 consecutive time periods is performed for wave parameters derived from the Steps 1-3.

## 20.5. Results

The analysis described in the previous section produces estimates of waveheight, centroid-period, wave- and wind-direction for each range cell for which the second-order echo exceeds the noise floor times a preset threshold factor. If there is consistency over range, which typically occurs during onshore winds/wave, these results can be averaged to improve stability. When winds are offshore, results are not consistent with range; e.g. waveheight increases with distance from the shore (i.e., with fetch), and results from different range cells must be viewed separately.

We now give examples of this interpretation process, using data sets with different wave/wind conditions from California and New Jersey. Derived results are compared with buoy measurements when available. Differences can arise in the comparisons, as radar data represent spatial averages, while buoy data represent results from a single point. Because of possible inhomogeneity at large ranges, we here restrict wave analysis to the first 10 range cells.

All times quoted are UTC.

### 20.5.1. Bodega Marine Lab., California

Our first example is based on a data set from Bodega Marine Lab., California, April 20-28, 2015. Fig. 20.3 shows the location of the radar (transmit frequency 12.91 MHz) and the offshore bathymetry. The closest NDBC buoy (Station 46013), used for comparisons with the radar results, is located at  $38^{\circ}14'17''$  N  $123^{\circ}18'27''$  W.

Fig. 20.4 shows examples of measured and best-fit model second-order spectra.

Winds and waves in this location are almost always onshore and shallow-water effects are minimal. Hence derived results are consistent vs. range. Examples of radar wave parameters for radar range-cells 2 and 10 are shown in Fig. 20.5, along with results from the buoy NDBC 46013.

The mean deviation between radar and buoy waveheights over this time period is -0.18 m (Range cell 2) and 0.02 m (Range cell 10); the corresponding RMS deviation is 0.34 m (Range cell 2) and 0.36 m (Range cell 10).

### 20.5.2. New Jersey, USA

Several radars operate from the New Jersey coast; see Fig. 20.6 for the locations of four of these radar sites and neighboring buoys.

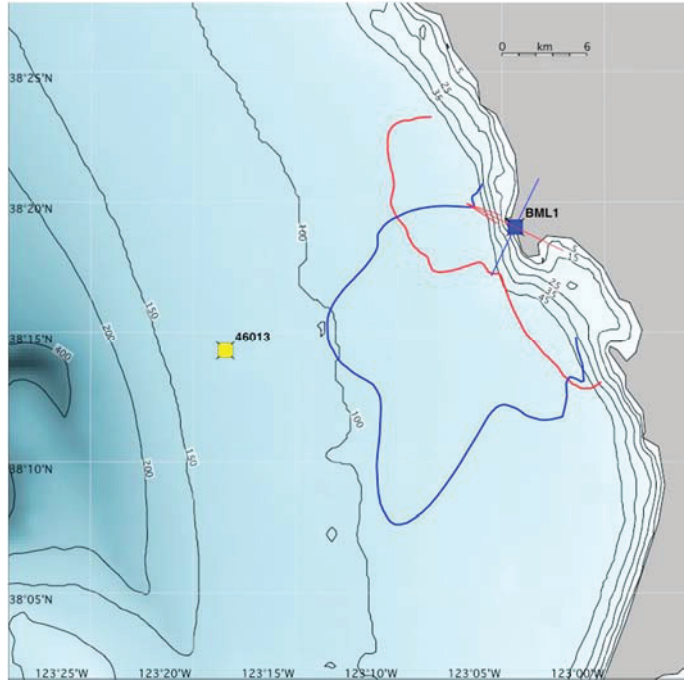


**Fig. 20.3.** The coastline and bathymetry with contour depths in meters around Bodega Marine Lab., California, showing the position of the radar and wave buoy 46013 (yellow dot). The antenna patterns are shown, the curves represent the loop signal amplitudes normalized by the monopole signal amplitude: Loop 1 (red), Loop 2. (blue). The red arrow at the radar site indicates the Loop 1 axis; the blue line indicates the Loop 2 axis, at right angles to the Loop 1 axis.

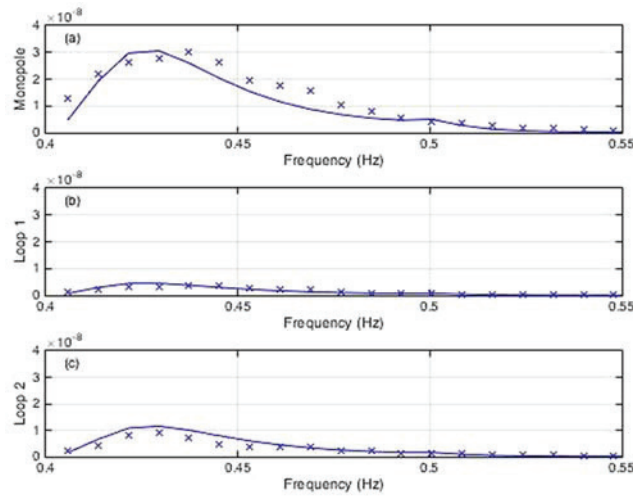
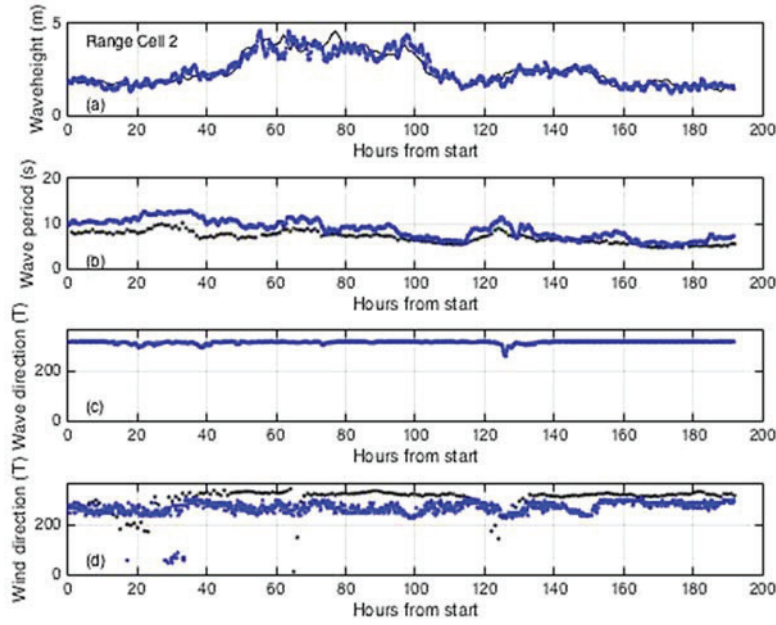
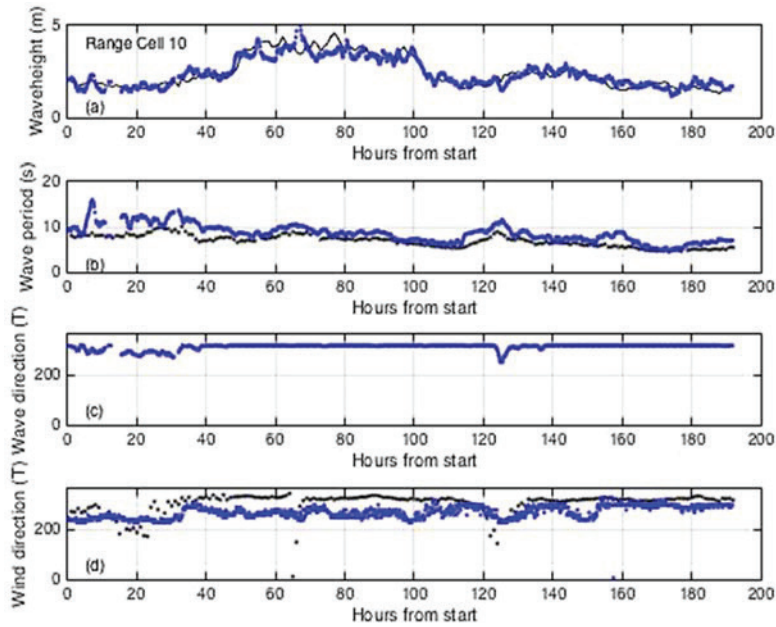


**Fig. 20.4.** Second-order radar self-spectra, voltage-squared, arbitrary units, (the outer sideband of positive Bragg peak for the second range cell), 2-4 km from shore, April 21, 3:10 am, 2015 plotted vs. Doppler frequency. Solid line: measured data, x: best-fit model. (a) Monopole; (b) Loop1; (c) Loop 2.





(A)



(B)

**Fig. 20.5.** Measured wave parameters from Bodega Marine Lab. Start time: April 20. 00:00 2015. (A) Range cell 2; (B) Range cell 10. (a) Waveheight: Radar (blue). Buoy (black); (b) Wave period: Radar centroid period (blue). Average buoy period (black); (c) Radar wave direction  $^{\circ}$ T (blue). No buoy wave direction measurements are available for this period. (d) Wind direction measurements: Radar (blue), Buoy (black).

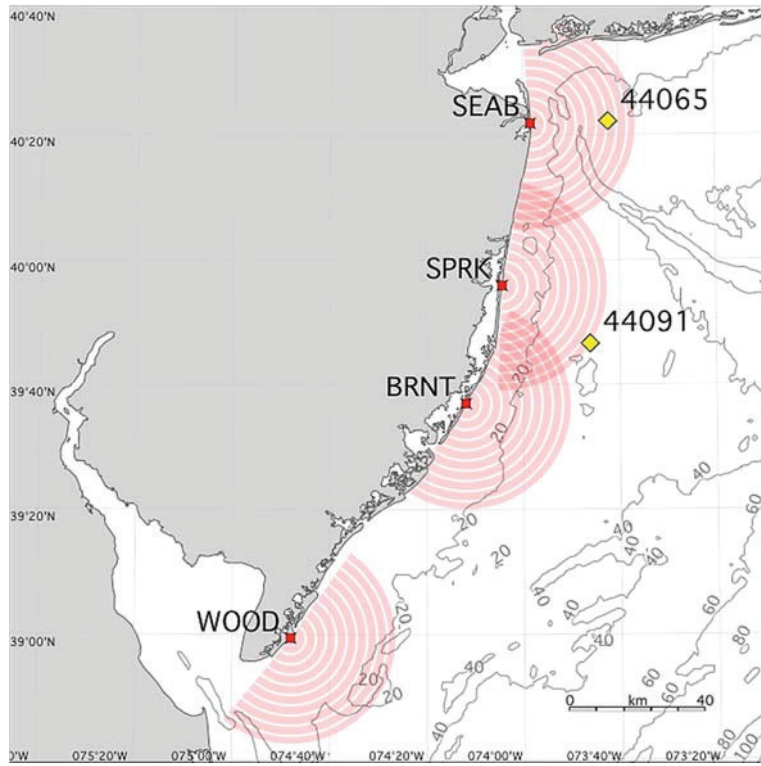


**Fig. 20.6.** The location of four New Jersey radar sites at Sea Bright (SEAB), Seaside Park (SPRK), Brant Beach (BRNT), North Wildwood (WOOD) and neighboring NDBC buoys. Ten 3-km range cells are plotted in red. Depth contours are marked in meters.

Both onshore and offshore winds and waves are common in this location. Because the New Jersey coast is aligned at approximately  $30^\circ$  clockwise from true North, onshore winds/waves have directions clockwise from  $30^\circ\text{T}$  to  $210^\circ\text{T}$ , and offshore winds/waves have directions clockwise from  $210^\circ\text{T}$  to  $30^\circ\text{T}$ . When winds are onshore, there is no significant range-dependence. Offshore winds produce wind waves that are barely developed nearest the coast. As the wave develops further from shore, wave height increases, which is the well-known effect of fetch.

In this Subsection, 20.5.2.1 gives a specific example of the effect on waveheight at SPRK of changing wind direction; 20.5.2.2 shows the effect on waveheight at the 4 radars of the passage of a front across the coastline; 20.5.2.3 gives examples of wave results taken over a 9-day period, with comparison to neighboring buoys.

#### 20.5.2.1. Effects of Wind Turning Offshore

Wind waves in various stages of development leading up to and during an offshore wind event were observed by the SPRK radar on March 22 and 23, 2017. Waveheights from three radar range cells and NDBC 44091 are shown in Fig. 20.7.

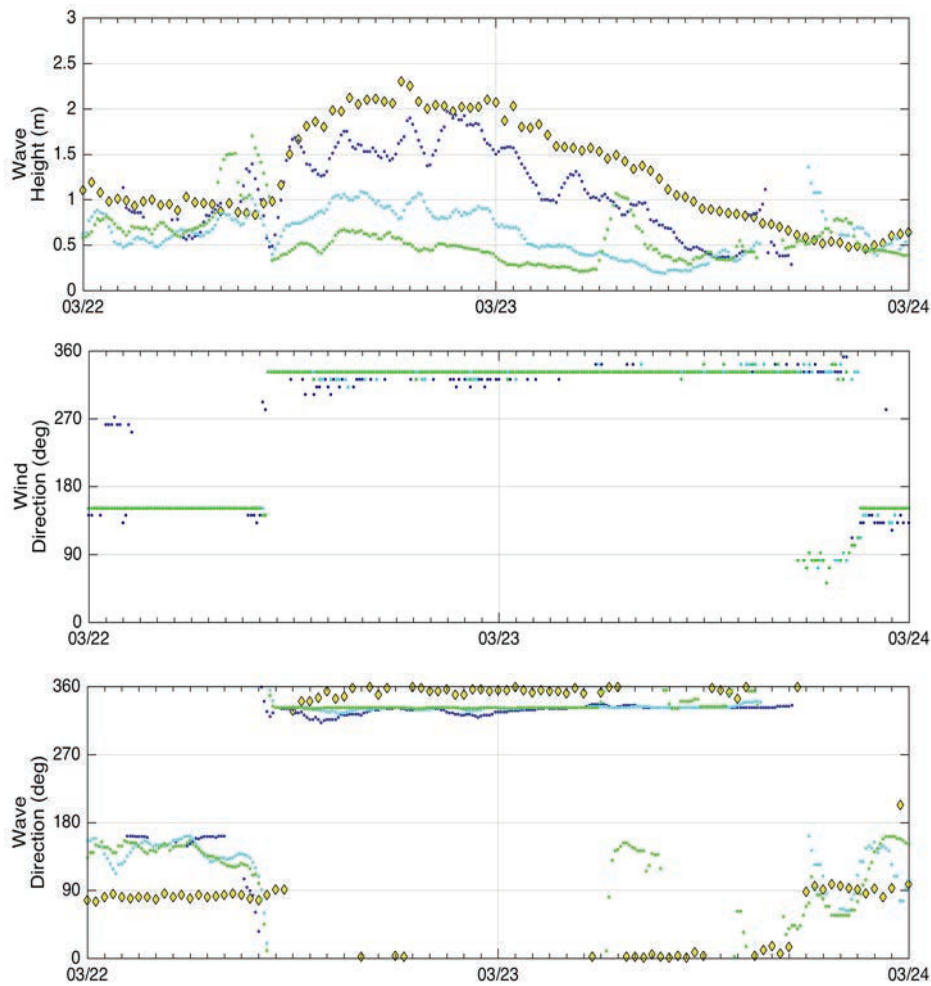


**Fig. 20.7.** Waveheight, wind and wave direction measured by the SPRK radar and NDBC 44091 plotted vs. time from March 22 00:00 to March 24 00:00. Radar Range cells: 10 (blue), 5 (cyan), 3 (green) and NDBC 44091 (yellow).

Wind and wave directions turn from onshore to offshore at approximately March 22 12:00, after which the waveheight increases with range from the radar, reflecting the ocean surface response to wind forcing for increasing fetch.

#### 20.5.2.2. Wave-height and Wind-Direction Observations that Reflect the Passage of a Front

Radar observations from the 4 radars traced the northward trajectory of a front on March 14, 2017, see Fig. 20.8.

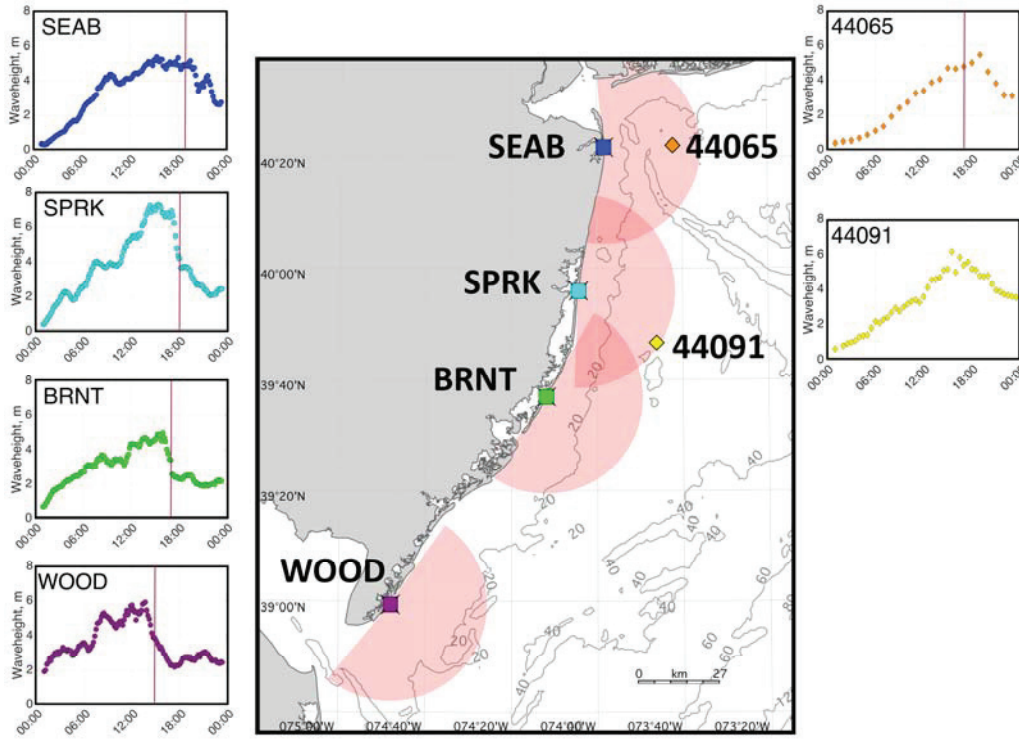


**Fig. 20.8.** Ocean waveheights for March 14, 2017 plotted vs. time for four New Jersey radar sites (Range cell 10) and NDBC 44065, 44091. The vertical lines indicate times at which the wind-direction changes from onshore to offshore: WOOD (14:00), BRNT (17:00), NDBC 44065 (17:30), SPRK (18:00), SEAB (19:00). NDBC 44091 does not provide wind direction measurements.

It can be seen that the first transition from onshore to offshore winds and waves occurs first at the south-most site (WOOD) and progresses northward. The trajectory is consistent with the northward tracking of the low pressure center as seen in NOAA National Weather Service, Daily Weather Map [17] shown in Fig. 20.9.

### 20.5.2.3. Examples of Measured Wave Results

Examples of radar wave parameters from the four New Jersey radars are shown in Fig. 20.10, together with buoy measurements for January 16-29, 2017. No significant effects due to shallow water were observed. As shown in Section 20.5.2.1, offshore winds lead to range dependence. Fig. 20.10 displays wave parameters from Range cell 10 (27-30 km from the radar), for which this effect is less than for close-in ranges.

The second-order radar echo is typically much lower than the first order echo (e.g. see Fig. 20.1). When the second-order echo dips below ambient radio noise levels in the Doppler spectrum, wave parameters cannot be determined. This can occur during low wave conditions, increased ambient radio noise or some combination of the two and leads to gaps in the wave parameter time series as shown in Fig. 20.10. These gaps do not occur



in the derived wind direction, which is derived from the stronger first-order Bragg peaks. Seaside Park (SPRK) typically has the lowest radio noise conditions and highest signal to noise ratio of the four sites and, therefore, has fewer gaps.

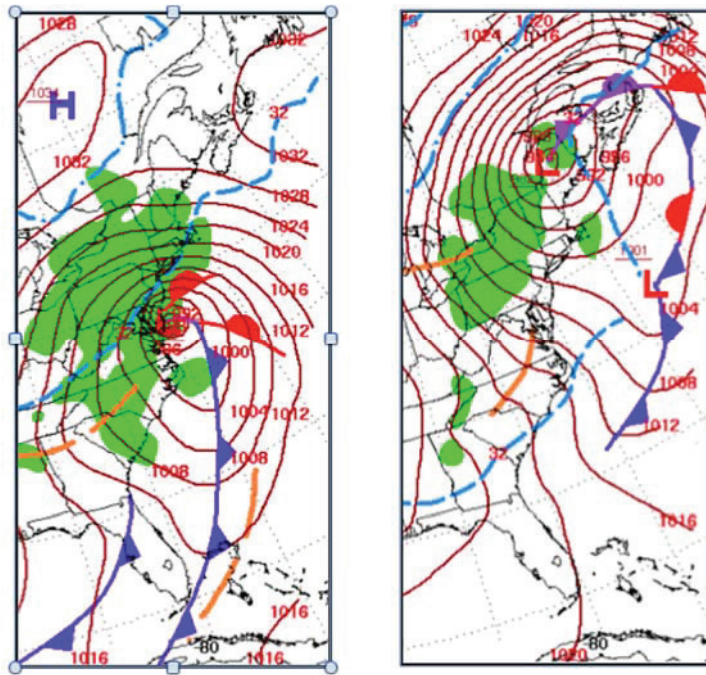


**Fig. 20.9.** Daily Weather Maps. Left: March 14 07:00 am EST, showing a low-pressure center just south of New Jersey. Right: March 17 07:00 am EST, showing that the low-pressure center has migrated northward.

The mean deviations between radar and buoy waveheights over this time period are 0.07 m (SEAB and NDBC 44065) and 0.02 m (SEAB and NDBC 44065); the corresponding RMS deviations are 0.65 m and 0.73 m. NDBC 44091 is the closest buoy to BRNT and WOOD. However, it is not within either radar coverage area for waves, see Figs. 20.6 and 20.8. NDBC 44091 data are included on Figs. 20.10(C), (D) for comparison purposes.

The mean deviations between radar and buoy waveheights over this time period are 0.07 m (SEAB and NDBC 44065) and 0.02 m (SPRK and NDBC 44065); the corresponding RMS deviations are 0.65 m and 0.73 m.

Waves turn from onshore to offshore at approximately 175 hours (WOOD), 200 hours (BRNT), 210 hours (SPRK), 212 hours (SEAB), indicating a front moving Northward, which is similar to that shown in Fig. 20.8. The waveheight decreases when the wind turns from onshore to offshore, which is similar to the event shown in Fig. 20.8. The maximum waveheights increase from WOOD to BRNT and from SEAB to SPRK, which is similar to those shown in Fig. 20.8.

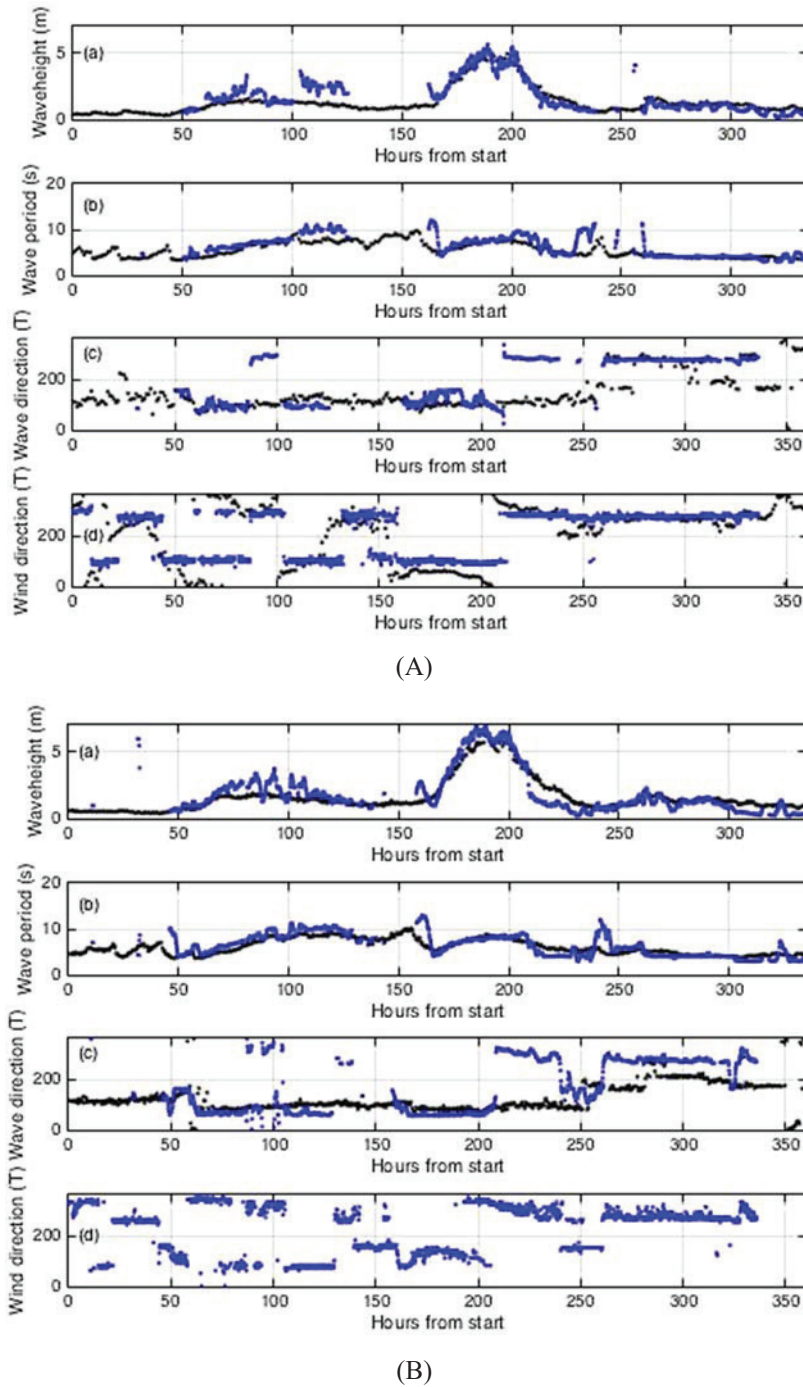
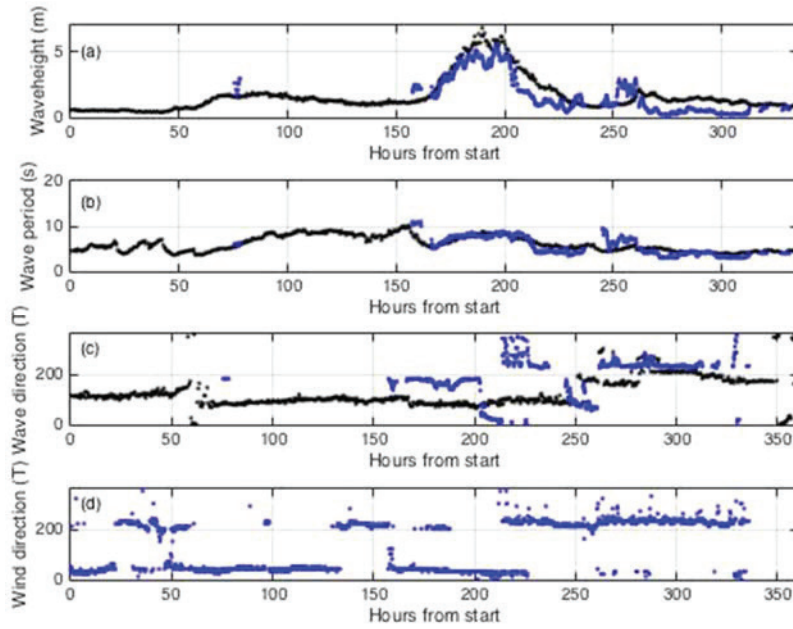
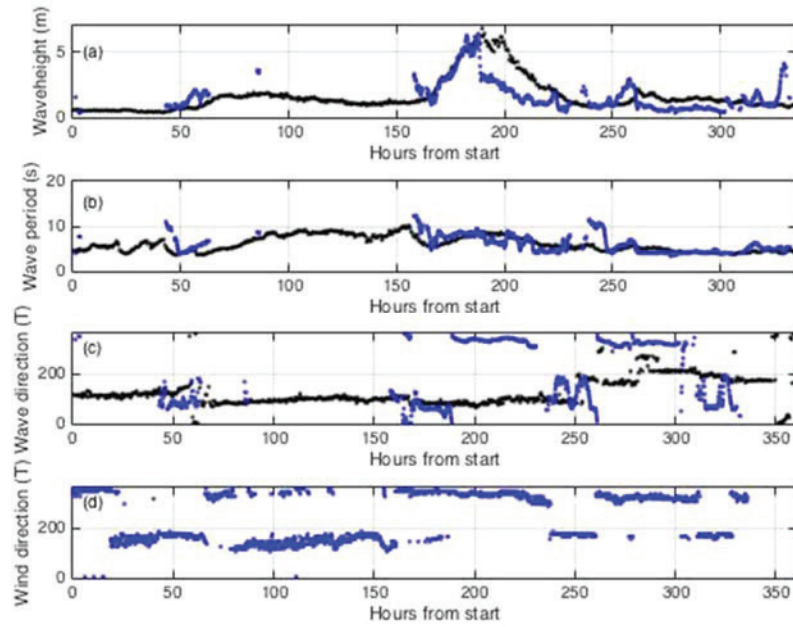


**Fig. 20.10 (A-B).** Wave measurements from the New Jersey radars and neighboring buoys; (A) Sea Bright, NDBC 44065 (B) Seaside Park, NDBC 44091. Start time: January 16 00:00 2017. (a) Waveheight: Radar (blue), Buoy (black). (b) Wave period: Radar centroid period (blue). Average buoy period (black). (c) Wave direction  $^{\circ}\text{T}$ : Radar (blue), Buoy (black) (d) Wind direction measurements  $^{\circ}\text{T}$ : Radar (blue), Buoy (black). NDBC 44091 does not provide wind directions.



(C)



(D)

**Fig. 20.10 (C-D).** Wave measurements from the New Jersey radars and neighboring buoys; (C) Brant Beach, NDBC 44091 (D) Wildwood, NDBC 44091. Start time: January 16 00:00 2017. (a) Waveheight: Radar (blue), Buoy (black). (b) Wave period: Radar centroid period (blue). Average buoy period (black). (c) Wave direction °T: Radar (blue), Buoy (black) (d) Wind direction measurements °T: Radar (blue), Buoy (black). NDBC 44091 does not provide wind directions.

## 20.6. Interpretation of the Radar Doppler Spectrum Using a Bimodal Ocean Wave Model

We illustrate the interpretation procedure using a data set from Espichel, Portugal, located at  $38^{\circ}24.928'N$ ,  $9^{\circ}13.001'W$  when bimodal waves often dominate. Fig. 20.11 shows the location of the radar (transmit frequency 12.91 MHz) and the offshore bathymetry. The closest wave buoy (the Lisbon buoy), owned by the Portuguese Hydrographic Institute, is located at  $38^{\circ}32'16''N$ ,  $9^{\circ}18'32''W$ , approximately 15 km from the radar. All times quoted are UTC.

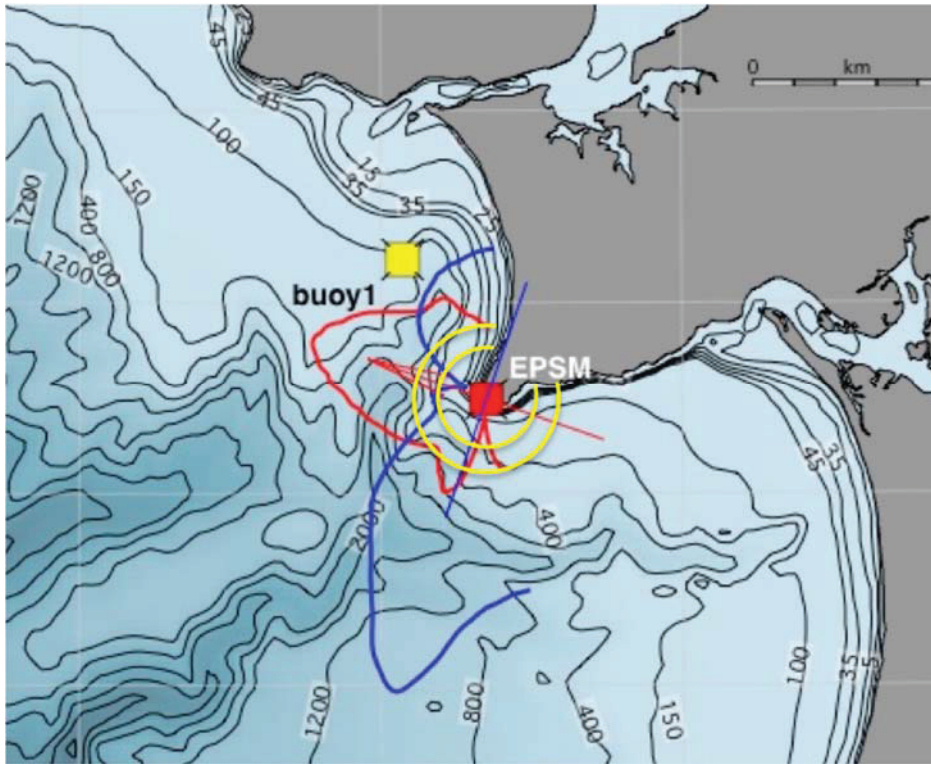


**Fig. 20.11.** The coastline and bathymetry (contours in meters) around Espichel, Portugal, showing the position of the radar and the Portuguese Hydrographic wave buoy. The antenna patterns are shown, the curves represent the loop signal amplitudes normalized by the monopole signal amplitude: Loop 1 (red), Loop 2. (blue). The red arrow at the radar site indicates the Loop 1 axis; the blue line indicates the Loop 2 axis, at right angles to the Loop 1 axis. The spherical boundaries of the second radar range cell used in the analysis are drawn in yellow.

Examination of second-order Doppler spectra reveals that contributions from two distinct ocean wave spectra can be identified, arising typically from swell and wind-waves. Wind-waves produce a broad second-order echo in the radar Doppler spectrum; see for example Fig. 20.1. Ocean swell can produce narrow spectral peaks in the second-order echo Doppler spectrum close to the Bragg frequency; see for example Fig. 20.12.



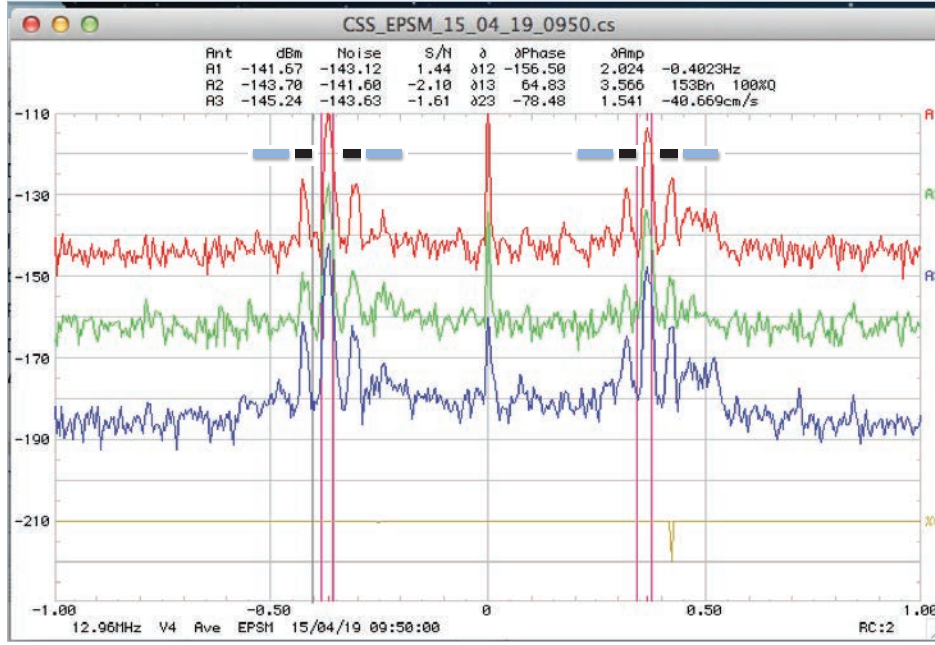


**Fig. 20.12.** An example of SeaSonde cross spectra for April 19, 2015, 9:50 am; Loop 1 (red), Loop 2 (green), Monopole (blue). The spectra exhibit narrow spectral peaks close to the first-order Bragg region produced by swell in addition to the broader echo from wind-waves further from the first-order Bragg region. The color bars at the top indicate the regions in the second-order spectrum dominated by swell (black) and wind-waves (blue).

Swell is commonly understood to be long-period waves arriving from a distant storm area. Wind waves are developed by local winds/storms in the observed area, and are more distributed in their frequencies and directions. In this section, we describe a method to interpret the radar Doppler spectrum in terms of two ocean wave spectra models (which we term bimodal): the P/M model (20.12) and a triangular swell model.

When the radar spectrum exhibits narrow swell peaks, these are interpreted using a simple triangular model for the ocean wave swell spectrum at wave frequency  $f$ :

$$\begin{aligned}
 S_{sw}(f, \varphi) &= A_{sw}(f) \delta(\varphi - \varphi_{sw}), |f - f_{sw}| < \Delta \\
 &= 0 \quad |f - f_{sw}| > \Delta,
 \end{aligned} \tag{20.13}$$

where  $f$  is defined in terms of the ocean wavenumber,  $k$ , by:

$$f = \sqrt{2gk} / 2\pi, \tag{20.14}$$

and  $\Delta$  defines the width of the swell peak centered at wave frequency,  $f_{sw}$ ;  $\varphi_{sw}$  is the swell direction;  $A_{sw}$  is an isosceles triangular function, with base width  $\Delta$ , that peaks at the swell period and decays to zero at the boundary

To interpret the spectrum, the following steps are carried out:

*Step 1:* A value for the outer boundary frequency defining the swell region is defined, as illustrated in Fig. 20.13.

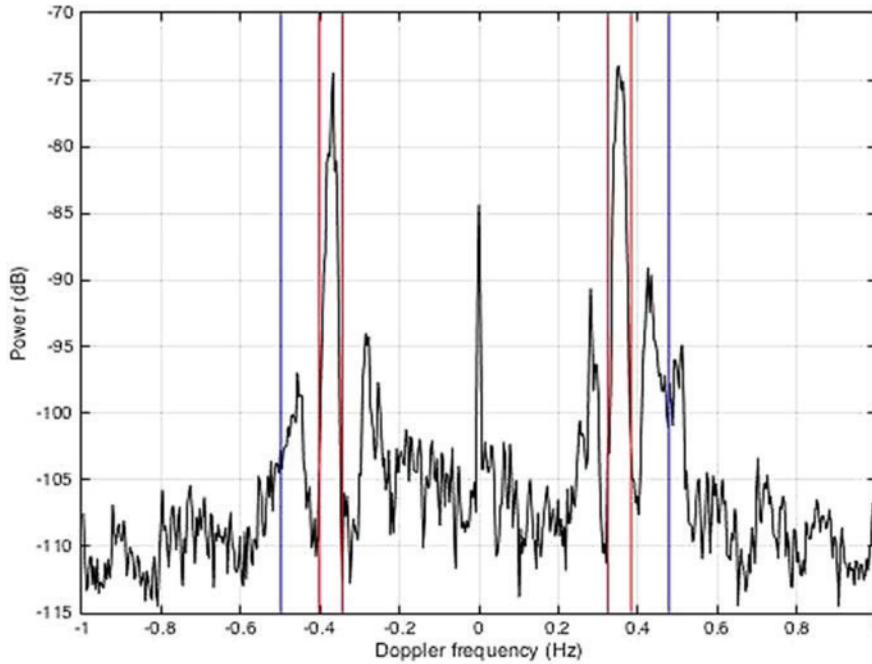


**Fig. 20.13.** Antenna 3 (monopole) self-spectrum for April 21, 7:20 am, 2015 plotted vs. Doppler frequency (Hz). Boundaries defining the first-order Bragg region are marked in red. The second-order swell peak is clearly visible for the outer, positive Doppler region, within the approximate outer boundary marked in blue.

Take the case when the initial value is set at 0.48 Hz. Using this value, when the Doppler frequency is above 0.48 Hz, the second-order spectrum is assumed to come from wind-waves only; when Doppler frequency less than 0.48 Hz, the second-order spectrum is assumed to be produced by echo from both swell and wind-waves, see for example Fig. 20.14, which illustrates the procedure for the monopole antenna.

*Step 2:* The radar spectra with Doppler frequency  $>0.48$  Hz are analyzed using the P/M wind-wave model defined by (20.12); measured values are shown in Fig. 20.14 (b) together with best-fit model values for the whole frequency range.

*Step 3:* The P/M model values in the region containing swell echo with Doppler frequency  $<0.48$  Hz are subtracted from the measured spectral values. The resulting differences define the contribution from swell alone, which is interpreted using the swell model defined by (20.13). The difference values and best-fit model values are plotted in Fig. 20.14 (c).

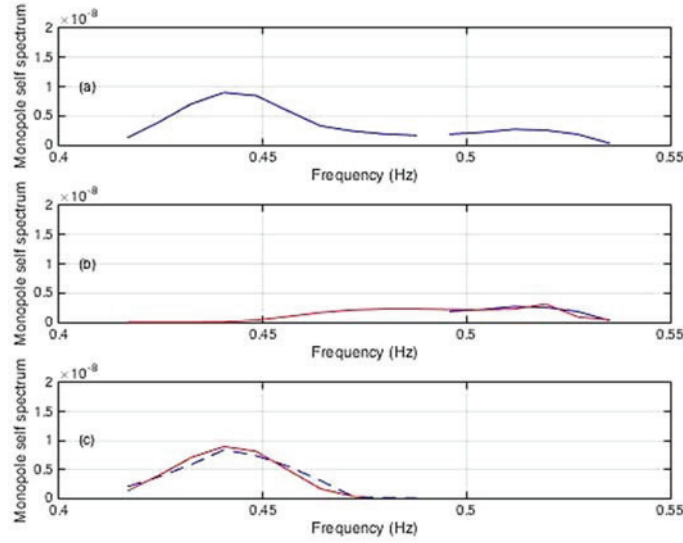


**Fig. 20.14.** Illustration of the procedure for April 21, 7:20 am, 2015 when both swell and wind-waves are present and the boundary frequency is set to 0.48 Hz. Spectra plotted are voltage-squared, arbitrary units. (a) Monopole radar spectral points plotted vs. Doppler frequency. For frequency  $> 0.48$  Hz: wind-waves only; for frequency  $< 0.48$  Hz: swell and wind-waves: The frequency-gap indicates the break selected between the two regions. (b) Wind-wave spectral values: Measured (blue), Best-fit model (red). (c) Swell spectral values: Measured spectra minus best-fit wind-wave model (blue dashed), best-fit swell model (red).

*Step 4:* The optimum value for the boundary frequency is set minimizing the least-squares sum. In this case it was determined to be 0.47 Hz.

The output ocean wave parameters derived are defined by the derived swell and wind-wave spectra:

- Wind-waves: significant height  $H_{ww}$ , centroid period, dominant wave direction.
- Swell-waves (when present): significant height  $H_{sw}$ , period, direction.
- The total waveheight  $H$ , which is given by:

$$H = \sqrt{H_{ww}^2 + H_{sw}^2}. \quad (20.15)$$

In the Appendix, models defined by (20.12) (P/M) and (20.13) (triangular swell) are least-squares fit to measured ocean wave spectra from the Lisbon buoy. It is shown that when the measured buoy peak-period is greater than about 12 s, the RMS deviations of the model-fit to the measured buoy data are significantly lower using the triangular swell model (20.13) at lower frequencies, indicating that the use of a bimodal model is required.

Fig. 20.15 shows the derived ocean wave parameters obtained over the entire period April 15-21, 2015. Radar waveheight is compared with that measured by the closest buoy. The

buoy gives two measures of wave period over the previous 10 minutes which are plotted in Fig. 20.15(c): the mean period  $T_z$  and the period defining the wave spectral maximum value  $T_{max}$ . No buoy wind direction measurements are available for this period.

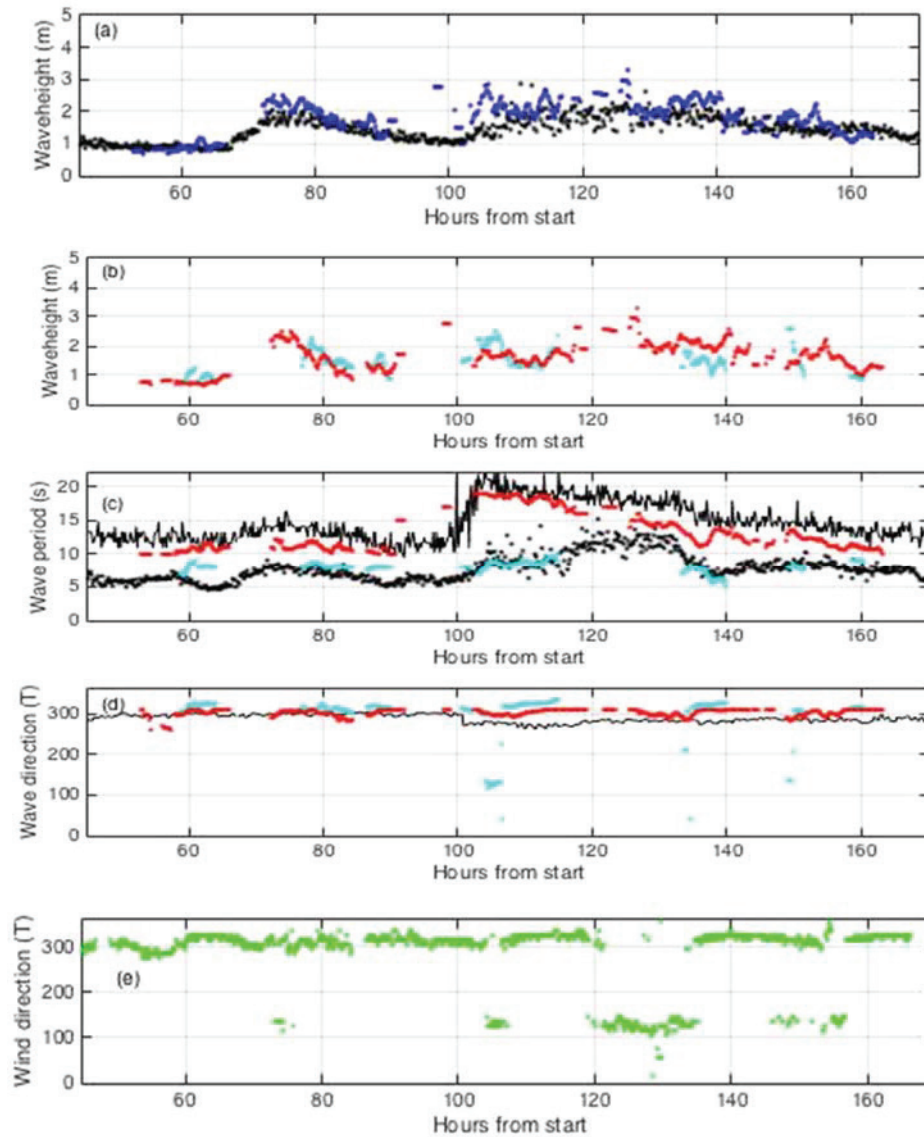


**Fig. 20.15.** Measured wave parameters obtained every 10-minutes from Espichel, Portugal. Start time: April 15, 12:30 am 2015. (a) Total waveheight: Radar (blue), Buoy (black) (b) Radar bimodal waveheight: Wind-wave (cyan), Swell (red) (c) Wave period: Radar bimodal centroid period: Wind-wave (cyan), Swell (red). Buoy wave periods (black): continuous line: Buoy  $T_{max}$ , dotted line: Average period  $T_z$ . (d) Radar bimodal wave direction: Wind-wave (cyan), Swell (red), Buoy (black) (e) Radar wind direction.



It follows from Fig. 20.15 (c) that the radar wind-wave period agrees well with the buoy mean wave period, while the radar swell period is somewhat less than the buoy maximum period, except for extremely long period waves. The time-gaps in the radar data, as shown in Fig. 20.15, usually occur for calmer wave conditions when the second-order echo dips below the higher noise/interference levels. This does not happen with the wind direction, which comes from the stronger first-order Bragg peaks, in contrast to the weaker second-order.

Use of the unimodal P/M model (20.12) rather than the bimodal model results in significant overestimation of the waveheight when swell is present, as shown in Fig. 20.16.

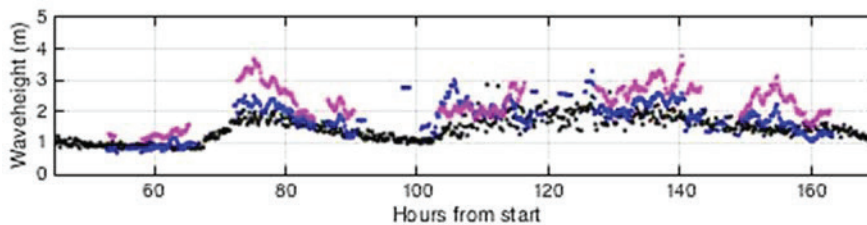


**Fig. 20.16.** Total waveheight obtained every 10-minutes. Start time: April 15. 12:30 am 2015. Radar results based on the bimodal model (blue), Radar results based on the unimodal model (magenta), Buoy (black).

## 20.7. Conclusion

There are approximately 650 SeaSondes worldwide, operating in the broad-beam, direction finding mode. They constitute approximately 85 % of the radars in operation; all others are different brands of phased arrays that form narrower beams and scan them in bearing. A large portion of SeaSondes in operation have track records of over a decade of continuous current measurements. Approximately 30 of these SeaSondes have been used for real time wave measurements, and hence can benefit from the methods described in this chapter.

We have described how measured antenna patterns can be included in the analysis for wave parameters from a broad-beam system; previously the analysis assumed ideal patterns. Measured patterns allow for more accurate current extraction, based on reducing bearing-angle errors for the scattering radar cell. They can also be used with the analysis methods presented here for improved wave estimates, in particular when there are large differences between measured and ideal patterns.

Existing SeaSonde wave software was developed to be applied to radars on the West Coast of the United States, where dominant waves are usually onshore; waves were programmed either to be onshore or to follow the wind. This assumption was found to be inadequate on the East Coast, where winds routinely turn from onshore to offshore as storms pass

through. In the software described here, the radar cross spectra are analyzed to indicate if onshore or offshore waves are dominant; offshore waves are programmed to follow the wind direction, which is determined from the first-order radar spectrum. Onshore wave directions are constrained by angles set by the user e.g. the coastline angles, which are now defined as a function of range, allowing use of the software in regions with complicated coastlines.

Recent operations with the Pierson/Moskowitz model for the ocean wave spectrum at different sites have uncovered situations where it is inadequate, resulting in significant overestimation of the waveheight. This appears to be due to peaks due to swell in the second-order radar spectra, as well as broader spectral components due to wind-waves. We are in the process of extending the analysis methods to handle these more complex bimodal scenarios and here give initial results from a radar located at Espichel, Portugal. The algorithm under development involves least-squares fitting of calculated echoes based on ocean wave spectral models to measured radar data and automatically selects the optimum model and its parameters. When the sea spectrum is bimodal, the algorithm provides heights, directions and periods for each ocean wave spectral component from analysis of the second-order Doppler spectrum, as well as wind direction extracted from the first-order echo.

Future research may allow the inclusion of some degree of variation over space for the directional wave spectrum as well as the inclusion of shallow water effects.

## Acknowledgments

We are grateful to Mason Kwiat for providing the maps shown in this chapter.

## References

- [1]. D. D. Crombie, Doppler spectrum of sea echo at 13.56 MHz, *Nature*, Vol. 75, 1955, pp. 681-682.
- [2]. D. E. Barrick, First-order theory and analysis of MF/HF/VHF scatter from the Sea, *IEEE Trans. Antennas Propagat.*, Vol. AP-20, 1972, pp. 2-10.
- [3]. D. E. Barrick, Remote sensing of sea-state by radar, in Remote Sensing of the Troposphere (V. E. Derr, Ed.), *U.S. National Oceanic and Atmospheric Administration*, 1972, pp. 12-1 – 12-46.
- [4]. L. R. Wyatt, J. J. Green, A. Middleditch, M. D. Moorhead, J. Howarth, M. Holt, S. Keogh, Operational wave, current, and wind measurements with the Pisces HF radar, *IEEE J. Oceanic. Engr.*, Vol. 31, 2006, pp. 819-834.
- [5]. D. Barrick, M. Evans, B. Weber, Ocean surface currents mapped by radar, *Science*, Vol. 189, 1977, pp. 138-144.
- [6]. B. J. Lipa, D. E. Barrick, Analysis Methods for Narrow-Beam High-Frequency Radar Sea Echo, Technical Report 420-WP, Vol. 56, *U.S. Department of Commerce, National Oceanic and Atmospheric Administration, Environmental Research Laboratories*, 1982.
- [7]. D. Savidge, J. Amft, A. Gargett, M. Archer, D. Conley, G. Voulgaris, L. Wyatt, K.-W. Gurgel, Assessment of WERA long-range HF-radar performance from the user's perspective,

- in *Proceedings of the IEEE/OES 10<sup>th</sup> Current, Waves and Turbulence Measurements Conference (CWTM'11)*, Monterey, CA, 2011, pp. 31-38.
- [8]. B. Lipa, B. Nyden, Directional wave information from the seasonde, *IEEE Journal of Oceanic Engineering*, Vol. 30, 2005, pp. 221-231.
  - [9]. R. Long, D. Barrick, J. Largier, N. Garfield, Wave observations from Central California: SeaSonde systems and in-situ wave buoys, *Journal of Sensors*, Vol. 2011, 2011, 728936.
  - [10]. B. Lipa, B. Nyden, D. Barrick, J. Kohut, HF radar sea-echo from shallow water, *Sensors*, Vol. 8, 2008, pp. 4611-4635.
  - [11]. CODAR Ocean Sensors, <http://www.codar.com/SeaSonde.shtml>
  - [12]. C. Ohlmann, P. White, L. Washburn, E. Terrill, B. Emery, M. Otero, Interpretation of coastal HF radar-derived surface currents with high-resolution drifter data, *Journal of Atmospheric and Oceanic Technology*, Vol. 24, 2007, pp. 668-680.
  - [13]. M. Hubbard, D. Barrick, N. Garfield, J. Pettigrew, C. Ohlmann, M. Gough. A new method for estimating high-frequency radar error using data from central San Francisco bay, *Ocean Science Journal*, 2013, pp. 1-12.
  - [14]. J. T. Kohut, S. M. Glenn, Improving HF radar surface current measurements with measured antenna beam patterns, *J. Atmos. Oceanic Technol.*, Vol. 20, 2003, pp. 1303-1316.
  - [15]. C. W. Evans, H. J. Roarty, E. M. Handel, S. M. Glenn, Evaluation of three antenna pattern measurements for a 25 MHz SeaSonde, in *Proceedings of the IEEE/OES 11<sup>th</sup> Current, Waves and Turbulence Measurement Conference (CWTM'15)*, St. Petersburg, FL, 2015.
  - [16]. L. Washburn, E. Romero, C. Johnson, B. Emery, C. Gotschalk, measurement of antenna patterns for oceanographic radars using aerial drones, *J. Atmos. Oceanic Technol.*, Vol. 34, 2017, pp. 971-981.
  - [17]. Daily Weather Map, <http://www.wpc.ncep.noaa.gov/dailywxmap/>

## Appendix

### Comparisons of Wave Spectral Models and Measured Frequency Spectra from the Lisbon Buoy

The Lisbon Directional Waverider buoy<sup>1</sup> is located offshore from Costa da Caparica village at 38° 32.683' N, 9° 18.547' W, ~5.4 km from the coast and in water of depth 110 m. It has three accelerometers (in the X, Y and Z planes) located on a horizontally stabilized platform. The time series that are acquired consist of displacements in the North-South and East-West and vertical directions. From this data wave parameters including height, period and direction are derived and transmitted every 10 minutes and wave spectra every 30 minutes.

Fig. 20.17 shows the nondirectional wave spectrum measured by the buoy at the same time as the radar spectrum shown in Fig. 20.12.

It can be seen that the second-order radar spectrum (Fig. 20.12) and the buoy wave energy spectrum (Fig. 20.17) both clearly display bimodal behavior: For the buoy, the swell peak

---

<sup>1</sup> The Lisbon Directional Waverider buoy is manufactured by Datawell and owned by the Portuguese Hydrographic Institute

occurs at about 0.05 Hz, in agreement with the radar swell peaks that are displaced about 0.05 Hz from the first-order echo. The broader wind-wave spectrum is at higher frequencies (buoy) and further displaced from the first-order spectrum (radar).

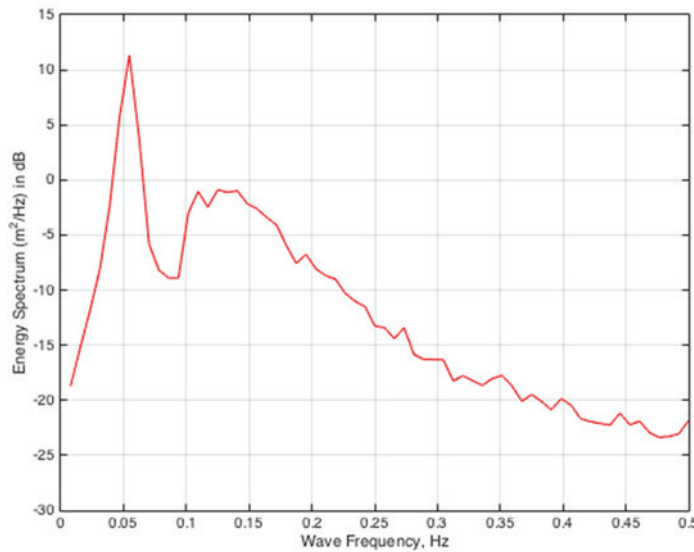


**Fig. 20.17.** The nondirectional spectrum measured by the Lisbon buoy at the same time as the radar spectrum shown in Fig. 20.3 (April 19, 2015, 9:50 am UTC).

The model ocean nondirectional spectra were least-squares fitted to buoy spectra measured from April 15 to 22 to give optimum model parameters using two procedures:

- i. The P/M model defined in (20.12) was assumed to apply at all frequencies.
- ii. The P/M model defined in (20.12) was assumed to apply at higher frequencies and the nondirectional triangular model defined in (20.14) was assumed to apply at lower frequencies, with the frequency boundary determined by the fitting procedure.

It was found that when the second-order spectrum is broad, using the P/M model for all frequencies provides an adequate fit, but when there are narrow, long-period peaks, it does not. An example of this effect is given in Fig. 20.18.

The RMS differences between measured buoy spectra and the best-fit model were calculated for the procedures (i) and (ii) over the 160-hour period; results are given in Fig. 20.19.

It can be seen from Fig. 20.19 that when the buoy peak period exceeds about 12 s indicating the presence of long-period swell, the RMS deviations for the bimodal model are significantly lower than those for the unimodal model, indicating that the bimodal model provides a better fit.



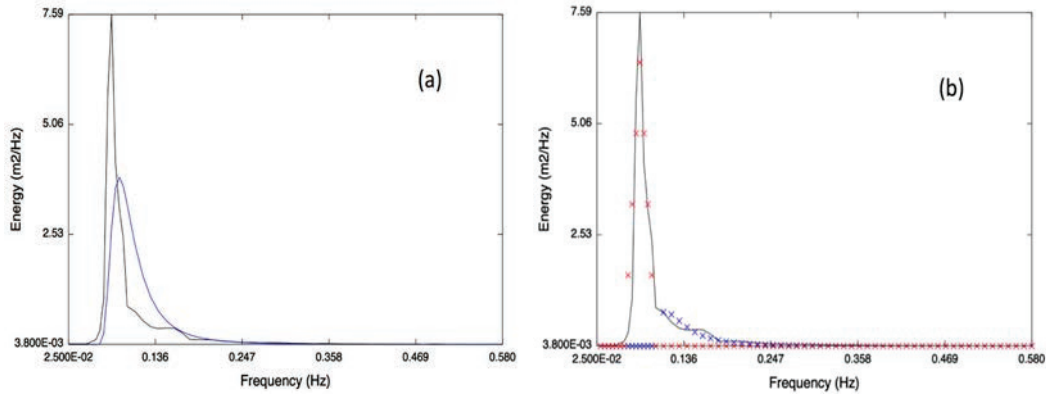


**Fig. 20.18.** An example of least-squares fitting of the measured buoy spectrum for April 12, 2015, 7:20 am. (a) Buoy (black), P/M model fit for all frequencies (blue line). The plot indicates a poor fit. (b) Buoy (black), P/M model fit for frequencies >0.1 Hz (blue crosses) and triangular swell model fit for frequencies <0.1 Hz (red crosses). Using the bimodal with two spectral peaks shows a much better overall fit to measured wave spectrum.

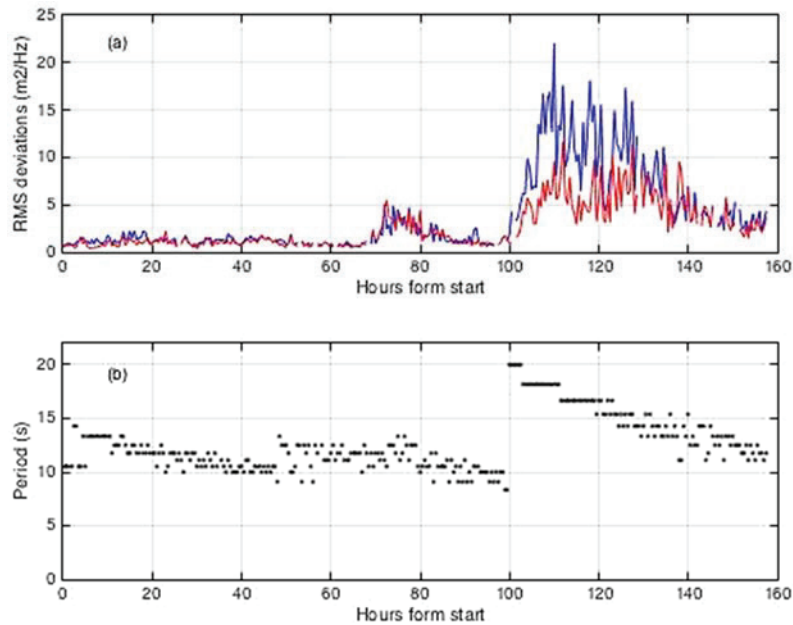


**Fig. 20.19.** (a) RMS differences between measured buoy and model-fit spectra, plotted vs. time. Start time April 15, 2015, 0:30 am Blue: Method i: P/M model for all frequencies (blue); Red: Method ii: Triangular swell model for lower frequencies and P/M wind-wave model for higher frequencies. (b) Measured buoy peak period plotted vs. time.





# The Global High Frequency Radar Network

Hugh Roarty<sup>1\*</sup>, Thomas Cook<sup>2</sup>, Lisa Hazard<sup>2</sup>, Doug George<sup>3</sup>, Jack Harlan<sup>4</sup>, Simone Cosoli<sup>5</sup>, Lucy Wyatt<sup>6</sup>, Enrique Alvarez Fanjul<sup>7</sup>, Eric Terrill<sup>2</sup>, Mark Otero<sup>2</sup>, John Largier<sup>3</sup>, Scott Glenn<sup>1</sup>, Naoto Ebuchi<sup>8</sup>, Brian Whitehouse<sup>9</sup>, Kevin Bartlett<sup>10</sup>, Julien Mader<sup>11</sup>, Anna Rubio<sup>11</sup>, Lorenzo Corgnati<sup>12</sup>, Carlo Mantovani<sup>12</sup>, Annalisa Griffa<sup>12</sup>, Emma Reyes<sup>13</sup>, Pablo Lorente<sup>7</sup>, Xavier Flores-Vidal<sup>14</sup>, Kelly Johanna Saavedra-Matta<sup>14</sup>, Peter Rogowski<sup>2</sup>, Siriluk Prukpitikul<sup>15</sup>, Sang-Ho Lee<sup>16</sup>, Jian-Wu Lai<sup>17</sup>, Charles-Antoine Guerin<sup>18</sup>, Jorge Sanchez<sup>19</sup>, Birgit Hansen<sup>20</sup> and Stephan Grilli<sup>21</sup>

## OPEN ACCESS

### Edited by:

Sabrina Speich,  
École Normale Supérieure, France

### Reviewed by:

Jeffrey Dean Paduan,  
Naval Postgraduate School,  
United States  
Rosemary Anne Morrow,  
UMR5566 Laboratoire d'Etudes en  
Géophysique et Océanographie  
Spatiales (LEGOS), France

### \*Correspondence:

Hugh Roarty  
hroarty@marine.rutgers.edu

### Specialty section:

This article was submitted to  
Ocean Observation,  
a section of the journal  
Frontiers in Marine Science

**Received:** 20 November 2018

**Accepted:** 15 March 2019

**Published:** 14 May 2019

### Citation:

Roarty H, Cook T, Hazard L,  
George D, Harlan J, Cosoli S,  
Wyatt L, Alvarez Fanjul E, Terrill E,  
Otero M, Largier J, Glenn S,  
Ebuchi N, Whitehouse B, Bartlett K,  
Mader J, Rubio A, Corgnati L,  
Mantovani C, Griffa A, Reyes E,  
Lorente P, Flores-Vidal X,  
Saavedra-Matta KJ, Rogowski P,  
Prukpitikul S, Lee S-H, Lai J-W,  
Guerin C-A, Sanchez J, Hansen B  
and Grilli S (2019) The Global High  
Frequency Radar Network.  
Front. Mar. Sci. 6:164.  
doi: 10.3389/fmars.2019.00164

<sup>1</sup> Department of Marine and Coastal Sciences, Rutgers, The State University of New Jersey, New Brunswick, NJ, United States, <sup>2</sup> Scripps Institution of Oceanography, Coastal Observing Research and Development Center, La Jolla, CA, United States, <sup>3</sup> Coastal and Marine Sciences Institute, University of California, Davis, Davis, CA, United States, <sup>4</sup> United States Integrated Ocean Observing System Program Office, NOAA, Silver Spring, MD, United States, <sup>5</sup> Ocean Graduate School and UWA Oceans Institute, The University of Western Australia, Crawley, WA, Australia, <sup>6</sup> School of Mathematics and Statistics, The University of Sheffield, Sheffield, United Kingdom, <sup>7</sup> Puertos del Estado, Madrid, Spain, <sup>8</sup> Institute of Low Temperature Science, Hokkaido University, Sapporo, Japan, <sup>9</sup> OEA Technologies Inc., Upper Tantallon, NS, Canada, <sup>10</sup> Ocean Networks Canada, Victoria, BC, Canada, <sup>11</sup> AZTI Marine Research, Pasaia, Spain, <sup>12</sup> Institute of Marine Sciences, National Research Council of Italy, Lerici, Italy, <sup>13</sup> ICTS SOCIB, Palma, Spain, <sup>14</sup> Instituto de Investigaciones Oceanológicas, Universidad Autónoma de Baja California, Ensenada, Mexico, <sup>15</sup> Geo-Informatics and Space Technology Development Agency, Bangkok, Thailand, <sup>16</sup> Kunsan National University, Gunsan, South Korea, <sup>17</sup> NARLabs, Taiwan Ocean Research Institute (TORI), Taipei, Taiwan, <sup>18</sup> Mediterranean Institute of Oceanography, University of Toulon, Toulon, France, <sup>19</sup> Qualitas Remos, Madrid, Spain, <sup>20</sup> HELZEL Messtechnik GmbH, Kaltenkirchen, Germany, <sup>21</sup> Department of Ocean Engineering, University of Rhode Island, Kingston, RI, United States

Academic, government, and private organizations from around the globe have established High Frequency radar (hereinafter, HFR) networks at regional or national levels. Partnerships have been established to coordinate and collaborate on a single global HFR network (<http://global-hfradar.org/>). These partnerships were established in 2012 as part of the Group on Earth Observations (GEO) to promote HFR technology and increase data sharing among operators and users. The main product of HFR networks are continuous maps of ocean surface currents within 200 km of the coast at high spatial (1–6 km) and temporal resolution (hourly or higher). Cutting-edge remote sensing technologies are becoming a standard component for ocean observing systems, contributing to the paradigm shift toward ocean monitoring. In 2017 the Global HFR Network was recognized by the Joint Technical WMO-IOC Commission for Oceanography and Marine Meteorology (JCOMM) as an observing network of the Global Ocean Observing System (GOOS). In this paper we will discuss the development of the network as well as establishing goals for the future. The U.S. High Frequency Radar Network (HFRNet) has been in operation for over 13 years, with radar data being ingested from 31 organizations including measurements from Canada and Mexico. HFRNet currently holds a collection from over 150 radar installations totaling millions of records of surface ocean velocity measurements. During the past 10 years in Europe,

HFR networks have been showing steady growth with over 60 stations currently deployed and many in the planning stage. In Asia and Oceania countries, more than 110 radar stations are in operation. HFR technology can be found in a wide range of applications: for marine safety, oil spill response, tsunami warning, pollution assessment, coastal zone management, tracking environmental change, numerical model simulation of 3-dimensional circulation, and research to generate new understanding of coastal ocean dynamics, depending mainly on each country's coastal sea characteristics. These radar networks are examples of national inter-agency and inter-institutional partnerships for improving oceanographic research and operations. As global partnerships grow, these collaborations and improved data sharing enhance our ability to respond to regional, national, and global environmental and management issues.

**Keywords:** remote sensing, high frequency radar, ocean currents, waves, tsunami, boundary currents, ocean observing system

## INTRODUCTION

Ocean currents regulate the climate by carrying warm water from the equator toward the poles. The ability to measure these currents will allow us to monitor and hopefully predict the trajectory of our climate. Western boundary currents are important areas for understanding and measuring the oceans impact on and response from climate processes (Send et al., 2009). Approximately 1.2 billion people (23% of the world population) live within 150 km of the coast (Small and Nicholls, 2003). These populations are projected to increase as more people migrate to the coast. This current and projected population will put a strain on coastal ecosystems because of the resources that humans extract from the coast as well as the waste we dispose of in the coastal ocean. Coastal ocean health is critical for human health because humans are exposed to disease causing organisms in this interface (Stewart et al., 2008). Therefore, it is essential to improve existing and develop new coastal management techniques and strategies in order to protect the world's most critical ecosystems (Boesch et al., 2000). Quantifying coastal ocean currents is one such tool to manage the ecosystem. There are several different methods in order to accomplish this. Surface drifters (Lumpkin et al., 2013) provide an accurate measurement of surface drift with high temporal resolution. The drawbacks of this platform are the short-lived nature of the surface floats (order 1 month in a given region like those used in the Global Drifter Program or due to battery life like those used by the United States Coast Guard). Acoustic Doppler Current Profilers (ADCPs) provide single-point or along-track velocity current data with high temporal resolution with measurements throughout the water column. ADCPs with a servicing interval on the order of 1 year carry with it the high cost of ship time to deploy and service the mooring. Satellite-altimetry derived currents provide valuable insights on large-scale geostrophic ocean circulation, but satellite observations of currents near the coast are poor for a few reasons: (i) the sampling strategy was not designed for near-coast regions, (ii) altimetry observations are of lower accuracy near the coast due to land contaminations (altimeter and radiometer), (iii) inaccurate removal of atmospheric effects

at the surface and incorrect tidal corrections (Vignudelli et al., 2005; Liu and Weisberg, 2007).

Oceanographic HFRs have been identified as a cost-effective complement to *in situ* systems by providing increased spatial coverage (Fujii et al., 2013). The measurement is typically confined to the coastal zone and can be effective to fill the gaps of other monitoring platforms, such as satellite-based sensors, but with much higher temporal resolution. HFR derived ocean surface currents are a remotely sensed measurement typically collected with land-based sensors, which reduces operations and maintenance budgets for collection of the data as compared to ship-based and moored sensors. There have been measurements with HFR in the open ocean aboard large oil platforms (Lipa et al., 1990) but the vast majority of platforms are located along coastlines. Additionally, HFR operates continuously, and with proper maintenance, is capable of observing time-series with high temporal resolution and longtime records (some sites operating for two decades). These measurements allow for both Eulerian and Lagrangian estimates of the flow field (Ohlmann et al., 2007).

Coastal radars typically operate in the HF and UHF radio bands (3–50 MHz), and transmit and receive a ground wave that couples to the salty sea water surface (Figure 1). There have been oceanographic applications of sky wave signals (Anderson, 1986; Headrick and Thomason, 1998) but the large size and cost of these systems have not made them a viable option for the oceanographic community. The traditional measurement of the HFR using groundwave propagation is a radial map of currents derived once an hour (Figure 2), but higher temporal resolution sampling schemes are occasionally utilized (Piedracoba et al., 2016). Because of the long radio wavelengths at HF (100 m – 10 m) the receive antennas are kept stationary to look in different directions compared to microwave antennas that are typically rotated to determine bearing. Bearing determination, as it relates to measuring ocean surface currents with HFR, describes the method used by the radar to determine direction of arrival of the signal echo. This processing step is divided into two groups, direction-finding and beam-forming (aka phased array). Direction-finding (compact array) radars, such as the Coastal Ocean Dynamic Application Radar (CODAR) SeaSonde



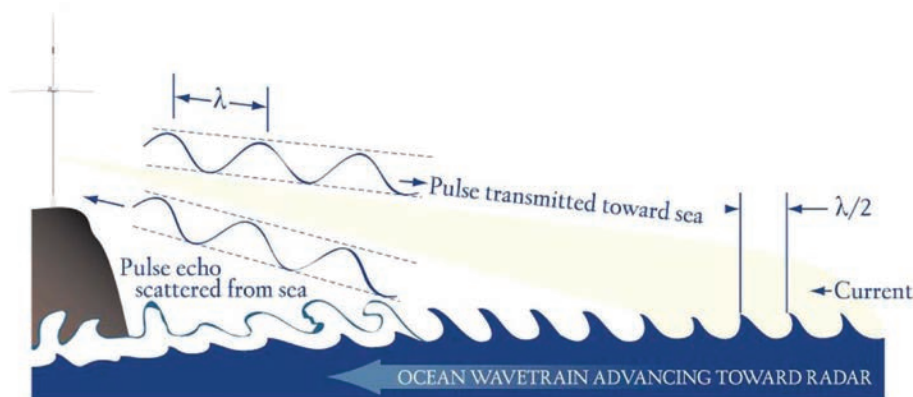


**FIGURE 1 |** Schematic figure depicting the Bragg scattering process that allows for ocean current measurements with High Frequency radio signals. The echo scattered from the sea is amplified when the transmitted radio signal encounters an ocean wave that has a wavelength that is half the wavelength of the radio signal.

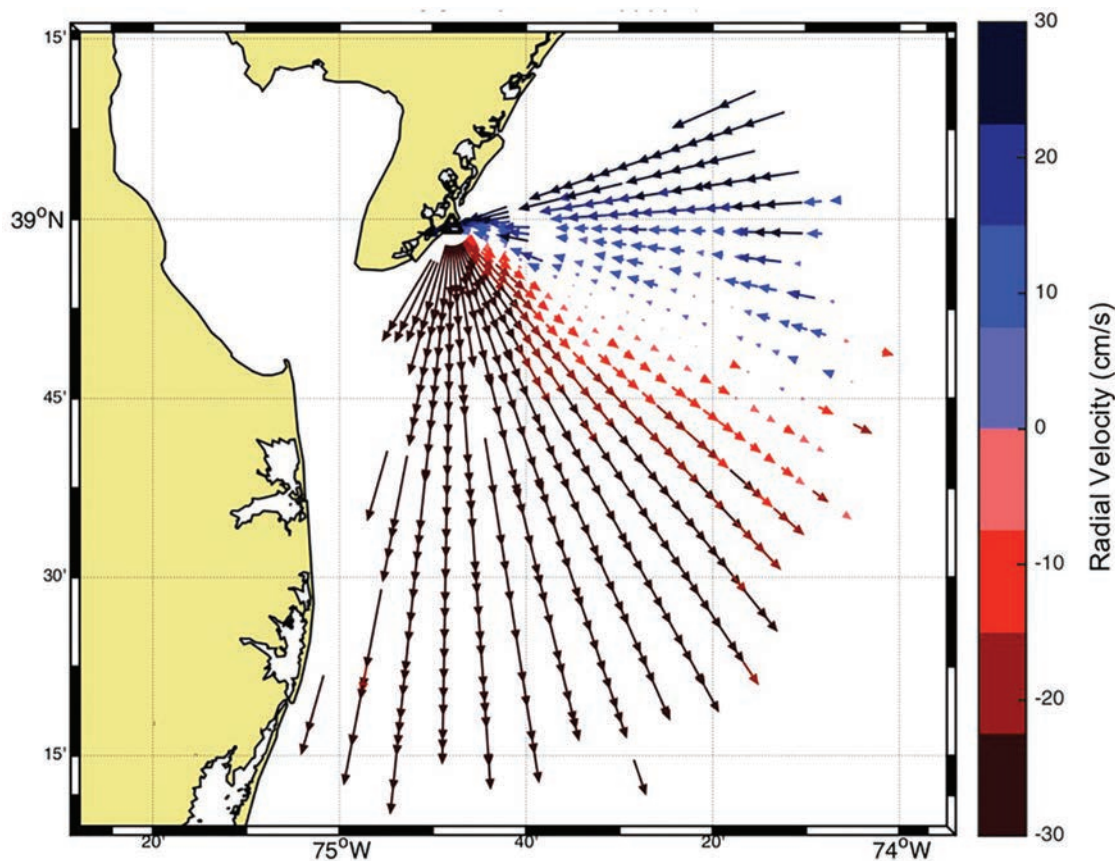


**FIGURE 2 |** Radial map of ocean currents derived from an HF radar station (triangle). The blue vectors denote surface currents towards the radar station while red vectors show currents away from the radar.

(Barrick and Lipa, 1985), compare the phases and amplitudes of radio signals received by closely spaced antenna elements coupled with various direction-finding inversion algorithms. Beam-forming radars adjust the amplitude and phase of the received signal through an array of antennas to determine bearing (de

Paolo and Terrill, 2007). Early versions of this radar type included the Ocean Surface Current Radar (OSCR) and Pisces. The radar models available as of this manuscript with a beam-forming design include the Pisces (Wyatt et al., 2006), the Wellen Radar -WERA- (Helzel et al., 2007) and LERA (Flament et al., 2016).

Regardless of the manufacturer, the positive contribution of commercial HFR systems to retrieve realistic wave and surface current information has been unequivocally proven.

A recent advancement in the radar technology is the bistatic measurement (Lipa et al., 2009; Baskin et al., 2016) where the transmitter and receiver are geographically separated which yields an elliptical map of ocean surface currents. The radial or elliptical measurements from multiple stations are combined via a variety of combining methods to produce an hourly map of total currents (**Figure 3**) typically, once an hour. An ensemble of total vector files can be used to generate a trajectory model of virtual surface drifters to demonstrate the fate of particles on the surface (**Figure 4**). The readers are referred to Paduan and Washburn (2013) for a thorough discussion of oceanographic HFR theory, development, and applications.

The information contained in the second order region, of much lower amplitude than the first order peak, are utilized to obtain the wave information, i.e., height, centroid period and direction or the full directional spectrum and derived parameters (Wyatt et al., 2011). Wave measurements are obtained using some version of the theory of Barrick (1977). The current techniques for wave measurements range from empirical methods, which relate wave parameters (significant wave height) to an integral of the second order Doppler spectrum, to full numerical inversions, which can provide the ocean wave directional spectrum if the quality of the radar data is good enough. The frequency of the radar determines the maximum and minimum wave height that can be measured by any system. The lower the frequency the higher the wave height that can be measured. For example, the maximum wave height that can be measured at 25 MHz is 4 m however it is 20 m at 5 MHz operating frequency (Lipa and Nyden, 2005). Below the minimum threshold, the lower-energy second-order spectrum is closer to the noise floor and more likely contaminated with spurious contributions that might result in wave height overestimation or limited temporal continuity in wave measurements. Above the maximum threshold, the first-order peak merges with the second-order one and the interpretation of the spectra becomes impossible with existing methods. In this context, recent efforts have been focused on the improvement of wave height estimation for highly variable sea states by using dual-frequency HFR systems (Wyatt and Green, 2009). HFR-derived wave measurements also have a broad range of practical applications and can be used as benchmark for wave model skill assessment (Lorente et al., 2018), as input for assimilation into SWAN or Wavewatch III models (Waters et al., 2013), or for the analysis of extreme wave height events (Atan et al., 2015).

HFR can also be used to estimate wind speed and direction but are not yet robust enough for operational use. The ratio of two first order peaks can be utilized to estimate wind direction (Fernandez et al., 1997; Wyatt, 2018). Estimates of wind speed have also been obtained from the second order peaks (Kirincich, 2016).

The initial “coming of age” for HFR occurred between 2000 and 2010, in which real-time HFR data was accepted as a reliable operational tool. For example, surface current data is ingested in the United States (US) by federal and state group for search

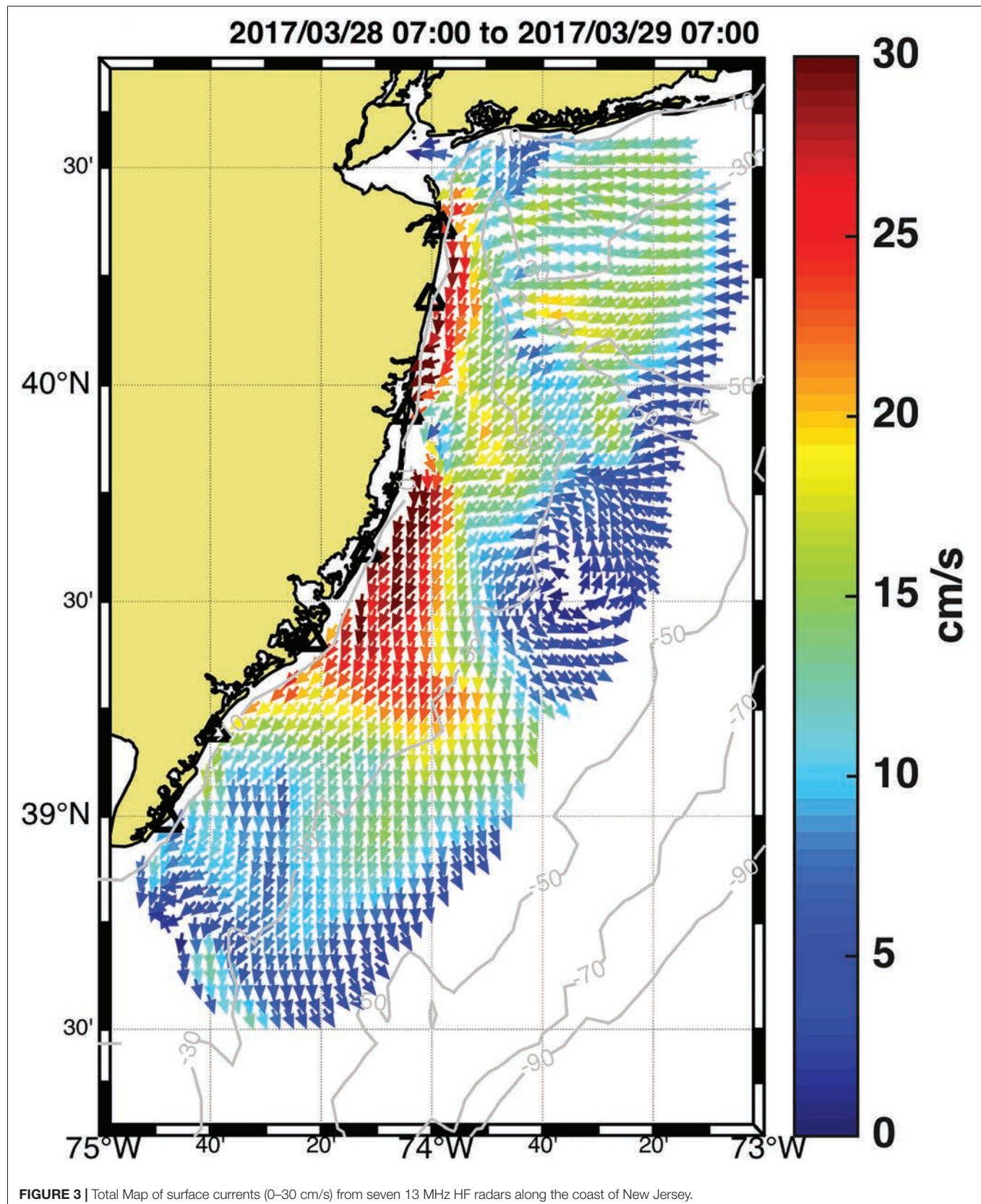
and rescue (SAR), oil spill and other operational protocols in coastal waters. Success stories have emerged over the past decade from the United States and elsewhere, as well as examples where the importance of HFR surface currents data was noted (e.g., Deep Water Horizon oil spill in the Gulf of Mexico). The next phase for HFR applications involves the recognition of the value of long-term, high-resolution surface currents for tracking environmental change and marine resources, including coastal water quality, coastal ecosystems and fisheries. This second coming of age is imminent with data sets of over 10 years now available from the west and east coasts of the United States as well as from northern Japan.

The Global High Frequency Radar Network was established in 2012 as part of the Group on Earth Observations 2012–2015 Work Plan (Roarty et al., 2014). A series of meetings were held to jump start the collaboration England 2012, Norway 2013, Taiwan 2014, Crete 2015, and finally the United States in 2016 (Roarty et al., 2016). This series of meetings introduced the radar network to global organizations like the Global Ocean Observing System (GOOS) and the Joint Technical Commission for Oceanography and Marine Meteorology (JCOMM). JCOMM coordinates oceanographic measurements, data and services between the Intergovernmental Oceanographic Commission (IOC) and the World Meteorological Organization (WMO). The GOOS is executed within the IOC. In 2017 the Global HFR Network along with ocean gliders were recognized by JCOMM as an observing network of GOOS.

## DEVELOPMENT OF NETWORKS

Academic, government, and private organizations from around the globe have established high frequency radar (HFR) networks at regional or national levels to support scientific and operational activities along the coast. The growth of the network remains steady with approximately 400 stations currently operating and collecting real-time surface current information. There are approximately 281 sites reporting to the GEO list as of 2018. The United States and Europe have tracked the growth of this sensor technology versus time (**Figure 5**). Approximately 140 installations are active in the Asia-Pacific region, and this number is expected to grow with new installations in the Philippines and Vietnam. HFR systems have also been recently installed in South Africa. The number of organizations displaying surface current information on the Global Network page has also increased from 7 in November 2016 to 13 in May 2017. The organizations currently providing surface current information to the Global Network are shown in **Table 1**.

The Global Network has been organized according to the International Telecommunication Union (ITU) regions (**Figure 6**). Region 1 encompasses Europe, Africa and northern Asia. Region 2 covers the Americas and Region 3 comprises southern Asia and Oceania. In 2012 Resolution 612 was passed by the ITU establishing the use of the radiolocation service between 3 and 50 MHz to support (high-frequency) oceanographic radar operations. This was an important first step for the community because it established the importance of HFR to





receive designation in frequency space for the operation of the radars. There is still more work to be done because while the ITU sets global standards, each region and country within will set specific service rules and licensing regulations. Acquiring a frequency allocation that allows HFR as a primary user is a current goal for the community, as interference within HF bands greatly impacts HFR performance.

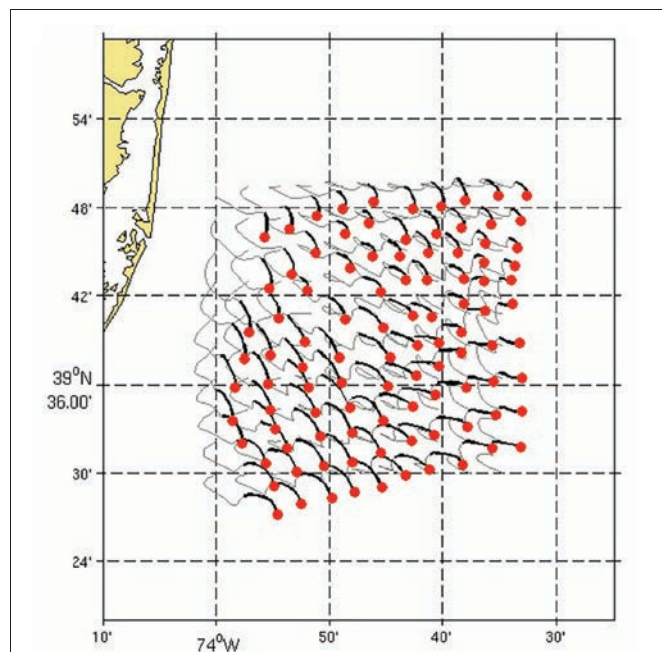


**FIGURE 4 |** Twenty four hour simulation of virtual trajectories from the surface currents in **Figure 3**. The virtual surface particles (red dots), the trajectory of the particle over the past 24 h (gray line) and the path of the particle over the past 6 h (black line) are shown.

Here is a brief description on the history and present status of HFR networks within the Global regions.

## Europe, Africa and Middle East (Region 1)

In Europe (EU), the use of HFR systems is growing with over 62 HFR sites currently operating and a number in the planning stage. A survey to catalog the status of different HFR systems available in the Europe was launched in June 2016 and has been maintained up to date (Mader et al., 2016). The survey gathered responses from 28 European institutions and information on more than 70 HFR systems. From 2004 until 2009 a moderate growth rate of two new HFRs per year was observed and, since 2009, it has increased to around six new HFRs installed per year and up to seven, since 2016 (**Figure 5B**). The most popular identified user of the EU HFR data was academia, followed by European or national maritime safety agencies and weather services (Rubio et al., 2017). The most popular research lines were those related to Lagrangian approaches to surface transport and connectivity (e.g., Menna et al., 2007; Abascal et al., 2009; Uttieri et al., 2011; Berta et al., 2014a; Berta M. et al., 2014b; Bellomo et al., 2015; Solabarrieta et al., 2016; Cianelli et al., 2017), data assimilation and the validation and calibration of numerical ocean forecasting models especially near the coast (e.g., Barth et al., 2008, 2011; Marmain et al., 2014; Stanev et al., 2015; Iermano et al., 2016; Lorente et al., 2016; Hernández et al., 2017) and small scale and mesoscale ocean processes (e.g., Sentchev et al., 2013; Berta et al., 2018; Hernández-Carrasco et al., 2018; Rubio et al., 2018a).

The European contribution to the Global Network is on a volunteer basis and no dedicated funding is allocated directly to the providers for a coordinated effort. The European coordination of HFR systems started with the EuroGOOS HFR Task Team (TT) in 2014, which increased the global visibility of the European HFR systems and enabled a joint integration

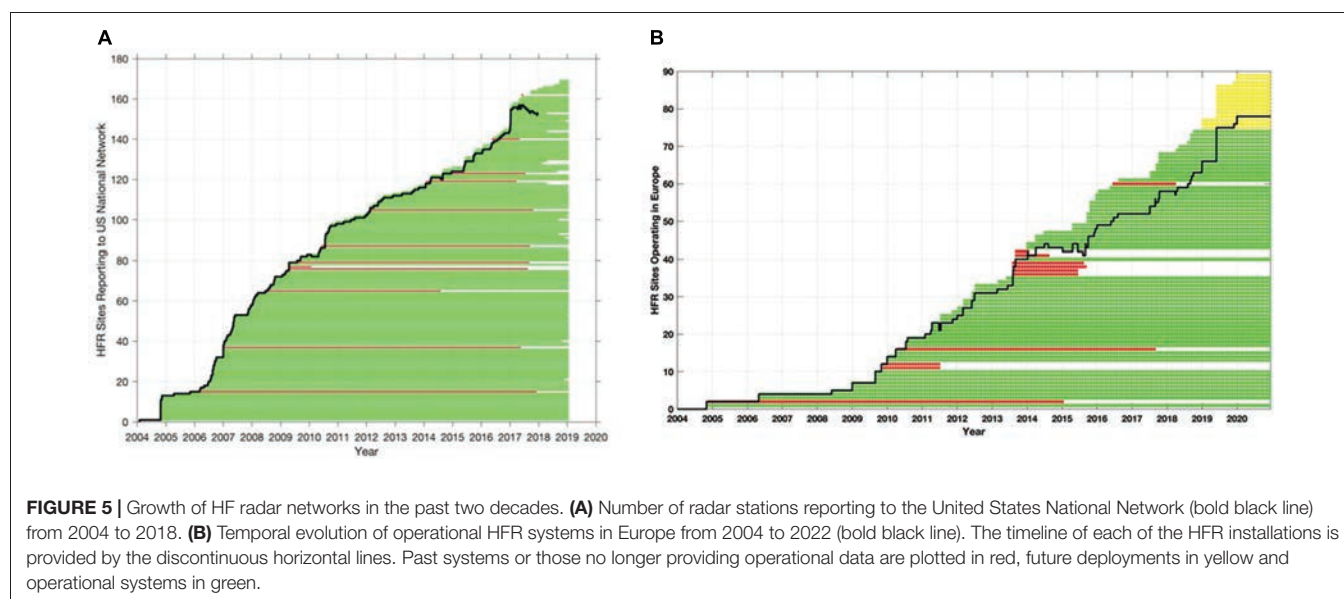


**FIGURE 5 |** Growth of HF radar networks in the past two decades. **(A)** Number of radar stations reporting to the United States National Network (bold black line) from 2004 to 2018. **(B)** Temporal evolution of operational HFR systems in Europe from 2004 to 2022 (bold black line). The timeline of each of the HFR installations is provided by the discontinuous horizontal lines. Past systems or those no longer providing operational data are plotted in red, future deployments in yellow and operational systems in green.



**TABLE 1** | List of countries and organizations providing surface current information to the Global HF Radar Network.

Number	Country	Organization
1	Australia	Integrated Marine Observing System
2	Canada	Ocean Networks Canada
3	Croatia	Institute of Oceanography and Fisheries
4	Germany	Helmholtz-Zentrum Geesthacht Centre for Materials and Coastal Research
5	Italy	CNR, Consiglio Nazionale delle Ricerche OGS, Istituto Nazionale di Oceanografia e di Geofisica Sperimentale
6	Malta	University of Malta, Physical Oceanography Unit (PO-Unit), International Ocean Institute-Malta Operational Centre (IOI-MOC)
7	Mexico	Observatorio de Corrientes Oceánicas MEXicanas (OCOMEX)
8	Spain	Puertos del Estado SOCIB, Balearic Islands Coastal Observing and Forecasting System Meteorological Agency ( <i>Euskalmet</i> ) INTECMAR Universidad de Vigo Universidad de Cádiz
9	Taiwan	TOROS (Taiwan Ocean Radar Observing System)
10	United States	Integrated Ocean Observing System (IOOS)

in the Global Network. From its conception the EuroGOOS HFR TT has ensured a close exchange with the GEO Global HF radar network and participated in GEO Global HF radar task meetings. The two European co-chairs of the GEO Global HF radar task are members of the EuroGOOS HFR TT core group, and this institutional collaboration should continue in the future. In addition, the definition of the EU HFR data standard has been developed by the EuroGOOS HFR TT in close collaboration with the EU and US.

In 2018, the HFR EU data node was created as a centralized European competence center to ensure the implementation of the HFR data stream (harvesting, harmonization, formatting, and distribution) from the data providers toward the different EU marine data portals and global data infrastructures. A plan for the inclusion of HFR data into the Copernicus Marine Environment Monitoring Service (CMEMS) through this EU data node is in progress. First steps toward this integration were carried out under the CMEMS INCREASE Project (Rubio et al., 2018b). A survey of the CMEMS community by the INCREASE project highlighted the interest shown in having access to HFR current data at a global level and to operational data derived from the advanced processing of the HFR backscatter signals, such as waves and maps of wind direction, which opens future working lines.

The CMEMS In Situ Thematic Centre (CMEMS-INSTAC), will start delivery of near-real time (NRT) total and radial HFR data from certain sites in April 2019 and April 2020, respectively. The data distribution will be made both at a global and regional level, aiming to foster the relationship between users, providers, and the INSTAC regional components inside

the regional alliances of EuroGOOS (ROOSes). Other European HFR operators will be supported in their preparation of their involvement, in order to achieve the final goal of distributing all European HFR data within CMEMS-INSTAC, SeaDataCloud and EMODnet platforms.

Inside CMEMS-INSTAC the HFR data set is considered part of a global product of ocean surface currents, and will be delivered jointly with the global surface drifter data set. The CMEMS structure is thus ready to embrace a global dimension for the HFR data. Work is underway to prepare for the inclusion of United States HFR data from the United States IOOS National HFR Node into the CMEMS-INSTAC Global Distribution Unit, planned for April 2020. This preparation phase is being developed with the MARACOOS (IOOS regional association in the Mid-Atlantic) network and is mainly focused on treating the dataflow and the few discrepancies between United States and European standard data models.

In parallel, the EU Project JERICO-NEXT is working to provide procedures and methodologies to enable HFR data to comply with the international standards regarding their quality and metadata, within the overall goal of integrating the European coastal observatories (Corgnati et al., 2018b).

The ongoing MyCoast project aims to build a coordinated coastal operational observatory in the Atlantic Ocean by improving the synergies between observational and forecasting systems. A dedicated work package is devoted to the analysis and enhancement of HFR-derived wave estimations and the subsequent application to extreme weather events and maritime safety. There is an ongoing effort and a considerable planned investment in the North-Western Mediterranean between Italy and France (Quentin et al., 2017), in the framework of the EU Interreg Maritime Program (projects IMPACT and SICOMAR-PLUS). The plan is to build a network of sixteen HFRs, nine of them already operating, covering 600 km of coastline between the two countries by the end of 2021. The general purpose, through the integration of the HFR data with numerical models and *in situ* measurements, is the development of operational tools in the field of SAR operations and protection of the marine environment. Lastly there is an effort in Europe taking place in the Malta Channel area between Sicily (Italy) and Malta where four HFRs are currently operating as part of the EU Interreg project CALYPSO. Three additional HFRs will be added inside 2019 to the CALYPSO network. The main goal of the CALYPSO project, led by the University of Malta and having the University of Palermo as the main Sicilian partner, is to support efficient response against the threat of marine oil spills and also to support SAR operations and improve security and safety at sea in the *trans-boundary* Mediterranean area between Malta and Sicily.

The reader is referred to Rubio et al. (2017) for a more thorough description of the HFR activities within Europe. Below are descriptions of new networks since this paper was published. In addition, we are aware of installations in Turkey, Israel, and South Africa that will be coming online soon.

## Morocco

The National Meteorological Directorate of Morocco (DMN) operates a network of two 5 MHz long-range HFRs (Bouksim et al., 2016) located in the Port of Casablanca and in

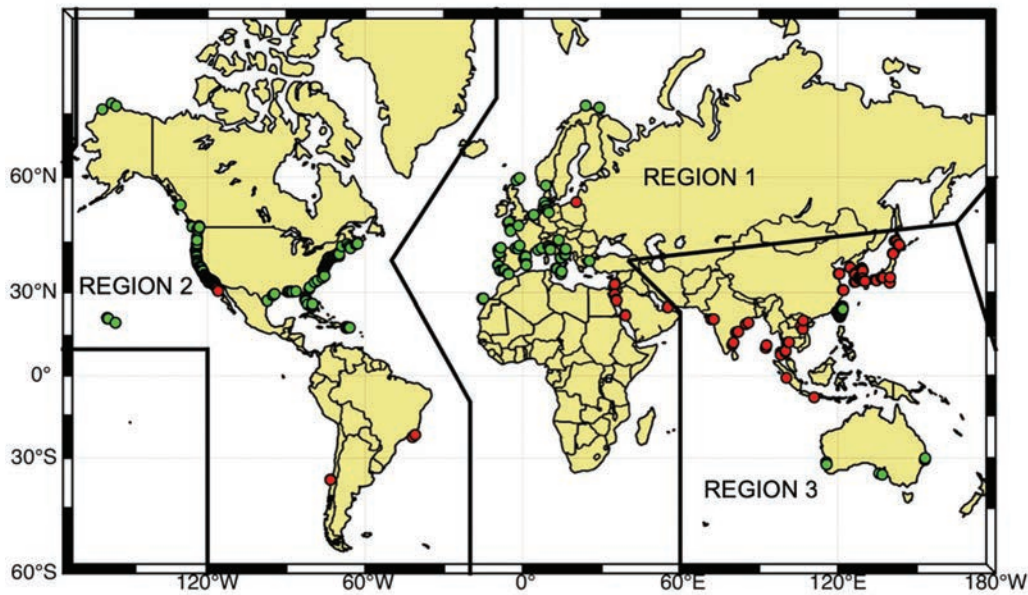


**FIGURE 6 |** Global distribution of HFR stations organized within the three regions of the International Telecommunications Union (ITU). The green dots indicate stations that are sharing their data through the global network and red dots indicate stations that are not currently sharing their data.

Temara with a measurement range of approximately 200 km offshore, covering an area of around 17,000 km<sup>2</sup> between Casablanca and Rabat. This network was commissioned in April 2016 and represents the first permanent HFR network deployed in Africa. DMN is initially applying HFR surface currents and wave data to validate their operational marine forecast models and to improve their knowledge of the hydrodynamics in this part of the Moroccan coast. In future work, data will also be used for SAR operations, safety in navigation and for better preparedness and response against marine pollution incidents in collaboration with the Royal Moroccan Navy, National Ports Agency and Civil Protection Authority.

Future DMN plans include the extension of the current network to the South to cover the energy port of Jorf Lasfar and the installation of two additional HFRs in Tanger Med and Cap Malabata to monitor the Strait of Gibraltar. Data exchange with Spain is also envisioned to combine data of this new network with the already existing HFR network in this area operated by the Spanish National Harbour Authority (Puertos del Estado) in order to cover the whole strait.

### Saudi Arabia

In 2015 King Abdullah University of Science and Technology (KAUST) and Saudi Aramco installed the first HFR network in the Kingdom of Saudi Arabia (KSA), composed of two 16 MHz HFRs, monitoring surface currents and waves in the central Red Sea (Solabarrieta et al., 2018). One HFR is located at a KSA Coast Guard station in Rabigh pairing with the other set on the KAUST campus in Thuwal. Both stations provide hourly surface currents measurements up to a range of 70–100 km with a spatial resolution of 3 km. The network was further expanded in 2017 to the North with the installation of two additional HFRs in Duba and Almuwaylih. KAUST owns two additional HFRs and plans to

install these two units in the Southern part of the Red Sea inside 2019. **Figure 7** shows the location of KAUST's current four radar network and envisioned location of the two additional units they plan to deploy in the Southern part of the Red Sea. Current use of the data is restricted to basic science, which will contribute to the Kingdom's fundamental understanding of ocean processes in the region. Some envisioned future applications include tracking of marine pollutants, fisheries management, safety of navigation and the design of marine protected areas.

### Portugal

The Portuguese Hydrographic Institute (IH), the main operational oceanography institution in Portugal, operates a network of five CODAR HFRs (Fernandes, 2014). The network consists of two 13 MHz HFRs deployed in 2010 deployed in São Julião and Espichel close to Lisbon and three 13 MHz CODAR HFRs installed along the coast of the Algarve in Vila Real, Alanzinha and Sagres inside the period 2012–2016 by the TRADE project<sup>1</sup>. The main goal of the TRADE network is to improve safety in navigation and port operations in the Gulf of Cadiz, from the Straits of Gibraltar (Spain) to Cape St. Vicente (Portugal). Use of the Portuguese HFR data includes validation of numerical surface currents models, tracking of marine pollutants and use in SAR cases. A CODAR Tsunami Detection Software Package has recently been also installed on the Sagres HFR station as part of the OCASO project in order to develop tsunami detection algorithms that are adapted to the very complex bathymetry of the area. The IH has a mid-term plan to extend its HFR network to a total of 20 stations.

<sup>1</sup><http://www.tradehf.eu>

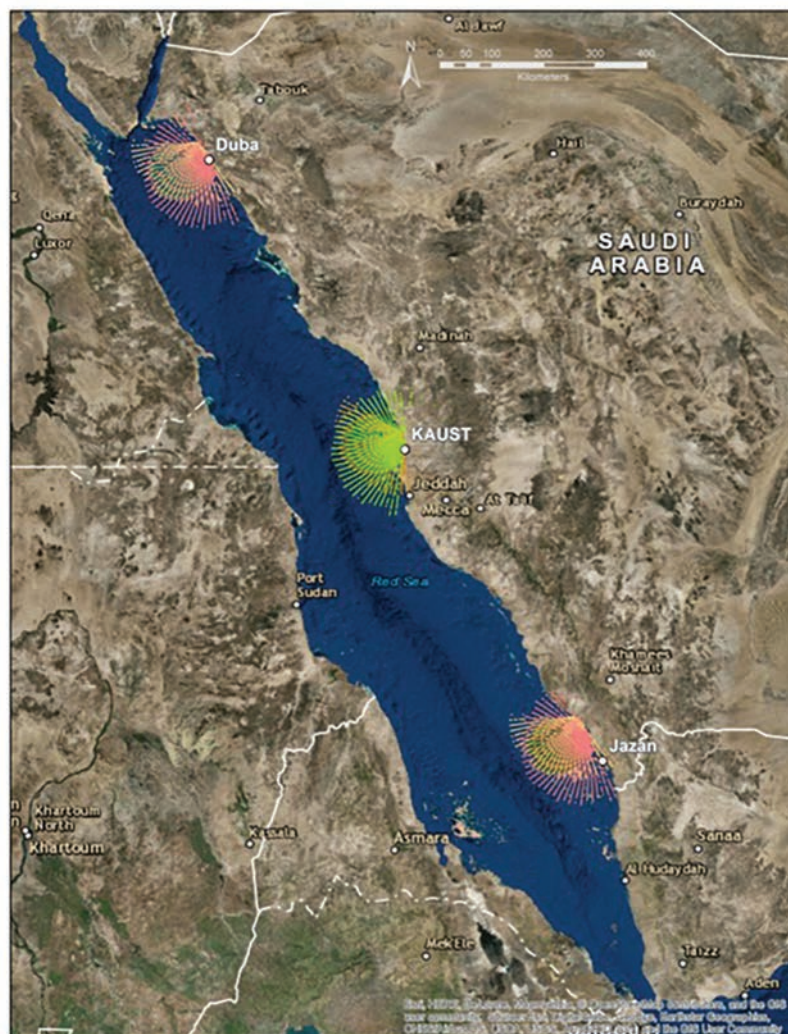


**FIGURE 7 |** HFR Network off the west coast of Saudi Arabia. The colors indicate typical radial coverage for the 6 HFR stations.

## The Americas (Region 2)

### Canada

Historically, Canada's coastal HFR activities have focused on vessel detection using phased-array systems on the Atlantic coast (Ponsford et al., 2003). This research and development continues as a component of Canada's defense research programs, but as of 2018 only one of Canada's 22 coastal HFRs falls within this category with an equal number of HFRs on the Pacific and Atlantic coasts. Sixteen of the HFRs are owned by universities and all but three are operated by universities. We make this distinction because the future of coastal HF radar in Canada is influenced by the fact that all of the existing radars and networks are research based and therefore financed through various finite research programs, as opposed to being components of the nation's operational maritime monitoring and surveillance infrastructure.

From an application perspective, vessel detection has the longest track record in Canada, but has yet to emerge from the R&D stage. Defence Research and Development Canada (DRDC)-Ottawa and Raytheon Canada Limited worked cooperatively for decades to develop over-the-horizon, phased-array HFR to detect vessels up to 200 nm from shore. Currently, DRDC Ottawa operates a 3rd generation HFR installed in 2015 near Halifax, Nova Scotia, Canada. The radar includes a spectrum management scheme that allows operation on a non-interference-basis.

Another defense research agency, DRDC Atlantic, is working cooperatively with Dalhousie University and the Marine Environmental Observation Prediction and Response (MEOPAR) Network, with a focus on oceanographic applications. Dalhousie is operating two of DRDC Atlantic's 5 MHz HFRs, which were installed in 2014 near Halifax, Nova Scotia, on either side of the above referenced phased-array



system owned by DRDC Ottawa. Dalhousie uses surface current data in its coastal circulation and ocean forecasting models. Its Department of Oceanography works cooperatively with Canada's Department of Environment and Climate Change, which is home to the nation's weather forecasting programs and operations. The Atlantic Pilotage Association has also expressed interest in this Halifax R&D network, but from a wave monitoring perspective in support of ship traffic operations.

On the Pacific coast, Ocean Networks Canada (ONC) (Heesemann et al., 2014) and the Department of Fisheries and Oceans own and operate coastal HFRs at various locations. ONC operates a WERA at Tofino (installed 2016), on Vancouver Island, four CODAR HF radars covering the Strait of Georgia (2011, 2012, 2016), and two CODARs covering Chatham Sound off Prince Rupert (2016, 2017). The WERA unit is used by German and American researchers to develop tsunami-detection algorithms. The CODARs are used by research programs run out of the University of British Columbia and the University of Victoria, but also by researchers located in Korea, China and other parts of Canada. There are also two ONC CODARs overlooking the Strait of Juan de Fuca, not fully installed, that await spectral allocation, and the Department of Fisheries and Oceans operates two long-range CODARs on either side of Hecate Strait (installed 2017). The Canadian Coast Guard has expressed interest in using surface current products arising from these and other Canadian HFR.

The longest running coastal HFRs in Canada are owned by the University of Maine, which since 2004 has operated a long-range CODAR in Nova Scotia and another in New Brunswick. Memorial University operates two WERA-like HFRs in Placentia Bay, Newfoundland, and the Université du Québec à Rimouski operates two standard CODARs and a WERA on the St. Lawrence River estuary.

## Chile

Sixteen counties of the Chilean Biobío Region share a border with the ocean, where important sea related economic activities are performed, among them fisheries, navigation, international commerce, infrastructure, defense, tourism, and recreational activities. Historically this region has been affected by natural disasters related to the ocean such as wave surges, heavy weather, tsunami, oil spills, sinking of ships, etc. causing strong social, economic and environmental damages. Several of these risks are associated with physical properties of the coastal waters such as sea waves, surface winds, and marine currents. The solution for these challenges is being answered by the Chilean Integrated Ocean Observing System (CHIOOS). The CHIOOS is based upon two WERA High Frequency (HF) ocean radar systems, which are installed along the coast and provide real-time measurements of physical properties of the coastal waters, and complemented by sensors for relevant biological and chemical ocean parameters. This project will be carried out in strong collaboration with Chilean national and regional agencies, among which are the Chilean Navy National Hydrographic and Oceanographic Service (SHOA), the Chilean Emergency Regional Office (OREMI), the local Maritime Authority (Gobernación Marítima de Talcahuano), the

national Ministry of Energy, municipalities of coastal counties, and harbor authorities<sup>2</sup>.

## Mexico

The Mexican HF radar Network has its origin starting in 2003, when the Autonomous University of Baja California (UABC) acquired two SeaSonde CODAR systems, which were operational from 2003 to 2005 on Rosarito Baja California. Later in 2005 another two WERA type radars were purchased through a research project funded by the Consejo Nacional de Ciencia y Tecnología (CONACyT, National Council of Science and Technology). Those two radars were installed in the Gulf of Tehuantepec, and were operational for almost 3 years (Flores-Vidal et al., 2014).

Those early installations in Mexico had a completely oceanographic research purpose (Flores-Vidal et al., 2011, 2013, 2018) but lacked operational continuity with gaps in the time series on the order of two to 3 months for the worse cases, and with absolutely no real time data transfer. In 2009 the four radars from UABC were installed in Todos Santos bay (100 km south from the United States-Mexico border) and for the first time provided a continuous real-time time series with reduced datagaps due to the ability of data quality control 24/7. The Mexican secretary of Marine corps (SEMAR) used the data during surveillance and SAR operations. In 2010 the Observatorio de Corrientes Mexicanas OCOMEX was created and obtained funding from CONACyT to purchase three more radars which were installed on Baja California producing long-range (~200 km offshore) with time-spatial resolution of 1 h and 3 km and real-time support. Up to today OCOMEX is still operational, producing two nested grids of sea surface currents, inside the Todos Santos Bay with resolution of 500 m and 15 min, and at the adjacent ocean (Southern California Coastal Current) with 3 km and 1 h of resolution (**Figure 8A**). With almost 10 years of measurements with research purposes on the southern California shore (Flores-Vidal et al., 2015, 2018) has brought operational success which supports Mexican federal agencies as well as the academic sector.

In 2015, the Mexican Secretary of Energy (SENER) along with CONACyT launched an unprecedented program for research, surveillance and mitigation in case of oil-spill in the Gulf of Mexico. UABC and OCOMEX were funded to purchase and install 15 radar units on the Gulf of Mexico. OCOMEX decided to install LERA radars (Flament et al., 2016) due to its performance, robustness, compact, and low power consumption design. Presently, the OCOMEX-UABC team operates 16 HFR in the Gulf of Mexico, spanning the states of Tamaulipas, Veracruz, Tabasco, Campeche, and Yucatan (**Figure 8B**). The installation, management and maintenance of this HFR network is being performed by a multi-institutional consortium which include more than 20 universities and research institutes in Mexico. Currently, OCOMEX operates 22 near real-time (NRT) HFR systems in Mexico and is actively working with United States-IOOS personnel to establish a relay to the HFRNet.

<sup>2</sup>[www.chioos.cl](http://www.chioos.cl)



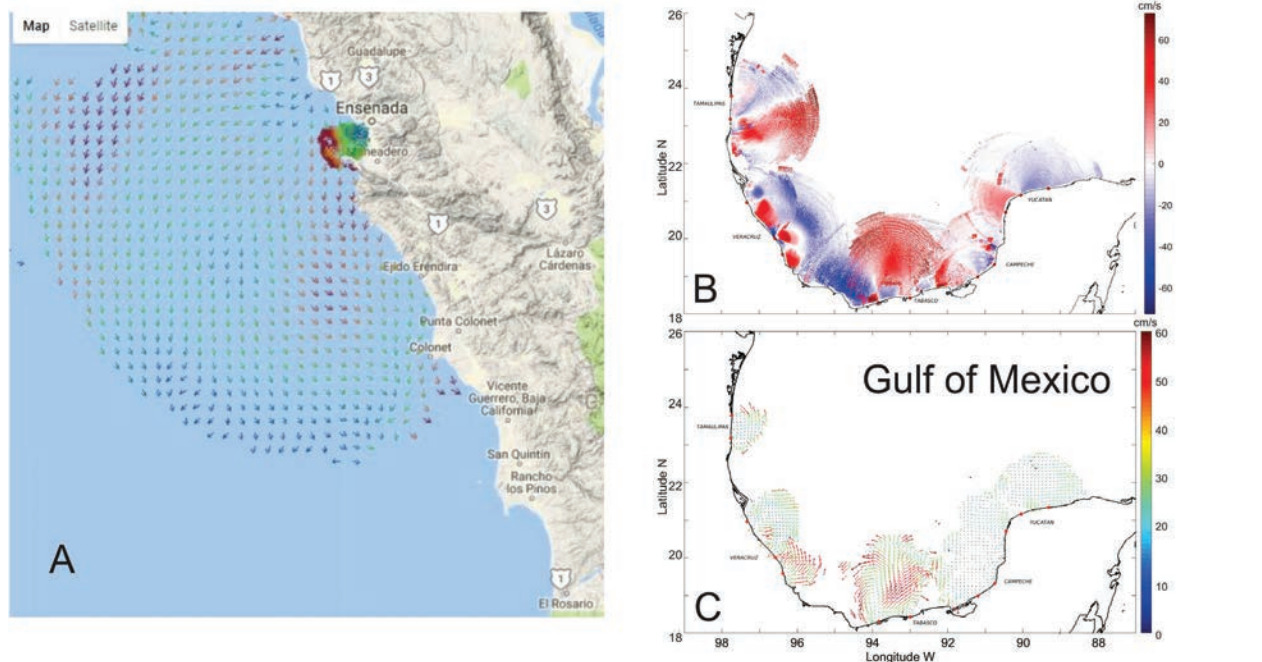


**FIGURE 8 | (A)** Sea surface currents mapped at high resolution (400 m and 15 min, respectively) inside of Todos Santos Bay, along with long-range (~200 km offshore) measurements simultaneously taken at the adjacent open ocean. Long-range measurements have a time spatial resolution of 3 km and 1 h, respectively. **(B)** Map of 11 radar stations (red dots) installed in the Gulf of Mexico from 2017 to 2018 showing radial currents toward the radar station (red) and away from the radar station (blue) **(C)** the radial measurements from **(B)** are combined to generate total vector currents between 0–50 cm/s.

## United States

In 2004 the United States led Integrated Ocean Observing System (IOOS) established a national network of HFR sites along the coastal United States, frequently referred to as the National Network (Harlan et al., 2010). The National Network differentiates sites by geographical area including the United States West Coast (USWC), United States East and Gulf Coast (USEGC), Hawaii (USHI), and Puerto Rico and Virgin Islands (PRVI). Additionally, when weather conditions allow (typically during summer months), HFR sites from Alaska North Shelf (AKNS) and Gulf of Alaska (GAK) are included. The technical basis of the National HFR Network was guided by a steering team of experts in the field, with the resulting documentation distilled into a National Surface Current Plan (U.S. Integrated Ocean Observing System [IOOS], 2015) which has been updated occasionally since its initial publication. The plan describes the design and implementation of the National HFR Network from the infrastructure of individual HFR stations, data management and dissemination, and HFR related product development. The report highlights the requirement to collect surface current given its societal importance, and established priority for the location of HFR stations within eleven regional associations (RAs) which guide development of regional ocean observing activities. Furthermore, the plan provides technical design of the National Network to acquire radial current maps from individual HFR stations, process the radial maps into a Real Time Vector (RTV) product and establish requirements for data standards, management and distribution, while providing a metric of performance which is monitored daily. The report

also recognized the importance of staffing structure through academia/federal partnerships.

The HFR National Network began collecting radial current maps from participating regions in 2006 (**Figure 9**). The geographic coverage for each region over the entire period of recording is shown for the main regions. Surface currents collected through IOOS HFR National Network are utilized by a number of federal agencies including United States Coast Guard (Search and Rescue), NOAA's Office of Response and Restoration (OR&R) (hazardous spill response), National Ocean Service Center for Operational Oceanographic Products and Services (CO-OPS) (ocean tidal prediction), as well as state and local agencies that use data in water quality management. Additionally, surface current data is distributed to various research and development groups that are assimilating HFR derived surface current into numerical models. The United States West Coast Ocean Forecast System (WCOFS) is developing a capability to assimilate HFR surface currents into the 2-km horizontal resolution, ROMS based numerical model run along the entire United States West Coast (Kurapov et al., 2017). Finally, the IOOS-funded Short-term Prediction System (STPS) uses real-time analysis of the HFR surface currents to predict trajectories that are fed to the United States Coast Guard SAR tools (Roarty et al., 2010; Harlan et al., 2015).

## Asia and Oceania (Region 3)

The status for HFR for Australia, China, Japan, Korea, and Taiwan was documented recently (Fujii et al., 2013). Here are recent advancements for some of these countries as

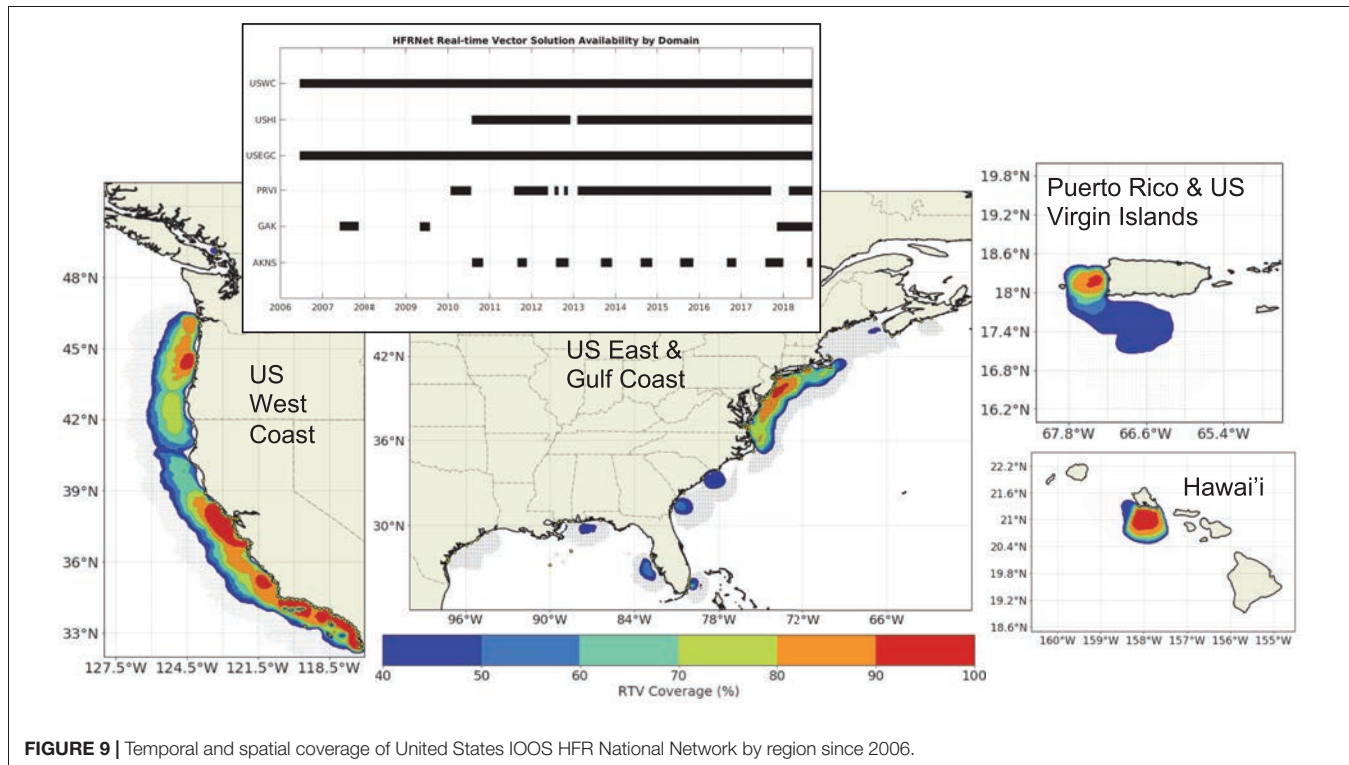


**FIGURE 9 |** Temporal and spatial coverage of United States IOOS HFR National Network by region since 2006.

well as a description of HFR in the recent networks of Vietnam and Thailand.

### Australia

The Australian Ocean Radar facility, based at the University of Western Australia is part of the Integrated Marine Observing System (IMOS), a national collaborative research infrastructure tasked with collection and dissemination of ocean data. The radar facility uses commercial direction-finding (SeaSonde) and phased-array (WERA) HFR systems. Each HFR node is configured primarily to sample ocean currents with a maximum range of over 200 km. Radar data, freely available from the IMOS portal<sup>3</sup>, are used for scientific research, operational modeling, coastal monitoring, fisheries and other applications (Kerry et al., 2016; Mihanovic et al., 2016; Archer et al., 2017, 2018; Mantovanelli et al., 2017; Schaeffer et al., 2017; Wandres et al., 2017). Between 2017 and 2018 asset relocation across the country was conducted, aimed at maximizing HFR coverage at a regional scale, and increasing data uptake. A new regional node was added to the network north of Sydney (New South Wales) composed of long-range (5 MHz) SeaSonde HFR systems, became operational in December 2017 but soon caused interference problems to primary users and has since been operated below its capabilities. The transmit power was reduced, typically below 1 Watt and sweep width reduced to less than 50% of the ITU allocated bandwidth, yet these settings were still causing interference to several users across the country. To date, operational uptime at this location is less than 50%. The spectrum management agency

within Australia (ACMA) is now enforcing a full implementation of ITU resolution 612 before operations can be resumed at this location. These requirements now include use of a directive transmit antenna, reduced bandwidth and employing a technique to allow multiple radars to operate on the same frequency. In 2018, the Federal Government approved operations for the 2018-2022 time period with potential to continue operation for additional 5 years, providing operational budget and injection of significant funds for the refurbishment and upgrade of the entire HFR systems, and replacement of the aging infrastructure. Additionally, the relocation of a decommissioned phased array HFR node from Queensland to the northwest shelf of Western Australia was approved through co-investment between IMOS and the oil and gas industries in the area, in support to development of an ocean monitoring tool for the Ningaloo reef, a world heritage area.

### Vietnam

Analysis of the spatial and temporal ocean circulation patterns of the Gulf of Tonkin are the focus of an ongoing collaborative effort between the Vietnamese Center for Oceanography (CFO), Vietnam Administration for Seas and Islands (VASI), and United States partners. Three long-range HF radar sites were installed in the spring of 2012 within the Gulf of Tonkin, Vietnam (Figure 10A). The temporal availability and spatial coverage of the radial data were strongly dependent on the seasonal monsoon cycles that drive observed circulation patterns within the predominantly low energy environment of the Gulf of Tonkin. Minimal radial coverage occurred during the summer monsoon seasons due to prevailing weak offshore wind directions. The

<sup>3</sup><https://portal.aodn.org.au/>

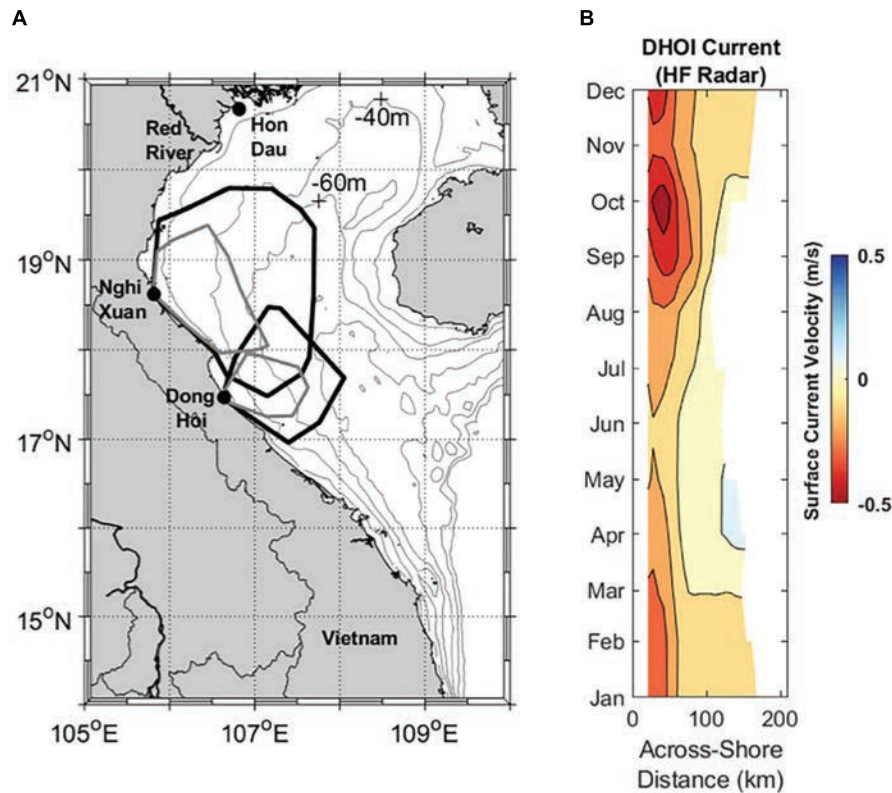


**FIGURE 10 | (A)** Map of Vietnamese coastal waters with HFR stations (black dots) overlaid with 20 m depth contours. The polygons indicate the 50% radial data coverage boundaries of the HF-radar during the winter season (black line) and summer season (gray line). **(B)** Hovmöller diagrams of HF radar alongshore surface currents located just north of the Dong Hoi radar site. Positive currents indicate poleward flow while negative values denote regions of equatorward flow. HF radar monthly averages are computed from a 2 year period from June 2014 to June 2016.

onset of the winter monsoon season results in a transition to an onshore flow resulting in better temporal availability and spatial coverage of radial data (**Figure 10A**).

Numerical simulations confirm coastal flows, originating from the Red River, are a prominent feature impacting the circulation of the western region of the Gulf of Tonkin. Two years of monthly averaged HF radar observations, from June 2014 through July 2016, were used to assess the seasonal temporal and spatial variability of coastal currents. The upcoast/downcoast surface currents along a shore normal 200 km transect just north of the Dong Hoi radar site for this period illustrates seasonal fluctuations in the coastal current that are consistent with model results (**Figure 10B**).

As a result of the successes from the United States – Vietnamese partnership, future efforts will build on the developed relationships to continue education and training in the use of emergent ocean technologies. This will include working with VASI and CFO as they begin to further develop their HF radar infrastructure along the Vietnamese coast.

## Korea

As Korean economy has increased, the importance of NRT surface currents measured in coastal and marginal seas around Korea has been recognized since 1995. Pukyong National

University (PNU) first installed HFR systems in the southeast coast in 1999 to monitor the East Korea Warm Current (EKWC). HFR systems gradually increased with oceanographic demands for 10 years (**Figure 11B**). The HFR network rapidly expanded from 9 radar sites in 2009 to 46 sites in 2016 in order to respond to increasing demands of the current data covering large areas with increased spatial and temporal resolution for fishing activities, maritime transportations, coastal zone developments and harbor constructions, and coastal environment managements.

The Korea Hydrographic and Oceanographic Administration (KHOA) has been focused on operational application of radar-derived currents around six major harbors with 31 HFRs where ship traffic is heavy, providing NRT data to the public and wide variety of end-users. Universities and research institutes have mainly applied HFR systems to scientific researches. Kunsan National University (KNU) has installed radars to examine the effects of large coastal development on the current structure and variation of river plumes (Son et al., 2007; Lee et al., 2013; Kim et al., 2018) and the observation-based current variabilities for the effective management and utilization of the mid-west coastal sea in the future. Seoul National University (SNU) has operated HFRs to map surface current along the mid-east coast where the East Korea Warm Current (EKWC) and North Korea Cold Current (NKCC) meet and frequently produce complicated



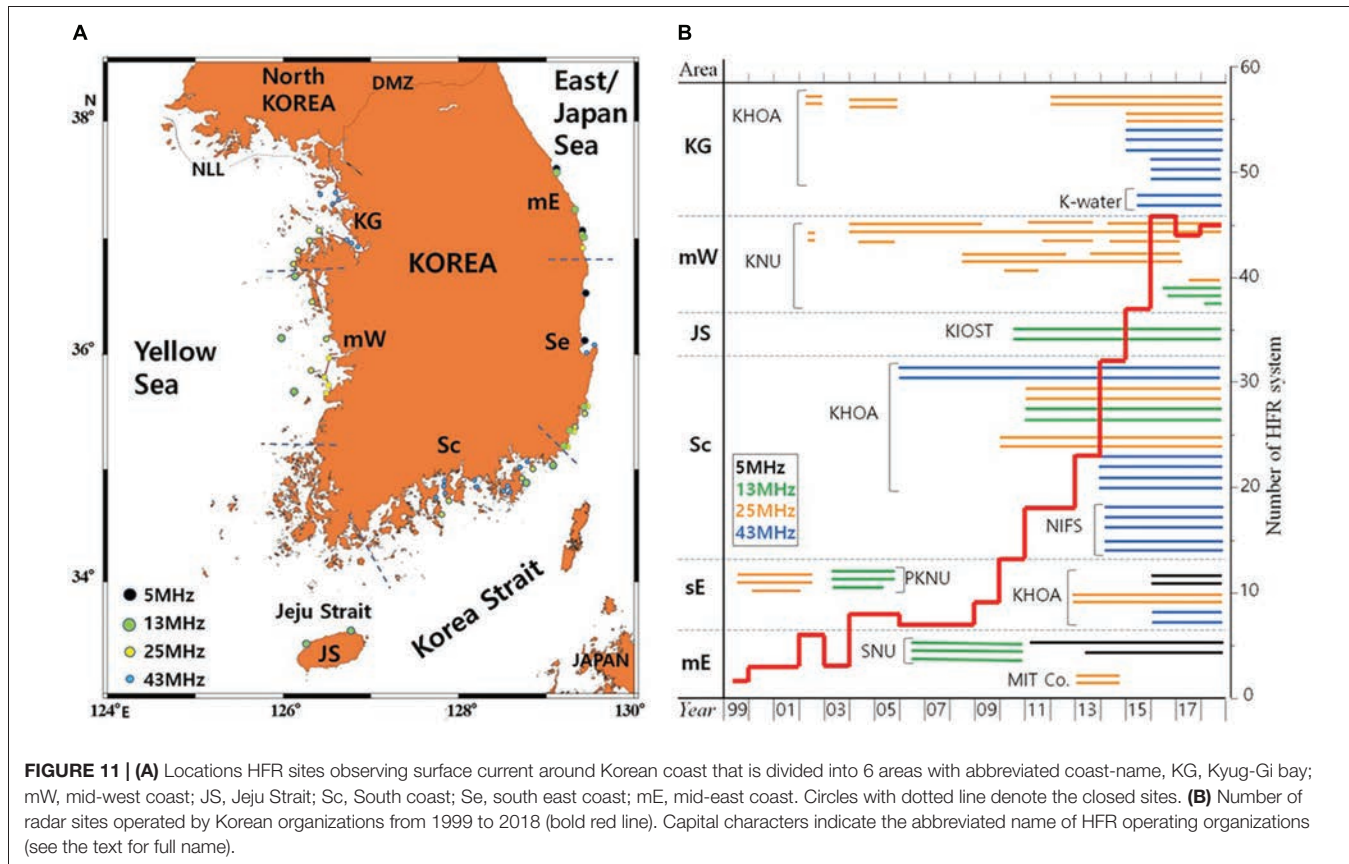


**FIGURE 11 | (A)** Locations HFR sites observing surface current around Korean coast that is divided into 6 areas with abbreviated coast-name, KG, Kyug-Gi bay; mW, mid-west coast; JS, Jeju Strait; Sc, South coast; Se, south east coast; mE, mid-east coast. Circles with dotted line denote the closed sites. **(B)** Number of radar sites operated by Korean organizations from 1999 to 2018 (bold red line). Capital characters indicate the abbreviated name of HFR operating organizations (see the text for full name).

flow patterns. Korea Institute of Ocean Science and Technology (KIOST) has operated two radars (13 MHz) since 2012 to observe the current structure and variability in the Jeju Strait. National Institute of Fisheries Science (NIFS) has operated an HFR network since 2014 to investigate the dispersion and residence time of pollutant materials in the inner bays along the south coast in order to plan the sanitation management and space requirements for aquaculture farms. Korea Water Resources Corporation (K-water) has monitored the outflow jet from the gate of Shihwa lake tidal power station to estimate effects of the jet flow on the coastal environment since 2015. Marine Information Technology Co. (MIT) has mapped currents and waves off the mid-east coast from 2013 to 2014 for a meteorological demand using the two HFRs that are a unique WERA system in Korea.

With the increase of HFR systems, the Korean HFR community recognized the necessity of cooperation between radar organizations to share experiences and information about radar operation and promote the efficient use of radar-derived data. The Korean Ocean Radar Forum (KORF) was established in 2011 for this purpose. KORF holds a workshop every year, and discusses issues that are common to operators and end-users in Korea. In May 2012, KORF organized the 1st Ocean Radar Conference for Asia-Pacific (ORCA) in Seoul Korea to share experiences on HFR network planning, operation, maintenance and data management, exchange ideas about application and research results, and build relationships across national boundaries (Lee and Heron, 2013; Fujii et al., 2013).

More than seventy persons from ten countries participated in the 1st ORCA and the conference has been successively held every 2 years.

Though 45 HFRs are presently operating in the Korean coast for public and scientific usages, partnership between KORF members has not established yet to organize a nation-wide data node to systematically respond to a wide array of end user's demands. Recently the Korean government recognized HFR as a valuable platform for building wide integrated surveillance of marine territory and launched a research project integrating satellite, AIS, HFR, UAV etc. data and platforms. The Korean HFR community is trying to establish a national organization to collect HFR-data to a data aggregation node, support technical and operational design for data standards, management and distribution, raise funds for a national network installation, and participate to the international observing programs over the next decade.

### Thailand

Thailand first began installing HFR systems in 2012 and are operated under the responsibility of Geo-Informatics and Space Technology Development Agency (GISTDA), which is located within the Ministry of Science and Technology. The purpose of the project is to understand the circulation pattern and wave characteristic in the Gulf of Thailand in both time and space continually in order to support the government's water management system from land into the coastal zone. The coastal



radar systems in Thailand use frequencies of 13 and 24 MHz covering the Gulf of Thailand and Andaman with a total of 19 stations. Installing the system was divided into two phases, consisting of the first phase from 2012 to 2015 which installed 13 stations in the Gulf of Thailand and the second phase from 2016 to 2018 which installed 4 stations in the Gulf of Thailand and 2 stations in the Andaman Sea. The HFR platforms in Thailand have also been outfitted with closed circuit television for displaying of wave and weather conditions to the public.

Geo-Informatics and Space Technology Development Agency has developed geographic information systems that integrate satellite imagery, coastal radar surface currents and other related remote sensor to monitor marine and coastal environments in the Gulf of Thailand and Andaman sea. This integrated product is paired with a vessel tracking system to analyze marine pollution by modeling the pollution situation and direction. These data are used as a tool for analyzing pollution sources, planning and situation management, including marine pollution alerts from oil spills or phytoplankton blooms. The HFR data is also utilized for monitoring waves and currents which are the factors affecting coastal zone change in Thailand, as well as for integrating approaches, project plans and budgets for coastal erosion management. Lastly, integration of coastal radar data with satellite imagery data and other information such as sea temperature and chlorophyll content for is helping fisheries management, water quality monitoring and marine resource conservation in Thailand.

Information from coastal radar systems has been used by government agencies, educational institutions, the private sector and the general public by accessing to the data via web-based applications and mobile applications. The development of coastal radar systems in Thailand under the implementation of GISTDA is another useful remote sensor for coastal area management. The application of this technology not only fulfills the mission of GISTDA, but it is a response to the mission of all marine and coastal sectors in Thailand. The use of such systems is diverse and focuses on the overall strategy of the country. Based on our past performance, lowering system maintenance costs is very important and future plans, we will continue to focus on the development of systems based on the integration of GISTDA and partner agencies expertise in geospatial information systems (GIS, satellite imagery, GNSS, remote sensors) to enhance capability of the people and coastal communities to utilize and access this information in order to improve the quality of life and safety in our coastal waters.

## Taiwan

Taiwan is an island on the margin sea between the western Pacific and the Eurasian shed. The interaction between the ocean and the residents is very close. The first set of HFRs introduced in Taiwan can be traced back to the 1990s. The Naval Meteorological and Oceanographic unit was responsible for operating the HFR system. They were expected to provide over-the-horizon ocean surface currents and wave information for the battlefield. Later, at the initiative of ocean scientists and disaster prevention experts, government departments such as science and technology, education and transportation systems

launched projects for the construction of High Frequency surface wave radars for ocean monitoring beginning around 2010. As of 2018, includes: 19 HFRs are operated by TOROS (the research organization for the establishment and maintenance of marine radars within the Taiwan Ocean Research Institute), two HFRs operated by the Naval Academy (called SCONET) and the two phased array radars operated by the Harbor and Marine Technology Center. Over the past 8 years these radar systems have provided continuous, NRT surface current maps of the surrounding waters around Taiwan and sea state information for the 14 commercial harbors and 225 fishing ports. The HFRs have played an important role in marine environmental information for coastal ocean science research, navigation or recreational safety, and maritime SAR.

Therefore, starting in 2019, the Central Weather Bureau of the Ministry of Transportation and Communications will construct an observation network consisting of three phased array radars in the northern Taiwan Strait to provide metocean information needed for transportation safety. The Harbor and Marine Technology Center will also implement a phased array radar in central Taiwan to monitor the sea state and vessel status within an offshore wind farm. Another network being developed entails monitoring the Luzon Strait between Taiwan and the Philippines which will form the Luzon Strait Ocean Observation System (LuSOOS).

## DATA PRODUCTS, QUALITY CONTROL, AND DISSEMINATION

### Deployment and Maintenance Best Practices

Given the need to collect high-quality observations from a number of independent organizations at varied coastal locations, IOOS has supported HFR technical and operation staff under the Radiowave Operators Working Group (ROWG). Founded in 2005 this group maintains an informational wiki<sup>4</sup> (password protected), email list, and computer code repository<sup>5</sup>. The group is open to HFR operators from the United States and international institutions and meets frequently to discuss standard practices, maintenance concerns and technology updates. The group has encapsulated best practices for HFR equipment setup and required maintenance into a living document called Deployment & Maintenance of a High-Frequency Radar for Ocean Surface Current Mapping: Best Practices (Cook et al., 2008). Topics include site setup of HFR equipment, power and cooling considerations, software/hardware configuration, data management and site maintenance. Additionally, HFR vendors provide guidance to HFR operators to assist with the goal of collecting the highest quality data as different locations may have specific issues and concerns and there is no “one size fits all” approach to HFR site deployment.

<sup>4</sup><http://rowg.org>

<sup>5</sup><http://github.com/rowg>

In Europe, the EuroGOOS HF Radar Task Team was established in 2014, with the goals of: (i) promoting joint progress through networking and scientific synergies for key questions; (ii) developing best practices and tools exchange; (iii) improving administrative procedures and regulations (e.g., the cross-border agreement for oceanographic radars in the 13–16 MHz band operating in the Western Mediterranean Sea in Spain, France and Italy was signed in February 2018); (iv) looking for complementary of HFRs with other multi-platforms and model products<sup>6</sup>. Simultaneously, definition of best practices in the implementation and use of HFR systems as well as the testing of methodological improvements on HFR retrievals and products is reported in the context of JERICO-NEXT project.

Dealing with one of the main risks foreseen in order to ensure HFR sites sustainability (i.e., downtime, outages and failures), the EU HFR data node, aligned with the leading efforts of MARACOOS, have shared best practices for the creation of HF Radar outages database (Updyke, 2017) as an aid for operations and maintenance. In spite of the fruitful collaborations between the HFR national networks, operators recognized the necessity for a centralization of methodologies and best practices documentation to increase efficiency, reproducibility and interoperability of the coastal HFRs network design, operation and maintenance tasks. In this context, the Ocean Best Practices (OBP) System<sup>7</sup> is emerging as the unified, sustained and readily global accessible knowledge based of interdisciplinary best practices in the ocean observing value chain to foster innovation and excellence. Particularly, in the case of HFR, best practices documentation related to the EU network current status, QA/QC HFR surface current data, deployment & setup of HFRs and HFR data management are currently available at the IODE OBP repository<sup>8</sup>. Nevertheless, an extra effort is required from the global HFR network to document best practices and to promote their propagation. Moreover, the involvement of HFR experts from different networks may contribute to the internal peer-review of best practices documents.

## Quality Assurance/Quality Control

Within the United States, IOOS strives to collect the high-quality data for 34 identified core variables, which include ocean currents. To this goal, the Quality Assurance/Quality Control (QA/QC) of Real-Time Oceanographic Data (QARTOD) Project Plan was finalized in 2012, and established quality control procedures for the 26 core variables representing physical, chemical, biological, and multidisciplinary ocean observations (U.S. Integrated Ocean Observing System [IOOS], 2017). Coordinated effort between manufacturers, academic researchers and federal scientists created the Manual for Real-Time Quality Control of High Frequency Radar Surface Current Data published in 2016 (U.S. Integrated Ocean Observing System [IOOS], 2016). The manual incorporates existing QA/QC procedures from a group of HFR experts, and identified a number of tests to ensure QA/QC of both radial current

measurement and total current vector measurement. Efforts to implement these tests in the real time data stream are ongoing and occurring at the radial current collection sites, and at the National Network.

In order to deliver high quality HFR data for scientific, operational and societal applications and to enforce discovery and access for HFR data, the European HFR community defined a standard model for data and metadata for producing NRT HFR surface current data, aimed at ensuring efficient and automated HFR data discovery and interoperability. This data model will be the operational data delivery model since the entry in service of HFR data distribution in CMEMS-INSTAC occurs in April 2019. The model has been implemented according to the standards of Open Geospatial Consortium (OGC) for access and delivery of geospatial data, and compliant with the Climate and Forecast Metadata Convention CF-1.6, to the Unidata NetCDF Attribute Convention for Data Discovery (ACDD), to the OceanSITES convention and to the INSPIRE directive. Furthermore, it has been defined following the guidelines of the DATAMEQ working group and it fulfills the recommendations given by ROWG. To enforce semantics and interoperability, controlled vocabularies are used in the model for variable short names and standard names. All the discussions and activities for the data model definition and implementation have been carried on in strict collaboration with the US colleagues through ROWG. Other important external contributions have been given by other networks, such as the Australian ACORN network. Moreover, representatives of all these groups meet periodically at ROWG and ROW meetings, Ocean Radar Conference for Asia Pacific (ORCA) meetings and there was one ad-hoc meeting (INCREASE HFR expert workshop La Spezia 2016).

The model specifies the file format (i.e., *netCDF-4 classic model*), the global attribute scheme, the dimensions, the coordinate, data and Quality Control (QC) variables and their syntax, the QC procedures and the flagging policy for both radial and total data (Corgnati et al., 2018b). A battery of mandatory QC tests to be performed on NRT HFR data has also been defined, in order to ensure the delivery of high-quality data, to describe in a quantitative way the accuracy of the physical information and to detect suspicious or unreliable data. These QC tests standard model to be applied to HFR radial (7 tests) and total (6 tests) data were defined according to the DATAMEQ working recommendations on real-time QC and building on the QA/QC of Real-Time Oceanographic Data (QARTOD) manual produced by the United States IOOS (Corgnati et al., 2018b).

The QC standard model will be the operational standard data model starting with delivery of HFR data distribution in CMEMS-INSTAC in April 2019. Until recently, the implementation of real time QA/QC procedures of the data was depending on the HFR operator experience level. NRT validation of the HFR surface currents against surface currents of point-wise current meters or from ADCPs located inside the HFR footprint area provides a systematic data evaluation, helping also to identify periods without data (e.g., no radial velocities produced by the site, hardware/software outage, power outage, communication lost) or periods of instrument malfunction (e.g., either from the radar or from the other instruments) when velocities suddenly appear unrealistic. Of course, the

<sup>6</sup><http://eurogoos.eu/download/Task-Team-updates-GA2016.pdf>

<sup>7</sup><https://www.oceanbestpractices.org>

<sup>8</sup><https://www.oceanbestpractices.net>

NRT validation should not substitute the traditional offline validation practices (performed at delayed-mode system), but it complements it. The most common delayed-mode validation of HFR currents performed so far are based on comparison with drifter trajectories and point-wise current meters and ADCPs located in the HFR footprint along with self-consistency checks at the midpoint of the overwater baseline (Lorente et al., 2014; Kalampokis et al., 2016; Corgnati et al., 2018a; Cosoli et al., 2018). Equally, a variety of validation exercises of HFR-derived wave measurements against *in situ* observations have been previously conducted (Atan et al., 2015; Gómez et al., 2015) in order to infer the accuracy of HFR remote-sensed estimations and quantify the uncertainties related to this technology.

## Open Source Software Tools

One benefit of organizing the network globally are the resources that can be shared across all networks. Free and open-source software packages available for managing and analyzing HFR data have been developed. A sampling of the open source tools are described in **Table 2** including its functionality, the link to the repository and the primary authors of the tools. Constant knowledge sharing on the existing software and further updates will bring continued benefits to the global network participants. By sharing these tools as a community new features and benefits can be developed faster and more effectively than internal teams. The use of open source code should be promoted to gain full visibility and to increase reliability with the HFR worldwide community supporting the code base.

## Data Access and Visualization

Within the United States, the HFR National Network data management system relies on robust communications between the individual HFR installations and centralized data repositories that are updated in NRT. Radial surface currents are measured hourly at HFR installations (a site) and synced with one of 9 local regional operations centers (a portal) that aggregate radial current data from all HFR sites within a RA. In turn, data from the portals are accumulated at two redundant data repositories (a node) which are housed at Scripps Institution of Oceanography (SIO) and the National Data Buoy Center (NDBC). The primary node, located at SIO, serves the hourly radial current files to HFRNet processing machines which produce near real-time total vector (RTV) product generated on grids with multiple resolutions (500 m, 1, 2, and 6 km). Distribution of the RTV and 25-hr average products is accomplished through a Thematic Real-time Environmental Distributed Data Services (THREDDS) server<sup>9</sup>. THREDDS provides an interface to data access using a number of open source protocols including OpenDap, Web Mapping Service (WMS), Web Coverage Service (WCS), NetCDF Subset, and others. Sample code is available for utilizing these services with popular data processing platforms such as MATLAB and Python/Matplotlib. Vector tiles of all RTV products are available to web mapping applications via a publicly accessible application programming interface<sup>10</sup>.

<sup>9</sup><http://hfrnet-tds.ucsd.edu/thredds>

<sup>10</sup><http://cordc.ucsd.edu/projects/mapping/api/>

In addition to RTV products, the diagnostic information included in the HFR radial files is stored in a database and displayed to site operators through the HFRNet diagnostics portal. Diagnostic information includes hardware specific data such as system voltages, transmitted and reflected power and radial vector data such as range, number of solutions and signal to noise ratio.

Finally, overall IOOS network performance is evaluated using diagnostics from individual sites contributing to HFRNet through a real-time metric that is reported to the IOOS program manager and site operators. This metric categorizes when a radial file passes certain criteria, which are based on long term statistics of similar sites within the HFRNet archive. These criteria include the arrival time of a radial file (file must be received at HFRNet within 24 h of its collection) and the number of solutions (the number of valid radial solutions in the file must exceed a baseline).

In addition to THREDDS for both NRT and delayed mode (DM) products, the Australian Ocean Data Network (AODN) is making publicly available aggregated HFR data through their portal<sup>11</sup>. This includes surface currents, wind and wave maps. Within Europe the major platform for marine data distribution are CMEMS-INSTAC and the SeaDataNet infrastructure (SDN/SDC). They operate through a decentralized architecture based on National Oceanographic Data Centers (NODC) Production Units (PUs) organized by region for the global ocean and the six European seas and a Global Distribution Unit (DU). The core of CMEMS-INSTAC and SDC is to guarantee for the users the quality of the product delivered is equivalent wherever the data are processed.

In this framework, in order to enforce and make operational the efficient management of HFR data for INSTAC PUs, other CMEMS Thematic Centers (TAC) and Marine Forecasting Centers (MFC), the establishment of the HFR data stream has to be organized in a coordinated way, in collaboration with the regional alliances of EuroGOOS and the regional and global components of the CMEMS *In Situ* TAC. The implementation of the HFR data stream will be operated by a centralized European competence center: the EU HFR Node. This implementation will be performed in the frame of CMEMS *In Situ* TAC with the established formats and standards on QC flags and tests, dimension, naming, definition and syntax of coordinated variables.

The EU HFR Node will act as focal point with the European HFR data providers, the key EU networking infrastructures and the Global HFR network. The key roles of the EU HFR Node will be the connection with data providers for NRT and reprocessed (REP) data, the connection with CMEMS-INSTAC for NRT and REP data, the connection with SeaDataNet for REP data. The node will also ensure optimal visibility of HF radar data and foster the applications based on HF radar data. The EU HFR Node will facilitate the management and integration of any potential data provider according to a simple and very effective rule: if the data provider can set up the total surface current data flow according to the defined standards, the HFR central node only has to link

<sup>11</sup><https://portal.aodn.org.au/>

**TABLE 2 |** Summary of open source software toolboxes for the processing and visualization of HFR surface current data.

Toolbox	Functionality	Programming Language	Primary Author/Link
HFR_Progs	Total currents generation, Open -boundary Modal Analysis, Interpolation and filtering, Tides, EOFs	MATLAB	Mike Cook, Naval Postgraduate School David Kaplan, Virginia Institute of Marine Science <a href="https://github.com/rowg/hfrprogs">https://github.com/rowg/hfrprogs</a>
Codar Processing	Python tools for working with radial and wave data. Loading ASCII data files, QC, exporting to NetCDF	Python Jupyter Notebook	Michael Smith, Rutgers University  <a href="https://github.com/rowg/codar_processing">https://github.com/rowg/codar_processing</a>
Hfr_gui	Graphical user interface (GUI) for processing and visualizing HFR data	MATLAB	Teresa Updyke, Old Dominion University  <a href="https://github.com/rowg/hfr_gui">https://github.com/rowg/hfr_gui</a>
JRADAR	Transformation of CODAR radial and total files into the European HFR data model	Java	Jose Luis Asensio, AZTI  <a href="https://github.com/llasensio/JRadar">https://github.com/llasensio/JRadar</a>
HFR_Combiner	Standard QC processing and combination of CODAR and WERA radial current into total current and generation of radial and total data into the European HFR data model.	MATLAB	Lorenzo Corgnati and Carlo Mantovani, CNR-ISMAR  <a href="https://github.com/LorenzoCorgnati/HFR_Node_tools">https://github.com/LorenzoCorgnati/HFR_Node_tools</a>
Total Conversion	Standard QC processing and transformation of Codar and WERA total current into the European HFR common data & metadata model	MATLAB	Lorenzo Corgnati and Carlo Mantovani, CNR-ISMAR  <a href="https://github.com/LorenzoCorgnati/HFR_Node_tools">https://github.com/LorenzoCorgnati/HFR_Node_tools</a>
HFRadarReports	Automatic generation of monthly reports, as a new product for HFR data quality assessment	Python and La Tex	Andreas Krietmayer, Charles Troupin, Grant Rogers and Emma Reyes, SOCIB <a href="https://github.com/socib/HFRadarReports">https://github.com/socib/HFRadarReports</a>

The table shows the name of the toolbox, its main features, the programming language it was written in, the author and URL to the GitHub repository.

and include the new catalog and data stream. If the data provider cannot setup the total data generation and flow (because of lack of experience, technical capacity, etc.), the HFR Node will work on harvesting the radial data from the provider, harmonize and format these data and make them available.

For all these reasons the establishment of a centralized HFR node is the cornerstone of the operational European HFR network. The EU HFR Node became pre-operational in November 2018 and fully operational in April 2019 for CMEMS-INSTAC and SDN/SDC data delivery. It is also designed to maximize the compatibility and the possibility of mutual integration with the United States HFRNet. Links to data access portals for each of the regions are given in Table 3.

APPLICATIONS

Search and Rescue

Public Agencies and private companies in charge of SAR missions, marine pollution response, and maritime traffic control are among the most significant targeted users of reliable surface currents. It is essential for NRT surface currents be reliable and current predictions be accurate for the specific marine SAR areas of responsibility as assigned by the IMO (International Maritime Organization).

HFR data and predictions are one important part of SAR in the United States, being used as operational input

**TABLE 3 |** Website links to the portal for the global network along with links for data access in each of the three regions.

Link to data	
Global Network	<a href="http://global-hfradar.org/index.html">http://global-hfradar.org/index.html</a>
Region 1	<a href="http://thredds.emodnet-physics.eu/thredds/HFRADARCatalog.html">http://thredds.emodnet-physics.eu/thredds/HFRADARCatalog.html</a>
Region 2	<a href="http://hfrnet-tds.ucsd.edu/thredds/catalog.html">http://hfrnet-tds.ucsd.edu/thredds/catalog.html</a>
Region 3	<a href="https://portal.aodn.org.au/">https://portal.aodn.org.au/</a> <a href="http://www.khoa.go.kr/koofs/kor/ports/">http://www.khoa.go.kr/koofs/kor/ports/</a>

to United States Coast Guard Search and Rescue Optimal Planning System (SAROPS) since May 2009. During 2016–2017, HFR data and statistical predictions ranked 6th most popular as a source for surface current information by the United States Coast Guard and the Mid Atlantic ROMS model with HFR data assimilation reached the 4th position. HFR surface currents have been shown to reduce the search area by a factor of three in comparison with HYCOM after 96 h, presenting much higher skill score than a global model (Roarty et al., 2010).

In Europe, significant efforts are being made to promote the use of the HFR data as reliable surface current input of the SAR emergency response and environmental modeling tools in the Iberian-Biscay-Ireland seas (e.g., the ongoing CMEMS User Uptake IBISAR project) and in Malta (Gauci et al., 2016). A first



coordinated approach in Mediterranean Sea on SAR applications was made during the Tosca Project (Bellomo et al., 2015), involving five HF Radar sites in different countries.

## Hazard Detection

A recent advancement is the use of HFR for detection of tsunami waves. The main principle for detection is that long wave orbital velocities induced by tsunamis can be detected by the HF radar as slowly varying surface currents with characteristic space and time scales. The theory for tsunami detection by HFR was first developed in the 1970s (Barrick, 1979). However, the first detection of a tsunami by an HFR did not occur until the March 2011 Tohoku tsunami in Japan, that propagated through the Pacific Ocean (Barrick and Lipa, 2011; Dzvonkovskaya et al., 2011; Lipa et al., 2011). At that time, HF radars were not equipped with real-time detection capabilities and the occurrence of the tsunami could only be identified a posteriori by analyzing the recorded data.

Real-time HFR detection of a tsunami was accomplished by a WERA HFR system installed in Tofino, Canada (Dzvonkovskaya et al., 2017). This event occurred on October 14th, 2016, when a series of severe storms were impacting the Eastern Pacific coasts. These storms were the remnants of Typhoon Songda, thus the triggering event was atmospheric in origin and there was no seismic alert issued at that time. An in-depth a posteriori analysis of the meteorological data gathered during the event, together with the recorded HF radar data in the light of an improved tsunami detection algorithm, clearly showed that two successive abnormal long waves impacted the coast, which was a meteotsunami (Guérin et al., 2018). This tsunami was first detected by the HFR 60 km offshore, about 45 min before its arrival on the coast. The meteotsunami cleared the lowest threshold of the WERA detection software and then triggered a detection at the higher threshold 20 min later, thereby confirming the presence of the oncoming wave. The current research effort is devoted to increasing the detection range (and warning time) of such events. This can be accomplished by the combination of improved detection algorithms and increased signal-to-noise ratio of the radar signal (Grilli et al., 2017). Other meteotsunami events associated with sudden changes in surface air pressure have been detected in the Netherlands (Dzvonkovskaya et al., 2018) and the East Coast of the United States (Lipa et al., 2013). New installations in Oman and the Philippines have also been motivated by the need to protect coastlines and coastal communities from hazards such as tsunamis and storm surges. It is important to remember that the performance of these systems to detect these hazards is dependent upon continuity in electrical power during such seismic or atmospheric events and this can be a problem in remote areas. Investments to increase the resiliency of the HFR systems against power outages and other failure modes should be made by the networks.

## Coastal Circulation

From long-term records, a unique view of seasonal and interannual variability in surface circulation in the coastal waters of the United States have emerged with unprecedented spatial detail, together with analysis of important differences between

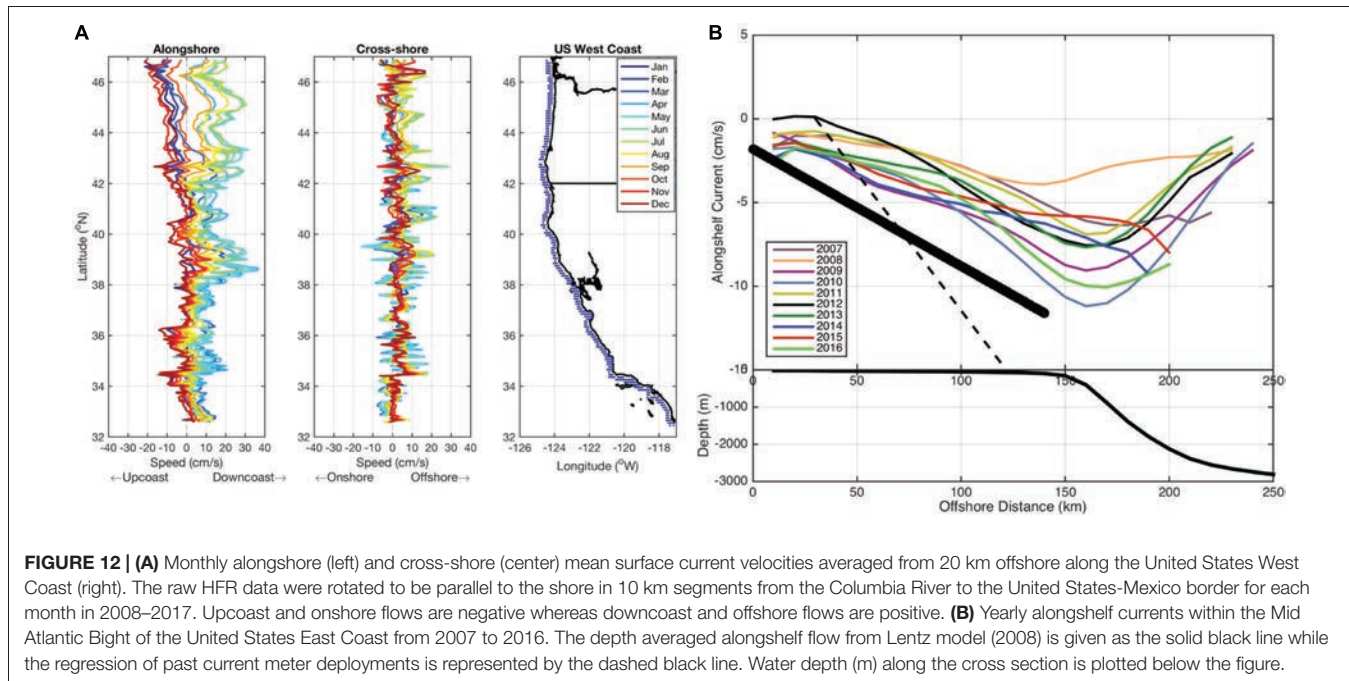
coastal and offshore circulation. Interannual anomalies in the NE Pacific include the 2014–2015 marine heat wave, the 2015–2016 El Niño, extreme freshwater runoff in 2017, and strong upwelling in 2009. The spatial coverage of HFR allows differentiation of features such as the upwelling jets and mesoscale eddies from wind-driven circulation over the shelf and from the large-scale California Current offshore while the temporal resolution allows resolution of the time-variation of each of these phenomena independently. Seasonal shifts in the alongshore current along the United States west coast (**Figure 12A**) characterize the upwelling season in spring-summer with persistent strong north winds, the relaxation season in autumn with weak winds, and the winter/storm season with strong southerly wind events (Garcia-Reyes and Largier, 2012). Cross-shore currents show strong seasonality at Cape Mendocino (~40N) and other major headlands, where topography can steer the currents (e.g., deflection of the strong alongshore current) and mesoscale eddies can develop and persist (e.g., 1-year persistence of 100-km eddy off Cape Mendocino in 2008, Halle and Largier, 2011).

Along the east coast of the United States, similar long-term datasets show the distinct differences in mean and seasonal surface circulation between coastal waters and the Gulf Stream offshore. Plots of annual mean alongshelf flow show a gradual increase with distance offshore in the Mid-Atlantic Bight reaching a maximum near the shelf break (**Figure 12B**). The interannual variability of the alongshore current measured so far has a range between 3 and 11 cm/s. New insights from HFR also elucidate the eddy-driven exchange of water between coastal and offshore regions here and elsewhere (e.g., Kim et al., 2011; Rypina et al., 2016).

Over a decade of HF Radar data is also available from northern Japan, providing an unprecedented view of the distinct seasonal variation in the Soya Warm Current. Hokkaido University, has operated five HF radars along the northern coast of Hokkaido since August 2003 (Ebuchi et al., 2006). The radars cover the Soya/La Perouse Strait between Hokkaido, Japan, and Sakhalin, Russia. The Soya Warm Current enters the Sea of Okhotsk from the Sea of Japan through this strait and flows along the coast of Hokkaido as a coastal boundary current. **Figure 13** shows the monthly averaged profiles of the alongshore surface current across the eastern outlet of the Strait with respect to the distance from the coast line of Hokkaido, Japan. The error bars indicate the standard deviation over 15 years from 2003 to 2018.

## Environmental Management

HF Radar data are increasingly being used in support of environmental management, including short-term pollution events and long-term resource management. Specifically, data have been used in tracking the fate of runoff (Rogowski et al., 2015) and wastewater discharges in southern California, residence time in Monterey Bay (Coulliette et al., 2007), and source-sink of water parcels off northern California (Kaplan and Largier, 2006). Further, HFR data have been used in identifying circulation features that account for plankton blooms, including harmful algal blooms imported to the Ria de Vigo (Piedracoba et al., 2016) and phytoplankton delivery to the rich ecosystems of Cordell Bank and the Gulf of



Farallones (Halle and Largier, 2011). Other unpublished work has used these surface current data in designing networks for marine protected areas, and assessment of transport of juvenile salmonids in coastal waters. Off the west coast of the United States, HFR data are also an important component of an index of the condition of the environment for ecosystem health (Sydeman et al., 2013), been used in fishery oceanography (Nishimoto and Washburn, 2002; Bjorkstedt et al., 2010) and a recent analysis has used these data to explain anomalous and unprecedented appearance of southern species during the 2014–2015 marine heat wave (Sanford et al., 2019). These are just some examples that use HFR data to address environmental questions and inform management agencies addressing water quality, marine resources, and marine conservation.

## Ocean Model Validation and Assimilation

In addition to direct use of HFR data in operational and retrospective assessment, HFR surface current data are distributed to various research and development groups that assimilate HFR-derived surface current into numerical models that simulate 3-dimensional circulation and water properties in the coastal ocean. Because of the large spatial extent and high-frequency sampling of surface currents that resolve tidal variability and small-scale topographic effects, the assimilation of these data has been shown to greatly improve model realism and confidence (e.g., Chao et al., 2018). Increasingly, this is a preferred way to deliver the value of HFR datasets as it combines the benefits of models and real data. A number of publications already exist on the assimilation of both surface currents and wave HFR data (Breivik and Sætra, 2001; Paduan and Shulman, 2004; Barth et al., 2008, 2011; Waters et al., 2013; Marmain et al., 2014; Ren et al., 2015; Sperrevik et al., 2015; Stanev et al., 2015; Iermano et al., 2016; Hernández et al., 2017, to mention only a few examples). For the entire United

States west coast, the large-scale, high-resolution West Coast Ocean Forecast System (WCOFS) is developing a capability to assimilate HFR surface currents into a 2-km-resolution, Regional Ocean Modeling System (ROMS) numerical model (Kurapov et al., 2017). Typically, radial data are used for assimilation into regional models. An effort is underway led by University of California Santa Cruz in evaluating the impact of ocean observing system measurements on ocean analysis and forecast systems – including assessment of the best data type and the best data locations in terms of improved model realism and confidence. The project is focused on advancing ROMS (Wilkin and Hunter, 2013) through use of 4-dimensional variational data assimilation diagnostic tools to assess the impact of observations on analysis and forecasts. Indeed, the combined assimilation of the data with satellite altimetry and multi-platform observations improve both the representation of small-scale features and the understanding of the impact of coastal processes on larger scales.

While data assimilation is an exciting recent development in the use of HFR data and in realizing and delivering its value, HFR data have long been used as a very valuable data set for evaluating high-resolution numerical simulations of coastal circulation. Compared with other multi-platform observations (e.g., gliders, fixed moorings, Lagrangian drifters), HFR data are preferred as the network provides routine data at high spatio-temporal resolution comparable with the models. This cross-validation has provided an unprecedented opportunity for model assessment and contributed valuable insights into the small-scale variability of coastal ocean currents. The comparison of the mean velocity fields between model and HFR surface currents detected circulation biases in coastal models at a scale that is not properly resolved by altimetry (Mourre et al., 2018). Operationally, HFRs are increasingly considered part of core validation systems (Lorente et al., 2016; Aguiar et al., 2018) and tools like the North Atlantic Regional Validation (NARVAL), the

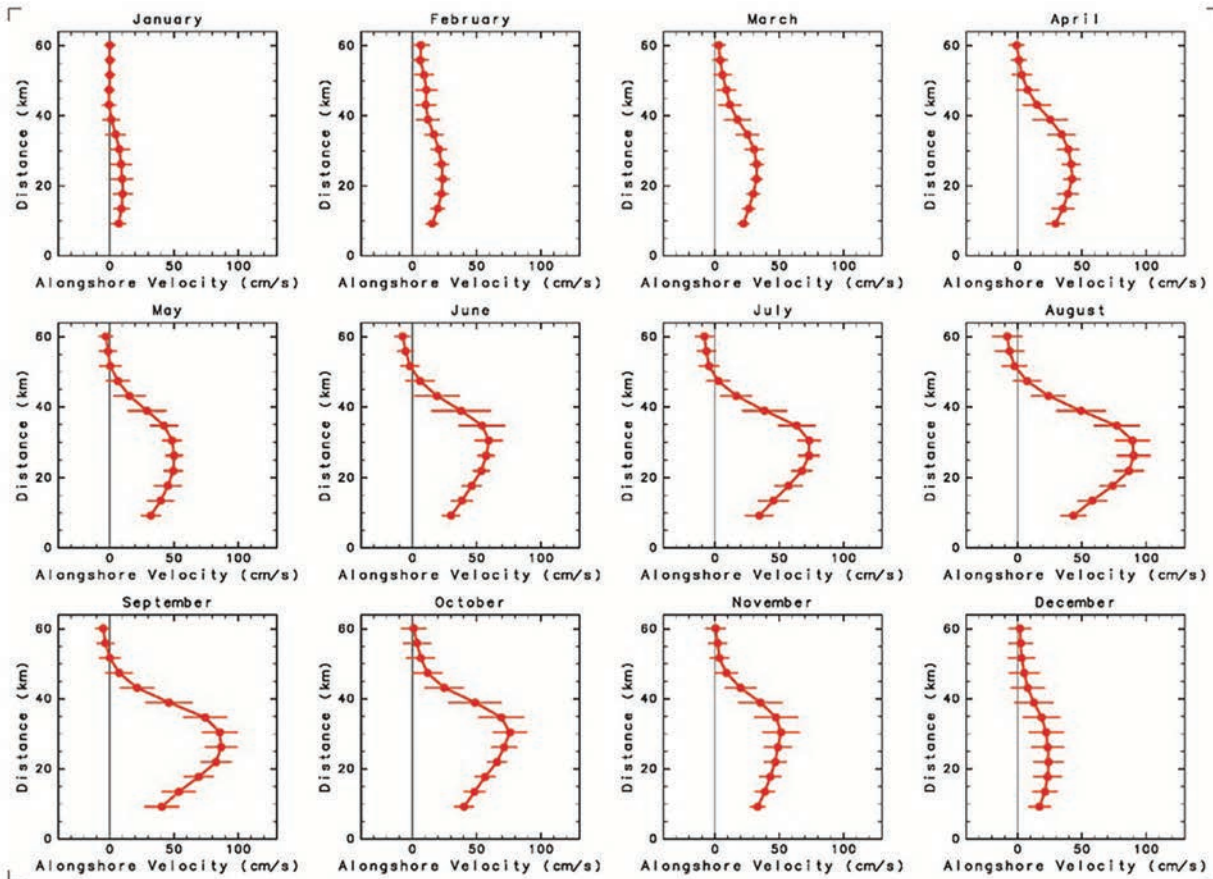


**FIGURE 13 |** Monthly averaged profiles of the alongshore surface current velocity component across the eastern outlet of the Soya/La Perouse Strait with respect to the distance from the coast line of Hokkaido, Japan. The error bars indicate the standard deviation over 15 years from 2003 to 2018.

IBI-MFC forecast system validation web tool (Sotillo et al., 2015) or the SOCIB- WMOP Operational Validation System (Juza et al., 2016) are used to systematically assess model outputs at different time scales. Complementarily, HFR systems play a primary role in multi-model comparison in overlapping regions since they help in judging the strengths and weaknesses of each forecasting system in the modeling of key ocean processes and also to deepen the understanding of discrepancies in model predictions. With CMEMS regional models special emphasis has been placed on the use of HFR measurements in the intercomparison of regional models against nested coastal model solutions in order to elucidate the added value of dynamical downscaling approaches (Hernandez et al., 2018).

## GAPS AND FUTURE CHALLENGES

High frequency radar technology for surface current mapping has been widely implemented in the last two decades, with a remarkable growth in applications in the last decade. In the context of the S-curve of technology development, HFR networks are in their middle age with the rapid development

of new insights, applications and benefits. Globally, HFR systems are and have been operated in 25% of the countries with an ocean coastline. The Global HF Radar Network will work to develop HFR capabilities in new countries and continue its mission to increase the number of coastal radars operating around the globe by maintaining a dialogue with organizations like the Group on Earth Observations (GEO), Intergovernmental Oceanographic Commission (IOC), Joint Technical Commission for Oceanography and Marine Meteorology (JCOMM), and Partnership for Observation of the Global Ocean (POGO).

High frequency radar has proven operational value that is also well recognized through inclusion in operational protocols in the United States and elsewhere. Value is recognized specifically in rapid-response (e.g., search and rescue; oil spill) and also more recently in hazard identification and warning (e.g., tsunami). Data are used directly as well as ingested by models with operational capabilities. Further, HFR time series comprised of hourly maps of surface currents have been sustained for 10–20 years in several locations, demonstrating the value of HFR networks for retrospective assessment of environmental change, including seasonal and interannual fluctuations in



coastal circulation and ecosystems. The Global Network has just begun conversations on developing the infrastructure to curate and serve these long data records. At the EU level, and following the recommendation given by the United States colleagues, best practices of operations and maintenance of the HFR sites are currently being developed. The development of troubleshooting guides, helping to minimize site downtime and the implementation of aids to operations and managements as well as the creation of EU technical steering teams, that could be related with the best practices working group advisor committee as expert panels are being considered in the framework of different joint proposals.

High frequency radar technology is a form of remote sensing that offers a relatively low-cost method for tracking coastal waters with both operational and environmental dividends. However, beyond the initial investment, a sustained commitment to operational up-time and data quality is essential to realize these dividends. This review of the current status of the HFR global network highlights the major challenges for data production and applications that can be addressed at a global level to properly inform choices to direct the future evolution of HFR networks as coastal ocean observing platforms. In terms of applications, further efforts are needed in the development of novel signal processing methodologies for allowing the operational delivery of other information (e.g., waves and wind maps) as well as to exploit synergy between HFR and other multi-platform observing systems (e.g., satellite, gliders, drifters). Secondly, the use of HFR surface-velocity fields for improving operational high-resolution forecast models through data assimilation is emerging strongly. Nevertheless, use of the surface current measurements to improve the model downward through the water column represents an additional challenge (Paduan and Washburn, 2013), as well as the combined assimilation of HFR data with satellite altimetry and multi-platform observations. Progress in this research will offer a unique opportunity to increase the understanding of small-scale features and their interaction with larger scale processes and feedback mechanisms. Simultaneously, the progress in observation and forecasting in the coastal ocean will allow us to develop new science-based products of high added value, enhancing the HFR data discovery and the visibility of the HFR work and applications. The development of more user-driven products will help to reinforce the HFR user's loyalty and to attract new communities, beyond academic and SAR agencies (e.g., environmental monitoring).

In terms of data production, a key overarching concern for the network is continued development of the HFR technology, sufficient supply of experienced HFR technicians and scientists and effective management of the frequency spectrum through national coordinating bodies which should hopefully limit the instances of radio frequency interference. HFR site sustainability has emerged as a challenge in those countries (e.g., Canada) where the HFR sites are owned and operated by universities in the context of finite research programs, and also in regions where HFR sites have been operated for a long time and confronted by "aging infrastructure" without renewal of hardware. One of the top priority issues is the maintenance of continued

financial support to preserve the infrastructure and core service already implemented, but also funding to extend the networks at diverse national scales for an overall spatial coverage. The need for data standardization, harmonization and integration has also emerged. The future integration of the HFR data from the MARACOOS network into CMEMS-INSTAC in April 2020 (tentative date) could be considered the first step toward this goal.

An active global HFR network is crucial for pushing forward HFR scientific developments, promoting training activities, encouraging the integration of the HFRs into operational maritime monitoring and environmental assessment, and boosting networking toward an integrated, evolving and sustained HFR global network over the next decade.

## AUTHOR CONTRIBUTIONS

HR, TC, PL, ER, SC, JL, and LW contributed to the main structure and content of all sections. LH contributed to Abstract, **Figure 1** and **Table 1**, and made substantial contributions to the Introduction and Development of Networks sections. EAF and PL contributed to the European Network and Ocean Model Validation and Assimilation sections. LC, CM, AG, JM, and AR contributed to the European Network, Deployment and Maintenance Best Practices, Quality Assurance/Quality Control, and Data Access and Visualization sections. ER made substantial contributions to the writing and revising of the manuscript, particularly at the Deployment and Maintenance Best Practices, Search and Rescue, Ocean Model Validation and Assimilation, and Gaps and Future Challenges sections. LW contributed to Introduction, Europe, Africa and Middle East (Region 1), and Hazard Detection sections. JS contributed to the description of HFR in Morocco, Saudi Arabia, and Portugal, and **Figure 7**. BW and KB contributed to the description of HFR in Canada. BH contributed to the description of HFR in Chile. XF-V and KS-M contributed to the description of HFR in Mexico and **Figure 8**. TC contributed to the description of HFR in United States. SC contributed to the description of HFR network, data uptake, and QC in Australia. PR contributed to the description of HFR in Vietnam and **Figure 10**. S-HL contributed to the description of HFR in Korea and **Figure 11**. SP contributed to the description of HFR in Thailand. J-WL contributed to the description of HFR in Taiwan. HR contributed to **Figures 2–4, 6, 12B**, and **Table 3**. TC and LH contributed to **Figures 5A, 9**. AR and JM contributed to **Figure 5B**. DG contributed to **Figure 12A**. NE contributed to **Figure 13**. ER and HR contributed to **Table 2**. C-AG and SG contributed to the Hazard Detection section. JH, ET, MO, and SG contributed to the content of all sections.

## FUNDING

Korean HFR Network is supported by the Ministry of Ocean and Fisheries through the project "Base Research for Building Wide Integrated Surveillance System of Marine Territory."



## ACKNOWLEDGMENTS

We would like to thank Zdenka Willis for the vision to establish the Global High Frequency Radar Network. We would also like to thank the NOAA IOOS, RITMARE, JERICO-NEXT,

INCREASE, SeaDataCloud, IMPACT, SICOMAR-Plus, SENER-CONACyT Hidrocarburos programs and Korean Ministry of Ocean and Fisheries. We are very grateful to all the people who kindly provided the information of their radar and related activities.

## REFERENCES

- Abascal A. J., Castanedo, S., Medina, R., Losada, I. J., and Álvarez-Fanjul, E. (2009). Application of HF radar currents to oil spill modelling. *Mar. Pollut. Bull.* 58, 238–248. doi: 10.1016/j.marpolbul.2008.09.020
- Aguiar, E., Mourre, B., Reyes, E., Hernández, J., Heslop, E., Juza, M., et al. (2018). Downscaling CMEMS Mediterranean model over the western basin: Impacts on mean flows and mesoscale eddies, in *Proceedings of the 20th EGU-General Assembly 2018 of the European Geosciences Union* (Vienna: EGU).
- Anderson, S. (1986). "Remote sensing with the JINDALEE skywave radar." *IEEE J. Ocean. Eng.* 11, 158–163. doi: 10.1109/JOE.1986.1145180
- Archer, M. R., Keating, S. R., Roughan, M., Johns, W. E., Lumpkin, R., Beron-Vera, F., Shay, L. K. (2018). The kinematic similarity of two western boundary currents revealed by sustained high-resolution observations. *Geophys. Res. Lett.* 45, 6176–6185. doi: 10.1029/2018GL078429
- Archer, M. R., Roughan, M., Keating, S., Schaeffer, A. (2017). On the variability of the east australian current: jet structure, meandering, and influence on shelf circulation. *J. Geophys. Res. Oceans* 122, 8464–8481. doi: 10.1002/2017JC013097
- Atan, R., Goggins, J., Hartnett, M., Nash, S., and Agostinho, P. (2015). "Assessment of extreme wave height events in Galway Bay using high frequency radar (CODAR) data," in *Proceedings of the 1st International Conference on Renewable Energies Offshore (RENEW)*, Boca Raton, FL: CRC Press, 49–56. doi: 10.1201/b18973-8
- Barrick, D. (1977). "Extraction of wave parameters from measured HF radar sea-echo doppler spectra." *Radio Sci.* 12, 415–424. doi: 10.1029/RS012i003p00415
- Barrick, D., and Lipa, B. (2011). Japan tsunami detected by HF radars on two continents. in *Proceedings of the OCEANS'11 MTS/IEEE KONA*. (Waikoloa, HI: IEEE).
- Barrick, D. E. (1979). "A coastal radar system for tsunami warning." *Remote Sens. Environ.* 8, 353–358. doi: 10.1016/0034-4257(79)90034-8
- Barrick, D. E., and Lipa, B. J. (1985). "Mapping surface currents with codar." *Sea Technol.* 26, 43–48.
- Barth, A., Alvera-Azcárate A., and Weisberg R. H. (2008). Assimilation of high-frequency radar currents in a nested model of the West Florida Shelf. *J. Geophys. Res.* 113:C08033. doi: 10.1029/2007JC004585
- Barth A., Alvera-Azcárate, A., Beckers, J. M., Staneva, J., Stanev, E. V., and Schulz-Stellenfleth, J. (2011). Correcting surface winds by assimilating HFR surface currents in the German Bight. *Ocean Dynam.* 61:599 doi: 10.1007/s10236-010-0369-0
- Baskin, C., Roarty, H., Kohut, J., and Glenn, S. (2016). Effectiveness of a bistatic system on high frequency radar resiliency. In *Proceedings of the OCEANS 2016 MTS/IEEE Monterey*. (Monterey, CA: IEEE). doi: 10.1109/OCEANS.2016.7761296
- Bellomo L., Griffo, A., Cosoli, S., Falco, P., Gerin, R., Iermano, I., et al. (2015). Toward an integrated HF radar network in the mediterranean sea to improve search and rescue and oil spill response: the TOSCA project experience. *J. Oper. Oceanogr.* 8, 95–107. doi: 10.1080/1755876X.2015.1087184
- Berta, M., Bellomo, L., Griffo, A., Magaldi, M. G., Molcard, A., Mantovani, C., et al. (2018). Wind-induced variability in the Northern Current (northwestern Mediterranean Sea) as depicted by a multi-platform observing system. *Ocean Sci.* 14, 689–710. doi: 10.5194/os-14-689-2018
- Berta, M., Bellomo, L., Magaldi, M. G., Griffo, A., Molcard, A., Marmain, J., et al. (2014b). Estimating lagrangian transport blending drifters with HF radar data and models: Results from the TOSCA experiment in the ligurian current (North Western Mediterranean Sea). *Progr. Oceanogr.* 128, 15–29. doi: 10.1016/j.pocean.2014.08.004
- Berta, M., Ursella, L., Nencioli, F., Doglioli, A., Petrenko, A., and Cosoli, S. (2014a). Surface transport in the Northeastern Adriatic Sea from FSLE analysis of HF radar measurements. *Cont. Shelf Res.* 77, 14–23. doi: 10.1016/j.csr.2014.01.016
- Bjorkstedt, E. P., Goericke, R., McClatchie, S., Weber, E., Watson, W., and Lo, N. et al. (2010). "State of the California current 2009-2010: regional variation persists through transition from La Niña to El Niño (and back)". *California Cooper. Ocean. Fish. Invest. Rep.* 51, 39–69.
- Boesch, D. F. and Field, J. C. and Scavia, D. (eds.) (2000). "NOAA Coastal Ocean Program Decision Analysis Series, 21." *The Potential Consequences of Climate Variability and Change on Coastal Areas and Marine Resources: report of the Coastal Areas and Marine Resources Sector Team, U.S. National Assessment of the Potential Consequences of Climate Variability and Change, U.S. Global Change Research Program*. (Silver Spring, MD: NOAA/National Centers for Coastal Ocean Science), 163
- Bouksim, H., Zaidouni, Z., Merrouchi, R., (2016). HF radar pilot project in Morocco, in *Proceedings of the WMO CIMO-TECO Conference*, (Madrid: World Meteorological Organization).
- Breivik, Ø., and Sætra, Ø. (2001). Real time assimilation of HF radar currents into a coastal ocean model. *J. Mar. Syst.* 28, 161–182. doi: 10.1016/S0924-7963(01)00002-1
- Chao, Y., Farrara, J. D., Zhang, H., Armenta, K. J., Centurioni, L., Chavez, F., et al. (2018). Development, implementation, and validation of a California coastal ocean modeling, data assimilation, and forecasting system. *Deep Sea Res. Part 2 Top. Stud. Oceanogr.* 151, 49–63. doi: 10.1016/j.dsr2.2017.04.013
- Cianelli, D., D'Alelio, D., Uttieri, M., Sarno, D., Zingone, A., Zambianchi, E., et al. (2017). Disentangling physical and biological drivers of phytoplankton dynamics in a coastal system. *Sci. Rep.* 7:15868. doi: 10.1038/s41598-017-15880-x
- Cook, T., Hazard, L., Otero, M., and Zelenke, B. (2008). *Deployment and Maintenance of a High-Frequency Radar for Ocean Surface Current Mapping: Best Practices*. La Jolla, CA: Southern California Coastal Ocean Observing System, 35.
- Corgnati, L., Mantovani, C., Griffo, A., Berta, M., Penna, P., Celentano, P., et al. (2018a). Implementation and validation of the ismar high-frequency coastal radar network in the gulf of Manfredonia (Mediterranean Sea) *IEEE J. Ocean. Eng.* doi: 10.1109/JOE.2018.2822518 [E-pub ahead of print].
- Corgnati, L., Mantovani, C., Rubio, A., Reyes, E., Quentin, C., Cosoli, S., et al. (2018b). *The European common data and metadata model for real-time High Frequency Radar surface current data, EGU General Assembly 2018*. Vienna: Geophysical Research Abstracts.
- Cosoli, S., Grcic, B. deVos, S., and Hetzel, Y. (2018). Improving data quality for the australian high frequency ocean radar network through real-time and delayed-mode quality-control procedures. *Remote Sens.* 10:1476. doi: 10.3390/rs10091476
- Coulliette, C., Lekien, F., Paduan, J. D., Haller, G., and Marsden, J. E. (2007). "Optimal pollution mitigation in Monterey Bay based on coastal radar data and nonlinear dynamics." *Environ. Sci. Technol.* 41, 6562–6572. doi: 10.1021/es0630691
- de Paolo, T., and Terrill, E. (2007). "Skill assessment of resolving ocean surface current structure using compact-antenna-style hf radar and the music direction-finding algorithm." *J. Atmosph. Ocean. Technol.* 24, 1277–1300. doi: 10.1175/JTECH2040.1
- Dzvonkovskaya, A., Figueroa, D., Gurgel, K., Rohling, H., Schlick, T. (2011). HF radar observation of a tsunami near Chile after the recent great earthquake in Japan. in *Proceedings of the 2011 12th International Radar Symposium (IRS)*. (Leipzig: IEEE).
- Dzvonkovskaya, A., Helzel, T., and Peters, H. (2018). Meteotsunami Observation by WERA Ocean Radar Systems at the Dutch Coast. in *Proceedings of the 2018 OCEANS - MTS/IEEE Kobe Techno-Oceans (OTO)*. (Kobe: IEEE).
- Dzvonkovskaya A., Petersen L., Insua TL (2017) "Real-time capability of meteotsunami detection by WERA ocean radar system". in *Proceedings of the*

- 8th International Radar Symposium (IRS). (Prague: IEEE). doi: 10.23919/IRS.2017.8008096
- Ebuchi, N., Fukamachi, Y., Ohshima, K. I., Shirasawa, K., Ishikawa, M., Takatsuka, T., et al. (2006). Observation of the soya warm current using HF ocean radar. *J. Oceanogr.* 62, 47–61. doi: 10.1007/s10872-006-0031-0
- Fernandes, C. (2014). Portuguese HF Radar Network – Future Plans and Consolidation, in *Proceedings of the proEuroGOOS HF radar Conference*, Lisbon.
- Fernandez, D. M., Graber, H. C., Paduan, J. D., Barrick, D. (1997). “Mapping wind directions with HF radar.” *Oceanography* 10, 93–95. doi: 10.5670/oceanog.1997.33
- Flament, P., Harris, D., Flament, M., Fernandez, I. Q., Hlivak, R., Flores, X. and Marie, L. (2016). *A Compact High Frequency Doppler Radio Scatterometer for Coastal Oceanography*. American Geophysical Union: Washington, DC.
- Flores-Vidal, X., Durazo, R., Castro, R., Navarro, L. F., Dominguez, F., Gil, E. (2015). *Fine-Scale Tidal and Subtidal Variability of an Upwelling-Influenced Bay as Measured by the Mexican High Frequency Radar Observing System*. *Coastal Ocean Observing Systems*. Amsterdam: Elsevier, 209–228. doi: 10.1016/B978-0-12-802022-7.00012-2
- Flores-Vidal X., Durazo, R., Zavala-Sanson, L., Flament, P., Chavanne, C., Ocampo-Torres, F. J., Reyes-Hernandez, C. (2014). Evidence of inertially generated coastal-trapped waves in the eastern tropical Pacific. *J. Geophys. Res.* 119:2014.
- Flores-Vidal, X., Durazo, R., Chavanne, C., Flament, P. (2011) Coastal circulation in the absence of wind in the Gulf of Tehuantepec, Mexico: high frequency radar observations. *Ciencias Marinas* 37, 493–512. doi: 10.7773/cm.v37i4A.1911
- Flores-Vidal, X., Flament, P., Chavanne, C., Durazo, R., Gurgel, K.W. (2013) High frequency radars: beam steering calibrations using ships as reflectors. *J. Atmosph. Ocean. Technol.* 30:638–648. doi: 10.1175/JTECH-D-12-00105.1
- Flores-Vidal, X., González-Montesa, S., Zertuche-Chanes, R., Rodríguez-Padilla, I., Marti, L. C., Imberger, J., et al. (2018). Three-dimensional exchange flows in a semi-enclosed bay: numerical simulations and high frequency radar observations *Estuar. Coast. Shelf Sci.* 210, 26–35. doi: 10.1016/j.ecss.2018.05.027
- Fujii, S., Heron, M. L., Kim, K., Lai, J.-W., Lee, S.-H., Wu, X., et al. (2013). “An overview of developments and applications of oceanographic radar networks in Asia and Oceania countries.” *Ocean Sci. J.* 48, 69–97. doi: 10.1007/s12601-013-0007-0
- García-Reyes, M., and Largier, J. L. (2012). Seasonality of coastal upwelling off central and northern California: new insights including temporal and spatial variability. *J. Geophys. Res.* 117:C03028. doi: 10.1029/2011JC007629
- Gauci, A., Drago, A., Abela, J. (2016) Gap filling of the calypso hf radar sea surface current data through past measurements and satellite wind observations. *Int. J. Navig. Observ.* 2016:2605198. doi: 10.1155/2016/2605198
- Gómez, R., Helzel, T., Wyatt, L., Lopez, G., Conley, D., Thomas, N., et al. (2015). “Estimation of wave parameters from HF radar using different methodologies and compared with wave buoy measurements at the Wave Hub”. *Paper presented at OCEANS 2015 – MTS/IEEE*, Genova. doi: 10.1109/OCEANS-Genova.2015.7271477
- Grilli, S. T., Guérin, C.-A., Shelby, M., Grilli, A. R., Moran, P., Grosdidier, S., Insua, T. L. (2017) “Tsunami detection by high frequency radar beyond the continental shelf: ii. extension of time correlation algorithm and validation on realistic case studies”. *Pure Appl. Geophys.* 174, 3003–3028. doi: 10.1007/s00024-017-1619-6
- Guérin, C.-A., Grilli, S. T., Moran, P., Grilli, A. R., Insua, T. L. (2018). “Tsunami detection by high-frequency radar in British Columbia: performance assessment of the time-correlation algorithm for synthetic and real events”. *Ocean Dynam.* 68, 423–438. doi: 10.1007/s10236-018-1139-7
- Halle, C. M., and Largier, J. L. (2011). Surface circulation downstream of the Point Arena upwelling center. *Cont. Shelf Res.* 31, 1260–1272. doi: 10.1016/j.csr.2011.04.007
- Harlan, J., Terrill, E., Hazard, L., Keen, C., Barrick, D., Whelan, C., et al. (2010). “The integrated ocean observing system high-frequency radar network: status and local, regional, and national applications.” *Mar. Technol. Soc. J.* 44, 122–132. doi: 10.4031/MTSJ.44.6.6
- Harlan, J., Terrill, E., Hazard, L., Otero, M., Roarty, H. (2015). The Integration Ocean Observing System HF Radar Network. in *Proceedings of the OCEANS 2015-MTS/IEEE*. Washington, DC. doi: 10.23919/OCEANS.2015.7404587
- Headrick, J. M., and Thomason, J. F. (1998). “Applications of high-frequency radar.” *Radio Sci.* 33, 1045–1054. doi: 10.1029/98RS01013
- Heesemann, M., Insua, T. L., Scherwath, M., Juniper, S. K., Moran, K. (2014). “Ocean Networks Canada: from geohazards research laboratories to smart ocean systems.” *Oceanography* 27, 151–153. doi: 10.5670/oceanog.2014.50
- Helzel, T., Knipphoff, M., and Petersen, L. (2007). Features and limitations of the modular oceanography radar system WERA. in *Proceedings of the OCEANS 2007-Europe*, Aberdeen. doi: 10.1109/OCEANSE.2007.4302421
- Hernandez, F., Smith, G., Baetens, K., Cossarini, G., Garcia-Hermosa, I., Drevillon, M. et al., (2018). “Measuring performances, skill and accuracy in operational oceanography: New challenges and approaches.” in *New Frontiers in Operational Oceanography*, eds E. Chassignet, A. Pascual, J. Tintoré and J. Verron (Tallahassee: GODAE OceanView), 759–796. doi: 10.17125/gov2018.ch29
- Hernández, J., Mourre, B., Reyes, E., Marmain, J., Orfila, A., Tintoré, J., (2017) *Model Velocities Assessment and HF Radar Data Assimilation in the Ibiza Channel*. Vienna: EGU General Assembly, 23–28.
- Hernández-Carrasco, I., Orfila, A., Rossi, V., Garçon, V. (2018) Effect of small scale transport processes on phytoplankton distribution in coastal seas. *Sci. Rep.* 8:8613. doi: 10.1038/s41598-018-26857-9
- Iermano, I., Moore, A. M., and Zambianchi, E. (2016). Impacts of a 4-dimensional variational data assimilation in a coastal ocean model of southern Tyrrhenian Sea. *J. Mar. Sys.* 154, 157–171. doi: 10.1016/j.jmarsys.2015.09.006
- Juza, M., Mourre, B., Renault, L., Gómara, S., Sebastián, K., Lora, S., et al. (2016) SOCIB operational ocean forecasting system and multi-platform validation in the Western Mediterranean Sea. *J. Operat. Oceanogr.* 9, s155–s166. doi: 10.1080/1755876X.2015.1117764
- Kalampokis, A., Uttieri, M., Poulain, P.-M., and Zambianchi, E. (2016) Validation of HF radar-derived currents in the Gulf of Naples with Lagrangian data. *IEEE Geosci. Remote Sens. Lett.* 13, 1452–1456. doi: 10.1109/LGRS.2016.2591258
- Kaplan, D. M., and Largier, J. L. (2006). HF-radar-derived origin and destination of surface waters off Bodega Bay, California. *Deep Sea Res. II* 53, 2906–2930. doi: 10.1016/j.dsr2.2006.07.012
- Kerry, C., Powell, B., Roughan, M., Oke, P. (2016). Development and evaluation of a high-resolution reanalysis of the East Australian Current region using the regional ocean modelling system (ROMS 3.4) and incremental strong-constraint 4-dimensional variational (IS4D-Var) data assimilation. *Geosci. Model. Dev.* 9, 3779–3801. doi: 10.5194/gmd-9-3779-2016
- Kim, H.-K., Kim, J.-H., Son, Y.-T., and Lee, S.-H. (2018). An overview of operations and applications of hf ocean radar networks in the korean coast. (review). *Korean J. Remote Sens.* 34, 351–375.
- Kim, S. Y., Terrill, E. J., Cornuelle, B. D., Jones, B., Washburn, L., Moline, M. A., et al. (2011). Mapping the U.S. West Coast surface circulation: a multiyear analysis of high-frequency radar observations. *J. Geophys. Res.* 116:C03011. doi: 10.1029/2010JC006669
- Kirincich, A. (2016). Remote sensing of the surface wind field over the coastal ocean via direct calibration of HF radar backscatter power. *J. Atmosph. Oce. Techn.* 33(7), 1377–1392. doi: 10.1175/JTECH-D-15-0242.1
- Kurapov, A. L., Erofeeva, S. Y., and Myers, E. (2017). Coastal sea level variability in the US West Coast Ocean Forecast System (WCOSFS). *Ocean Dyn.* 67, 23–36. doi: 10.1007/s10236-016-1013-4
- Lee, S.-H. and Heron, M. L., (2013). Development of oceanographic radar networks, data management and applications in asia and oceania countries. *Ocean Sci. J.* 48, 67–68. doi: 10.1007/s12601-013-0006-1
- Lee, S.-H., Kang, C.-Y., Choi, B.-J., and Kim, C.-S. (2013). Surface current response to wind and plumes in a bay-shape estuary of the eastern Yellow Sea: Ocean radar observation. *Ocean Sci. J.* 48, 117–139. doi: 10.1007/s12601-013-0010-5
- Lipa, B., Arrick, D. B., Saitoh, S., Ishikawa, Y., Awaji, T., Largier, J. and Garfield, N. (2011). Japan tsunami current flows observed by HF Radars on two continents. *Remote Sens.* 3, 1663–1679. doi: 10.3390/rs3081663
- Lipa, B., Parikh, H., Barrick, D., Roarty, H., Glenn, S. (2013) High-frequency radar observations of the June 2013 US East Coast meteotsunami. *Nat. Hazards* 74, 109–122. doi: 10.1007/s11069-013-0992-4
- Lipa, B., Whelan, C., Rector, B., and Nyden, B. (2009). “HF radar bistatic measurement of surface current velocities: drifter comparisons and radar consistency checks.” *Remote Sens.* 1, 1190–1211. doi: 10.3390/rs1041190

- Lipa, B. J., Barrick, D. E., Isaacson, J., and Lilleboe, P. M. (1990). "CODAR wave measurements from a North Sea semisubmersible." *IEEE J. Ocean. Eng.* 15, 119–125. doi: 10.1109/48.50697
- Lipa, B., and Nyden, B. (2005). "Directional wave information from the SeaSonde." *Ocean. Eng.* 30, 221–231. doi: 10.1109/JOE.2004.839929
- Liu, Y., and Weisberg, R. H. (2007). "Ocean currents and sea surface heights estimated across the West Florida Shelf." *J. Phys. Oceanogr.* 37, 1697–1713. doi: 10.1175/JPO3083.1
- Lorente, P., Piedracoba, S., Soto-Navarro, J., and Álvarez-Fanjul, E. (2014). "Accuracy assessment of high frequency radar current measurements in the Strait of Gibraltar." *J. Operat. Oceanogr.* 7, 59–73. doi: 10.1080/1755876X.2014.11020300
- Lorente, P., Sotillo, M. G., Aouf, L., Amo-Baladrón, A., Barrera, E., Dalphin, A., et al. (2018). "Extreme wave height events in nw Spain: a combined multi-sensor and model approach." *Remote Sens.* 10:1. doi: 10.3390/rs10010001
- Lorente, P., Piedracoba, S., Sotillo, M. G., Aznar, R., Amo-Balandron, A., Pascual, A., et al. (2016). "Ocean model skill assessment in the NW Mediterranean using multi-sensor data." *J. Operat. Oceanogr.* 9, 75–92. doi: 10.1080/1755876X.2016.1215224
- Lumpkin, R., Grodsky, S. A., Centurioni, L., Rio, M., Carton, J. A., and Lee, V. (2013). Removing spurious low-frequency variability in drifter velocities. *J. Atmos. Oceanic Technol.* 30, 353–360. doi: 10.1175/JTECH-D-12-00139.1
- Mader, J., Rubio, A., Asensio, J. L., Novellino, A., Alba, M., Corgnati, L., et al. (2016). *The European HF Radar Inventory*. Pasaia: EuroGOOS publications.
- Mantovanelli, A., Keating, S., Wyatt, L. R., Roughan, M., Schaeffer, A. (2017). "Lagrangian and Eulerian characterization of two counterrotating submesoscale eddies in a western boundary current." *J. Geophys. Res. Oceans* 122, 4902–4921. doi: 10.1002/2016JC011968
- Marmain, J., Molcard, A., Forget, P., Barth, A. (2014). Assimilation of HF radar surface currents to optimize forcing in the North Western Mediterranean Sea, *Nonlinear Process. Geophys.* 21, 659–675. doi: 10.5194/npg-21-659-2014
- Menna, M., Mercatini, A., Uttieri, M., Buonocore, B., Zambianchi, E. (2007). Wintertime transport processes in the Gulf of Naples investigated by HF radar measurements of surface currents. *Nuovo Cimento* 6, 605–622.
- Mihanovic, H., Pattiaratchi, C., Verspecht, F. (2016). "Diurnal sea breezes force near-inertial waves along rotnest continental Shelf, Southwestern Australia." *J. Phys. Oceanogr.* 46, 3487–3508. doi: 10.1175/JPO-D-16-0022.1
- Mourre, B., Aguiar, E., Juza, M., Hernández-Lasheras, J., Reyes, E., Heslop, E., et al. (2018). Assessment of high-resolution regional ocean prediction systems using multi-platform observations: Illustrations in the Western Mediterranean Sea, in *New Frontiers in Operational Oceanography*, eds E. P. Chassignet, A. Pascual, J. Tintoré, J. Verron (Tallahassee: GODAE OceanView), 815. doi: 10.17125/gov2018.ch24
- Nishimoto, M. N., and Washburn, L. (2002). Patterns of coastal eddy circulation and abundance of pelagic juvenile fish in the Santa Barbara Channel, California, USA. *Mar. Ecol. Progr. Ser.* 241, 183–199. doi: 10.3354/meps241183
- Ohlmann, C., White, P., Washburn, L., Emery, B., Terrill, E., and Otero, M. (2007). "Interpretation of coastal HF radar-derived surface currents with high-resolution drifter data." *J. Atmos. Ocean. Technol.* 24, 666–680. doi: 10.1175/JTECH1998.1
- Paduan, J. D., and Shulman, I. (2004). HF radar data assimilation in the Monterey Bay area. *J. Geophys. Res. Oceans* 109, 1–17. doi: 10.1029/2003JC001949
- Paduan, J. D., and Washburn, L. (2013). High-frequency radar observations of ocean surface currents. *Ann. Rev. Mar. Sci.* 5, 115–136. doi: 10.1146/annurev-marine-121211-172315
- Piedracoba, S., Rosón, G., and Varela, R. A. (2016). Origin and development of recurrent dipolar vorticity structures in the outer Ría de Vigo (NW Spain). *Cont. Shelf Res.* 118, 143–153. doi: 10.1016/j.csr.2016.03.001
- Ponsford, A. M., Dizaji, R. M., and McKerracher, R. (2003). HF surface wave radar operation in adverse conditions. In *Proceedings of the International Conference on Radar (IEEE Cat. No. 03EX695)*, IEEE doi: 10.1109/RADAR.2003.1278808
- Quentin, C. G., Zakardjian, B., Marié, L., Rubio, A., Dumas, F., Sentchev, A., et al. (2017). "Progress towards a french high frequency ocean surface wave radar network." *Merc. Ocean J.* 55, 25–38.
- Ren, L., Nash, S., and Hartnett, M. (2015). Observation and modeling of tide- and wind-induced surface currents in Galway Bay. *Water Sci. Eng.* 8, 345–352. doi: 10.1016/j.wse.2015.12.001
- Roarty, H., Hazard, L., and Alvarez, E. (2016). *Growing Network of Radar Systems Monitors Ocean Surface Currents*. Washington, DC: EOS.
- Roarty, H., Hazard, L., Wyatt, L., Harlan, J., and Alvarez Fanjul, E. (2014) *The Global High Frequency Radar Network* Available at: <https://earthzine.org/the-global-high-frequency-radar-network/> (accessed October 30, 2014).
- Roarty, H. J., Glenn, S. M., Kohut, J. T., Gong, D., Handel, E., Rivera Lemus, E., et al. (2010). "Operation and application of a regional high frequency radar network in the mid atlantic bight." *Mar. Technol. Soc. J.* 44, 133–145. doi: 10.4031/MTSJ.44.6.5
- Rogowski, P. A., Terrill, E., Schiff, K., and Kim, S.-Y. (2015). An assessment of the transport of southern California stormwater ocean discharges. *Mar. Poll. Bull.* 90, 135–142. doi: 10.1016/j.marpolbul.2014.11.004
- Rubio, A., Caballero, A., Orfila, A., Hernández-Carrasco, I., Ferrer, L., González, M., et al. (2018a) Eddy-induced cross-shelf export of high Chl-a coastal waters in the SE Bay of Biscay. *Remote Sens. Environ.* 205, 290–304. doi: 10.1016/j.rse.2017.10.037
- Rubio, A., Mader, J., Corgnati, L., Mantovani, C., Griffa, A., Novellino, A., et al. (2018b). "Present and future of the European HF radar network: outcomes of the INCREASE project. A, 2018," in *Proceeding of the 4th Orca meeting*, Okinawa.
- Rubio, A., Mader, J., Corgnati, L., Mantovani, C., Griffa, A., Novellino, A., et al. (2017). HF radar activity in European coastal seas: next steps towards a pan-European HF radar network, *Front. Mar. Sci.* 4:8. doi: 10.3389/fmars.2017.00008
- Rypina, I. I., Kirincich, A., and Lentz, S. J. (2016). Investigating the eddy diffusivity concept in the coastal ocean. *J. Phys. Oceanogr.* 46, 2201–2218. doi: 10.1175/JPO-D-16-0020.1
- Sanford, E., Sones, J. L., García-Reyes, M., Goddard, J. H. R. and Largier, J. L. (2019). "Widespread shifts in the coastal biota of northern California during the 2014–2016 marine heatwaves." *Sci. Rep.* 9:4216. doi: 10.1038/s41598-019-40784-3
- Schaeffer, A., Gramouille, A., Roughan, M., Mantovanelli, A. (2017). Characterizing frontal eddies along the East Australian current from HF radar observations. *J. Geophys. Res. Oceans* 122, 3964–3980. doi: 10.1002/2016JC012171
- Send, U., Davis, R., Fischer, J., Imawaki, S., Kessler, W., Meinen, C., et al. (2009). "A global boundary current circulation observing network," in *Proceedings of OceanObs'09: Sustained Ocean Observations and Information for Society*, Venice.
- Sentchev, A., Forget, P., Barbin, Y., Yaremchuk, M. (2013). Surface circulation in the Iroise Sea (W. Brittany) from high resolution HF radar mapping. *J. Mar. Syst.* 109–110, S153–S168. doi: 10.1016/j.jmarsys.2011.11.024
- Small, C., and Nicholls, R. J. (2003). A global analysis of human settlement in coastal zones. *J. Coast. Res.* 19, 584–599.
- Solabarrieta, L., Aspey, R., Jones, B., (2018). "A New Insight into the Physical Processes of the Red Sea Using High Frequency Radar Data," in *Proceedings of the Ocean Sciences Conference*, Portland, 11–16.
- Solabarrieta, L., Frolov, S., Cook, M., Paduan, J., Rubio, A., González, M., et al. (2016). Skill assessment of HF radar-derived products for Lagrangian simulations in the Bay of Biscay. *J. Atmos. Oceanic Technol.* 3, 2585–2597. doi: 10.1175/JTECH-D-16-0045.1
- Son, Y.-T., Lee, S.-H., Kim, C.-S., Chul Lee, J., and Lee, G.-H. (2007). "Surface current variability in the Keum River Estuary (South Korea) during summer 2002 as observed by high-frequency radar and coastal monitoring buoy." *Cont. Shelf Res.* 27, 43–63. doi: 10.1016/j.csr.2006.08.008
- Sotillo, M. G., Cailleau, S., Lorente, P., Levier, B., Aznar, R., Refray, G., et al. (2015) The MyOcean IBI ocean forecast and reanalysis systems: operational products and roadmap to the future copernicus service. *J. Operat. Oceanogr.* 8, 63–79. doi: 10.1080/1755876X.2015.1014663
- Sperrevik, A. K., Christensen, K. H., and Röhrs, J. (2015). Constraining energetic slope currents through assimilation of high-frequency radar observations. *Ocean Sci.* 11, 237–249. doi: 10.5194/os-11-237-2015
- Stanev, E. V., Ziemer, F., Schulz-Stellenfleth, J., Seemann, J., Staneva, J., Gurgel, K.-W. (2015). Blending surface currents from HF Radar observations and numerical modeling: tidal hindcasts and forecasts. *J. Atmos. Ocean. Technol.* 32, 256–281. doi: 10.1175/JTECH-D-13-00164.1
- Stewart, J. R., Gast, R. J., Fujioka, R. S., Solo-Gabriele, H. M., Meschke, J. S., Amaral-Zettler, L. A., et al. (2008). "The coastal environment and human health:

- microbial indicators, pathogens, sentinels and reservoirs". *Environ. Health* 7:S3. doi: 10.1186/1476-069X-7-S2-S3
- Sydeman, W. J., Thompson, S. A., Garcia-Reyes, M., Kahru, M., Peterson, W. T., and Largier, J. L. (2013). Multivariate ocean-climate indicators (MOCI) for the central California current: Environmental change 1990-2010. *Prog. Oceanogr.* 120, 352–369. doi: 10.1016/j.pocean.2013.10.017
- U.S. Integrated Ocean Observing System [IOOS] (2015). *A Plan to Meet the Nation's Needs for Surface Current Mapping, 2015 Prepared for the Interagency Working Group on Ocean Observations*. Silver Spring, MD: IOOS, 62.
- U.S. Integrated Ocean Observing System [IOOS] (2016). *Manual for Real-Time Quality Control of High Frequency Radar Surface Currents Data: A Guide to Quality Control and Quality Assurance of High Frequency Radar Surface Currents Data Observations*. Silver Spring, MD: IOOS, 58.
- U.S. Integrated Ocean Observing System [IOOS] (2017). *QARTOD Project Plan Accomplishments for 2012-2016 and Update for 2017-2021*. Silver Spring, MD: IOOS.
- Updyke, T. (2017) *A study of HF Radar Outages in the Mid-Atlantic*. Galveston: Radiowave Operators Working Group (ROWG).
- Uttieri, M., Cianelli, D., Buongiorno Nardelli, B., Buonocore, B., Falco, P., Colella, S., Zambianchi, E. (2011). Multiplatform observation of the surface circulation in the Gulf of Naples (Southern Tyrrhenian Sea), *Ocean Dyn.* 61, 779–796. doi: 10.1007/s10236-011-0401-z
- Vignudelli, S., Cipollini, P., Roblou, L., Lyard, F., Gasparini, G. P., Manzella, G., et al. (2005). Improved satellite altimetry in coastal systems: case study of the Corsica Channel (Mediterranean Sea). *Geophys. Res. Lett.* 32:L07608. doi: 10.1029/2005GL022602
- Wandres, M., Wijeratne, E. M. S., Cosoli, S., Pattiaratchi, C. (2017). The effect of the Leeuwin Current on offshore surface gravity waves in southwestwestern Australia. *J. Geophys. Res. Oceans* 122, 9047–9067. doi: 10.1002/2017JC013006
- Waters, J., Wyatt, L. R., Wolf, J., and Hines, A. (2013). "Data assimilation of partitioned HF radar wave data into Wavewatch III". *Ocean Model.* 72, 17–31. doi: 10.1016/j.ocemod.2013.07.003
- Wilkin, J. L., and Hunter, E. J. (2013). An assessment of the skill of real-time models of Mid-Atlantic Bight continental shelf circulation, *J. Geophys. Res. Oceans* 118, 2919–2933. doi: 10.1002/jgrc.20223
- Wyatt, L. R. (2018). A comparison of scatterometer and HF radar wind direction measurements. *J. Oper. Oceanogr.* 11, 54–63. doi: 10.1080/1755876X.2018.1443625
- Wyatt, L. R., Green, J. J., Middleditch, A., Moorhead, M. D., Howarth, J., Holt, M., et al. (2006). "Operational wave, current, and wind measurements with the pises HF radar." *IEEE J. Ocean. Eng.* 31, 819–834. doi: 10.1109/JOE.2006.888378
- Wyatt, L. R., and Green, J. J. (2009). "Measuring high and low waves with HF radar", in *Proceedings of the OCEANS 2009-EUROPE*. Bremen: IEEE. doi: 10.1109/OCEANSE.2009.5278328
- Wyatt, L. R., Green, J. J., and Middleditch, A. (2011). "HF radar data quality requirements for wave measurement". *Coast. Eng.* 58, 327–336. doi: 10.3390/s150407412

**Conflict of Interest Statement:** BW was employed by company OEA Technologies, Inc. BH was employed by company HELZEL Messtechnik GmbH. JS was employed by company Qualitas Remos.

The remaining authors declare that the research was conducted in the absence of any commercial or financial relationships that could be construed as a potential conflict of interest.

Copyright © 2019 Roarty, Cook, Hazard, George, Harlan, Cosoli, Wyatt, Alvarez Fanjul, Terrill, Otero, Largier, Glenn, Ebuchi, Whitehouse, Bartlett, Mader, Rubio, Corgnati, Mantovani, Griffa, Reyes, Lorente, Flores-Vidal, Saavedra-Matta, Rogowski, Prukpitikul, Lee, Lai, Guerin, Sanchez, Hansen and Grilli. This is an open-access article distributed under the terms of the Creative Commons Attribution License (CC BY). The use, distribution or reproduction in other forums is permitted, provided the original author(s) and the copyright owner(s) are credited and that the original publication in this journal is cited, in accordance with accepted academic practice. No use, distribution or reproduction is permitted which does not comply with these terms.



## RESEARCH ARTICLE

10.1029/2020JC016368

## Key Points:

- A decade of hourly surface current maps were used to calculate annual and seasonal means along with interannual and intra-annual and seasonal variability
- Mean flows are cross-shore near the coast and southward alongshore with greater speeds offshore
- Wind velocity and river discharge are used to explain the most significant interannual variability

## Supporting Information:

- Supporting Information S1

## Correspondence to:

H. Roarty,  
hroarty@marine.rutgers.edu

## Citation:

Roarty, H., Glenn, S., Brodie, J., Nazzaro, L., Smith, M., Handel, E., et al. (2020). Annual and seasonal surface circulation over the Mid-Atlantic Bight Continental Shelf derived from a decade of High Frequency Radar observations. *Journal of Geophysical Research: Oceans*, 125, e2020JC016368. <https://doi.org/10.1029/2020JC016368>

Received 6 MAY 2020









Accepted 6 OCT 2020

Accepted article online 12 OCT 2020

©2020. The Authors.

This is an open access article under the terms of the Creative Commons Attribution License, which permits use, distribution and reproduction in any medium, provided the original work is properly cited.

# Annual and Seasonal Surface Circulation Over the Mid-Atlantic Bight Continental Shelf Derived From a Decade of High Frequency Radar Observations

Hugh Roarty<sup>1</sup> , Scott Glenn<sup>1</sup> , Joseph Brodie<sup>1</sup> , Laura Nazzaro<sup>1</sup>, Michael Smith<sup>1</sup>, Ethan Handel<sup>1</sup>, Josh Kohut<sup>1</sup> , Teresa Updyke<sup>2</sup> , Larry Atkinson<sup>2</sup> , William Boicourt<sup>3</sup> , Wendell Brown<sup>4</sup>, Harvey Seim<sup>5</sup>, Mike Muglia<sup>6</sup>, Haixing Wang<sup>7</sup> , and Donglai Gong<sup>7</sup>

<sup>1</sup>Center for Ocean Observing Leadership, Rutgers University, New Brunswick, NJ, USA, <sup>2</sup>Center for Coastal Physical Oceanography, Old Dominion University, Norfolk, VA, USA, <sup>3</sup>Center for Environmental Science, University of Maryland, Cambridge, MD, USA, <sup>4</sup>School for Marine Science and Technology, University of Massachusetts Dartmouth, New Bedford, MA, USA, <sup>5</sup>Department of Marine Sciences, University of North Carolina-Chapel Hill, Chapel Hill, NC, USA, <sup>6</sup>Department of Coastal Studies, East Carolina University, Wanchese, NC, USA, <sup>7</sup>Virginia Institute of Marine Science, College of William and Mary, Gloucester Point, VA, USA

**Abstract** A decade (2007–2016) of hourly 6-km-resolution maps of the surface currents across the Mid-Atlantic Bight (MAB) generated by a regional-scale High Frequency Radar network are used to reveal new insights into the spatial patterns of the annual and seasonal mean surface flows. Across the 10-year time series, temporal means and interannual and intra-annual variability are used to quantify the variability of spatial surface current patterns. The 10-year annual mean surface flows are weaker and mostly cross-shelf near the coast, increasing in speed and rotating to more alongshore directions near the shelfbreak, and increasing in speed and rotating to flow off-shelf in the southern MAB. The annual mean surface current pattern is relatively stable year to year compared to the hourly variations within a year. The 10-year seasonal means exhibit similar current patterns, with winter and summer more cross-shore while spring and fall transitions are more alongshore. Fall and winter mean speeds are larger and correspond to when mean winds are stronger and cross-shore. Summer mean currents are weakest and correspond to a time when the mean wind opposes the alongshore flow. Again, intra-annual variability is much greater than interannual, with the fall season exhibiting the most interseasonal variability in the surface current patterns. The extreme fall seasons of 2009 and 2011 are related to extremes in the wind and river discharge events caused by different persistent synoptic meteorological conditions, resulting in more or less rapid fall transitions from stratified summer to well-mixed winter conditions.

**Plain Language Summary** A coordinated High Frequency Radar network operated between Cape Cod, MA, and Cape Hatteras, NC, generates hourly maps of ocean surface currents. A decade-long study revealed the detailed structure of the surface flows. These flows were compared to wind and river flow data to explain the patterns observed in the flow. Near the coast, the average currents flow offshore. Away from the coast, the average currents flow along the coast toward the south. Fall is the season with the most variability from year to year. Its higher variability can be traced to different regional weather patterns that change the wind fields and the amount of freshwater delivered by the rivers to the coastal ocean. This is the first study to use a decade of observed surface current maps that uniquely and simultaneously observe the changing patterns of the average flow structure along a segment of eastern United States. The improved understanding of the coastal circulation over a wide area, and what drives its variability, has implications for pollutant transport, plankton transport at the base of the food chain, fish and shellfish reproduction, and multiple ocean-based human activities including fishing, marine transportation, and offshore wind energy development.

## 1. Introduction

The coastal ocean is an intricate system that forms the boundary between the land and the deep ocean. For shallow and wide continental shelves, such as those on the U.S. East Coast, dynamical factors such as

topography, large-scale circulation, wind, fresh water input, and turbulent dissipation play key roles in governing shelf circulation and dynamics. While the deep ocean experiences independent air-ocean and ocean-benthos interactions, the benthos of the shallow ocean affects the surface layer and in turn the associated along and cross-shelf transport (Soulsby et al., 1993). Wind and buoyancy forcing are critical to the flow and can quickly change the dynamics on time scales ranging from hours and days to seasons and years.

The Middle Atlantic Bight (MAB) supports a complex marine ecosystem, and it has been a focus of coastal oceanographic research since the early 1900s (Bigelow & Sears, 1935). The continental shelf of the MAB extends from Cape Hatteras, NC, in the south to Georges Bank off Cape Cod, MA, in the north. The prominent topographic features in this region are the Hudson Shelf Valley (HSV; Lentz et al., 2014), Nantucket Shoals (Beardsley et al., 1985; Limeburner & Beardsley, 1982), and Great South Channel (Chen et al., 1995). The width of the shelf gradually decreases from ~120 km south of Cape Cod down to ~40 km east of Cape Hatteras. The isobaths are roughly parallel to the coastline except near the HSV and the many shelfbreak canyons distributed throughout the MAB.

Beardsley and Boicourt (1981) present a review of the estuarine and coastal circulation of the MAB. The first dynamical model for the MAB showed a southwest drift of shelf and slope waters from Cape Cod toward Cape Hatteras (Sverdrup et al., 1942). Miller (1952) later showed that there was strong variability about this mean drift in the form of eddies and current filaments. Using arrays of long-term moorings, Lentz (2008) showed that the depth-averaged flow is aligned along the isobaths with the exception of the HSV where the mean flow is shoreward up the shelf valley. Chapman and Beardsley (1989) suggest that the origin of the shelf water is from glacial melt along the southern Greenland coast that propagates south to the MAB as a buoyant coastal current. Beardsley and Winant (1979) show that the southwest flow of this cold glacial water is primarily driven as a boundary current connected to the larger-scale circulation of the western North Atlantic Ocean (Fleming, 2016; Levin et al., 2018; Pringle, 2018).

Technology allowed for more long-term measurements of currents, water temperature and salinity, and meteorological forcing in the 1960s. Beardsley and Boicourt (1981) describe much of the work using these longer time series confirming that transient currents modulate the mean southwest drift. The focus of dynamical research in the 1970s shifted from the mean southwest flow to the current variability. Beardsley et al. (1976) suggest that the current variability of the MAB is mostly wind driven. Moores et al. (1976) show that the wind forcing driving this variability is predominately from the west/northwest except in the summer months when the wind is typically from the southwest. Ou et al. (1981) go on to show observationally that the variability is composed of a wind forced component and a larger-scale free-wave component that is not correlated with the wind and propagates downshelf. Using numerical simulations, Beardsley and Haidvogel (1981) confirm that these current fluctuations do have a local and nonlocal response. The local response is related to local geometry, topography, and forcing while the nonlocal response is due to forcing “distant in time and space.”

Beginning in the late 1990s and early 2000s, High Frequency Radar (HFR) surface current mapping technology was introduced to the region. These networks have supported circulation research in the region including nearshore studies off the coast of New Jersey (Kohut et al., 2004), the response of the shelf water to tropical storms (Kohut et al., 2006), and the seasonal variability of the shelf circulation (Castelao et al., 2008; Dzwonkowski et al., 2009, 2010; Gong et al., 2010). In the MAB, numerous studies have validated the HFR surface currents against more traditional in situ measurements (Haines et al., 2017; Kohut & Glenn, 2003; Kohut et al., 2006, 2012; Ullman & Codiga, 2004) and, as a result, these data now support U.S. Coast Guard Search and Rescue operations in the MAB and throughout the United States (Roarty et al., 2010; Ullman et al., 2006).

Since 2007, the Mid-Atlantic Regional Association Coastal Ocean Observing System (MARACOOS) has operated a regional HFR network consisting of approximately 41 radars. These systems have been maintained through a regional collaboration of eight separate organizations (University of North Carolina [Chapel Hill], Center for Innovative Technology, Old Dominion University, Rutgers University, University of Connecticut, University of Rhode Island, University of Massachusetts [Dartmouth], and Woods Hole Oceanographic Institution). The network provides hourly measurements of ocean surface currents (i.e., representative of water depths of 0.3–2.5 m) within ~250 km of the coast, over an area encompassing more than 190,000 km<sup>2</sup> of the ocean's surface, at resolutions of 1, 2, and 6 km. In this study, we focus on

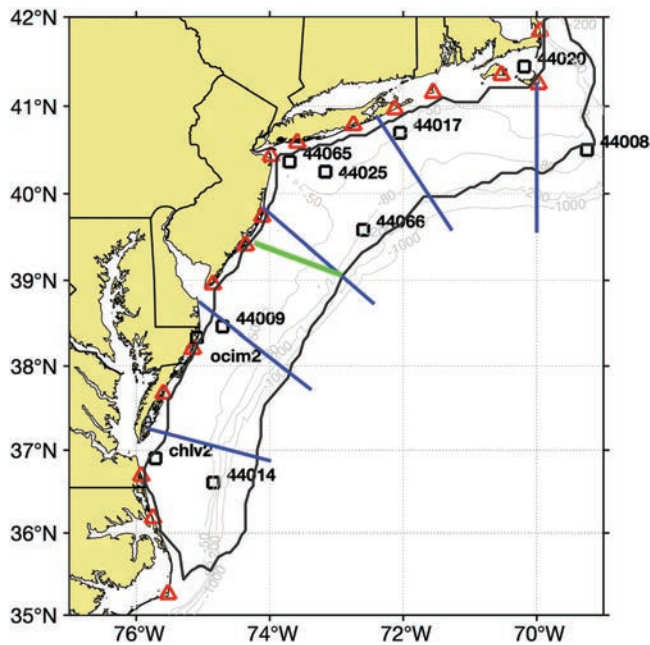


**Figure 1.** Map of the Mid-Atlantic Bight from Cape Hatteras, NC, up to Cape Cod, MA. The locations of the 5-MHz HF radar stations are denoted as red triangles. NOAA NDBC stations are marked as black squares and labeled. The 50-, 80-, 200-, and 1,000-m isobaths are marked along with the 50% total vector coverage for the study period shown as the thick black line. The Tuckerton endurance line is marked in green. The continental shelf was divided into six regions following definitions used by Wallace et al. (2018). From north to south, the regions are Eastern New England (ENE), Southern New England (SNE), New York Bight 1 (NYB1), New York Bight 2 (NYB2), Southern Shelf 1 (SS1), and Southern Shelf 2 (SS2).

10 years of shelf-wide surface current data provided by this network to examine the response of the surface current fields to local wind forcing and river input over seasonal to annual time scales. The study utilizes wind measurements from several coastal and at-sea wind sensors and river discharge data to describe the response of the two-dimensional structure of the ocean surface flow to these drivers and place that response in the context of atmospheric and oceanic flow features. The paper is divided into the following sections. In section 2, we describe the methods used to collect and process the MARACOOS surface current data set, the National Oceanic and Atmospheric Administration (NOAA) weather buoy and Coastal-Marine Automated Network (C-MAN) station wind data, and the U.S. Geological Service (USGS) river discharge data. In section 3, we characterize the mean and variability of the surface flow, the mean wind over the area, and the seasonality of the surface currents. In section 4, we will discuss the results and draw conclusions in section 5.

## 2. Methods and Data

### 2.1. Surface Currents

Surface current measurements were collected in the MAB from 2007 to 2016 using data from sixteen 5 MHz SeaSondes manufactured by CODAR Ocean Sensors (Figure 1). The SeaSonde is a HFR that uses the Doppler shift of radio signals reflected off ocean surface wind waves to measure the component of the ocean current along a radial line toward or away from the station. The average depth of the measurement varies with radar frequency and is proportional to  $\lambda/8\pi$ , where  $\lambda$  is the radar wavelength (60 m at a 5 MHz transmit frequency). This equates to an average depth measurement of 2.7 m (Paduan & Graber, 1997; Stewart & Joy, 1974). The 60-m radio waves are resonant with ocean waves having a wavelength of 30 m, which equate to waves with a period of 4.3 s in deep water. Each HFR station generated 3-hr-averaged radial component velocity maps

every hour; the data collection period for each hourly file was the file timestamp  $\pm 90$  min. Each radar utilized a 1-Hz sweep rate for the radio signal and a 1,024-point fast Fourier transform (FFT) for the Doppler processing. This resulted in a radial velocity resolution of approximately  $\pm 1.5$  cm/s for each hourly radial vector map.

The hourly radial files were combined into hourly total surface currents using the optimal interpolation scheme (Kim et al., 2008; Kohut et al., 2012). The optimal interpolation parameters used for the total combination were  $420 \text{ cm}^2/\text{s}^2$  for signal variance and  $66 \text{ cm}^2/\text{s}^2$  for error variance. The radials were weighted based on an exponential decay defined by the decorrelation scales in the north ( $S_y$ ) and east ( $S_x$ ) directions. The decorrelation scales in the MAB are larger along the isobaths (Beardsley & Boicourt, 1981; Kohut et al., 2004), so  $S_y$  (25 km) was set to 2.5 times that of  $S_x$  (10 km) and rotated along isobath. This processing is similar to that utilized in the Kohut et al. (2012) study. Total surface currents were computed on the 6-km national HFR grid (Terrill et al., 2006). For each year of surface current data from December 2006 through November 2016, the `t_tide` toolbox in MATLAB (Pawlowicz et al., 2002) was used to detide data in annual segments (1 December to 30 November; Gong et al., 2010). A 30-hr low-pass filter was then applied to the detided data in order to remove any remaining high-frequency variability. Only grid points with at least 50% coverage (Gong et al., 2010) at a normalized uncertainty level under 0.6 (Kohut et al., 2012) in both the  $u$  and  $v$  components over the year were included in this analysis. All means, variance, and root mean square (RMS) described below are calculated using the detided and low-pass filtered data that met these quality criteria.

Single-year seasonal means (winter: 1 December to 29 February; spring: 1 March to 31 May; summer: 1 June to 31 August; autumn: 1 September to 30 November) were created by averaging the hourly data over the 3-month period wherever the temporal coverage was at least 50%; annual means were calculated with all hourly data over the 12-month period from 1 December to 30 November, since it had already passed the 50% temporal coverage criterion. Decadal means for each season and for the full year were calculated by

**Table 1**  
*List of River Discharges That Were Utilized in the Study*

Major River	Minor River	Location	USGS Station No.
Connecticut Hudson		Thompsonville, CT	01184000
	Hudson	Fort Edwards, NY	01327750
	Mohawk	Cohoes, NY	01357500
	Passaic	Little Falls, NJ	01389500
Delaware Chesapeake	Raritan	Bound Brook, NJ	01403060
		Trenton, NJ	01463500
	Susquehanna	Conowingo, MD	01578310
	Potomac	Washington, DC	01646500
	Patuxet	Laurel, MD	01592500
	Rappahannock	Fredericksburg, VA	01668000
	Choptank	Greensboro, MD	01491000
	James	Cartersville, VA	02035000
	Appomattox	Matoaca, VA	02041650
	Pamunkey	Hanover, VA	01673000
	Mattaponi	Beulahville, VA	01674500

*Note.* The Hudson and Chesapeake were an amalgamation of several rivers.

taking the mean of all 10 previously calculated means, so each year was weighted equally. Each grid point had to contain at least five individual yearly means (i.e., 50% coverage) to be included in the decadal mean.

For each single-year seasonal and annual mean, a corresponding within-year variance was calculated for both eastward and northward velocities using the hourly surface current data. The decadal seasonal and total intra-annual variance was calculated by taking the mean of the 10 individual-year seasonal and total variances. The interannual variance was calculated by taking the variance of the eastward and northward components of the 10 individual-year seasonal and annual mean current fields. For each within- and between-year variance estimate, a corresponding RMS value was calculated by taking the square root of the sum of the eastward and northward variance values; this RMS considers variation in both current speed and current direction. The same 50% coverage requirements applied to the mean currents were also used for variance and RMS.

The confidence interval of the surface currents on the continental shelf was computed for the decadal mean as well as the seasonal means on the continental shelf following Thomson and Emery (2014). The 95% con-

fidence interval was calculated using the equation  $1.96\sigma/(N^*)^{1/2}$ , where  $\sigma$  is the standard deviation and  $N^*$  is the effective degrees of freedom.  $N^*$  was calculated using this equation,  $N^* = N\Delta t/T$ , where  $N$  is the number of samples,  $\Delta t$  is the sampling interval (1 hr), and  $T$  is the integral time scale.  $T$  was calculated to be 19 hr from a year's worth of data at midshelf offshore of New Jersey; hence,  $N^*$  was 4,870 for the decade of data and was 1,218 for each of the seasons. The uncertainty amounted to  $\pm 0.2$ – $0.6$  cm/s for the decadal mean and within  $\pm 0.4$ – $1.0$  cm/s for the seasonal means.

## 2.2. Winds

Wind data from 10 NOAA National Data Buoy Center (NDBC) stations (44008, 44009, 44014, 44017, 44020, 44025, 44065, 44066, chl2, and ocim2) were used for the wind analysis. Hourly wind data over the 10-year record from 2007 to 2016 were accessed online (<https://www.ndbc.noaa.gov>). A minimum of 50% temporal coverage was required of the annual or seasonal record to be included in the analysis. The wind data were averaged in the same manner as the current data to generate the seasonal means. The statistics of the wind speed and direction were performed by converting wind speed and direction into an east and north vector; all the east vectors were averaged, and all the north vectors were averaged, and then the resulting two vectors were combined to obtain a mean wind vector. The wind velocity data were then converted to wind stress using the wind stress function found in the Climate Data Toolbox for MATLAB (Greene et al., 2019).

## 2.3. River Discharge

Daily river discharge data were collected from the U.S. Geological Survey (USGS) water data available online (<http://waterdata.usgs.gov/nwis>) for the Connecticut and Delaware rivers. Discharge data from the Hudson, Mohawk, Passaic, and Raritan rivers were combined into a single product and labeled the Hudson River. Discharge data from the Susquehanna, Potomac, Patuxent, Rappahannock, Choptank, James, Appomattox, Pamunkey, and Mattaponi rivers were combined into a single data set and labeled the Chesapeake. The USGS station number corresponding to each river is given in Table 1. The discharge data from the individual stations were merged following the methodology of Chant et al. (2008) and Zhang et al. (2009). The final discharge data sets are made available on the Rutgers ERDDAP server ([http://tds.marine.rutgers.edu/erddap/tabledap/ROMS\\_DISCHARGE.graph](http://tds.marine.rutgers.edu/erddap/tabledap/ROMS_DISCHARGE.graph)). The yearly and seasonal mean and standard deviation of river discharge data are provided in Table 2.

# 3. Results

## 3.1. Decadal Mean Surface Currents

Throughout the manuscript, wind direction will follow the meteorological convention where direction indicates where the wind is blowing from and the currents will be described in the oceanographic convention



**Table 2**  
Annual and Seasonal Mean River Discharge Along With One Standard Deviation

	Annual		Winter		Spring		Summer		Fall	
	Mean	$\pm s$	Mean	$\pm s$	Mean	$\pm s$	Mean	$\pm s$	Mean	$\pm s$
Connecticut	675	551	659	378	1,096	611	485	337	457	301
Delaware	630	626	704	417	884	579	449	290	447	337
Hudson	770	629	855	395	1,165	692	538	389	557	346
Chesapeake	2,524	2,521	3,073	1,865	4,242	2,322	1,311	728	1,483	1,276

where direction indicates where the current is flowing toward. The wind field as observed by the 10 wind sensors in the region shows a mean wind from the west northwest that increases speed with distance offshore and rotates slightly to be out of the northwest near the shelfbreak (Figure 2a). Wind variability is denoted by ellipses that represent two standard deviations in the data shown with a scale of 15 m/s. The mean surface flow over the 10-year period (2007–2016) as measured by the MARACOOS long-range HF radar network was offshore and equatorward with a speed of 2–12 cm/s (Figure 2b) with the mean across the entire field of 7 cm/s. The alongshelf currents increase with increasing water depth, consistent with Lentz (2008). Compared to the mean, the currents are most steady along the shelfbreak and most varied near the coastline, essentially varying in offshore direction in concert with the change in coastline orientation. North of the HSV, the currents are toward the southwest while south of the HSV the currents are toward the southeast rotating clockwise toward the southwest with distance offshore. This agrees with

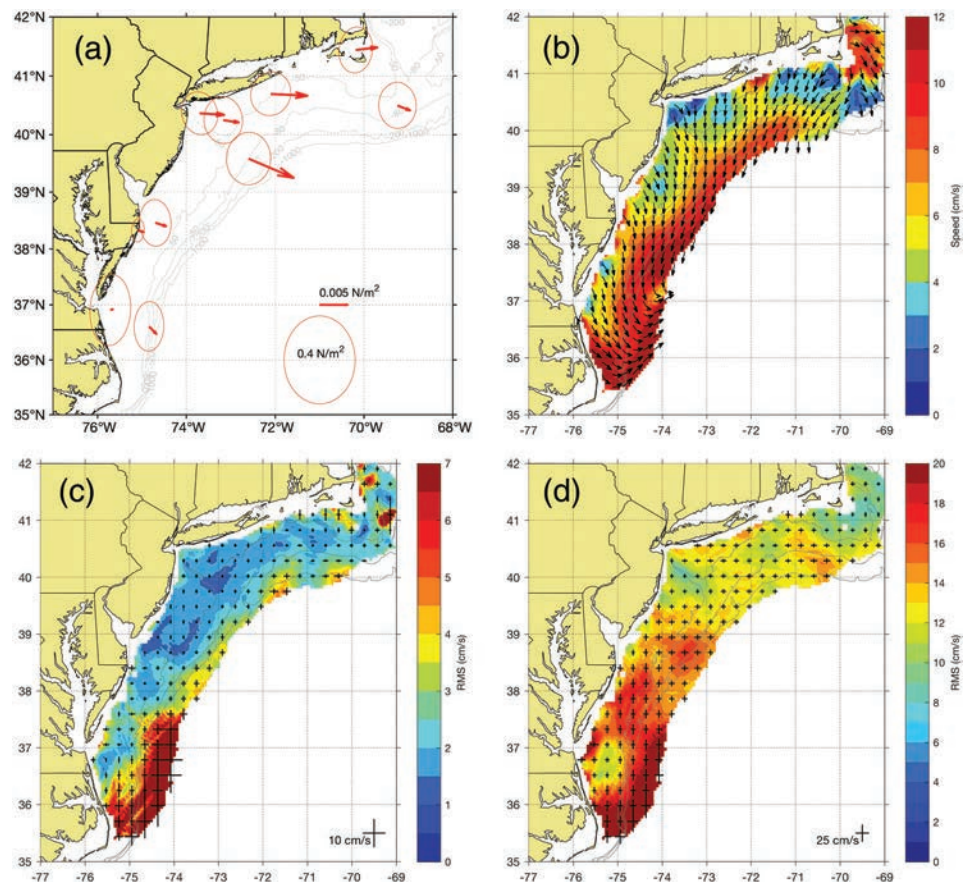


**Figure 2.** (a) Mean and 95% data ellipse of wind stress ( $N/m^2$ ) from NDBC stations for 2007–2016. The reference vector of 0.005 and 0.4  $N/m^2$  variability ellipse is given in the lower right. (b) Mean surface current for the Mid-Atlantic Bight (cm/s) colorbar indicates magnitude and vectors indicate direction toward of surface current. (c) Interannual standard deviation of the surface currents (cm/s). (d) Intra-annual standard deviation of the surface currents (cm/s).

the earlier work by Gong et al. (2010), who observed the HSV divides the flow into two regimes north and south of the valley. The currents gradually transition from SE to SW with increasing depth; southward currents are centered along the 50-m isobath from Virginia to New Jersey. The surface currents strengthen seaward of the 50-m isobath with speed increasing to 7–11 cm/s with faster flow observed further south. South of the Chesapeake Bay (CB), the flow then turns offshore and merges with the Gulf Stream. The broad band of fast flowing current over the outershelf and shelfbreak is persistent throughout most of the year, and it is thought to be associated with the meandering shelfbreak jet (Linder & Gawarkiewicz, 1998). However, other factors such as buoyancy-driven flow from the rivers also likely contributed to this enhanced flow feature. For our purpose, we will continue to call it the shelfbreak jet, but please keep in mind that this is only in a statistical sense. Any synoptic realization of the shelfbreak jet will likely look very different than this average view.

The surface flow east of Cape Cod is predominantly to the southeast. Below Cape Cod, the flow turns toward the southwest to join the flow south of Rhode Island. Moving south from Cape Cod, the mean surface flow is along isobath toward the equator, consistent with previous studies that analyzed the depth-averaged flow with current meters (Beardsley & Boicourt, 1981; Lentz, 2008) and HF radar (Gong et al., 2010).

The weakest flow regions are observed near the New York Bight apex and south of Cape Cod where the surface currents drop to between 1 and 3 cm/s. The strongest flows in the region are observed near the Gulf Stream, east of Cape Cod, and Nantucket and a strong coastal current along the coast of North Carolina (Lentz et al., 2003).

The influence of the rivers can be seen as the increased velocity regions near the eastern end of Long Island, south of the HSV, south of the Delaware Bay (DB), and the strengthened coastal current along the coast of North Carolina off of the Chesapeake.

### 3.2. Variability of Surface Currents

The variability of the surface current is significant compared to the mean. The standard deviation within a year (Figure 2) is between 10 and 20 cm/s for the entire field reaching a peak of 20 cm/s off Cape Hatteras where the variability in the position of the Gulf Stream factors significantly (Andres, 2016). Marks representing one standard deviation in the east/west and north/south direction for every fifth grid point are shown with a reference of 25 cm/s in the lower right of the figure. The average standard deviation for the entire field is 15 cm/s. The standard deviation in the northern portion of the domain is of the order 10 cm/s and gradually increases to 20 cm/s in the southern portion of the domain. While the climatological mean is toward the equator, the daily mean can be poleward or opposite the mean flow for several days if the wind conditions are from the south or southwest (Bumpus, 1969; Frey, 1978). Two regions of lower variability are seen over the New Jersey shelf and off the Virginia/North Carolina coast.

The variability from year to year is much less than the variability within the year. The average variability between years is 4 cm/s for the entirety of the domain (Figure 2c). Marks representing one standard deviation in the zonal and meridional direction for every fifth grid point are shown with a reference of 10 cm/s in the lower right of the figure. The variability between years increases across the shelf most likely due to the position of the shelfbreak jet (Fratantoni & Pickart, 2003; Linder & Gawarkiewicz, 1998). The variability between years is highest in the southern region extending up to 37.5°N latitude where the location of the Gulf Stream may influence this variability.

### 3.3. Seasonal Mean Flow

The surface current and wind data were seasonally averaged following Flagg et al.'s (2006) climatological analysis of the subsurface currents on the outer shelf and Gong et al.'s (2010) analysis of the surface currents on the shelf. The following is a discussion of the seasonally averaged winds (Figure 3) and currents (Figure 4). Again, the variability in the wind is denoted by ellipses that represent two standard deviations in the data. The variability of the wind is two to three times the mean in the MAB, which is reflected in the surface currents. Note that the maps of the seasonal winds and currents are arranged with winter in the upper left and progressing clockwise through the seasons to make it easier for the reader to identify the season-to-season changes in adjacent maps.

To describe the regional differences in surface transport, the continental shelf off the northeast United States is divided into four distinct regions, by combining some of the same regional definitions used by Wallace et al. (2018) in their hydrographic analysis. From north to south, the four analysis regions are Region 1

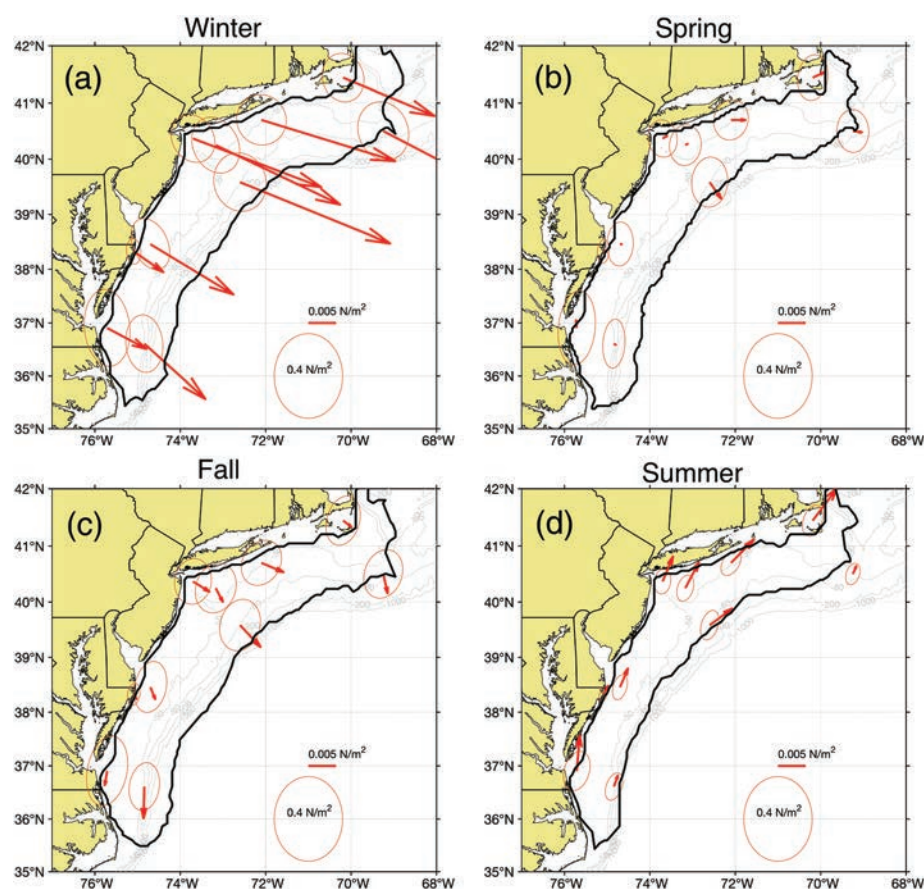


**Figure 3.** Map of mean and two standard deviation data ellipse of wind stress by season (a) winter, December–February; (b) spring, March–May; (c) fall, September–November; and (d) summer, June–August. The reference vector of 0.005 and 0.4  $\text{N/m}^2$  variability ellipse is given in the lower right of each figure. The 50% total vector coverage boundary for each season is shown as the thick black line.

encompassing Eastern New England (ENE), Region 2 encompassing Southern New England (SNE) and New York Bight 1 (NYB1), Region 3 encompassing New York Bight 2 (NYB2) and Southern Shelf 1 (SS1), and Region 4 encompassing Southern Shelf 2 (SS2). In addition, we defined the MAB region as encompassing the three southernmost regions (similar to the regions defined by Mountain, 2003, but modified to better encompass the inner-shelf domains). These regions are illustrated in Figure 1. We focused the wind analysis on four stations as being representative of the wind field within the particular regions: Region 1 (44008), Region 2 (44025), Region 3 (44009), and Region 4 (44014).

The seasonal maps of the 10-year average HFR surface current and NOAA buoy winds reveal the following:

**Winter:** From December to February, strong winds from the west-northwest are present over the entire area (Figure 3a), and the flow is similar to the long-term mean (Figure 4a). The ocean surface currents are predominantly offshore, only slightly to the right of the winds with peak velocities between 7 and 12 cm/s. The core of the shelfbreak jet has moved offshore to over the 1,000-m isobath. The current response was divided into four subregions, which allows for a finer description of the flow (Figure 1). (1) ENE: Flow to the east over Nantucket Shoals diverges to east and south. (2) SNE and NYB1: Currents are toward the south on inner shelf turning to the south southwest as they cross the shelfbreak. The low current area south of Nantucket has slightly increased speeds compared to the decadal mean, and currents are directed much more to the south. (3) NYB2 and SS1: Currents are offshore toward the southeast over the inner shelf turning south as they cross the shelfbreak. And lastly, Region (4) SS2: Currents are alongshelf turning counterclockwise to transport water off of the shelf into the Gulf Stream.



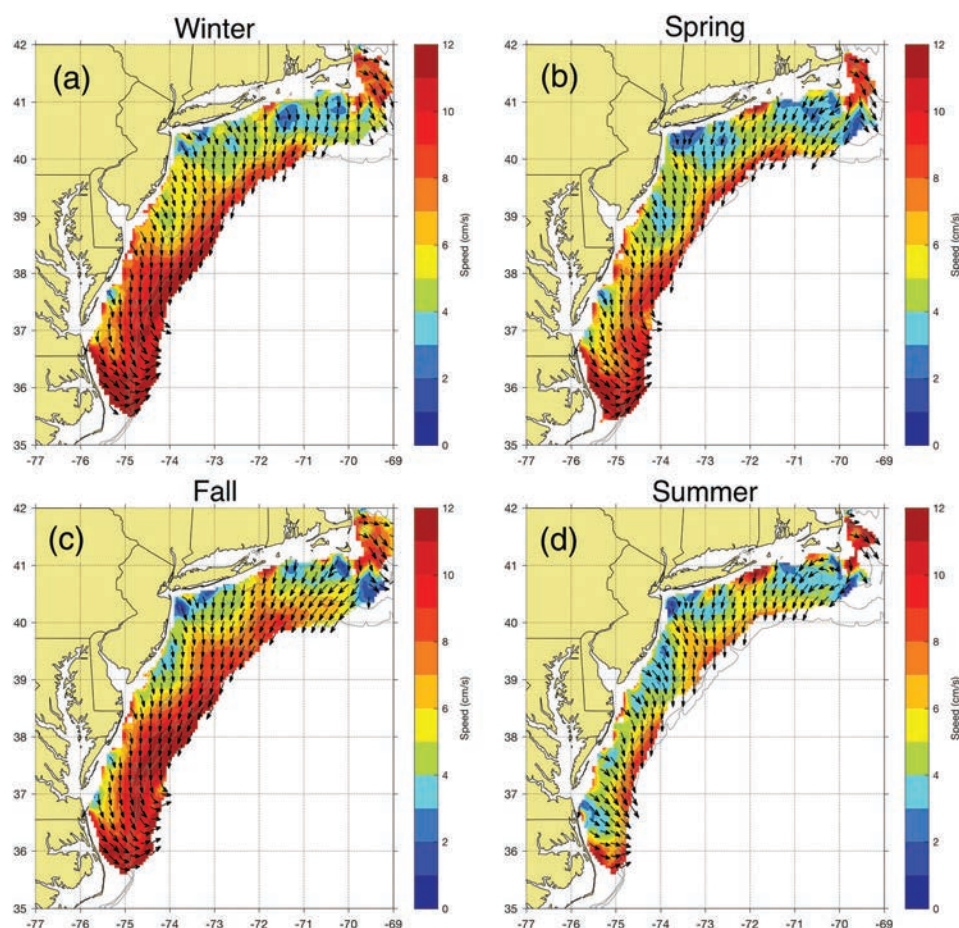


**Figure 4.** Mean surface currents (2007–2016) by season (a) winter, December–February; (b) spring, March–May; (c) fall, September–November; and (d) summer, June–August. Colorbar indicates magnitude (cm/s) and vectors indicate direction toward of surface current.

Spring: From March to May, weak winds from the west are present nearshore (Figure 3b) with slightly stronger winds in the eastern portion of the domain. The currents inshore of the 100-m isobath are weaker than winter with velocities of 3–6 cm/s. Stronger alongshore currents persist offshore of the 100-m isobath in the range of 9–12 cm/s (Figure 4b). There is a distinct continuous shelfbreak jet, with a wide peak that starts south of Martha's Vineyard and runs continuously until it turns offshore before reaching Cape Hatteras. (1) ENE: Again, currents are to the southeast and south to the right of the wind are observed. (2) SNE and NYB1: Currents are to south southwest over most of the shelf with south and south-southeast currents near the HSV. South of Nantucket, there are weak currents to the southwest, opposite of the wind. (3) NYB2 and SS1: currents to the southeast over inner shelf, turning to southwest over outer shelf. (4) SS2: Outflow hugs the coastline, turns with the coast, and is then transported offshore into the Gulf Stream. There is a pathway from the shelf/slope front to the east into the Gulf Stream as far north as CB.

Summer: From June to August, the winds are at the midrange of speeds (1.0 to 1.9 m/s) and from the southwest (Figure 3d), typical of the large-scale response to the summer Bermuda high (Zhu & Liang, 2013). Summer has the weakest flows of all the seasons with currents of 3–6 cm/s over most of the shelf (Figure 4d). The currents along the 100-m isobath are slightly faster than those inshore of that isobath. Currents are predominantly offshore, about 90° to the right of the winds in this highly stratified season with peak velocities, 6–8 cm/s, over the 100-m isobath. (1) ENE: There is an area of weak currents and divergence southeast of Nantucket. North of this, there are strong currents to the southeast. (2) SNE and NYB1: Currents are south-southwest over most of the shelf. South of Nantucket and Martha's Vineyard, there are weak west to southwest flows, and a small area south of Nantucket has northwest to north-northwest



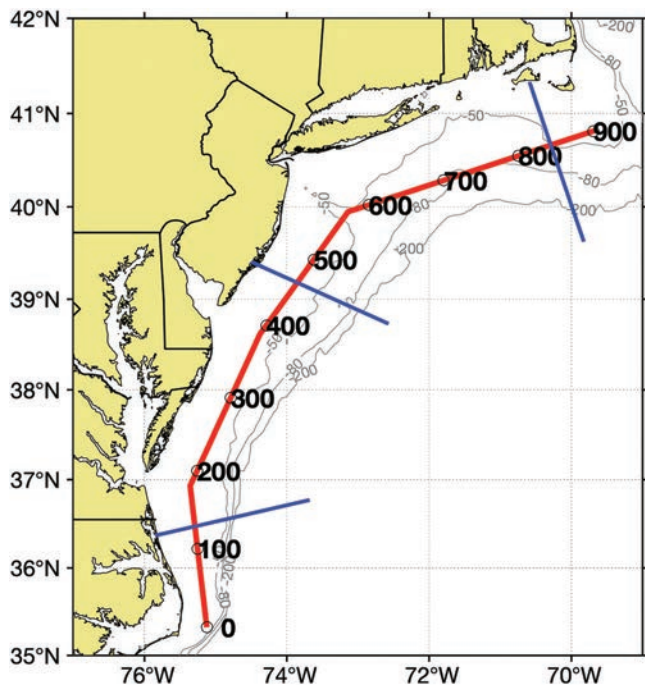


**Figure 5.** Reference line along the midshelf (red) used to calculate the cross-shelf and alongshelf flow along the Mid-Atlantic Bight. The numbers represent distance in kilometers along the reference line from south to north. The blue lines are the cross section lines that are shown in Figure 7.

flow that is not present in any other season. Strong flows from Long Island and Block Island Sounds are offshore to the southwest. (3) NYB2 and SS1: The cross-shelf flow extends further out over the shelf before turning more alongshore, and the inner-shelf flow is weaker than in other seasons. (4) SS2: weaker flow and directed more cross-shelf than in the other seasons, transporting water to the southeast off the shelf toward the Gulf Stream.

Fall: From September to November, it has similar medium wind speeds as summer but turned to be from the northwest, in the offshore direction (Figure 3c). Fall displays the fastest currents of all the seasons with currents greater than 6 cm/s over most of the shelf (Figure 4c). Compared to summer, the currents across most of the shelf increase in speed, especially off Maryland and Virginia where they accelerate to 13 cm/s along the 80-m isobath. The shelfbreak jet is the strongest and widest in fall with peak currents beginning south of Martha's Vineyard. The broad peak extends between the 60- and >1,000-m isobaths. This feature flows all the way south to join the Chesapeake outflow and flow offshore to the Gulf Stream in one wide region. (1) ENE: The flow is to east over Nantucket Shoals. Southeast of Nantucket, there are slower currents directed to the southeast. (2) SNE and NYB1: South-southwest currents on the inner shelf turn slightly to the southwest over the outer shelf, accelerating in the alongshelf direction. (3) NYB2 and SS1: On the inner shelf the currents are offshore and toward the south, turning to alongshelf over the middle to outer shelf. At the outer shelf and in the slope water the currents are alongshelf, 90° to the right of wind. (4) SS2: Outflow along the coast is strong and joins the shelfbreak jet over the shelf and both flow offshore in one current

The seasonal mean and standard deviation of the discharge ( $\text{m}^3/\text{s}$ ) for each of the four major rivers in the MAB are shown as Table 2. The outflows from the Connecticut, Delaware, and Hudson are of the same order

while the outflow from the Chesapeake is two to four times larger than each of these rivers. The freshwater outflow analysis is from the four major rivers within the Mid-Atlantic and not fresh water from the Gulf of Maine. The largest outflow is in the spring accounting for 40% of the fresh water into the system with the lowest discharge in the summer only accounting for 15%. This pattern also holds true for the variability with the spring accounting for 21% of the variability (one standard deviation) and the summer accounting for only 6% of the variability.

### 3.4. Alongshelf and Cross-Shelf Flows

In this section a quantitative description of the seasonal flow in the MAB is provided. The alongshore and cross-shore current was calculated over a midshelf line (Figure 5a), and the distance in kilometers along the line is overlaid on the line where the origin is east of Cape Hatteras and increases toward the north. The bearing along this line was used to rotate the surface currents into an alongshelf and cross-shelf coordinate system. The new current components were then plotted as a function of distance along the isobath as shown in Figure 6a for the alongshelf flow and Figure 6b for the cross-shore flow. The approximate location of where the four major estuaries connect to the shelf water are drawn as horizontal lines in Figure 6, CB at distance marker 150 km, DB at 350 km, Hudson River at 550 km, and Long Island Sound (LIS) at 700 km.

Three distinct regions emerge from these plots. The first region from 0 to 150 km is where the shelf slope front turns offshore and the CB plume accelerates along the coast, and the two flows join with the Gulf Stream to be advected to the northeast. Within this region there is an increase in both the alongshelf flow and cross-shelf flow. The cross-shelf flows are consistent from season to season. Winter and fall display the greatest alongshelf flow while summer exhibits the weakest alongshelf flow. Spring resides in the middle with an alongshelf flow of 4 cm/s near CB accelerating to 9 cm/s near Cape Hatteras.

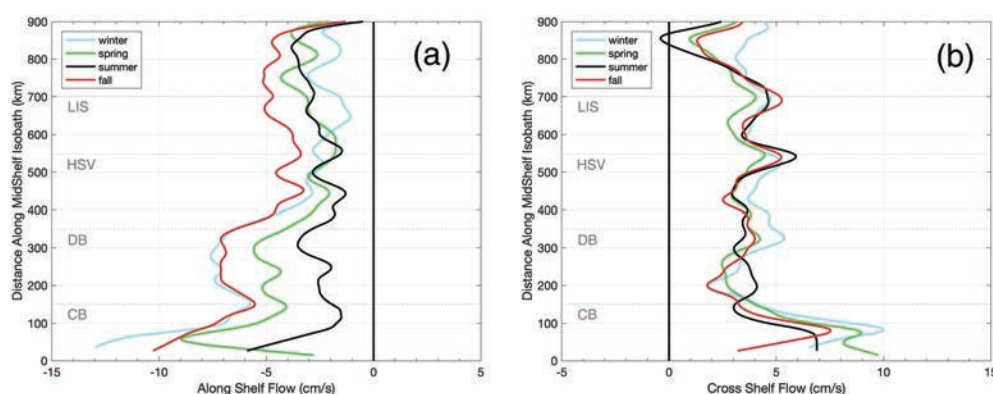


**Figure 6.** (a) Alongshelf current plotted by distance along the midshelf line (Figure 5a) by season winter (blue), spring (green), summer (black), and fall (red). (b) Cross-shelf current plotted by distance along the midshelf line. The locations of the four major estuaries are denoted by the dotted lines Long Island Sound (LIS), Hudson Shelf Valley (HSV), Delaware Bay (DB), and Chesapeake Bay (CB).

In the middle region between 150 and 800 km shows a consistent alongshelf flow from 800 to 350 km near DB and then an increase in alongshelf flow south of this location during some seasons. The alongshelf flow is strongest in the fall and weakest in the summer. The cross-shelf flow is offshore for each season, and the alongshelf flow is equatorward in each season. The cross-shelf flow is consistent between the seasons. There are local maximum points in the cross-shelf flow near the major estuaries at LIS, HSV and DB. The cross-shelf flow then accelerates when it reaches CB at 150 km. South of the 350-km distance marker, there is an increase in the alongshelf flow except in summer. It is in this middle zone where all the variation in space and seasonality takes place. In winter when the water column is well mixed, the flow will be more influenced by topography while in the summer it will be influenced by the stratification. Lastly, the region from 800 to 900 km exhibits an alongshelf flow that is consistent between the four seasons. The cross-shelf flow is 1–4 cm/s while winter exhibits the strongest cross-shore flow due to the strong winds from the northwest.

The findings for distances 0–800 km along the midshelf line show a stronger cross-shelf flow than measured by Lentz (2008), who found the cross-shelf flow to be between 1 and 3 cm/s near the surface. This is understandable, as the Lentz near-surface velocities were from the shallowest measurement of an acoustic current meter within 20 m of the surface while the HFR measurement is within 3 m of the surface. Any shear in the water column would explain these differences. Lentz (2008) also noted that the current meter records showed stronger offshore flows in the northern MAB and weaker cross-shelf flows in the southern MAB. This agrees for the area off Cape Cod. We note an area of increased cross-shelf flow off of Cape Hatteras.

Next, cross sections were taken through the seasonal flows to look at the variability of the along and cross-shelf flow in relation to their location within the MAB. Figure 7 shows the alongshelf velocity (top panel), cross-shelf velocity (middle panel), and water depth (lower panel) for the three cross sections (blue lines) from Figure 5. The three cross sections fall within three of the subregions Southern Shelf 2 (SS2), New York Bight 2 (NYB2), and Southern New England (SNE), which can be thought of as the entrance, middle, and exit of the flow through the MAB, respectively. The alongshelf and cross-shelf flow are plotted against distance offshore (km). Positive alongshelf flow is toward the northeast, and positive cross-shelf flow is offshore. The largest seasonal variability at the entrance (Region SS2) to the MAB is displayed in the alongshelf current while the exit (Region SNE) exhibits the strongest seasonal variability in the cross-shelf. The seasonal variability in the middle of the MAB (Region NYB2) is at a minimum, which is in contrast to the highly variable winds in each season as shown in Figure 3. This suggests that the mean alongshelf flow is not influenced by the wind but is driven by a large-scale alongshelf pressure gradient (Lentz, 2008). Each of the cross sections display a coastal current that is toward the equator and an increasing alongshelf flow with distance offshore. Region NYB2 displays a linearly increasing alongshelf flow while Region SS2 reaches a maximum alongshelf flow at 120 km offshore just past the shelfbreak and then transitions to cross-shelf flow in the vicinity of the Gulf Stream.

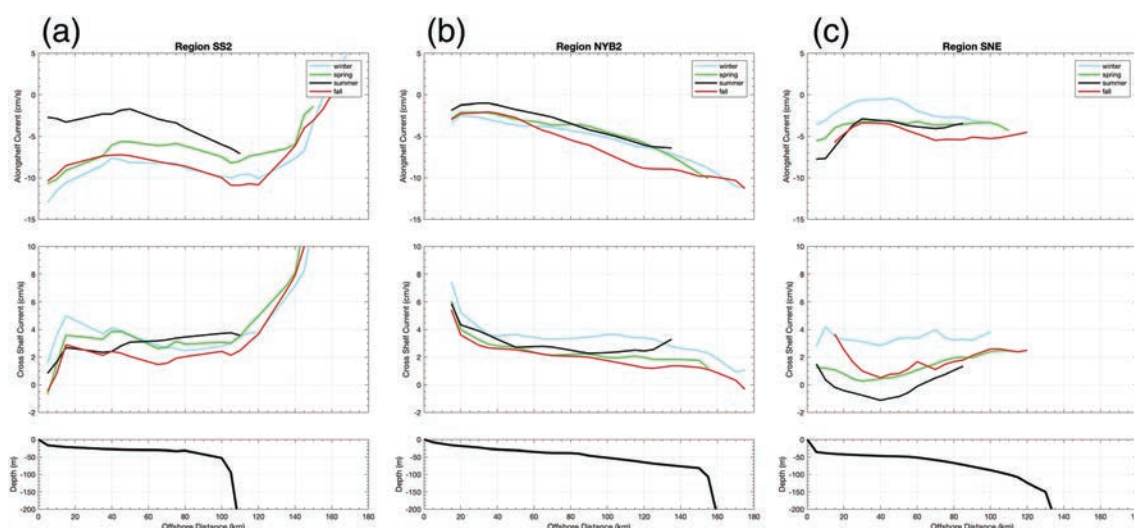


**Figure 7.** Alongshelf current (top) and cross-shelf current (middle) as a function of distance offshore (km) by season winter (blue), spring (green), summer (black), and fall (red) for three cross sections through MAB: (a) Southern Shelf 2 (SS2), (b) New York Bight 2 (NYB2), and (c) Southern New England (SNE). The bottom panel depicts water depth along each of the three cross sections.

### 3.5. Seasonal Variability

Next, we examined for each season the variability of the surface flow within the years (intra-seasonal variability) and the variability between the years (inter-seasonal variability). Intra-seasonal variability (Figure 8) is found by calculating the standard deviation of the hourly data each season and then averaging the results for all 10 years so that each year is equally weighted. This provides a measure of the short-term variability expected within a season. Inter-seasonal variability (Figure 9) is calculated by taking the standard deviation of the 10 annual averages. This provides a measure of the year-to-year variability in the seasonal averages.

For the intra-seasonal statistics, summer is the least variable with a standard deviation of 11.9 cm/s averaged over the entire field. Winter and fall exhibit the highest variability at 15.4 cm/s. Spring is in between at 14.5 cm/s. Comparing Figure 8 with Figure 4, the standard deviation of the short-term variability is greater than the mean flow speeds. The variability decreases with higher latitude in each of the seasons. Winter, spring, and fall all display less variability over the HSV. As noted by Gong et al. (2010), the spatial variability of the surface currents is affected by different forcing mechanisms at different scales. Wind forcing and stratification operate at shelf wide scales while topography can influence the flow on scales of tens of kilometers.

The inter-seasonal variability is one third the value of the intra-seasonal, implying that the seasonal averages are relatively stable from year to year. For the inter-seasonal statistics, again, summer is the least variable with a standard deviation of 3.5 cm/s for the whole field. The most significant year-to-year variability in the domain occurs in the southern half of the MAB, either along the shelfbreak jet or along on the southern MAB shelf itself, where the strong currents turn toward the shelfbreak and the Gulf Stream. The variability between summers is high near the eastern side of LIS, which match the findings of Ullman and Codiga (2004), who found a surface-intensified jet that is strongest in the summer and essentially absent in winter. The variability is high between springs at the shelfbreak near 40°N, 71°W, an area where Gulf Stream warm core rings are known to impact the shelf (Zhang & Gawarkiewicz, 2015). The variability between seasons is relatively constant at 3 cm/s along the New Jersey and New York coast. The fall is unique in having both high inter-seasonal and intra-seasonal variability. We will focus on the variability associated with this season in section 4.

## 4. Discussion

### 4.1. General Overview: Variability of Surface Circulation in MAB

A 10-year time series of surface ocean currents mapped with a long-range HFR network identified important patterns and pathways in the mean and variance of the surface flow over annual and seasonal time scales.



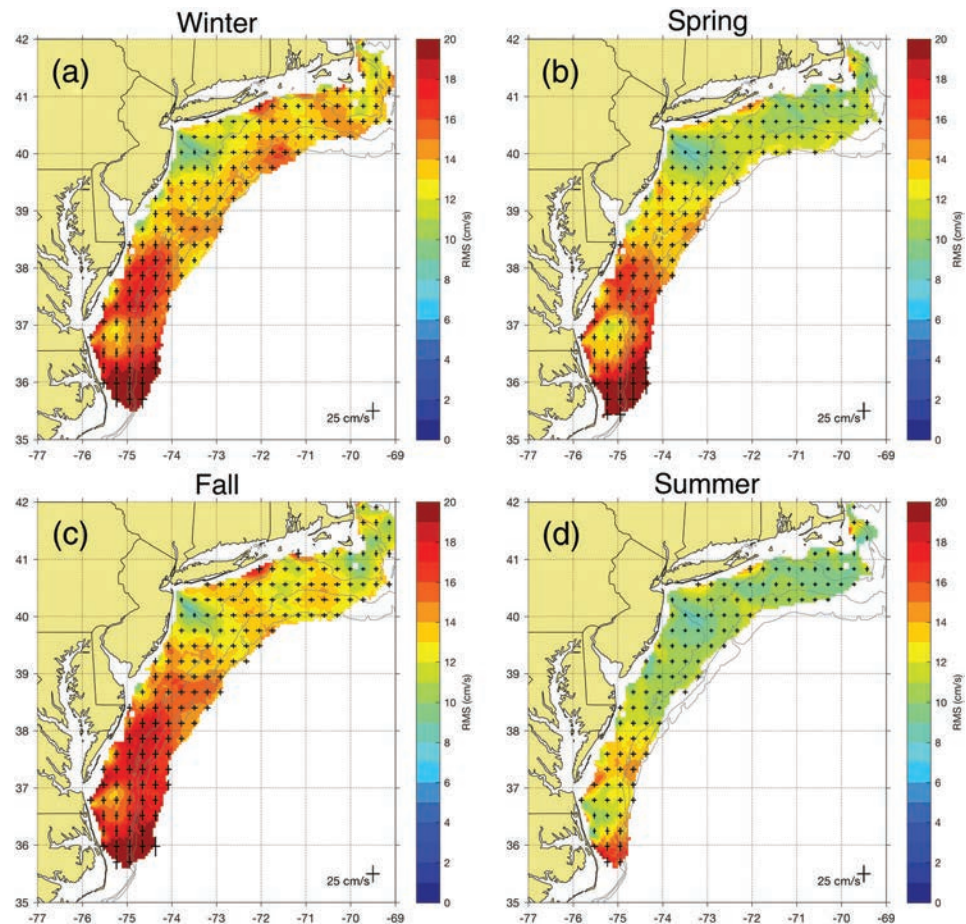


**Figure 8.** Intraseasonal standard deviation of the surface current (cm/s) in the Mid-Atlantic from (a) winter, December–February; (b) spring, March–May; (c) fall, September–November; and (d) summer, June–August. One standard deviation marks in the east/west and north/south directions are shown for every fifth grid point (30-km spacing) with a reference scale of 25 cm/s in the lower right.

These data show that the variability in the flow over these time scales is twice the magnitude of the mean, driven by similar variance in the local winds. The largest variability in the surface currents was typically seen in the fall and winter seasons when the MAB transitions from a highly stratified water column to a well-mixed water column. During these seasons, energetic wind events and buoyancy inputs drive the observed variability.

The seasonally averaged winds and the variabilities of the winds for the MAB are shown in Figure 3. Autumn and winter generally exhibit stronger winds in the cross-shore direction from the northwest, with more spatial variability in the autumn when the winds are slightly weaker. Progressing from spring into summer, the weaker winds are more alongshore from the southwest, with more spatial variability in the weaker spring. Freshwater input can also be divided into two types of response but offset in time from the winds. Freshwater input is typically largest in winter and spring and lowest in summer and fall. In fall and winter, cross-shore winds are dominant with low riverine flow in the fall and high flow in the winter. On the other hand, spring and summer seasons exhibit predominately alongshore winds with high riverine flow in the spring and low flow in the summer.

The seasonal mean currents from Figure 4 indicate that fall and winter currents are very similar, with the weakest currents inshore in the northern half of the MAB and the highest flows near the shelfbreak and across the entire shelf in the southern MAB. In winter, the spatially consistent strong winds from the northwest may act to diminish the westward alongshore component of flow in the northern MAB. This is quite different from the southern MAB where the relative angle of the wind and shelf geometry is close to



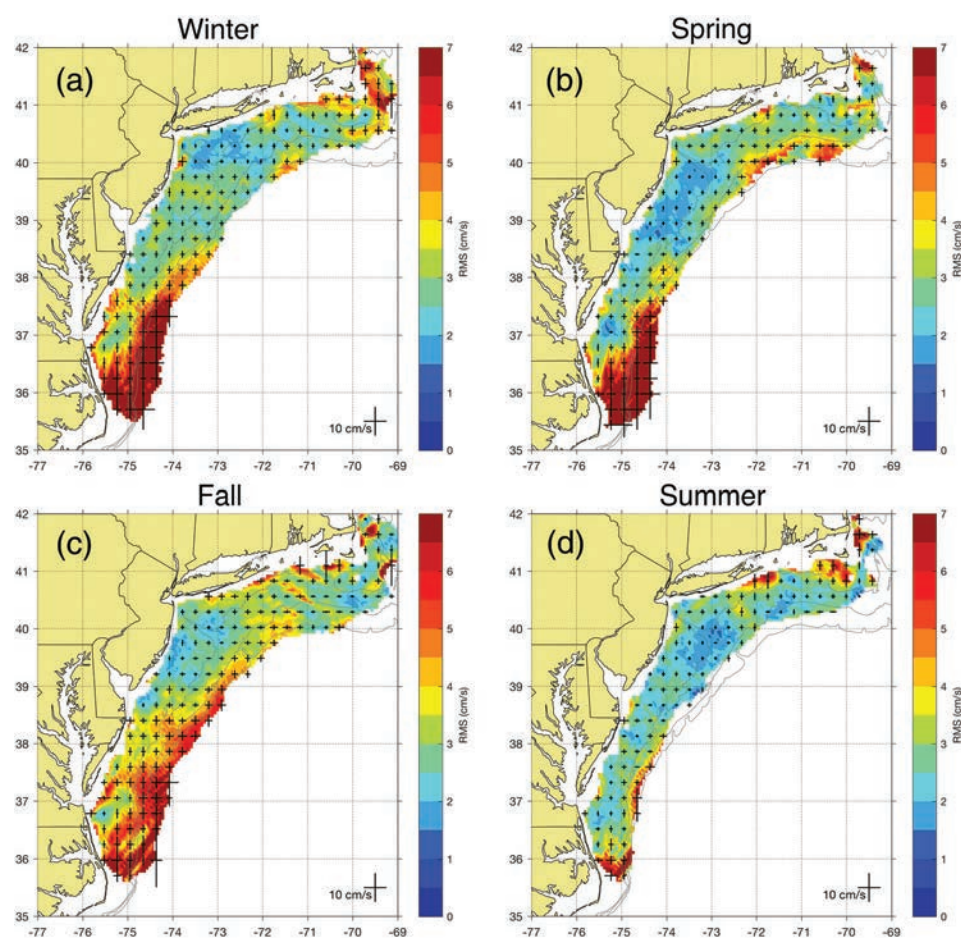


**Figure 9.** Interseasonal standard deviation of the surface current (cm/s) in the Mid-Atlantic from (a) winter, December–February; (b) spring, March–May; (c) fall, September–November; and (d) summer, June–August. One standard deviation marks in the east/west and north/south directions are shown for every fifth grid point (30-km spacing) with a reference scale of 10 cm/s in the lower right.

orthogonal and the alongshore transport is enhanced by winds in the fall. During this transition season, the flow is directed more alongshore. Spring and summer currents are similar in that both have weaker currents nearshore along the entire MAB, increasing in magnitude with distance offshore, with the strongest currents near the shelfbreak. The cross-shelf pathways are prominent in both the high-flow spring and the low-flow summer. During the high-flow spring, the currents reach speeds similar to the wind driven currents of fall and winter despite having very little average wind forcing.

In general, moving from north to south along the midshelf line with the main current, the alongshore current speeds increase, peaking in Region 4 SS2 (Figure 6a). The alongshore current rapidly increases as the strong current turns offshore and exits the shelf over a seasonally variable 150- to 200-km-wide region. Alongshore currents in the spring and summer are similar with the wind opposing the flow. Fall and winter have the largest alongshore currents, when the wind is cross-shore and the water column is generally less stratified. The alongshore flow is strengthened in the southern MAB in the fall and winter where there is a rotation in the wind to align with alongshore toward the south. Alongshore currents in the winter are the lowest in the northern MAB where they are opposed by the local wind (Figure 7, top right). At midshelf, cross-shelf currents are nearly 2–4 cm/s over much of the MAB. Local peaks in the cross-shelf flow occur at LIS, HSV, and DB (Figure 6b).

Intraseasonal variability is similarly large in fall (high winds speeds) through winter (medium wind speeds and medium river flow) and into spring (low winds and high river flow), with significantly lower variability in the summer. Spring variability is smaller in the northern half of the MAB when winds are very low and

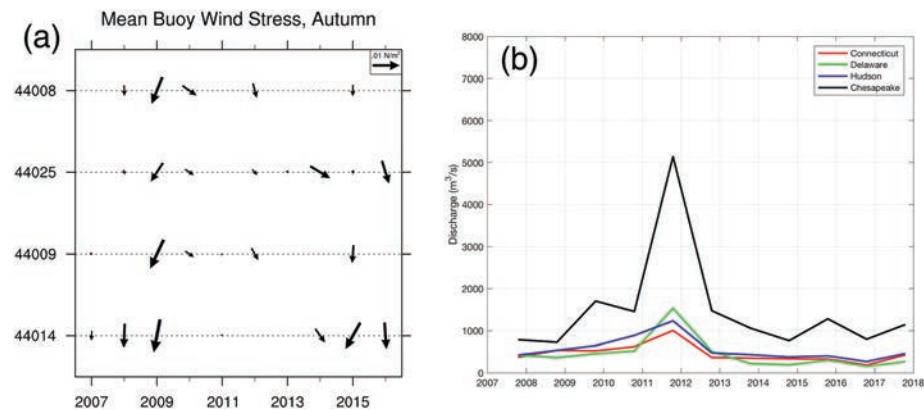


**Figure 10.** (a) Mean wind stress from the four NDBC buoys in the fall season by year. (b) River discharge from four major rivers/estuaries for the fall season by year: Connecticut (red), Delaware (green), Hudson (blue), and Chesapeake (black).

the rivers have not had their influence. In the southern MAB, the variability during the high-flow season from the Chesapeake is similar to the variability during the fall and winter.

Interseasonal variability shows that the year-to-year variation is greatest in the southern MAB offshore in the outflow region. The observation that the mean and variable currents increase to the south can be explained by the converging isobaths and barotropic flows will be steered along contours of constant  $f/H$ , where  $f$  is the Coriolis parameter and  $H$  represents ocean depth; therefore, the flow will accelerate. Most of the year-to-year variability in the rest of the MAB is near the outer and inner edges of the shelf. Away from the outflow region, the fall has the largest variability, extending across the entire shelf. We therefore chose to look at the variability in the wind forcing and buoyancy inputs during the fall when we expect to see the most implications for shelf wide- differences.

#### 4.2. Detailed Case Study: A Tale of Two Falls

The fall seasonal average wind velocity is plotted for the four main NDBC buoys in Figure 10a. The years 2009 and 2011 stand out as being different from the rest. For the fall 2009 season the winds are the strongest with little spatial variability over the entire MAB. The fall of 2009 was an anomalous wind year in that the winds were stronger and shifted clockwise to be more from the northeast rather than from the northwest typically observed in the fall. This was due in large part to the passage of seven coastal low-pressure systems through the MAB including the extratropical system Nor'Ida (Olabarrieta et al., 2012). The passage of each of these systems stalled in the bight apex, which allowed for the counterclockwise flow around the cyclone to drive surface winds and, consequently surface currents, down the shelf (Figure 11a). The surface currents were aligned toward the southwest with weak cross-shelf transport south of the bight apex.

The fall of 2011 was another anomalous fall for a different reason. This season had the weakest winds between the two buoys that reported. In 2011 there was a large amount of freshwater discharge due to the passage of Hurricane Irene (Glenn et al., 2016) and Tropical Storm Lee (Munroe et al., 2013). These weather systems delivered three times the typical seasonal rainfall (Figure 12) and hence discharge to the northern half of the region as evidenced by the discharge from the Connecticut, Delaware, and Hudson Rivers. These storm systems made an even greater impact on the southern region of the domain by delivering five times the normal fall precipitation and discharge onto the shelf as measured by the discharge from the Chesapeake gauges (Figure 10b). The outflow from rivers is relatively steady, but if an anomalous discharge like that of 2011 occurs, the ocean response is seen across the entire shelf. The response of the currents on the shelf to this increased discharge can be seen as a pronounced offshore surface transport near the exits of the four major estuaries with lower offshore transport between these pathways (Figure 11b).

In order to evaluate overarching meteorological conditions which may be influencing this interannual variability we saw in 2009 and 2011, the synoptic weather types for each fall during the 10-year period were examined using a synoptic typing data set (Siegert et al., 2017; Suriano & Leathers, 2017). Synoptic typing

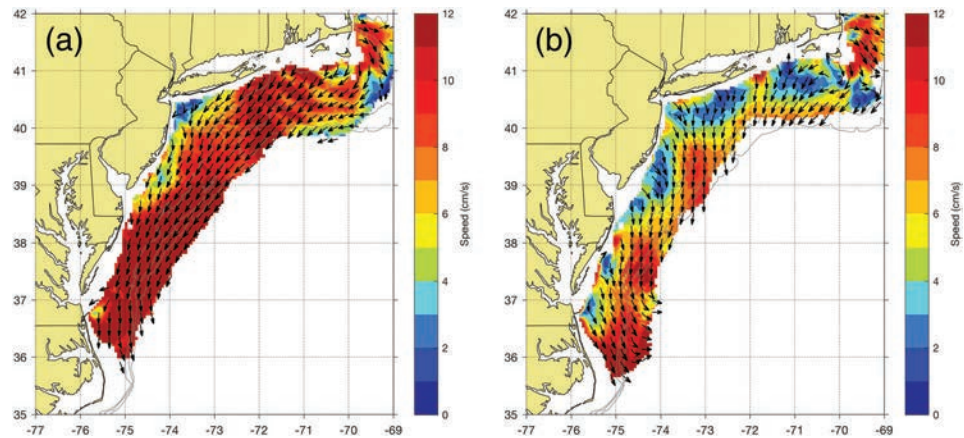


**Figure 11.** Mean surface currents during the fall, September to November, of (a) 2009 and (b) 2011. Colorbar indicates magnitude (cm/s) and vectors indicate direction toward of surface current.

aims to quantify common features in the daily synoptic weather conditions in order to identify days that are similar using daily surface observations and spatial NCEP/NCAR daily reanalysis data (Kalnay et al., 1996). This synoptic typing data set has been used to evaluate hydroclimatology in the Mid-Atlantic (Siegert et al., 2017), snowfall in the Great Lakes region (Suriano & Leathers, 2017), wind ramp events in the MAB (Veron et al., 2018), and high ozone pollution events in Delaware (Archer et al., 2019), showing broad applicability to weather-related studies throughout the region.

We examined the daily distribution of synoptic types for the fall season (September/October/November 2007–2016), covering the 10 years of the HF radar record. From this analysis, the synoptic type classified as having a strong high-pressure center over New England (spatial average in Figure 13b) emerged as the most prevalent synoptic type during fall 2009, with 26 occurrences out of 92 days in the season, more than any other year in the 10-year period. The New England High is centered overland to the north of the region, producing large-scale winds from the northeast over the MAB. Additionally, several of these days included a

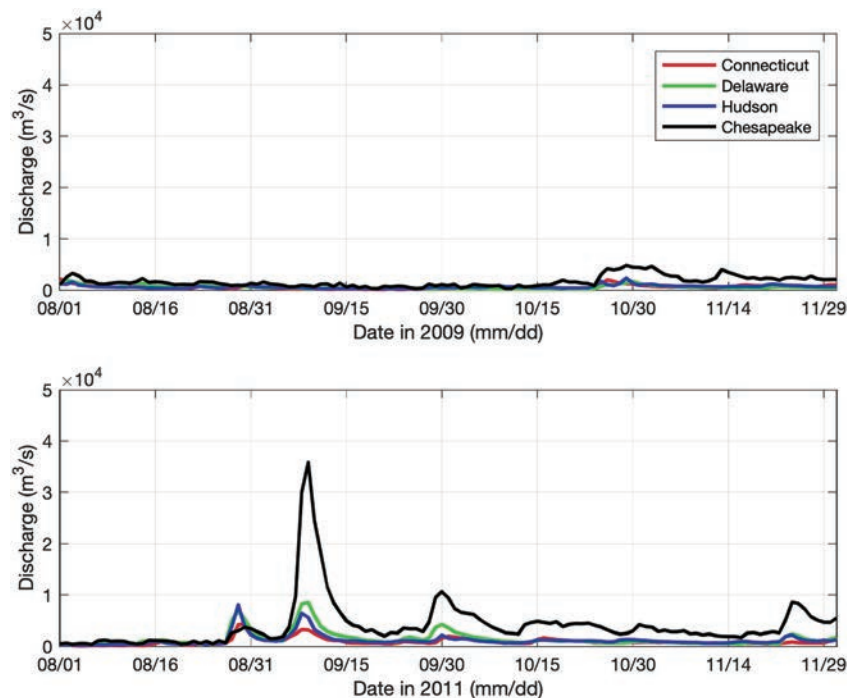


**Figure 12.** Time series plot of river discharge from four major rivers/estuaries for the fall of 2009 (top) and 2011 (bottom): Connecticut (red), Delaware (green), Hudson (blue), and Chesapeake (black).



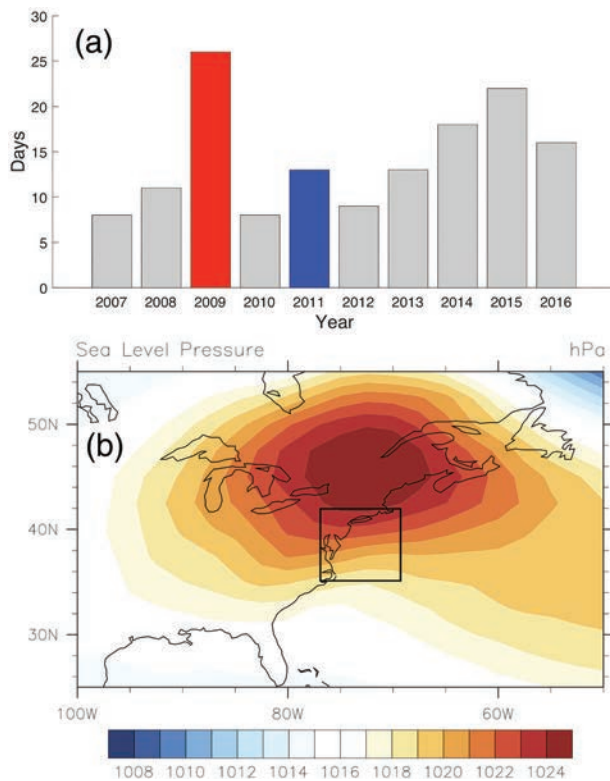


**Figure 13.** New England High synoptic type classification for the period 2007–2016 where (a) shows the annual distribution of the synoptic type identified in the fall months (September/October/November). The 2009 year is highlighted in red, and the 2011 year is highlighted in blue. (b) The average map of sea level pressure from NCEP/NCAR reanalysis based on all days in the full synoptic data set (1946–2015) for New England high pressure center (type 4,010).

coastal low pressure over the South Atlantic Bight, further reinforcing this onshore wind flow pattern. This indicates that the overall flow pattern over the MAB was likely dominated by both the New England High and earlier discussed coastal storms (Olabarrieta et al., 2012), helping to explain the strong average wind from the northeast seen in Figure 10a during 2009. However, 2011 (Figure 13a, blue bar) has a more typical occurrence of the New England High, and so the river discharge and buoyancy forcing would likely be more important forcing factors to help explain the surface current response in the fall of 2011. The events responsible for the high river discharge anomaly experienced in 2011 are compared to 2009 in Figure 12. River discharge for 2009 is low and steady over the entire fall. In contrast, river discharge in 2011 shows the impact of several storms, including two named tropical storms (Irene & Lee) and additional northeasters. Tropical storms like Irene transited the MAB in less than 12 hr, but the increase in river discharge from the tropical storm rains can last for days.

The fall seasonally averaged surface current maps are compared for 2009 and 2011 in Figure 11. The fall 2009 currents (Figure 11a) are strong across the entire shelf, running alongshelf in nearly the same direction as the wind until reaching the southern MAB where the current turns more offshore. In the fall of 2011 (Figure 11b), currents are weak over the inner shelf, and stronger over the outer shelf, with an offshore component nearly equal to the downshelf component. Unlike 2009, offshore transport at the shelfbreak is observed along the entire Mid-Atlantic, not just in the far southern region. The strong cross-shelf current regions extend inward nearly to the coast near the four estuaries. In between the four estuaries, the weak inner-shelf currents extend to midshelf. The vastly different surface regimes experienced in 2009 and 2011 point to the possibility that different subsurface regimes are also present. Strong surface currents in the direction of the wind in 2009 are consistent with shallow water

Ekman theory for an unstratified shelf. The large buoyancy inputs from the estuaries in 2011 are expected to enhance stratification, which acts to decouple the surface boundary layer from the bottom boundary layer (Chant et al., 2008).

### 4.3. Oceanographic and Ecological Implications

The implication of the different forcing on the shelf goes beyond those described in the surface current fields above. As has been stated, the fall season marks a significant transition in the MAB as it shifts from a strongly stratified two-layer system to a well-mixed homogenized water column. Using autonomous underwater glider sections along the Endurance Line from Tuckerton, NJ, to the shelfbreak (Castelao et al., 2008), we describe the oceanographic implications on the shelf hydrography (Figure 14). A glider deployed in the fall of 2009 as part of an Observing System Simulation Experiment (Schofield et al., 2010; Wang et al., 2013) indicates that the surface was cool (around 18°C; Figure 14a) with relatively high salinity nearshore (Figure 14c). The water column was well mixed nearshore, and thermocline was at a depth of 40 m. Cross-shelf temperature and salinity sections indicate that the windy 2009 fall transition to well-mixed conditions was nearly complete by mid-November. The core of the cold pool was offshore, starting at the 50-m isobath and extending to the 80-m isobath. The strong winds and resulting surface currents drove strong downwelling throughout the season, pushing the warm surface water up against the coast and forcing the cold pool offshore, resulting in a well-mixed water column on the inner shelf. Upwelling of the cold pool had occurred on the inner side of the stratified zone, with the well-mixed shallow area cutting off access to the coast (Austin & Lentz, 2002). Over much of the continental shelf this year, the wind influence extends to the bottom.



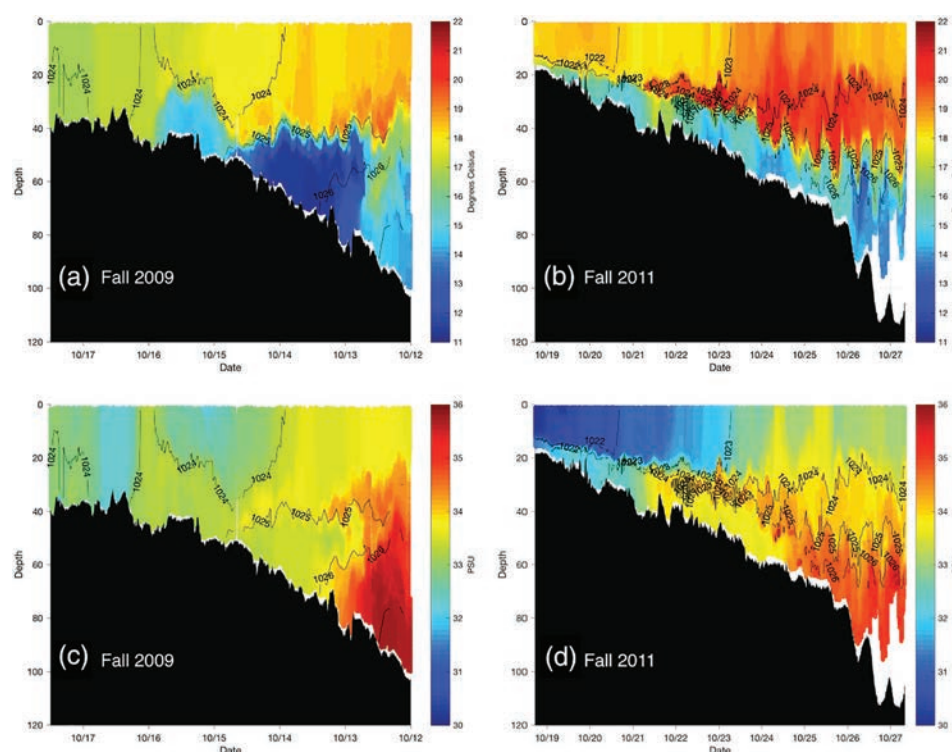


**Figure 14.** Temperature (top) and salinity (bottom) sections along the Tuckerton Endurance Line offshore of New Jersey for the fall of 2009 (left) and fall of 2011 (right).

In contrast, during the fall of 2011, a glider deployed in support of the Mid-Atlantic Regional Association Coastal Ocean Observing System (MARACOOS) (Brown et al., 2012) indicates that the surface waters were warmer at 20°C (Figure 14b) and the salinity nearshore was much lower (Figure 14d). These lower salinities are the result of much more freshwater discharged from multiple storms including Irene and Lee that moved through the area. The stratification was much stronger in 2011 with the thermocline present over the entire shelf with a depth of 20 m nearshore deepening to 40 m offshore. This intense MAB temperature and salinity stratification persisted at least through late November. This cross-shelf section indicates that the cold pool extended across the entire shelf, even inshore of the 20-m isobath. The strong stratification results in what Chant et al. (2008) characterize as a more slippery interface between the surface and bottom layers, working to decouple the surface layer response from the influence of the bottom. In the fall of 2011, the wind influence is confined to the surface layer over this glider section, while the bottom layer response is dominated by cross and alongshelf pressure gradients.

The 2009 and 2011 fall seasons exemplify the significant variability in the forcing, ocean surface response, and hydrography throughout the water column and across the shelf. Consequently, these physical characteristics have impacts on the marine life in this region. Some 321 species of fish call the MAB home (Able & Fahay, 1998). These species have evolved with seasonal dependent phenologies that anticipate and take advantage of this physical variability. For example, certain flounder species, such as the summer flounder, will time their spawn with the MAB fall transition. Adults two or more years old spawn as they migrate in September through November (Wilk et al., 1980). Their larvae are neutrally buoyant and adrift at the surface for 30 days. Therefore, the connection between summer flounder spawning grounds and nursery grounds is based upon the transport of larvae in the fall. Given the observed currents in our 10-year data set, the transport of these larvae and their success to recruit into the fishery depend on the local forcing (Brodziak & O'Brien, 2005). In 2009, when the alongshore currents were strong and to the southwest, these larvae were rapidly advected south. In 2011, when significant freshwater outflow lead to a more cross-shore transport pathway, the larvae likely moved offshore much faster than down the shelf.

## 5. Conclusion

Surface current patterns on the MAB's broad seasonally stratified continental shelf are highly influenced by variability in the wind field and the riverine inflow of fresh water. This study used a decade of hourly surface current maps from an HFR network that spans the full MAB combined with wind observations from meteorological buoys and coastal stations as well as river discharges from the national stream gauge network. Ten-year annual and seasonal means, along with their interannual and intra-annual variability, were calculated to study the spatial patterns of the mean surface currents and their relation to the mean wind and riverine forcing.

Generally, the 10-year annual mean surface currents are (a) offshore and weaker, about 3–6 cm/s, near the coast; (b) increase in speed to about 8–10 cm/s and rotate to an alongshore direction on the outer shelf; and (c) similarly increase in speed and rotate to flow offshore toward the Gulf Stream in the southern MAB. The year-to-year interannual variability is low, with a standard deviation of about 1–3 cm/s over most of the shelf, but the variability within a year is much greater, with a typical standard deviation of 10–20 cm/s over the same region.

Compared to the annual mean, the four 10-year seasonal mean surface current maps generally exhibit similar spatial patterns but with different current magnitudes and slightly different directions, with winter and summer more cross-shore and the transition seasons of fall and spring more alongshore. Fall and winter, with their strong cross-shore mean winds, have the strongest mean currents, while summer, with its opposing alongshore mean winds, has the weakest mean currents. Again, compared to the seasonal means, the seasonal interannual variability is lower, and the seasonal intra-annual variability is higher.

The season with the most variability was the fall, when the MAB transitions from highly stratified summer conditions to well-mixed winter conditions. Examination of the annual wind and river discharge records indicates that fall of 2009 experienced an anomalously strong and coherent wind field over the MAB, while the fall of 2011 had anomalously high river discharges due to a series of tropical and extratropical rainstorms. The spatial patterns of surface currents for these two fall seasons are different, with the relatively windy dry fall of 2009 exhibiting strong (8–10 cm/s) alongshore currents to the southwest over the entire MAB, while the low wind but rainy fall of 2011 exhibited weak (1–4 cm/s) cross-shelf currents over much of the inner shelf with cross-shelf peaks near the rivers. Cross-shelf temperature and salinity sections indicate that the windy 2009 fall transition to well-mixed conditions was nearly complete by mid-November, but that in the wet fall of 2011, the intense MAB temperature and salinity stratification persisted at least through late November.

The MAB is the southern half of the Northeast U.S. Large Marine Ecosystem (LME). Long-term surface current observations, especially over seasonal time scales, provide insights into the physical conditions organisms have adapted to in these productive waters. Larvae that are neutrally buoyant are advected by these currents. Temperature sensitive fish migrate across-shelf based on the timing of the seasonal transitions. The MAB is also a densely populated urbanized coast that supports multiple human activities, including fishing, marine transportation, and a developing offshore wind energy industry. Improved understanding of the mean currents and their variability will enable more informed development, better management of pollutants, and response to events, both natural and human made.

## Data Availability Statement

Data sets for this research are available in these in-text data citation reference: Roarty (2020), (Creative Commons Attribution 4.0 International).

## References

- Able, K. W., & Fahay, M. P. (1998). *The first year in the life of estuarine fishes in the Middle Atlantic Bight*. New Jersey: Rutgers University Press New Brunswick.
- Andres, M. (2016). On the recent destabilization of the Gulf Stream path downstream of Cape Hatteras. *Geophysical Research Letters*, 43, 9836–9842. <https://doi.org/10.1002/2016GL069966>
- Archer, C. L., Brodie, J. F., & Rauscher, S. A. (2019). Global warming will aggravate ozone pollution in the US Mid-Atlantic. *Journal of Applied Meteorology and Climatology*, 58(6), 1267–1278. <https://doi.org/10.1175/JAMC-D-18-0263.1>
- Austin, J. A., & Lentz, S. J. (2002). The inner shelf response to wind-driven upwelling and downwelling. *Journal of Physical Oceanography*, 32(7), 2171–2193. [https://doi.org/10.1175/1520-0485\(2002\)032<2171:TISRTW>2.0.CO;2](https://doi.org/10.1175/1520-0485(2002)032<2171:TISRTW>2.0.CO;2)

## Acknowledgments

The authors would like to recognize the effort of the technical team that kept the radar stations operating during this 10-year period that included Rich Arena, Chris Jakubiak, Zhitao Yu, and Colin Evans. The MARACOOS HFR network was supported from 2007–2010 by NOAA Award Number NA07NOS4730221 “Phased Deployment and Operation of the Mid-Atlantic Regional Coastal Ocean Observing System (MARCOOS)” and from 2011–2016 by NOAA Award Number NA11NOS0120038 “Towards a Comprehensive Mid-Atlantic Regional Association Coastal Ocean Observing System (MARACOOS).” Sponsor: National Ocean Service (NOS), National Oceanic and Atmospheric Administration (NOAA) NOAA-NOS-IOOS-2011-2002515/CFDA: 11.012, Integrated Ocean Observing System Topic Area 1: Continued Development of Regional Coastal Ocean Observing Systems. The MARACOOS HFR network was supported from 2016–2021 by NOAA Award Number NOAA-NOS-IOOS-2016-2004378 “MARACOOS: Preparing for a Changing Mid-Atlantic.”

- Beardsley, R., & Winant, C. (1979). On the mean circulation in the Mid-Atlantic Bight. *Journal of Physical Oceanography*, 9(3), 612–619. [https://doi.org/10.1175/1520-0485\(1979\)009<0612:OTMCIT>2.0.CO;2](https://doi.org/10.1175/1520-0485(1979)009<0612:OTMCIT>2.0.CO;2)
- Beardsley, R. C., & Boicourt, W. C. (1981). On estuarine and continental-shelf circulation in the Middle Atlantic Bight. In B. A. Warren & C. Wunsch (Eds.), *Evolution of Physical Oceanography: Scientific Surveys in Honor of Henry Stommel* (Vol. 1, pp. 198–233). Cambridge, MA: MIT Press.
- Beardsley, R. C., Boicourt, W., & Hansen, D. (1976). Current variability and mean circulation in Middle Atlantic Bight. In *Transactions American Geophysical Union* (Vol. 57, pp. 262–262). Washington DC: American Geophysical Union.
- Beardsley, R. C., Chapman, D. C., Brink, K. H., Ramp, S. R., & Schlitz, R. (1985). The Nantucket Shoals Flux Experiment (NSFE79). Part I: A basic description of the current and temperature variability. *Journal of Physical Oceanography*, 15(6), 713–748. [https://doi.org/10.1175/1520-0485\(1985\)015<0713:TNSFEP>2.0.CO;2](https://doi.org/10.1175/1520-0485(1985)015<0713:TNSFEP>2.0.CO;2)
- Beardsley, R. C., & Haidvogel, D. B. (1981). Model studies of the wind-driven transient circulation in the Middle Atlantic Bight. Part 1: Adiabatic boundary conditions. *Journal of Physical Oceanography*, 11(3), 355–375. [https://doi.org/10.1175/1520-0485\(1981\)011<0355:MSOTWD>2.0.CO;2](https://doi.org/10.1175/1520-0485(1981)011<0355:MSOTWD>2.0.CO;2)
- Bigelow, H. B., & Sears, M. (1935). Studies of the waters on the continental shelf, Cape Cod to Chesapeake Bay. II. Salinity. *Papers in Physical Oceanography and Meteorology*, 4, 94.
- Brodziak, J., & O'Brien, L. (2005). Do environmental factors affect recruits per spawner anomalies of New England groundfish? *ICES Journal of Marine Science*, 62(7), 1394–1407. <https://doi.org/10.1016/j.icesjms.2005.04.019>
- Brown, W., Boicourt, W., Flagg, C., Gangopadhyay, A., Schofield, O., Glenn, S., & Kohut, J. (2012). Mapping the Mid-Atlantic Cold Pool evolution and variability with ocean gliders and numerical models. *2012 Oceans*. <https://doi.org/10.1109/oceans.2012.6404970>
- Bumpus, D. F. (1969). Reversals in surface drift in Middle Atlantic Bight area. *Deep-Sea Research*, 17–23.
- Castelao, R., Glenn, S., Schofield, O., Chant, R., Wilkin, J., & Kohut, J. (2008). Seasonal evolution of hydrographic fields in the central Middle Atlantic Bight from glider observations. *Geophysical Research Letters*, 35, L03617. <https://doi.org/10.1029/2007GL032335>
- Chant, R. J., Glenn, S. M., Hunter, E., Kohut, J., Chen, R. F., Houghton, R. W., et al. (2008). Bulge formation of a buoyant river outflow. *Journal of Geophysical Research*, 113, C01017. <https://doi.org/10.1029/2007JC004100>
- Chapman, D. C., & Beardsley, R. C. (1989). On the origin of shelf water in the Middle Atlantic Bight. *Journal of Physical Oceanography*, 19(3), 384–391. [https://doi.org/10.1175/1520-0485\(1989\)019<0384:OTOOSW>2.0.CO;2](https://doi.org/10.1175/1520-0485(1989)019<0384:OTOOSW>2.0.CO;2)
- Chen, C., Beardsley, R. C., & Limeburner, R. (1995). Variability of currents in late spring in the northern Great South Channel. *Continental Shelf Research*, 15(4–5), 451–473. [https://doi.org/10.1016/0278-4343\(94\)00056-S](https://doi.org/10.1016/0278-4343(94)00056-S)
- Dzwonkowski, B., Kohut, J. T., & Yan, X.-H. (2009). Seasonal differences in wind-driven across-shelf forcing and response relationships in the shelf surface layer of the central Mid-Atlantic Bight. *Journal of Geophysical Research*, 114, C08018. <https://doi.org/10.1029/2008JC004888>
- Dzwonkowski, B., Lipphardt, B. L. Jr., Kohut, J. T., Yan, X.-H., & Garvine, R. W. (2010). Synoptic measurements of episodic offshore flow events in the central Mid-Atlantic Bight. *Continental Shelf Research*, 30(12), 1373–1386. <https://doi.org/10.1016/j.csr.2010.05.004>
- Flagg, C. N., Dunn, M., Wang, D. P., Rossby, H. T., & Benway, R. L. (2006). A study of the currents of the outer shelf and upper slope from a decade of shipboard ADCP observations in the Middle Atlantic Bight. *Journal of Geophysical Research*, 111, C06003. <https://doi.org/10.1029/2005JC003116>
- Fleming, N. E. (2016). *Seasonal and spatial variability in temperature, salinity and circulation of the Middle Atlantic Bight*, PhD Thesis. Rutgers: The State University of New Jersey-New Brunswick.
- Fratantoni, P., & Pickart, R. (2003). Variability of the shelf break jet in the Middle Atlantic Bight: Internally or externally forced? *Journal of Geophysical Research*, 108(C5), 3166. <https://doi.org/10.1029/2002JC001326>
- Frey, H. R. (1978). Northeastward drift in the Northern Mid-Atlantic bight during late spring and summer 1976. *Journal of Geophysical Research*, 83(C1), 503–504. <https://doi.org/10.1029/JC083iC01p00503>
- Glenn, S., Miles, T., Seroka, G., Xu, Y., Forney, R., Yu, F., et al. (2016). Stratified coastal ocean interactions with tropical cyclones. *Nature Communications*, 7(1), 10887. <https://doi.org/10.1038/ncomms10887>
- Gong, D., Kohut, J. T., & Glenn, S. M. (2010). Seasonal climatology of wind-driven circulation on the New Jersey Shelf. *Journal of Geophysical Research*, 115, C04006. <https://doi.org/10.1029/2009JC005520>
- Greene, C. A., Thirumalai, K., Kearney, K. A., Delgado, J. M., Schwanghart, W., Wolfenbarger, N. S., et al. (2019). The climate data toolbox for MATLAB. *Geochemistry, Geophysics, Geosystems*, 20, 3774–3781. <https://doi.org/10.1029/2019GC008392>
- Haines, S., Seim, H., & Muglia, M. (2017). Implementing quality control of high-frequency radar estimates and application to Gulf Stream surface currents. *Journal of Atmospheric and Oceanic Technology*, 34(6), 1207–1224. <https://doi.org/10.1175/JTECH-D-16-0203.1>
- Kalnay, E., Kanamitsu, M., Kistler, R., Collins, W., Deaven, D., Gandin, L., et al. (1996). The NCEP/NCAR 40-year reanalysis project. *Bulletin of the American Meteorological Society*, 77(3), 437–471. [https://doi.org/10.1175/1520-0477\(1996\)077<0437:TNYRP>2.0.CO;2](https://doi.org/10.1175/1520-0477(1996)077<0437:TNYRP>2.0.CO;2)
- Kim, S. Y., Terrill, E. J., & Cornuelle, B. D. (2008). Mapping surface currents from HF radar radial velocity measurements using optimal interpolation. *Journal of Geophysical Research*, 113, C10023. <https://doi.org/10.1029/2007JC004244>
- Kohut, J., Roarty, H., Randall-Goodwin, E., Glenn, S., & Lichtenwalner, C. (2012). Evaluation of two algorithms for a network of coastal HF radars in the Mid-Atlantic Bight. *Ocean Dynamics*, 62(6), 953–968. <https://doi.org/10.1007/s10236-012-0533-9>
- Kohut, J. T., & Glenn, S. M. (2003). Improving HF radar surface current measurements with measured antenna beam patterns. *Journal of Atmospheric and Oceanic Technology*, 20(9), 1303–1316. [https://doi.org/10.1175/1520-0426\(2003\)020<1303:IHRSCM>2.0.CO;2](https://doi.org/10.1175/1520-0426(2003)020<1303:IHRSCM>2.0.CO;2)
- Kohut, J. T., Glenn, S. M., & Chant, R. J. (2004). Seasonal current variability on the New Jersey inner shelf. *Journal of Geophysical Research*, 109, C07S07. <https://doi.org/10.1029/2003JC001963>
- Kohut, J. T., Glenn, S. M., & Paduan, J. D. (2006). Inner shelf response to Tropical Storm Floyd. *Journal of Geophysical Research*, 111, C09S91. <https://doi.org/10.1029/2003JC002173>
- Kohut, J. T., Roarty, H. J., & Glenn, S. M. (2006). Characterizing observed environmental variability with HF Doppler radar surface current mappers and acoustic Doppler current profilers: Environmental variability in the Coastal Ocean. *IEEE Journal of Oceanic Engineering*, 31(4), 876–884. <https://doi.org/10.1109/JOE.2006.886095>
- Lentz, S. J. (2008). Observations and a model of the mean circulation over the Middle Atlantic Bight Continental Shelf. *Journal of Physical Oceanography*, 38(6), 1203–1221. <https://doi.org/10.1175/2007JPO3768.1>
- Lentz, S. J., Butman, B., & Harris, C. (2014). The vertical structure of the circulation and dynamics in Hudson Shelf Valley. *Journal of Geophysical Research: Oceans*, 119, 3694–3713. <https://doi.org/10.1002/2014JC009883>
- Lentz, S. J., Elgar, S., & Guza, R. (2003). Observations of the flow field near the nose of a buoyant coastal current. *Journal of Physical Oceanography*, 33(4), 933–943. [https://doi.org/10.1175/1520-0485\(2003\)33<933:OOTFFN>2.0.CO;2](https://doi.org/10.1175/1520-0485(2003)33<933:OOTFFN>2.0.CO;2)



- Levin, J., Wilkin, J., Fleming, N., & Zavala-Garay, J. (2018). Mean circulation of the Mid-Atlantic Bight from a climatological data assimilative model. *Ocean Modelling*, 128, 1–14. <https://doi.org/10.1016/j.ocemod.2018.05.003>
- Limeburner, R., & Beardsley, R. C. (1982). The seasonal hydrography and circulation over Nantucket Shoals. *Journal of Marine Research*, 40, 371–406.
- Linder, C. A., & Gawarkiewicz, G. (1998). A climatology of the shelfbreak front in the Middle Atlantic Bight. *Journal of Geophysical Research*, 103(C9), 18,405–18,423. <https://doi.org/10.1029/98JC01438>
- Miller, A. R. (1952). *A pattern of surface coastal circulation inferred from surface salinity-temperature data and drift bottle recoveries*, WHOI Tech. Rep. 52–28. Woods Hole, Massachusetts: Woods Hole Oceanographic Institution. 14 pp
- Moores, C. N., Fernandez-Partagas, J., & Price, J. F. (1976). *Meteorological forcing fields of the New York Bight (first year's progress report)*, Tech. Rep. TR76–8. Miami Florida: Rosenstiel School of Marine and Atmospheric Science.
- Mountain, D. G. (2003). Variability in the properties of shelf water in the Middle Atlantic Bight, 1977–1999. *Journal of Geophysical Research*, 108(C1), 3014. <https://doi.org/10.1029/2001JC001044>
- Munroe, D., Tabatabai, A., Burt, I., Bushek, D., Powell, E. N., & Wilkin, J. (2013). Oyster mortality in Delaware Bay: Impacts and recovery from Hurricane Irene and Tropical Storm Lee. *Estuarine, Coastal and Shelf Science*, 135, 209–219. <https://doi.org/10.1016/j.ecss.2013.10.011>
- Olabarrieta, M., Warner, J. C., Armstrong, B., Zambon, J. B., & He, R. (2012). Ocean-atmosphere dynamics during Hurricane Ida and Nor'Ida: An application of the coupled ocean-atmosphere-wave-sediment transport (COAWST) modeling system. *Ocean Modelling*, 43, 112–137. <https://doi.org/10.1016/j.ocemod.2011.12.008>
- Ou, H. W., Beardsley, R. C., Mayer, D., Boicourt, W. C., & Butman, B. (1981). An analysis of subtidal current fluctuations in the Middle Atlantic Bight. *Journal of Physical Oceanography*, 11(10), 1383–1392. [https://doi.org/10.1175/1520-0485\(1981\)011<1383:AAOSCF>2.0.CO;2](https://doi.org/10.1175/1520-0485(1981)011<1383:AAOSCF>2.0.CO;2)
- Paduan, J. D., & Graber, H. C. (1997). Introduction to high-frequency radar: Reality and myth. *Oceanography*, 10(2), 36–39. <https://doi.org/10.5670/oceanog.1997.18>
- Pawlowicz, R., Beardsley, B., & Lentz, S. (2002). Classical tidal harmonic analysis including error estimates in MATLAB using T\_TIDE. *Computers & Geosciences*, 28(8), 929–937. [https://doi.org/10.1016/S0098-3004\(02\)00013-4](https://doi.org/10.1016/S0098-3004(02)00013-4)
- Pringle, J. M. (2018). Remote forcing of shelf flows by density gradients and the origin of the annual mean flow on the Mid-Atlantic Bight. *Journal of Geophysical Research: Oceans*, 123, 4464–4482. <https://doi.org/10.1029/2017JC013721>
- Roarty, H. J., Glenn, S. M., Kohut, J. T., Gong, D., Handel, E., Rivera Lemus, E., et al. (2010). Operation and application of a regional High Frequency Radar network in the Mid Atlantic Bight. *Marine Technology Society Journal*, 44(6), 133–145. <https://doi.org/10.4031/MTSJ.44.6.5>
- Roarty, H. (2020). *2007–2016 surface circulation over the Mid Atlantic Bight continental shelf derived from a decade of High Frequency Radar observations (Version 01) [data set]*. Meyrin, Canton of Geneva, Switzerland: Zenodo. <http://doi.org/10.5281/zenodo.3770921>
- Schofield, O., Glenn, S., Orcutt, J., Arrott, M., Meisinger, M., Gangopadhyay, A., et al. (2010). Automated sensor networks to advance ocean science. *Eos, Transactions of the American Geophysical Union*, 91(39), 345–346. <https://doi.org/10.1029/2010EO390001>
- Siegert, C., Leathers, D., & Levia, D. (2017). Synoptic typing: Interdisciplinary application methods with three practical hydroclimatological examples. *Theoretical and Applied Climatology*, 128(3–4), 603–621. <https://doi.org/10.1007/s00704-015-1700-y>
- Soulsby, R. L., Hamm, L., Klopman, G., Myrhaug, D., Simons, R. R., & Thomas, G. P. (1993). Wave-current interaction within and outside the bottom boundary layer. *Coastal Engineering*, 21(1–3), 41–69. [https://doi.org/10.1016/0378-3839\(93\)90045-A](https://doi.org/10.1016/0378-3839(93)90045-A)
- Stewart, R. H., & Joy, J. W. (1974). HF radio measurements of surface currents. In *Deep sea research and oceanographic abstracts* (Vol. 21, pp. 1039–1049). Great Britain: Elsevier. [https://doi.org/10.1016/0011-7471\(74\)90066-7](https://doi.org/10.1016/0011-7471(74)90066-7)
- Suriano, Z. J., & Leathers, D. J. (2017). Synoptic climatology of lake-effect snowfall conditions in the eastern Great Lakes region. *International Journal of Climatology*, 37(12), 4377–4389. <https://doi.org/10.1002/joc.5093>
- Sverdrup, H. U., Johnson, M. W., & Fleming, R. H. (1942). *The oceans: Their physics, chemistry, and general biology*. New York: Prentice-Hall.
- Terrill, E., Otero, M., Hazard, L., Conlee, D., Harlan, J., Kohut, J., et al. (2006). Data management and real-time distribution in the HF-radar national network. In *OCEANS 2006* (pp. 1–6). Boston, MA: IEEE. <https://ieeexplore.ieee.org/document/4099038>
- Thomson, R. E., & Emery, W. J. (2014). *Data analysis methods in physical oceanography*. Newnes. Waltham, MA: Elsevier B. V.
- Ullman, D. S., & Codiga, D. L. (2004). Seasonal variation of a coastal jet in the Long Island Sound outflow region based on HF radar and Doppler current observations. *Journal of Geophysical Research*, 109, C07S06. <https://doi.org/10.1029/2002JC001660>
- Ullman, D. S., O'Donnell, J., Kohut, J., Fake, T., & Allen, A. (2006). Trajectory prediction using HF radar surface currents: Monte Carlo simulations of prediction uncertainties. *Journal of Geophysical Research*, 111, C12005. <https://doi.org/10.1029/2006JC003715>
- Veron, D. E., Brodie, J. F., Shirazi, Y. A., & Gilchrist, J. R. (2018). Modeling the electrical grid impact of wind ramp-up forecasting error offshore in the Mid-Atlantic region. *Journal of Renewable and Sustainable Energy*, 10(1), 013308. <https://doi.org/10.1063/1.4990684>
- Wallace, E. J., Looney, L. B., & Gong, D. (2018). Multi-decadal trends and variability in temperature and salinity in the Mid-Atlantic Bight, Georges Bank, and Gulf of Maine. *Journal of Marine Research*, 76, 163–215. <https://doi.org/10.1357/002224018826473281>
- Wang, X., Chao, Y., Thompson, D. R., Chien, S. A., Farrara, J., Li, P., et al. (2013). Multi-model ensemble forecasting and glider path planning in the Mid-Atlantic Bight. *Continental Shelf Research*, 63, S223–S234. <https://doi.org/10.1016/j.csr.2012.07.006>
- Wilk, S. J., Smith, W. G., Ralph, D. E., & Sibunka, J. (1980). The population structure of summer flounder between New York and Florida based on linear discriminant analysis. *Transactions of the American Fisheries Society*, 109(3), 265–271. [https://doi.org/10.1577/1548-8659\(1980\)109<265:PSOSFB>2.0.CO;2](https://doi.org/10.1577/1548-8659(1980)109<265:PSOSFB>2.0.CO;2)
- Zhang, W. G., & Gawarkiewicz, G. G. (2015). Dynamics of the direct intrusion of Gulf Stream ring water onto the Mid-Atlantic Bight shelf. *Geophysical Research Letters*, 42, 7687–7695. <https://doi.org/10.1002/2015GL065530>
- Zhang, W. G., Wilkin, J. L., & Chant, R. J. (2009). Modeling the pathways and mean dynamics of river plume dispersal in the New York Bight. *Journal of Physical Oceanography*, 39, 1167–1183. <https://doi.org/10.1175/2008JPO4082.1>
- Zhu, J., & Liang, X.-Z. (2013). Impacts of the Bermuda high on regional climate and ozone over the United States. *Journal of Climate*, 26(3), 1018–1032. <https://doi.org/10.1175/JCLI-D-12-00168.1>





## OPEN ACCESS

## EDITED BY

Juliet Hermes,  
South African Environmental Observation  
Network (SAEON), South Africa

## REVIEWED BY

Marc Le Menn,  
Service Hydrographique et Océanographique  
de la Marine (SHOM), France  
Antonio Novellino,  
ETT SpA, Italy

## \*CORRESPONDENCE

Hugh Roarty  
✉ hroarty@rutgers.edu

RECEIVED 07 December 2023

ACCEPTED 09 February 2024

PUBLISHED 06 May 2024

## CITATION

Roarty H, Updyke T, Nazzaro L, Smith M,  
Glenn S and Schofield O (2024) Real-time  
quality assurance and quality control for a  
high frequency radar network.  
*Front. Mar. Sci.* 11:1352226.  
doi: 10.3389/fmars.2024.1352226

## COPYRIGHT

© 2024 Roarty, Updyke, Nazzaro, Smith, Glenn  
and Schofield. This is an open-access article  
distributed under the terms of the [Creative  
Commons Attribution License \(CC BY\)](#). The  
use, distribution or reproduction in other  
forums is permitted, provided the original  
author(s) and the copyright owner(s) are  
credited and that the original publication in  
this journal is cited, in accordance with  
accepted academic practice. No use,  
distribution or reproduction is permitted  
which does not comply with these terms.

# Real-time quality assurance and quality control for a high frequency radar network

Hugh Roarty <sup>1\*</sup>, Teresa Updyke <sup>2</sup>, Laura Nazzaro <sup>1</sup>,  
Michael Smith <sup>1</sup>, Scott Glenn <sup>1</sup> and Oscar Schofield <sup>1</sup>

<sup>1</sup>Center for Ocean Observing Leadership, Department Marine and Coastal Sciences, Rutgers University, New Brunswick, NJ, United States, <sup>2</sup>Center for Coastal Physical Oceanography, Ocean and Earth Sciences, Old Dominion University, Norfolk, VA, United States

This paper recommends end to end quality assurance methods and quality control tests for High Frequency Radar Networks. We focus on the network that is operated by the Mid Atlantic Regional Association Coastal Ocean Observing System (MARACOOS). The network currently consists of 38 radars making real-time measurements of the surface currents over the continental shelf for a variety of applications including search and rescue planning, oil spill trajectory modelling and providing a transport context for marine biodiversity observing networks. MARACOOS has been delivering surface current measurements to the United States Coast Guard (USCG) since May 2009. Data quality is important for all applications; however, since the USCG uses this surface current information to plan life-saving missions, delivery of the best quality data is crucial. We have mapped the components of the HF radar data processing chain onto the data levels presented in the NASA Earth Science Reference Handbook and have applied quality assurance and quality control techniques at each data level to achieve the highest quality data. There are approximately 400 High Frequency radars (HFRs) deployed globally and the presented techniques can provide a foundation for data quality checks and standardization of the data collected by the large number of systems operating today.

## KEYWORDS

ocean currents, high frequency radar, remote sensing, best practice, quality assurance, quality control

## 1 Introduction

Measuring ocean currents is crucial for a wide range of activities, including, but not limited to, tracking pollutants, aiding search and rescue missions, monitoring harmful algal blooms and supporting marine navigation. High Frequency radar has emerged as the cost effective and low impact sensor to efficiently measure ocean surface currents within 200 km of the coast. Ocean.US, the predecessor to the United States (U.S.) Integrated Ocean Observing

System (IOOS) (Snowden et al., 2019), established the Surface Current Mapping Initiative (SCMI) in September 2003. A steering committee was appointed to address critical technical issues associated with implementation of a surface current mapping system for coastal U.S. waters. At the time there were approximately forty HFR systems operating in coastal U.S. waters. SCMI designed a framework for a national system to measure surface currents and identified the following six issues: governance, radar siting, frequency coordination, product development, research topics and vessel tracking. The report concluded that HF radar was the most viable and cost effective sensor for continuous surface current mapping over large coastal areas and it described a vision for a national backbone of long range (180 km) radars with higher resolution systems nested where desired (Paduan et al., 2004; Harlan, 2015).

In 2004, shortly after this report was published, the Mid-Atlantic Regional Association Coastal Ocean Observing System (MARACOOS) was established as one of the eleven Regional Associations (RAs) comprising the coastal component of U.S. IOOS. The MARACOOS area of responsibility encompasses 378,000 km<sup>2</sup> (Roarty & Shivock, 2022) covering the ocean and estuaries from Cape Cod, MA to Cape Hatteras, NC. The RAs cover a broad range of ecosystems and are central to driving the development of observing systems tailored to address regional and local priorities defined by diverse stakeholders, non-governmental organizations, academia, industry and members of the general public. Together, the RAs coordinate through the IOOS Association to establish linkages to ensure that the needs of the region are reflected in national policy.

## 1.1 HFR surface currents societal benefit areas

Remote sensing data play a pivotal role in operational oceanography and provide society with a wide spectrum of useful products. The Framework for Ocean Observing (Lindstrom et al., 2012) is organized around sustained and routine observations of physical, biogeochemical and biological essential ocean variables (EOVs). U.S. IOOS has defined 34 core variables to detect and predict changes in the ocean. Currents and surface waves are 2 EOVs where HF radar can make a direct measurement and wind direction and speed can be indirectly measured by HFR. U.S. IOOS has focused on seven societal benefit areas (SBA) to meet the nation's need for ocean information. They are listed here along with how HFR surface current measurements are supporting each one of the SBAs.

### 1.1.1 Improve predictions of climate and weather and their effects on coastal communities and the nation

As defined by a US National Research Council committee, a Climate Data Record (CDR) is “a time series of measurements of sufficient length, consistency and continuity to determine climate variability and change.” HFR surface current measurements are now

reaching 20 years in length and have provided annual and seasonal estimates surface current flow along the coast (Roarty et al., 2020). Standardization to guarantee a consistent time series is critical if the data will be useful for any climate focused studies that require a clear data quality and precision understanding. This represents an opportunity for IOOS to provide climate relevant data.

### 1.1.2 Improve the safety and efficiency of maritime commerce

The NOAA National Ocean Service established the Physical Oceanographic Real-Time System (PORTS) to provide accurate and reliable real-time information about environmental conditions in seaports. PORTS currently serves about one-third of the 175 major seaports in the US. HFR surface current data and tidal current predictions have been available in three PORTS (New York Harbor, Chesapeake Bay and San Francisco Bay) since April 2014 (Gradone et al., 2015). HFR are presently assimilated into the real-time ocean forecast models including DOPPIO (Levin et al., 2021) and an experimental version of NOAA's West Coast Operational Forecast System (WCOFS) (Kurapov et al., 2017; Kurapov et al., 2022). The HFR data could also provide a validation source for the Operational Forecast models or could be assimilated into more models for the most accurate nowcast (Roarty and Shivock, 2022).

### 1.1.3 More effectively mitigate the effects of natural hazards

NOAA has developed the Nearshore Wave Prediction System (NWPS) to provide on-demand and high-resolution wave guidance to coastal forecasters of the National Weather Service. A probabilistic rip current forecast model has been coupled with NWPS to provide guidance on the likelihood of rip currents developing. Rip currents are a leading cause of fatalities amongst coastal hazards and fourth leading cause of death amongst weather fatalities (US Department of Commerce, N, 2019). HFR waves can aid in the validation of NWPS and the rip current model. NWPS currently utilizes significant wave height ( $H_s$ ) from NDBC buoys to validate the model. The one drawback to that is that most NDBC buoys are far offshore. The wave measurements from HF radar are much closer to the coast and in the case of winds coming from land, the wave field nearshore can be quite different due to differences in fetch.

### 1.1.4 Improve public safety and national homeland security

The Office of Naval Research (Roarty et al., 2010), US Navy (Roarty et al., 2012c), and Department of Homeland Security (Roarty et al., 2011; Roarty et al., 2013b) have all researched the possibility of utilizing the HFR network as a dual use system, which would deliver ocean currents on an hourly basis as well as detecting ships in coastal waters and delivering that information for maritime domain awareness. The radars can effectively detect vessels that have a vertical dimension greater than  $\frac{1}{4}$  the radar wavelength e.g. at 13 MHz the SeaSonde is capable of detecting vessels with a height greater than 6 m or 20 ft. DHS completed its external review of

over-the-horizon HF radar technology and determined that it is a cost-effective surveillance gap-filler between satellites with global coverage but low revisit intervals and line-of-sight microwave radars deployed near-shore. The cost effectiveness is achieved by deploying a distributed network of compact HF radars that are linked in a multi-static configuration.

### 1.1.5 Reduce public health risks

Harmful algal blooms and marine debris can pose health risks to those who use coastal waters for recreation or their living (O'Halloran, 2011; Heil & Muni-Morgan, 2021). HFR derived surface currents have been utilized on several occasions to estimate surface drift in response to a marine debris incident (Brunner & Lwiza, 2019). The New Jersey Department of Environmental Protection used HFR surface currents to determine the origin of medical waste that washed up on the shores of Long Beach Island. The spill caused the closure of five beaches for one day at the beginning of the 2012 beach tourism season as officials determined the extent of the pollution. The surface currents from the HFR network were used to perform a reverse drift simulation to determine the source of the medical waste.

### 1.1.6 More effectively protect and restore healthy coastal ecosystems

Every year, there are approximately 8,000 marine accidents (National Transportation Statistics, 2021) that have the potential to result in the release of oil or chemicals into the environment, either due to accidents or natural disasters. Incidents involving spills in coastal waters, whether accidental or deliberate, pose risks to both people and the environment. Moreover, they can lead to significant disruptions in marine transportation, potentially causing widespread economic consequences. The Emergency Response Division of NOAA's Office of Response and Restoration (OR&R) plays a crucial role by providing scientific expertise to support incident responses and initiating assessments of natural resource damage. The division deals with around 150 spills annually, and the frequency of such incidents is increasing. To aid in spill response efforts, high-resolution surface current maps provide context for the response (Abascal et al., 2009). This data has been incorporated into the General NOAA Operational Modelling Environment (GNOME) (Harlan et al., 2011), and it is now accessible on the GNOME Online Oceanographic Data Server. NOAA utilized HFR measurements throughout the Deepwater Horizon oil spill to provide guidance on the choice of model that was providing the most accurate forecast of spill trajectories (Howden et al., 2011). Previous studies in the area showed that assimilation of HFR data into the Navy Coastal Ocean Model resulted in a 25-30% better skill in predicting surface drifter trajectories (Yaremchuk et al., 2016).

### 1.1.7 Enable the sustained use of ocean and coastal resources

Conventional approaches to fisheries or plankton surveys, which rely on fixed grid or stratified random designs, may not adequately capture the complexities of the coastal ocean. These environments are influenced by dynamic and episodic processes

that can amplify, subside, or shift significant features such as fronts during a survey. It is crucial for field studies to remain attuned to changes in the study area and be flexible in adapting to evolving conditions. Bio-acoustic surveys conducted in the New York Bight have incorporated near real-time surface current data (Kohut et al., 2006a) to specifically target features of interest. The integration of real-time surface current products could revolutionize how NOAA fisheries sample the coastal ocean (Kohut et al., 2021).

## 1.2 High frequency radar network description

The Mid Atlantic High Frequency Radar Network (Figure 1) was established in 2007 and is coordinated through a central office at Rutgers University with sub-regional technology centers at the University of Connecticut, University of Massachusetts Dartmouth, Woods Hole Oceanographic Institution and Old Dominion University. Roarty et al. (2010) described the network in its infancy and this manuscript provides an update of the network now that it has been in operation for over a decade. The network consists of 18 radar stations that operate at 5 MHz (typical range 180 km, spatial resolution 6 km), 9 stations that operate at 13/16 MHz (typical range 80 km, spatial resolution 3 km), and 15 radar stations that operate at 25 MHz (typical range 30 km, spatial resolution 1 km). The 5 MHz network covers the Mid Atlantic Bight Shelf from Cape Hatteras to Cape Cod. Four of the 5 MHz stations in this network are operated by partners in the Southeast Coastal Ocean Regional Association (SECOORA). The 13 MHz network measures the New Jersey shelf and was developed to assess and quantify the offshore wind resource (Seroka et al., 2012; Roarty et al., 2012a). The 16 MHz network covers New England and was also developed for offshore wind and coastal ocean studies (Kirincich et al., 2019; Rypina et al., 2021). The 25 MHz network is the oldest of the three and covers the major estuaries (Chesapeake Bay, Delaware River, New York Harbor, Long Island Sound and Block Island Sound). Throughout the manuscript the place name of the radar station will be provided by the four-letter site code that is assigned to each station. For instance, the 13 MHz station in Sea Bright, NJ is given the site code SEAB. The MARACOOS technical workforce consists of a regional coordinator and radar operators stationed within each of three sub-regions (north, central and south) all within a day's drive of any shore station in the sub-region.

In 2016, U.S. IOOS certified MARACOOS as a full member of the national IOOS system. Being certified as a Regional Information Coordination Entity (RICE) places it under the authority of the Integrated Coastal and Ocean Observation System Act of 2009 (ICOOS Act). Certification of IOOS Regional Associations is a detailed review and assessment process and provides NOAA and its interagency partners a means to verify a Regional Association's organizational and operational practices meet recognized and established standards set by NOAA. This includes all aspects of data collection and management. The IOOS certification process does not follow an international standard; however there is a

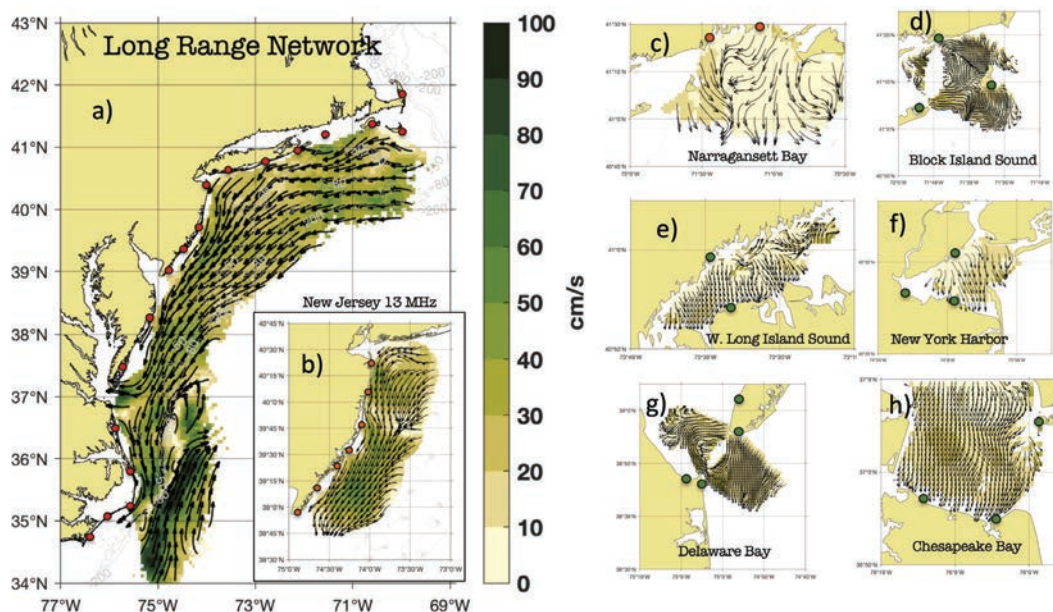


FIGURE 1

Map of the MARACOOS HF Radar Network (A) 5 MHz network consisting of 18 stations (B) 13 MHz network consisting of 7 stations in New Jersey (C) 16 MHz network covering Narragansett Bay with 2 stations and 25 MHz network consisting of 15 stations distributed over 5 domains (D) Block Island Sound (E) Western Long Island Sound (F) New York Harbor (G) Delaware Bay and (H) Chesapeake Bay.

rigorous process for becoming a certified Regional Information Coordination Entity that is documented on the IOOS website <https://ioos.noaa.gov/about/governance-and-management/certification/>. As part of the certification process, each RICE is required to describe its data quality control procedures for the data it collects and distributes. All data shall be quality controlled and procedures shall be employed following quality assurance of real-time ocean data (QARTOD). In 2021, MARACOOS was recertified for another five years.

This manuscript describes an HF radar processing methodology, representing the combination of a suite of widely used QA/QC practices that are implemented in an efficient way through the use of automated diagnostic plots and community quality control software. The further development of HFR community software packages allows for the standardization of these practices on a wider scale. These methodologies have been conceptualized, tested and hardened over the past 20 years while operating High Frequency radar systems in the Mid Atlantic of the United States. Quality control practices are constantly evolving and we provide here a summary of at present QA/QC methods that we hope to update regularly which in itself is a best practice (Pearlman et al., 2019). Currently the MARACOOS team meets once a week to discuss existing data quality and develop new methods for improving data quality. We submit a description of our practices to the oceanographic community for consideration as a “Best Practice”. Section 2 describes the data flow from radar to total vector map and the associated best practices and QA/QC methods applied at each level. Section 3 discusses how the quality control techniques impact the comparison of HFR data with ADCP and drifter data. Section 4 is a discussion of QC flags, best practices and the challenges faced by the radar network. Section 5 provides concluding remarks.

## 2 Methods

An overview of the HFR data processing is provided in Figure 2. All but two of the radars in MARACOOS are the SeaSonde model manufactured by CODAR Ocean Sensors and the processing descriptions in this paper apply to those systems. The SeaSonde utilizes a three-element receive antenna mounted on a single post. The receive antenna consists of two directionally dependent cross-loops and a single omnidirectional monopole. The SeaSonde utilizes frequency modulation to determine range and direction finding for bearing (Barrick & Lipa, 1997; Kohut & Glenn, 2003). Radials are generated at the station and sent to data assembly centers (DAC) which combine the radial data into a total surface current map on a regular grid. These gridded total vectors are made available for applications such as the assimilation into the statistical and dynamic models operated in the region (Wilkin & Hunter, 2013) and the calculation of NOAA tidal current predictions.

The components of the HF radar data processing chain have been mapped onto the data levels presented in the NASA Earth Science Handbook (Parkinson et al., 2006). There are a total of 5 layers with Level 0 representing the unprocessed instrument data at full resolution and Level 4 signifying derived products. We declared that the radial velocity data from the radar should correlate with Level 2 data, which are derived geophysical variables. Level 3 represents data on a uniform space-time grid and corresponds with the total vector currents. Level 0 to 2 data is processed at the individual radar stations while processing levels 3 and 4 take place at the DAC or at locations of external data users. This HFR mapping framework was first proposed at an Marine Technology Society OCEANS Conference (Roarty et al., 2016b) and has now been adopted by others in the community (Mantovani et al., 2020). Mapping the HF radar processing chain onto a common



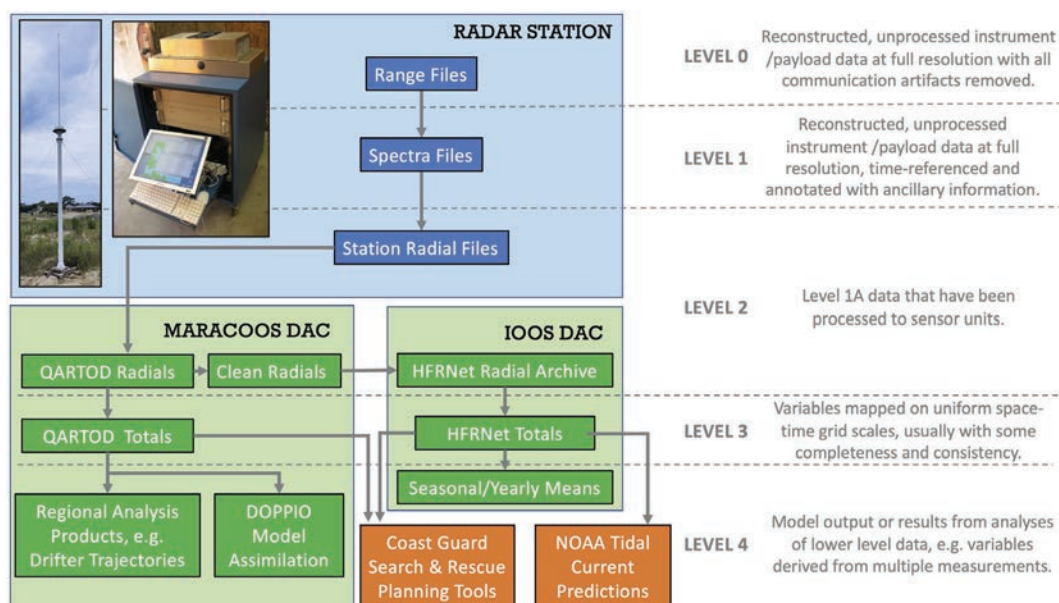


FIGURE 2

Flow chart of the HF radar processing chain from Level 0 data (quality assurance and range series files) to Level 4 data (derived products). The blue region indicates processing at the radar station, green for processing at the data assembly center and orange for usage by external stakeholders.

template with other remote sensing methods may identify ways to leverage QA/QC methods or practices that have been developed in other communities of practice (Kerfoot et al., 2016; Smith et al., 2017).

## 2.1 Level 0

We associate Level 0 data with any quality assurance methods that are conducted at the radar station. These include proper site setup and maintenance, remote monitoring, on-site inspections, and calibration with antenna pattern measurements. Technical expertise for operations and maintenance is shared during regular conference calls with operators in the region and spare hardware resources are shared amongst partners.

Some of the ancillary equipment we deploy at the station to ensure proper operation of the hardware includes an enclosure for the radar equipment, an air conditioning unit to remove humidity from the enclosure and keep radar equipment cool in the summer months, a lightning protection kit for the antennas, additional station lightning protection to minimize damage from a direct lightning strike, an uninterruptible power supply (UPS) to condition the incoming power and keep the station operating for short periods of time (under one hour) if power is lost at the station, a remote power switch that allows us to remotely cycle power to any component of the radar system and lastly a router to manage the communication to the station and communicate with the UPS and Web Power Switch. These supporting assets are similar to hardware accessories used by other operators (Mantovani et al., 2020). The stations utilized phone lines for communication early on, but these have been completely replaced with cellular modems.

We remotely inspect the radar station once a week by remotely logging into the station computer or viewing the hardware and radial diagnostic data through the stations' Radial Web Server to

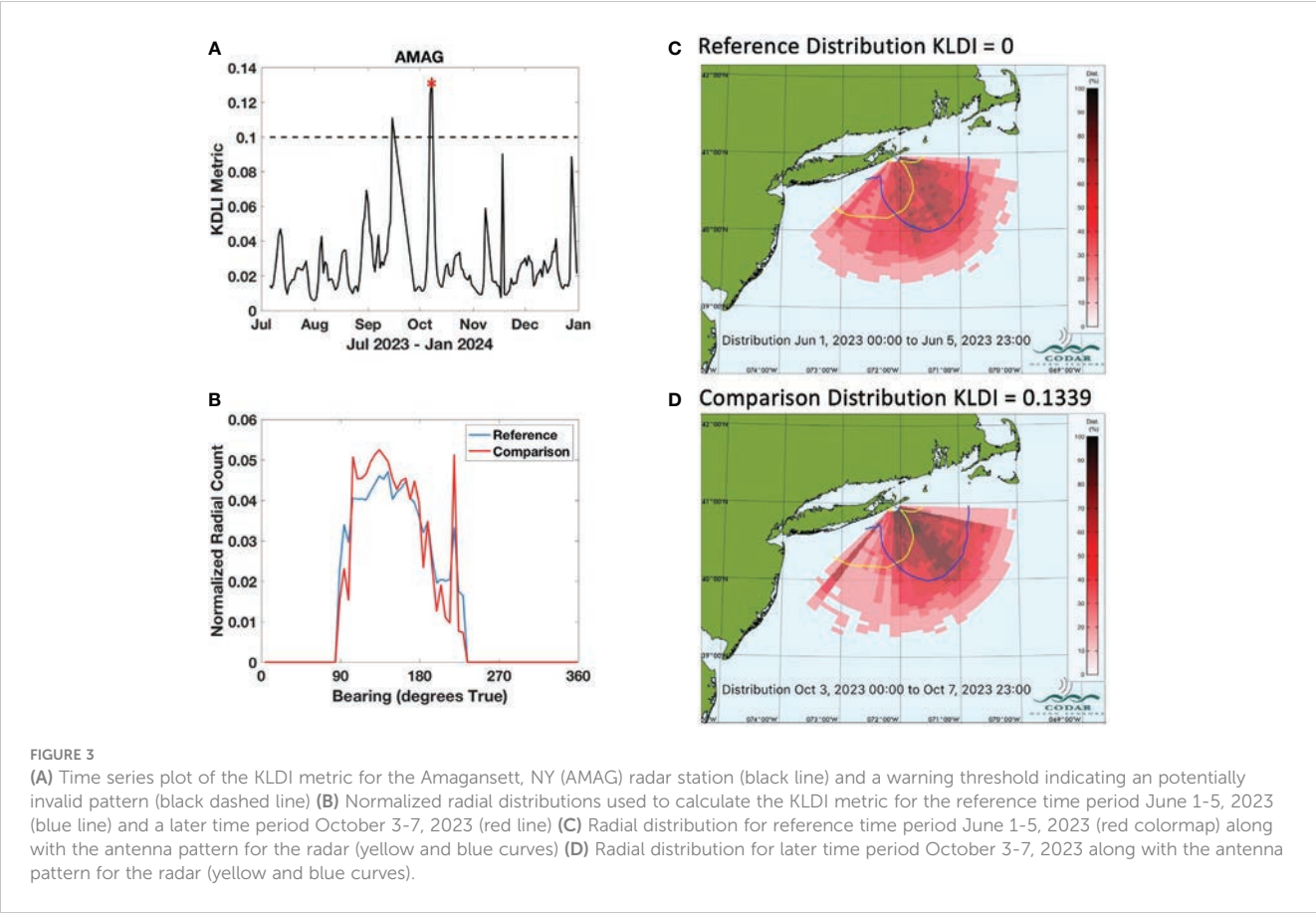
perform an inspection following guidance from the manufacturer (Barrick et al., 2011) and the HF radar community (Cook et al., 2008). The technicians visit the stations at least once every 6 months to physically inspect the radar hardware and ancillary equipment.

The pattern of the receive antenna should be re-measured once a year or if data quality degrades (Kohut & Glenn, 2003; Laws et al., 2010). An antenna pattern is measured through a variety of methods: walking, boat, drone or AIS (Evans et al., 2015; Whelan et al., 2018). MARACOOS has implemented a real-time metric that checks for significant changes in measured pattern radial distributions over time based on a method developed by CODAR Ocean Sensors. It compares the distribution of the last five days of radial maps to a reference distribution using five days of maps generated after the most recent measured pattern was installed on the site using a Kullback–Leibler divergence index (KLDI) (Figure 3). This index is a statistical measurement that quantifies the difference between one probability distribution and a reference probability distribution, with higher values representing greater differences. Time series plots of the KLDI metric for each station are updated daily and posted online<sup>1</sup>. KLDI values that increase and remain above a certain threshold indicate that a station's measured pattern is no longer working well. If the metric remains above 0.1 for more than a week, a new antenna pattern is requested.

## 2.2 Level 1 – spectra

Level 1 data focuses on the step of generating velocity spectra from the radar. The settings for spectra collection for each of the

<sup>1</sup> [https://rucool.marine.rutgers.edu/codar/data\\_quality/plots/index\\_kldi.php](https://rucool.marine.rutgers.edu/codar/data_quality/plots/index_kldi.php).



frequencies are provided in Table 1. The relevant first-order scatter from the sea (Bragg echo) needs to be correctly extracted from the spectra for further processing into radial vectors. Rodriguez-Alegre (2022) presents a thorough description and explanation of the first order identification algorithms. We currently use the SeaSonde software to delineate the first order region of the spectra. Alternative methods (Kirincich, 2017; Rodriguez-Alegre, 2022) utilize image processing techniques and machine learning to draw this boundary and we are evaluating the impact of this new methodology. If a more efficient methodology for extracting the first order Bragg region becomes available, radial maps can be reprocessed using spectra which are archived at each operator’s institution.

Each operator makes a monthly inspection of the first order delineation in the self-spectra to see if any of the processing parameters need to be adjusted to better capture the Bragg echo. The shape of the Bragg echo varies based upon the type of current that is being measured. Figure 4 shows the self-spectra (CSS) from the three frequencies operated within the Mid Atlantic, including a 5 MHz station in Loveladies, NJ (LOVE), a 5 MHz station in Buxton, NC (HATY), a 13 MHz system located in Seaside Park, NJ

TABLE 1 SeaSonde Doppler, spectra and radial vector file processing parameters for each of the three frequencies operated within MARACOOS.

	5 MHz	13 MHz	25 MHz
Doppler Bins (#)	1024	512	1024
Sweep Rate (Hz)	1	2	4
Velocity Resolution (cm/s)	2.9	4.4	2.4
Spectra CSQ Averaging (min)	17.1	4.3	4.3
Spectra CSS Averaging (min)	60	15	15
Spectra CSS Output Rate (min)	30	10	10
Radial Coverage Time (min)	180	75	75
Number of CSS in Each Radial File	5	7	7
Radial Output (min)	60	60	60

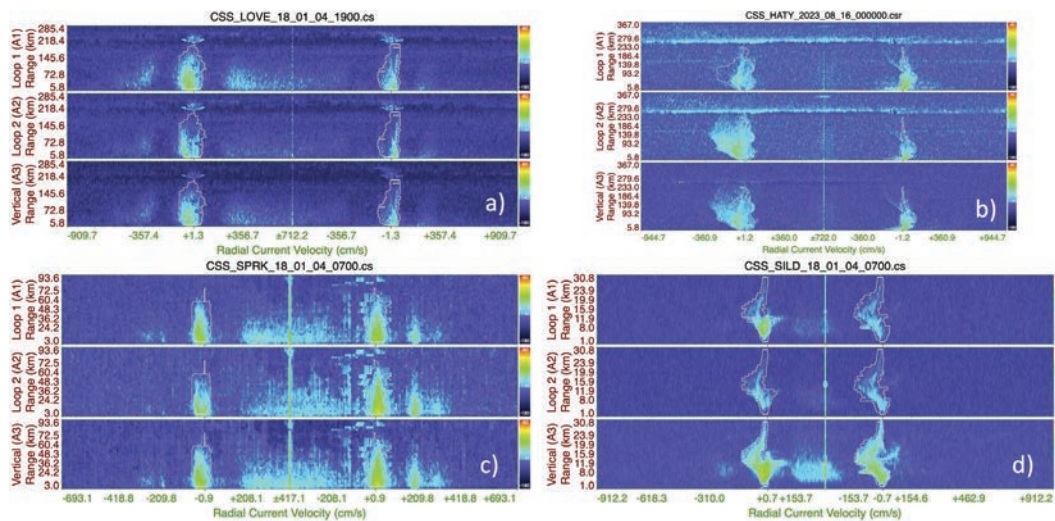


**FIGURE 4**  
Spectra files from (A) 5 MHz system that covers the shelf (B) 5 MHz system that covers the Gulf Stream (C) 13 MHz system that covers the shelf (D) 25 MHz system that covers the entrance to NY Harbor with strong tidal currents.

(SPRK) and a 25 MHz station in Staten Island, NY (SILD). In these plots, the x-axis represents radial velocity (cm/s), the y-axis represents range (km) and the color indicates echo signal strength (dB). The first order Bragg echoes appear as the flame-like shapes with the strongest signals and the white lines are delineations of that first order echo by the SeaSonde software. Second order echoes are not always present, but they may appear on either side of first order. In Figure 4C, second order peaks are visible in the positive radial velocity side to the right of the first order Bragg. For a majority of the stations within the Mid Atlantic the shape of the first order echo is a simple rectangle (Figures 4A, C). However, when the flow field is strong and variable as in the case of the Gulf Stream currents offshore of HATY or the water exiting NY Harbor measured by SILD, the shapes can be complex and it may be challenging to delineate the first order region for radial current processing.

## 2.3 Level 2 – radials

Generation of radial files involves several processing steps that take place at the radar station. The first order spectra from Level 1 are passed to the direction-finding algorithm MUSIC, which uses an ideal or measured antenna pattern to determine the bearings associated with first order reflections so that radial speeds can be properly mapped (Lipa et al., 2006; Cook et al., 2007). MUSIC processing produces radial metric files, which are then processed to short term radial files. The short-term radial files are concatenated and the median velocity in each range and angular bin is chosen as the velocity for the merged hourly file. The software is configured to require at least two vectors in the short-term radial ensemble in order to output a velocity measurement in the hourly file. The requirement of two vectors minimizes the error in the velocity measurement (Kohut et al., 2006b). On each radar station, a custom

angular segment filter (named AngSeg\_XXXX.txt located in the station configuration folder where XXXX is the four-letter site code for the station) is applied to the merged radial file. This filter is used to flag radial vectors that are placed in unreasonable locations, i.e. over land or behind islands. This also limits the angular coverage of the radial file to flag radial vectors derived from radar signals that would have excessive land paths back to the receive antenna. Radial files generated with a measured antenna pattern are referred to as measured radials and those generated with an assumed ideal antenna pattern are referred to as ideal radials. For a further description of the SeaSonde analysis procedure see (Lipa et al., 2006; de Paolo & Terrill, 2007; Kirincich et al., 2012).

The radial files are transferred back to the regional DAC at Rutgers once an hour via rsync over secure shell. As soon as a radial file arrives, a watchdog program initiates software that performs QC on that file. The radials are quality controlled according to the most recent version of the Quality Assurance/Quality Control of Real-Time Oceanographic Data (QARTOD) for High Frequency Radar surface current data (Bushnell & Worthington, 2022). The software used to perform the QARTOD tests is found in HFRadarPy (Smith et al., 2022), a Python package designed for exploration, cleaning and manipulation of HFR data. The quality tests applied to the radial data include file syntax, maximum speed, valid location, radial count and spatial median. All radial vectors are marked according to the QARTOD flagging definitions of pass (1), not evaluated (2), suspect (3) or fail (4) (Gouldman et al., 2017).

Primary and secondary flags are written to the radial file based on the QARTOD tests. The primary flag is meant to provide users with an overall assessment of data quality and can be used to quickly filter out bad data. The secondary flags are the results of individual QC tests. The primary flag for a radial vector is set to a fail code (4) if any of the specified secondary flags has a fail code. Radials that fail are excluded from the total vector calculation. The new radial QC file retains the same name as the original radial file and keeps all of the



information from the original file. QC test metadata is added to the file header and the flag code results for each test are appended to the CODAR main data table in separate data columns. When an entire file fails based on a test such as syntax or radial count, fail flags are set for every vector in the file (Updyke et al., 2021). Lastly a cleaned version of the radial file is created, which only contains data that has passed quality control (primary flag not equal to 4). This file is then passed to the IOOS surface current data assembly center (HFRNet) for total vector processing.

Monitoring practices at the MARACOOS DAC help streamline the processing as well as alert operators to any problems. The radial metadata are inserted into a Mongo database to allow for quick retrieval of station diagnostic information and to monitor which sites in the network have contributed a radial file for a particular hour. The latest radial information from each of the stations can be found on the Radial Diagnostic Dashboard<sup>2</sup> hosted on the Rutgers University website. The Dashboard displays the timestamp of the latest radial file, the radial vector count of the file, transmit frequency and preferred radial type (ideal or measured) that will be used in the total processing. If the most recent radial data is older than 12 hours the background color of the radial station changes to alert the technicians to the deficiency. An outage report is automatically created and the technicians also receive an email alert. Information for each outage, including duration and cause, is saved in the database and displayed online.

In addition to monitoring for data gaps, the DAC creates several automated plots that operators use to evaluate data quality. Figure 5A shows a plot of a typical radial file. Radial maps are made with the blue/red colormap where blue indicates vectors that are travelling towards the radar and red vectors indicating currents that are travelling away from the radar, consistent with redshift and blueshift from electromagnetic Doppler phenomenon. This two-color map aids in quick identification of areas that have contrasting directions of flow, which may signify flow dynamics of particular interest or indicate vectors that have potential data quality issues. We utilize the 25-hour mean radial map (Figure 5B) and a weekly plot of average radial velocity and radial vector count (Figure 6) as quick diagnostics for station health. These diagnostics are similar to those of previous researchers (Kim, 2015). Abnormally low radial counts are caused by a low radar signal to noise ratio (SNR) and the reason for the low SNR must be investigated. When low SNR is due to equipment failure or high background noise levels, the radials are likely to be of poor quality. Other initial QC checks include those for spatial consistency within each station map and between neighboring station maps. Figure 5A shows smooth transitions in radial flow and no spatial outliers in speed or direction. The southern section of this map shows radial flow directed away from the antenna. If for example, a single bearing in that section included vectors directed towards the antenna, this would be a spatial inconsistency of concern. The radial maps in Figure 5 indicate a general flow towards the southwest; however, if nearby radar stations all indicated flow to the north, this would indicate a quality issue. The current flow must be physically reasonable.

Another quick check of this in our region is to see that the periodicity of the average radial velocity time series (Figure 6) is visually consistent with the ebb and flow of a semi-diurnal tide. We have also found that a consistent average radial bearing (Roarty et al., 2012b) is an indication of a properly operating station and if this measurement has a step change or becomes erratic then that is an indication of a failure somewhere within the system. Whenever inconsistencies are found, the data are considered suspect and the operator will update a configuration file in the database to either remove the radial station from the total vector processing or change its preferred pattern type for processing. The operator will then begin an inspection of the system to identify any problems.

## 2.4 Level 3 – totals

The processing of total vectors runs once an hour to combine the radial velocity measurements into an evenly gridded total surface current product. When the total generation script runs it checks the Mongo database to see what radials are available at that time. The software also checks back 168 hours (1 week) to see if any radials were late in arriving at the DAC and will reprocess the total file if a radial file is now present. The MATLAB community toolbox HFRProgs (available on GitHub) is used to generate the total vector files. The radial vectors are screened so only vectors without fail codes in the primary flag are included in total vector generation. The configuration file within the database sets the pattern type (ideal or measured) to be used in the processing. The preferred radial type for total generation is measured; however, the ideal type may be used if the measured file is not available or found to be questionable.

The radial files are combined with two methods, unweighted least squares (UWLS) and optimal interpolation (OI), to produce two distinct total vector products. The configuration parameters for the UWLS and OI total surface current products are given in Table 2. In areas of good geometry and radial data coverage the algorithms are similar, however the OI outperformed the UWLS in the prediction of a surface drifter over 12 hours (Kohut et al., 2012). The surface drifter is the preferred instrument the Coast Guard uses for evaluation of surface currents during search and rescue missions (Allen, 1996) and the 12-hour threshold is the maximum length of drift scenario that would be used by the Coast Guard; therefore we chose the OI product as the one we would deliver to the Coast Guard and other stakeholders as the operational product.

Currently, only radials from similar frequency and averaging parameters are combined to form total vector products within the region. The combining grids were provided by the US National HF Radar Network (Terrill et al., 2006). The radials from the 5 MHz radars are combined on a 6 km grid, the 13/16 MHz radials on a 2 km grid and 25 MHz radials on a 1 km grid. This is unlike the U.S. National Network that combines radials from multiple frequencies and processing configurations into its 6 km and 2 km products. It has been noted that radial velocity maps with higher spatial resolution would produce a bias in the total vector map if combined with radial files with lower spatial resolution (Kim et al., 2011), so the decision was made to only generate totals with radials with similar averaging

<sup>2</sup> <https://hfradmin.marine.rutgers.edu/status/radials>



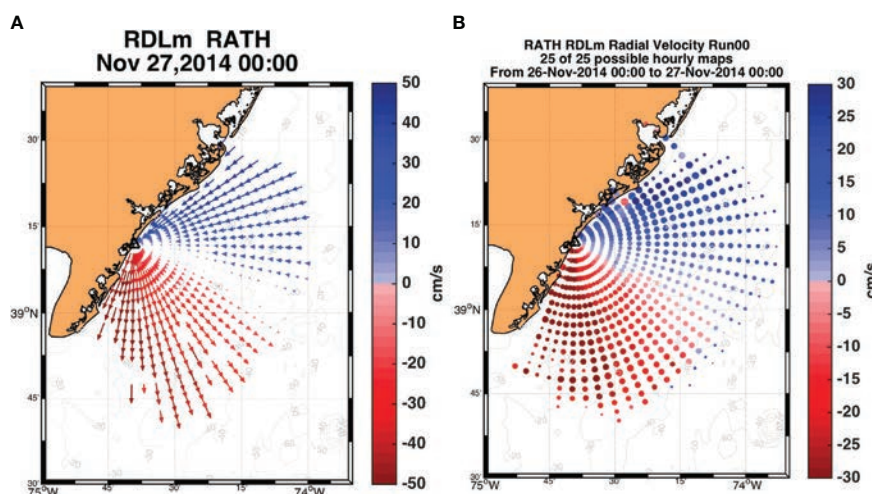


FIGURE 5

(A) Example of a radial map for a 13 MHz station. (B) 25-hour mean of radial velocities. The average velocity is represented by the color and the standard deviation by the size of the dot.

and processing schemes. Also, the temporal averaging differs for the frequencies that are operated in the region, 180 minutes for the 5 MHz radars and 75 minutes for the 13 and 25 MHz radars. Operators have experimented with shorter averaging intervals for the 5 MHz (Roarty et al., 2013a) and 25 MHz (Chant et al., 2008) but have not implemented them operationally.

The total vector files are quality controlled according to the HFR QARTOD manual (Bushnell & Worthington, 2022). The total vector data are subject to the data density (a minimum of three radial velocities must be sourced from at least two radar stations in order to compute a total velocity vector), maximum speed (total velocities > 300 cm/s are flagged as failing), valid location and velocity uncertainty tests. The u component (eastward) and v component (northward) velocity uncertainties are normalized uncertainties that are calculated as part of the optimal interpolation algorithm. A value of 0 is good and a value of 1 is poor. In the Mid-Atlantic, a previous study by Kohut et al., 2012 showed that a threshold value of 0.6 improved data quality while preserving good data coverage in the total vector maps.

The total vector data are saved in MATLAB (.mat) files in the HFRProgs TUV data structure as well as climate and forecast (CF) compliant NetCDF files. The quality control flags are stored in the MATLAB files as additional fields of the TUV structured array. In the NetCDF files, the flags are represented as additional variables and those variables include attributes that describe the flags and the tests. The radial and total vector files are served to the oceanographic community and public through several methods. The data files can be accessed and downloaded through the Thematic Real-time Environmental Distributed Data Services (THREDDS)<sup>3</sup> (Unidata, 2017) interface or via ERDDAP<sup>4</sup> (Simons, 2017). The surface current maps can be visualized through the MARACOOS data portal OceansMap available at <http://oceansmap.maracoos.org>, the National HF-Radar

Network <https://cordc.ucsd.edu/projects/hfrnet/> or the National Data Buoy Center <https://hfradar.ndbc.noaa.gov>

The hourly gridded total maps are the data product of interest for most applications at this time. The maps are reviewed to look for errant vectors. If a total map has suspect vectors, the radial files in the vicinity of the suspect area are plotted. If a particular radial file/station is found to have errant vectors, the cause of the error is investigated and adjustments are made to the processing to eliminate the error in future maps.

## 2.5 Level 4 – derived products

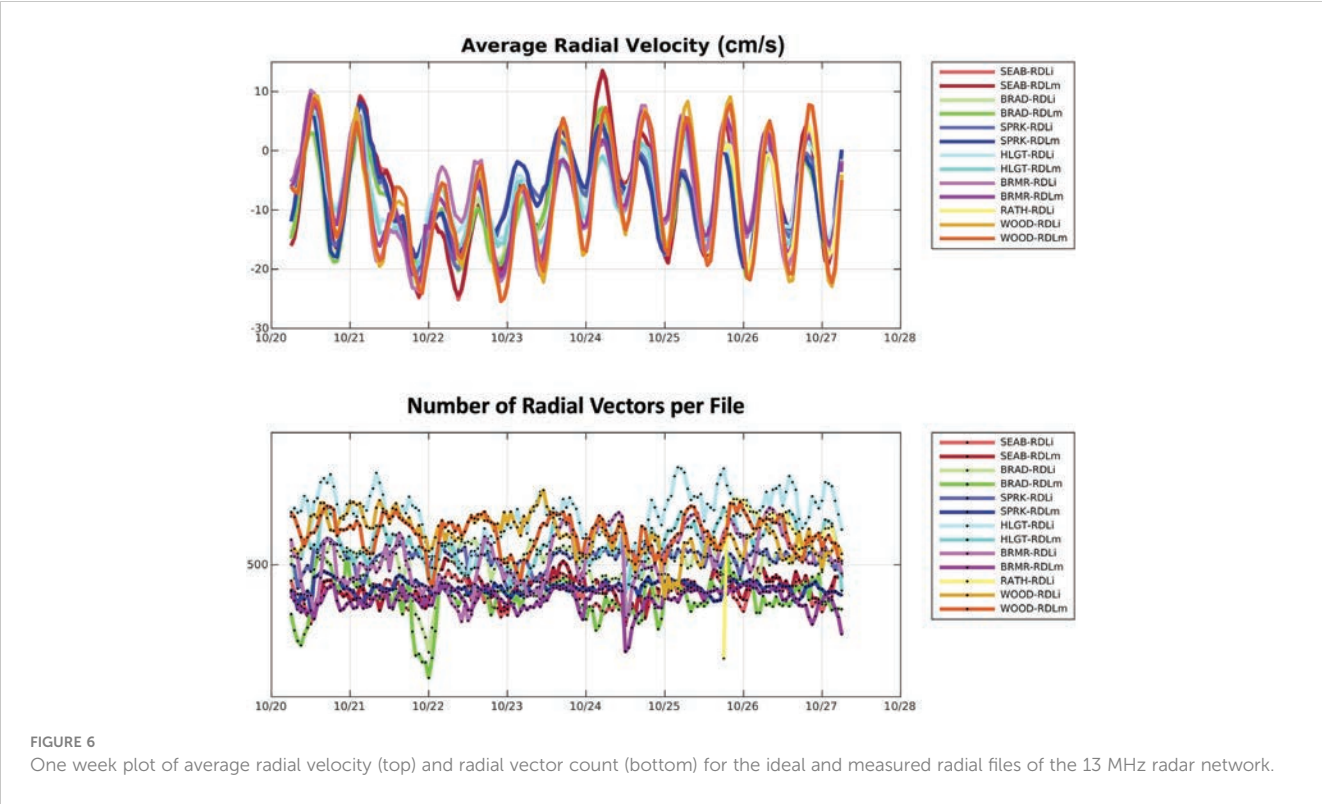
Level 4 data is treated as analyses from lower Level 3 data i.e. variables derived from multiple measurements. The types of products that are generated include daily, seasonal and annual means of the Mid Atlantic surface currents (Gong et al., 2010; Roarty et al., 2020), virtual Lagrangian drifter trajectories (Roarty et al., 2016a; Roarty et al., 2018) and Eulerian velocity time series at any point in the field of coverage. For daily, monthly or yearly maps of the surface currents we typically require 50% temporal coverage and the OI normalized velocity uncertainty to be below 0.6 (Kohut et al., 2012) at a grid point in order for a vector to be displayed.

## 2.6 Network performance metric

The MARACOOS 6 km surface current product has been operational with the Coast Guard for search and rescue since May 4, 2009. A requirement from the Coast Guard for this new data product was consistent temporal coverage and spatial coverage over a majority of the Mid Atlantic. Therefore, a spatial and temporal coverage metric was developed to gauge network performance which in turn helped guide the efforts of the technical staff operating the network. The goal is to achieve 80%

<sup>3</sup> [https://tds.marine.rutgers.edu/thredds/cool/codar/cat\\_totals.html](https://tds.marine.rutgers.edu/thredds/cool/codar/cat_totals.html)

<sup>4</sup> <http://hfr.marine.rutgers.edu/erddap/index.html>



temporal coverage over 80% of the Mid Atlantic over a six-month period, which is the reporting interval for MARACOOS. The spatial coverage entailed the 6 km grid beyond the 15 m isobath within 150 km of the coast between latitude 35° to the south and 42° to the north. The 15 m isobath was chosen as the inward boundary because the measurements from the 5 MHz radars will include a bias in water depths shallower than this threshold. The radio wavelength for the 5 MHz radars is 60 m and these radio waves scatter off ocean wavelengths of 30 m. From linear wave theory, wave speed is altered when  $d/\lambda < 0.5$ , where  $d$  is the water depth and  $\lambda$  is the ocean wave length. The 150 km outer boundary was chosen as the minimum nighttime range of the 5 MHz radars.

Figure 7 presents the network coverage from June 2011 to February 2022. This is a marked improvement over the network performance that was first published in 2012 (Roarty et al., 2012b). MARACOOS was able to exceed the 80/80 goal for nearly all progress, even during the December 2012 period just after Hurricane Sandy badly damaged the network (Malakoff, 2012). The four failures to meet the goal were due a combination of factors.

The coverage of the network has degraded recently as the funding has not kept up with inflation and the equipment continues to age with many of the radars older than 20 years. The COVID-19 pandemic also impacted technician response time and hardware repair turnaround times. One of the biggest contributing factors to missing the goal was due to the locations of the particular stations that experienced extended outages. In the northern section of the region, adjacent sites had extended outages at the same time. Whenever adjacent stations are offline, this has a much greater negative impact on the spatial coverage of the total map product. In areas where radars are more densely spaced along the coast, such as New Jersey, losing one station will not create as much of a data gap since overlapping radials from the neighboring stations are still available to generate totals for much of the area. An extended outage for the Cedar Island station on the Eastern Shore of Virginia also created a large spatial gap as there are not many suitable powered locations for radar stations along that section of coastline and the neighboring stations are far enough apart that overlapping radial coverage is limited.

TABLE 2 Processing parameters and velocity thresholds for the unweighted least squares (UWLS) and optimal interpolation combining methods.

	Radial Velocity Threshold (cm/s)	Total Velocity Threshold (cm/s)	Model Variance (cm <sup>2</sup> /s <sup>2</sup> )	Error Variance (cm <sup>2</sup> /s <sup>2</sup> )	Sx (km)	Sy (km)	UWLS Spatial Threshold (km)
6 km	110-280	300	420	66	15	15	10
2 km	110	200	420	66	5	5	3
1 km	120-200	300	420	66	2.5	2.5	1.5

Sx and Sy refer to decorrelation length scales for east and north components respectively. For description of configuration settings, see Kohut et al., 2012.

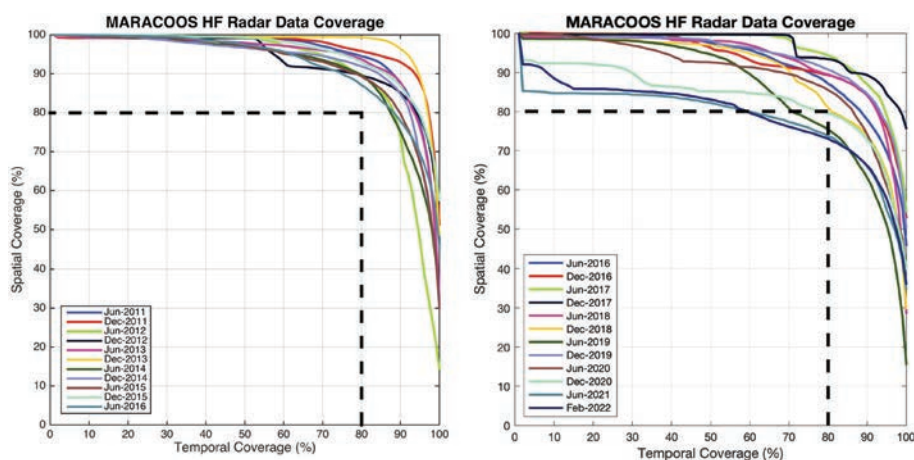


FIGURE 7

Total surface current performance metric for the 6 km product. The x-axis represents temporal coverage and the y-axis represents spatial coverage. Each of the colored solid lines represent the network performance for the 6-month progress periods within MARACOOS. The dashed black line at 80/80 is the goal for network performance as established with the Coast Guard Office of Search and Rescue. The left panel represents the progress periods from 2011–2016 and the right panel shows network coverage from 2016–2022.

### 3 Results

This section first describes two previous studies that were performed in 2016 to quantify the impact of these quality control concepts. We discuss the difficulties in assessing the value of QC with these approaches and then report on recent analysis that seeks to better characterize the value from a wider perspective. In the 2016 studies, HFR data (with and without additional radial QC tests applied), were compared to *in-situ* measurements of surface currents from an Acoustic Doppler Current Profiler (ADCP) and to surface drifter data provided by the Coast Guard Office of Search and Rescue.

A four-month data set of HF radar surface currents from the New York Bight Midshelf Front Experiment (NYBMFE) (Kohut et al., 2012; Ullman et al., 2012) was compared to measurements taken from the closest surface bin of an ADCP. We then quantified the impact of using additional radial QC tests on the HFR data before making the comparison. We also assessed the difference between using measured pattern radials and using ideal pattern radials in the comparison. Preliminary results were previously published in conference proceedings (Roarty et al., 2016b). When the NYBMFE was conducted, only a limited number of radial QC tests were in place including a syntax test, over-water test, and a global range (maximum velocity) test. Three additional radial tests were used in reprocessing for this experiment: 1) local range (maximum velocity), which tests whether a velocity measurement falls outside a pre-defined range 2) stuck sensor, which tests if the velocity measurement has repeated occurrences of the same value and 3) temporal gradient, which tests if changes between successive measurements fall outside a predetermined range.

First, appropriate thresholds needed to be defined for each of the tests. The local range (maximum velocity) test thresholds were selected after reviewing one year of radial velocity measurements at different locations. Greater flow speeds and larger variability are associated with the Gulf Stream and the currents in New York

Harbor, while shelf currents are slower and less variable. A local range threshold of 150 cm/s was chosen for stations observing shelf waters not located near the Gulf Stream and a higher threshold of 250 cm/s was set for stations observing strong tidal currents in estuaries or those measuring the Gulf Stream. Note that the maximum velocity thresholds reported in the methods section above were developed later and not in use when this analysis took place.

The stuck sensor test checks for repeating values in the time series. If successive measurements do not exceed the resolution of the measurement for a certain amount of time, the values are considered “stuck” and will fail the QC test. The resolution defined for the purpose of this test was 0.01 cm/s. The time threshold was set to three hours. The stuck sensor test identified gaps in velocity solutions at a particular range and bearing cell. The radar processing picks the median velocity from the ensemble of radial short files. If there are missing solutions over an averaging period then the median velocity repeats and is flagged by the stuck sensor test. The temporal gradient threshold was established using the ADCP record. The ADCP surface bin was rotated into a radial and cross radial coordinate system relative to the radar station at Wildwood, NJ (WILD). The temporal derivative over one hour in the radial direction was calculated for the four-month velocity record. The median of that record was  $-1.15 \times 10^{-4}$  cm/s<sup>2</sup> and mean was  $-2.5 \times 10^{-8}$  cm/s<sup>2</sup>, both close to zero. The 95<sup>th</sup> percentile value of 0.005 cm/s<sup>2</sup>, was chosen as the gradient threshold. This equates to a velocity change of 18 cm/s over an hour and any radial velocity with a temporal derivative greater than this threshold was flagged as failing the test.

The thresholds explained above were used to flag the HF radar measurements. MARACOOS follows the flagging scheme established by the Quality Assurance of Real-Time Oceanographic Data (QARTOD) (Gouldman et al., 2017). The radial velocities with fail flags were then removed from the record and the remaining data was compared to the full ADCP record. Then eight combinations of the three tests were utilized to determine if the comparison between the radial velocity from the WILD radar station closest to the ADCP would be improved. Test 1 kept all the HFR data while Test 8

removed any radar data that failed the local range, stuck sensor or temporal gradient test. The statistics for the comparison between the ADCP and the ideal and measured radials are given in Table 3. In this experiment, the use of ideal or measured radial files was comparable. In the ideal radial comparison, there was a 4% improvement in root mean square difference (RMSD) for test 8, which utilized all three quality control tests; however, 9% of the data was removed. For the measured radial comparison, both correlation and RMSD decreased with the use of all three quality control tests. There was no discernible change in the correlation between the HFR and ADCP data through the use of the QC tests.

Recognizing the limited scope of the first study as a comparison at a single location for one radar station, the next test of the quality control concepts used surface drifters so that given the Lagrangian nature of the drifter current measurements, larger areas of radar coverage for multiple stations could be tested. The analysis presented here was conducted as part of a validation experiment of the radar network in conjunction with the Coast Guard Office of Search and Rescue. Three clusters of Coast Guard surface drifters (Allen, 1996) were released: one cluster along the 30 m isobath in the northern area of the 5 MHz network, one along the 70 m isobath in the northern area of the 5 MHz network and one along the 30 m isobath in the central region of the 5 and 13 MHz network (Roarty et al., 2018). The average surface drift is towards the southwest so the hope was that the drifters deployed in the northern region of the network would drift through the majority of the network coverage. The drifters remained in the northern and central region for the experiment so the full network wasn't tested near Virginia and North Carolina, but the drifters endured for an average of 36 days providing a robust data set.

The drifters reported position data every 30 minutes. The drifter data were interpolated to hourly intervals to match the temporal sampling of the radar data. If a drifter passed through the coverage area of one of the radar stations, the velocity of the drifter was rotated into a radial velocity relative to the particular radar station. Then the closest radial velocity from the radar station was paired with the radial velocity of the drifter for comparison. An example of this comparison is shown in Figure 8 where drifter 43346 was compared

to the radial velocity from the radar station at Brant Beach, NJ (BRNT). This comparison was repeated for each of the seven drifters against eleven radar stations. The radial velocity correlation and root mean square error (RMSE) between the drifter and radar station are shown in Table 4. Seven of the stations showed high correlation with the surface drifters. The radar stations that showed low correlation (Martha's Vineyard, MVCO; Nantucket, NANT and Misquamicut, MISQ) were due to hardware problems at the stations that had not been repaired yet. Three stations (AMAG, MRCH and BLCK) displayed low correlation with the same drifter 43104 so there may have been errors in the position reporting of that particular drifter.

A subsequent analysis compared the skill of predicting drifter tracks with two datasets of HFR surface current maps, real-time and reprocessed, from the year 2017. The results quantify the impact of the use of additional QA/QC in the reprocessed data. The real-time dataset for radials included 1) operator review of hardware and radial diagnostic plots, 2) operator review of radial maps and radial distributions, 3) operator evaluation of which radial type to use in totals (ideal or measured pattern), 4) removal of data over a set maximum speed at the spectra level using manufacturer software, 5) flagging of invalid locations using manufacturer software and 6) radial file syntax requirements. Additional QA/QC for reprocessed maps included 1) a systematic review of data and diagnostics by the MARACOOS QC group to remove questionable data, 2) reprocessing radials from spectra if more suitable calibration patterns were available, 3) applying radial metric QC (Haines et al., 2017) to North Carolina radar stations, 4) applying QARTOD radial count and spatial median radial QC tests, which were not in use in real-time data in 2017 and 5) re-calculating totals with radials that did not fail any of the QC tests. Table 5 compares the performance of each dataset using a Lagrangian skill score (Liu & Weisberg, 2011). Skill at predicting a drifter track was improved significantly by using the reprocessing dataset for drifter 65247790 near the Outer Banks. The skill for drifter 63804280 was higher using the real-time dataset; however, it is worth noting that this case had an extremely low skill score count. For other drifters, skills were the same or slightly improved. These results provide comparisons throughout the Mid-Atlantic although the

TABLE 3 Correlation ( $r$ ), root mean square error (rms error cm/s), number of samples ( $N$ ) and percentage decrease of the original data record based on 8 combinations of quality control tests for the WILD ideal (left) and measured (right) radial files.

Test		Ideal Radial Files				Measured Radial Files			
		$r$	rms error	$N$	% Decrease	$r$	rms error	$N$	% Decrease
1	All Data	0.67	13.44	2080	0%	0.68	13.47	2080	0%
2	Local Range	0.66	12.85	2042	2%	0.66	13.48	2066	1%
3	Stuck	0.66	13.67	1944	7%	0.68	13.57	1938	7%
4	Gradient	0.68	13.07	2074	0%	0.68	13.47	2075	0%
5	Local Range & Stuck	0.66	13.05	1906	8%	0.66	13.58	1924	8%
6	Local Range & Gradient	0.67	12.74	2038	2%	0.66	13.48	2061	1%
7	Stuck & Gradient	0.68	13.28	1938	7%	0.68	13.57	1933	7%
8	Local Range, Stuck & Gradient	0.66	12.94	1902	9%	0.66	13.58	1919	8%



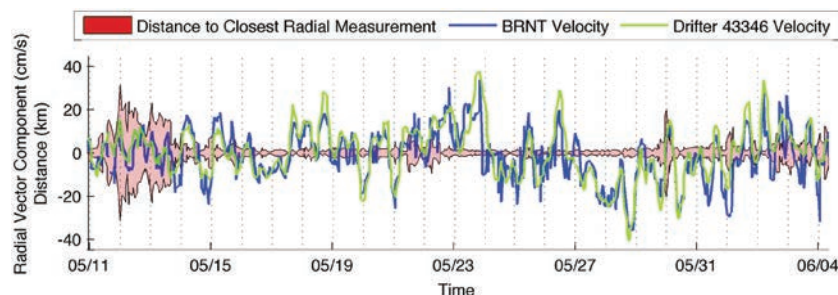


FIGURE 8

Radial velocity of drifter 43346 (green) relative to radial velocity of radar station at Brant Beach, NJ (BRNT) (blue). The distance between the drifter and the nearest radial velocity at a particular instance of time is shown as the shaded red region.

comparisons are only available for the duration of time that the drifter is located within the radar coverage. Each skill score represents a comparison over six hours so based on the number of scores per drifter, the minimum duration of a comparison was 12 hours (2 scores for drifter 63804280) and the maximum was 384 hours (64 scores for drifter 63783850).

We have used comparisons of HFR data with currents measured by other instruments to evaluate the effectiveness of quality control; however, this is not the only way to assess benefits of QA/QC. Poor quality is sometimes evident and can be identified even when a separate verification data set is not available. One source of measurement error is the processing of spectra that is not sea echo and an example of this is the processing of ionospheric reflections that are recorded in the spectra. All the radars operate with the manufacturer supplied filter that is applied to each Doppler spectra, where interference that is detected is removed from further processing. However, the existing filter does not catch all ionospheric interference. Ionospheric interference is characterized by increased signal strength stretching across the Doppler cells but confined to a few range bins. Those reflections in the radar data are of interest to researchers who study the ionosphere (Kaeppeler et al., 2022); however, this interference can lead to large velocity vectors being added to the radial maps, which in turn, cause errant patches of high velocity data in the total maps. Figure 9 shows an hourly map when the Duck, North Carolina (DUCK) radar station exhibiting ionospheric interference as the large red vectors and the same map where the ionospheric interference has been removed through the use of the spatial median test. Figure 10 shows the positive impact that flagging and removing these types of erroneous vectors can have on the surface current maps. The high velocity patch seen in the map on the left of the figure is caused by the noise being processed to radial vectors and that patch is removed when QC tests, including the spatial median test, are applied in the processing.

## 4 Discussion

### 4.1 Utilizing flag information

The total count of flags for each of the individual radial tests (syntax, maximum velocity, valid location, radial count, spatial median, temporal gradient and stuck sensor) and the primary flag

are plotted as a time series for the past week<sup>5</sup>. This online visualization allows the operators to detect any changes with respect to the radar operations by identifying time periods with high numbers of suspect or fail flags. The plots include two radial QC tests, temporal gradient and stuck sensor, that are staged for implementation at a future date. Tests under evaluation are added to the real-time processing, but the results are not considered when assigning a value to the primary flag; this means that those tests will not affect which radials are included in total vector calculations. However, the results of the tests are written to the QC version of the radial file and also plotted, which is useful because the plots of flag counts can be viewed to see if the new tests and test thresholds are working as expected. For example, if there are too many fail flags for a test at a certain site, a closer investigation of the performance of the test can be pursued and test thresholds could be adjusted for that station. When a new test is working well, it may be approved for inclusion in calculation of the primary flag.

### 4.2 QC challenges

The processing of ionospheric and other types of radio interference remains a significant QC challenge. The exact origin of interference might not be known, but it may still be visually apparent in a spectra colormap that other signals are being confused with sea echo (e.g. interference appearing as vertical or horizontal stripes covering wide areas of the spectra are also covering the first order sea echo). Radial vectors that contribute to unrealistic spatial patterns in the current maps can often be traced back to the locations in the spectra where interference intersected with the first order region. Flagging and removing these erroneous vectors from the maps can significantly improve data quality. In an application such as search and rescue planning, a high velocity patch such as that in Figure 10, would influence virtual drifter trajectories, carrying drifters further than they should travel in the time period for the search scenario and expanding the size of a search area. The QARTOD spatial median test occurs at the radial level; it can miss problems when there are few neighboring radials or a patch of erroneous data is large enough that the vectors in the

TABLE 4 Correlation (r), root mean square error (RMSE, cm/s) and number of data points (N) between radar station radial data (ideal and measured) and surface drifter.

Site	Frequency	Drifter	Ideal			Measured		
			r	RMSE	N	r	RMSE	N
AMAG	5	38824	0.76	12.23	590	0.76	12.59	590
BLCK	5	38824	0.73	12.02	594	0.66	13.54	594
MRCH	5	38824	0.68	14.14	594	0.66	14.4	594
MVCO	5	38824	0.2	23.01	594	0.26	20.05	594
NANT	5	38824	0.34	20.11	589			
AMAG	5	43104	0.39	16.32	590	0.37	16.06	594
BLCK	5	43104	0.51	14.57	594	0.4	15.93	594
MRCH	5	43104	0.33	17.44	594	0.32	17.24	594
MVCO	5	43104	0.14	22.73	594	0.07	21.95	594
NANT	5	43104	0.16	21.09	589			
AMAG	5	43241	0.74	12.59	590	0.74	12.39	590
BLCK	5	43241	0.8	11.27	594	0.84	9.82	594
MVCO	5	43241	0.13	22.82	594	0.42	17.71	594
NANT	5	43241	0.24	24.58	589			
BRAD	13	43340	0.72	10.46	587	0.72	10.48	587
BRNT	13	43340	0.85	7.57	586	0.79	8.74	586
LOVE	5	43340	0.71	9.17	586	0.72	8.97	586
SPRK	13	43340	0.8	8.49	536	0.84	7.44	536
BRNT	13	43346	0.84	7.13	586	0.82	7.63	586
LOVE	5	43346	0.75	8.6	586	0.78	7.97	586
SPRK	13	43346	0.83	7.94	536	0.84	7.33	535
BISL	25	43372	0.37	22.07	490	0.4	21.97	490
BLCK	5	43372	0.69	17.96	490	0.77	15.19	490
MISQ	25	43372	0.09	27.16	490	0.24	24.94	490
MVCO	5	43372	0.38	23.32	490	0.41	21.69	490
NANT	5	43372	0.18	31.83	490			
BRNT	13	43411	0.83	6.95	586	0.81	7.4	586
LOVE	5	43411	0.67	8.35	586	0.76	7.15	586
SPRK	13	43411	0.8	7.93	535	0.8	7.71	534

middle of the patch pass the test. The development of additional QC measures to address interference at the spectra level would be an even better approach. QC is applied in the SeaSonde software to remove interference at the range and spectra level, but at the present time, it is only partially effective for some types of interference.

4.3 Best practices

The subject of quality control and best practices (Bushnell et al., 2019) has been a topic within the HF radar community for quite

some time. The Radiowave Operators Working Group was formed in 2004 to help develop best practices for the burgeoning field of operational HFR remote sensing. The charter of ROWG aims to foster collaboration between new and experienced HFR operators, develop procedures governing HFR operations and provide recommendations to HFR stakeholders (data users, instrument manufacturers and program managers). The organization meets in person approximately every 18 months, maintains a listserv of approximately 140 members where members can communicate between meetings and supports a wiki [www.rowg.org](http://www.rowg.org) that serves as a knowledge repository for the operators. The operators also maintain

TABLE 5 HFR skill at predicting drifter tracks of Coast Guard drifters deployed in the Mid Atlantic in 2017.

Drifter	Average Skill Score		Number of Scores		Area
	Real-time	Reprocessed	Real-time	Reprocessed	
63783850	0.25	0.26	64	64	Virginia Beach
63804280	0.71	0.47	2	17	Cape Cod
64065020	0.28	0.32	7	12	Outer Banks
64116430	0.52	0.55	21	20	New Jersey
64502470	0.43	0.43	5	6	Outer Banks
64529230	0.46	0.50	61	50	Cape Cod
65241210	0.37	0.37	57	58	New Jersey
65247790	0.21	0.47	26	25	Outer Banks

several software repositories that are utilized in the management of HFR data and can be found at <https://github.com/rowg>. It should be noted that the HFR community was the first to update their QARTOD manual to provide community guidance and a roadmap for the ocean observing community.

HFR operators have also published several documents on best practices and quality assurance/quality control. Operators in California, USA developed the first best practices document on the deployment and maintenance of High Frequency radar stations (Cook et al., 2008). Operators in Europe have also made strides to document best practices and quality control (Rubio et al., 2017; Mantovani et al., 2020) as well as practitioners in Australia (Cosoli & Grcic, 2019). Both the Mantovani and Cosoli paper discuss best practices for both beam forming and direction finding radar systems while this paper focuses solely on the direction finding SeaSonde radar. Also, the Mantovani paper discusses the siting of new radar installations while this paper focuses on existing

installations. One thing to note is that Australia utilizes UNESCO (Commission, I. O, 1993) flag codes while European HFR operators use the flag codes from the ARGO network (Wong et al., 2023). Both of these flagging conventions are slightly different from the QARTOD codes. The ability to manage these differing flagging schemes can be done through the use of a translation table (Bushnell et al., 2019). The unique aspect of our best practice manuscript is that we describe quality control tools that include dashboards and real-time automated plots that are implemented at the regional level.

4.4 Future QC work

Future QC plans include developing further use of radial metric QC (Haines et al., 2017) as well as implementing real-time baseline comparisons (Capodici et al., 2019) between stations and synthetic

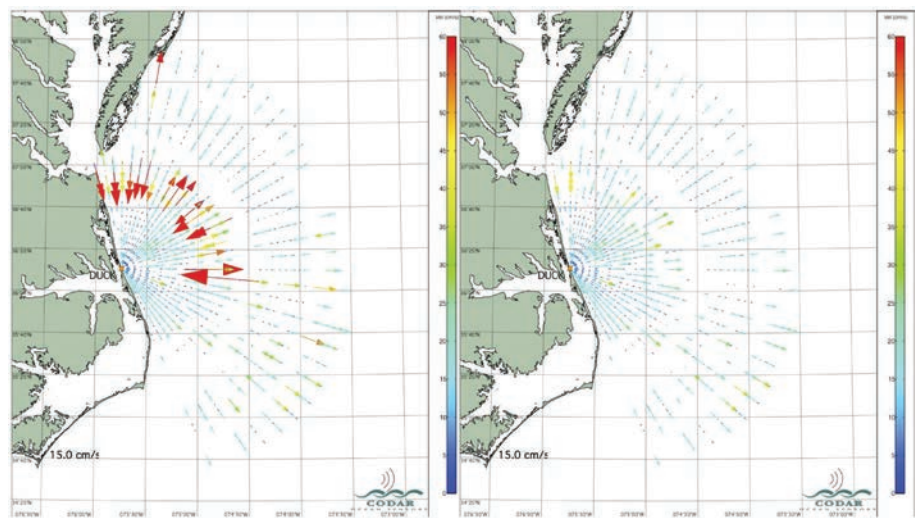


FIGURE 9 Map of radial files from the Duck, North Carolina radar station for November 9, 2016 23:00 UTC. Left panel: Map including erroneous high velocity radials caused by processing of ionospheric interference. Right panel: Map after applying a spatial median QC test to flag and remove spatial outliers.

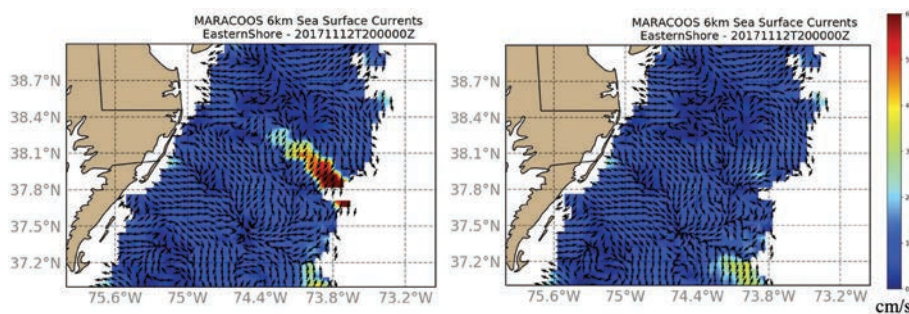


FIGURE 10

Surface current map for November 12, 2017 20:00 UTC. Left panel: Map calculated using real-time radials contaminated by ionospheric interference. Right panel: Map calculated with radials that had additional QC applied to flag and exclude spatial outliers from processing.

radial comparisons (Emery et al., 2022) for additional layers of quality control. Synthetic and baseline radial comparisons are a means of quantifying consistency with other HF radar measurements as a metric of quality. These are useful metrics given the unique spatial and temporal coverage of the HF radar, which complicates the evaluation of the data quality by means of comparison to data collected by other instruments, such as satellites, drifters or ADCPs.

This manuscript provides the most up to date summary of real-time delivery of surface currents from the Mid Atlantic High Frequency Radar Network. We are beginning to develop methods and the workflow to deliver a post-processed science quality product (Updyke et al., 2019; Smith et al., 2021) in addition to the real-time data stream. The quality control tests for reprocessed data may be applied somewhat differently from the tests for the real-time product. For example, the temporal QC test, such as gradient or stuck sensor, can be applied over time periods that extend further into the future as well as the past.

## 4.5 Operational challenges

There are two major challenges facing the network for continued success in the future: aging infrastructure and the development of offshore wind in the Mid Atlantic.

The radars that were first deployed in the region are reaching their end-of-life status. The MARACOOS radar community has designated the service life for radar chasses (receiver and transmitter) as 20 years. The exposed elements have shorter working life spans: 15 years for transmit antennas and 10 years for receive antennas which contain more sensitive electronics. Service life of the cables depends on the type of conduit and exposure, but is estimated at 10 years. Platform components like air conditioning units have a 10-year service life and computers are typically replaced every 5 years. The US network was envisioned to contain 321 radars (Harlan, 2015). At the current rate of expansion (26 stations added between 2017 and 2019, 9 per year), this will be completed in 2038. In order to complete the network by the end of the decade 25 new radars would need to be added to the network each year and 15 aging radars should be replaced each year.

The other challenge to the network is the 50 GW of offshore wind envisioned by the Mid Atlantic states. Land-based High Frequency (HF) Radars provide critically important observations of the coastal ocean that will be adversely affected by wind turbine interference (WTI). Pathways to mitigate the interference of turbines on HF radar observations exist for a small number of turbines; however, a greatly increased pace of research is required to understand how to minimize the complex interference patterns that will be caused by the large arrays of turbines planned for the U.S. outer continental shelf.

CODAR Ocean Sensors led a series of studies funded by the Bureau of Ocean Energy Management (BOEM) to understand the problem. The key findings of the first study (Trockel et al., 2018) are that the interference is caused by the amplitude modulation of the turbine's radar cross section. The location of the interference is predictable and can be determined from the rotation rate of the turbine. The turbines interfere with HF radar processing in three ways: 1) raising the background noise level which affects the sea echo identification algorithm 2) changing the boundaries of the sea echo peaks by mischaracterizing turbine echoes as part of the sea echo and 3) affecting the bearing determination of radial current vectors by causing the turbine echoes to be convolved with the sea echo. The second BOEM study (Trockel et al., 2021) tested the mitigation strategies outlined in the first report. The overall result of the mitigation strategies led to a reduction of 86% of WTI in the first order region of SeaSonde spectra collected from a 5 MHz radar for a single month (March 2021). To assess the full impact of WTI on the HF radar enterprise, additional frequencies and longer evaluation periods will be needed.

The HF radar community self-organized to identify a roadmap for the next five years to tackle this problem (Kirincich et al., 2019). This led to the NOAA IOOS funded program (2020-2024) to advance the WTI mitigation from research into regular operations via a coordinated set of system integration, validation and verification activities. The radar community has identified three mitigation methods (Trockel et al., 2023) for the WTI: 1) increasing the sweep rate of the radar so the spread of the WTI peaks is reduced 2) flagging and removing the WTI peaks in the radar spectra and 3) increasing data redundancy by adding additional



monostatic radial or bistatic (Lipa et al., 2009) elliptical measurements. It should be noted that there are drawbacks to each method but when used together, WTI can be effectively mitigated in HFR data streams.

## 5 Conclusion

This paper summarizes the configuration and operation of the Mid Atlantic High Frequency Radar Network for the measurement of ocean surface currents. We have summarized the data processing chain from site installation and operation, recording of spectra, generation of hourly radial velocity vectors, assembly of the radial velocity files from several shore stations into a total surface current product and then distribution of total surface currents and derived products to a multitude of users. The HFR surface current processing steps were mapped onto the data levels established for remote sensing measurements of the NASA Earth Observing System. Defining the data levels onto the HFR processing chain allows for improved data quality by ensuring that measurements have undergone the necessary checks and corrections at each level, facilitates data interoperability and improves data access and distribution by allowing researchers to access the data levels that align with their goals and expertise.

At each data level, quality assurance methods and quality control procedures were explained. The performance of the network over the past thirteen years was documented. The coverage was higher in the first half of the period than the last, however we have plans to raise the coverage levels to previous values by replacing aging equipment. The quality assurance procedures and quality control data tests were applied in two experiments. One focused on the comparison of radial vector data with an upward looking ADCP and the other experiment compared radial vector data with velocity data derived from several surface drifters. Both experiments highlighted the case that well performed quality assurance reduces the need for quality control.

Both radial and total vector data are being generated in realtime with quality descriptor flags satisfying the first QARTOD Data Management Law that “Every real-time observation distributed to the ocean community must be accompanied with a quality descriptor”. The pursuit of a best QA/QC practice is a never-ending task, so we will continue to develop new and revisit previous quality assurance and quality control procedures to improve the surface current measurements. The methodology and procedures outlined in this paper will hopefully serve as a template for other High Frequency Radar Networks that are operating around the globe.

## Data availability statement

The datasets presented in this study can be found in online repositories. The names of the repository/repositories and accession number(s) can be found below: <http://hfr.marine.rutgers.edu/erddap/index.html>.

## Author contributions

HR: Conceptualization, Methodology, Project administration, Writing – original draft. TU: Conceptualization, Formal Analysis, Methodology, Writing – original draft. MS: Software, Writing – original draft, Data curation. LN: Software, Writing – original draft, Visualization. SG: Supervision, Writing – review & editing. OS: Writing – review & editing, Supervision.

## Funding

The author(s) declare financial support was received for the research, authorship, and/or publication of this article. This work was funded by NOAA Award Number NA16NOS0120020 “Mid-Atlantic Regional Association Coastal Ocean Observing System (MARACOOS): Powering Understanding and Prediction of the Mid-Atlantic Ocean, Coast, and Estuaries”. Sponsor: National Ocean Service (NOS), National Oceanic and Atmospheric Administration (NOAA) NOAA-NOS-IOOS-2021-2006475, Integrated Ocean Observing System Topic Area 1: Implementation and Development of Regional Coastal Ocean Observing Systems. The activities described in this manuscript were funded through a contract from the National Academy of Science, Engineering, and Medicine – Gulf Research Program – Understanding Gulf Ocean Systems (NASEM-GRP-UGOS) to the GulfCORES research consortium.

## Acknowledgments

We would like to thank the HF radar partners in SECOORA (Harvey Seim, Sara Haines, Mike Muglia, Trip Patterson and Anthony Whipple) for their collaboration in operating the radars and analysis of the data in the southern MAB. Thank you to Art Allen and the United States Coast Guard for providing the surface drifters used in this experiment. Thanks to Gerhard Kuska and Mary Ford for their continued leadership at MARACOOS. Thanks to all of the Mid Atlantic radar operators for their efforts in maintaining the radar systems.

## Conflict of interest

The authors declare that the research was conducted in the absence of any commercial or financial relationships that could be construed as a potential conflict of interest.

## Publisher's note

All claims expressed in this article are solely those of the authors and do not necessarily represent those of their affiliated organizations, or those of the publisher, the editors and the reviewers. Any product that may be evaluated in this article, or claim that may be made by its manufacturer, is not guaranteed or endorsed by the publisher.

## References

- Abascal, A. J., Castanedo, S., Medina, R., Losada, I. J., and Alvarez-Fanjul, E. (2009). Application of HF radar currents to oil spill modelling. *Mar. Pollut. Bull.* 58, 238–248. doi: 10.1016/j.marpolbul.2008.09.020
- Allen, A. (1996). Performance of GPS/Argos self-locating datum marker buoys (SLDMBs). *OCEANS '96. MTS/IEEE. 'Prospects 21st Century'*, p.857–861. doi: 10.1109/OCEANS.1996.568341
- Barrick, D., Parikh, H., Aguilar, H., and Whelan, C. (2011). Remote monitoring checklist. *CODAR Ocean Sensors* 6, 1–6.
- Barrick, D. E., and Lipa, B. J. (1997). Evolution of bearing determination in HF current mapping radars. *Oceanography* 10, 72–75. doi: 10.5670/oceanog
- Brunner, K., and Lwiza, K. M. (2019). “The impact of storm-induced coastal trapped waves on the transport of marine debris using high-frequency radar data,” in *2019 IEEE/OES Twelfth Current, Waves and Turbulence Measurement (CWTM)* (San Diego, CA: IEEE). doi: 10.1109/CWTM43797.2019
- Bushnell, M., Waldmann, C., Seitz, S., Buckley, E., Tamburri, M., Hermes, J., et al. (2019). Quality assurance of oceanographic observations: Standards and guidance adopted by an international partnership. *Front. Mar. Sci.* 6, 706. doi: 10.3389/fmars.2019.00706
- Bushnell, M., and Worthington, H. (2022). *Manual for real-time quality control of high frequency radar surface current data: a guide to quality control and quality assurance for high frequency radar surface current observations*. Available online at: <https://repository.library.noaa.gov/view/noaa/15482>.
- Capodici, F., Cosoli, S., Cirao, G., Nasello, C., Maltese, A., Poulain, P.-M., et al. (2019). Validation of HF radar sea surface currents in the Malta-Sicily Channel. *Remote Sens. Environ.* 225, 65–76. doi: 10.1016/j.rse.2019.02.026
- Chant, R. J., Glenn, S. M., Hunter, E., Kohut, J., Chen, R. F., Houghton, R. W., et al. (2008). Bulge formation of a buoyant river outflow. *J. Geophys. Res.* 113, C01017. doi: 10.1029/2007JC004100
- Commission, I. O. (1993).
- Cook, T. M., DePaolo, T., and Terrill, E. J. (2007). Estimates of radial current error from high frequency radar using MUSIC for bearing determination. *OCEANS 2007*, 1–39. doi: 10.1109/OCEANS.2007.4449257
- Cook, T., Hazard, L., Otero, M., and Zelenke, B. (2008). *Deployment and Maintenance of a High-Frequency Radar for Ocean Surface Current Mapping: Best Practices* (San Diego, CA: Southern California Coastal Ocean Observing System), 35. Available at: <https://repository.oceanbestpractices.org/handle/11329/368>.
- Cosoli, S., and Grcic, B. (2019). *Quality Control procedures for IMOS Ocean Radar Manual, Version 2.1*. Available online at: <https://repository.oceanbestpractices.org/handle/11329/1173>.
- de Paolo, T., and Terrill, E. (2007). Skill assessment of resolving ocean surface current structure using compact-antenna-style HF radar and the MUSIC direction-finding algorithm. *J. Atmospheric Oceanic Technol.* 24, 1277–1300. doi: 10.1175/JTECH2040.1
- Emery, B., Kirincich, A., and Washburn, L. (2022). Direction finding and likelihood ratio detection for oceanographic HF radars. *J. Atmospheric Oceanic Technol.* 39, 223–235. doi: 10.1175/JTECH-D-21-0110.1
- Evans, C. W., Roarty, H. J., Handel, E. M., and Glenn, S. M. (2015). “Evaluation of three antenna pattern measurements for a 25 MHz seasonde,” in *Current, Waves and Turbulence Measurement (CWTM)*, 2015 IEEE/OES Eleventh (St. Petersburg, FL: IEEE). doi: 10.1109/CWTM.2015.7098147
- Gradone, J., Roarty, H., Evans, C., Glenn, S., Handel, E., Baskin, C., et al. (2015). Assessing HF radar data in the New York Harbor: Comparisons with wind, stream gauge and ocean model data sources. In *OCEANS 2015-MTS/IEEE Washington* (pp. 1–8). IEEE.
- Gong, D., Kohut, J. T., and Glenn, S. M. (2010). Seasonal climatology of wind-driven circulation on the New Jersey Shelf. *J. Geophys. Res.* 115, 25. doi: 10.1029/2009JC005520
- Gouldman, C. C., Bailey, K., and Thomas, J. O. (2017). *Manual for real-time oceanographic data quality control flags*.
- Haines, S., Seim, H., and Muglia, M. (2017). Implementing quality control of high-frequency radar estimates and application to Gulf Stream surface currents. *J. Atmospheric Oceanic Technol.* 34, 1207–1224. doi: 10.1175/JTECH-D-16-0203.1
- Harlan, J. (2015). *A Plan to Meet the Nation's Needs for Surface Current Mapping* (Silver Spring, MD: NOAA IOOS), 64. Available at: [https://cdn.ioos.noaa.gov/media/2017/12/national\\_surface\\_current\\_planMay2015.pdf](https://cdn.ioos.noaa.gov/media/2017/12/national_surface_current_planMay2015.pdf).
- Harlan, J., Allen, A., Howlett, E., Terrill, E., Kim, S. Y., Otero, M., et al. (2011). National IOOS high frequency radar search and rescue project. *OCEANS 2011*, 1–9. doi: 10.23919/OCEANS.2011.6107090
- Heil, C. A., and Muni-Morgan, A. L. (2021). Florida's harmful algal bloom (HAB) problem: Escalating risks to human, environmental and economic health with climate change. *Front. Ecol. Evol.* 9, 646080. doi: 10.3389/fevo.2021.646080
- Howden, S., Barrick, D., and Aguilar, H. (2011). “Applications of high frequency radar for emergency response in the coastal ocean: utilization of the Central Gulf of Mexico Ocean Observing System during the Deepwater Horizon oil spill and vessel tracking”, *Proc. SPIE 8030, Ocean Sensing and Monitoring III*, 80300O (11 May 2011). doi: 10.1117/12.884047
- Kaeppler, S. R., Miller, E. S., Cole, D., and Updyke, T. (2022). On the use of high-frequency surface wave oceanographic research radars as bistatic single-frequency oblique ionospheric sounders. *Atmospheric Measurement Techniques* 15, 4531–4545. doi: 10.5194/amt-15-4531-2022
- Kerfoot, J., Baltes, R., Bushnell, M., Campbell, L., and Knee, K. (2016). “The US National glider network: Application of QARTOD recommended quality control methods to glider CTD data sets,” in *OCEANS 2016 MTS/IEEE Monterey* (Monterey, CA: IEEE). doi: 10.1109/OCEANS.2016.7761356
- Kim, S. Y. (2015). Quality assessment techniques applied to surface radial velocity maps obtained from high-frequency radars. *J. Atmospheric Oceanic Technol.* 32, 1915–1927. doi: 10.1175/JTECH-D-14-00207.1
- Kim, S. Y., Terrill, E. J., Cornuelle, B. D., Jones, B., Washburn, L., Moline, M. A., et al. (2011). Mapping the U.S. West Coast surface circulation: A multiyear analysis of high-frequency radar observations. *J. Geophysical Research: Oceans* 116, C03011. doi: 10.1029/2010JC006669
- Kirincich, A. (2017). Improved detection of the first-order region for direction-finding HF radars using image processing techniques. *J. Atmospheric Oceanic Technol.* 34, 1679–1691. doi: 10.1175/JTECH-D-16-0162.1
- Kirincich, A. R., de Paolo, T., and Terrill, E. (2012). Improving HF radar estimates of surface currents using signal quality metrics, with application to the MVCO high-resolution radar system. *J. Atmospheric Oceanic Technol.* 29, 1377–1390. doi: 10.1175/JTECH-D-11-00160.1
- Kirincich, A., Emery, B., Washburn, L., and Flament, P. (2019). Improving surface current resolution using direction finding algorithms for multiantenna high-frequency radars. *J. Atmospheric Oceanic Technol.* 36, 1997–2014. doi: 10.1175/JTECH-D-19-0029.1
- Kohut, J. T., and Glenn, S. M. (2003). Improving HF radar surface current measurements with measured antenna beam patterns. *J. Atmospheric Oceanic Technol.* 20, 1303–1316. doi: 10.1175/1520-0426(2003)020<1303:IHRSCM>2.0.CO;2
- Kohut, J., Glenn, S., and Schofield, O. (2006a). Phased implementation of the Mid-Atlantic regional HF radar system. *2006 IEEE US/EU Baltic Int. Symposium*, 1–7. doi: 10.1109/BALTIC.2006.7266158
- Kohut, J., Oliver, M. J., Wark, K., Breece, M., and Nazzaro, L. (2021). “A new blue economy: connecting ocean information with the needs of the recreational and commercial fishing industry,” in *Preparing a Workforce for the New Blue Economy* (Cambridge, MA: Elsevier), 151–159. doi: 10.1016/B978-0-12-821431-2.00056-1
- Kohut, J. T., Roarty, H. J., and Glenn, S. M. (2006b). Characterizing observed environmental variability with HF doppler radar surface current mappers and acoustic doppler current profilers: Environmental variability in the coastal ocean. *Oceanic Engineering IEEE J.* 31, 876–884. doi: 10.1109/OE.2006.886095
- Kohut, J., Roarty, H., Randall-Goodwin, E., Glenn, S., and Lichtenwalner, C. (2012). Evaluation of two algorithms for a network of coastal HF radars in the Mid-Atlantic Bight. *Ocean Dynamics* 62, 953–968. doi: 10.1007/s10236-012-0533-9
- Kurapov, A., Pelland, N., and Rudnick, D. (2017). Seasonal and interannual variability in along-slope oceanic properties off the US West Coast: Inferences from a high-resolution regional model. *J. Geophysical Research: Oceans* 122, 5237–5259. doi: 10.1002/2017JC012721
- Kurapov, A. L., Rudnick, D. L., Cervantes, B. T., and Risien, C. M. (2022). Slope and shelf flow anomalies off oregon influenced by the el niño remote oceanic mechanism in 2014–2016. *J. Geophysical Research: Oceans* 127, e2022JC018604. doi: 10.1029/2022JC018604
- Laws, K., Paduan, J. D., and Vesecky, J. (2010). Estimation and assessment of errors related to antenna pattern distortion in CODAR seaSonde high-frequency radar ocean current measurements. *J. Atmospheric Oceanic Technol.* 27, 1029–1043. doi: 10.1175/2009JTECHO658.1
- Levin, J., Arango, H. G., Laughlin, B., Wilkin, J., and Moore, A. M. (2021). The impact of remote sensing observations on cross-shelf transport estimates from 4D-Var analyses of the Mid-Atlantic Bight. *Adv. space Res.* 68, 553–570. doi: 10.1016/j.asr.2019.09.012
- Lindstrom, E., Gunn, J., Fischer, A., McCurdy, A., and Glover, L. K. (2012). *A Framework for Ocean Observing*. By the Task Team for an Integrated Framework for Sustained Ocean Observing. (Paris: UNESCO). doi: 10.5270/OceanObs09-FOO
- Lipa, B. J., Nyden, B., Ullman, D. S., and Terrill, E. J. (2006). SeaSonde radial velocities: Derivation and internal consistency. *Oceanic Engineering IEEE J.* 31, 850–861. doi: 10.1109/OE.2006.886104
- Lipa, B., Whelan, C., Rector, B., and Nyden, B. (2009). HF radar bistatic measurement of surface current velocities: Drifter comparisons and radar consistency checks. *Remote Sens.* 1, 1190–1211. doi: 10.3390/rs1041190
- Liu, Y., and Weisberg, R. H. (2011). Evaluation of trajectory modeling in different dynamic regions using normalized cumulative Lagrangian separation. *J. Geophysical Research: Oceans* 116, 1–13. doi: 10.1029/2010JC006837
- Malakoff, D. (2012). Scientists assess damage from sandy's deadly punch. *Science* 338, 728–729. doi: 10.1126/science.338.6108.728

- Mantovani, C., Corgnati, L., Horstmann, J., Rubio, A., Reyes, E., Quentin, C., et al. (2020). Best practices on high frequency radar deployment and operation for ocean current measurement. *Front. Mar. Sci.* 7, 210. doi: 10.3389/fmars.2020.00210
- National Transportation Statistics (2021).
- O'Halloran, C. L. (2011). *Oceans and human health: harmful algal blooms and acute health symptoms among surfers and lifeguards* (Berkeley: University of California).
- Paduan, J. D., Kosro, P. M., and Glenn, S. M. (2004). A national coastal ocean surface current mapping system for the United States. *Mar. Technol. Soc. J.* 38, 102–108. doi: 10.4031/002533204787522839
- Parkinson, C. L., Ward, A., and King, M. D. (2006). “A guide to NASA's earth science program and earth observing satellite missions,” in *Earth Science Reference Handbook* (Washington D.C.: NASA), 291. Available at: <https://atrain.nasa.gov/publications/2006ReferenceHandbook.pdf>.
- Pearlman, J., Bushnell, M., Coppola, L., Karstensen, J., Buttigieg, P. L., Pearlman, F., et al. (2019). Evolving and sustaining ocean best practices and standards for the next decade. *Front. Mar. Sci.* 6, 277. doi: 10.3389/fmars.2019.00277
- Roarty, H., Allen, A., Glenn, S., Kohut, J., Nazzaro, L., and Fredj, E. (2018). Evaluation of environmental data for search and rescue II. 2018 OCEANS - MTS/IEEE Kobe Techno-Oceans (OTO), 1–3. doi: 10.1109/OCEANS-Kobe39585.2018
- Roarty, H. J., Barrick, D. E., Kohut, J. T., and Glenn, S. M. (2010). Dual-use compact HF radars for the detection of mid- and large-size vessels. *Elektrik Turkish J. Electrical Eng. Comput. Sci.* 18, 373–388. doi: 10.3906/elk-0912-15
- Roarty, H., Glenn, S., and Allen, A. (2016a). Evaluation of environmental data for search and rescue. *OCEANS 2016 - Shanghai*, 1–3. doi: 10.1109/OCEANSAP.2016.7485535
- Roarty, H., Glenn, S., Brodie, J., Nazzaro, L., Smith, M., Handel, E., et al. (2020). Annual and seasonal surface circulation over the Mid-Atlantic Bight Continental Shelf derived from a decade of High Frequency Radar observations. *J. Geophysical Research: Oceans* 125, e2020JC016368. doi: 10.1029/2020JC016368
- Roarty, H., Kerfoot, J., Kohut, J., Glenn, S., Whelan, C., and Hubbard, M. (2013a) in *Improving the measurements of high frequency radar: Reduced averaging times and bistatics*, OCEANS - Bergen, 2013, MTS/IEEE (Bergen, Norway: IEEE).
- Roarty, H., Lemus, E., Handel, E., Glenn, S., Barrick, D. E., and Isaacson, J. (2011). Performance evaluation of seaSonde high-frequency radar for vessel detection. *Mar. Technol. Soc. J.* 45, 14–24. doi: 10.4031/MTSJ.45.3.2
- Roarty, H., Palamara, L., Kohut, J., and Glenn, S. (2016b). “Automated quality control of high frequency radar data II,” in *OCEANS 2016 MTS/IEEE Monterey* (Monterey, CA: IEEE). doi: 10.1109/OCEANS.2016.7761250
- Roarty, H., Riscica, J., Palamara, L., Bowers, L., Seroka, G., Kohut, J., et al. (2012a) in *Analysis of the wind resource off New Jersey for offshore wind energy development*, 2012, Oceans (Hampton Roads, VA: IEEE).
- Roarty, H., and Shivock, C. (2022). “Surface current coverage of the mid atlantic United States,” in *OCEANS 2022, Hampton Roads* (Hampton Roads, VA: IEEE). doi: 10.1109/OCEANS47191.2022.9977344
- Roarty, H. J., Smith, M., Glenn, S. M., and Barrick, D. E. (2013b). Real-time beyond the horizon vessel detection. *Proc. SPIE 8714 Radar Sensor Technol. XVII*, 87140Z–87140Z. doi: 10.1117/12.2015871
- Roarty, H. J., Smith, M., Handel, E., Glenn, S. M., and Barrick, D. E. (2012c) in *Expanding the coverage of HF radar through the use of wave powered buoys*, 2012, Oceans (Hampton Roads, VA: IEEE).
- Roarty, H., Smith, M., Kerfoot, J., Kohut, J., and Glenn, S. (2012b) in *Automated quality control of High Frequency radar data*, 2012, Oceans (Hampton Roads, VA: IEEE).
- Rodriguez-Alegre, I. (2022). *Determining First-Order Boundaries in High-Frequency Radar Sensing of Ocean Surface Currents: A Proposed Method Using Bayesian Estimation* (Santa Cruz: University of California). Available at: <https://login.proxy.libraries.rutgers.edu/login?url=https%3A%2F%2Fwww.proquest.com%2Fdissertations-theses%2Fdetermining-first-order-boundaries-high-frequency%2Fdocview%2F2649953876%2Fsc-2%3Faccountid%3D13626>.
- Rubio, A., Mader, J., Corgnati, L., Mantovani, C., Griffa, A., Novellino, A., et al. (2017). HF radar activity in european coastal seas: Next steps toward a pan-european HF radar network. *Front. Mar. Sci.* 4, 8. doi: 10.3389/fmars.2017.00008. Review.
- Rypina, I. I., Kirincich, A., and Peacock, T. (2021). Horizontal and vertical spreading of dye in the coastal ocean of the northern Mid-Atlantic bight. *Continental Shelf Res.* 230, 104567. doi: 10.1016/j.csr.2021.104567
- Seroka, G., Dunk, R., Glenn, S., Bowers, L., Kerfoot, J., Crowley, M., et al. (2012). “Rutgers university coastal ocean observation laboratory (RU-COOL) advanced modeling system developed to cost-effectively support offshore wind energy development and operational applications”, in 2012 Oceans Hampton Roads, VA: IEEE, 2012, Oceans.
- Simons, R. A. (2017). *ERDDAP* (Monterey, CA: NOAA/NMFS/SWFSC/ERD). Available at: <https://coastwatch.pfeg.noaa.gov/erddap>.
- Smith, M., Belabbassi, L., Garzio, L., Knuth, F., Lichtenwalner, S., Kerfoot, J., et al. (2017). Automated quality control procedures for real-time ocean observatories initiative datasets. *OCEANS 2017-Anchorage*, 1–4.
- Smith, M., Glenn, S., Merz, C., Liu, Y., Weisberg, R., Shay, L., et al. (2021). A unified approach to HF radar radial quality control for understanding gulf ocean systems. *OCEANS 2021: San Diego-Porto*, 1–5. doi: 10.23919/OCEANS44145.2021.9705910
- Smith, M. J., Updyke, T., and Haines, S. (2022). *Open-source software to support high frequency radar data analysis and quality control* (Hampton Roads: OCEANS 2022). doi: 10.1109/OCEANS47191.2022.9977323
- Snowden, J., Hernandez, D., Quintrell, J., Harper, A., Morrison, R., Morell, J., et al. (2019). The U.S. Integrated ocean observing system: governance milestones and lessons from two decades of growth. *Front. Mar. Sci.* 6. doi: 10.3389/fmars.2019.00242
- Terrill, E., Otero, M., Hazard, L., Conlee, D., Harlan, J., Kohut, J., et al. (2006). Data management and real-time distribution in the HF-radar national network. *OCEANS 2006*, 1–6. doi: 10.1109/OCEANS.2006.306883
- Trockel, D., Rodriguez-Alegre, I., Barrick, D., and Whelan, C. (2018). *Impact Assessment and Mitigation of Offshore Wind Turbines on High Frequency Coastal Oceanographic Radar* Vol. 53 (Sterling, VA: US Department of the Interior, Bureau of Ocean Energy Management. OCS Study BOEM), 49.
- Trockel, D., Trockel, J., and Whelan, C. (2021). *Coastal High Frequency Radar Wind Turbine Interference Mitigation* (Sterling, VA: US Department of the Interior, Bureau of Ocean Energy Management). 37 p.
- Trockel, J., Emery, B., Kirincich, A., Muglia, M., Roarty, H., Taylor, P., et al. (2023). Strategies for Operating HF Radars in Field of View of Offshore Wind Turbines. In *OCEANS 2023-MTS/IEEE US Gulf Coast* (pp. 1–6). IEEE.
- Ullman, D. S., Codiga, D. L., Hebert, D., Decker, L. B., and Kincaid, C. R. (2012). Structure and dynamics of the midshelf front in the New York Bight. *J. Geophysical Research: Oceans* 117, 1–17. doi: 10.1029/2011JC007553
- Unidata (2017). *Thematic Real-time Environmental Distributed Data Services (THREDDS)* (Boulder, CO: UCAR/Unidata). doi: 10.5065/D6N014KG
- Updyke, T. G., Roarty, H. J., Smith, M., and Nazzaro, L. (2019). “The impact of reprocessing efforts on the mid-atlantic's surface current product,” in *OCEANS 2019 MTS/IEEE SEATTLE* (Seattle, WA: IEEE). doi: 10.23919/OCEANS40490.2019
- Updyke, T. G., Roarty, H. J., Smith, M., and Nazzaro, L. (2021). Implementation of quality flags in the processing of high frequency radar surface current data. *OCEANS 2021: San Diego-Porto*, 1–6. doi: 10.23919/OCEANS44145.2021.9706013
- US Department of Commerce, N. (2019). *Weather related fatality and injury statistics*.
- Whelan, C., Hubbard, M., Trockel, D., and Parikh, H. (2018). “Benefits of multiple antenna pattern measurement methods for maintaining a regional HF radar network,” in *Proceedings of the ORCA Conference* (Okinawa, Japan: ORCA).
- Wilkin, J. L., and Hunter, E. J. (2013). An assessment of the skill of real-time models of Mid-Atlantic Bight continental shelf circulation. *J. Geophysical Research: Oceans* 118, 2919–2933. doi: 10.1002/jgrc.20223
- Wong, A., Keeley, R., and Carval, T. (2023). *Argo quality control manual for CTD and trajectory data* (Brest, France, Ifremer).
- Yaremchuk, M., Spence, P., Wei, M., and Jacobs, G. (2016). Lagrangian predictability in the DWH region from HF radar observations and model output. *Deep Sea Res. Part II: Topical Stud. Oceanography* 129, 394–400. doi: 10.1016/j.dsr2.2013.05.035





<https://doi.org/10.1038/s43247-025-02101-x>

# Lagrangian coherent structures influence the spatial structure of marine food webs



Jacquelyn M. Veatch<sup>1,2</sup>✉, Matthew J. Oliver<sup>3</sup>, Erick Fredj<sup>4</sup>, Hank Statscewich<sup>5</sup>, Kim Bernard<sup>6</sup>, Ashley M. Hann<sup>6,7</sup>, Grant Voirol<sup>3</sup>, Heidi L. Fuchs<sup>1</sup>, William R. Fraser<sup>8</sup> & Josh T. Kohut<sup>1</sup>

The patchy distribution of prey in marine environments has a large effect on upper trophic level foraging strategies and distributions. While currents can disperse or concentrate low-motility plankton into patches that reflect the dynamic fluid environments they inhabit, it remains unclear whether surface flows affect motile zooplankton. Here, we used an in-situ optical dataset to detect phytoplankton patches, active acoustics to observe krill, and GPS-tagged penguins to observe three levels of the food web. These data allowed us to investigate whether the local food web overlaps with small-scale surface transport patterns as evidence that dynamic flows structure marine food webs. In Palmer Deep Canyon, Antarctica, we deployed High Frequency radars to measure hourly ocean surface currents, which were subsequently applied to estimate attractive Lagrangian Coherent Structures. We found that phytoplankton patches, Antarctic krill (*Euphausia superba*), Adélie penguins (*Pygoscelis adeliae*) and gentoo penguins (*Pygoscelis papua*) were preferentially located in attracting Lagrangian Coherent Structure features. These results provide evidence that Lagrangian Coherent Structures act as hotspots for prey and associated foraging predators, thus spatially focusing the food web. Results highlight the role of small-scale currents in food web focusing and the importance of transport features in maintaining the Palmer Deep Canyon ecosystem.

Distributions of planktonic and nektonic marine organisms are continuously shaped by the dynamic ocean environments in which they reside and are typically patchy in space and time. Phytoplankton and zooplankton are both known to form discrete patches<sup>1,2</sup>, with predators that seek out these patches of prey<sup>3</sup>, which leads to a form of spatial control on the ecosystem known as food web focusing<sup>4</sup>, where small scale fluid flows (hours-days and 1–100 km) structure the relationship between different trophic levels. Here, we are using the term “food web focusing” to describe transient and spatially variable prey patches, as opposed to prey aggregations associated with fixed spatial structures like seamounts<sup>4</sup>. Understanding the mechanisms that control “patchiness” seen in primary producers, primary consumers, and their predators requires integrating environmental observations of physical processes and community structure at relevant temporal and spatial scales<sup>5,6</sup>. These interactions between marine organisms and physical ocean processes are crucial to understanding their distribution within and reliance on the dynamic ocean habitat in which they reside.

Low-motility plankton with low and intermediate Reynolds numbers ( $Re \sim 10^{-2} - 10^3$ ), such as phytoplankton and zooplankton, are transported by ocean currents<sup>8</sup>. (Here, Reynolds numbers ( $Re$ ) refer to how the fluid flows around the animals rather than how the fluid flows on its own). Foraging species with high Reynolds numbers ( $Re \sim 10^6$ )<sup>7</sup> and greater mobility can employ various foraging strategies to seek out their zooplankton prey, which swim more slowly and are less able to move independently of ocean currents. The transport of low-motility plankton is particularly noticeable in areas with strong currents, often associated with features such as ocean fronts and eddies<sup>9</sup>. In order to understand distributions of phytoplankton, zooplankton, and top predators, we must investigate patterns in ocean transport.

Patterns in ocean transport can be elucidated through particle release experiments within observed ocean velocity fields. By integrating over Lagrangian particle trajectories, attracting structures are quantified within evolving velocity fields using an analysis known as Lagrangian Coherent Structures (LCS)<sup>10</sup>. Several types of LCS exist with different definitions of

<sup>1</sup>Department of Marine and Coastal Sciences, Rutgers, The State University of New Jersey, New Brunswick, NJ, USA. <sup>2</sup>Department of Applied Ocean Physics and Engineering, Woods Hole Oceanographic Institution, Woods Hole, MA, USA. <sup>3</sup>College of Earth, Ocean and Environment, University of Delaware, Lewes, DE, USA. <sup>4</sup>Computer Science Department, The Jerusalem College of Technology, Jerusalem, Israel. <sup>5</sup>College of Fisheries and Ocean Sciences, University of Alaska, Fairbanks, AK, USA. <sup>6</sup>College of Earth, Ocean, and Atmospheric Sciences, Oregon State University, Corvallis, OR, USA. <sup>7</sup>National Oceanic and Atmospheric Administration Uncrewed Systems Operations Center, Silver Spring, MD, USA. <sup>8</sup>Polar Oceans Research Group, Sheridan, MT, USA. ✉e-mail: [jveatch@whoi.edu](mailto:jveatch@whoi.edu)

“attraction” and “repulsion” to quantify the strength of transport features. In this study, we use Finite Time Lyapunov Exponents (FTLE) as a metric to identify attracting LCS, and test if these attracting LCS are acting as a hotspot for low-motility plankton. FTLE were chosen as they provide flexible integration time, allowing for the identification of ocean features at the scale of interest, and have been shown to identify transport features associated with increased phytoplankton patch presence in our study area<sup>11</sup>. LCS can quantify transport patterns in ocean velocities that cannot be seen by studying Eulerian velocity fields alone, allowing for the investigation of the role of transport in food web focusing.

LCS have been shown to overlap with bioactivity on different levels of the marine food web, shaping large phytoplankton blooms<sup>12–15</sup>, correlating with the presence of middle trophic levels (fishes)<sup>16</sup>, and appearing along the tracks of top predators<sup>17,18</sup>. Much of this previous work has been conducted on larger, geostrophic currents characteristic of open ocean (pelagic) ecosystems. On these scales, satellite-observed ocean color is often used to track the evolution of large phytoplankton patches and Global Positioning System (GPS) tags are used to track movements of large marine animals in relation to LCS calculated from satellite altimetry<sup>12</sup> or long range radars<sup>14</sup>. However, predator and prey patches likely interact at much smaller scales than measured by these systems.

Distributions of zooplankton affect prey availability for many higher trophic level predators<sup>6</sup> including whales<sup>19</sup> and commercially important fishes<sup>20</sup>. Therefore, a major interest in marine spatial ecology has been understanding and quantifying the factors that affect the preyscape of a marine ecosystem. While both phytoplankton and predators have been associated with attractive LCS features, the relationship between zooplankton and LCS are more difficult to obtain as they require in-situ acoustic measurements and/or net tows, and the factors that influence their distribution can be driven by both zooplankton behavior and advection.

Many of the studies linking LCS to top predators assume that, similarly to phytoplankton, zooplankton are also concentrated by attractive LCS features, though these assumptions are typically made without coincident zooplankton measurements. The few studies that have linked zooplankton

to LCS were conducted over relatively large scales using data from mesoscale ocean model output<sup>21,22</sup> and long-range (low frequency) radars<sup>23</sup>. These findings suggest links between zooplankton biomass and the presence of LCS at scales of days to weeks and tens of kilometers. Other studies have associated zooplankton distributions with mesoscale eddy kinetic energy<sup>24</sup>, tidal cycles phases<sup>25,26</sup>, and wind events<sup>25,27</sup> suggesting connections between ocean dynamics and zooplankton swarms. Larger top predators such as whales have also been shown to select for LCS-identified prey concentrating features over larger scales<sup>23</sup>. However, predators likely seek prey patches on much smaller scales<sup>28,29</sup>, meaning these coarser-scale associations between LCS and predators could be averages of finer scale processes. Using an Antarctic submarine canyon as our natural laboratory, we resolved the food web at scales of hours to days across spatial scales of hundreds of meters to kilometers and observed transport features experienced by near-shore patches of phytoplankton, zooplankton and associated predators. To our knowledge, the following study is the first, to the best of our knowledge, to include concurrent high-resolution observations of zooplankton, phytoplankton and upper trophic predators in relation to LCS-identified ocean features.

For this study, we focus on the local food web of Palmer Deep Canyon along the Western Antarctic Peninsula (WAP). Here, Antarctic krill (*Euphausia superba*, hereafter referred to as krill) serve as a keystone species and a major food source for marine predators including whales, seals, and penguins<sup>27,30–34</sup>. Local Adélie (*Pygoscelis adeliae*) and gentoo (*Pygoscelis papua*) penguins are both central place foragers, meaning they return to a nest after each foraging trip, with overlapping foraging areas centered over Palmer Deep Canyon (Fig. 1b). Penguin populations in Palmer Deep Canyon have persisted for hundreds of years<sup>35–37</sup>, their diets dependent at least in part on the elevated biomass of krill<sup>38</sup> that persists here in relation to neighboring regions<sup>37,39,40</sup>, establishing Palmer Deep Canyon as a “biological hotspot”. Consequently, Palmer Deep Canyon’s ecosystem hinges on the availability of krill as the trophic link between phytoplankton at the base of the food web and higher predators<sup>41</sup>. In this study, we investigate current-driven controls on the distributions of phytoplankton patches and krill

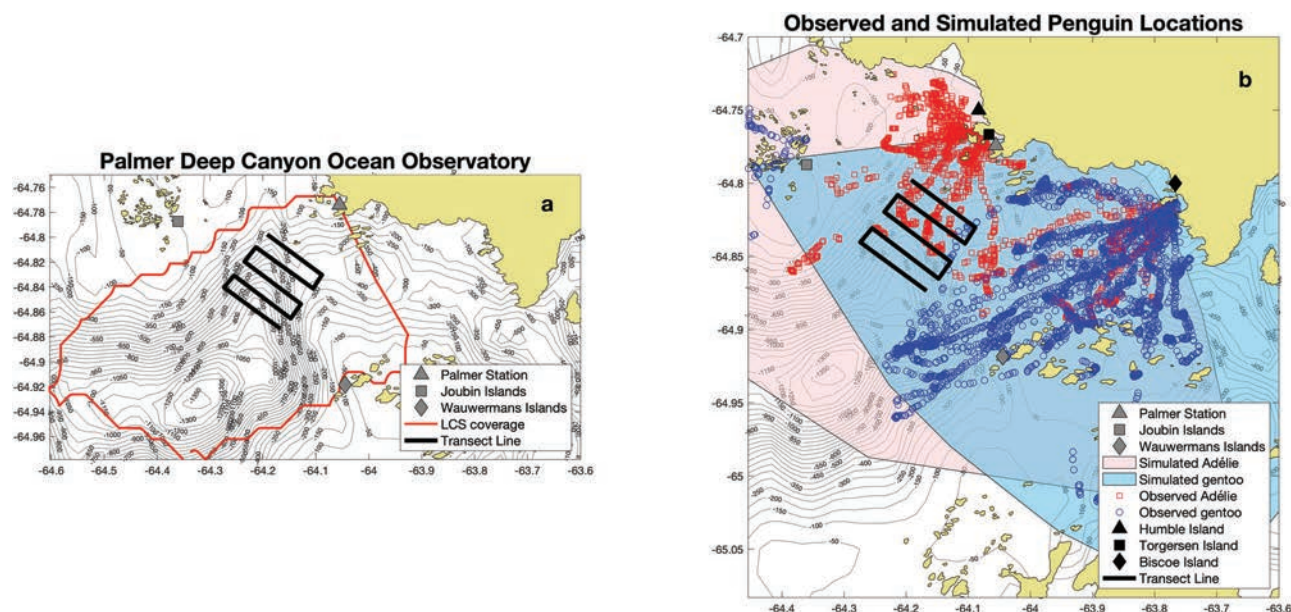


**Fig. 1 | Ocean observatory around Palmer Deep Canyon.** **a** Palmer Deep Canyon study region with the location of the three High Frequency Radars shown with polygons and the area of LCS results contoured. Within the LCS footprint is the transect line of the active acoustic survey used to detect krill and optical survey used to detect phytoplankton patches. Canyon bathymetry is contoured in 50 m isobaths. **b** Penguin positions observed with GPS tags for Adélie (red squares) and gentoo (blue circles) penguins. Convex hulls of simulated Adélie and gentoo penguins are shown in red and blue respectively, the smallest convex polygon that contains the set

of points produced by the simulated penguin tracks. Penguin nests are shown in black polygons. Adélie breeding colonies are located on Humble Island, Torgerson Island, and Biscoe Island, and gentoo breeding colonies on Biscoe Island. Transect line for the surveys that observed krill swarms and phytoplankton patches is shown with a solid black line. Canyon bathymetry is shown in contours of 50 m isobaths. Note that the seemingly straight penguin tracks are likely penguins returning to their nests after satiation.

swarms at the scales of penguin foraging through the use of a multi-platform ocean observing system (Fig. 1a). Integration of multiple observing platforms provides the rare opportunity to analyze the overlapping physical processes and trophic interactions on time and space scales relevant to understanding the physical mechanisms that concentrate high density patches of prey that predators use to efficiently forage.

When integrating both biological and physical observations of an ecosystem, it is important to investigate them at the appropriate space and time scales<sup>42</sup>. Palmer Deep Canyon is a coastal system, characterized by sub-mesoscale ocean currents, strong tidal influences, and short (2–7 days) surface residence times<sup>43</sup>. Similarly, phytoplankton patches have been shown to move through this system quickly (6 h decorrelation)<sup>11</sup>, and most penguin foraging trips are between 6 and 24 h<sup>44</sup>. Previous work has established Palmer Deep Canyon as a fast-moving oceanic habitat, characterized by dynamic physical conditions and a similarly variable biological ecosystem. In this study, we determine if the distribution of krill and foraging penguins at these shorter time and space scales show similar association with LCS-identified transport features as previously observed with phytoplankton<sup>11</sup>, suggesting small-scale and current-driven controls on food web focusing. The present study maps each level of the food web onto dynamic ocean currents at resolutions that resolve interactions between near-shore creatures and complex coastal flow, providing a unique opportunity to deepen our understanding of potential small-scale physical mechanisms of spatial ecology.

## Results

### Dynamic feature mapping with Lagrangian Coherent Structures

In this study we used a high-resolution High Frequency Radar (HFR) network to calculate attracting FTLE, projected at the temporal and spatial resolution of inputted HFR data (1 h, 1 km). FTLE is a metric used to characterize the Lagrangian structure in fluid flows. It measures the rate of separation of initially close particles over a finite time interval, providing insights into the stability and chaotic behavior of the flow (see section 5.7 for details). FTLE maps were calculated each hour with a 1 km spatial resolution (Fig. 2 and Supplementary Movie 1), the same spatial and temporal resolution as the HFR velocity field data. Higher values of LCS indicated a higher influence on the attraction of nearby drifting particles. This analysis produced a time resolved 2-dimensional field of attracting features.

### Phytoplankton patches occurring in transport features

Phytoplankton patches were observed with an ACROBAT, a towed instrument that undulates between the surface and ~50 m depth (see Section 5.3 for details), outfitted with a Wetlabs Ecopuck optical sensor (chlorophyll-a, CDOM fluorescence, and optical backscatter at 700 nm) and a fast-sampling (16 Hz) Seabird 43 FastCAT CTD (conductivity, temperature, and pressure) following transect lines within the HFR footprint (Fig. 1a). MLD was calculated as the depth of maximum buoyancy frequency for each profile<sup>11,45</sup> using data collected via the towed ACROBAT. Phytoplankton patches were determined following methods in Veatch et al.<sup>11</sup> as profiles with an integrated mixed layer backscatter greater than a threshold, and re-analyzed in this study for direct comparison with krill and penguin foraging observations (Section 5.3, Supplementary Fig. 2).

Previous results found phytoplankton patches were associated with higher FTLE values (indicative of stronger attracting features) than a null model<sup>11</sup>. The distribution of FTLE values associated with phytoplankton patches are shifted towards higher FTLE values, peaking around  $0.3 \text{ hr}^{-1}$  while the distribution of FTLE values associated with randomized phytoplankton patches (null model) were more symmetrical, peaking around  $0.22 \text{ hr}^{-1}$  (Fig. 3). Randomized phytoplankton patches were created by generating survey transects in random locations and associating them with LCS (see section 5.6 for details). The distribution of FTLE values associated with observed phytoplankton patches were significantly higher than those of randomized phytoplankton patches (Fig. 3a), according to a one-sided Kolmogorov-Smirnov (KS) test ( $p = 0.01187$ ) which tests whether one sample distribution tends to have greater values than the other. Results were

the same when the null model was confined to the area of the observed transect (see section 5.6 for details) passing a one-sided KS test ( $p = 2.54 \times 10^{-11}$ ).

### Krill swarms occurring in transport features

Krill swarms (Fig. 4) were concurrently mapped using active acoustics during small boat surveys within the HFR footprint (Fig. 1a) during daytime surveys. The small boat was equipped with a hull-mounted EK80. Krill were acoustically detected and parameterized following methods previously used in Palmer Deep Canyon<sup>28,46–48</sup>. Mixed layer depth (MLD) was also observed using a CTD aboard a towed ACROBAT instrument (see Sections 3.2, 5.3). Of the 1749 total krill swarms detected, 687 (~39%) were observed above the MLD. A null model representing random distribution of krill aggregations across the survey area was created to compare to observations.

Observed krill swarms as well as randomized krill swarms from a null model were matched in space and time with FTLE. The density distributions of FTLE for krill swarms (above the MLD, below the MLD, and total) are skewed towards higher FTLE with the peak around  $0.35 \text{ hr}^{-1}$  for krill above the MLD,  $0.33 \text{ hr}^{-1}$  for krill below the MLD, and  $0.35 \text{ hr}^{-1}$  for all krill swarms (Fig. 3b). In contrast, the density distributions of FTLE for randomized krill swarms is relatively symmetrical in shape, peaking at a lower value around  $0.25 \text{ hr}^{-1}$ . A KS test between density distributions of FTLE for observed and randomized krill swarms showed that the distribution of true krill swarms is skewed toward higher FTLE values compared to randomized krill swarms. There was a significant difference between total krill swarms and randomized krill swarms ( $p = 9.57 \times 10^{-14}$ ). This was also true for krill swarms both above and below the MLD ( $p = 0.0028$  and  $p = 5.56 \times 10^{-12}$ , respectively) (Fig. 3b). When all krill swarms were compared to null model confined to the area of the observed transect (see section 5.6 for details) results were the same, passing a one-sided KS test ( $p = 7.16 \times 10^{-39}$ ).

### Adélie and gentoo penguins selecting for transport features

Penguin diving locations, tracked using Fastloc GPS archival tags, showed preference for higher values of FTLE. Similar to the krill swarms, density distributions of FTLE associated with observed Adélie penguin diving locations indicated that Adélie penguins tended to forage in regions with higher FTLE compared to the simulated Adélie penguin tracks (KS test,  $p = 2.7 \times 10^{-5}$ ). Adélie locations with dives less than 10 m deep (KS test,  $p = 2.2 \times 10^{-15}$ ) and locations with dives greater than 10 m deep (KS test,  $p = 0.0017$ ) both showed higher density distributions of FTLE compared to null models, with 10 m representing the average MLD calculated from the towed ACROBAT instrument. Like Adélie penguins, the density distributions of FTLE associated with observed gentoo penguin diving locations was shifted towards higher FTLE values compared to randomized gentoo penguin foraging locations (KS test,  $p < 1.66 \times 10^{-15}$ ). Observed gentoo penguin foraging locations were also associated with higher FTLE values compared to randomized foraging locations for dives with maximum depths above and below 10 m ( $p < 1.15 \times 10^{-13}$  and  $p < 9.6 \times 10^{-12}$ , respectively). The density distributions of FTLE for Adélie and gentoo penguins are shifted towards higher FTLE (Fig. 3c, d). In contrast, the density distributions of FTLE for simulated Adélie and gentoo penguins are relatively symmetrical in shape. For all three of these comparisons (all dives, dives shallower than 10 m, and dives deeper than 10 m), we systematically removed one penguin from the analysis and recomputed the KS test, as each sampling group was O10 penguins. The resulting distributions showed that no individual penguin was driving the shift of Adélie or gentoo penguins toward higher FTLE values (see the grey shaded area in Fig. 3c, d).

## Discussion

In this study, we observed that food web focusing by small-scale currents shapes the spatial ecology of a coastal marine food web at the patch scale of foraging (hours and 100 s of meters to kilometers). Our results show that phytoplankton, krill, and penguins are found in higher attracting FTLE features (LCS), suggesting aggregation of plankton from horizontal ocean



**Fig. 2 | Example FTLE results calculated from High Frequency Radar observed surface currents.** Locations of three HFR stations are denoted with polygons. FTLE results on January 21st 2020 at 16:00 GMT are shown in greyscale with higher FTLE values corresponding with stronger attracting ocean features.

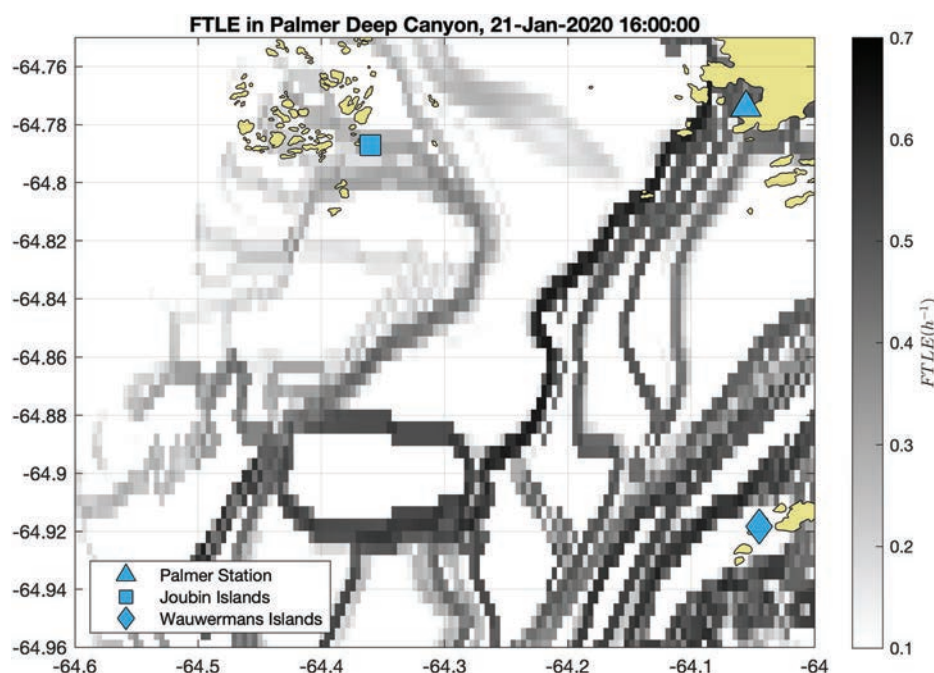
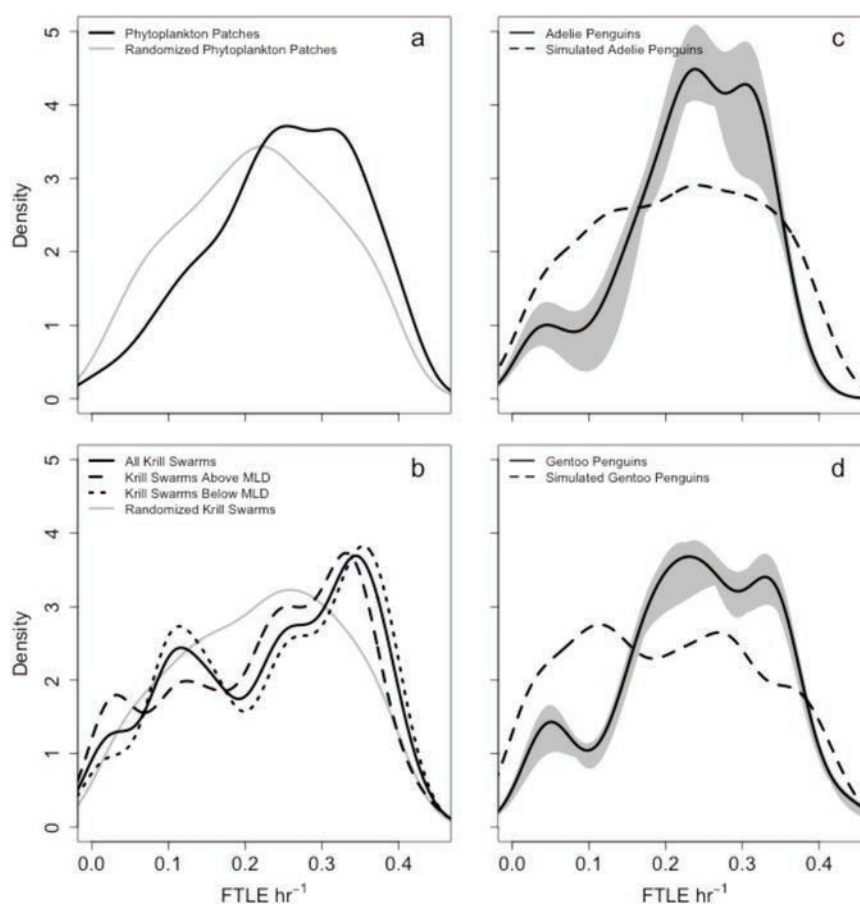


**Fig. 3 | Density distributions of FTLE.** **a** Density distributions of FTLE associated with observed phytoplankton patches (black line) and randomized phytoplankton patches (grey line) previously published in Veatch et al.<sup>11</sup>. Phytoplankton patch FTLE value density distribution were skewed toward higher values compared to randomized phytoplankton patches (KS test,  $p = 0.01187$ ). **b** Density distributions of FTLE associated with observed krill swarms (solid line) above (dashed line) and below (dotted line) the mixed layer depth. All three of these distributions are skewed toward higher FTLE values than randomized krill swarms (grey line) (KS test,  $p = 9.57e-14$ ,  $0.0028$ ,  $5.56e-12$ ). **c** Adélie and **d** gentoo tagged penguin FTLE values shown in solid line and randomized penguin FTLE values with dashed line. Grey regions represent the distributions of either Adélie or gentoo penguins if individual birds were systematically excluded from the analysis. This was done to determine if an individual bird was driving the results. Both Adélie and gentoo FTLE distributions were skewed toward higher values compared to FTLE values with simulated penguins (KS test,  $p = 2.7e-5$ ,  $p < 1.66e-15$ ). All curves are kernel density estimates computed with a density function within the statistic package of  $R^{36}$ , with the bandwidth of the kernel smoother set to 0.03. These density curves visualize the frequency of the underlying data.



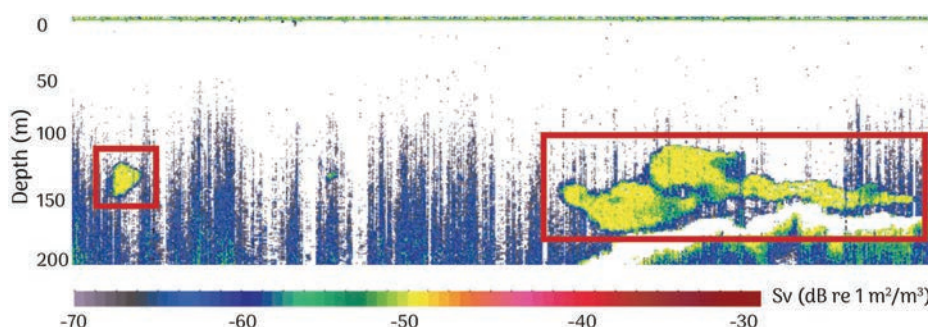
transport is an important factor in the spatial ecology of Palmer Deep Canyon and providing the first evidence, to the best of our knowledge, of LCS selection at these scales across primary producers, primary consumers, and predators.

#### Interactions with ocean transport from each trophic level

The three trophic levels tested in this study span a wide range of Reynolds numbers with significant differences in their behavior and in the dependence of their movement on ocean currents. The passive particles used in



**Fig. 4 | Example of acoustic detection of krill swarms.** Echogram from survey (see Fig. 1a for survey path) with ACROBAT deployment. Dense yellow regions outlined in red boxes were detected as krill using a threshold of  $-70$  to  $-30$  dB. Raw acoustic data was processed in Echoview software, following methods of Tarling et al.<sup>47,48</sup> to identify krill swarms from all other backscatter.



LCS calculations most closely approximate the non-motile characteristics of phytoplankton at the scales of this study ( $Re \sim 10^{-2}$ , estimated from length scale<sup>7</sup>). The correlation between phytoplankton patches and LCS, their immobility, and their slow growth rates compared to local surface residence time<sup>43</sup> suggests that these patches are formed through horizontal ocean transport.

Unlike the largely passive phytoplankton cells, krill exhibit movement behavior relative to local ocean currents ( $Re \sim 10^3$ ) and migrate vertically based on the sun angle<sup>49</sup>, which means they can both be transported by ocean currents and swim somewhat independently of them. Our analysis used only passive particles and current velocities at the surface, yet surprisingly, high FTLE values indicated that krill both above and below the MLD were preferentially associated with surface concentrating features. Dynamics below the mixed layer are outside the scope of this study, but we can speculate why krill below the MLD would have higher FTLE values than a null model using surface particles. Krill below the MLD may have recently migrated down from within the mixed layer, and have not yet become decorrelated with surface currents. It is also possible that the velocity field below the MLD may be similar to that in the mixed layer, concentrating sub-surface krill in similar patterns to those reflected in the surface. Similarities between the surface and the sub-surface velocity fields could be driven by this region's barotropic tides<sup>50</sup>, creating similar concentrating features in the sub-surface as in the surface velocities used to calculate FTLE. Finally, krill may be attracted to locally concentrated phytoplankton in higher FTLE values, indicating that both advection and behavior explain their affinity for LCS features with high FTLE values. Regardless of the mechanism, these results suggest that the distribution of krill in Palmer Deep is affected by food web focusing driven by small scale currents.

Foraging penguins have very high Reynolds numbers ( $Re \sim 10^6$ ), indicating that they may move independently of currents. As a result, their distribution is expected to be most unlike the passive particles used in the LCS calculations. Results from this study show that penguin foraging behavior leads to spatial distribution in which there is more frequent penguin dives around locations with strong concentrating features (high FTLE). This suggests that while penguins may not actively seek out LCS, they are more likely to dive once they reach these features and find concentrated prey. Similar conclusions were drawn by a previous study investigating elephant seals interacting with larger scale currents<sup>51</sup>, showing that elephant seals increase their foraging dives when at distinct oceanographic features. Unlike the elephant seals, Adélie and gentoo penguins will return straight to their nests once satiated, which creates the directed return journeys in the penguin tracks (Fig. 1b).

Penguin dives above and below the MLD, associated with stronger FTLE values, suggest that while penguins may use surface cues to initiate dives, they do not limit their foraging to the surface layer. This result is consistent with findings in krill distributions, where krill swarms both above and below the MLD were associated with strong FTLE. Penguins and other marine mammals transit near the ocean surface from where they dive to search and forage for their prey, exhibiting a variety of movement modes<sup>52–54</sup>. Although dive location and frequency can be quantified, little is

known about the selective interactions of animals during their foraging trips that produce these patterns<sup>55</sup>, including whether animals actively search for prey or use environmental cues associated with prey<sup>56</sup>. Emerging theories suggest that selection for environmental cues is likely<sup>57</sup>, but it is unknown if Adélie or gentoo penguins respond to prey or environmental cues. Further research is needed to identify the surface cues Adélie and gentoos use to decide when to dive for prey.

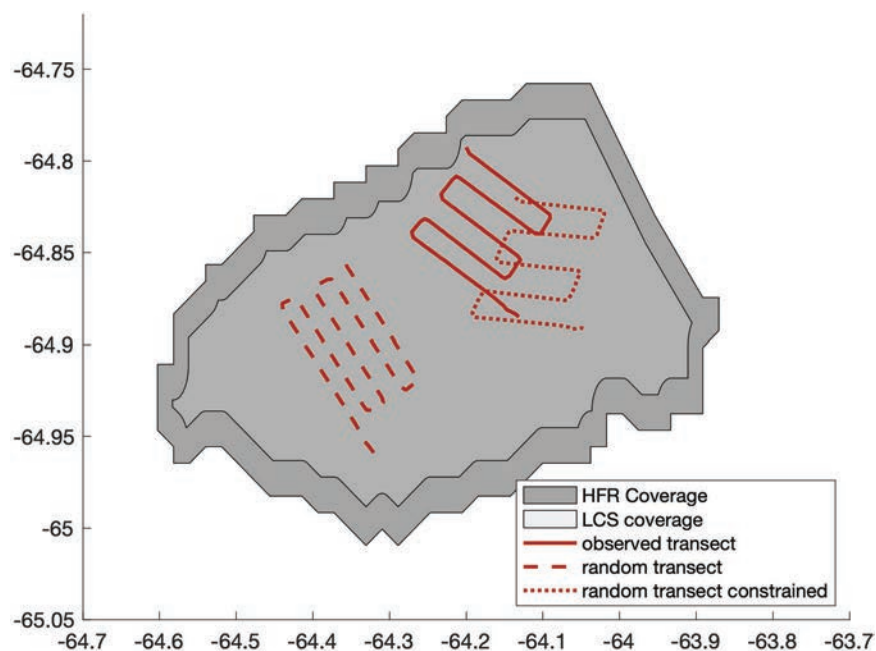
Despite the wide range in the Reynolds numbers of our study species, each species showed selectivity for horizontally concentrating features (LCS) derived from passive particle trajectories. As species size and Reynolds number increases, so does the complexity of their relationship to LCS. Phytoplankton have low Reynolds numbers, and their distributions are likely dominated by ocean transport. Krill have intermediate Reynolds numbers, and their selection for LCS likely reflects a combination of physical concentration by attractive features and behavioral attraction to phytoplankton patches. Lastly, Penguins have high Reynolds numbers and behavior-driven distributions, so their selection for LCS is likely dominated by foraging behavior concentrated at krill patches. Such selectivity across species with varying Reynolds numbers demonstrates the importance of ocean transport to multiple levels of the food web.

### Observations of small-scale ocean transport with Lcs

Selection by multiple levels of the food web for LCS quantified by FTLE at a 6-h integration suggests that FTLE capture transport patterns that create small-scale (sub-tidal) food web focusing. FTLE is a paired particle tracking technique, meaning that it uses relative distances between neighboring particles to quantify attraction and repulsion. This allows FTLE to quantify attracting features with little influence of the particle's starting position, unlike the single particle tracking methods<sup>11</sup>. FTLE also assigns scalar quantities to attracting features based on separation rate of neighboring particles (backwards in time, particle accumulation rate), allowing FTLE to account for rate of change of particle position rather than position alone. Additionally, FTLE integrate over particle trajectories, adding “memory” of particle position to the calculation of attracting features. Yet another strength of this method is the integration over time, which pairs well with the high temporal resolution of the HFR velocity data. The incorporation of relative particle motion and integration over particle trajectories makes FTLE a powerful tool for quantifying small-scale transport compared to the use of particle trajectories on their own.

FTLE patterns at these scales are highly variable in space and time, yet ubiquitous throughout the study system (Supplementary Movie 1 and Fig. 1). The null model sensitivity test showed similar results when the null model was constrained to the area closer to the observed transect rather than the entire LCS bounds (Fig. 5). Therefore, FTLE are not concentrated over the observed transect but throughout the study region. It is unknown whether penguins select their colony locations based on proximity to heightened LCS features. This study sets the groundwork for future investigations into whether coastal regions on the WAP near persistent penguin colonies have heightened FTLE activity compared to regions without such colonies.

**Fig. 5 | Example of null model.** The area of LCS coverage is plotted in light grey, shrunk from HFR coverage (dark grey) to exclude edges of data. The transect where phytoplankton patches and krill swarms were observed is plotted with a solid red line, and one of the randomly rotated and translated transects is plotted with a dashed red line. A sensitivity test was conducted on the null model, constraining “randomly generated” transects to the northeast of the solid black line. A randomly rotated and translated transect confined to northeast of the black line is plotted with a dotted red line. Figure modified from Veatch et al.<sup>11</sup> Fig. 3.



In addition to identifying areas of attraction, strong FTLE will appear as horizontal transport barriers, which manifest as horizontal buoyancy gradients (fronts and edges of eddies) in ocean velocity fields. This makes areas of high FTLE oceanographically distinct from areas with low FTLE values. While attractive transport is likely to be a large reason why phytoplankton and zooplankton are associated with high FTLE values, it is unclear if Adélie and gentoo penguins are able to select for areas of high FTLE based on a learned oceanographic cue or if they are able to perceive large krill swarms and those happen to be at areas of high FTLE. Future work is needed to investigate penguin (and other forager) behavior that leads to their association with areas of high FTLE.

### Limitations and caveats

There are several biological processes that limit the conclusions that can be made with these observational data. Mapping of prey, which was conducted through small boat surveys twice weekly, provides a snapshot in time of a prey field that is constantly evolving. The timing of observation within the process of food web focusing is unknown. For example, an area where there was an LCS-identified transport feature could have been observed shortly after a predator fed on a krill swarm. Our observations would show that an LCS-identified transport feature was there without presence of food web focusing, when in fact there was. Our observations could have also occurred before the ecosystem was able to respond to the presence of the LCS, perhaps showing high phytoplankton but no krill, or krill swarms but no penguin foraging. Additionally, far fewer predators (penguins) exist than prey (krill), making it more difficult to correlate predators to food web focusing events. With these caveats in mind, the patterns that were observed likely underestimate the food web focusing effect of small-scale transport.

### Local and global implications

Results and conclusions from this study increase our understanding of how a coastal biological hotspot is maintained in the context of a larger marine ecosystem. Palmer Deep Canyon was once considered to be a location where phytoplankton production is driven by local upwelling<sup>40</sup>. Recent studies provide evidence against this, showing instead almost no stratified summertime occurrence of nutrient-rich Upper Circumpolar Deepwater in the photic zone<sup>58</sup>. Further, production is light limited rather than nutrient limited<sup>59</sup>, suggesting little reliance on locally upwelled nutrient rich waters.

Furthermore, a deep, recirculating eddy driven by the bathymetry of Palmer Canyon has the ability to trap krill performing diurnal vertical migration<sup>60</sup>. This feature may provide a seasonal reservoir of krill, which migrate to the surface, and are then aggregated in surface LCS structures. Emerging theories propose that high concentrations of phytoplankton<sup>40</sup> are advected from the shelf break where upwelling of nutrient-rich Upper Circumpolar Deep Water fuels phytoplankton blooms<sup>61,62</sup>. Future work is needed to further investigate larger scale, regional transport that reflects climate scale impacts in the WAP region. Our results further emphasize the importance of ocean transport in this system not just for local phytoplankton abundance but throughout the food web. Oceanographic transport patterns that reliably concentrate prey could be a reason penguins colonies have persisted in this region over ecological time scales<sup>37</sup>. As Palmer Deep Canyon and other ecosystems along the WAP experience rapid warming<sup>63–65</sup>, sustained observations are needed to determine if these transport patterns that local food webs rely on will change. Future work must also investigate the fate of the sources of plankton that are being delivered to the system in order to predict Palmer Deep Canyon’s resistance to changing climate. A depletion of these sources could be detrimental to Palmer Deep Canyon’s ecosystem even if transport patterns are maintained.

Selectivity of LCS calculated with short integrations by intermediate and upper trophic levels illustrates the importance of small-scale transport features in the spatial ecology of coastal systems. This not only supports the emerging theory of trophic focusing by physical ocean processes<sup>4</sup>, but demonstrates that these processes occur on the sub-mesoscale. Correlations between LCS and phytoplankton, zooplankton, and top predators stress the importance of incorporating LCS as a covariate in predictions of spatial ecology in marine systems.

Our study provides a link between the preyscape of a coastal ecosystem and ocean transport. This relationship fills the gap in previous studies that link phytoplankton and top predators’ distributions to ocean transport without considering the critical mid-trophic level zooplankton. Results also provide a useful tool for the marine ecological community to quantify ocean transport features, namely FTLE. FTLE, although more computationally complex than single particle tracking techniques such as Relative Particle Density<sup>11,66</sup>, have been shown to quantify transport features that are selected by each level of the Palmer Deep Canyon food web, justifying their use in dynamic coastal environments. Connections between ocean movement and spatial ecology improve current understanding of how local populations use

their ocean habitats, enabling more informed conservation strategies to protect areas of prey accumulation, mitigating anthropogenic impacts on coastal ecosystems.

## Methods

An ocean observatory was deployed around Palmer Deep Canyon during January–March 2020, mapping phytoplankton, zooplankton, and penguin foraging behavior onto physical ocean processes. The following section describes the small boat surveys that were conducted along a transect twice weekly to observe phytoplankton and zooplankton as well as the HFR array observations and tagged penguin measurements that overlapped with this transect.

### High Frequency radar

Three High Frequency Radars were deployed around Palmer Deep Canyon, using doppler-shifted radio waves backscattered from ocean waves to produce vector maps of surface current velocities each hour. HFRs were deployed on the Joubin Islands, Wauwermans Islands, and at Palmer Station (Fig. 1). Remote sites (Joubin and Wauwermans) were each accompanied by a remote power module, described in refs. 67,68. Radial components from each radar<sup>69</sup> were added together with an optimal interpolation algorithm<sup>70</sup> and gap filled<sup>71</sup> as described in refs. 11,72. The resulting data product is an evolving hourly map of ocean surface currents over a 1 km spatial grid.

### Calculating mixed layer depth

On the active acoustic survey transects (Fig. 1a), an ACROBAT (Autonomous Conductivity, temperature, and depth Rapidly Oscillating Biological Assessment Towed) was towed, equipped with a fast-sampling (16 Hz) Seabird FastCAT CTD (conductivity, temperature, and pressure). This instrument undulated between the surface and about 50 m depth, profiling the upper water column about every 300 m in the horizontal. For each profile, MLD was determined as the depth with the maximum buoyancy frequency following methods in Carvalho et al.<sup>45</sup>. MLD measurements were used to calculate mixed layer optical backscatter (Section 5.3) and to determine if krill swarms were above or below the MLD (section 5.4). ACROBAT profiles were matched with observed krill swarms in space and time, assigning a MLD to each krill swarm. If the depth of the krill swarm was shallower than the ACROBAT observed MLD, the swarm was considered to be within the mixed layer.

### Optical surveys

Towed ACROBAT surveys were conducted twice weekly collecting optical measurements of the water column along transects shown in Fig. 1a. Methods for identifying phytoplankton patches with ACROBAT optical measurements followed those in Veatch et al.<sup>11</sup>, and are explained thoroughly there. In short, the ACROBAT profiled between the surface and about 60 m, completing a profile about every 300 m of horizontal distance traveled. Profiles were determined as “within a phytoplankton patch” or “not in a phytoplankton patch” based on a daily threshold of integrated mixed layer optical backscatter. In this system, optical backscatter is a good proxy for phytoplankton biomass and avoids the problem of non-photochemical quenching that is associated with measuring phytoplankton fluorometrically. Consecutive profiles designated as “within a phytoplankton patch” were assumed to be in the same phytoplankton patch (Supplementary Fig. 2).

Each ACROBAT profile was assigned an FTLE value based on the closest FTLE grid point to the profile in space and time. Phytoplankton patches made up of multiple profiles were assigned an FTLE value based on the average FTLE value assigned to the profiles within that phytoplankton patch.

### Acoustic surveys

Active acoustic surveys were conducted twice weekly using a hull-mounted SIMRAD EK80 single-beam, single frequency (120 kHz) echosounder

**Table 1 | Tagged penguins by colony**

Colony	Penguins tagged	Trips recorded
Adélie - Humble Island	12	23
Adélie - Torgersen Island	13	24
Adélie - Biscoe Island	5	13
Gentoo - Biscoe Island	14	32

Number of individual Adélie and gentoo penguins tagged per colony.

(Kongsberg Maritime) along transects shown in Fig. 1a. The echosounder was configured with a 1 s ping rate, 512  $\mu$ s pulse duration, and 24  $\mu$ s sampling duration. Calibrations of the echosounder were performed in the vicinity of Palmer Deep Canyon using a tungsten sphere (diameter = 38.1 mm) during February, 2020. Acoustic data were processed in Myriax Echoview software version 11.1 following methods from Tarling et al.<sup>47</sup> and Tarling et al.<sup>48</sup>. Raw data were processed to consider the echosounder calibration and in situ ocean acoustic conditions via incorporation of onboard CTD data, and to remove background noise and other interferences via the Background Noise Removal<sup>73</sup> and Impulse Noise Removal<sup>74</sup> algorithms in Echoview. Krill were then detected using a target strength threshold of  $-70$  dB to  $-30$  dB<sup>47,48</sup> in Echoview following similar parameterization and protocols to Nardelli et al.<sup>28</sup> and Reiss et al.<sup>75</sup> (Fig. 3).

All acoustically detected krill swarms were manually reviewed before exporting the acoustic data in Nautical Area Scattering Coefficient (NASC) values, a common proxy for organism presence in acoustic measurements. NASC values were calculated per detected swarm and exported along with depth, GPS position (longitude and latitude), swarm height, swarm length, and backscatter (Sv). These methods for acoustic surveys and processing of subsequent acoustic data follow those in Hann et al.<sup>46</sup>.

### Penguin tagging

Adélie penguin colonies were located on Humble Island (64°45'S, 64°05'W), Torgersen Island (64°46'S, 64°04'W), and Biscoe Island, (64°48'S, 63°46'W), with the latter location also including a colony of gentoo penguins (Fig. 1b). Both species were double tagged with GPS tags and time-depth recorders measuring pressure at 0.5 Hz while wet. Penguins were GPS tagged with either a Lotek FastGPS (F5G 234B, 35 g), Sirtrack Fastloc 3 loggers (30 g) or IgotU GT-600 (35 g, Mobile Action Technology, Taiwan). IgotU loggers were encased in adhesive-line heat shrink tubing. The time-depth recorders were either a Lotek LAT1810 (10 g) or StarOddi DST CTD (22 g). Tags were adhered to the anterior feathers on the lower dorsal area of the penguin. All protocols were carried out in accordance with the approved guidelines of the Columbia University (Assurance #AAAS2504) Institutional Animal Care and Use Committee for the 2019–2020 season. Tags were generally deployed on individuals for 2–4 days before being removed and reattached to another penguin. We tagged 30 Adélie and 14 gentoo penguins over the course of the austral summers (Table 1).

Drift in the depth data for tags was zero offset corrected using the *calibrateDepth* function in the R package *diveMove*<sup>76</sup>. Drift was not corrected for 7 deployments, as on 6 of these deployments (all Adélies, 5 Humble Island, 1 Torgersen Island) depth recordings shallower than 1 meter were not taken, and on 1 deployment (1 Adélie, Humble Island) depth recordings shallower than 5 meters were not taken. GPS data were filtered for erroneous locations based on improbable swimming speeds ( $>2.8$  m s<sup>-1</sup>). GPS location and TDR data were time matched and dives were identified using the *diveStats* function in *diveMove*<sup>76</sup>.

Penguin data collection was conducted by Polar Oceans Research Group (PORO) as part of project SWARM.

### Creating null models

Distribution of LCS where phytoplankton patches and krill swarms were observed in our transects were compared to those along simulated “null model” phytoplankton patches and krill swarms. The phytoplankton and krill null models were created by randomly moving the observed



distribution of phytoplankton and krill within the LCS field (Fig. 5), maintaining the observed phytoplankton patch and krill swarm size and distribution along the transect. Each of the thirteen surveys were rotated and translated 100 times, creating 100 randomized locations of each observed phytoplankton patch and krill swarm while maintaining the shape of the survey. This ensured that the survey shape did not contribute to differences found between observed and null model phytoplankton patches and krill swarms. These randomized locations make up the phytoplankton and krill null model. Methods for using the survey transect to create the null model were adapted from Veatch et al.<sup>11</sup>.

A sensitivity study was conducted on the null model to test if the differences between the null model and observations were due to the area where the survey was conducted having more FTLE than elsewhere in the study area. A new model was created following above methodology but requiring the randomly moved transects to be within a smaller area closer to the observed transect (northeast of the black line in Fig. 5). This constrained null model produced the same results as the original null model (see Results).

Distribution of LCS selected by penguin GPS locations were compared to those along simulated “null model” penguin tracks. Penguin null models were created with simulated Brownian motion of central place foragers (simmm.bb in the adehabitatLT R package)<sup>77</sup>, having the simulated penguin tracks return to the Adélie and gentoo colonies at the end of each trip (Fig. 1b). Each day that we had overlapping penguin observed data and LCS results from HFR-observed surface currents, ten penguin trips were simulated for each species. These trips were limited to 24 h, and simulated penguin speeds were normally distributed around a mean of 4 km hr<sup>-1</sup> with a maximum of 8 km hr<sup>-1</sup>. These limitations were set to mimic average foraging trip duration (6–24 h)<sup>44</sup> and swimming speeds<sup>78</sup> of Adélie and gentoo penguins. The Brownian motion used to create these tracks is uncorrelated. Therefore, simulated tracks represent random foragers that do not select for environmental features or remembering previous feeding locations. Simulated penguin locations were used as a null metric for all the available LCS values for non-selecting central place foragers. Methods for the creation of simulated Adélie and gentoo tracks were adapted from Oliver et al.<sup>66</sup>.

### Calculating Lagrangian Coherent Structures

LCS were calculated from the HFR observed surface currents using the FTLE metric. FTLE were calculated beginning with a velocity field over a selected time interval (in this case, 6 h). Then, from the derivative of the flow map the Cauchy-Green strain tensor field (C) and eigenvector field ( $\lambda_i$ ) were computed to be used in Eq. (1):

$$S(x_0) = [\max_{i=N^{\lambda_i}} (C(x_0))]^{1/2} \quad (1)$$

where  $S(x_0)$  is the maximum stretching around point  $x_0$ . FTLE is then computed over a finite time (T)<sup>10,79–81</sup>. The resulting FTLE field changes in space and time with inputted HFR observed velocity field. These methods follow those in Veatch et al.<sup>11</sup>.

### Matching observed presence of null models to LCS

To associate krill and penguin presence with LCS, observations were matched in both space and time. LCS results were calculated each hour and at a 1 km spatial resolution to match the resolution of inputted HFR velocity data. Krill swarms and penguin locations were matched to the nearest hour of LCS map. This means that for the LCS results computed for 13:00 on January 15th, all krill and penguin location observations between 12:30 and 13:30 on January 15th were compared to the LCS results from 13:00. To match krill and penguin presence with LCS in space, a haversine function<sup>82</sup> was used to find the closest LCS result grid point (using the center of the grid point) to the krill or penguin location. The LCS value in that grid point for the LCS results on the nearest hour were associated with the krill or penguin observation. The same was done for null models.

### Kolmogorov-Smirnov tests

Two-sample Kolmogorov-Smirnov (KS) tests<sup>83</sup> were used to determine if there are significant differences between the empirical distribution functions of observations and null models. KS tests are conducted using Eq. (2):

$$D = \sup_x |F_{n,1}(x) - F_{n,2}(x)| \quad (2)$$

where D is the test statistic,  $F_{n,1}(x)$  and  $F_{n,2}(x)$  are the empirical distribution functions of the two samples. A small *p*-value from the KS test means that the two samples come from different distributions. One-sided KS tests are especially good at determining if the tails of two cumulative distributions are significantly different from each other.

### Reporting summary

Further information on research design is available in the Nature Portfolio Reporting Summary linked to this article.

### Data availability

Data and code used in this study are publicly available on NSF funded project SWARM's BCO-DMO site and GitHub. High Frequency Radar observed surface currents are available in the gap-filled version used in this study on BCO-DMO<sup>84</sup>. Lagrangian Coherent Structure Results for FTLE metrics are available on BCO-DMO<sup>85</sup>. EK80 acoustic data used to detect krill swarms are available on BCO-DMO ACROBAT data used to detect phytoplankton patches are available on BCO-DMO<sup>86</sup>. Penguin GPS tag data are available University of Delaware's public archive ([http://modata.ceoe.udel.edu/public/Antarctica\\_2020/SWARM\\_Penguin\\_CSVs/](http://modata.ceoe.udel.edu/public/Antarctica_2020/SWARM_Penguin_CSVs/)). Any questions can be directed to Jacquelyn Veatch (jveatch@whoi.edu).

### Code availability

Code used to gap-fill High Frequency Radar data are available on GitHub ([https://github.com/JackieVeatch/SWARM\\_CODAR](https://github.com/JackieVeatch/SWARM_CODAR)). The code used to produce LCS results can be found on GitHub ([https://github.com/JackieVeatch/SWARM\\_LCS](https://github.com/JackieVeatch/SWARM_LCS)). The code was modified from open-source MATLAB library<sup>80</sup> for use on HFR data. All other code for analysis can be found on GitHub ([https://github.com/JackieVeatch/SWARM\\_analysis](https://github.com/JackieVeatch/SWARM_analysis), [https://github.com/JackieVeatch/SWARM\\_Krillanalysis](https://github.com/JackieVeatch/SWARM_Krillanalysis), and [https://github.com/JackieVeatch/SWARM\\_PenguinAnalysis](https://github.com/JackieVeatch/SWARM_PenguinAnalysis)). Any questions can be directed to Jacquelyn Veatch (jveatch@whoi.edu).

Received: 9 September 2024; Accepted: 5 February 2025;

Published online: 20 February 2025

### References

- Marquet, P. A. et al. Ecological and evolutionary consequences of patchiness: a marine-terrestrial perspective in *Patch dynamics* 277–304 (Berlin, Heidelberg: Springer Berlin Heidelberg, 1993).
- Cheriton, O. M. et al. Effects of mesoscale physical processes on thin zooplankton layers at four sites along the west coast of the US. *Estuaries Coasts* **30**, 575–590 (2007).
- Benoit-Bird, K. J. et al. Prey patch patterns predict habitat use by top marine predators with diverse foraging strategies. *PLoS ONE* **8**, e53348 (2013).
- Genin, A. Bio-physical coupling in the formation of zooplankton and fish aggregations over abrupt topographies. *J. Mar. Syst.* **50**, 3–20 (2004).
- Stommel, H. Varieties of oceanographic experience: the ocean can be investigated as a hydrodynamical phenomenon as well as explored geographically. *Science* **139**, 572–576 (1963).
- Benoit-Bird, K. J. Resource patchiness as a resolution to the food paradox in the sea. *Am. Nat.* <https://doi.org/10.1086/727473> (2023).
- Mann, K. & Lazier, J. *Dynamics of Marine Ecosystems* (3rd ed.) (Wiley, 2013).
- Power, J. H. Simulations of the effect of advective-diffusive processes on observations of plankton abundance and population rates. *J. Plankton Res.* **18**, 1881–1896 (1996).



9. Keister, J. E., Di Lorenzo, E., Morgan, C., Combes, V. & Peterson, W. Zooplankton species composition is linked to ocean transport in the Northern California current. *Glob. Change Biol.* **17**, 2498–2511 (2011).
10. Haller, G. Lagrangian coherent structures. *Annu. Rev. Fluid Mech.* **47**, 137–162 (2015).
11. Veatch, J. M., Kohut, J. T., Oliver, M. J., Statscewich, H. & Fredj, E. Quantifying the role of submesoscale Lagrangian transport features in the concentration of phytoplankton in a coastal system. *ICES J. Mar. Sci.* **81**, 760–773 (2024).
12. Lehahn, Y., d'Ovidio, F. & Koren, I. A satellite-based lagrangian view on phytoplankton dynamics. *Annu. Rev. Mar. Sci.* **10**, 99–119 (2018).
13. Lehahn, Y., d'Ovidio, F., Lévy, M. & Heifetz, E. Stirring of the northeast Atlantic spring bloom: a Lagrangian analysis based on multisatellite data. *J. Geophys. Res. - Oceans* **112**, C08005–C08005 (2007).
14. Hernández-Carrasco, I., Orfila, A., Rossi, V. & Garçon, V. Effect of small scale transport processes on phytoplankton distribution in coastal seas. *Sci. Rep.* **8**, 8613–8613 (2018).
15. Huhn, F., von Kameke, A., Pérez-Muñuzuri, V., Olascoaga, M. J. & Beron-Vera, F. J. The impact of advective transport by the South Indian Ocean Countercurrent on the Madagascar plankton bloom. *Geophys. Res. Lett.* **39**, n/a (2012).
16. Baudena, A. et al. Fine-scale structures as spots of increased fish concentration in the open ocean. *Sci. Rep.* **11**, 15805 (2021).
17. Emilie Tew, K. et al. Top marine predators track lagrangian coherent structures. *Proc. Natl. Acad. Sci. USA* **106**, 8245–8250 (2009).
18. Fahlbusch, J. A. et al. Blue whales increase feeding rates at fine-scale ocean features. *Proc. R. Soc. B, Biol. Sci.* **289**, 20221180 (2022).
19. Goldbogen, J. A. et al. Mechanics, hydrodynamics and energetics of blue whale lunge feeding: efficiency dependence on krill density. *J. Exp. Biol.* **214**, 698–699 (2011).
20. Lomartire, S., Marques, J. C. & Gonçalves, A. M. M. The key role of zooplankton in ecosystem services: a perspective of interaction between zooplankton and fish recruitment. *Ecol. Indic.* **129**, 107867 (2021).
21. Maps, F. et al. Linking acoustics and finite-time Lyapunov exponents reveals areas and mechanisms of krill aggregation within the Gulf of St. Lawrence, eastern Canada. *Limnol. Oceanogr.* **60**, 1965–1975 (2015).
22. St-Onge-Drouin, S., Winkler, G., Dumais, J.-F. & Senneville, S. Hydrodynamics and spatial separation between two clades of a copepod species complex. *J. Mar. Syst.* **129**, 334–342 (2014).
23. Fahlbusch, J. A. et al. Submesoscale coupling of krill and whales revealed by aggregative Lagrangian coherent structures. *Proc. R. Soc. B* **291**, 20232461 (2024).
24. Santora, J. A. et al. Krill space: a comparative assessment of mesoscale structuring in polar and temperate marine ecosystems. *ICES J. Mar. Sci.* **69**, 1317–1327 (2012).
25. Bernard, K. S. et al. Factors that affect the nearshore aggregations of Antarctic krill in a biological hotspot. *Deep-Sea Res. Part I: Oceanogr. Res. Pap.* **126**, 139–147 (2017).
26. Bernard, K. S. & Steinberg, D. K. Krill biomass and aggregation structure in relation to tidal cycle in a penguin foraging region off the Western Antarctic Peninsula. *ICES J. Mar. Sci.* **70**, 834–849 (2013).
27. Warren, J. D., Santora, J. A. & Demer, D. A. Submesoscale distribution of Antarctic krill and its avian and pinniped predators before and after a near gale. *Mar. Biol.* **156**, 479–491 (2009).
28. Nardelli, S. C. et al. Krill availability in adjacent Adélie and gentoo penguin foraging regions near Palmer Station, Antarctica. *Limnol. Oceanogr.* **66**, 2234–2250 (2021).
29. Pickett, E. P. et al. Spatial niche partitioning may promote coexistence of *Pygoscelis* penguins as climate-induced sympatry occurs. *Ecol. Evol.* **8**, 9764–9778 (2018).
30. Chapman, E. W., Hofmann, E. E., Patterson, D. L. & Fraser, W. R. The effects of variability in Antarctic krill (*Euphausia superba*) spawning behavior and sex/maturity stage distribution on Adélie penguin (*Pygoscelis adeliae*) chick growth: a modeling study. *Deep Sea Res. Part II: Topical Stud. Oceanogr.* **57**, 543–558 (2010).
31. Nicol, S. et al. Krill (*Euphausia superba*) abundance and Adélie penguin (*Pygoscelis adeliae*) breeding performance in the waters off the Béchervaise Island colony, East Antarctica in 2 years with contrasting ecological conditions. *Deep Sea Res. Part II: Topical Stud. Oceanogr.* **55**, 540–557 (2008).
32. Nowacek, D. P. et al. Super-aggregations of krill and humpback whales in Wilhelmina Bay, Antarctic Peninsula. *PLoS ONE* **6**, e19173 (2011).
33. Santora, J. A. & Reiss, C. S. Geospatial variability of krill and top predators within an Antarctic submarine canyon system. *Mar. Biol.* **158**, 2527–2540 (2011).
34. Santora, J. A., Reiss, C. S., Cossio, A. M. & Veit, R. R. Interannual spatial variability of krill (*Euphausia superba*) influences seabird foraging behavior near Elephant Island, Antarctica. *Fish. Oceanogr.* **18**, 20–35 (2009).
35. Fraser, W. R. & Trivelpiece, W. Z. Factors Controlling the Distribution of Seabirds: Winter-Summer Heterogeneity in the Distribution of Adélie Penguin Populations 257–272 (American Geophysical Union, Washington, D. C, 1996).
36. Emslie, S. D., Fraser, W., Smith, R. C. & Walker, W. Abandoned penguin colonies and environmental change in the Palmer Station area, Anvers Island, Antarctic Peninsula. *Antarct. Sci.* **10**, 257–268 (1998).
37. Schofield, O. et al. Penguin biogeography along the west Antarctic Peninsula: testing the canyon hypothesis with palmer LTER observations. *Oceanography* **26**, 204–206 (2013).
38. Fraser, W. R. & Trivelpiece, W. Z. Palmer LTER: relationships between variability in sea-ice coverage, krill recruitment, and the foraging ecology of Adélie penguins. *Antarct. J. U. S.* **30**, 271 (1995).
39. Fraser, W. R. & Trivelpiece, W. Z. Factors controlling the distribution of seabirds: Winter-summer heterogeneity in the distribution of Adélie penguin populations. *Found. Ecol. Res. West Antarct. Penins.* **70**, 257–272 (1996).
40. Kavanaugh, M. T. et al. Effect of continental shelf canyons on phytoplankton biomass and community composition along the western Antarctic Peninsula. *Mar. Ecol. Prog. Ser.* **524**, 11–26 (2015).
41. Schofield, O. et al. Antarctic pelagic ecosystems on a warming planet. *Trends Ecol. Evol.* **39**, 1141–1153 (2024).
42. Root, T. L. & Schneider, S. H. Ecology and climate: research strategies and implications. *Science* **269**, 334–341 (1995).
43. Kohut, J. T. et al. Variability in summer surface residence time within a West Antarctic Peninsula biological hotspot. *Philos. Trans. R. Soc. Lond. Ser. A: Math., Phys., Eng. Sci.* **376**, 20170165–20170165 (2018).
44. Oliver, M. J. et al. Adélie penguin foraging location predicted by tidal regime switching. *PLoS ONE* **8**, e55163–e55163 (2013).
45. Carvalho, F., Kohut, J., Oliver, M. J. & Schofield, O. Defining the ecologically relevant mixed-layer depth for Antarctica's coastal seas. *Geophys. Res. Lett.* **44**, 338–345 (2017).
46. Hann, A. M., Bernard, K. S., Kohut, J., Oliver, M. J. & Statscewich, H. New insight into *Salpa thompsoni* distribution via glider-borne acoustics. *Front. Mar. Sci.* **9**, <https://doi.org/10.3389/fmars.2022.857560> (2023).
47. Tarling, G. A. et al. Variability and predictability of Antarctic krill swarm structure. *Deep Sea Res. Part I: Oceanogr. Res. Pap.* **56**, 1994–2012 (2009).
48. Tarling, G. A. et al. Varying depth and swarm dimensions of open-ocean Antarctic krill *Euphausia superba* Dana, 1850 (Euphausiacea) over diel cycles. *J. Crustacean Biol.* **38**, 716–727 (2018).
49. Brierley, A. S. Diel vertical migration. *Curr. Biol.* **24**, R1074–R1076 (2014).
50. Padman, L., Erofeeva, S. Y. & Fricker, H. A. Improving Antarctic tide models by assimilation of ICESat laser altimetry over ice shelves. *Geophys. Res. Lett.* **35**, <https://doi.org/10.1029/2008GL035592> (2008).

51. Della Penna, A., De Monte, S., Kestenare, E., Guinet, C. & d'Ovidio, F. Quasi-planktonic behavior of foraging top marine predators. *Sci. Rep.* **5**, 18063 (2015).
52. Berg, H. C. *Random Walks in Biology* (Princeton University Press, 1993).
53. Klafter, J. & Sokolov, I. M. Anomalous diffusion spreads its wings. *Phys. World* **18**, 29 (2005).
54. Okubo, A. & Levin, S. A. *Diffusion and Ecological Problems: Modern Perspectives*. Vol. 14 (Springer, 2001).
55. Nathan, R. et al. A movement ecology paradigm for unifying organismal movement research. *Proc. Natl. Acad. Sci. USA* **105**, 19052–19059 (2008).
56. Fraser, W. R. & Ainley, D. G. Ice edges and seabird occurrence in Antarctica. *BioScience* **36**, 258–263 (1986).
57. Wilson, R. P. et al. Luck in food finding affects individual performance and population trajectories. *Curr. Biol.* **28**, 3871–3877. e3875 (2018).
58. Hudson, K. et al. Reevaluating the canyon hypothesis in a biological hotspot in the Western Antarctic Peninsula. *J. Geophys. Res. Oceans* **124**, 6345–6359 (2019).
59. Carvalho, F. et al. Testing the canyon hypothesis: evaluating light and nutrient controls of phytoplankton growth in penguin foraging hotspots along the West Antarctic Peninsula. *Limnol. Oceanogr.* **65**, 455–470 (2019).
60. Hudson, K. et al. A recirculating eddy promotes subsurface particle retention in an antarctic biological hotspot. *J. Geophys. Res. Oceans* **126**, n/a (2021).
61. Prézélin, B. B., Hofmann, E. E., Moline, M. & Klinck, J. M. Physical forcing of phytoplankton community structure and primary production in continental shelf waters of the Western Antarctic Peninsula. *J. Mar. Res.* **62**, 419–460 (2004).
62. Dinniman, M. S. & Klinck, J. M. A model study of circulation and cross-shelf exchange on the west Antarctic Peninsula continental shelf. *Deep Sea Res. Part II: Topical Stud. Oceanogr.* **51**, 2003–2022 (2004).
63. Gorodetskaya, I. V. et al. Record-high Antarctic Peninsula temperatures and surface melt in February 2022: a compound event with an intense atmospheric river. *NPJ Clim. Atmos. Sci.* **6**, 202–218 (2023).
64. Vaughan, D. G. et al. Recent rapid regional climate warming on the Antarctic Peninsula. *Climatic Change* **60**, 243–274 (2003).
65. Hugh, W. D. et al. West Antarctic Peninsula: an ice-dependent coastal marine ecosystem in transition. *Oceanography* **26**, 190–203 (2013).
66. Oliver, M. J. et al. Central place foragers select ocean surface convergent features despite differing foraging strategies. *Sci. Rep.* **9**, 157–157 (2019).
67. Statscewich, H. & Weingartner, T. A high-latitude modular autonomous power, control, and communication system for application to high-frequency surface current mapping radars. *IEEE* **54**, 1–3 (2012).
68. Kohut, J. Marine Technology; Study data from University of Alaska update understanding of marine technology (studying the impacts of local oceanographic processes on Adelie Penguin Foraging Ecology). *Ecol. Environ. Conserv.* **750**, 25–34 (2014).
69. Barrick, D. E., Evans, M. W. & Weber, B. L. Ocean surface currents mapped by radar. *Science* **198**, 138–144 (1977).
70. Kohut, J. T., Roarty, H. J. & Glenn, S. M. Characterizing observed environmental variability with hf doppler radar surface current mappers and acoustic doppler current profilers: environmental variability in the coastal ocean. *IEEE J. Ocean. Eng.* **31**, 876–884 (2006).
71. Fredj, E., Roarty, H., Kohut, J., Smith, M. & Glenn, S. Gap filling of the coastal ocean surface currents from HFR data: application to the mid-atlantic bight HFR network. *J. Atmos. Ocean. Technol.* **33**, 1097–1111 (2016).
72. Veatch, J., Fredj, E. & Kohut, J. High Frequency Radars as Ecological Sensors: Using Lagrangian Coherent Structures to Quantify Prey Concentrating Features in *OCEANS 2022, Hampton Roads, Hampton Roads, VA, USA*, pp. 1–7. (2022)
73. De Robertis, A. & Higginbottom, I. A post-processing technique to estimate the signal-to-noise ratio and remove echosounder background noise. *ICES J. Mar. Sci.* **64**, 1282–1291 (2007).
74. Ryan, T. E., Downie, R. A., Kloser, R. J. & Keith, G. Reducing bias due to noise and attenuation in open-ocean echo integration data. *ICES J. Mar. Sci.* **72**, 2482–2493 (2015).
75. Reiss, C. S., Cossio, A. M., Walsh, J., Cutter, G. R. & Watters, G. M. Glider-Based estimates of meso-zooplankton biomass density: a fisheries case study on antarctic krill (*Euphausia superba*) around the northern antarctic peninsula. *Front. Mar. Sci.* **8**, 604043 (2021).
76. Luque, S.P. Diving Behaviour Analysis in R. *R News* **7**, 8–14 (2007)
77. Calenge, C. The package “adehabitat” for the R software: a tool for the analysis of space and habitat use by animals. *Ecol. Model.* **197**, 516–519 (2006).
78. Ainley, D. *The Adélie Penguin: Bellwether of Climate Change* (Columbia University Press, 2002).
79. Dosio, A., Vilà-Guerau de Arellano, J., Holtslag, A. A. M. & Builtjes, P. J. H. Relating eulerian and lagrangian statistics for the turbulent dispersion in the atmospheric convective boundary layer. *J. Atmos. Sci.* **62**, 1175–1191 (2005).
80. LCS tool: a computational platform for lagrangian coherent structures (<<https://github.com/jeixav/LCS-Tool-Article/>>).
81. Haller, G. Distinguished material surfaces and coherent structures in three-dimensional fluid flows. *Phys. D.* **149**, 248–277 (2001).
82. distance calculation using Haversine formula (<https://www.matchworkds.com/matlabcentral/fileexchange/27785-distance-calculation-suing-haversine-formula>, 2024).
83. Massey, F. J. Jr The Kolmogorov-Smirnov test for goodness of fit. *J. Am. Stat. Assoc.* **46**, 68–78 (1951).
84. Veatch, J., Klinck, J. M., Oliver, M., Statscewich, H., Kohut, J. High Frequency Radar (HFR) observed surface currents at Palmer Deep Canyon in the coastal ocean west of the Antarctic Peninsula in 2020 BCO-DMO version 1, <https://doi.org/10.26008/1912/bco-dmo.917884.1> (2024).
85. Veatch, J., Klinck, J. M., Oliver, M., Statscewich, H., Kohut, J. Results from Finite Time Lyapunov Exponent calculations using High Frequency Radar observed surface currents around Palmer Deep Canyon from January to March of 2020 BCO-DMO version 1, <https://doi.org/10.26008/1912/bco-dmo.917914.1> (2024).
86. Bernard, K. S., Hann, A., Veatch, J. Krill swarms detected with active acoustic EK80 onboard small boat surveys in Palmer Deep Canyon, Antarctica during January-March 2020 BCO-DMO version 1, <https://doi.org/10.26008/1912/bco-dmo.949922.1> (2025).

## Acknowledgements

This project was funded through the National Science Foundation, award # OPP 1745009. Many thanks to the Antarctic Support Contractor and their teams aboard the ARSV Laurence M. Gould, at Palmer Station, and headquarters in Denver, CO without whom a study of this scale would not be possible. Thank you to the students and field assistants for their valued involvement in the SWARM project in particular, Dr. Katherine Gallagher, Dr. Jerome Pinti, Dr. Thilo Klentz, Ethan Handel, and Jordi Maisch. We thank the Palmer Long-Term Ecological Research team and the Commission for the Conservation of Antarctic Marine Living Resources for their advice and collaboration, in particular the Seabird team of the Palmer Long-Term Ecological Research who were instrumental in the deployment of penguin tags.

## Author contributions

J.V. contributed by writing the original draft of this manuscript, leading the formal analysis, validation and visualization of data, and contributed equally

to data curation, developing methodology, and the conceptualization of this manuscript. J.K. contributed by leading the funding acquisition and supervision of this manuscript and contributed equally to the conceptualization, data acquisition, development of methodology, and reviewing and editing of this manuscript. M.O. contributed equally to data acquisition, development of methodology, analysis, and reviewing and editing of this manuscript, led the visualization of penguin tagged data, and contributed supporting supervision. H.S. contributed a leading role to the data acquisition and contributed equally to the conceptualization of this manuscript. E.F. contributed equally to the conceptualization and development of methodology in this manuscript and contributed supporting supervision. K.B. contributed equally to data validation, conceptualization, development of methodology, and reviewing and editing of this manuscript. H.F. contributed equally to conceptualization and reviewing and editing of this manuscript. W.F. contributed to penguin foraging data acquisition, conceptualization, reviewing and editing of this manuscript. A.H. led the validation of the active acoustic data and contributed equally to reviewing and editing of this manuscript. G.V. led the validation of the penguin tagged data and contributed equally to reviewing and editing of this manuscript.

### Competing interests

The authors declare no competing interests.

### Additional information

**Supplementary information** The online version contains supplementary material available at <https://doi.org/10.1038/s43247-025-02101-x>.

**Correspondence** and requests for materials should be addressed to Jacquelyn M. Veatch.

**Peer review information** *Communications Earth & Environment* thanks Alberto Baudena and the other, anonymous, reviewer(s) for their contribution to the peer review of this work. Primary Handling Editors: Heike Langenberg, Aliénor Lavergne. A peer review file is available.

**Reprints and permissions information** is available at <http://www.nature.com/reprints>

**Publisher's note** Springer Nature remains neutral with regard to jurisdictional claims in published maps and institutional affiliations.

**Open Access** This article is licensed under a Creative Commons Attribution-NonCommercial-NoDerivatives 4.0 International License, which permits any non-commercial use, sharing, distribution and reproduction in any medium or format, as long as you give appropriate credit to the original author(s) and the source, provide a link to the Creative Commons licence, and indicate if you modified the licensed material. You do not have permission under this licence to share adapted material derived from this article or parts of it. The images or other third party material in this article are included in the article's Creative Commons licence, unless indicated otherwise in a credit line to the material. If material is not included in the article's Creative Commons licence and your intended use is not permitted by statutory regulation or exceeds the permitted use, you will need to obtain permission directly from the copyright holder. To view a copy of this licence, visit <http://creativecommons.org/licenses/by-nc-nd/4.0/>.

© The Author(s) 2025

